SP-414
Volume I

Third ERS Symposium on

Space at the service of our Environment

- SOIL MOISTURE
- HYDROLOGY
- LAND USE
- FORESTRY
- DEM
- GEOLOGY
- HAZARDS

Florence, Italy, 14-21 March 1997

European Space Agency
Agence spatiale européenne

SP-414
Volume I
May 1997

Third ERS Symposium on

Space at the service of our Environment

• Soil Moisture • Hydrology
• Land Use • Forestry
• DEM • Geology • Hazards

Florence, Italy, 14-21 March 1997

European Space Agency
Agence spatiale européenne

Cover image

Multitemporal view of Florence and its surroundings, obtained from three images acquired by ERS-1 and ERS-2 during 1996: Red: *ERS-1 (7 January)* — Green: *ERS-1 (30 June)* — Blue: *ERS-2 (14 October).*
[ERS images and multitemporal products are processed at the Italian Processing & Archiving Facility (I-PAF), Matera, Italy]

ESA SP-414: *Proceedings of the Third ERS Symposium*
Space at the service of our Environment

Published by: ESA Publications Division
ESTEC, Noordwijk, The Netherlands

Compiled by: T.-D. Guyenne & D. Danesy

Price Code: 200 Dfl (the set of 3 volumes)

ISBN 92-9092-656-2 Printed in The Netherlands

These Proceedings *(SP-414,* 3 vol.) contain the majority of the papers presented at the Symposium and received in camera-ready form. Volume III includes an Appendix containing 15 late papers.

Volume III

Winds and Waves

***Chair*: P. Janssen & A. Stoffelen**

L.-A. Breivik & al.
Assimilation of ERS-SAR wave spectra in a wave prediction model 1123
E. Bauer & al.
Comparison of assimilation results from an optimal interpolation and the Green's function method using ERS-1 SAR wave mode spectra 1131
L. Wilson & al.
Impact of the assimilation of ERS-1 & 2 data into a North Atlantic regional version of WAM 1137
P. Heimbach & al.
A three-year global intercomparison of ERS-1 SAR wave mode spectral data with WAM model data 1143
C. Davies & al.
Altimeter estimates of wave period 1151
P.D. Cotton & al.
Analysis of inter-annual variability of altimeter measured global wave climate 1157
V. Kerbaol & B. Chapron
A global comparison between AMI scatterometer data and ERS-SAR wave mode products 1163
D. Lemaire & al.
Scattering by the ocean surface under non-fully developed state: two-scale model validation & inversion of radar measurements 1169
C. Mejia & al.
Comparison of the neural network GMF's of the ERS-1 & NScat scatterometers 1175
L.-A. Breivik & H. Schyberg
Assimilation of scatterometer wind pairs & altimeter wind speeds in a limited area weather-forecast model 1181
A. Bentamy & al.
Wind climatology from ERS scatterometer 1187
Eva Bauer
Statistical comparison of winds from ERS-1 scatterometer & ECMWF model in time & wave number domain 1195
E. Arabini & al.
Wind field over Lampedusa island observed by ERS-1 scatterometer & implemented by ground observations 1201
J. Horstmann & al.
Wind fields from ERS-SAR compared with a mesoscale atmospheric model near to the coast 1205
E. Korsbakken & al.
Coastal wind field retrievals from ERS-SAR images 1211
S. Pouliquen & al.
ERS-2/NScat collocated database 1217
H. Schyberg & L-A. Breivik
A method for two-dimensional variational analysis of ocean-surface winds based on ERS altimeter & scatterometer data 1219
A. Bartoloni & Cl. D'Amelio
A fieldwise approach to the wind field retrieval from scatterometer data 1225

Posters
H. Schyberg & L-A. Breivik
Optimal scatterometer ambiguity removal using a successive correction method 1229
Y. Quilfen & al.
High-resolution scatterometry in preparation for the Ascat instrument 1233
Fr. Ocampo-Torres
Significant wave height from ERS altimeter for shallow water wave studies in coastal regions 1239
F. Nirchio & al.
ERS-PRI products for wave parameters estimation on the Mediterranean Sea 1243

Coastal Zones

***Chair*: H. Wensink**

W. Alpers & al.
Study of mesoscale atmospheric phenomena over the ocean by ERS-SAR and numerical models 1017
H. Hajji & D. Bonichel
Use of SAR images to study coastal processes 1023
K. Hessner & al.
The Rhine outflow studied by the analysis of ERS-SAR data and numerical simulations 1029
A. Yu Ivanov & al.
Lake Ladoga surface features on the ERS-1 SAR imagery 1035
O.M. Johannessen & al.
COASTWATCH '95 - using SAR imagery for monitoring coastal currents, surfactants & wind fields 1041
M. Schwäbisch & al.
Coastline extraction using ERS-SAR interferometry 1049
G. Hesselmans & al.
Mapping of seabed topography to and from SAR 1055
V.R. Wismann & K. Boehnke
Coastal topography derived from ERS-SAR imagery 1059
C. Mastenbroek & C.F. de Valk
Satellite-based shelf sea climate assesment system 1065

Posters
J-P. Rudant & al.
Distinction entre formations végétales littorales et continentales dans leur rapport avec la géomorphologie: Intérêt des images ERS-1 1069
H. Greidanus & al.
Speckle reduction in low-contrast areas by dedicated-SAR processing 1075
D.C. Mason & al.
Improving inter-tidal digital elevation models constructed by the waterline technique 1079
D.W.S. Lodge & al.
Application of satellite remote sensing to land/coastal interaction studies 1083
A. Raouf & J. Lichtenegger
Integrated use of SAR and optical data for coastal zone management 1089

Global Change

***Chair*: M. Drinkwater**

B. Candy
The conversion of ATSR sea-surface temperatures for use in a climate database 1097
L. Fenoglio-Marx & E. Groten
Geodetic aspects of long-term sea-level variations in European seas from altimetry & tide gauge data 1103
M.R. Drinkwater & X. Liu
ERS satellite microwave radar observations of Antarctic sea-ice dynamics 1109
H. Rott & al.
Significant ice retreat in the region Patagonia - Antarctic Peninsula observed by ERS-SAR 1115

R.M. Frolich C.S.M. Doake
Detecting changes in ice movement over the Antarctic Ice Sheet by SAR interferometry 895
H.A. Phillips & al.
Comparison of ERS altimeter and GPS heights on the Amery Ice Shelf, East Antarctica 899

Sea Ice
Chair: O Johannessen

O.M. Johannessen & al.
ICEWATCH - Realtime sea-ice monitoring of the Northern Sea Route using satellite radar technology 907
J. Capdevila & al.
Observation of sea-ice & ice-free structures in the Bransfield Strait and S. Drake Passage with ERS-1 SAR 917
P.B.G. Dammert & al.
Sea-ice displacement measured by ERS-1 SAR interferometry 923
V. I. Lytle & al.
Floe sizes in the East Antarctic sea ice zone estimated using combined SAR and field data 931
R.G. Onstott
Study of the temporal nature of Arctic leads during Spring using ERS-1 SAR 937
S. Lehner & al.
Estimation of wind, wave and ice parameters at the ice boundary using ERS active microwave systems 943

Posters
M. Thomas & R. Roth
Mesoscale sea-ice dynamics in the Weddell Sea 949
M. Thomas & al.
Measuring changes of iceberg attitudes by SAR interferometry 955
R. Schmidt & G. Heygster
Use of ocean wave imaging to detect the marginal ice zone in ERS-SAR images 959
G. Chen & al.
Regional characteristics of sea-level variation in the Southern Ocean with relation to Antarctic Sea Ice 963

Ice Dynamics
Chair: N. Young

R. Goldstein & Ch. Werner
Radar ice motion interferometry 969
I. Joughin & al.
Interferometric estimation of ice sheet motion and topography 973
M. Fahnestock & al.
Interferometric study of the ice stream in interior NE Greenland 979
D.P. Winebrenner & al.
Interferometric SAR for observation of glacier motion and firn penetration 983
J.J. Mohr & al.
ERS Tandem study of glacier dynamics in NE Greenland 989
C.S. Lingle & al.
Dynamic behaviour of the Bering glacier Bagley icefield system during a surge, and other measurements of Alaskan glaciers with ERS-SAR imagery 995
A.L. Gray & al.
Experiments at CCRS using ERS Tandem mode data 1001
N.W. Young & G. Hyland
Applications of time series of microwave backscatter over the Antarctic region 1007

Ph. Watts & A.J. Baran
A survey of tropical cirrus particle size and shape using ATSR-2 visible/near infrared data 773
Fr. Flechtner & al.
Modeling of the ionosphere with PRARE 779
S.-A. Boukabara & al.
Coupled analysis of active & passive microwave measurements. Retrieval improvement of geophysical parameters 785
Y. Xue & al.
Use of ATSR data to estimate surface fluxes over land and sea 791
A.M. Zavody & al.
Cloud detection algorithms used in the processing of ATSR data into sea-surface temperature 795

Ice Properties and Ice Sheet Topography

***Chair*: P. Pampaloni**

T. Furukawa &N.W. Young
Comparison of microwave backscatter measurements with observed roughness of the snow surface in East Queen Maud Land, Antarctica 803
C. Schneider & al.
Validation of energy balance estimates from snow-covered areas of the Antarctic Peninsula based on ERS PRI images 809
E. Rignot
Ice discharge from North and Northeast Greenland as observed by ERS radar 815
B.K. Lucchitta & Ch.E. Rosanova
Thwaites Glacier and Marie Byrd Land Coast, Antarctica 819
F. Gohin & al.
Five years of AMI-wind sea-ice backscatter grids on a CD-ROM 825
R.E.J. Kelly & al.
Characteristic snow and ice properties on a Norwegian ice cap determined from complex ERS-SAR data 831
M. Stenoien & Ch.R. Bentley
Topography estimation in W. Antarctica directly from level-2 radar altimeter data 837
J. Bamber & al.
A digital elevation model of the Greenland Ice Sheet and validation with airborne laser altimeter data 843
Fr. Rémy & B. Legrésy
Antarctica Ice Sheet dynamics derived from ERS-1 precise topography 849

Posters
S. Wunderle & al.
Derivation of glacial catchments of the Antarctic Peninsula by means of interferometric techniques 853
V.R. Wismann & K. Boehnke
Monitoring snow properties in Greenland with ERS scatterometer and SAR 857
E. Rignot & D.R. MacAyeal
Ice velocity at the ice front of the Filchner-Ronne Ice Shelf as observed with ERS interferometry 863
A.W. Bingham & W.G. Rees
Satellite data synergies for monitoring Arctic ice masses 867
J. Piesbergen & al.
Multi-source snow cover monitoring in Eastern Switzerland 871
U. Müller & al.
SAR data exploitation for monitoring Antarctic ice sheets and glaciers 877
Vl. V. Melentyev & al.
ERS-SAR retrieval of ice cover parameters for some oil and gas fields at the Russian Arctic Shelf 881
B. Legrésy & Fr. Rémy
Antarctic Ice Sheet snow properties derived from ERS altimeter data 887
H. Le Core & D. Llewellyn-Jones
ATSR data and hydrodynamic models to investigate physical processes in Lake Baikal, Siberia 891

S. Ponte
ERS Tandem data for earthquake prediction: Preliminary results 499
C. Reigber & al.
The Antofagasta 1995 Earthquake: Crustal deformation patterns as observed by GPS and D-INSAR 507
B. Theilen-Willige
Earthquake hazard zonation in the Lake Constance area: Contribution of satellite radar (ERS-1, SIR-C) data 515
C. L. Werner & al.
Detection of a seismic creep along the San Andreas Fault near Parkfield (CA) with ERS-1 interferometry 521
R. J. Stow & P. Wright
Mining subsidence land survey by SAR interferometry 525
L. Marinelli & al.
Flood mapping using ERS Tandem coherence image: A case study in Southern France 531

Posters
L. C. Smith & D. E. Alsdorf
Flood mapping from phase decorrelation of ERS Tandem: The Ob River, Siberia 537
D. Raymond & J.-P. Rudant
ERS-SAR interferometry: Potential and limits for mining subsidence detection 541
G. Peltzer & al.
Crustal deformation in Southern California using SAR interferometry 545
U. Münzer & al.
Recent interdisciplinary research in the neovolcanic zone of Iceland using SAR data 549
H. van Leeuwen & al.
Flood monitoring study in the Jamuna & Ganges floodplain in Bangladesh using ERS-1 555
O. Laugier & al.
High temporal detection and monitoring of flood dynamics : The 1993-94 Camargue flood events 559
P. Clemente-Colon & al.
Evolution of oil slick patterns as observed by SAR off the coast of Wales 565
F. Z. Garcia & al.
Analysis of ERS SAR & Spot-P data for the mapping of Pinatubo lahar & pyroclastic flow deposits 569
M. Haynes & al.
Major urban subsidence mapped by differential SAR interferometry 573
F. Kervyn
Recent tectonic features evidenced by SAR interferometry in the East African rift 579

Volume II

GOME

***Chair*: J. Burrows & P. Simon**

J. P. Burrows & al.
The global ozone monitoring experiment (GOME): Mission, instrument concept & first scientific results 585
D. Loyola & al.
Ground segment for ERS-2 GOME sensor at the German D-PAF 591
Cl. Zehner
GOME instrument performance monitoring 597
D.N.C. Pemberton
GOME diffuser and dark signal trends 603
C. Caspar & K. Chance
GOME wavelength calibration using solar and atmospheric spectra 609
R. Siddans & al.
Height-resolved ozone information in the troposphere from GOME 615
R. J.D. Spurr
Development of a prototype algorithm for the operational retrieval of height-resolved products from GOME 621
J.-Ch. Lambert & al.
Pole-to-pole validation of the ERS-2 GOME level-2 products with the ground-based SAOZ network 629
A. J.M. Piters & al.
GOME validation using data assimilation 637

W. Rathman & al.
A preliminary comparison between TOVS and GOME level-2 ozone data 641
D. Perner & al.
First results on tropospheric observations by GOME 647
M.C. Krol & al.
Tropospheric studies using GOME 653
K. Chance
Quantitative spectroscopy for the analysis of GOME data 659
R. B.A. Koelemeijer & al.
Spectral surface albedo derived from GOME data 663
P. Stammes & al.
GOME polarisation validation study 669
M. Eisinger & al.
SO2, OClO, BrO and other minor trace gasses from GOME 675
E. Hegels & al.
Global distribution of BrO by GOME 681
R. Guzzi & al
Aerosol optical thickness from GOME data. Methodological approach and preliminary results 687
G. A.A. Koppers & al.
Aerosol optical thickness retrieval from GOME data in the oxygen A band 693
Ph. Peeters & P.C. Simon
GOME solar irradiance validation using UARS SOLSTICE data 697

Posters
M. Bittner & al.
Planetary-scale waves in total ozone from ERS-2 GOME data 703
J. Callies & al.
The Global Ozone Monitoring Experiment (GOME) on board of ERS-2 707
I. Aben & al.
First results of GOBELIN project: breadboard model characterisation under ambient & vacuum conditions 711
E. Schoubs & D. De Muer
Validation of GOME with ground-based ozone measurements at Uccle (Belgium) 715
Ph. Peeters & P.C. Simon
MgII core-to-wing index from high-resolution GOME data 719
M. Mochi & al.
GOME data processing at I-PAF: The aerosol optical thickness retrieval from GOME spectra 723
J.-Ch. Lambert & al.
Validation of the ERS-2 GOME ozone products with the NDSC/Alpine stations 729
R.M. Koopman
Analysis of GOME stray light 733
R. B.A. Koelemeijer & al.
Intercomparison of GOME and ATSR-2 reflectivity measurements 739
M.R. Dobber
GOME moon measurements, including instrument characterisation and moon albedo 743
R. de Beek & al.
Ozone profile retrieval from GOME satellite data: Part I - Algorithm description 749
K.-U. Eichmann & al.
Ozone profile retrieval from GOME satellite data: Part II - Validation and Applications 755

Atmosphere and Climate

***Chair*: C. Mutlow**

Th. Popp & al.
Exploiting GOME and ATSR-2 data: First results of the PAGODA project 761
R.M. Dundas & al.
Measurement of radiative properties of global atmospheric aerosols using data from ATSR 767

A. Bégué & al.
Characterisation of the landuse cover in the Congo rainforest with optical and microwave data 385
N. Stussi & al.
Landcover classification using ERS-SAR/INSAR data on coastal region of Central Sumatra 391

DEMs
Chair: F. Adragna

M. Dowson & P.A.M. Berry
Potential of ERS-1 derived orthometric heights to generate ground control points 399
P.A.M. Berry & al.
Retracking ERS-1 altimeter waveforms over land for topographic height determination:
An expert systems approach 403
A. Brenner & al.
Topography over South America from ERS altimetry 409
C. S. Nielsen & al.
Merging of elevations from SAR interferometry, satellite altimetry GPS & laser altimetry in Greenland 415
M. Seymour & I. Cumming
INSAR terrain height estimation using low-quality sparse DEMs 421

Geology
Chair: J. Bodechtel

K. S. Rao & Y. S. Rao
Field experiments synchronous with ERS Tandem mission for the simulation of neotectonic movement 429
H. Yesou & al.
Assessment of two methodologies of ERS mixing for geological investigations: ERS time series and
optical-radar fusions 435
C. Streck & U. Wegmüller
Investigation of ERS-SAR data of the Tandem mission for planning & monitoring of Siberian pipeline tracks 441

Posters
D. Closson & al.
Etude de faisabilité: Détection de sites archéologiques et cartographie géomorphologique en Syrie par
l'exploitation d'images ERS-1 et Spot-2 intégrées dans un SIG 449
M. K. Hsu & al.
Mapping of sand waves and channels in the Taiwan Tan area with ERS-SAR 453
A. Legeley-Padovani & al.
Texture analysis of ERS-1 SAR images from South Cameroon 457

Hazards
Chair: J. Bodechtel

J. Chorowicz & al.
SAR-ERS imagery for the study of relationships between tectonics & volcanism in Iceland & Anatolia 463
G. Wadge & al.
Volcano monitoring using interferometric SAR 469
K.-H. Thiel & al.
ERS Tandem interferometric observation of volcanic activities in Iceland 475
M. J. Wooster & D. A. Rothery
Volcano monitoring using data from the ERS-ATSR 481
R. Hanssen & S. Usai
Interferometric phase analysis for monitoring slow deformation processes 487
Y. Cornet & al.
Use of ERS Tandem data to produce DEMs and study of land movements in Calabria and Jordan 493

W. Stroobants & al.
Apport de la fusion multidate pour l'interprétation des images ERS-1 en milieu tropical 241
A. Sowter & al.
Requirements for the selection & processing of SAR data for operational agricultural applications in Europe 247
Y. Smara & al.
Multisource ERS-1 & optical data for vegetal cover assessment & monitoring in a semi-arid region of Algeria 251
M. Simard & al.
Sensitivity analysis of ERS-SAR signal to multiscale structures of tropical forests using the wavelet transform 261
B. Schieche & al
Monitoring of intensive and extensive landuse with multitemporal ERS and Landsat-TM datasets in the district of Göttingen (Lower Saxony, Germany) 265
E. Parlow & al.
Satellite-based climate analysis of Basel, Switzerland 271
A. Luckman & J. Baker
Interferometric coherence measurements of tropical, temperate and boreal forests 275
H. van Leeuwen & M. Borgeaud
Regional application of ERS1/2 SAR data in the Flevoland agricultural area in The Netherlands 279
D. Kosmann
RAPID - a joint proposal using INSAR 283
A. Valverde & al.
Preliminary results of landcover analysis of Calanda area using ERS1/2 SAR and Landsat-TM data 289
V. De Cauwer & R. De Wulf
Potential use of ERS-SAR data to discriminate natural & degraded woody vegetation types in Central Africa 295
A. Legeley-Padovani & al.
Classification d'une image radar: cartographie automatique de la mangrove (région de Douala, Cameroun) 301
G. Abbate
Heat island study in the area of Rome by integrated use of ERS-SAR and Landsat-TM data 305
W. Ang & S. E. Hobbs
Weather effects on radar backscatter from crops 311
C. Keithley & al.
Examining agricultural and wetland vegetation using ERS-1 imagery 317
G. M. Henebry & H. J.H. Kux
Spatio-temporal analysis of SAR image series from the Brazilian Pantanal 321
O. M. Johannessen & al.
Environmental monitoring of the St. Petersburg region using ERS data 325
G. H. Griffiths & K. H. White
Monitoring processes of dryland degradation from ERS-SAR data 331

Forestry

***Chair*: J-P. Malingreau**

J. Askne & al.
Interferometric SAR observations of forested areas 337
M. E. Engdahl & J. M. Hyyppä
Forest inventory using interferometric SAR techniques 345
F. Ribbes & al.
Forest mapping in tropical region using multitemporal and interferometric ERS1/2 data 351
T. Strozzi & U. Wegmüller
Forest mapping with ERS-SAR interferometry 357
E. S. Kasischke & al.
Monitoring the effects of fire in North American boreal forests using ERS-SAR imagery 363
V. V. Donchenko & al.
Synergistic use of ERS-SAR and other satellite data for the polluted areas identification for boreal forests of St Petersburg region 369
F. De Grandi & al.
Wither radar global mapping of the tropical forest: New avenues from the TREES ERS-1 Central Africa Mosaic 377

N. I. Fox & al.
Retrieval of soil moisture content from naturally vegetated upland areas using ERS-1/2 SAR 107
C. Prietzsch & al.
Identification of parameters & phenomena of hydrological restoration processes in lowland bog areas 111
P. Pampaloni & al.
ERS-1 SAR sensitivity to hydrological parameters: A comparison with SIR-C and AIRSAR data 115
E. Nezry & al.
Retrieval of environmental & geophysical parameters through Bayesian fusion of ERS & Radarsat data 119

Land Use

Chair: H. De Groof & A. Sowter

G. Lemoine & al.
Methodological advancements in using ERS-SAR data for crop area estimation 125
R. Kidd & al.
Integration of ERS-SAR classification products in the MARS activity B 'Rapid Area Estimation' 131
G. Kattenborn & H-G. Klaedtke
Classification of ERS-1 SAR data over Seville (Spain) for agricultural statistics 139
E. Auquière & al.
ERS-SAR time series analysis for maize monitoring using experimental and modeling approaches 147
S. C. Liew & al.
Delineation of rice cropping systems in the Mekong delta river using multitemporal ERS-SAR 153
K. Dabrowska-Zielinska & al.
Soil moisture investigation for the different agricultural crops using ERS-1 and ERS-2 data 159
E. Mougin & al.
Monitoring seasonal vegetation dynamics in the Sahel with ERS wind scatterometer data 163
M. C. Edwards & al.
Mapping and monitoring of arid land vegetation in Jordan using ATSR-2 data 169
G. M. Henebry
Advantages of principal components analysis for land cover segmentation from SAR image series 175
Y. Ban & P. J. Howarth
Orbital effects on the ERS-1 temporal backscatter profiles of agricultural crops 179
G. Mackay & al.
Comparison of directional reflectance & radar backscatter from desert surfaces: The eastern desert of Jordan 185
J. Verhoeye
Research on the capabilities of ERS-SAR for monitoring of land use changes in the Neotropics 191
D. C. Rundquist & al.
Using ERS-1 data to measure and map selected conditions related to the production of methane in a wetland environment: The Nebraska sandhills, USA 197
R. Stolz & W. Mauser
Evaluation of ERS data for biomass estimation of meadows 203
A. Shepherd & al.
Angular dependence of radiometric surface temperature for sparse vegetation 209
M. C. Perrin & A. C. Millington
Monitoring biomass burning in Bolivia using ATSR-2 data 215

Posters

M. Günzl & al.
ERS-SAR data for land information systems 221
S. Usai & R. Hanssen
Long time scale INSAR by means of high coherence features 225
H. Yesou & al.
Pastures monitoring and land-surfaces characteristics analysis in a sahelian region: The Chad case of study 229
L. Basly & al.
ERS-SAR imagery for urban climate studies 233
S. P. Vyas & al.
Leaf area estimation for sugar beet yield prediction using ERS-SAR data 237

Contents

Volume I

Opening Addresses
L. Emiliani, ESA Directorate of Observation of the Earth & its Environment *xix*
H. J. Allgeier, European Commission: *Earth Observation and Space - European Perspective* *xxi*

Keynote Addresses
C. J. Rapley, Executive Director, IGBP: *The Earth from Space: What Next for Europe?* *xxiii*
F. Rocca & al., Politecnico di Milano: *An Overview of ERS-SAR Interferometry* *xxvii*

Symposium Summary 1

Soil Moisture
***Chair*: T. Le Toan**

K. J. Tansey & al.
Comparison of modelled backscatter response and ERS-1 SAR data for desert surfaces: The Eastern Badia of Jordan 21
M. Rombach & W. Mauser
Multi-annual analysis of ERS surface soil moisture measurements of different land uses 27
K. Boehnke & V. Wismann
Detecting soil thawing in Siberia with ERS scatterometer and SAR 35
P. Saich & al.
Development & demonstration of soil moisture determination & INSAR for catchment hydrological monitoring 41
U. Wegmüller
Soil moisture monitoring with ERS-SAR interferometry 47
B. Dousset
Interpretation of ERS-SAR images over urban surfaces 53

Hydrology
***Chair*: W. Mauser**

K. Fellah & al.
Potentials and limitations of multitemporal SAR data in a quantitative approach for multiscalar hydrological applications. Synthesis of ERS Alsace/Camargue Pilot Project 61
E. S. Kasischke & al.
Monitoring hydropatterns in South Florida ecosystems using ERS-SAR data 71
W. Mauser & al.
The contribution of microwave data to distributed hydrologic modelling 77
F. Portmann & H.-G. Mendel
Soil moisture estimation in hydrological mesoscale modelling using ERS-SAR data 85
P. A. Troch & al.
Spatial organisation of hydrological processes in small catchments derived from advanced SAR image processing - Field work and preliminary results 93

Posters
N. Verhoest & al.
Spatial soil moisture mapping through multitemporal analysis of ERS-SAR PRI data 99
W. Klaassen & al.
SAR sensing of vegetation wetness: The first results 103

Altimetry
Chair: J. Lillibridge

Ph. Moore & al.
Calibration of the ERS-1 range bias through tide-gauge data 1519
P. Bonnefond & al.
Calibration of radar altimeters & validation of orbit determination in the Corsica-Capraia area 1525
S.-A. Boukabara & L. Eymard
In-flight calibration/validation of the ERS-2 microwave radiometer – Comparison with ERS-2, SSM/I & Topex radiometers 1529

Poster
Ph.A.M. Berry & M. Leigh
Towards validation & correction of global DEMs with ERS-1 altimetry 1535

Marine Geoid
Chair: A. Cazenave

M. Anzenhofer & al.
Global sea-level analysis based on ERS-1 altimeter data 1541
S.W. Laxon & D.C. McAdoo
Polar marine gravity fields from ERS-1 1547
R. Cullen & al.
Global altimetric mean sea-surface derived from the geodetic phase of ERS-1 mission utilising a spectral least squares collocation technique 1553

Posters
P. Knudsen & O. Baltazar Andersen
Improved recovery of marine gravity field from combining ERS-1with Seasat geodetic mission altimetry 1559
M.J. Fernandes & al.
Combining ERS altimetry and surface gravimetry in the Azores region for local geoid determination 1563
H.J. Boomkamp & P. Moore
A gravity field solution based on unified ERS-1 and Topex/Poseidon altimetry 1567
O. Baltazar Andersen & P. Knudsen
Global gravity field from the ERS-1 and Geosat geodetic mission altimetry in the Mediterranean Sea 1573

Meteorology
Chair: T. Liu

A.K. Laing & al.
ERS scatterometer observations of airflow around mountainous islands 1579
W.T. Liu & W.Q. Tang
Application of ERS scatterometer winds to typhoon, monsoon, rain & El Niño studies 1585
G.J. Marshall & J. Turner
ERS scatterometer observations of katabatic winds over a polynya 1591
J. Turner & G. Marshall
The use of ERS scatterometer data to investigate the surface circulation of Antarctic mesocyclones 1597
D. Kasilingam & al.
Investigation of tropical rain cells with ERS-SAR imagery and ground based weather radar 1603
G.D. Quartly (*Poster*)
Retrieving rainfall rates from ERS altimeter data 1609

ATSR Instrument Performance

Chair: C. Mutlow

I. Parkes & al.
The Mutsu Bay experiment – An investigation into the physical processes of the ocean/atmosphere boundary using ATSR data and in situ measurements 1617
S. Tamba & al.
The relationship between SST measured from ATSR to the spatial & temporal behaviour of the ocean skin temperature as observed with an in situ thermal infrared camera 1623
D.L. Smith
Calibration of the ATSR-2 visible channels using desert scenes 1629

Orbits

Chair: R. Scharoo

S. Bedrich & al.
PRARE system performance 1637
R. Scharroo & P. Visser
ERS Tandem orbits: is 5 cm still a challenge? 1643
R.J. Walmsley & al.
Analysis of PRARE data for ERS-2 1649
Fr.-H. Massmann & al.
Quality of D-PAF ERS orbits before and after inclusion of PRARE data 1655
Th. Gruber & al.
D-PAF global Earth gravity models based on ERS data 1661
R. Zandbergen & al.
Progress in ERS orbit and tracking data analysis 1669
K. Singh & al. (*Poster*)
Baseline estimation in interferometric SAR 1681

Interferometry

Posters

U. Wegmüller & Ch. Werner
Gamma SAR processor and interferometry software 1687
S. Goze & al.
Three-dimensional exploitation of tandem imagery acquired with Libreville mobile station 1693
I. Cumming & W. Xu
Comparison of phase unwrapping performance using a noisy interferogram 1697
M. Costantini
Validation of a novel phase unwrap algorithm using true & simulated ERS Tandem SAR interferometric data 1701
P. C. Smits & al.
Iterative model reconstruction for phase unwrapping 1707
S. Dupont & al.
Atmospheric artifacts in ERS DTM.ISTAR's experience over multiple sites & large areas 1711

JERS/ERS Synergy

Chair: A. Rosenqvist

H. Wakabayashi & F. Nishio
Ice cover monitoring on Lake Saroma using ERS-1 SAR data 1723
P. Pampaloni & al.
The potential of C- and L-band SAR in assessing vegetation biomass: ERS-1 & JERS-1 experiments 1729

P. Heimbach & al.
Comparison of significant wave heights derived from ERS-1, Topex, Geosat & Seasat altimeters and retrieved from ERS-1 SAR wave mode spectra 1247
F. Aversa & al.
A software package for the quality assessment of the low bit rate Mediterranean scatterometer & altimeter products: ERS-1.WSC.DWP and ERS-1.ALT.MPR 1253

Sea-Surface Temperature & Oceanography

***Chair*: A. Cavanie, D. Ollewellyn-Jones & W. Alpers**

M.-K. Hsu
Kuroshio front & oceanic phenomena near Taiwan & in the Southern Okhotsk Sea from ERS-SAR data 1259
D. Lyzenga & C. Wackerman
Detection & classification of ocean eddies using ERS-1 and aircraft SAR images 1267
D. S. Kirby & al.
SAR remote sensing of wind-driven circulation in the Gulf of Tehuantepec, Mexico 1273
V. E. Jensen & al.
Mesoscale studies in the Indian Ocean using altimeter data 1279
W. Alpers & al.
Observations of internal waves in the Andaman Sea by ERS-SAR 1287
E.K. Oikonomou & I.S. Robinson
Effect of wind field in observing internal wave phenomena over the continental slope on ERS-SAR imagery 1293
S.A. Ermakov & al.
ERS-SAR imaging of long-period internal (tidal) waves 1299
J.C. da Silva & al.
The character of short-period internal waves ERS-SAR signatures at very low wind speeds 1305
A.K. Liu & al.
Evolution of non-linear internal waves in the China Seas 1311
I.K. Ridley & al.
Use of ATSR-measured ocean skin temperatures in ocean and atmosphere models 1317
Lei Guan & al.
Use of ATSR data & in-situ observations to study ocean dynamics near the Kuroshio boundary 1323
G.M. Johnson & al.
Observations of phytoplankton dynamics in Lake Ontario using ATSR-2 imagery 1331
I.S. Robinson & J. Johannessen
Opportunities for combining SAR & ATSR ocean observations during ERS Tandem mission 1337
M.S. Jones & al.
Comparison of altimetric sea-surface height & radiometric SST in the South Atlantic 1343
P. Knudsen & al.
Annual cycles of ERS-1 altimetric sea-surface height data & ATSR sea-surface temperature data 1349
M.C. Naeije & K.F. Wakker
Global analysis of sea-surface height and temperature 1355
H.A. Espedal & al.
ERS-1/2 SAR detection of natural film on the ocean surface 1361
P.W. Vachon & al.
Comparison of ERS and Radarsat SARs for wind and wave measurement 1367
Ming-Xia He & al.
Research & application of ERS-1 data in the China Seas and NW Pacific Ocean 1373
T.H. Guymer & al.
Remote sensing & in situ measurements of bio-optical variability in a Mediterranean mesoscale system 1379
N.R. Stapleton & al.
Study of ERS-SAR Tandem imagery of the Malin-Hebrides shelf 1385
A.G. Ramos & al.
Satellite-derived scatterometer/ERS-1 wind stress sea-surface curl in the oceans 1391

Posters
S.T. Dokken & H. Laur
Ocean and ice features detection using the ERS-SAR browse images 1397
H.M. Snaith & al.
ERS, Shipborne and aircraft observations of circulation in the Almeria-Oran front region 1403
I.S. Robinson
Intercomparison of ATSR & ATSR-2 brightness temperatures during the ERS Tandem mission 1407
I-I Lin & V. Khoo
Computer-based algorithm for ship detection from ERS-SAR imagery 1411
T. Hamre & H.A. Espedal
Operational use of wind data for slick detection 1417
G. Corsini & al.
Estimation of directional sea spectra from ERS-SAR images of the Mediterranean area: A case study 1423
A. Martinez & I.S. Robinson
Fronts & eddy features in coincident ERS-2 SAR & AVHHR-IR images for a case of offshore wind forcing 1427
O. Chic & al.
ERS-2 SAR near-realtime data used in the sampling strategy of an oceanographic cruise in the Western Mediterranean 1433
D. Ballestero & al.
Remote sensing & modeling primary productivity in upwelling systems 1439

Ocean Circulation

***Chair*: P. Le Traon**

P-Y. Le Traon & al.
Sea-level variability from ERS-1, ERS -2 and Topex/Poseidon 1445
J. Lillibridge & al.
Real-time altimetry from ERS-2 1449
R. Barzaghi & al.
Stationary SST estimation using ERS-1 & Topex/Poseidon data in the Western Mediterranean area 1455
G.M.R. Manzella & al.
Potential use of satellite data to infer the circulation dynamics in a marginal area of the Mediterranean Sea 1461
B.B. Nardelli & al.
Mediterranean sea-level anomalies & 3D structure of the sea from LIWEX & ERS/Symplex experiments 1467
P. Cipollini & al.
The potential of ERS for the detection of Rossby waves in the NE Atlantic 1473
K.J. Heywood & Y.K. Somayajulu
Eddy activity in the South Indian Ocean from ERS-1 altimetry 1479
S. Marullo & al.
A combined use of ERS & Topex/Poseidon data to study the mesoscale dynamics in the Mediterranean Sea 1485
E. Romaneessen
Transport estimates from altimeter data in the South Atlantic Ocean 1491
C. Bouzinac & al.
CEOF analysis of ERS & Topex/Poseidon combined altimetric data in the Algerian Current region 1497

Posters
A. Pauluhn
Principal oscillation pattern analysis of sea-surface temperature data 1501
Ch. W. Hughes & al.
Propagation of features in the Southern Ocean, using ATSR and altimetry 1505
A. Tejera & al.
Mesoscale variability in the Canary region from altimetry 1509

J.M. Kellndorfer & al.
Multi-ecoregion vegetation mapping using combined ERS/JERS SAR imagery 1735
Y. Rauste & al.
Preliminary assessment of complementary ERS-1/JERS-1 SAR observations in the TREES-GRFM Central Africa Mosaic projects 1741

Products and Services

Posters

Th. Gruber & al.
Improvements of D-PAF altimeter products 1749
J.I. Sanchez & H. Laur
The ERS-SAR performances, products & systems 1753
Cr. Celani & al.
Processing & validation of the ERS-1 radar altimeter data at the Italian PAF 1759
V. Thouvenin & al.
CLIOSAT: Validation & calibration of satellite data 1763
M. Tonon
An operational ERS data application: Map coverage of French Guyana by space triangulation of ERS images 1769
R. Loizzo & al.
New I-PAF products & services 1773

Appendix – Late Papers 1777

List of Participants

OPENING ADDRESS

Lanfranco Emiliani

ESA Director, Observation of the Earth and its Environment

Ladies and Gentlemen,

May I first say what a great pleasure it is for me to be here today and to join you for this symposium where many of the results from the ERS-1 and ERS-2 missions will be presented and discussed by the scientific community. I welcome all of you on behalf of the European Space Agency and its Director General, Mr. Jean-Marie Luton. The initiative to convene the third ERS Symposium here in Florence draws its origin from a request made by the 'Agenzia Spaziale Italiana' back in 1994, and I am pleased that we have been able to support and realise it.

This meeting today, and until the end of this week, gives a third opportunity to researchers and applications experts, who are taking part in the ERS-1 and ERS-2 projects and have convened here from all over the world, to present and compare their findings following presentations of initial results back in 1992 in Cannes and additional results a year later in Hamburg. I believe that even more exceptional findings will be revealed on this occasion, particularly as we had the opportunity to operate the two satellites in tandem for nearly a year in the 1995-1996 timeframe.

Looking at the programme and the topics to be covered, one cannot help but be impressed by the number and breath of the subjects and by the very wide spectrum of users involved. I am particularly pleased to see further confirmed the international dimension of the project, a key factor in the success of the programme, and I should like to welcome those colleagues who have come from overseas to join us today for this event. The ERS programme can certainly be counted amongst the brightest successes of the European Space Agency. Both satellites have performed outstandingly since their launch back in July 1991 and April 1995 respectively, and are fulfilling our expectations completely. I believe this achievement is the outcome of highly successful European scientific and technological cooperation and a tangible sign that the investment in space research and technology by our Member States has been well placed.

It is not my purpose here to address the specific mission objectives of ERS other than to stress that answers to the environmental problems facing mankind, such as those derived from ERS, are important not only for the specialist but also for the man in the street who shares these concerns and wants positive actions to be taken in this respect. Thus, in the context for instance of events such as this symposium, if we are able to confirm that our programmes are responsive to these concerns, a broader and stronger support will naturally follow.

I would like to take this opportunity to inform you that our current plans foresee the extension of the ERS mission up until end of 1999 when Envisat will take over. In addition to the specific objectives of this mission, emphasis has been put on the continuation and extension of the data services provided by the ERS system. This new mission will thus support the provision of long-term datasets which are essential for both the operational application of spaceborne remote-sensing systems and climatological and environmental research.

Beyond Envisat and the new meteorology missions, namely Meteosat Second Generation and Metop, ESA is currently preparing future Earth Observation missions, i.e. the *Earth Explorer* and *Earth Watch Missions*. Here I would like to say that, following the User Consultation Meeting of May 1996 in Granada, in which many of you were active participants, we were authorised, subject only to the funds which we expect to become available soon, to initiate feasibility study activities for four candidate missions, namely:

- The Gravity and Steady-State Ocean Circulation Mission
- The Atmospheric Dynamics Mission
- The Earth Radiation Mission
- The Land-Surface Processes and Interactions Mission.

As international cooperation has always played and will continue to play an important role in the European space programmes, cooperation with other

space-faring nations remains an essential feature of ESA's Earth-Observation policy. We are committed to continuing this close relationship in the context of the new missions, the Earth Explorers and the Earth Watches, with our traditional partners, both within and outside Europe, as well as with newer partners as the opportunities arise. Finally, meetings where scientists gather to consider the impact that data obtained from space are having on our knowledge and understanding of factors determining our environment are essential elements to secure the required political support. I am confident that your contribution in this symposium will further enhance the support we all need to sustain our common quest for a better understanding of our planet.

I thus wish you all a very successful, stimulating, and productive meeting.

EARTH OBSERVATION AND SPACE — EUROPEAN PERSPECTIVE

Herbert J. Allgeier

Director Aeronautics Task Force, Space Coordination Group
European Commission, Brussels

Ladies and Gentlemen,

It is a great pleasure and an honour for me to have the opportunity to address this Third ERS Symposium organised by the European Space Agency and to do so on behalf of the European Commission, and specifically on behalf of Commissioner Mme Edith Cresson, who personally takes a great interest in Europe's achievements in space.

Indeed, the European remote-sensing satellite ERS is a fine example of Europe's achievements and the large number of participants present here for the next few days testifies to the very strong interest shown in this unique undertaking by the Earth-observation community and its users worldwide.

Since its very beginning in 1991 the ERS programme has caught the attention of a growing number of scientists and Earth-observation specialists from Europe and around the World. I am therefore very pleased to represent the European Commission at this important manifestation, of course sharing one more thing with all of you: the pleasure of being in the beautitul city of Florence, one of the crown jewels of European Culture.

As many of you know, over the years space activities have received growing attention from the European Commission, and, through a wide variety of programmes and projects, the Commission is actively involved in the field of satellite communication, navigation and position fixing and Earth observation at different levels: (i) through the activities of the Joint Research Centre of the Commission, and (ii) more generally through the Framework Programme for Research and Development, (iii) as a kind of pioneer user of data in a variety of fields, but (iv) also by actions of a more political or operational nature, for example in the field of international co-operation, competition or position fixing e.g. EGNOS.

In Earth observation, incidentally, the Commission is, as you know, the biggest single European customer of satellite data. Always in close co-operation and co-ordination with the main actors, above all ESA. To be sure this involvement is likely to increase in the future. Not because of, as some will say, the general trend of europeanisation. No, there is no need, be cause the European space programme is already European... one of the European success stories.

But the advent of the information society, the changes in the geopolitical situation, and the changing rules of global competition and co-operation require that the main actors introduce a new dynamics in their partnership to develop new synergies... This is the message of the Commission Communication recently transmitted to Council and Parliament entitled *The European Union and Space.* It proposes:

– to introduce a new dynamics in the relationship of the European partners, first of all with ESA;

– to create more synergy with the policies of the European Union, and to use the strength of European Union policies, the political and economic dimension of the European Union to protect, valorise and exploit Europe's position and achievements in Space.

Earth observation is one of the areas that will have to be addressed. Indeed, in many applications, Earth-observation data from space already provide more reliable and more comprehensive information to monitor our environment, to evaluate the agricultural production in a timely manner, to design regional policies for land use, or to plan actions for developing countries than other means. And the Union, as a political entity, can play a major role in stimulating the use of space techniques to support the implementation of its various policies or in direct response to a variety of users needs. There is both a direct and an indirect role for the Commission – the EU.

And there are many successful applications and we can point out important achievements. And there is more demand... Nevertheless, we still have difficulties in showing convincing evidence of the often quoted 'imminent commercialisation' of Earth observation. Therefore, I believe that it is important

to take stock and look at new ways of organising ourselves if we want to make a quantitative jump in this direction, that is commercialisation bringing market forces to work. And this together with ESA, with international agencies such as Eumetsat and with space agencies in Member States as well as with the private sector. One idea is an emerging initiative aiming at the creation of a European GIS which could provide the supporting wide area platform for the development of new services. Also it will be necessary to look at the convergence of communication, position fixing and observation to provide new added-value services.

This, Ladies and Gentlemen, is the background against which you should see the interest of the European Commission in Space in general and in Earth observafion in particular, and against which I am very keen to underline here the essentially European nature and the central role of the ERS programme.

The launch of ERS-1 in 1991 did indeed herald a new and promising phase for Europe in space. Since then, it has provided, without interruption, an impressive amount of data on the condition of the Earth surface, land and oceans. The information sent down to Earth by ERS-1, and since 1995 by ERS-2, has revolutionised the way we look at our environment. Let us not forget to pay tribute to the ingenuity and hard work of the countless scientists, engineers, technicians, operators and managers who have devoted long hours, years of their professional life and a good part of their career to this undertaking. Thanks to them, Europe is now recognised as a world leader in radar technology and ESA has demonstrated that advanced Earth-observation technologies can be put to the service of the citizens. Let me note a few of ERS' achievements which I believe are of particular relevance to Europe:

– First I should note the contribution of the ERS radar instrument in ship routing, thanks to its ability to monitor sea-ice movements and the possibility to characterise sea-surface conditions. Such developments are likely to have a major impact on the way we do business in maritime transport.

– Second, we all know that European nations are very sensitive to the quality of our environment and are, in this context, particularly concerned about natural disasters which so often threaten life, affect economic activities or destroy property. It is therefore that we followed with expectations, and noticed with interest, the growing importance of ERS radar data in the monitoring of flooded areas. The capability of the radar to map the extent of the floods under all-weather conditions is obviously a major advantage offered by the ERS system.

– A third example of the success of ERS is the tremendous progress in the study of the Earth's crust, again thanks to the radar information.

European scientists have, indeed, reported spectacular advances in measuring terrain movements which could be precursors to volcanic eruptions or earthquakes. European science can here be seen at its best, putting Europe in a leading position in the study of tectonic and volcanic risks. It is with additional satisfaction that we have recently seen the emergence of initiatives by the private sector using this up-to-date satellite radar technology to provide operational services to regional entities concerned with risk assessment and disaster mitigation.

Finally, I would like to mention the fact that the Joint Research Centre of the Commission has successfully developed and promoted the use of ERS data for agricultural statistics and monitoring and for assessing trends in deforestation in tropical areas. This is one more area where the advantages of radar data have been well demonstrated and they are a significant complement to other means of evaluating agricultural production or of assessing the environmental consequences of large-scale deforestation in the tropical belt. On a different level, allow me to stress the importance that the fraud combat team in the Commission's Directorate General for Agriculture attaches to a timely availability of ERS data on an operational basis.

Ladies and Gentlemen, during the next few days you will have ample opportunity to get better acquainted with many more exiting results of instruments like the Synthetic Aperture Radars, the Along-Track Scanning Radiometers, the Radar Altimeters or the more recent GOME atmospheric chemistry instrument. The ERS mission has opened the door to many technological and scientific breakthroughs as a whole. The ERS mission demonstrates that benefits can be derived which are directly delevant to European environmental, security and other political concerns. It is that dimension which, in closing, I would like to emphasise because it represents progress in the way we use technology for the benefit of society.

Let me in concluding congratulate the European Space Sgency for the ERS programme as a whole and for having organised this milestone Symposium.

I wish all of you a very fruitful and pleasant meeting.

THE EARTH FROM SPACE: WHAT NEXT FOR EUROPE?

Prof Chris Rapley
Executive Director

International Geosphere-Biosphere Programme
Royal Swedish Academy of Sciences

Box 50005, Lilla Frescativägen 4
S-104 05 Stockholm, Sweden

Mr Chairman, Ladies and Gentlemen,

It is a pleasure to be here to give this talk. During the period 1981 to 1994, as a 'remote sensing' academic based in the UK, I was closely involved in many aspects of the ERS programme. For the last three years I have been preoccupied with another task. This leaves me in a position to view ERS from a fresh perspective, whilst being aware of the details of its history. My aim is to take stock of where European Earth Observation (EO) was 15 years ago, where it is now, and what the EO community might aim for over the next 15 years.

Let's start by considering ERS's origins. These can be traced back to 1978 and the flight of NASA's highly successful, but short-lived, Seasat radar oceanographic mission. The enormous interest which this generated stimulated a number of ESA studies and planning exercises culminating on 28 October 1981 with the Member States plus Norway and Canada approving ERS-1. The mission objectives were to:

- increase scientific understanding of coastal zones, global ocean processes, and polar regions ...
- develop and promote economic / commercial applications

It is interesting to note that at the time of approval, although emphasis was placed on support for the World Climate Research Programme, the word 'environment' did not feature strongly in any of the project literature. The fact that subsequently ERS-1 and 2 have come to be seen as archetypal 'environmental' missions is a measure of the extent to which our world view has evolved. This needs to be borne in mind when considering goals and strategies for the 2010 time-frame.

What was the status of European EO in 1981? Through the efforts of a number of university groups and research institutes, of ESA and the national space agencies, of industry, and of the meteorological services, there was an established track record in the development of visible and infra-red sensors, space systems, and in the use of space data for research and operational weather forecasting. However, there was no experience in the development or exploitation of space radars, and only limited experience in the data processing, archiving and delivery systems required to handle large quantities of remotely sensed data. The research community was small, dispersed, and poorly networked. Research funding and the commercial market were both very limited.

For Europe to exploit fully the potential of ERS, a major capacity building exercise was necessary. Fortunately, visionaries both inside and outside ESA recognised the need, and stimulated a series of workshops, conferences, and funding opportunities. Events held at Igls, Alpbach, Schliersee, and numerous other locations, combined with a variety of study activities, not only provided the basis for the successful design and execution of the ERS system, but also laid the foundations for the development of an expert user community. The result was a snowball effect in which young researchers, committed to the exploitation of EO data, trained new generations and drew in workers (and hence new ideas) from related fields. With a cycle time of 3 years or less, and the benefit of expanding research budgets and increasing industrial interest, rapid growth in the size and strength of the skill pool occurred.

Following the successful launch of ERS-1 in July 1991, and the approval, and successful launch of the follow-on ERS-2, European (and other) users have had access to the most advanced and comprehensive data sets of their kind. The result has been that the research and applications communities have expanded and matured out of all recognition. The point is underscored by the statistics of this symposium, which has attracted over 700 participants from 30 nations.

Other outcomes of the programme include:

- a fully functional space segment consisting of two operational satellites, one currently held in reserve
- a state of the art ground segment delivering a wide variety of near-real-time and off-line data products
- new scientific knowledge, skills and capabilities extending over topics well beyond those originally envisaged
- established research funding mechanisms

- a set of demonstrated practical applications of the data
- a small but growing community of operational users

Thus, an investment of approximately 2bn ecu of European taxpayers' money has resulted in an operational state-of-the-art EO system designed to address critical issues of the environment, an embryonic commercial sector, and a massive increase in the associated technical and scientific skill pool.

The human resource is especially important. In addition to providing the foundation for the development of future generations of European EO missions, it is critical to the understanding of the Earth system and hence to achieving a sustainable society. Possibly even more important, is its potential role as a 'reaction force', capable of diagnosing Earth system behaviour and formulating policy advice in response to global change surprises.

The legacy of ERS therefore comprises major physical and human assets of global as well as European significance. So the answer to the question 'Is ERS a success?' is a confident 'yes', both on the basis of the original objectives, and using much wider criteria.

Given such success, it is surprising to find that the long-term future of EO is uncertain. How can this be?

Of particular significance is the fundamental change in attitudes towards science which has occurred since the glory days of the 1980s. Gone is the concept of the 'endless frontier' in which the scientist's obligation is simply to 'fill the reservoir of knowledge'. Budgetary stringencies and the doctrine of accountability now require that science justifies itself in terms of its direct benefits to society. The consequences are profound and the transition is still incomplete. For example, although the title of this symposium reflects the new realities, the abstracts of the papers tell a different story, with a continuing heavy bias towards basic research, and less emphasis on practical applications.

An example of prevailing political attitudes is provided by the pamphlet 'Inventing Tomorrow' in which the ministers of the European Commission state that:

"...apart from generating new knowledge, we would like science to contribute to general well-being and social balance. We want to see scientific progress and innovation making a major contribution to Europe's future..."

EO is not alone in facing such challenges. Similar pressures are being felt widely, and especially within Global Change research Programmes such as the World Climate Research Programme (WCRP), International Geosphere-Biosphere Programme (IGBP), and the International Human Dimensions Programme (IHDP). These were established in the 80s with a mandate to 'reduce uncertainties' concerning the functioning and behaviour of the Earth system. They are increasingly being encouraged to address the regional consequences and human impacts of global change, to develop integrated assessment models, and to carry out cost-benefit analyses concerning policy options. Strong political interest is expressed in 'answers now'.

The response has been to develop new research activities focused on practical, regional objectives. An example is the recently inaugurated joint WCRP/IGBP/IHDP project on 'Climate Variability Prediction and Agriculture in Monsoon Asia', in which, for a network of selected sites, climate variability predictions on the scale of months to a year will be generated with a view to improving management and decision-making concerning crop production. This combines a set of challenges to the researchers working on basic science (climate variability prediction, crop models, etc.), with a practical outcome.

Before developing that concept further, it should be noted that EO faces specific problems and criticisms. In a recent publication 'Earth Observation from Space, History, Promise and Reality', the Space Studies Board of the US National research Council observes that:

"The ability to make earth observations from space is one of the great achievements of the space age. For both scientists and operational users of the data, however, the success has been tempered with disappointment. The promise of the technology has not yet been realized, nor is it evident that current activities are leading towards a timely realization of that promise."

Although this statement addressed the US EO programme, it applies within Europe, notwithstanding the ERS success. The problems derive from a variety of causes including:

- long mission gestation times (which limit both the rate of progress and responsiveness to changing knowledge and circumstances)
- high costs
- institutional problems (such as the lack of an agency responsible for operational EO missions)
- lack of financial commitment from the institutional environmental authorities (the only realistic source of funding for 'repeat' missions and operational systems)
- the tendency of industry and the research community to focus on demonstrations (technical and scientific) and 'curiosity-driven' activities, rather than missions focused on the provision of specific services to society.

More fundamentally, in spite of some preliminary efforts of ESA, the EU and Eumetsat, there is a lack of a clearly-defined vision of EO's future, both as regards the balance between science and commerce, and the purpose of the science. The scientific community has only limited influence over the financial and institutional issues, but it has substantial influence, and indeed responsibility for contributing to such a vision. So it is on this topic that I will conclude. In doing so I will draw heavily on Francis Bretherton's excellent paper 'Making Earth System Science Policy Relevant'.

The key source of contention between scientists and their political masters is the balance between 'curiosity-driven' research and the delivery of 'goods and services of value to society'. An over-emphasis on either will be unsatisfactory to one or other party. The smart way forward, is to develop activities which satisfy both. This is the approach being adopted by the Global Change research programmes, and it is the approach proposed by Bretherton. Table 2 of Bretherton's paper defines a series of deliverables, stated in a language which the policy maker user community can understand and appreciate, which push the limits of existing scientific knowledge, and at the same time are of value to society. Three examples, in increasing order of difficulty and timescale are:

- regularly scheduled, ongoing predictions one year ahead of interannual climate fluctuations associated with El Niño, together with *regional impact and forecast utilization studies*

- ability to determine national sources and sinks for atmospheric CO_2 and other greenhouse gases and aerosols, *for application as part of a monitoring system for an international greenhouse gas emissions reduction agreement*

- understanding of the major interactions of human societies with the global environment, *enabling quantitative analyses of existing and anticipated patterns of change*

The first example is already being addressed by the International Research Institute (for Seasonal to Interannual Climate Prediction). Regarding the second example, the Third Conference of the Parties of the Framework Convention on Climate Change will take place in Kyoto in late 1997 with the goal of signing binding international agreements on carbon emissions. Thus, the development of a system to monitor and verify greenhouse gas sources and sinks is highly significant issue, providing the science community with a tremendous opportunity. The third example points in the direction of seamless multi-disciplinarity, and a heavy emphasis on integration and synthesis, a process already under way within the global change research programmes.

In my view, the prospects for European (and global) EO are very bright. There is a need to minimise costs and maximise value, to engage users who can and will pay, and to balance 'blue skies' research and tangible deliverables. The challenge is yours.

Reference

Bretherton, F., 1995, 'Making Earth System Science Policy Relevant', in *'The State of Earth Science from Space: Past Progress and Future Prospects'*, Ghassem Asrar and David Jon Dokken Eds., 1995 the American Institute of Physics.

AN OVERVIEW OF ERS-SAR INTERFEROMETRY

F. Rocca, C. Prati, A. Ferretti
Dipartimento di Elettronica e Informazione- Politecnico di Milano
Pzza. L. da Vinci, 32, 20133 Milano. Italy
Tel: +39-2-23993573 Fax: +39-2-23993413
E-mail: rocca@elet.polimi.it

April 11, 1997

1. Summary

In this presentation we propose an overview of SAR interferometry discussing its possibilities and limits, making reference to the TANDEM experiments carried out with ERS 1 and 2. The coherence of the interferometric pair is an important parameter, that combined with the more usual backscatter amplitudes, leads to useful images segmentation. Due to the 1 day delay between passes of the two satellites, the coherence is high but on highly forested areas; very useful DEM's are obtainable from the fringes. The combination of several passes can reduce the dispersion due to atmospheric artifacts. Millimetric motion of large areas of the terrain or of corner reflectors can be measured with good reliability and therefore the possibility has been demonstrated to measure subsidence, landslides, volcanoes deflation, and coseismic motions.

2. Introduction

Synthetic Aperture Radar (SAR) systems record both amplitude and phase of the backscattered echoes. The phase of each pixel of a focused SAR image is the sum of three distinct contributions:

1 - the two-ways travel path (sensor-target-sensor: hundreds of kilometers in the satellite case) that, divided by the used wavelength (a few centimeters), corresponds to millions of cycles;

2 - the interaction between the incident e.m. waves and the scatterers within the ground resolution cell;

3 - the phase shift induced by the processing system used to focus the image.

Therefore, the phase of a single SAR image is of no practical use. On the contrary, if two SAR images from slightly different viewing angles are considered (*interferometric pair*) their phase difference (*interferometric fringes*) can be usefully exploited to generate Digital Elevation Maps (DEMs), to monitor terrain changes and to improve the range resolution. The interferometric fringes image is derived as the phase of the SAR *interferogram*, that is the complex image formed by cross-multiplying the two SAR images. The relation between the interferometric fringes and ground elevation is usually explained by means of the *monochromatic approach* [24, 14]. It is based on the assumption that the RF bandwidth is so small (and this is the case of most satellite systems including SEASAT, ERS-1, JERS-1, ERS-2 and RADARSAT) to be negligible. Thus the system is considered monochromatic. However, if the finite bandwidth of the system is considered (*wavenumber shift* approach), a relative shift of the ground wavenumber spectra dependent on the baseline and the local slope is found. A few important consequences come out from this result [16, 5]. Using the simpler monochromatic approach we show the relationship between the relative terrain elevation and the interferometric fringes. Then we will determine the quality of the Digital Elevation Model derived from interferometry. Two sections (6 and 8) will be dedicated to the description of other applications of SAR interferometry: small terrain motion detection and uses of the coherence for image segmentation. Symbols that will be used through the text and the main parameters values of the ERS-1 SAR system (that will be assumed as typical parameters of SAR from satellites) are shown in table 1.

3. The monochromatic approach

Let us consider two complex SAR images taken from two slightly different viewing angles (see figure 3.1), v_1 and v_2. Even if non simultaneous acquisitions are considered, we shall suppose, for now, that the terrain backscatter did not change.

Let us now exploit the "monochromatic approximation": the relative system bandwidth is so small (i.e. in the ERS-1 case its value is $3 \cdot 10^{-3}$) to be neglected. The phase difference ϕ between correspondent complex pixels in v_1 and v_2 is proportional to the travel path difference $2\Delta r_\circ$ (the factor 2 accounts for the two ways travel path):

$$\phi = \frac{4\pi}{\lambda} \Delta r_\circ \tag{3.1}$$

(λ is a constant). The interferometric phase ϕ of a single pixel is still of no practical use. The travel path

difference $2\Delta r_o$ is usually much greater than the wavelength λ (in most of the practical cases, the travel path difference from the satellite can be as large as a few hundred meters whereas the used wavelength is of the order of a few centimeters) and the measured phase ϕ shows an ambiguity of many cycles. On the other hand, passing from one pixel to its neighbor (only a few meters apart in the slant range direction), the variation of the travel path difference ($\Delta(\Delta r_o)$) may be much smaller than λ and the variation of the interferometric phase $\Delta\phi$ is not ambiguous. Moreover, a simple relation between $\Delta\phi$ and the relative terrain elevation can be derived.

Table 1

Symbol	Meaning
λ	wavelength
$f_o = c/\lambda$	central frequency
W	system bandwidth
f_s	sampling frequency
$f_{Ny} = f_s/2$	Nyquist frequency
θ	off-nadir angle
α	local terrain slope (range)
H	platform altitude
ρ_s	slant range resolution
Δr	slant range sampling interval
ρ_g	ground range resolution
B	baseline
B_n	normal baseline
B_r	radial baseline
B_{nc}	critical baseline
r	slant range axis
r_o	sensor-target distance
y	ground range axis
z	elevation axis
k_y	ground range wave number
ϕ	interferometric phase
Symbol	**ERS-1 value**
λ	5.66cm
$f_o = c/\lambda$	5.3GHz
W	16MHz
f_s	18.96MHz
θ	23deg.
H	780km
ρ_s	9 meters
B_{nc}	1100 meters

In figure 3.1 we have indicated the position of the two SAR sensors (S_1 and S_2) and their relative displacements parallel (B_r) and normal (B_n) to the slant range direction. We have also indicated the position of two point scatterers and their relative displacements parallel (r_p) and normal (n_p) to the slant range direction. Let us assume as a reference the positions of S_1 and P_1 with their relative distance r_o. By changing the sensor and target position by (B_n, B_r) and (r_p, n_p) respectively the sensor-target distance becomes:

$$r = \sqrt{(r_o + r_p - B_r)^2 + (n_p - B_n)^2} \tag{3.2}$$

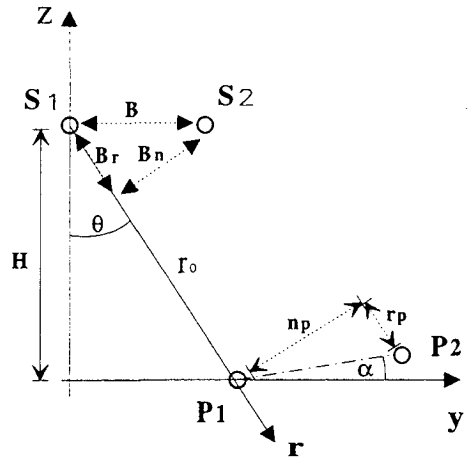

Figure 3.1: Interferometric SAR geometry in a plane orthogonal to the rectilinear platforms (S_1 and S_2) trajectory.

Since the distance between the two SAR sensors is generally much smaller than the sensor-target distance r_o (a few hundred meters compared with 800km, in the ERS-1 case), the following expression of the interferometric phase variation holds:

$$\Delta\phi = \frac{4\pi}{\lambda}\Delta(\Delta r_o) = \frac{4\pi \cdot B_n \cdot n_p}{\lambda \cdot r_o} \tag{3.3}$$

This result shows that if we know the relative displacement of the two orbits normal to the slant range direction B_n, the distance r_o and the value of the SAR wavelength λ, then the phase difference $\Delta\phi$ depends only on the n_p value, i.e. the elevation difference between the points displayed in figure 3.1, measured in the direction normal to the slant range axis. Thus the interferometric phase image represents a map of the relative terrain elevation with respect to the slant range direction. A linear term can then be subtracted from the interferometric phase so that the phase corresponding to the flat horizontal terrain is a constant. After some algebra, the version of equation 3.3 that refers to the relative elevation $q = \Delta z$ with respect to a flat terrain becomes:

$$\Delta\phi = \frac{4\pi \cdot B_n \cdot q}{\lambda \cdot r_o \cdot \sin\theta} = 2\pi\frac{q}{q_0} \tag{3.4}$$

where we have indicated with q_0 the *altitude of ambiguity*, i.e. the elevation change correspondent to a 2π phase shift.

4. Phase unwrapping

Up to now it has been assumed that the phase difference $\Delta\phi$ of equation 3.4 would be directly obtained

from the interferometric fringes. However such an assumption is in some way misleading. In fact, from the interferogram, the complex values $e^{j\Delta\phi}$ can be determined but not the $\Delta\phi$ values themselves. What is measured is not the phase difference value $\Delta\phi$, but its principal value $\Delta\phi_p$, limited between $-\pi$ and $+\pi$. The interferometrical fringes show typical discontinuities like those shown in figure 4.1.

Figure 4.1: ERS-1 - Mt. Vesuvius (Italy) August 27th and September 5th, 1991. - Interferometric fringes. The estimated normal baseline is $B_n = 193$ meters.

Two adjacent discontinuities separated by a constant elevation increment, corresponding to a 2π phase drop, represent the height contours of the terrain elevation map. However, since the real phase values are " wrapped" around a 2π interval, to obtain the correct map (and, thus, the correct labels of each contour line), a map of the multiples of 2π to be added to the "wrapped" phase should be carried out (*phase unwrapping*). At the beginning of the studies on SAR interferometry (1988-89), the phase unwrapping problem was investigated assuming that only two SAR images were available. That was the actual situation at that time since the only few interferometric SAR images were from the SEASAT and the JPL single pass airborne systems. Many techniques of phase unwrapping of interferometric SAR images have been proposed [7, 6, 19]. A summary of these techniques is out of the scope of this paper.

More recently, however, a different strategy to solve the phase unwrapping problem has been considered. With the huge amount of SAR images from the European satellites ERS-1 and ERS-2 together with the availability of Digital Elevation Models (typically from the optical stereo SPOT) the basic assumption changed: all the available information should be exploited to get a DEM [20]. Then, an available Digital Elevation Model (DEM) can be transformed into the SAR geometry and subtracted from the interferogram. Depending on the DEM accuracy and on the normal baseline B_n the phase of the residue can be so small to show a single fringe with no need of phase unwrapping.

4.1. The multibaseline approach

An alternate approach to phase unwrapping comes from the comparison of images with different baselines [3]. Theoretically it would be enough to have three interferograms with baselines that are prime with respect to each other to remove ambiguities (Chinese remainder theorem). In a practical case, where data are noisy and baselines random, the use of multiple interferograms increases significantly the elevation ambiguity level. Precise location of the flight paths together with a good estimation of the standard deviation of the phase noise allows the use of Maximum Likelihood (ML) and Maximum A Posteriori (MAP) techniques to estimate the height difference of each pixel with respect to a reference one, taking into account *a priori* information.

The conditional density function of the elevation for each interferogram is periodic with a different period (the altitude of ambiguity) dependent on the baseline. In each period the higher is the quality of the fringes (the coherence) the sharper is the histogram. The product of the conditional densities shows a neat peak whenever the coherence is not close to zero and the baseline errors are not too high. The sharper is the global peak, the higher is the reliability of the results i.e. the probability that the correct value of the height variation lies inside a given interval.

The benefits of the multibaseline approach are twofold. First, combining all the information it is possible to limit the impact of the noise. Besides, there is minor risk of aliasing with respect to conventional single interferogram phase unwrapping: working simultaneously on more interferograms, phase unwrapping is possible even if the phase is undersampled. Of course the higher the noise, the worse the reliability and the more likely the phase unwrapping errors.

As a conclusion, even if a fully automatic phase unwrapper that works in all conditions is not available yet, phase unwrapping does not appear to represent a serious problem in SAR interferometry anymore.

5. Digital Elevation Map preparation

The elevation map derived from SAR interferometry lies on a plane where the reference axes correspond to the azimuth and slant range directions.

Such a coordinates system is different from the reference systems in the azimuth-ground range plane used in the usual elevation maps. Thus it is necessary to transfer the unwrapped phase from the slant range coordinates system to the ground range system; the ob-

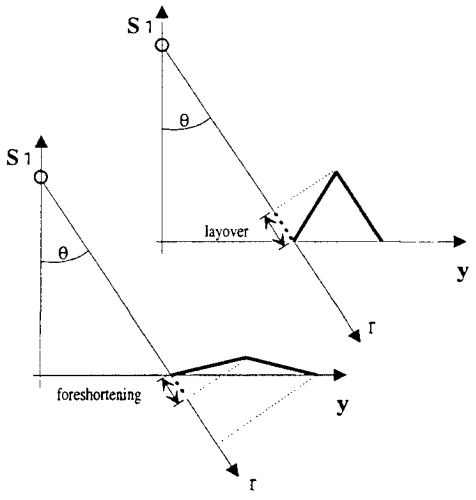

Figure 5.1: Typical geometric deformations introduced by SAR (foreshortening and layover).

tained values must be interpolated and resampled in terms of uniform ground range cells.

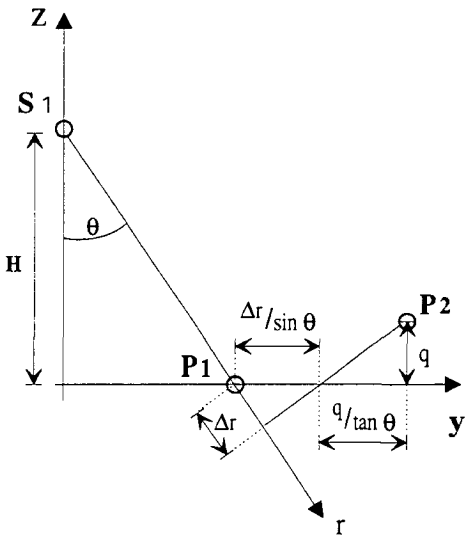

Figure 5.2: Cross-section of the SAR system geometry normal to the azimuth direction. The ground range coordinate depends on both the range position and the point elevation.

5.1. Rectification of the elevation map

From Figure 5.2 it is evident that the horizontal position of a backscatterer depends on both the slant range coordinate and the elevation. Through simple geometrical expressions the relation between these three parameters can be found. The ground range coordinate with respect to the initial point, indicated by y, is the sum of two components: the first is the horizontal displacement in the case of flat terrain, the second caused by a non-zero elevation drop.

$$y(r,q) = \frac{\Delta r}{\sin\theta} + \frac{q(r)}{\tan\theta} \tag{5.1}$$

Since the position of the points depends on its elevation, the correspondence between ground range and slant range is quite irregular. In fact, the well known foreshortening effect causes a compression of the areas with ascending slope and a spread of the descending areas. As a consequence the ground difference, corresponding to a constant slant range displacement, will be much larger in the case of ascending slopes. Furthermore, when layover effects occur several areas of the earth's surface can disappear from the SAR image (see figure 5.1).

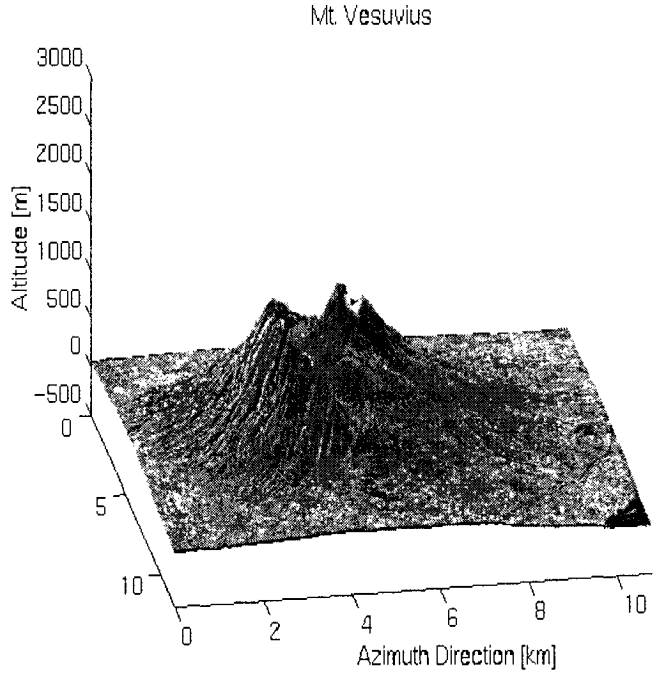

Figure 5.3: A perspective view of Mt. Vesuvius obtained from ERS descending orbits interferograms.

In a ground range reference system the obtained elevation map will have a quite uneven sampling interval. Thus to obtain a regular sampled map the elevation values must be interpolated. For our purposes a linear interpolation is quite adequate. In fact, in flat or descending areas the interpolating points are fairly close, whereas with an ascending slope the foreshortening effect produces such a large slant range compression that the interpolating points lie much further away and no interpolator would operate correctly. The results of the rectification process, performed for the SAR image of the area near the Vesuvius is shown in figure 5.3.

5.2. Combination of ascending and descending orbits data

Any current DEM estimate is very useful for unwrapping. In fact, data from different takes and therefore with different baselines can be combined, but only if properly positioned in space; in the case of a flat region, uninteresting for the unwrapping problem, the coregistration can be carried out using ephemerides. Not so in complex topography situation, where the registration is DEM dependent. We arrive to an iterative procedure where the available data are combined in such a way to achieve a progressive improvement of the DEM. In this operation, the combination of data from ascending and descending orbits could be very helpful[13]. First, to unravel the layover areas, that, if not in shadow, may appear well behaved with the other orbit. Second, and equally relevant, the combination of the two views is only possible if the DEM is correct; hence, it is a powerful check of its quality, to remove blunders, reduce the elevation dispersion, etc.

6. Monitoring terrain changes

If the SAR acquisitions are not simultaneous, the interferogram phases (*fringes*) are also affected by the possible terrain changes. Two types of temporal terrain evolution can be identified by means of multitemporal interferometric SAR images: decorrelation changes and small terrain motions; a very interesting report on the possibility of monitoring terrain changes can be found in [2].

Decorrelation changes. A random change of the position and physical properties of the scatterers within the resolution cell can be detected as low coherence of the images and will be dealt with in section 8.

Small terrain motions. Local centimetric relative motions in slant range, generate large local phase shifts in the interferogram. The phase difference $\Delta\phi_s$ thus generated is governed by a mathematical relation completely different from that of the interferometric fringes (that, in order to avoid any confusion we shall indicate with $\Delta\phi_T$) described by equation 3.3. It is, in fact, proportional to the ratio between the relative motion Δs along the slant range direction and the transmitted wavelength λ. Thus, if we have a non simultaneous interferometric SAR pair with a given baseline B_n and a small terrain relative motion occurs between the two acquisitions, the following expression of the interferometric phase difference holds:

$$\Delta\phi = \Delta\phi_T + \Delta\phi_s = \frac{4\pi B_n n_p}{\lambda r_o} + \frac{2\Delta s}{\lambda} \qquad (6.1)$$

From equation 6.1, it is clear that the two terms $\Delta\phi_T$ and $\Delta\phi_s$ should be separated in order to recover the terrain relative motion. The simplest way to estimate small motions consists of choosing an image pair with a very small baseline (zero or a few meters would be sufficient in the case of ERS-1) so that the first term is much smaller than the second. An interesting example of such a solution is shown in figure 6.1. Two ERS-1 images of the area of Nice on the border between France and Italy, with a time interval of 9 days and a baseline B_n = 6m, have been used to generate an interferogram. In figure 6.1 the interferometric fringes are shown. Due to the very small baseline the fringes do not show rapid variations (even if the topography of that area is not flat at all) but for a small area close to the center of the map. In that area a very active landslide has being monitored by the group of the Institute de Physique du Globe (IPG) in Paris[1]. From the ERS-1 interferometric data, an average landslide velocity of about 1cm per day has been estimated. The result is in good agreement with the data provided by the IPG group. Moreover, the ERS-1 interferometric SAR image provides a set of measurements of the landslide relative motion on a very dense grid (4×20 meters) at a cost that is much smaller than that of any other traditional techniques. The accuracy of the motion measurement offered by such a technique has been tested with an ERS-1 experiment (the "Bonn experiment"), where elevation change as small as 9 mm of a few artificial radar targets (corner reflectors) has been detected with no ambiguity [9, 15].

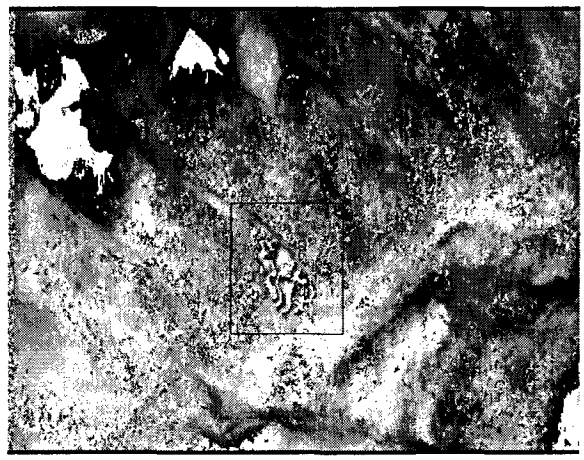

Figure 6.1: ERS-1 SAR interferometry. Fringes generated from two images of the area of Nice on the border between France and Italy, with a time interval of 9 days and a baseline B_n = 6m.

If a stereo SAR pair with a very small baseline is not available, the topography contribution to the interferometric phase ($\Delta\phi_T$) must be subtracted from the fringes. It can be accomplished in two different ways. If a topographic map of the area of interest is available, it has to be transformed in the azimuth slant range coordinates and scaled proportionally to the baseline of the interferometric pair in order to have an estimate of the phase component $\Delta\phi_T$. Then, it should be subtracted from the fringes (an impressive example of this technique has been shown by CNES [10] for the Landers

earthquake). As an alternative, an additional SAR image can be exploited in order to have an interferometric SAR pair with no terrain changes [4]. For the sake of simplicity, let us label the three SAR images with 1, 2 and 3 with no regard to their time consecution. Let us also assume that during the first two images no terrain changes occur. Thus, the fringes generated from the first two images will be proportional to the phase $\Delta\phi_t$ to be subtracted from the fringes generated either from the couple $1-3$ or $2-3$. From equation 3.3, it is clear that the proportionality coefficient is given by the ratio of the two baselines B_{n12} and B_{n13} (or B_{n23}). However, since the proportionality holds on the phases and not on their principal values[1], the fringes obtained from the couple $1-2$ must be first unwrapped and then scaled.

Other extremely interesting results on the use of this technique for studies of volcano deflation (Etna) or glacier motion can be found in [11, 8].

Table 2: The Vesuvius data set

SAT	ORB	DATE	Bn
ERS-1	20794	07/07/95	
ERS-2	**1121**	**08/07/95**	**39**
ERS-1	21295	11/08/95	
ERS-2	**1622**	**12/08/95**	**57**
ERS-1	22297	20/10/95	
ERS-2	**2624**	**21/10/95**	**135**
ERS-1	22798	24/11/95	
ERS-2	**3125**	**25/11/95**	**220**
ERS-1	23299	29/12/95	
ERS-2	**3626**	**30/12/95**	**253**
ERS-1	23800	02/02/96	
ERS-2	**4127**	**03/02/96**	**146**
ERS-1	24802	12/04/96	
ERS-2	**5129**	**13/04/96**	**106**

7. Atmospheric effects

In repeated pass SAR interferometry from satellite, different propagation velocities along the scene due to atmospheric changes (at the time of the two surveys) could be responsible of interferometric phase variations that *cannot* be related either to the topography or to relative terrain motions[25]. Multibaseline techniques can be usefully exploited to get a DEM that is less affected by artifacts by averaging the uncorrelated atmospheric contributions coming from the single interferograms [3]. When the ML DEM is generated it is possible to get the phase difference with respect to each interferogram. These phase residues are proportional to atmospheric changes.

[1] Apart from the special case of an integer ratio between B_{n12} and B_{n13} (or B_{n23}).

7.1. Experimental results

Seven ERS-1/ERS-2 Tandem interferometric pairs have been used to generate a DEM of Mt. Vesuvius [3]. Orbits number, dates and normal baselines are summarized in the following table.

As an example the phase residues obtained by subtracting the ML DEM from the April, July and August interferograms of the Vesuvius data set are shown in figures 7.1, 7.2 and 7.3.

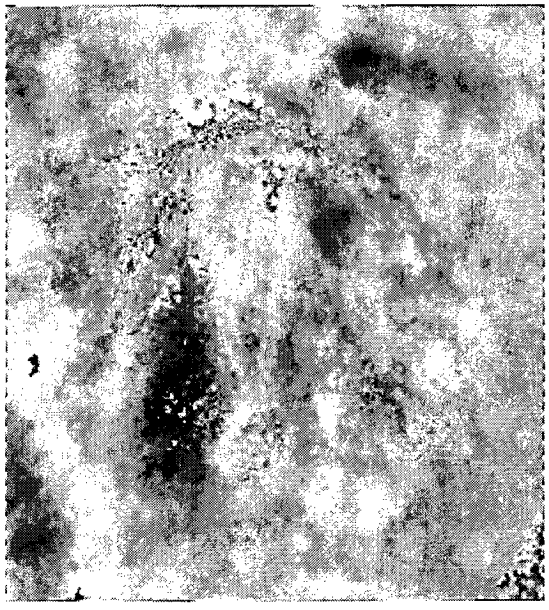

Figure 7.1: Vesuvius: differential interferogram generated subtracting the ML DEM from the April 1996 Tandem interferogram (B_n= 106 m).

The phase variations (about one fringe peak to peak) with very low spatial frequency (more than one kilometer in both directions) visible in the figure are generated by atmosphere changes within the surveys. These effects appear to be the major limitation to the use of SAR interferometry as a technique for generating highly accurate Digital Elevation Models and for detecting small surface deformations. However, the interferometric phase depends on the relative elevation through a coefficient that is directly proportional to the baseline (see equation 3.3): the higher the baseline, the higher the phase variation correspondent to the same topography. On the other hand, the phase variations due to atmospheric changes are independent of the baseline. Thus, the higher is the baseline of the interferometric pair the smaller is the topographic error due to parasitic effects. Moreover, if many interferometric pairs of the same area are available, "outliers" can be identified and eliminated from the database. The remaining results can be combined to "filter out" the effects of atmospheric changes.

An example of outliers identification is shown in figure 7.4. Here seven elevation profiles (along a range line) generated with the tandem pairs of the Vesuvius

Figure 7.2: Vesuvius: differential interferogram generated subtracting the ML DEM from the July 1995 Tandem interferogram (B_n= 39 m).

Figure 7.3: Vesuvius: differential interferogram generated subtracting the ML DEM from the August 1995 Tandem interferogram (B_n= 57 m).

data set are superposed. It can be clearly seen that for some range positions there is a good consensus of five profiles and two outliers coming from the small baseline (39 and 57 meters) interferograms.

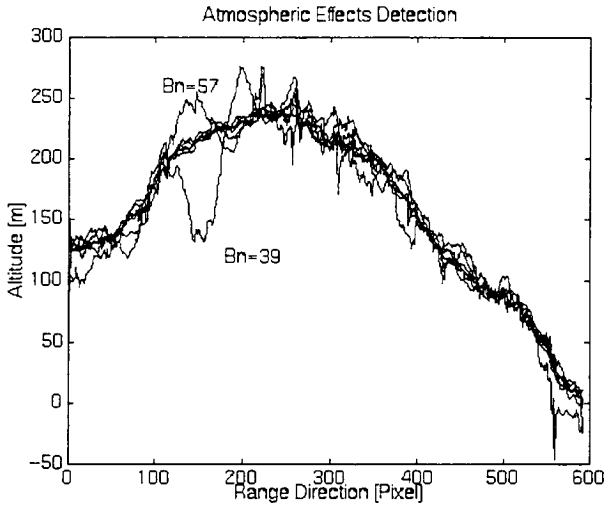

Figure 7.4: Example of atmospheric outliers. Seven elevation profiles (along a range line) generated with the tandem pairs of the Vesuvius data set are superposed.. For some range positions there is a good consensus of five profiles; two outliers come from small baseline (39 and 57 meters) interferograms.

In a companion paper [3], it is shown that by eliminating the outliers from the database and by weighting properly the different DEMs, the rms difference found between ML and SPOT DEMs is less than 10 meters.

It should be mentioned here that once an accurate DEM is available, also low coherence interferometric pairs (typically from the 35 days repeat cycle or its multiples) can be usefully exploited to get info on terrain deformations with low spatial frequency and/or atmospheric artifacts. Low-pass filtering the differential interferogram that contains low frequency signal plus white spectrum noise, allows us to extract useful information. An example is shown in the following figure 7.5. Here the phase of the low-pass filtered differential interferogram of the Valle del Bove (Mt. Etna) is shown. Low frequency phase variations that occurred in 36 days are clearly visible.

More differential images could then be used to identify the time evolution of the phase variations. Possible terrain deformations might be separated from atmospheric artifacts by fitting a deformation model to the time evolution of the phase variations [11].

8. Coherence

The quality of the interferometric phase depends on the amount of noise that, in general, comes from distinct sources [14, 18]: i- system noise; ii- terrain change (non

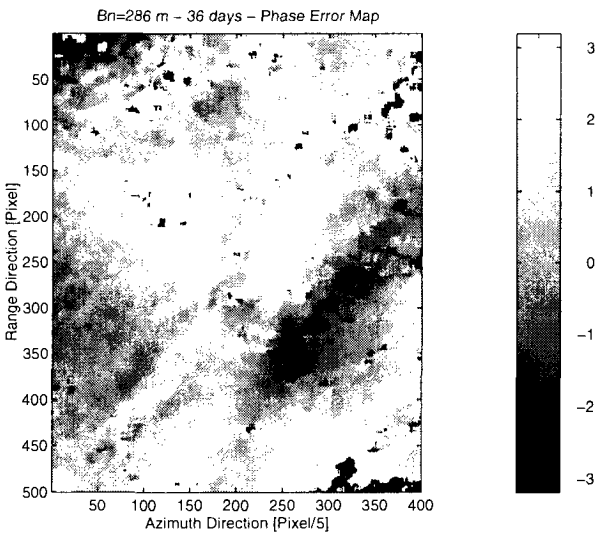

Figure 7.5: Etna 36 days interferogram. The topographic contribution has been compensated and low frequency distortions are visible.

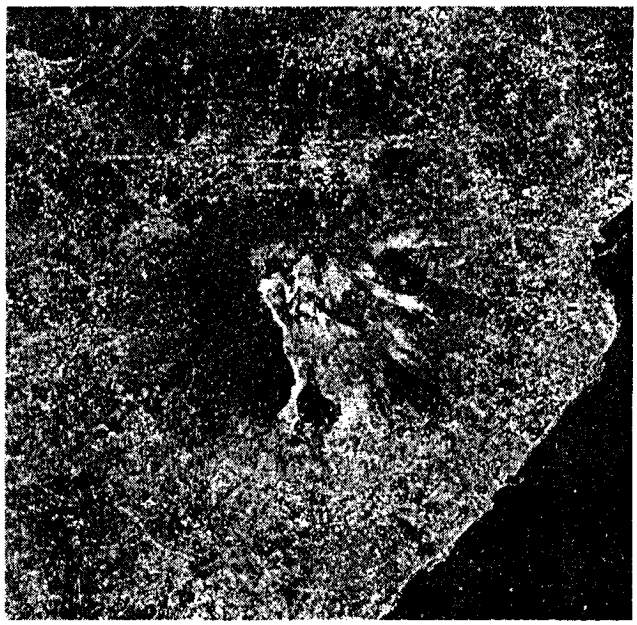

Figure 8.1: Coherence map of Mt. Vesuvius.

simultaneous acquisitions); iii- images misregistration; iv- approximate and unequal focusing of the two passes; v- decorrelation due to the baseline ("geometric" decorrelation). It is obvious that there is no way to avoid the first two sources of noise. On the other hand, as far as the last three sources are concerned, they can be taken under control. In other words, since in most cases the system noise is quite small compared with the usually sensed signals, and the processor noise is well under control if it is designed to be **phase preserving** [14], it can be seen that the fringes quality is degraded by scattering change in time and volumetric effects only. The coherence γ of two complex SAR images v_1 and v_2, is defined as follows [16]:

$$\gamma = \frac{E[v_1 v_2^*]}{\sqrt{E[\mid v_1 \mid^2] E[\mid v_2 \mid^2]}} \tag{8.1}$$

where E[.] means the expected value (that in practice will be approximated with a sampled average) and * the complex conjugate. The absolute value of γ is a fundamental information on the exploitability of SAR interferograms. The signal (usable fringes) to noise ratio Ξ can be usefully expressed as a function of the coherence:

$$\Xi = \frac{\mid \gamma \mid}{1 - \mid \gamma \mid} \tag{8.2}$$

Thus, it is clear that every effort should be dedicated to avoid coherence loss during the interferogram generation process (section 8).

The statistical confidence of the estimated coherence (sampled coherence) and of the derived measurements, depends on the number of independent samples (n) that can be combined for the computation. As a first approximation, the standard deviation of the estimator is proportional to $1/\sqrt{n}$. Thus, whenever uniform areas (in the statistical sense) are identified, the sampled coherence can be computed as:

$$\widehat{\gamma} = \frac{\sum_n v_1 v_2^* e^{-j\phi}}{\sqrt{\sum_n \mid v_1 \mid^2 \sum_n \mid v_2 \mid^2}} \tag{8.3}$$

In fact, since the coherence is estimated from the combination of the phases of a few pixels at the very least, the topography effects on the interferometric phase ϕ proportional to the known terrain changes have to be removed from the result. Thus, in order to compensate this unwanted effect, the vectors at the numerator of equation 8.3 must be *deskewed* before summing. It is also clear that, in order to generate an interferogram, the pixels of the images gathered in the two different images must be registered accurately, so that the random variates corresponding to the reflectivity are properly aligned. A single pixel shift, if the focusing processor is a good one, is enough to practically zero the correlation. In the following we will not consider the effects due to misregistration and system noise, since they can be avoided with a good system or with a proper processing. The elevation error σ_n of maps generated by means of SAR interferometry will follow the value of Ξ as:

$$\sigma_n = \frac{\lambda r_o \sin\theta}{2\pi n_s} \sqrt{\frac{1}{2\Xi}}$$

As an example, the coherence map of the area of Mt. Vesuvius in Italy observed from ERS-1 on August 27th and September 5th 1991 is shown in figure 8.1 (see also the fringes obtained with the same passes that are shown in figure 4.1). The sampled coherence has been computed on small rectangles 16 × 4 (azimuth, slant

range) pixels large ($n = 64$) that reasonably belong to uniform areas. The coherence map can be converted into an elevation error map (apart from systematic errors). As expected, areas covered by thick vegetation or in foreshortening or layover show an almost zero coherence and are not usable for SAR interferometric applications (e.g. DEM generation and super-resolution).

8.1. Multi-Interferogram Coherence Maps

A multi-interferogram approach can be usefully exploited to estimate the coherence using an ensemble average instead of a space one. When a good DEM is available with the same resolution of the SAR images, it is in fact possible to combine all the data to compute a multi-baseline coherence map γ_m of the area of interest on a fine spatial resolution: the increased number of freedom degrees (due to multiple interferograms) allows to get high resolution products (say 20×20 m).

First the topographic contribution on the phases of each interferogram is compensated for using the DEM. Then the phases are high-pass filtered to eliminate local distortions due to atmospheric effects. Finally the mean phase value is subtracted in each interferogram so that all the data can be considered phase aligned. The estimation is then straightforward:

$$\widehat{\gamma_m} = \frac{\sum_{i,n} v_{1i} v_{2i}^* e^{-j\Phi}}{\sqrt{\sum_{i,n} \mid v_{1i,n} \mid^2 \sum_{i,n} \mid v_{2i,n} \mid^2}} \qquad (8.4)$$

where $\sum_n$ is the standard space average on the $i-th$ interferogram (this time using a small estimation window). The achieved coherence map highlights what remains unchanged during the time interval between the first and the last acquisition and could be exploited for image segmentation and classification; it gives a measure of SNR on a fine spatial resolution.

8.2. Applications to image segmentation

SAR coherence is an additional source of information with noticeable diagnostic power. In the following we shall enumerate some of the most relevant applications. In [12] it was first observed that forests, that appeared with variable reflectivity in the ERS - 1 detected images, appeared almost black in the coherence images: this effect is due to the scarce penetration of C band radiation in the vegetated canopy, so that small variations of the positions of leaves and smaller branches were enough to change the disposition of the scatterers and therefore practically annihilate coherence; likewise happens for water bodies, that appear always with negligible coherence. In [17, 23, 22] it was also observed that cultivated field changed their coherence after plowing, harvesting etc., so that it was possible to detect anthropogenic effects in multitemporal sequences of takes of the same area, by looking at sudden coherence losses. In general, the combination of multitemporal observation both of detected images and coherence allows a very good segmentation of agricultural areas; it is thus possible to identify cultures (potatoes are harvested in that month, whereas corn matures in that other ..). Other authors [21] observe that from the phase of the interferometric takes the height of the trees and therefore the biomass can be estimated.

9. Conclusions

In this overview, we have seen that interferometry is speckle free, since its effect disappears from the differential phase. Further, we have seen that the fringes, given the short revisiting times of the TANDEM mission, may give a very good DEM, with a vertical resolution that could be in the tens of meters range, using the combination of several passes to combat atmospheric effects. Millimetric motion of large areas of the terrain or of corner reflectors have been measured with good reliability and therefore the possibility of using the system to measure subsidence, landslides, coseismic motion has been demonstrated. However, several conditions have to be met, the most important being the maintenance of some coherence of the scatterers during the entire experience. This is possible in the case of exposed rocks, but in other cases artificial reflectors may be needed to link together scattering structures that may change due to vegetation, floods, storms, etc. Coherence is an important clue, that combined with the more usual backscatter amplitude, leads to high quality images segmentation. The combination of multiple images will improve resolution.

References

[1] Carnec, C. Interferometrie SAR differentielle, Application à la detection des mouvements du terrain, Thèse de doctorat de l'Université de Paris 7, 1996.

[2] Dixon, T., Editor, SAR Interferometry and Surface Change Detection, 1994, Report of the Workshop in Boulder, February 3 and 4, 1994, http://southport.jpl.nasa.gov/ scienceapps/dixon/index.html

[3] Ferretti A., Prati C., Rocca F., Monti Guarnieri A. "Multibaseline SAR Interferometry for automatic DEM reconstruction" Proc. 3rd ERS Symposium - Florence 1997 - http://florence97.ers-symposium.org/

[4] Gabriel A.K., Goldstein R.M., Zebker H.A., Mapping small elevation changes over large areas: differential radar interferometry , J.G.R., Vol.94, N.B7, July 1989, pp.9183-9191.

[5] Gatelli F., Monti Guarnieri A., Parizzi F., Pasquali P., Prati C., Rocca F., 1994, Use of the spectral shift in SAR interferometry: applications to ERS-1, IEEE Trans. on GARS, Vol. 32 , No 4, July 1994, pp.855-865.

[6] Giani M., Prati C., Rocca F., 1992, "SAR interferometry and its applications", ESA report N.8928/90/F/BZ.

[7] Goldstein R.M., Zebker H.A., Werner C.L., 1988, Satellite radar interferometry: Two-dimensional phase unwrapping, Radio Science, Vol.23, N.4, pp. 713-720.

[8] Goldstein R.M., Engelhardt H., Kamb B., Frolich R.M., "Satellite radar interferometry for monitoring ice-sheet motion: Application to an Antarctic ice stream" Science, Vol. 262, p.1525, 1993.

[9] Hartl Ph., Reich M., Thiel K., Xia Y., SAR Interferometry applying ERS-1 - Some preliminary test results, Proc. First ERS-1 Symposium, Cannes, 4-6 November 1992, pp. 219-222.

[10] Massonnet D. et al., The Displacement Field of the Landers Earthquake Mapped by Radar Interferometry, Nature, Vol.364, July 8, 1993, pp.138-142.

[11] Massonnet, D., Briole, and A. Arnaud, 1995, Deflation of Mount Etna monitored by space radar interferometry. Nature, Vol. 375, pp. 567 - 570.

[12] Monti Guarnieri A., Parizzi F., Pasquali P., Prati C., Rocca F., Developments in ERS-1 SAR interferometry, Proc. of 1st Workshop FRINGE, ESA-ESRIN, Frascati, 12 Ottobre 1992.

[13] Pasquali P., Pellegrini R., Prati C., Rocca F., "Combination of Interferograms from Ascending and Descending Orbits" IGARSS 94 - Pasadena, California USA - p. 733-735.

[14] Prati C., Rocca F., Monti Guarnieri A., Damonti E., 1990, Seismic migration for SAR focusing: Interferometrical applications, IEEE Transactions on GARS, Vol.28, N.4, pp.627-640.

[15] Prati C., Rocca F., Monti Guarnieri A., SAR interferometry experiments with ERS-1, Proc. First ERS-1 Symposium, Cannes, 4-6 November 1992, pp. 211-218.

[16] Prati C., Rocca F., 1993, Improving resolution of stationary objects with multiple SAR surveys, IEEE Transactions on AES, Vol. 29, No.1, 135-144

[17] Prati C., Rocca F., Monti Guarnieri A., 1994, Topographic Capabilities of SAR exemplified with ERS-1, Geo-Information-Systems, Vol. 7, No.1, February 1994, pp.17-22.

[18] Rodriguez E., Martin J.M., 1992, Theory and design of interferometric synthetic aperture radars, IEE Proceedings-F, Vol.139, No.2, pp.147-159.

[19] Spagnolini U., 1993, 2-D Phase Unwrapping and Phase Aliasing, Geophysics, Vol.58, N.9, pp.1324-1334.

[20] Tarayre H., 1996, Extraction de modele numeriques de terrain par interferometrie radar satellitaire: algorithmie et artefacts atmospheriques, These de doctoeur de l'I. N. Polytechnique de Toulouse.

[21] Ulander L. M. H., Dammert, P. B. G., Hagberg, J. O., 1995, Measuring tree height using ERS - 1 SAR Interferometry, Proc. IGARSS 1995, Florence, Italy.pp 2189-2191, 1995c.

[22] Wegmueller U., and Werner C. L., 1995, Farmland monitoring with SAR interferometry, Proc. IGARSS 1995, Florence, Italy. pp. 544 - 546, 1995b.

[23] Werner C., Hensley S., Goldstein R.M., Rosen P.A., Zebker H.A., Techniques and applications of SAR interferometry for ERS-1: Topographic mapping, change detection, and slope measurement, Proc. First ERS-1 Symposium, Cannes, 4-6 November 1992, pp. 205-210.

[24] Zebker, H. Goldstein R., 1986, Topographic Mapping from SAR Observation, Journal of Geophysical Research, Vol. 911, pp. 4993 - 4999.

[25] Howard A. Zebker, Paul A. Rosen "Atmospheric Artifacts in Interferometric SAR Surface Deformation and Topographic Maps" Submitted to J.Geophys.Res.- Solid Earth - http://www-ee.Stanford.EDU:80/~zebker/

Symposium Summary Report

Symposium Report

From 17 to 21 March 1997, the ESA Directorate for Observation of the Earth and its Environment held its Third ERS Symposium. This event – following similar ones in Cannes in 1992 and Hamburg in 1993 – marked a milestone in the evolution of ERS data exploitation. The large number of attendees (some 700) from 35 countries representing the full range of Earth observation data users from scientific, operational, institutional and commercial entities, demonstrated the wide interest in ERS data. The good atmosphere of the Conference was proof of the well established co-operation between all user groups and the Agency.

The outstanding quality of the 420 presented contributions reflected the evolution from instrument and performance validation and very general utilisation plans in the 1991-92 timeframe over the era of familiarisation with the data, algorithm and the product tuning in 1993-94 up to the real exploitation of ERS data in all areas of EO application.

Six years after the launch of ERS-1, that is, earlier than most previous EO missions, the ERS mission has started to reach its 'real exploitation phase' and, accordingly, the focus of most projects and presentations has turned back from technology to the real application.

Scientific work is ongoing to integrate Altimeter and Scatterometer data for land applications. This is just one example for newly emerging applications of these which were not foreseen during definition of the mission and designing of the instruments. Nevertheless instrument validation and improvement of algorithms and products will continue in parallel to the exploitation of the data.

The 32 Sessions were organised by application subject – not by instrument utilisation as in previous Symposia – and covered subjects such as Land Use, Forestry, Geology, Hazards, Global Change including the monitoring of polar ice caps, sea ice, glaciers, oceanography, sea-surface temperature, the assimilation of Wind and Wave data, Ocean Circulation, Marine Geoid and Meteorology.

The Symposium for the first time included some 30 contributions on monitoring of the Atmosphere using the only new instrument on ERS-2: GOME. It has been demonstrated that in addition to the trace gases ozone and nitrogen-dioxide, GOME also provides information on minor trace gases like BrO and OClO.

Summary of Thematic Sessions

Soil Moisture

A sound theoretical basis has been established for the use of radar backscattering data from C-band SAR and scatterometers for the estimation of soil moisture. A soil moisture retrieval strategy, based on a log-linear relationship, has been developed for the use of ERS data taking into account the limitations introduced by surface canopy and surface roughness effects.

Operational applications were demonstrated over desert areas with stable roughness and over areas with sparse vegetation. Regional correction algorithms for roughness and vegetation effects were developed.

Interferometric coherence is used to delineate dielectric (soil moisture & freezing) and roughness effects. This technique requires short revisit times such as during the three-day repeat orbit and the ERS-1/ERS-2 tandem mission.

New information was presented on the monitoring of thawing/freezing phenomena by large-scale observations with high temporal resolution using the scatterometer. Archived tandem data shall be further exploited and further tandem acquisitions should be considered.

Hydrology

The entire session was devoted to the use of ERS SAR data. SAR was demonstrated as an established tool for flood monitoring. Flooding causes sufficient image contrast for reliable detection and mapping of flooded areas without applying complex retrieval algorithms. By fortunate coincidence of the ERS overpass and the flooding event it was shown that SAR actually can see the flood wave in a river.

A reliable relationship between radar backscattering and accumulated rainfall in a region was established. ERS SAR data are being assimilated in hydrological models through soil moisture estimation derived from radar backscattering.

ERS SAR images clearly show human impact (road construction) in environmentally sensitive areas and SAR is used as an operational tool to design counter measures against these impacts. Planned future studies on the use of phase information (interferometry) and on rain effects need ERS tandem data. Limitations in this application are due to the long acquisition repeat cycle i.e. 35 days.

Land Use

Within the MARS project framework, former studies have already demonstrated the capability of ERS SAR data to drive early crop estimates. New methodologies aiming at the improvement of the system have been presented.

- A colour-coded classified product is generated by the combination of 4 optimal acquisitions of ERS data during the winter and the spring seasons. Eight distinct classes of crops are discriminated with 80% of accuracy for winter combinations.
- The integration of ancillary data such as agricultural practices, meteorological data and soil types into a structured and coherent database has been tested. It allows the analysis of crop effect on the backscatter, the planning of satellite acquisitions and queries at a site and point level.
- A crop information system has been successfully developed and used over MARS test sites in UK, integrating ancillary data and satellite data for agriculture monitoring and production of agricultural statistics. This automatic system can be further customised for specific needs, as has been done for the Ministry of Agriculture in Paraguay.

The ERS capabilities to monitor specific crops is still investigated:

- The row direction of the maize cultivation was modelled and correlated to the radar backscatter. The discrimination between physiological stages was shown and extend to other crops.
- The production of composite ERS SAR images from change index maps allowed the discrimination of different rice cultivated systems but the validation of results still needs to be done.
- The mapping of agricultural and non agricultural areas from ERS SAR data has been validated in Senegal, at a regional scale. It was the first spatial presentation of agricultural acreage. Because of the low density of the vegetation and the small size of the fields, it was impossible to discriminate cotton cultivation. Further investigation need to be performed over an intensive cotton production area.

Good correlation between the backscatter and soil moisture for different crops was found when soil moisture is estimated through the Water Deficit Index calculated from NOAA AVHRR data. Further development will be performed using ATSR data.

ERS scatterometer data can also be used to estimate vegetation parameters such as the biomass. A modelling approach has been developed over the Sahel. Extension and validation to other sites in the region will be done as well as the combination of ERS scatterometer data with data from other sensors.

ATSR-2 data have been tested for mapping and monitoring of land cover. The correlation of the vegetation index and the percentage of vegetation is poor, due to the presence of a sparse vegetation. Good correlation was found through a simulation of the bi-dimensional reflectance distribution function of ATSR-2 pixels over dry land surfaces. Further methodological work is still necessary to improve the results.

The second session on Land Use was comprised of 19 presentations and 24 posters. New results were reported on post-processing in applying principal component analysis on multitemporal datasets. The 1st component represents a well despeckled image.

The effect of the incidence angle was discussed: up to 3dB was found as difference between near and far range with respect to corn fields backscatter. In wetland monitoring, the dampening effects of the vegetation was used to improve the classification. For biomass estimations with SAR the importance of comprehensive auxiliary data was stressed. For banana plantation classification SAR was reported to be perfectly adapted with 95% classification accuracy.

A interesting result was reported with ATSR-2: there is a good correlation between these data and geophysical vegetation parameters (temperature, coverage) and also grass-fires could be well detected.

Forestry

As a result of the availability of data from the 3-day repeat cycle of ERS-1 in 1994 and from the ERS-1 and ERS-2 Tandem Mission, several projects/studies in the domain of forestry have made use of interferometric SAR information with promising results.

The recognised limitations of the radar backscattering intensity (in the ERS configuration in particular) for thematic classification have been overcome both for boreal forest and tropical forest through the use of coherence images.

At the same time, the operational perspectives of SAR interferometry techniques for forest inventory issues have been demonstrated in countries like Finland, with a long, consolidated tradition in the utilisation of optical data as a primary source of satellite information. The understanding of the interferometric signature has improved, leading to a much wider set of applications in the domain of forest-related issues.

In contexts like boreal forest fires, the contribution of SAR can be seen rather than in the monitoring phase where AVHRR/ATSR play a major role, in the post-phenomena phase (burned areas assessment), i.e. when the fire signatures observed on SAR imagery are analysed and processed.

For what relates to the complete double coverage over Central Africa made available through the CAMP Project, further interesting developments are in progress, both for thematic applications, processing techniques and extensions to other sensors such as TM or NASDA J-ERS (GRFM Programme by the JRC SAI MTV to pull together a network of interested partners for the CAMP thematic interpretation). This will ensure in the short term a rapid expansion of the original, innovative concept of CAMP, i.e. to serve as a catalogue database for further navigation and information extraction.

As to particular aspects of forestry, the Session has offered the opportunity to consider the application of microwave remote sensing to forest vitality monitoring. Here investigations are based on the information that microwave signatures can provide on one of the main tree components, i.e. water content.

Scientists and Project Leaders need to spend further effort on transferring their most significant findings into easily understandable and applicable concepts for use in an operational context.

Digital Elevation Models (DEMs)

A global DEM has been produced using the ERS Radar altimeter WAP (Waveform Altimeter Product) data from both of the 168-day repeat Geodetic Mission phases. This DEM has been interpolated to a 10-km spacing grid and appears accurate on the metric scale for flat, homogeneous regions with the height error increasing rapidly in areas of rough terrain (local slopes >1 deg). Nevertheless, this DEM represents the most accurate source of topographic information today for many areas of the world (e.g. parts of S-America and the Polar Ice Sheets). A full validation of the accuracy of this global DEM is in progress.

The detailed characteristics of the RA waveform returns indicate the possibility to distinguish specific types of waveform that are related to the type of land surface involved.

Regarding the generation of high (spatial) resolution DEMs from SAR interferometry, progress has been made in the development of an automatic technique to generate the best consensus DEM from a number of ERS Tandem acquisitions, typically 5/6 pairs. This technique removes DEM outliners due to variations in the atmospheric conditions between acquisitions. The technique generates a DEM error map, with expected rms errors in the range of about 5m. The method has been applied to the test areas of Vesuvius and Etna in Italy, and first validations of the consensus DEM accuracy lead to figures of under 10 m rms, possibly due to errors in the reference DEMs used to perform the validation. Maps of the topographic error due to the atmosphere can be generated by differencing the consensus DEM with a single-pair DEM.

The fusion of DEMs from ascending and descending passes of the same area shows a clear improvement in the combined DEM quality by filling in layover and shadow regions and reducing height error by half (from 20 to 10 m rms) even outside these regions. This analysis was performed on 3-day and 35-day repeat data for Catalunya in Spain. A corresponding analysis of Tandem data for the same region is in progress.

Several applications related uses of ERS DEMs generated by SAR interferometry were presented, including:

- Ice-mass balance determination in E. Greenland
- Climatic change history through the tilting and orientation of alluvial fans
- Coastal uplift & inland subsidence associated with tectonic movements in Chile,
- Volcanic subsidence through 3-year ERS differential INSAR in California.

Geology

6 papers and 4 posters were presented. Traditional geological mapping techniques on SAR imagery have been further developed, emphasising especially the information enhancement using ERS-SAR stereopairs, through image-summation to improve significantly the spatial resolution, as well as by applying optical/microwave merges. It can be considered now as a matured and well established application. SAR data integration into a GIS environment has also be successfully achieved, whereas SAR is considered to contribute more to local mapping in contrast to LANDSAT TM used for regional geological evaluations.

Successful applications of SAR interferometry were reported for Siberian Pipeline Track monitoring and land subsidence measurements. The last one has reached commercial exploitation in the US for oil-well environment monitoring, despite the fact that the 35-day repeat cycle is too large for some of the earth movements to be observed.

Hazards

17 papers and 15 posters were presented. In 20 papers out of 32, the use of interferometric techniques were reported. The subject most frequently treated was tectonics (8) followed by volcanoes (6) and floods (4).

In using ERS-SAR imagery, accurate mapping for geological applications and for floods was reported. The volcanic eruption in Iceland has turned out to be an attractive testbed for fast response from ERS SAR interferometry. To meet the user community's requirements ESA decided at short notice to operate both satellites again for a short period of time. But also Etna remains in the centre of the attention: after having demonstrated that the whole mountain was subsiding after the most recent eruption, now also local deformations due to the weight of recent lavaflow has been observed.

With respect to tectonic movements, the creeping along the San Andreas fault could be astonishingly well mapped and quantified, and the dangerously locked part of the fault identified. Observations are also ongoing both in the Chilean Desert, comparing GPS and SAR interferometry successfully; and also in an earthquake prone zone of Southern Italy.

For land subsidence measurements e.g. in coal mining areas, using again differential interferometry the data applications are close to operational. The problems caused by atmospheric effects could largely be overcome by using multiple datasets.

For flood monitoring, the introduction of GIS is proposed in order to get information also in urbanised areas and in forests. For the mapping of flooded areas in Siberia the coherence between two acquisitions were used to improve the image content of multitemporal datasets.

ATSR has also been identified and proposed to monitor globally volcanic activities by using the 1.6 μm band on night-passes. Both the building-up of the temperature prior to the eruption and also post-vents such as the characteristics of the cooling of lava could be detected on volcanos in different parts of the world.

The second part of the session on Hazards included, among other, issues covering ground deformations caused by earthquakes or volcano activity, use of ERS-1/ERS-2 SAR interferometry and differential interferometry products in studies in seismic areas, joint ERS SAR and SIR-C use for seismic risk analysis. It appeared that most of the achievements were obtained through the experimental, combined use of all possible sources like GPS, DEMs, SIR-C, ERS INSAR and Tandem data.

New fields of investigation in the domain of hazards include measurements of elevation changes deriving from mining activities with the contribution of SAR interferometry.

The economic interest in minimising the damage at surface is likely to push these types of application towards further development.

Along the way to pre-operational demonstration projects in flooding it has to be remarked that some limitations in the use of SAR still exist. These are represented by the fact that in some instances only a static detection at a given date is possible if the flood peak is missed due to the data acquisition constraints.

The Tandem coherence images may give the additional information necessary to optain sufficient classification accuracy as demonstrated in the case of Beziers floods in Southern France.

GOME

Instrument performance, calibration, processing

In general, the instrument is showing an excellent performance and stability. The diffuser, essential element in the radiometric calibration path, is showing within the signal-to-noise limit of the method no sign of degradation. The change in radiometric response detected early in the programme and believed to be due to coating off-gassing could in principle be confirmed to the Gobelin measurements with the GOME BBM. Increase of dark current and noise due to accumulated radiation is within the range of expectation and does not have a significant impact on the quality of the measurements. Internal straylight levels are low and therefore hard to quantify. Further improvements are necessary for the wavelength calibration, in particular in those regions of the spectrum in which the calibration lamp provides only few, weak or uncomfortably distributed lines. Use of Fraunhofer lines to improve the wavelength registration has been demonstrated to work in principle.

For most of the identified problems, solutions have been implemented in the GOME data processor, which otherwise works routinely and stable.

GOME Level 1 Product

GOME sun spectra are in good agreement with UARS/Solstice measurements.
Better than 10% in Channel 1.
Better than 4% in Channels 2-4
GOME measurements have a very low noise which allows MgII index calculation to monitor solar variability.

GOME Level 2 Product (Other than O_3 and NO_2)
Non Official Products
GOME demonstrated the capability to measure trace gasses in the troposphere beside O_3 and NO_2:
SO_2 was measured in the troposphere during a volcanic eruption in Africa
B_rO can be measured on global scale in the troposphere and stratosphere.
OCLO can be measured in the stratosphere during pre-ozone hole conditions
HCHO was measured during biomass burning events over Africa and over the cities Los Angeles and Mainz. HCHO is an important species in the oxidation process in the troposphere.

Aerosols could be retrieved mainly over sea with some preliminary data over land (especially desert). Surface reflectance: albedo in the visible can be retrieved to be used for climate models (ground pixel size of 40x80 km). The Polarisation Measurement Devices are useful to get information about cloud cover which is important for the retrieval and studies of trace gases. Good spectroscopy data (measured in laboratories) are needed to improve the accuracy of the retrieval of trace gasses.

UV and visible radiance/irradiance of Earth/Sun/Moon
The high precision of the solar irradiance measurements enables the derivation of MgII indices for the characterisation of solar activity. The observed long term drift in the irradiance measurements over several months might only in part be a true instrument degradation (at least for the UV regions, but this was expected) but might be caused by other effects. Work to pin down the real cause is in progress, but has to rely on further long term observations. The use of moon calibration data, limited by the moon visibility and the complicated evaluation process, may be of help on the long term to distinguish possible causes.

Total Ozone Column
Comparisons of GOME derived total ozone columns with ground based measurements performed by various networks (Dobson, Brewer, SAOZ, NDSC) show good agreement at mid-latitudes but various biases at other regions and solar zenith angles. This is confirmed by processing GOME data with an adapted TOMS algorithm. The main reasons for that have been identified to be the climatology used to calculate the air mass factors, and a wrong slit function for the convolution of the oxygen reference spectrum, leading to systematically too high fractional cloud measurements and air mass factor computations. Work to compute new air mass factor tables to overcome this problem is I progress.

The precision of the derived ozone values is excellent: from the assimilation of total ozone values into global advection models, and comparison of the advected with the true distribution, a precision of better than 2% could be quantified.

Ozone Profiles
Several groups could demonstrate the potential to retrieve ozone profiles from the GOME data. The novelty is that, because of the extended wavelength range, the range could be extended into the troposphere down to ground level. Comparison with MLS and Ozone sonde data show, within the resolution of the method, good agreement.

Aerosol, Surface reflectivity and Clouds
Various groups report initial success in attempts to derive aerosol amounts and classifications from the GOME data. The results of intercomparison of GOME derived cloud cover with independent data sources (ATSR-2, METEOSAT) confirms the overestimation of fractional cloud cover (see paragraph on total ozone column)). Use of the polarisation detectors by means of sub-pixel RGB indices improves on the accuracy of cloud detection. The spectral range of the GOME instrument enables interesting studies of reflectivity, albedo, and polarisation properties of surfaces and clouds.

Conclusion
The data provided by GOME instrument in general stand up to the high expectations. Further improvements and additions are necessary for the ground segment to fully exploit the potential.

Atmosphere using ATSR, PRARE and GOME data in synergy

Aerosols play a very important role in the atmosphere studies, climate effect and satellite measurement. During this session it has been demonstrated that the use of satellite data provides very useful (and unique) information about aerosol. The combined use of ATSR-2 visible and NIR and GOME allow the derive the aerosol mixture and the UV-B fluxes.

In complement, the double view capacity and the brightness temperature of ATSR-2 give the possibility to detect aerosol concentration both in terms of quantity and quality. This result was validated with volcano aerosol after the Pinatubo eruption and with Sahara dust detection.

The ATSR-2 visible and NIR channels provide the capacity of determining the optical depth, the size and shape of cirrus cloud crystals. Thanks to the stereoscopic ability of ATSR-2, it is possible to determine, with an error margin of 3 km, the height of the clouds and top temperature using the thermal channel.

A more complete study of cloud detection has been made and its results have been incorporated in the operational ATSR processor, providing a more reliable SST retrieval.

A on-going study demonstrates the interest in using ATSR-2 for deriving sea-land-atmosphere heat fluxes. This parameter is very important for climate study and again satellite data is a powerful tool at regional and global scale for measuring this flux.

PRARE, through a network of stations, gives information about the orbit determination, the ionospheric connection and the total electron content. There are plans to include PRARE in ERS-2 altimeter data and to generate and distribute PRARE data in 1997.

Finally, a study for coupling passive and active microwave measurement has been presented. Satellites like ERS and Topex carry both radiometer and altimeter instruments. Even if the emisivity and reflectivity are dependent, the calibration is made independently and apparently there is an incompatibility between the two calibrations. There could be a way to calibrate the altimeter using the radiometer. (The connection to be applied seems to be a linear connection of about 2dB).

The satellite data appear to be very useful for atmosphere study (aerosol, cloud, ionosphere, heat flux). The combined use of instrument data (ATSR/GOME, radiometer/altimeter) seems to improve our knowledge about atmosphere features.

Ice Properties and Ice Sheet Topography

The physical interaction of the instrument signal with the ground target is being understood to a degree where applicative use of the data is feasible.

The different instruments of ERS are strengthening each others' findings through measurement of physical phenomena by different observation techniques.

Scatterometer

- Routine derivation of sea ice parameters, free distribution to users
- Some physical phenomena can be observed over ice shelves
    - predominant wind directions (tentative)
    - melt signatures
    - percolation line

Altimeter

- Calibration of signal for extraction of DEM is advancing fast, and is currently at a level where applicative use of DEM is feasible. ~1m height accuracy RMS for gentle slopes, somehow less accurate for steeper slopes, but here further improvements through pulse analysis is feasible.
- The derived DEM has numerous applications linked to glaciological studies. Science can now be done at a global ice shelf scale. New features have been identified and are being studied more closely with complementary techniques.

SAR Detected Image

- Physical understanding of interaction with snow/ice is being derived through in-situ measurements and modelling.
- Feature tracking has been established as a tool for movement monitoring, but cross calibration with optical data remains.
- Snow cover monitoring is feasible if ground cover knowledge is sufficient to allow removal from signal.

SAR Interferometry

- Discharge measurements at grounding line are radically changing the estimates of ice discharge from Greenland Ice Shelf. This may become a serious contribution from ERS to global change studies. Ref: Presentation by E Rignot, JPL.

Sea Ice

A total of 9 papers were presented during this session. The Nansen Center, Bergen, Norway presented a report on operational use of radar data within the Icewatch project. Some concerns about practical constraints were expressed by the audience, but it was agreed about the importance of remote sensing data for operational ice monitoring.

This first presentation also pointed out the high value of synergistic use of RS data which was underlined by a paper from M Shokr about sea ice studies within the Canadian ice monitoring program. This work and the talk of P Nielsen about mapping of sea ice around Greenland gave some details about first experiences with Radarsat images for sea ice research in comparison with ERS SAR. Several case studies with more or less comprehensive in situ measurements have been presented. Two papers about Antarctic sea ice conditions from M Garcia and V Lytle and a detailed work about Arctic leads by R G Onstott.

Two papers came up with new techniques of using SAR data for sea ice research. P Dammert reports about a first try to use interferometry for ice movement detection. S Leher closes the session with a presentation of an interesting method to use the complex SAR data to retrieve short time (<1 sec) dynamical features of ocean waves and sea ice.

Ice Dynamics

ERS-1/2 3-day repeat and Tandem SAR data has been successfully used through a combination of ascending and descending acquisitions to separate and measure, with high accuracy, the surface topography and the 3-D ice motion vectors for many large ice flows and glaciers using the technique of SAR interferometry. Outstanding results have been obtained for many areas in Greenland, Alaska and Canada. Surface topography agrees with laser altimetric and GPS data to less then 10 m rms. Ice velocity directions are accurate to within a few degrees and speeds are as good as available in-situ data. When combined with measurements of ice thickness from radar sounding campaigns, this new information on ice dynamics allows reliable computation of ice flux and discharges to be made, that appear to be three times bigger than conventional estimates made by observing iceberg calving. Less spectacular results have been achieved for inland areas in Antarctica and Patagonia, mainly due to strong wind affects causing a loss in surface coherence due to the local summer conditions. Clear evidence of phase corruption due to a change in atmospheric conditions has been observed in the arctic. The origin of this effect is unknown, but when present it can significantly effect the accuracy of retrieved topography and ice motion. This area requires further investigation. In addition, work is in progress to model the complex process due to backscattering at depths of the order of meters in permanently dry snow zones. If successful, this approach may allow the measurement of additional snow parameters from SAR interferometry.

ERS Scatterometer has been used to generate long timescale (yearly) sequences of normalised radar backscatter for the entire Antarctic continent. Further analysis will link with a surface map from the ERS altimeter. This time series demonstrates clearly the large-scale variations in surface snow melt conditions, with a strong snow melt in the summer of 91/92 observed. Cooler (low melt) conditions in following summers, possibly connected with the eruption of Mt Pinutubo, return to normal melt 1995/96 - 96/97.

In addition, several large icebergs have been tracked calving and circulating around Antarctica, providing valuable information on ocean currents and first measure of erosion of icebergs with time using active microwave instrument. The high spatial resolution of information regarding topography and ice velocity provided by SAR interferometry provides an unprecedented opportunity to understand the dynamics of ice flows and glaciers allowing further insight into discharge and surge processes. Further Tandem acquisitions are strongly recommended to fully understand the evolution of ice dynamical processes.

Coastal Zones, Ocean Dynamics and Features

For coastal zone application we are now seeing the architecture of Shallow Water Bathymetry, wetland and river delta operational system in which SAR images play an important role. In shallow waters (< 30 m) where the current exceeds about 1 knot (0.5 m/s) the surface expression related to bottom topographic features such as sand banks and channels are clearly found. As such it provides a powerful data source for monitoring shallow water conditions (complemented with traditional depth soundings from ships). This information is important in navigation safety. River outflow and plume advection from major rivers are also expressed in SAR images with different characteristics during the tidal cycles. It is demonstrated that the details of these observations make it a valuable data source for validation of high resolution models of river outflow interaction with coastal currents.

SAR imaging of oceanic fronts, eddies, natural film and atmospheric boundary layer conditions and wind speed have advanced to a point where we now see more and more quantitative interpretations. In particular, wind speed estimates are derived from SAR images with very good agreement to in-situ observations suggesting promising capabilities in coastal regions where the wind field can undergo rapid changes as influenced by the land-ocean boundary. Moreover, characteristic SAR image expressions of fronts and eddies agree well with conceptual radar backscatter models suggesting that both current shear and convergence pattern can be obtained from the images. This combined with the SAR imaging of surface film (and oil spill) demonstrates new and promising retrieval capabilities for process studies in the upper ocean and atmospheric boundary layer.

Global Change

Seven papers were presented in a session which covered both regional and global aspects of climate change. Data from the ATSR, SAR, altimeter and scatterometer were used, together with additional data from TOPEX-Poseidon and NSCAT, in the analysis of climate processes.

Three papers related to the role of the Antarctic region provided significant scientific results. The first used scatterometer data (ERS and NSCAT) to measure variations in sea ice extent which was then used to characterise the pathway provided by Antarctic sea ice in connection with ENSO and monsoon events. In addition, sea ice variations were linked to the production and outflow of Antarctic bottom water and hence to thermohaline circulation. A second presentation used SAR data to characterise the extent of glaciers in regions of the Antarctic where the environment was close to the crucial point for glacier preservation. Such glaciers are extremely sensitive indicators of local warming and SAR data were found to be an effective tool for their monitoring.

Radar altimeter data were used to deduce that there was no secular variation in ice sheet elevation of the Antarctic. The climatic implications of this null trend in elevation were entirely dependent on the spatial correlation of temporal fluctuations in mass and density of the ice which require some 10, 20 or 100 year time series of measurements in order to be properly characterised. It is possible, however, that the altimeter time series can be used to reduce uncertainties in the mass balance from 400 GT/year to 85 GT/year.

Three presentations were also made regarding ATSR data.
A characterisation of surface fluxes at a number of test sites in Australia was presented and the excellent agreement of ATSR and ground based radiometers was emphasised, leading to a quantification of short wave surface flux in clear sky conditions of better than 10 W/M^2 broadband. The long-wave component of the surface flux was more problematic however.

Another result with implications for global models concerns the use of global SST values in climate models. A presentation from UKMO described an attempt to reduce the level of variability between ATSR measured skin temperatures and buoy measurements of bulk temperatures as a preliminary task prior to global conversion of all ATSR SST measurements to bulk temperatures for use in a climate database. Unfortunately, the skin to bulk temperature conversion remains unsolved.

As a conclusion, we are now starting to see the benefits of a continuous time series of ERS observations for global change analysis. It was pointed out however, that even the current time series is not sufficient and more measurements are required.

Winds

Operational Assimilation of scatterometer winds started in several European Meteorological Centres during the last two years, in particular with the availability of three-dimensional variational techniques which provide an appropriate solution to the ambiguity removal problem. The assimilation of scatterometer winds using this technique gives a clear improvement of the analysed and first guess surface winds, as well as in the short range forecasts, in particular in the southern hemisphere.

Four-dimensional variational methods were shown to give better analyses and forecasts, in particular with the inclusion of scatterometer winds, as this technique gives a better vertical projection of the surface information.

Tandem ERS scatterometer assimilation shows that data coverage (only one swath) is the main limitation.

Along with this major theme, four other aspects are being developed.

Climatology
Long term wind atlases have been generated through collocation of ERS data with other data sets such as in-situ buoy data, analysis, and other instruments (for example Nscat).

Wind comparison
Various methods and strategies have been developed to compare and validate different data sets, for example comparison in the spectral domain or triple collocations.

These new methods allow an estimation of errors in each observation system, which is important information for the use of the data to derive fluxes of momentum, humidity or heat, or to drive ocean waves or circulation models.

Wind direction ambiguity removal
Variants of Variational methods have been developed to improve the ambiguity removal method which remains the main problem when the scatterometer data are directly used in an application. This problem is largely solved by manual intervention and for automatic ambiguity removal, variational techniques are most satisfactory.

This is an important subject to be investigated in order to promote the direct use of wind products.

Use of SAR images for mesoscale wind analysis
SAR images give access to small scale features in the wind structure, in particular close to the coast. This information is very useful to validate mesoscale atmospheric models, which are becoming more and more common. The correction for the derivation of wind direction remains a problem.

Waves

During recent years, operational assimilation data systems have been developed in order to allow the integration of ERS data into wave prediction models. it is proved that this integration presents overall positive results. However, in order to get full advantage of the information contained in SAR wave products and to eliminate differences which can be identified when comparing real data with the wave models, further improvement is needed in the SAR and RA wave products themselves and in the assimilation models.

In addition, new applications are appearing, like the wave period calculation by using RA data or the analysis of long-term trends in global wave climate.

The possibility of using SAR Wave data in order to retrieve wind speed information or as a high-resolution scatterometer is being analysed. All these improvements are complemented by new data exploitation techniques, such as neural networks.

Sea-Surface Temperature

Six papers were presented in this session, all involving the ATSR. The first three concentrated on the use of the ATSR for describing marine processes, while the latter three were investigations of the synergy between ATSR and m-wave measurements in the retrieval of oceanographic information. One of the main results (highlighted in two papers) was the confirmation of a correlation between SSH and SST variations using the ATSR and radar altimeter. The maximum correlation was shown to occur for areas where mesoscale activity is high, something supported by the fact that the wavelength where this maximum correlation occurs is of the order of 600-800 km.

The tandem phase allowed the joint use of the ERS SAR and ATSR instruments to observe the same ocean features with a delay of only 30 minutes. Although searches through the data archives were impeded to a certain degree by the lack of browse ATSR data frontal structures were observed a number of times in the North Atlantic by both instruments. In addition, bathymetric structure in the southern North Sea was observed in both SAR imagery and ATSR-2 visible channels. Some features were more prominent in one sensor than the other (and vice versa) suggesting there is scope for further useful work.

A further result of interest to the oceanographic community concerned the analysis of the bi-modality of the Kuroshio extension current using ATSR SST data and CDT measurements. Additional SST measurements off the coast of Peru, together with UKUO analysis fields showed that the direct current mode coincides with wind stress anomalies east of the Philippines and SST anomalies in the equatorial Pacific.

Two other papers were presented on the ATSR. This confirmed the assumption made in the processing chain that the emissivity of the sea surface remains unchanged as the wind speed increased. The effect of foam remains to be investigated. The second paper demonstrated the possibility of using the visible channels of ATSR-2 to study phytoplankton dynamics in Lake Ontario. This paper showed that ATSR-2 does indeed have potential in this area despite the fact that the gains and wavelengths were optimised for land applications.

Several speakers had made use of the ATSR ASST product (available for research purposes on CD-ROM from RAL) which is very well suited to the study of mesoscale and larger scale phenomena.

Ocean Circulation

The ocean circulation session hosted many regional applications, half of which based in the Mediterranean Sea. Most results were based on merged Topex-Poseidon and ERS altimetric data, often using Letraon-AVISO's Sea Level Anomaly dataset. It was clearly established that complementary datasets of at least two satellites are required to monitor ocean circulation. Low-energy mesoscale features are now resolved in the Mediterranean Sea.

Altimetry

Good ERS radar altimeter data sets now exist and are being widely used. The Geophysical Data Records have reached a high level of maturity. It was stressed by the participants that they would like ESA to reprocess all the past geophysical records to the highest level of quality, thus ensuring homogeneity of the long time series of ERS-1 and ERS-2.

Finally, the work on the ERS-2 Radar Altimeter and Microwave Radiometer calibration was reported and various absolute calibration methods involving tide gauges and transponders were presented as well as some plan for Envisat calibration.

Marine Geoid

The availability of the ERS-1 geodetic phase data led to the full declassification of the Geosat Geodetic Mission data, making thus available a complete dataset covering the earth surface very densely. The geoid could hence be determined with the unprecedented resolution of a few kilometres. The gravity-field anomalies have also been mapped with the same resolution, revealing features unknown so far, and the seafloor topography could also be inferred. The detailed knowledge of the mean sea surface and the existence of a long altimetric time series have generated also a new potential application: sea level change detection, which would be a major step in the knowledge of the environment. This application requires an instrumental accuracy and stability around two orders of magnitude better than specified, but this is not unachievable.

Finally, the general feeling of the community is that the results of these studies could be of interest to other groups, and in this perspective it would be advisable to gather the various models concerning delta-g, geoid, mean sea surface and seafloor topography on a CD and make it available to the public for promotion.

Meteorology

The meteorological session consisted of six presentations and one poster. The authors have been working with all active ERS Sensors, but mainly with the scatterometer. Data assimilation aspects were not included in the session. Most meteorological users are now exploring the possibility of using scatterometer information to explore phenomena which are missed by numerical models due to a coarse resolution. This is the case for the airflow changes induced by mountainous islands. A methodology has been developed for New Zealand. The scatterometer can also depict katabatic winds over a polynya and surface circulation of Antarctic mesocyclones. The latter applications suffer from problems related to the dealising, which may be wrong due to erroneous analyses in data sparse areas. Other better known meteorological use of the scatterometer refer to the following of typhoons, investigations of monsoons and El Nino as well as rainfall estimate.

The work related to the use of SAR images concentrates mainly in the tropical rain cells, whose structure can be related to SAR signatures: gust from, convergence zone, downdraft area and associated rainfall. Finally, a model has been proposed to prove the use of the ERS radar altimeter to infer rain rate as this dampens the microwave signal. A general recommendation from this session was that a further exploitation of synergy between SAR and scatterometer was needed. The availability of NSCAT was also welcome, as it complements nicely ERS scatterometer coverage, especially in areas where SAR is frequently used.

ATSR Instrument Performance

ATSR-1, after 5 years of operation, is still able to provide data of good quality, better than AVHRR. After the anomaly of ATSR-2, from December 95 to July 96, ATSR-2 is now fully operational. All the parameters indicate a very good stability and good quality, better than ATSR-1. The on-board visible calibration system works well and in situ observations yield drift less than 1.7% per year for the visible channel. In situ experiments, like the Mutsu Bay experiment, have allowed the validation of the SST. The results found give an accuracy of about 0.3°C, which was initially requested by the climate user community.

Orbits

The PRARE instrument works very well, and the network of PRARE stations covers both hemispheres. PRARE shows up as a very good system for precision fast-delivery orbits. The initial precision of the ERS-1 precise orbits was around 50 cm. The orbit has now reached the unprecedented radial accuracy of 7-8 cm, due to the recent improvements in the gravity models, which were based on the altimeter measurements during the geodetic phase.

Furthermore, today's work demonstrates the use of ERS tailored models and the use of simultaneous determination of ERS and Topex orbits through dual crossover analysis. This reduces the error to 5 cm, which is better than the basic requirement for global oceanography. Envisat will strongly benefit from theses achievements in the ERS orbit determination and related gravity models.

Envisat Special Session

The special session dedicated to the presentation of the Envisat mission has attracted about 200 participants and consisted in an introduction to the mission objectives, to the payload elements and their individual objectives and to the main mission operation concepts. It was concluded by a special presentation by K. Soerensen of NIRA (Norway) on the application potential of MERIS (Medium-Resolution Imaging Spectrometer), one of the most innovative instruments flying on Envisat.

The Envisat mission, to be launched in 1999, is dedicated primarily to environmental monitoring on local, regional and global scales. The complex payload allows to address issues in the domains of atmospheric chemistry, physical oceanography, marine biology, glaciology and ice processes, coastal processes, land and vegetation studies and climatology. The Envisat payload will also allow the continuation of several measurement series currently provided by ERS: wind speed and wave height, wave spectra, sea-surface temperature, SAR imaging and interferometry. For some of these measurements it will make available, in combination with ERS, continuous measurements over a time frame of 14-15 years.

The same payload will substantially contribute to the monitoring and management of earth resources at local and regional scales. ASAR and MERIS, with their operational flexibility will allow to prefigure future operational mission configurations in support of specific applications. The same instruments will support commercial projects. The whole payload allows to provide support to operational entities in various domains (and with different degrees of readiness): meteorology, environmental monitoring, climate monitoring, sea ice monitoring, navigation, oil pollution monitoring, etc.

The mission will provide the capability to record on board most of the datasets, ensuring a global coverage for all low-rate instruments. High-rate instruments (ASAR and MERIS full resolution) will be acquired by regional stations or through the Artemis data relay satellite, thus ensuring a quasi global coverage. A well defined set of ESA products will be available through several sources, both in near real time and off-line. Co-operation with national facilities of participating states will allow a progressive enlargement of the services proposed to users.

More information is available through Internet (web site through the ESA home page, ESA programmes, Earth observation) and on a brochure distributed at the meeting and available on request from the Mission Management Office, ESA HQ, 8-10 rue Mario Nikis, 75738 Paris CEDEX 15.

Working Sessions

On top of the oral presentations and the poster presentations, working sessions were organised to discuss specific questions.

Atmospheric Artefacts in SAR Interferometry

Variations in atmospheric conditions between repeat pass INSAR lead to spurious signatures in the interferogram. The dominant effects are believed to be due to variations in the tropospheric water content and in the ionospheric electron density. The phase signal is independent on the altitude of ambiguity. When fringes are converted into heights for generation of DEMs the artefacts can add considerable error to the small baseline (large ambiguity) interferograms. With increasing baseline the effects of atmospheric variations decrease, but the fringe unwrapping of the interferogram becomes more challenging at the same time as the common spectrum of the two acquisitions decrease, resulting in lower coherence. The understanding of the artefacts and the techniques which will allow applicative use of the Tandem dataset are still under development. Based mainly on an analysis by ISTAR the status of atmospheric artefacts in ERS SAR interferometry today can be summarized as follows:

Some 10% of the interferograms they have processed over temperate zones (EU, USA) contain localised artefacts (1 to 3 cycles) with spatial scale smaller than 10 km. A low amplitude signal of 1/3 to 1/2 phase cycle is generally present in all interferograms with spatial scale smaller than 50 km.

There is ongoing work in trying to identify a correlation between atmospheric artefacts and tropospheric cloud inhomogeneities through use of IR and visual data collected over the site close in time to the acquisition. If a close correlation is found there is a high probability that identification of acquisitions with optimal conditions can be implemented. The generation of masks for areas with high artefact levels may be possible, and in particular cases it may be possible to derive phase corrections from the auxiliary data. The feasibility of this approach is, however, to be confirmed. Tropospheric artefacts created by air/land interaction have been observed in interferograms. It is a known fact that topography influences the local atmospheric conditions. Examples of such effects are mountains barring the way of cloud systems and creating leeway wakes. The presence of ionospheric artefacts should be most pronounced close to the poles and close to equator. At mid latitudes they should not contribute significantly to the artefacts. The ionospheric phase delay can be measured by GPS ground stations. In areas where the spatial density of such stations is good enough one can generate maps of ionospheric electron density. This can be used to investigate scientifically the link between ionospheric activity and artefacts, but the generalisation of this methodology is precluded by the limited areas with high enough GPS station density.

Modelling of ionospheric activity based upon sunspot activity may be an approach to removal of the large scale ionospheric variations, but the spatial detail of such corrections will probably preclude the possibility of removing the finer variations in the ionospheric clouds. Efforts are being undertaken to establish tools for identification of Tandem pairs with low probability of artefacts. The first approach has been to gather world climatological data and compare the probabilities for cloud cover and precipitation for each month throughout the world with the acquired Tandem dataset. Further work needs to be done to assess the potential of this technique in identifying Tandem acquisitions with low levels of atmospheric artefacts.

Polimi presented a technique for removal of artefacts through the use of multiple interferograms and maximum consensus decision process has been developed. This allows the generation of artefact masks as well as quantitative measurements of the artefacts. The technique currently needs up to 6 interferograms with reasonable coherence and a range of baselines from around 100m to 300m to yield optimised results. With further development it should be possible to limit these somewhat stringent requirements to allow a larger portion of the Tandem dataset to be used in applications requiring artefact removal. The application of this technique in areas where the coherence is good after 35 days is an additional possibility. In this case one can expect larger areas to be covered with data suitable for application purposes.

During the session a range of recommendation were proposed by the participants and commented on by ESA. A second Tandem mission of at least 6 months for acquisition of a higher baseline dataset (the current dataset has baseline in the lower range of the useful spectrum) and for the addition of multiple takes over new areas to allow removal of artefacts through the maximum consensus technique. It was mentioned that for many foreign stations, such a campaign will have to be planned up to 8 months ahead due to the station logistics.

Comment: The addition of a shorter Tandem campaign can be foreseen to fill in holes in the existing coverage. Although there are areas (e.g. in Europe and parts of Northern America) covered today with a large number (>6) of tandem pairs there will only be on average less than 2 pairs covering all land surfaces. The cost in operations, the availability of the receiving stations and lifetime shortening in obtaining 3 to 4 tandem acquisitions over the whole world appears to be prohibitive. If an additional campaign is to be launched it will have to be limited to areas where there is a real market value for a DEM. There is therefore a need to assign market based priorities prior to the planning of such a campaign.

Coherence and phase confidence maps should be made avaible to VACs and users to allow to determine whether a specific area is sufficiently covered with interferometric products to allow the successful derivation of a customer product (DEM). It was suggested that the quick-look prototype demonstrated by ESRIN should be used for this purpose. This interferometric quick-look processor prototype, which was developed by POLIMI and further developed by ACS, is not yet fully operational. It has been however suggested to start up a limited demonstration operation where selected parts of the Tandem archive are processed in cooperation with VACs active in the field.

As an alternative to a new Tandem campaign a 3-day repeat cycle was proposed. This cycle, however, would not allow for global coverage at lower latitudes and would reduce the application potential of some of the Low-Bit Rate instruments.

Observation of Landcover from ATSR Data

The purpose of this session was to discuss the ATSR-2 potential or possible problems for study over land. ATSR-2 presents three features, different from previous existing sensors which should help the land use community:

- Narrow band in visible-NIR: we expect to observe vegetation change with a much better sensitivity.
- Two angle views (initially designed for SST). This should help in atmospheric correction and give much new information about bi-directional effect.
- On-board visible calibration system. This provides a very accurate calibration for the visible and NIR channels.

A presentation was given about the angular dependence of radiometric surface temperature for sparse vegetation. At an incidence angle of 55° (corresponding to ATSR-2 forward view) over sparse vegetation the bi-directional emissivity effect can reach a difference of about 2° C.

The effect of atmosphere being negligible in this experiment. This study needs to be completed with more ATSR-2 data. Using Principal Component Analysis, it has been demonstrated that, due to spectral channel definition of ATSR-2, the spectral resolution of ATSR-2 is similar to that of Landsat.

The 1.6 μm channel provides for distinction of organic and mineral soil types. This makes ATSR (1 and 2) a powerful tool for mapping of forests and burnt surfaces.

Overland a problem of miscollocation between nadir and forward view has been noticed. This is caused by the relief. For precise collocation nadir/forward, the relief effect needs to be corrected.

Combining the spatial resolution of 1km (already demonstrated to be very useful by AVHRR experience) and the good spectral resolution ATSR-2 is a very good tool for land studies. Different studies or projects using ATSR-2 over land are still ongoing (heat budget over urban area, fire detection, volcano monitoring, forest mapping).

However, this promising perspective needs to be confirmed and demonstrated operationally. There is a perception by many potential users that AVHRR is easier and less expensive to obtain. This acts as a deterrent. The ATSR-2 data promotion and distribution need to be improved.

JERS/ERS Synergy

This session, arranged as a result of an ESA-NASDA cooperative working group, provided a useful opportunity for international scientific participants to this symposium to discuss progress in developing applications projects which can exploit the complementary capabilities of the currently orbiting ERS C-band and JERS L-band SARs.

The session was well attended (standing room only) and topics covered included ice-cover monitoring in climatically sensitive regions around Japan, as well as a comparative assessment of the interferometric capabilities of the two SAR systems. Six of the eight presentations addressed the joint use of ERS and JERS for vegetation monitoring, particularly for forestry applications. Two papers gave a brief summary of progress on understanding and modelling the underlying microwave scattering mechanisms, with emphasis on the wavelength, polarisation and incidence-angle dependencies which determine the characteristic responses of each SAR over specific vegetation types, environmental and observation conditions. Based on this, the complementarity of the two systems, as well as their limitations, are well understood. This provides a sound basis for exploiting the operational observation capabilities of the two SARs for achievable goals within well defined applications.

In two presentations the capability to distinguish between different tree species using composite JERS/ERS imagery was reported. In a study conducted over test sites in West Malaysian plantations it proved possible to distinguish rubber trees from palm trees in composite imagery. Results obtained from a classification scheme aimed to produce vegetation maps at 1:200,000 scale utilising JERS and ERS SARs were also reported and ability to discriminate according to a standard physiognomic vegetation classification scheme were presented for conditions ranging from desert to rain forest. Classification accuracy up to 90% was reported for certain vegetation classes with ground truth for test sites.

Two major projects aiming to exploit the global-scale potential of the ERS and JERS SARs for forestry monitoring in the coming year were presented. A campaign of nearly simultaneous ERS/JERS acquisitions over Siberian Boreal forest zone, for which the DLR transportable station will be located in Ulan Bator is planned for June 1997. A similar exercise, linked to the on-going JERS Global Rain Forest Mapping Project, will compile several SAR (ERS, Radarsat, JERS) data sets at over the African tropical rain forests, building on the techniques and results already obtained by JRC Ispra within the TREES project, was reported.

In both these projects the objective is, using orbiting SAR systems, to generate semi-continental image mosaics and maps of vegetation parameters over climatically sensitive forest regions for which no other comparable data set is available.

These presentations highlighted the usefulness and complementarity of the ERS and JERS SAR missions. Participants from ESA and NASDA acknowledged the benefits of this type of scientific exchange in view of the forthcoming C-band and L-band SAR missions currently being prepared by the Agencies. NASDA representatives expressed their thanks to ESA for arranging this session.

Conclusions and Recommendations

Plenary Session

The closing Plenary session was held to round up and to invite the audience to add some general comments and recommendations. A number of specific points were addressed by the audience or ESA during the Plenary Session:

Future Announcements of Opportunity

AOs have proved to be a suitable tool to stimulate and advance exploitation of ERS data. However, after several years of ERS data exploitation, further new AOs shall be more limited, focused and dedicated to specific subjects. Over and above the Envisat AO which will be issued in summer 1997, several options for such dedicated AOs for the exploitation of ERS data can be envisaged, namely:

- for the exploitation of the large archives e.g. data older than 6 months
- for the exploitation of new station coverages
- for the exploitation of atmospheric data GOME and ATSR
- dedicated to open up and demonstrate new 'commercial applications' and 'business cases'
- for the preparation of Envisat e.g. definition of products, algorithms, cal/val etc
- for developing countries
- for the development of new technologies, e.g. in processing.

Next Conference

The total number of data users and participation to dedicated conferences has increased greatly. Nevertheless, ESA intends to maintain the dual concept of

- large symposia (to stimulate the synergy and commonality of the instruments on the same mission) and
- smaller dedicated workshops focused on one particular application subject.

Since the second series of AOs are still ongoing, in 1998 ESA will continue the series of application work-shops which was started in Toledo, Zurich and Frascati. One such workshop could cover 'Application of WSC data over Land and Ice' to build upon the fairly new application results presented in Florence.

A large symposium can be envisaged for end 1998 or early 1999 and will then focus on the transfer from ERS data exploitation to Envisat. Preliminary project plans of the Envisat AO could already be presented by then.

Utilisation of Instruments in Synergy

While in the early phase of the ERS mission projects were focusing on utilisation of data from one instrument, now the complementarity of the different ERS instruments such as DEMs generated at different scales by RA and SAR or the complementarity of different satellites such as the ERS C-band SAR and the JERS L-band SAR have been recognised and combined datasets are used.

SAR Low-Resolution Fast-Delivery Data Service

The SAR low-resolution fast-delivery service is currently offered on a commercial basis in Europe by the stations of Tromso and West Freugh. Participants to the Symposium, mainly from the operational and scientific ice community, request that this service be offered free of charge for the National Ice Services.

Future Tandem Operations

Further ERS-1/2 tandem operation was requested by participants. However first priority shall be given to a full exploitation of the existing tandem dataset. As a second priority proper justification should be sought (large-size projects/financial contributions etc) for:

- parallel operations of SAR, rather than full operations of all instruments,
- selected acquisitions for a short period (say 1-2 cycles)

The current planning of lifetime together with the financial planning aims at the end of Envisat commissioning phase. If a strong requirement to extend lifetime in parallel to Envisat were to arise, further and longer parallel operations will be even more critical. ERS-1 in the meantime has already exceeded twice its specified lifetime.

Continuity in Data Services and Preparation of New Missions

In order to stimulate users to further extend and invest in the utilisation of remote sensing data, a long-term perspective is vital. ESA was requested to present and ensure such a long-term plan for data provision through Earth Observation instruments. Also a political sign on continuity was mentioned by the participants as a condition for future investment in this technology, which has now demonstrated its capabilities.

On top of the operational and commercial aspects requiring a long-term strategy, a number of scientific objectives (e.g. in monitoring atmosphere and geoid) can also be met and trends can be determined only through acquisition of long time series of data.

ESA was therefore requested to proceed with the preparation of the Earth Explorer Missions and to start immediately the definition of the Earth Watch Missions to ensure confidence in the private sector on a continutity of data services following Envisat.

Future ESA Radar Altimeter Mission

Participants stressed that no further altimetric mission is yet planned by ESA following Envisat. A continuation of ESA's Radar Altimetry missions was requested complementing the Jason series of Franco-American altimetric missions in order to:

- increase spatial and temporal resolution, particularly for significant wave height and mesoscale monitoring;
- monitor ice sheets and broaden altimetric land applications.

Long Time Series of Data for Atmospheric Sciences

Atmospheric Sciences require long data series (i.e. at least 15 years).
ESA was requested to investigate and plan for operations of the ERS GOME in parallel to Envisat for as long as possible. A firm commitment for another atmospheric mission after the Envisat time frame was requested by the atmospheric user groups..

Final remarks

One of the original targets in the exploitation of the ERS mission was to broaden the use of remote sensing data; the increasing number of participants, papers and the variety of application subjects of the conferences clearly demonstrate that this objective has been.

The progress in the understanding of the ERS data potentialities is impressive. The utility of ERS is now beyond question. The use of ERS data has become routine for many projects. This meets a second objective of this mission.

Also the complementarity within the ERS instruments or with instruments from other Earth Observation Missions has found its way into application; examples are the DEMs generated by RA and SAR data or the use of JERS and ERS SAR data for vegetation/forest mapping.

One generation of scientists has been paving the way to get ERS approved and working. Now a new generation of scientists has emerged to who access to and exploitation of ERS data in Earth Sciences is not a question anymore.

The co-operation between the user and ESA has reached an extremely fruitful level. The outstanding results presented during this Symposium now need to be translated into the necessary political and financial actions to ensure continuity in data services through ERS, Envisat and follow-on missions and to benefit from and build on these results on the long term.

Therefore this Symposium shall not be seen as the end of the exploitation efforts of the ERS Programme, even though most of the mission objectives have been reached, but as one milestone in the process of European Earth Observation applications' development and confirm the long-term strategy through the series of European programmes and missions.

Soil Moisture

Chairperson: **T. Le-Toan**

COMPARISON OF MODELLED BACKSCATTER RESPONSE AND ERS-1 SAR DATA FOR DESERT SURFACES, THE EASTERN BADIA OF JORDAN

Kevin J. Tansey, Andrew C. Millington

Department of Geography, University of Leicester, University Road, Leicester, LE1 7RH, UK
phone: +44 (0)116 2523822, fax: +44 (0)116 2523854, e-mail: kjt7@le.ac.uk, acm4@le.ac.uk

Kevin White

Department of Geography, University of Reading, Whiteknights, Reading, RG6 6AB, UK
phone: +44 (0)1734 875123 Ext. 7752, fax: +44 (0)1734 755865, e-mail: k.h.white@geography.rdg.ac.uk

Anwar Battikhi

Faculty of Graduate Studies, University of Jordan, Amman, Jordan

ABSTRACT

The objective of this paper is to investigate the use of theoretical surface scattering models to simulate the backscatter coefficient for a range of dryland surfaces. *In-situ* measurements of soil moisture, surface roughness and soil texture have been used in the Kirchoff and Small Perturbation models. Comparison of the results of this modelling with ERS-1 SAR data indicate good agreement between the predicted and observed backscatter coefficient ($R^2 > 0.8$). An analysis of the suitability of the Integral Equation Model is also presented. The modelling has demonstrated the need for accurate and representative surface roughness parameterisation for the retrieval of soil moisture. Further research is aimed at increasing the sample dataset, deriving surface roughness characteristics and to develop a greater understanding of the interactions between microwaves and desert surfaces.

Keywords: ERS SAR, soil moisture, surface roughness, desert, modelling.

1. INTRODUCTION

The retrieval of information related to physical surface parameters is a major objective of many studies in remote sensing investigations. With the deployment of ERS-1 Synthetic Aperture Radar (SAR) and more recently ERS-2 SAR (C-band, VV polarisation with an incidence angle of 23°) estimates of soil moisture have been extensively exploited in such disciplines as agriculture and hydrology. Other satellite radar systems such as JERS-1 and RADARSAT complement and increase our knowledge of interactions between radar and natural surfaces. The optimal configuration, as stated by Ulaby *et al.* (1978), for maximum soil moisture sensitivity was a C-band system operating at an incidence angle between 10 and 20°, but compared with the configuration of ERS SAR, consideration must be made of other surface parameters notably surface roughness and soil texture which influence backscatter.

One approach to understanding interactions between radar and natural surfaces is through modelling. In this paper, theoretical models of surface scattering, described in section 2, are validated using *in-situ* measurements of surface parameters for an arid climatic region of the Jordanian Badia, described in sections 3 and 4. Using backscatter values derived from ERS-1 SAR PRI imagery, described in section 5, at overpass times contemporous with field data collection, comparison with modelled values are made. The results, displayed in section 6, are encouraging but are interpreted to indicate where problems in using the models as predictive tools may occur. These problems are addressed with respect to the retrieval of soil moisture parameters. Conclusions and recommendations for future research are described in section 7.

2. THEORETICAL MODELS

Simple models of rough surface scattering help us to understand and interpret the nature of wave scattering and to extract information from radar images. The models used in this study are the Small Perturbation Method (SPM), the Kirchoff Method (comprising the Geometrical Optics (GO) and the Physical Optics (PO) models) and the Integral Equation Model (IEM). For a full description of the SPM, GO and PO models see Ulaby *et al.* (1982). In simple terms, the SPM assumes that variations in surface height, parameterised as root mean square (RMS) height (σ), are small compared to the wavelength (λ) of the radar signal ($\lambda \equiv 5.66$cm for

ERS-SAR). Also, that the surface slope parameter, *m*, is small (where $m = \sigma/l$ where *l*, the correlation length, can be considered as the horizontal distance beyond which two points are approximately statistically independent), (Ulaby *et al.*, 1982). The GO solution is valid when RMS height is large compared to the wavelength. The PO solution is valid when RMS height is small compared to the wavelength.

The IEM developed by Fung *et al.* (1992), is less restrictive in its validation domain. The complex version of the model accounts for a wide range of roughness and frequencies. For the purpose of this study an approximate solution is used, the only limitation being for surfaces with large RMS heights compared to the wavelength. Two further assumptions are made; firstly, only the real part of the dielectric constant (ε) is used, a reasonable approach for soil moisture retrieval (Sreenivas *et al.*, 1995); and secondly, the autocorrelation function, a descriptor of the correlation between two points over a horizontal scale as the distance between the points change, is assumed isotropic and represented by a Gaussian or exponential distribution function (Altese *et al.*, 1995; Su and Troch, 1996).

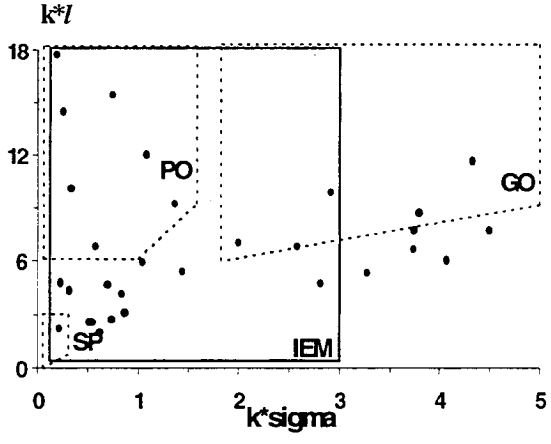

Figure 1 - Validity domains of the Small Perturbation Method (SP), Geometrical Optics (GO), Physical Optics (PO) and Integral Equation Models (IEM), shown against measured roughness values for desert surfaces. $k \cong 1.11$, *l* is the correlation length and sigma is the RMS height

The validation domains of these models can be identified in the ksigma-kl feature space (figure 1) where k is the free space wavenumber ($k = 2\pi/\lambda \cong 1.11$ for ERS SAR). Plotted within this feature space are measured roughness values from field sites. It can be seen that there are sites for which none of the models are valid (especially for the SPM, GO and PO model domains). The output from the models, the backscattering coefficient (σ^0 or Sigma 0) measured in decibels (dB), is expressed as a function of the radar frequency, polarisation, incidence angle; surface RMS height, correlation length, autocorrelation function and the dielectric constant, the latter calculated from volumetric soil moisture and soil texture using an empirical relationship given by Hallikainen *et al.* (1985).

3. STUDY AREA

The majority of soil moisture experiments using radar remote sensing have focused on systems where human activity has altered the land surface. This study looks at a wide range of natural and non-natural desert surfaces characteristic of the eastern Badia of Jordan (figure 2).

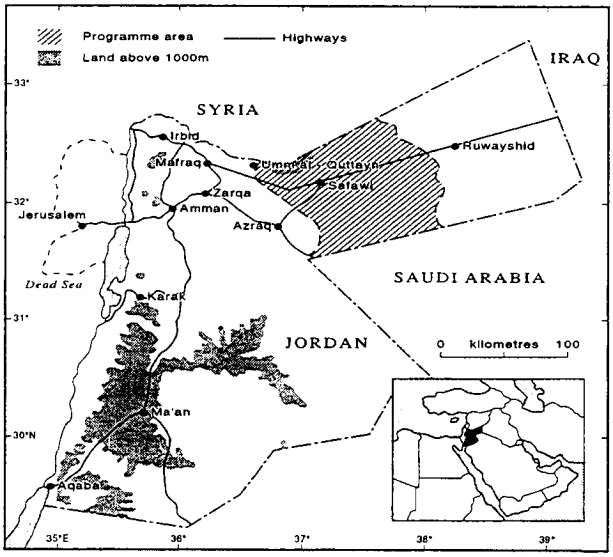

Figure 2 - Location of the Jordan Badia Research and Development Programme Area

The Jordan Badia Research and Development Programme area, bounded by Syria to the north and Saudi Arabia to the south, covers a total of 11,210 km^2. The eastern and western margins follow a perimeter of Tertiary-Quaternary basalt flows and tuffs, known locally as *harrat*, comprising parts of the Harrat Ash-Shaam Basaltic Super-group (Ibrahim, 1993). The land surface towards the south of the programme area comprises of mainly sedimentary rocks and cherts, known locally as *hammad*. Thin layers of sand cover the *hammad* in the far south and south-eastern reaches of the area, termed sand veils in this paper. Within these major geomorphic units are drainage systems, forming what are known locally as *qaa* and *marab*. *Qaas* are characteristically flat, silt-clay loam surfaces that act as sinks for sediment and water fluxes. Desiccation cracking is also a feature of these surfaces. *Marabs* are areas of natural vegetation usually

associated with channel systems and outwash plains. Vegetation covers are low, primarily due to limited rainfall and also grazing in the programme area with almost all areas having less than 10% cover (Edwards *et al.*, 1996). Some cultivation is practised within the programme area.

An arid desert climate exists within the Badia. Mean annual rainfall totals vary from 200mm in the north to less than 50mm in the south. Annual equivalent evaporation rates range from 1500mm to 2000mm along a gradient from north to south (Al-Homoud *et al.*, 1995).

4. METHODOLOGY

Study sites were chosen within each major landcover unit that were considered homogeneous over approximately a square kilometre. Two field campaigns were completed in November-December 1995 and April-May 1996. Soil moisture data were collected using a dielectric probe that produced an estimate of the volumetric soil moisture content from the upper 6cm of surface material. 30 samples were taken at random locations within a 30 by 30m area and the average value derived. Surface roughness data were collected with a profilometer recording height measurements along transects between 1.5 and 3m in length at a sampling resolution of 5mm. The profiles were digitised and statistical descriptors of the surface properties derived. The RMS height (σ) and the correlation length (l) were calculated following the recommendations of Ulaby *et al.* (1982) and Cox (1983). Analysis of the surface height distributions showed that the majority of sites were characterised by approximate Gaussian distributions. Calculation of the surface slope parameter, m, defined in section 2, was made for either exponential or Gaussian autocorrelation functions based on goodness-of-fit observations of these theoretical distributions to actual distributions (see Oh *et al.*, 1992). Soil texture information were partially derived from comprehensive soil maps of the programme area and from analysis of field samples.

5. ERS-1 SAR IMAGERY

Backscatter coefficients were derived from ERS-1 SAR PRI imagery, acquired in conjunction with collection of field data, using the comprehensive equation by Laur *et al.* (1996). The dates of image acquisition were (day-month-year); 23-11-95, 09-12-95, 12-12-95, 11-04-96, 01-05-96 and 16-05-96. The raw images were transformed to geographic co-ordinates using ground control points, identifiable both on imagery and in the field. Nearest neighbour resampling was used with an RMS transformation error of approximately one pixel. This enabled accurate identification and location of sites within the SAR image. As no algorithm for speckle reduction was applied to the images, thus maintaining original pixel DN, the backscatter coefficient was derived from an average of 25 by 20 pixel DN, approximately equivalent to 300 by 250m on the ground. Original site selection criteria assumed homogeneity for at least a square kilometre.

6. RESULTS AND DISCUSSION

Estimates of the backscatter coefficient were calculated using sites that satisfied the validation domains of the models shown in figure 1. From a total of 30 sites, only 13 lie within the criteria set by the SPM, GO and PO models whereas 23 sites lie within the criteria of the IEM. Predicted backscatter values are plotted against observed backscatter values, using the SPM, GO and PO models (figure 3), giving a correlation coefficient of 0.82. Some points are very well predicted by the models while other sites (e.g. sand veils) show that the models are not representative of the scattering processes. For example, in figure 3, sites indicated by hollow symbols are sand veil surfaces.

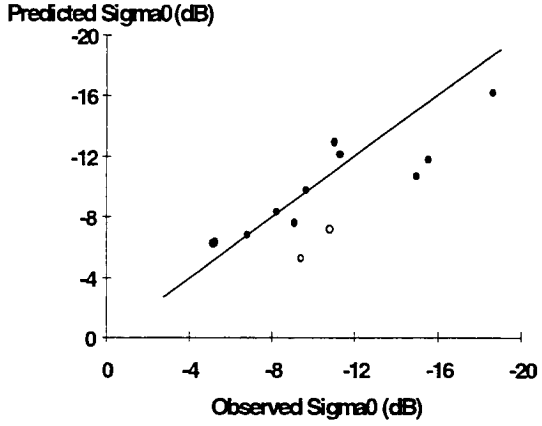

Figure 3 - Modelled backscatter values (predicted Sigma 0) plotted against ERS-1 SAR derived values (observed Sigma 0) for sites satisfying SPM, GO and PO model criteria for all surfaces. Sand veil surfaces are shown as green circles, $R^2 = 0.82$

The results of the IEM validation are similar (figure 4). The correlation coefficient between the predicted and observed backscatter values is improved to 0.87 using the 23 sites that satisfy the model validation criteria. This is an encouraging result given that the model is predicting the backscatter response for a variety of natural surfaces and is based on field measurements. Further analysis of the scatterplot shows that the model overpredicts (indicated by the fact that the model predicts a greater backscatter coefficient should be detected (lower negative dB value) than that indicated by the SAR data) the backscatter response for quite a

number of sites. This was further indicated in figure 3 where some surfaces were not well predicted by the models, the sand veil sites for example.

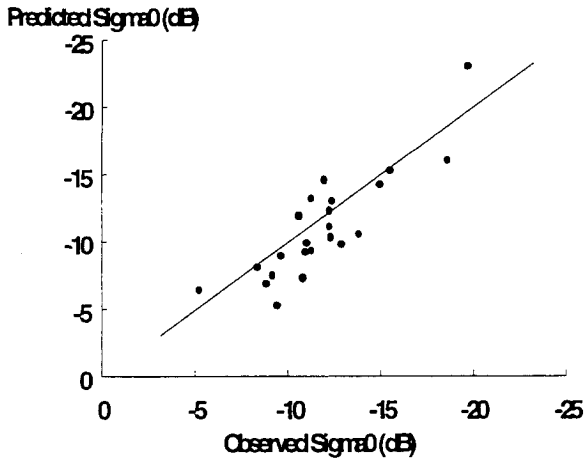

Figure 4 - Modelled backscatter values (predicted Sigma 0) plotted against ERS-1 SAR derived values (observed Sigma 0) for sites satisfying the IEM criteria, $R^2 = 0.87$

The inaccuracies of the models can be explained in a variety of ways based on an understanding of model theory and may be attributable to the following:

(i) The models are derived from surface scattering principles. Volume scattering in especially dry, sandy areas, such as those existing towards the south-east of the programme area may be a significant process.

(ii) Vegetation in the *marabs* could possibly influence the radar signal even though present in low amounts. Therefore observations of the change in backscatter response over the year will be crucial in understanding the contribution of vegetation to the backscatter signal.

(iii) Natural surfaces are not entirely homogeneous over the spatial scales observed by ERS-SAR. Distribution of moisture and hence dielectric properties are likely to vary. Sarabandi *et al.* (1996) investigate these problems by modelling the surface as a inhomogeneous random layer comprising two-dimensional humps of varying size, shape and dielectric constant overlying a smooth, uniform impedance layer. The same approach could be adopted to derive an average dielectric constant for the *harrat* and *hammad* surfaces where basaltic and sedimentary rocks overlie a soil surface. The models, as they are, assume only a soil surface when calculating the dielectric constant.

(iv) Natural surfaces rarely have autocorrelation functions that fit either Gaussian or exponential theoretical functions.

(v) The measurement of surface roughness may be a potential limitation of the data. For example, Engman and Wang (1987) found correlation coefficients between the backscatter coefficient (σ°), and RMS height, and σ° and correlation length to be 0.59 and 0.04 respectively. This indicates there is little relationship between backscatter and the correlation length for the large number of bare, dry fields the authors' studied. The general theory behind derivations of roughness parameters that adequately describe topographic variation appears unclear especially for remote sensing applications. Other methods seem more suitable, although data collection and analysis are time consuming. In a unifying approach, Greenwood (1984) stated that a complete description of a random surface's topography can be derived in terms of the PDF and the power spectrum of the surface profile. However, for power spectrum analysis, profiles of different sampling resolutions are required and a large number of independent profiles are desirable to reduce noise (Farr, 1992). The uncertainty of the roughness parameters used in the models can be argued through interpretation of the work by Sayles and Thomas (1978), who show through Gaussian statistics that the variance of the height distribution of a random structure is linearly related to the length of the sample involved. This implies that the RMS height increases as profile length increases and, through fractal analysis the function describing this relationship cannot be described and varies significantly with observation frequency (Brown and Scholtz, 1985). This invokes an uncertainty over what profile length should be used for radar studies and demonstrates the need for more accurate and representative measures of surface roughness.

(vii) Errors in determining the soil dielectric constant for very dry, structureless desert soils.

(viii) Calibration errors deriving σ° from ERS-SAR imagery.

The outcome of the model depends on field parameters that may be unrepresentative of the surface conditions. Another approach, less demanding of data than an empirical approach, would be to use the models to derive a roughness parameter through model inversion, simulate soil moisture and RMS height variation, and subsequently monitor the sensitivity of the backscatter coefficient to these variations. Correlation lengths (the roughness parameter) were derived for different land cover types using the SPM, GO and PO models that yielded values of backscatter corresponding most closely to those observed from the imagery. Using actual values of RMS height, the sensitivity of the radar backscatter to changes in volumetric soil moisture from 0.0 to 0.4 m^3 (water)/ m^3 (soil) were simulated (figure 5).

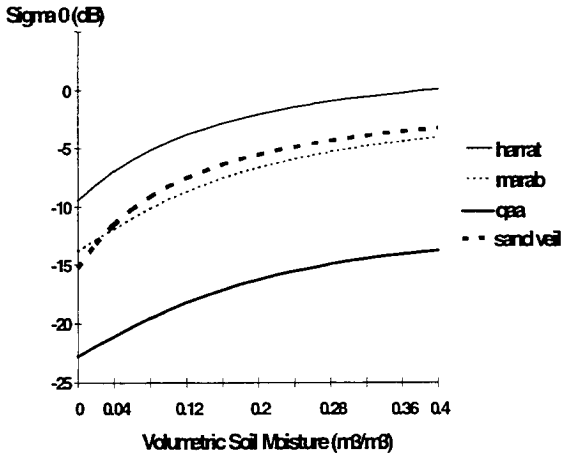

Figure 5 - Backscatter response to changes in soil moisture for various land cover types simulated with the SPM, GO and PO models. RMS heights (cm) are 3.9 (*harrat*), 1.23 (*marab*), 0.18 (*qaa*) and 0.94 (sand veil)

The simulation indicates that surface roughness has little effect on the sensitivity of the backscatter coefficient to changes in soil moisture i.e. the curves all have a similar form. What is also important is a greater sensitivity to changes in soil moisture from very dry to small volumes of water, which is the most likely range of values found in desert areas. The influence of soil type can also be seen especially at low values of soil moisture by examining the curve for a *qaa* surface dominated by clay-sized particles. The slope of the backscatter response is seen to be approximately constant over the range of soil moistures with only a small increase in sensitivity as the soil becomes dryer. Comparing this to the curve for a coarse-textured sandy site (sand veil) it can be seen in the latter that backscatter reaches an asymptote more quickly as the soil gets drier. The difference can be explained by the fact that, for a given low value of volumetric soil moisture, there is generally more water available in a sand to influence the dielectric constant than a clay.

The sensitivity of the backscatter to small variations in topographic roughness are displayed in figure 6 for the same surface types. For flat surfaces (*qaa* surfaces and some of the smoother *marabs* present in the study area) very small changes in surface roughness have a large effect on the backscatter. This sensitivity is reduced significantly for surfaces with a RMS height in excess of approximately 1cm and for the *harrat* rock surfaces, changes in roughness over similar scales has a negligible effect on the backscatter response.

The implications for soil moisture monitoring and retrieval using ERS SAR imagery, based on the model

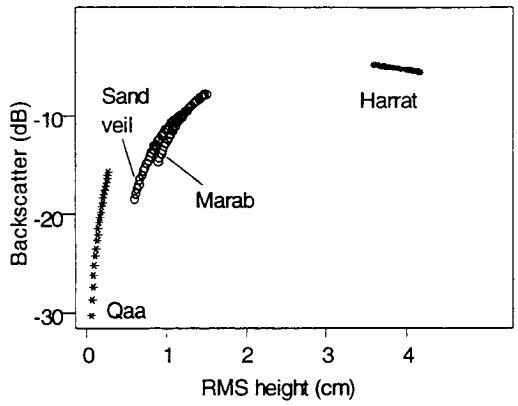

Figure 6 - Backscatter response to changes in RMS height for various land cover types simulated with the SPM, GO and PO models. Soil moisture values are approximately constant

simulation, are that the radar backscatter is sensitive to changes in soil moisture for a wide range of surfaces if surface roughness is assumed constant. Le Toan *et al.* (1993) suggest this may be the case for many natural surfaces. For example, if surface roughness remained constant over a year in a vegetated marab, then any changes in backscatter would most probably be due to soil moisture and vegetation fluctuations. However, processes such as wind erosion causing deflation and deposition of surface sediments; and surface swelling and desiccation of smectitie clay-rich surfaces, that each operate over relatively short timescales, need to be accounted for by taking roughness measurements during different seasons. An absence of saline soils within the programme area reduces the effect that salt crystal growth has on backscatter (Wadge *et al.*, 1994).

7. CONCLUSION

Surface scattering models have been validated using field data acquired during two field campaigns in late 1995 and early 1996. The backscatter coefficients have been compared to values derived from ERS-1 SAR PRI imagery collected at similar times. Good agreement was found; the correlation coefficients were 0.82 when validated with the SPM, GO and PO models and 0.87 when validated with the IEM. Further field campaigns will increase the number of sites that can be used for validation. The experiment also highlights the limitations of using the models to monitor and retrieve soil moisture information for a wide range of desert surfaces, unless certain assumptions are made. If it is assumed, that surface roughness is constant over an annual timescale, then retrieval of soil moisture should be possible. Model simulation shows that this is relatively independent of RMS height. If surface roughness does change over the year then soil moisture

information will be erroneous; greatest for the smooth surfaces (*qaas*, smooth *marabs*) and negligible for rough surfaces (*harrat*, rough *marabs*) unless the magnitude of the variations are known. This problem is being approached by making roughness measurements during different climatic seasons and using the range of backscatter coefficients derived from multi-temporal ERS SAR imagery as a guide to indicate what surface processes may be occurring. Future research will be focused on:

(i) Increasing the sample dataset for model validation using ERS-2 SAR data.

(ii) Investigate alternative and complimentary measures that characterise surface roughness such as power spectrum analysis.

(iii) Investigate the influence of arid dryland vegetation on the backscatter response both qualitatively, by comparing image texture with field observations, and quantitatively with field measurements of vegetation parameters.

8. ACKNOWLEDGEMENTS

Imagery was obtained under an ESA PI to White and Millington (A02.UK.125). Kevin Tansey is supported by NERC award (GT4/95/154/D). The author's wish to express their thanks to Leland Pierce of the University of Michigan, USA and Zhongbo Su of the DLO Staring Centre for Integrated Land, Soil and Water Research, Netherlands for supplying the models and providing useful feedback. The authors also acknowledge assistance given by George Mackay and Marianne Edwards in the field and the staff at the Higher Council for Science and Technology and Safawi Field Centre, Jordan, University of Jordan, Amman and the Centre for Overseas Research and Development, University of Durham, UK.

9. REFERENCES

Al-Homoud, A.S., Allison, R.J., Sunna, B.F. and White, K., 1995, Geology, geomorphology, hydrology, groundwater and physical resources of the desertified Badia environment in Jordan, *Geojournal*, 37, 51-67.

Altese, E., Bolognani, O., Mancini, M. and Troch, P.A., 1996, Retrieving soil moisture over bare soil from ERS-1 synthetic aperture radar data: Sensitivity analysis based on a theoretical surface scattering model and field data, *Water Resources Research*, Vol. 32, 3, 653-661.

Brown S.R., and Scholz, C.H., 1985, Broad bandwidth study of the topography of natural rock surfaces, *Journal of Geophysical Research*, Vol. 90, B14, 12575-12582.

Cox, N.J., 1983, On the estimation of spatial autocorrelation in geomorphology, *Earth Surface Processes and Landforms*, Vol. 8, 89-93.

Edwards, M.C., Al-Eisawi, D. and Millington, A.C, 1996, The use of ERS ATSR-2 data for monitoring rangeland vegetation in the eastern Badia, Jordan, *Proceeding of RSS96, 22nd Annual Conference of the Remote Sensing Society*, 11-14 September 1996.

Engman, E.T. and Wang, J.R., 1987, Evaluating roughness models of radar backscatter, *IEEE Transactions on Geoscience and Remote Sensing*, Vol. GE-25, 6, 709-713.

Farr, T.G., 1992, Microtopographic evolution of lava flows at Cima Volcanic Field, Mojave Desert, Calafornia, *Journal of Geophysical Research*, Vol. 97, B11, 15171-15179.

Fung, A.K., Li, Z. and Chen, K.S., 1992, Backscattering from a randomly rough dielectric surface, *IEEE Transactions on Geoscience and Remote Sensing*, Vol. 30, 2, 356-369.

Greenwood, J.A., 1984, A unified theory of surface roughness, *Proceedings of the Royal Society of London, Series A*, 393, 133-157.

Hallikainen, M.T., Ulaby, F.T., Dobson, M.C., El-Rayes, M.A. and Wu, L.K., 1985, *IEEE Transactions on Geoscience and Remote Sensing*, Vol. 23, 1, 25-34.

Ibrahim, K., 1993, The geologic framework for the Harrat Ash-Shaam Basaltic Super-Group and its volcanotectonic evolution, *1:50,000 Geological Mapping Series, Geological Bulletin, The Hashemite Kingdom of Jordan*, Natural Resources Authority.

Laur, H., Bally, P., Meadows, P., Sanchez, J, Schaettler, B. and Lopinto, E., 1996, *Derivation of the Backscattering Coefficient* σ^0 *in ESA ERS SAR PRI Products*, ESA Publication, Document No: ES-TN-RS-PM-HL09, Issue 2, Rev. 2.

Le Toan, T., Smacchia, P., Souyris, J.C., Beaudoin, A., Merdas, M., Wooding, M. and Lichteneger J., (1994), On the retrieval of soil moisture from ERS-1 SAR data, *Proceedings Second ERS-1 Symposium*, Hamburg, Germany, 11-14 October, 1993, 883-888.

Oh, Y., Sarabandi, K. and Ulaby, F.T., 1992, An empirical model and an inversion techniques for radar scattering from bare soil surfaces, *IEEE Transactions on Geoscience and Remote Sensing*, Vol. 30, 2, 370-381.

Sarabandi, K., Oh, Y. and Ulaby, F.T., 1996, A numerical simulation of scattering from one-dimensional inhomogenous dielectric random surfaces, *IEEE Transactions on Geoscience and Remote Sensing*, Vol. 34, 2, 425-432.

Sayles, R.S. and Thomas, T.R., 1978, Surface topography as a nonstationary random process, *Nature*, Vol. 271, 431-434.

Sreenivas, K.,Venkataratnam, L. and Narasimha-Rao, P.V., 1995, Dielectric properties of salt-affected soils, *International Journal of Remote Sensing*, Vol. 16, 641-649.

Su, Z., and Troch, P.A., 1996, Soil surface parameters and radar backscattering, *Paper presented at the 21st General Assembly of the European Geophysical Society*, the Hague, 6-10 May, 1996.

Ulaby, F.T., Baltlivala, P.P. and Dobson, M.C., 1978, Microwave backscattering dependence on surface roughness, soil moisture and soil texture, part 1- bare soil, *IEEE Transactions on Geoscience and Remote Sensing*, Vol. GE-16, 4, 286-295.

Ulaby, F.T., Moore, R.K. and Fung, A.K., 1982, *Microwave remote sensing: Active and passive, Vol. II: Radar remote sensing and surface scattering and emission theory*, Addison-Wesley, Reading, MA.

Wadge, G., Archer, D.J. and Millington, A.C., 1994, Monitoring playa sedimentation using sequential radar images, *Terra Nova*, Vol. 6, 391-396.

MULTI-ANNUAL ANALYSIS OF ERS SURFACE SOIL MOISTURE MEASUREMENTS OF DIFFERENT LAND USES

Markus Rombach & Wolfram Mauser
Institute for Geography
Dept. of Geography and Geographical Remote Sensing
Ludwig-Maximilians-University of Munich
Luisenstrasse 37, D-80333 München Germany
phone: +49(0)89-5203 335, fax: +49(0)89-5203 321
e-mail: M.Rombach@ieee.org

ABSTRACT

This paper describes a new approach to convert ERS backscatter signals from different test sites within Germany into surface soil moisture values over several years.
Because the radar backscatter signal depend mainly on soil type, vegetation development, vegetation structure and water content of the soil, vegetation and soil dependencies were eliminated to receive the backscatter signal only influenced by the amount of soil moisture.
To retrieve a soil type independent relationship between surface soil moisture and the radar backscattering signal, all in situ measured surface soil moisture values were converted into dielectric constant values using the relationship of dielectric constant and volumetric soil moisture established by Hallikainen et al. (1985).
The influence on the backscattering signal of different agricultural use of the test fields were corrected by using a roughness criteria for each crop type under investigation. The correction of this influence was done by including roughness parameter into this approach, based on investigations by Ulaby (1992).
The approach was successfully used for corn, barley, oat and harvested fields. A common nonlinear regression curve is now available for these crops. For meadows, a very common land use in the Bavarian Alpine Foreland, an additional vegetation parameter (biomass) had to be included, to compensate the attenuation effect of strong radar effective vegetation structure changes within the period of observation. On the basis of these results, an attempt was made to determine the temporal development and spatial distribution of the course of the top soil moisture, using the corrected ERS backscattering coefficients of each field in the whole test site.

1. INTRODUCTION

Point measurements of one of the most important parameters in water cycle, the soil moisture, will not lead to a realistic view of the spatial moisture distribution. Therefore, not much is known of the course of moisture in different soils and under different land uses. The reason for this is the great spatial inhomogeneity of soil moisture and the expensive, complicated and labor intensive soil moisture point measurement available now.
Therefore it is worthwhile to investigate the potential of remote sensing as a source of environmental data, which is already spatially distributed and available. Once correlations are established between remote sensing data and environmental parameters this can be used to improve the quality of model input data sets and finally to reduce the number of conventional point measurement stations, still maintaining the quality of data.
Both, theoretical considerations and measurements using ground based scatterometer and aircraft based radar systems in the 70s and 80s, have proven, that the fraction of a RADAR pulse, which is backscattered from the surface, mainly contains information on the dielectric properties and roughness of the imaged surface (HALLIKAINEN et al., 1985; ULABY et al., 1982-1986). Further influencing factors on the backscattered intensity and polarisation are the incidence angle, the wavelength of the microwave and the properties of the soil both in terms of geometry and material. The value of the dielectric constant is dominated by the water content of the soil because the dielectric constant of water has approx. 20-30 times the value of the soil matrix. Therefore, the dielectric constant of the soil water mixture changes strongly with soil water content.
The new approach is eliminating separately the effects of different soil types, different land use and for meadows the varying biomass on the backscatter signal of ERS. Then the remaining radar signal information are converted into surface soil moisture values over the test site.

2. TEST SITES

Between 1991 and 1994 two test areas were investigated within an ERS-PI-project. During the Commissioning Phase of ERS-1 in 1991 investigations

were carried out in the Freiburg test site. A new test area near Munich was chosen for investigations from 1992 until 1994. This test site is situated near the town of Weilheim.

2.1 The test site near Freiburg

The Freiburg test site is situated about 20 km West of Freiburg within the Upper Rhine Valley. The geographical location of the test area is at approx. 48° North and 8° East. It covers a total area of approx. 50 km^2.

The average annual temperature in the test site is 10 °C with an average July temperature of 19.9 °C. Precipitation in the test site varies between 550 mm/a and 650 mm/a. Coarse grained sandy soils in the central part of the valley force farmers to irrigate corn fields to stabilize yield. The test site is geomorphologically situated on the lower terrace of the river Rhine (very flat area). Detailed soil information of the test area exists in the form of the Special Soil Survey of Germany (former "Reichsbodenschätzung") of 1934. The maps of these investigations were digitized and converted into GIS raster data layers with a resolution of two meters.

The ground water table in the Freiburg test site lies between 3-10 m below surface. Therefore no contact exists between the roots of the plants (even for forests) and ground water.

The land use in the test site is very inhomogeneous. Intensive agricultural land use covers approx. 60 % of the test site whereas the forested areas cover approx. 25 %. The remaining 15 % are covered with artificial lakes, gravel pits and villages.

The agricultural land use in 1991 consisted of corn (50%), cereals (20 %, mainly barley and wheat), potatoes (4 %) and whine (17 %). The percentage relate to the total agricultural use in the test site. The average field size is 1.5 ha, which leads to a strong heterogeneity of the test area.

As conclusion the test site near Freiburg covers a large variety of natural surface and climate conditions. It ranges from very light to heavy soils, from thick forests to gravel pits without vegetation, a large variety of agricultural plants and a variety of soil moisture conditions due to different soils, plants and a gradient in rainfall across the test area.

2.2 The test site near Weilheim

The Weilheim test area is situated at 48° North and 11° East approx. 60 km South of Munich in the Upper Bavarian Forelands around the town of Weilheim and covers an area of 100 km^2.

The landscape in the test area was formed by glaciers during the ice ages. It consists of a former glacier valley, which is bound by moraines to the East and the West. In the North, Lake Ammer forms a natural boundary of the test area. In the South the geological step of the "Guggenberg Molasse" forms the border of the test site.

The average elevation of the test site is 550 m a.s. The elevation and the nearby Alps result in cool average annual temperatures of 7-8 °C in the test site. The average temperature in January is -2 °C. The average annual precipitation in the test site is 1050-1200 mm/a with a slight gradient from the North to the South. During summer, rainfall appears mainly in form of heavy thunderstorms whereas in winter time advective rainfall predominates. The distribution of the soils in the Weilheim test site were digitized from the "Bodengütekarte von Bayern, 1959" using the soil type classification of the Special Soil Survey of Germany.

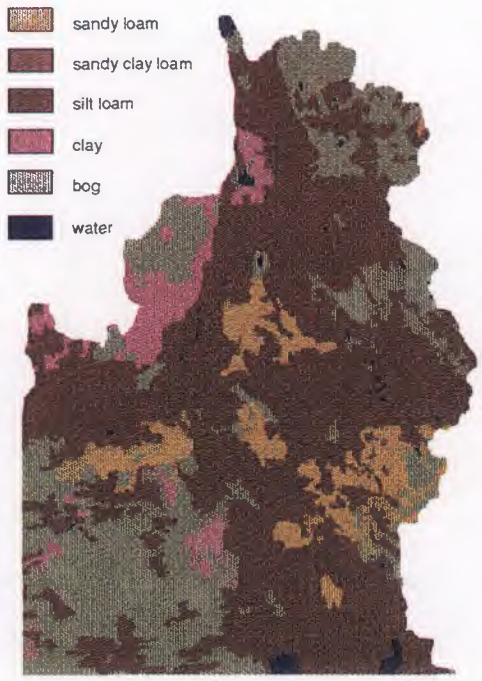

Figure 1: Digital soil type map of the test site near Weilheim (from: "Bodengütekarte von Bayern", 1959)

Figure 1 shows the distribution of the soil type in the test site. The distribution of the soils in the test site follows a general pattern. The lighter loamy gravel soils can be found to the East and West of the test site on the moraines surrounding the Ammer valley. Within the valley loamy and clay soils predominate. Where bogs developed on the clay soils today boggy soils with a high content of organic matter can be found.

The test site is predominantly covered with agriculture. The forests in the test area can be found on the moraines.

Figure 2 shows the land use distribution in the Weilheim test site in 1992 derived from Landsat TM classification (details see STOLZ & MAUSER,

1997a). As can be seen, more than half of the test area is covered with agriculture, 24 % is covered with forest and 10 % with villages. Superficially, these percentages are comparable with those in the Freiburg test site. A deeper analysis shows, that the dominance of grassland and meadows makes the Weilheim test site very different from the Freiburg one in the sense, that it is much more uniform, than the intensive agricultural region in the Rhine valley.

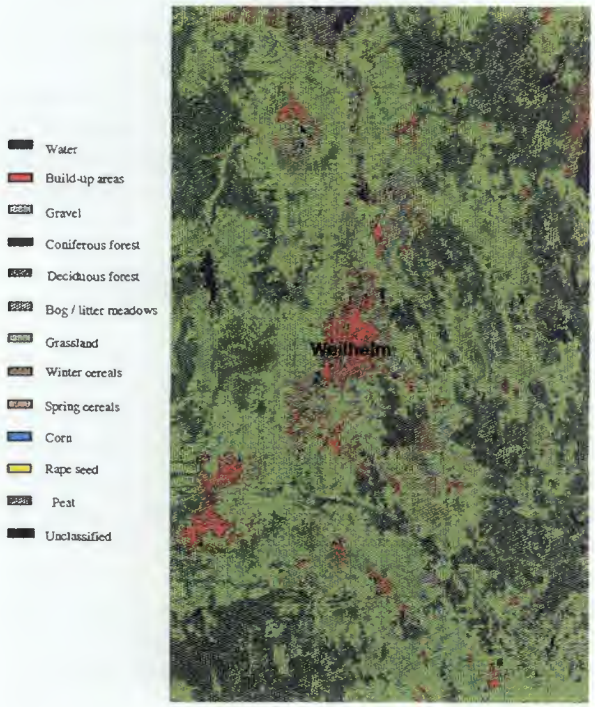

Figure 2: Digital land use map of the test site near Weilheim derived by TM classification (STOLZ & MAUSER, 1997a)

3. GROUND TRUTH

3.1 Soil moisture

To determine the amount of soil moisture in the first 2-4 cm of a test field, it is necessary to proof all data sets, taken at the field. First because of the principal problems of the measurement (different sensor techniques measure different soil moisture), second because of the nearly unlimited interference factors (registration of extreme events, influence of animals in the area near the station of measurement, different quantity of irrigation of a field, impairment of the electronic registration of data, mistakes in calibrations, etc.). Therefore it is very important to use different measurement techniques, to measure soil moisture and to use them on different places in the test fields to control themselves as well (tensiometer, electrical resistors (gypsum blocks), Time Domain Reflectometry (TDR), gravimetrical measurements, electrical capacity measurements, etc.).

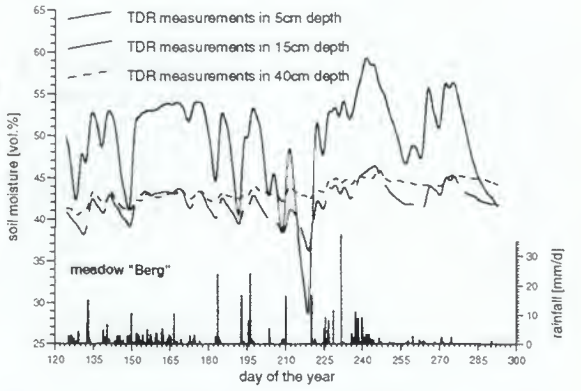

Figure 3: Measured soil moisture courses (TDR) of a meadow in three different depths

This was done for both test sites during the vegetation periods (April to October) of the years 1991 until 1994 (see Figure 3). Almost 30 different test fields with different land use were monitored for temporal and spatial soil moisture development together with other permanent soil physical parameters (porosity, soil bulk density, soil suction curves, grain size distribution, a.o.).

3.2 Meteorological data

Additional to hourly measurements of radiation, wind speed and direction, temperature (wet and dry), rainfall data were collected by rain gauges installed through the research group of the Institute of Geography (hourly measurements) and from meteorological stations of the German Weather Service (DWD) three times a day.

3.3 Plant Parameters

The aim of the detailed measurement of plant parameters on selected test fields is to acquire sufficient data to verify models for the backscattering behavior of natural surfaces and to deliver synchronious data of plant canopy parameters during the overflights of ERS.

During the vegetation period of the years 1991 until 1994 plant parameters were measured on almost 45 test fields.

Measurements took place once every week not taking into account the actual dates of the overpass of the satellite. The following parameters were measured on each selected field on a regular basis: phenology, plant height, leaf area index, wet/dry biomass and plant density.

4. RADAR DATA

All radar data were received either from the German or EECF Processing and Archiving Facility.

Test site Freiburg (1991):
38 ERS-1 SLC quarterscenes (descending mode)
37 ERS-1 SLC quarterscenes (ascending mode)
03 ERS-1 PRI full coverage (ascending mode)
Thus an almost complete data set of the images of the Commissioning Phase 1991 (August until October) is available.

Test site Weilheim (1992):
06 ERS-1 SLC quarterscenes (descending mode)
05 ERS-1 PRI full coverage (descending mode)
The images were taken between April 27 and November 23 1992 during the Mapping Phase.
Due to sensor problems no data of the test site were acquired at August 12 1992.

Test site Weilheim (1993):
06 ERS-1 SLC quarterscenes (descending mode)
04 ERS-1 SLC quarterscenes (ascending mode)
The data were acquired during the period from February 1 to November 24 1993.

Test site Weilheim (1994):
04 ERS-1 SLC quarterscenes (descending mode)
02 ERS-1 SLC quarterscenes (ascending mode)
The data were acquired during the period from May 11 to October 6 1994.

5. PREPARATION OF THE DATA SETS

5.1 Ground truth data

All field data (soil moisture, plant parameter, rainfall, radiation, wind speed, photographs, a.o.) are stored in a digital database after a careful check of their correctness.
When analysing the soil moisture values of meadows, we had to face the problem of measuring the water content of organic material as well, if taking probes from the top soil layer. This was leading to very high values (up to 80 vol. %) of soil moisture. Per definition these are no *soil* moisture values. By comparing the measurements of a lower horizon (15 cm depth) of the same soil at full saturation, we were able to calculate the real soil moisture values for the top soil layer. A special analysis of the organic content of the top soil layer confirmed this procedure.

5.2 Remote sensing data

The existing ERS SLC data were, converted into intensity (power) images, coregistrated and then calibrated (algorithm published by LAUR, 1993). No geometrical changes were made with these images.
For the test site near Freiburg images with per field averaged backscatter coefficients were generated. This was done with the help of a digital field number map of the test site and a statistical software package implemented within the image processing software FAP, developed at the Institute for Geography (MAUSER & BACH, 1993). For the test site near Weilheim the ERS images were averaged by using a gaussian and afterwards a median filter (each with a 3x3 box). They are produced to calculate the backscattering behavior on a field size raster, when field boundary maps does not exist, but averaged backscatter values per field are needed. No radiometric correction of local incidence angle influence on to the backscatter signal were applied, because in both test sites only flat test fields were investigated.

6. DESCRIPTION OF THE APPROACH

The backscatter of the ERS radar system is basically influenced by the soil type, vegetation development, vegetation structure, the water content of soil and the surface roughness. To retrieve the surface soil moisture from radar data, all influences contributing to the main signal, apart from the water content must be eliminated. This was done by finding the corresponding relations between each ground truth parameter and the backscatter signal for different land use classes. The next step is the correction of the main radar signal performed with the knowledge of existing ground truth data and their contribution to the signal. Afterwards the remaining signal is only sensitive to surface soil moisture content and can be converted.

7. IMPLEMENTATION OF THE APPROACH

Results of investigations based only on the test site near Freiburg in 1991 are documented in several publications (DEMIRCAN et al., 1993 a/b; ROMBACH et al., 1993; MAUSER & ROMBACH, 1994). It was not possible to generalize these results and use them straight forward on the test site near Weilheim. Therefore this new approach was developed.
All ground measured surface soil moisture values of both test sites, for each overflight of ERS, were converted into dielectric constant values (DC). This was done using the algorithm published by Hallikainen et al. (1985) (see Figure 4).
First all soil type classes had to be transformed into grain size distribution functions as input in the transformation formula. Problems occurred, when finding the necessary grain size distribution curves for soils with high organic content. To overcome this problem, the function of volumetric soil moisture vs.

dielectric constant published by Roth et al. (1992) was used when bog soils were found within the test sites (added in Figure 4). After this procedure of converting soil moisture into dielectric constants, the soil type effects on the backscatter signal are eliminated.

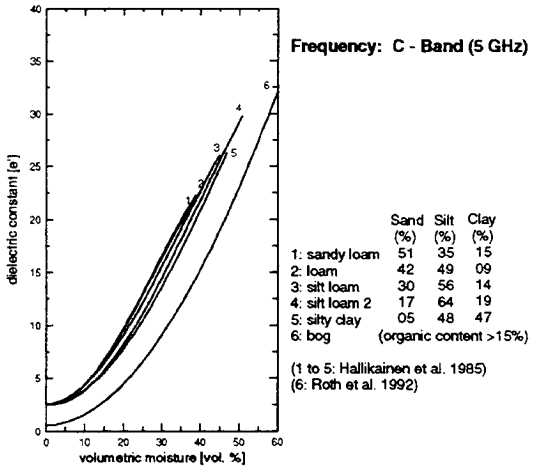

Figure 4: Relations between volumetric soil moisture and dielectric constant for one frequency on different soil types (from: HALLIKAINEN et al., 1985 and ROTH et al., 1992)

Vegetation development (roughness) effects are taken into account by establishing separate relations between dielectric constant and the backscattering signal depending on each land use under investigation. This is possible, due to the fact, that images are only taken into the analysis, where crops reached a growing development, from which onwards, no radar effective roughness changes appear (for example: when the height of corn plants are greater than 1 m). Therefore only the crop type is responsible for a different backscatter behavior when all other influencing parameters are stable. Harvested fields are treated as a different "land use" class. As an example for other crops under investigation, Figure 5 shows a resulting regression curve for corn fields. The bold line shows a MIMICS simulation (Michigan Microwave Canopy Scattering Model) of the backscattering behavior on bare soils for the ERS configuration (ULABY, 1992). The measured soil moisture values (converted in DC) of corn fields (plant height is already above 1 m) agree well to the simulation. The meaning of the equal course of these curves is, that for corn fields from a certain phenology stadium onwards, the ERS signal reflect almost like a bare soil with a roughness (RMS) height of 0.7 cm. This behavior can be found on rye, barley, oat and fallow fields but, of course, with different roughness agreements calculated by the MIMICS model.
These roughness parameters were assigned to the corresponding crop type.

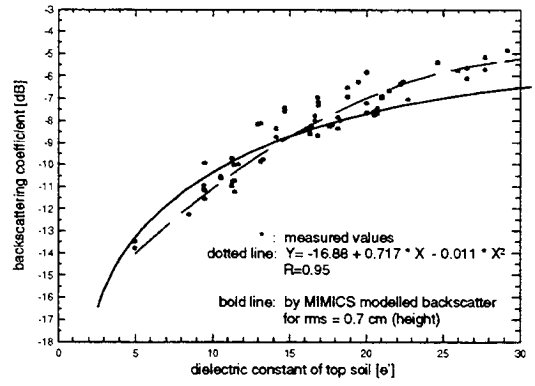

Figure 5: Regression analysis between dielectric constant and backscatter coefficient for corn fields

To eliminate the roughness influence on the backscatter signal, all backscatter coefficients were shifted from their estimated roughness class (crop type dependent) to the radar ineffective roughness class (RMS height > 2.4 cm).

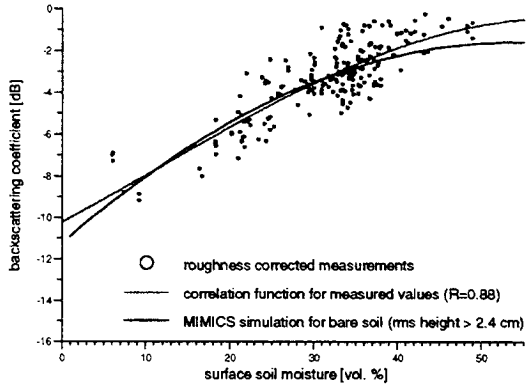

Figure 6: Roughness corrected relation between surface soil moisture and backscattering coefficient for all crop types under investigation

Figure 6 shows the results of this correction for over 200 measurements calculated for a standard soil (sand: 40 %, silt: 40 %, clay: 20 %) The dotted line is the nonlinear regression curve for these measurements with a correlation coefficient of 0.88. The bold line indicates the same relation derived by Ulaby (1992) for bare soils with a roughness height greater than 2.4 cm.

The influence of vegetation structure changes on the backscattering behavior is very strong within the major land use in the test site near Weilheim. Meadows change their phenotype within a vegetation period, not only, but also through cultivation activities of farmers. This structure change can be quantified by dry biomass measurements in the fields. Comparing this biomass

changes and the transmissivity of the backscatter for meadows in the test site, two relations of different meadow types can be distinguished. A stronger attenuation was observed, especially for extensive cultivated meadows. This kind of meadows seem to absorb the signal stronger than intensive cultivated meadows (see STOLZ & MAUSER, 1997b).

Ulaby et al. (1996) derived a transmissivity function depending on dry biomass per square meter for a radar system configuration with 5 GHz frequency, 20 degrees incidence angle and HH polarization with the MIMICS model. The graph in Figure 3 shows the estimated attenuation effects of extensive and intensive cultivated meadows measured in the test site near Weilheim, compared to the modeled results derived by Ulaby.

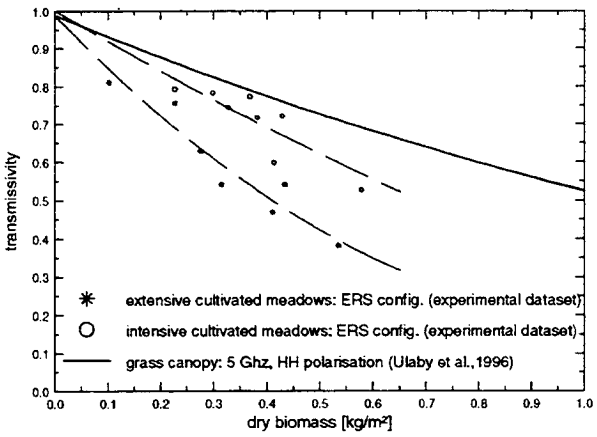

Figure 7: Transmissivity behavior of meadows in the test site compared to MIMICS simulation results with grass canopy

The simulated transmissivity is higher than the observed values. This can be explained by the different radar system parameters of ERS and the model and by different meadow types observed.
Using the temporal biomass measurements of meadows in the test site, all backscattering coefficients of meadows were corrected for vegetation structure changes with the transmissivity function of Figure 7.

8. RESULTS OF THE APPROACH

For corn, barley, oats, harvested and fallow fields nonlinear relations between the backscattering coefficients of ERS and the soil type independent dielectric constants are established. With these curves the roughness height (RMS) were estimated, based on the results of the Michigan Empirical Model. The offset from the ineffective ERS radar roughness height (< 2.4 cm) were calculated for each land use. The effects of vegetation structure changes on the backscattering signal of meadows are eliminated with relations between dry biomass and transmissivity.
A common regression curve between soil moisture and radar backscatter for crops under investigation were found, which is independent of vegetation and roughness effects (see Figure 6). A summary of the results can be found in Table I at the end of this paper.

9. SURFACE SOIL MOISTURE MAPS

For the purpose of hydrologic modeling, especially for floods and water yield, the knowledge of the spatial distribution and temporal change of the top soil moisture is essential to bring the existing models to a new level of accuracy and applicability. Recently hydrologic models are emerging, which explicitly model the spatio-temporal distribution of soil moisture from rainfall, meteorological data (radiation, temperature etc.) and runoff. Presently there is a considerable lack in methods for the validation and calibration of these models. To conduct a first test of the applicability of the proposed method to determine soil moisture for model validation purposes the model PROMET (MAUSER & SCHÄDLICH, 1997a; MAUSER et al., 1997b) was used. PROMET is based on a SVAT (Soil-Vegetation-Atmosphere-Transfer) scheme and was developed to determine the spatial water balance on different scales using as much remote sensing data as possible. It considers meteorology, plant development, soil differentiation and relief. PROMET models the spatial distribution of soil moisture on hourly basis. To be able to compare the results of PROMET with the measured soil moisture from ERS surface soil moisture maps are generated using the unified relation between backscattering coefficient of ERS images and soil moisture (Figure 6).

For the calculation of surface soil moisture maps two distinct ERS images from 1992 were chosen: one at the end of a drought period in spring (June 1) and one five weeks later after intensive rainfall (July 6) to test the sensitivity of the approach. The night before June 1 a small rainfall event of about 8 mm occurred, most of which evaporated from the wetted vegetation cover before the overpass of the satellite. The rest infiltrated into the top soil layer and partly filled it up. Before July 6 of the same year, rainfall was quite regular and intensive with a heavy rainfall the day before the overpass. After masking of forested areas, for which no relation between the ERS signal and soil moisture was derived, the backscatter was converted into soil moisture using the existing land use information for a selected test site near Weilheim.

The result is shown at the bottom of Figure 8. At the top of Figure 8 the model results from the days of the

satellite overpass are shown. They are cut out from a continuous stream of hourly model calculations, which started on March 1, 1992.

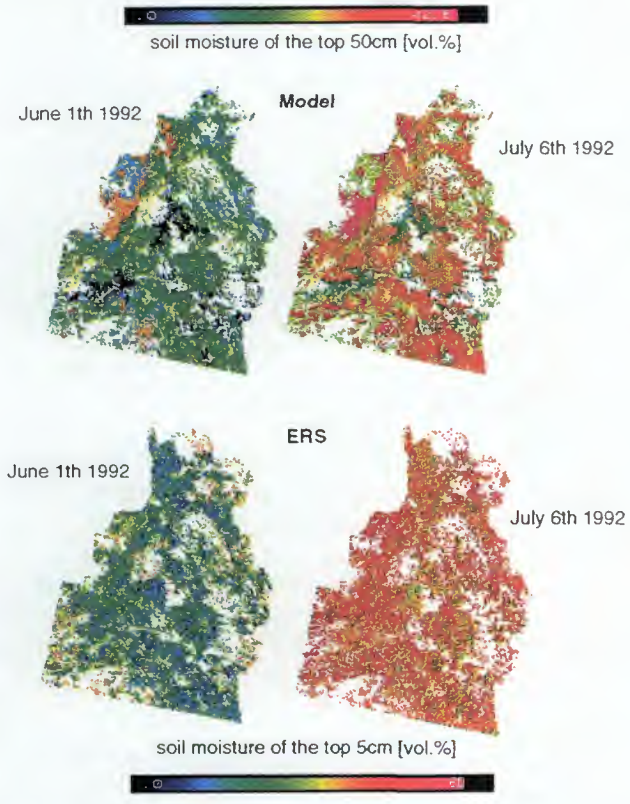

Figure 8: Soil moisture maps derived with the model PROMET and extracted from ERS radar data of the test site near Weilheim for two days in 1992.

The change in soil moisture between both days is clearly visible in both image pairs as much as differences in scale between satellite derived and modeled soil moisture allows. This is mainly due to the different depths for which the model and the satellite considers soil moisture (50 cm in the model vs. approx. 5 cm from ERS). Due to the light rainfall before the first overpass the surface is slightly wetter in the ERS image in June. This tendency even increases in July because the antecedent rainfall has filled up the top soil layer. The deeper layers of the soil are still drier than usual due to the drought in spring. The average surface soil moisture of the test site measured by ERS is about 20 vol. % in the June and 42 vol. % in the July image. The corresponding model results are 14 vol. % for June and 26 vol. % for July respectively. The larger changes in the topsoil moisture measured by ERS show the much larger soil moisture dynamics at the surface than in the deeper soil layers. Still the overall trend is visible.

For easier comparison Figure 9 shows the over and under estimation of soil moisture, calculated with ERS data in percentage relative to the soil moisture values received from the model.

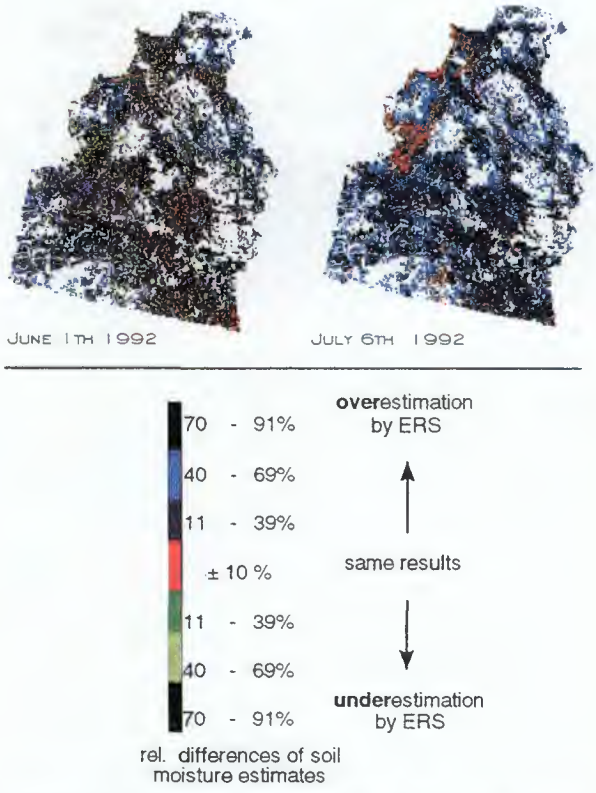

Figure 9: Comparison of ERS (top 5 cm) and modeled (top 50 cm) soil moisture results

The absolute soil moisture difference, calculated from the image in Figure 9, varies for June within 0.4 vol. % and 6 vol. % and for July from 1.5 vol. % up to 14 vol.%.

11. CONCLUSIONS

The principle possibility to measure surface soil moisture with the ERS radar system can be confirmed by the approach of this paper. Several limitations have to be taken care of. These are:

- existence of a land use map
- existence of a soil type map
- knowledge of the actual biomass of meadows
- soils under crops can only be monitored, when these crops passed a vegetation developing stadium from which onwards no radar effective changes take place.
- the approach is only validated for the crops investigated within this survey (corn, barley, rye, harvested and fallow fields and meadows).

If these additional information are available, surface soil moisture maps can be calculated, for all temporal

and spatial coverage of ERS. To use these surface soil moisture maps for modeling (as a starting parameter and for verification purposes), a multi layer soil moisture module must be implemented within the used SVAT model.

TABLE I

	dB vs. DC	R	RMS height (cm)	dB offset (approx.)	transmissivity vs. biomass
corn	$dB = -16.88 + 0.71\,DC - 0.0011\,DC^2$	0.95	0.7	4.6	-
barley	$dB = -24.07 + 1.17\,DC - 0.0020\,DC^2$	0.94	0.45	7.5	-
oats	$dB = -25.20 + 1.20\,DC - 0.0180\,DC^2$	0.94	0.43	7.9	-
harvested fields	$dB = -15.44 + 0.42\,DC - 0.0047\,DC^2$	0.90	0.65	5.3	-
fallow fields	$dB = -14.57 + 0.33\,DC - 0.0045\,DC^2$	0.97	0.55	6.5	-
meadows intensive	$dB = -16.53 + 0.53\,DC - 0.0055\,DC^2$	0.96	0.68	4.9	transm.= 1.0 - 0.84 biom. + 0.15 biom.^{2}
meadows extensive	$dB = -16.53 + 0.53\,DC - 0.0055\,DC^2$	0.96	0.68	4.9	transm.= 0.98 - 1.46 biom. + 0.67 biom.^{2}

dB vs. DC: function for the relation between backscatter and dielectric constant; *R*: correlation coefficient for the "dB vs DC function"; *RMS height:* estimated roughness; *dB offset*: approximated offset for roughness correction; *dB:* backscattering coefficient; *DC:* dielectric constant; *biom.*: dry biomass; *transm.*: transmissivity;

12. REFERENCES

Demircan, A., Rombach, M., Mauser, W. (1993a): Extraction of Plant- and Soil Parameters from Multitemporal ERS-1 SLC-Data of the Freiburg Test site. Proceedings First ERS-1 Symposium Cannes 1992, ESA SP-359, Vol. II 631-634.

Demircan, A., Rombach, M., Mauser, W. (1993b): Extraction of soil moisture from multitemporal ERS-1 SLC Data of the Freiburg Test Site. Proceedings IGARSS'93 Tokyo, Vol. IV, pp. 1794-1796.

Hallikainen, M., et al. (1985): Microwave Dielectric Behavior of Wet Soil - Part I: Empirical Models and Experimental Observations. IEEE Trans. Geosci. Remote Sensing, Vol. GE-23, No. 1, p. 25-34.

Laur, H. (1993): ERS-1 SAR RADIOMETRIC CALIBRATION. SAR Calibration Workshop, ESA WPP-048, ESTEC, Noordwijk.

Mauser, W. & Schädlich, S. (1997a): Modeling the Spatial Distribution of Evapotranspiration using Remote Sensing Data and PROMET. Accepted in J. of Hydrology.

Mauser, W. et al (1997b): The Contribution of Microwave Data to Distributed Hydrologic Models. Proceedings Third ERS-1 Scientific Symposium, Florence.

Mauser, W., Bach H. (1993): "FAP - Flächendaten Analyse Programm Version 2.0". Institut für Geographie, Lehrstuhl für Geographie und geographische Fernerkundung, LMU München, 182 S.

Rombach, M., Demircan, A. & Mauser, W. (1994): Correlation between Soil Moisture and the Backscattering Coefficient of ERS-1 Data. Proceedings Second ERS-1 Symposium Hamburg 1993, ESA SP-361, Vol. II p. 861-864.

Rombach, M., Kellndorfer, J., Mauser, W. (1993): Application oriented Requirements to SAR-Data Calibration - The Soil Moisture Case. SAR Calibration Workshop Noordwijk 1993, ESA WPP-048, S. 9-12.

Roth, C.H., Malicki, M.A. & Plagge, R. (1992) Empirical evaluation of the relationship between soil dielectric constant and volumetric water content as the basis for calibrating soil moisture measurements by TDR. Journal of Soil Science, 43, p. 1-13.

Stolz, R. & Mauser, W. (1997a): Knowledge-based multisensoral approach for land-use classification and biomass monitoring. Remote Sensing of Vegetation and Sea, Giovanna Cecci, Guido D'Urso, Edwin T. Engman, Preben Gudmandsen, Editors, Proc. SPIE 2959, 49-58.

Stolz, R. & Mauser, W. (1997b): Evaluation of ERS Data for Biomass Estimation of Meadows. Proceedings Third ERS-1 Scientific Symposium, Florence.

Ulaby, F.T., Moore, R.K. and Fung, A.K. (1982-1986): Microwave Remote Sensing: Active and Passive, Vol.II - Vol.III.

Ulaby, F. (1992): Modeling Radar Backscatter from Vegetation. Short Course Notes, DLR, Oberpfaffenhofen.

Ulaby, F., et al. (1996): Radar mapping of surface soil moisture. Journal of Hydrology 184, p. 57-84.

ACKNOWLEDGEMENT

The authors would like to thank the Deutsche Agentur für Raumfahrtangelegenheiten (DARA) for making this study possible through their funding of the projects "Land-Use, Pedology and Soil Moisture from Multitemporal ERS-1 Data" and "The Pre-Operational Use of ERS-Data in Hydrology and Agriculture". The authors also want to thank ESA for providing the necessary ERS images through its PI-program.

DETECTING SOIL THAWING IN SIBERIA WITH ERS SCATTEROMETER AND SAR

Kai Boehnke and Volkmar Wismann

Institute for Applied Remote Sensing, Bahnhofstraße 54, 22880 Wedel, Germany
T: +49-(0)4103-13922; F: +49-(0)4103-7469; E: ifars@compuserve.com

ABSTRACT

Based on multi-temporal radar backscatter measurements obtained from the ERS-1 scatterometer at various incidence angles, a method was developed for monitoring the state (frozen/thawed) of the upper layer of the soils in arctic to temperate climate regions. In spring and to some lesser extent in fall, the normalised radar cross section (NRCS) data show distinct variations which can be attributed to thawing and freezing soils. ERS SAR imagery was used to study the temporal and spatial behaviour of the radar cross section during the thawing process. The application of a change detection algorithm to the average radar cross sections derived from ERS scatterometer data for the Siberian test site reveals maps of the isochrons of thawing. The signatures detected in these maps are well represented in geographical distribution and the interannual variability of air temperature reanalyses and SSM/I derived snow cover. Overall, thawing commences in the south/south-west and progresses towards northern central Siberia. The thawing of mountainous regions is delayed compared to regions of lower elevation. Due to the huge extent of the Siberian test site, it takes more than three months for the entire region to be thawed. On average, interannual variations are up to one month, whereas locally, the "onset of thawing" can be several months apart.

INTRODUCTION

In the course of improving our understanding of the global climate, highly complex models describing the dynamics of the atmosphere and oceans play an important role. Only minor attention has been paid to the bio- and geospheric processes which influence our climate. Mainly due to the lack of sufficient data, exchange processes across these boundaries were treated as being static or in any event rough estimates of the dynamics of these processes had to hold. More recently, a more realistic description of these processes in numerical models evokes a need for high quality bio-and geophysical data. Of prime interest to climate modelers is the geophysical parameter soil moisture. So far, this parameter cannot be derived from remotely sensed data on scales applicable to climate modeling. However, in this study we show that information on the state of the soils (frozen/thawed) can be inferred from ERS scatterometer data (Boehnke and Wismann, 1996a, 1996b). This is an important environmental parameter since evapotranspiration and gas exchange processes change significantly when going from one state to the other and represents a first step towards soil moisture estimation.

When the vegetation cover is sparse or absent, the NRCS at C-band, VV polarization, depends mainly on the moisture content of the soil, the dielectric constant, the penetration depth and the surface roughness. The radar backscatter increases with soil moisture and with surface roughness. When liquid water in soil freezes, the dielectric constant of the soil falls dramatically. This process is reversed in spring when the soil thaws. From NRCS time series it can be seen that in spring, during snow melt, the radar cross section first decreases by up to 5 dB and shortly later, when the soils start thawing, increases dramatically (Wismann et al., 1996a). ERS-1 SAR images obtained simultaneously reveal this behavior in more detail. Within three days the radar return of the complete area has changed dramatically. In the following 3 weeks, the number of wet snow patches and melt water ponds - responsible for the low radar return - gradually decrease as the soils thaw and the water percolates the ground.

ALGORITHM DEVELOPMENT

The NRCS data are re-sampled to a grid with a resolution of 0.5° in latitude and 1° in longitude which corresponds roughly to the instrument resolution of 50 by 50 km. For three day intervals, an average radar cross section (σ_{40}) is computed for each grid point by linear regression between the measured NRCS and their respective incidence angles. σ_{40} is the value of this regression line at an incidence angle of 40° (Wismann et al., 1996b). This procedure accounts for the incidence angle dependence of the NRCS which is highly variable in spring when the backscattering mechanism changes from volume to surface scattering depending on snow cover, snow wetness, soil moisture and penetration depth of the microwaves. Moreover, irregular distributions of NRCS measurements with respect to the

incidence angle due to sampling and orbital characteristics have little influence on σ_{40}. Fig. 1 shows two typical time series of σ_{40} for two grid points in Siberia, their geographical positions are given in the figure. Note the extreme temporal stability of the radar cross section during early spring and the large variations (>5 dB) associated with the onset of thawing.

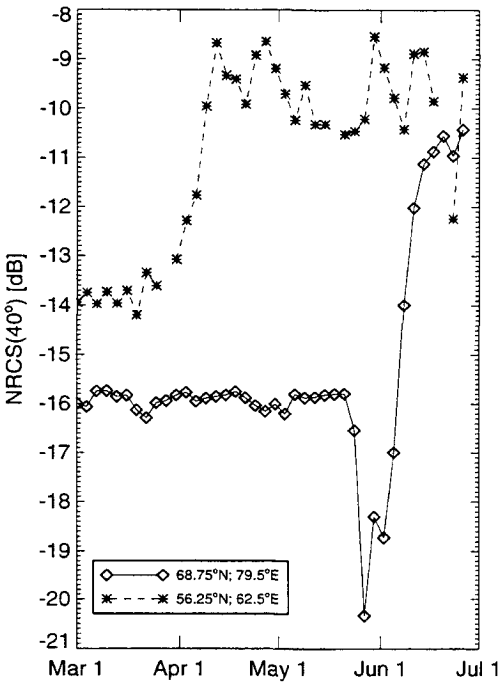

Fig.1: Time series of σ_{40} for two grid points in spring 1993.

The next step involves determining the monthly means for February and July of each year and finally, detecting the point of time of thawing. The latter is achieved by analyzing the σ_{40} time series during the spring (for the time period March, 1 to July, 1) for the step-like increase seen in Fig. 1. The change-detection algorithm marks a grid point as thawed when two consecutive σ_{40} values exceed 50% of the difference between the monthly mean of σ_{40} for July and February of the respective year. The constraint of requiring two values above the threshold eliminates spikes which are not removed when computing σ_{40} and single events which are not connected to the thawing process.

In Fig. 1 the onset of thawing is detected at the beginning of June for the grid point located in the north, whereas for the grid point further south, the algorithm detects thawing at the beginning of April. As can be seen from the σ_{40} time series of the northern grid point, spring snow melting leads to a strong short-term decrease of up to 5 dB. This drop in σ_{40} can be explained by the increasing wetness of the snow leading to an enhanced absorption of the microwaves and the subsequent low radar return from melt water ponds formed on the frozen grounds when infiltration is still blocked.

Further evidence for the interpretation of the radar cross section behaviour during the snow melt - soil thaw succession comes from a sequence of five ERS-1 SAR images acquired over northern Siberia between May 20 and June 27, 1995. The overlapping area is 26 km by 69 km wide and is centred at 70.75° N 77° E. Fig. 2 displays this sequence of SAR scenes marked A-E which are snapshots taken at various stages of the snow melt - soil thaw succession. On May 20 (SAR scene A), the ground is snow covered and lakes and rivers which are still frozen appear as bright patches. Only three days later, SAR scene B shows an overall lower radar return. A reduction of approximately 4 dB can be delineated from the histograms displayed to the right side of each SAR scene in Fig. 2. The air temperature has exceeded 0°C and initiated snow melting resulting in low radar return from wet snow.

SAR scenes C and D show two intermediate stages which can be described as follows: In the low regions in the vicinity of the rivers (meandering signatures nicely visible in scene D), the snow has melted rapidly but the melt water cannot infiltrate the ground since it is still frozen. Also, melt water run off is hindered as the rivers are at their highest water level at this time of year. Radar return from these regions is extremely low. The snow melt in slightly higher regions with more rigid terrain (bottom centre of the SAR scenes) has basically also taken place between May 20 and May 23. An increase in contrast such that the relief seems to become more evident, can be explained by wet snow and melt water accumulating in the valley regions whereas the hilly areas are already exposed. This diversity in surface conditions and thus in NRCS leads to the double peaks in histograms C and D. SAR scene E in Fig. 2 reveals the situation after all the snow and melt water has disappeared and the soil has thawed. On June 27, of all the scenes, the highest NRCS is measured. From this scene one can clearly delineate that the contributions of lakes and rivers to the overall NRCS is very small and can be neglected.

Fig. 3 depicts the time series of the NRCS measured by the scatterometer at the same location where the SAR scenes were taken. The scatterometer data were referenced to 23° of incidence angle and mean NRCS values were calculated from the histograms of the SAR scenes A-E (see Fig. 2) and included in the graph. Both the NRCS obtained from scatterometer and SAR experience a strong decrease as soon as the air temperatures exceed 0° C in the third week of May (NCEP, 1996). The NRCS continuously increases when air temperatures above freezing persist from the second

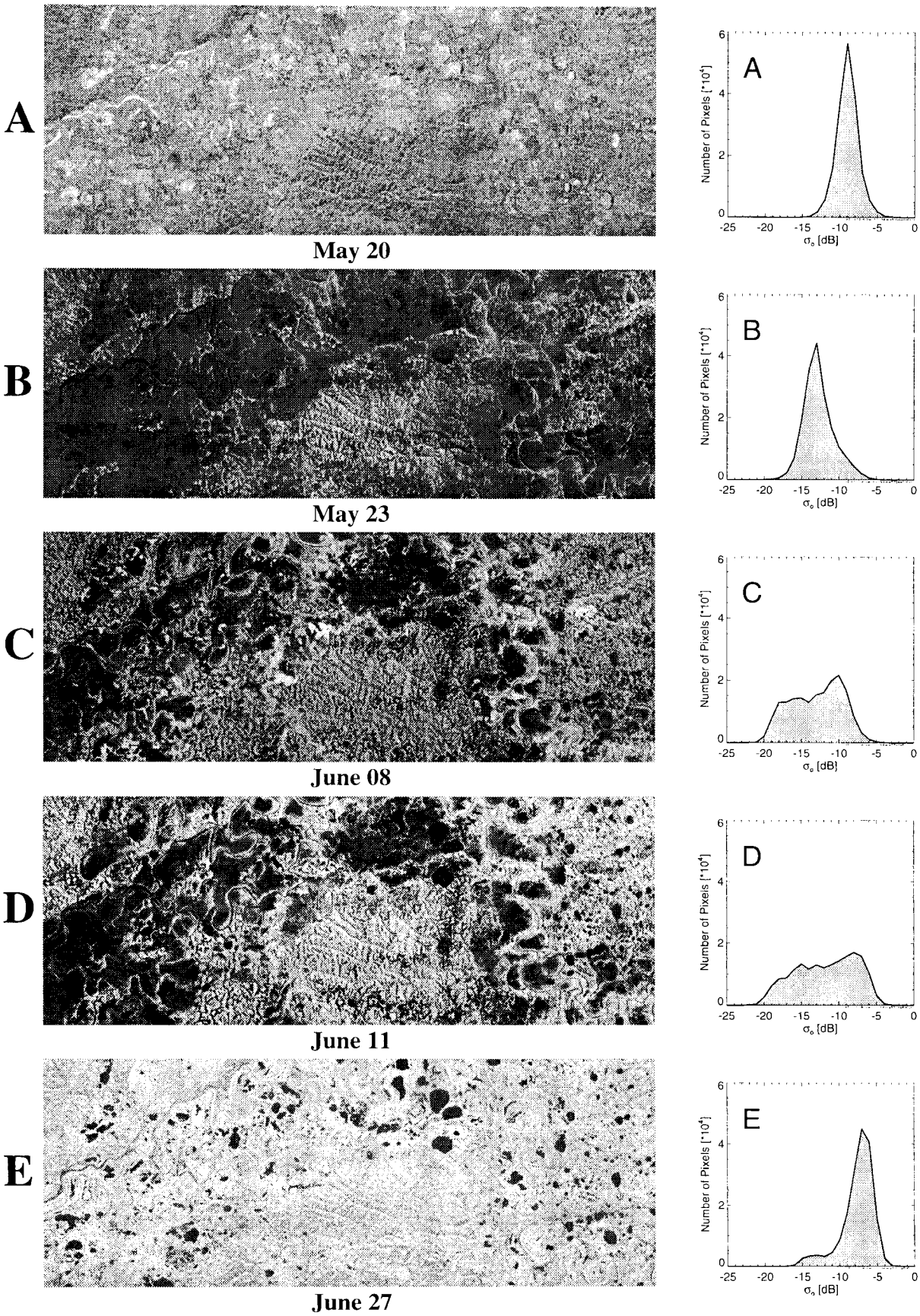

Fig. 2: Sequence of ERS-1 SAR scenes (frame 2169, © ESA 1995) and the respective histograms of the NRCS. The scenes cover an area of 26 km by 69 km centred on 70.75° N 77° E

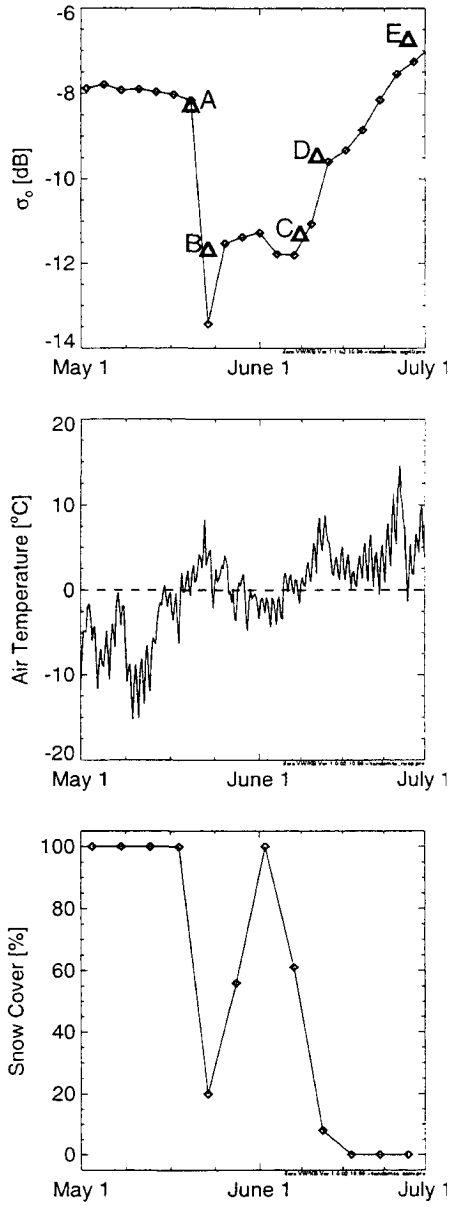

Fig. 3: Time series of NRCS from scatterometer (top), air temperature (middle), and snow cover (bottom). Average NRCS values derived from SAR images A-E of Fig. 2 are included for comparison (top).

week of June on. For comparison, the bottom plot in Fig. 3 shows the snow cover percentage derived from SSM/I radiometer data (Grody, 1991). These data reproduce the first snow melt onset correctly, whereby the SSM/I seem to respond more sensitive to a refreezing of the remaining snow surface at the beginning of June. Here only a slight increase in NRCS was observed.

MAPPING THE ONSET OF THAWING

The algorithm detecting the freeze / thaw transition has been applied to the scatterometer data for the Siberian test site, which extends from 50° N to 80° N and from 42° E to 172° E. For the years 1992 to 1996, maps of the isochrons of thawing were constructed which reveal the geographical distribution and the interannual variability of the "onset of thawing". These maps are shown in Fig. 4 for the years 1992 to 1996. Each colour represents the area thawed before the date marked under the colour scale. Each of the 16 colour codes corresponds to a time step of 8 days and thus the observation time period from March 1 to June 28 is spanned. Superimposed are contour lines marking elevation levels of 100, 250, 500 and 1000 m (Lee and Hastings, 1995).

The temporal and spatial evolution of the onset of thawing differs significantly over these years. In 1992, the onset of thawing is late. After the southern part of the test site starts thawing in April, thawing gradually moves towards the north coincident over the complete range of longitudes. By the middle of May, thawing has reached most of Siberia with the exception of the Central Siberian Plateau. For 1995, thawing commences early in the southwest and progresses towards the northeast somewhat slower than in 1992, so that by the middle of May in both years, approximately the same area has thawed (green to grey colours). At last, in both years, the Central Siberian Plateau starts thawing in June.

On a regional scale, the onset of thawing follows orographic particulars. As expected, mountainous regions (e.g. Ural, Werchojansk, Stanowoi) thaw later than regions of lower elevation. It is remarkable how well some isochrons - especially in eastern Siberia - are in accordance with the elevation contour lines.

There is no evidence, that different types of vegetation influence the detectability of the "onset of thawing" using the proposed technique. The Siberian test site spans several classes of natural vegetation, i.e., from forested steppe in the south over boreal forests (central Siberia) and mixed forests (eastern Siberia) to the Tundra region with negligible vegetation cover in the north. Surely, the σ_{40} time series vary over these different terrains, which is why we cannot rely on the strong dip in NRCS shown in Fig. 1 (northern grid point) as an indicator for the thawing of the soils, since this signature is typical for the Tundra region. Nevertheless, the patterns better match topographic maps where local thaw-detection coincides with elevation, whereas the overall thawing depends on the regional meteorological conditions.

INTERANNUAL VARIABILITY

For a sub-region of the Siberian test site encompassing the West Siberian Lowland and the Central Siberian Plateau (55°-70° N; 50°-120° E), the interannual variability was estimated. For each time step of 3 days, the area classified as thawed was calculated for each individual year. The slope of the area versus time curves is rather constant for all the years except 1992 (see Fig. 5 top). For the years 1993 to 1996, the thawed area gradually increases throughout the entire time period, whereas in 1992, the onset of thawing is late, but then the majority of the Siberian sub-region thaws much quicker than in the other years. In 1995 thawing begins very early and in 1996 very late. The overall large scale interannual variability is on the order of one month.

Analogous area versus time plots were created for the SSM/I snow cover data (Fig. 5 middle) and the air temperature data (Fig. 5 bottom). The large scale characterizations of "spring" from the scatterometer data, the SSM/I data and the air temperature data agree well. The early progress in 1995 and the rapidity of the "onset of spring" in 1992 are consistent. Discrepancies are found for 1992, where the "onset of spring" in the SSM/I data - the area no longer covered with snow - is detected very early. The step-like increases in the plot constructed from the air temperatures arise from the large areal extent of a grid point (2.5° by 2.5°).

DISCUSSION

A method has been developed for monitoring the state of the soils in arctic to temperate climate regions. It was demonstrated that the proposed algorithm reveals reasonable geographical distributions and temporal evolution of the thawing of the soils. In general, thawing commences in the South and then progresses towards the North whereby regions of higher elevation thaw later than lower regions.

Presently, only the very first thawing event is detected within the time period March 1 to July 1 since the change-detection algorithm does not account for refreezing. Here, a more stringent formulation of the algorithm must be found and the radar signal of the thaw/freeze transition must be understood. The freezing of soils as well as the build-up of a snow cover express themselves as gradual decreases in σ_{40} making it more difficult for an algorithm to react quickly enough, e.g., compare the slight dip in the σ_{40} time series in Fig. 3 (top) just before SAR data take C and the corresponding air temperature curve in Fig. 3 (middle) which shows temperatures below freezing for one week around the first of June.

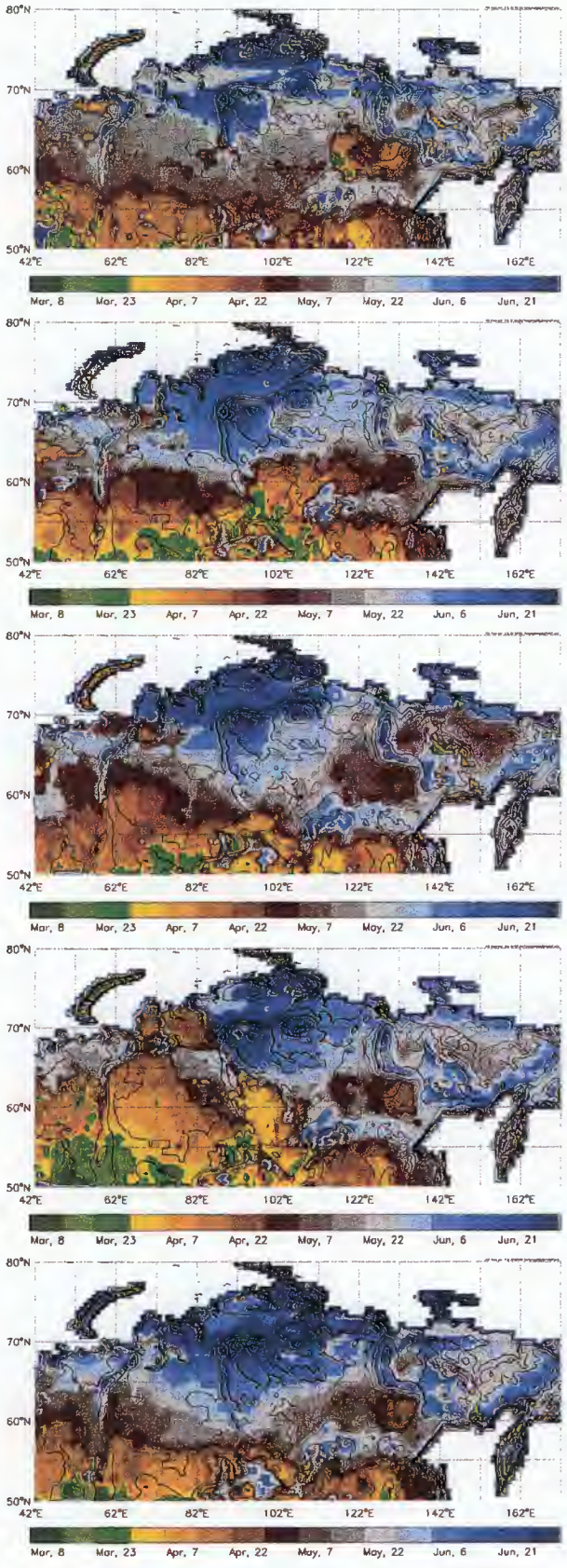

Fig. 4: Maps of Siberia, depicting isochrons of the "onset of spring" defined by scatterometer derived thawing of soils for 1992-1996 (top to bottom). See text for details.

One free parameter in the proposed method is the definition of the time of thawing. The accuracy with which this parameter can be determined depends on the temporal resolution and quality of the in situ data. In this respect, the question arises how representative a singular point measurement is for the state of an area of 50 by 50 km viewed by the scatterometer. SAR scenes C and D (Fig. 2) give an impression of the spatial variability associated with the thawing in spring. The patchiness of the SAR scenes and the double-peak histograms indicate that single point measurements within a scatterometer resolution cell are not representative for the environmental conditions encountered. On the other hand, as one can see from Fig. 1, any other definition of the point of time of thawing can only lead to a relative time shift of a few days. In general, large scale interannual variations detected from the evaluation of the scatterometer data are of the order of one month and agree well with those detected in SSM/I derived snow cover data and air temperature data.

One advantage of the proposed method is, that with minor modifications, the proposed technique is suitable for operational use and, thus, could make soil state information available in near real-time. This would provide a good data basis for climate models which are very sensitive to changes in the evapotranspiration exchanges between the atmosphere and the ground which essentially depend on the soil state.

ACKNOWLEDGEMENT

A part of this work was conducted under ESA study contract No. 11103/94/NL/CN. The ERS-1 scatterometer data were provided by ESA as Fast Delivery Product Copies (FDC) from Centre ERS d´Archivage et de Traitement (CERSAT) the French Processing and Archiving Facility (F-PAF). Global temperature data in form of the NCAR/NCEP reanalysis were provided by the NOAA Climate Diagnostics Center. Global snow cover and precipitation data derived from SSM/I radiometer data were provided by Ralph Ferraro, Microwave Sensing Group, NOAA/Satellite Research Laboratory.

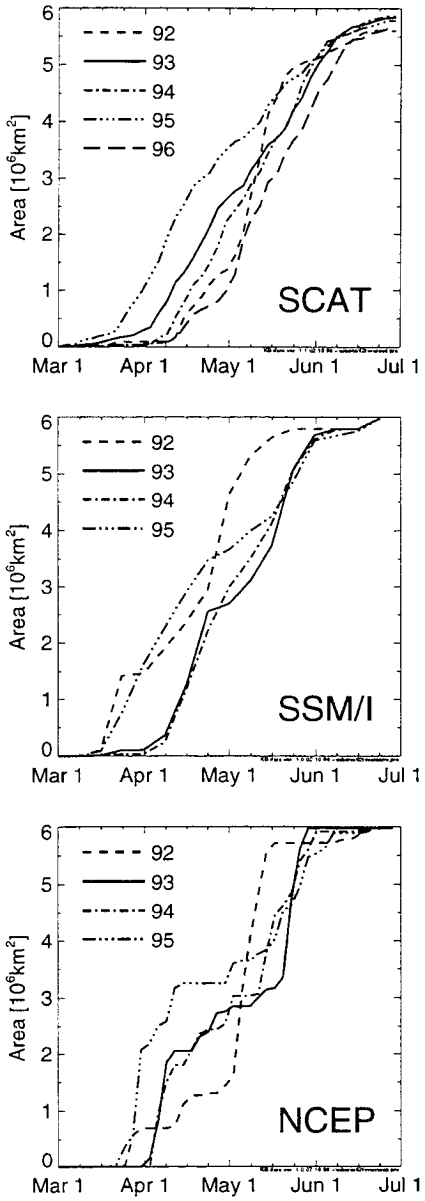

Fig. 5: Time series of the extent of the area detected as thawed (top), depleted of snow cover (middle), and with mean air temperatures above 0°C (bottom).

REFERENCES

Boehnke, K. and V. R. Wismann, ERS Scatterometer Land Applications: Detecting the Thawing of Soils in Siberia, *Earth Observation Quarterly, ESA Publication Division*, 52, 4-7, 1996a

Boehnke, K. and V. R. Wismann, Thawing of Soils in Siberia Observed by the ERS-1 Scatterometer Between 1992 and 1995, Proceedings of the International Geoscience and Remote Sensing Symposium - IGARSS'96, Lincoln, USA, May 27-31, Volume IV, 2264-2266, 1996b.

Grody, N. C., Classification of snow cover and precipitation using SSM/I, J. Geophys. Res., 96, 7423-7435, 1991.

Lee, W. R. III and D. Hastings, TerrainBase Global DTM Version 1.0 (on CD-ROM), National Geophysical Data Center and World Data Center-A for Solid Earth Geophysics, Boulder, Colorado, USA, 1995.

NCEP, NCAR/NCEP reanalysis data provided through the NOAA Climate Diagnostics Center (http://www.cdc.noaa.gov/), 1996.

Wismann, V., A. Cavanie, D. Hoekman, I. Woodhouse, K. Boehnke and C. Schmullius, Land surface observations using the ERS-1 scatterometer - Final Report Part I, ESTEC Contract 11103/94/NL/CN, 57 pages, 1996a.

Wismann, V., K. Boehnke A. Cavanie, R. Ezraty, F. Gohin, D. Hoekman, and I. Woodhouse, Land surface observations using the ERS-1 scatterometer - Final Report Part II, ESTEC Contract 11103/94/NL/CN, 65 pages, 1996b.

DEVELOPMENT AND DEMONSTRATION OF SOIL MOISTURE DETERMINATION AND INSAR FOR CATCHMENT HYDROLOGICAL MONITORING

P.J. Saich, R.J. Miller
Space Division, GEC-Marconi Research Centre, Chelmsford, Essex CM2 8HN, UK
tel: +44-1245-242654, fax: +44-1245-475244, email: paul.saich@gecm.com

A.J. Sephton
Space Systems Finland, Keilaranta 8, Espoo, Finland

C.G. Collier, N.I. Fox
Telford Research Institute, University of Salford, Salford M5 4WT, UK

ABSTRACT

ERS SAR data acquired during the Tandem Mission have been used to determine catchment slopes and monitor soil moisture as inputs to a hydrological model for predicting the potential for floods in the catchment area of the River Irwell in the U.K. A Digital Elevation Model (DEM) has been derived for the area using a pair of ERS SAR images acquired one day apart. This DEM has been validated against maps of the area and provides estimates for the local terrain slopes. The soil moisture retrieval makes use of an algorithm that has been motivated by a theoretical scattering model. The algorithm has been developed and tested using ERS SAR data and in-situ measurements acquired over a five month period. The algorithm and the radar measurements are found to give a good retrieval of the soil moisture but there are distinct differences between the results from descending and ascending orbits.

Keywords: SAR, Radar, Hydrology, Interferometry, Soil Moisture

1. INTRODUCTION

A significant proportion of the world's population reside in areas that are prone to flooding, such as low-lying floodplains or regions in which convective rainfall and local ground conditions lead to surface run-off. In many of these areas reliable and accurate information for predicting the likely extent of the floods is often unavailable. Existing methods such as telemetering of river levels and rain gauge data may not be possible or even adequate in many regions and it is often these regions that suffer most from a lack of resources for coping with flooding. Remote sensing data would provide an ideal source of information allowing the likelihood of flooding to be estimated on a routine basis and enabling scarce resources to be directed most efficiently. This project aims to construct and test a hydrological model for predicting flood potential due to convective rainfall. The model is driven by two sources of remote sensing data - optical / IR and synthetic aperture radar (SAR). The model and overall strategy have been developed and tested at the River Irwell catchment area in Northern England. In the future this will be extended to a more realistic site in Africa. In this paper, the overall project philosophy is first outlined, including the way in which the sources of remote sensing data are combined into the hydrological model. Following this, a more complete description of the role of SAR data is given, covering the generation of accurate topographical information and the retrieval of soil moisture as a boundary condition to the hydrological model.

2. PROJECT PHILOSOPHY

The overall idea of the project is that models for convective rainfall can be both driven by and combined with appropriate remote sensing information on local surface conditions to predict the strength of heavy showers and the amount of this that flows out of the catchment area as surface run-off. A structure diagram for the model is given in figure 1. Information on surface temperature (from either the ATSR instrument on board ERS or NOAA's AVHRR instrument) and the soil moisture (from the SAR) are combined in an atmospheric boundary layer model to predict the amount of convective rainfall. This is then combined with information on general land-use (from optical / IR measurements) and terrain slopes (from the SAR) to predict the amount of surface run-off.

3. THE ROLE OF SAR DATA IN HYDROLOGICAL MODELLING

Generation of Terrain Slopes by INSAR

A pair of complex quarter-scene (50km x 50km) ERS SAR images has been acquired over the River Irwell test site during the Tandem phase of the

ERS-1 and 2 missions. The images have a temporal separation of one day (11th/12th October 1995), an interferometric baseline of 343m and were acquired via the Matra-Marconi Space (MMS) Rapid Acquisition and Information Dissemination System (RAIDS). The test site covers an area of approximately 35km x 35km and a range of elevations up to approximately 500m.

Complex image handling has been conducted using an interferometric processor developed at GEC-Marconi Research Centre (MRC) which performs image registration, interferogram generation and then generation of a number of associated products such as the DEM or coherence maps. The interferogram generation requires phase unwrapping which has been done using a "valley seeking" method known as the Minimum Phase Difference Seeking (MPDS) algorithm [Ref. 1]. This method, which uses the phase gradient to determine the optimal unwrapping path, does not rely on the detection of phase singularities (such as "cut and branch" unwrapping methods [Ref. 2]) or fringe line detection [Ref. 3] and has been found to work successfully on a variety of data. The method also has the advantage of unwrapping the "least reliable" regions last so that any errors resulting from large phase gradients are contained within relatively small neighbourhoods.

The DEM generated from this approach is shown in figure 2. The DEM covers an area of 25.6km (range) by 43.77 km (azimuth) and has a horizontal resolution of 55m. Its vertical accuracy has been validated by comparison with Ordnance Survey DEMs. Some large errors (greater than 100 m) are apparent, associated with phase unwrapping artifacts in the most rugged areas. Elsewhere accuracies appear to be of order 15 m. The terrain slopes can be generated directly from the DEM. In place of this, a "mean slope index" for the catchment area is determined and used as input to the calculation of the surface run-off.

Determination of Soil Moisture by SAR

The other role of the SAR is to provide a means of monitoring the local soil moisture conditions. To study this, a sequence of seven ERS SAR images of the area has been acquired and analysed in conjunction with in-situ soil moisture data. Six of the images are from descending ERS orbits and the other is from an ascending orbit. In-situ soil moisture measurements have been made using a dielectric probe at an experimental facility operated by the University of Salford. The vegetation cover around the test site is mainly grass.

The SAR images have been acquired using RAIDS. These images are 24-look (to smooth speckle), the pixels are 100m square and the resolution is approximately 200 and 170 m across and along-track respectively. In the following comparison between radar and in-situ measurements, we work with the single pixel backscatter corresponding to the test site at which soil moisture is measured. This is identified to the nearest pixel (approximately 100m).

Many existing studies look for a correlation between soil moisture and SAR backscatter and quantify this correlation with linear regression. When this has been done, the resulting expression can be rewritten in the form of a linear "retrieval algorithm" of the form $m_s=\alpha+\beta\sigma^0_{dB}$, where m_s and σ^0_{dB} are the volumetric soil moisture and backscatter coefficient (dB) respectively, and α and β are the parameters of the regression.

Instead of this, we have chosen to begin with a physical model for the surface scattering and simplify this to a form suitable to be used in the regression against the observed data. The advantage of this is that we will be able to identify precisely the meaning of the "free parameters" that are used in the fitting and conjecture how their behaviour might be quantitatively different in other contexts. The model we use is for scattering from a surface with an optically thin layer of vegetation. The surface scattering is described by the Kirchhoff Geometrical Optics model and the effect of the optically thin vegetation layer is to act as an attenuator of the ground scattering - the vegetation does not itself contribute directly to the radar backscatter. With this simplification, the backscatter coefficient in natural units is

$$\sigma = e^{-2\tau}\sigma_s \qquad (1)$$

for optical depth τ where the ground scattering term σ_s is

$$\sigma_s = \frac{|R|^2 e^{-\tan^2\theta/2s^2}}{2s^2\cos^4\theta} \qquad (2)$$

In (2), R is the Fresnel reflection coefficient for vertically polarised waves at normal incidence, θ is the local incidence angle and s is the rms surface slope. It is through the dependence of the reflection coefficient on the surface permittivity that we gain the dependence on soil moisture. To isolate this,

note that if we integrate (1) over probability distributions in both the optical depth and the surface roughness, we obtain

$$\sigma_{dB} = A + 20\log_{10}|R| \qquad (3)$$

where

$$A = 10\log_{10}\iint \frac{e^{-2\tau-\tan^2\theta/2s^2}}{2s^2\cos^4\theta} p(\tau)p(s)d\tau ds \qquad (4)$$

Though A has a complicated form we could in principle estimate it by numerical simulation (using theoretical scattering models). Rather than this, we have chosen to determine its value experimentally by using (3) as a model function to use in non-linear regression against the in-situ data. For the relationship between the Fresnel coefficient and the volumetric soil moisture content we use R= $(\sqrt{\varepsilon}-1)/(\sqrt{\varepsilon}+1)$ where the permittivity, ε, depends upon the soil texture and moisture according to the model of [Ref. 4].

In figure 3 we show the backscattered powers for the area of the test site and against this have plotted the best fit using equation (3). Note that in the fitting we have chosen to ignore the single ascending pass, where the backscatter is approximately -3.3 dB. The empirical value for the constant A is determined to be 0.6213 and we now use (3) in conjunction with this value as a retrieval algorithm to operate on the backscattered data. The results are shown in figure 4 and compared with the in-situ measurements. The comparison between these is quite good, especially in terms of tracing the decrease and subsequent increase in soil moisture near day 240. However, it is clear that the dynamic range of the retrievals is quite small - ideally we would like to see this tested over a wider range of soil moisture conditions.

As a final point we note that the single ascending pass gave a backscatter much higher than any of the descending passes (see figure 3). We have concerns that the low resolution dataset we are processing contains complex features in the local terrain whose responses may differ significantly between the ascending and descending imaging geometries. Examination at higher spatial resolution will be required to confirm this. We note that differences between the images are apparent in the distribution of backscatter values from the entire area. This has a characteristic shape for each of the descending passes that differs markedly for the ascending pass. By assuming typical values for the variation in vegetation optical depths, soil roughnesses and local incidence angles across the region, we find that the width of the distribution is most strongly affected by the local incidence angle.

4. CONCLUSIONS

The role of SAR in hydrological monitoring for determining catchment area terrain slopes and local soil moisture has been identified and tested. The generation of a DEM is found to be relatively straightforward for this test site and yields reasonably good results. The soil moisture study has indicated that even in areas with a thin vegetation covering it is possible to monitor the changes in soil moisture and a model for this relationship has been suggested. The results are fairly good though require validation over a wider range of soil moisture variations and for other sites. A strong difference between descending and ascending orbits has been identified.

5. ACKNOWLEDGEMENTS

This work has been supported by the British National Space Centre (BNSC) under the BNSC Earth Observation Link Programme (project R1/012), and by Matra-Marconi Space (MMS). Many thanks also to the European Space Agency for the use of ERS data acquired during the Tandem Mission.

6. REFERENCES

[1] Partington, K.C., Rye, A.J., Wright, P.A. & Smith, P.J., 1995. "High Level Software Design for the Production of SAR-Derived Digital Elevation Models", GEC-Marconi Research Centre Document MTR 95/52A.

[2] Goldstein, R.M., Zebker, H.A. & Werner, C.L., 1988. "Satellite Radar Interferometry: Two Dimensional Phase Unwrapping", Radio Science, Vol. 23, 713.

[3] Lin, Q., Vesecky, J.F. & Zebker, H.A., 1992. "New Approaches in Interferometric SAR Processing", IEEE Trans. Geosci. & Remote Sensing, Vol. 20,

[4] Hallikainen, M., Ulaby, F.T., Dobson, M.C., El-Rayes, M.A. & Wu, L. -K., 1985. "Microwave Dielectric Behaviour of Wet Soil - Part 1: Empirical Models and Experimental Observations", IEEE Trans. Geosci. & Remote Sensing, Vol. 23, 25 - 34.

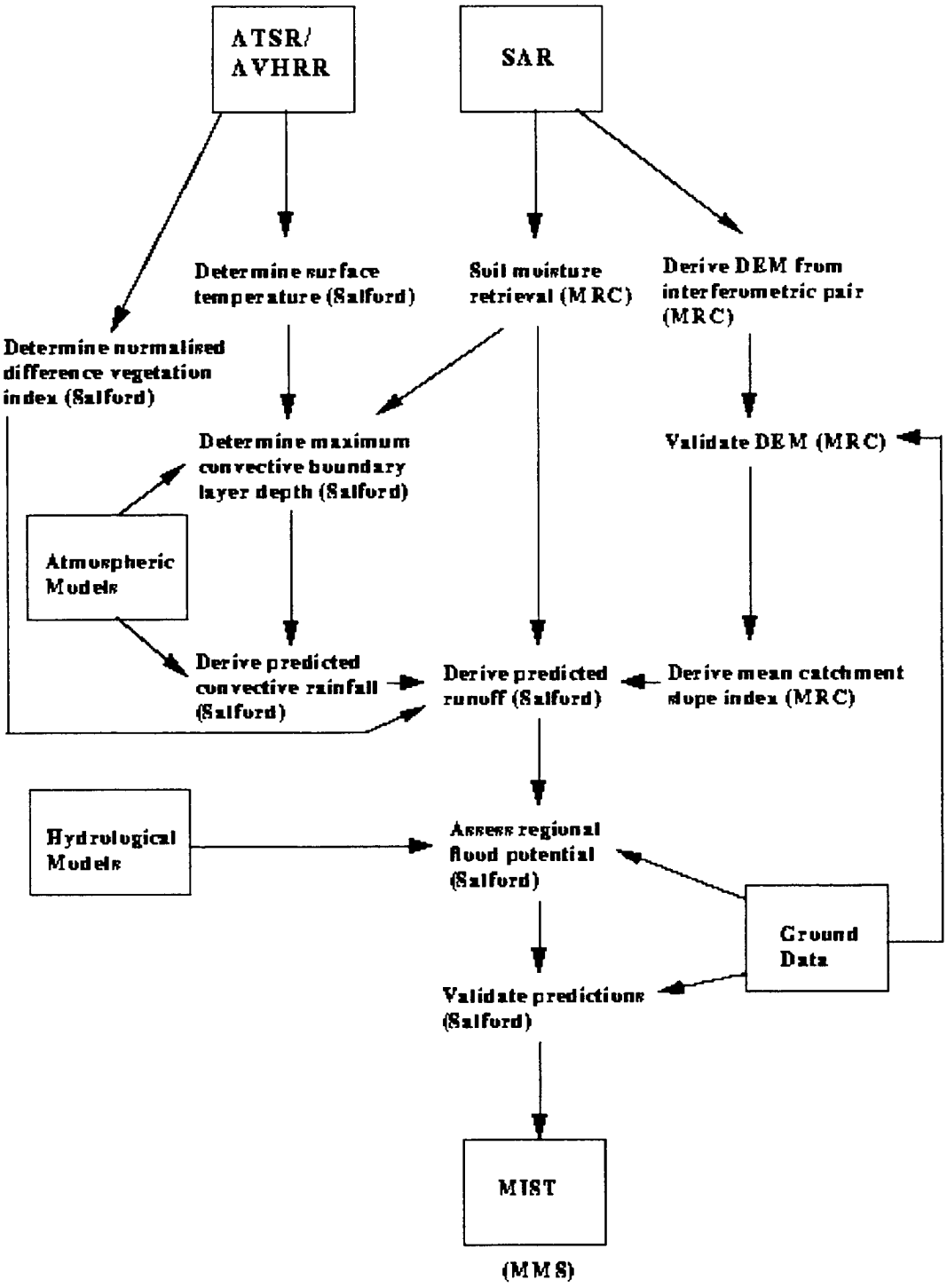
ATSR/
AVHRR
SAR
Determine surface temperature (Salford)
Soil moisture retrieval (MRC)
Derive DEM from interferometric pair (MRC)
Determine normalised difference vegetation index (Salford)
Determine maximum convective boundary layer depth (Salford)
Validate DEM (MRC)
Atmospheric Models
Derive predicted convective rainfall (Salford)
Derive predicted runoff (Salford)
Derive mean catchment slope index (MRC)
Hydrological Models
Assess regional flood potential (Salford)
Ground Data
Validate predictions (Salford)
MIST
(MMS)

Figure 1.

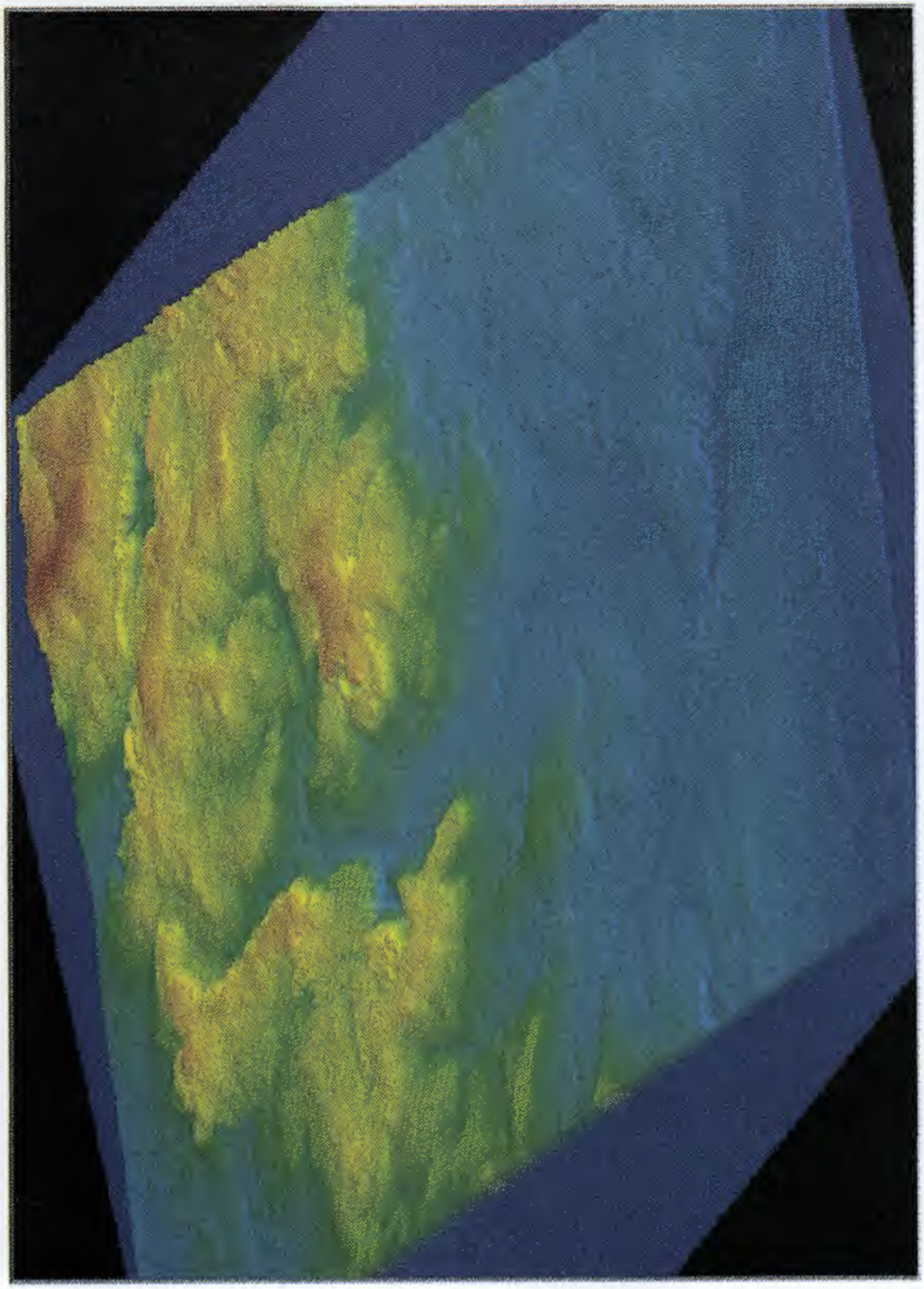

Figure 2.

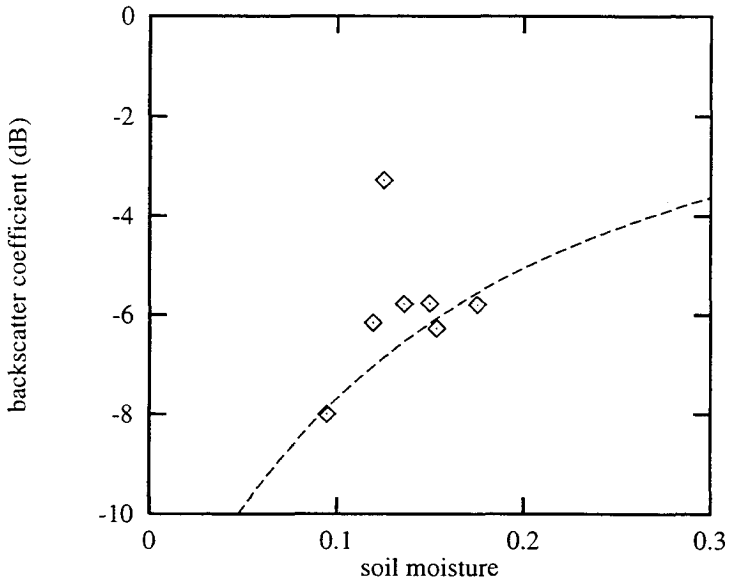

Figure 3 SAR Backscatter compared with measured soil moisture. The point at -3.3 dB is an ascending pass, the others are all descending

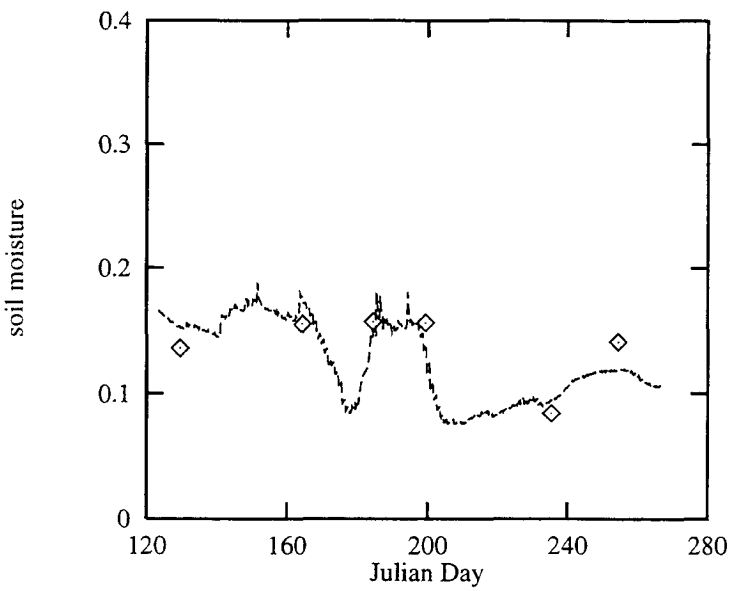

Figure 4 Retrieved soil moisture in comparison with measured soil moisture. Descending passes only

SOIL MOISTURE MONITORING WITH ERS SAR INTERFEROMETRY

Urs Wegmüller

Gamma Remote Sensing, Thunstrasse 130
CH-3074 Muri b. Bern, Switzerland
Tel: +41(0)31-951.70.05, Fax: +41(0)31-951.70.08
email: gamma_rs@pingnet.ch

ABSTRACT

Soil moisture monitoring with repeat-pass ERS SAR data using interferometric signature analysis was investigated using data acquired over Middle Zeeland, The Netherlands, between January and March 1994 during 3-day repeat orbits. Bare and sparsely vegetated fields with constant surface roughness were identified based on its interferometric signatures. Such areas are most useful for soil moisture monitoring. Under the assumption of limited vegetation scattering and constant surface roughness, multi-temporal microwave backscattering data show a clear dependence on the soil moisture content of the upper most soil layer. For eight bare fields without roughness change the backscattering was related to the in-situ measured soil moisture and used to derive retrieval algorithms for the relative soil moisture change and the soil moisture. The relative soil moisture change is retrieved from the relative backscatter change (defined as difference of backscatter values in dB, or ratio [in dB] of absolute backscattering values). The absolute soil moisture can be estimated if the soil moisture is known for one reference data set. In the case of the Middle Zeeland data acquired during a period with frozen soils, i.e. very low soil moisture content, was used as moisture reference. The influence of the surface roughness on the soil moisture retrieval algorithm were also investigated. In a further step, the algorithms were applied to fields without in-situ data, allowing to retrieve soil moisture maps for larger areas.

1. INTRODUCTION

One of the most often proposed application of microwave remote sensing is the retrieval of soil moisture. The scattering properties of a soil surface are dominated by its geometry and its permittivity or dielectric constant. The permittivity itself depends strongly on the soil moisture content because of the very high permittivity of liquid water. Therefore, the suggested approach is to relate the measured backscattering to the permittivity and the latter to the soil moisture, or what is done even more often, to relate the backscattering coefficient directly to the soil moisture. In practice, it turns out that soil moisture measurement based on the microwave backscattering coefficient is a very difficult task. In order to better understand the scatter properties theoretical models were developed. Based on such models the physical understanding was much improved. Forward models can reasonably well predict the observed backscattering coefficient. The inversion of the models is, unfortunately, much less reliable.

Most studies to retrieve soil moisture from microwave backscattering are restricted to bare soils. In addition the approach can be further simplified by interpreting time series of data over specific areas. As long as the surface roughness does not change for those areas the backscatter change originates from the permittivity, respectively soil moisture, change. Under the assumption of constant surface roughness quite reliable soil moisture estimates are obtained from the microwave backscattering coefficient. Surface roughness changes may result in severe errors in the moisture estimate, though.

Here, a new technique is proposed to improve the potential of SAR data for hydrological applications. Repeat-pass SAR interferometry, as successfully demonstrated with data from the ERS satellites, is very sensitive to temporal change (Wegmüller et al., 1995a, Wegmüller et al, 1995b). In a multi-temporal data set this allows to identify areas of unchanged geometry, that is constant surface roughness. The relative changes of the backscattering for those areas can then be used to monitor the soil moisture.

2. TEST SITE AND DATA

Interferometric signatures were extracted from ERS-1 data acquired between January and March 1994 over Middle Zeeland, The Netherlands. Middle Zeeland was selected because of the available in-situ data. Borgeaud et al. (1995) investigated ERS-1 SAR data acquired during the 3-day repeat orbits of Phase D (January to March 1994) together with very detailed descriptions of the soil surfaces of test-fields in Middle Zeeland. The orbital mode (three day repetition rate) together with the detailed in-situ information collected during the ground campaigns and the detailed analysis of the backscatter intensity data (Borgeaud et al., 1995) make this data set ideal for an investigation of the interferometric signatures of bare soils.

The Middle Zeeland site is very flat. The location of the 8 test fields is shown in Figure 1. Relatively large fields were selected for the ground campaign (2-10 ha). During field campaigns the air temperature (Figure 2), soil moistures and surface roughness were measured (Bakker and Huizing, 1994). Based on the 1.5 m long

surface height profiles the standard deviation of the surface height and the correlation lengths were computed (Bellini, 1994). In Table 1 rms surface height values averaged for each field over the entire observation period are listed. The volumetric soil moisture was measured at depths of 0-5 cm and 0-10 cm. The measurements were repeated in order to monitor soil moisture and surface roughness on the selected fields during ERS-1 Phase D. For a certain period temperature dropped below 0° C and the soils froze. Field averages for the soil moisture of the 0-5 cm depth layer are shown in Figure 3. For days with frozen soil the soil moisture was set to 3%, in accordance with earlier experiments (Wegmüller et al., 1990). The observed soil moistures cover the entire range from the "very dry" (i.e. very low liquid water content) frozen soils to the close to saturated soils often observed during the winter.

Figure 1: Map of the Middle Zeeland test site with the selected 8 bare soil fields shown in black.

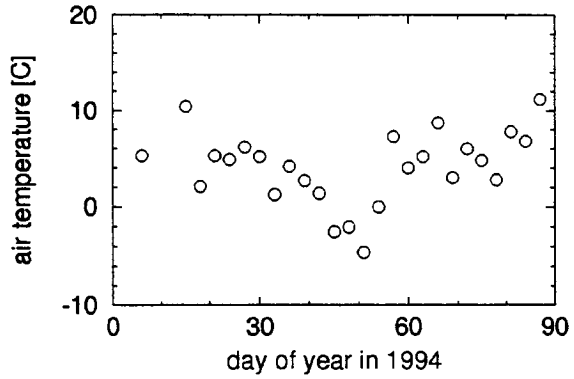

Figure 2: Middle Zeeland experiment winter 1994: Temporal development of air temperature.

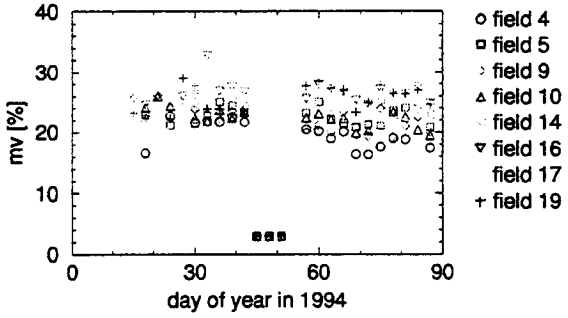

Figure 3: Middle Zeeland experiment winter 1994: Temporal development of volumetric soil moisture m_v (given in %) for selected bare soil fields. For frozen fields the soil moisture (corresponding to liquid water, only) was set to 3% in accordance with earlier experiments (Wegmüller et al., 1990).

Table 1: Average standard deviation of surface height for 8 test-fields at Middle Zeeland observed in winter 1994.

Field number	<rms-height> [cm]
4	1.85
5	2.01
9	4.39
10	2.79
14	1.57
16	3.24
17	1.93
19	0.86

Our investigation focused on the soil moisture monitoring on bare and sparsely vegetated fields. Vegetated fields as well as fields with changing surface roughness are identified based on its low interferometric correlation. For the bare fields without roughness change the backscattering was related to the in-situ measured soil moisture and used to derive retrieval algorithms for the relative soil moisture change and the soil moisture.

The algorithms were developed based on the SAR and in-situ data for the 8 test fields. In a second step the algorithms were applied to fields without in-situ data, allowing to retrieve soil moisture information for a larger area.

The influence of the surface roughness on the soil moisture retrieval algorithm was also investigated.

3. ALGORITHM DEVELOPMENT

3.1. Relative Soil Moisture Change

Based on the multi-temporal interferometric correlation (Figure 4), data not useful for soil moisture retrieval were excluded from the analysis. For field 4, data showing low correlation values at the beginning of the time series and, for all fields, data with wet snow (day

54) were excluded. For frozen fields the volumetric soil moisture (liquid water content) drops to very low values. In accordance with ground-based experiments over frozen soils, the volumetric soil moisture was set to 3% (Wegmüller, 1990).

For the 8 test fields the average backscatter intensities were extracted and plotted versus the in-situ measured soil moisture (Figure 5). The backscattering [in dB] shows a clear dependence on the volumetric soil moisture. The linear regressions calculated separately for each field (see Figure 5) have high correlation coefficients between 0.94 and 0.99. The slopes of the regression curves vary only between 0.20 dB/% and 0.27 dB/% (average 0.24 dB/%), the intercepts between -11.9 dB and -7.5 dB (average -9.5 dB).

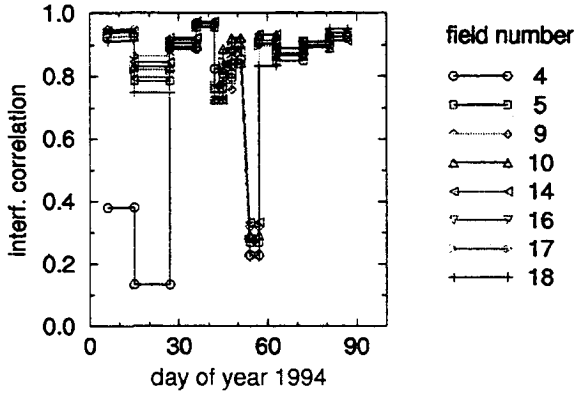

Figure 4: Interferometric correlation of consecutive ERS-1 data acquisitions for 8 bare fields at Middle Zeeland, January to March 1994.

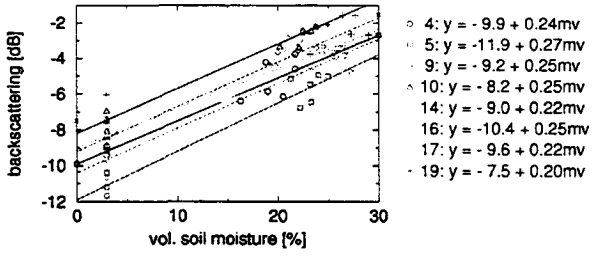

Figure 5: Average backscatter intensities versus in-situ measured soil moisture.

Taking advantage of the result that the slope of the regression curves in Figure 5 is almost the same for all test fields and soil moisture changes, we may retrieve

$$\Delta m_v = m_{v,2} - m_{v,1} \quad (1)$$

using

$$\Delta m_v = 0.042 \Delta\sigma^\circ \,[\mathrm{dB}] \quad (2)$$

where $\Delta\sigma^\circ$ is the backscatter change

$$\Delta\sigma^\circ = \sigma_2^\circ[\mathrm{dB}] - \sigma_1^\circ[\mathrm{dB}]. \quad (3)$$

The advantage of this method is that the errors due to the unknown roughness remain relatively small. The exact slope of the regression slope is approximated with an accuracy of ±10% leading to a relative soil moisture change estimation error of 10% or an error of 0.01 for a moisture change of 0.1. Another advantage is that calibration errors (for instance caused by local topography, unknown antennae diagram, or other unknown calibration factors) do not affect the quality of the result as long as the same calibration is off by the same factor in both cases. In this relative method most of the influence of the incidence angle dependence of the backscattering coefficient is removed and may therefore be neglected. The main disadvantage of the method is that it is only an estimation of the moisture change but not of the absolute soil moisture level. We conclude that this method is very useful to map moisture changes and particularly to map small moisture changes because the main errors are relative to the change occurring.

The algorithm was first applied to the 8 test fields for four different interferometric image pairs. No frozen soils were included. The soil moisture change estimated from the backscatter change was compared to the in-situ observations of the soil moisture change in Figure 6. Based on the observed in field variability, vertical moisture inhomogeneity, and measurement errors, an uncertainty of at least 0.03 (3%) is expected for a single soil moisture measurement. The difference of two statistically independent measurements with an accuracy of 0.03 is around 0.04 (4%). The accuracy of the estimation of the backscatter change introduces the main error in the moisture estimation. An estimation accuracy of below 0.5 dB may only achieved for very large fields. An error of 0.5 dB translates into a soil moisture change estimation error of 0.02. The soil moisture changes occurring during the experiment were only small, in the range of the errors of both the in-situ and remote sensing method. Therefore, Figure 6 is not sufficient for a profound validation of the algorithm.

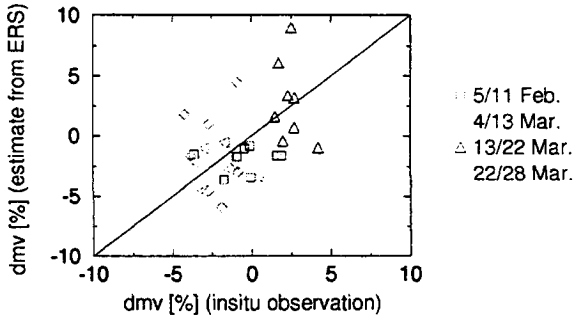

Figure 6: Change in volumetric soil moisture [in %] estimated from ERS data using Equation (2) versus in-situ measured soil moisture change.

3.2. Soil Moisture

The algorithm discussed above can be extended to absolute soil moisture estimation if the soil moisture is known for one data set

$$m_v = m_{v,0} + 0.042\left(\sigma^\circ[\mathrm{dB}] - \sigma_0^\circ[\mathrm{dB}]\right) \quad (4)$$

where σ_0^o is the backscattering coefficient for the known soil moisture $m_{v,0}$.

Even without in-situ data the soil moisture may be known quite reliably under certain conditions as in the case of frozen soil or very wet (moisture near field capacity) soil after extensive rain.

In Equation (4) the differences in the intercepts shown in Figure 5 were not considered. However, the intercepts may be a measure of the roughness of the fields. Plotting the slope of the regression curves found for the different test fields versus the intercept a high negative correlation is found (Figure 7). Ignoring the one point located far away from the regression curve leads to a correlation coefficient of 0.89 and to a linear regression function as indicated in Figure 7. The fact that the two quantities are related was used to improve the soil moisture retrieval algorithm by replacing the constant slope value with a roughness dependent slope, s, estimated from the intercept, i. According to

$$\Delta i = \sigma_0^o - m_{v,0} \cdot s \tag{5}$$

and $$s = 8.56 - 1.56 \cdot i \tag{6}$$

we found

$$i = \frac{\sigma_0^o - 8.56 \cdot m_{v,0}}{1 - 1.56 \cdot m_{v,0}} \tag{7}$$

The soil moisture retrieval algorithm is therefore

$$m_v = \frac{\sigma^o - i}{8.56 - 1.56 \cdot i} \tag{8}$$

Having two or more data sets with known soil moistures, for example a frozen and a saturated soil, allows to conduct a regression analysis and derive both slopes and intercepts directly from the data.

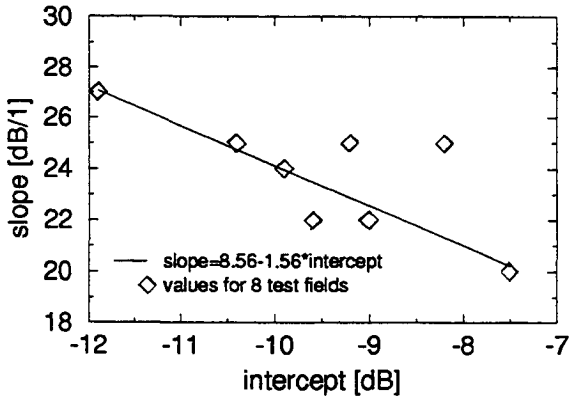

Figure 7: Slope of the regression curves for the different test fields versus the intercept. A high negative correlation is found between the two quantities. Ignoring the point located far away from the regression curve leads to the correlation coefficient of 0.89 and the indicated linear regression function

4. RESULTS

The described algorithms were applied to the Middle Zeeland data. This allowed to retrieve soil moisture information for fields distributed over the entire ERS scene. The application of the described algorithms is done in two steps, first the classification step and second the parameter retrieval step.

4.2 Retrieval of Relative Soil Moisture Change

In order to retrieve soil moisture change over bare soils the *appropriate* bare soils are first classified based on high interferometric correlation (> 0.7) and low image texture (< 0.5). *Appropriate* as used here means bare soil without roughness change between the acquisitions of the two data sets. The low texture condition was used to distinguish the bare or sparsely vegetated fields from urban areas (with high texture).

The soil moisture change was then determined using Equation (2). In the estimation of the backscatter change the speckle noise has to be taken into account. It is recommended to use large enough averaging/filtering windows to determine average backscattering coefficients before the ratio is taken. For the example discussed we applied minimum mean square error (MMSE) filter (Frost et al., 1982) to 7x7 5-look pixels. The ratio was then calculated for averages of 15 x 15 5 look pixels (using a linearly decreasing weighting function). Equation (2) was then applied to calculate the soil moisture change.

The classification and soil moisture change results were then combined. The resulting image contains the soil moisture change values and zero values for areas without soil moisture change estimate. To visualize the result a color scale was used to display the soil moisture change. For the image brightness one of the backscatter images was used. The results obtained for the changes occurred between 4 and 13 March 1994 and between 13 and 22 March 1994 are shown in Figure 8. For most areas the observed soil moisture change was small (blue color), as expected from the in-situ observations. Decreasing soil moisture (turquoise color) was observed for small parts of the area on the 13 / 22 March pair.

4.1 Soil Moisture Retrieval

For simplicity only fields without geometric change throughout the entire experiment were used for the soil moisture monitoring. This was achieved by conducting a classification using the interferogram pair between the first and last data takes, applying a high interferometric correlation (> 0.7) and low image texture (< 0.5) criteria. In order to have a good reference data set with known soil moisture, the backscattering of the three days with frozen soil were used. The data were first averaged, then a minimum mean square error filter (Frost et al., 1982) with a window size of 7x7 5-look pixels, and finally a running average filter (window size 15x15 5-look pixel) with linear weighting was applied. The result

was taken as backscatter reference with an assumed (liquid) soil moisture content of 0.03. The backscatter images to be used for the soil moisture retrieval were treated in the same way as the reference data, i.e. MMSE and average filtering. The resulting backscatter coefficient were then used to estimate the soil moisture using Equation (8).

The classification result and the soil moisture retrieval output were then combined. The resulting soil moisture map contains soil moisture values and zero values for areas without soil moisture estimate. In order to visualize the result a color scale was used to display the soil moisture change. For the image brightness one of the backscatter images was used. The results obtained for the data on 11 and 14 February 1994 are shown in Figure 9. On 11 February soil moisture values around 0.25 were detected (blue color), with values below 0.20 for a few fields (turquoise color). On 14 February very low soil moistures were detected for all fields as a result of freezing.

5. ROUGHNESS ANALYSIS

The detailed surface roughness data was also used to investigate a possible dependence of the interferometric correlation on the surface roughness. The differences between the fields on a certain date and between the data of one field on different dates do not show a clear indication of a dependence of the interferometric correlation on the surface roughness. More important factors may be the effects of meteorological conditions, sparse vegetation, acquisition time difference, baseline, etc.

Nevertheless, as mentioned above, the sensitivity of the backscattering to soil moisture change depends on the surface roughness. The intercept of the backscattering versus soil moisture regression curve depends on the surface roughness as well. A multi-temporal data set with some in-situ or meteorological data as the one over the Zeeland test-site allows to retrieve surface roughness parameters. The relationship between the slope and the rms-height is shown in Figure 10. Instead of the rms-height, the slope value itself can be considered as a roughness parameter. This may actually be a more useful description of the "surface roughness as seen by microwaves".

6. CONCLUSIONS

The focus of this study is on soil moisture retrieval with ERS SAR interferometry. Data acquired over Middle Zeeland between January and March 1994 during 3-day repeat orbits were used. The soil moisture monitoring was applied to bare and sparsely vegetated fields with constant surface roughness, which were identify by means of the high interferometric correlation. For 8 bare fields without roughness change, where in-situ data were collected, the backscattering was related to in-situ

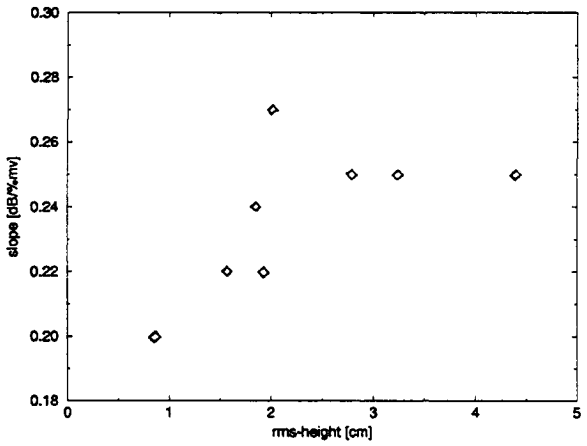

Figure 10: Relation between the slope of the regression curves between the backscatter in dB and the volumetric soil moisture and the rms-height for test fields in Middle Zeeland.

measured soil moisture. The dependence of the backscattering on the volumetric soil moisture was used to derive retrieval algorithms for the relative soil moisture change and the soil moisture. The algorithms are based on the intercepts and slopes of the regression curves calculated between backscattering and volumetric soil moisture. The algorithm for the retrieval of the relative moisture change is in particular suitable for the map of small moisture changes because the errors are relatively small. The absolute soil moisture can be estimated if the soil moisture is known for one reference data set. In this case study, data acquired during a period with frozen soil were used as reference. The algorithms were then applied to fields without in-situ data available, leading to soil moisture maps of large areas. At last, the influence of the surface roughness on the soil moisture retrieval algorithm was investigated. In a possible extension of this study, fields with vegetation cover, which decreases the sensitivity of the backscattering to soil moisture, may be investigated.

7. ACKNOWLEDGMENTS

This work was supported by ESA ESTEC under ESA/Contract 11740/95/NL/PB(SC).

8. REFERENCES

Bakker J., Huizing J., 1994: Ground-data collection Zeeland ERS-1 1994 - Phase D Experiment - January - March 1994. *Synoptics - Integrated Remote Sensing & GIS applications*, May, Wageningen, The Netherlands.

Bellini A., 1994: Analysis of surface scattering models for remote sensing applications. *ESTEC Working Paper No. 1803*, ESA-ESTEC/XEP.

Borgeaud M., Attema E., Salgado-Gispert G., Bellini A., Noll J., 1995: Analysis of bare soil surface roughness parameters with ERS-1 SAR data. In: *Proceedings of Int. Symp. on Retrieval of Bio- and Geophysical Parameters from SAR data for Land Applications*, October 17 -20, Toulouse, France.

Frost V.S., Stiles J.A., Shanmugan K.S., Holtzman J.C., 1982: A model for radar images and its application to adaptive digital filtering of multiplicative noise. *IEEE Trans. Pattern Analysis and Machine Intelligence, 4(2)*, 157-165.

Wegmüller U., 1990: The effect of freezing and thawing on the microwave signatures of bare soils. *Remote Sensing of Environment, 33(2)*, 123-135.

Wegmüller U., Werner C. L., Nüesch D., Borgeaud M., 1995a: Land-surface analysis using ERS-1 SAR interferometry. *ESA Bulletin, 81*, pp. 30-37.

Wegmüller U., Werner C. L.,1995b: Farmland monitoring with SAR interferometry. In: *Proceedings of IGARSS'95*, July 10-14, Firenze, Italy, pp. 544-546. (Code TUA 07)

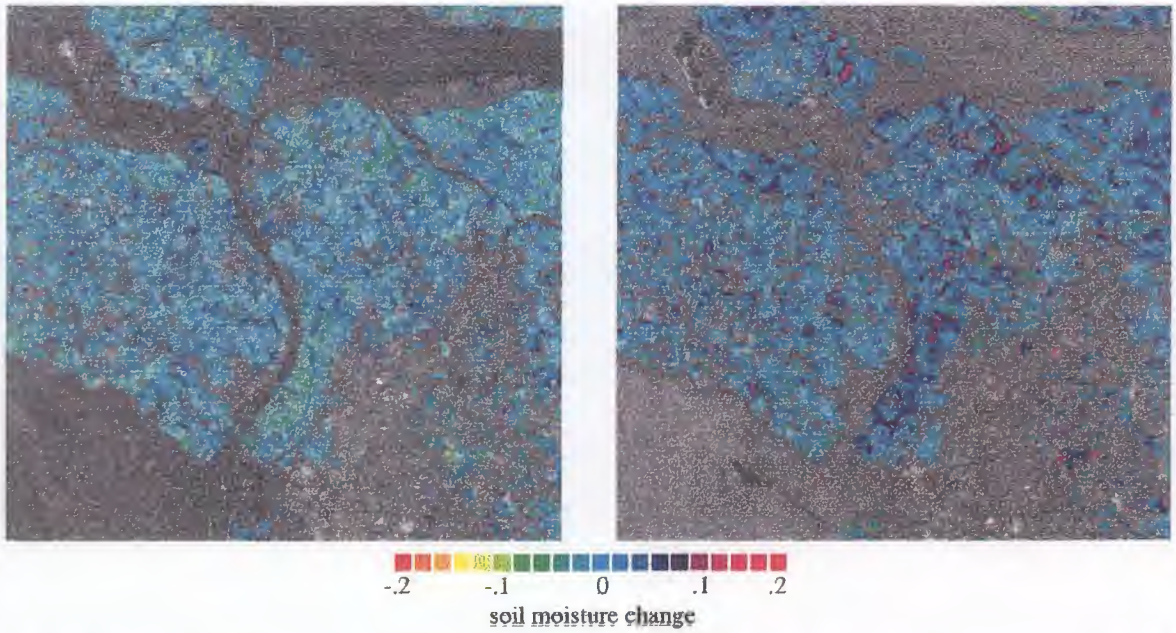

Figure 8: Soil moisture change for Middle Zeeland (NL) test-site occurring between 4 and 13 March 1994 (a, left side) and 13 and 22 March 1994 (b, right side) retrieved from multi-temporal ERS-1 SAR data. The soil moisture change is displayed using the indicated color scale, the image brightness corresponds to the backscattering on the first date. In order to improve the reliability soil moisture, change was estimated exclusively over bare and sparsely vegetated fields with unchanged surface roughness. For gray areas no soil moisture change information was retrieved.

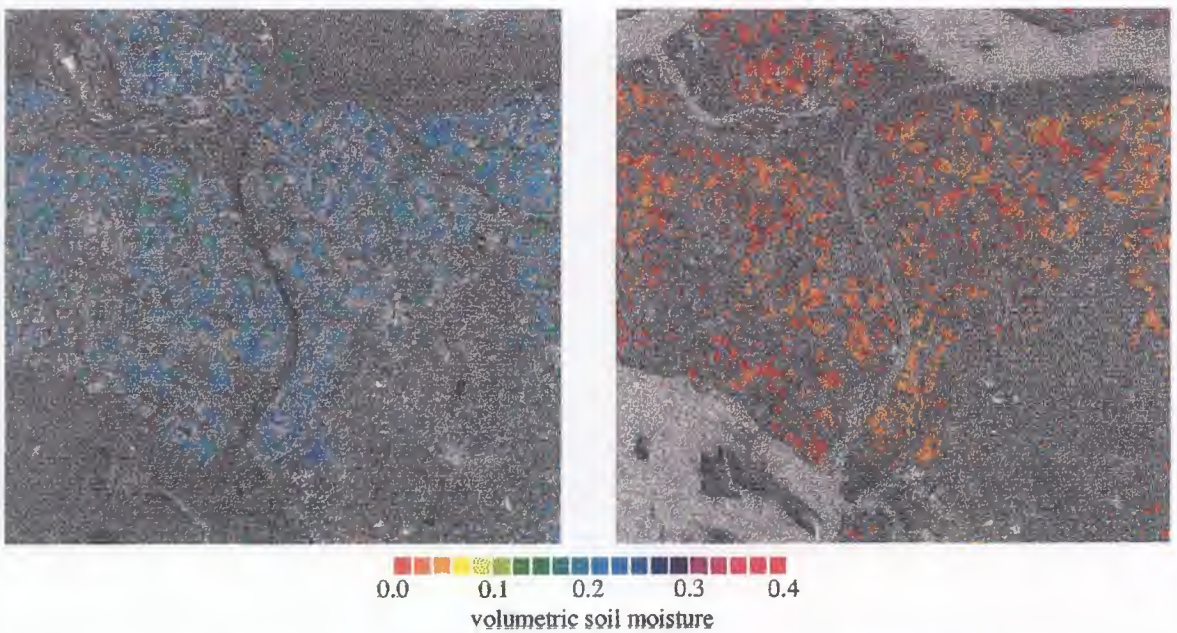

Figure 9: Volumetric soil moisture at 0 to 5 cm depth for Middle Zeeland (NL) test-site on 11 February 1994 (a, left side) and 14 February 1994 (b, right side) estimated from multi-temporal ERS-1 SAR data. The low moisture values on 14 February are a result of freezing. The soil moisture is displayed using the indicated color scale, the image brightness corresponds to the backscattering on the first date. For gray areas the volumetric soil moisture was not retrieved.

INTERPRETATION OF ERS-SAR IMAGES OVER URBAN SURFACES

Bénédicte Dousset

Hawaii Institute of Geophysics and Planetology, University of Hawaii
2525 Correa Road, Honolulu, Hawaii 96822 U.S.A.
phone:+ 808 956 6418, fax: + 808 956 9225
e-mail: bdousset@soest.hawaii.edu

ABSTRACT

Large variations of backscatter intensities were observed in between and within ERS-SAR images of the Los Angeles metropolitan area. Low intensities backscatter were found over smooth pavement and asphalt, and higher ones over industrial and commercial areas, indentified using a SPOT-HRV image classified for land-use. Highest backscatter anisotropy occurred when the flight direction of the SAR was parallel to the alignment of streets. These contaminations mask the backscatter variations due to surface roughness and to soil moisture, and indicate that the retrieval of moisture availability from ERS-SAR images, is contingent upon eliminating backscatter contamination from processes inherent to the urban structure.

1. INTRODUCTION

Urbanization modifies the nature and properties of the surface and atmosphere. It alters the radiative, thermal, hydrological and aerodynamics components of the energy fluxes and their interaction with the surface. The understanding of urban microclimate perturbations relays on our ability to model the alteration of these components and of their interaction. In particular we need to better understand the physical processes that determine the partition of radiative energy into sensible and latent heat fluxes.

Energy fluxes components such as Land Surface Temperature (LST), albedo, vegetation density, aerosols and cloudiness can efficiently be collected by radiometers on board polar orbiting satellites. For example, urban LST have been derived from infrared sensors such as NOAA-AVHRR (Dousset 1989), ERS-ATSR or LANDSAT-TM.

Soil moisture is an important forcing factor. As shown in Fig. 1, there is a strong negative correlation between averaged summer afternoon LST and the Normalized Difference Vegetation Index over Los Angeles. In fact, the moisture availability of residential areas allows for a great fraction of radiant energy to be converted into latent heat flux, lowering the sensible heat flux, hence the surface temperatures (Dousset 1991). Such properties could be applied to mitigate heat island effects by a proper spatial distribution of permeable materials, vegetation and urban parks.

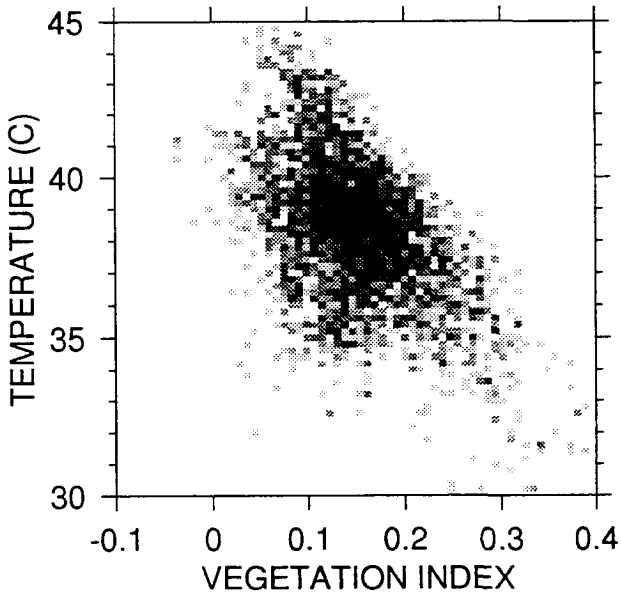

Figure 1. Joint distribution of the summer Los Angeles Land Surface Temperature at 14:50 PDT (averaged over 15 NOAA-AVHRR IR images), versus the Normalized Difference Vegetation Index computed from NOAA-AVHRR channels 1 and 2.

The application of microwave sensing to the retrieval of moisture content of bare soil and vegetation canopy, such as forest or crops, have been extensively studied through physical observation and theoretical modeling. Conversely, there have been few applications over urban areas due in part to the heterogeneity and roughness of their surfaces. Moisture availability is still inferred indirectly from a combination of thermal remote sensing and inverse modeling, as described in

Carlson et.al, (1981), and Gillies et al., (1995). The lack of moisture monitoring from remote sensing limits our ability to close the urban surface energy balance, and to model the LST amplitude.

The retrieval of soil moisture from Synthetic Aperture Radar systems such as ERS-SAR is based on the dielectric properties of the surfaces, influencing the intensity of backscattered electromagnetic waves. Sensing of soil moisture arises from the large difference between the dielectric constant of water and that of dry soil (Dobson and Ulaby, 1986).

Here, we present a preliminary analysis of ERS-SAR series of images collected over the Los Angeles basin to explore the applicability of microwave remote sensing to the study of the energy balance at the urban surface.

2. TEST SITE AND DATA ACQUISITION

The test site is the Los Angeles metropolitan area, located in a coastal plain bounded by mountains, centered at 118°W-34°N. It is characterized by a high degree of urbanization and a low density population of ~15 million. The climate of Los Angeles is semi-arid, with sporadic periods of high rainfall associated to global climatic cycles, resulting in a large annual and interannual amplitude of soil moisture. The topography of the Los Angeles basin is rather uniform, simplifying the interpretation of SAR backscatter.

The analysis is based on the following co-located data:

- 19 ERS-SAR images in C band (6cm) VV polarization, sensed in between July 1992 and January 1996 spanning all seasons.
- 1 SIR-C image in L band HH and HV polarizations, and C band HV polarization, sensed in October 1994.
- 1 Multispectral 20 m resolution SPOT-HRV image, sensed in June 1986.
- Near-continuous monitoring of Land Surface Temperature from NOAA-AVHRR imaging.

The different inclination of the ERS satellite orbits and both ascending and descending passes allows for the analysis of backscatter variations with illumination azimuth. The images cover the entire Los Angeles basin, however the observations were principally focussed on the area comprised between downtown Los Angeles and Long Beach harbor (Fig.3).

The SPOT-HRV image was classified and the Normalized Difference Vegetation Index computed. The classification (Fig. 3) arises from the joint distribution of the visible HRV-1 and near-infrared HRV-3 channels, and the vegetation index results from their normalized difference.

3. ERS-SAR DIFFERENCE AND MEAN IMAGES

An ERS-SAR image difference (not shown here) was derived from a pair of descending images. The images were aligned using the coastline and reference points from the harbor structures in Long Beach. The texture of the image difference revealed distortions amounting to ~4-5 pixels, precluding interferometry without first remapping the images by a bilinear or higher order transform to a reference image.

The ERS-SAR mean image (not shown here) was derived from the same pair of images. It was remapped to a smaller SPOT HRV image, and corresponds to area with little distortion, ~1-2 pixels. The mean image emphasizes the urban structures such as highways, roads, airport runways, bridges upon the Los Angeles River, and the delineation of land covers such as parks and asphalt by reducing speckle.

Fig. 2, shows the joint distribution of the ERS-SAR mean image and SPOT-HRV Vegetation Index. The distribution displays two clusters: the small one at the bottom left corresponds to the ocean, the larger one at the center left corresponds to land surfaces devoid of vegetation. These latter exhibit the highest backscatter, probably due to surface roughness and contamination inherent to the urban structure. The points comprised between 0.1-0.5 vegetation index and 0-2000 backscatter intensity indicates the relatively large amount of vegetation in this urban area, and the relationship of backscatter intensity to vegetation, related to moisture availability and evapo-transpiration. This figure also demonstrates the need to mask pixels with high backscatter from urban surfaces devoided of vegetation, (industrial, commercial or densely built) and from moving vehicles, before attempting to retrieve soil moisture. Therefore, I focus here on the backscatter anisotropy and its relationship to the morphology of different urban land-uses/covers.

4. OBSERVATION OVER DIFFERENT URBAN LAND-USES

Large variations of backscatter intensity were observed among and within the images. The response of each land-use class (Fig.3) was examined separately and is shown in Figs. 4 and 5.

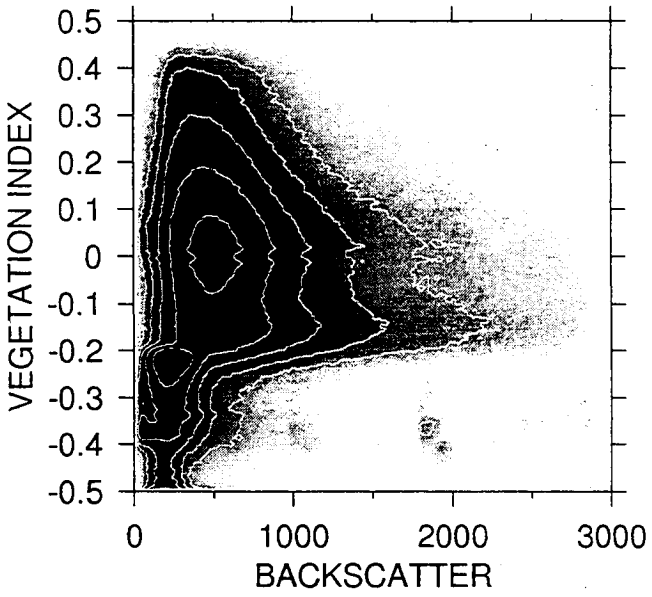

Figure 2. Joint distribution of Backscatter intensity from the mean ERS-SAR image and the Normalized Difference Vegetation Index from the SPOT-HRV image.

Commercial-industrial

The areas classified as devoid of vegetation based on the SPOT image, correspond actually to three different subclasses in the SAR images: smooth paved surfaces, industrial metallic structures, commercial /industrial buildings. Very low backscatter occurs on asphalt, pavement and bare soil, such as airport runaways (Long Beach airport, A), freeways and storm channels (Los Angeles river, B). Low backscatter results both from the surface smoothness, that reduces Bragg scattering, and from low soil moisture, that reduces subsurface scattering. Random contamination occurs along many freeways, possibly due to vehicles acting as crude corner reflectors. Some may be Doppler-shifted, explaining the lateral displacement seen in enlarged images (Fig.6).

Within the same SPOT class, pixels with very high backscatter intensity correspond to industrial structures, for example chemical industries (fuel tanks, pipelines, oil wells) in Carson (C), and harbor structures (containers, cranes, ships) in Long Beach (D). Comparing the different images, the high reflectance appears rela tively isotropic, presumably because many of these structures have either curved surfaces (tanks, ships) or are randomly oriented (cranes, oil wells).

In contrast, distinctly anisotropic properties are found where streets and tall buildings are regularly aligned.

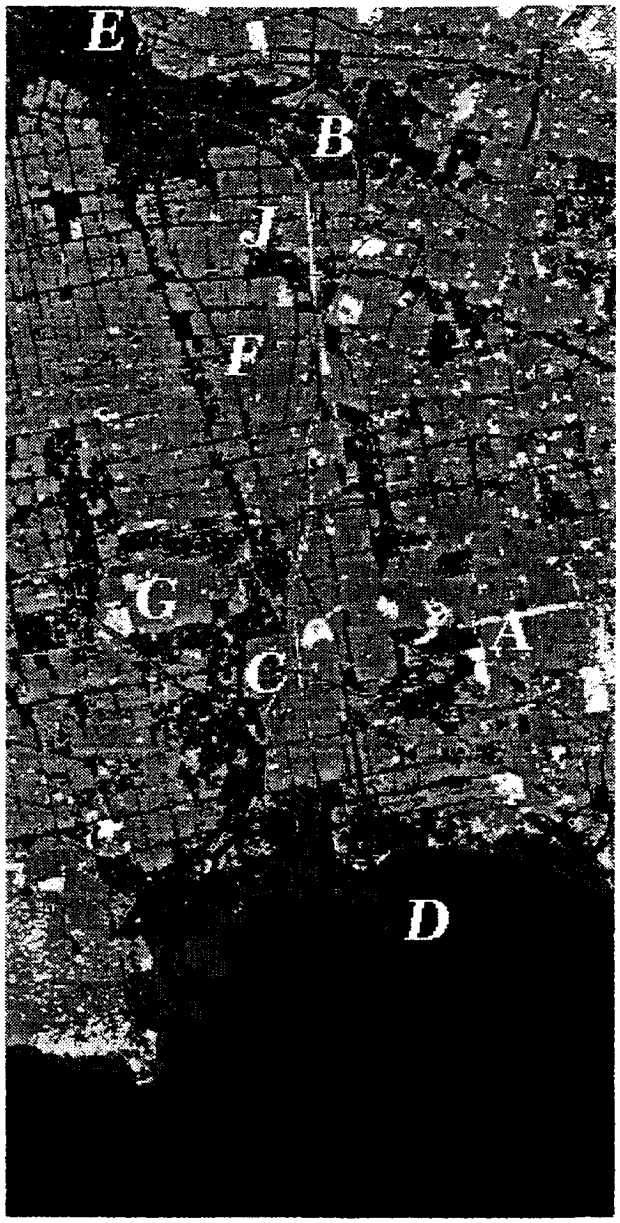

Figure 3. Main Los Angeles land-uses, derived from multispectral SPOT HRV image: vegetation and parks are displayed in white, residential areas in light grey, commercial and industrial areas devoid of vegetation in dark grey, water in black.

For example, downtown Los Angeles (E) and commercial districts along the main boulevards (Alameda, F) have intensities depending on the illumination azimuth. In these areas, the regular geometry of reinforced concrete walls, metalized roofs and steel beams provides numerous dihedral reflectors, resulting in greatly enhanced backscatter when the illumination azimuth is orthogonal to the buildings.

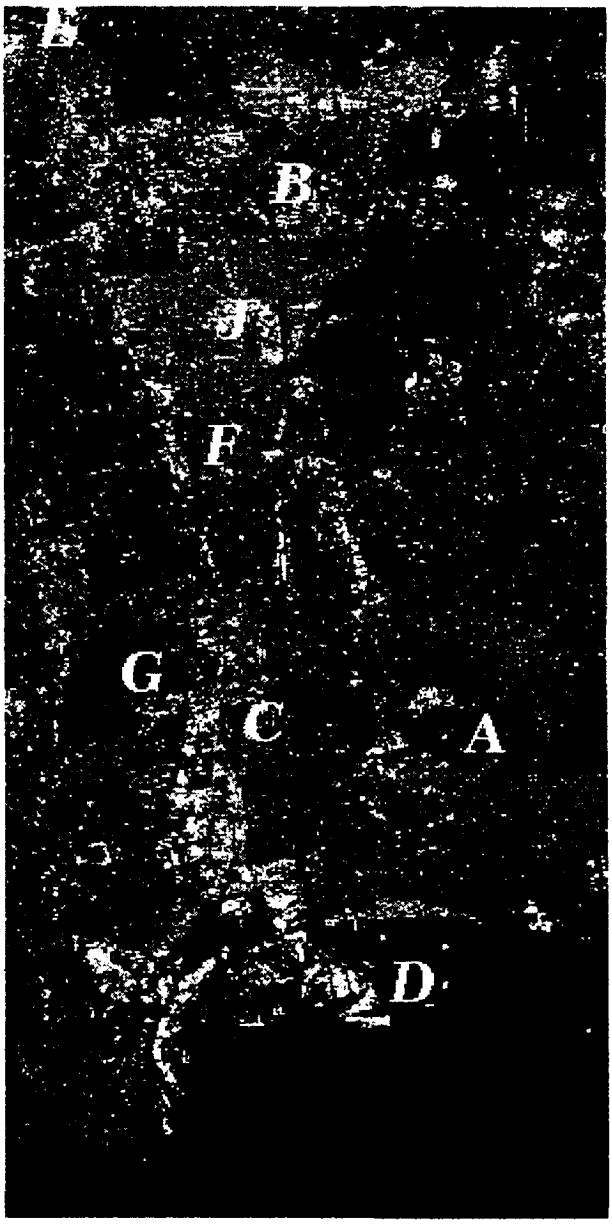

Figure 4. ERS-1 SAR band C image of Los Angeles, November 24, 1993 at 18:31 UTC, descending pass.

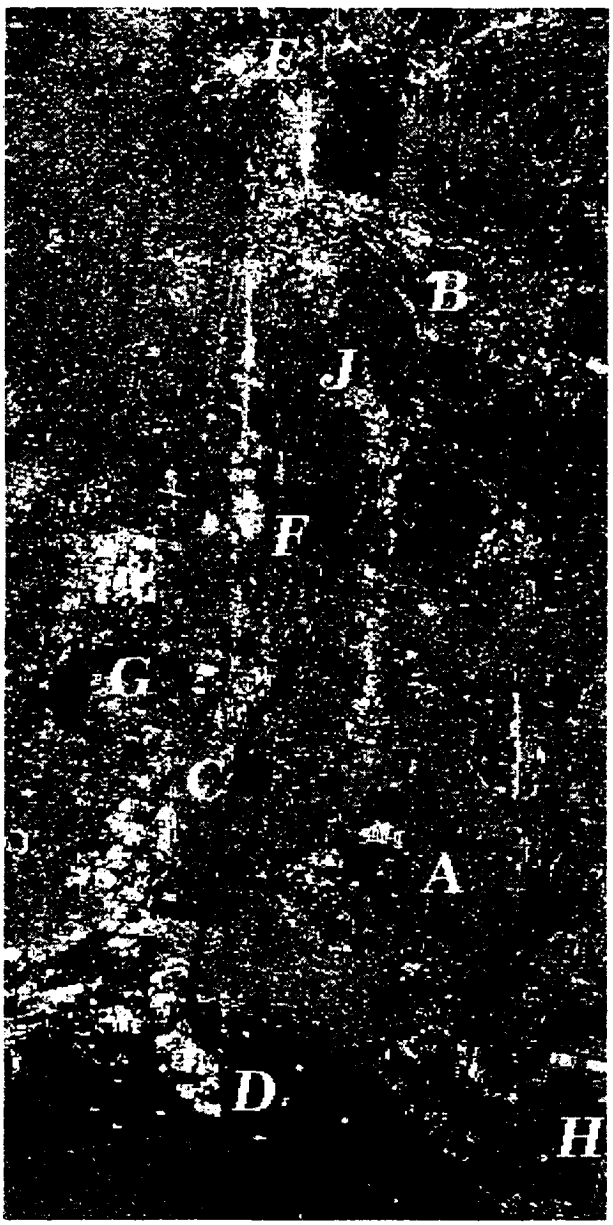

Figure 5. ERS-1 SAR band C image of Los Angeles, November 5, 1992, at 06:13 UTC, ascending pass.

Parks and vegetation

Areas classified as vegetation such as urban parks, golf-courses, grass in undeveloped blocks and airports have in general low isotropic backscatter. Examples in Fig. 4 and 5 are the Victoria park and golf course in Carson (G), and Seal Beach Naval Weapon Station (H).

Residential

Areas classified as residential have considerable speckle, with average backscatter larger than the vegetation class. The additional soil moisture due to irrigated lawns is unlikely to be the cause of this increased intensity. Instead, the presence of numerous sub-pixel metallic scattering targets such as vehicles, utility lines, electrical wiring and appliances in houses is likely to increase backscatter to a level higher than vegetation. Some residential blocks feature a significant imaging anisotropy. A striking example is provided by the districts of Huntington Park and South Gate (J). These districts are alternately brighter (Fig. 4) and darker (Fig. 5) than average in the pair of ERS-1 images.

A close examination of city maps reveals that the streets of these districts are nearly exactly aligned with the flight direction for Fig. 4, but not for Fig. 5. A similar enhanced backscatter correlated with street alignment can be seen in the SIR-C image over Burbank and Santa Monica (not shown). This anisotropy is somewhat unexpected, and suggests that even light constructions based on wood and stucco walls may be favorable to dihedral reflections.

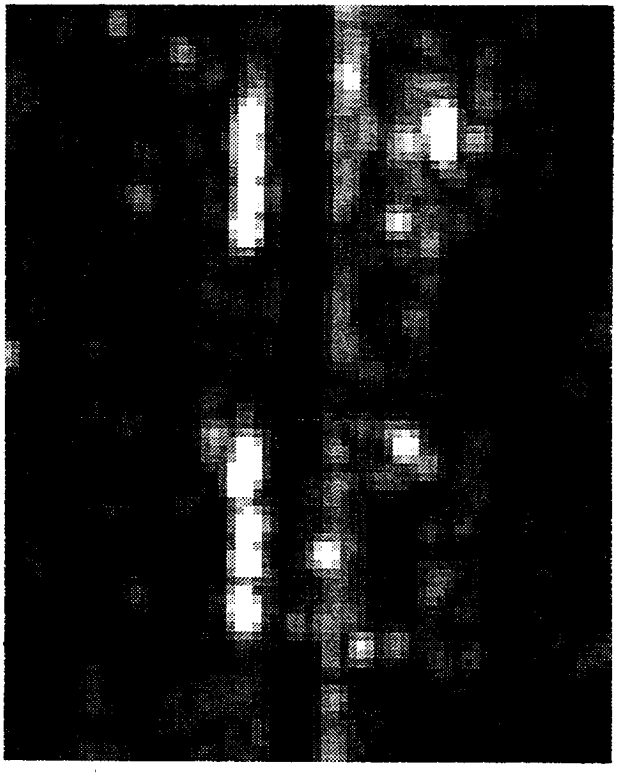

Figure 6. Doppler-shifted vehicles on the sides of the Los Angeles Freeway 10.

5. CONCLUSION

In many areas of the Los Angeles basin, imaging anisotropies mask the variations of backscatter due to other processes, illustrating the complexity of extracting quantitative information from SAR images of urban surfaces. Over industrial and commercial areas, high backscatter from concrete and metallic structures appears to hopelessly contaminate the signal, precluding the extraction of information on the ground surface. Over some low density residential areas, the increases of backscatter intensity correlated with the angle between the radar illumination and the streets. With no further corrections, the estimation of urban surface properties such as roughness and soil moisture should be limited to areas devoid of constructions. Selecting those areas requires a priori knowledge of land use which can be derived from multispectral SPOT or LANDSAT images.

Future work will attempt to model the anisotropy based on a series of images with different illumination azimuths and a database on urban topography, and to derive a backscatter intensity corrected for these contaminations.

6. ACKNOWLEDGEMENTS

The author thanks the European Space Agency for providing the ERS-SAR data, and the National Aeronautics and Space Administration for support under grant NAGW-4940. The work was performed at the Oceanography Satellite Laboratory of the University of Hawaii.

7. REFERENCES

Carlson, T.N., J.K. Dood, S.G. Benjamin, and J.N. Cooper, "Satellite estimation of surface energy balance, moisture availability and thermal inertia," *J. Applied Met.*, vol. 20, pp. 67-87 (1981).

Dobson, M.C and F.T Ulaby, "Active microwave soil moisture research," *IEEE Trans. Geosci. Remote Sens.*, vol. GE-24, no. 1, pp. 23-36 (1986).

Dousset, B., "Surface temperature statistics over Los Angeles: the influence of land use," in *Proceedings of IGARSS-91*, I.E.E.E., Helsinki.

Dousset, B., "AVHRR-derived cloudiness and surface temperature patterns over the Los Angeles area and their relationship to land use," in *Proceedings of IGARSS-89*, pp. 2132-2137, I.E.E.E., Vancouver (1989).

Gillies, R.R. and T.N. Carlson, "Thermal Remote Sensing of Surface Soil Water Content with Partial Vegetation Cover for Incorporation into Climate Models," *J. Applied Met.*, vol. 34, pp. 745-756 (1995).

Hydrology

Chairperson: **W. Mauser**

POTENTIAL AND LIMITATIONS OF MULTI-TEMPORAL SAR DATA IN A QUANTITATIVE APPROACH FOR MULTI-SCALAR HYDROLOGICAL APPLICATIONS. SYNTHESIS OF ERS ALSACE/CAMARGUE PILOT PROJECT.

FELLAH K., MEYER C., LAUGIER O., CLANDILLON S. and DE FRAIPONT P.

SERTIT, Boulevard Sébastien Brandt, F-67400 Illkirch, Tel : +33 (0)3 88.65.52.00, e-mail: sertit@sertit.u-strasbg.fr
http://sertit.u-strasbg.fr

ABSTRACT

The potential of multi-temporal ERS SAR data in hydrological applications is investigated in two areas - the Alsace and Camargue regions - where wetland and flood monitoring analysis are performed. In the Alsace test site, a large data base has been built up in order to dissociate and analyse the different factors influencing the ERS backscattering coefficient. Firstly, a review of the different findings is summarised showing that: 1) At a regional scale, there is a strong correlation between ERS-1 SAR backscattering coefficient and a soil moisture parameter; 2) A minimum spatial scale can be defined at which the backscattering coefficient measurement of ERS can be achieved with a given level of confidence in order to derive quantitative bio-geophysical information. Then, in order to determine the optimal conditions for soil moisture retrieval using ERS SAR data, the influence of vegetation parameters has been analysed. The NDVI, derived from synchronous SPOT imagery for different classes of cropland and grassland, was used to estimate different vegetation states. The study of the spatial and temporal backscattering coefficient's behaviour vis-à-vis the vegetation state, over a multi-year period, allows the determination of an empirical relationship between those parameters to be determined. In the Camargue Region, high temporal ERS acquisitions, recorded in a 3-day mode before, during and after the 1993 and 1994 floods, are used to evaluate ERS SAR data potential in flood detection and monitoring. Additionally, the ERS SAR data acquired after the 1994 flood, are used for the study of the backscattering coefficient's temporal behaviour with respect to the hydrological state of the soils (i.e. flooded, saturated, moist). This study permits a trend curve, relating the ERS backscattering coefficient and the hydrological state of the soils, to be established.

1. INTRODUCTION

Since the launch of ERS-1, several studies have shown experimental results relating ERS-1 SAR backscattering coefficient to a number of land surface bio-geophysical parameters (Bouman and Uenk, 1992 ; Demircan *et al* ., 1993 ; Wooding *et al.*, 1994). With its system configuration parameters (C-band, VV polarisation) and an incidence angle of 23°, the use of ERS-1 SAR should provide near optimal sensitivity to soil moisture in combination with a minimal sensitivity to surface soil and vegetation roughness (Ulaby, 1974). Intensive theoretical and experimental studies have been conducted with the results showing a strong correlation between the ERS backscattering coefficient and soil moisture (Wooding *et al.*, 1993; Fellah *et al.*, 1994; Le Toan *et al.*, 1994; Mohan *et al.*, 1994). In order to determine the optimal condition for soil moisture retrieval, the other factors influencing the backscattering coefficient have to be taken into account. In fact, several studies (Ulaby *et al.*, 1976; Attema *et al.*, 1978; Wang 1985; Prevot *et al.*, 1993) have shown that an estimation of the soil water content can be derived for grassland and cropland under specific conditions (flat terrain, surface roughness, biomass, ...).

Within the ESA pilot project AO2-F122, sponsored by the CNES and the Conseil Régional d'Alsace, a study aiming to evaluate the potential of multi-temporal ERS data for hydrological applications during normal and exceptional hydrological conditions in the Alsace plain and Camargue Region, has been carried out.

In the Alsace plain, a quantitative approach for soil moisture retrieval was investigated. After a short review of the main results obtained previously and which have already been published (Fellah *et al.*, 1994, 1995a), a study of the influence of the vegetation parameters on the backscattering coefficient was performed in order to define the optimal conditions for soil moisture retrieval. This work was performed within a Geographical Information System using an extensive multi-source regional data base.

In the Camargue region high temporal flood zone detection and monitoring using ERS data, acquired in 3 mode, during the exceptional hydrological conditions of 1993 and 1994, was performed. This study pinpointed the usefulness of ERS SAR data in the precise cartography of flood limits and therefore, in the provision of flood dynamic information (Laugier *et al.*, 1997). A second objective, which is presented hereafter, was to analyse the temporal backscattering coefficient's behaviour over zones which pass from

flooded to different moisture states during soil drainage. This was done by using ERS SAR data acquired with a 3 day cycle after the flood event in January 1994.

2. THE ALSACE TEST SITE

The study area, the Ried Centre Alsace, is situated between Strasbourg and Colmar on the Alsace plain (North-eastern France). It is a very flat area and an environmentally sensitive biotope which is strongly influenced by hydrological processes and is therefore affected by new EU environmental and CAP directives. The landuse in this region comprises intensive agriculture which consists essentially of corn but also areas of grassland.

2.1. DATA BASE

A large regional database was developed aimed at isolating information which relates to soil moisture by dissociating and analysing the importance of the numerous parameters that affect the SAR signal return. The data base contains calibrated ERS-1 SAR and optical satellite data, plus exogenous data, all integrated within a GIS.

- ERS-1 data

More than thirty essentially springtime or autumnal ERS-1 images were selected between 1991 and 1995. These periods are interesting as these seasons reflect contrasting hydrological regimes. Meteorological data was used in choosing ERS-1 scenes enabling the differentiation between moisture due to rainfall and that caused by other factors (soil moisture retention, water table, etc..).

- Optical satellite data

SPOT XS scenes which are quasi-synchronous to ERS SAR acquisitions acquired between 1991 and 1995, allowed the realisation of a precise landuse classification. This thematic classification allowed the spatial and temporal ERS backscattering coefficient to be analysed per landuse.

- Exogenous data

There are comprised of a DTM, scanned cartographic data (piezometric, pedological and substrate deposits data), providing information on the natural environment, administrative cadastral coverage, meteorological information and, particularly, mapped antecedent precipitation indexes prior to ERS acquisitions. These were complimented by synchronous aerial photos and field surveys.

2.2. QUANTITATIVE MEASUREMENTS OF BIO-GEOPHYSICAL PARAMETERS

A review of the different stages of this study are summarised below. The radar's backscatter behaviour relating to different land covers is studied. Then, the sensitivity of ERS SAR data to soil moisture variation is investigated. The impact of observational scale on SAR radiometric resolution is analysed. Finally, the results of the influence of the vegetation parameters on the backscattering coefficient are presented in more detail.

The backscattering coefficient has been calculated using the method described by Laur *et al.* (1992, 1996). In order to enable the comparison of backscattering coefficients obtained for all scenes, it is important to ascertain the spatial and temporal calibration of the ERS signal and the influence of the incidence angle per theme considered. A test was therefore performed for several land cover types taken from a multitemporal SPOT XS classification on two ERS-1 scenes acquired 12 hours apart with no rainfall being recorded within the time interval. In this case, no change in the landscape is assumed. The backscattering coefficient calculated for the grassland, cropland and forest themes on both ERS-1 images is calculated with an excellent backscattering measurement stability being noted (less then 0,15 dB variation). It is therefore possible to define a temporal thematic signature for each theme taken into account.

2.2.1 Effect of landcover on the backscattered signal

An analysis of backscattering coefficient's temporal variations vis-à-vis the following landcover themes, forestry, grasslands and croplands was carried out between Spring 1992 and Autumn 1993 by using 12 ERS-1 data sets. Forestry's backscattering coefficient is practically stable at -7.7dB +/-0.2dB. Between Spring and Autumn, the backscattering coefficient for both grassland and cropland rises respectively by 2dB and 3dB. These seasonal variations are, in particular, explained by the evolution of the vegetal cover between Spring and Autumn. A backscattering coefficient variation for the grassland and cropland themes was also observed in the case of temporally close acquisitions (a few days) for which landuse would have not changed. The reason for these variations is most likely linked to soil moisture variations due to rainfall.

2.2.2 Sensibility of ERS-1 SAR data to soil moisture variation

A first study aiming to test the sensitivity of ERS SAR backscattering coefficients was carried out. For this purpose, rainfall prior to SAR acquisitions was

spatialised by using information provided by METEO FRANCE from 27 rain gauges in the study area. The backscattering coefficient was calculated over bare soil and short grassland in relation to the gradient of antecedent precipitation index. A strong correlation was shown between the ERS-1 SAR backscattering coefficient for bare soil (0.94) and short grassland (0.92), calculated at a regional scale, with soil moisture being linked to recent plotted rainfall events. The results, as obtained, open interesting fields of applications for large scale hydrological applications and inversion algorithms are therefore being investigated. Furthermore, this study points out that, due to the statistical properties of speckle in SAR imagery and the effect of local parameters, the accuracy level of the soil moisture estimate depends on the scale at which the backscattering coefficient is determined and therefore seems to create limitations for local scale applications.

2.2.3 Impact of observation scale on backscattering coefficient measurement accuracy

In order to test the potential and limitations of ERS-1 SAR in local to global scale applications, the impact of observation scale on SAR radiometric resolution and therefore on the level of accuracy of soil parameter estimation has to be investigated. A relationship between the observation scale and the accuracy of the backscattering measurement has been established and validated in the case of ERS-1 SAR data. (Bally and Fellah, 1995). Taking into account the user requirements in terms of measurement accuracy for soil moisture estimation, this relationship permits a minimum spatial scale to be calculated for which the quantification of the soil parameter can be determined at a sufficient confidence level. There is therefore a limitation of the use of ERS SAR data in estimating a soil moisture parameter, or any other parameter, at local scales (Fellah, 1995b). For example, considering the theoretial and experimental results obtained by Borgeaud (1993), who concludes that to retrieve soil moisture information to a 5% accuracy a backscattering coefficient precision of +-0.5 db is necessary. The use of the relationship derived above between observation scale and backscattering coefficient measurement accuracy leads to a minimal spatial scale of 3.5 hectares.

2.2.4 Influence of vegetation parameters on the ERS Radar Backscatter

The analysis of the vegetation parameters influence on the backscattered signal is investigated for Spring seasons, during crop grown, with ERS SAR data acquired between 1991 and 1993. The NDVI derived from SPOT data, which are quasi-synchronous to processed ERS SAR acquisitions, is used to estimate different vegetation states. The NDVI is calculated for all the SPOT data using Equation 1 below:

$$NDVI = [\,[\,(XS3 - XS2) / (XS3+XS2)\,] + 1\,] * 128. \qquad (1)$$

For each SPOT image, the mineral/vegetal threshold was calculated, the retained NDVI value is 159 for all the data. The NDVI values included between the mineral/vegetal threshold and the maximum are grouped into about ten different classes, each class for 5 NDVI values (Table 1). These classes enable the biomass of vegetation for cropland and grassland to be estimated.

Classes	Intervals
1	159-163
2	164-168
3	169-173
4	174-178
5	179-183
6	184-188
7	189-193
8	194-198
9	199-203
10	204-208

Table 1: NDVI classes

The backscattering coefficient is calculated for these two themes, for each NDVI class and for each ERS-1 SAR image. As an example, Figure 1 shows the backscattering coefficient behaviour for cropland and grassland relating to NDVI classes calculated with a SPOT scene, acquired the 17/05/92, which is quasi-synchronous to the Spring ERS SAR image acquired on the 22/05/92.

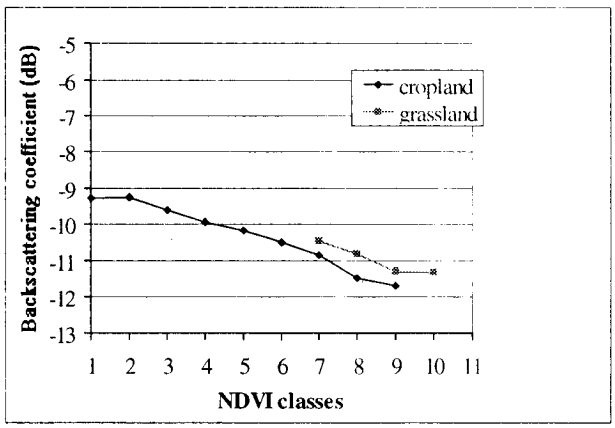

Figure 1: Behaviour of the backscattering coefficient calculated using 22/05/92 ERS SAR data with respect to NDVI classes calculated using 17/05/92 SPOT data

Correlation between NDVI classes and Radar backscatter

Figure 1 shows that there is a linear relationship between ERS backscattering coefficient and NDVI classes, and that the backscattering coefficient is slightly different for cropland and grassland which have the same NDVI values. This last point shows that complementary information from ERS SAR data could be derived about vegetation parameters (structure and/or water content).

The same linear decline of the backscattering coefficient with respect to NDVI (Radar backscatter decrease is about 2dB between minimal and maximal NDVI classes) is found for croplands in all the acquisitions recorded during the Spring period. This is only the case when rainfall effects on the backscattered signal are negligible and when the SAR and optical acquisitions are sufficiently synchronous. Therefore, using 6/05/92, 22/05/92 and 26/05/93 measurements, a relation between the backscattering coefficient and NDVI was investigated. A linear regression was found with a correlation coefficient greater than 0,92 for these three dates (figure 2).

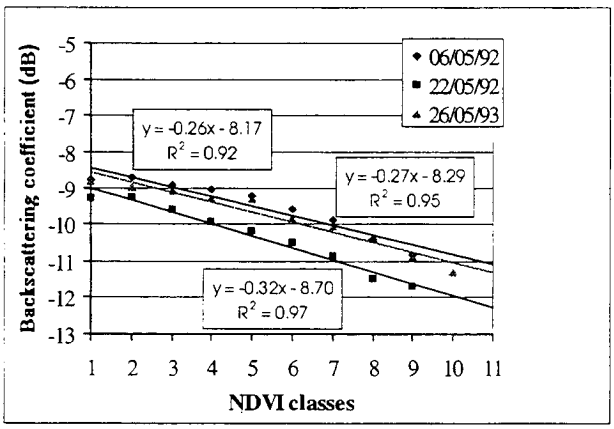

Figure 2: Behaviour of the backscattering coefficient calculated using 06/05/92, 22/05/92 and 26/05/93 ERS SAR data with respect to NDVI classes calculated using 17/05/92 and 18/05/93 SPOT scenes and their respective linear regressions.

These correlations show that an empirical relation between NDVI classes and the ERS backscattering coefficient can be established in this area for agricultural lands. The inversion and the spatialisation of this parameter over agricultural lands using ERS SAR data can therefore be carried out and is currently being investigated.

3. THE CAMARGUE TEST SITE

Located in the delta of the Rhône river in the South of France near the town of Arles, the Camargue region is a very flat plain normally protected from Rhône floods by embankments. A few months after the October 1993 flood, the Camargue region was flooded again in January 1994 after the formation of breaches in the Rhône river dykes. During the flood-level rise, Rhône water spread successively from breaches to the four Camargue flood basins (Vianet, 1994). These flood basins are the Saliers, Tête de Camargue, Bernacles and Grand Mar basins.

Within this project, the potential of multi-temporal ERS SAR data, during exceptional hydrological conditions, for flood detection and monitoring was presented by Laugier *et al.*, 1997. In the following section, an analysis of the backscattering coefficient's behaviour during soil drainage, which followed the 1994 Camargue flood, is presented.

3.1. THE DATA BASE

A data base has been built up in order to acquire historic background knowledge concerning the 1994 Camargue flood and to acquire information concerning the natural environment of the Camargue region. This data base is composed of satellite and exogenous data.

- Satellite Data

The satellite data include a SPOT XS scene plus fourteen ERS-1 SAR scenes acquired before, during and after the 1994 flood. These scenes were acquired during a three day ERS-1 acquisition mode (phase D). The SPOT XS scene was acquired on the 26th of March 1993 and was used to derive landcover information. The ERS data were acquired between the 3rd of January 1994 and the 16th of March 1994.

- Exogenous data

The exogenous data include topographic, pedological and soil maps as well as meteorological information and a flood report (Vianet, 1994). The meteorological data, which include daily precipitation for the period lasting from December 1993 to March 1994, were recorded by METEO FRANCE at the Tour du Valat station located in the Camargue region.

3.2. RADAR BACKSCATTER BEHAVIOUR DURING SOIL DRAINAGE

The backscattering coefficient's behaviour was analysed over surfaces during soil drainage after the flood. This allows the description of the backscattering coefficient's behaviour on surfaces at different hydric states during the transition from saturated to moist soil states. In fact, over a range from typically 10-40% soil moisture content, most studies show a linear increase and correlation between the backscattering coefficient

and soil moisture. In the case of very moist or saturated soil, the backscattering coefficient's behaviour is not well known. This knowledge is nevertheless important especially in the study of wetland evolution which frequently comprise very moist soil near saturation point. Two studies (Merot and Chanzy, 1991; Brun *et al.*, 1990) had shown that the backscattering coefficient, calculated using sensors with similar parameters as ERS-1 (i.e. wavelength, polarisation and incidence angle), increases when soils pass from a flooded to a moist state.

3.2.1 Approach for the backscattering coefficient measurements

The backscattering coefficient was calculated using the method described in Laur *et al.*, (1996). In order to study the backscattering coefficient's behaviour during soil drainage, measurements were done per image (every 3 days) and per "flood ring". Flood rings are defined as zones which are included between two consecutive flood zone limits (Fig. 3). These limits result from the cartography of the 1994 Camargue flood established using multi-temporal ERS SAR images and auxiliary information as detailed in Laugier *et al.* (1997).

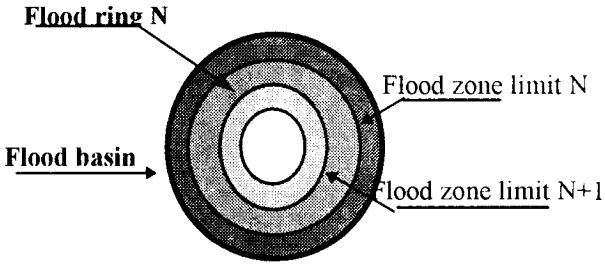

Figure 3: Principle of the "flood ring"

Measurements are performed for the four basins together and individualy as they could have their own hydrological characteristics.

As a first step, the backscattering coefficient measurements were carried out on 3 large reference fields (more than 3 hectares). These fields comprised one grassland and two rice fields located in agricultural zones within the Camargue region but outside flood zones. The figure 4 shows the temporal behaviour of the backscattering coefficient related to ERS-1 SAR acquisitions. Histograms of rainfall amount are also superimposed on this figure. For the reference fields, the trend of the curves is globally the same. One can also notice that globally their peaks follow important rainfalls and that radar backscatter decreases during dry periods, showing again, the effect of rainfall events in the ERS backscatter signal.

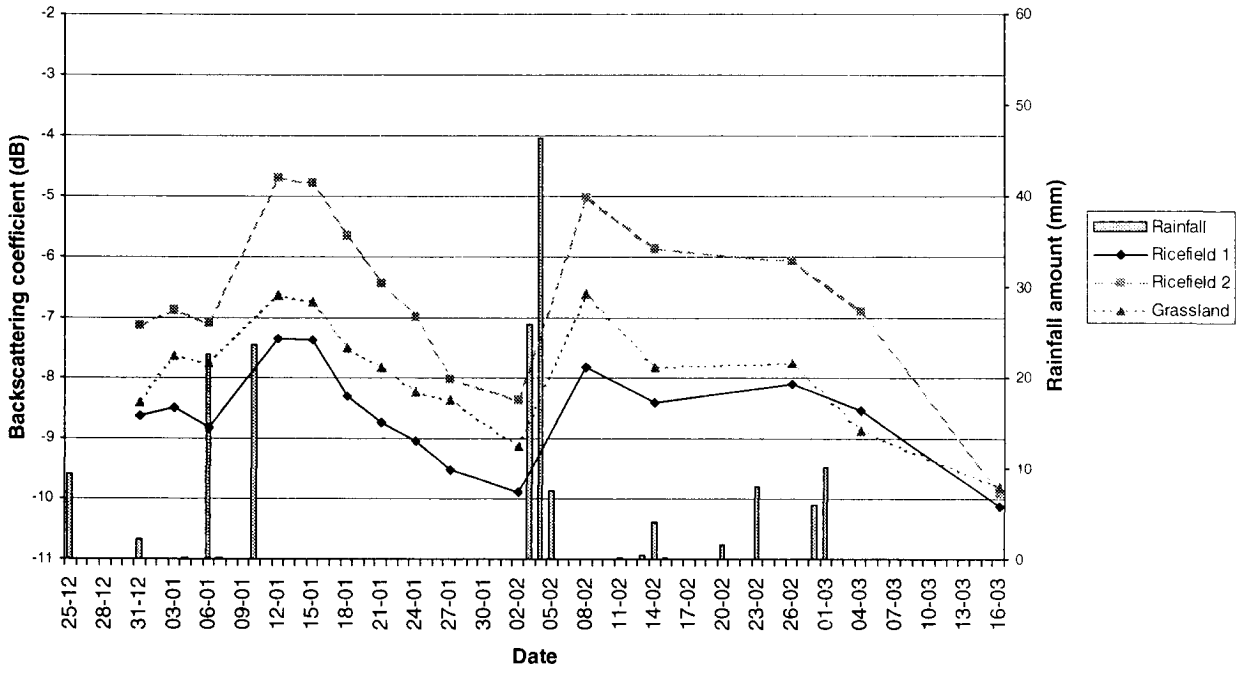

Figure 4: Temporal backscattering coefficient behaviour in the reference fields.

3.2.2 Analysis of the backscattering coefficient's behaviour during soil drainage

The temporal behaviour of the backscattering coefficient in each flood ring, for respectively, the ensemble of basins and independently for the 4 individual basins was analysed. Between each acquisition, seperated by only 3 days, the landscape is considered constant The surface which are considered within each flood ring consists of agricultural land without vegetation cover. Surface roughness and soil maps have been considered in the analysis of the temporal backscattering coefficient's behaviour, but it has been shown that under this experimental conditions, soil moisture was the predominant dynamic factor and therefore had the predominant effect on the backscatter signal analysis. Figure 5 shows the temporal backscattering coefficient's behaviour per flood ring for the basin set. The Bernacles basin is taken as an example to illustrate the analysis per flood basin (Figure 6). In fact, the behaviour of the backscattering coefficient in the other flood basins are very similar except for the Grand Mar basin. The difference in the Grand Mar basin is explained by the land cover which is essentially composed of natural marshlands contrary to the other flood basins which are agricultural areas without vegetation cover. Due to the presence of marshlands in the Grand Mar flood basin, the backscattering coefficient's measurements from this basin will not be discussed further.

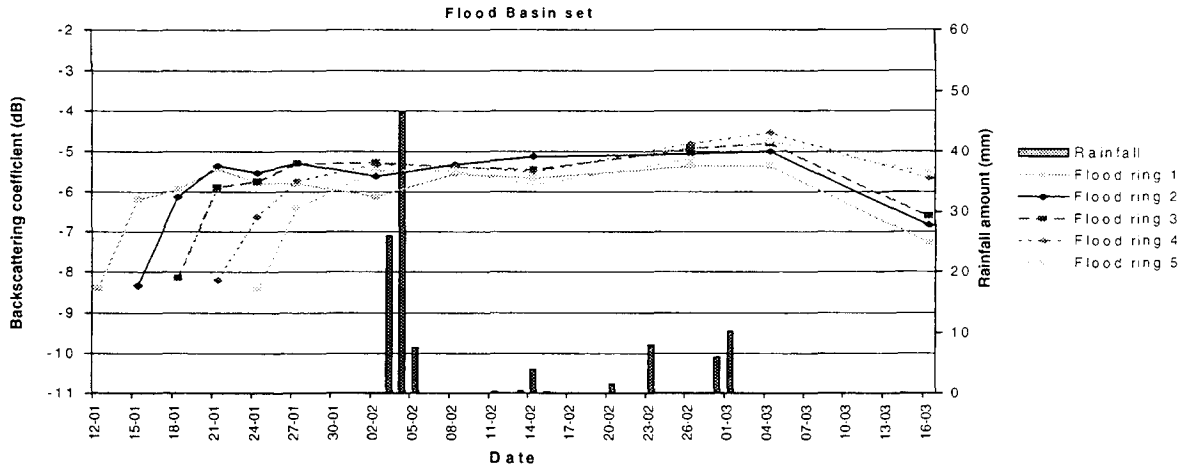

Figure 5: Temporal backscattering coefficient behaviour in each food ring for the ensemble of basins.

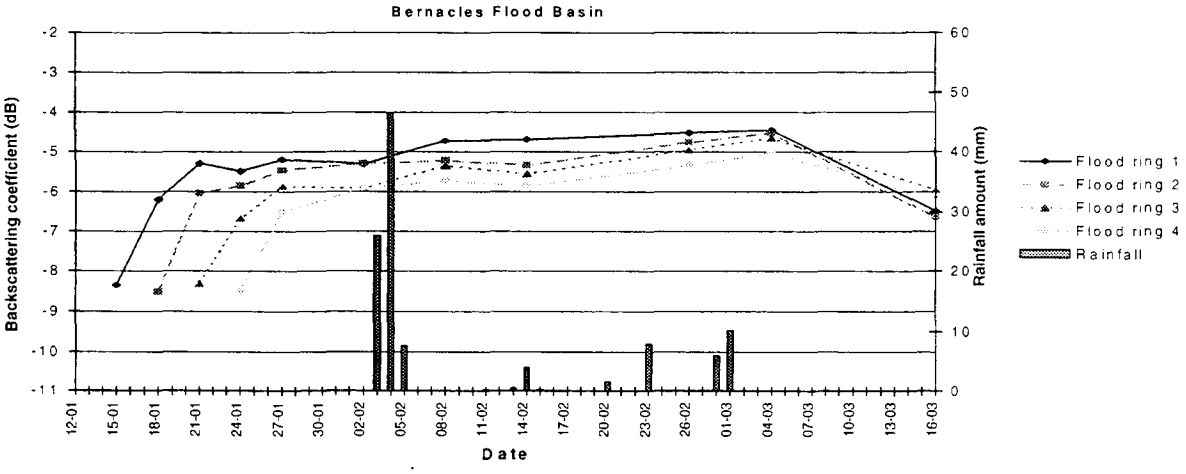

Figure 6: Temporal backscattering coefficient behaviour in each food ring for the Bernacles basin.

In Figure 5 and 6, the backscattering coefficient increases when the area of the flood rings pass from flooded to saturated and moist. One can note that contrary to the reference fields, the rainfall in the period between the 2nd and 5th of February do not correspondingly increase the backscattering coefficient value calculated over the flood rings. This means that an increase in soil moisture for very wet surfaces does not automatically mean an increase in the backscatter signal.

The temporal backscattering coefficient's behaviour for the flood basin set and the Bernacles flood basin

versus time interval since the start of soil drainage are respectively presented in Figures 7 and 8. In order to avoid rainfall influence on the backscattering coefficient, the measurements used stop before the 2nd of February. The curve trend of Figure 7 and 8 clearly shows that the backscattering coefficient increases as an asymptotically towards a peak situated between -5dB and -4 dB before becoming stable or diminishing slightly.

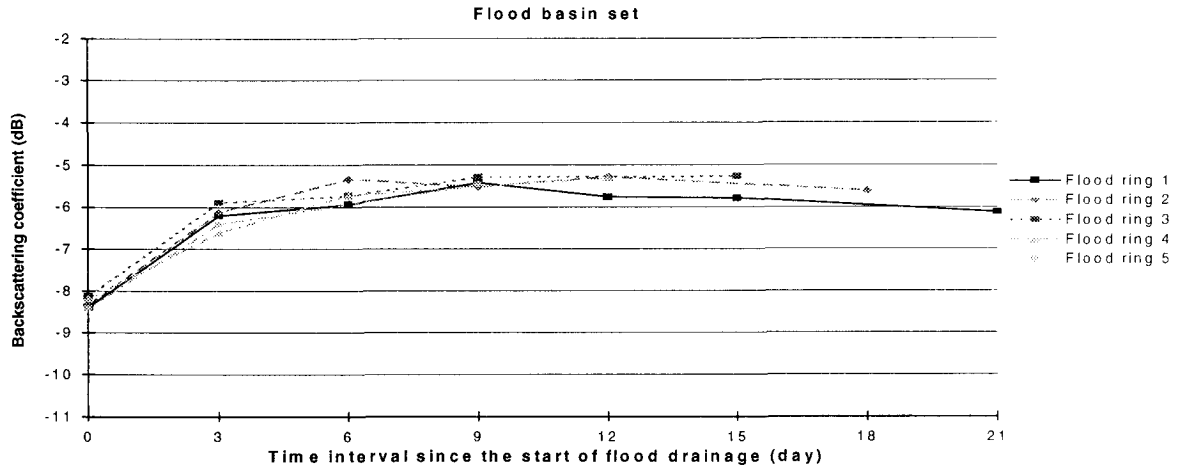

Figure 7: Backscattering coefficient behaviour in each food ring with respect to time interval since the start of flood drainage for the ensemble of basins.

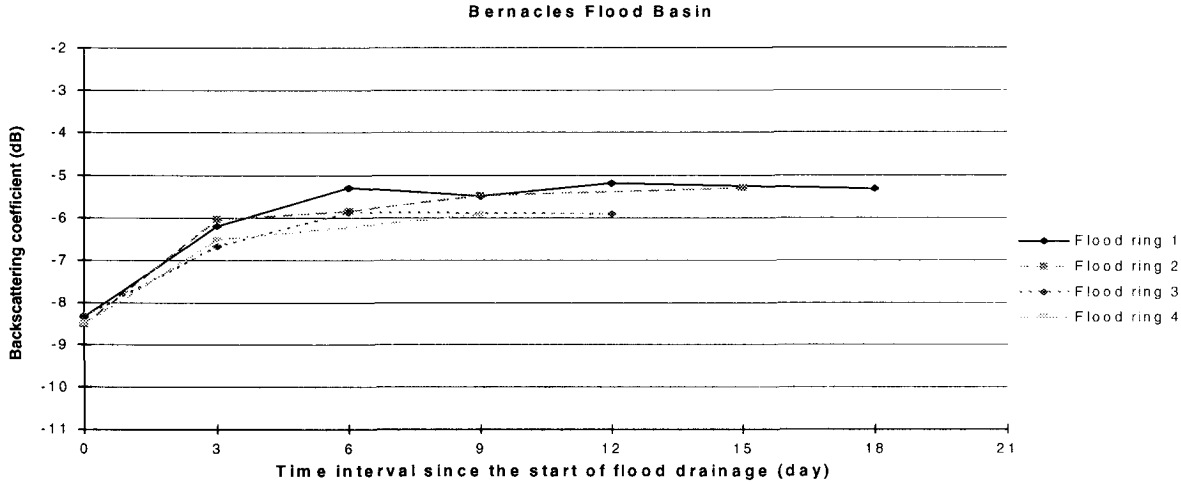

Figure 8: Backscattering coefficient behaviour in each food ring with respect to time interval since the start of flood drainage for the Bernacles basin.

Trend curve elaboration and discussion

The analysis of the temporal behaviour of the backscattering coefficient's during soil drainage enables a trend curve to be drawn, showing the backscattering coefficient behaviour versus the hydric state of the soil.(Fig. 9).

The main remarks to be made following this analysis are that firstly, a soil under two different hydrological states could have the same backscattering coefficient and secondly, after a certain soil moisture level the backscattering coefficient increases asymptotically.

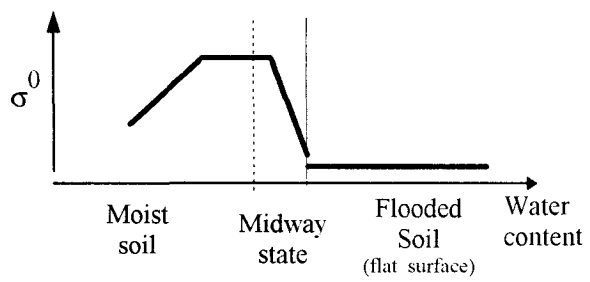

Figure 9: Trend curve showing the backscattering coefficient (σ^0) with respect to soil hydrological states

LES INONDATIONS DE JANVIER 1994 EN CAMARGUE
COMPLEMENTARITE DES DONNEES ERS ET SPOT

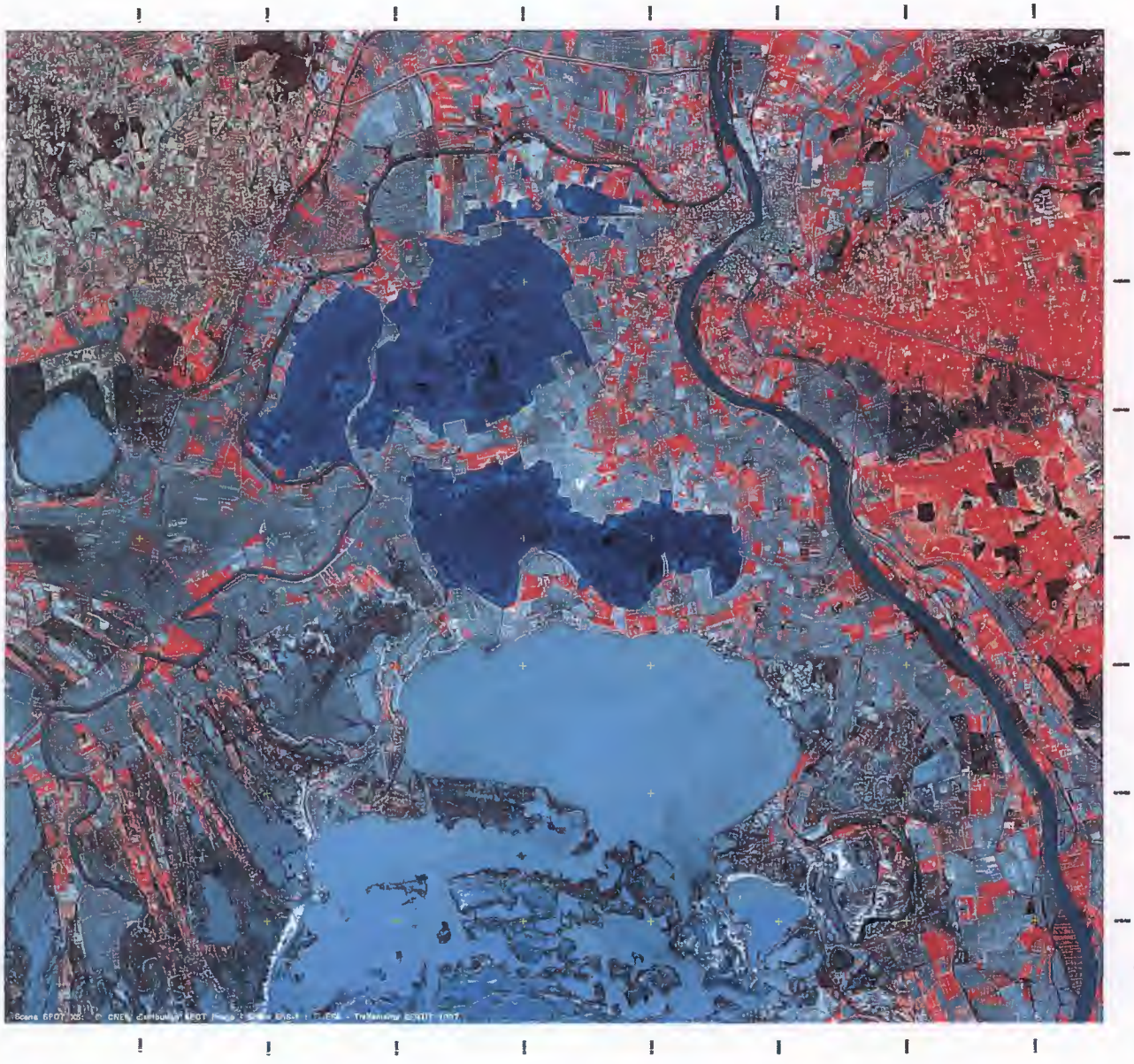

Sur l'image SPOT XS ci-dessus, les terres détectées inondées au 18/01/94 apparaissent sous un masque bleu. Les limites des champs d'inondation ont été déterminées à partir de l'analyse d'une série temporelle d'images ERS-1 acquises lors des inondations de 1994 et de données exogènes. Cette image illustre la complémentarité des données SPOT et ERS pour la prévention, l'impact et le suivi de catastrophes environnementales.

Service Régional de Traitement d'Image et de Télédétection
Boulevard Sébastien Brandt - 67400 Illkirch - France
Tel: +33 (0)3 88 65 52 00 http://sertit.u-strasbg.fr

4. CONCLUSION

The work carried out in these two regions using multi-temporal ERS SAR data together with auxiliary information has led to main results listed below :

In the Alsace test site where a quantitative approach towards soil moisture retrieval was carried out, the work has shown that:

There is a strong correlation between the ERS SAR backscattering coefficient calculated over large surfaces and soil moisture content. This has been noted for bare soils and short grassland during the Spring period.

A springtime multi-year study on the ERS backscattering coefficient versus an NDVI derived from synchronous SPOT data allows an empirical relationship between those parameters to be determined in this region. This can be used to determine the optimal conditions for soil moisture retrieval using ERS SAR data and pinpoints the potential of SAR data for the evaluation of vegetation parameters.

A relationship between SAR radiometric resolution and observational scales has been investigated, established and validated in the case of ERS-1 SAR products. This permits the determination of a minimum spatial scale at which the backscattering coefficient measurement can be achieved with a given level of confidence in order to derive quantitative bio-geophysical information. This pinpoints therefore some limitations in the use of ERS SAR data in quantifying bio-geophysical parameters at local scale.

In the Camargue region, 3 day mode ERS SAR data acquired before, during and after the 1993 and 1994 floods were processed. This study shows the high potential of ERS SAR data in the precise cartography of flood mapping and therefore in the provision of flood dynamic information. Furthermore, the analyse of the backscattering coefficient's behaviour during soil drainage has enabled the building up of a trend curve showing the backscattering coefficient's behaviour with respect to different soil hydrological states.

This study has underlined important aspects that must be considered in applications of ERS SAR data. The implications of this study open interesting perspectives in the field of hydrological ERS applications, as it seems that useful information could to be extracted at a regional scale and therefore open environmental applications for example in the wetland studies domain. In addition, the use of ERS SAR data during exceptional hydrological conditions demonstrates that operational use of this data can be envisaged in flood applications.

ACKNOWLEDGEMENTS

The ERS-1 SAR data were available under ESA Pilot Project A02-F112. This study was supported by CNES within the AVAL SAR programme and the Conseil Régional d'Alsace. The authors would wish to thank, METEO FRANCE, the Mairie d'Arles and the Parc Naturel Régional de Camargue.

REFERENCES

ATTEMA E., ULABY F., 1978, Vegetation Modelled as a Water Cloud, Radio Sci., Vol. 13, pp 357-364.

BALLY P., FELLAH K., BESNUS Y., MEYER C., RAST M. and de FRAIPONT P., 1995 - Impact of SAR radiometric resolution in hydrological and agro-environmental applications, Proceedings of the international Symposium «retrieval of bio- and geophysical parameters from SAR data for land applications», Toulouse, 10-13 Oct. 1995, 337-346.

BOUMAN B.A.M., UENK D., 1992, Crop Classification Possibilities with Radar in ERS-1 and JERS-1 Configuration, Remote Sensing Environ., Vol 40, pp.1-13.

BORGEAUD M., NOLL J., BELLINI A., 1994, Use of ERS-1 SAR data for land applications, Proceedings of the Second ERS-1 Symposium Space at the service of our Environment, Hambourg, 11-14 Octobre 1993, ESA SP-361, pp.845-847.

BRUN C., BERNARD R., VIDAL-MADJAR D., GASCUEL-ODOUX C., MEROT P., DUCHESNE J., NICOLAS H., 1990, Mapping Saturated Areas With a Helicopter-Born C Band Scatterometer, Water Resources Research, Vol. 26, No 5, pp 945-955.

DEMIRCAN A., ROMBACH M., MAUSER W., 1992, Extraction of Plant- and Soil- Parameters from Multi-temporal ERS-1 SLD-Data of the Freiburg Testsite, Proceedings First ERS-1 Symposium, Cannes, ESA SP-359, Vol 2, pp 631-634.

FELLAH K., BESNUS Y., CLANDILLON S., ETTAJANI A., MEYER C. and de FRAIPONT P., 1994, Multi-temporal ERS-1 SAR data in environmental studies: researching a quantitative approach for soil moisture retrieval. Proceedings of the First ERS-1 Pilot Project Workshop, Toledo, 22-24 June 1994, ESA SP, 85-92.

FELLAH K., BALLY P., BESNUS Y., MEYER C., RAST M. and de FRAIPONT P., 1995a - Impact of SAR radiometric resolution in hydrological and agro-environmental applications, Proceedings of the International Symposium «retrieval of bio- and geophysical parameters from SAR data for land applications», Toulouse, 10-13 Oct. 1995, 337-346.

FELLAH K., 1995b - The impact of the observation scale in hydrological applications of SAR data, ESA-ESTEC/VRL, Earth Sciences Division, Land/Surface Unit, Stagiaire report, Avril 1995. 35 pp.

LAUGIER O., FELLAH K., THOLEY N., MEYER C. and de FRAIPONT P., 1997, High temporal detection and monitoring of flood zone dynamic using ERS data around catastrophic natural events: the 1993 and 1994 Camargue Floods events, Proceedings of the 3rd ERS Symposium, Florence 18-21 March, 1997.

LAUR H., 1992, ERS-1 SAR Calibration, Derivation of Backscattering Coefficient in ERS-1 SAR PRI products, Rapport de l'Agence Spatiale Européenne, N°1, 16 pages.

LAUR H., BALLY P., MEADOWS P., SANCHEZ J., SCHAETTLER B., LOPINTO E., 1996, Derivation of the Backscattering Coefficient σ^0 in ESA ERS SAR PRI products, ERS SAR Calibration, Issue 2, Rev. 2, N° ES-TN-RS-PM-HL09, ESRIN, ESA.

LE TOAN T., SMACCHIA P., SOUYRIS J., BEAUDOIN A., MERDAS M., WOODING M. and LICHTENEGER J., 1994, On retrieval of soil moisture from ERS-1 SAR data, Proceedings of the Second ERS-1 Symposium Space at the service of our Environment, Hambourg, 11-14 Octobre 1993, ESA SP 361, pp.883-889.

MERET P., CHANZY A., 1991, Mesure de l'humidité d'un sol nu par radar dans des conditions d'excès d'eau, Mesures Physiques et Signatures en Télédétection, Courchevel, France, SP-319, ESA, Vol 1, pp. 293-296.

MOHAN S., MEHTA N.S., MEHTA R.L., PATEL P., RAJAK D.R., SRIVASTAVA H.S., DAS D.K., SHARMLA S., SAXENA C.M., SUTRODHAR A.K., 1994, Soil moisture estimation using ERS-1 SAR data, Proceedings of the Second ERS-1 Symposium : Space at the service of our Environment, Hambourg, ESA SP 361, 875-878.

PREVOT L., CHAMPION I., GUYOT G., 1993, Estimating Surface Soil Moisture and Leaf Area Index of a Wheat Canopy Using a Dual-Frequency (C and X Bands) Scatterometer., Remote Sensing Environ., Vol. 46, pp 331-339.

THOLEY N., de FRAIPONT P., CLANDILLON S., FELLAH K., YESOU H., 1995, Monitoring Flood Events with Remote Sensing Data: An Example of ERS-1'S Contribution to Flood Events in Northern and Southern France Regions, 26-27 June 1995, First ERS Thematic Working Meeting on Flood Monitoring, Italy, ESRIN, ESA.

ULABY F.T., 1974, Radar Measurements of Soil Moisture Content. IEEE Trans. on Antennas and Propagation, Vol. AP-22, N°2, 1974, pp 257-265.

ULABY F.T., BUSH T.F., 1976, Monitoring Wheat Growth with Radar, Photogrammetric Engineering and Remote Sensing, Vol. 42, pp 557-568.

VIANET R., 1994, Rapport sur les inondations, Parc Naturel Régional de Camargue (unpublished).

WANG J.R., 1985, Effect of Vegetation on Soil Moisture Sensing Observed from Orbiting Microwave Radiometers, Remote Sensing of Environment, Vol. 17, geophysical parameters from SAR data for land applications», Toulouse, 10-13 Oct. 1995, 337-346.

WOODING M.G., GRIFFITHS G.H., EVANS R., 1993, Temporal Monitoring of Soil Moisture using ERS-1 SAR data, Producing First ERS-1 Symposium - Space at the Service of our Environment, Cannes, France, 4-6 Novembre 1992, ESA SP 359, pp 641-648.

WOODING M.G., ZMUDA A.D., GRIFFITHS G.H., 1994, Crop discrimination using multi-temporal ERS-1 SAR data, Proceedings of the Second ERS-1 Symposium Space at the service of our Environment, Hambourg, 11-14 Octobre 1993, ESA SP 361, pp.51-56.

MONITORING HYDROPATTERNS IN SOUTH FLORIDA ECOSYSTEMS USING ERS SAR DATA

E.S. Kasischke, L.L. Bourgeau-Chavez, and K. Smith

Earth Sciences Group, Environmental Research Institute of Michigan, Ann Arbor, MI USA
phone (313) 994-1200 -- *fax* (313) 994-5824 -- *email* ekas@erim.org

E. Romanowicz and C.J. Richardson
Nicholas School of the Environment, Duke University, Durham NC USA

ABSTRACT

This paper summarizes the results of an ongoing study of ERS SAR imagery collected over the southern Florida, an area containing numerous wetlands. This study showed that the signatures from the wetlands in this region observed in the ERS SAR imagery vary widely throughout the year. The seasonal differences in these signatures are shown to be primarily due to variations in water levels.

Keywords: wetlands, flooding,, ERS SAR, Florida Everglades, Big Cypress National Preserve

INTRODUCTION

Southern Florida contains one of the largest complexes of freshwater wetlands found anywhere in the world. While the Everglades is the largest and most noteworthy of these systems, numerous other wetlands types are indigenous to this region, such as the wet marl prairies and cypress forests found in the Big Cypress National Preserve located northwest of the Everglades. Most wetland ecosystems in southern Florida have been heavily impacted by human activities, with the temporal patterns of flooding or inundation partially or entirely disrupted. Even though the scientific community has long recognized the importance of these wetlands, it has only been recently that the general public and policy making communities have begun to accept the need for intensive wetland restoration and mitigation.

A key challenge facing the scientific and management communities is monitoring the temporal and spatial patterns of flooding in wetland ecosystems, e.g., the hydropattern. While the remote sensing community has long recognized that longer-wavelength SARs (such as Seasat and JERS-1) are capable of monitoring flooding in forested wetlands (Hess et al. 1990), it has only been recently recognized that the ERS SAR can be used to detect and monitor flooding in wetlands dominated by herbaceous vegetation (Morrissey et al. 1994; Kasischke et al. 1997). Since a high percentage of the wetlands in southern Florida are non-wooded, it has been realized that ERS offers a unique means for monitoring flooding in this region (Kasischke and Bourgeau-Chavez 1997).

In this paper, we review recent research using ERS SAR imagery to monitor the patterns of flooding within the Everglades National Park (ENP) and the Big Cypress National Preserve (BCNP), both of which are located in southern Florida. First, we present examples of ERS SAR imagery illustrating dramatic variations in image intensity over both the ENP and BCNP and discuss the sources of these variations. Next, we illustrate how color compositing of different dates of ERS SAR data can be used as an effective tool for monitoring changes in water levels and soil moisture conditions.

ERS SAR IMAGERY OF SOUTH FLORIDA

Figure 1 presents a series of ERS SAR images collected over the south Florida region during late 1995 and 1996. For references purposes, Figure 2 presents the major geographic features of the imaged area and Figure 3 summarizes monthly precipitation during this time period.

Southern Florida is located within the tropics and has distinct wet and dry seasons. From Figure 3, it can be seen that the 11 December 1995 to 30 April 1996 images were collected during the dry season, while the 4 June to 17 September images were collected during the wet season. Figure 3 shows that the precipitation during the wet season in 1996 was slightly below the average for the past 30 years. Overall, there is an increase in radar image intensity as the dry season progresses and a decrease in image intensity as the wet season progresses. There are areas within the images where the opposite trend exists.

To understand why these image intensity variations occur, one needs a basic understanding of the sources of microwave or radar scattering from vegetated surfaces. One of the major sources is direct scattering of energy from the vegetation. Up until a certain point, as the density and biomass of a canopy increases, so does the radar scattering from that vegetation. A certain amount of the microwave energy passes through the vegetation, however,

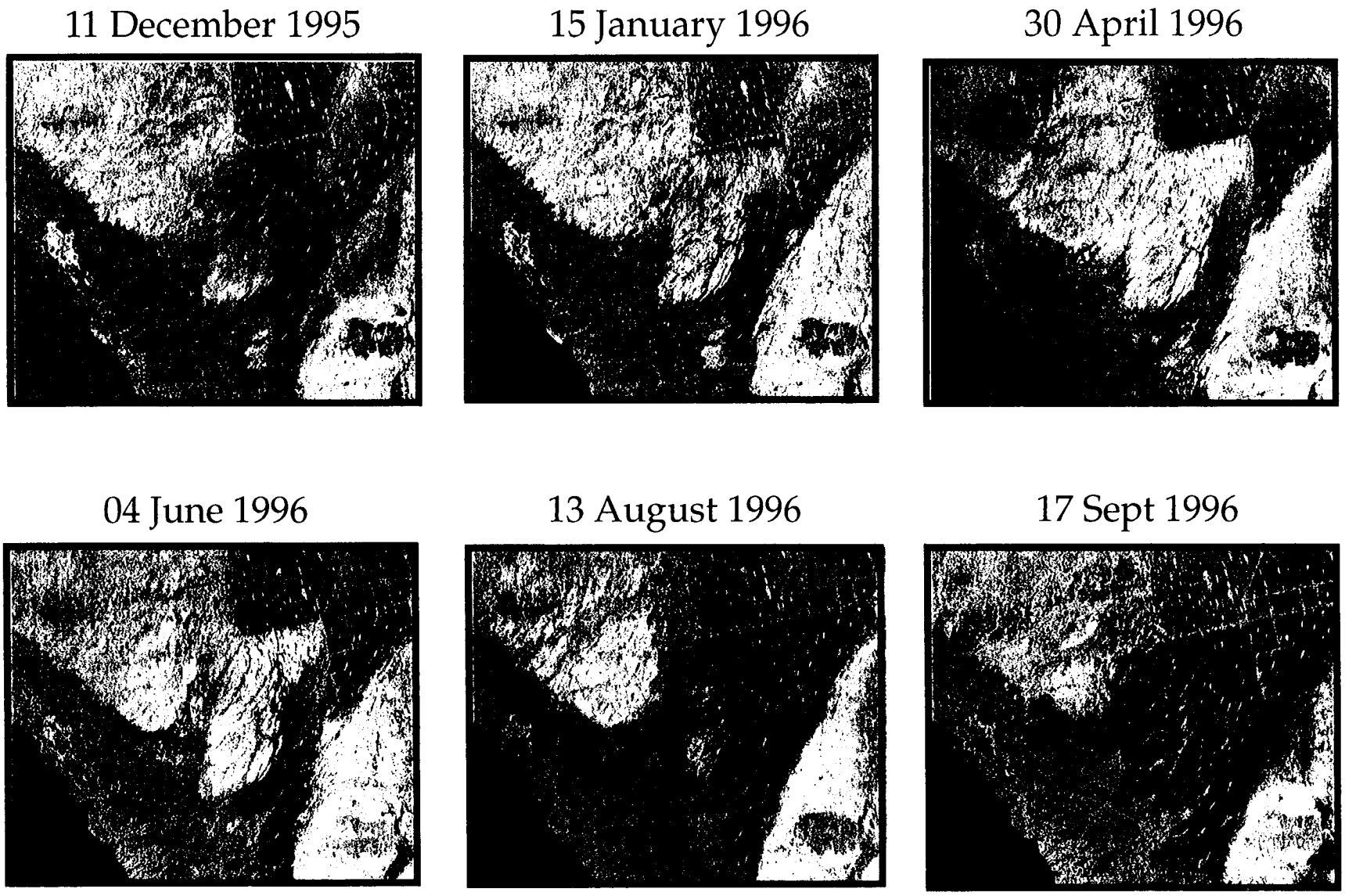

Figure 1. ERS SAR Images of Southern Florida (Images Copyright European Space Agency 1995, 1996)

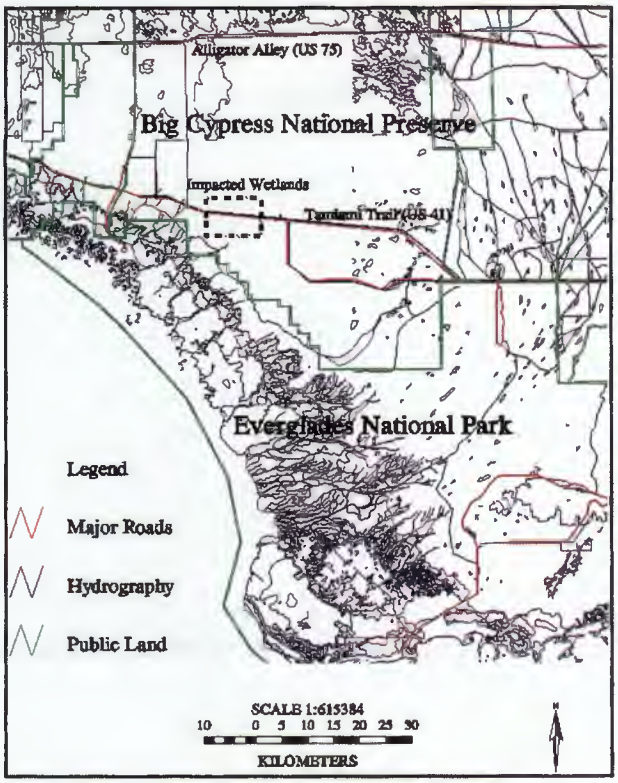

Figure 2. Schematic Diagram Illustrating the Major Geographic Features of the Areas within the ERS Images in Figure 1.

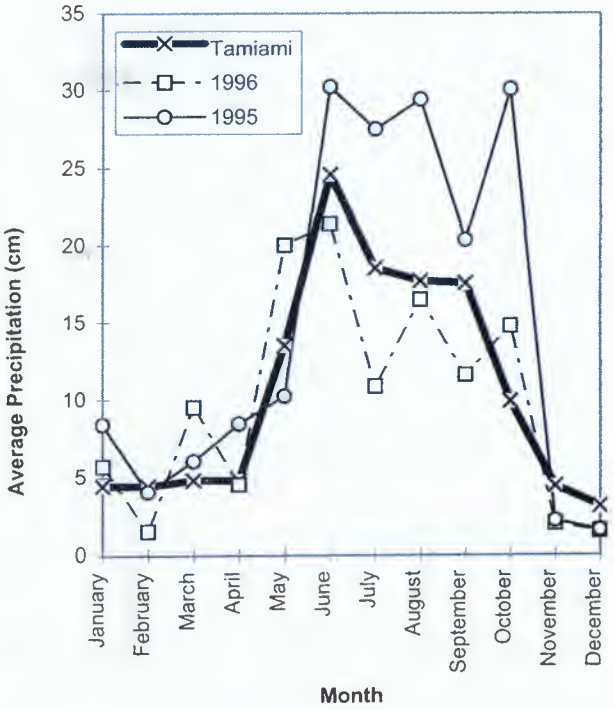

Figure 3. Average Monthly Precipitation for Southern Florida.

and reaches the ground surface. Here, the energy is either absorbed, scattered back to the radar system or is scattered in a forward direction away from the radar. For unflooded surfaces, the degree of scattering from the ground is directly proportional to soil moisture. If a layer of water covers the ground surface (which occurs in a flooded wetland), then all the radar energy is reflected away from the radar receiver. A third scenario for a radar signature exists if a wetland contains woody vegetation (trees or shrubs). In this case, the microwave energy that is scattered away from the radar transmitter is intercepted by tree branches or boles, and reflected back to the radar.

In summary, there are three potential sources of scattering from a vegetated surface: (1) direct scattering from the vegetation canopy; (2) direct scattering from the ground; and (3) multiple reflection scattering from between the ground and vegetation.

Figure 4 illustrates the types of scattering which occurs in two different wetland types found in southern Florida: dwarf cypress and wet marl prairies. This diagram illustrates the sources of radar scattering as function of variations in soil moisture and flooding. Relative to a dry ground surface, wet soils would increase the radar signature from both wetland types. In contrast, relative to the wet soil surface, a flooded surface would: (1) increase the radar signature from the dwarf cypress because of the enhance ground-to-tree scattering but; (2) reduce the radar signature in the wet marl prairie because of the total reflection of the microwave energy away from the radar.

ANALYSIS OF A TWO-DATE ERS SAR IMAGES

Figure 5 presents two color color-composite images generated from ERS SAR imagery collected at the end of the dry season (April/May) and towards the end of the wet season (August). The two images presented in Figure 5 were generated from data collected in 1995 and 1996. Note from Figure 3 that the rainfall during the wet season of 1995 was significantly greater that during the same time period in 1996.

These images are from an area which has two dominant vegetation covers: prairie wetlands and cypress/hardwood forests. The normal pattern of inundation in these two wetland types is for there to be standing water during the wet season, and very little or no standing water, but very

Figure 4. Illustration of the effects of vegetation, soil moisture, and flooding on ERS radar signatures.

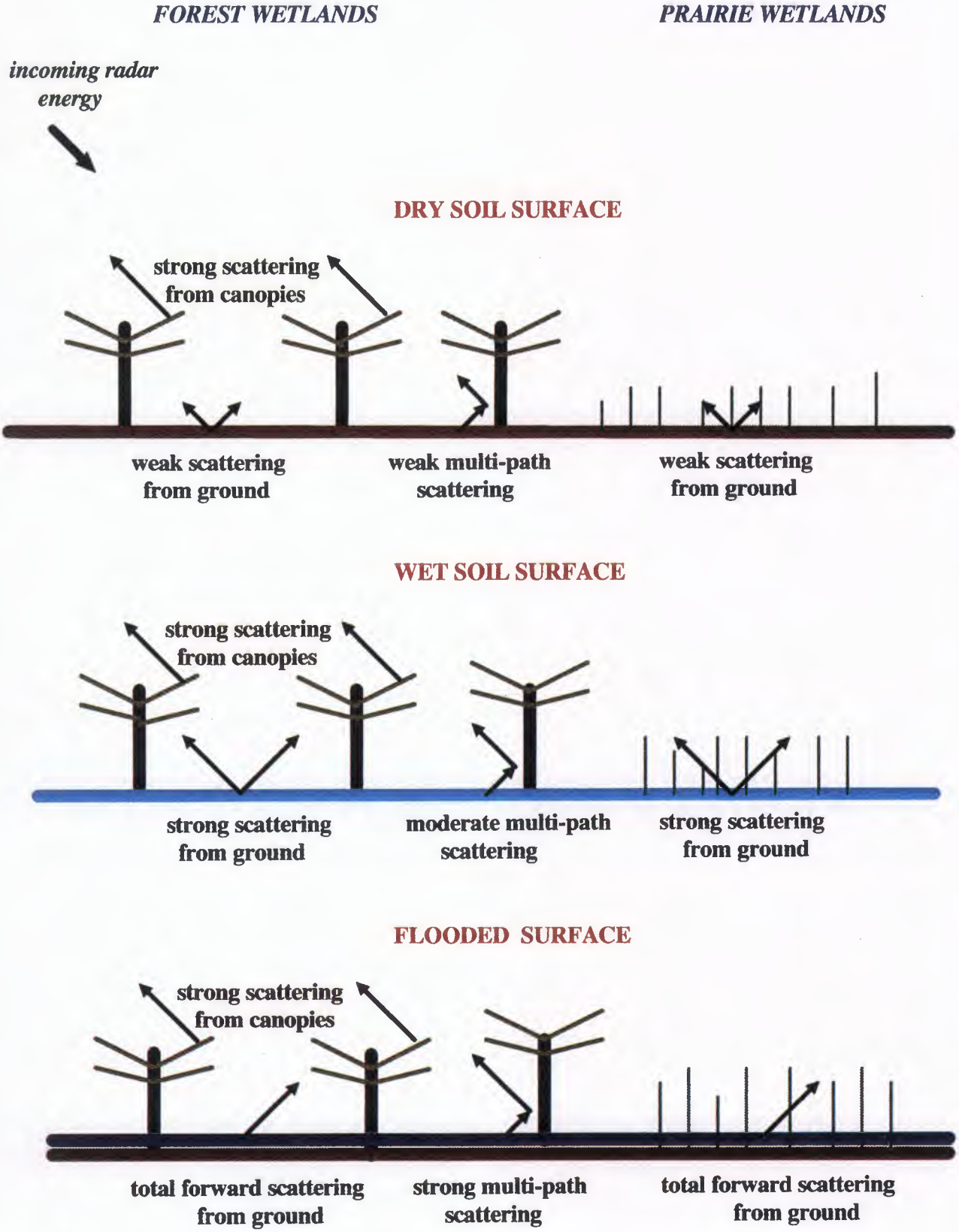

1995 , 1996 ERS-1 SAR Multi-date Composites

Big Cypress National Preserve

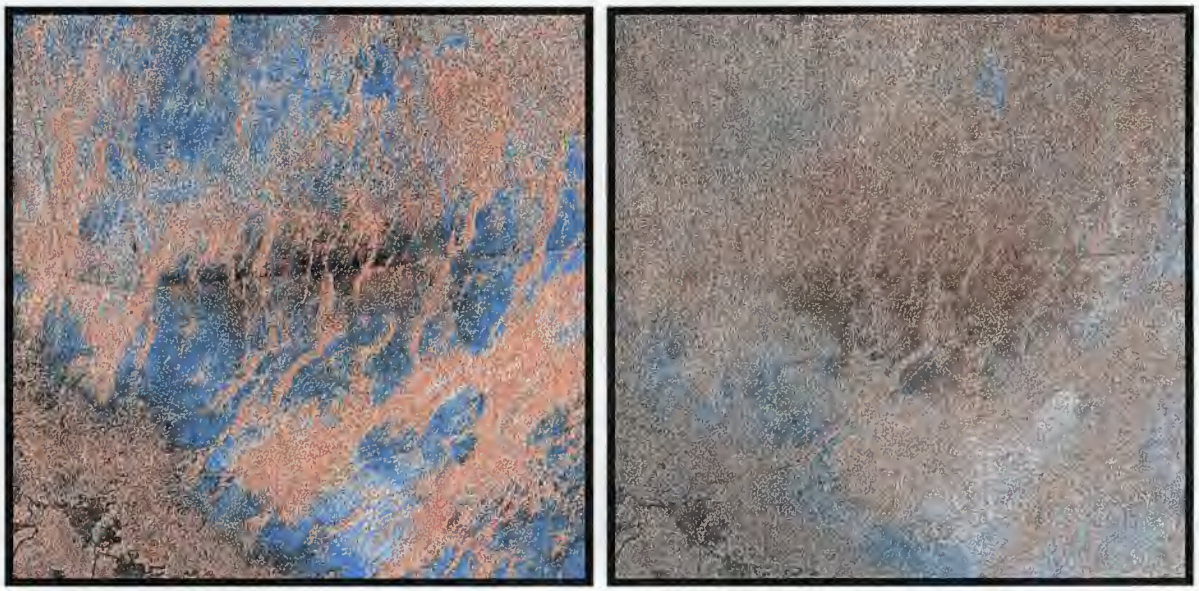

28 August 1995 (Wet Season)

15 May 1995 (Dry Season)

13 August 1996 (Wet Season)

30 April 1996 (Dry Season)

Thematic Mapper Derived Vegetation Classification

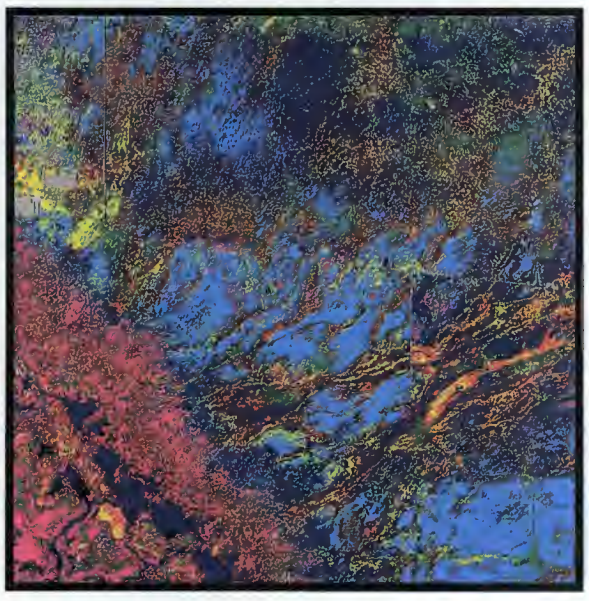

Tropical Hardwood/ Cypress Forests

Shrub Wetlands

Pine Uplands

Sawgrass Prairie Wetlands

Freshwater Marl Prairie Wetlands

Mangroves

Figure 5. Two-Color Composite ERS Images and Vegetation Map Over Big Cypress National Preserve.

moist soils during the dry season. This normal inundation pattern would result in the forested stands having brighter signatures during the wet season than in the dry season because of the enhanced multiple-bounce scattering from the flooded surface. In contrast, the prairie wetlands would have a much brighter signature during the dry season because of the higher direct scattering from the moist soil.

The color-composite images in Figure 5 were generated by assigning the dry season image the color blue and the wet season image the color red. Thus, forest stands with a normal inundation pattern appear red in the 1995 composite image in Figure 5, while prairie wetlands appear blue.

Some of the prairies adjacent to the Taimiami Trail do not exhibit a color associated with the normal inundation pattern in the 1995 composite image in Figure 5. In particular, there are prairie wetlands on the north side of the road which have a "dark" signature and on the south side of the road which have a red signature. These variations from normal are thought to be caused by the road itself. On the north side, a borrow pit runs continuously parallel to the road, forming a canal. This canal serves to drain the prairie wetlands north of the road, and significantly reduces the soil moisture in these prairies during the dry season. These dry soil would have a darker radar signature compared to areas with wet soils. Because the road blocks the normal north-to-south flow of surface water during the wet season, the prairies immediately to the north of the road flood during the wet season, as do prairies not affected by the road. Thus, the prairies north of the road have a dark signature in both the wet and dry seasons, resulting in a dark signature on the composite image in Figure 5. The blocking of normal surface flow affects the prairies to the south of the road as well. Because of the blocking of the normal surface flow in the wet season, these areas tend to become: (1) drier than normal prairies during the dry season; and (2) do not become flooded during the wet, but have wet soils at this time. Thus, these areas have a brighter signature (from wet soils) during the wet season, resulting in the red signatures on the composite radar image in Figure 5.

The absence of the extensive blue signatures in the wetland prairies in the 1996 composite ERS SAR image indicates that these wetlands most likely did not flood during that year's wet season. The almost white signature in many of the prairie wetlands indicates these areas had wet soils in both the wet and dry seasons. The darker red signatures in some of the wetland prairies, especially along the Taimiami Trail, are indicative of dry soils during the dry season and moist, but unflooded soils during the wet season. Comparison of the two SAR composite images in Figure 5 clearly shows that inter-seasonal variations in hydropattern can be detected using ERS data.

SUMMARY

This study has shown that the imaging radar onboard the ERS satellite is uniquely suited to monitor variations in surface inundation and soil moisture in several different wetland ecosystems in southern Florida. Studies are currently underway to explore the utility of ERS radar imagery, as well as that collected by the Radarsat satellite, to monitor patterns of inundation in all the different wetland communities in this region. Because of its ability to monitor large areas in a single image, ERS radar imagery provide a valuable resource monitoring tool which compliments efforts to monitor water levels using point-source measurements. In particular, this technology may be quite appropriate for: (1) identifying areas where human built structures have influenced the natural flow of water; and (2) monitoring the effects of efforts specifically designed to restore the natural flow of surface water within wetland ecosystems in this region.

ACKNOWLEDGEMENTS

The research reported in this paper was supported by a research grant from NOAA and by EPA through award number R 825156-01-0 to ERIM. Although this research was supported by EPA, it has not been subject to agency review and therefore does not necessarily reflect the view of the agency and no official endorsement should be inferred. The ERS imagery was provided by ESA through experiment AO2.USA133. The continuing support of ESA in providing access to ERS data has been a great benefit throughout the years this study has been ongoing.

REFERENCES

Kasischke, E.S. and L.L Bourgeau-Chavez, 1997
Monitoring wetland vegetation type and inundation in southern Florida using ERS-1 SAR imagery, *Photogram. Eng. Remote Sens.* **63**, pp. 281-291.

Hess, L. L., *et al.* , 1990
Radar detection of flooding beneath the forest canopy: a review, *Int. J. Remote Sens.* **11**, pp. 1313-1325.

Kasischke, E.S., *et al.*, 1997
The use of imaging radars for ecological applications - a review, *Remote Sens. Env.* (in press).

Morrissey, L. A., *et al.*, 1994
Use of SAR in regional methane exchange studies, *Int. J. Remote Sens.***15**, pp. 1337-1342.

THE CONTRIBUTION OF MICROWAVE DATA TO DISTRIBUTED HYDROLOGIC MODELING

Wolfram Mauser[1], Heike Bach[2], Aslan Demircan[1], Beate Eibl[1], Gertrud Riegler[1], Karl Schneider[1]

[1]Institute for Geography, Dept. of Geographical Remote Sensing, University of Munich, Luisenstr.37, D-80333 Munich, Germany, Fax.: ++49-89-5203-321, e-mail: W.Mauser@iggf.geo.uni-muenchen.de
[2]Vista - Remote Sensing Applications in Geosciences, Anton-Ferstl-Str. 11, D-82234 Wessling, Fax.: ++49-8153-952204, e-mail:100640.1506@compuserve.com

ABSTRACT

Remote sensing data offer spatial information on the state of a large variety of environmental parameters, which determine land surface processes. To model these processes, of which the water cycle plays a central role, the PROMET-family of spatial evapotranspiration models was developed. PROMET was given a structure, with allows to maximize the input of remote sensing data on the field- as well as micro- and mesoscale. The model-family consists of a kernel model (a SVAT based on the Penman-Monteith equation and a plant-physiological model for the influence of environmental parameters on canopy resistance) and a spatial modeller, which provides and organizes raster input data on the field-, micro- and mesoscale. Input data from different remote sensing data sources are presently used (ERS-AMI, LANDSAT, NOAA-AVHRR and METEO-SAT) both to gather input-data for the model and to validate model results. Model results on the field scale show good agreement with measurements. Spatial data is set up using remote sensing and conventional data sources for a 800 km² watershed in Upper Bavaria. Several examples show the presently possible utilization of remote sensing data and especially microwave data in the model. From these examples a concept for future utilization scenarios for microwave data in hydrologic models is derived.

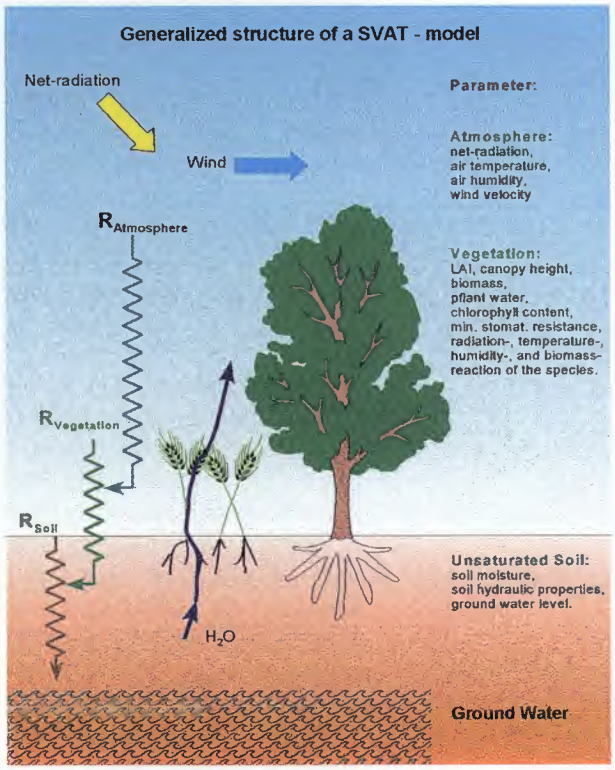

Fig.1: Generalized SVAT-Scheme

1. INTRODUCTION

Understanding evapotranspiration (aET) on the land surface is the key to the hydrologic cycle because evapotranspiration rules the partitioning of energy and matter. Evapotranspiration is affected by a multitude of processes at the interface between soil, vegetation and atmosphere. Actual evapotranspiration and the related processes are responsable for app. 70 percent of the lateral global energy transport. Since agricultural production is closely related to evapotranspiration and the water consumption by plants, it also is the key parameter for a secure future food supply. Any change of aET either through a change in vegetation or a change in climate directly affects the available water resources and runoff. Changes in vegetation-cover through human influences are taking place both on the field scale through an expansion of agricultural areas and an introduction of new or modified species in agriculture and forestry and on the regional scale through deforestation, irrigation and man-induced erosion. To be able to quantify the effect of these changes on the energy- and water-balance of the surface, physically based and distributed models have to be established to describe the distributed nature of the evapotranspiration process on different scales.

A whole wealth of measurements of aET conducted over different land covers and under different climatic conditions at the point scale have demonstrated the large variety and complexity of the evapotranspiration process. Through these measurements energy supply, soil-moisture, temperature and plant development were identified as major limiting factors influencing aET. On the basis of these measurements powerful physically based soil-vegetation-atmosphere-transfer-(SVAT)-models were formulated (see Fig.1), which describe the processes involved on different levels of complexity for homogeneous surfaces at the point scale [Ref.1,2,3]. The most widely applied of these models was developed by Penman and modified by Monteith [Ref.4]. It combines the energy-balance of the land surface with the concept of

a species dependent surface resistance for water-vapour release. Only lately have these SVAT-models been extended from single fields to landscapes [Ref.5,6,7,8], which became possible through the use of remote sensing data for the determination of slowly changing parameters like land-use or topography. Nevertheless this has proven difficult because the models and data-structures used were not optimized for the use of remote sensing data. To maximize the utilization of remote sensing data for modeling the hydrologic cycle and to derive sound model-requirements in terms of spatial, spectral and temporal resolution for synergistic remote sensing data from a variety of proposed future missions the model-family PROMET (**Pr**ocess **O**riented **M**ultiscale **E**vapotranspiration) was developed.

2. MODELING AND INFORMATION FLOW WITHIN PROMET

The information flow within PROMET is shown in Fig.2. PROMET is based on a flexible data handling shell, which serves three purposes:

- organization of input data streams into the system. Spatial data from three different areas can be input to PROMET:
  - land cover and its change over time (LAI, plant height, albedo)
  - soil physics and its change over time (soil-moisture)
  - meteorology (radiation, temperature, wind, humidity).

Currently derived parameters from METEOSAT, NOAA-AVHRR, LANDSAT and ERS are used in the model.

- organization and synchronization of different sub-models, which use the spatial input data streams. Currently sub-models for radiation, evapotranspiration, soil-moisture and ground water recharge are implemented.
- organization of output data streams from the system, production of time series, digital videos etc.

At the interface between PROMET and remote sensing data sources parameter-models are located, which transform time series of remote sensing observations into meaningful model-parameters.

2.1 ALGORITHM FOR MODELING ACTUAL EVAPOTRANSPIRATION

The kernel model of PROMET uses the Penman-Monteith equation, which regulates evapotranspiration through a canopy resistance, which represents the influence of the environment on plants. This influence is simulated by a coupled plant physiological and a soil hydraulic model. It takes into account plant species, plant growth and soil moisture status through a set of parameters. Each species is represented in the model through the following set of parameters: photosynthetically active radiation (PAR), min. stomatal resistance, increase of stomatal resistance with photosynthetically active radiation, cardinal temperatures consisting of minimum, optimum and maximum air temperature for stomatal resistance, decrease of stomatal resistance with humidity, soil suction, at which stomatal closure starts, slope of the increase of stomatal resistance with soil suction beyond this point.

The influence of plant growth on canopy resistance and energy balance in the model is represented through the temporal evolution of the following parameters: green leaf area index (LAI) , plant height and albedo. These parameters and their change with time, which represents plant growth, should be determined through remote sensing.

Soil water balance, soil suction and moisture in the root-zone are determined through a simplified

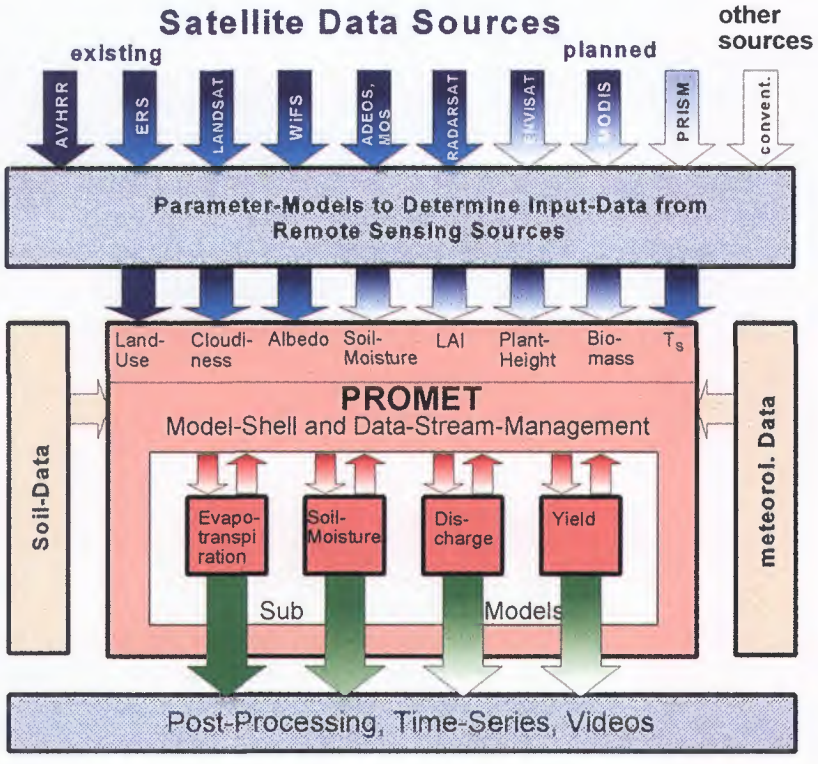

Fig2: Information Flow and General Structure of PROMET

solution of the Richards-equation. The static soil parameters needed to do the calculations are: pore volume, pore size distribution index, bubbling preasure head. The soil-model presently assumes one vertically homogeneous soil layer, which is represented by the the average root depth. A more detailled description of PROMET can be found in [Ref.7, 19].

Fig.3: LANDSAT-TM and ERS based land-use classification of the Ammer-watershed

3. THE STUDY REGION

To study the spatial distribution of evapotranspiration using remote sensing data within PROMET a typical Central European landscape was chosen. This landscape is characterized through elevation differences, heterogeneous soils and land use, which is mainly man-made in its distribution. The region chosen for this study is the Ammer watershed, which lies in the Northern Alpine Forelands of Upper Bavaria in Germany, a region with undulated to steep terrain, varying soils from clay to sandy loam and high rainfall rates (average >1000 mm/a). The elevation difference between the North and the South of the study region is approximatelly 1200 m. This and the influence of the Alpes introduce a strong N-S gradient in temperature, humidity and rainfall with the tendency of decreasing temperatures and increasing humidity and rainfall towards the Alpes.

In Fig.3 an image of test region as a LANDSAT-TM land-use classification overlayed on a digital terrain model is shown [Ref.9]. Landscape units like cities, forests, lakes and agricultural regions can be seen. As can be seen clearly land-use changes with elevation in the test area.

4. REMOTE SENSING INPUTS

Tab.1 gives an overview of the most important parameters, that enter PROMET together with an estimation of the temporal observation frequency necessary to adequatly observe the parameter.The two most time-critical parameters are soil-moisture and emergence date, a plant development parameter. For most of the other parameters aweekly to bi-weekly reliable observation is necessary. The rightmost column gives an estimate of the principle capabilities of remote sensing to cover the considered parameter under the assumption that an adequate observing system exists.

Input and internal model parameters	**Required temp. observation frequency**	**Potential of remote sensing observation**
vegetation type	1 year	✔
leaf area index	7 - 14 days	✔
vegetation height	7 - 14 days	✔
biomass	7 - 14 days	✔
fractional vegetation cover	7 - 14 days	✔
surface albedo	7 - 14 days	✔
emergence date	1 - 3 days	✔
root zone depth	7 - 14 days	-
soil-moisture	1 - 3 days	✔
soil-hydraulic properties	once	-
bare soil roughness	7 - 14 days	✔
topography	once	✔
surface temperature	-	✔

Tab.1: Summary of the spatial parameter requirements of PROMET

Presently remote sensing data, which can serve as source for input parameters to PROMET is rare. The reason for this lies in the high demand for multitemporal data and is due to the rapid growth of the vegetation canopy which is described by the parameters LAI (leaf area index), plant height and albedo, as well as the rapid change of soil moisture which for proper observation demand time intervals of 1 day to 1 week respectivelly. This temporal coverage is very rarely fullfilled with the present high

resolution remote sensing systems. No available microwave system can give this coverage. Optical systems with this kind of temporal coverage exist but at the price of degraded spatial resolution. Therefore an attempt is made to demonstrate the current possibilities at the mesoscale using coarse resolution data, before a future scenario to operate PROMET with remote sensing data on a regional scale is presented.

Four examples should serve as demonstration of the utilization of present remote sensing data to derive input parameters into the model:

- Stolz [Ref.10, included in this publication] shows a strong dependency of the backscatter of grassland on growth height for multitemporal ERS images in the Ammer test area.
- Rombach [Ref.11, included in this publication] shows, that surface soil-moisture can be derived from ERS-images independent of agricultural cover type for different geographical regions. He also shows, that model results of the soil-moisture content in the Ammer test area using PROMET correspond well with ERS-derived soil-moisture distributions.
- The next two examples (derivation of temporal albedo changes and large scale soil-moisture index) show, that information on temporal changes of input parameters can even be determined with coarser spatial resolutions.

4.1 Derivation of temporal albedo changes

A time-series of all available cloud-free NOAA-14 AVHRR images of 1995 over Southern Germany was used to determine the temporal development of albedo in the Ammer-watershed. The NOAA-imgages after geometric correction were calibrated and atmospherically corrected taking into account elevation based on LOWTRAN-7 [Ref.12]. Large enough grassland areas were selected in the Ammer-watershed to be able to compare the NOAA-derived temporal course of albedo with the course that has been used within PROMET and which was basically derived from literature. Fig.4 shows the comparison of NOAA-AVHRR-derived albedo, the standard literature values and, as an orientation, the literature and measured values of plant height for the corresponding year. Clearly a similarity can be seen between the changes in the NOAA-albedo and the measured plant height. Albedo tends to increase when plant height of the grassland decreases through cutting (before and after day 190). The measured plant heights as well as the course of albedo do not correspond with the standard literature values because due to a warm Spring in 1995 the onset of vegetation growth was unusually early. What can also be seen clearly is a systematic difference between the absolute value of albedo from literature and derived from NOAA-time series. The literature values are generally too high because literature is usually based on measurements from standard weather stations with short grass. This example clearly shows, that the availability of remote sensing measurements would enable a realistic inclusion of albedo depending on the actual plant development in the model.

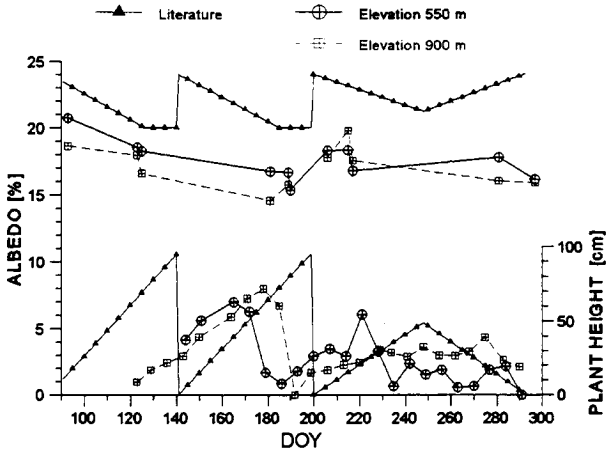

Fig.4: Comparison between measured albedo (NOAA) and plant height (field) and the literature values presently used in PROMET.

4.2 Derivation of a large scale soil-moisture index

An operational data source suitable for mesoscale soil moisture measurement with a spatial resolution comparable to AVHRR data is not available yet. Ground measurements prove the existence of large spatial differences in soil moisture. The potential of using ERS-SAR-data for soil moisture estimates has been shown previously [Ref. 13, 14, 15, 16]. However, these studies were limited to small test sites and not applicable for mesoscale models. Thus, by spatially degrading ERS data to a resolution of 500 and 1000 m and thereby increasing the radiometric fidelity of the sensor, the applicability of microwave data to determine soil moisture patterns suitable for mesoscale modelling was studied in the Weser watershed in North-Germany (A=40.000 km²).

4.2.1 Methodology

The determination of mesoscale soil moisture patterns is based on the following assumptions: The radar backscatter provided by ERS in agricultural areas depends primarily on soil moisture and surface roughness [Ref.13], other influencing factors such as row direction average out on mesoscale pixels. Build up areas, forests and lakes do not provide information on soil moisture. Each vegetation type has a typical microwave surface roughness which does not change within the scene [Ref.17]. Thus given the landuse types within a pixel and the specific backscatter for each landuse type, the effect of the surface roughness can be corrected by normalising the signal to a reference crop. Investigating a large number of ERS 1/2 images (13 images) proved, that the backscatter coefficients of wheat and barley do not show significant differences, also sugar beet and potatoes can be treated jointly. Thus only two

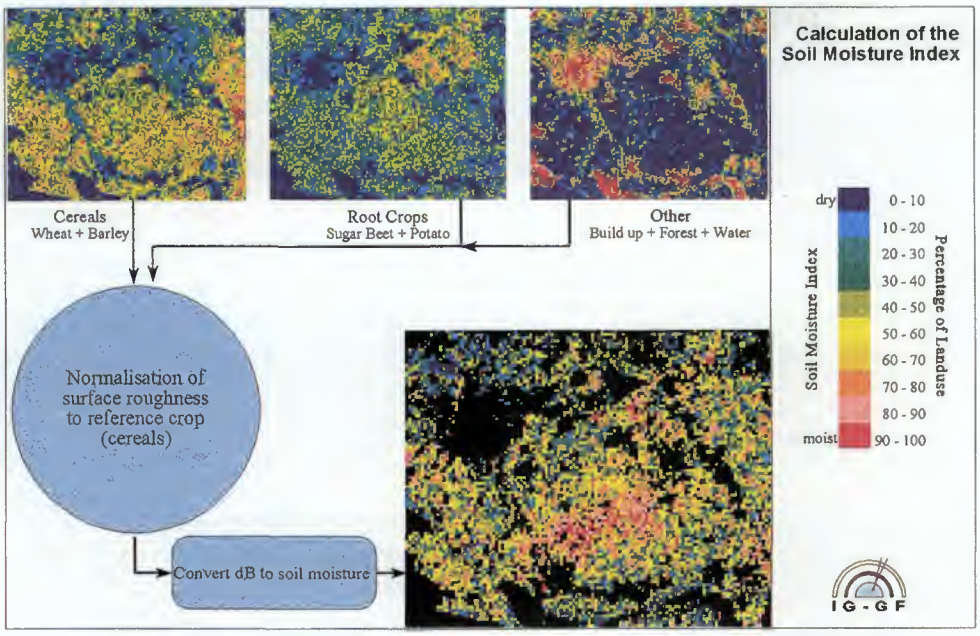

Fig.5: Schematic scetch for the derivation of the soil-moisture index on spatially degraded ERS-images (spatial resolution: 500 m).

agricultural landuse types had to be separated within the test site: cereals and root crops. Cereals were selected as reference crop to which the backscatter should be normalized because of their global occurance. The normalisation of the measured backscatter (B) to this reference crop is done according to the following equation:

$$\text{Eq.1: } B_{NORM} = \frac{B_M - B_F * F_F - B_W * F_W - B_B * F_B + F_R * (B_C - B_R)}{(F_R + F_C)}$$

where B stands for backscatter coefficient, F stands for fractional cover of a given land-use within a 500-1000 m resolution pixel, subscript $_{NORM}$ stands for normalized to cereal, subscripts $_{F,W,B,R,C}$ stands for forest, water, build up area, root crops and cereals respectively. The fractional cover of the different landuse classes crop was derived by unmixing a NOAA / AVHRR time series of 17 images to determine the fractional cover of the required land-use types. The specific backscatter for each land-use typ was determined from a small section of the ERS image in which the soil moisture was assumed to be constant. The normalized backscatter values were converted to dB and a regression model developed by Rombach [Ref.18] for barley was used to calculate the soil moisture from the normalised backscatter. Since the results are to some extend dependent upon the surface roughness of the reference crop the calculated moisture may require further adjustments to account for the reference crop surface roughness. However, the resulting image will show spatial differences of the surface soil moisture. Thus the results are given as relative units in the form of a soil moisture index instead of volumetric soil moisture.

Ground truth campaigns conducted in 1996 for three different ERS overflights were used to validate the soil moisture index. Soil moisture was determined over a large number of transsects using TDR-probes. Fig.6 shows the strong relationship between the calculated soil moisture index and the measured soil moisture. Prior to calculating the soil moisture index, the radar backscatter was normalised to the reference crop as described above. Without the normalization no correlation can be found between calculated soil moisture index and measured soil moisture in Fig7.

ERS-images of 1995 were used to create maps of the soil moisture index. Since they are presently hard to validate they were compared with precipitation patterns. An example of the mesoscale soil moisture variability is given in Fig.5. The black spots in the scene are pixels with a combined coverage of more than 50 % of build up area, forest or water. These pixels were excluded from calculation of the soil moisture index.

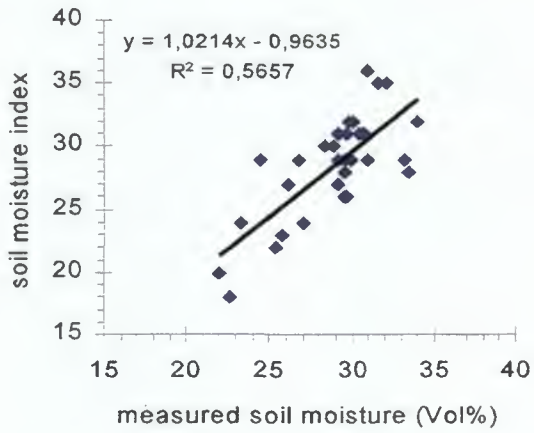

Fig.6: Comparison of measured soil-moisture and calculated soil-moisture index with normalization to reference crop

The soil moisture index for July 25, 1995 shows increased moisture in the central part of the test site in yellow and red colors. Three days prior to the overflight no precipitation was recorded in the test area. However, considerable precipitation differences were measured

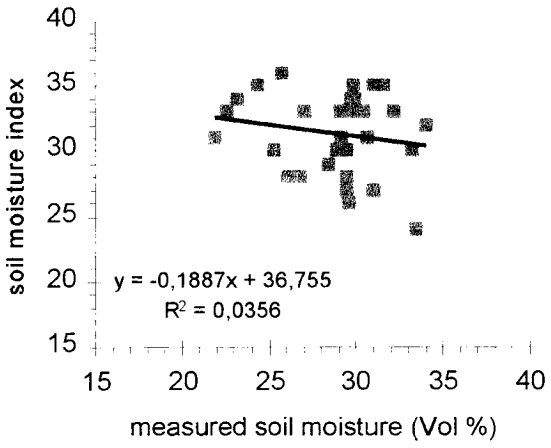

Fig.7: Comparison of measured soil-moisture and calculated soil-moisture index without normalization to reference crop

during the most recent precipitation period which started 11 days and ended 6 days prior to the overflight. Hildesheim located closest to the soil moisture peak reported 44.9 mm whereas the measured rainfall in the surrounding area was measured at 12-30 mm. Generally the soil-moisture patterns show good agreement with the measured rainfall patterns. Beyond these first indications and good correlations on the field scale more validation effort is necessary to prove the validity of the observed patterns.

The examples demonstrate, that a broad palette of input parameters to PROMET can be derived both from optical and microwave remote sensing data. In this context microwave data can serve both as input data (plant height, biomass, aerodynamic roughness) and as validation parameter, which can proof, that model calculations are correct (soil-moisture). The examples also clearly demonstrate, that the available microwave data from spaceborne sensors can not yet satisfy the data need of realistic, spatially distributed hydrological and land-surface process models. Based on the experience with the data profile, that PROMET requires, strategies were derived for the optimal utilization of remote sensing data in PROMET as well as requirements for future microwave data.

5. SCENARIOS FOR FUTURE MICROWAVE DATA INTEGRATION INTO MODELS

Remote sensing data can be utilized within PROMET in different ways, which are described in the following chapter. Common to all applications is, that remote sensing data has to be converted into a meaningful input or internal parameter through a parameter model, which serves as the interface between remote sensing data and model calculation.

5.1 Determination of model input parameters

The simplest way of using remote sensing data is to provide model input parameters, which are static and do not change with time. These parameters can be obtained by specific parameter models. Examples are land-use or topography.

5.2 Update of model input parameters through forcing

If a model input parameter is needed more frequently, because it changes with time, multitemporal remote sensing data should be used to update the parameters through model forcing (Fig.8).

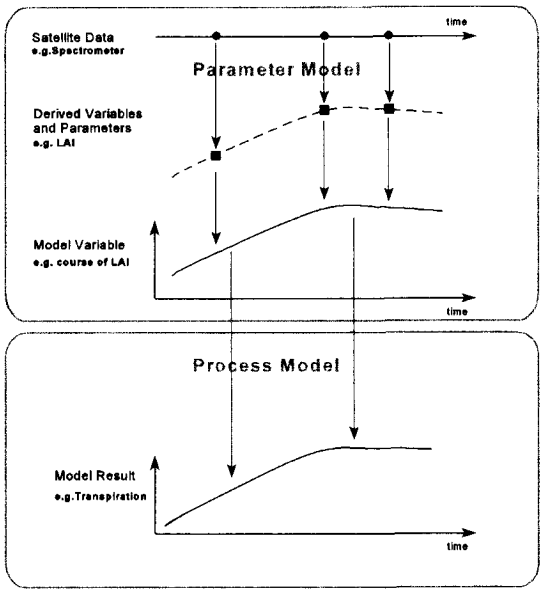

Fig.8: Updating of model input parameters through model forcing

The remote sensing data sources (in this case optical) deliver data in the form of radiances in irregular time intervals (dots in Fig.8). A parameter model converts the measurements into model input parameters (rectangles). In a second step the discretly available measurements from remote sensing sources are converted into a continous stream of values of model parameters through intelligent interpolation (course of LAI in Fig.8). This information can then be used directly in the calculations of the process model, which results in transpiration values.

5.3 Recalibration of internal model parameters

Beyond the use of remotely-sensed observations as surrogate values for one or more conventional parameters in the model, they can also be used to adjust the model during execution. This is illustrated in Fig.9, where the soil-moisture is provided. Soil-moisture is an internal model parameter. It is a required input for the calculation

of transpiration and evaporation and at the same time an output of the calculations of the soil water balance.

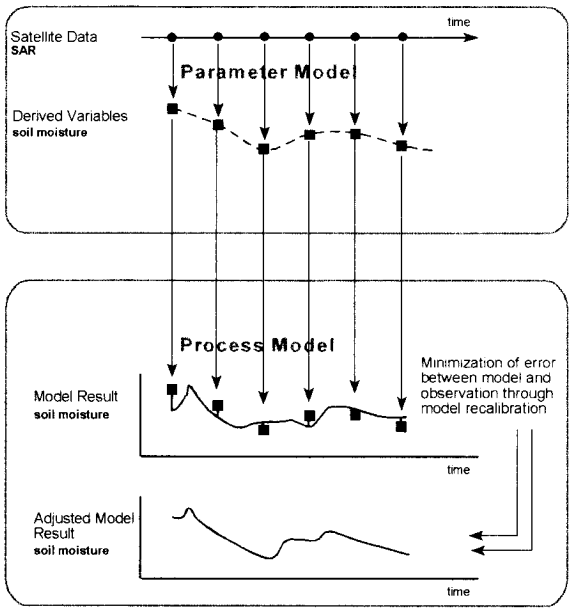

Fig.9: Recalibration of internal model parameters

In the example of Fig.9 a SAR-sensor delivers backscatter values in regular intervals (dots). A parameter model is applied to convert the backscatter values to soil-moisture values of the soil surface (rectangles). Soil-moisture is non-linearly dependent on precipitation, evapo-transpiration, percolation and capillary rise and can therefore not simply be interpolated. The temporal resolutions of existing and planned SAR-sensors are also too coarse for this task. Therefore, soil-moisture observations can not be directly used as model input. But one can compare the observations at certain points in time with the soil-moisture, that results from the continous modeling of the soil water balance (lower part of Fig.8). The difference between modeled and observed soil-moisture can then be minimized through recalibration of the SVAT-model. The result is an adjusted course of the soil-moisture, which is externally controlled through measured values.

5.4 Parameter determination through model inversion

A further step can be conducted, if one not just recalibrates the process model, but inverts it on the basis of the observations to determine land surface parameters. Through parameter optimization using inverse modeling scale dependent effective soil hydraulic functions can be inferred. On the basis of measurements of evapotranspiration and soil-moisture in different depth the hydraulic properties of the soils are determined inversely.

A simplified illustration of this type of model inversion is given in Fig.10. A multi-layer model of the soil-water balance is run under the assumption of three different soil types (sand, sandy loam and clay). The model result of surface soil-moisture is then compared to soil-moisture measurements conducted with microwave sensors. The model is inverted by determing the soil-type, for which the temporal patterns of measured and calculated surface-soil-moisture fit best. Weighting functions for the relative importance of the retrieved surface soil-moisture using different SAR-frequencies, which correspond to different penetration depths, must be taken into account for in this approach. In Fig.10 the SAR-measurements show, that the soil in the example is a sandy loam. This is expected to be obtained in the future when multifrequency and multipolarization SAR-data is available.

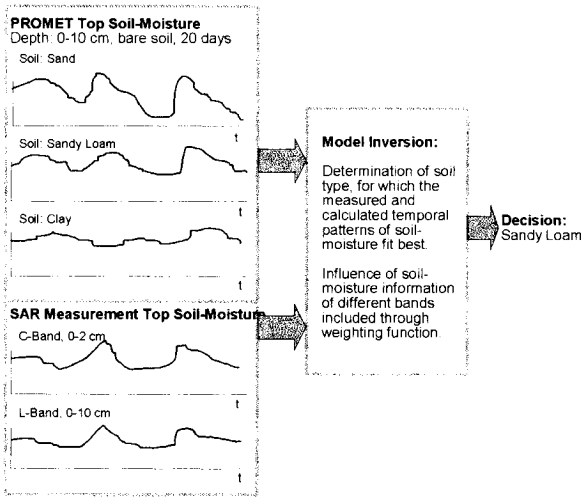

Fig.10: Soil-physical parameter determination through model inversion

6. CONCLUSIONS

From these four scenarios presented on the utilization of remote sensing data for hydrologic modeling on the land surface and from the large body of evidence on the possibility to extract land-surface parameters from remote sensing data through dedicated parameter models the following points seem to be evident:

- to guide remote sensing towards application, data fusion with conventional data and integration of remote sensing derived information into land-surface models is necessary.
- it has been shown that hydrologic models (as example for land surface process models) are evolving, which can make extended use of remote sensing data. They should be further developed.
- for land-surface application on the regional scale temporal resolution is at least adequatly important to spatial and spectral resolution in terms the demand of the evolving hydrologic process models.

- successfull use of microwave remote sensing data in hydrologic models can best be achieved through a synergistic and coordinated utilization together with improved optical remote sensing data sources.
- as a first starting point multifrequency / multipolarization coarse resolution microwave sensors are needed, which gather information about the land surface complementary to NOAA-AVHRR.

7. ACKNOWLEDGEMENT

The authors wish to thank the Deutsche Agentur für Raumfahrtangelegenheiten (DARA) for funding through the project "The Utilization of Remote Sensing Data in Hydrologic Modeling", the Bundesministerium für Bildung und Forschung (BMBF) for funding through the project "Derivation of a soil-moisture index from ERS-data" in the frame of the German National Climatic Research Program and ESA for supplying ERS-data through their PI-program. Parts of the paper are based on an ESA study on "Combination of Synthetic Aperture Radar and Optical Spectroradiometer Data for Aggregated Models" conducted as collaboration between the Institute for Radio Frequency Technology, DLR-Oberpfaffenhofen (D. Hounam, J. Nithack, C. Schmullius) and Vista - Remote Sensing Applications in Geosciences.

8. REFERENCES

[1] Shuttleworth, W. J., J.S. Wallace (1985): Evaporation from sparse crops - an energy combination theory. Qart. J. R. Met. Soc., 111:839-855

[2] Famiglietti, J.S., E.F. Wood (1994): Multiscale modeling of spatially variable water and energy balance processes. Wat. Res. Research, 30:3061-3078

[3] Raupach, M.R. (1995): Vegetation - atmosphere interaction and surface conductance at leaf, canopy and regional scales. Agric. For. Meteorol., 73: 151-179

[4] Monteith, J.L. (1965): Evaporation and the environment. Symp. Soc. Expl. Biol., 19: 205-234

[5] Ford, R., S. Runnings, R. Nemani (1994): A modular sysem for scalable ecological modeling. IEEE Computational Science and Engineering, Fall 1994: 32-44

[6] White, J.D, S.W. Running (1994): Testing scale dependent assumptions in regional ecosystem simulations. Jou. of Veget. Sci., 5:687-702

[7] Mauser, W. (1991): Modeling the spatial variability of soil-moisture and evapotranspiration with remote sensing data. Proc. Int. Symp. Remote Sensing and Water Resources, Enschede, Aug. 20-24, 1990, R. van Ackern Pub., Lingen

[8] Bastiaanssen, W.G.M., D.H. Hoekman, R.A. Roebeling (1994): A method for the assessement of surface resistance and soil water storage variability at mesoscale based on remote sensing measurements. IAHS Special Publ. No.2 , Institute for Hydrology, Wallingford

[9] Stolz, R., Mauser, W. (1997): Knowledge based multisensoral approach for landuse classifcation and biomass moonitoring, in: Remote Sensing of Vegetation and Sea. Proc. Europics Conference Taormina 1996. SPIE Proc. Series, Vol. 2959, pp.49-58

[10] Stolz, R., Mauser, W. (1997): Evaluation of ERS Data for Biomass Estimation of Meadows, Proc. 3rd ERS Scientific Symposium, Florence, Mar. 1997, ESA-SP-394 (this publication)

[11] Rombach, M., Mauser, W. (1997): Multi-annual Analysis of ERS Surface Soil Moisture Measurements of Different Land Uses, Proc. 3rd ERS Scientific Symposium, Florence, Mar. 1997, ESA-SP-394 (this publication)

[12] Bach, H., Mauser, W. (1994): Atmospheric Correction of Hyperspectral Data in Terms of the Determinationof Plant Parameters, in: Advances in Remote Sensing and Hyperspectral Remote Sensing. EUROPTO Series, SPIE, Vol.2318, pp.52-62

[13] Ulaby, F.T. (1992): 'Short Course Notes', DLR, Oberpfaffenhofen

[14a] Wooding, M.G., G.H. Griffiths, R. Evans (1992): 'Temporal Monitoring of Soil Moisture Using ERS-1 SAR Data' Proc. 1st ERS-1 Symposium, Cannes, pp. 641-648

[14b] Wooding, M.G., A.D. Zmuda, G.H. Griffiths (1993): 'SAR Calibration Requirements for Crop and Soil Studies. The Soil Moisture Case' Proc. CEOS Calibration/ Validation Working Group: SAR Calibration Workshop, Noordwijk, ESA WPP-048, pp 13

[15] Rombach, M., Mauser, W. (1996): Spatial and temporal Soil Moisture retrieval using microwave Remote Sensing and GIS Techniques. In: Application of Geographic Information Systems in Hydrology and Water Resources Management. Holzmann,H. & Nachtnebel, H.P.(Eds.), Poster Paper Volume of the Int. Conf. HydroGIS' 96, Vienna, April 1996.

[16] Mauser, W., M. Rombach, H. Bach, A. Demircan, J. Kellndorfer (1995): 'Determination of Spatial and Temporal Soil Moisture Development using multi-temporal ERS-1 data' SPIE Vol. 2314, pp. 501-515

[17] Fellah K., Y. Besnus, S. Clandillon, A.Ettajani, C. Meyer, P. de Fraipont (1994): 'Multi-Temporal ERS-1 SAR Data in Environmental Studies: Researching a Quantitative Approach for Soil Moisture Retrieval.'

[18] Rombach, M., Kellndorfer, J., Mauser, W. (1993): Application oriented Requirements to SAR-data Calibration - The Soil Moisture Case, SAR Calibration Workshop Noordwijk 1993, ESA WPP-048, pp.9-12

[19] Mauser, W., Schädlich, S. (1997): Modeling the Spatial Distribution of Evapotranspiration On Different Scales Using Remote Sensing Data, accepted for publication in: Journal of Hydrology, Summer 1997

SOIL MOISTURE ESTIMATION IN HYDROLOGICAL MESOSCALE MODELLING USING ERS SAR DATA

Felix Portmann, Herrmann-Gregor Mendel

Federal Institute of Hydrology
Kaiserin-Augusta-Anlagen 15-17, D-56072 Koblenz, F.R.G.
phone: +49 261 1306-217 / -218, fax: +49 261 1306-280

ABSTRACT

The moisture in the top soil layer is considered as a key element in the runoff process. Facilitation and improvements of the computation of runoff, particularly in flood events, and water balance is readily acknowledged if this value were known for the whole catchment or at least for representative sub-areas. Direct measurements on the ground at all sites are impossible because of the unjustifiable expenditures, and indirect estimates are inacceptable because of their high degree of uncertainty. Remote sensing from satellite, especially radar satellites like ERS, being independent from weather conditions, is expected to offer an alternative. Therefore, the derivation of soil moisture from satellite synthetic aperture radar (SAR) data is expected to be a key element in a state-of-the-art runoff process modelling. Yet, the derivation of the volumetric soil moisture is, up to now, readily available to a certain extent only for bare soil. The framework conditions, e.g. inclination of the terrain, surface texture / roughness, flooding of an area increase the uncertainty in the respective derivative function. Ground-truth information is needed for the calibration of that function. For a flat area in Northern Germany, a relationship for bare soil conditions between the standardised backscattering coefficient sigma zero ($\sigma°$) and volumetric soil moisture could be established, resulting in an R^2 of 0.7 without outliers. Outlying values have to be discussed individually with respect to deviation due to soil probing accuracy, vegetation cover/texture, specular reflection. Their inclusion significantly reduces the goodness of fit to an R^2 of 0.3.

1. BACKGROUND

The moisture in the top soil layer is considered as a key element in the runoff process. If this value were known for the whole catchment or at least for representative sub-areas, this would greatly facilitate (and improve) the computation of runoff, particularly in flood events.

Direct measurements on the ground are often not available, because either only at some selected sites soil moisture is probed by the official meteorological services, either a representative probing would ensue extremely high costs. Remote sensing from satellite, especially radar satellites like ERS, which can operate independently from weather conditions, offers an alternative to rough indirect estimates.

The influence of soil characteristics including soil moisture on the backscattering of the microwave signal is the principal aspect on which its use in hydrology is based. The backscattering signal is essentially influenced by two factors:

- Terrain and soil structures (e.g. surface roughness, vegetation cover, slope, soil type), and
- the moisture in the top soil layer (as dielectricity of water dominates the soil's dielectricity).

Moreover, the scattering of the satellite signal depends on its wavelength [Ref. 10]. ERS uses the radar wavelength 5.6 cm (C band) in vertical VV polarisation.

The best relationships between soil moisture and the standardised backscattering coefficient sigma zero ($\sigma°$) are achieved when the soil is free of vegetation cover. Ref. 1 established a linear relationship of $\sigma°$ with the volumetric soil moisture in the C band in VV polarisation and with an angle of incidence of 23°, the characteristics of the ERS-SAR device. Ref. 2 found similar relations for vegetation-covered areas.

Within the framework of the second "Announcement of Opportunity" scheme of the European Space Agency (ESA), the Federal Institute of Hydrology (Bundesanstalt für Gewässerkunde, BfG), Koblenz, Germany, has submitted an application via the German Aerospace Agency (Deutsche Agentur für Raumfahrtangelegenheiten, DARA). Results of the ongoing study (AO2.D136) are presented in this paper.

Proc. 3rd ERS Symp. on Space at the service of our Environment, *Florence, Italy, 17–21 March 1997* (ESA SP-414, 3 Vols., May 1997)

2. LOCATION OF THE TEST SITE

Among several sites a primary test site was chosen. It is a location within the former floodplain of the River Elbe, between the cities of Wittenberge and Hamburg, at about 11°25'E and 53°05'N around stream-kilometre 489 (cf. Fig. 1). The terrain is mostly flat, with elevations ranging 14 - 18 m above mean sea level for most of the study area. To the North, former ground moraines form the margin of the local catchment area. The soil consists of mainly sandy soils, with additions of loam, silt and partly clay lenses, following former fluvial deposition. The region is dominated either by agricultural use (arable land and meadows) or, to a smaller extent, by forestry on the moraine hills. Lakes as a consequence of subrosion of salt domes in the underground occur.

The test site properly speaking is an agricultural plot of about 1.2 km by 1.2 km near the community of Mödlich, situated only about 100 m north of the protection dike of the river Elbe. The plot is used for cultivation of grain by a cattle-raising farm. The plot is divided in three parts with N-S arrangement, named Mödlich-West, Mödlich-Centre Mödlich-East, cultivated in different cycles (Fig. 2). For most of the time the Eastern and Western parts were cultivated similarily, whereas the central part was used in a different way.

3. METHODOLOGY

The study aims to clarify the relationship between backscattering coefficient and soil moisture. Therefore, soil samples with cylindrical corers were taken simultaneously during the selected passes of the satellite and their water content was measured gravimetrically. TDR (time-domain reflectometry) probes were used to measure further ground truth reference data in the test areas. Both techniques covered the top 10 cm of the soil, a depth considered representative for the upper soil layers and easily to be probed. A smaller sampling depth could result in fairly higher sampling errors and inaccuracies, as the soil surface texture eventually is not homogeneous due to the cultivating practices of plowing and harrowing, which sometimes leave the surface in small clods (Fig. 3).

For satellite data, GTC (georeferenced terrain coded) SAR products were used to obtain maximum spatial accuracy and georeferencing quality. The backscattering coefficient σ° was determined analogically to Ref. 6 with the support of the Institute of Space Sensors (Prof. M. v. Schönermark and Mr. A. Weimann) of the German Aerospace Research Establishment - Institute of Space Sensors (Deutsche Forschungsanstalt für Luft- und Raumfahrt - Institut für Weltraumsensorik, DLR-WS) at Berlin-Adlershof.

The methodology of Ref. 6 was selected for its simplicity and the availability of large homogeneous areas at the test site. The computation of standardised backscattering coefficient σ° was done for each sub-area of the test plot (West, Central, East) when soil moisture probing was executed. Periods of time of fallow or only small vegetation cover when the soil was not frozen were chosen. Typically, these periods of time were in spring and autumn.

4. RELATIONSHIP BETWEEN SOIL MOISTURE AND STANDARDISED BACKSCATTERING COEFFICIENT σ°

The primary aim was to established a linear relationship of the σ° with the volumetric soil moisture similar to those found by Ref. 1 and Ref. 2.

The standard volumetric soil moisture was obtained by standardised gravimetric techniques (long-term drying at 105°C; cf. Ref. 5). This assured results comparable to traditional soil probing methods applied in soil science.

Table 1. lists the results of the evaluations, comparing mean σ° in decibel and mean volumetric soil moisture.

The respective relationship is visualised in Fig. 3. They diagram shows, that a broad linear relationship exists, even if some deviations occur, which are marked by circular or square frames. These are considered outliers bound to specific acquisition conditions, as they can be related either to certain dates (cases „a" and „b") or certain sampling conditions (e.g. case „a": flooding). For one acquisition, the deviations might be influenced by calibration differences of ERS-1 and ERS-2 (case „b"), too.

The reasons for the deviations are considered to be:

1. inaccuracy of soil moisture probing (measurement errors, bad representativity)
2. extreme texture conditions
2.1 vegetative cover
2.2 coarser soil surface texture, e.g. after plowing
2.3 silting of the soil (surface smoothing) with an increase of backscattering
2.4 smooth water surfaces, e.g. of inundated areas in case of flood events or high rainfall intensity,

obviously reducing the backscattering by specular reflection (case „a" in Fig. 3)

The relationship between $\sigma°$ in decibel and volumetric soil moisture could be established by linear regression.

The selection of viable measurements, accepting minor deviating conditions, results in a goodness of fit, expressed as R^2, of 0.7, showing a manageable relationship with the following equation (Fig. 4):

$$VolSoilMoisture[\%] = 35.4 + 1.68*\sigma° \text{ [dB]}$$

Inclusion of all measurements considerably reduces the R^2 to only 0.2. Therefore, the consideration of the causes of the deviation is a main task when the relationship is established. More knowledge about the causes is expected when the evaluation of all of the imagery is completed.

5. RELIABILITY OF SOIL MOISTURE VALUES

As mentioned before, for additional sampling of soil moisture information, TDR probes were used to characterise the variability of the gravimetric soil moisture regarded as a representative standard.
The TDR, according to theory, directly measures the water content of the medium surrounding the pair of wave transmitter, looking like a fork with two (or more) peaks. The principle is based on the differences in wave transmission velocity according to the water content of the medium [Ref. 9, Ref. 4]. The calibration of the TDR probes by transformation of velocity to volumetric soil moisture is not always an easy task, and depends also on the TDR measurement technique. Either conventional relationships, often fit by polynoms, or, for the TRIME measurement principle applied in this study, linear relationships are applied. The conventional method shows non-linear behaviour especially below volumetric soil moisture of 15 % or above 40 %, depending on the probe type [Ref. 9]. Here, the supplied standardised voltage output [0..1V] of the TRIME TDR probe was directly transformed to percentage volumetric soil moisture, as soil characteristics were expected to differ from probing site to probing site, inhibiting specific calibration.
Five TDR measurements of soil moisture were taken, one exactly at the location of the soil corer, four additional ones in the neighbourhood of about 1.5 m, limiting the time required for probing to an acceptable quantity.
The results of the TDR probing were expected to deliver information on soil moisture variability by a simple and efficient technique.

The comparison of mean gravimetric volumetric soil moisture and mean TDR volumetric soil moisture at the soil probing locations shows a broad positive relationship. Although, generally lower values by the TDR method than by the gravimetric method were observed, a deviation which was surprising (Fig. 5). The respective linear regression only results in an R^2 of 0.6, i.e. 60% explained variance. The reasons of the poor fit, even more evident for individual pairs of gravimetric and direct TDR values, are not clear yet, as the probing depth is exactly the same for both methods. Further information is given in the scattergram of mean TDR value versus the variation coefficient (standard deviation * 100 / mean) of the five TDR values at the probing sites (Fig. 6): It shows an increase in relative variability with a decrease of the soil moisture, whereas the absolute variability is almost independent from soil moisture, ranging from 1 to 9 Vol.-% at almost all soil moisture conditions (not shown here).

6. CONCLUSIONS AND OUTLOOK

The derivation of the standardised backscattering coefficient $\sigma°$ for greater areas according to the method developed by Ref. 6 seems to be a possible approach for the estimation of volumetric soil moisture in the top soil from ERS-SAR imagery. Although, some inconveniences of this methodology have been observed:
- Deviations of the ideal conditions are observed, whose causes have to be further studied.
- The replacement of gravimetric measurements of soil moisture by readily available, efficient TDR measurements is not as easy as it was supposed to be: a systematic underestimation and a high variability in the relationship between the parameters were observed. This renders difficult the estimation of the gravimetric soil moisture regarded as the standard value to refer to. The reasons will have to be studied more deeply before any estimation of soil moisture by the use of TDR only is undertaken.
- The variability of the soil moisture increases with a decrease in absolute moisture. This seems also to be related to the soil bulk density, strongly affected by management practices (plowing, harrowing, etc.)
- The technique seems to be only applicable to conditions of bare soil or sparse vegetation. For higher vegetation cover, which is present during a longer period of time during spring, summer, and autumn, the soil moisture may be derived by modelling techniques. These may encompass either the modelling of plant growth during the vegetative period at a certain plot, or the regional transfer of soil moisture information from one site, whose characteristics are better known, to the other ones (cf. Ref. 7, Ref. 3). The second method may be

assisted by Geographical Information Systems (GIS).
- Once the transfer functions of soil moisture were known, the estimation of the soil moisture by SAR would enable to compute input data and parameters for hydrological models using e.g. estimations of prior soil saturation for computation of flood hydrographs [Ref. 8].

7. REFERENCES

[1] Chanzy A & L Bruckler & P Bertuzzi 1990, Modelling evaporation on bare soil using microwave data, comparison between a mechanistic and a simplified model, *International symposium on remote sensing and water resources*, Enschede, 20-24 August 1990, Proceedings, R. van Acken GmbH, Lingen (Ems), pp. 261-270

[2] Cognard A-L & C Loumagne & M Normand & P Olivier & C Ottlé & D Vidal-Madjar & S Louhala & A Vidal 1995, Evaluation of ERS 1 / synthetic aperture radar capacity to estimate surface soil moisture, two-year result over the Naizin watershed, *Water Resources Research*, 31, 975-982

[3] Crave A & C. Gascuel-Odoux, 1997, The influence of topography on time and space distribution of soil surface water content, *Hydrological Processes*, 11, 203-210

[4] Disse M, 1995, *Modellierung der Verdunstung und der Grundwasserneubildung in ebenen Einzugsgebieten [Modelling of Evapotranspiration and groundwater recharge in flat catchments]*, Karlsruhe, pp. 180

[5] Hoffmann G, 1991, *Methodenbuch, Band I: Die Untersuchung von Böden [Methodologies, Volume 1: The examination of soils]*, Darmstadt, pp. 200

[6] Laur H 1992, *Derivation of backscattering coefficient σ° in ERS-1.SAR.PRI products*, ESRIN, Frascati, Italy, Issue 1, Review 0, 17th October 1992, pp. 17

[7] Merot P & A Crave & C Gascuel-Odoux, S Louhala, 1994, Effect of saturated areas on backscattering coefficient of ERS 1 synthetic aperture radar: First results, *Water Resources Research*, 30, 175-179

[8] Singh V, 1995, Computer models of watershed hydrology, Highlands Ranch, CO, pp. 1130

[9] Stacheder M 1996, Die Time Domain Reflectometry in der Geotechnik [The time domain reflectometry in geotechnics], Karlsruhe, pp. 170

[10] Ulaby F T & R K Moore & A K Fung, 1982, *Microwave remote sensing. Active and passive. Volume II: Radar remote sensing and surface scattering and emission theory*, Reading, MS, pp. 457-1064

8. TABLES

Table 1. Mean volumetric soil moisture and standardised backscattering coefficient σ° at the test sites from 27th April 1995 until 8th November 1996.

Date of scene (ERS-SAR)			Soil moisture [Vol.-%]			Backscattering coefficient σ° [dB]		
Orbit	Frame	Date	West	Central	East	West	Central	East
19778	2529	27.04.95	27.5	30.8	-	-	- 8.92	-
21782	2529	14.09.95	31.9	-	30.0	- 3.38	-	- 4.37
22283	2529	19.10.95	17.2	19.9	22.5	- 9.18	- 8.68	- 7.2
22784	2529	23.11.95	31.6	32.1	26.8	- 2.64	- 1.89	- 1.9
24287	2529	07.03.96	37.4	38.4	38.1	- 2.75	- 4.38	- 2.89
24516	2529	23.03.96	34.6	26.3	28.0	-5.18	-5.98	-5.09
24788	2529	11.04.96	24.7	24.2	24.2	-5.81	-3.9	-4.32
25017	2529	27.04.96	31.2	29.5	29.2	-5.1	-4.16	-2.29
25518	2529	01.06.96	27.4	31.3	26.2	-6.83	-8.68	-6.39
8182	2529	08.11.96	25.5	31.0	29.7	-12.13	-10.27	-10.25

9. FIGURES

Figure 1. ERS multitemporal SAR imagery of selected test site Mödlich (11°25'E and 53°05'N) on the River Elbe (3 * 3 filtered).
Colour coding: red: 23-Mar-1996, green: 24-Apr-1996, blue: 11-Apr-1996.

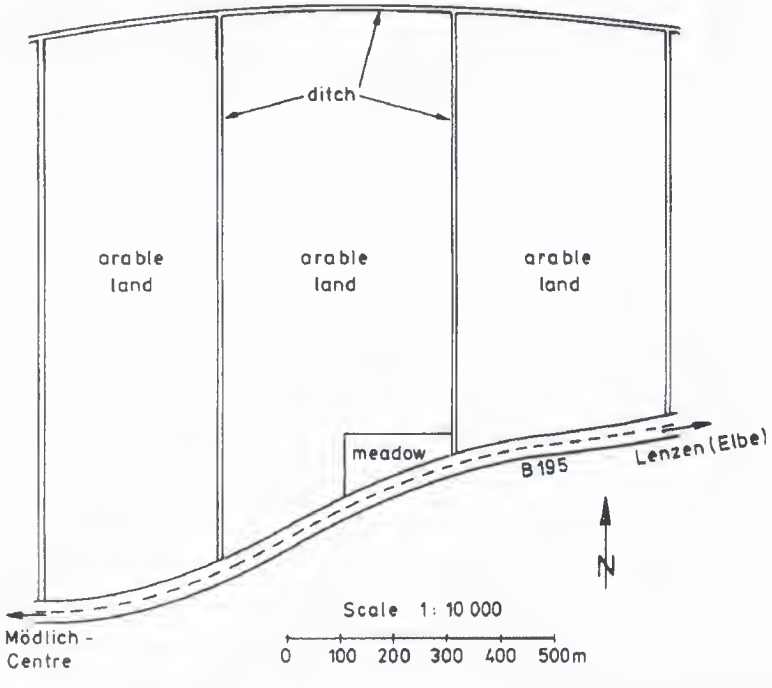

Figure 2. Detailed view of test site Mödlich with sub-areas West, Central, and East.

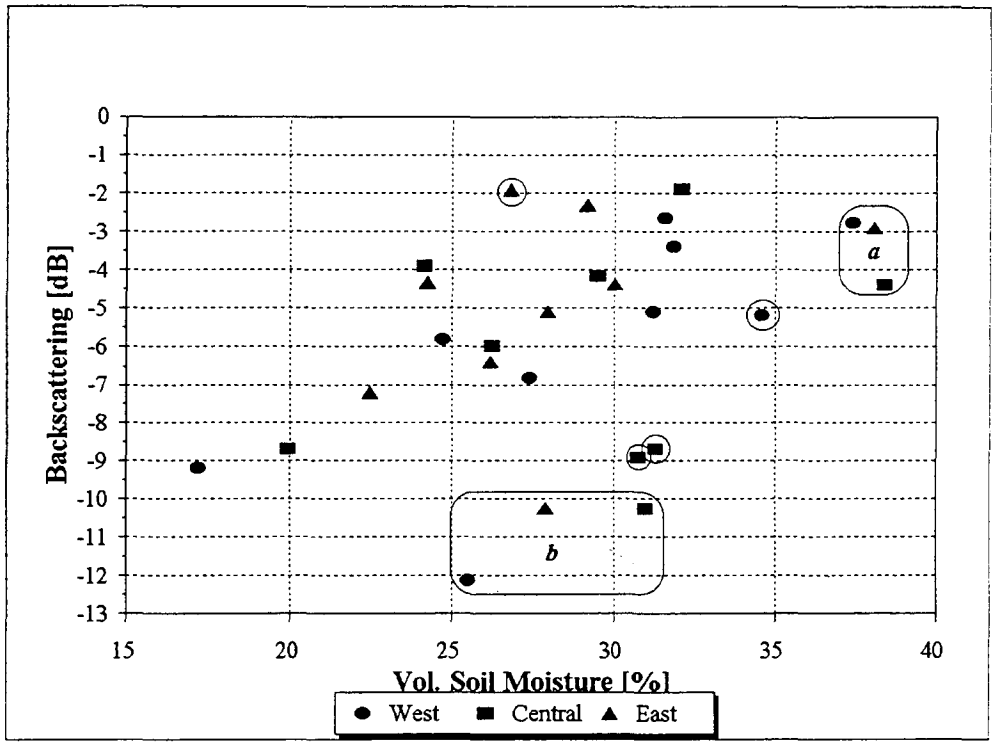

Figure 3. Scattergram of relationship between mean volumetric soil moisture and standardised backscattering coefficient σ° at the test site with deviations (encircled).

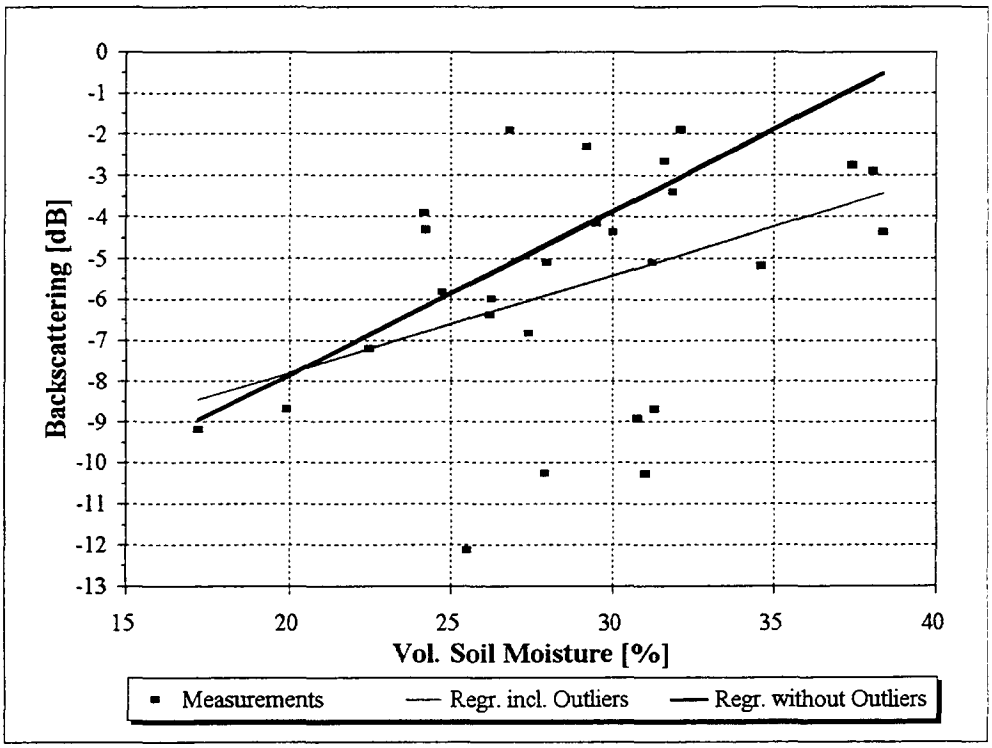

Figure 4. Linear regressions of relationship between mean volumetric soil moisture and standardised backscattering coefficient σ° at the test site.

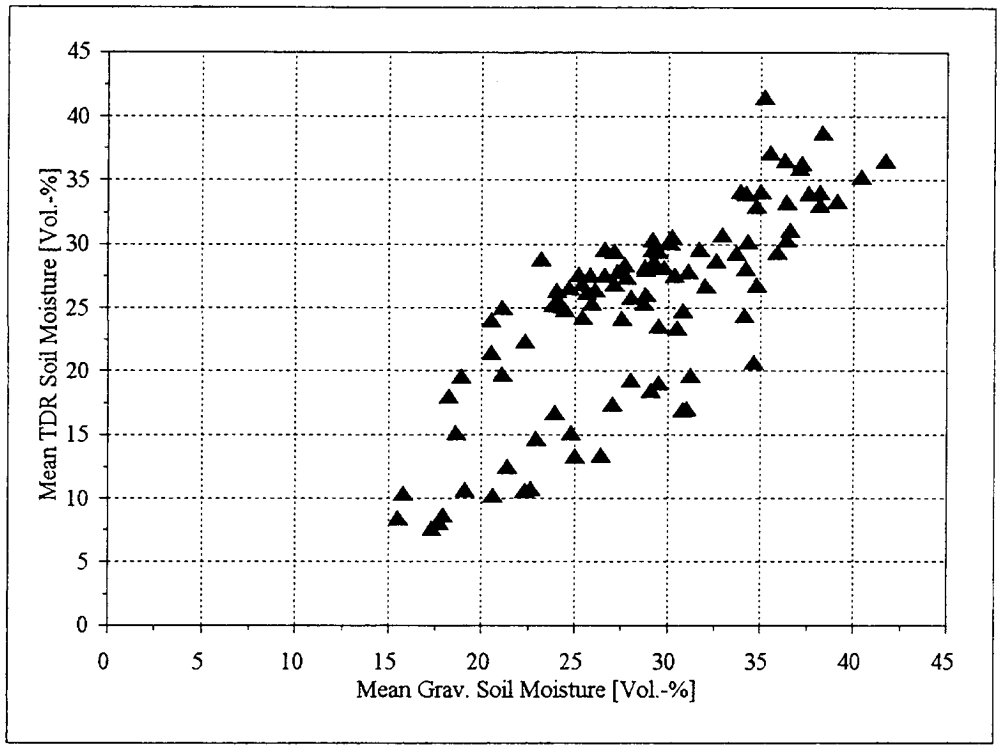

Figure 5. Scattergram of relationship between mean gravimetric soil moisture and mean TDR soil moisture.

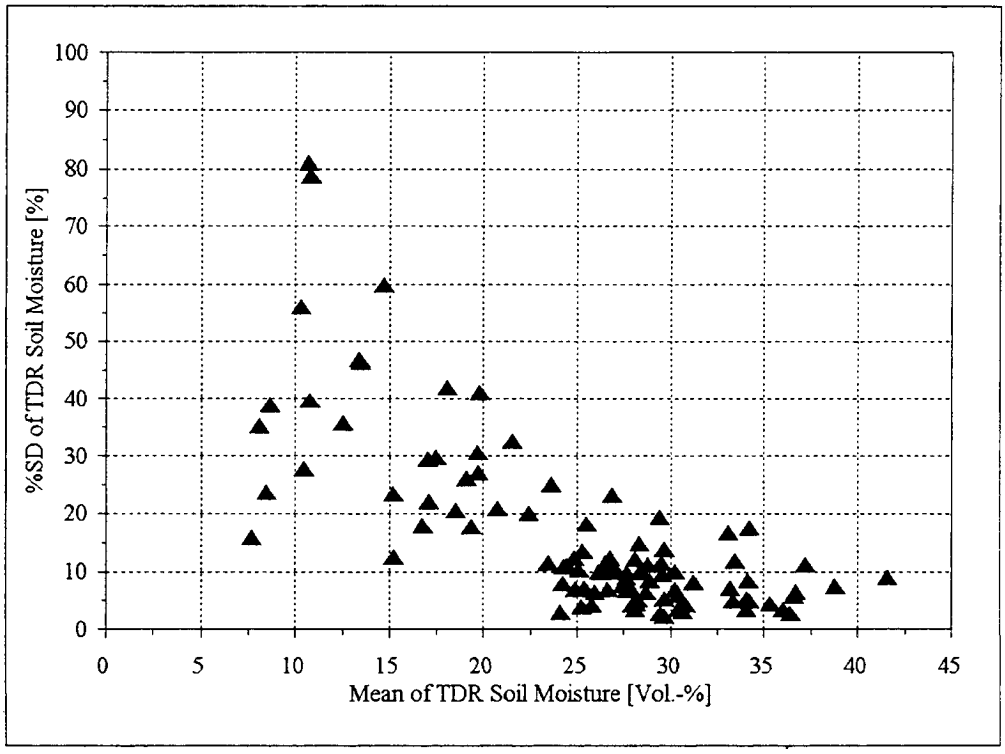

Figure 6. Scattergram of relationship between mean TDR soil moisture and variation coefficient.

SPATIAL ORGANIZATION OF HYDROLOGICAL PROCESSES IN SMALL CATCHMENTS DERIVED FROM ADVANCED SAR IMAGE PROCESSING: FIELD WORK AND PRELIMINARY RESULTS

P. A. Troch, F. P. De Troch, R. Grayson[†], A. Western[†], D. Derauw[‡], C. Barbier[‡]

Laboratory of Hydrology and Water Management
University of Gent, Gent , Belgium
[†]Centre for Environmental Applied Hydrology
University of Melbourne, Melbourne, Australia
[‡]Centre Spatial de Liege
University de Liege, Liege, Belgium

Abstract. The presented research focusses on the use of active microwave observations to retrieve hydrologically relevant information of surface characteristics (i.e. soil moisture and surface roughness) in river catchments. Given the availability of pairs of SAR data from the tandem mission the following research issues are addressed: (1) development and testing of improved retrieval algorithms for surface characteristics based on the combined use of phase and magnitude information of the return signal from active microwave sensors; (2) use of high resolution field collected data and remotely sensed data to test and validate theories for the catchment scale estimation of soil moisture integrated over soil depth. In particular questions to be investigated include: (2a) what spatial resolution is required for estimation of spatial average soil moisture patterns over a range of scales; (2b) what temporal resolution is required for accurate estimation of the time series of soil moisture.; (2c) what spatial and temporal resolution of data is required to obtain information about the dynamics of soil moisture redistribution within the soil profile using distributed hydrological modelling; (3) study of the influence that spatial organization of soil moisture and vegetation on SAR-based soil moisture retrieval, and of the ability to identify such organization using ERS data.
In order to accomplish these objectives extensive field campaigns are organized in two small experimental catchments (Tarrawarra near Melbourne, Australia and Wijlegemse beek near Gent, Belgium). For both catchments a number of ERS-1/2 tandem scenes have been collected. Both Single Look Complex (SLC) and Precision Image (PRI) data will be required to carry out the different steps in the proposed project.

1. INTRODUCTION

Since the launch of ERS-1 in 1991 a number of investigations to use SAR PRI data for the retrieval of land surface characteristics useful in hydrologic studies have been reported. Initially, these studies used an empirical approach to relate the backscattering coefficient to, for instance, moisture content of the upper 5 cm soil layer under different land use. Later, the conversion of the backscattering coefficient to volumetric soil moisture content was based on theoretical surface scattering models (*Fung et al.*, 1994; *Altese et al.*, 1996). All these studies demonstrated the potential of the use of SAR data for spatial and temporal mapping of soil moisture at field scale and over larger areas. However, these studies identified also some of the critical problems related to the accurate retrieval of surface soil moisture from PRI data. Basically, these technical problems are related with the (lack of) detailed knowledge of the surface roughness characteristics. Recently, based on data from an airborne remote sensing campaign (EMAC'94), *Su et al.* (1996) developed a method to retrieve both soil moisture and surface roughness (expressed in terms of the roughness slope, i.e. the ratio between the root mean square height difference and the correlation length) using two successive SAR scenes in different frequencies. They also demonstrate that accurate soil moisture retrieval at the field scale is possible through the use of this so-called effective roughness slope.

The availabillity of the ERS-1/2 tandem offers the possibility to test another approach to improve SAR-soil moisture retrieval algorithms. Change detection in surface characteristics is possible when a pair of single frequency SAR scenes are analysed for both amplitude and phase. The idea is to combine retrieval algorithms based on

theoretical surface scattering models with coherence maps calculated from phase information in single look complex (SLC) data. Two radar echoes will be coherent if each of them represents nearly the same interaction with a set of scatterers (*Derauw*, 1995). Lack of coherence is explained by changes in surface characteristics between the two data takes. In the event of changes in, e.g., the dielectric properties of the surface due to drydown or heavy rainfall, the coherence map should contain information about the amount of change. It is therefore anticipated that the combined use of both amplitude (i.e. backscattering coefficient to be derived from PRI data) and phase (i.e. coherence maps from SLC data) should allow a more accurate determination of soil moisture changes in catchments.

Blöschl et al. (1993) demonstrated that the spatial organization of soil moisture influences hydrology at both the hillslope and catchment scale. They showed that a traditional geostatistical approach to distribute soil moisture spatially can either underestimate or overestimate catchment scale runoff compared to a more realistic distribution based on topography, depending on the rainfall. Remote sensing has potential for providing information about the spatial distribution of soil moisture and its link with topography. Simulation studies (e.g. *Entekhabi et al.*, 1994) suggest that these data may be extrapolated to give soil depth profiles of soil moisture.This project aims at using ERS data to test these hypotheses.

2. EXPERIMENTAL PLAN AND DATA REQUIREMENTS

2.1. SAR-soil moisture inversion algorithms

Since microwave remote sensors do not measure soil moisture directly, a retrieval algorithm is needed to extract this information from the measured signals which are often contaminated with noise. From a mathematical point of view, this is equivalent to solving an inverse problem closely related to forward modelling. Forward modelling develops a set of mathematical relationships to simulate the instrument's response for a given set of model parameters. In the context of soil moisture remote sensing, these parameters generally include soil properties and the geometry and phenology of the overlying vegetation canopy. To solve the inverse problem, it is crucial to start from a forward modelling procedure which is able to adequately describe the observations. It is also important to know the number of model parameters used to describe the subjects being measured and to know which parameters most sensitively influence the returned signal.

Consider the problem of microwaves impinging upon a layer of vegetation canopy overlying a rough ground surface. The waves penetrate the layer and interact with various parts of the inhomogeneous vegetation canopy and with the top soil matrix, resulting in a series of absorption and scattering reactions. A portion of the scattering waves returns to the radar's receiver and carries within it dielectric information regarding the illuminated vegetation-soil medium. In essence, this backscattering process can be subdivided into three components: (1) a component representing the scattering contribution of the vegetation canopy; (2) a component representing the surface-volume interaction contribution; (3) a component representing the ground backscattering contribution, including the two-way attenuation caused by vegetation.

The problem of wave scattering from a randomly rough ground surface has been studied theoretically using both low- and high-frequency approximations. Among the high-frequency scattering models, the Kirchhoff formulation (KF) is the most commonly used. The basic assumption of this method is that the total scattered field at any point on the surface can be computed as if the incident wave is impinging upon an infinite plane tangent to the point. Analytic solutions have been developed for surfaces with a large standard deviation (σ) of surface heights, using the stationary phase approximation in conjunction with the Kirchhoff formulation, and for surfaces with small slopes and small σ using a scalar approximation. For a ground surface whose σ and correlation length are much smaller than the wavelength, the small perturbation method (SPM), which is a low-frequency solution, can be used to estimate the backscattering contribution. The region of validity of the SPM has been extended to higher values of σ using a perturbation expansion of the phase of the surface field. Attempts have also been made to unite the KF and the SPM in order to extend the range of validity. This led to the development of two-scale models. More recently, *Fung* (1994) has developed a surface scattering model based on the surface field integral equations called the Integral Equation Model

(IEM). The IEM reduces to the SPM when the surface is smooth, and to the standard Kirchhoff model when σ is much larger than the incident wavelength.

Microwave scattering models for a vegetation canopy can be categorised into two classes: empirical (or phenomenological) models, and physical (or theoretical) models. The empirical models are based on intuitive understanding of the relative importance of various vegetation parameters, then summing up the contributions from each component believed to be important. The physical models are based upon the modelling of the interactions between microwaves and the various scattering elements of a vegetation canopy (*Lang et al.*, 1986). The major difficulties in modelling these interactions are the determination of the canopy geometry and the multiple-scattering pattern. It is common practice to model the vegetation canopy either as a continuous medium with specific dielectric properties, or as a mixture of discrete scatters randomly distributed in an inhomogeneous layer.

2.2 Interferometric SAR data analysis

For years synthetic aperture radar has been used to produce photograph-like images of terrain features. While complex data (both phase and amplitude) are collected to produce the SAR image, only magnitude information is withheld and the phase information is discarded. Radar interferometry, on the other hand, depends on phase information. Together, SAR interferometry provide additional information to that of a conventional SAR. InSAR (interferometric SAR) can e.g. detect slight changes in scene content. Changes in surface features (e.g. dielectric properties and/or roughness characteristics) can be detected through coherence measurements. Coherence is a measure of the correlation between two signals (*Derauw*, 1995). Two radar echoes will be coherent if each represents nearly the same interaction with a set of scatterers. If the scene changes between the two takes, the phase will vary and a loss of coherence will occur. The combined use of conventional SAR and InSAR offers new opportunities for the retrieval of geophysical parameters of the Earth's surface. SAR observations of the same area over a very short time interval is required to relate loss of coherence to well defined atmospheric circumstances (e.g. rainfall, strong dry-down due to solar insolation). These conditions are met for the first time for space observation through the ERS tandem mission.

2.3 Ground truth data acquisition

2.2.1 description of test sites

Tarrawarra catchment, near Melbourne (Australia): The Tarrawarra site is located within the square bounded by 145°26' E, 145 °27' E, 37 °39' S, 37 °40' S. The catchment has an area of 10 ha. The catchment elevation is approximately 100m. The maximum relief is 27m and the hillslopes typically have slopes of 11-14%. The main drainage line has a mean slope of 4%. The land is used for dryland grazing of dairy cows and has improved pastures. Tarrawarra has a temperate climate with a mean annual rainfall of 1000mm and a class A pan evaporation of 1200mm. The major soil type is a duplex soil with a loam-clay loam A horizon which has a bleached A2 horizon. The B horizon is a heavy yellow-grey mottled clay. The A horizon is 30-35cm deep over the majority of the catchment and the B horizon varies between 0.5m and more than 1.4m thick.

Wijlegemse beek catchment, near Gent (Belgium): The Wijlegemse beek catchment is located in the Zwalm catchment and has an area of 250 ha. The Zwalm catchment is situated in East-Flanders, Belgium, and is a tributary of the Scheldt river. The drainage divide of the catchment expands from 50°45'48" to 50°54'16" N latitude and from 3°40'17" to 3°50'15" E longitude. The total drainage area is 114.3km^2. The three main soil types are sandy loam, loam, and clay. The depth of the eolic sandy loam to loam cover is estimated to range between 0 and 10 m. The topography of the basin is characterized by rolling hills and mild slopes. The maximal elevation difference in the basin is equal to 150 m. Climatic conditions can be described as humid temperate. The mean yearly rainfall is 775 mm and is distributed almost uniformly over the year. The catchment was a test site during the last EMAC'94 (ESA) campaign and during the SIR-C/X-SAR (NASA) campaign. The catchment was also test site for the EV5V-CT94-0446 E.C.-project in the third framework Environment Programme.

2.2.2 ground truth data acquisition

Tarrawarra test site

(1) Permanent instrumentation: An automatic weather station has been installed in the catchment and is monitoring: dry bulb temperature, wet bulb temperature, ground surface temperature, soil temperature at 2, 5, 10, 20 and 50 cm, rainfall, global radiation, net radiation, wind speed, and wind direction. Data from this weather station is used to determine rainfall inputs and evaporative fluxes. A flume has also been installed to monitor surface runoff continuously.

(2) Soil moisture monitoring: Soil moisture monitoring at this site is probably the most detailed one undertaken anywhere in the world so far. Soil moisture is being monitored in two ways. Time Domain Reflectometry (TDR) is being used to monitor soil moisture on regular grids within the catchment. This is being done using a Terrain Data Acquisition System (TDAS). TDAS employs an all-terrain vehicle with a position fixing system (GPS) which allow the operator to drive to predetermined sampling locations. It carries four TDR probes which are inserted hydraulically. In this way the mean soil moisture in the top 30cm of the soil profile is being measured. A 10mx20m sampling grid is used across the whole catchment. More detailed measurement can further be made in parts of the catchment using a 2mx2m grid. Secondly, Neutron Moisture Meters are used to provide information on the vertical movement of soil water. This will assist the interpretation of observed changes in the spatial soil moisture pattern. Twenty neutron probe access tubes have been installed. These access tubes were placed in the drainage line, on the midslopes and at or near the drainage divide. For each of the satellite passes, over 500 TDR readings will be taken, along with depth profiles from the neutron moisture meter sites.

(3) Soil characterization: Currently, a significant effort is being made to characterize the hydrologic characteristics of the soils in the catchment. A detailed soil map of the catchment is prepared including information on soil type and the depth of the A horizon. Vertical and lateral hydraulic properties of the soil (A and B horizons) are being measured. Particle size distribution and bulk density are also measured and used to characterize spatial changes in soil properties. Also ground penetrating radar (GPR) is going to be used to assist in describing the spatial characteristics of the soil profile.

(4) Digital elevation model: a detailed (1500 spot elevations accurate to 5 cm) ground based topographic survey has been completed for Tarrawarra.

Wijlegemse beek test site

(1) Permanent instrumentation: An automatic weather station has been installed in the catchment and is monitoring: dry bulb temperature, wet bulb temperature, ground surface temperature, soil temperature at 2, 5, 10, 20 and 50 cm, rainfall, global radiation, net radiation, wind speed, and wind direction. Data from this weather station is used to determine rainfall inputs and evaporative fluxes. A flume has also been installed to monitor surface runoff continuously. A transect of 20 piezometers is installed perpendicular to the main stream of the basin, in order to study the phreatic groundwater table position and fluctuations.

(2) Portable surface flux stations: During intensive field campaigns the surface fluxes of latent and sensible heat can be determined using a portable Bowen ratio station and a portable eddy correlation station.

(3) Soil moisture monitoring: In the vicinity of the automatic weather station a vertical profile consisting of 4 TDR probes is installed to monitor vertical water movement in the top 50 cm of the soil layer. During the time of satellite overpass soil moisture is measured using handheld TDR probes and gravimetric sampling techniques.

(4) Soil characterization: A detailed soil map exists for the catchment (scale 1/20,000). This map contains information on the soil texture, drainage conditions, and profile development. In addition the determination of hydraulic properties is planned in the framework of a research project to be financed by the University of Ghent.

(5) Digital elevation model: a detailed (4x4 m) digital elevation model has been constructed based on the 1/10,000 scale topographic maps available for the site.

2.3. Spatial patterns of soil moisture and geomorphic terrain features

Blöschl and Sivapalan (1995) discuss the nature of spatial variability and hetero-geneity in a review of scale issues in hydrology. Of particular interest in this project is the concept of organization. Organization is similar to regularity or order but tends to relate to a more complex form of regularity. In some cases, spatial organization may reflect adaptive landscape development, while in others it may reflect water routing processes or spatial pattern of precipitation and evapotranspiration. Spatial organization of a variable implies that its variation in space is characterized by the presence of complex spatial relationships. Because of this, traditional geostatistics are not sufficient to fully characterize the spatial patterns. Many geostatistical applications rely upon the intrinsic hypothesis of second order stationarity of the difference between a variable at two different points. Generally, this hypothesis is not met when organization is present. *Blöschl et al.* (1993) demonstrated the importance of organization of soil moisture patterns at the hillslope and catchment scale. They simulated runoff hydrographs based on organized and random spatial patterns of antecedent soil moisture, hydraulic conductivity and precipitation. While the covariance structure of the organized and random cases was identical, the runoff response was vastly different. Remote sensing obviously has potential for providing the spatial data required to further our understanding of the spatial characteristics of catchments. However there are problems with interpretation of remotely sensed soil moisture data which need to be addressed before it will see routine applications in hydrology. This research proposal aims at resolving some of these technical difficulties. One of the concepts often applied in catchment hydrology is the wetness or topographic index. Wetness indices have been used to predict the spatial distribution of soil moisture. The effect of this spatial organization upon radar retrieval of soil moisture, possible interaction with vegetation cover, and the ability to identify spatial organization with SAR are important questions for which definitive answers are yet to be developed.

References

Blöschl, G., D. Gutknecht, R.B. Grayson, M. Sivapalan and I.D. Moore, Organization and randomness in catchments and the verification of hydrologic models, EOS, Trans. Am Geophys. Union, 74, 317, 1993.

Blöschl, G. and M. Sivapalan, Scale issues in hydrological modelling: a review, in: Scale Issues in Hydrological Modelling, Eds. J.D. Kalma and M. Sivapalan, Adv. Hydrol. Processes, J. Wiley & Sons, 9-48, 1995.

Derauw, D., Development of an interferometric SAR processor, Proc. SPIE, 319-324, 1995.

Entekhabi, D., H. Nakamura and E.G. Njoku, Solving the inverse problem for soil moisture and temperature profiles by sequential assimilation of multifrequency remotely sensed observations, IEEE Trans. Geosc. Remote Sensing, 32(2), 438-448, 1994.

Fung, A.K., Microwave Scattering and Emission Models and Their Applications, Artech House, Norwood, Mass., 1994.

Lang, R.H., S. Saatchi and D.M. LeVine, Microwave backscattering from an anisotropic soybean canopy, Proc. IGARSS'86 Symp., Zurich, 8-11 Sept., 1107-1112, 1986.

Su, Z., P.A. Troch and F.P. De Troch, Remote sensing of soil moisture using ESAR/EMAC data, Int. J. Remote Sensing, submitted, 1996.

Western, A., G. Blöschl, G.R. Willgoose, T.A. McMahon and R.B. Grayson, Field investigations of spatial organization of soil moisture in a small catchment, 23rd Hydrology and Water Resources Symp., Hobart, 23-26 May, in press, 1996.

Wood, E.F., D.S. Lin, M. Mancini, D. Thongs, P. Troch, J. Famiglietti and T.J. Jackson, Intercomparison between passive and active microwave remote sensing and hydrological modelling for soil moisture, Adv. Space Res., 13, (5)167-(5)176, 1993.

SPATIAL SOIL MOISTURE MAPPING THROUGH MULTI-TEMPORAL ANALYSIS OF ERS-SAR PRI DATA

N. Verhoest, P. A. Troch, J. Deckmyn+, C. Paniconi*, and F.P. De Troch

Laboratory of Hydrology and Water Management
University of Gent, Gent, Belgium
+ Programa para el manejo del Agua y del Suelo
Universidad de Cuenca, Cuenca, Ecuador
* CRS4, Cagliari, Italy

Abstract

The scattering of microwaves from soil depends on several surface characteristics, such as the roughness, vegetation and the moisture content of the top layer. Knowledge of the temporal and spatial distribution of this last parameter is of major importance to hydrologic, meteorologic and climatologic modelling. However accurate measurements of the spatial distribution of soil moisture with classical methods have always been a difficult task. Owing to its dependency on soil moisture and its spatial character, radar remote sensing holds much promise. Several empirical and physically based scattering models have been proposed to retrieve soil moisture values from SAR data, but problems occur with the identification of the roughness and vegetation parameters. This can be partly overcome through the use of multi-frequency and/or multi-polarization radar, but this option is often not available on spaceborne platforms. However, single frequency and single polarization data allows one to map saturation-prone areas using a multi-temporal analysis. The use of multi-temporal data makes it possible to retrieve spatial soil moisture patterns within the studied catchment by applying statistical methods to the time series of images.

Two methods for the analysis of a winter time series of ERS-1 and ERS-2 images, for which constant roughness and vegetation conditions can be assumed, are suggested. The first method is based on the temporal coefficient of variation. Since the variability of soil moisture is expected to be smaller near a stream then further upslope from the stream, a smaller temporal coefficient of variation of the returned signal is observed near streams. The second method makes use of principal component analysis of the winter time series of images. Both methods lead to a representation of the spatial distribution of the soil moisture at the catchment scale. However, principal component transformation performs better since it can separate the soil moisture component in the backscattered signal from other influencing factors such as topography and land use.

Keywords Soil moisture, Coefficient of variation, Principal component analysis.

1. INTRODUCTION

Radar remote sensing has been shown to be a useful tool for the determination of the spatial soil moisture distribution within a catchment. Nevertheless, to get exact values for this parameter, a lot of information has to be known, such as the roughness characteristics of the soil and the vegetation characteristics. It has been shown that with multi-frequency data the soil moisture content and effective roughness parameters could be derived for bare soil surfaces [Su *et al.*, 1996]. This procedure cannot be used for single-frequency single-polarization satellite data, such as from ERS satellites.

The first part of this paper presents the time series of images for the analysis. In the second section the use of the temporal coefficient of variation for deriving soil moisture patterns is discussed. Section three discusses principal component analysis for this purpose. Finally, differences between both methods are discussed.

2. EXPERIMENTAL SITE AND DESCRIPTION OF DATA

The selected study area for the analysis is the Zwalm catchment which is located about 20 km south of Gent, Belgium. The land use in the catchment is mostly agricultural, but the southern is forested. The degree of urbanization is about 10%.

For temporal analysis of soil moisture using radar images, it is desirable to examine a period over which marginal changes in roughness and vegetation are expected. In our application the winter period of October 1995 to March 1996 was chosen. During this period it can be assumed that changes in backscattering are mainly due to changes in moisture content of the toplayer. Figure 1 gives an overview of the daily rainfall during the selected period and also shows the data takes of ERS-1 and ERS-2 which are used in the analysis.

4 descending ERS-1 and 4 descending ERS-2 images were selected, on the following dates:

31/10/1995: ERS-1, D-PAF
01/11/1995: ERS-2, D-PAF
05/12/1995: ERS-1, I-PAF
06/12/1995: ERS-2, I-PAF
13/02/1996: ERS-1, I-PAF
14/02/1996: ERS-2, D-PAF
19/03/1996: ERS-1, I-PAF
20/03/1996: ERS-2, I-PAF

All images share the same frame and track (resp. 2583 and 423), for which the local incidence angle for each pixel can be assumed to be constant in time. This is an important consideration since effects of changes in incidence angles can be noticed on the backscattering [Altese *et al.*, 1996].

After georeferencing, the images were resampled to 30 by 30 meter pixels. Since the images were obtained from two different Processing and Archiving Facilities (PAFs), all images were calibrated to the same reference (ERS-1 I-PAF). The final preliminary image processing step to be performed is speckle reduction. In our study we applied the Gamma MAP filter designed by Lopez *et al.* [1990], which gives very high speckle reduction.

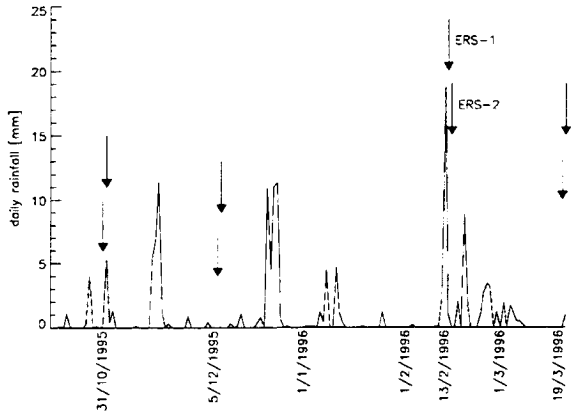

Figure 1: Daily rainfall for the 1995-1996 winter period. Also indicated are the ERS-1 and ERS-2 data takes.

3. TEMPORAL COEFFICIENT OF VARIATION

For the analysis of a series of ERS-1 images, Gineste and Mérot [1996] suggested 4 different parameters, called radar indices. One of these indices is the temporal coefficient of variation (CV), which can be calculated as the temporal standard deviation of a pixel divided by its temporal mean value.

Since the variation of soil moisture near rivers is expected to be small compared to the variation in upslope areas, this analysis should produce less signal variation and thus a smaller CV near rivers, and increasing signal variation further away.

After calculating the coefficient of variation on the sequence of 8 images, lower CV values are indeed observed near the rivers, as shown in Figure 2. However, the influence of topography and land use can also clearly be seen: forested areas in the south of the catchment and scattered urbanized areas also produce low CV values.

4. PRINCIPAL COMPONENT ANALYSIS

The principal component transformation is a linear transformation which uses image data statistics to define a rotation of original images in such a way that the new axes are orthogonal to each other and point in the direction of decreasing order of variances. In optical remote sensing

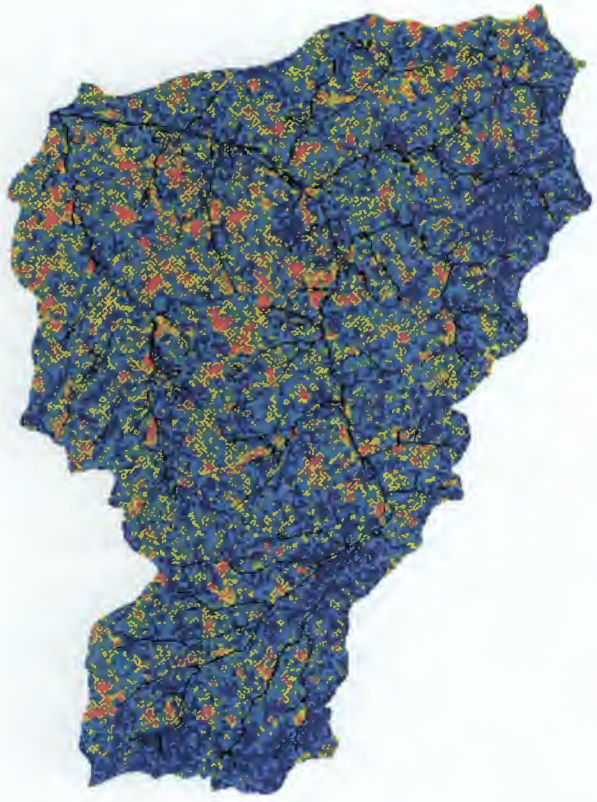

Figure 2: Coefficient of variation over the 8 ERS images. The stream network (black) is draped on top of the image.

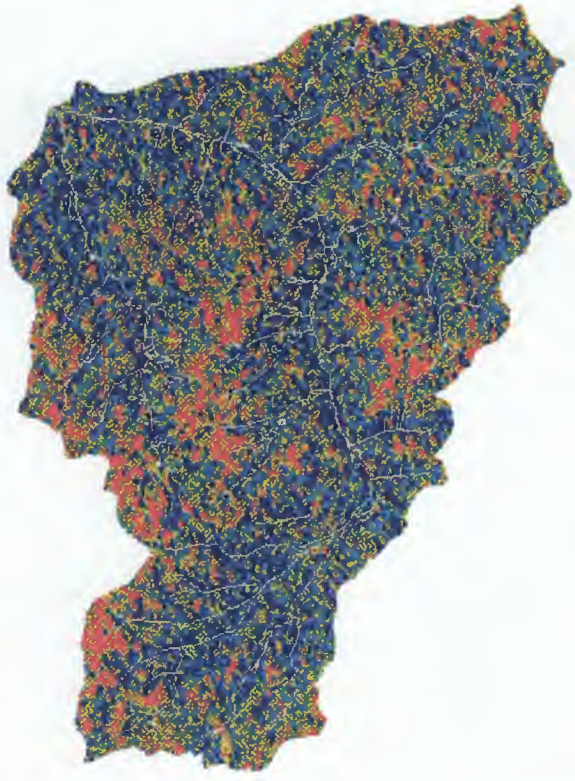

Figure 3: Third principal component retrieved from the 8 ERS images. The stream network (white) is draped on top of the image.

this transformation has been widely used for image enhancement, digital change detection, data compression and classification [Richards, 1986; Gonzales and Wintz, 1987; Singh, 1989]. Principal component analysis has not been widely used in radar remote sensing. One example is provided by Lee and Hoppel [1992], who use a modified principal component transformation on multifrequency polarimetric SAR imagery for reducing speckle and information compression.

Subjecting the 8 ERS images to a principal component analysis leads to the separation of the signal into several components which can be assigned to different factors influencing the backscattering. After ordering the eigenvalues in a descending sequence, the corresponding eigenvectors point in the direction of decreasing variances (see Table 1).

For our application, 87.6% of the variance (information) within the image is explained by the first component. This component will correspond to the mean behaviour of the catchment towards backscattering during this period, and will be influenced mainly by topography (e.g. larger backscattering on the slopes facing the satellite). The second principal component in our analysis accounts for 3.77% of the variance within the image. This component appears to be mainly influenced by urbanized areas and land use.

The third principal component appears to map those pixels that have similar behaviour in soil moisture dynamics, as can be seen in Figure 3. The dentritic network is clearly visible and is extended by those pixels that have constantly high soil moisture content. It can be reasoned that these areas are related to the variable source areas generating saturation excess overland flow during rainstorms.

The fourth and subsequent components are probably characterized mostly by noise, and account for the remaining 5.59% of the variance in

Table 1: The Coefficients of the Eigenvectors for each Principal Component (PC) and the Percentage of the Total Data Variance Accounted for in each Principal Component.

Matrix of Eigenvectors								Var.(%)
-0.33	-0.32	-0.30	-0.27	-0.45	-0.39	-0.38	-0.35	87.6
-0.32	-0.27	-0.35	-0.41	0.70	0.20	0.04	-0.01	3.77
0.32	0.32	-0.06	-0.21	0.34	-0.79	0.06	0.00	3.02
-0.33	-0.28	0.00	-0.04	-0.22	-0.29	0.60	0.56	2.53
-0.39	-0.27	0.58	0.44	0.35	-0.28	-0.16	-0.17	1.51
-0.58	0.68	0.27	-0.35	-0.09	0.08	0.04	-0.06	0.70
0.31	-0.33	0.61	-0.63	-0.08	0.08	0.05	-0.07	0.54
0.01	-0.02	-0.07	0.09	-0.03	0.02	0.68	-0.72	0.31

the images.

5. CONCLUSIONS

For the determination of soil moisture patterns using temporal SAR data, we have selected a series of 8 ERS images taken over a winter period, all sharing the same frame and track, to minimize the effects of local incidence angle, vegetation, and soil surface characteristics. In this paper two methods were presented for the determination of the soil moisture distribution in a catchment. A first method makes use of the temporal coefficient of variation. Low values of CV are observed near the stream and higher values occur in upslope areas. The main drawback of this analysis is that it is impossible to distinguish between the influences of topography, land use, and soil moisture on backscattering, which results in corrupted maps of saturation-prone areas.

The second method applied is a principal component analysis on the SAR images. This statistical technique makes it possible to separate the soil moisture effects from the governing topographical and land use influences on the backscattering, and thus allows us to map the soil moisture distribution within the catchment during a winter season.

Acknowledgements

This study was supported in part by ESA and the Belgian 'Federale Diensten voor Wetenschappelijke, Technische en Culturele Aangelegenheden' (DWTC) through grant no T3/02/35, the E.C. Environment Research Programme under contract no EV5V-CT94-0446, and the Sardinia Regional Authorities. We thank our colleagues B. Cosyn and M. Marrocu for technical support and helpful discussions.

REFERENCES

Altese, E., Bolognani, O., Mancini, M., and Troch, P. A. (1996). Retrieving soil moisture over bare soil from ERS-1 synthetic aperture radar data: Sensitivity analysis based on a theoretical surface scattering model and field data. *Water Resour. Res.*, *32*(3), 653-661.

Gineste, P., and Mérot, P. (1996). ERS-1 SAR data spatio-temporal analysis for soil moisture and saturated areas assessment over a small agricultural watershed. In *Proc. of Second EV5V-CT94-0446 Workshop* (p. 28-55). Rennes, France.

Gonzales, R. C., and Wintz, P. (1987). *Digital Image Processing.* Addison-Wesley.

Lee, J., and Hoppel, K. (1992). Principal components transformation of multifrequency polarimetric SAR imagery. *IEEE Trans. Geosc. Rem. Sens.*, *30*(4), 686-696.

Lopez, A., Laur, H., and Nezry, E. (1990). Statistical distribution and texture in multilook and complex SAR images. In *Proc. International Geoscience and Remote Sensing Symposium (IGARSS)* (p. 2427-2430). Washington DC., USA.

Richards, J. A. (1986). *Remote Sensing Digital Image Analysis.* Springer-Verlag.

Singh, A. (1989). Digital change detection techniques using remotely-sensed data. *Int. J. Rem. Sens.*, *10*(6), 989-1003.

Su, Z., Troch, P. A., and De Troch, F. P. (1996). Remote sensing of soil moisture using EMAC/ESAR data. *Int. J. Remote Sensing.* (submitted)

SAR SENSING OF VEGETATION WETNESS: THE FIRST RESULTS

Wim Klaassen, Marco van der Linden

Department of Physical Geography, University of Groningen,
Kerklaan 30, 9751 NN Haren, the Netherlands,
phone: +31 50 3636141, fax: +31 50 3635205,
email: W.Klaassen@biol.rug.nl

Albert Ballast
Department of Theoretical Physics, University of Groningen
Nijenborg 4, 9747 AG Groningen, the Netherlands.

ABSTRACT

Interception of rainfall by vegetation constitutes a large fraction of total water use and an important feedback mechanism in the hydrological cycle. Research used to be restricted to in situ observations at the patch scale. We present ERS-SAR observations to scale-up local observations.
Microwave backscatter increases with the amount of rain water collected on the leaves. At the canopy scale, sensitivity of SAR to vegetation wetness is still present, as well as sensitivity to wetness of the upper soil layer.
ERS-SAR data recorded just before and after rainfall are being analysed. Radar backscatter increases for almost all surfaces after rainfall. Preliminary we conclude:
1) ERS-SAR is useful to estimate vegetation wetness;
2) Best results are obtained when soil wetness and reflectivity are known;
3) The satellite determination of vegetation wetness may become more accurate when a larger angle of incidence is used.

1. INTRODUCTION

Interception is that part of the rain that falls on the vegetation and evaporates without reaching the ground. Interception is thought to be a significant part of the water budget, especially for aerodynamically rough vegetation, like forests. The significance of interception is caused by the high evaporation rate of wet surfaces. Interception is found to be 10-50% of the precipitation on forest and accounts for even a larger fraction of total water use.
Interception is generally measured as the difference of rainfall outside and inside the forest patch. Due to spatial variability of rainfall, the use of local parameters may result in a severe overestimation of rainfall interception in climate models (e.g. Dolman and Gregory, 1992). Also, the patchy structure of most forests results in an underestimation of the time required to dry up wind exposed forest edges (Klaassen et al, 1996). Finally, direct observations using microwave transmissivity suggest that forest may store a factor two more rain water than calculated from common theory (Klaassen et al., 1997). In the latter study it was recommended to use direct observations of water storage in future interception studies.

Several studies have indicated the sensitivity of ERS-SAR to vegetation wetness. Backscattering of tropical forest has shown to be remarkably constant, suggesting that rainforest can be used to calibrate ERS-SAR (Bernhard and Vidal-Madjar, 1989). However, in the same study backscatter was found to increase by 0.5 dB after a rain shower. Dobson et al. (1991) even found increases of 2-3 dB at C-band backscattering during a break between rain showers for several coniferous and northern hardwood forest species. For low vegetation an increase of 4 dB was found. The sensitivity of ERS-SAR to vegetation wetness was further confirmed by Brown et al. (1993), Rignot et al. (1994) and Pulliainen et al. (1996). In these studies, the sensitivity to vegetation wetness was only noticed as a side effect.

The aim of the present study is to analyse the potential of ERS-SAR for rainfall interception studies. We expect that ERS-SAR may improve the understanding of spatial variability of interception and thus improve the simulation of interception in climate models. Moreover, ERS-SAR may increase our understanding of the influence of species composition and leaf area index on rain water storage. Finally, we may expect that the drying time after the last shower varies over the area covered by the SAR image, and thus we may gain a better insight into the drying of vegetation after rainfall.

Proc. 3rd ERS Symp. on Space at the service of our Environment, *Florence, Italy, 17–21 March 1997* (ESA SP-414, 3 Vols., May 1997)

2. THEORY

The sensitivity of ERS-SAR to vegetation wetness was theoretically investigated. Special emphasis was placed on leaf scale processes. Assuming a water film of 0.2 mm on a small leaf of 0.2 mm thickness and 60% gravimetric water content the backscatter would increase with 8 dB due to leaf wetness. A leaf film of 0.2 mm would result in a water storage of 1 mm for a forest with leaf area index 5, and may be taken as a common value for many forests. Especially on young leaves, however, rain water is not stored as a film, but as droplets on the leaves. Fortunately, as long as the leaf dimensions are small as compared to the radar wavelength, it is mainly the amount of water, and not the spatial distribution, that accounts for backscatter. For coniferous vegetation with small needles, it is not the individual needle that should be taken as the basic backscattering entity, but the shoot with a cloud of needles. In that case the backscatter is slightly less sensitive to vegetation wetness, as the emissivity of the basic entity is already increased by the presence of the shoot.

It is concluded that at the leaf scale C-Band backscatter is increased by up to 8 dB by stored rainwater. The sensitivity of backscatter to water storage may depend on leaf type but should hardly depend on the distribution of water on the leaves.

To scale up the backscatter of leaves to canopy backscatter, we used the model of Karam et al. (1992). A very dense canopy with Leaf Area Index (LAI) = 10 implies that almost all backscatter arises from the canopy. Backscatter by the wet canopy is increased by 1 - 2 dB. The values are smaller as compared to single leaves because increased absorption by wet leaves results in less reflection from deeper layers in the canopy.

A medium dense canopy with LAI = 5 results in a contribution of the soil to the total backscatter. Table 1 shows the simulation results for a soil with 50% sand and a varying percentage of water. Other input parameters are:
Leaf radius: 2.5 cm
Leaf thickness: 0.2 mm
Gravimetric leaf water content: 60%
Thickness water on wet leaves: 0.2 mm
Roughness of soil: 2 cm

TABLE 1
Backscatter (in dB) of Wet and Dry Forest

Soil water (% water)	dry	wet	wet-dry
0	-9.9	-8.2	1.8
10	-9.5	-8.2	1.4
20	-9.2	-8.1	1.1
30	-9.0	-8.1	0.8
40	-8.8	-8.1	0.7
50	-8.7	-8.1	0.5

Theoretical analysis indicates that it is possible to estimate vegetation wetness using ERS-SAR. The reflectivity in wet conditions arises almost entirely from the canopy. A dry canopy results in a larger transmissivity, and some sensitivity to soil conditions. The calculations suggest that it would be advantageous to use three recordings: 1) wet canopy and wet soil; 2) dry canopy and dry soil; and 3) dry canopy and wet soil.

From the theoretical analysis it is recommended to use a measurement method that diminishes soil reflectivity. The following strategies might improve the estimation of vegetation wetness:
1) Use a higher frequency with stronger attenuation in the canopy
2) Use cross polarization: Karam's model suggests little cross-polarized backscatter from the soil and 2 dB increase of cross-polarized backscatter from wet vegetation
3) Use a larger observation angle with the vertical, thus increasing the length of the radar beam through vegetation and decreasing the backscatter of the soil in the direction of the observation.

3. DATA

Data from the ERS Tandem mission are used for experimental validation. Image pairs were selected with one image recorded with dry vegetation and the other with wet vegetation. Detection of the change of backscatter between these images would experimentally show the sensitivity of ERS-SAR to vegetation wetness. Data were selected from an area in the North of the Netherlands, where two field campaigns on rainfall interception were executed.
Figure 1 presents the very first result. It shows the difference in reflectivity between 7 and 8 september 1995. It was the end of a dry summer with only 23 mm precipitation in the last month

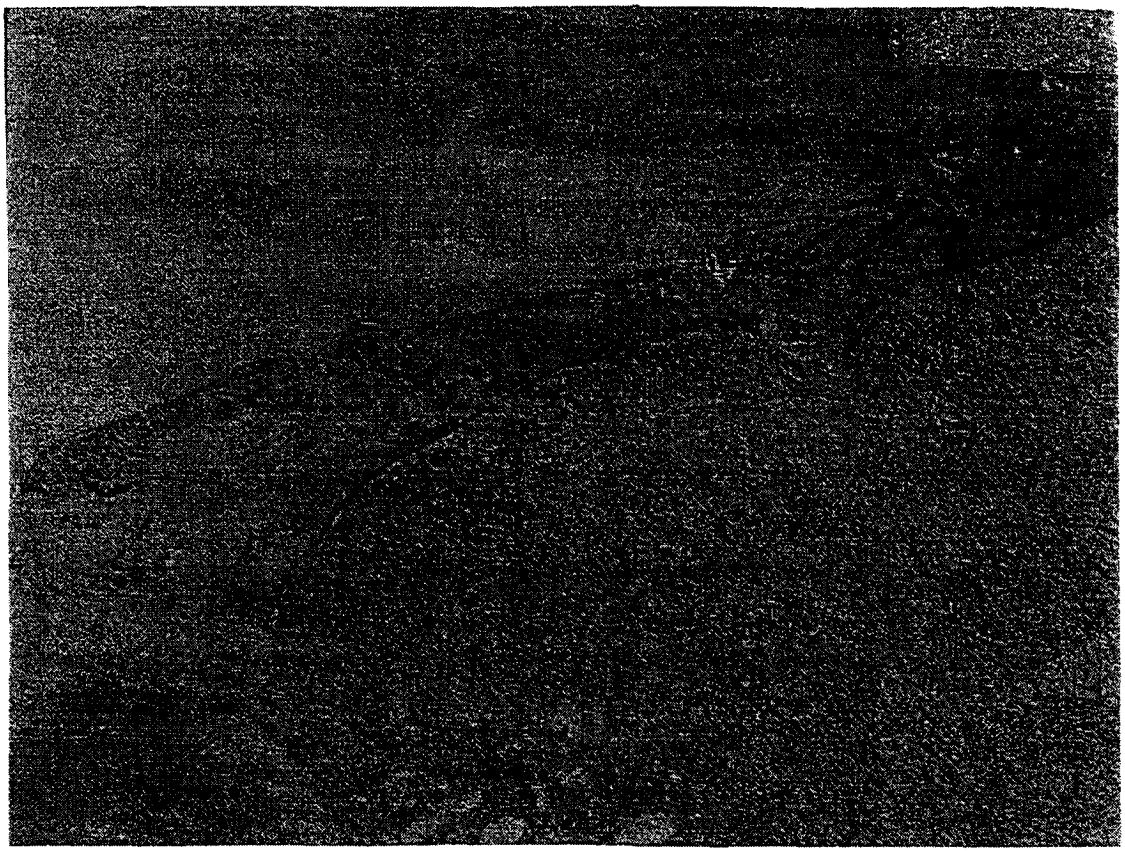

Figure 1: Difference in ERS-SAR reflectivity between 7 and 8 september 1995 in the Wadden Sea area. Surface conditions were dry on 7 september and wet on 8 september. Light colors are more reflectivity on the first day and dark colors are more reflectivity on the wet day. See text.

before the first observation. So the observation was made in dry conditions. A showery cold front with 7 mm rain passed at the end of the afternoon followed by drizzle in the early night. It can safely be assumed that the vegetation was still wet the following morning at 10:34 UTC when the second observation was made. Air temperature was 15 ^{0}C, mean wind velocity 5 m/s with a heavy overcast sky in the period between the recordings.

4. RESULTS

Figure 1 shows that reflectivity increases with surface wetness, see table 2

TABLE 2
Difference in reflectivity between wet and dry surfaces

Surface	Wet - Dry (dB)
rain above sea	-2
open water	0
grassland	1
forest	1.5
arable land	2
salt marsh	9.5

The largest increase in reflectivity is found in salt marsh. This is caused by flooding of the sea and shows that soil wetness may account for differences in reflectivity of the order of 10 dB. For arable land the result for arable land is a rough estimate as it is averaged between bare soil and vegetated surfaces. The results for grassland and forest agree well with the theoretical result of table 1. However, the increase for grassland is smaller than for forest, in disagreement with Dobson et al (1991). We suggest that the relatively small increase for grassland is caused by the wet soils that prevail in this part of the country, even in dry summers. In contrast, forests are usually situated on the dryer soils and this may

explain the larger increase of reflectivity due to wetting of the forest.
We plan to continue this study by analysing ERS-SAR recordings from other dates and places. Moreover we will try to use these data in a more quantitative way to estimate the amount of water on vegetation, the areal extend of wetting and the drying time after rainfall.

5. CONCLUSIONS

The theoretical analysis shows that ERS-SAR has the potential to measure vegetation wetness. However, when analysing radar data, care should be taken to distinghuish between soil and vegetation wetness. Soil influences are diminished using a larger angle of incidence of the radar beam.
Empirical evidence agrees with the modelling effort that ERS-SAR is indeed sensitive to vegetation wetness. Further study is planned to analyse the potential of ERS-SAR for quantitative studies on rainfall interception by vegetation.

6. REFERENCES

Bernhard, R and Vidal-Madjar, D, 1989: C-Band radar cross section of the Guyana rain forest: Possible use as a reference target for spaceborne radars, *Rem. Sens. Env.* 27, 25-36.

Brown, Bedard, Brisco and Naunheimer, 1993: Crop discrimination using multi-temporal ERS1-SAR data. *Proc. 2^0 ERS1 Symp. ESA SP361*, 57-62.

Dobson, MC, Pierce, K, McDonald, K and Sharik, T, 1991: Seasonal change in radar backscatter from mixed conifer and hardwood forest in Northern Michigan. *IGARSS 91,* Helsinki, 1121-1124.

Dolman, AJ and Gregory, 1992: The parameterization of rainfall interception in GCM's. *Q.J.R. Meteorol. Soc.* 118, 455-467.

Karam, MA, Fung, AK, Lang, RH and Chauhan, NS, 1992: A microwave scattering model for layered vegetation. *IEEE Tr. Geo. Rem. Sens.* 30, 767-783.

Klaassen, W, Lankreijer, HJM and Veen, AWL, 1996: Rainfall interception near a forest edge. *J. Hydrol.* 185, 349-361.

Klaassen, W, Bosveld, F and De Water, E, 1997: On water storage and evaporation as constituents of rainfall interception. *J. Hydrol.* (submitted).

Pulliainen, JT, Mikkelä, PJ, Hallikainen, MT, and Ikonen, JP, 1996: Seasonal dynamics of C-Band backscatter of boreal forests with applications to biomass and soil moisture estimation. *IEEE Tr. Geo. Rem. Sens.* 34, 758-770.

Rignot et al., 1994: Monitoring of environmental conditions in Taiga forests using ERS1-SAR. *Rem. Sens. Env.* 49, 145-154.

RETRIEVAL OF SOIL MOISTURE CONTENT FROM NATURALLY VEGETATED UPLAND AREAS USING ERS-1/2 SYNTHETIC APERTURE RADAR

Neil I. Fox[1], Paul Saich[2], Chris Collier[1], Robert Miller[2]

[1]Telford Institute of Environmental Systems
University of Salford, Salford, M5 4WT, UK
phone: 44 161 2953916, fax: 44 161 745 5060
email: n.i.fox@civils.salford.ac.uk

[2]Space Division, GEC-Marconi Research Centre
Chelmsford, Essex, CM2 8HN, UK

ABSTRACT

A novel algorithm has been used to derive soil moisture content from SAR imagery. Based upon a simplified Kirchhoff scattering model, the algorithm separates the contribution to the backscatter into that from the soil and that due to the surface roughness and slope effects. It is designed not to require intense ground calibration.

The method has been tested over a naturally vegetated hillside in the West Pennine Moors in Lancashire, England where a field site has been established. Comparative measurements have been made using a capacitance probe and a weighing lysimeter. The algorithm produces good estimates of soil moisture from SAR data when compared to root-zone measurements made with the capacitance probe, thereby showing the potential for SAR in this field.

Comparisons with the column soil moisture content measured by the lysimeter show the limitations of remotely sensed soil moisture when moisture is present only at depth. This is most important in the derivation of evapotranspiration rates and surface heat fluxes using remotely sensed soil moisture values.

1. INTRODUCTION

The observation of soil moisture content (SMC) over wide areas is crucial to the understanding and modelling of boundary layer convection, as well as aiding the distribution of irrigated supplies of water for agricultural usage. The availability of moisture for evapotranspiration (ET) is a critical parameter in the partition of energy at the Earth's surface and the quantity of water entering the atmosphere will regulate cloud formation and precipitation. If SMC could be monitored accurately on a regular basis then ET can be deduced.

There are a number of methods of observing SMC currently used, many of these (eg. neutron probes, Penman Monteith methods) use point measurements at the surface which then have to be extrapolated to give an areal estimate. L-band passive microwave observations have been shown to be effective (Njoku and Entekhabi, 1996) but will suffer when the canopy height is large or if there is cloud cover.

The problem of cloud cover is solved by using an active device such as the SAR. Concern has been expressed as to the effectiveness of a method involving SAR data to retrieve SMC from naturally vegetated and hilly areas and experimental work has therefore concentrated on flat, homogeneously vegetated or bare soil areas (Ulaby *et al*, 1996).

2. EXPERIMENT

The study described here was part of a larger program concerned with the prediction of potential flood events in data sparse areas (Saich *et al.*, 1997). A section of the project deals with the derivation of a SMC measuring tool using SAR data. To this end a physically based model of the surface scattering was used to divide the radar backscatter into components due to the surface roughness and the soil dielectric properties. This is detailed in Saich *et al.* in this volume.

The radar backscatter (σ_{dB}) is related to the Fresnel reflection coefficient (R) by the equation

$$\sigma_{dB} = A + 20\log_{10}|R| \qquad (1)$$

A is a constant that could be determined by numerical simulation of the surface scattering characteristics but in this case was empirically found by fitting to the ground truth data. The SMC is retrieved from the value of R by its relationship to the permittivity (Saich *et al.*, 1997). This method implies the need for some ground measurements to initialise the value of A if one is to achieve an absolute measure of SMC.

Comparisons were made between the six values of SMC

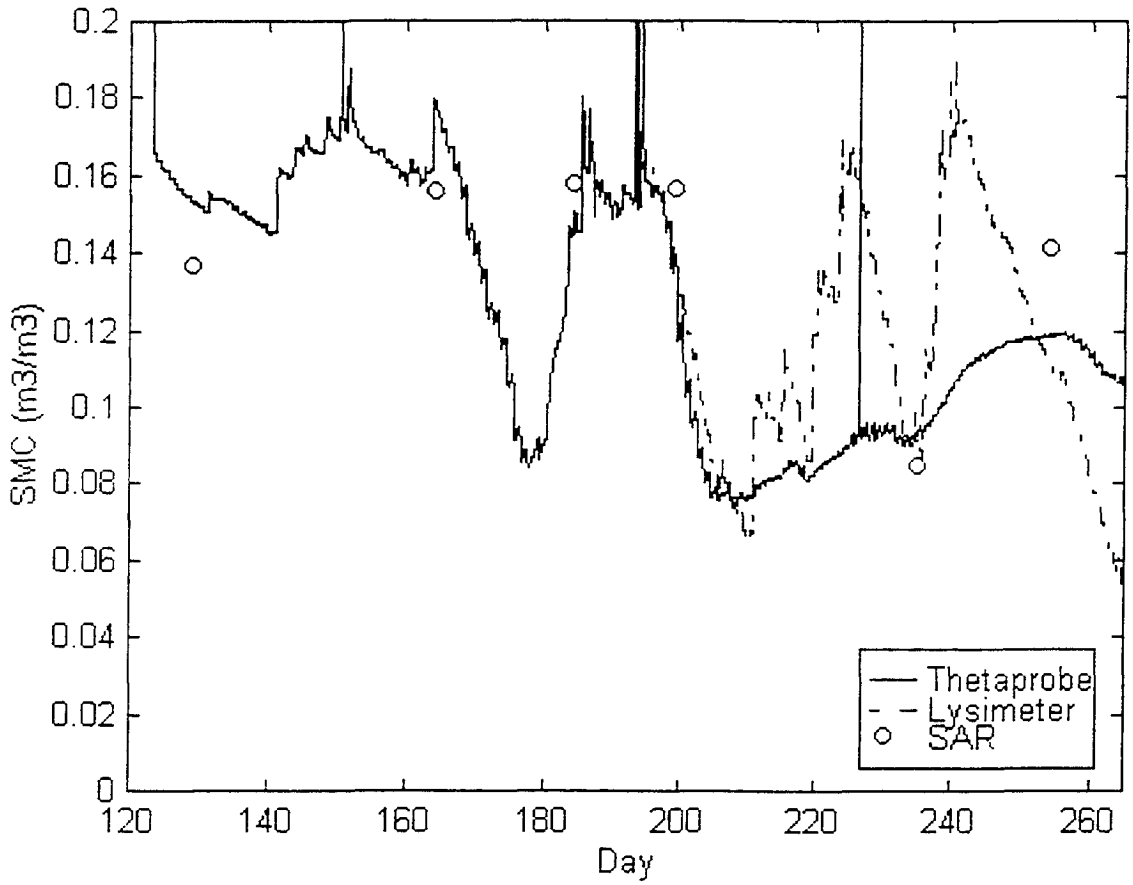

Figure 1: Comparison of SAR retrieved values of SMC with those found *in situ* using a capacitance probe and a weighing lysimeter.

derived from the SAR data through the summer of 1996 and *in situ* measurements. These latter were made with a theta-probe (manufactured by Delta-T Instruments, Cambridge, UK) and a weighing lysimeter (constructed at the Institute of Terrestrial Ecology, Merlewood, UK). The theta-probe is a time domain reflectometry (TDR) device and was installed for the entire measuring period. It was buried at a depth of between 5cm and 10cm and therefore is sensitive to the SMC within the root-zone. The weighing lysimeter contained an undisturbed soil column of diameter 31cm and length 37cm topped by natural grass. It was installed on July 12th 1996.

The test site for the experiment is located at Haslingden Grane in Lancashire, Northwest England. The area is part of the West Pennine Moors and as such has some steep slopes. The vegetation is mainly long, growing grass but there are stands of trees in the vicinity, as well as reservoir surface and hill tops with some bare rock outcrops. The grass was of the order of 10cm in length at the time of the initial observations in May, increasing to up to 30cm by September.

3. RESULTS

Six measurements of SMC found from the SAR imagery of the single 100m pixel containing the field site are compared to the ground measurements shown in figure 1.

A seventh image acquired from an ascending pass showed distinct characteristics from the six descending passes and is not shown. The 'spikes' in the theta-probe record are artifacts created when the power supply is renewed.

It is apparent that there exists considerable correspondence between the values of SMC found from the SAR data and that from the theta-probe, however there are insufficient data to determine the reliability of the technique. It is evident that the SAR discriminates between the wetter conditions earlier in the period from the dry conditions around day 240. The agreement with the theta-probe is perhaps to be expected as both instruments should respond similarly to the dielectric constant of the top few centimetres of soil. As the soil column retains water at its base for longer and fills up more quickly after rainfall it can be seen that the column SMC as measured by the lysimeter is not well represented by the SAR estimates.

4. EVAPOTRANSPIRATION

If one assumes that the SAR will measure the surface layer SMC in a similar way to the theta-probe then one can use the probe measurements to simulate ET values that could be derived from remotely sensed SMC. (It is perhaps worth noting that passive microwave methods would show similar behaviour). Such areal ET measurements are important in assessing the surface energy budget and would be of great benefit to climate modelers and

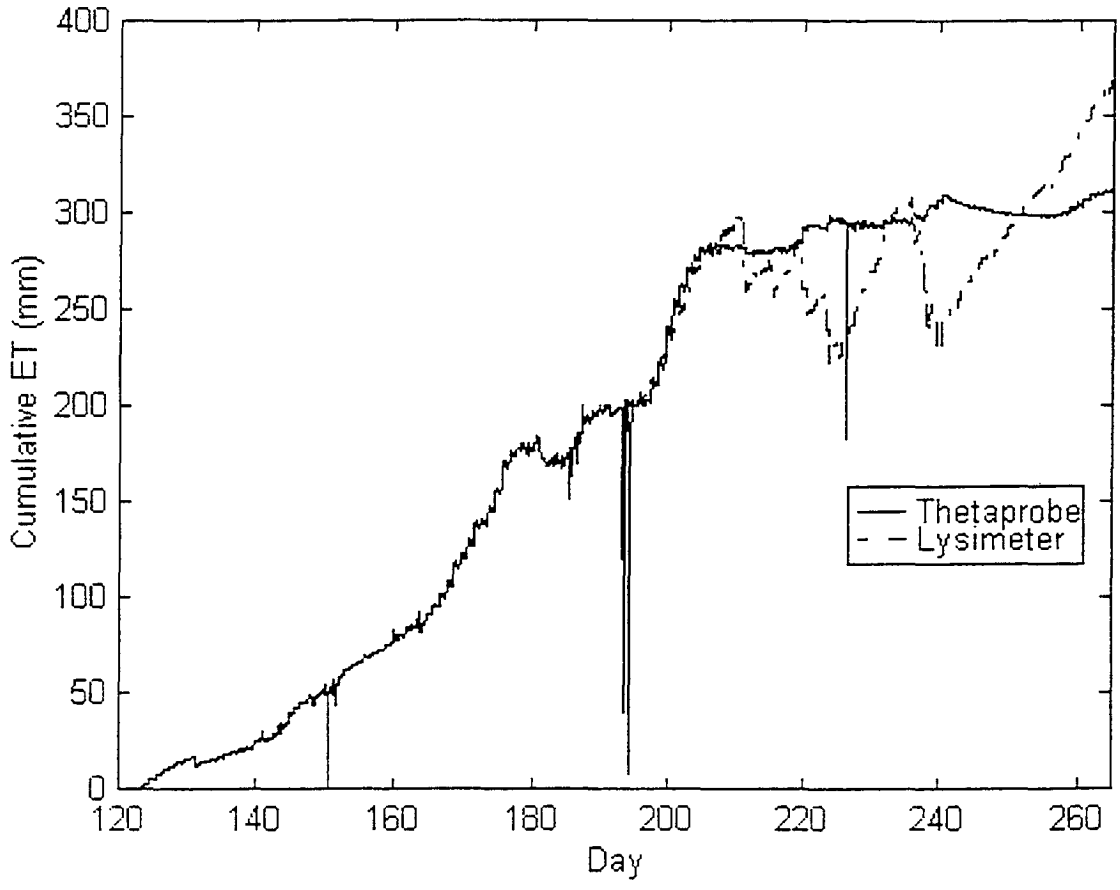

Figure 2: Comparison of evapotranspiration derived from measurements of the theta-probe and the lysimeter

boundary layer meteorologists.

In the area of Northwest England over which this study took place the SAR has a return period of 35 days so that an application such as the one being discussed is not practical. However a theoretical instrument which makes a daily pass would still have the limitations detailed in this section.

By adding the component of the water balance due to rainfall measured at the field site one can deduce the ET from the differences in the SMC recorded by the theta-probe and the lysimeter. The 2 methods are compared in figure 2.

It is seen that initially, when the lysimeter was installed on day 194, the two instruments produce values of ET that are in excellent agreement. At this stage there is still moisture available in the top layer of the soil. When the hot dry spell continues this surface layer dries out completely and no further ET takes place to deplete the SMC observed with the theta-probe. The lysimeter, on the other hand, continues to show that ET is taking place as water is drawn by deeper roots to the canopy from where it is evaporated.

6. DISCUSSION

It is evident that caution is required if remote sensing methods are to be used for the areal observation of SMC and ET. If one assumes that one can accurately determine the condition of the surface one may still need to make some surface investigation to correctly deduce the moisture available for crop use and ET. For instance, it may be useful to know the total soil depth, type and root penetration.

Once the surface is dry and there is no further change in the remotely sensed SMC one would have to extrapolate the ET by assuming, primarily that water remains deeper in the soil and secondly, that climatological factors remain reasonably constant and one has knowledge of the behaviour of the vegetation with regard to water under such conditions.

5. CONCLUSIONS

It has been demonstrated that SAR offers a possible way of monitoring SMC changes and, if calibrated, absolute values in areas of varied, natural vegetation and steep slopes. This is a useful application of SAR as much can be deduced from the surface layer SMC. However, more data is required to complete a detailed assessment of the effectiveness of the technique.

The response of the lysimeter to the column soil moisture content suggests that care must be taken if one wishes to use remotely sensed SMC measurements for boundary layer modelling or agricultural applications.

6. ACKNOWLEDGEMENTS

This work was undertaken as part of the British National Space Centre (BNSC) Earth Observation Link Programme. We would also like to thank Dave Benham of the Institute of Terrestrial Ecology for his work on the lysimeter, Mike Knowles of the UK Environment Agency for raingauge data and NorthWest Water Ltd. for providing the Haslingden Grane site.

7. REFERENCES

Njoku and D. Entekhabi, 1996: Passive remote sensing of soil moisture. *J. Hydrology,* **184, 101-129.**

Saich, P.J., R.J. Miller, A.J. Sephton, C.G. Collier and N.I. Fox, 1997: Development and demonstration of soil moisture determination and INSAR for catchment hydrological monitoring, *Proc.* 3rd ERS Scientific Symposium, Florence, Italy.

Ulaby, F.T., P.C. Dubois and J. Van Zyl, 1996: Radar mapping of surface soil moisture. *J. Hydrology,* **184,** 57-84.

IDENTIFICATION OF PARAMETERS AND PHENOMENA OF HYDROLOGICAL RESTORATION PROCESSES IN LOWLAND BOG AREAS USING ERS SAR DATA

PRIETZSCH, C.° & A. BACHEM° & O. DIETRICH* & H. KRETSCHMER*& H. PFEFFER* & S. EHLERT*

° Institute of Landscape Modelling, ZALF, Müncheberg, Germany, cprietzsch@zalf.de, abachem@zalf.de
phone: + 33432 - 82 239, fax: +33432 - 82 334
* Institute of Hydrology, ZALF, odietrich@zalf.de, phone: + 33432 - 82 305, fax: +33432 - 82 212
* Institute of Land Use Systems, ZALF, hkretschmer@zalf.de, phone: +33432 - 82 314, hpfeffer@zalf.de
phone: +33432 - 82 311, sehlert@zalf.de, phone: +33432 - 82 266

ABSTRACT

A pixel-based neural network classification of a multitemporal ERS-1 and ERS-2 SAR data set in a mainly grassland area in Brandenburg Germany is presented. The results are preliminnary but give hope on an alternative way to deduct restoration recommendations for a former wetland area as opposed to a hydrological approach based on a DTM and ground water table depths which serves as a comparison.

1. INTRODUCTION

The renaturalization and rewetting of formerly drained low moor areas in northeast Germany can only be achieved based on detailed knowledge of the occuring organic and mineral soil substrates, the terrain characteristics and the available surface and groundwater resources. A research project funded by BMBF [Ref. 1], [Ref. 2], [Ref. 3] (see acknowledgement) analysed the possibilities of renaturalization of three different areas in the state of Brandenburg one of these was the area 'Rhinluch' and delineated areas are preferable for rewetting and thus restoreation of the former status. This analysis was based on a DTM (digital terrain model), extensive measurements of the hydraulic characteristics of the area and hydrologic model. The ecological development concept of the same area was provided by [Ref. 4]. Since the necessary field measurements are costly and time consuming, it is tried to reach the same recommendation results on the basis of ERS DATA, which is partly represented here, and LANDSAT-TM data as to analyses the contribution of optical satellite data for this purpose and possible disadvantages and/or benefits. Related work in nortwest Germany can be found in [Ref. 5] and [Ref. 6]. The method developed for Rhinluch is going to be transfered to two other study area in northeast Germany (Finow Valley near Eberswalde and Friedland Great Meadows near Torgelow).

2. MATERIAL

A local GIS of the investigation area Rhinluch, includes a biotope and landuse map with 17 classes: forests on mineral soils, decideous trees on moist to wet sites, riverine woods, shrubs on moist and wet sites, undergrowth on moist to wet sites, tall herbaceous plants, high diversity pasture on wet sites, high diversity pasture on variably wet sites, fallows on wet sites, fallows on variably wet sites, sowed grassland, sedge, reeds, aquatics with floating leaves, agriculturally used areas, towns and buildings, lakes and ditches.

A soil map with 9 subclasses shows the heterogeneity of organic and mineral soils in the area. The digital terrain model calculated from 12 topographic maps in the scale 1 : 10 000 and the measured ground water table depth which was acquired during field campaigns was used to calculate the possible rewetting areas during the planned renaturalization process.

The image data were acquired from April 1995 to April 1996 by ERS-1 and ERS-2 so that a time series of 17 data takes of geocoded and terrain corrected products (GTC) is available. The full scenes converted to 8-bit data keeping track of the linear scaling parameters, were then subsetted and the subscenes of the region of interest were coregistered according to their common UTM coordinates. The image stack was then transformed into a transverse Mercator reference system with Gauss-Kruger net and Bessel ellipsoid for easy comparison and overlay with the GIS data. A LEE-filter with a 5x5 window was applied to the image data in order to reduce image speckle. Here a preliminnary analysis with a neural network approach for biotope type classification are presented.

3. METHODS

Based on the reference data (biotope type map) and optical data from LANDSAT-TM, the distinguishable

biotope types were delineated on the image to extract sample areas. The use of additional optical data was appropriate, because the reference map seemed to be generalized to an inappropriate degree. This was especially the case in built-up areas, where gardens and shrubs were mixed with this class also.

During this analysis it was obvious that especially those biotope types that occur only in small areas or enlongated fringes are not suited for the classification due to their low spatial extension (undergrowth on variably sites, aquatics with floating leaves). Therefore only the following 15 classes were extracted: forests on mineral soils, deciduous trees on variably wet sites, riverine woods, shrubs on moist and wet sites, tall herbaceous plants, high diversity pasture on wet sites, high diversity pasture on variably wet sites, green fallows on wet sites, green fallows on variably wet sites, sowed grassland, sedge stands, reed stands, agriculturally used areas, towns and buildings, lakes and ditches.

The overall number of sample areas was 290 which is about 5% of the investigation area. The normalized mean and the standard deviation (values ranging between 0...1) were used as input patterns for the neural network approach. The coding of the output patterns was achieved by a one-out-of-n-coding, that means the unit that equals the class number is assigned a value 1.0, whereas all others receive the value 0.0.

The applied neural network approach was a backpropagation network with momentum term in online mode which is an implementation of the University of Stuttgart (SNNS software package). A learning rate 0.01 was used, while the momentum term was set to 0.9. The activation function had sigmoidal characteristics. Learning was stopped after 1000 epochs. The applied network architecture was 30-30-15, i.e. 30 input units due to two parameters per image layer (mean and standard deviation for each of the 15 dates), one layer of 30 hidden units and 15 output units due to the formerly specified 15 desired classes.

For the final classification of the image data set a 5 by 5 window was moved across the image to calculate the mean and standard deviation in the neighborhood of the center pixel over all image layers (dates). The results were fed into the trained neural network, in which the unit with the highest output value formed the new class value.

4. RESULTS

This classification was a first approach which still has to be refined. The classification results are shown in Fig. 1 and in Fig. 2 the actual biotope types from the aerial image interpretation and field investigations by [Ref. 4] can be compared to this.

Visual interpretation of the classfication results shows that most of the area is dominated by sowed grassland, which has been well recognized by the neural network approach pretty well. Also, the lakes received the correct class assignment, except for the long lake in the upper middle of the image, which was totally misclassified as reeds.

The misclassification of the other areas are partly due to missing training patterns (areas outside the polygon overlay) for which no land use information was available. The overall confusion matrix in Tab. 1 was

Tab. 1: Results of the neural network classification approach on test site Rhinluch, Germany. Comparison of full investigation area.

		Classes after Neural Network Classification															
	Field data	**1**	**2**	**4**	**5**	**6**	**7**	**9**	**10**	**11**	**12**	**13**	**14**	**15**	**16**	**17**	**Sum**
0	Background	0.60	0.12	3.32	32.87	4.65	3.02	1.27	0.12	15.29	2.48	0.36	0.48	3.93	15.53	15.95	100
1	Built-up	**3.27**		7.62	39.38	9.44	4.17	1.63	0.91	7.26	1.45		0.18	2.00	9.26	13.43	100
2	Lakes, ditches and rivers	50.00				50.00											100
3	Aquatic with floating leaves																
4	Riverine woods																
5	Shrubs	6.12		16.33	**57.14**	4.08				2.04	2.04		6.12		4.08	2.04	100
6	Deciduous woods																
7	Forest on mineral soils			2.48	53.96	8.42	3.96	0.99	0.50	17.82	0.99	1.98		4.46	1.49	2.97	100
8	Undergrowth				25.00	25.00									50.00		100
9	Reed stands																
10	Sedge stands																
11	Tall herbaceous plants			4.00	12.00	9.33	2.67			**36.00**				13.33	9.33	13.33	100
12	High diversity grassland, wet sites																
13	High diversity grassland, variably wet sites	12.50													87.50		100
14	Green fallows, variably wet sites				23.68	10.53	6.58			17.11	1.32			14.47	14.47	11.84	100
15	Green fallows, wet sites																
16	Sowed grassland				23.39	1.02	1.02	5.76		12.88	1.36		1.02	1.69	**40.00**	11.86	100
17	Agriculture			0.36	29.04	0.91	2.18	0.36	0.54	21.23	3.27	0.91	0.36	2.36	13.25	**25.23**	100

Class assignments are given in %. Classes 3 and 8 were not present in the neural network approach.

created using the full investigation area (field based reference map) and the neural network classification. For each reference class the percentage of misclassifications was counted. It is striking that shrubs, sowed grassland, agriculture and tall herbaceous plants were best recognized. Most of the forest on mineral soils was misclassified as shrubs. Also between the different grassland types a high confusion can be recognized. This is not too surprising, because the geometry of the plants is nearly the same. Herein the demand for the design of more geometry oriented classes arises.

5. CONCLUSION

The classification results are promising, but have to be further improved by data set optimisation (selection of most significant images) and by the application a more advanced neural network approach that takes into account neighboring pixels at the design of the training patterns. Moreover the transferability to other investigation areas and the comparison with optical data classification of biotope types with conventional and neural network approaches will be investigated within the scope of AO2.128.

6. REFERENCES

[Ref. 1] Dietrich, O. & R. Dannowski & J. Quast & R. Tauschke (1996): Untersuchungen zum Wasserhaushalt nordostdeutscher Niedermoore. ZALF-Bericht, Nr. 25, Müncheberg.

[Ref. 2] Dietrich, O. & R. Dannowski & J. Quast (1995): Gis-based water balance analyses for fen wetlands. Int. Conf. Appl. GIS Hydrol. Wat. Res. Man., HydroGis'96, April 16-19, Vienna, Vol. Poster Papers, 83-90.

[Ref. 3] Dietrich, O. & R. Dannowski (1996): GIS-gestützte Untersuchungen zum Wasserhaushalt von Niedermooren. Tagungsbeitrag 'GIS im Naturschutz', 11.-12. April, Verlag Westarp-Wissenschaften, Braunschweig (in press).

[Ref. 4] Kretschmer, H. & E. Beyer & O. Dietrich & w. Haberstock & K. Hierlscher & J. Jüttner & H. Lehrkamp & H. Pfeffer & R. Tölle & J. Zeitz (1995): Ökologisches Entwicklungskonzept oberes Rhinluch. ZALF Müncheberg und Humboldt Universität Berlin, unpublished.

[Ref. 5] Reinke, E. (1995): GIS-gestützte Analyse von Fernerkundungsdaten zur Bestimmung des Grünlandanteils im Bereich des Dümmers. Unpublished Thesis. University of Vechta.

[Ref. 6] Schelling, K. (1996): GIS-gestützte Auswertung von Fernerkundungsdaten zur Bestimmung von Moorzustand und -nutzung am Beispiel Goldenstedter Moor. Unpublished Thesis. University of Vechta.

7. ACKNOWLEDGEMENT

The project 'Ecosystem Management for Lowmoors' was funded by the German Federal Ministry of Education and Research (BMBF, FKZ 0339507A and FKZ0339508A). The image data were kindly provided by ESA and are analysed in the scope of project AO2.D128.

Fig. 1: Neural network classification results of biotope types.

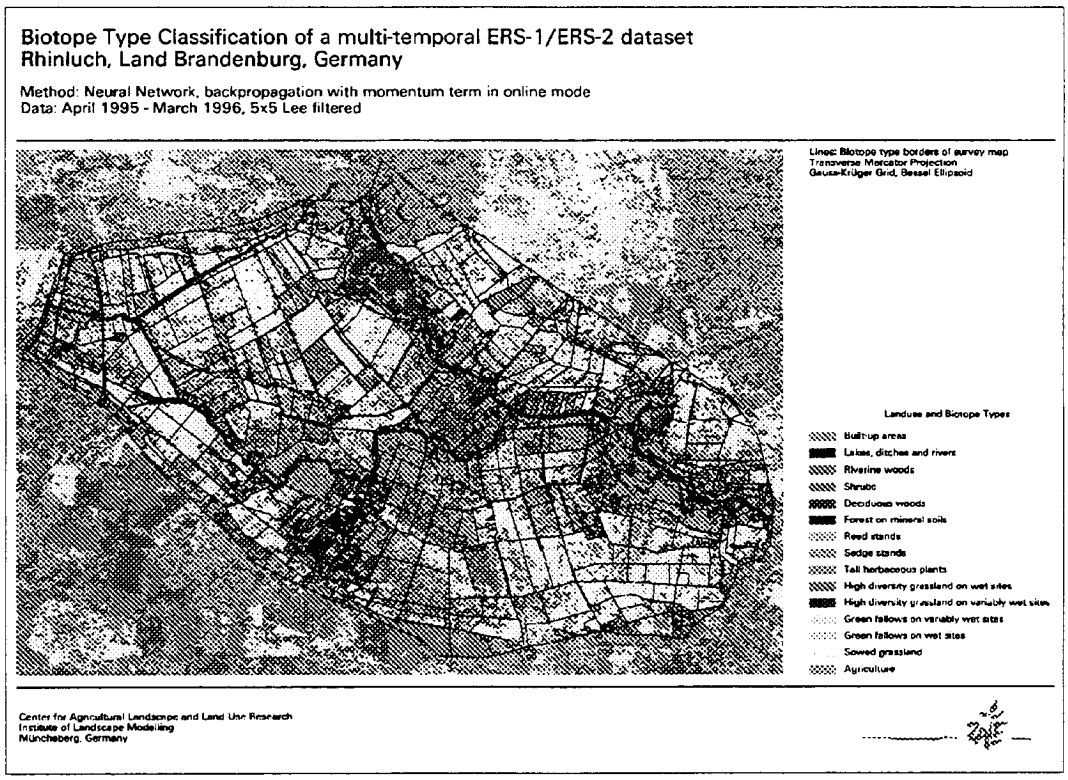

Fig. 2: Terrestric biotope type reference map.

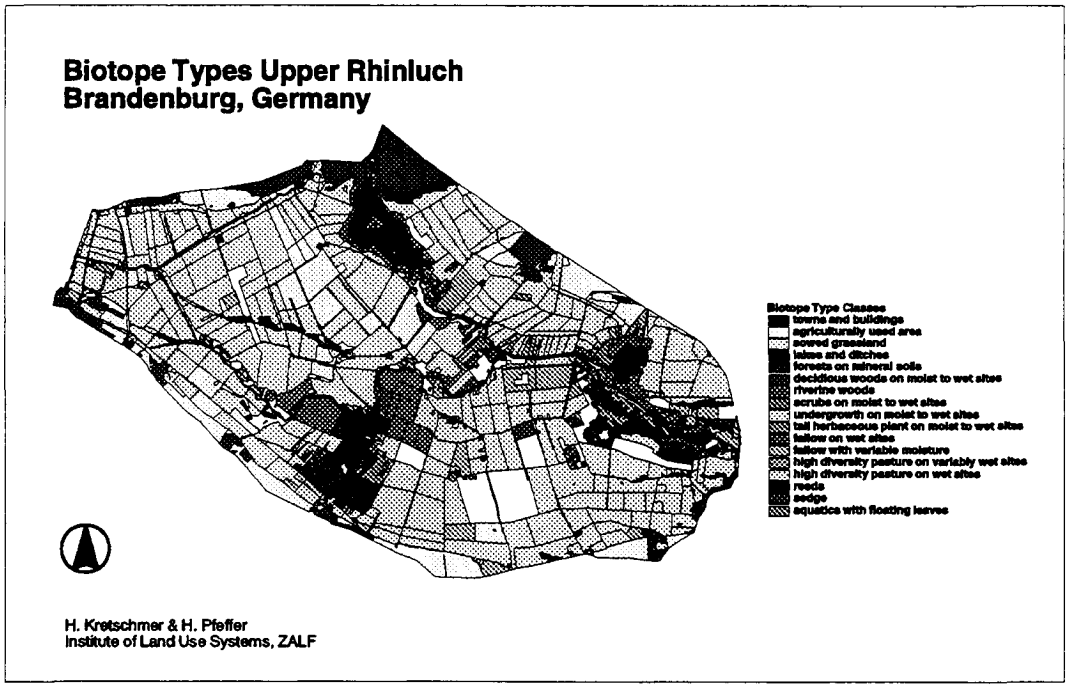

ERS-1 SAR SENSITIVITY TO HYDROLOGICAL PARAMETERS: A COMPARISON WITH SIR-C AND AIRSAR DATA

P. Pampaloni, G. Macelloni, S. Paloscia and S. Sigismondi
Istituto di Ricerca sulle Onde Elettromagnetiche - CNR
Via Panciatichi 64, 50127 Firenze, Italy
fax: +39 55 4235290, phone: +39 55 4235 205, e-mail: microrad@iroe.fi.cnr.it

ABSTRACT

The sensitivity of radar backscattering to surface roughness and soil moisture have been studied comparing experimental data collected with ERS-1 C-SAR, AIRSAR and SIR-C/X-SAR on Montespertoli test site (Italy) with analytical and semiempirical models. It has been found that co-polar L - band data give the highest information content for estimating soil moisture and surface roughness. At the observation parameters of ERS-1 C-SAR the sensitivity to soil moisture on a spatial scale is rather low. However, considering data collected at different dates on the same area, a very good correlation and sensitivity to soil moisture has been found.

1. INTRODUCTION

The operational capability of remote sensing for monitoring hydrological parameters in large watersheds is not yet fully explored and extensive research is being carried out to evaluate the potential of microwave sensors and to assess the achievable accuracies of measurements.

A research activity, which aims at a better understanding of the information achievable from Synthetic Aperture Radar to be used in hydrology, has been carried out in Italy on the test site of Montespertoli. A significant phase of this study consists of investigating the sensitivity of radar backscattering to some important parameters (soil moisture, surface roughness, vegetation cover and biomass) which are of primary importance in modelling the geophysical processes of the hydrological cycle. Although the detection of these parameters has been the subject of many investigations, carried out in past years with ground based and airborne sensors, only a very few preliminary investigations have been carried out using data collected with spaceborne sensors, [e.g. Ref 1- 3]. A major problem in retrieving the hydrological parameters is that each of them affects the radar backscattering in a different way and separating the effects requires the use of appropriate multi-frequency polarimetric algorithms.

In this paper we investigate the sensitivity of backscattering coefficient, to surface roughness and soil moisture by correlating remote sensing data to ground truth. To do that we use data collected on different dates at L- and C- bands, with ERS-1/ C-SAR, AIRSAR and SIR-C.

2.THE TEST SITE AND THE EXPERIMENT

The test site is a representative area of the landscape and climate of central Italy. About half of the area is hilly with wood, agricultural fields and some urbanization, while the remaining part is flat with agricultural fields and urbanization. In the whole site two sub areas were selected for detailed experiments:

a) an agricultural area along the Pesa river cultivated with vineyards, wheat, barley, sunflower, alfalfa and corn.

b) a sub-basin of Pesa river (Virginio) where a station for the measurement of total sediment transport is located.

The area was equipped with two trihedral corner reflectors of 180 cm and one of 240 cm, deployed parallel to flight line. In addition a few homogeneous fields, whose stability and backscatter characteristics were known from previous investigations, had been specifically prepared, to be used as cross reference between flights.

Ground truth measurements included: moisture, roughness and dielectric characteristics of soils, crop maps, and vegetation parameters. Only the roughness parameters measured on profiles parallel to the observation direction (which are in this case parallel to the rows) have been taken into account for the model analysis.

	Freq. Band	Pol.	Obs. Angle	Ground res. (m)	Dates
AIRSAR	C, L, P	Quad	20° 35°- 50°	12.2 x 6.6	22-29/6 1991 14/7/91
ERS-1	C	VV	23°	30 x 26.3	29/5/92 07/8/92 24/4/94
JERS-1	L	HH	35°	18.3x24.6	24/6/92 14/4/94
SIR-C/ X-SAR	L, C, X	Quad VV	23°-55°	25x25	12-17/4, 1994 3-14/10, 1994

TABLE I: Summary of processed SAR data

The site was imaged several times between April and October, at various incidence angles by different SAR

systems: the C-band ERS-1, the L-band JERS-1, and the multi-frequency polarimetric AIRSAR and SIR-C/X-SAR. Weather was dry in June when vegetation was well developed. On the contrary the average soil moisture was rather high (generally around 20%) both in April and October when most agricultural fields were bare or covered with small vegetation. A summary of data collected during the experiments is shown in TABLE I.

3. EXPERIMENTAL RESULTS AND DATA ANALYSIS

A comparison of calibrated ERS-1 C- band SAR data delivered by ESA/ESRIN with data collected at the same frequency and incidence angle with AIRSAR and SIR-C shows that the achieved data sets are quite consistent. As an example Fig. 1 shows the backscattering coefficient of the same fields and forests, measured at C-band, VV pol.

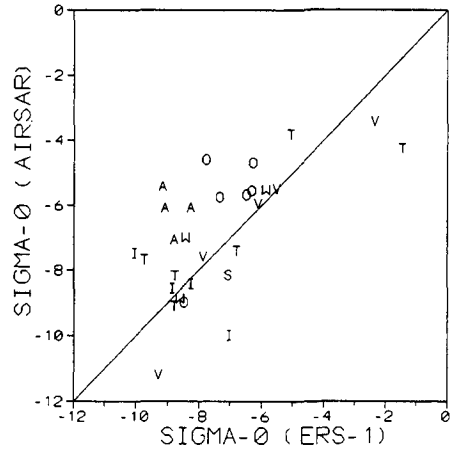

Figure 1 - σ°_{VV} C-band, $\theta = 23°$ measured on various cover types with ERS-1 SAR and airborne AIRSAR. (T = forest, O = oliveyard, V= vineyard, W = wheat, A= alfalfa, I = uncropped, S = sorghum)

and 23° incidence angle with AIRSAR and ERS-1. Due to the different observation dates and azimuth angle, σ° of a certain crop is not the same, being related to the development stage (for wheat, barley etc.) and row directions (especially for vineyard) of vegetation. Conversely, points representing forests, which are much more stable targets, are very close to the bisecting line. This intercalibration test allowed us to combine measurements from different sensors in order to relate the backscattering to geophysical parameters.

Surface type discrimination

The analysis of experimental data collected on Montespertoli site has shown that multifrequency radar systems are effective in separating agricultural fields from other types of surface and in discriminating among agricultural species [Ref. 3]. At P- and L- bands, there is a continuous increase of backscatter as the scatterer dimensions increase from the small leaf vegetation to the bigger forest trees. The SAR data at L-band can identify agricultural crops when they are well-developed and characterized by large stems and leaves. In particular well-developed 'broad leaf' crops, such as sunflower and corn, and plants with large stems and pods, such as colza, can be separated from bare soils and other crops with smaller plant constituents. The discrimination capability can be improved using C-band data. Indeed, the backscattering coefficient in this band is sensitive to small stems and leaves too. A simple algorithm which uses combined polarimetric data at P-, L and C-bands has been developed and tested with data collected with ERS-1/C-SAR, AIRSAR, SIRC-C and JERS-1/L-SAR. Nine classes have been separated: urban area, water body, forest, vineyards, olive groves, bare soil, sunflower, colza, and a class of mixed vegetation including wheat, alfalfa and pastures [Ref. 4]

Sensitivity to surface roughness

Since our data base includes data from P to X band at various polarization and incidence angles, we have investigated the influence of frequency, polarization and incidence angle on the response of various surface types. The highest sensitivity to soil roughness, at least in the investigated range of height standard deviations, has been noticed at L-band, copol, and $\theta = 35° - 50°$ [Ref.5].

A comparisons of experimental data with theory has been carried out considering direct relations between the backscattering coefficient and the surface roughness and soil moisture content. Since the degree of roughness of a surface is defined in terms of electromagnetic wavelength, a typical parameter used to investigate the variations of the backscattering coefficient with roughness is the product (ks) of the height standard deviation s with the wave number k ($k = 2\pi/\lambda$, λ = electromagnetic wavelength).

Experimental data have been compared with the Integral Equation Model [Ref. 6] implemented for single scattering. In the model the dielectric constant of soil was simulated by using a polynomial fit [Ref. 7], we assumed a soil with a mean value of texture (70% sand and 30% silt+clay), moisture SMC = 20 % and an exponential autocorrelation function with a correlation length l = 6 cm. Fig. 2 shows that the model (continuous line) reproduces quite well the data up tp $ks = 2$ where multiple scattering effects can be neglected. It should be noted that, whereas at L-band σ° gradually increases with ks, at C-band the saturation confirms that the same surface may appear rougher at C- than at L-band.

According to a semiempirical model developed by Oh et al. [Ref. 8] the parameters $p = \sigma^\circ_{HH}/\sigma^\circ_{VV}$ and $q = \sigma^\circ_{HV}/\sigma^\circ_{VV}$ can be related to ks, and to soil reflectivity Γ

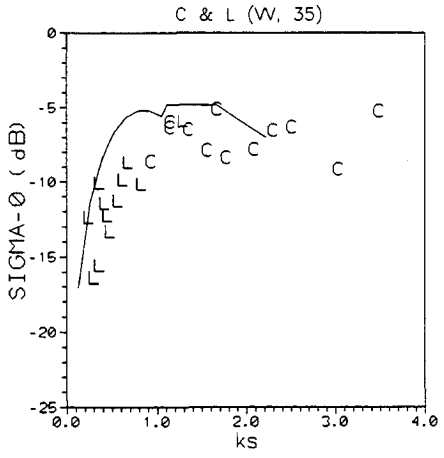

Figure 2 - σ°_{VV} at L- [L] and C-[C] band, $\theta = 35°$ (AIRSAR + SIR-C) as a function of *ks*. Continuous line represents the IEM model computed for l = 6 cm and SMC = 20 %.

The latter parameters can be retrieved with a satisfactory accuracy provided 0.1<ks<6 and 2.6<kl<19.7. Once Γ has been retrieved the correspondent soil moisture value can be computed trough an appropriate model [Ref.9]. The comparison between measured and retrieved height standard deviation of surface roughness is shown in Fig.3. We see that, in spite of some overestimation the obtained result appears rather satisfactory.

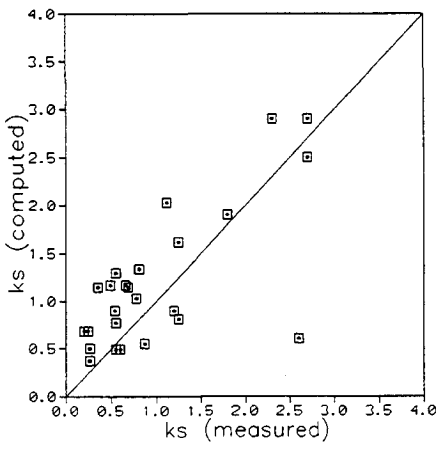

Figure 3 - Comparison of the retrieved and measured height standard deviation (normalized to wavelength)

Sensitivity to soil moisture

The sensitivity of a radar signal to moisture of smooth bare soils has been proven in many experiments carried out over the past years [Ref. 9]. However the radar signal is strongly influenced by surface roughness and vegetation cover as well, and separating the effects is not an easy task. The spurious effects are reduced for observation at incidence angle close to the nadir, but in this case the quality of SAR images is affected by the poor spatial resolution. According to data collected at Montespertoli, the highest correlation ($r^2 = 0.63$) and sensitivity (0.66 dB/ % SMC) to soil moisture is at L-band, HH pol., $\theta \sim 20°$ (Fig. 4).

A direct comparison of ERS-1 and SIR-C C-band backscatter with soil moisture of single fields shows that the correlation is rather low ($r^2 = 0.4$) (Fig. 5).

However, comparing data collected at different dates with ERS-1, SIR-C and AIRSAR, on the same area which includes twenty bare or scarcely vegetated fields (fig. 6), the correlation significantly increases ($r^2 = 0.9$). The average value of $\sigma°$ increases of about 5 dB as the SMC

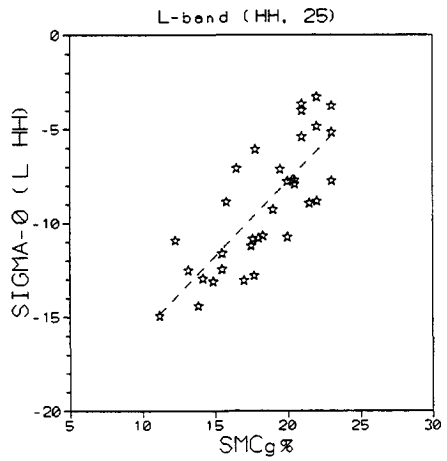

Figure 4 - σ°_{HH} at L-band, $\theta = 25°$ (AIRSAR + SIR-C) as a function of SMC of bare and scarcely vegetated (plant water content < 1 Kg/m^2) fields.

(gravimetric) increases from 5 % to 20%, which correspond to a sensitivity of 0.3 dB per % gravimetric soil moisture. A similar result has been obtained at L-band HH pol, $\theta = 25°$ with AIRSAR and SIR-C data.

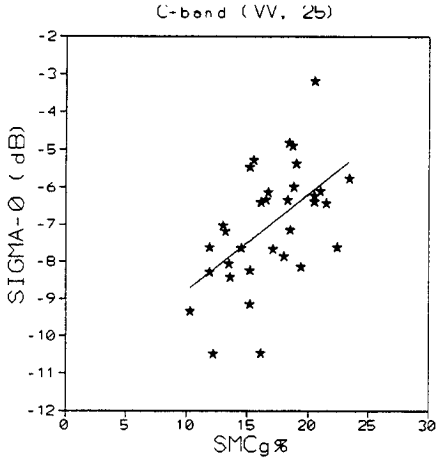

Figure 5 - σ°_{VV} at C-band, θ= 23° (ERS-1 + SIR-C), as a function of SMC of bare and scarcely vegetated (plant water content < 1Kg/m^2) fields.

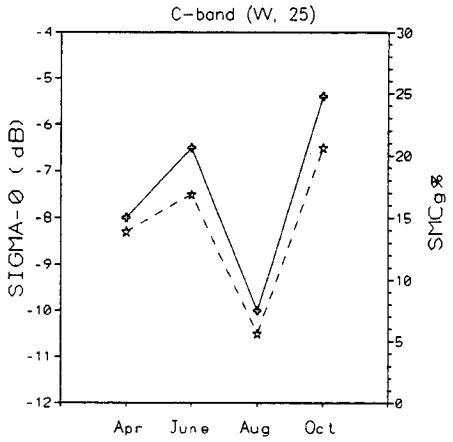

Figure 6 - σ°_{VV} at C- band, θ = 23° (ERS-1 + SIR-C) (continuous line) and SMC (dotted line) of an area comprising 20 bare or scarcely vegetated fields as a function of time.

4.FINAL REMARKS

The analysis carried on Montespertoli site using multi-frequency, multitemporal SARdata indicate that:

- multifrequency radar systems are quite effective in separating agricultural fields from other kinds of targets and in discriminating among agricultural species.
- in the scale of surface roughness typical of agricultural areas, a co-polar L- band sensor observing at two incidence angles (close to 20° and 35°/50°) gives the highest information content for estimating soil moisture and surface roughness.
- at the observation parameters of ERS-1 C-SAR the sensitivity to soil parameters on a spatial scale is rather low. However, considering data collected at different dates on the same area, the correlation and sensitivity to soil moisture is significant.
- good agreement has been found between experimental data and simulations with Integral Equation Model

5. REFERENCES

1. Dobson, M.C., Ulaby, F.T., Pierce, L.E. Sharik, T.L., Bergen, K.M., Kellindorfer, J., Kendra J.R., Li, E., Lin,Y.C., Nashshibi, A., Sarabandi, K., and Siqueira P. 1995, Estimation of Forest Biophysical Characteristics in Northern Michigan with SIR-C/X-SAR, *IEEE Trans. Geosci. Remote Sens.*, **33**, 877 - 895

2. Dubois P.C., van Zyl J.J., and Engman T., 1995, Measuring Soil Moisture with Imaging Radars, *IEEE Trans. Geosci. Remote Sens.*, **33**, 896 - 904.

3.Baronti S., F. Del Frate, S. Paloscia, P. Pampaloni and D. Solimini, 1995, SAR polarimetric features of agricultural areas, *Int. J. Remote Sensing*, 16, 2639-2656.

4. Ferrazzoli, P., Paloscia, S., Pampaloni, P., Schiavon, Sigismondi S. and Solimini, D., 1997, The potential of multifrequency polarimetric SAR in assessing agricultural and arboreous biomass . *IEEE Trans. Geosci. Remote Sensing,* Ge 35, 5-17.

5. Coppo P., G. Macelloni, P. Pampaloni, S. Paloscia and S. Sigismondi, 1996, The SIR-C /X-SAR experiment: the sensitivity of microwave backscattering to surface roughness of bare soils, *Proc. Int. Geosci. Remote Sensing Symp. (IGARSS96)*, Lincoln, Nebraska, 2131,2133.

6. Fung A.K., 1994, Microwave scattering and emission models and their applications Artech House Inc., Boston

7. Hallikainen M.T., Ulaby F., Dobson M.C., El Rayes M.A., Lin Ku Wu, 1985, Microwave dielectric behavior of wet soils - Part I: Empirical models and experimental observations", *IEEE Trans. Geosci. Remote Sensing*, vol. GE-23, pp. 25-33

8. Oh, Y. Sarabandi K. and Ulaby F.T., 1992, An empirical model and an inversion technique for radar scattering from bare soil surfaces, *IEEE Trans. Geosci. Remote Sens.* **30**, 370-381.

9. Ulaby F.T., Moore, R.K. and Fung, A.K., 1986, Microwave Remote Sensing: Active and Passive. Vol.III - *Surface Scattering and Emission Theory*, Artech House, Dedham, MA.

RETRIEVAL OF ENVIRONMENTAL AND GEOPHYSICAL PARAMETERS THROUGH BAYESIAN FUSION OF ERS AND RADARSAT DATA

Edmond Nezry, Francis Yakam-Simen, Iwan Supit, Francis Zagolski

PRIVATEERS NV Private Experts in Remote Sensing
42 De Weaver Drive, Philipsburg, Netherlands Antilles
Phone/Fax: (+39) 332-781494 / (+33) 61991724;
E-mail: edmond.nezry@iol.it / 106341.2602@compuserve.com
Internet Homepage: http://www.treemail.nl/privateers/

ABSTRACT

Two new Bayesian vector speckle filters have been developed for multi-channel SAR images. This filters incorporate first and second order statistical descriptions of the scene and of the speckle in multi-channel SAR images. Since these new filters present the structure of data fusion control systems, speckle filtering should be regarded as the first step of application oriented control systems to exploit the synergy between SAR sensors. Such a control system allowing the retrieval of soil roughness and soil moisture as well as the identification of snow covered areas from ERS and Radarsat images through Bayesian data fusion is presented. Results show that: 1) the new speckle filters present convincing performances for speckle reduction as well as for texture preservation and for small scene objects detection, 2) the retrieval of soil roughness and soil moisture as well as the identification of snow covered areas through Bayesian data fusion of ERS and Radarsat data provide valuable results.

1. INTRODUCTION

Important issues of interest in the field of multi-channel SAR images processing remain still open. Among them, the introduction of A Priori knowledge (or guess) in the processing of multi-SAR's images and multi-date SAR images. In the case of mono-channel SAR images, a Bayesian method, the Maximum A Posteriori (MAP) filtering method has already proved to be particularly suited for the restoration of both the radar reflectivity and the textural properties of natural scenes [1].
In the case of multi-channel detected SAR images, as described in [1,2], the i^{th} component R_i (channel i) of the radar reflectivity vector R is obtained when:

$$\partial \mathrm{Ln}(P(I/R))/\partial R_i + \partial \mathrm{Ln}(P(R))/\partial R_i = 0 \quad \text{for } R_i = \hat{R}_{i\,MAP} \qquad (1)$$

where I is the speckled intensity vector available in the actual SAR data. $P(I/R)$ is the joint probability density function (pdf) of the speckle. $P(R)$ is the joint pdf of the radar reflectivity, introduced as statistical A Priori information in the restoration process. The first term of Eq. 1, (Maximum Likelihood) accounts for the effects of the compound imaging system. The second term (Maximum A Priori) represents the prior statistical knowledge of the imaged scene. In the Bayesian inference process, induction is influenced by the prior expectations allowed by the prior knowledge of $P(R)$. Also the non-linear system and scene effects are taken into account by the restoration process. Therefore MAP speckle filtering can be considered as a controlled restoration of R, where A Priori knowledge controls the inference process, allowing an accurate estimation of the radar backscattering coefficients σ°_i.
At this point, additional Bayesian processes can be designed to retrieve important environmental and geophysical parameters, in a cascade of control processes.

2. MULTI-CHANNEL SCENE MODEL

It is now well established that a Gamma pdf would be the most suitable representation of the first order statistical properties of a natural scene. However, to describe these properties as viewed by diverse SAR sensors (different scene physics) or at different dates (scene evolution), there is no analytic multivariate Gamma pdf available. Therefore, we will use in the following a multivariate Gaussian pdf as analytic multi-channel (*i.e.* coupled) scene statistical model. This statistical model is convenient to preserve the mathematical tractability of the problem. In addition, the Gaussian model is still commonly used to describe the statistical properties of natural scenes.

3. SPECKLE MODELS AND MAP FILTERS

Let first consider the case of very different SAR sensors (very different wavelengths, for instance). In this case, it is justified to consider that the speckle is independent between the N image channels. Under this assumption, $P(I/R)$ can be modelled as a set of N independent Gamma distributions. Under this assumption, the *Gamma-Gaussian MAP filter for multi-channel detected SAR images* (N channels) comes down to the resolution of a set of N scalar equations [2]:

$$\begin{aligned} &L_i\,(I_i/R_i^2 - 1/R_i) - {}^t(1_i).C_R^{-1}.(R-\langle R\rangle) \\ &- {}^t(R-\langle R\rangle).C_R^{-1}.(1_i) - 1/2\ \mathrm{Tr}[C_R^{-1}.\partial C_R/\partial R_i] \\ &+ {}^t(R-\langle R\rangle).C_R^{-1}.\partial C_R/\partial R_i.C_R^{-1}.(R-\langle R\rangle) = 0 \end{aligned} \qquad (2)$$

where C_R is the covariance matrix of the scene, (1_i) is a vector where all components but the i^{th} are equal to zero, and the L_i are the Equivalent Numbers of Looks (ENL) of the individual SAR images.
Replacing the speckle noise model by the convenient optical noise model in the concerned image channels, this filter adapts easily to the case of multi-channel optical and SAR images. Thus, the introduction of coupling between the scene statistical representations is already a data fusion process.

On the other hand, in the case of multi-date images acquired on repeat-pass by the same SAR sensor, or of a set of images acquired by diverse SAR's with similar properties (similar orbit, track, frequency and resolution, with only different polarisation configuration, or small differences in incidence angle, for example), the correlation of the speckle between SAR image channels should be taken into account to deal optimally with system effects in the series. In theory, $P(I/R)$ should be a multivariate Gamma pdf. Nevertheless, since there is no analytic multivariate Gamma pdf available, another reasonable choice for $P(I/R)$ must be done for the sake of mathematical tractability: Lee [3] has shown that, in the case of multilook SAR images (more than 3-looks), $P(I/R)$ can be reasonably approximated by a Gaussian distribution. Under this assumption, the *Gaussian-Gaussian MAP filter for multi-channel detected multilook SAR images* is the set of equations [2]:

$$
\begin{aligned}
&{}^t(1_i).C_S^{-1}.(I-R) + {}^t(I-R).C_S^{-1}.(1_i) - 1/2\ \mathrm{Tr}[C_R^{-1}.\partial C_R/\partial R_i\ ] \\
&+\ {}^t(R-\langle R\rangle).C_R^{-1}.\partial C_R/\partial R_i\ .C_R^{-1}.(R-\langle R\rangle) \\
&-\ {}^t(1_i).C_R^{-1}.(R-\langle R\rangle) - {}^t(R-\langle R\rangle).C_R^{-1}.(1_i)\ = 0 \qquad (3)
\end{aligned}
$$

where C_S is the covariance matrix of the speckle.

4. MAP FILTERS AND CONTROL SYSTEMS

These filters offer numerous advantages, which are described in [2]: non linear image restoration, preservation of high-resolution through the correction of the effects of the compound multi-sensor imaging system, improvement of the probability of detection of thin scene structures due to both the diversity and redundancy aspects of information in all the channels.

Nevertheless, the most remarkable feature is that they present the structure of control systems. Both Eqs. (2) and (3) can be rewritten as Riccati's algebraic equations:

$$- A X - X\ {}^tA - Q + X\ {}^tC\ P^{-1}\ C\ X = 0 \qquad (4)$$

Equation (4) represents the optimal state controlled reconstruction at constant gain of linear invariant processes (R and textures of the channels) perturbed by white noises (speckle, pixel spatial mismatch between channels). It can easily be shown that the scene A Priori model acts as a command, and that the covariance matrices act as multipoles or controls.

5. FILTERING OF ERS / RADARSAT DATA SET

This new filtering technique is evaluated on a couple of Radarsat (C-HH) and ERS-1 (C-VV) SAR images, acquired along descending passes within 4 hours on Feb. 13, 1996. Figure 1 (left column) shows a detail of the Radarsat (up) and ERS-1 (bottom) images, around the Schipol-Amsterdam airport in the Netherlands.
The Radarsat and ERS SAR's operate at the same frequency from a very similar orbit (similar altitude and inclination angle). In this case, the angles of incidence are also very similar and image superimposition is possible without geometrical corrections over wide areas. The two sensors differ only in polarisation configuration, so that they are sensitive to similar physical properties of extended land areas, even if these properties do not contribute in the same amount to the backscattered signal. However, their different sensitivity to structural scene elements is of major interest for the identification of these particular targets. In this context, it is appropriate to use the new Gaussian-Gaussian MAP filter. The filtered images are shown in Figure 1 (right images). Thin details such as roads, runways, airport terminals, planes, point targets in the built-up areas, are very well denoised and preserved, as it is also the case for field edges. On the other hand, speckle noise is strongly filtered within the surrounding homogeneous agricultural fields (ENL=120 for Radarsat, ENL=100 for ERS-1). For both images, the filtered images were found superior in quality to the images filtered using the mono-channel Gamma-Gamma MAP filter [1] using the same structure detection algorithm [4].

6. BAYESIAN RETRIEVAL OF SOIL PARAMETERS

Haddad & Dubois [5] have developed a Bayesian estimation method of soil roughness and soil moisture. Although their method present some built-in limitations (the imaginary part of the dielectric constant ε is not taken into account, no dependence on the surface correlation, *cf.* [6]), it is based on the same principle as our new filtering method and present common theoretical advantages.
Since our data are accurately filtered and calibrated, instead of the model presented in [5], we can use directly the soil backscattering empirical model of Dubois *et al.* [7]:

$$
\begin{aligned}
\sigma^\circ_{HH} &= m = M_1\ (\theta,\lambda)\ .\ f(\varepsilon,h) \qquad (5)\\
\sigma^\circ_{VV} &= n = M_2\ (\theta,\lambda)\ .\ g(\varepsilon,h)
\end{aligned}
$$

where θ is the wave incidence angle, λ is the radar wavelength, ε is the soil dielectric constant, and h is the r.m.s. height (soil roughness).

Using Bayes' theorem, the unnormalised version of the conditional joint probability of (ε,h) verifies [5]:

$$P(\varepsilon,h|m,n) = P(\varepsilon,h) / [\, f(\varepsilon,h).g(\varepsilon,h) \,] \,.\, P(M_1, M_2) \qquad (6)$$

The optimum unbiased estimator for $X \in \{\varepsilon,h\}$ that has minimum variance is the conditional mean [5]:

$$\hat{X} = \int X \,.\, P(\varepsilon,h|m,n)\, d\varepsilon.\, dh \qquad (7)$$

Finally, the dielectric constant is converted to volumetric soil moisture through a set of empirical curves [8].

With our data accurately filtered and calibrated, the nature of the randomness present in (m,n) can only be due to relief. Since our Netherlands area present negligible relief, $P(M_1 , M_2)$ is reasonably assumed a Dirac distribution. This results in a straightforward estimation of $P(\varepsilon,h|m,n)$, *i.e.* a drastic simplification of the process and potentially more accurate results.

Results of this method, applied over the Netherlands (area size 73x63 km), are shown in Figure 2. Note that at this period of the year (February), the low/non-existent vegetation layer does not affect significantly the retrieval of soil parameters over agricultural areas (crops/pasture). As shown in this figure, snow covered areas (thin snow layer of a few centimeters), difficult to identify in the original SAR images, can be identified by simple classification of the soil moisture and roughness maps.

The interest of the quantitative results (especially soil moisture) for the initialisation of agro-meteorological and growth models has already been widely expressed. In addition, since soil roughness (in red) allows also the identification of cultivated areas, such a result can be a useful as a photo-interpretation tool, to support other agriculture applications such as crop surfaces estimation [9], or to monitor special environmental conditions (snow cover, frozen lakes, etc.).

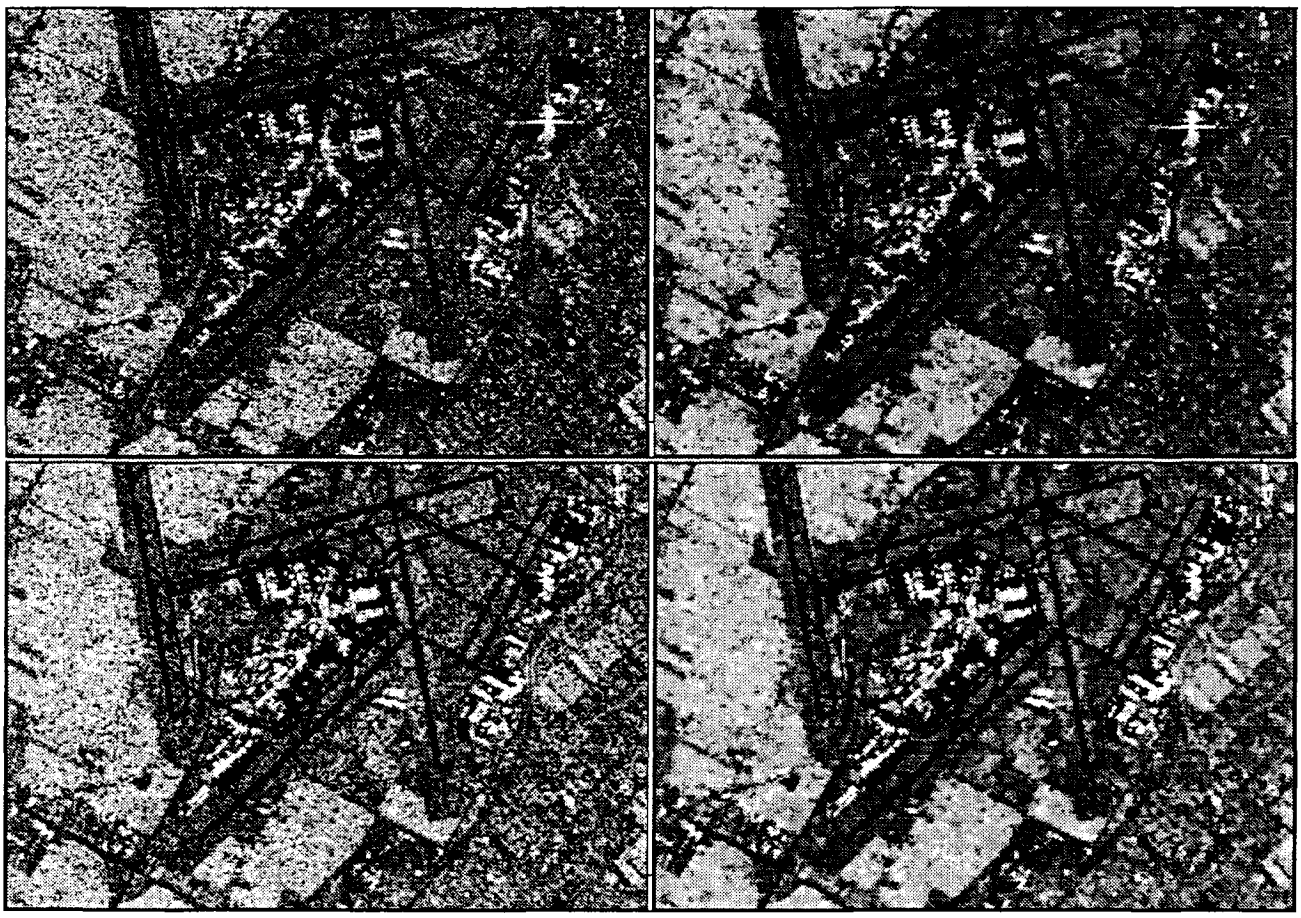

Figure 1: Upper images: original ERS-1 PRI image (13 Feb. 1996, ©ESA/Eurimage 1996) and its filtered version. Bottom images: original Radarsat Standard Beam image (13 Feb. 1996, ©Radarsat International 1996) and its filtered version (Gaussian-Gaussian MAP filter for multi-channel detected SAR images, 9x9 basic window size).

7. CONCLUSION

Two new Bayesian speckle filters have been developed for multi-channel SAR images, with very convincing results. The Gaussian-Gaussian MAP filter SAR images is suitable to process series of images from the same SAR system operating in repeat-pass mode or from diverse SAR's systems with relatively close properties. The Gamma-Gaussian MAP filter is suitable to process series of images originating from different SAR systems (different frequencies, incidence angles, or spatial resolution, but same spatial sampling). Combined with the two-points statistics based algorithm presented in [4], these filtering techniques are able to produce filtered images without loss in spatial resolution. Within homogeneous areas, speckle noise is strongly filtered, allowing the accurate estimation of σ° required by most of the remote sensing SAR applications such as the retrieval of soil parameters (roughness and moisture).
The major interest of this technique is that we apply pure control systems. This offers wide possibilities for the choice and the design of additional commands (statistical/physical models) for further data exploitation. In this view, speckle filtering should be regarded as the first step of integrated application oriented control systems rather than of processing chains.

ACKNOWLEDGEMENT

The ERS-1 and Radarsat images have been provided by the European Space Agency (Project PE-FRNE2) and the Canadian Space Agency (Project ADRO#581).

REFERENCES

[1] A. Lopes, E. Nezry, R. Touzi, H. Laur: "Structure detection and statistical adaptive speckle filtering in SAR images", *IJRS*, Vol.14, n°9, pp.1735-1758, June 1993.
[2] E. Nezry, F. Zagolski, A. Lopes, F. Yakam-Simen: "Bayesian filtering of multi-channel SAR images for detection of thin structures and data fusion", *Proc. of SPIE*, Vol.2958, pp.130-139, EUROPTO II, Taormina (Italy), 23-26 Sept. 1996.
[3] J.S. Lee: "Digital image enhancement and noise filtering by use of local statistics", *IEEE Trans. on PAMI*, Vol.PAMI-2, n°3, 165-168, March 1980.
[4] E. Nezry, M. Leysen, G. De Grandi: "Speckle and scene spatial statistical estimators for SAR image filtering and texture analysis: some applications to agriculture, forestry, and point targets detection", *Proc. of SPIE*, Vol.2584, pp.110-120, EUROPTO II, Paris (France), 25-29 Sept. 1995.
[5] Z.S. Haddad, P.C. Dubois: "Bayesian estimation of soil parameters from remote sensing data", *Proc. of IGARSS'94*, Vol.3, pp.1421-1423, Pasadena (CA), 8-12 Aug. 1994.
[6] M.S. Dawson, A.K. Fung, M.T. Manry, 1995: "Tools for soil moisture retrieval from radar measurements", *Retrieval from bio- and geophysical parameters from SAR data for land applications*, pp.295-305, Toulouse (France) 10-13 Oct. 1995.
[7] P.C. Dubois, J. van Zyl, T. Engman: "Measuring soil moisture with imaging radars", *IEEE Trans. on GRS*, Vol.33, n°4, pp.915-926, July 1995.
[8] M. Hallikainen, F.T. Ulaby, M.C. Dobson, M.A. El-Rayes, L. Wu: "Microwave dielectric behaviour of wet soil - Part 1: Empirical models and experiment observations", *IEEE Trans. on GRS*, Vol.GE-23, n°1, pp.25-34, Jan. 1985.
[9] E. Nezry, G. Genovese, G. Aa. Solaas, S. Rémondière: "ERS based early estimation of crop areas in Europe during the winter 1994/1995", *Proc. of the 2nd ERS Applications Workshop*, ESA SP-383, pp.13-20, 6-8 Dec. 1995.

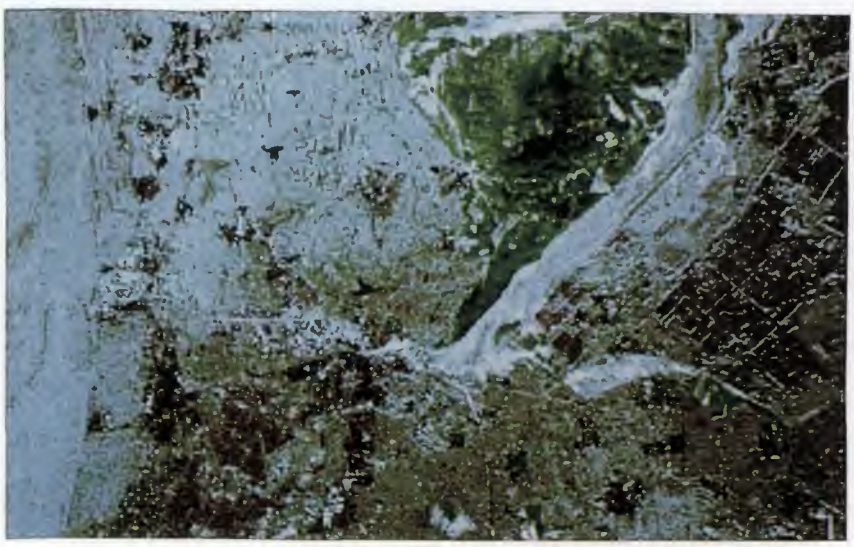

Figure 2: The Netherlands on February 13, 1996. Area size: 73x63 km. Red: soil roughness map. Green: soil moisture map. Blue: snow cover map. Maps produced using ERS-1 and Radarsat SAR imagery.

Land Use

Chairpersons: **H. de Groof & A. Sowter**

METHODOLOGICAL ADVANCEMENTS IN USING ERS SAR DATA FOR CROP AREA ESTIMATION.

Guido Lemoine, Richard Kidd, Hans van Leeuwen

SYNOPTICS, Integrated RS & GIS Applications BV, P.O. Box 117, 6700 AC Wageningen, the Netherlands,

Phone: +31 317 421221 Fax : +31 317 416146 E-mail: main@synoptics.nl

Hugo de Groof

Joint Research Centre, Space Applications Institute, MARS-AIS Unit

Phone : +39 332 785048 Fax : +39 332 789074 E-mail: hugo.de-groof@jrc.it

ABSTRACT

The paper reports the results of methodological research into the use of multi-temporal ERS SAR data for crop area estimation. This work has been carried out as part of the pilot project on the use of ERS SAR data for rapid area estimates of agricultural crops which was initiated by the DG VI of the European Commission with the technical and scientific support from the MARS Agricultural Information Systems unit of the Joint Research Centre. In the paper, an innovative methodological framework is presented to generate multi-temporal ERS image composites for optimal crop classification. The use of this method for early season and full season time series is presented and discussed. We show that soil moisture and surface roughness induced variation in backscattering signatures needs careful consideration in a crop classification approach. The use of calibrated geocoded and speckle filtered ERS image data has lead to a classification accuracy, which for the given sites and crops, can be considered superior than those obtained with SPOT optical/IR data. It is shown that the further integration of ERS-derived crop area estimates in the MARS operational activities is feasible and recommendable, under the condition that certain operational constraints are met.

Keywords: Agriculture, crop classification, constraints, MARS project

INTRODUCTION

The use of ERS SAR data for early season crop area estimation in the Monitoring Agriculture with Remote Sensing (MARS) program has reached a pre-operational status with the launching of an effort to produce area estimates in winter and spring for 60 sites in Western Europe. This effort is financed directly by the Directorate General VI (Agriculture) of the European Commission, and technically and scientifically supervised by the Agricultural Information Systems Unit of the MARS project of the Institute for Space Applications at the Joint Research Centre.

The 1997 activity, which is carried out by a consortium lead by NRSC Ltd (UK) and including SYNOPTICS, *Integrated Remote Sensing and GIS Applications BV* , follows a dedicated research effort in 1995 (SYNOPTICS, 1996a) and an experimental evaluation phase in 1996 (GAF *et al*, 1997). During the 1995 and 1996 projects, a number of critical items and constraints on the use of SAR data for crop area estimation have been addressed. This has lead to (1) the definition of the main requirements for SAR post-processing, (2) the development of a novel method for interpretation of SAR time series, and (3) the configuration of an interpretation environment in which a range of ancillary products are introduced in support of classification of temporal SAR signatures. The first of these items is further detailed in Sowter *et al*, 1997, and the latter in Kidd *et al*, 1997. This paper is concerned mainly with the description of the interpretation method.

The paper is structured as follows: in the following section, the methodology is described. The performance is illustrated with two examples for the Great Driffield (UK) and Bernburg (Germany) site. In the discussion, we address the accuracy in comparison with SPOT data for the same site, and illustrate some other interesting applications which are possible within the interpretation chain. We conclude with some remarks on expected further developments.

METHODOLOGY

The Activity B of the MARS project is focused on deriving crop area statistics for 60 sites in Western Europe. The operational of this exercise is based on the analysis of optical imagery during the growing season. For each site, between 1 and 4 optical images are

acquired for producing area coverages for all sites. The use of optical imagery allows production of the first reliable area estimates starting at the end of April after the first images have been processed. The use of optical images requires an appreciable reflection signal (hence, sufficient illumination by the Sun) and vegetation development (differentiation between bare and vegetated fields). Severe constraints due to cloudiness and haze are well known.

It has been recognised at an early stage that the use of SAR might advance the earliest date of crop area generation because microwave backscattering that underlies SAR image formation is sensitive to surface roughness change as well. Thus, in principle, the separation of soil surfaces by roughness type could lead to an early indication of generic crop classes, such as grass land, winter crops (smooth seedbeds at the onset of winter) and spring/summer crops (rough fields). Furthermore, in a multi-temporal approach, one should be able to follow transitions in surface roughness, which are indicative of soil tillage, and, while crop-specific, useful in further specification of crop classes. The potential of using autumn and spring SAR imagery for crop area estimation was reported previously (Lemoine *et al*, 1995, Nezry *et al*, 1996).

Because backscattering values are geo-referenced and calibrated it is possible to carry out SAR image interpretation in a quantitative manner, as long as a number of ancillary data are available. Information content in single SAR images is often limited, at least for agricultural scenes, and especially in the autumn to spring period. Therefore, a multi-temporal approach is usually adopted. A first advantage of such an approach is the possibility to reduced speckle, but also to follow transitions over time with calibrated backscattering signatures. In most studies, multi-temporal time series are combined in a composite and then classified, usually after some clustering has been performed. The success of such a classification is dependent on the parameter settings of the clustering algorithm, and the expertise of the operator in assigning specific clusters to definite crop classes.

In the 1996 project, we have tested the performance of a classification approach based on the use of synthetic channel composites (Nezry *et al*, 1996). In a synthetic channel composite statistical parameters of the time series are combined in a 3 channel composite. In our case, we have used the mean of the series, the range (difference between maximum and minimum) and the date of maximum backscattering. Mean, range and date of maximum are calculated on a per pixel basis. Classification was then based on an isodata clustering followed by regrouping of clusters and class assignment (GAF *et al*, 1997).

The evaluation of the classification performance with information from dedicated field surveys (SYNOPTICS, 1996b and 1996c) and MARS Action 6 surveys revealed that the results were non-optimal (SYNOPTICS, 1996d). This was partly due to several factors that influenced the quality of the individual images (geocoding, speckle filtering, adverse surface conditions), but also due to difficulties in the interpretation of the synthetic channel composite information content. A main drawback of the applied synthetic channel composite technique is the effect of soil moisture on the range and date of maximum backscattering. In the classification, one is mainly interested in separation of roughness and roughness transition events. In fact, soil moisture induced backscattering change constitutes an unwelcome noise factor that needs to be compensated first.

The evaluation led to an improvement of a method proposed during the study phase in 1995 (SYNOPTICS, 1996a). The so-called byte-sliced composite method recognises the fact that in typical SAR imagery for the autumn and spring periods, delineation of classes of agricultural fields is typically limited. The method codifies this observation by interactively slicing the SAR image (calibrated filtered geocoded (CFG) data) into 4 classes. In this way, an image can be stored with 2 bit per pixel. A logical OR operation on bit-shifted images creates a composite in which the indices are directly related to the membership of the various slices in the individual images. Since the limits of the slices are known, a direct correspondence with backscattering coefficient limits exists. The procedure to generate byte-sliced composites is illustrated in Figure A, for an combination of 3 images. The result is a composite in which the indices range from 0 to 63 (4^3-1). Extension into integer or even long-integer composites is possible.

The use of the composite has the following advantages:

- Up to 4 images can be combined in one byte (up to 8 in an (unsigned) integer, etc.)
- The effect of soil moisture is compensated partly by the introduction of the histogram quantile stretch, assuming a multiplicative effect of soil moisture change on the backscattering coefficients of bare soil
- Since all processing steps are documented, a full retracing of the procedure is possible.
- The calibrated signature values can be used in a signature data base. Automation of the interpretation procedure may be realised.

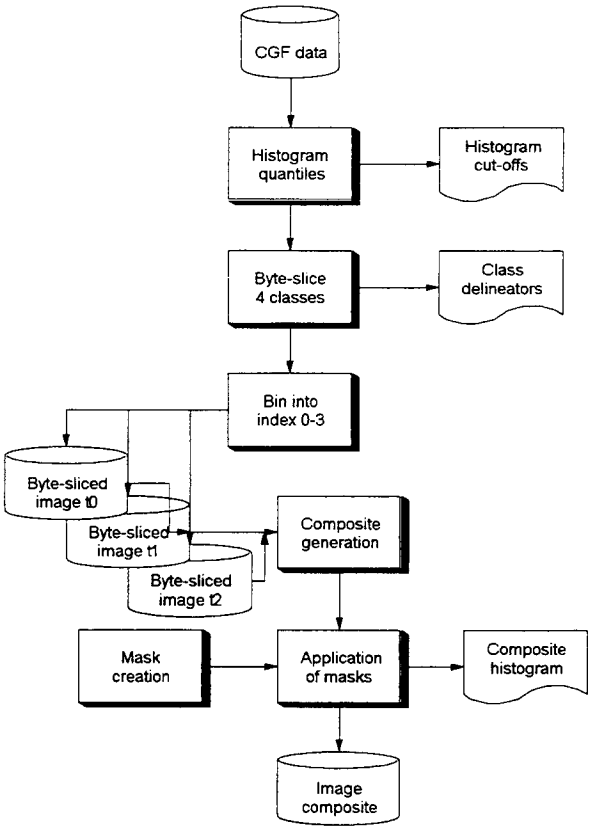

Figure A. Byte-sliced composite generation for SAR image interpretation.

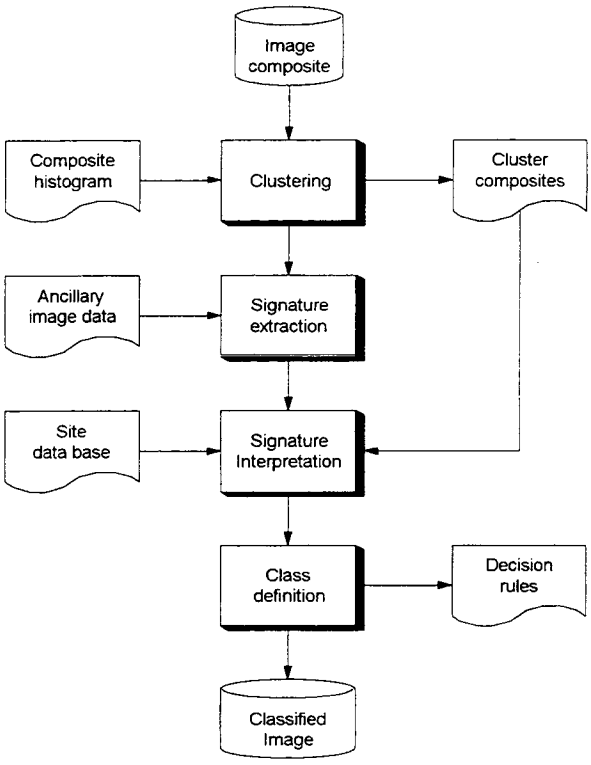

Figure B. The workflow in the image interpretation procedure.

The image composite is input into an image interpretation scheme, that is not very different from other image classification exercises (Figure B). Apart from the composite a number of other ancillary image products are used e.g. previous classification results, optical imagery, digital elevation models and raster maps as well as non-image data (meteorological records, crop calendar information (Kidd *et al*, 1997)). All these products are combined in support of interpretation of the temporal signatures that lead to the generation of a certain index in the byte-sliced composite. For instance, if one has a series of 3 images from autumn and spring, then index 0 in the composite means that the pixel (or field) has been assigned to the lowest slice in all 3 images (and is grassland in this case). Index 63 means membership of the three highest slices for all instances.

For autumn and spring combination, membership to slices is mainly determined by surface roughness conditions, which determine the backscattering coefficient of the bare and partly vegetated fields. For combinations that include summer imagery as well the characteristic signature of the crop canopy is another determinant.

RESULTS.

The use of the byte-sliced composite is illustrated with an example ERS time series of the Great Driffield MARS site in the United Kingdom. This site is characterised by a large area of arable land in the centre of the site, with winter and spring cereals, oil rape seed, potato and sugar beet as main crops. In the lower areas of the site, grass land is found more frequently. The site is located on the East coast, with its centre at approximately 54 N and 0 W. Annual precipitation amounts to some 600 mm and temperature extremes are typically between -5 and 25 degrees.

In Figure C, the results for a combination of 3 winter and spring images is shown (26 December 1995, 25 February and 31 March 1996). In this image, grass land, winter crops and spring and summer crops are delineated. The differentiation between spring and summer crops is the most difficult, since the spring of 1996 was unusually cold, with snow covers still present in half March. The classification results were assessed with field survey data that were collected in the second half of March (SYNOPTICS, 1996b). An accuracy of approximately 70 percent is reached, with apparent confusion between grass land and winter crops. This confusion is due to the spectral proximity of these two

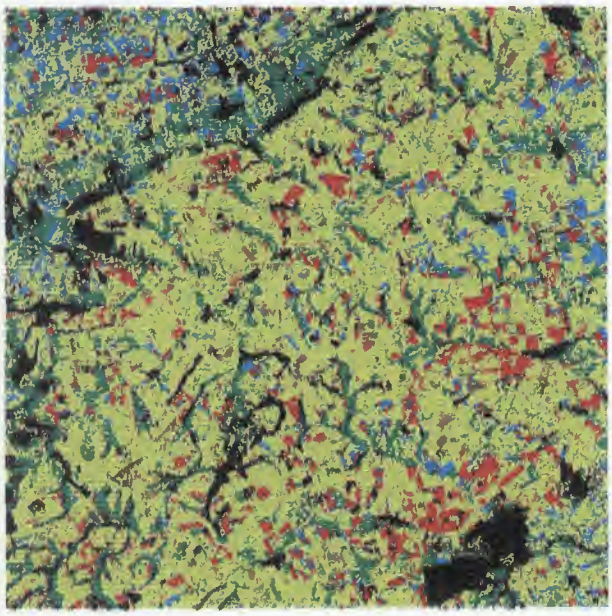

Figure C. Crop classification result for the Great Driffield MARS site, using autumn and spring ERS SAR images.

classes (which are effectively smooth bare fields, with little vegetation). In Kidd *et al*, 1997, we have presented the classification of a 4 image composite (25 February, 23 April, 9 June and 14 July 1996). In it, at least 6 distinct classes can be separated. The distinct signatures and contrast in the summer images cause a crisp delineation of field boundaries. The most interesting features of this combination are the distinction between winter wheat and winter barley, and the classification of oil rape seed (these are the major crops in the area that are supported with EU subsidies). In fact, the choice of the image combination was tuned to this purpose. Again, the classification was quality assessed with the ground survey data that were collected in March and those of dedicated surveys on cereals in June and July (SYNOPTICS, 1996c). The overall accuracy is around 80 percent (for details, see Kidd *et al*, 1997). The winter cereal classification has an accuracy higher than 90 percent. The separation between winter barley and winter wheat is possible since cereal ripening has a distinct effect on the crop backscattering signature, and barley ripens approximately 3 to 4 weeks earlier than wheat. The June and July images are exactly timed around this period. The separation of oil rape seed is possible, because the backscattering strongly increases after the end of April. Most summer crops (potato, sugar beet) also have a relative high signature in summer, but development is somewhat later, and the February image is used to separate these from oil seed rape because of their rough (ploughed) surface conditions. The inclusion of this early spring image is also essential in the separation of grassland.

A comparison of the classification results with SPOT derived results could only be made with the intermediate classification results for April, May and June imagery. This has shown that the SAR derived product performs better, especially with respect to the delineation of distinct crop classes. In the SPOT imagery, crop class specification is often limited to generic classes, even after the (third) acquistion in June. The separation between winter barley and winter wheat seems not to be possible in SPOT imagery. On the other hand, early spring SPOT imagery is very useful in fine-tuning separation between bare soil, winter crops and grass land. Limited synergetic efforts show positive effects of combining this image with early season SAR series. Also, field delineation is usually much better in single data SPOT imagery. Combinations with later SPOT images do not show significant improvements, unless the SPOT image captures a distinct spectral event, such as the flowering of oil seed rape at the Bernburg site in early June.

A further example is shown in figure d. The classification result for the Bernburg MARS site in Germany is shown. The composite method was extended to integers to create compositions of 6 sliced-images. Note that this creates 4096 different indices that need to be combined in clusters. The set of indices is dominated, however, by a subset of indices that relates to the signatures of distinct crop classes. In fact, some 200 indices constitute more than 65% of the pixels, with another 23% pixels included as masks. Thus, the majority of the indices belong to small fragments, that somehow need to be clustered. In the example image, these small fragments have been left unassigned to illustrate this point.

SAR image combinations in general are very effective in highlighting effects that are of use in image interpretation exercises. For instance, the separation of spring cereals can be improved with additional images in early April and May. An example combination that shows the effect of the soil is shown in Figure E. The image is a composition from the March 31 and April 9 acquisitions. During this period, there was no rain. With relatively little vegetation development because of low temperatures, the composite shows the effect of differential drying in the scene. A comparison with the 1:1,000,000 soil map of Europe is shown. The effect of drying is largest (4-6 dB) for the loamy soil in the centre area of the site, and much smaller for the lower areas that are characterised by clayey soils which suffer from water logging. Note also that roughness changes are included in this image, but the clear drop in backscattering values for winter cereals indicate that soil moisture change is the main mechanism (vegetation coverage is below 25% at the time). Other combinations are useful in emphasising roughness effects. For example, an ascending and descending

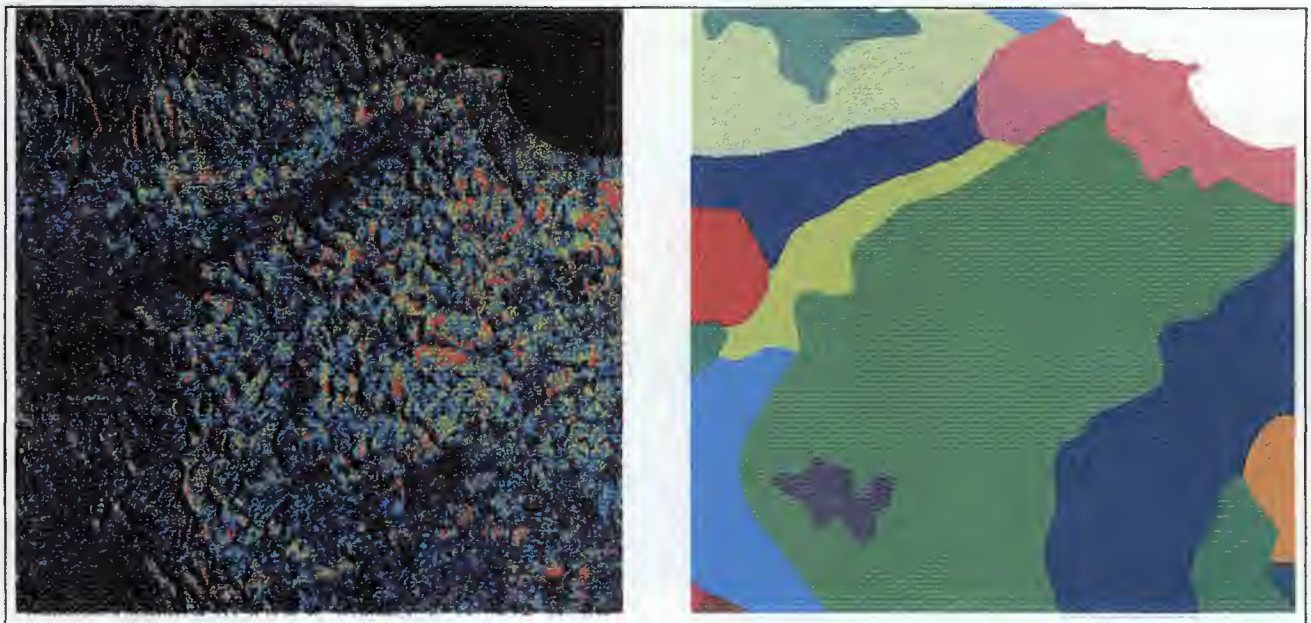

Figure E. A SAR image combination (left) for the Great Driffield site spanning a short period of drying in early April. The image is compared to the soil map in the right image.

combination in April clearly show the effect of look modulation for rough field with clear row patterns (ploughed fields and potato ridges).

Another aspect of signature analysis is the use of reference fields that are used to compensate for soil moisture change. Winter crop fields in the autumn and early spring, and potato fields up to the end of June serve this purpose very well. We have used this approach to highlight backscattering features that are related to roughness change and vegetation development. This shows that the major trends for the Great Driffield and Bernburg sites are very similar, though different in absolute levels. We expect this to be related to both soil and crop canopy differences. In an experiment for winter cereals, we have used the different sensitivity to soil moisture change in summer for the Great Driffield and Bernburg sites to highlight canopy attenuation effects that clearly differ between the two sites (SYNOPTICS, 1996f). It is speculated that this effect is due to lower wet biomass of the cereal canopy at the Bernburg site because of soil water deficit.

Figure D. A byte-composite classification for the Bernburg site (6 image combination).

CONCLUSIONS.

We have presented a simple technique for deriving crop classification products from multi-temporal SAR series. The method is based on the fact that in single SAR imagery only a limited amount of backscattering classes can be delineated, especially in the autumn to spring period. A recombination of scattering classes leads to a better separation of image clusters that are directly related to distinct backscattering signatures. The interpretation of these signatures into crop classes is then driven by the use of ancillary data resources.

We have shown that the performance of the proposed method is satisfactorily for separation of generic crop classes in early season imagery. Performance with image combination that include summer acquisitions was shown to be better than those currently produced in the optical image interpretation exercise in the MARS Action 4 project (at least for the Great Driffield site). Especially the more reliable timing of SAR image

interpretation exercises is of considerable importance in the context of crop area estimation. Furthermore, the method can easily be extended to include any combination between 2 and 16 images (although a selection of 6 seems to set a practical limit).

The rigorous documentation requirements of the method allow a full reproducibility and evaluation of processing steps. Since all intermediate products are stored, small errors are easily corrected.

Other image recombinations were shown to be helpful in delineating backscattering features that are useful for determination of soil and vegetation cover effects. Such features can then be used in the assessment of biophysical parameters or specific crop types.

It should be emphasised that the application of the method requires precise geocoding of SAR imagery and a good performance of speckle filtering and image calibration. Also, an image pre-screening exercise is necessary to filter out images with sub-optimal class delineation characteristics (e.g. due to snow, frost or drought). Obviously, successful implementation of a agricultural monitoring exercise with SAR data requires close interaction between the data supplier and the data user. Also, pricing policy should be tailored to wide area coverage and multi-temporal series in order to generate statistically significant crop sampling. Decentralised image reception on location could very well enhance the acceptance of SAR imagery in such agricultural monitoring exercises.

Since the MARS project constitutes an advanced operational framework for remote sensing applications in agricultural monitoring, ample possibilities exist to carry out further research in SAR dat use. In fact, the various SAR activities has led to the creation of a formidable data set. Future efforts will be directed to integration with optical data sets, improvement and automation of the interpretation cycle and testing of wide area sampling.

ACKNOWLEDGEMENTS

This work has been partly carried out under contract OJ 95/C203/07 which was funded by DG VI and supervised by the MARS project.

REFERENCES

GAF, SYNOPTICS and NRSC, 1997, A pilot project on the use of active microwave sensors for the rapid area estimation of Agricultural crops, Final Report O.J.95/C203/07, 700+ pp.

Kidd, R., Lemoine, G., and de Groof, H., 1997, Integration of ERS SAR Classification Products in the MARS Activity B "Rapid Area Estimation" Methodology, Proc. 3rd ERS Scientific Symposium, Florence, Italy, 17-20 March 1997.

Lemoine, G., van Leeuwen, H., and de Groof, H., 1995, Proc. ERS Applications Symposium, London, Dec 4-8, 1995.

Nezry, E., Solaas, G., Remondiere, S., and G. Genovese, 1995, Mapping of next season's crops during the winter using ERS SAR. Earth Observation Quarterly, No 50 Dec 1995.

NRSC, 1996, Evaluation of the SAR Processing Chain. Project Report O.J.95/C203/07, National Remote Sensing Centre, Ref DG-TR-NRL-AP-001, Issue 1.0, July 1996

Sowter, A., Lemoine, G., and de Groof, H., 1997, , Proc. 3rd ERS Scientific Symposium, Florence, Italy, 17-20 March 1997.

SYNOPTICS, 1996a, ERS-1 Data Analysis, Final Report MARS Contract Study 10946-ISP NL.

SYNOPTICS, 1996b, Spring field survey report, Project Report O.J.95/C203/07, Ref O.J.95/C203/07/1.1 /GGL.

SYNOPTICS, 1996c, Cereal field survey report, Project Report O.J.95/C203/07, Ref O.J.95/C203/07/3.1 /GGL.

SYNOPTICS, 1996d, Methodological Advancements, Project Report O.J.95/C203/07, Ref O.J.95/C203/07/5.1 /GGL.

SYNOPTICS, 1996e, Assessment of Crop Separability, Project Report O.J.95/C203/07, Ref O.J.95/C203/07/5.1 /GGL.

INTEGRATION OF ERS SAR CLASSIFICATION PRODUCTS IN THE MARS ACTIVITY B "RAPID AREA ESTIMATION" METHODOLOGY

Richard Kidd, Guido Lemoine

SYNOPTICS, Integrated RS & GIS Applications BV, P.O. Box 117, 6700 AC Wageningen, the Netherlands,

Phone: +31 317 421221 Fax : +31 317 416146· E-mail: main@synoptics.nl

Hugo de Groof

Joint Research Centre, Space Applications Institute, MARS-AIS Unit

Phone : +39 332 785048 Fax : +39 332 789074 E-mail: hugo.de-groof@jrc.it

ABSTRACT

The MARS Activity B "Rapid Area Estimation" has been an operational project for the last 5 years. It is based on the interpretation of high resolution optical imagery, collected throughout the growing season, for 60 sites in the EU to derive estimates on crop area changes at the level of the European Union. Within the MARS Agricultural Information System, a number of ancillary data products are routinely collected which may aid the image interpretation. This paper addresses the use of these ancillary products in support of the interpretation of ERS SAR time series for area estimation. The work has been carried out as part of a pilot project on the use of ERS SAR data for rapid area estimates of agricultural crops which was initiated by the DG VI -Agriculture of the European Commission under the scientific and technical supervision of the MARS AIS unit of the Joint Research Centre. While the analysis of backscattering signatures has been presented in a separate paper, we concentrate on the methods used for, and constraints placed upon the use of ERS images for crop area estimation. Methods for the fusion of ERS data with other spatial and non-spatial data sets in a dedicated information system are presented. Limitations and constraints of the different data sets are documented and recommendations made. Although currently carried out in a separate data analysis environment, we show that integration in a dedicated interpretation software environment is highly feasible.

Keywords: Agriculture, crop classification, operational, MARS project

INTRODUCTION

This paper offers an outline of the MARS data sets as used in the context of the DG VI project "A Pilot project on the use of active microwave satellite remote sensing data for rapid area estimation of agricultural crops". After a brief overview of the MARS project, the application and incorporation of these data sets into a SAR classification methodology is then presented, along with the inherent limitations, before finally drawing conclusions from the use of, and recommendations for the future implementation the MARS data sets.

The MARS Project (Monitoring Agriculture by Remote Sensing) has been operational since 1988 when it was launched as a pilot project for remote sensing applied to agricultural statistics. The overall operational aims of MARS project,(MARS-STAT) (Vossen, 1994) are twofold: firstly to distinguish, identify and measure, on a yearly basis, the area of economically important crops in Europe. Secondly, derivation of estimates of crop production early in the year. This rapid estimation of agricultural crop area is implemented within the framework of Activity B, (Action 4) of the MARS project. These estimates are presently derived from analysis of high-resolution optical satellite images acquired either from SPOT or from Landsat Thematic Mapper.

Action 4 is based upon the derivation of crop area estimations at a European level, with results extrapolated from a series of 60 sites. Each of these sites, distributed over the member states of Europe, covers an area of 40 x 40 km, thus offering a total coverage of 4% of the agricultural area within Europe.

The accurate identification of crop types depends on the availability of images acquired within specific time windows throughout the crop growing season. The timeliness and the quality of information derived from passive optical systems suffers from a number of constraints, for example extensive cloud cover in Northern Europe throughout the agricultural season. It is also noted that the discrimination of crops early in the growing season based solely upon their radiometric signatures in the optical domain, is inherently limited.

The on-board Synthetic Aperture Radar (SAR) systems of ERS satellites are, to all extents, independent of

cloud cover and daylight conditions. These capabilities are of particular interest for the MARS Action 4 test sites lying in Northern Europe, where the ability to collect optical imagery within relatively narrow time windows is problematic.

But along with this SAR has a great potential for early crop identification. The sensitivity of this instrument to changes in surface structure and moisture, allow for the identification and classification of soil surfaces being prepared for different crop types during autumn and winter. Therefore allowing a possible approach to an early identification of crops and, consequently, crop areas.

During the course of its activities the MARS Project has collected, and archived large amounts of data and gained experience in the fields of remote sensing, agronomy and related statistical analysis. These data sets held within the MARS Project vary from remotely sensed data, agronomic data, meteorological data along with derived products, and other types of spatial and statistical material.

In the context of the DG VI project "A Pilot project on the use of active microwave satellite remote sensing data for rapid area estimation of agricultural crops" several of the above mentioned data sets of the MARS project have been utilised in the development of the SAR interpretation methodology. Although this project was only aimed at providing area estimations for 20 Action 4 sites within Northern Europe, the rationale behind this paper is that the methodology for the use of these data sets can be applied to all Action 4 sites.

DESCRIPTION OF DATA SETS

In this classification methodology six unique sources of ancillary data have been identified. Specifically these are high resolution optical data products, meteorological data, digital elevation models, soils information, agronomic data sets, and ancillary site information.

High resolution Optical Products

For all of the 60 Action 4 sites of MARS Project, high resolution optical imagery (SPOT and Landsat TM) are acquired up to 4 times a year. The analysis of this imagery forms the foundation of the MARS Project activities in the area of yield prediction. The output from this analysis results in two data products, per image, at a site level. Firstly the unclassified optical imagery, and secondly a visually interpreted classification of the optical imagery. Over the operational lifetime of the MARS project the MARS archives now holds approximately 1750 raw optical images, along with all corrected and classified imagery.

The optical imagery undergoes a complete correction procedure. For each image radiometric, atmospheric and geometric correction is applied. In order to minimise data handling procedures data extraction is required. For SPOT XS images all 3 channels are extracted, whilst for TM images only channels 2,3,4 and 5 are extracted. The final product is then resampled to 20m pixels. (Noting that the final product is orientated to the SPOT imagery.)

The classified, interpreted, imagery is available at two levels. The main product is a final composite classification, which has been updated and corrected with ground survey observations, and is available on a yearly basis. In the classification procedure a series of processing steps are applied including the application of specific masks for non-agricultural areas. Secondly the intermediate visual interpreted classification is available for all optical images.

Meteorological Data

The MARS Project meteorological database contains historical daily weather observations from several hundred meteorological stations across Europe. The spatial extent of this data includes coverage of the new EU member states. This data set is updated on a decadal basis, with a hiatus of 4 days for processing and validation of data This is then extrapolated to give meteorological data scaled to a 50 by 50 km grid coverage of Europe, as implemented in the CGMS (Crop Growth Monitoring System) (van der Voet *et al*, 1994) system of the MARS Project. This data set is available either as diurnal measurements or decadal (10 day) averages. In order to exploit this information each site of interest must be related to the 50 by 50 km grid coverage of Europe.

Digital Elevation Models

Digital elevation models (DEM) exist in two formats. The first is a set of low resolution DEMS, as used in the within the GRIPS (Geographic and Radiometric Image Processing System) software for the pre-processing of the optical high resolution imagery. These offer the complete coverage of each Action 4 site, and have pixel resolutions in the order of 160 to 640 m.

Further to these DEMS a series of high resolution (50 m resolution) DEMS exist clipped to each Action 4 site.

Soils Information

The MARS Project activities include the development and maintenance of the European Soils Database (via the European Soils Bureau). This database is presently available for 12 Member States of the EU, and also covers extensions into Central and Eastern Europe. For

the remaining three EU member States work is being scheduled

The European Soil Database (King *et al,* 1995) is based on the 1:1,000,000 FAO soil map, and consists of soil mapping units (SMU) as its basic polygons. The SMU's describe the basic soil characteristics in terms of physiographical parameters (e.g. geological parent material, altitude, land use and limiting factors). Every SMU can have several soil topological units (STU), which correspond to soil types. Soil types are given using the FAO soil name. For a number of STUs detailed information on soil texture, slope and agricultural restrictions are available.

Agronomic Data Sets

The MARS Project Action 6 yield and ground survey data is a point-based system that has been operational since 1994. The sampling points are located in a grid of segments that are distributed across the sites. The positioning of the segments depending upon agricultural stratification of the site. These segments are 1440m by 1440m and contain 40 points distributed on a grid. For each point, the crop class, yield, and cropping information is registered on a yearly basis during a summer survey. Each site has a maximum of 16 segments, giving a maximum total of 640 points of data per site.

This point based agronomic data set is also reinforced by documentary agronomic information as compiled for use within CGMS.

Ancillary Site Information.

This collated data set consists of geographic information at a site level, detailing site and point locations, locations of sites with respect to European grid coverage, and image projection information.

MANAGEMENT OF DATA SETS

In the scope of this project there is obviously a necessity to provide effective management and access to all the ancillary data sets and data products. To realise this requirement a structured coherent data base has been developed and implemented (SYNOPTICS, 1996a). Along with the ancillary data sets from the MARS archives, a number of other data sets, collected within the context of this project are also stored. Specifically these include the results from the dedicated field surveys carried out by SYNOPTICS in the spring and summer of 1996 (SYNOPTICS, 1996b and SYNOPTICS, 1996c), and extracted (polygon based) signatures from ERS and SPOT imagery (SYNOPTICS, 1996d and SYNOPTICS, 1996e)

Within this database data for 20 sites is included. Field survey data for 1996 comprises 5000 Action 6 point locations, nearly 1900 polygons for 8 sites surveyed in the spring and over 400 polygons for the Bernburg and Great Driffield sites in summer. Over 25,000 ERS backscattering coefficients have been included for the various ground locations.

The 47 data base tables have been organised into 7 thematically related groups, as listed in table a. By structuring all relevant site information in this way, access and retrieval of information has been vastly improved.

Table A. Organisation of thematic groups in data base.

Groups	*Description of content*
Site information	Site information
Crop calendars	Crop calendars for sites
Soil map information	Soil map legends and codes
Meteorological records	Meteorological data for sites
SPOT quick looks	Information related to (external) SPOT quick looks
Ground surveys	All information related to the survey data
Signatures	ERS and SPOT signatures for known ground locations

INCORPORATION OF DATA SETS IN THE ERS METHODOLOGY

All of the above mentioned data sets have particular roles in the processing and classification of multi-temporal SAR imagery. In order to emphasis the specific uses of the data sets, the two aspects of the processing (figure 1) and classification methodology (figure 2. 2) are approached and presented separately. The specific uses of these data sets are summarised in table b.

Data Processing

Data screening is performed to ensure the quality of any imagery before the product is ordered. Initially temporal windows of opportunity are identified for dates of optimal image acquisition, (optimal in the sense of the possibility for identification of distinct crop types). Imagery is then selected on a basis of complete site coverage occurring during the optimal dates, and a quick look of the image acquired. Meteorological data

for dates preceding image acquisition is required to check for any meteorological events (heavy rain occurring at time of acquisition, frost, snow, etc.) that are likely to influence the quality of the imagery.

As the final composite (SAR) image is only required for the area extents of each specific site all images are subset to the Action 4 site and projected in SPOT image coordinates.. This requires the use of precise site location and rotation knowledge. Within this project all image data has been processed with the dedicated TSAR (Topographic SAR Processor) system at NRSC Ltd. (NRSC, 1996) using the 50 meter spaced DEM for detailed calibration and terrain correction. The data used in this study are derived from calibrated, geo-referenced GMAP (Nezry *et al,* 1993) filtered PRI data (termed CFG data in this report).

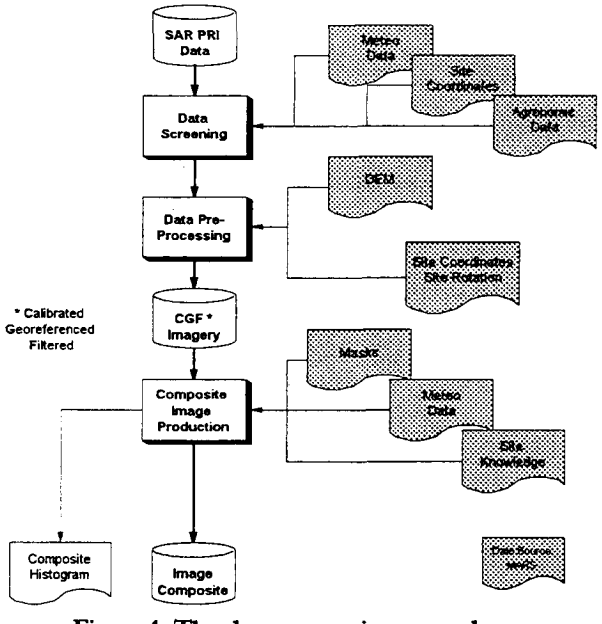

Figure 1. The data processing procedure

In the production of the Composite Imagery , (byte sliced image composite, Lemoine *et al,* 1997), it is necessary to have an understanding of the site specific agricultural conditions at the time of acquisition. Firstly to remove areas of potential confusion in the image non agricultural areas can be masked out using the masks derived from the optical classified imagery. Information with respect to the crop types and practices in the area can be determined from both agronomic data sets and from the explicit classes identified in the final verified optical classifications. By incorporating this knowledge with the historical agronomic information, crop rotation schemes can be determined, and hence the likelihood of finding certain crop types in certain areas can be evaluated. The meteorological data is here used not only to determine the likelihood of extreme or adverse conditions, but also, in conjunction with the soils data sets, for estimation of the surface moisture conditions at the time of image acquisition.

Classification Methodology

The classification procedure applied is analogous to the well known unsupervised classification methodology. It is imperative that within this procedure each interpreter working on a per site basis has as much relevant information as possible. By using these data sets the interpreter must develop a complete understanding of not only the topography of the area, but also how this relates to the expected agricultural practices at the time of image acquisition. Furthermore the interpreter must have a complete understanding of the physical nature of the cover types present, and also an understanding of the effects of agricultural practices upon the backscattered signal.

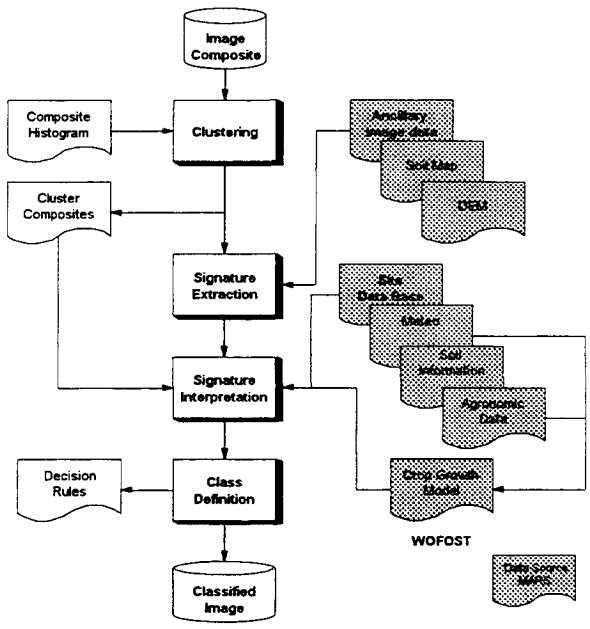

Figure 2. The workflow in the Classification Procedure

Data Products	*Purpose*
Activity B optical imagery	Site familiarisation, crop statistics and spatial distribution, reference geometry, Site Mask Production
Meteorological data	Data screening, interpretation of backscattering signatures for PI, soil/surface moisture estimation
Soil data	Site information, relation with crop distribution, backscattering modelling, potential for stratification of site.
Digital Elevation Models	Geo-coding of ERS data, site information
Agronomic information	Crop calendar knowledge, crop rotation.
Ancillary Site Information	Site Location and Image Processing routines.

Table B. Summary of use of data Products

In areas where there is a lack of *a priori* knowledge about certain cover types, it is also possible to incorporate outputs from agronomic models, such as the WOFOST crop growth model (Supit *et al, 1994*), to predict cover development stages.

A summary outlining the main uses for the MARS derived data sets is given in table b.

RESULTS.

To illustrate the benefits of the inclusion of these data sets in our classification methodology, we present in Figure 3 a comparison between our knowledge steered classification and an unsupervised isodata classification. Data is shown for a 20 by 20 km subset of the Great Driffield MARS Action 4 site in the UK. Four CGF images were used (dates: 25/02/96, 23/04/96, 09/06/96, 14/07/96). The timing of this series of images is considered optimal for the discrimination of the main crop types across this site (a total of 13 images between November 1996 and August 1996 were available).

In our classification the following five distinct classes can be delineated: oilseed rape (RAP), spring barley (SBA), grass land (GRA), winter barley (WBA) and winter wheat (WWH). For the summer crops, a distinction can be made between the peas/sugar beet (PEA/SBT) fields and other summer crops (SUM, mainly potato (POT), spring oil seed rape).

The classification accuracies have been assessed with the field survey results for spring and summer. The spring survey, carried out at the end of March concentrated on separation of winter crops and early spring and summer crops (the latter two both at bare soil stage). The summer survey, carried out in mid June and Mid July was focused on separation of cereal types. The results are summarised in table c and table d.

Table C. Classification accuracy assessment with spring field survey data. The top table is for the ISODATA classification, the bottom table for the byte-composite method.[1]

Crop	BSM	BSR	BSS	PEA	POT	RAP	SBA	SBT	STB	WBA	WWH
GRA										2	3
OTH			1								5
PEA/SBT		1				1			4	7	
RAP	3	1		3		26		1	2		1
SBA	6	4		1			3	1	1		14
SUM	20	4	1	4	6	1					
WBA	2									20	2
WWH		1					1		2	2	30

Crop	BSM	BSR	BSS	PEA	POT	RAP	SBA	SBT	STB	WBA	WWH
GRA	1								5		2
PEA/SBT	11	2	2	5	2	1			1		
RAP	1				1	24			1		1
SBA	4	2					2	1			17
SUM	13	6		3	3	3	1	2			1
WBA	1									25	1
WWH		1					1		2	6	31

[1] Other crop codes used in table c to table e are: BSS=smooth bare soil; BSM=medium rough bare soil; BSR=rough bare soil; STB=stubble; WIN=winter crop; SPR=spring crop; MIX=mixed class; FAL=fallow; FOD=fodder; OAT=oats; MSK=image masks.

In the tables, the polygons that are rightly classified are printed **boldface**, those that are wrongly classified are underlined. Ambiguous cases are in normal typeface. The total number of fields are 187 and 186 for the ISODATA and byte-composite classification, respectively. The total number of polygons was 205 (a 30% threshold was used, and small classes have been removed). The number of rightly classified fields for the ISODATA classification is 124 (66.3%), the number of wrongly classified fields 53 (28.3%). For the byte-composite these number are 130 (69.9%) and 47 (25.3%) respectively.

Looking at confusion between spring barley and winter wheat is the most obvious. This is most likely due to the late timing of the available April acquisition. It seems more appropriate to aggregate the classes SBA and WWH. In that case, the number of rightly classified fields increases to 139 (74.3%) and 148 (79.6%) for ISODATA and byte-composite classification respectively.

Table D. Classification accuracy assessment with summer survey data.

	ISODATA					BYTE-COMPOSITE				
Crop	GRA	OAT	SBA	WBA	WWH	GRA	OAT	SBA	WBA	WWH
GRA	2			2	3	3			3	1
OTH		1	1	1	9					
PEA/SBT				8			1	1	1	2
RAP				2					1	
SBA			10	1	27			10	1	26
SUM			1	2	1			1	2	1
WBA			1	41	3				46	2
WWH		2		6	75		2	1	8	86

In table d the results for the summer survey are shown. A total of 208 fields were sampled. 199 field were used in the assessment for both methods. The number of rightly classified fields is 129 (64.8%) and 145 (72.9%) for ISODATA and byte-composite methods respectively. Aggregation of SBA and WWH yields 156 (78.4%) and 172 (86.4%).

Although the overall performance improvement of 5% seems not too impressive, other observations point out a generally better performance of the byte-composite classification method. For instance, the various summer crop types are better delineated in the byte-composite classification. This is due to the fact that cluster assignment is better controlled in the byte-composite method. During signature analysis and interpretation, special weights can be given to backscattering features that relate to a certain crop type, while ISODATA classification lacks this option. Of importance also is that we have used *a priori* information to tune the number of clusters in the ISODATA classification. Thus, also simple ISODATA classification benefit from the use of ancillary data.

As a last quality assessment step, we have generated area estimates for the complete site for both classification, and compared these to the results generated with SPOT data (3 images) during the Action 4 activity in 1995 (table e). There are a number of interesting observations in this table. The first is related to the definition of the classes in the SPOT and SAR-based classifications. The SPOT classification includes fallow land and fodder. Since separation of this class is not possible in the SAR classification, we expect this class to be aggregated in the GRA class for SAR (considering that surface conditions are approximately equal). The ISODATA classification might have grouped these in the class OTH. The difference in WWH percentages is found back in the SBA class for the SAR. Apparently, neither SPOT nor SAR is successful in separating these classes. RAP separation is by far superior in SAR data than in the SPOT data. POT stands out better in SPOT data. The SPOT classification includes 13.3% of mixed classes, while the byte-composites class has only 1.8% unknown pixels (which are mainly distributed randomly across the site).

Table E. Area estimates derived from various classification products for the Great Driffield site.

Crop	SPOT 1995	Byte-composite	ISODATA
WWH	31.2	21.3	15.5
WBA	9.8	9.3	8.9
RAP	0.5	6.2	8.4
POT	4.4		
FAL	9.4		
FOD	0.2		
GRA	10.2	17.7	8.2
WIN	9.2		
WIN/SPR	0.8		
MIX	3.3		
SUM		8.4	6.5
PEA/SBT		6.1	10.4
SBA		9.1	11.3
OTH		1.8	10.4
MSK	20.9	21.1	20.4

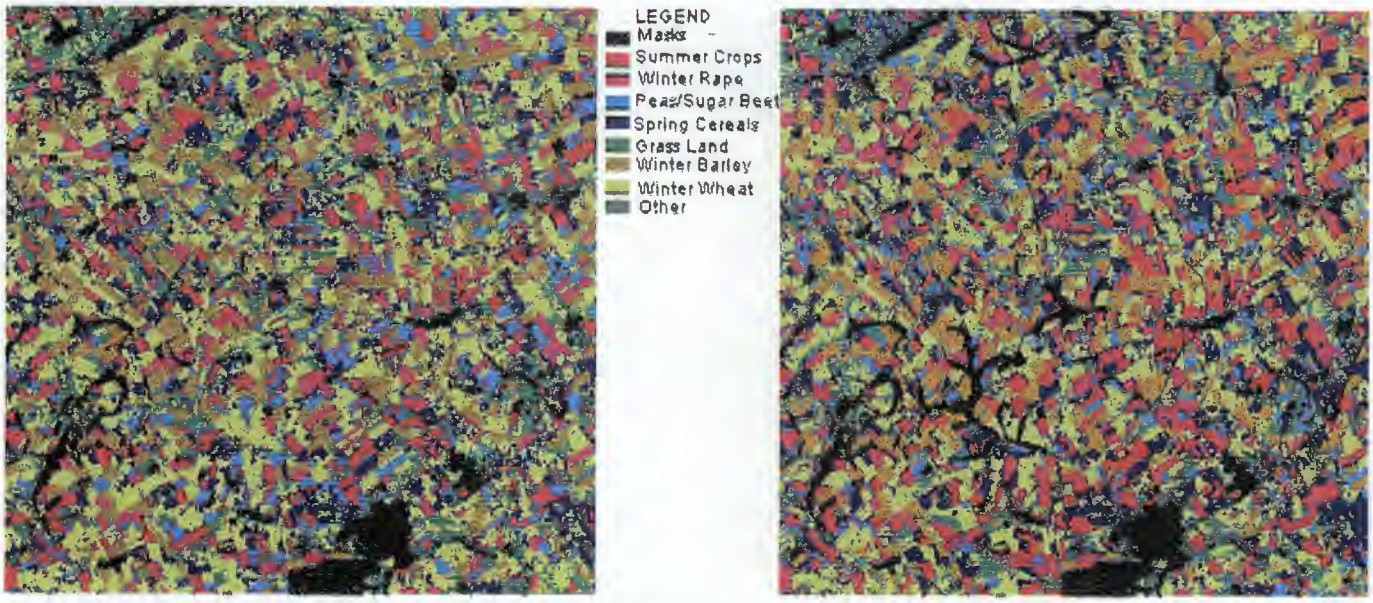

Figure 3. Colour coded classification result for Great Driffield, using an optimal 4date composite. Knowledge steered classification (left image), and an unsupervised ISODATA classification (right image).

CONCLUSIONS.

We have presented the use of a SAR classification methodology within the operational framework of the MARS program. The methodology is based on a sound analysis of SAR backscattering signatures with the support of a large set of ancillary data sets that are part of the MARS archives. The relevance of the different data sets has been described in detail.

In the SAR processing methodology, ancillary data sets already play an important role at data planning (crop calendars, previous classification results) and data screening (meteorological data, soil maps, crop maps). During interpretation this set, together with site knowledge, significantly improves the accuracy of cluster assignment.

The method was illustrated in comparison to an unsupervised ISODATA classification (which was partly guided by *a priori* information). An improvement in classification accuracy of approximately 5 percent was found for the example SAR series for the Great Driffield site. A comparison of area estimates derived from both byte-composite and ISODATA classifications against SPOT 1995 results, suggest that the byte-composite method can generate crop area statistics that are better than those derived from SPOT imagery. It should be noticed that although the results presented in this paper are for one site only, consistent improvement have also been found for the Bernburg site (Germany).

Confirmation of these results would need extrapolation to other MARS sites. This is currently done in a follow-up project, funded by DG VI.

With respect to improvement in ancillary data sets, we have found that ground survey data on a field polygon basis are more advantageous in classification accuracy assessment than Action 6 ground survey data (point based) that are part of the MARS archive. Soil maps sometimes show a shift in location, due to the rather large scale. At the moment, the MARS project team is considering the creation of a 1:250,000 soil map data base. Crop information might be further improved with information on tillage methods and their effect on surface conditions.

Ancillary image sets might include segmented optical images for better field boundary detection and topographical maps for better registration of SAR imagery at geocoding stage.

ACKNOWLEDGEMENTS

This work has been carried out under contract OJ 95/C203/07 which was funded by DG VI and supervised by the MARS project. The authors would like to thank Iwan Supit and Carmelo Attardo of the MARS project for critical contributions to this work. Further appreciation goes out to SYNOPTICS staff Leon Schouten and Onno Luimstra for carrying out the field surveys and Hans van Leeuwen for comments and support.

REFERENCES

King, D., Burrill, A., Daroussin, J., Le Bas, C., Tavernier, R., van Ranst, E., 1995: The EU Soil Geographic Database, European Land Information Systems For Agro-Environmental Monitoring, Eur 16232 EN, pp 43-60

Lemoine, G., Kidd, R., van Leeuwen, H., de Groof, H., 1997, Methodological advancements in using ERS SAR data for crop area estimation,. In Proceedings 3rd ERS Scientific Symposium, Florence, Italy, 17-20 March 1997

Nezry, E, 1993, The Refined Gamma-Gamma MAP Speckle Filter, EEC Expert Contract n°EARS 92-0004-FR, pp74, 1 June 1993

NRSC, 1996, Evaluation of the SAR Processing Chain. Project Report "A pilot project on the use of active microwave sensors for the rapid area estimation of Agricultural crops" O.J.95/C203/07, National Remote Sensing Centre, Ref DG-TR-NRL-AP-001, Issue 1.0, July 1996

Supit, I.., Hooijer, A.., A.., van Diepen, C., A., 1994, System Description of the WOFOST 6.0 Crop Simulation Model Implemented in CGMS, Volume 1: Theory and Algorithms. An Agricultural Information System for the European Community, EUR 15956 EN, pp144

SYNOPTICS, 1996a, Site Data Base Description, Report O.J.95/C203/07, Ref O.J.95/C203/07/7.1 /GGL.

SYNOPTICS, 1996b, Spring field survey report, Project Report "A pilot project on the use of active microwave sensors for the rapid area estimation of Agricultural crops" O.J.95/C203/07, Ref O.J.95/C203/07/1.1 /GGL.

SYNOPTICS, 1996c, Cereal field survey report, Project Report "A pilot project on the use of active microwave sensors for the rapid area estimation of Agricultural crops" O.J.95/C203/07, Ref O.J.95/C203/07/3.1 /GGL.

SYNOPTICS, 1996d, Assessment of Crop Separability, Project Report "A pilot project on the use of active microwave sensors for the rapid area estimation of Agricultural crops" O.J.95/C203/07, Ref O.J.95/C203/07/5.1 /GGL.

SYNOPTICS, 1996e, Potential of Data Combinations, Report O.J.95/C203/07/6.1 /GGL.

van der Voet, P., van Diepen, C., A., Oude Voshaar, J., 1994, Spatial Interpolation of Daily meteorological data. A knowledge based procedure for the regions of the European Communities. Report 53.3. The Winland Staring Centre, Wageningen, The Netherlands, Joint Research Centre, Ispra, Italy

Vossen, P, 1994, Early Crop Production Assessment of the European Union: The Systems Implemented By the MARS-STAT Project, Workshop For Central and Eastern Europe on Agrometeorological Models: Theory and Applications in the MARS Project., Ispra, 21-25 November 1994, pp 21-57

CLASSIFICATION OF ERS-1 SAR DATA OVER SEVILLE (SPAIN) FOR AGRICULTURAL STATISTICS

G. Kattenborn* and H-Gg. Klaedtke**

*Dep. Remote Sensing and Landscape Information Systems, University Freiburg, Tennenbacherstr. 4, D-79106 Freiburg, Phone: +49-761-800 937, Fax: +49-761-800 934, E-mail: kattenborn@t-online.de
**Institute for Navigation, University Stuttgart, Geschw.-Scholl-Str. 24D, D-70174 Stuttgart, Phone: +49-711-121 3418, Fax: +49-711-121 2755, E-mail: joerg@nav.uni-stuttgart.de

ABSTRACT

A time series of nine ERS-1 SAR images of the MARS sample site Seville, four SPOT XS images and ground surveys of 17 MARS segments all from 1992 have been available for the study. Preliminary masks of non-agricultural areas derived from thematic maps are refined by multi-temporal, unsupervised classification of optical satellite data. Stratification was performed using visual interpretation of SPOT data for refining macro-structural units of the region around Seville extracted from relevant literature. During preliminary investigations it turned out, that significance of supervised classification is limited due to limitations of the available ground truth. A robust, transferable approach is presented, which allows to retrieve crop types/single crops from ERS-1 SAR data on the base of unsupervised clustering. The recombination of clusters to classes is performed using ancillary knowledge (e.g. local agricultural practice, parcel structure). The method is detailed with the example of a single stratum. Application to the other strata of the Seville site proved functionality of the method. There are significant indications, that ERS-1 SAR data could be used as complement or substitute to optical satellite data. With regard to the operational needs of the MARS project the potential for an operationalisation of the approach seems to be high.

Keywords: ERS SAR, MARS, Masking, Stratification, Unsupervised Classification

1. INTRODUCTION

The MARS (Monitoring Agriculture with Remote Sensing) project includes an activity to derive area statistics for agricultural crops based on satellite imagery. The Joint Research Centre (JRC) decided to select more than 50 sites spread over Europe as an area frame sampling scheme. For the sample sites each of 40 km * 40 km size SPOT or Landsat TM data are acquired nominally four times during a growing season (*MEYER-ROUX, J. and VOSSEN, 1994*). The main drawback consists in the fact, that cloud cover often hinders acquisition of optical images. ERS Synthetic Aperture Radar (SAR) data will allow to fill temporal gaps of optical coverage, as well as to ensure all over the year coverage of the sample sites. Considering potential of ERS SAR data for agricultural use (e.g. *KOHL et al., 1994; HARTL et al., 1995*), it is intended to introduce these data into the MARS project in order to

- get complementary or additional information to optical data
- substitute optical data, especially in the early growing season

in the framework of MARS rapid estimates (RE). For a corresponding study the area around Seville, one of the important agricultural regions of Spain, with a wide range of crops, was selected. The scientific and practical results, achieved with this study, should be made transferable to other sample sites and to operational applications like RE aiming at a possible integration of ERS-1 SAR data into the operational system of MARS.

2. TEST SITE

Most of the Seville testsite belongs to the lowlands of Andalusia, which are characterised by the Guadalquivir valley. Morphologically this landscape is slightly hilly (Campinas) except of some steep slopes close to the Guadalquivir. Between the southern part of Seville and the delta of Guadalquivir flat marshland (Marismas) is located. Corresponding to *MADUEÑO (1991)* the region around Seville can be stratified into 13 different macro-structural agro-physical units. Only 11 out of 13 units are covered by the area under investigation.

In principal climate in Andalusia is typical Mediterranean with hot, dry, summers and mild winters. Due to few rainfall during summer months this area belongs to the semiarid region. This implies, that either irrigation or dry farming is practised for successful agriculture. The mosaic of soils in the area of interest is rather different. Main soil types are Tirs soil, recent Terra Rossa, relicts of Terra Rossa with lime and marl, Marsh soils.

Grown *permanent cultures* in Andalusia are to olives, wine, fruits (citrus, peaches), eucalyptus, pine trees, pastures, horticulture. Grown *temporary crop types* in Andalusia wheat, barley, oats, sunflower, maize, sugar beet, safflower, soya, sago, sorghum, potatoes, rice, cotton, broadbeans, chickpeas, water- and sugarmelons, tomatoes, lucerne, herbs *(MADUEÑO (1991)*.

There are two cultivation practices of *temporary crops*:

- Traditional dry-farming,
- so called wet farming (artificial irrigation).

Dry farming (two or three field rotation with a long period of fallow) has decreased within the last years. Traditional crops for dry-farming were cereals, maize, and crops grown on fallow land like broadbeans, chickpeas, and other fodder plants. If wet farming is practised, rice, sugar beet, potatoes, and legumes are grown but with

minor importance. Because of EU-activities some crops were added to the traditional crop catalogue like sunflowers, soya, and sago. Therefore the traditional crop rotation has also changed.

3. DATASET AN PRE-PROCESSING

Satellite and ground truth data delivered by SAI/AIS of JRC (Space Applications Institute/Agricultural Information System) have been implemented on the computer system at the Institute for Navigation (INS) of Stuttgart University. Additionally topographic and thematic maps of the Seville area as well as statistical and geographical information have been acquired. For the Seville MARS sample site there have been chosen 17 instead of regularly 16 MARS segments. This 17 segments were visited by field survey teams during May and June 1992. Tab. 1 contains a list of the available ERS-1 SAR PRI and SPOT XS acquisitions.

Tab. 1: Acquisition date of Satellite data

ERS-1 SAR	Day of year	SPOT	Day of year
22.04.1992	112	23.03.1992	082
27.05.1992	147	08.06.1992	159
01.07.1992	182	01.07.1992	182
05.08.1992	217	26.08.1992	238
09.09.1992	252	-	-
14.10.1992	287	-	-
18.11.1992	291		
23.12.1992	326		
27.01.1993	27	-	-

Additionally a SPOT-PAN scene of 28.02.92 was added giving an overview and orientation in fine resolution, and allowing photo-interpretation of details (Fig. 1).
Pre-processing for ERS-1 SAR PRI images partly applied at SAI/AIS partly at INS comprises extraction of subframes, image resampling to 20 m * 20 m pixel size, compression of 16- to 8-bit data, speckle filtering (*LOPES et al. 1993)*, and full calibration (*LAUR, 1992*).
The available SPOT-PAN ortho-image was used as master image for the geocoding of the ERS-1 SAR images. Due to the use of an ortho-image, i.e. a map representation at sea level as master image it is not absolutely necessary to introduce a DEM into the geocoding process. During geocoding by polynomials of n-th order and during following resampling, orbit and relief introduced distortions are corrected. A set of 45 ground control points and a first order polynomial was used for this procedure resulting in standard errors of about 100 m in East and about 50 m in North direction.

4. POTENTIAL OF ERS-1 SAR DATA FOR CLASSIFICATION

A test has been performed based on means and standard deviations of training areas (*DOBSON et al., 1992)* in order to assess the potential of supervised classification using the polygons of MARS segments as training areas. Results show, that only very limited differentiation of landcover and crop types is possible. According to a detailed examination also most of the histograms showed up multimodal distributions, i.e. several spectral classes within one ground truth class. It also turned out, that the number of samples available for a crop or landcover type was not sufficient in many cases with respect to statistical (i.e. minimum number of samples >100*)* or physical considerations.
Due to these restrictions it was necessary to modify the approach in the sense, that first a statistically sound procedure has to be applied to identify the intrinsic information content ERS-1 SAR data, followed by an appropriate input of ancillary information for a final classification (*NEZRY ET AL., 1995*). The following main prerequisites for this approach have been identified and considered to be fulfilled for the Seville dataset:

- Homogeneous scene conditions (as provided by masking and stratification see chapters 5 and 6),
- knowledge about occurring land use / crop classes,
- knowledge about phenological development and related spectral reflectance / backscatter behaviour of the occurring crop classes.

On the one hand the method should be objective and reliable leading to an overall classification of the Seville site. On the other hand it should be transferable and operational within the MARS project. Following this considerations a processing chain consisting of four hierarchical levels has been developed.
Within *level one* the introduction of expert knowledge and ancillary data allows a reduction of spatial, spectral, and temporal dimensions of the dataset by masking and stratification.
Within *level two* the intrinsic information content of the remaining dataset (respectively single stratum) is isolated by means of a statistical sound algorithm like ISODATA clustering. This process is supported by ancillary information regarding the potential number of clusters and the number of iterations during clustering.
Within *level three* the final land use/crop classes are identified through deductive interpretation of the ERS SAR clusters using simultaneously general knowledge regarding agriculture (main crop types present on the site, crop calendars, tillage practices), physics (interaction of electromagnetic waves and target), and statistics (examination of cluster structures). Special emphasis has to be laid on the parcel structure/ geometry within the clustered dataset. Clusters which fit together in the corresponding parcel structure are combined and assigned to one land use/crop class.
Validation is carried out within *level four* using ground truth data for comparison with the classification results. In case of substantial errors interpretation flow returns back to level three, where a new clustering with different parameters has to be carried out.

5. MASKING

For an accurate classification of agricultural land use considering the limited information content of single frequency spaceborne SAR data it is useful to mask non-agricultural areas like roads, urban areas, water surfaces

and forests in order to avoid misclassifications. Compared to agricultural fields these areas are characterised by their permanent surface cover types, i.e. signals detected by satellite sensors over these areas are relatively stable during a year or by year to year. Thus, reliable masks of non-agricultural land use can be created from optical satellite data already available for the MARS sites.

⇒ Applied method

For creation of masks of non-agricultural areas an interactive hierarchical classification approach of SPOT XS data was applied (*KATTENBORN et al., 1996*). A separate evaluation for each theme - roads, sealed areas, forest - was performed. In a first step so called "rough masks" are created. Supported by thematic maps clearly recognisable areas of the desired classes are delineated on the screen. In a second step for every mask type a principal component analysis (PCA) is carried out using these rough masks as reference for the statistical input. In a third step for each type of mask an unsupervised cluster analysis is performed using the transformed SPOT XS bands followed by an selective assignment of resulting clusters to the respective theme. In a final step all derived masks are combined to a single mask of „non-agricultural use".

6. STRATIFICATION

On the base of a signature analysis using MARS ground truth and corresponding SPOT reflectivities or ERS-1 SAR backscatter profiles no indications for a possible stratification of the Seville site have been recognisable., since no systematic variations of signatures with respect to the geographic diversity of the site could be found. Contrary to this visual interpretation of the available satellite images (SPOT XS and PAN, ERS-1 SAR) allows a clearly recognisable differentiation of photomorphologic units of the Seville site.

This technique was used to prepare the available information (macro-structural units, *MADUEÑO, (1991)*) by correcting and homogenising it for further use in ERS-1 SAR data evaluation. Important criteria for the stratification have been differences in site condition, topography, parcel structure, irrigation, number of harvests per year, and the regional agricultural practice. For practical reasons it was necessary to restrict the number of strata, but still to take into account essential differences of their agricultural use. With respect to these criteria five strata (Fig. 1) of the Seville testsite have been defined. However, the 17 MARS segments foreseen for the validation of the adopted classification approach are distributed non-uniformly over the strata; strata two and four contain each six segments, stratum five still four, stratum one only one; for stratum three ground truth is completely missing.

7. CLASSIFICATION RESULTS

The classification approach has been tested with all strata of the Seville site. Using „stratum 1" the single steps of the method are elaborated including a thorough analysis of results based on the available ground truth.

Results Stratum 1

- Description of stratum 1

Stratum 1 encloses the flat marshland of the Marismas (*MADUEÑO 1991*). The area is intensively cultivated, because of sufficient water supply and good soil fertility. A high proportion of rice is grown there but also winter cereals, maize, sunflower, and other summer crops (e.g. cotton) are cultivated. In most of the ERS-1 images parcel structure is discernible. This clearly recognisable geometric pattern results from dams, irrigation canals, and country lanes between the parcels. For the only existing MARS segment (No. 11) in this stratum ground survey delivered rice, maize, sunflower, water and urban areas as land use /crop types.

- Clustering

According to crop calendars many crops are already harvested half-way through the year. On these areas mostly fallow can be found after harvesting. In some areas probably the following crop was already sown respectively field preparation was done. The corresponding signals acquired with late year satellite measurements are therefore superimposed on the desirable information of spring/summer acquisitions leading to confusions during the clustering process. Thus, cluster analysis was carried out using only ERS-1 SAR data of 22.04.92, 27.05.92, 01.07.92, and 05.08.92.

According to the available a priori information five main crop types have to be expected for the stratum, namely rice, maize, winter cereals, sunflower, and other summer crops. Thereby summer crops have been considered as collective class, where no further discrimination is possible. In order to consider the backscatter variations within single crop classes due to different environmental conditions and locally varying agricultural management a sufficient number of initial clusters has to be provided to obtain homogeneous clusters with a reasonable low standard deviation. Thus, a maximum potential number of clusters of 13 was used.

- Recombination of clusters to crop classes

For the recombination and assignment of clusters to crop classes different levels and types of information have been used simultaneously. Only clusters are combined, which fit into parcel structure, i.e. which „fill up" single parcels. It has to be pointed out, that in practice smaller parts of parcel structure cannot be fully completed this way due to inhomogeneities of cluster results. Assignment of clusters to crop types was done using a priori knowledge concerning the occurring crop types and related cultivation practice , and by interpretation of backscatter signatures and statistics of the clusters. Thus, 12 resulting clusters have been finally assigned to land use classes as listed in Tab. 2.

Tab. 2: Cluster assignment to crop types and corresponding areas for stratum 1 of the Seville site.

Cluster No.	Assigned crop type	Area [ha]
1	Winter cereals	1011
2, 6, 12	Maize (1-3)	4138
3, 9	Summer crops (1, 2)	1387
4, 5, 7, 8, 11	Rice (1-5)	4565
10	Sunflower	666

- Spectral separability of clusters

Using the Bhattacharrya distance *(RICHARDS, J. A., 1986)* a separability test based on the backscatter signatures of the resulting clusters was carried out in order to assess, how far a discrimination of assigned clusters respectively crop types is possible using only their backscatter behaviour (Tab. 3). Values below 1.0 indicate a poor, between 1.0 and 1.9 a medium, and above 1.9 a good separability. In no case a poor separability was obtained. Surprisingly different clusters assigned as rice have a medium separability to other crop types but a good separability to each other (not listed in Tab. 3). By visual interpretation using parcel structure these clusters could be assigned as rice despite the more pronounced backscatter similarity to other crop types. Thus, even if separability of backscatter signatures of clusters is limited, they can reasonably be assigned using parcel structure and expert knowledge.

Tab. 3: Mean of signature separabilities for assigned clusters respectively crop types of one stratum of the Seville site estimated as Bhattacharrya distance.

	Winter cereals	Sun-flower	Summer crops	Maize
Sunflower	1.98			
Summer crops	1.99	1.52		
Maize	1.84	1.54	1.66	
Rice	1.82	1.91	1.96	1.90

- Visual inspection

Visual inspection of ERS-1 SAR classification results for the MARS segments is exemplarily shown with segment 11 in stratum 1. Every quarter of Fig. 2 shows the same subframe of the Seville site (4.6 km * 4.6 km) covering MARS segment 11 and the surrounding area.

Upper left quarter depicts the five land use classes available as ground truth within MARS segment 11.

Upper right quarter shows a histogram stretched color composite of SPOT data of 01.07.92 (RGB = band 3,2,1). Vectors of segment 11 are overlaid in yellow. With a close look to the parcels at upper right and opposite upper left corner of MARS segment 11 a pronounced difference in color can be distinguished. According to MARS ground truth both parcels are mapped as maize fields. The difference in color visible in the SPOT data therefore indicate a fault in ground truth stated also by the ERS-1 SAR data classification result (lower right quarter of Fig. 2).

Lower left quarter shows the ERS-1 SAR acquisition of 01.07.92, i.e. of the same date as the SPOT data. Again vectors of segment 11 are overlaid in yellow. Flooded areas and water surfaces appear dark in this data, because of the low ERS SAR backscatter of water. From these areas the Guadalquivir can easily be recognised, others are visually identified as rice fields.

Lower right quarter shows the classification result obtained with cluster analysis of four different ERS-1 SAR images (22.04., 27.05., 01.07., 05.08.92). Legend below indicates the assigned crop types. Because of missing round truth e.g. for cotton is was not possible to further differentiate summer crop types.

- Comparison with ground truth:

Taking into account the above discussed confusion of rice and maize in MARS ground truth 830 pixels of the ground truth for rice comprising 844 pixels, i.e. 98.3%, have been correctly identified. In comparison 99 pixels of the ground truth of maize (reduced to 120 pixels), i.e. 82.5 % are actually classified as maize. From the 27 ground truth ground truth pixels of sunflower 9, i.e. 33.0 % have been correctly identified. In the case of smaller ground truth polygons like sunflower confusions, related to inaccuracies of geocoding cause major effects on the accuracy of the classification. It has to be taken also into consideration, that with the placement of segment 11 large areas of rice fields are covered. However, sunflower or maize fields are only slightly touched. Therefore, statistics for this classes just reflect the situation at the boarders of the sunflower and maize fields (Fig. 2), which is characterised by effects of mixed pixels and inaccuracies of geocoding. The remaining ground truth classes have been considered being too small for a reasonable analysis of results in this way.

RESULT STRATUM 3

During the application to the different geographical and agro-ecological conditions of the remaining strata emphasis was put on a technically understandable transfer and test of the approach. It turned out, that in certain cases the assignment of cluster results was limited to aggregated classes of crop types with the respect to restrictions of the available ERS-1 SAR time series (Tab. 1, missing data from Jan.-Mar. 1992). Due to the above discussed lack of representative ground truth a validation was performed using the available SPOT time series as shown with the example of stratum 3 in the following paragraph.

- Evaluation of stratum 3

Stratum 3, as it was originally defined on the base of macro-structural units corresponding to *MADUEÑO (1991)* is mainly composed of the valley of the Guadalimar river - a fertile plain with alluvial deposits. No MARS segment is located in this area.

Results of first experimentally performed clustering of the overall stratum 3 delivered inhomogeneous results, which had to be rejected. If resulting clusters have been recombined following the parcel structure of the northern part of the stratum it was not possible to simultaneously reach acceptable results for the southern part and vice versa. This can be related to differences in agricultural character and crop rotation practices between both parts of the stratum. Within the northern part almost no irrigation is applied. Within the southern part irrigation is applied to most of the area similar to stratum 1. Thus, further evaluation was performed separately for both parts of the stratum (see Fig. 3) and results have been combined afterwards.

Following available crop calendars and with respect to the limited size of stratum 3 for both parts of the stratum an initial number of 13 clusters has been fixed. The

respectively resulting 12 clusters have been combined to 5 aggregated classes. The ERS-1 SAR classification result corresponds very close to SPOT NDVI information (23.03.92, 08.06.92, and 01.07.92) as it can be seen in Fig. 3, where aggregated classes are represented in colors similar to the visual appearance of the SPOT NDVI image. A general interpretation key for the SPOT NDVI composite is as follows. With regard to the sensitivity of the NDVI to photo-synthetic active biomass the color series of red, yellow, green, cyan, and blue enhances areas respectively parcels covered by a high amount of green biomass corresponding to the acquisition dates of the SPOT time series. White color indicates masked areas.

It is obvious, that with ISODATA clustering of ERS-1 SAR data and aggregation of clusters a result similar to the SPOT NDVI composite is obtained. Areas covered by an high amount of green biomass during spring time recognisable due to their red color in the SPOT NDVI composite (predominance of the SPOT NDVI image of 23.03.92) are mostly also identified by the ERS-1 SAR classification. Using a priori knowledge these areas can be considered to be winter cereals or also grassland. From Fig. 3 it is obvious, that in the northern part of stratum 3 more winter crops or grassland are found than in the southern part.

Areas covered by a high amount of green biomass during summer time recognisable due to their cyan color in the SPOT NDVI composite (predominance of the SPOT NDVI images of 08.06.92 and 01.07.92) and mainly occurring in the southern part of the stratum can be interpreted as summer crops.

Also with respect to parcel structure in the SPOT NDVI composite as well as in ERS-1 SAR classification results the differences in cultivation practice as applied in the northern and the southern part of stratum 3 are evident. More detailed descriptions of results for stratum 1 and 3 as well as evaluation and results for the remaining strata of the Seville site can be found in *KATTENBORN, G., et al. (1996).*

8. CONCLUSION

A time series of nine ERS-1 SAR images of the MARS sample site Seville, four SPOT XS images and ground surveys of 17 MARS segments all from 1992 have been available for the study. During preliminary investigations it was figured out, that significance of supervised classification results is limited. First available input data (MARS segment ground truth) are not representative for the overall testsite respectively for single strata. Second separability between the ERS backscatter signatures of ground truth polygons is poor. Additionally histograms of most of the backscatter signatures showed up multimodal distributions.

Thus, a newly developed robust approach, also transferable to other MARS sites was developed.

In order to exclude areas with permanent use from ERS SAR classification preliminary masks derived from thematic maps were refined by multi-temporal, unsupervised classification of optical satellite data in order to create masks of main permanent land use classes (roads, water surfaces, urban areas, forest). Stratification was performed using visual interpretation of SPOT data with respect to agro-ecological phenomena.

For the following classification ERS-1 SAR data are statistically segmented. Precise knowledge about the local agricultural practice, i.e. especially the crop rotation scheme, is necessary in order to identify all useful acquisition dates of the available ERS-1 SAR time series. With respect to crop calendars more ERS-1 SAR acquisitions than available for this study are required especially in the early growing season.

Recombination of clusters to classes is performed using ancillary knowledge (local agricultural practice, former agricultural statistics) and parcel structure (road and country lane network or a cadastral data base).

The method was developed and analysed in detail with the example of a single stratum delivering excellent results. The transfer to the other strata of the Seville site proved functionality of the method and delivered reasonable results just limited to a preliminary level by the lack of sufficient a priori information. The method proved robust against effects superimposing the desirable information (local agricultural management, agro-ecological conditions and related phenological differences, geographical diversity). It was shown, that ERS SAR data supply information similar to SPOT NDVI images, thus giving significant indications, that ERS SAR data could be used as complement or even as substitute to optical satellite data.

In terms of the operational needs of the MARS project the potential of the approach seems to be high. With regard to the processing of ERS-1 SAR data necessary algorithms are available as standard software. With regard to masking and stratification site-dependent effort is required. If once GIS data for masking and stratification have been compiled and implemented only periodical updates are necessary. In future additional data sources can be expected from administrational data bases in most European countries (e.g. ATKIS in Germany). The recombination and assignment of clusters requires interactive control, but can also be supported by GIS information up to a certain extent. For the rationalisation of this task expert systems will possibly play an important role in future. In conclusion a comprehensive and robust concept for the operational use of the continuous ERS SAR data flow for agricultural statistics was developed and its plausibility demonstrated.

ACKNOWLEDGEMENTS

This study was funded by JRC/Ispra under contract No. 10161-94-04 F1ED ISP D. We would like to thank Dr. Hugo De Groof, Dr. Hans Kohl and Dr. Edmond Nezry for their co-operation and effective support.

REFERENCES

DOBSON, M. C., PIERCE, L., SARABANDI, K., ULABY, F. T. and SHARIK, T. (1992): Preliminary analysis of ERS-1 SAR for forest ecosystem studies. IEEE Trans.Geosci. Rem. Sens., Vol.30, pp. 203-211.

HARTL, P., GÜTH, S., KLAEDTKE, H.-G., PALUBINSKAS, G., REICH, M. and WÖRZ, K. (1995): Application of multi-temporal ERS-1 SAR data: Some results of the PASTA project. Interim Report to ESA, Institute of Navigation, University of Stuttgart, Stuttgart, 27 pp.

KATTENBORN, G., KLAEDTKE, H.-G., GÜTH, S. and REICH, M. (1996): Potential of ERS-1 SAR for agricultural statistics. Final Report, JRC/CEC Contract no. 10161-94-04 F1ED ISP D. 143p.

KOHL, H. G., NEZRY, E. and DE GROOF, H. (1994): Crop acreage estimation with ERS-1 PRI images. Earth Observation Quarterly, 46, December 1994, pp. 6-9.

LAUR, H. (1992): ERS-1 SAR calibration: derivation of the backscattering coefficients in ERS-1 SAR PRI images. Technical Note, ESA/ESRIN, 17 pp.

LOPES, A., NEZRY, E., TOUZI, R. and LAUR, H. (1993): Structure detection and statistical adaptive speckle filtering in SAR images. Int. J. Remote Sensing, Vol.14, No. 9, pp.1735-1758.

MADUEÑO, J.M.M. (1991): Capacidad de uso y erosion de suelos. Una aproximación a la evaluación de tierras in Andalucía. Junta de Andalucía, Agencia de Medio Ambiente, 446 pp.

NEZRY, E., GENOVESE, G., SOLAAS, G. A., REMONDIERE, S, AND KATTENBORN, G. (1995): Early crop identification and area estimation in Europe using ERS winter images. Accepted by IEEE Trans. Geosci. Rem. Sens.

RICHARDS, J. A. (1986): Remote sensing digital image analysis. Springer Verlag, Berlin, Heidelberg, New York, London, Paris, Tokyo, pp. 206 - 225.

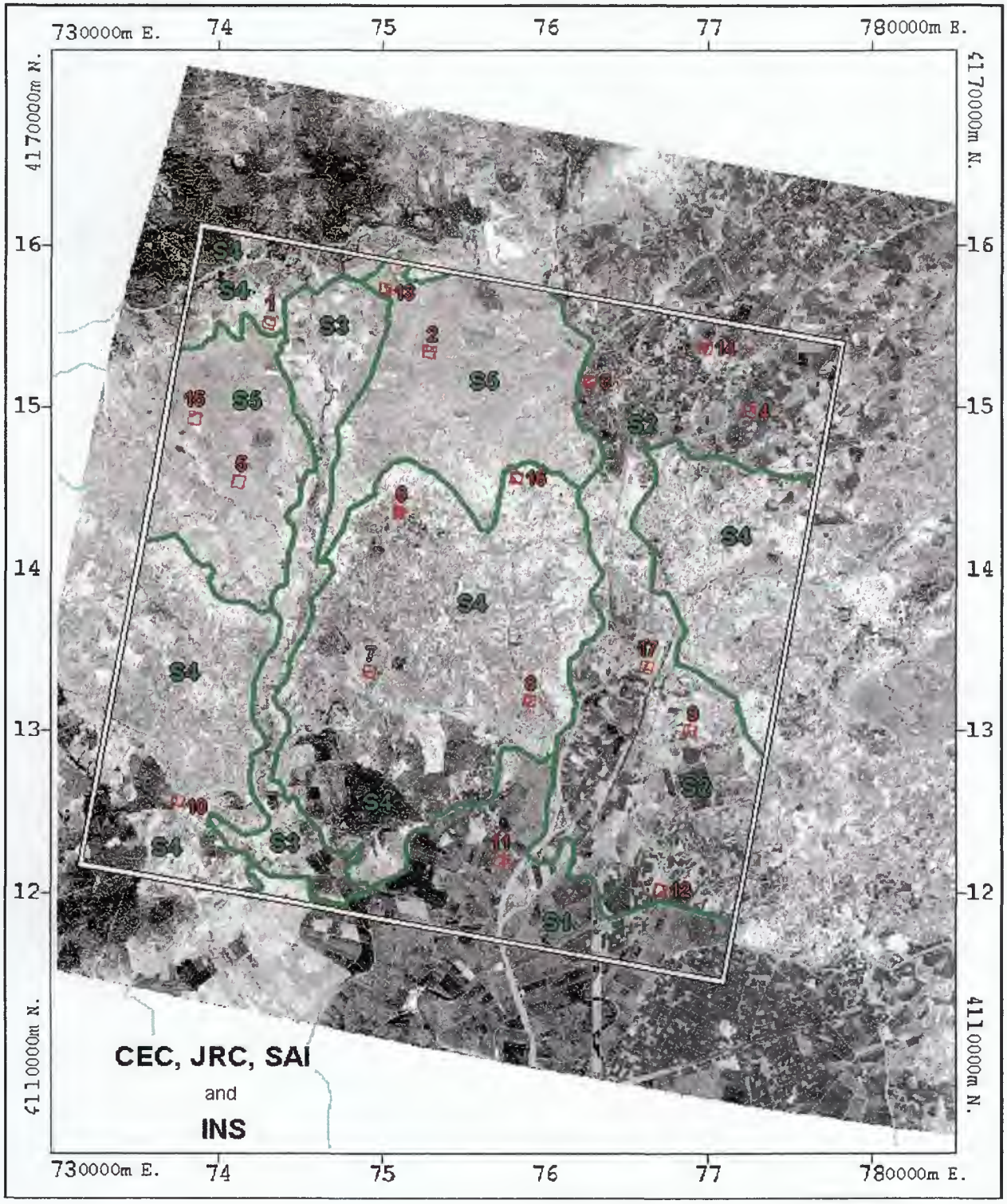

Fig. 1: Panchromatic SPOT scene from 28.12.92 of the Seville site overlaid with vectors of area under investigation (white), macro-structural units (corr. to *MADUEÑO, 1991*, green, small) defined strata S1...S5 (green, broad) and MARS segments 1...17 (red).

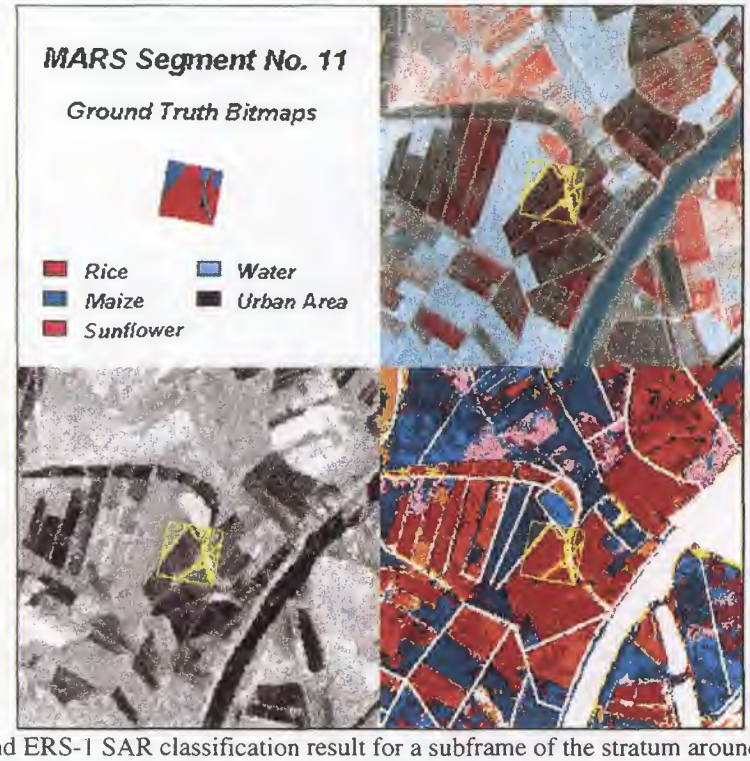

Fig. 2: Satellite data and ERS-1 SAR classification result for a subframe of the stratum around MARS segment 11 of the Seville site. UL: Ground truth bitmaps; UR: SPOT false color composite of 01.07.92; LL: ERS-1 SAR acquisition of 01.07.92; LR: ERS-1 SAR classification result in pseudocolor representation.

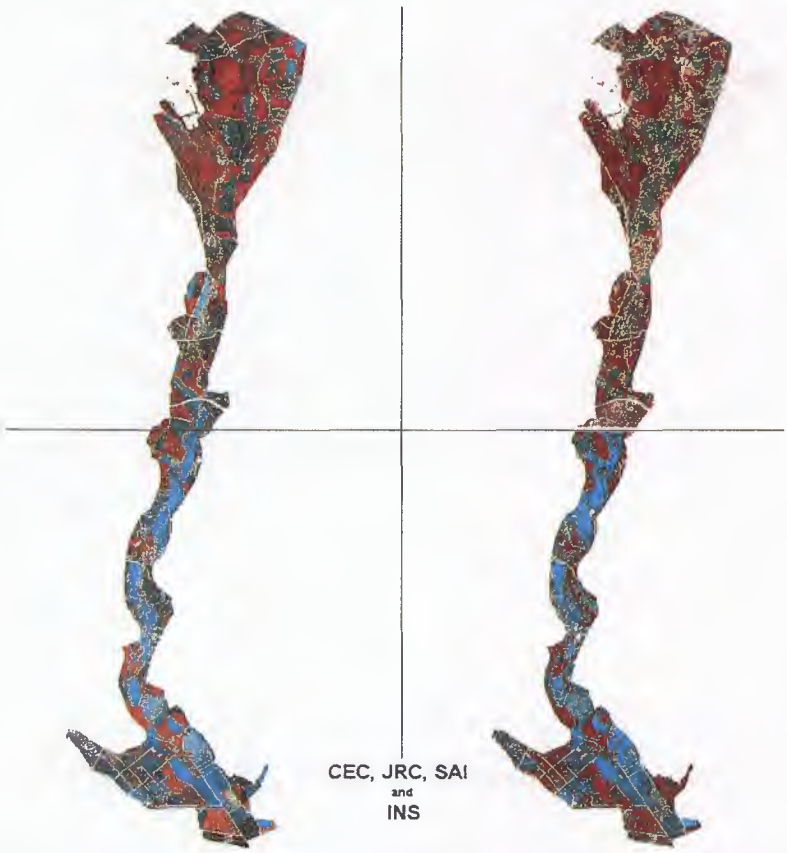

Fig. 3: Multi-temporal SPOT NDVI false color composite (23.03.92, 08.06.92, and 01.07.92) of stratum 3 of the Seville site (UL and LL): Pseudocolor presentation of ERS-1 SAR classification result (22.04.92, 27.05.92, and 01.07.92) of stratum 3 (UR and LR).

ERS SAR TIME SERIES ANALYSIS FOR MAIZE MONITORING USING EXPERIMENTAL AND MODELING APPROACHES

Auquière Eric, Defourny Pierre

Department of Environmental Sciences and Land Use Planning,
Université Catholique de Louvain, 2, bte 16, Place Croix du Sud, B-1348 Louvain-La-Neuve, BELGIUM
auquiere@mila.ucl.ac.be, defourny@mila.ucl.ac.be

Baltazart Vincent, Guissard Albert

Telecommunications and Remote Sensing Laboratory,
Université Catholique de Louvain, 2, Place du Levant, B-1348 Louvain-La-Neuve, BELGIUM
baltazar@inrets.fr, guissard@tele.ucl.ac.be

ABSTRACT

The study aimed at documenting the effective ERS-1 capabilities to monitor maize growth using field and SAR measurements over a large area (6000 km²). During the summer 1995, a first ground campaign was carried out to determine the row orientation and the relief of 555 fields. Secondly, bio- and geophysical parameters such as fresh and dry biomass, plant height and soil moisture were measured on 75 fields simultaneously to SAR image acquisitions. In total, 12 ERS-1 products were acquired. The results show that no specific maize crop temporal backscattering signature can be determined and that the soil moisture still influences the backscattering when the crop has reached is maximum height. However, the temporal evolution of the averaged field variation coefficient revealed the effect of the vegetation. A stratification approach was thus used to account for the soil moisture and to determine the crop parameters effect on the signal. A correlation coefficient of 0.9 between the σ° (dB) and the dry matter quantity per ha was obtained on fields larger than 2 ha. Finally, the row orientation was shown to have an influence on the attenuation by the canopy. These findings lead to the development of a water cloud model formulation dedicated to crops with a row-structured canopy.

1. INTRODUCTION

SAR remote sensing could play a major role in agriculture monitoring. However, exploitable results in an operational framework are still expected, particularly for early determination of crop acreages and yield forecasting. This ESA Pilot Project aims at documenting the effective ERS-1 capabilities to monitor crop growth cycle using theoretical modeling and a comprehensive data set of field and SAR measurements. A single crop was chosen to allow intensive measurements and the maize case was selected because it is considered as one of the most transparent crop. This paper briefly presents the results of this two year study.

Based on a field campaign focused on a single crop, the study objectives are to document the various factors influencing the signal, i.e. soil moisture, vegetation cover and field size, and to assess the signal sensitivity to crop parameters. Furthermore, the row-structure effect on the signal is also investigated using modeling and empirical approaches.

2.STUDY AREA

The study area was selected as large as possible to be representative of the maize crop in Belgium. It covers a total surface area of 6000 km² (see fig. 1). The soil is constituted of a Pleistocene loam deposit with a very stable textural composition (80 % of loam, 10 to 15 % of clay and 5 % of silt). The relief is slightly undulating and the mean slope of the fields is about 2 or 3 per cent. These characteristics allow us to avoid major interference related to soil type and topography.

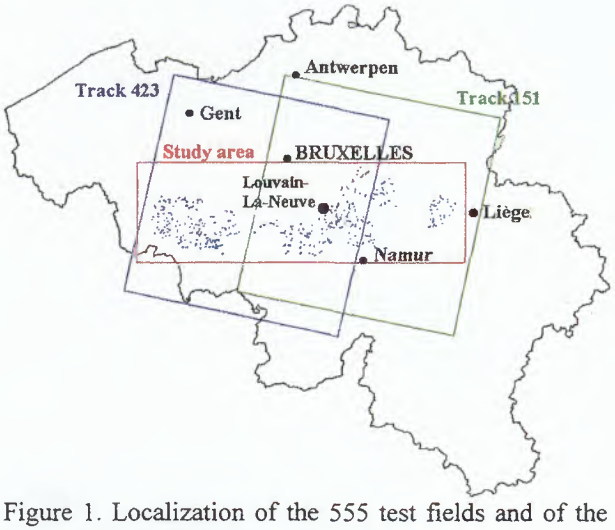

Figure 1. Localization of the 555 test fields and of the two image sets over the study area.

3.GROUND TRUTH MEASUREMENTS

Ground truth data have been collected in a two-step field campaign. During the first one - at the

beginning of the growing season - 555 maize fields were identified and localized (see fig. 1). For each, we recorded the row direction, the crop type of the surroundings, a rough scheme of the relief and the mean slope of the field. According to this last parameter, the fields were classified into three distinct categories (slope <1%: no relief; slope = 2 or 3 %: light relief; slope >4%: high relief)
A sub-sample of 76 maize fields constitutes the data set of the fully monitored maize fields for the second ground campaign. These were systematically visited at each of the satellite overpasses between mid-June and mid-October to proceed to biophysical parameters (leaf stage, plant height, wet biomass and plant moisture content) and gravimetric soil moisture measurements.
Daily meteorological parameters between 1st April 1995 to 31st October 1995 were also collected thanks to the national meteorological network. Temperatures, rainfall, sunshine and solar radiation data are respectively available for 11, 19, 4 and 1 meteorological stations.

ERS-1 SAR DATA

The whole study area is covered by two contiguous and descending SAR ERS-1 set of images. The revisiting period is 35 days but the common area of the two sets is overflown twice the period. Twelve images - in fact, six of each set - have been acquired between April and October 95. Figure 1 shows the localization of the two contiguous sets over the study area.
The data provided in a PRI format have been calibrated on a pixel basis using calculations stemmed from the procedure of H. Laur (1992). The two sets of images were separately geo-referenced in order to facilitate the localization of the fields. This was made thanks to the SPOT mosaic and partly to a set of airborne pictures acquired in May 95. The fields boundaries were drawn on each multi-temporal SAR image and used to extract for each field and each date :

- $\sigma^\circ\ (m^2/m^2) = \frac{1}{N} \cdot \sum_{i=1}^{N} \left(\sigma^\circ\right)_i$;
- $s = \frac{1}{N-1} \cdot \sum_{i=1}^{N} \left(\left(\sigma^\circ\right)_i - \sigma^\circ\ (m^2/m^2) \right)^2$;
- $\sigma^\circ\ (dB) = 10.\log_{10}(\sigma^\circ\ (m^2/m^2))$.

where:

N is the number of pixels for one field;

- $\left(\sigma^\circ\right)_i$ is the backscattering coefficient in (m^2/m^2) for pixel i.

4.RESULTS

4.1 Temporal signature of maize fields

The temporal backscattering signature is shown on figure 2. Each point represents the mean s° (dB) for the 150 fields located in the overlap area of the two image sets and the vertical bars, the standard deviation of the sample. This curve has a saw-tooth profile which can not been explained by the evolution of the crop biophysical parameters also represented on the graph. As already illustrated by Clevers *et al.* (1996) for other crops, the mean backscattering coefficient time profiles for maize will not present any standard pattern comparable from year to year.

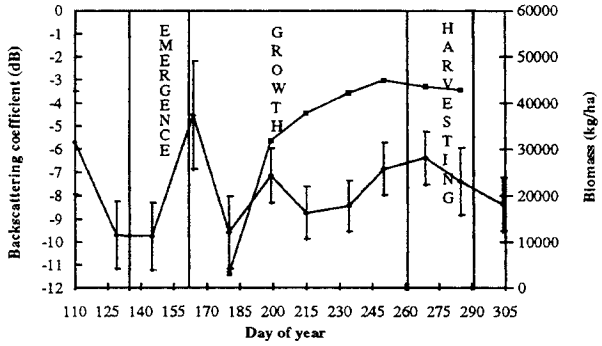

Figure 2. Temporal evolution of the averaged σ°(dB) obtained from the 150 fields located in the overlap area of the two image sets. Vertical bars represent the standard deviation of the samples. Main crop phases and the temporal evolution of the biomass are also illustrated.

At the end of the season, the mean biomass is calculated on fields which have not been harvested.
As documented in the litterature (Engman, 1991), the behavior of the ERS-1 signal is found to be related to the soil moisture variability. Figure 3 presents on the same graph the temporal signature of the signal and the evolution of the precipitation index defined as the sum of the precipitations of the six days before the image acquisition.

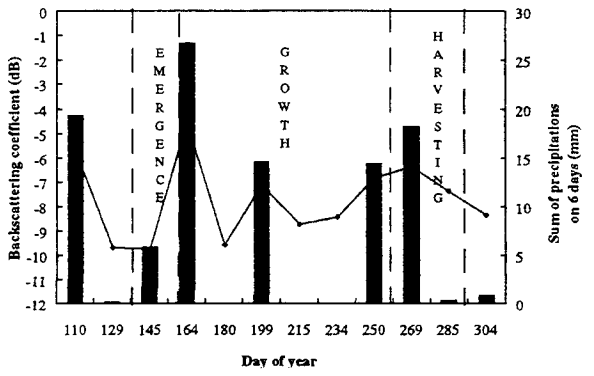

Figure 3. Comparison of the temporal evolution of the mean σ° (dB) and of the mean precipitation index.

Peaks and drops in the radar backscatter curve corresponds to periods of dryness and wetness. Thus, the maize canopy must be considered as partly transparent to the microwaves even at fully developed stages.

4.2 Sensitivity to soil moisture

To confirm the soil moisture effect during the vegetation phase of the crop, the backscattering coefficient has been plotted against the gravimetric soil moisture for 67 fields on figure 4. The test-sample has been set up with the two following constraints:

- first, a sufficient range of humidity has to be covered which imposes to work on measurements collected at different dates;
- secondly, the soil moisture has to be the main variable. Consequently, the crop status at the selected dates must be similar in order to avoid important biomass variations.

Moreover, no field repetition is included to keep the sample independence.

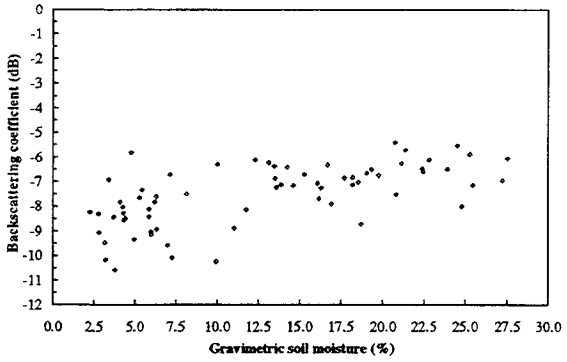

Figure 4. σ° (dB) against gravimetric soil moisture for the 67 selected fields. ρ is equal to 0.63

The correlation coefficient between the two variables is greater than 0.6. Assuming a linear relationship, it means that 40% of the sample variability is explained by the soil moisture. Nevertheless, the remaining variability is still important.

At this stage, the sample contains some fields of very small size. According to the theory (ESA, 1995), this could lead to a significant uncertainty due to speckle noise. In figures 5 and 6, we plotted two sub-samples according to the size of the fields. The limit has been fixed at 192 pixels or 3 ha for a PRI image.

The correlation coefficient of the first sub-sample is almost two times smaller than the one of the second population. A test of equality of the correlation coefficients was made for the two populations. The null hypothesis ($\rho 1=\rho 2$) is rejected at a level of 0.05 and the difference can be considered as highly significant.

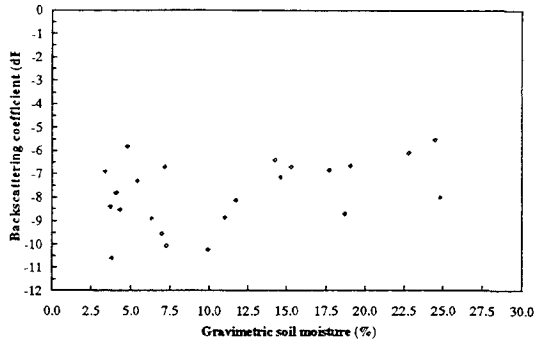

Figure 5. σ° (dB) against gravimetric soil moisture for the 25 fields with size smaller than 3 ha. $\rho 1 = 0.42$

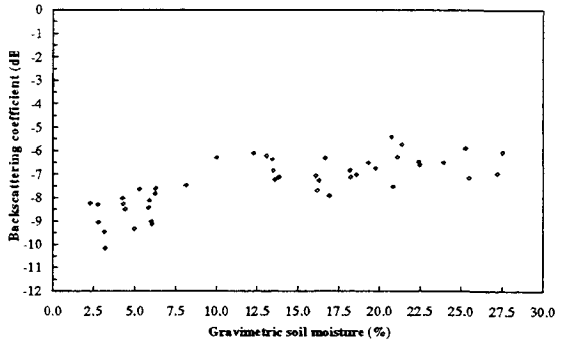

Figure 6. σ° (dB) against gravimetric soil moisture for the 43 fields with size higher than 3 ha. $\rho 2 = 0.76$.

4.3 Vegetation effect

In spite of the influence of soil moisture, the temporal signature of the averaged variation coefficient shows a pattern compatible with a vegetation effect (see fig. 7). The mean variation coefficient has been computed for 150 fields as follows :

$$\bar{C}_v = \sum_{j=1}^{M} \left(\frac{s_j}{(\sigma^\circ)_j}\right)$$

where :

- M is the number of fields, i.e. 150;
- s_j is the standard deviation of the pixels for the field j;
- $(\sigma^\circ)_j$ is the backscattering coefficient (m^2/m^2) for the field j.

According to statistical properties of radar images, the standard deviation of a target without texture is proportional to the mean and the variation coefficient is a constant equal to 0.58 ($=1/\sqrt{N}$ where N is the number of look of the radar image and is equal to 3 in this case). For a textured target, the variation coefficient increases with its heterogeneity (Laur, 1989). The mean variation coefficient is higher than 0.58 during all the season but presents a strong decrease corresponding to the canopy closure between day 180 and day 200. This characteristic pattern is not visible on temporal signatures of the variation coefficient for single fields.

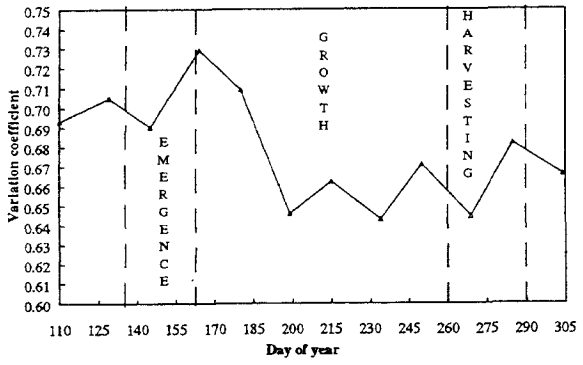

Figure 7. Temporal evolution of the variation coefficient averaged for 150 fields.

To integrate the crop biophysical parameter influence on the signal, the soil contribution had to be accounted for. This has been done using a stratification approach for the setting-up of test samples. Fields were distributed among different classes on the basis of their soil moisture. As in the previous section, measurements realized on the same field at different dates were avoided and smaller fields (inferior to 2 ha) were rejected.

On figures 8 and 9, the backscattering coefficient has been plotted respectively against the dry matter quantity per hectare (dmh) and the dry matter quantity per unit of volume (dmv) for the only class containing sufficient data. The 16 selected fields have a soil moisture between 10 and 14 % and comes from three SAR scenes.

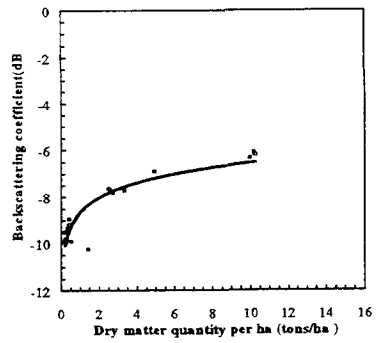

Figure 8. σ° (dB) as a function of the quantity of dry matter per ha for the 16 fields of the sample.

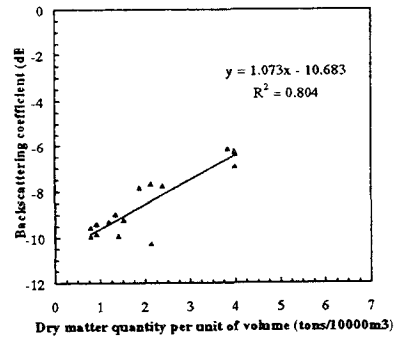

Figure 9. σ°(dB) as a function of the dry matter quantity per unit of volume for the same fields. $\rho = 0.9$.

In the first case, the relationship between the two variables seems to correspond to a negative exponential law. For the second canopy parameter, the vegetation height is accounted for in the denominator and the relationship between the two variable is approximately linear. For this graph, a correlation coefficient of 0.90 was found.

Further tests were made to assess the effect of the row direction on the signal. Indeed, the maize crop has a row-structured canopy clearly visible during the early phenological stages of the crop. First, the previous sample was enlarged to account for fields with soil moisture going from 7 % to 14% and the 28 fields finally retained were divided into two groups depending on the row orientation.

For fields with a relative row orientation between 0 and 45°, figure 10 shows that the relationship between the backscattering coefficient and the dry matter quantity hectare is worse than on figure 8 while it is not affected for fields having a relative row orientation between 45 and 90° (see fig. 11). This could be related to the fact that the number of rows to be penetrated by the radiation increases with the view angle.

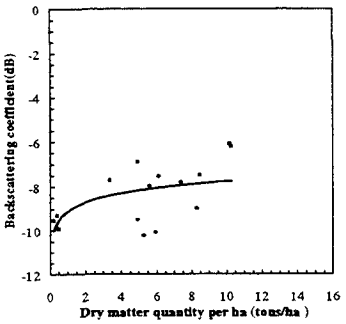

Figure 10. σ° (dB) as a function of the quantity of dry matter per ha for 15 fields with soil moisture between 7 and 14 % and row-direction between 0 and 45°.

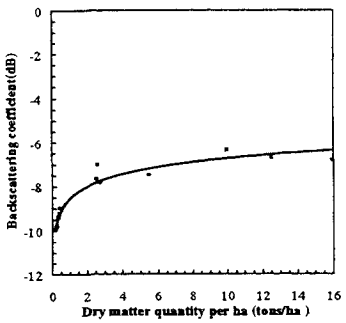

Figure 11. σ° (dB) as a function of the quantity of dry matter per ha for 13 fields with soil moisture between 7 and 14 % and row direction between 45° and 90°.

The canopy structure effect is also confirmed on figure 12 where the $\sigma 0$ (dB) has been plotted against the radar look direction , that is to say the azimuth angle ϕ between the ground projection of the antenna beam, for 33 fields with soil moisture and biomass considered as similar.

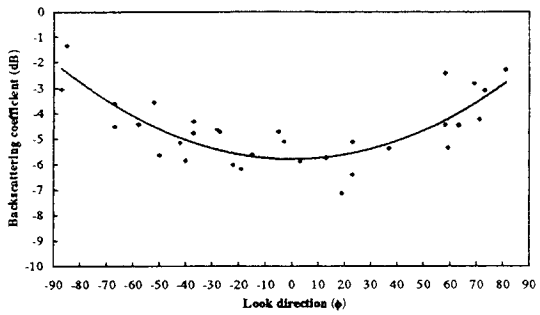

Figure 12. Plot of the backscattering coefficient against the look direction ϕ for 33 fields located near each other. The backscattering coefficients were extracted on the SAR scene of the 13/06/95, after the emergence of the crop; the canopy height is approximately 40 cm. A look direction of 0° signifies that the beam of the incident angle is parallel to the row direction.

4.4 Modeling approach

Considering these results, the water-cloud model (Ulaby et al., 1986) has been extended to crops which present a row structured canopy at early growth stages such as maize and sugar beet.

As in the original formulation, the total backscattered power is computed as the incoherent sum of both the underlying ground σ^o_{surf} and the vegetation contribution σ^o_{veg} where:

$$\sigma^{o}_{surf} = \sigma^{o}_{soil}.T(h)$$

The quantity represent the backscattering over the bare soil. However, in the new formulation, the vegetation backscattering coefficient is no longer integrated on the whole height of the canopy.

On figure 13, we see that the canopy is considered as σ^{o}_{soil} a succession of adjacent rows of height h, row-spacing D, and row-width d. Other parameters are the incidence angle q and the angle Y between the row-direction and the SAR view angle. As shown on figure 14 for the particular case Y = 90°, the triplet of parameters {D, d, htanq} allows us to discriminate between growth stages.

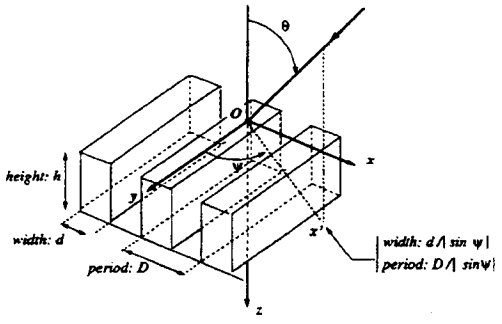

Figure 13. Row-structure of the canopy.

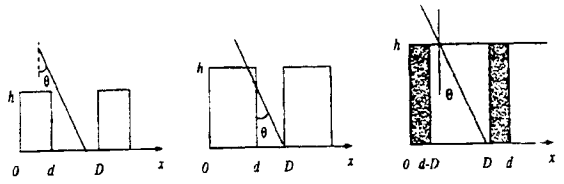

Figure 14: Scenario associated to the growth stages to be considered in the modeling. Radiation are orthogonal to the row direction, i.e. $\psi = 90°$.

Because of the canopy structure, the radar cross-section (*rcs*) depends on the position x along the axis with period D. The simple shape of the canopy implies that the total *rcs* is the incoherent sum of four terms σ_i, each one being the solution over a spatial subinterval Ω_i. We thus write the backscattering coefficient as follows:

$$\sigma^{o}_{veg} = \frac{1}{D} \sum_{i=1,...,4} \sigma_i ,$$

with: $\sigma_i = \int_{\Omega_i} \sigma_i^o(x).dx$,

where the calculation of the backscattering coefficient $\sigma_i^o(x)$ follows the original formulation by Ulaby *et al* (1986), but with the bounds of integration over the (Oz) axis changing accordingly to the intervals Ω_i. The bounds of the four domains Ω_i depend on growth stages, incidence angle, crop characteristics, i.e. large or small row-width in comparison to either the row-spacing or the quantity $h\tan\theta$, and on the amount of rows which interacts with the radar signal. The details and the whole set of solutions has been described by Baltazart *et al.* (1996).

First simulations have shown the negative trend of the two-way attenuation through the vegetation layer with increasing ψ angle from 0 to 90 degrees, and a positive trend of about the same magnitude for the backscattering by the vegetation alone, i.e. σ^o_{veg}. However, the trend of the total backscattering coefficient appears to be mostly driven by the backscattering sensitivity over bare soil. Backscattering sensitivity to look direction over bare soil varies the same way as σ^o_{veg} with a magnitude depending on the tillage and drainage patterns and seed bed preparations. The vegetation cover gradually conceals most of this sensitivity. This is illustrated over sugar beet crops by the following simulation on figure 15.

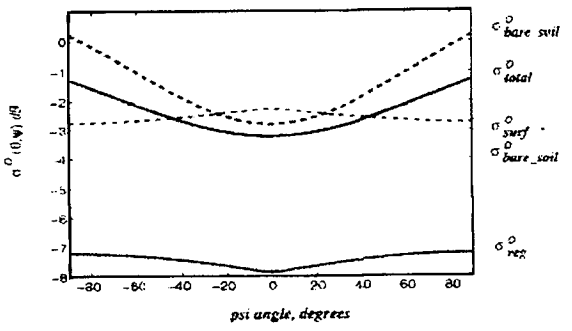

Figure 15. Contribution of the different terms to the backscattering coefficient. Extinction coefficient κ_e = 2.5 Np / m, scattering coefficient η = 2.2 m^{-1}, canopy height h = 0.3 m, row-spacing D = 0.4 m, row-width d=0.2 m, frequency =5.3Ghz, incidence angle θ = 23 degrees and VV polarisation. σ0 of the bare soil is deduced from Müller et al. (1993).

CONCLUSIONS

The aim of this project was to assess the capabilities of the ERS-1 SAR data to retrieve quantitative biophysical and geophysical variables in the perspective of crop monitoring. The methodology was based on the complementary contributions from theoretical and empirical approaches.

The theoretical approach focused on the understanding of the backscattering by row structured crop canopies at early growth stages (e.g. maize, sugar beet, vineyard and sorghum). The research leads to the development of a semi-empirical model accounting for the structure and orientation of the canopy rows and which could be used for the early prediction of crop yield. The empirical study was based on a very intensive ground campaign set up during summer 95 over 555 maize fields. The collected data were put together in a relational data-base with meteorological data and ERS-1 backscattering coefficients extracted from 12 ERS-1 SAR images acquired over the whole season.

Due to the structure of its canopy, maize is generally be considered as one of the most transparent crops to microwaves. Soil properties under maize canopy influence the signal backscattering all over the growth season. As a consequence, the mean backscattering coefficient time profiles for maize crops do not present any standard pattern comparable year to year. This study confirms the sensitivity of the ERS-1 SAR signal to soil moisture. For fields larger than 3 ha at full vegetation stage, i.e. canopy at its maximum height, a correlation coefficient of 0.76 was found.

However, the temporal evolution of the averaged variation coefficient of the fields revealed some effect of the vegetation. A stratification approach was used to account for the soil moisture and to assess the effect of the crop parameters on the ERS-1 signal. A correlation coefficient of 0.9 between the σ° (dB) and the dry matter quantity per ha was obtained on fields larger than 2 ha. This minimum field size requirement was imposed for reducing the speckle effect on the estimation uncertainty.

Finally, further work focused on the study of the row direction effect on the ERS-1 SAR signal. We found that during the early growth stage of the crop, backscattering coefficients extracted from large flat fields with homogeneous soil moisture conditions can vary of approximately 2 or 3 dB in relation with the canopy row orientation.

ACKNOWLEDGMENTS

The authors would like to thank the Belgian Federal Office for Scientific, Technical and Cultural affairs for his financial support and ESA organization for providing SAR images in the framework of this pilot project.

REFERENCES

Baltazart, V., Auquière, E., Guissard, A., Defourny, P., 1996 (submitted), On The Extension Of The Water Cloud Model To A Row-Structured Canopy, in *IEEE on Geoscience and Remote Sensing.*

Clevers, J., van Leeuwen, H., Hoekman, D., Nieuwenhuis, G., Kramer, H., Vissers, M., 1996, *Application of JERS-1 data for agriculture, forestry and land use*, NRSP report 95-33 of the BCRS project 3.2/TO-06, Netherlands Remote Sensing Board, Delft, 95 p.

Engman, E.T., 1991, Applications of Microwave Remote Sensing Of Soil Moisture for Water Resources and Agriculture, in *Remote Sensing of Environment*, Vol. 35, n° 12, pp. 213-226.

ESA SP-1185, 1995, Satellite Radar in Agriculture, Experience with ERS-1, ESA Publications Division, Noordwijk, 71 p.

Laur, H., 1989, *Analyse d'images radar en télédétection: discriminateurs radiométriques et texturaux*, Thèse, Université Paul Sabatier, Toulouse.

Laur, H., 1992, *Derivation of backscattering coefficient in ERS-1 SAR PRI products*, ESA-ESRIN, Issue 1, Rev. 0, 17, 17 p.

Müller, U., Löcherbach, T., Förstner, W., Kühbauch, W., 1993, Suitability of ERS-1 SAR PRI-data for multitemporal agricultural land-use mapping, in *Proc. ERS-1 Symposium*, ESA SP-361, Noordwijk, pp. 69-74.

Ulaby, F.T., Moore, R.k., Fung, A.K., 1986, *Microwave Remote Sensing*, Vol. III, Artech House, pp. 1065-2162.

DELINEATION OF RICE CROPPING SYSTEMS IN THE MEKONG RIVER DELTA USING MULTITEMPORAL ERS SYNTHETIC APERTURE RADAR

S. C. Liew[a], S. P. Kam[b], T. P. Tuong[b], P. Chen[a],
V. Q. Minh[c], L. Balababa[d] and H. Lim[a]

[a]Centre for Remote Imaging, Sensing and Processing,, National University of Singapore,
Lower Kent Ridge Road, Singapore 119260.
Tel: (+65) 7723220, Fax: (+65) 7757717, email: phyliew@nus.edu.sg
[b]International Rice Research Institute, P.O. Box 933, 1099 Manila, Philippines
[c]Department of Soil Science, Faculty of Agriculture, University of Can Tho, Can Tho, Vietnam
[d]Natural Resources Program, Asian Institute of Technology, Bangkok., Thailand

ABSTRACT

The aim of this study is to use multitemporal ERS-2 satellite synthetic aperture radar (SAR) images in delineating and mapping areas under different rice cropping systems in the Mekong river delta, Vietnam. Five change index maps were generated from the six images acquired between June and December, 1996. Using a 3-dB threshold, the pixels in each change index map were classified into one of three classes: increasing, decreasing or constant backscattering. The five change index maps were used to generate a composite map with 243 possible change classes. After discarding the minority classes, and merging the dominant classes with similar backscatter time series, the thematic classes of rice cropping systems practiced in the study area were delineated.

1. INTRODUCTION

Rice cultivation in the Mekong river delta is largely governed by hydrology, rainfall pattern and the availability of irrigation. Given the diversity of the cropping systems, it would be very difficult, if not impossible, to discriminate the areas under different planting systems using one single-date image. Multi-temporal images are required to monitor the spatial and temporal growth patterns of the rice crops and subsequently to identify the cropping systems practiced at a particular region. Multispectral visible/near infrared images such as those from the SPOT or LANDSAT satellites could be used for this purpose. Unfortunately, a large part of the rice growing season coincides with the rainy period resulting in limited availability of cloud-free images throughout the growing season. The use of cloud penetrating SAR would overcome this problem.

The objective of this study is to use multi-temporal ERS-2 SAR data to delineate and map the spatial distribution of the various rice cropping systems in the Mekong River Delta. The study was confined within a 100 km by 100 km area covered by one ERS-2 SAR scene, (track 75, frame 3411 shifted 30%) which includes parts of Soc Trang and Bac Lieu provinces in the Mekong river delta, Vietnam (see Fig. 1 and inset for the location map).

II. RICE CROPPING SYSTEMS IN THE MEKONG RIVER DELTA

There are three main rice seasons in the Mekong river delta (see Table 1). Two of the seasons (HT and M) coincide with the rainy season which typically starts in May and lasts until November. The annual rainfall in the study area varies from 1600 to 2000 mm. The three rice seasons, in various combinations governed by hydrology, rainfall pattern and availability of irrigation, constitute the variety of rice-based cropping systems practiced in the Mekong river delta [1].

The major rice cropping systems in this area are the single rice crop (SC), double rice crop (DC) and triple rice crop (TC) systems (see Table 2). The single rice crop is invariably the *Mua* (M), which has traditionally been the rainfed rice cropping system using local, traditional varieties with a longer growth period. It is practiced mainly in the tidally-inundated coastal area subjected to salinity intrusion prior to the rainy season. The double cropping system may be the *Dong Xuan-He Thu* (DX-HT) or the *He Thu-Mua* (HT-M) system. The DX crop, planted at the end of the rainy season, needs to be irrigated. In areas affected by deep flooding during the rainy season, the second crop (HT) is planted earlier in April, depends on pump-irrigation for its water, and is harvested before the onset of the flood. In areas where flooding is not severe or commences later, the HT crop is planted in May/June and makes use of rain water. The HT-M system is typically practiced in the salinity affected areas and in areas where irrigation is not available. Both crops are rainfed. Hence the crop calendar varies each year, depending on the onset of the rainy season. The rice crops may be planted using the transplanting or the direct seeding methods. In the direct seeding method, the seeds are either sown onto dry fields prior to the start of the rainy season (dry direct seeding) or pre-germinated seeds may be sown onto wet fields (wet direct seeding). The HT crop is generally wet or dry direct seeded while the M crop may be transplanted or wet direct seeded. The triple crop system combines all three rice seasons (DX-HT-M) and is practiced in limited riverine areas with favourable hydrological conditions and availability of irrigation for the DX crop.

Table 1: Rice Seasons in the Mekong River Delta

	Season	Planting	Harvest
Dong Xuan (DX)	Winter - Spring	Nov/Dec	Feb/Mar
He Thu (HT)	Summer - Autumn	May/Jun	Aug/Sep
Mua (M)	Rainy Season	Jul/Aug	Dec/Jan

Table 2: Major Rice Cropping Systems in the Mekong River Delta

	Cropping Type	Rice Seasons
1.	Single Rainfed	*Mua* (M)
2.	Double Irrigated	*Dong Xuan* (DX) - *He Thu* (HT)
3.	Double Rainfed	*He Thu* (HT) - *Mua* (M)
4.	Triple Irrigated-Rainfed	*Dong Xuan* (DX) - *He Thu* (HT) - *Mua* (M)

III. RADAR BACKSCATTERING CHARACTERISTICS OF RICE PLANTS

Various studies on the backscattering of radar from rice plants [2, 3, 4] indicate that the radar backscatter generally increases with time after planting during the vegetative phase when there is a rapid increase in plant biomass. The backscatter saturates at the reproductive phase of the growth cycle when the plants start flowering. Theoretical simulation [4] shows that the scattering mechanism is dominated by double scattering between the water surface and the rice plants. The backscattering coefficient is found to increase from −16 dB or less at the beginning of the growth cycle when the field is inundated and there is little biomass in the field, to about −8 dB at the saturation level [4].

Hence, it should be possible to monitor the rice growth stage by measuring the backscattering coefficient from the plants as a function of time if radar images are acquired at appropriate time intervals. ERS-2 SAR images can only be acquired in the same mode (either descending or ascending) at 35-day intervals. Although the backscatter time series obtained at 35-day intervals would not have sufficient temporal resolution to capture the rapid increase in biomass during the vegetative phase for the short growth duration rice, which is about 30 days, it would still be able to capture the changes in backscatter between the beginning of the planting cycle and the end of the reproductive stage. Generally, the beginning of a rice season would be identified by a low backscatter in the time series when the field was inundated while the end of the reproductive stage is characterised by a high backscatter.

IV. IMAGES AND DATA ACQUISITION

Seven descending mode ERS-2 synthetic aperture radar images at 35-day repeat intervals were acquired (track 75, frame 3411 shifted down by 30% to cover areas of interest in Soc Trang and Bac Lieu provinces) during the following dates in 1996: May 5, Jun 9, Jul 14, Aug 18, Sep 22, Oct 27 and Dec 1. A reasonably cloud-free SPOT multispectral image of the part of the study area was also acquired on Jun 19, 1996. This image served as a useful aid in the interpretation of the earlier radar images. Ground truthing field trips were also carried out on dates coincidental with or close to the dates of SAR image acquisition. Over 90 plots of rice fields, each about 100 x 100 m^2 in size were monitored for general field conditions, date of planting and crop growth stage. A final field check was carried out after completion of the radar data processing to ascertain the delineated spatial pattern of the rice cropping systems.

V. IMAGE PREPROCESSING

The ERS-2 scenes were acquired and processed into the calibrated SAR Precision Image (PRI) format at the ground station of the Centre for Remote Imaging, Sensing and Processing (CRISP), Singapore. Each PRI product was first converted to 8-bit images by dividing the 16-bit pixel Digital Numbers (DN) by 4, low-pass filtered using a 5x5 averaging window and then downsampled to 50-m pixel size. An edge-preserving speckle removal filter based on the adaptive Wiener filter for multiplicative noise was applied followed by a 3x3 median filter. For ease of analysis, the ocean and Cu Lao (island) Dung on the left bank of the Hau Giang (one of the branches of the Mekong River) appearing in the scene were masked out. Multitemporal colour composite images were then generated to show the changes in the backscattering coefficients during the rice growing seasons. An example of such images is shown in Fig. 1 which is composed of the ERS images of May 5, Jun 9 and Jul 14 in the red, blue and green bands respectively. The multitude of colours illustrates the variety of rice cropping systems in the study area. The areas which appear grey are where the backscattering coefficient remained relatively constant throughout the season. These areas correspond to relatively invariant surface features such as the inland melaleuca forests, the coastal mangrove forests, the linear settlements, homestead gardens and orchards along canals and roads; and the built-up areas.

VI. CLASSIFICATION METHOD AND RESULTS

Classification of the rice cropping systems in this region was made by thresholding the change indices derived from the series of multitemporal SAR images. For each consecutive pair of images 1 and 2, a change index map was generated. The change index (CI) was defined as the change in the backscattering coefficient expressed in dB,

$$CI = \Delta\sigma_0\ (dB) = 20 \log_{10}(DN2/DN1) \qquad (1$$

where DN1 and DN2 are the pixel digital numbers of the images 1 and 2 respectively. Six change index maps were generated from the series of seven SAR images. An arbitrary threshold was then applied to each change index map to produce a threshold-change-index (TCI) map. A threshold value of 3 dB was found to be suitable for delineating the different classes of rice cropping systems. For each TCI map, the pixels were classified as having a constant (-3dB < CI < +3dB), decreasing (CI < -3dB) or

increasing (CI > +3dB) backscattering over the corresponding time period. Five TCI maps (covering the period from Jun 9 to Dec 1) were used in the classification. By combining these five TCI maps, a total of 243 possible classes could be formed. Each pixel was assigned a class number according to

$$\text{class no.} = \sum 3^{i-1} t_i \qquad (2$$

where t_i (i = 1, 2, ..., 5) is the pixel value of the ith TCI map, which assumes one of the values 0 (constant backscatter), 1 (decreasing backscatter) or 2 (increasing backscatter). Since these classes were obtained from the threshold change indices, they will be referred to as the "change classes" in the following paragraphs.

The change class of value zero corresponds to the regions in the scene where the radar backscattering coefficient remained relatively constant throughout the period of observation. These areas are the non-rice areas, covered with relatively permanent surface features described in the previous section. Of the 243 possible classes, 30 classes were found to account for 86.7% of the pixels with non-zero class value, i.e. where the backscatter changed by 3 dB or more in at least one of the series of TCI maps. These change classes are listed in Table 3 in descending order of dominance in terms of pixel numbers.

Table 3: Cumulative percentage for 30 dominant change classes derived from five TCI maps

Class No.	Cum. Percent	Class No.	Cum. Percent	Class No.	Cum. Percent
189	15.8	196	65.0	54	79.5
7	25.5	2	67.0	61	80.4
27	32.2	18	68.8	209	81.3
191	38.5	33	70.5	192	82.1
81	44.7	212	72.1	163	83.0
162	49.4	29	73.6	21	83.8
195	53.7	45	75.1	190	84.5
6	57.2	210	76.5	19	85.3
1	60.6	169	77.5	208	86.0
207	63.0	194	78.6	164	86.7

A number of change classes were associated with and merged into a thematic class of rice cropping system on the basis of similarity in their time series of radar backscattering (σ_0 in dB) as well as their geographical distribution pattern. Field knowledge about the type of rice cropping system that might be practiced in a particular geographical region was also considered when assigning the thematic classes. Of the 30 dominant change classes, 24 could be assigned to the major thematic classes of rice cropping systems. Six change classes remained unclassified. They were very likely the non-rice classes. The resulting thematic map of the rice cropping systems is shown in Fig. 2. The backscatter time series of the dominant change classes were grouped and graphed for the major thematic classes of rice cropping systems (see Fig. 3a to 3h).

VII. DISCUSSION

The major rice cropping systems listed in Table 2 (except the triple crop system) have been delineated by thresholding the change index maps derived from the multitemporal SAR images. Some variations of these major systems have also been identified. Their backscatter time series characteristics are described in the following paragraphs.

The single crop system (rainfed *Mua*), planted with long growth duration rice, is predominantly confined to the coastal areas where there is still saline intrusion during the dry season (coloured red in Fig. 2). The backscatter time series is characterised by a sharp drop in the backscattering coefficient between Jun 9 and Jul 14 (see Fig. 3a), corresponding with the start of the *Mua* rice crop. The backscatter then increases and remains high till the end of the monitoring period in Dec 1. The shrimp-rice system (coloured brown in Fig. 2) is practiced in the low depression areas, where there is late planting of *Mua* crop (a sharp increase in σ between Aug 18 and Sep 22; see Fig. 3b) after the harvest of shrimps and flushing out of saline water by the rains.

There are two main variations of the irrigated, double rice cropping (DX-HT) system. The irrigated DX-HT areas coloured yellow in Fig. 2 are low-lying and are subjected to severe flooding in Aug-Oct. To avoid the floods, the HT crop is planted early, in April, and is at the earlier part of the crop season Correspondingly the backscatter time series shows a generally increasing σ from May 5, peaking at Jul 14 (see Fig. 3c). The drop in σ between Jul 14 and Aug 18 is probably due to flooding after the harvest of the HT crop. The fields remain fallow until the planting of the DX crop in December.. The increase in σ between Aug 18 and Sep 22 is probably due to weed emergence. The drop in σ at the end of Oct coincides with the peak of flooding, while the subsequent increase in σ in December marks the start of the DX crop.

The backscatter time series for the area coloured magenta in Fig. 2 is characterised by a distinct drop in σ on Oct 27, followed by a steep increase in backscatter (see Fig. 3d). The earlier part of the profile shows a slight drop in σ on Jun 9, followed by a gradual increase of radar backscatter, reaching a peak on Sep 22. This category is found predominantly in areas where the second variation of the irrigated DX-HT cropping system occurs. In these areas which are not so severely affected by flooding during the rainy season, the HT crop is planted later, in May/June, to take advantage of the rains. The increasing σ from July to September indicates the HT crop in the fields. The drop in σ on Oct 27 may be due to the peak floods. It was also noted that in the irrigated area, the class number 27 (the backscatter series of which is included in Fig. 3d) occurs mainly in the periphery of the rice areas, just behind the linear settlements and

associated homestead orchards and miscellaneous planting. Field investigation and interviews with the local residents reveal that these locations are associated with the sugarcane-rice (HT) cropping system.

The magenta-coloured pixels (Fig. 2) also occur scattered in the rainfed areas, with some concentrations along the main road leading from Soc Trang to Bac Lieu. Ground observations indicate that the rainfed HT-M system is practiced in some parts of this area, where the dry direct-seeded HT crop is planted between May/June and Aug/Sep, followed by the Mua crop in Oct. Because of the similar crop calendar of the HT crop for both the irrigated DX-HT and the rainfed HT-M cropping systems, it is coincidental that these two systems exhibit similar characteristics in their backscatter time series. For the HT-M system, the increase in backscatter between Oct 27 and Dec 1 is probably due to the *Mua* crop, while in the case of the DX-HT system, the increase could be due to weed emergence. This backscatter time series probably also reflects the sugarcane-HT rice cropping system mentioned above.

Four other variations of the double cropping rainfed HT-M systems which exhibit distinctive backscatter time series can be identified. The system practiced mainly in the Bac Lieu province (coloured light green in Fig. 2) is characterised by two distinct drops in the backscatter time series, i.e. on Jun 9 and Oct 27 (see Fig. 3e). In these areas which are lower-lying, the fields are flooded in June, hence the corresponding drop in σ in the Jun 9 scene. The wet field conditions allow for wet direct seeding of the HT crop. The increase in σ after October corresponds with the *Mua* crop. The bright green pixels which appear within the irrigated DX-HT magenta area west of Phung Hiep correspond with swampy areas which are not cultivated. It is also coincidental that the backscatter time profile of this swampy area resembles that of the wet direct seeded HT-M cropping system.

On the other hand in most of Soc Trang province which is on relatively higher ground (coloured cyan in Fig. 2), there is no distinct dip in σ in the backscatter time series (see Fig.3f); there was no early season inundation of the rice fields. The HT crop is mainly dry direct seeded, hence the corresponding increase in backscatter between Jul 14 and Aug 18.. As is the case of the light green areas, the increase in σ after October corresponds with the *Mua* crop.

In the more inland region of Bac Lieu province (coloured dark green in Fig. 2), the HT-M system is characterised by two dips in the backscatter time series on Jul 14 (late HT) and Oct 27 (Fig. 3g). Roughly east of Soc Trang town, close to the Hua Giang river, is a small but rather homogeneous area coloured dark blue (Fig. 2) which has a distinctive backscatter time series (see Fig. 3h). The cropping system in this area is similar to that of the cyan-coloured area of Soc Trang province. However as this area can be subjected to tidal inundation, the backscatter profile could be altered.

The triple crop system has not been identified. Since this system is not commonly practiced, it is most probably included under the minority classes not considered in this study.

VIII. CONCLUSIONS

In conclusion, the dominant rice cultivating systems practiced in the study area have been delineated in this study by thresholding the change index maps derived from multitemporal SAR images followed by human interpretation of the radar backscatter time series. The thresholding process produces 243 possible change classes characterised by their unique signature of radar backscatter time series. The dominant change classes are merged into one of the several thematic classes of rice cropping systems based on their similarity in the backscatter time series and their geographical distribution. However, ambiguity still exists in assigning some change classes to their respective thematic classes. For example, one of the rainfed HT-M systems has similar radar backscatter time series as the irrigated DX-HT system, and possibly with a rice-nonrice cropping system. An acquisition in April or sometime during the peak of the DX crop is probably needed to resolve this ambiguity. Use of ascending mode images may help to increase the temporal resolution of the backscatter time series. However, mixing the two modes of acquisition may complicate the interpretation of the backscatter time series due to the different orientations of the ground with respect to the SAR line of sight.

REFERENCES

1. T.P. Tuong, C.T. Hoanh and N.T. Khiem. 1991. "Agro-hydrological factors as land qualities in land evaluation for rice cropping patterns in the Mekong Delta of Vietnam," in P. Deturck and F.N. Ponnamperuma (eds.) *Rice Production on Acid Soils of the Tropics*. Institute of Fundamental Studies, Kandy, Sri Lanka.
2. T. Le Toan, H. Laur, E. Mougin, and A. Lopes. "Multitemporal and dual-polarization observations of agricultural vegetation covers by X-band SAR images," *IEEE Trans. Geosci. Remote Sensing*, vol 27, pp. 709-717, 1989.
3. T. Kurosu, M. Fujita, and K. Chiba, "Monitoring of rice crop growth from space using ERS-1 C-band SAR," *IEEE Trans. Geosci. Remote Sensing*, vol 33, pp. 1092-1096, 1995.
4. T. Le Toan, F. Ribbes, L.-F. Wang, N. Floury, K.-H. Ding, J. A. Kong, M. Fujita, and T. Kurosu, "Rice crop mapping and monitoring using ERS-1 data based on experiment and modeling results," *IEEE Trans. Geosci. Remote Sensing*, vol 35, pp. 41-56, 1997.

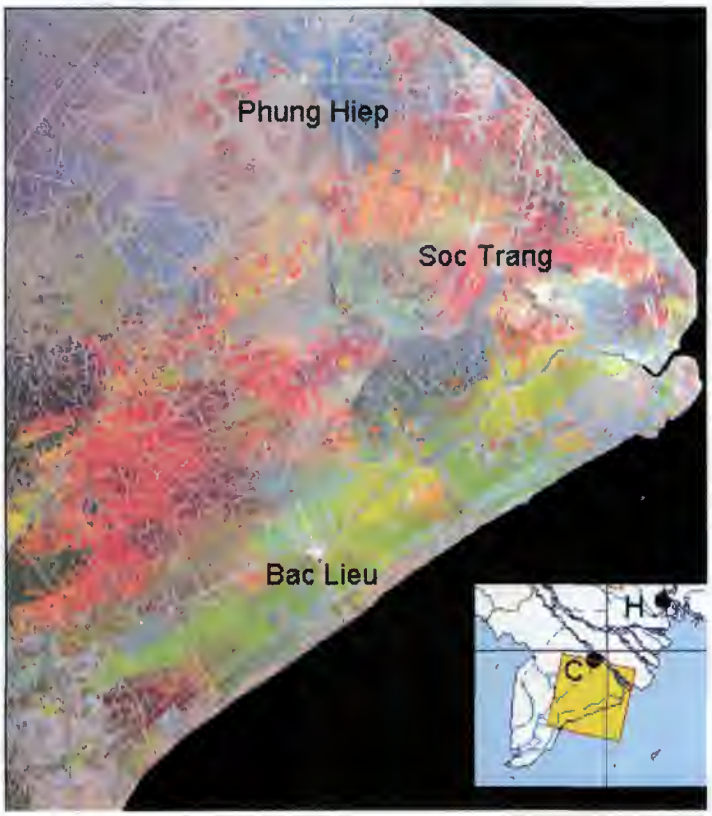

Fig. 1: Multitemporal SAR colour composite image of the test area. (Red: May 5. Green: Jun 9. Blue: July 14. 1996). Inset: Location map of the test area. C: Can Tho town. H: Ho Chi Minh City.

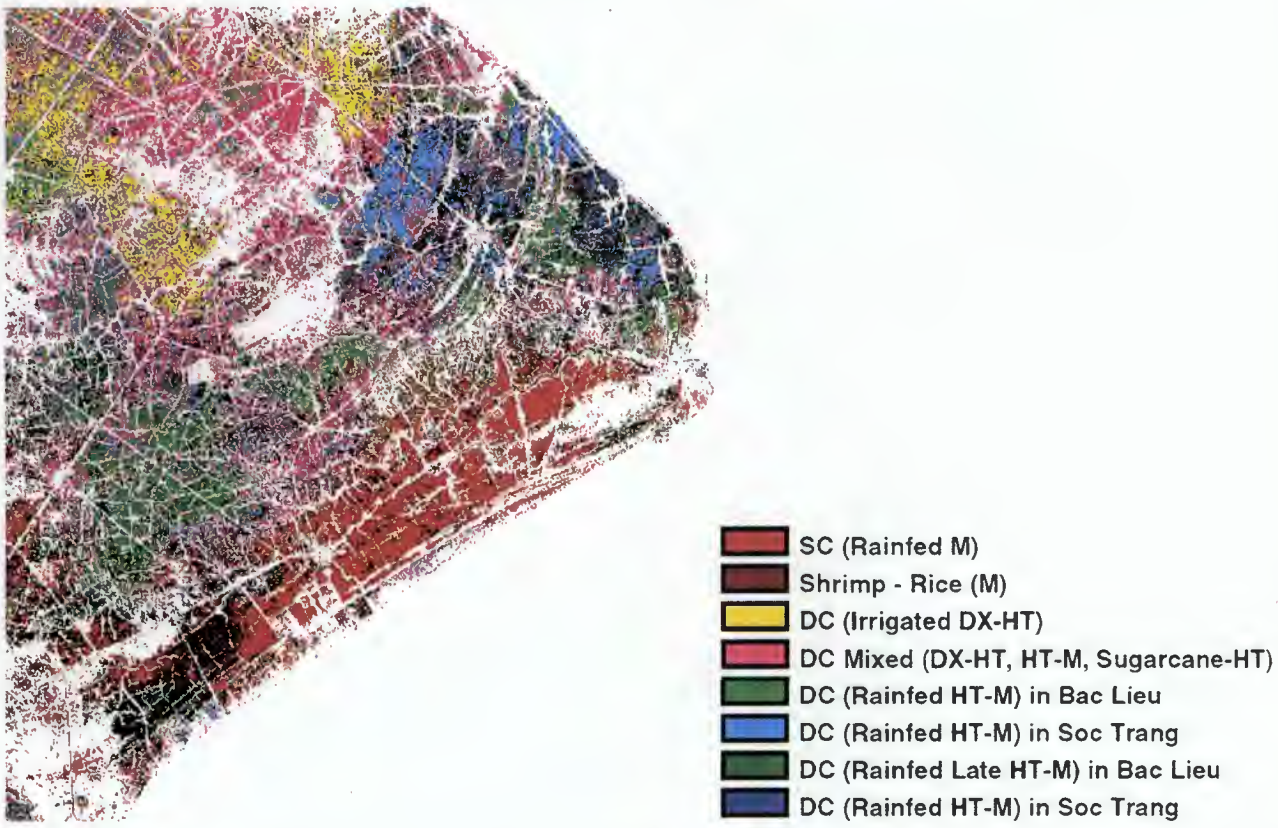

Fig. 2: Thematic classes of rice cropping systems in the Mekong river delta derived from five SAR threshold-change-index maps.

a: SC (Rainfed M)

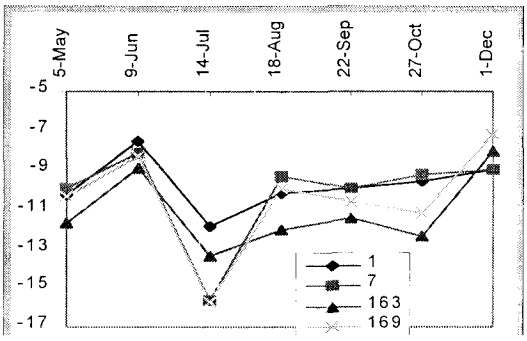

b: Shrimp - Rice (Rainfed M)

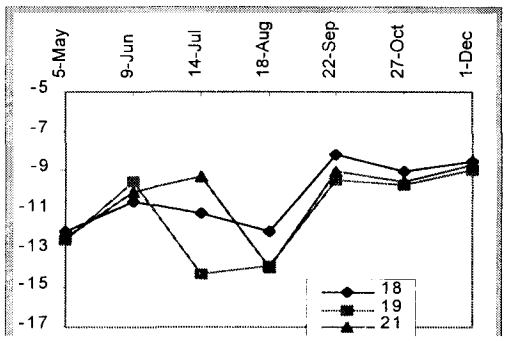

c: DC (Irrigated DX-HT)

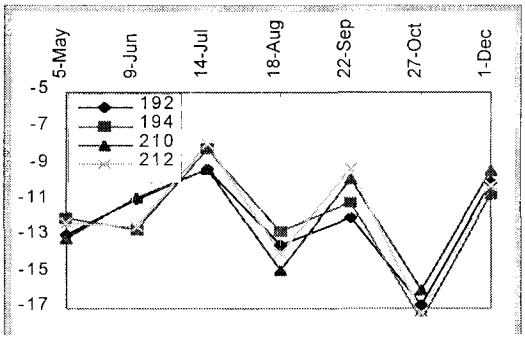

d: DC Mixed (Irrigated DX-HT, Rainfed HT-M, sugarcane-HT)

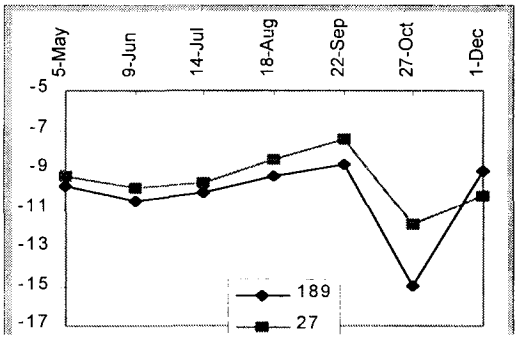

e: DC (Rainfed HT-M) in Bac Lieu Prov.

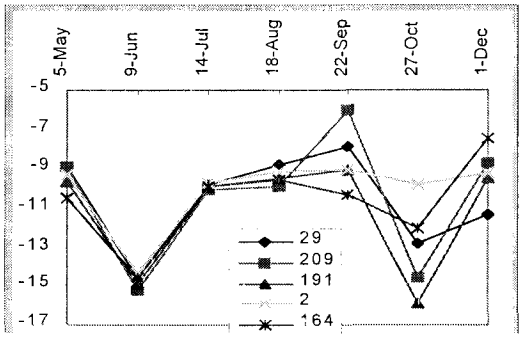

f: DC (Rainfed HT-M) in Soc Trang Prov.

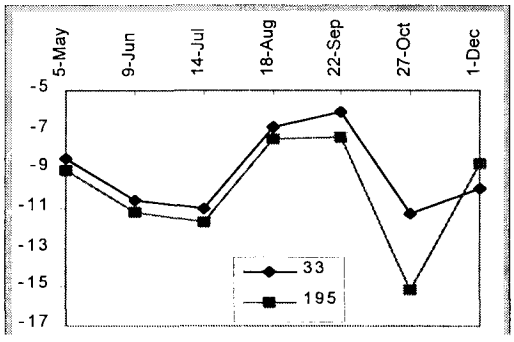

g: DC (Rainfed Late HT-M) in Bac Lieu Prov.

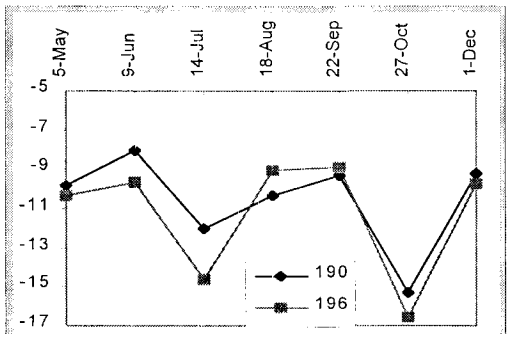

h: DC (Rainfed HT-M) in Soc Trang Prov. (variation)

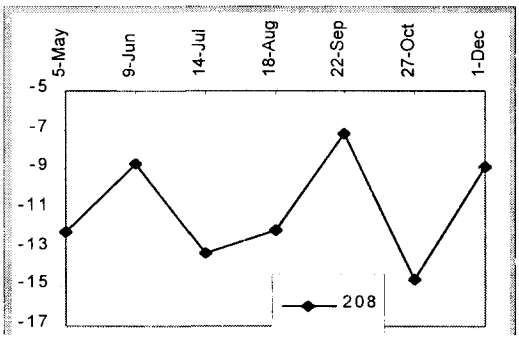

Fig.3: Backscattering time series of the dominant change classes merged into thematic classes. The vertical axis in each graph is the class average backscattering coefficient in dB for the change classes.The standard deviation of most data points range from 1 to 2 dB.

SOIL MOISTURE INVESTIGATION FOR THE DIFFERENT AGRICULTURAL CROPS USING ERS-1 AND ERS-2 DATA

K.Dabrowska-Zielinska, M.Gruszczynska, K.Stankiewicz, M.Janowska, U.Raczka,

Institute of Geodesy and Cartography
Remote Sensing and Spatial Information Center
Jasna 2/4, 00-950 Warsaw, Poland
phone: 48/22 8270328, fax: 48/22 8270328

Abstract

Within the Project AO2.PL102 sponsored by ESA the following paper has been prepared. The data applied for the project include images obtained for Pilot Project PP.PL-4 for 1992-1994. **SAR and ATSR-1 data are used for soil moisture assessment for different agricultural crops.** For 1992-1996 growing seasons the various soil-vegetation ground measurements have been carried out at the time of ERS-1/2 overpasses. Also, survey was undertaken to record crop type with their actual development stage and crop condition. Meteorological parameters as air temperature, wind speed, solar and net radiation were also measured. Obtained SAR.PRI and ATSR-1 descending images have been rectified to Landsat TM georeferenced image. Backscattering coefficient and ATSR data (albedo and surface temperature) have been extracted for the chosen agricultural test site. **SAR data were taken as an average value for the each whole plot as well as for measurement point (from block of 9x9 pixels). Also NOAA/AVHRR data have been registered closed to ERS-1/2 overpasses and processed to obtain NDVI and surface temperature values.** ATSR and AVHRR/NOAA pixels covered nearly the same area on Landsat TM image. **From SAR data average backscatter for the area of each NOAA and ATSR pixel has been extracted. Comparison of ground data with SAR data gave good results for soil moisture under separated surface vegetation roughness classes represented by LAI values. From AVHRR/NOAA and ATSR data soil moisture index WDI has been calculated.** This index which reflects crop water condition has been compared to SAR backscatter values for the area of different crops and growing vegetation stages. The results are going to be presented at the 3rd ERS Symposium.

INTRODUCTION

The project has been carried out for the test site situated in South-West part of Poland in the Obra Valley. The considered area is covered by agricultural fields with the following dominant crops: wheat, rye, triticale, barley, oat, rape, maize, sugar beet and potatoes. The crop types for the considered fields varied from 1992 to 1996. The first ERS-1 SAR images for years 1992-1995 were acquired (towards the end of May) when winter crops were in their heading or flowering stage, spring crops were in their tillering or jointing stage, root crops and maize were in their emergence or germination stage and grass in the flowering stage before harvest. The ATSR-1 images were available for 1995. The predominate soil types for crops are sandy and sandy loam. The area of the test site is flat.

Throughout each of the growing seasons and simultaneously to ERS-1,2 descending overpasses the measurements of soil and vegetation parameters were carried out at 30 points chosen for different crops. The parameters measured were:

- volumetric soil moisture [%],
- wet and dry biomass [g/m^2],
- gravimetric vegetation moisture [%],
- leaf area index (LAI),
- height of the vegetation [m].

These measurements were based on samples taken at the sites which represent the whole field. Also, surveys were undertaken to record crop type with their actual development stage and grass growing condition.

ERS-1.SAR.PRI data acquired during the 35-day repeat orbit were obtained from ESA for Project AO2.PL.102 and PP.PL-4. From each of the ERS-1.SAR images a sub-scenes corresponding to the area of the test site were geometrically transformed to the georeferenced Landsat TM image.

Backscatter coefficient values (sigma) for each of the ground truth points were calculated and averaged for blocks of pixels 9x9. The ground sample point was placed in the middle of each block. Also for the whole field the backscatter coefficient was calculated as well as for the area covered by each of AVHRR/NOAA and ATSR pixel. Such backscatter signature values have been included in the subsequent data analysis.

RESULTS AND DISCUSSION

The intensive study during the previous years tried to answer the question to what extend the value of backscatter depends on surface roughens and soil plant moisture. In this paper we wanted to present the spatial

distribution of backscatter and its relation to soil moisture and roughness for different roughness-moisture conditions in order to determine the relative influence of the parameters on backscattering signal and perform the statistical analysis. The first part of the studies presents the variation of backscattering coefficient and soil moisture as point measurements for 1992 - 1996. The second part presents statistical analyses for satellite data (ERS-1/2.SAR, ATSR, NOAA/AVHRR).

Generally the simple correlation between sigma and soil moisture for each of the crop during vegetation season was poor. Only for spring triticale (r=0.7) and spring wheat (r=0.5) correlation was stronger.

The Figure 1 presents the relation between backscattering coefficient and soil moisture for the fields covered by cereals for the period of 1992-1996. The surface roughness has not been considered. The correlation was poor. It is difficult to present the surface roughness when the soil is covered by vegetation.

One of the approach that has been considered in this research was to measure Leaf Area Index (LAI) for different vegetation growing stages. LAI values change during the growth of vegetation from the low at the beginning of growth reaching maximum at heading stage of cereals and then at the stage of ripening. In our research LAI values represent surface roughness. Figure 2 presents the relationship between backscattering coefficient of ERS/SAR and calculated using LAI and soil moisture values. The correlation is better, correlation coefficient equals to 0.70.

Also considering different LAI classes for cereals the relationship between soil moisture and backscattering coefficient has been considered. The Figure 3 presents the relation between backscattering coefficient and soil moisture for one of LAI class i.e. 3-4. For separated LAI classes the correlation between sigma and soil moisture for cereals is as follows:

LAI from 1 to 2 - r= -0.68,
LAI from 2 to 3 - r= 0.46,
LAI from 3 to 4 - r= 0.62,
LAI>4 - r= 0.82.

In order to eliminate the surface roughness or to consider it as constant the relationship between backscattering coefficient and soil moisture has been examined. The best correlation between sigma and soil moisture for cereals was for high LAI values when crops are in their maximum biomass (and of jointing to heading). At the stage of similar surface roughness (heading/graining and ripening for the year 1992 - 1996) the soil moisture values varied from 3% to 19%. The results of correlation between backscatter and soil moisture at this stage of the crop for spring wheat were significantly better, r= 0.73, Fig. 4.

At the same time of ERS-1/2 overpasses the ground measurements of surface albedo and radiative temperature have been carried out in order to calculate Normalized Vegetation Index (NDVI) and Water Deficit Index (WDI). These indices were considered as an indication of surface roughness (NDVI) and soil moisture (WDI) which also controls the ability of plant soil system to water loss to the atmosphere. Water Deficit Index (WDI) developed by Moran et al. indicates soil - vegetation status. It takes into account the actual soil water conditions in relation to potential and drought. The index considers the percentage of vegetation cover. The Fig. 5 presents the relationship between backscattering coefficient and WDI (calculated using measurements from the ground level) for spring wheat (between 1992 - 1996). The best relation between backscattering coefficient and Water Deficit Index is for the ripening stage of vegetation what confirmed the results presented at the Fig 4.

The second approach to this study has been to use only satellite data to determine the relation between backscattering coefficient and soil-vegetation moisture and roughness. For the study area covered by ERS/SAR image the NOAA/AVHRR data were introduced. Block of ERS/SAR pixels was extended to the size of NOAA/AVHRR pixels. The grid of NOAA pixels was overlaid on ERS/SAR image. For each of NOAA pixels NDVI and WDI indices were calculated. The NDVI represented surface roughness and WDI soil - vegetation water deficit. The Figure 6 presents three curves. First represents the values of backscattering coefficient averaged for the area of each of NOAA pixels. The next curve represents the values of NDVI and the third the values of WDI for the same pixel. The study area was registered by SAR on 20 05 95 and by NOAA on 23 05 95. The backscattering coefficient fluctuated from -13 to -8 dB. The high values of the coefficient i.e. -8 dB represented wet soil water condition, where Water Deficit Index was 0.75 (pixel 44-48). Dry soil water conditions occurred for the area represented by pixel 68-70, for which backscatter was equal to -13 dB and WDI was close to 1. The NDVI values represented area roughness. One as the surface structure which was constant (like tillage direction or infrastructure), and the other which depend on crop structure and vegetation status. The Fig. 7 shows the differentiation of backscatter values for the year 1992 - 1996. The 1992 and 1996 year was the most dry, the sigma values were the lowest. The examination of changes of backscatter values for different years for the same pixels will show the changes of soil - vegetation conditions across the years.

The examination of relation of ERS/SAR data to NOAA data gave the possibility to examine the potential to apply the ATSR data for better understanding of soil - vegetation water conditions.

For the arable area we have examined radiative temperature measured by Along - Track Scanning Radiometer (ATSR) for two dates i.e 20.05.1995 and

28.07.1995. The grid of ATSR pixels (20.05.1995) was overlaid on ERS/SAR image (20.05.1995). The sigma values were averaged within the block of 80 SAR pixels which corresponded to an area of one ATSR pixel.
The Figure 8 presents the variation of three curves. One represents the backscattering coefficient, second radiative temperature and the third Water Deficit Index (WDI).
The values of backscattering coefficient for the pixel 72 and 73 were equal to -12 dB and for the pixel 64 and 65 were equal to -10 - 10.5 dB. The soil - vegetation moisture for the area covered by pixels 64 and 65 were much better than these at the area covered by the pixel 72 and 73, what reflected in lower values of Water Deficit Index (WDI).
The Figure 9 presents the curves of NDVI values calculated from AVHRR data for ATSR pixels and radiative temperature from ATSR and backscatter values obtained from ERS/SAR for 28, 29 July. For the area of temperature increment what indicated the decrease of soil moisture the values of backscatering coefficient lowered.
The visible and infrared range of electromagnetic spectrum gives the information about crop status and allows to examine and understand better the influence of soil - vegetation complex on radar signal.
The project is being continued and the other data of SAR, ATSR and ground observations will be added.

LITERATURE

Bamler, R., 1992, A comparison of Range-Doppler and Wavenumber Domain SAR focusing algorithms, IEEE Trans. on Geoscience and Remote Sensing, Vol. 30.

Dabrowska-Zielinska, K., Gruszczynska, M., Janowska, M., Stankiewicz, K., Bochenek, Zb., 1994, Use of ERS-1 SAR data for soil moisture assessment, Proc. of the First Workshop on ERS-1 Pilot Projects, Toledo, s. 79-84.

Dabrowska-Zielinska, K., Moran, M. S, Janowska M., Gruszczynska M., Stankiewicz K. 1995, Visible, infrared and microwave data as a source of information about vegetation status. Proc. the Meteorological Satellite Data Users Conference, Winchester, U.K.

Laur, H., 1992, Derivation of backscattering coefficient in ERS-1 SAR.PRI products, ESA Esrin.

Moran, M. S., Clarke, T. R., Inoue, Y., Vidal, A., 1994, Estimating crop water deficit using the relation between surface-air temperature and spectral vegetation index. Remote Sensing of Environment, s. 246-263.

Nghiem S.V., T. Le Toan, J.A. Kong, H.C.Han, M. Borgeaud 1993, Layer model with random spheroidal scatterers for remote sensing of vegetation canopy. Journal of Electromagnetic Waves and Applications, Vol.7, No.1,pp.49-75.

Wooding M.G., G.H. Griftiths, R., Evans, P. Bird, D. Kenward, G.E. Keyte 1992, Temporal monitoring of soil moisture using ERS-1 SAR data. Proc. First ERS-1 Symposium, Cannes, pp 641-648

T. Le Toan, P. Smacchia, J.C. Souyris, A. Beaudoin, M.Merdas, M.Wooding, J.Lichteneger 1993, On the retrieval of soil moisture from ERS-1 SAR data. Proc. Second ERS-1 Symposium

Ulaby, F.T., 1980 Microwave response of vegetation ; 23rd Ann. Conf. of Committee on Space Res. (COSPAR Adv. Space Res., vol.1 pp 55-70

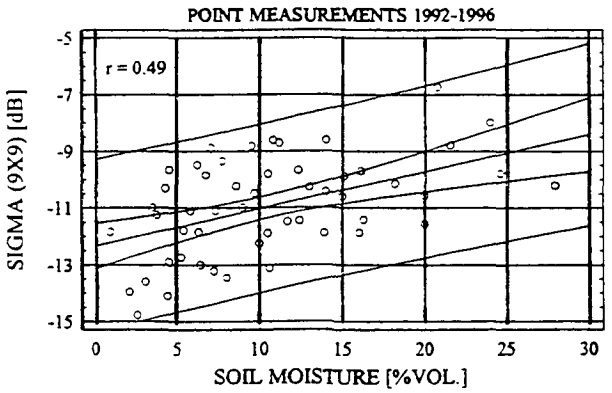

Fig.1. Relation between ERS-1/2.SAR backscatter (SIGMA) and soil moisture from ground measurements for cereals.

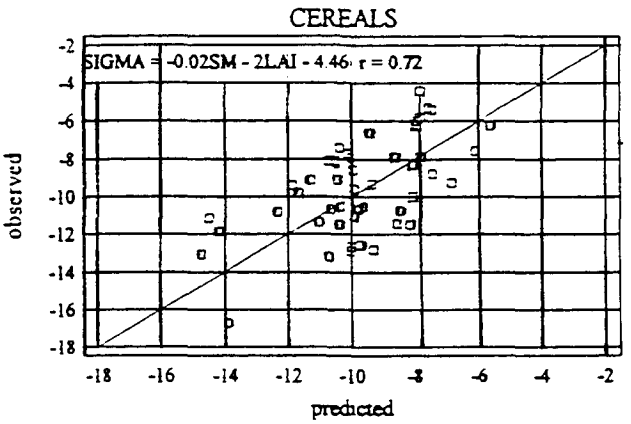

Fig.2. Relation between backscatter observed from ERS-1/2.SAR (SIGMA) and backscatter predicted from soil moisture and LAI point measurements (1992-1996).

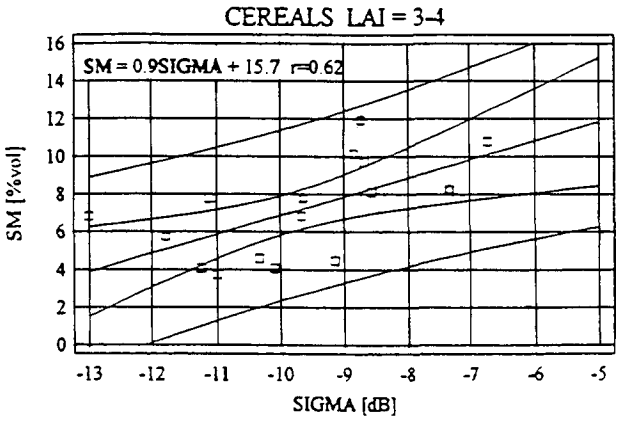

Fig.3. Relation between backscatter from ERS-1/2.SAR (9x9) and soil moisture from point measurements.

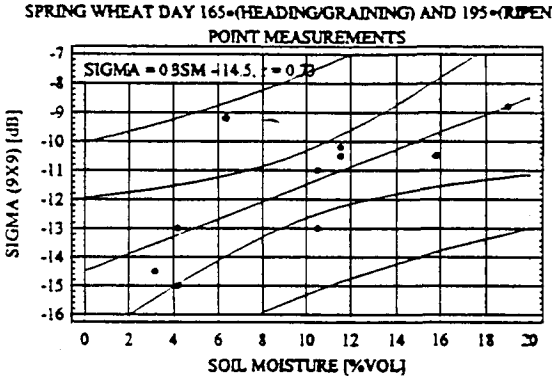

Fig. 4. Relation between backscatter from ERS-1/2.SAR (SIGMA) and soil moisture (SM) from point measurements (1992 - 1996) for spring wheat.

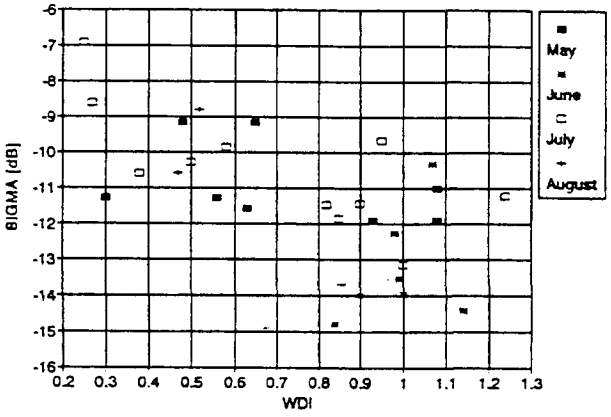

Fig. 5. Relation between backscatter from ERS-1/2.SAR (SIGMA-9x9) and WDI from point measurements for spring wheat for 1992 - 1996.

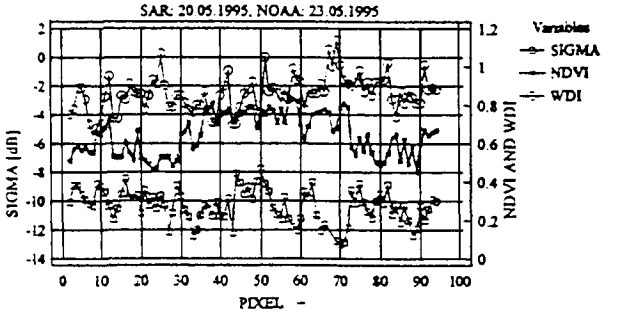

Fig. 6. Temporal evolution of backscatter averaged for NOAA pixels and NDVI and WDI from NOAA.

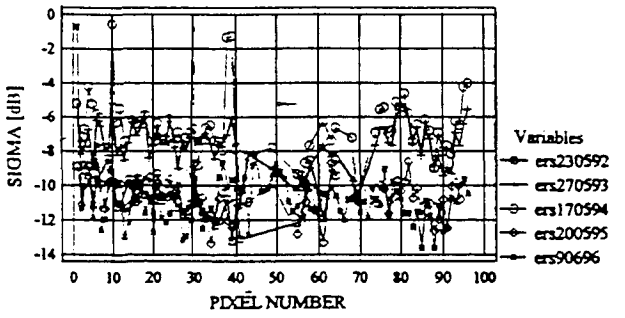

Fig. 7. Temporal evolution of backscatter from May 1992-1996 averaged for NOAA pixels.

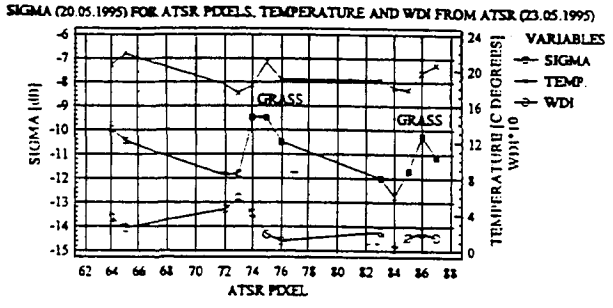

Fig. 8. Plot of backscatter (SIGMA) averaged for ATSR pixels and surface temperature and WDI from ATSR.

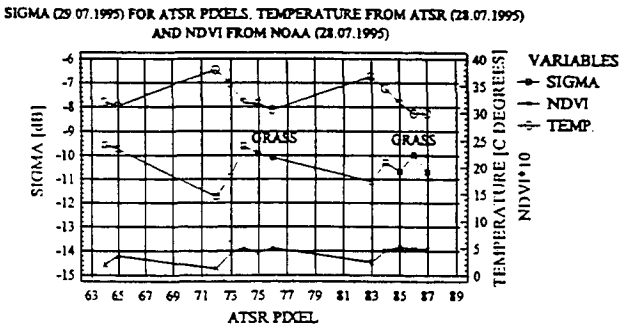

Fig. 9. Plot of backscatter (SIGMA) averaged for ATSR pixels, surface temperature from ATSR and NDVI from NOAA.

MONITORING SEASONAL VEGETATION DYNAMICS IN THE SAHEL WITH ERS WIND SCATTEROMETER DATA

Eric Mougin, Pierre-Louis Frison

CESBIO (CNES-CNRS-UPS)
18 Ave. E. Belin 31401 TOULOUSE CEDEX FRANCE
mougin@cesbio.cnes.fr

Pierre Hiernaux

International Livestock Research Institute
Centre Sahélien de l'ICRISAT, NIAMEY NIGER
P.Hiernaux@cgnet.com

ABSTRACT

ERS-1 wind-scatterometer data acquired over a saharo-sahelian region located in the Gourma, Mali during the period 1992-1995, are analysed. Experimental observations show that $\sigma^{\circ}(45)$ temporal data display a marked seasonality associated with the development and senescence of annual grasses during the successive rainy seasons. The interpretation of the temporal σ° plots is performed with the assistance of a semi-empirical backscattering model combined with an ecosystem grassland model. The backscattering model is parameterised as a function of two surface parameters, namely the soil volumetric water content and the total biomass. The use of this simplified model allows the total biomass to be estimated with a 33% error.

1. INTRODUCTION

Low resolution spaceborne scatterometers such as the instruments on board ERS-1 and ERS-2, have recently shown considerable potential for monitoring vegetation dynamics at global and regional scales (*e.g.* Mougin et al., 1993a; Wismann et al., 1993; Kerr and Magagi, 1993; Frison and Mougin, 1996a; 1996b). Scatterometers operate in the microwave domain and provide a measurement of the bi-directional reflectivity of the observed surface, expressed as the backscattering coefficient σ°. The later mainly depends on the dielectric properties of the surface (vegetation and soil), on the vegetation density, on the relative size of vegetation components with respect to the incident wavelength, as well as on soil surface roughness (Ulaby et al., 1982). At a given frequency, dielectric properties of vegetation and soils are closely linked to their respective water content (Hallikainen et al. 1985; Ulaby and El Rayes, 1987). As green living plants contain a high percentage of water, it was expected that σ° measurements could be used to monitor biomass during the growing season. At a regional scale, this hypothesis was confirmed when comparing wind scatterometer (WSC) σ° temporal plots, acquired at large incidence angles, with Normalised Difference Vegetation Index (NDVI) values for numerous vegetation types (Frison and Mougin, 1996b). Particularly, a very good concordance was found between these two data sets for arid and semi-arid regions of West-Africa. In the case of sparse vegetation like the sahelian one, σ° data displayed a large dynamic range between the dry and the rainy seasons, whereas little variation was observed over regions showing higher vegetation density. Furthermore, no saturation in the σ° values was observed even at the peak of standing biomass which occurs toward the end of the wet season. In contrast, the signal may saturate over more humid savannahs, thus leading to a lesser sensitivity of σ° data to the vegetation development. For all these considerations, the Sahel is retained as a study region for assessing the potentialities of the ERS-1 wind-scatterometer.

In this paper, we analyse multi-temporal ERS-1 WSC data acquired during the period 1992-1995, over a saharo-sahelian region located in the northern Gourma (Mali). Emphasis is put on the monitoring of the seasonal and inter-annual vegetation dynamics. We also investigate the capability of the ERS-1 WSC for retrieving herbaceous biomass.

2. DESCRIPTION OF THE STUDY REGION

The 50 x 50 km² study region is located in the northern part of the Gourma region, Mali (Figure 1). This area lies between 17°N to 16.5°N and from 1.5°W to 2°W, and belongs to the bioclimatic zone defined as the saharo-sahelian transition (Le Houérou, 1989). The landscape is characterised by gently undulating sandy soils partially covered with a low herbaceous layer and a very scattered shrub layer. For the period 1992-1995, annual rainfall ranged from 59 mm to 233 mm with a mean value of 155 mm. The phenology of vegetation is mainly determined by rainfall. Grass development starts after the first rains in June and senescence is associated with the end of the rainy season in September. During

Proc. 3rd ERS Symp. on Space at the service of our Environment, *Florence, Italy, 17–21 March 1997* (ESA SP-414, 3 Vols., May 1997)

the long dry season, there is no green vegetation apart from a few shrubs.

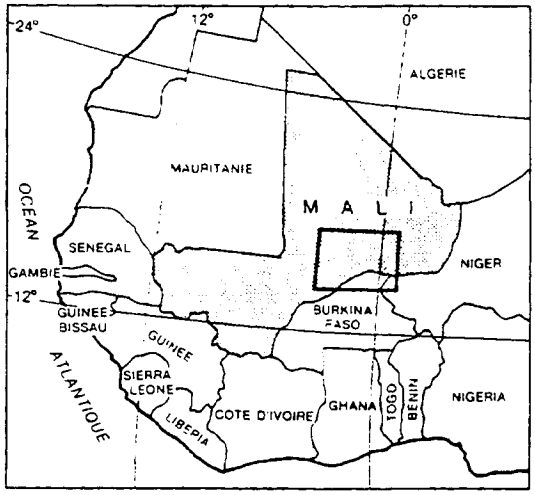

Figure 1: Location of the study region.

Ground data consist of measurements of the total herbaceous above-ground biomass performed at the end of the growing season *i.e.* in September or October. Total biomass corresponds to green and dead components of the standing biomass, and is expressed in kg dry matter per ha (kg DM ha^{-1}). In the area under consideration, measurements are performed in 4 sample sites distributed along a North-South transect. Each sample site is 1 km square and is located within homogeneous environment over at least 4x4 km^2. During the period 1992-1995, maximum biomass is ranging from 240 kg DM ha^{-1} (in 1995) to 1050 kg DM ha^{-1} (in 1994). In each sample site, the associated uncertainty on the means of biomass is about 15%. Within the study region, soil texture is very homogeneous, characterised by a sand content of about 90%. Daily rainfall data is obtained from the meteorological station of Gourma Rharous (16.9°N, 1.9°W) located at the northern edge of the study region.

Simulation of vegetation parameters

Measurement at sample sites provide an estimation of above-ground biomass at the end of the growing season from which a mean value is calculated for the study region. In order to compare with σ^o temporal plots, the daily evolution of biomass is simulated using the sahelian grassland *STEP* model (Mougin et al., 1995). In the following sections, the *STEP* model is used to simulate the vegetation parameters (biomass, vegetation cover, canopy height and vegetation volume fraction) and the volumetric water content in the upper soil profile. Model parameters such as the growth efficiency are obtained by fitting simulations to field measurements of above-ground biomass.

3. DESCRIPTION OF THE WSC DATA

The ERS-1 WSC operates at C-band (5.3 GHz) with VV polarisation. Data are given with a pixel size of 25 km but the actual resolution is about 50 km. The radar signal is continuously delivered and analysed by three sideway antennae : one pointing normal to the satellite flight path (midbeam antenna) and the two others pointing 45° forward (forebeam antenna) and 45° backward (aftbeam antenna). The three antennae illuminate a 500 km wide swath, in a quasi-simultaneous mode, as the satellite moves along its orbit. Across the swath, local incidence angles are ranging from about 18° to 47° for the midbeam and from 25° to 59° for the two other antennae. General characteristics and performance of the ERS-1 WSC instrument can be found in Frison and Mougin (1996a). In the case of the 35-day repeat cycle, the theoretical temporal repetitivity is about 4-5 days. In the following sections, only radar data acquired around 20° and 45° of incidence angles are retained. Data recorded by the three antennae are considered together and are averaged over a 10-day period.

4. EXPERIMENTAL OBSERVATIONS

Temporal profiles of the backscattering coefficient σ^o for the period January 92 - December 95 are depicted in Figure 2. Daily precipitation and daily simulated biomass expressed in terms of its volumetric water content (in kg m^{-3}) are also plotted.

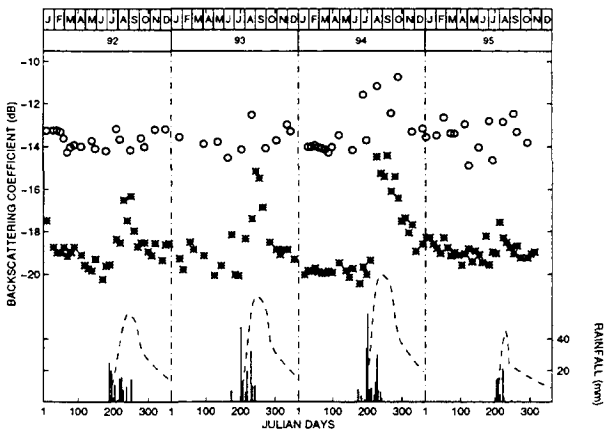

Figure 2 : temporal variation of σ^o at 20°(o) and 45°(*) of incidence angle. Januray 92-December 95.

The saharo-sahelian region shows a marked seasonality associated with the development and senescence of annual grasses during the rainy season. This vegetation cycle is well depicted by the $\sigma^o(45)$ plots. Low σ^o values are observed during the dry season (December-May) when the soil is dry and green vegetation is absent. During this period, the mean backscattering is about -19 dB and -13.5 dB for $\sigma^o(45)$ and $\sigma^o(20)$, respectively. Discrepancy around this mean value is attributed to the spatial heterogeneity of the region in terms of surface

roughness. In 1994, data acquired during the period of the 3-day repeat cycle (between January and March) can be easily identified. Following the first rains, the lowest σ° values are observed at the end of the dry season in June, probably resulting from a decrease of the surface roughness. In July, the vegetation growth is associated with an increase in the $\sigma^\circ(45)$ values up to a maximum occurring in either August or September and corresponding approximately to the maximum of herbaceous biomass. The peak in the $\sigma^\circ(45)$ data is followed by a prompt decrease. The yearly dynamic range is large and appears to be strongly correlated with annual rainfall; it reaches about 4.4 dB, 5.1 dB, 6.7 dB and 2.4 dB for 1992, 1993, 1994 and 1995, respectively. In contrast, the $\sigma^\circ(20)$ temporal plots do not display such a characteristic signature. Overall, $\sigma^\circ(20)$ data show a large scatter in their values. The highest values are nevertheless found during the rainy season but relatively high values are also observed during the dry season. This is particularly the case in 1995. The annual dynamic range reaches about 1 dB, 1.5 dB, 3 dB and 2 dB in 1992, 1993, 1994 and 1995, respectively.

5. MODELLING APPROACH

Due to the size of a resolution cell, only a semi-empirical approach can be undertaken. The objective of the modelling approach is to develop a simple semi-empirical, but physically-based model which might provide a realistic description of the main scattering processes occurring within a resolution cell.

Geometry of the model

At the scale under consideration *i.e.* at the scale of a resolution cell, the sahelian landscape is mainly seen as an integration of contributions from two components (bare soil and herbaceous vegetation). Furthermore, as the herbaceous vegetation is sparsely distributed, the two components can be taken as independent *i.e.* interactions between bare soil and vegetation are neglected. The backscattering coefficient of the observed scene, σ°_{scene} , is given as the incoherent sum of the two previous components after being linearly weighted by their respective cover fractions (Ulaby et al., 1982; Mougin et al., 1993b; Magagi and Kerr, 1997). This simple area additive σ° model therefore implies that the vegetation is confined in a fraction v_c of a considered resolution cell. Hence, by assuming that there is no azimuthal dependency on σ°, which is a reasonable assumption (Frison and Mougin, 1996a), the backscattering coefficient σ°_{scene} , as seen by the three antennae is written :

$$\sigma^\circ_{scene}(\theta_i) = (1 - v_c)\,\sigma^\circ_{bare\ soil} + v_c\,\sigma^\circ_{canopy} \qquad (1)$$

where $\sigma^\circ_{bare\ soil}$ and σ°_{canopy} denote the contribution of the bare soil and the vegetation canopy, respectively and where θ_i is the incidence angle.

Modelling the soil backscattering

The model used here is the Oh et al.'s model which has been validated with radar data acquired for numerous roughness and moisture conditions (Oh et al., 1994). This empirical model is given in terms of the *rms* height, s, and the relative dielectric constant of the soil surface, $\varepsilon_{r,s}$; this later being estimated by an empirical model (Hallikainen et al., 1985) which relates $\varepsilon_{r,s}$ to soil texture (sand and clay content) and soil volumetric water content H_v.

Modelling the vegetation backscattering

The vegetation canopy is modelled as a collection of discrete, randomly oriented scatterers representing the vegetation components, above a rough surface. Within the considered layer, all the scatterers are assumed to be uniformly oriented in azimuth. For the calculations, the stems are neglected and the leaves are modelled as elliptic discs whose axe dimensions are chosen to represent typical C_4 leaves. The scattering matrix of a single scatterer is obtained by applying the Generalised Rayleigh-Gans approximation (Karam et al., 1988). This approximation holds for thin leaves smaller than the wavelength.

The backscattering coefficient of the vegetation canopy, σ°_{canopy} , is given as the zeroth-order solution (soil scattering) and the first order solution (vegetation scattering and surface-vegetation interaction) of the radiative transfer equation (Karam et al. 1992;1995). The backscattering coefficient is written :

$$\sigma^\circ_{canopy} = L^2\,\sigma^\circ_{soil} + \sigma^\circ_{vegetation} + \sigma^\circ_{interaction} \qquad (2)$$

where L is the canopy transmission factor and the terms σ°_{soil} , $\sigma^\circ_{vegetation}$ and $\sigma^\circ_{interaction}$ denote the contributions of the soil beneath the vegetation layer, the contribution of the vegetation volume and the interaction component between the soil and the vegetation, respectively. The explicit content of $\sigma^\circ_{interaction}$ can be found in Karam et al. (1995). For the VV polarisation, the vegetation term has the following expression :

$$\sigma^\circ_{vegetation} = 4\pi \cos\theta_i\, n_o \langle |f_{vv}(-\hat{\imath},\hat{\imath})|^2 \rangle \left[\frac{1 - L^2}{2\kappa_e}\right] \qquad (3)$$

where κ_e is the extinction coefficient for V polarisation given by $n_o \langle \sigma_t \rangle$, σ_t is the extinction cross section, n_o is the density of scatterers per unit volume, $f_{vv}(-\hat{\imath},\hat{\imath})$ is the scattering amplitude in the backscattering direction, L is the loss factor given by $\exp(-\kappa_e\, h_c / \cos\theta_i)$, and $\langle\ \rangle$ denotes the ensemble average over the probability density functions of orientation of the scatterers. For elliptic leaves, the three Eulerian angles of orientation (α, β, γ) are needed to describe the leaf orientation.

The dielectric constant for leaves $\varepsilon_{r,v}$, is computed with the dispersion Ulaby and El Rayes' model (1987).

The Sahelian vegetation backscattering model

Equations (1) and (2) yields the following expression for the backscattering coefficient :

$$\sigma^\circ_{scene}(\theta_i) = (1 - v_c)\,\sigma^\circ_{bare\ soil} + v_c L^2\ \sigma^\circ_{soil} + v_c\,(\sigma^\circ_{vegetation} + \sigma^\circ_{interaction}) \quad (4)$$

The computation of $\sigma^\circ_{vegetation}$ requires the knowledge of the three Eularian angles. As no information is available about leaf orientation at the considered scale, the inclination β parameter is derived from a reasonable guess. Here, the inclination distribution of leaves is chosen to be erectophile due to the predominance of C_4 grasses, and the angle γ is taken as a fitting parameter. Best results are obtained for a γ value of 45°. Leaf dimensions are assumed to be constant throughout the growing season apart from the length which is equal to canopy height up to a maximum of 20 cm. The other necessary parameters v_c and h_c are simulated by the *STEP* model. The number density of scatterers n_o is derived from the simulated vegetation volume fraction f_v which can be expressed as a function of the total biomass B_t (in kg DM ha^{-1}), the canopy height h_c and the gravimetric water content of vegetation H_p.

Soil roughness is assumed to be constant throughout the growing seasons; its value being adjusted with the σ° measurements acquired at the end of the first dry season (May 1992).. Soil surface moisture content H_v is provided by the *STEP* model. Simulated daily values are averaged over a 10-day period in order to get more representative data for the whole study area.

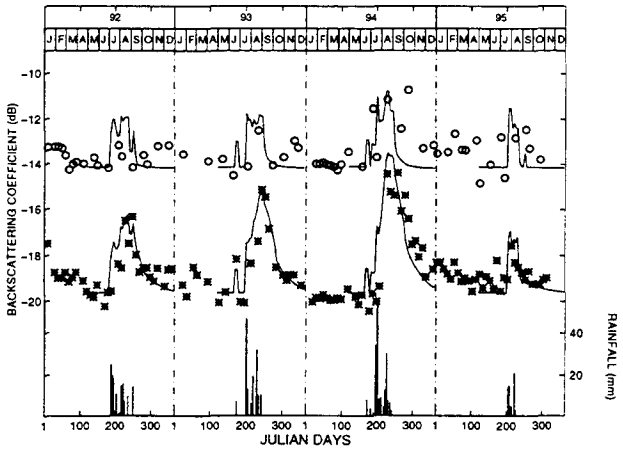

Figure 3 : Comparison of simulated (—) and observed σ° temporal profiles. January 92 - December 95.

The evolution of the soil and vegetation parameters are fed into equation (4) to compute the variation of σ°_{scene} throughout the four successive growing seasons. Figure 3 shows the comparison between the measurements and the simulations for the period 1992-1995. For each year, simulations are performed from May, 1 till December, 31 with a 5-day time scale.

At 45° of incidence angle, there is an overall good concordance between the simulations and measurements. Particularly, the annual σ° dynamic range is very well described by the model. At the peak of backscattering, the differences between measurements and simulations never exceed 1 dB. In contrast, there are obviously some difficulties in simulating the beginning of the growing period when the vegetation cover is still very low. Particularly, in 1992 there is a time shift of about 3 weeks between the observed increasing in the σ° values and the simulations. Also, this difference is about 10 days in 1993 and in 1994. During this period, the magnitude of the backscattering mainly depends on the moisture content of the soil surface which, within a resolution cell, is highly variable. Here, it is apparent that we fail to simulate an appropriate soil moisture from the rainfall data recorded at only one meteorological station. On the other hand, when vegetation is sufficiently developed, the contribution of the soil decreases and the agreement between the experimental data and the model is good.

At 20° of incidence angle, the comparison between simulations and measurements is difficult due to the small number and the discrepancy of the experimental data. Overall, maximum observed values are pretty well simulated during the rainy seasons apart from 1992. At the beginning of the dry season, the increasing in the experimental data (particularly in 1992 and 1993) is not understood.

Contribution of the soil and vegetation to the scene backscattering

The sahelian backscattering model allows the different contributions to be analysed.

At 45° of incidence angle, only the contributions of the vegetation and the bare soil are significant. The soil always dominates at the beginning of the rainy season when the vegetation is not fully developed. The magnitude of the soil contribution, resulting from the variation of its surface moisture, is nevertheless limited, given that sandy soils have a small field capacity of about 10%. Accordingly, the characteristic temporal profiles and in particular the peaks of σ° essentially depend on the vegetation term. While the vegetation contribution remains weak for 1995, the peak of σ° mainly results from the vegetation component in 1994. In 1992 and 1993, the vegetation and soil contributions have similar values. From these observations, it can be seen that the maximum σ° is coincident with the peak of the vegetation volumetric water content and not with the peak of green biomass. Due to the continuous decrease

of the leaf moisture content since grass emergence, there is a time lag of about three weeks between the two peaks. At the end of the growing season, the soil dries and the shape of the temporal plot mainly results from the vegetation contribution. Finally, as vegetation dries out at the beginning of the dry season, the backscattering only originates from the dry soil.

At 20° of incidence angle, the total backscattering mainly results from the soil component. Overall, the vegetation canopy has little effect on the radar signal apart from the 1994 growing season for which its contribution may reach about 20% of the total backscatter at the end of the growing season.

Parameterisation of the model

From the above considerations, the sahelian backscattering model can be simplified under the following forms :

$$\sigma^{\circ}_{scene}(20) = \sigma^{\circ}_{bare\ soil} \quad (5)$$

$$\sigma^{\circ}_{scene}(45) = (1 - v_c)\,\sigma^{\circ}_{bare\ soil} + v_c\,\sigma^{\circ}_{vegetation} \quad (6)$$

Furthermore, in order to parameterise equation (6), the vegetation component, given by equation (3), can be expressed as a function of the standing biomass B_t , which is the only parameter estimated from field measurements. Empirical relationships are therefore sought between the physical parameters (extinction coefficient κ_e and the radar cross section $\sigma_s = 4\pi |f_{vv}(-\hat{i},\hat{i})|^2$) and B_t . From a physical point of view, the two previous quantities are related to a density of scatterers per unit volume and not to a density of scatterers per unit surface. However, as the canopy parameters are strongly inter-correlated (Mougin et al., 1995), it is nevertheless possible to find a relationship between the physical parameters and B_t. This approach is valid if the scatterers do not to change as a function of time, in terms of shape, size, orientation and dielectric constant. As the later varies with B_t , we can attempt to find a general relationship. To this end, the *STEP* model is run till the peak biomass for the years 1992, 1993 and 1994 and equation (3) is used to compute κ_e and σ_s . The 1995 growing season is not included because of the very limited development of the vegetation. The general regression relationship, derived from the simulation study, is written :

$$\kappa_e \text{ (or } \sigma_s) = exp(a_2 B_t^2 + a_1 B_t + a_0) \quad (7)$$

where a_i (i=1,2,3) are empirical parameters.

At 45° of incidence angle, the simplified sahelian backscattering model is therefore given by equation (6) combined with equation (7). The parametric model is similar to the water cloud model proposed by Attema and Ulaby (1978), the two contributions being weighted by their respective cover fractions. Furthermore, the vegetation cover v_c can be written as a function of the above-ground biomass (Mougin et al, 1995). Expressed under this form, the model has only two unknown parameters, the soil volumetric water content H_v and the total biomass B_t .

6. INVERSION

Emphasis is put on biomass retrieval. The inversion approach follows a two-step procedure. Firstly, the Oh et al.'s model is used to derive a linear relationship between $\sigma^{\circ}_{scene}(20)$ and H_v , from which a maximum value of the surface soil moisture during the rainy season, is estimated. Second, a procedure which minimises the differences between the experimental data and the simulated $\sigma^{\circ}_{scene}(45)$ data is performed using the simplex method (Nelder and Mead, 1985). This later is run with two constraints: on one hand, the soil moisture value to be retrieved must be smaller or equal than the maximum value previously found, and on the other hand, the biomass must follow a 2-parameter logistic function simulating its temporal evolution. Results of the biomass retrieval are given in Figure 4.

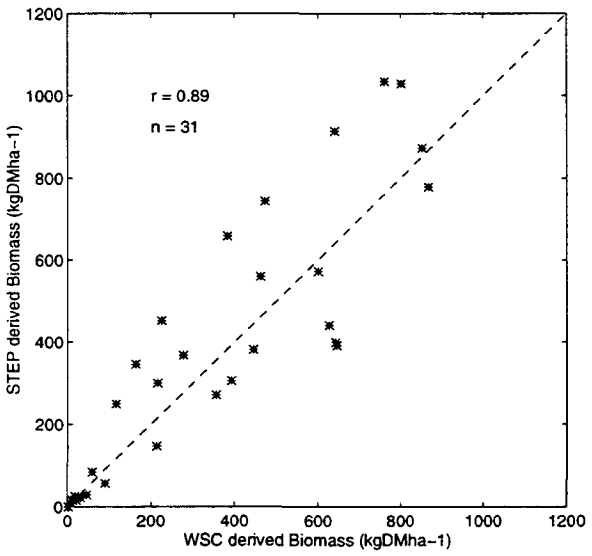

Figure 4 : Comparison between WSC-Derived Biomass and STEP-Derived Biomass. Growing seasons 92-94.

The associated error is about 33% indicating that biomass retrieval can be performed with a certain degree of confidence. Particularly, the maximum retrieved biomass equal to 500, 650 and 900 kg DM ha^{-1} compare well with the field-estimated values equal to 400, 620 and 1050 kg DM ha^{-1} for 1992, 1993 and 1994, respectively.

7. CONCLUSION

ERS-1 wind-scatterometer data acquired over a saharo-sahelian region located in the Gourma, Mali during the period 1992-1995, are analysed. Experimental observations show that $\sigma^{\circ}(45)$ temporal data display a marked seasonality associated with the development and senescence of annual grasses during the successive rainy seasons. The interpretation of the temporal σ° plots is performed with the assistance of a semi-empirical backscattering model combined with the ecosystem grassland model *STEP*. Contributions of the various components of the Sahelian landscape to the total backscattering are identified. Overall, the soil contribution is always large but the $\sigma^{\circ}(45)$ temporal plots reflect well the biomass variation. Particularly, it is shown that the maximum backscattering coefficient is associated with the peak of the vegetation volumetric water content which is not coincident with the peak of green biomass. Finally, the backscattering model is parameterised as a function of two surface parameters, namely the soil volumetric water content and the total biomass. The use of this simplified model allows the total biomass to be estimated with a 33% error.

ACKNOWLEDGEMENTS

The authors thank ESA for providing us the ERS-1 scatterometer data used in the present study (project AO2.F121). This work was partly supported by the 'Pôle Espace' of the Région Midi-Pyrénées, France.

8. REFERENCES

Attema, E.P.W., and Ulaby, F.T. (1978), Vegetation modeled as a water cloud, *Radio Science*, 13:357-364.

Frison, P.L., and Mougin, E. (1996a), Use of ERS-1 wind scatterometer data over land surfaces, *I.E.E.E. Trans. Geosc. Remote Sens.*, 34:1-11.

Frison, P.L., and Mougin, E. (1996b), Monitoring global vegetation dynamics with ERS-1 wind scatterometer data, *Int. J. Remote Sens.*, 17(16):3201-3218.

Hallikainen,M.T., Ulaby, F.T., Dobson, M.C., El-Rayes M.A., and Wu, L-K. (1985), Microwave dielectric behavior of wet soil. Part I: Empirical models and experimental observations, *I.E.E.E. Trans. Geosci. Remote Sens.*, 23:25-34.

Karam, M.A., Fung, A.K, Lang, R.H., and Chauhan, N.S. (1992), Microwave scattering model for layered vegetation, *I.E.E.E. Trans. Geosci. Remote Sens.*, 30:767-784.

Karam, M.A., Fung, A.K, Amar, F., Mougin, E., Lopes, A., Levine, D.M., and Beaudoin, A. (1995), A microwave polarimetric scattering model for a forest canopy based on vector radiative transfer theory. *Remote Sens. Environ.*, 53:16-30.

Karam, M.A., Fung, A.K, and Antar Y.M.M., (1988), Electromagnetic wave scattering from some vegetation samples, *I.E.E.E. Trans. Geosci. Remote Sens.*, 26:799-808.

Kerr, Y.H., and Magagi, R.D. (1993), Use of ERS-1 windscatterometer data over land surfaces. *Proceed. 2nd ERS-1 Symposium , Hamburg, 11-14 Oct., ESA SP-361,* pp. 381-388.

Le Houérou, H.N. (1989), *The Grazing Land Ecosystems of the African Sahel*, Ecological Studies 75, Springer-Verlag, Berlin, 282 pp.

Lo Seen, D., Mougin, E., Rambal, S., Gaston, A., Hiernaux, P. (1995), A regional Sahelian grassland model to be coupled with multispectral satellite data. II. Towards the control of its simulations by remotely sensed indices. *Remote Sens. Environ.*, 52:194-206.

Magagi, R.D., and Kerr, Y.H (1997), Characterization of surface parameters over arid and semi-arid areas by use of ERS-1 wind-scatterometer, *Remote Sensing Review*, (to appear).

Mougin, E., Lopes, A., Proisy, C., Warich, A., Frison, P.L., Lo Seen, D., and Lecomte, P. (1993a), Analysis of ERS-1 scatterometer data over land surfaces. Preliminary results. *Proceed. 2nd ERS-1 Symposium , Hamburg, 11-14 Oct., ESA SP-361,* pp. 393-397.

Mougin, E., Lo Seen, D., Frison, P.L., and Rambal, S. (1993b), Assessing the complementarity of microwave and optical data for ecosystem modelling in arid regions, *Proceed. Satellite Remote Sensing Symposium, Europto, Rome, 26-30 Sept.*

Mougin, E., Lo Seen, D., Rambal, S., Gaston, A., and Hiernaux, P. (1995), A regional Sahelian grassland model to be coupled with multispectral satellite data. I. Description and validation. *Remote Sens. Environ.*, 52:181-193.

Nelder J.A. and Mead. R. (1985), A simplex method for function minimization. *Computer Journal*, vol 7., p. 308-313.

Oh, Y., Sarabandi, K., and Ulaby, F.T. (1992), An empirical model and inversion technique for radar scattering from bare soil surfaces, *I.E.E.E. Trans. Geosci. Remote Sens.*, 30:370-381.

Ulaby, F.T., Moore, R.K., and Fung, A.K. (1982), Microwave remote sensing : active and passive, vol. II., *Addison-Wesley Publishing Company.*

Ulaby, F.T., and El-Rayes, M.A. (1987), Microwave dielectric spectrum of vegetation. Part II: Dual-Dispersion model, *I.E.E.E. Trans. Geosci. Remote Sens.*, 25:550-557.

MAPPING AND MONITORING OF ARID LAND VEGETATION IN JORDAN USING ATSR-2

Marianne C Edwards, Jane Wellens, Andrew C Millington

Department of Geography, University of Leicester, University Road, Leicester, LE1 7RH, UK.
phone: +44 (0)116 2525148, fax: +44 (0)116 252385
e-mail: mce1@le.ac.uk, jw27@le.ac.uk, acm4@le.ac.uk

Dawud Al-Eisawi

Faculty of Graduate Studies, University of Jordan, Amman, Jordan.

ABSTRACT

The narrow wavebands (0.545-0.565, 0.649-0.669, 0.855-0.875, 1.58-1.64 μm) and dual look angle (nadir and 55° forward) of ATSR-2 should enhance the ability to detect vegetation of very low densities from remotely sensed data. This paper looks at the application of ATSR-2 to the mapping and monitoring of sparse vegetation in the eastern desert region of Jordan, an area used extensively for grazing. Imagery was compared with contemporaneous field data. Results indicate that indices utilising combinations of near infrared/red reflectance are of limited use for differentiating vegetation due to bright soil backgrounds; this limits the ability to extract a characteristic spectral response of dry chenopod vegetation, particularly at vegetation densities of less than 10 %. An alternative approach is to simulate the bi-directional reflectance distribution function (BRDF) of ATSR-2 pixels over dryland surfaces in order to develop a model, which can be inverted to estimate vegetation characteristics. Ongoing research considers the use of linear mixture modelling incorporating different look angles as data layers and the potential information held in the directional dependence of red/near infrared feature space.

INTRODUCTION

The Along Track Scanning Radiometer (ATSR-2) was launched on-board ERS-2 in April 1995. Designed as a research satellite, ATSR-2 provides the opportunity to study the effects of off-nadir viewing particularly in relation to vegetation mapping and monitoring. Using a conical scan mechanism, locations on the Earth's surface are scanned twice - at nadir and at a forward look angle of 55°. Narrow wavebands in the visible and near infrared (0.545-0.565, 0.649-0.669, 0.855-0.875 μm) provide detailed information on those areas of the electromagnetic spectrum where the influence of vegetation is most commonly detected.

This paper describes current research examining the usefulness of ATSR-2 data for the study of vegetation in arid environments. In these regions, vegetation is characteristically of low densities exhibiting wide spatial and temporal variations. Off nadir viewing of such areas using ATSR-2 should enhance the detection of sparse vegetation. Furthermore the coarse resolution (1km), relatively large swath (500 km) and 6 day coverage cycle should help capture temporal and spatial variability over a large area. Overgrazing and land degradation are problems found in many arid areas. These are areas that equally face population growth and increased pressure on finite resources. It is therefore important to study these areas effectively mapping their past histories, understanding their development and making informed predictions for the future.

VEGETATION MAPPING AND MONITORING

The use of vegetation indices to detect and map vegetation is widely accepted. Such indices focus on the use of red and near infrared wavebands where differential reflectance by photosynthetically active vegetation gives a low red and a high near infrared response. Indices range from a simple red/near infrared ratio to more complicated indices that include terms relating to background soil conditions and atmospheric effects. The Normalised Difference Vegetation Index (NDVI) is one of the most commonly used vegetation index and numerous examples can be found of it's application in drylands. Kennedy (1989) used the NDVI calculated from Advanced Very High Resolution Radiometer data to study vegetation in Tunisia, whilst Ringrose and Matheson (1987) considered its application to rangeland in Botswana. The Soil-Adjusted Vegetation Index (SAVI), a modified version of the NDVI was proposed by Huete (1988). It 'calibrates' a vegetation index, effectively normalising differences in soil substrate, thus allowing a more accurate estimate of vegetation cover. Equations for the NDVI and SAVI are given below:-

$$NDVI = \frac{NIR - R}{NIR + R}$$

$$SAVI = \frac{NIR - R}{NIR + R + L} * (1 + L)$$

where L = 1 for low vegetation densities.

Results by Gutman (1991) show an increase in NDVI in a forward scatter direction using AVHRR data. Coincidence of the forward look of ATSR-2 with the direction of forward scatter should increase vegetation indices. An oblique view will also mean that proportionally more vegetation is viewed by the sensor - vegetation indices should be higher accordingly.

An alternative to the use of vegetation indices is to adopt a more direct modelling approach. Modelling the spectral response of a surface can take a number of different forms from theoretically based models and the use of radiative transfer and geometric optics to more empirically based models. Modelling the spectral response of vegetation has been attempted by a number of authors. Many such as Rosema *et al.* (1992), Hall *et al.* (1995) and Li and Strahler (1985) consider forest canopies. The methods and assumptions they use relate well to trees but are more difficult to apply to the shrubby vegetation found in arid regions. Modelling vegetation in an arid environment should have advantages over a similar task in a tropical or temperate environment. The vegetation is characteristically sparse and fairly uniform in shape. A common geometric shape (e.g. spheres or cones) can be assumed and the proportion of shadow is easily calculated. Due to single plants on a soil background, multiple scattering between different canopy layers can be ignored. Having said that, in this environment, background soil conditions are considerable and pure homogenous pixels from which to extract pure endmembers are difficult to find.

In this study, an initial attempt at modelling the spectral response of vegetation in arid regions has focused on the method described by Jasinski (1996). Jasinski's model is essentially a hybrid model using a physical modelling approach to interpret the information held in the red/near infrared feature space derived from a single multispectral satellite image. The canopy is considered as geometric elements randomly positioned on a horizontal soil surface. Using a reflectance model, the reflection of a given pixel can be described in terms of canopy transmittance - and proportions of illuminated and shaded canopy, and illuminated and shaded background (see equation 1 below).

$$\rho(\lambda) = [m_i + m_S\,\tau\,(\lambda)]\{\rho_\infty(\lambda)[1-\tau^2(\lambda)] + \rho_{gi}\,(\lambda)\tau^2(\lambda)\} + \rho_{gi}(\lambda)[g_i + g_S\,\tau\,(\lambda)] \quad (1)$$

λ = the wavelength of the band centre
m_i = fraction of illuminated canopy
m_S = fraction of shaded canopy
g_i = fraction of illuminated ground
g_S = fraction of shaded ground
τ = bulk canopy transmittance
ρ_{gi} = illuminated ground reflectance
ρ_∞ = canopy reflectance at zero transmittance

Within this equation, each reflectance term is considered to have a random or Poisson distribution. This moves away from the commonly made assumption of constant endmembers and takes account of spatial variability relating to differences in soil texture, organic content, soil moisture, canopy height and leaf area. Treating plants as randomly distributed objects on a planar surface allows the estimation of ground shadow, g_S, in terms of η, a nondimensional solar geometric similarity parameter equating to the ratio of the mean shadow area cast by a single tree to the mean projected area.

$$g_S = 1 - m - (1 - m)^{\eta + 1} \quad (2)$$

m_S is similarly defined in terms of β, a constant that is derived from plant geometry and the solar zenith angle. The values for bulk transmittance and zero transmittance are estimated using values held in the red/near infrared scattergram. For more details on parameter derivation, see Jasinski (1989, 1996). Jasinski's model estimates the variables in equation 1 and uses them to predict lines of constant canopy cover. This method is invertible and little or no ground information is needed.

THE STUDY AREA

Research is being carried out in association with the Jordan Badia Research and Development Programme, a collaborative project between the Royal Geographical Society in the U.K. and the Higher Council for Science and Technology in Jordan. This programme focuses on an area of 11,210 km^2 in north-east Jordan between Syria to the north and Saudi Arabia to the south. A basalt regolith overlies the northern half of the area whilst the south is covered by cherts, limestone and other sedimentary rocks. The Badia experiences a generally arid desert climate with a mean annual rainfall of between 200 mm in the north and 50 mm in the south, and a potential evaporation of 1500 mm to 2000 mm per annum (Al-Homoud *et al.* 1995). Vegetation in the area is spatially variable occurring naturally on very low angle gravel fans that extend out

from wadis (known as marabs) into seasonally inundated mudflats (known as qaas).

METHODOLOGY

FIELD DATA COLLECTION

Field work was carried out in November-December 1995 and March-May 1996. A Landsat TM image was used to locate large homogeneous vegetated sites - seven vegetated sites were visited on each occasion and measurements taken of percentage vegetation cover, biomass, plant dimensions, density and spacing, soil moisture, soil type and ground radiometric properties. Three random 30m quadrats were sampled within a central 1 km^2 sampling frame. Within each quadrat, vegetation measurements were taken along ten 20m transects. The length of transect covered in vegetation in relation to the total transect length was used to give an estimate of percentage vegetation cover.

IMAGE ACQUISITION AND PRE-PROCESSING

An ATSR-2 image dating from 1st December 1995 was used in this work. The image was obtained as a gridded brightness temperature (GBT) product. It is 512 * 512 km and contains information on seven spectral wavebands in the nadir and forward look directions. The geolocation information supplied with the product was used to apply a geometric correction. Having converted digital counts to top of atmosphere reflectances using supplied calibration tables, an atmospheric correction was carried out. A detailed description of the method of atmospheric correction can be found in Mackay and Millington (1997).

Following geometric and atmospheric correction of the imagery, vegetation indices were calculated for the areas of field study. Each index was calculated using values in a 3 * 3 grid of pixels. This includes the central 1 km sampling frame and ensures accurate location of field sites (Justice and Townshend 1981).

In order to apply Jasinski's model of pixel reflectance, a computer programme was written in C to solve equation 1. Equation 1 was used to calculate red and near infrared reflectances at different vegetation coverages and soil reflectances. Table 1 gives details of the input parameters used. As an initial form of analysis, many of the figures are taken from Jasinski's own work in Walnut Gulch, Arizona. Vegetation in Walnut Gulch is shrubby with very little herbaceous understory. It is structurally similar to that of the Badia. Running the computer model gives a series of data pairs as output. These can be plotted and superimposed on the red/near infrared scattergrams giving lines of increasing vegetation cover.

RESULTS AND DISCUSSION

Figure 1 shows the results obtained from the application of vegetation indices to the ATSR-2 data. Correcting for the soil effect using SAVI decreases the index but both the NDVI and SAVI show that no obvious relationship exists between the indices and percentage vegetation cover. Ringrose and Matheson (1987) describe how an increase in vegetation cover in arid environments is often associated with a darkening effect due to leaf absorbency and the effects of shadowing. In this case, vegetation amounts are too small to manifest a relationship in any direction. Figure 1 does however indicate a difference between the forward and nadir bands of ATSR-2. This difference is not always positive. As discussed in Edwards *et al.* (1996), many factors (e.g. resolution, soil reflectance and the nature of the vegetation) influence the sensor recorded signal. Using vegetation indices, the effect of vegetation on the off nadir signal cannot be ascertained from the imagery at the very low coverages examined here.

Figure 2 shows the red/near infrared scattergram derived from an ATSR-2 image of Jordan. Percentage vegetation cover lines imposed are those derived using Jasinski's model. The scattergram shows a characteristic triangle, and a soil line such as that described by Baret *et al.* (1993) can be identified. With reference to the image, values lying to the right of the soil line represent areas of snow accumulation on the Jebel Drouz and water such as the Dead Sea, whilst those to the extreme left correspond to sites of high vegetation cover in the Jordan Valley. Field sites in the Badia where vegetation cover is known all correctly lie between the soil and 10 % cover lines.

The question arises as to what extent the location of points between 0 and 10 % cover can be attributable to vegetation. As Jasinski (1989) describes, the soil line pivots around a mean according to such factors as soil moisture, soil mineralogy and shadow. These are factors that vary across the Badia region. Future work will aim to follow Jasinski's model further, calculating probability functions relating to the many combinations of soil reflectance, vegetation cover, transmittance and reflectance that yield the same red/near infrared data pair. Scene simulation should make it possible to establish the point at which vegetation reflectance dominates over soil reflectance.

Paramount to this work is the hypothesis that viewing in a forward look direction will enhance vegetation detection. The acquisition of more ATSR-2 data will allow Jasinski's model to be extended to compare scattergrams derived from forward and nadir looks. Considering viewing geometry in relation to AVHRR,

Gutman (1991) stresses the need for bidirectional surface models that incorporate the fact that vegetation is anisotropic. Further fieldwork will study the nature of plant response in arid environments and gain field measurements of factors such as canopy transmittance to input into Jasinski's model. The accuracy of the parameters derived from feature space must be tested.

The influence of resolution will also be studied. Jasinski's work was carried out with reference to a Landsat TM scene. Transferral of this method between field measurements at the metre scale, Landsat TM at the 30m scale and ATSR-2 and AVHRR at the kilometre scale needs to be investigated. Advantages to vegetation detection gained by using the forward look at ATSR-2 may be negated by the coarse resolution of the sensor.

Research using ATSR-2 data and field sites in the Badia region of Jordan has shown that the sparse vegetation cannot be detected using conventional vegetation indices. Through sampling on a pixel by pixel basis, vegetation is not identified. Consideration of subpixel processes is needed.

There are many ways of modelling arid land vegetation. Work presented here gives the results from the initial consideration of Jasinski's model (1996). Future work needs to take this further considering feature space boundary probabilities and the application of the model to the forward look bands of ATSR-2. It must also be recognised that modelling simplifies complex processes. There will be a degree of error involved. Future field work must aim to test the accuracy of assumptions made comparing simulated data with actual ground measurements and imagery.

ACKNOWLEDGEMENTS

Marianne Edwards is supported by a Leicester University Studentship. Imagery was obtained under an ESA PI to White and Millington (A02.UK.125). The authors wish to express their thanks to Michael Jasinski at the NASA Goddard Space Flight Center, Washington for his advice and help with model implementation, to George Mackay, Kevin Tansey and Kevin White for their help with fieldwork and to all at the Higher Council for Science and Technology, Amman, the University of Jordan and Safawi Field Centre for their assistance with field campaigns.

BIBLIOGRAPHY

Al-Homoud, A.S., Allison, R.J., Sunna,B.F., and White,K., 1995, Geology, geomorphology, hydrology, groundwater and physical resources of the desertified Badia environment in Jordan. *Geojournal* 37 pp 51-67.

Baret, F., Jacquemoud, S., and Hanocq, J.F., 1993, The soil line concept in remote sensing. *Remote Sensing Reviews* Vol. 7. pp 65-82.

Edwards, M.C., Al-Eisawi,D., and Millington,A.C., 1996, The use of ERS ATSR-2 data for monitoring rangeland vegetation in the eastern Badia, Jordan. *Proceedings of the 22nd Annual Conference of the Remote Sensing Society* 11-14th September 1996. University of Durham.

Gutman, G.C., 1991, Vegetation Indices from AVHRR: An update and future prospects. *Remote Sensing of Environment* Vol. 35. pp 121-136.

Hall, F.G., Shimbakuro, Y.E., and Huemmrich,K.F., 1995, Remote sensing of forest biophysical structure using mixture decomposition and geometric reflectance models. *Ecological Applications* Vol. 5 (4). pp. 993-1013.

Huete, A.R., 1988, A soil-adjusted vegetation index. *Remote Sensing of Environment* Vol. 25 pp. 295-309.

Jasinski, M.F. and Eagleson, P.S., 1989, The structure of red-infrared scattergrams of semivegetated landscapes. *IEEE Transactions on Geoscience and Remote Sensing* Vol. 27. No. 4. pp. 441-451.

Jasinski, M.F., 1996, Estimation of subpixel vegetation density of natural regions using satellite imagery. *IEEE Transactions on Geoscience and Remote Sensing* Vol. 34. No. 3. pp. 804-813.

Justice, C.O. and Townshend, J.R.G., 1981, Integrating ground data with remote sensing, in Townshend , J.R.G, (ed), *Terrain analysis and remote sensing,* London, George Allen and Unwin.

Kennedy, P.J., 1989, Monitoring the phenology of Tunisian grazing lands. International Journal of Remote Sensing Vol. 10. Nos 4 and 5. pp. 835-845.

Li, X, and Strahler, A.H., 1985, Geometric-optical modelling of a conifer forest canopy. *IEEE Transactions on Geoscience and Remote Sensing* Vol. 32. No. 5. pp. 705-720.

Mackay, G, and Millington, A.C., 1997, Application of a dual angle atmospheric correction for ATSR-2 solar reflecting channels, submitted to *International Journal of Remote Sensing* February 1987.

Ringrose, S and Matheson, W., 1987, Spectral assessment of indicators of range degradation in the Botswana hardweld environment. *Remote Sensing of Environment* Vol. 23. pp 379-396.

Rosema, A., Verhoef, W., Noorbergen,H., and Borgesius, J.J., 1992, A new forest light interaction model in support of forest monitoring. *Remote Sensing of Environment* Vol. 42. pp. 23-41.

Table 1: Input parameters used to apply Jasinski's model

Parameter	Value used
Solar zenith angle, θ	55.3
Solar geometric similarity parameter, η	1.19
Bulk canopy transmittance (red), τ	≈ 0 *
Bulk canopy transmittance (nir), τ	0.47 *
Reflectance at zero transmittance (red), ρ_∞	0.07 *
Reflectance at zero transmittance (nir), ρ_∞	0.25 *
Soil line slope, α	1.29
Soil line intercept, γ	0.08
* values taken from Walnut Gulch	

Figure 1: Percentage vegetation cover plotted against NDVI and SAVI

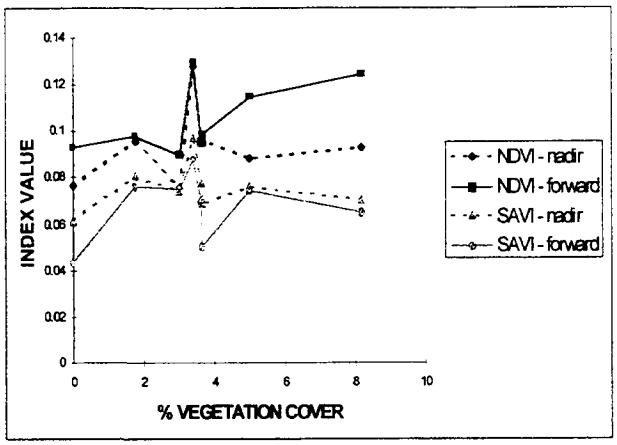

Figure 2: Red/Near infrared scattergram derived from ATSR-2

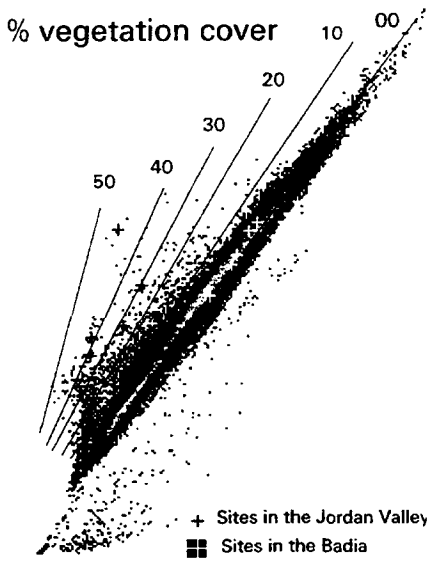

ADVANTAGES OF PRINCIPAL COMPONENTS ANALYSIS FOR LAND COVER SEGMENTATION FROM SAR IMAGE SERIES

Geoffrey M. Henebry

Department of Biological Sciences, Rutgers University
Newark, NJ, 07102 USA
phone: +1 201 648 5053, fax: +1 201 648 5518

ABSTRACT

Two interrelated difficulties could hinder the widespread use of SAR imagery in land cover mapping and monitoring: speckle and georeferencing. Speckle poses problems for both scene segmentation and georeferencing: high-frequency, spatially random multiplicative noise hinders clustering algorithms and obscures landmarks. Most despeckling techniques trade spatial information for noise reduction. Using multiple image dates, noise can be reduced with little loss of spatial resolution. Furthermore, image time series enable assessment of land cover variation, whether due to seasonality or disturbance. Principal components analysis (PCA) on SAR image series can identify a landscape's dominant spatio-temporal modes of backscattering. The first principal component yields a very low noise image that contains information about temporally invariant terrain features (roads, rivers, slope/aspect), which can aid georeferencing. I illustrate the approach using a SAR image series for 12 sub-orbital repeats acquired during the 1995 growing season. PCA was performed on a scene containing Konza Prairie Research Natural Area, a scientific preserve for tallgrass ecology, and surrounding lands. The first four principal components held significant spatial information, while higher order components were dominated by speckle. A surprising result was the ability of PCA to pick out isolated riparian woodlands amidst a hilly prairie landscape. A kind of poor man's interferometry, this feature arises out of the differential backscattering caused by a 4 degree nominal shift in incidence angle between sub-orbital repeats.

1. INTRODUCTION

Principal components analysis (PCA) is an important tool for analysis of image time series. However, most applications have been to optical imagery (e.g., Townshend *et al.*, 1985; Eklundh and Singh, 1993; Benedetti *et al.*, 1994). The rare employment of PCA for SAR image studies likely arises for two reasons: (1) a general lack of availability of SAR image series until the past few years and (2) the presence of a well-defined scene model for most SAR applications. This last point merits some discussion.

A scene model can be broadly construed as some prior understanding of the spatio-temporal arrangement of stuff that interacts with the illuminating radiation (Strahler *et al.*, 1986). What constitutes this "stuff" are the objects of interest in the imaged scene, e.g., agricultural fields, ice fields, geological lineaments. Given how few orbital SAR sensors had flown until 1990s and the technical requirements needed to understand and manipulate the data effectively, it is not surprising that the application domains for SAR data have been restricted until recently to disciplines where the scene objects were well-defined in advance of data acquisition. Land cover monitoring requires a rather loosely-defined prior scene model due to the typically heterogeneous mix of dynamic surfaces and textures. As a result, land cover segmentation and mapping involves aspects of data mining and statistical pattern recognition.

PCA of SAR image series has several advantages, most of which have been well demonstrated for optical data. PCA of a high temporal resolution image series can attenuate temporal autocorrelation, thereby increasing the suitability of the data for

Proc. 3rd ERS Symp. on Space at the service of our Environment, *Florence, Italy, 17–21 March 1997* (ESA SP-414, 3 Vols., May 1997)

image segmentation and classification procedures (Benedetti *et al.*, 1994). Furthermore, the principal components (PCs) are of intrinsic interest because they effectively summarize the dominant spatio-temporal modes of radiometric variation in the data in terms of linear combinations of image frames. The PC loadings, i.e., weights assigned to each image date, provide important information about what sort of thing each PC is summarizing, which points to its potential utility for land cover discrimination.

PCA has another potentially important use in the analysis of SAR image series: it could attenuate two interrelated difficulties that hinder the widespread use of SAR imagery in land cover mapping and monitoring – speckle noise and georeferencing. Speckle noise poses problems for both scene segmentation and georeferencing: high-frequency, spatially random multiplicative noise hinders clustering algorithms and obscures landmarks. Most despeckling techniques trade spatial information for noise reduction. Using multiple image dates, noise can be reduced with PCA resulting in minimal loss of spatial resolution. Furthermore, image time series enable assessment of land cover variation, whether due to seasonality or disturbance.

2. METHODS

A series of 11 ERS-1 SAR images (uncalibrated data in MLD format from CCRS) were acquired during the 1995 growing season. I selected image subscenes to include Konza Prairie Research Natural Area, the City of Manhattan Airport, Kansas River floodplain, Interstate Highway 70, and neighboring grazing and agricultural lands. Using the Khoros warpimage program, scenes were coregistered to the 19MAY scene using between 50 and 80 tiepoints; the resulting areal extent used in the analysis was about 233 km^2. I chose not to calibrate the data because terrain variation was very significant and no fine-resolution DEM exists for the entire study area, so calculation of local incidence angle was not feasible. (We are working to remedy this deficiency using SAR interferometry.) A datacube of 11 time-ordered scenes was then submitted to the PCA program in ERDAS Imagine; principal component images, eigenvalues, and eigenvectors (loadings) were received as the output.

3. RESULTS

The first PC captured the consistently bright and dark features in the scene and explained 47% of image series variance (Figure 1). Radiometrically bright features are predominantly slopes with easterly aspects and some agricultural fields; dark features include airport runways, the Kansas River, highways I-70 and K-18, and terrain in radar shadows. Since these are persistent features in the scene, the loadings were nearly uniform across dates (Figure 2); PC1 summarized the stable scene elements.

The second PC captured the distinction between burned and unburned prairie as well as some discrimination among agricultural fields. Burned areas are also typically grazed. Explaining about 9.5% of series variance (Figure 1), the loadings exhibited a definite seasonality (Figure 2).

The third PC revealed a surprising aspect of the image series: it captured look angle differences and thereby explained 8.3% of variance (Figure 1). The over-lapping orbital paths, 69 and 341, yielded different look angles, about 24.4° and 20.2° respectively, for this landscape. This difference translated into an enhanced sensitivity to local height variations. Riparian wooded areas were clearly distinguishable, even in complex upland drainages. In addition to picking out ribbons of trees amid the grasslands, the look angle difference generated registration artifacts from hills with the brighter eastern aspect slopes. The alternating loadings confirm the association of PC3 with orbital path (Figure 2).

The fourth PC, explaining 7.2% of datacube variance (Figure 1), captured the seasonality of agricultural production in the larger riparian landscapes. However, PC4 also exhibited a sensitivity, albeit weaker, to orbital path (Figure 2), which was manifested in "dark" registration artifacts associated with "bright" artifacts of PC3.

Higher order PCs exhibited little spatial localization and thus are attributable either to smaller patches of weaker radiometric change or to speckle noise. The total variance explained by the remaining 7 PCs is about 29%. Note the significant drop in explanatory power between PC4 and PC5 (Figure 1). Speckle noise is characterized by high spatial frequency and is usually treated as spatially random. The relatively slow decay of variance in the higher order PCs results from each PC skewering a high-dimensional cloud of effectively random points: every PC "skewer" explains *some* variance, just not very much. I have observed in optical image series this phenomenon of high-order PCs being dominated by noise elements and leading to slow variance decay (Henebry and Rieck, 1996).

The major consequence of the PCA pushing speckle into the higher order components is a greatly improved signal-to-noise ratio for the first PC. This low noise image has no significant of spatial resolution (although there is some negligible loss during coregistration). PCA speckle reduction is accomplished by sacrificing temporal resolution to maintain spatial resolution. PCA enables a time-for-space substitution to achieve a lower noise image that is well-suited for georeferencing. Crucial spatial detail needed for precisely locating ground control points is frequently obscured by speckle but can be recovered through PCA. In addition, the PC1 image provides a high resolution scene for multi-sensor fusion. All the low-order PCs provide important spatio-temporal information that can be exploited by segmentation and classification algorithms.

PCA uses a statistical decision rule to arrive at the components and these components are simply linear combinations of the variables -- here scenes from different dates. How robust are the PCs? Does their explanatory power extend beyond the particular dataset used to derive them? Clearly, particular sets of PCs will have limited extrapolatory power at best for different landscapes; but how well has a particular set captured the dominant spatio-temporal modes of backscattering in that landscape? One approach to this question is to increase or decrease the number of scenes submitted to the PCA and observe the changes in loading patterns and PC image structure. I guessed that adding a scene to the end or beginning of the growing season should have a marginal overall effect on the loadings but could give some indication of the robustness of particular PCs. Of particular interest are the first few PCs, since they are readily useful. To test for their robustness I added a twelfth image from late October to the datacube and reran the PCA.

To compare the results of the first PCA (PCA-11) with the second (PCA-12), I regressed the loadings for each corresponding principal component. The first three PCs were highly positively correlated; the fourth PC was highly negatively correlated; and the correlation of higher order components ranged from moderate to very low (Figure 3). The images produced by first four PCs of PCA-12 were virtually indistinguishable from those produced by PCA-11, except for the negative switch in PC4.

4. CONCLUSIONS

Principal components analysis appears to have one fundamental use in land cover analysis of SAR image series: speckle reduction. From this perspective some significant advantages accrue: (1) identification of dominant spatio-temporal modes of backscattering within the scene; (2) partitioning of this variance into a set of discrete images that can be submitted to segmentation and classification algorithms; and (3) production of a high spatial resolution, low spatial noise image that can serve as a template for georeferencing and multi-sensor fusion.

There are limitations of PCA that relate to sampling rate relative to scene dynamics. In scenes with high intrinsic temporal variability, sampling frequency must at least meet the Nyquist criterion, but PCA works better when there is a high degree of temporal autocorrelation (Henebry and Rieck, 1996). In the absence of temporal oversampling in dynamic landscapes, PCA still segregates speckle to higher order components and lower order PCs tend more towards lower noise images of individual dates. (I have observed this in a seven date image series from the Brazilian Pantanal; see Henebry and Kux, this volume.) As SAR image series become more

readily available over the next decade and as interest in land cover monitoring increases, there is a need for new approaches to spatio-temporal analysis. While not a new technique to remote sensing, PCA offers distinct advantages for SAR data analysis that should be further explored.

5. ACKNOWLEDGEMENTS

I gratefully acknowledge support from ESA through project AO2.USA126 and from NSF through grant DEB-9696229. Thanks to Shawn Hutchinson for assistance with image coregistration.

6. REFERENCES

Benedetti, R. *et al.*, 1994, Vegetation classification in the middle mediterranean area by satellite data,, *Int. J. Remote Sens.*, 15, 583-596.

Eklundh, L., and Singh, A. 1993, A comparative analysis of standardised and unstandardised principal components analysis in remote sensing, *Int. J. Remote Sens.*, 14, 1359-1370.

Henebry, G.M., and Kux, H.J.H., 1997, Spatio-temporal analysis of SAR image series from the Brazilian Pantanal, *this volume*.

Henebry, G.M., and Rieck, D.R., 1996, Applying principal components analysis to image time series: effects on scene segmentation and spatial structure, *Proc. IGARSS '96*, pp. 448-450.

Strahler, A.H., *et al.*, 1986, On the nature of models in remote sensing. *Remote Sens. Environ.*, 20, 568-588.

Townshend, J.R.G., *et al.*, 1985, Multitemporal dimensionality of images of normalized difference vegetation index at continental scales, *IEEE Trans. Geo. Rem. Sens.*, GE-23, 888-895.

Figure 1: explanatory power of PCs

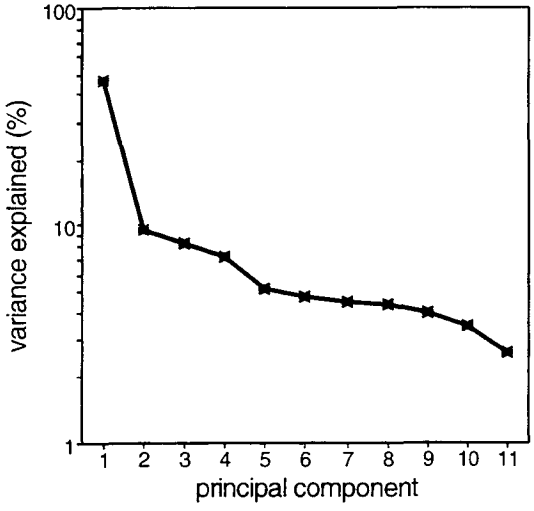

Figure 2: loadings for PCA-11

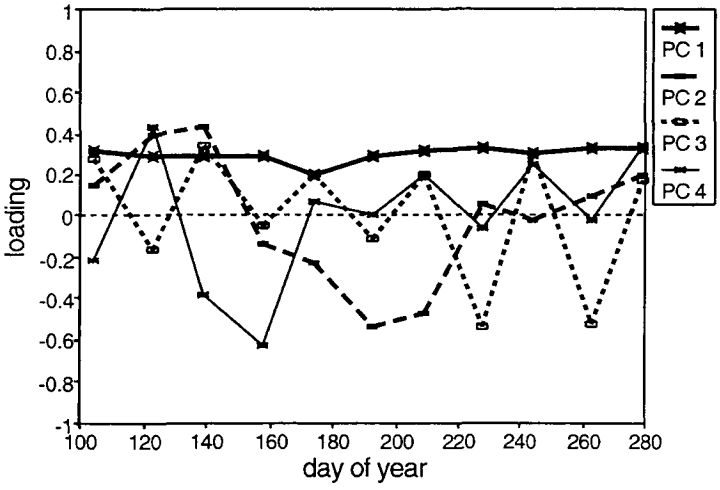

Figure 3: regression of PCA-11 & PCA-12

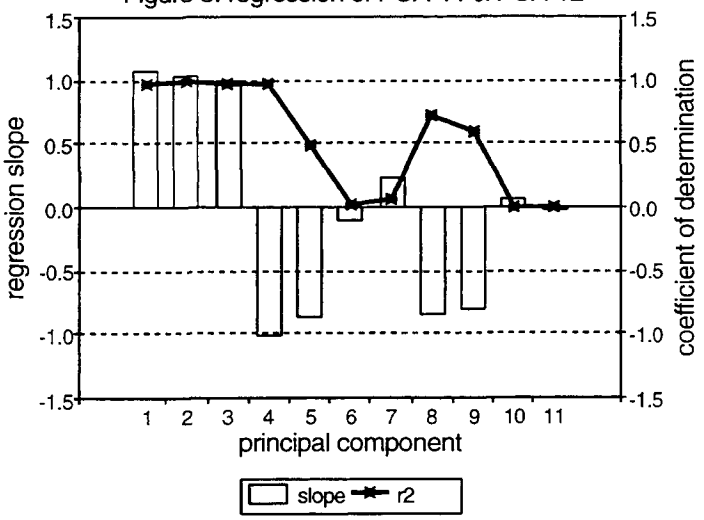

ORBITAL EFFECTS ON ERS-1 SAR TEMPORAL BACKSCATTER PROFILES OF AGRICULTURAL CROPS

Yifang Ban

Division of Geoinformatics
Department of Geodesy and Photogrammetry
Royal Institute of Technology
S-10044 Stockholm, Sweden
Phone: +46-8-790 7348, Fax: +46-8-790 7343
yifang@geomatics.kth.se

Philip J. Howarth

Waterloo Laboratory for Earth Observations
Department of Geography
University of Waterloo
Waterloo, Ontario, Canada N2L 3G1
Phone: +1-519-888-4567 ext. 3404, Fax: +1-519-888-6768
howarth@watleo.uwaterloo.ca

ABSTRACT

Multitemporal radar backscatter characteristics of crops and their underlying soils are analyzed for an agricultural area in southwestern Ontario, Canada using nine dates of ERS-1 SAR imagery acquired during the 1993 growing season. From the calibrated data, SAR temporal backscatter profiles were generated for each crop type. It was found that the radar backscatter coefficients varied considerably from one date to the next. Attempts were made to explain the variations based on changes in environmental conditions or potential variations due to characteristics of the SAR system. The results of the study indicate that small changes in incidence-angle can have strong impacts on radar backscatter. Thus, attention must be given to local incidence-angle effects when using ERS-1 SAR data, especially when comparing backscatter coefficients of the same area from different scenes or different areas within the same scene.

1. INTRODUCTION

Spaceborne SAR is potentially an important data source for agricultural applications. It satisfies a basic agricultural requirement for reliable and frequent imaging throughout the crop growing season. Before the launch of the long-duration spaceborne SAR systems, airborne studies had demonstrated that multitemporal SAR data can enhance the ability to distinguish between various crop types (e.g., Brisco *et al.*, 1984; Brown *et al.*, 1984; Fischer and Mussakowski, 1989; Foody *et al.*, 1989; Dobbins *et al.*, 1992). However, comparatively few datasets have been available for study because of the increased cost and logistics of generating multitemporal SAR data with airborne platforms (Brisco *et al.*, 1992). With the launch of ERS-1&2, JERS-1 and RADARSAT, world-wide spaceborne SAR data became routinely available. To be able to extract information from multitemporal spaceborne SAR, it is important to understand the radar backscatter behaviours of individual crops throughout the growing season and to determine what factors are likely to cause variation in backscatter between different dates.

In this study, we analyze the multitemporal radar backscatter characteristics of crops and their underlying soils over the growing season and attempt to relate the variations between dates to agricultural/environmental parameters and SAR system parameters.

2. STUDY AREA AND DATA DESCRIPTION

The study area is situated in an agricultural area in Oxford County, southern Ontario, Canada (Figure 1). Approximately 15 km x 4 km, this area has been selected as one of the few representative agricultural 'supersites' across Canada at which the relationships between radar data and agriculture are being studied (Brown *et al.*, 1991).

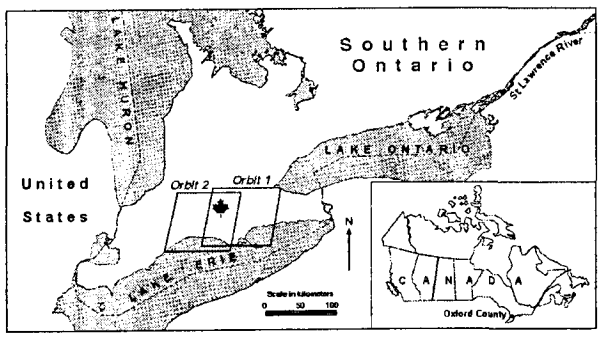

Figure 1. The study area and the ERS-1 satellite orbits

The ERS-1 C-VV SAR data were acquired on nine dates during two descending passes in the 1993 growing season (Figure 1, Table 1). Extensive ground data were collected by field teams at the times of the satellite overpasses. It included observations and measurements of the crops (e.g., crop type, growth stage, percentage cover, canopy height, row spacing, plant condition) and their soil characteristics (e.g., soil type, surface roughness, moisture content, row direction). The field boundaries were digitized from a SPOT image.

Table 1. ERS-1 Data

Date	Orbit
May 31, 1993	2
June 16, 1993	1
July 5, 1993	2
July 21, 1993	1
Aug. 9, 1993	2
Aug. 25, 1993	1
Sept. 13, 1993	2
Sept. 29, 1993	1
Oct. 18, 1993	2

3. METHODOLOGY

3.1 Preprocessing

Field-Boundary Preparation

Since the development of image segmentation techniques is not the aim of this study, the geocoded (i.e., Universal Transverse Mercator (UTM) coordinates) field-boundary file for the study area was generated using a PAMAP GIS. First, the field-boundary file was converted from a vector format to a raster format; then a 5-pixel buffer was applied to the field boundaries to eliminate the effects of field boundary pixels and minor image registration errors on crop discrimination. The file was then imported into the PCI EASI/PACE image processing system.

SAR Data Radiometric Calibration and Geometric Correction

Quantitative comparisons of the multitemporal SAR data require calibrated images. Thus, the SAR data used in this study were corrected for SAR antenna pattern and compensated for range-spreading loss at ESA D-PAF, Germany. The calibration accuracy is $\pm$ 0.42 dB (Laur *et al.*, 1993).

The SAR images were then geometrically corrected to field boundaries with a 12.5 m pixel spacing using a second-order polynomial and a nearest-neighbour resampling algorithm.

3.2 Derivation of the Radar Backscatter Coefficient σ°

The generation of ERS-1 SAR temporal backscatter profiles of agricultural crops requires relating pixel digital numbers (DN) on SAR images to backscatter coefficients of corresponding distributed targets in the scene. According to Laur (1992), the complete equation to be applied to determine the backscatter coefficient σ° of an area located at incidence angle α is:

$$\sigma^\circ = \frac{<I>}{K(\alpha)} = \frac{<I>}{K} \bullet \frac{\sin\alpha}{\sin\alpha_{ref}} \bullet \frac{R^3}{R^3_{ref}} \bullet \frac{1}{g^2(\theta)}$$

where: $K = K(\alpha_{ref} = 23^\circ)$

R is the slant range distance at the distributed target location and R_{ref} is a reference slant range distance; i.e., the mid-swath slant-range distance R_{ref} = 847.0 km

$g^2(\theta)$ is the two-way antenna pattern profile and θ is the look angle at the distributed target location

Since the ESA SAR PRI products have compensated for range spreading loss and antenna pattern, the equation can be simplified to:

$$\sigma^\circ = \frac{<I>}{K} \bullet \frac{\sin\alpha}{\sin\alpha_{ref}}$$

where :

$$<I> = \frac{1}{N} \bullet \sum_{i=1}^{i=N} DN_i^2$$

DN_i is the digital number of a given pixel *i* and is proportional to the square-root of the intensity I_i received from the ground resolution cell corresponding to pixel *i*.

N is a large pixel number (more than 500) to ensure statistical validity to the estimation of the mean intensity.

Expressed in decibels ($\sigma^\circ(dB) = 10 \bullet \log_{10} \sigma^\circ$), we have:

$$\sigma^\circ(dB) = <I>(dB) - K(dB) + \beta(dB)$$

where $K = 58.63$ dB

$$\beta(dB) = 10 \bullet \log_{10}\left(\frac{\sin\alpha}{\sin\alpha_{ref}}\right)$$

In PRI images, the range of incidence angles α is typically from 19.5° at the near-range to 26.6° at the far-range. The correction factor β can vary from - 0.7 dB to +0.6 dB with image swath (Laur, 1992).

3.3 Temporal Backscatter Profile Generation

SAR temporal backscatter profiles were generated in EXCEL for major crop types (i.e., corn, soybeans, winter wheat, barley/oats, alfalfa and pasture). First, the temporal backscatter profile for each individual field was generated; then the general temporal backscatter profile for each crop was generated by averaging the σ° of all fields for that crop type on each date.

4. RESULTS AND DISCUSSION

A wide range of parameters affects the backscatter of microwaves from vegetation and soil. The important system parameters, however, are frequency, polarization and incidence angle. The crucial features of the target in determining the proportion of radiation returning to the sensor are plant canopy (e.g., plant type, height, density, biomass, water content and growth stage) and soil parameters (e.g., soil moisture content, roughness and tillage direction). The SAR temporal backscatter profiles for each crop show the complexity of the relationship between microwave and agricultural parameters over the growing season.

Using multitemporal ERS-1 SAR data during the 1993 growing seasons, the radar backscatter characteristics of crops and their underlying soils were analyzed. The SAR temporal backscatter profiles were generated for each crop type (Figure 2). In general, radar backscatter was primarily influenced by soil in the early season when fields were bare or exhibited a limited crop canopy. With crop development, radar backscatter decreased due to attenuation and absorption by vegetation canopies. The decreasing trend continued until crops were at the seed development stage. Then the backscatter started to increase as the crops reached the senescent stage (Figures 2 & 3).

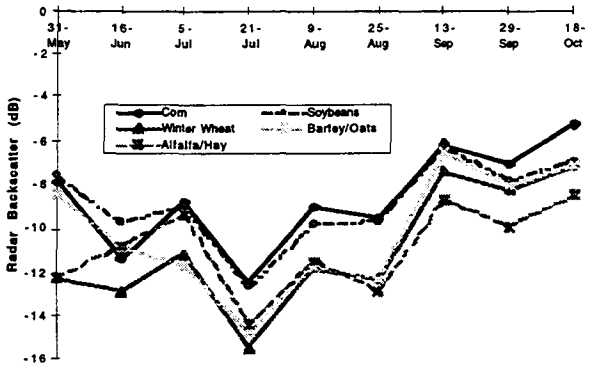

Figure 2. ERS-1 SAR temporal backscatter profiles for major crops during the 1993 growing season

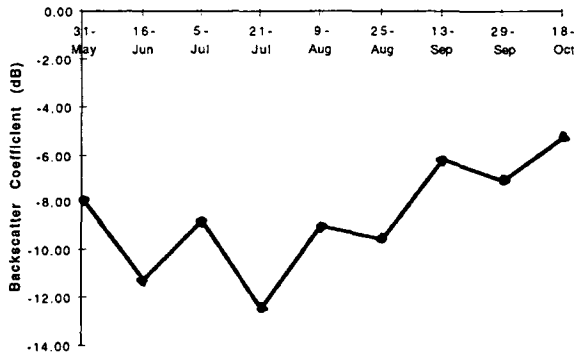

Figure 3. ERS-1 SAR temporal backscatter profile for corn

Although Figures 2 and 3 match the general trend described earlier, the radar backscatter coefficients varied considerably from one date to the next. Given the absolute calibration accuracy of +/- 0.42 dB, these variations could not be related to SAR calibration. Attempts to explain the variations based on changes in environmental conditions, such as local meteorological conditions and crop development, were unsuccessful.

Attention was then turned to potential variations due to characteristics of the SAR system. For individual crop types, SAR temporal backscatter profiles were generated separately for each orbit. It was found that the profiles were relatively smooth when the two orbits were separated (Figure 4).

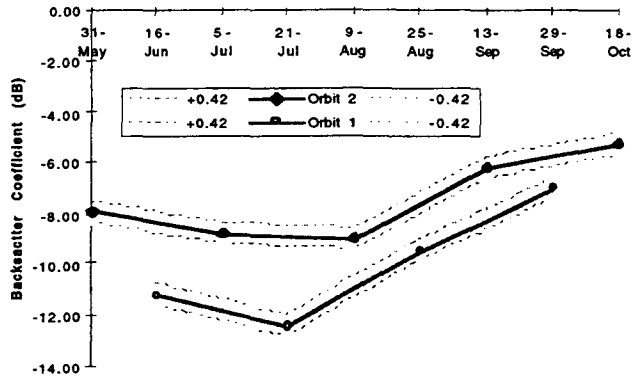

Figure 4. ERS-1 SAR temporal backscatter profiles for corn derived from two orbits: error buffers included

ERS-1 orbital (incidence angle) effects were observed on all crops (Figures 5 - 8). For the 4° difference of incidence angle between the two orbits in the study area (about 21.5° for orbit 2 and 25.5° for orbit 1), the average difference of radar backscatter was approximately

3 dB. This finding is comparable to the results of Ulaby *et al.* (1986, Figure 9). Using C-HH SAR, Ulaby *et al.* (1986) measured incidence-angle effects on a corn canopy. The estimated change of backscatter is about 3-4 dB from incidence-angle 20° to 25°.

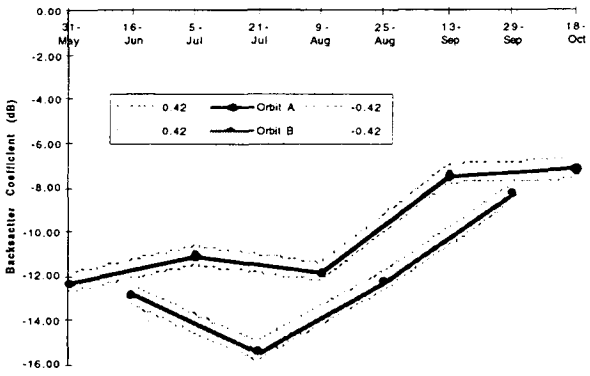

Figure 5. ERS-1 SAR temporal backscatter profiles for wheat derived from two orbits: error buffers included

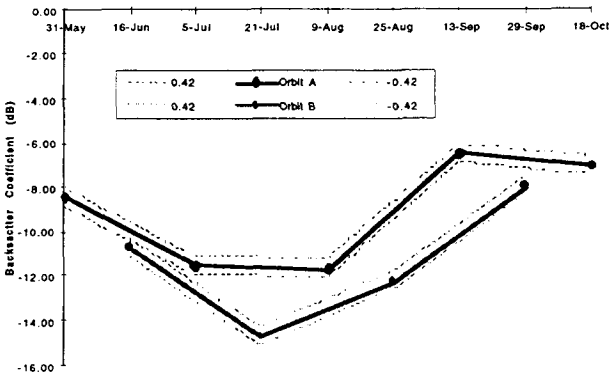

Figure 6. ERS-1 SAR temporal backscatter profiles for barley/oats derived from two orbits: error buffers included

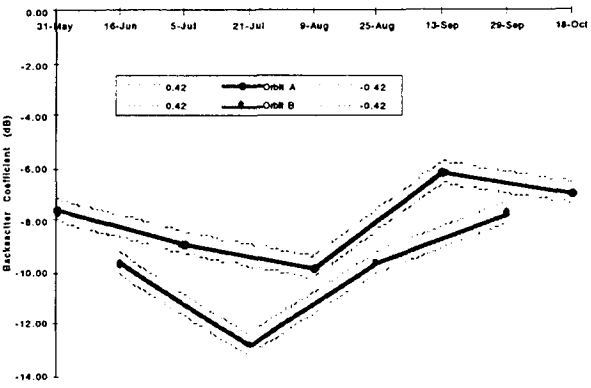

Figure 7. ERS-1 SAR temporal backscatter profiles for soybeans derived from two orbits: error buffers included

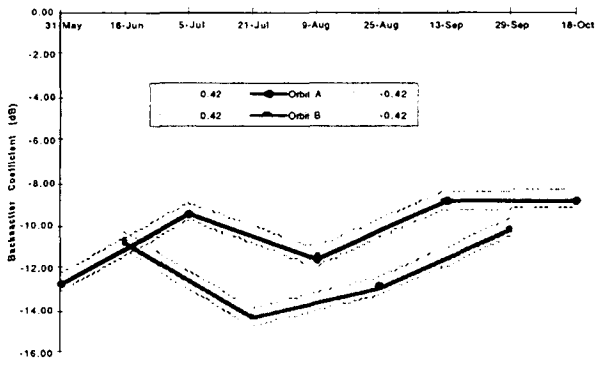

Figure 8. ERS-1 SAR temporal backscatter profiles for alfalfa/hay derived from two orbits: error buffers included

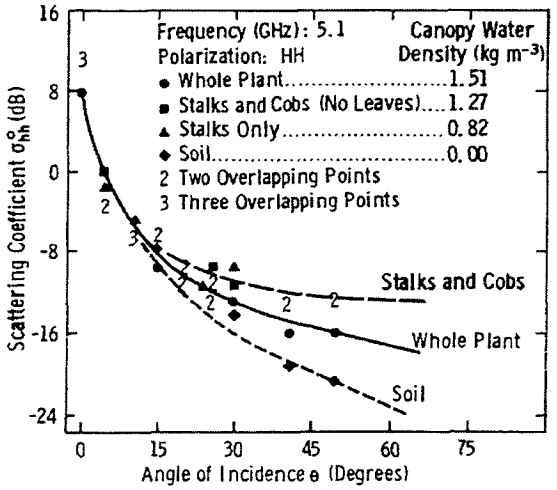

Figure 9. Measured δ° of a fully mature corn canopy in four consecutive stages of defoliation; all the measurements were made on the same day (Ulaby *et al.*, 1986)

5. CONCLUSIONS

Multitemporal radar backscatter characteristics of crops and their underlying soils were analyzed for an agricultural area in southwestern Ontario, Canada. Nine dates of ERS-1 SAR imagery were acquired for two descending passes during the 1993 growing season. These data were corrected for SAR antenna pattern and compensated for range-spreading loss at ESA D-PAF. For major crop types, SAR temporal backscatter profiles were generated. It was found that the radar backscatter coefficients varied considerably from one date to the next. Given the absolute calibration accuracy of +/- 0.42 dB, these variations could not be related to SAR calibration. Attempts to explain the variations based on changes in environmental conditions, such as local meteorological conditions and crop development, were also unsuccessful.

Attention was then turned to potential variations due to characteristics of the SAR system. For individual crop types, SAR temporal backscatter profiles were generated separately for each orbit. It was found that the profiles were relatively smooth when the two orbits were separated. For the 4° difference of incidence angle between the two orbits in the study area, the average differences in backscatter coefficients were approximately 3 dB. These results indicate that small changes in incidence-angle can have strong impacts on radar backscatter. Thus, attention must be given to local incidence-angle effects when using ERS-1 SAR data, especially when comparing backscatter coefficients of the same area from different scenes or different areas within the same scene.

6. ACKNOWLEDGEMENTS

Financial support for this project was provided by a Centre of Excellence Grant from the Government of Ontario, Canada to the Institute for Space and Terrestrial Science and through an NSERC Research Grant awarded to P. J. Howarth. Special thanks to ESA/ESRIN ERS Help Desk and ESA D-PAF for their assistance with image calibration.

7. REFERENCES

Brisco, B, F.T. Ulaby, and R. Protz. 1984. Improving crop classification through attention to the timing of airborne radar acquisitions. *Photogrammetric Engineering and Remote Sensing*, Vol. 50, No. 6, pp. 739-745.

Brisco, B., R. J. Brown, J. G. Gairns and B. Snider. 1992. Temporal ground-based scatterometer observations of crops in western Canada. *Canadian Journal of Remote Sensing*. Vol. 18, No. 1, pp. 14-21.

Brown, R. J., B. Guindon, P.M. Teillet and D. G. Goodenough. 1984. Crop type determination from multitemporal SAR imagery. *Proceedings, 9th Canadian Symposium on Remote Sensing*, St. John's, Newfoundland, Canada, pp. 683-691.

Brown, R.J., R. Leconte, B.G. Brisco, C.A. Hutton, D. Mullins, J.G. Gairns, Q.H.J. Gwyn, R. Protz, J. Fischer, P.J. Howarth, P.M. Treitz, J.B. Boisvert, and K.P.B. Thomson. 1991. Oxford County Soil Moisture Experiment (OXSOME) Overview. *Proceedings, 14th Canadian Symposium on Remote Sensing*, Calgary, Alberta, Canada, pp. 512-518.

Dobbins, R., K. Korporal, P. Nixon, B. Brisco and R. Brown. 1992. A comparison between multi-date C-HH and C-VV SAR digital imagery for potato crop monitoring. *Proceedings, 15th Canadian Symposium on Remote Sensing*. June 1-4, Toronto, Ontario, Canada, pp. 245-250.

Fischer, J.A., and R.S. Mussakowski. 1989. Preliminary evaluation of multi-date SAR data for the identification of agricultural crops in Southern Ontario. *Proceedings, IGARSS'89 / 12th Canadian Symposium on Remote Sensing*, Vancouver, British Columbia, Canada, Vol. 2, pp. 430-433.

Foody, G.M., P.J. Curran, G.B. Groom, and D.C. Munro. 1989. Multi-temporal synthetic aperture radar data for crop classification. *Geocarto International*, Vol. 4, No. 3, pp. 19-29.

Laur, H. 1992. *ERS-1 SAR Calibration: Derivation of Backscattering Coefficient σ° in ERS-1.SAR.PRI Product,* ESRIN/ESA Document, Issue 1, Rev. 0, 17pp.

Laur, H., P. Meadows, J.I. Sanchez, and E. Dwyer. 1993. ERS-1 SAR radiometric calibration. Proceedings of *SAR Calibration Workshop: CEOS Calibration Working Group SAR Calibration Sub-Group*, pp. 257-281, September 20-24, ESTEC/ESA, Noordwijk, The Netherlands.

Ulaby, F.T., R.K. Moore, and A.K. Fung. 1986. From Theory to Applications. *Microwave Remote Sensing: Active and Passive*, Vol. III, Addison-Wesley, Reading, Massachusetts.

COMPARISON OF DIRECTIONAL REFLECTANCE AND RADAR BACKSCATTER FROM DESERT SURFACES, THE EASTERN DESERT OF JORDAN

George Mackay[1], Kevin J. Tansey[2], Andrew C. Millington[3]

Department of Geography, University of Leicester, University Road, Leicester, LE1 7RH, UK
phone: +44 (0)116 2523822, fax: +44 (0)116 2523854,
e-mail: [1]gm20@le.ac.uk, [2]kjt7@le.ac.uk, [3]acm4@le.ac.uk

Kevin White

Department of Geography, University of Reading, Whiteknights, Reading, RG6 6AB, UK
phone: +44 (0)1734 875123 Ext. 7752, fax: +44 (0)1734 755865, e-mail: k.h.white@geography.rdg.ac.uk

ABSTRACT

In this paper we present preliminary results of an investigation into the relationship between optical directional reflectance properties and surface roughness, and compare the measure of optical roughness obtained from field spectroradiometer measurements for surfaces in the eastern desert of Jordan with the corresponding estimates derived from surface profilometer measurements. A measure of the optical roughness is assumed using the ratio, R, of the slope to the intercept determined in a simple linear fit of directional reflectance expressed as a function of the phase angle. Observations demonstrate that R increases linearly as a function of the standard deviation of surface height with a correlation coefficient of 0.88. The implication of this work is that optical directional reflectance data could be used in conjunction with SAR data to constrain surface roughness estimates in a multisensor approach to retrieve surface environmental parameters. An analysis of simulated directional reflectances obtained with the SOILSPECT model is used to determine the sensitivity of R to the surface albedo and the particular illumination conditions. A 36% change in R was associated with the change in surface albedo and illumination conditions used in our analysis. These factors would need to be corrected to make use of the optical data for reliable estimates of surface roughness.

Keywords: directional reflectance, surface roughness, ERS SAR, desert surfaces

INTRODUCTION

Most Earth surfaces are distinctly non-Lambertian reflectors and information on their physical properties are contained within directional reflectance data. An understanding of the directional reflectance properties of the Earth surface materials is also crucial for determining accurate estimates of surface albedo. Considerable attention has been given to the elaboration of analytical models to describe these effects (references are cited in Roujean *et al.* 1992).

These models can be inverted to retrieve the properties of the Earth surface from remotely sensed data. The inversion of an appropriate model to retrieve estimates of the model parameters is dependent on having a sufficient number of well distributed radiance measurements against which to invert the model ('well distributed' refers to the angular distribution of the measurements over the viewing hemisphere). In practice, the range of observation angles over which such data can be collected using spaceborne instruments is conditioned by the geometry of the sensor and the orbital characteristics of the satellite on which it is mounted. Further limitations are imposed by the length of time it takes to acquire the sample set of multi-angle measurements with the satellite-borne sensors. Cabot *et al.* (1994) tested the possibility of confidently fitting a selection of published directional reflectance models with the kind of limited sampling obtained with operational satellites; if the sampled plane is not the solar principal plane the ability of the models to predict the reflectance in different directions becomes difficult or impossible. When used operationally, it may be difficult to retrieve more than two or three parameters from directional reflectance model inversion (Barnsley *et al.* 1996).

With the second Along Track Scanning Radiometer (ATSR-2) there is the potential to provide coincident data on the state of the atmosphere and the surface directional reflectance properties. The unique conical scanning system of the ATSR-2 provides a dual-look capability with nominal viewing zenith of 55°, on the leading edge of the detector cone, and at nadir, on the trailing edge of the detector cone (Prata *et al.* 1990). The optical data obtained in the four solar reflecting channels denoted as channel-V1 (0.545-0.565μm), -V2 (0.649-0.669μm), -V3 (0.855-0.875μm), and -1b (1.58-

1.64μm) can be combined to provide the directional reflectances and the atmospheric extinction (Mackay *et al.* 1997). Provided with a single overpass of the ATSR-2 we can attempt to estimate a two parameter BRDF.

In this paper we determine the use of a simple two parameter linear fit applied to directional data to describe the directional reflectance properties of bare desert surfaces. The benefits of developing such a simple model is the potential to monitor the dynamic temporal changes in the directional reflectance characteristics of the surface (associated with both the surface and the atmospheric variation) using the ATSR-2 sensor. We also consider the potential of using the simple two parameter model to provide an estimate of surface roughness. The reflectance from anisotropic rough soil surfaces is strongly correlated with the area of shadowing which depends on the degree of soil roughness as well as the viewing and illumination geometry (Cierniewski 1987; 1989).

In this preliminary study we test the ability to fit the linear model to a data set of directional reflectance measurements and compare the goodness of the fit with the three parameter empirical model of Walthall *et al.* (1985). The comparison is evaluated in terms of the RMS difference in the directional reflectances between the empirical fit and the measured values. We have also used contemporaneous estimates of the surface roughness obtained in the field to demonstrate that a measure of the optical roughness can be obtained using the ratio, R, of the slope to the intercept in the linear fit. The implication is that optical directional reflectance data could be used in conjunction with ERS-1 SAR data to constrain surface roughness estimates within a multisensor approach to retrieve surface environmental parameters. The relationship between R, obtained from the directional reflectance data and the ERS-1 SAR backscatter values is demonstrated.

The directional effect also depends on the contrast between the areas of illumination and shadow and becomes less pronounced if the fraction of diffuse illumination is high and shadows are less dark. The directional effect is therefore a function of the particular illumination conditions (the solar position and atmospheric conditions). Further, when the soil albedo is high (e.g., with a sand) multiple scattering will affect the directional reflectance. The variation in R resulting from changing solar zenith, surface albedo, and the fraction of diffuse illumination has been studied using simulated directional reflectances from the SOILSPECT model of Jacquemoud *et al.* (1992). The results of this analysis are presented.

THE RADIOMETRIC FIELD MEASUREMENTS

The fieldwork and research detailed in this work is conducted within phase II of the Eastern Badia Research and Development Programme and is part of a more extensive study into the application of remotely sensed data to the study of this arid environment. The Programme area is located within the eastern desert of Jordan (latitude limits: 31°30'N - 32°40'N; longitude limits: 36°30'E - 38°00'E) and is bounded by Syria in the north and Saudi Arabia in the south. Field spectral radiometric measurements were taken during a field campaign in May 1996 using an ASD Fieldspec radiometer with an 8° field of view aperture. The radiometer provides spectral reflectance measurements from 300-2500 nm. Reflectance was measured as the ratio of radiance measured over a target to that measured over a horizontal barium sulphate reference panel, corrected for the non-unity response of the reference reflectance panel. The measurements were confined to relatively good to excellent circumstances with almost cloudless skies and a clear atmosphere (the total optical depth at 550 nm was estimated to be less than 0.2 on each of three separate dates on which atmospheric measurements were performed).

The reflectance was measured in 17 viewing directions around each radiometer set-up and comprise a nadir observation and observations at view zenith of 25° and 55°, at 45° intervals of relative azimuth from 0° to 315°. The measurements were performed at sites representing the main geomorphic units in the area which comprise: (i) regolith pavements of coarse, basaltic stones formed over lava flows, (ii) desert pavements of small angular fragments of flint and limestone, (iii) areas of thin aeolian sand cover, (iv) outwash plains of gravel and sand, and (v) broad areas of fine-grained alluvial fills. A total of 10 sets of directional reflectance measurements were performed at each site. The measurements taken in each viewing direction were averaged to remove the effects of local anisotropy. The contemporaneous measurements of the surface roughness and the derivation of the standard deviation of surface height are described in Tansey *et al.* (1996).

The equivalent above surface reflectance corresponding to ATSR-2 channels -V1, -V2, and -V3 were then obtained from the spectral reflectance data by convolving the spectral reflectances with the sensor spectral response and the solar spectral irradiance. The spectrometer data obtained in the shortwave infra-red above 1100nm appeared noisy, therefore, the directional reflectance measurements were not used to simulate the corresponding above surface reflectance for the ATSR-2 channel-1b.

THE OPTICAL EQUATION AND COMPARISON OF SURFACE ROUGHNESS EFFECTS

Soil bi-directional reflectance distributions arise mainly from shadowing effects of aggregates. The shadowing is zero if the soil surface is observed from the direction convergent to the solar direction. The shadowing increases as the phase angle, ψ, described as the angle between the directions of illumination and observation, increases. The two parameter equation to fit the directional reflectance data is given by,

$$r_s = i + s\psi, \quad (1)$$

where

$$\cos \psi = \cos \theta_s \cos \theta_v + \sin \theta_s \sin \theta_v \cos \Delta\phi,$$

r_s is the directional reflectance, i and s are the intercept and slope derived using a least-squares fitting procedure; θ_s and θ_v are the solar zenith and view zenith, respectively, and $\Delta\phi$ is the relative azimuth between the illumination and viewing directions. Equation 1 was compared with the use of the three parameter empirical model of Walthall *et al.* (1985), expressed as,

$$r_s = a\theta_v^2 + b\theta_v \cos(\Delta\phi) + c, \quad (2)$$

where a, b and c are coefficients derived in a least-squares fitting procedure.

Overall, the RMS difference in reflectance between equation 1 and measured values ranged from 0.001 to 0.0068, for 14 desert sites using three spectral directional reflectance data sets corresponding to the three ATSR-2 spectral channels, and from 0.0012 to 0.0044 using equation 2. The average RMS difference for equation 1 is only slightly higher in each of the three spectral intervals. Results of the least squares fitting of equation 1 and equation 2 are presented in table 1 for the equivalent above surface reflectances in channel-V3. A demonstration of the linear fit to the directional reflectance data for two of the desert sites is provided in figure 1.

The ratio, $R=s/i$, in the three separate spectral channels, obtained for each desert site, generally agree to within 10% with R tending to increase from channel-V1 to channel-V3. The exception are for the sites representing areas of fine-grained alluvial fill. For these surfaces R approaches zero; the directional effect is less pronounced and there is a component of forward scattering around the specular direction

In figure 2, R_{V3} is plotted against the standard deviation of surface height derived from contemporaneous profilometer measurements obtained at 11 of the desert sites, and gives a correlation coefficient of 0.88. The relationship between R_{V3} and ERS-1 SAR backscatter values for the sites obtained from the overpass nearest to the time of field data acquisition is also provided in figure 2. The values used in the plots are listed in table 1.

THE EFFECTS OF SURFACE ALBEDO AND ILLUMINATION CONDITIONS

The SOILSPECT model (Jacquemoud *et al.* 1992) was used to determine the sensitivity of the ratio, R to the illumination conditions and the surface albedo. The model has six parameters, ω, the single scattering albedo (the ratio of the scattered energy to the total energy either scattered or absorbed by the particle), a roughness parameter, h, and four coefficients of the phase function to explain both backscattering and forward scattering, b, c, b', c'. A description of 26 soil samples and the corresponding soil reflectance model parameters can be found in Baret *et al.* (1993).

The roughness parameter and the phase function parameters are fixed for a particular soil (Baret *et al.* 1993). The model was run for ω equal to 0.3 and 0.6, θ_s equal to 30° and 60°, and for a diffuse illumination fraction from 0.0 to 0.7. In each run the directional reflectances were determined for a nadir observation and for observations at view zenith of 25° and 55°, at 45° intervals of relative azimuth from 0° to 180°. The ratio, R was then derived for each set of directional reflectance. The results of the analysis for a dry pebble surface are plotted in figure 3; the four lines represent the ratio, R, for ω/θ_s equal to *0.3/30°*, *0.6/30°*, *0.3/60°*, and *0.6/60°*, plotted as a function of the fraction of diffuse illumination. The range of diffuse illumination corresponding to the four ATSR-2 channels, for a solar zenith in the range from 30° to 60° and for clear to turbid atmospheric conditions (aerosol optical depth at 550nm from 0.1 to 0.7) was determined using the Simulation of the Sensor Signal in the Solar Spectrum (5S) code (Tanre *et al.* 1990). The ranges are indicated toward the base of the plot.

The effect on R of the changing fraction of diffuse illumination is clearly demonstrated in figure 3. This effect would be minimised by determining R in channel-1b where the variation in the fraction of diffuse illumination is limited to a range from 0.02 to 0.20. The combined effect of the increase in the single scattering albedo and the solar zenith produce a 20% fall in R. Combine this with a change in the fraction of

diffuse illumination from 0.0 to 0.2 and there is a reduction in R of 36% (from 0.438 to 0.320).

DISCUSSION

The directional reflectance measurements for the desert surfaces can be approximated using the simple two parameter model expressed as a function of phase angle. The RMS differences for the directional reflectance data are marginally higher than for the three parameter model of Walthall *et al.* (1985) using the equivalent above surface reflectances for ATSR-2 channels-V1, V2, and V3. There has been no special consideration in the measurement procedure given to sampling the "hot spot" or the forward scattering in the specular direction. Models with additional parameters are required to characterise these effects.

The range of values for R_{V3} determined for the desert surfaces are from 0.476 to 0.011 (rad^{-1}) and correspond to a range in the standard deviation of surface height from 3.484 to 0.261 (cm), with a correlation coefficient of 0.88. The optical directional reflectance data sets were obtained with a high sun and a clear atmosphere. Changing the fraction of diffuse illumination, the solar zenith angle, and the surface albedo all have a significant effect on the retrieved ratio. With the ATSR-2 sensor the particular illumination conditions could be approximated from the contemporaneous atmospheric correction procedure which provides the possibility of correcting for these additional effects.

ACKNOWLEDGEMENTS

The radiometric equipment used in this study was supplied by the NERC Equipment Pool for Field Spectroscopy (EPFS), Southampton. The authors would like to express their appreciation to Mohammed Shahbaz, Higher Council for Science and Technology, Jordan, and the field personnel at the Safawi Research Centre for their assistance during the field campaign. Also, to Marianne Edwards for her significant contribution to the field measurement activities.

REFERENCES

Baret, F., Jacquemoud, S., Hanocq, J. F., 1993, The soil line concept in remote sensing, *Rem. Sens. Reviews*, 7, 65-82.

Barnsley, M., Disney, M., Lewis, P., Hesley, Z., Muller, P., 1996, On the intrinsic dimensionality of the BRDF: implications for the retrieval of land surface biophysical properties. *Proc. 22nd Ann. Conf. Remote Sensing Society*, Durham,69-70.

Cabot, F., Qi, J., Moran, M., Dedieu, G., 1994, Test of surface bidirectional reflectance models with surface measurements: results and consequences for the use of remotely sensed data. *Proc. 6th Int. Symp. Physical Measurements and Signatures in Remote Sensing*, Val d'Isere, France, 627-634.

Cierniewski, J., 1987, A model for soil surface roughness influence on the spectral response of bare soils in the visible and near-infrared range, *Rem. Sens. Environ.*, 23, 97-115.

Cierniewski, J., 1989, The influence of the viewing geometry of bare soil surfaces on their spectral response in the visible and near infared, *Rem. Sens. Environ.*, 27, 135-142.

Jacquemoud, S., Baret, F., Hanocq, J. F., 1992, Modelling spectral and bidirectional soil reflectance. *Rem. Sens. Environ.*, 41, 123-132.

Mackay, G., Millington, A. C., 1997, Application of a dual-angle atmospheric correction for ATSR-2 solar reflecting channels. Submitted to *Int. J. Remote Sensing*.

Prata, A. J. F., Cechet, R. P., Barton, I. J., Llewellyn-Jones, D. T., 1990, The along track scanning radiometer for ERS-1 - scan geometry and data simulation, *IEEE Transactions on Geoscience and Remote Sensing*, 28, 1, 3-13.

Roujean, J. L., Leroy, M., Deschamps, P. Y., 1992, A bidirectional reflectance model for the Earth's surface for the correction of remote sensing data, *J. Geophys. Res.*, 97, D18, 20,455-20,468.

Tanre, D., Deroo, C., Duhaut, P., Herman, M., Morcette, J. J., Perbos, J., Deschamps, P. Y., 1990, Description of a computer code to simulate the satellite signal in the solar spectrum: the 5S code, *Int. J. Remote Sensing*, 11, 4, 659-668.

Tansey, K., White, K. H., Battikhi, A., Millington, A. C., 1996, Relationships between surface roughness and ERS-1 SAR backscatter on desert surfaces in eastern Jordan: preliminary results. *Proc. 22nd Ann. Conf. Remote Sensing Society*, Durham, 45-52.

Walthall, C. L., Norman, J. M., Welles, J. M., Campbell, G., Blad, B. L., 1985, simple equation to approximate the bidirectional reflectance from vegetative canopies and bare soil surfaces. *Applied Optics*, 24, 383-387.

	Optical data									
			Linear		Walthall				RMS	σ°
	θ_s	i	$R=s/i$ rad^{-1}	RMS	a rad^{-2}	b rad^{-1}	c	RMS	Height (cm)	(dB)
Regolith pavements										
	19.	.180	.476	.0030	-0.039	0.046	.139	0.0034	3.484	-6.61
	23.	.435	.316	.0068	-0.049	0.098	.359	0.0044	3.328	-8.30
	41.	.217	.283	.0029	-0.032	0.044	.178	0.0029	4.125	-5.84
	23.	.207	.354	.0053	-0.017	0.057	.162	0.0038	4.077	-7.98
	23.	.443	.208	.0024	-0.054	0.046	.403	0.0035	-	-7.23
Desert pavements										
	20.	.437	.099	.0039	-0.007	0.038	.410	0.0023	0.625	-8.53
	18.	.486	.119	.0040	-0.016	0.044	.454	0.0023	0.707	-8.25
	25.	.339	.217	.0014	-0.049	0.035	.309	0.0025	-	-9.01
Outwash plains										
	27.	.429	.072	.0013	-0.012	0.019	.411	0.0016	1.043	-11.96
	19.	.401	.119	.0028	-0.027	0.020	.381	0.0033	0.627	-12.77
Alluvial fills										
	49.	.471	.020	.0029	0.021	0.010	.451	0.0020	-	-20.05
	37.	.565	.011	.0014	0.005	0.006	.557	0.0013	0.261	-18.04
Aeolian sand cover										
	23.	.384	.115	.0021	-0.022	0.023	.363	0.0026	1.442	-10.56
	16.	.427	.101	.0023	-0.021	0.021	.408	0.0024	2.009	-10.48

Table 1 : Optical data are the results of least squares fitting of the above surface directional reflectances in ATSR-2 channel V3 to equation 1 and equation 2. The solar zenith in column 2 is the value assumed for the time of the acquisition of the directional reflectance data. The RMS surface height, and ERS-1 SAR backscatter values determined for desert sites are also provided.

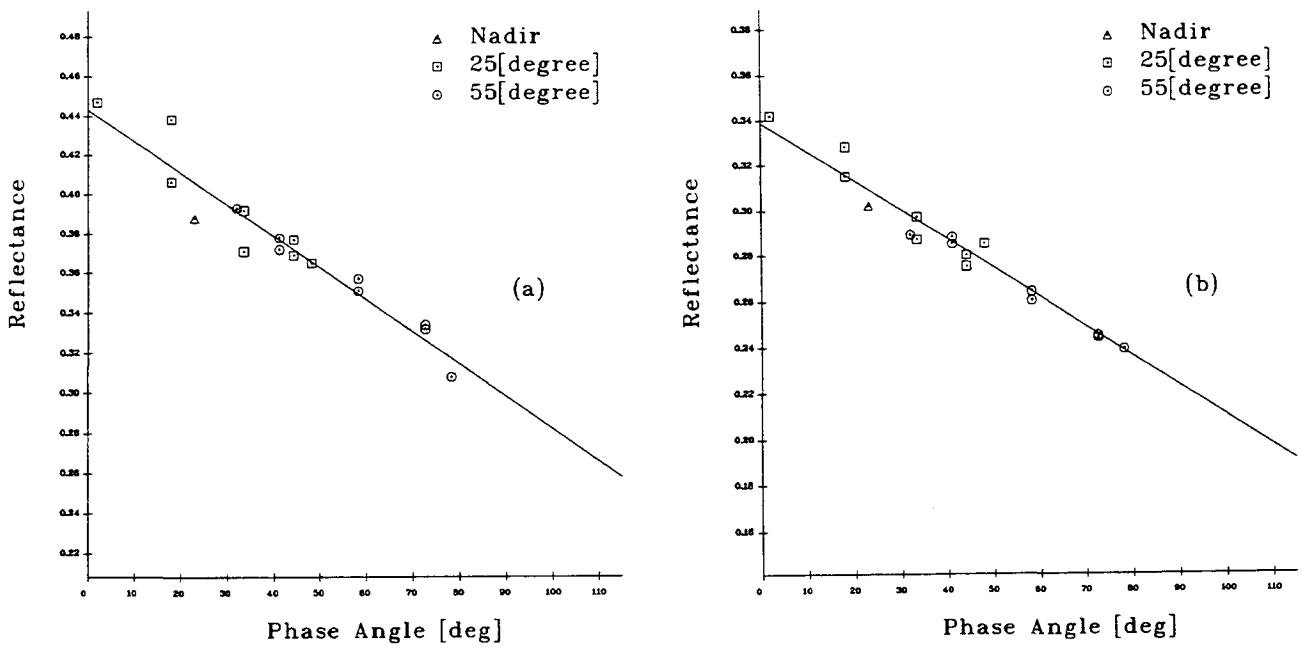

Figure 1 : Directional reflectance measurements as a function of the phase angle determined for desert surfaces, (a) a regolith pavement of coarse basaltic stone, and (b) a desert pavement with a covering of angular chert fragments.

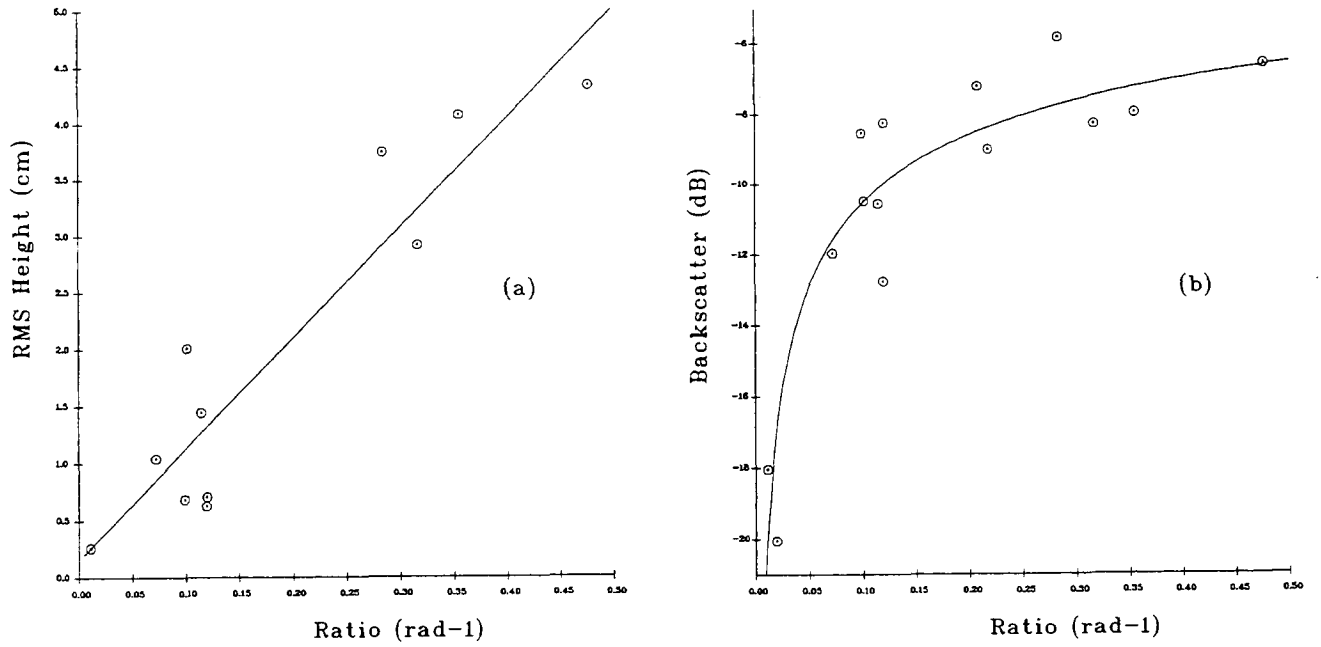

Figure 2 : The optical ratio, *R*, related to measured surface roughness and ERS-1 SAR backscatter for desert surfaces: (a) *R* versus the RMS surface height, and (b) *R* versus the SAR backscatter.

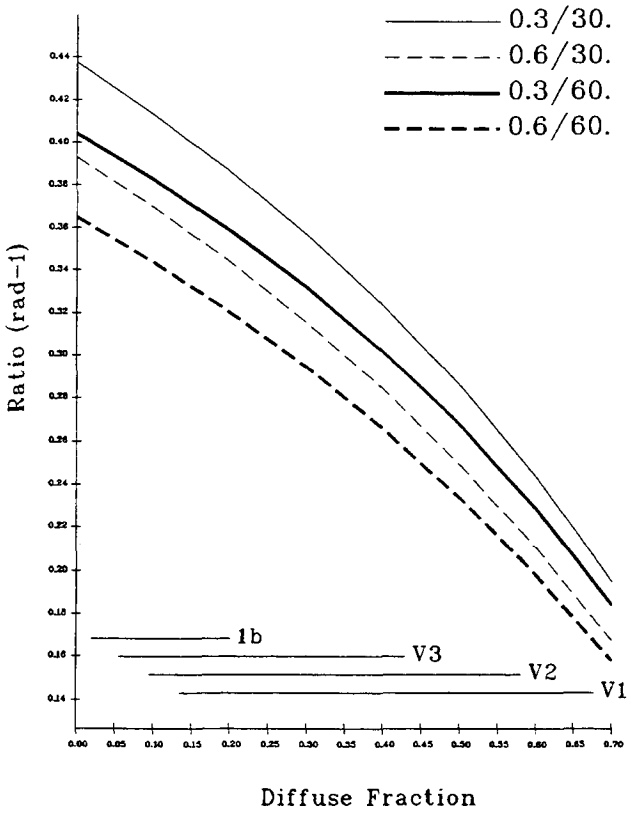

Figure 3 : The ratio, *R*, determined for SOILSPECT simulations plotted as a function of the changing fraction of diffuse illumination for ω/θ_s combinations given as: *0.3/30°*, *0.6/30°*, *0.3/60°*, and *0.6/60°*.

RESEARCH ON THE CAPABILITIES OF ERS.SAR FOR MONITORING OF LAND USE CHANGES IN THE NEOTROPICS

Jan Verhoeye

University of Gent, Department of Forest and Water Management
Coupure Links 653, B-9000 Gent, Belgium
Tel : +32 9 264 60 91 Fax : +32 9 264 62 40
Jan.Verhoeye@rug.ac.be

ABSTRACT

Land use maps at a scale of 1:200.000 exist for the whole of Costa Rica. They were produced in 1985 from Landsat-TM images and aerial photographs. Given the frequent cloud cover, regular updating of those maps via optical satellite data is problematic.
The north-east of Costa Rica is a region with a nearly flat relief and some isolated hills. Most of the land is covered with pasture and wet tropical forest. During the last decade a significant portion of the area has been converted into plantations, mostly of banana.
A procedure has been developed for producing land cover maps and an associated measure of accuracy. It consists of calibration, resampling, filtering, segmentation, principal component transformation and supervised classification of multitemporal radar images. As input to this processing chain any number of SAR.PRI images or derived texture images can be used. The output consists of a land cover map and an accuracy assessment. The procedure has been applied to a series of 4 SAR images, which yielded a map with an overall accuracy of 78 %. The high precision with which the large banana plantations can be mapped is most interesting, both for its economics importance as for environmental monitoring.
By combining this map with the land cover map of 1986 it is possible to detect the changes over the period 1986-1995.

Keywords: land cover change, banana plantation, ERS-SAR

1. INTRODUCTION

Land use maps are important tools for regional land use planning. Not only should these maps contain the correct thematic information, but this information should also be up-to-date.
In tropical areas the updating of the land use maps by use of optical satellite imagery (SPOT, Landsat,...), is often problematical because of the frequent cloud cover. Quite often it will take years in order to obtain a reasonably cloud free image, and in the mean while the value of the extant maps may decrease to a point where they are almost useless.
Since the launch of ERS-1 and ERS-2 by ESA, SAR-images are available that are weather independent and which cover the whole surface of the globe on a regular basis. So it is quite understandable that the question has been raised as to what extent these images can be used to produce new land cover maps, and with what accuracy this can be done.
These are the questions to which this article will try to find an answer.

2. MATERIAL AND METHODOLOGY

2.1 Study area

The study area is situated approximately between 9° 30' N and 11° N, 83° W and 84° W (figure 1) in the Atlantic Zone of Costa Rica (Central America) and covers some 425 000 hectares. The area is virtually flat, with a few isolated hilltops reaching 170 meters. Most soils are well drained, with the exception of a more than ten kilometre wide zone along the Caribbean coast. The southern half is rather densely populated, with Puerto Viejo de Sarapiquí, Guápiles, Guácimo and Siquirres as main population centres.

Figure 1 : Study area

Until a few decades ago the area was completely covered in wet tropical forest. The vegetation in the

coastal swamps is characterised by the presence of the *yolillo*-palm (*Raphia taedigera*) (Janzen, 1983). Recent colonisation of the area has brought important changes to the original vegetation. Nowadays land use in the southern part is dominated by cattle ranches. Less important activities include the cultivation of ornamental plants, palm heart (*Bactris gasipaes*), plantations of *Gmelina arborea* and *Tectona grandis* (Stoorvogel and Eppink, 1995).

During the last decade banana plantations have expanded dramatically, and the Atlantic zone has become a major production area. The banana production plays a very important role in Costa Rica's economy. It is the country's leading source of foreign exchange (Science in the Rainforest), with the total income for 1993 estimated at USD 560 million. The banana industry also is an important employer. An estimated 43 000 Costa Ricans are directly dependent on banana production for their livelihood, not even including part-time-employment or the domestic service industries that support the banana producers. But there is a less bright side to the picture too. The banana production is dependent on large volumes of pesticides, herbicides and fertilisers and much of this is washed away or dissipates before the plants can benefit from it. An estimated 90 % of fungicides are lost in this way. Another problem is posed by the solid waste generated during the banana production. For each ton of banana exported, three tons of waste is produced, mostly consisting of leaves and stems of the banana plants (Hernandez and Scott, 1996). Furthermore, streams are diverted and channelled, and contaminated with sediment and chemicals. It should be clear that monitoring of this activity is of interest to governmental as well as non-governmental institutions.

2.2 Available data

The available data consist of four ERS-1 images, dating from November 9 1992, August 16 1993, September 20 1993 and October 25 1993, and one cloud-free Landsat-TM image dating from February 6 1986. Collateral data consist of aerial photographs at scale 1:60 000 dating from 1992 and 1993 and more than 1200 field observations of land use for 1995.

2.3 Digital processing of the radar image

A suite of tools has been designed for the processing of ERS.SAR.PRI images and has been described in Verhoeye and De Roover (1996). One or more PRI-images, possibly together with synthetic channels such as texture images, serve as input. The output consists of a classified image and a measure of accuracy.

As a rule the chain has been implemented using commercially available software (Earth View by Atlantis Scientific Systems Group Inc., ISI-2 by Intergraph Corporation). Only when these are inadequate additional software programs has been developed. This is the case for the calibration, segmentation and evaluation modules.

First the images are read from tape onto the computer hard disk, after which the header files of the PRI-images are analysed in order to extract the parameters needed for the calibration. A program for calibration of ERS-images has been developed using the formulas proposed by ESA (Laur, 1992). Subsequently the calibrated images are imported into the image processing software. At this point a first data volume reduction is obtained by linearly rescaling the 16-bit data into 8-bit data.

After georeferencing, the images, originally measuring approximately 8000 by 8000 pixels, are reduced to 2000 by 2000 pixels by applying an averaging procedure. While at the one hand allowing faster processing by further reducing the data volume, the averaging also removes some of the speckle. The resolution of resultant images is 60 meters.

In an effort to further reduce the speckle, the images are subjected to filtering. Next a principal components transformation (PCT) is applied to the filtered images. The analysis yields Eigenvalues, which will be used as weighting factors during the segmentation.

Despite the fact that the application of filters can eliminate a considerable amount of speckle, it is accepted that the accuracy can be further improved if the radar image is segmented prior to the classification (ESA, 1995). Segmentation techniques partition the image into multi-pixel regions that represent discrete objects or regions in the image. The method applied here is based on the multiresolution Pixel Linking" algorithm, which uses a "pyramid" of images at successively lower resolutions. It establishes links between pixels at successive levels of the pyramid and uses these links to move the values of the top level down to the base level, resulting in a segmented image (Burt, 1984; Hong, 1982; Rosenfeld, 1984). The segmentation algorithm has been discussed in more detail in Verhoeye and De Roover (1996).

The segmented images are then used as input to a supervised classification, applying the Maximum Likelihood algorithm and using the field observations of 1995 as training data. In order to be able to assess the accuracy of the classification result, it has to be confronted with the ground truth, which will be provided by the results of the interpretation of the 1993 aerial photographs. Different measures of classification accuracy can be calculated after constructing a confusion matrix (Lillesand and Kiefer, 1994).

3. RESULTS

3.1 Land cover map for 1993

An exhaustive evaluation of the processing chain revealed that the optimum classification result was obtained using the following settings :

- multitemporal input (four images)
- inclusion of textural information as a fifth channel
- sigma filtering using (window 7 by 7 pixels)
- principal components transformation
- segmentation using a pyramid consisting of seven levels, root level at level one, two root intervals
- classification (Maximum Likelihood, 6 classes)
- no modus filtering.

Ground truth is provided by stereoscopic interpretation of aerial photographs at scale 1:60.000. The total area for which ground truth has been interpreted covers some 70.000 hectares. As can be seen in table 1, no ground truth data are available for the *yolillo* class. This is due to the fact that the aerial photographs taken over these extensive swamp forests contain no features (like cross-roads, bridges,...) that can be referenced to the topographical maps.

The classification result can be seen in figure 2. The patches "not classified" within the study area correspond to isolated hills that have been masked out because the effects of layover and radiometric distortion do not allow a correct classification. The general picture is largely consistent with the land cover as interpreted from the aerial photographs and the field observations : *yolillo* swamps along the Caribbean coast, forests in the northern half of the study area, extensive grasslands and large scale banana plantations in the south.

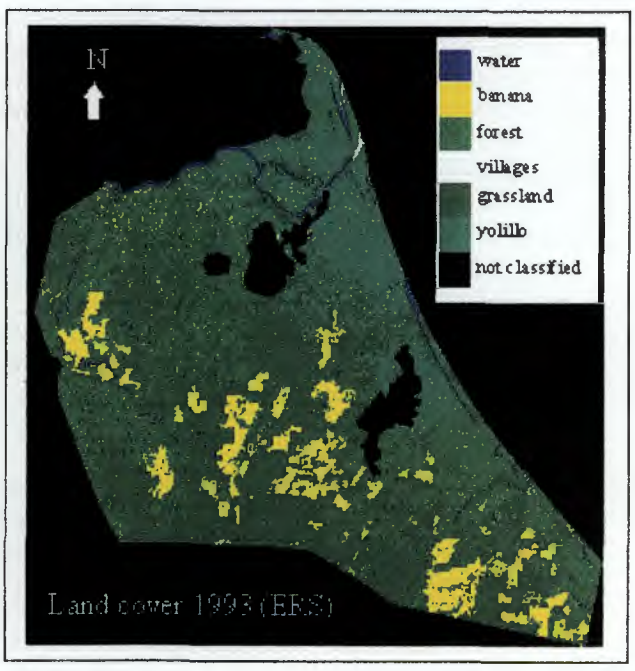

Figure 2 : Land cover 1993

A more detailed picture can be obtained by studying the confusion matrix (table 1), the producer's accuracies (table 2) and the consumer's accuracies (table 3). Overall accuracy is 78 %, which falls within the range (65 % to 80 %) cited by ESA (1995) for land cover classification in Thailand. Striking is the misclassification of villages. This should come as no surprise as houses in the study area are widely scattered along the roads and their surroundings are very heterogeneous, typically containing a lot of trees and small fields. Considering the spatial resolution of the images used (60 meters), pixels inevitably become mixed.

Quite a lot of confusion exists between forest and grassland. The largest error is that of commission, with 40 % of the forest land cover actually belonging to the grassland class. This is probably related to the ranching practices applied in the study area : even intensively used grassland contain a fair amount of remaining tree groups and stems. More extensively used pastures tend to be invaded rapidly by scrubs and bushes eventually leading to a dense and entangled secondary vegetation. This creates a rough surface and will lead to higher values of backscatter which apparently are confused with those of forest. Similar observations have been made in the Brazilian rain forest (Keil et al., 1996) and on Borneo (Kuntz et al., 1996).

On the other hand, the accuracies for classifying grassland and banana are fairly high : both producer's and consumer's accuracy range between 83 % and 87 %. Especially the monitoring of banana plantations could prove to be an important operational application, as these plantations represent important economic values as well as pose severe environmental threats (Science in the Rainforest; Hernandez and Scott, 1996). When the confusion matrix is evaluated after regrouping into two classes (banana versus non-banana) it becomes clear that the accuracy is extremely high (95 %) (table 4). Another indication of the reliability of ERS-images for monitoring banana plantations can be found when calculating the total surface of these plantations (44 600 hectares). This compares very well to the surface (44 187 hectares) calculated from the 1993 aerial photographs at scale 1 : 60 000 for the same area (Stoorvogel and Eppink, 1995).

The results discussed till now are produced by multitemporal input, meaning that images dating from several (in this case four) dates are processed simultaneously. It would be interesting to know how these compare to the results from monotemporal input. From table 4 it can be seen that the accuracy for discriminating banana from other land cover is equally high in monotemporal as in multitemporal processing!

3.2 Change detection for 1986-1993

The classification of the 1986 Landsat-TM image yields a land cover map with 90 % accuracy. By applying the post-classification comparison technique, it is possible to detect the changes in land cover that have occurred between 1986 and 1996.

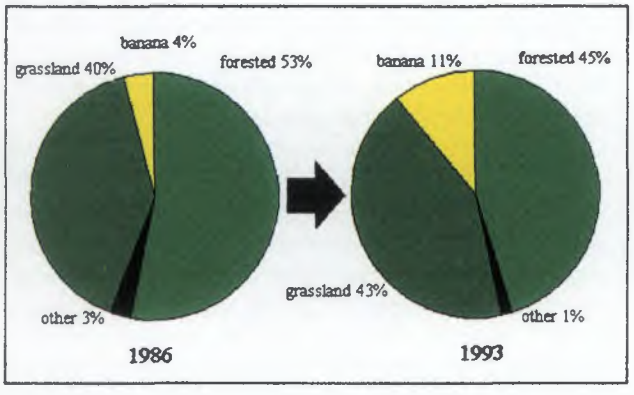

Figure 3 : Land cover change 1986-1993

The expansion of the banana plantations is very obvious (from 4% to 11%). While there is only a small increase of grassland, the rate of forest loss is significant : 2% of the forested area disappears annually (figure 3). These figures would seem to confirm the opinion (Science in the Rainforest) that the expansion of the banana plantations occurs at the expense of the rain forest. A more detailed interpretation of the land cover change maps leads to a somewhat different conclusion : it appears that that the majority of the new banana plantations are established in former grasslands in the southern half of the study area, while new pastures are being created at the fringes of the forests in the north and the south-east.

4. CONCLUSIONS

It has been shown that land cover maps with a fair degree of accuracy can be produced using ERS.SAR.PRI as input data. This can be achieved by applying a series of digital operations, most of which can be done using commercially available software. A notable exception is the segmentation, for which a software module has been developed *in house*. Although the overall accuracy of the land cover map may not be as high as can be achieved using optical images, the accuracy with which banana plantations can be detected is very high. This holds true both for multi- and monotemporal datasets. These findings point to a potentially important operational application.

5. ACKNOWLEDGEMENTS

Funding for this project was provided by the Belgian Federal Office for Scientific, Technical and Cultural Affairs (OSTC). The ERS-1.SAR.PRI images were made available by ESA.

6. REFERENCES

Burt, P.J., 1984: The pyramid as a structure for efficient computation. In: Rosenfeld, A., Multiresolution Image Processing and Analysis. Springer-Verlag, Berlin Heidelberg New York Tokyo: pp 8-35.

ESA, 1995: Satellite Radar in Agriculture. Experience with ERS-1. ESA SP-1185. ESA Publications Division. ESTEC, Noordwijk, The Netherlands. ISBN 92-9092-339-3.

Hernandez, C.E., Scott, G.W., 1996: Evaluating and Managing the Environmental Impact of Banana Production in Costa Rica : A Systems Approach. Ambio, Vol. 25, May 1996 : pp. 171 - 178.

Hong, T.H., 1982: Image smoothing and segmentation by multiresolution pixel linking : Further experiments and extensions. IEEE Transactions on Systems, Man, Cybernetics, pp. 611 - 622.

Janzen, D. H., 1983: Costa Rican natural history. The University of Chicago Press. ISBN 0-226-39334-8.

Keil, M., Scales D., Winter R., Kux H., dos Santos J.R., 1996: Tropical rainforest investigation in Brazil using multitemporal ERS-1 SAR data. Proceedings of the Second ERS Applications Workshop, London, UK, 6-8 December 1995 (ESA SP-383, February 1996) : pp. 77 - 82. ISBN 92-9092-215-X.

Kuntz, S., Streck C., Siegert F., 1996: Multitemporal Evaluation of ERS-SAR Data for Monitoring Deforestation Tropical Forest. Proceedings of the Second ERS Applications Workshop, London, UK, 6-8 December 1995 (ESA SP-383, February 1996) : pp. 83 - 94. ISBN 92-9092-215-X.

Laur, H., 1992: Derivation of backscattering 0 in ERS-1.SAR.PRI products. ESA/ESRIN.

Lillesand, T.M., Kiefer R.W., 1994: Remote sensing and image interpretation. Third Edition. John Wiley & Sons, Inc. New York - Chichester - Brisbane - Toronto - Singapore. ISBN 0-471-57783-9.

Rosenfeld, A., 1984: Some useful properties of pyramids. In: Rosenfeld, A., Multiresolution Image Processing and Analysis. Springer-Verlag, Berlin Heidelberg New York Tokyo: pp. 8 - 35.

Science in the Rainforest : "Smart Banana" Program at http://www.pbs.org/tal/costa_rica/res2/costbanana.html

Stoorvogel, J., G.P. Eppink, 1995: Atlas de la Zona Atlántica Norte de Costa Rica. Programa Zona Atlántica (CATIE-UAW-MAG). Guápiles, Costa Rica.

Verhoeye, J., B. De Roover, 1996: Research on the Capabilities of ERS-SAR for Monitoring of Land Use Changes in the Neotropics : Preliminary Results. Proceedings of the Second ERS Applications Workshop, London, UK, 6-8 December 1995 (ESA SP-383, February 1996): pp. 463 - 468.

Confusion matrix						
	Ground truth					
Classified as	banana	forest	villages	grassland	yolillo	total
banana	24349	1779	184	2646	0	28958
forest	2207	24014	154	17746	0	44121
villages	224	95	196	247	0	762
grassland	1784	13238	354	99781	0	115157
yolillo	7	389	6	44	0	446
total	28571	39515	894	120464	0	189444
Overall accuracy (%)	78					

Table 1 : Confusion matrix

Producer's accuracy (%)					
	banana	forest	villages	grassland	yolillo
banana	85	4	21	2	-
forest	8	61	17	15	-
villages	1	0	22	0	-
grassland	6	34	40	83	-
yolillo	0	1	1	0	-
total	100	100	100	100	-

Table 2 : Producer's accuracy (%)

Consumer's accuracy (%)						
	banana	forest	villages	grassland	yolillo	total
banana	85	6	1	9	0	100
forest	5	54	0	40	0	100
villages	29	12	2	33	0	100
grassland	2	12	0	87	0	100
yolillo	2	87	1	10	0	100

Table 3 : Consumer's accuracy (%)

Input data	4 dates	Nov 9 1992	Aug 16 1993	Sep 20 1993	Oct 25 1993
Overall accuracy (%)	95	95	94	94	95

Table 4 : Accuracies for classifying banana in multi- and monotemporal datasets

USING ERS-1 DATA TO MEASURE AND MAP SELECTED CONDITIONS RELATED TO THE PRODUCTION OF METHANE IN A WETLAND ENVIRONMENT: THE NEBRASKA SANDHILLS, USA

Donald C. Rundquist, Bryan C. Leavitt, Steven L. Payton
Center for Advanced Land Management Information Technologies
University of Nebraska, Lincoln, NE, USA 68588-0517
phone: 402-472-7536, fax: 402-472-2410

Ram M. Narayanan
Department of Electrical Engineering
University of Nebraska, Lincoln, NE, USA 68588-0511
phone: 402-472-5141, fax: 402-472-4732

ABSTRACT

Wetlands are important as both sources and sinks for methane, a trace gas implicated in greenhouse warming. Information necessary for estimating fluxes of methane includes plant species and primary production. Measuring and monitoring the spatial and temporal variations in these parameters should facilitate modeling fluctuations in global greenhouse gas amounts.

Three ERS-1 and two Landsat-TM datasets, acquired over large wetland sites in the Western Sandhills of Nebraska, were obtained during the 1995 growing season. The SAR images were despeckeled, and both ERS and TM were resampled to a 30m spatial resolution, rectified to a UTM coordinate system, and segmented to exclude uplands using a digital National Wetlands Inventory (NWI) dataset. In-situ reference data were obtained at various sites within the study area in conjunction with satellite overpasses. The ERS data were classified in an attempt to identify and map the distribution of wetlands at two levels: 1) specificity roughly equivalent to that of the NWI; and 2) at the species level, with emphasis on *Typha, Scirpus, and Phragmites*. The TM scenes were also classified and compared to the SAR result. Finally, a combined ERS and TM dataset was classified. Both SAR backscatter and TM reflectance were correlated to field measures of above-ground biomass. Results were considered with regard to C- and L-band (VV and VH) scatterometer data acquired at close-range over experimental plots containing *Typha* and *Phragmites*.

Landsat-TM seems better than ERS for generalized classification and mapping, and for emulating the NWI product. However, TM is limited with regard to identification of individual wetland species, and sparse stands of emergent, floating, and submergent macrophytes. ERS seems better than TM for detecting individual species, and sparse stands of emergent, floating, and submergent macrophytes. But, the ERS multi-temporal classification is not easily adapted for most practical mapping applications. Wind must be considered when classifying ERS in shallow lake systems. Potential exists for ERS/TM classification, but more work is needed. Biomass estimation, while encouraging, needs refinement. C- and L-band scatterometer data suggest that polarization is more important in distinguishing *Typha* and *Phragmites* than frequency.

1. BACKGROUND

Our research is aimed at the synergistic use of ERS-SAR and Landsat Thematic Mapper (TM) digital data for characterizing, mapping, and monitoring wetland vegetation in the Sandhills of Nebraska, USA. Classifying and mapping wetlands in that region, generally done for evaluation of wildlife habitat, has been a priority in Nebraska for over 40 years (Seevers *et al.*, 1975; Rundquist, 1983). Therefore, it seemed natural to consider ERS as a potential opportunity to improve on-going efforts to monitor wetlands of the study area.

The work is also linked to another project involving estimation of methane fluxes in the large wetland communities of the Sandhills (Verma *et al.*, 1996). These wetlands are significant as both sources and sinks for methane, a trace gas implicated in "greenhouse warming" (Mitsch and Gosselink, 1993). Parameters for estimating fluxes of methane in a marsh include, among other things, plant species and primary production. Speciation is useful because there are differences in both amount of gas released to the atmosphere and the actual mechanism of transfer, from one species to the next (Vanyarkho and Arkebauer, 1995). Productivity is important because it corresponds to total amount of

organic material available for decomposition. Measuring and monitoring the spatial and temporal variations in speciation and production may ultimately facilitate modeling fluctuations in global greenhouse gas amounts.

1.01. OBJECTIVES

The general goal of the project was to improve on previous classifications of wetlands in the study area by using ERS. Therefore, we sought, first of all, to test the utility of the SAR for identifying and mapping wetlands at a "general" level. The research consideration, then, was whether or not one could use ERS data, either alone or in combination with Landsat-TM, to classify wetlands at the level of detail provided by the U.S. National Wetlands Inventory (NWI) (Cowardin *et al.*, 1979). At a more specific level, the research focused on two parameters, plant species and primary production, both linked to methane flux. With regard to plant species, we aimed to: 1) examine the utility of ERS data for classifying *Typha, Scirpus*, and *Phragmites*; 2) compare ERS results to a similar classification based on multi-temporal TM data; and 3) evaluate the potential for enhancing TM classifications of wetlands by combining the Landsat data with ERS. We also assessed the utility of both ERS and TM in estimating the above-ground biomass in Sandhills wetlands. As a final objective, we evaluated C-and L-band (VV and VH) scatterometer returns for distinguishing *Typha* and *Phragmites*.

1.02. STUDY AREAS

The study area was in the Western Sandhills of Nebraska (Figure 1). The region consists of a virtual "sea" of sand dunes that are generally stabilized by a veneer of grass. Deflation hollows are present where the grass cover has been interrupted. Low-lying, flat-floored valleys, some wet and some dry, are prevalent throughout the region. The wet meadows contain lush vegetation, which exists in sharp contrast to the sparsely vegetated uplands and dry valleys. Rainfall results in virtually no runoff because of the sandy soils, so recharge is rapid and extensive. As a result, there is a tremendous reserve of ground water beneath the Sand Hills, and the hundreds of shallow lakes and wetlands in the western portion of the region are, for the most part, surface expressions of the water table. Dominant species of wetland emergents in the study area are broadleaf cattail (*Typha latifolia*), hardstem bulrush (*Scirpus acutus*), and common reed (*Phragmites communis*).

The specific study site for this paper was at the Crescent Lake National Wildlife Refuge (CLNWR). Our brief discussion will focus primarily on the expanse of wetlands surrounding Island Lake (refer to Figure 1).

A secondary study site was at the University of Nebraska Agricultural Research and Development Center (ARDC), located near Lincoln, Nebraska. Our research group operates a facility at ARDC for collecting spectral data over homogenous stands of wetland species under tightly controlled conditions. The cultivation of wetland species at ARDC began in early 1992, when four experimental plots, each approximately 5x5m were constructed. In more recent years, plot size has increased beyond 30x30m. Rhizomes of several species including *Typha, Scirpus, Phragmites*, and others were purchased from commercial nurseries and planted in separate plots. Optical data (Spectron SE-590) have been acquired numerous times in each growing season since original planting.

2. METHODOLOGY

2.01. SATELLITE DATA

Three ERS-1 images, acquired over the Western Sandhills on June 3, July 8, and September 16, 1995, comprise the principal datasets for the study. Corrections to data prior to our receipt included adjustments for slant angle, antenna pattern, and radiometric fall-off. We were unable to calibrate backscatter because we lacked proper ground-calibration targets. The ERS images were despeckeled using a Lee-sigma filter, and a 3x3 moving average. Each image was normalized so that its minimum value was always zero. This was accomplished by simply subtracting the lowest data value within an image from all data comprising that image.

Two Landsat TM scenes, acquired over the study area on June 14 and August 17, 1995 were obtained to supplement the ERS data. Digital numbers were converted to reflectance using standard procedures (Markham and Barker, 1986). The ERS and TM datasets were both resampled to a 30m spatial resolution using a nearest-neighbor algorithm, and rectified to a UTM coordinate system.

2.02. FIELD RADAR-SCATTEROMETER DATA

Radar data at the ARDC experimental site were acquired at approximately weekly intervals during the 1996 growing season over pure stands of *Typha* and *Phragmites*. The *Scirpus* plot was deemed too sparse for meaningful data collection in 1996. The van-mounted radar scatterometer acquired data at both C-band (5.3

Ghz) and L-band (1.275 Ghz) at incidence angles of 0, 12, 24, 36, and 48 degrees. Polarizations included HH, HV, VH, and VV. All measurements were made at 2.5m above the top of the canopy. Ancillary data included spectroradiometer data (Spectron SE-590) in visible and near-infrared spectral regions, canopy-light extinction (Li-Cor LAI-2000), and digital photography of the canopies (Kodak DC-40).

2.03. IN-SITU VEGETATION DATA

In-situ above-ground biomass data were obtained at 41 sites along 7 transects around the Island Lake site concurrent, or nearly so, with satellite overpasses. The location of each sampling site was determined to approximately 2m using differential GPS. All vegetation in an area of 0.25m squared was clipped and bagged. Other measurements, such as height, numbers of green plants, etc. were made. Upon returning to Lincoln, material was sorted and to separate green from senesced vegetation and then weighed.. Samples were oven-dried and re-weighed. Identical procedures were employed at the ARDC-controlled site, except that the areas sampled were 0.10m squared, due to relatively small plot sizes. Surface cover and species identification were also recorded at 46 sites within and around Island Lake during the 1995 growing season. The location of each site was again determined using differential GPS. These sites were ultimately used as control points to check the accuracy of the classified images. Unfortunately, *Phragmites* sites were not identified during the 1995 field survey.

2.04. CLASSIFICATION PROCEDURES

Data for topographic uplands were removed from all ERS and TM scenes using the NWI as a "cutter file." Therefore, only lowland areas were digitally classified. Three separate classifications were executed: 1) three dates of C-band, like-polarized ERS (i.e., three channels of information); 2) two dates of green, red, and near-infrared TM (i.e., six channels); and 3) two dates of green, red, and near-infrared TM combined with one date (July 8) of ERS (i.e., seven channels). The clustering was accomplished with an unsupervised minimum spectral distance algorithm in Erdas IMAGINE. Results were evaluated in two ways: 1) by overlaying the digital NWI classification for the Island Lake area; and 2) by relating pixel locations to GPS reference points and corresponding documentation acquired during in-situ vegetation sampling.

3. RESULTS AND DISCUSSION

3.01 MULTI-TEMPORAL ERS

The first classification used three separate ERS scenes, June 3, July 8, and September 16, as input. The lake surface was rough in the June and September images and smooth in the July image. Backscatter from areas of emergent vegetation was relatively low to moderate in June, moderate to high in July, and low to moderate in September. Backscatter from areas of near-surface submergents was relatively high in June, very low in July, and moderate in September. Therefore, we believe that it may be possible, under some conditions, to distinguish between emergent and submergent vegetation, especially by using multi-temporal ERS images where one image contains a smooth lake surface and another a rough lake surface. It seems that the necessary conditions for detecting submergents include plants being at or very near the surface where they impact wave action.

From the classification, a total of 50 clusters resulted, and these were reduced to seven, based on both ground-truth and other first-hand knowledge of the site. Results are depicted in Figure 2. Notice the "salt-and-pepper" appearance of the classified multi-temporal ERS data. This is due to the fact that the radar backscatter is impacted by all vegetation, however small, "emerging" from water surface, as well as any floating algal mats or debris. The result is a classified image that seems "noisy," with an appearance of "almost too much information." Our conclusion is that ERS data are not easily adapted for classifying wetlands at the generalized NWI level (compare Figures 2 and 3).

We believe the ERS to hold potential for classifying wetlands at the level of individual species. However, when the ERS classification is compared to ground-reference sites, the result is rather unimpressive. It should be noted, though, that the relatively low number of ground-control points, the difficulty of isolating pure stands of individual species in the field and the resulting necessity of including a "mixed class" of vegetation, the lack of reference sites specifically for *Phragmites*, and the 30m pixel size may all have contributed to the low classification accuracy.

A positive finding in using multi-temporal ERS-1 data was that it allowed detection of sparse stands of emergent, floating, and submergent (near-surface) macrophytes. It has, in the past, been difficult for us to detect the presence of these vegetative groups.

We also determined that wind is a factor in classification of ERS data in Sandhills wetlands. Areas with emergent vegetation and areas with large amounts of near-surface submergents show a lower radar backscatter, compared to the water itself, when the water surface is rough. Conversely, when the water surface is smooth, areas with emergent vegetation show a higher backscatter than the water. The decrease of backscatter in vegetated areas, when the water surface is rough, is probably due to the dampening of wave action by the plants. Thus, while wind seems, at first to be detrimental to successful classification, it can be beneficial when classifying wetlands in shallow lakes using orbital SAR.

3.02 MULTI-TEMPORAL TM

The classification using TM data was certainly "smoother" than that for ERS, and it was easily adapted to emulate the NWI map for the area (compare Figures 3 and 4). On the "negative side," however, Island Lake contains innumerable small, sparse stands of emergent macrophytes (mostly Scirpus), floating, and submergent macrophytes. The preponderance of those stands were invisible to the TM. Despite these omissions, the TM classification was "statistically" slightly better at the "species level" than that for ERS (refer to Table 1). Once again, however, the reader should be reminded of the potential accuracy-assessment shortcomings noted in a previous paragraph (section 3.01).

3.03 COMBINED ERS AND TM

The classification involving six TM (green, red, near-infrared for two dates) and one ERS (July 8) datasets is shown as Figure 5. The result seems, from a practical mapping point of view, to be a rather nice "compromise" between the relatively high level of detail provided by the ERS and the relatively lower level of specificity provided by the TM. The high percentage of incorrectly identified land cover at the control-point sites (Table 1) seems rather incongruous, and further work on accuracy assessment is warranted. The identification of submerged / near surface vegetation was diminished when the TM data were merged with ERS. Most of the error seems to have occurred in three areas: misidentification of bulrush as water or mixed vegetation; inability to distinguish between the mixed and cattail classes; and lack of submergent detection. It seems reasonable that the single date radar image was "overwhelmed" by the TM data. In retrospect a better classification may have been attainable if fewer TM bands had been used.

3.04 BIOMASS ESTIMATION

Additional research is clearly required in the instance of biomass estimation with ERS, TM, and/or ERS/TM. Scatterplots show distinct clusters of points by species, but correlations were relatively low. Despite the low correlations, it seems that potential exists for using ERS and TM synergistically to predict biomass over the study area.

3.05 FIELD RADAR-SCATTEROMETER

Scatterometer data from the 1996 growing at the ARDC site provide some insight into potential problems encountered when classifying ERS data for the Sandhills study area. Both C- and L-band VV and VH data are summarized in Figure 6. The graphic suggests that wavelength is not as important as polarization in distinguishing *Phragmites* from *Typha*. However, results are very preliminary, and more data collection is required. We anticipate continuing our scatterometer work over controlled wetland sites during the 1997 field season.

4. SUMMARY AND CONCLUSIONS

Although the results are preliminary, the work suggests to us that Landsat-TM is superior to ERS if one is concerned with mapping wetland communities at a very general level, such as the classes provided in the U.S. National Wetland Inventory. However, TM does not allow easy identification of individual species, and sparse stands of emergent, floating, and submerged macrophytes. Despite our very limited quantitative assessment of accuracy in classification, multi-temporal ERS would seem to hold great potential for detecting individual wetland species. The ERS backscatter should ultimately allow us to better characterize the architecture of vegetation canopies in Sandhills wetlands. Despite the lack of quantitative proof, we believe that merged ERS and TM datasets will ultimately improve our ability to analyze, map, and monitor the spatial extents of conditions pertinent to the natural production of trace gases, including methane.

Other findings can be briefly reiterated. Our cursory evaluation of biomass estimation with both ERS and TM yielded inconclusive results, and more work is clearly necessary. Wind may be considered both detrimental and beneficial in classifying wetlands in shallow lakes using orbital SAR. On the negative side, water surfaces roughened by wind complicates classification; on the positive side, a comparison of backscatter when lake

surfaces are rough versus smooth may facilitate the identification of sparce stands of emergent, floating, and submergent species. Preliminary field-scatterometer results suggest that the single-polarization (VV) characteristic of the ERS may inhibit successful classification of certain wetland species.

5. REFERENCES CITED

Cowardin, L.M., V. Carter, F.C. Golet, and E.T. LaRoe, 1979. Classification of Wetlands and Deepwater Habitats of the United States. Office of Biological Services, Fish and Wildlife Service, U.S. Department of the Interior, Washington, D.C.

Markham, B.L. and J.L. Barker, 1986. Landsat MSS and TM post-calibration dynamic ranges, exoatmospheric reflectance and at-satellite temperatures. EOSAT: Landsat Technical Notes, No. 1, August.

Mitsch, W.J. and J.G. Gosselink, 1993. Wetlands (2nd Ed.). New York: Van Nostrand Reinhold.

Rundquist, D.C., 1983. Wetlands inventories of Nebraska's Sandhills. Resource Report #9, Conservation and Survey Division, University of Nebraska-Lincoln, 46 pp.

Seevers, P. R. Peterson, D. Mahoney, D. Maroney, and D. Rundquist, 1975. An inventory of Nebraska wetlands with the use of imagery from the Earth Resources Technology Satellite. Proceedings, 4th Annual Remote Sensing of Earth Resources Conference, 281-292.

Vanyarkho, O. and T.J. Arkebauer, 1995. Responses of *Phragmites australis* and *Scirpus acutus* leaf and canopy gas exchange to environmental conditions. Ecological Society of America, 80th Annual Meeting, Snowbird, Utah.

Verma, S.B., T.J. Arkebauer, F.G. Ullman, D.P. Billesbach, J. Kim, R.J. Clement, D.W. Valentine, D.S. Schimel, and E.A. Holland, 1996. An integrated investigation of carbon dioxide and methane fluxes in mid-latitude prairie wetlands: micrometeorological measurements, process-level studies and modeling. Third Annual Report, Great Plains Regional Center for Global Environmental Change, U.S. Department of Energy, 87-92.

CLASS	TM	RADAR/TM	RADAR
Bulrush	55.6	22.2	44.4
Cattail	55.6	33.3	33.3
Floating	0.0	33.3	33.3
Mixed	66.7	41.7	50.0
Submerged	0.0	0.0	50.0
Water	100.0	80.0	80.0

Table 1. Percent of correctly identified species for each classification.

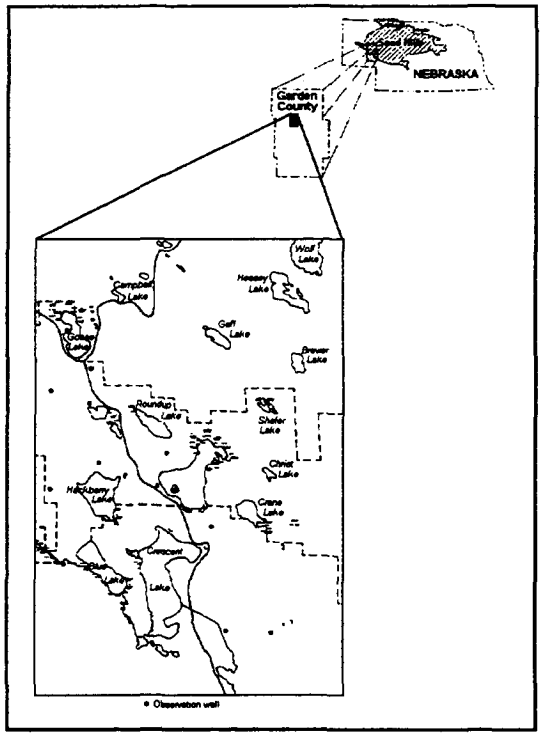

Figure 1. Location of study site.

Figure 2. ERS-1 classification.

Figure 3. National Wetland Inventory classes.

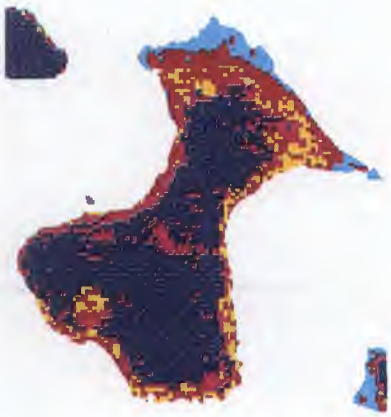

Figure 4. TM classification.

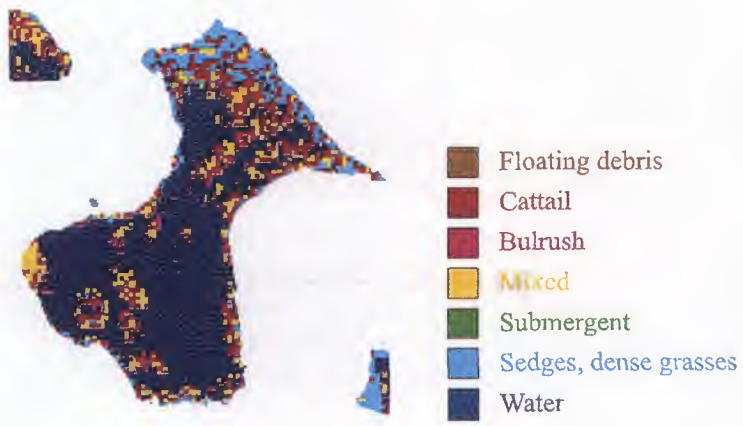

Figure 5. TM/ERS-1 classification.

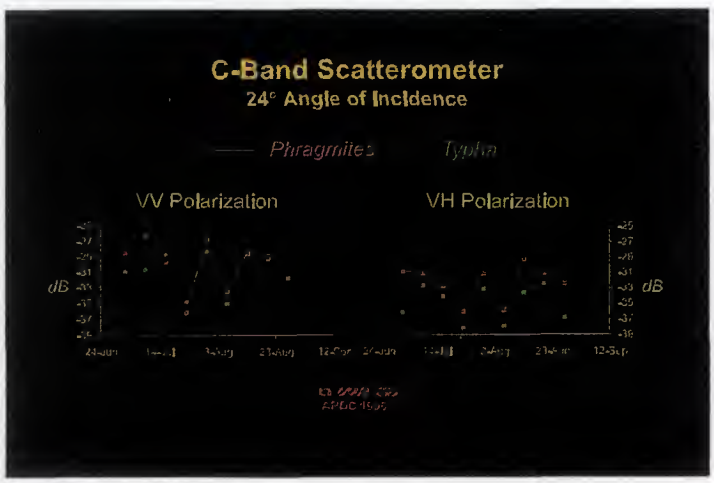

Figure 6. C-Band Scatterometer data.

EVALUATION OF ERS DATA FOR BIOMASS ESTIMATION OF MEADOWS

Roswitha Stolz, Wolfram Mauser
Institute for Geography
Dept. of Geography and Geographical Remote Sensing
Ludwig-Maximilians-University of Munich
Luisenstrasse 37, D-80333 Muenchen, Germany
phone: ++49 (0) 89-5203 326, fax:++49 (0) 89-5203 321
e-mail: R.Stolz@iggf.geo.uni-muenchen.de

Abstract

The knowledge about the amount of biomass is necessary to determine the impact of the landcover on the hydrological cycle due to the fact that different plants show significant differences in evapotranspiration. The study area of this work is the catchment of the Ammer River, which covers about 800 km² in the Bavarian Alpine Foreland. Since grassland in various forms is the dominating agricultural landuse in the testsite investigations were made on the utilisation of radar data for the determination of the temporal development of grassland. ERS data were used for this task. For verification data from several meadows which were investigated from 1992-1994 are used. The plant parameters height, wet and dry biomass were measured on a weekly base during the vegetation period. Statistical approaches were applied to investigate whether one of the plant parameters can be correlated to the backscatter signal. It is shown that there is a correlation between the signal density and the vegetation height of meadows. Due to the fact that the plant height correlates with the biomass, the grassland biomass can be estimated.

1. INTRODUCTION AND BACKGROUND

To calculate or model the spatial distribution of part of the hydrological cycle, such as evapotranspiration besides other parameters the landuse distribution and the biomass developement is of need. In our case to get a highly accurate landuse classification a knowledge based fuzzy logic approach was carried out using optical LANDSAT TM data [8]. The biomass of crops can also be determined using TM data and the phenological state of the crops [1, 2]. But the estimation of the biomass of grassland seems to be not possible with the present optical satellite systems. The determination is more difficult due to the fact that there are different forms of grassland with a high variety of species and which does not show homogeneous phenotypes. Furthermore grassland in different forms is the dominating ecosystem on earth, covering an area of about 17% of the land surface [6]. Besides the natural forms, such as prairie and savanna, intensively used grassland plays an important role within the agricultural production, for example in the Alps and alpine Foreland.

In this paper it is investigated whether ERS-SAR data show a potential for estimating biomass of grassland. In literature both theoretical considerations and measurements have proven that the backscatter signal contains different informations about the surface material, such as roughness and water content (HALLIKAINEN, 1985; ULABY, F.,1986; DOBSON, C./ ULABY,F., 1989; SAATCHI, S., 1995; TROCH, P. et al, 1996). So an attempt is made to analyse whether biomass information can be extracted from the radar data.

2. TESTSITE

2.1. Overview

The investigations were carried out in the catchment of the Ammer river, located southwest of the city of Munich in the Bavarian Alpine Foreland. It covers an area of about 800 km² with elevation differences between 500 m in the valley of the Lake Ammersee and 1700 m in the alpine foothills. Due to the variety in geology, the rugged terrain and gradients in climate the testsite shows a high heterogeneity in landuse. Especially the change in precipitation from about 1000 mm in the northern part and 1600mm in the southern part of the testsite and the rugged terrain causes changes in the agricultural landuse structure from the north to the south. The precipitation variation is on one hand connected to the topography, on the other hand the topographical influence is overlied by the barrier effect of the alps, which results in an increase of precipitation in the southern part of the testsite. This leads to a high precipitation rate in the valleys of the alpine margin, although they show elevations as low as 650 -700 m. The same holds for temperature and the duration of snowcover. Due to the hilly terrain and the high precipitation rate, grassland is dominating landuse here. Arable landuse is mainly related to the flat valley of the Ammer river and pleistocene gravel fields in the northern part of the testsite. Nevertheless 65% of the agricultural landuse there is grassland. It increases to almost 100% in the alpine part of the testsite. So investigations in grassland are of major interest.

2.2. The grassland in the testsite

Three different types of grassland are appearing in the testsite:
- pasture: mainly in rugged terrain and steep slopes
- meadows: intensively and extensively used
- natural grassland which is mainly located in nature reserves.

Due to the fact that the investigations were carried out mainly in the slightly undulated terrain of the northern part of the testsite, investigations were concentrated on meadows which are the dominating form of grassland in this area.
Two major types can be differentiated:
- intensively used meadows with a mowing rhythm of 3-4 times during the vegetation period. They are highly ferilised.
- extensively used meadows: they are cut only 1-2 times a year and are not fertilised. One form are so called litter meadows which mainly grow on turfy soils.

The structure of the canopy varies depending on the height of the plants and on the species spectra. When grass is short, it has a structure which is dominated by broad leafed herbages. As grass grows the blades bind and lodge, thus creating another structure [6]. A second layer is then developing consisting of the narrow leafs, stems and the heads. Most intensively used meadows are cut before the grass species are developing heads and flowering.
Both types have developed a layer of thatch or detritus material which covers the soil. Due to different cultivation methods the thatch layer of extensively used grassland is better developed.

3. A CASE STUDY FOR DERIVING BIOMASS DATA FROM ERS RADAR DATA

3.1. Data set

The ERS data set contains 11 ERS-1-SLC scenes, both descending and ascending, acquired during the vegetation period May to September 1992 to 1994. The data were converted to intensity values, corregistrated and calibrated using an algorithm published by LAUR [4]. Calibration is done under the assumption of the ellipsoid model. Because the local incidence angle is not considered, the calibration is only valid for flat terrain. Therefore only meadows located in the flat parts of the test site could be considered. The radiometric accuracy of the calibrated data is of about 0.5 dB. No further treatment, such as filtering, was applied on the data.

3. 2. Ground truth data

Beginning from 1992 plant parameters for different agricultural landuse were measured on selected test fields. Besides corn and grain fields meadows were considered as well. All together 11 meadows, 7 intensively used and 4 extensively used, were investigated in the northern part of the testsite. The following parameters were measured on a weekly base:
- growth height: the lower height of the herbage layer and the average maximum growth height. Both values are averaged to a mean growth height
- wet and dry biomass per m^2
- from the biomass the plant water content was calculated

The measurements were taken at four locations and averaged to a mean value for the meadow.
All together more than 40 measurements are taken into account :
1992: 3 dates (only descending)and investigations on 3 meadows
1993: 4 dates (only descending), one meadow
1994: 5 dates (ascendening and descending) and 6 meadows.

3.3. Approach

A spatial measurement of the biomass and the biomass development for a large area is an important information for different applications, e.g. hydrologic and climatic models or yield prediction. A weather independent, operational system would be an ideal tool especially in areas with high amount of cloud cover. Due to the fact that in the testsite meadows are the dominant landuse the evaluation of ERS data for the estimating of grassland biomass is investigated in this paper.
Grassland is investigated in the testsite since 1992. But due to the rugged terrain in the southern part, only the results of meadows in the only slightly undulated terrain of the northern part of the testsite were used in this approach, because the data are not yet corrected according to the local incidence angle.
Besides sensor specific parameters such as frequency, polarisation and incidence angle, terrain specific factors are influencing the backscatter intensity. The signal returning from grassland is formed by the backscatter behavior of a variety of parameters:
- Roughness
- Biomass
- Geometrical factors of the canopy
- Interception water on the plants
- Soil moisture conditions

To what extent the soil moisture is still influencing the signal depends on the degree of development of a thatch layer.
Due to the fact that only data of a single frequency - single polarisation system are used, it can only be investigated whether the signal contains information on plant parameters. But it is not possible to give exact values without further investigations.
In this approach the two major plant parameters, biomass and plant height, were compared to the backscatter coefficient σ°. The biomass is a measure for the plant water content and has therefore an infuence on the dielectric constant. The plant height influences the roughness and the

geometrical factors in the canopy varies during growth. The two parameters, growth height and biomass, are correlating strongly for the investigated meadows in the testsite (*Fig. 1*). In the field two plant heights were measured due to the development of two layers on the meadows. The mean growth height was calculated through averaging the height of the herbage layer and the maximum growth height.

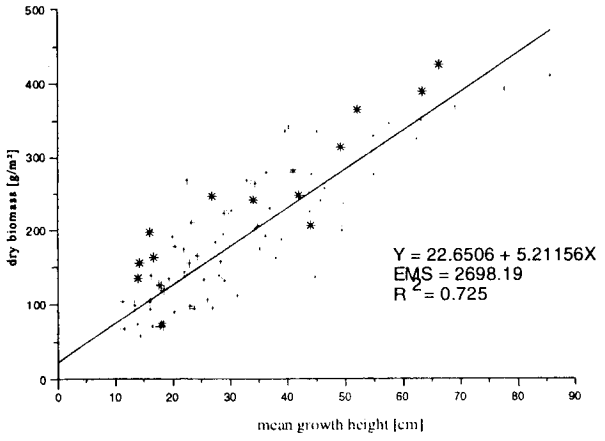

Fig. 1: Correlation between the dry biomass and the mean growth height derived from all investigated meadows 1992-1994

For applying statistical analysis methods on the ERS data, the average backscatter values were derived for the investigated meadows. Due to the speckle influence this can only be done on a field basis. The backscatter intensity of all pixels in the considered field were averaged and the average converted into σ°. These backscatter coefficencies were then related to the plant parameters.

4. RESULTS

4.1. Determination of a relationship between plant parameters and signal intensity

The measured biomass of the investigated meadows is statistically correlated to the fieldwise derived backscatter values of all available scenes (*Fig. 2*). The curve shows a linear course of the regression, but only with a relatively poor correlation. With increasing biomass the backscatter signal is deceasing. A higher amount of biomass causes an attenuation of the signal [9]. The possibility of deriving biomass estimations through this regression gives no satisfying result.

According to *Fig. 1* in a second attempt it was investigated, whether there is any relation between the growth height and the backscatter signal. Additionally the possibility of an influence ofintercepted rainfall on the backscatter behavior was checked. The statistical regression of the mean growth height and the backscatter coefficient shows a significant correlation. The differentiation between data acquired during rainy and dry weather conditions additionally improves the result concerning the dry scenes additionally. It seems that the higher dielectric constant due to water

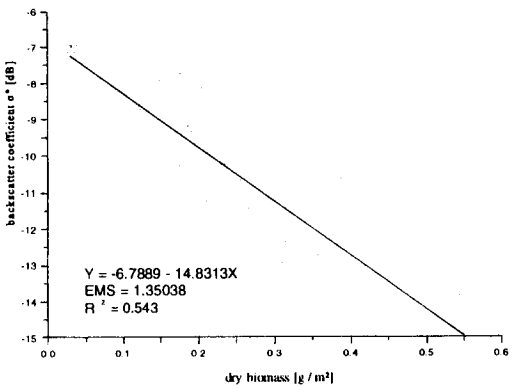

Fig 2: Correlation between the dry biomass and the backscatter coefficient of all investigated meadows

droplets on the plants increases the signal significantly only for higher canopy (*Fig. 3*). For further investigations, only the data of the dry acquisition dates are taken into account. This reduces the number of measurements which can be used. With increasing plant height the attenuation on the signal increases as well. For this fact two parameters can be taken into account: the possible change in roughness (depending on the species) and the change of geometrical properties in the canopy. The developed stalks and heads of a second layer can lead to the attenuation [7].

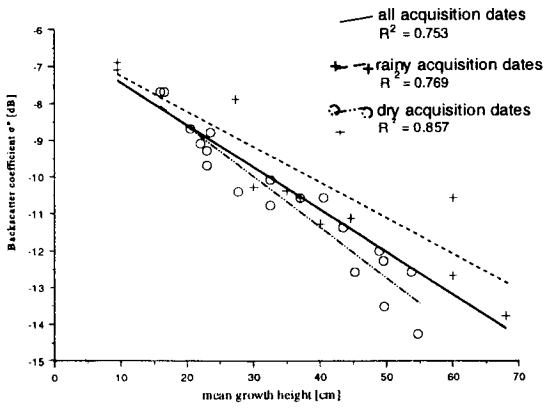

Fig. 3: Correlation between the mean growth height of the investigated meadows and the backscatter coefficient of all available acquisition dates and differenciated between dry and rainy weather conditions during acquisition.

4.2. Differentiation between meadows of different cultivation intensities

In the previous shown attempts no differencies were made between the different types of meadows. No influence of the different phenotypes can be seen in the correlation of the backscatter coefficient and the growth height.

But the analysis of the biomass development in relationship

geometrical factors in the canopy varies during growth. The two parameters, growth height and biomass, are correlating strongly for the investigated meadows in the testsite (*Fig. 1*). In the field two plant heights were measured due to the development of two layers on the meadows. The mean growth height was calculated through averaging the height of the herbage layer and the maximum growth height.

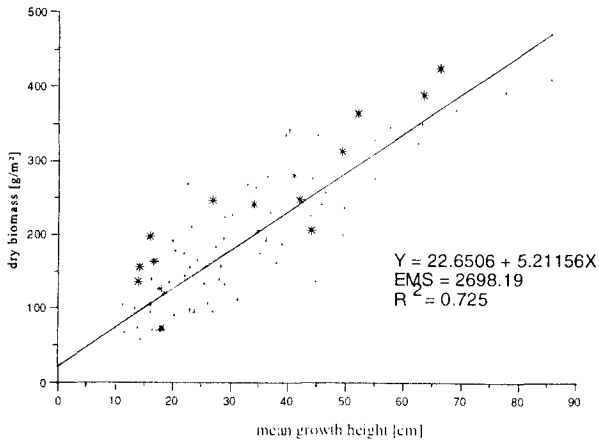

Fig. 1: Correlation between the dry biomass and the mean growth height derived from all investigated meadows 1992-1994

For applying statistical analysis methods on the ERS data, the average backscatter values were derived for the investigated meadows. Due to the speckle influence this can only be done on a field basis. The backscatter intensity of all pixels in the considered field were averaged and the average converted into σ°. These backscatter coefficencies were then related to the plant parameters.

4. RESULTS

4.1. Determination of a relationship between plant parameters and signal intensity

The measured biomass of the investigated meadows is statistically correlated to the fieldwise derived backscatter values of all available scenes (*Fig. 2*). The curve shows a linear course of the regression, but only with a relatively poor correlation. With increasing biomass the backscatter signal is deceasing. A higher amount of biomass causes an attenuation of the signal [9]. The possibility of deriving biomass estimations through this regression gives no satisfying result.

According to *Fig. 1* in a second attempt it was investigated, whether there is any relation between the growth height and the backscatter signal. Additionally the possibility of an influence ofintercepted rainfall on the backscatter behavior was checked. The statistical regression of the mean growth height and the backscatter coefficient shows a significant correlation. The differentiation between data acquired during rainy and dry weather conditions additionally improves the result concerning the dry scenes additionally. It seems that the higher dielectric constant due to water

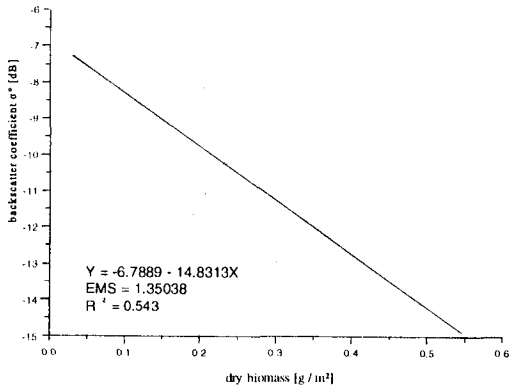

Fig 2: Correlation between the dry biomass and the backscatter coefficient of all investigated meadows

droplets on the plants increases the signal significantly only for higher canopy (*Fig. 3*). For further investigations, only the data of the dry acquisition dates are taken into account. This reduces the number of measurements which can be used. With increasing plant height the attenuation on the signal increases as well. For this fact two parameters can be taken into account: the possible change in roughness (depending on the species) and the change of geometrical properties in the canopy. The developed stalks and heads of a second layer can lead to the attenuation [7].

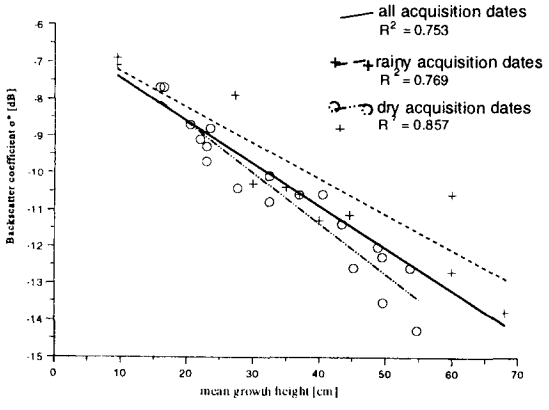

Fig. 3: Correlation between the mean growth height of the investigated meadows and the backscatter coefficient of all available acquisition dates and differenciated between dry and rainy weather conditions during acquisition.

4.2. Differentiation between meadows of different cultivation intensities

In the previous shown attempts no differencies were made between the different types of meadows. No influence of the different phenotypes can be seen in the correlation of the backscatter coefficient and the growth height.

But the analysis of the biomass development in relationship

5. CONCLUSION

Using ERS- SAR data it is possible to estimate the biomass distribution of meadows in the testsite. An influence of the biomass / plant growth height on the signal was clearly established. Through separate investigations of meadows of different cultivation (intensive / extensive), it is shown that most stable correlations between the mean growth height and the backscatter coefficient exist for extensively used meadows (which are similar to natural grassland) due to the development of a thatch layer. Correlations for intensively used grassland are somehow weaker. Using ERS radar data without additional information does not lead to stable results. Information which has to be considered is:

- a digital field boundary map to derive fieldwise data
- information about the grassland type
- information about the weather conditions during the acquisition

This can be only done with a combination of the Radar data with optical remote sensing data and conventional GIS data layers. A synergistic approach is then increasing the evaluation of the data.

6. REFERENCES

[1] Bach, H. (1995): Die Bestimmung hydrologischer und landwirtschaftlicher Oberflächenparameter aus hyperspektralen Fernerkundungsdaten.
Münchner Geographische Abhandlungen B 21.

[2] Demircan, A. , Mauser, W. (1996): Yield estimations by remote sensing data. *Proc. of the Int.Symposium on appliedAgrometeorology and Agroclimatology*, Volos, Greece

[3] Dobson, M.C. , Ulaby, F. , Pierce, L. (1995): Land-Cover Classification and Estimation of Terrain Attributes Using Synthetic Aperture Radar.
Remote Sensing of Environment, **51**, pp.199-214

[4] Laur, H. (1992): Derivation of backscatter coefficient σ° in ERS- SAR PRI products. *Issue 1, Rev.0*, ESA

[5] Rombach, M., Mauser, W., Bach, H., Demircan, A., Kellndorfer, J. (1994): Determination of spatial and temporal soil-moisture development using multi-temporal ERS-1 data, *European Symposium on Satellite Remote Sensing, Rome,* CNR, SPIE, Vol. 2314, pp. 502-515

[6] Saatchi,S., Lang, R., LeVine, D., 1991: Microwave backscattering and Emission Model for Grass Canopies, *Proceedings of the IGARSS`91 Conference,* Helsinki, pp. 1889-1891

[7] Schmullius, C., Nithack, J. (1997): Temporal multiparameter airborne DLR E-SAR images for crop monitoring: summary of the CLEOPATRA campaign 1992. *Proc.of Europtics Conference Taormina 1996.* SPIE Proceedings Series, vol. 2959, pp. 37-48

[8] Stolz, R., Mauser, W. (1997): Knowledge based multisensoral approach for landuse classification and biomass monitoring. In: Remote Sensing of Vegetation and Sea. *Proc.of Europtics Conference Taormina 1996.* SPIE Proceedings Series, vol. 2959; pp. 49-58

[9] Ulaby, F., Dobson, M.C. (1989): Handbook of Radar Scattering Statistics of Terrain.Artech House, Norwood.

[10] Troch, P.A. et al. (1997): Active Microwave Soil Moisture Sensing under Vegetation Cover. In: Remote Sensing of Vegetation and Sea. *Proc.of Europtics Conference Taormina 1996.* SPIE Proceedings Series, vol. 2959, pp. 84-93

7. ACKNOWLEDGEMENT

The authors would like to thank the Deutsche Agentur für Raumfahrtangelegenheiten (DARA) for making this study possible through their funding of the projects "Land-Use, Pedology and Soil Moisture from Multi temporal ERS-1 Data" and "The utilisation of remote sensing data in hydrological models". The authors also want to thank ESA for providing the necessary ERS images through its PI-program. And last but not least we want to thank Mr. Markus Rombach for providing us with calibrated field data.

ANGULAR DEPENDENCE OF RADIOMETRIC SURFACE TEMPERATURE FOR SPARSE VEGETATION

A. Shepherd

Dept. Earth Observation Science, Leicester University, LE1 7RH, UK, Tel:0116 2525264, Fax: 0116 2525262, email:as39@le.ac.uk

J.B. Stewart

Dept. Geography, Southampton University, SO17 1BJ, UK, Tel:01703 593289, Fax:01703 593295, email:jstewart@soton.ac.uk

M. Lupankwa

Dept. Geology, University of Zimbabwe, Harare, Zimbabwe, email:LUPANKWA@geology.uz.zw

ABSTRACT

Surface heat fluxes can be determined from the difference between surface and air kinetic temperatures using the aerodynamic resistance for the transfer of heat. To obtain representative fluxes on a regional scale remotely sensed radiometric surface temperatures have to be used in place of the kinetic surface temperature required in such models.

The Along Track Scanning Radiometer (ATSR) provides improved measurements of thermal radiance's from approximately 1 km squares on the earth's surface at frequent intervals and has the unique ability to view the scene at two angles, which enables determination of the atmospheric correction over oceans and hence enhances retrieval accuracy. There is far greater spatial heterogeneity over the land, so that it is uncertain whether the dual look capability could determine acceptable atmospheric corrections.

To investigate the utility of the dual look angle data, radiometric temperatures of a semi-arid sparse grassland site were measured using a number of ground based radiometers set up at different view angles. On a typically cloudless day differences of up to 3.5 K were observed between the nadir view (0 degrees from zenith) and the forward view (55 degrees from zenith) of the same surface and a linear relationship between the two temperatures was inferred. Studies of possible mechanisms causing this difference showed that it is much greater than previously observed angular variations in the emissivities of soils.

INTRODUCTION

The hydrological balance in semi-arid regions is particularly sensitive because of the extreme temporal and spatial variability in precipitation they experience.

The distribution of vegetation cover is often severely affected by water stress, resulting in large spatial variability in surface temperatures and heat and water vapour fluxes (see Kustas et al, 1989, Humes et al, 1994). Whilst the appropriate aggregation schemes for these fluxes are still uncertain, it is clear that their estimation is required at a variety of scales, from field to regional, for agricultural and meteorological purposes.

Latent and Sensible heat fluxes can be related to the kinetic surface temperature, which can be estimated using radiometric surface temperatures, or brightness temperatures, remotely sensed from satellite platforms.

The Along Track Scanning Radiometer (ATSR) can sense surface radiance's from approximately 1km squares, at two different view angles, almost simultaneously. Assuming the mean emissivity within a pixel is known, the two radiometric temperatures can be used to determine the atmospheric correction for the satellite data, and enhance the accuracy to which the surface kinetic temperature can be determined (e.g. Labed & Stoll, 1993). This method works well across uniform bodies such as the oceans, where the angular emissivity profile is well known and the kinetic temperature is uniform, but a typical land surface consists of multiple components resulting in a much more complicated aggregate emission (e.g. Van de Griend et al, 1991). Without any accurate knowledge of the angular variation in surface emission it is not possible to determine the atmospheric correction using the two views of ATSR.

Approaches towards modelling land surface emission have been made, and the influential factors are the component emissivities and their respective kinetic temperatures (Chehbouni et al, 1995, Norman et al, 1995). Typically a land surface can be divided into two components, soil and vegetation, for which emissivity profiles have been determined.

In semi-arid regions, considerable variability in temperature will exist horizontally across the surface and, to a lesser extent, vertically throughout the vegetation canopy, where temperature gradients are often forced through heat conduction from the soil. The temperature heterogeneity is, however, predominantly due to surface composition, and essentially there will be some discrete mean kinetic temperatures, T_V and T_S , which can be attributed to the vegetation and soil respectively within a region. Such an approximation is based upon the assumption that the vegetation as a whole will share a common radiative exchange mechanism, which will be substantially different to that of the soil when ambient temperatures are extreme and water is scarce. There will always be some thermodynamic interaction between the vegetation and soil, and partitioning the surface energy balance in this way can only be successful at the macro-meteorological scale. Using such a parameterisation for the ensemble emission the radiometric surface temperature is strongly dependent upon the fractional occupancy of each component.

Deriving land surface kinetic temperatures from the dual view of ATSR is further complicated because of the three dimensional nature of a vegetated surface.

The fractional occupancy of vegetation, and hence the ensemble radiometric surface temperature, will be dependent upon the angle at which the surface is observed (Lagouarde et al, 1995, Kimes et al, 1980).

The proportion of the scene occupied by vegetation will typically increase from a minimum in the nadir view (θ=0) to a maximum when viewing parallel to the surface (θ=90), assuming the vegetation is infinite in extent. In such circumstances any decrease in radiance observed in the forward view of ATSR, or off centre pixels retrieved from other satellite instruments, cannot wholly be attributed to increased atmospheric attenuation because of the greater optical path length.

The fractional occupancy of vegetation can be described in certain instances using analytical models of the canopy architecture (e.g. Norman et al, 1995). Existing models do not, however, qualitatively describe a semi-arid grassland environment well, where the vegetation is sparse and columnar in nature.

In order to benefit from ATSR's stereoscopic viewing over land the angular variation in radiance needs to be quantified for each surface studied. By measuring the directional radiometric surface temperature of a semi-arid site with ground based instruments, orientated in the same configuration as the ATSR, the angular variation in surface emission can be observed in absence of any significant atmospheric attenuation. To fully characterise the directional behaviour of the surface radiometric temperature, continuous diurnal measurements were collected to encompass all possible differences between T_V and T_S. Temperatures were recorded on 3 separate occasions in winter and summer representing maximum and minimum in vegetation density.

THEORY

Given estimates of the net radiation (Rn), sensible heat flux (H), and the soil heat flux (G), and neglecting miscellaneous processes such as photosynthesis and transpiration, evaporation from a surface can be inferred from the latent heat flux (λE) using the energy balance (Eq. 1)

$$Rn + H + G + \lambda E = 0 \qquad \text{(Eq. 1)}$$

Typically, G is a minor component of the energy budget so that net radiation, which can be estimated from meteorological data, is dissipated primarily as sensible and latent heat according to water availability.

Assuming similarity with turbulent molecular transport, of water vapour, for example, sensible heat from the surface is the advection of heat solely through mass motion within the atmosphere (e.g. Brutsaert, 1982).

Under such a parameterisation, H is then related to the difference between the aerodynamic surface and air kinetic temperatures, T_{as} and T_{air} , via the aerodynamic resistance to heat transfer, r_{ah} (e.g. Verma et al, 1978) so that

$$H = \rho c_p (T_{as} - T_{air})/r_{ah} \qquad \text{(Eq. 2)}$$

where ρ is the density and c_p is the specific heat of air at constant pressure.

The directional radiative surface temperature, $T_{RAD}(\theta)$, is frequently substituted as the best approximation to the areally averaged T_{as} (e.g. Stewart et al, 1994, Vining and Blad, 1992), and r_{ah} is then formally the resistance to heat transport from a surface at $T_{RAD}(\theta)$ to T_{air} .

By equating the emission from a source to that from a grey body of directional emissivity $\varepsilon(\theta)$, the radiative temperature $T_{RAD}(\theta)$ can be obtained through inversion of the Planck function integrated over the desired wavelength interval.

For a surface of mixed composition, the ensemble radiative surface temperature can be described as a linear combination of the component radiances, so that

$$T_{RAD}(\theta) = [\ (1/\langle\varepsilon(\theta)\rangle)\ \Sigma_i\ f(\theta)_i\ \varepsilon(\theta)_i T_i^n\ ]^{1/n} \qquad \text{(Eq. 3)}$$

where $f(\theta)_i$ is the fractional occupancy of the scene at an observation angle θ by component i, at temperature T_i and directional emissivity $\varepsilon(\theta)_i$, $\langle\varepsilon(\theta)\rangle$ is the aggregate surface emissivity and n is the appropriate power of temperature to satisfy the Planck integration

requirements. For full spectrum radiation Stefans law states that n=4, and for broadband thermal infra-red wavelengths (8-14μm) a value of n=4.5 is a reasonable approximation.

In general $T_{RAD}(\theta=0) \neq T_{as}$ and when calculating H in this manner adjustments have to be made to the classical formulation for r_{ah} to compensate for the inequality.

Radiometric surface temperatures, $T_{RS}(\theta)$, or brightness temperatures, are remotely sensed from satellite based instruments, such as the ATSR, with frequent temporal and spatial coverage. The radiometric surface temperature is the temperature of a black body that would emit the same radiance as that observed by the radiometer, which includes preferential reflection of the hemispherical sky radiative temperature (T_{SKY}) from the surface (Eq. 4).

$$T_{RS}(\theta) = [\ <\varepsilon(\theta)>\ T_{RAD}(\theta)^n + (1-<\varepsilon(\theta)>)\ T_{SKY}^{\ n}\ ]^{1/n} \quad \text{(Eq. 4)}$$

Radiative surface temperature can be derived from $T_{RS}(\theta)$ given an estimate of T_{SKY}, and in the case of satellite retrieved radiances an estimate of the atmospheric opacity. T_{SKY} can be estimated using empirical formulations which relate the longwave sky radiation to surface vapour pressure and air temperature (e.g. Idso, 1981).

The ATSR measures brightness temperatures from above the earth's atmosphere at two different view angles, and the atmospheric path length in the forward swath is approximately twice that of the nadir (Fig. 1).

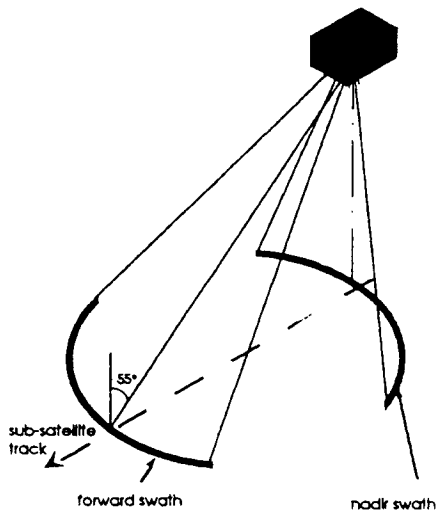

Figure 1. The viewing geometry of the along track scanning radiometer (ATSR)

If the surface is homogenous and the directional emissivity is known then stereoscopic brightness temperatures from ATSR can be used to determine the atmospheric correction and obtain the radiometric surface temperature at ground level.

EXPERIMENT

SITE DESCRIPTION

The site is characteristically semi-arid grassland and is predominantly sandy soil with a short, sparse grass canopy covering an area of some 2500 square kilometres to the north east of Zimbabwe, southern Africa (31.4 - 31.6 E, 18.0 - 18.3 S). At an altitude of approximately 1550 m the region receives annually around 1000 mm of rainfall, higher than the national average, and is populated mainly by subsistence farmers. The terrain is typically rolling hillsides and the intervening basins are classified as regions known as *dambos* , or *vleis* , where the hydrology is of particular interest because of their increased water capacity.

Dambos are nationally protected wetlands but it is understood that their cultivation is widespread through necessity. The hydrological balance within this area is particularly sensitive because of the systematic deforestation and unrestricted cultivation that has occurred.

Normal fractional vegetation cover was estimated to vary between 50% and 66% annually with an associated increase in the mean canopy height from 0.01 to 0.04cm. The vegetation is suppressed through overgrazing and bears little resemblance to that within nearby rigorously protected areas where the canopy is over 2m in height.

METHOD

Angular radiometric surface temperatures were recorded as part of a wider field campaign and data were collected on 3 separate occasions (2/10/95,19-20/5/96). Between 4 and 6 Everest Interscience* infra-red thermometers were used to sense the radiometric surface temperature of representative sites during each period of measurement.

The instruments have a spectral bandpass of 8-14μm and a field of view of 15 degrees. This intermediary field of view is sufficiently large to enable sensing the temperature of a reasonably sized area, relative to the scale of the surface heterogeneities, and small enough to exclude any overlaps between the required view angles. The temperature retrieved using a finite field of view will in general be different to the unique angular radiometric temperature because it is an average of temperatures from a range of angles around the central orientation. If the vegetation is tall enough to exhibit a pronounced vertical temperature distribution then this smoothing could significantly bias the radiometric temperature because the central

temperature would in reality be some non-linear aggregate over the field of view instead of a simple average. This effect is not anticipated over a low canopy where the dominant factor affecting ensemble temperature is assumed to be the component fractional occupancy, which averages linearly in typical canopy architectures.

Radiometers were configured to record either the nadir (zenithal) or forward (55 degrees to zenith) temperature of approximately the same area simultaneously. Forward viewing instruments were azimuthally orientated along the ERS-1 sub-satellite track (8.5 degrees East of North during daytime overpasses) to reproduce the viewing geometry of the ATSR. The sensors were located approximately 2.5m from the surface on tripods capable of holding 2 radiometers each. The height of each radiometer above the canopy was adjusted so that measurements were taken through similar atmospheric path lengths at both angles, primarily to ensure mismatches in target area were not extreme. At nadir inclination the radiometers observed an area of approximately 0.35 m^2, increasing to roughly 0.6 m^2 when inclined at 55 degrees.

The mean length of roughness elements within the canopy was estimated to be 0.02 m.

By using 2 or more radiometers at each angle any errors in targeting the sensors could be minimised through the overlaps in the field of view of individual instruments. This duplicity of instrumentation also increases the effective target area and indicates the extent of surface sampling heterogeneities present within the test region.

All radiometers were calibrated against a Working Standards WS153* reference blackbody source before and after each field campaign. The calibrations were performed across a complete range of temperatures and each sensor response is accurate to within 0.15 C at room temperature. Studies have indicated that the instrument response is uncharacteristic when subjected to thermal shocks, and to reduce the chances of this occurring during field measurements they were shielded from direct solar heating.

Air temperature at a height of 1m was recorded during the experiment and was observed to vary between 17.5 and 27 C.

*Trade name implies no recommendation or endorsement by the author and is for the benefit of the reader only.

RESULTS & DISCUSSION

Radiometric surface temperatures, $T_{RS}(\theta)$, were collected over sparse vegetation from 2 different observation angles (0 and 55 degrees to the zenith) using between 4 and 6 infra-red thermometers set at an azimuthal angle of 8.5 degrees East of North. Temperatures were sampled at 1 second intervals and were recorded as 10 minute averages to compensate for instantaneous fluctuations in influential factors such as the wind speed.

Meteorological information collected nearby was used to estimate the radiative sky temperature, T_{SKY}, on each day of the experiment. The mean surface vapour pressure was 9.1 mbar and the mean air temperature was 20.9 C, so that (after Idso, 1981) a value of T_{SKY}=4 C is appropriate. Clear skies were present on the first day of measurements (2/10/95) with low intermittent cumulus disturbing the surface energy balance at time periods typically less than the (10 minute) sampling interval on subsequent days (19-20/5/96).

Surface temperature responds rapidly to changes in net radiation, such as cloud intervention, through an almost instantaneous change in the sensible heat flux, in contrast to evaporation and soil heat fluxes.

A histogram of estimated radiance standard deviations (Fig.2) indicates that 70% of all data points deviate by less than 3% of the observed radiance, and the modal cloudless deviation was 1.0-1.5 C.

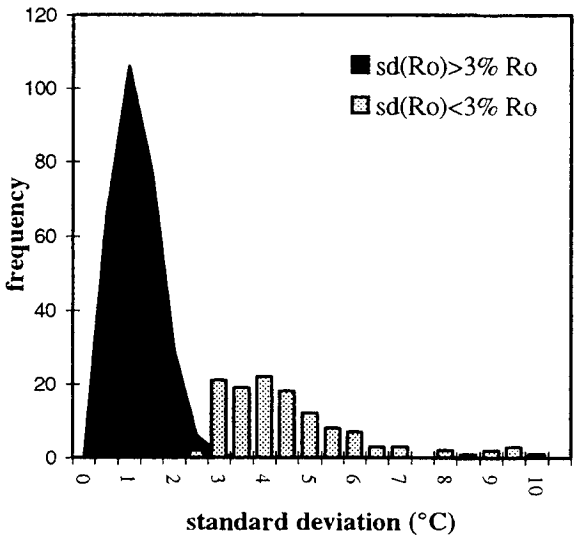

Figure 2. Histogram of radiance standard deviations estimated from radiometric surface temperatures sampled over 10 minute intervals. Data is separated into distributions representing cloudy and clear sky observations.

Surface radiances with proportionally high standard deviations were selectively removed from the original data set, under the assumption that these represent inappropriate temporal averages. The resultant cloudy and clear sky distributions obtained using this simple cloud clearing algorithm qualitatively describe independent distributions derived from the original bimodal distribution (Fig.3).

Results are presented from both the original and the adjusted (clear sky) data sets, and in general inclusion of cloudy data does not significantly affect any empirical relationships derived.

The mean absolute temperature differences (MATD) between individual radiometers at nadir inclination was 0.8 C for both the original and the adjusted data set.

The angular variation in thermal emissivity has been investigated for a number of soil types (Labed and Stoll, 1991, Nerry et al, 1988) categorised by composition and granularity. In general larger decreases in emissivity with zenithal view angle are apparent in agricultural soils, and the soil within the region is fine, compressed and silica rich.

All data from individual days are combined to characterise the angular variation in the radiometric surface temperature of a sparsely vegetated surface (Fig.3) in contrast to the estimated variation for SiO2 sand (after Labed & Stoll).

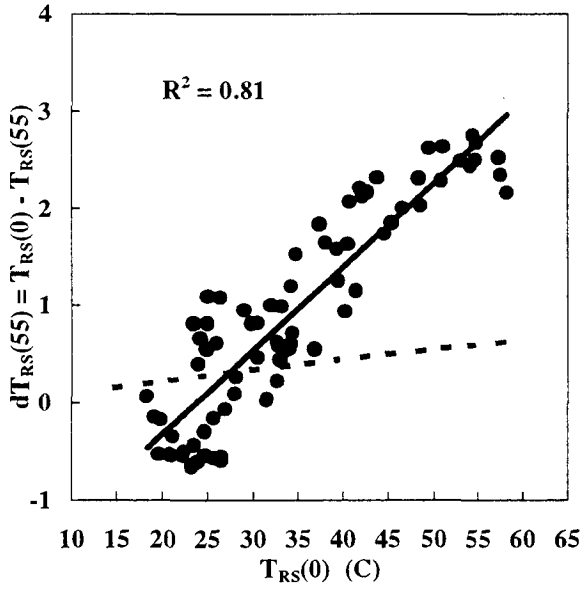

Figure 3. Difference between nadir (zenithal) and forward (55 degrees to zenith) radiometric surface temperature as a function of nadir radiometric surface temperature for a) sparse grassland canopy b) SiO2 sand (after Labed & Stoll, 1991) using estimated T_{SKY} (dotted line)

The observed difference $dT_{RS}(55)=T_{RS}(0)-T_{RS}(55)$, shows strong correlation with the nadir temperature, and the empirical relationship

$$dT_{RS}(55) = a\ T_{RS}(0) + b \qquad \text{(Eq.5)}$$

is consistently valid for the sparse canopy.

For the original data set, a=0.084 and b=-1.88 C, and the mean absolute temperature difference from the linear approximation is 0.41 C, and for the adjusted data set, a=0.086 and b=-2.03 C, MATD = 0.40 C.

Using such a parameterisation for the angular variation in surface temperature a maximum of 3.2 C difference between the forward and nadir views can be predicted, with typically a 0.5-1.5 C difference at the time of satellite overpass.

Lagouarde et al (1995) observed similar variations over various plant canopies and concluded that this was a standard feature over vegetation due to it's vertical structure. The strongest angular dependence determined by Lagouarde et al was over corn, with a smaller but still significant variation over grass. Both of these canopies were unstressed and the vegetation height was 1.1m and 0.2m for the corn and grass respectively. Because of the limited range in surface temperatures the absolute maximum $dT_{RS}(\theta)$ observed by Lagouarde et al were between 2 and 3.5 C, although these differences occured at much lower nadir temperatures and substantial dependence on $T_{RS}(0)$ can be inferred from their results over both canopies. Much larger differences have been presented over a wheat canopy (Kimes et al, 1980) but no angular relationship can be inferred from these results.

The comparatively small differences observed here can be explained by the nature of the sparse canopy, in particular the relatively low height of the vegetative elements. Physically, a pronounced thermodynamic interaction will exists between the soil and vegetation within such a short canopy, which will result in lower differentials between the vegetation and soil kinetic temperatures, particularly during periods of water stress. This will lead to a lower variability in the ensemble radiative temperature $T_{RAD}(\theta)$ as it is strongly related to the relative component temperatures.

Significantly, $dT_{RS}(55)$ reduces to zero at low temperatures, as one would expect, since essentially thermodynamic equilibrium exists when there is no solar heating.

It is evident that angular variations in soil emissivity alone are not sufficient to produce the difference in surface temperatures observed in this experiment. Two factors could introduce a significant increase in the predicted angular difference, specifically the inclusion of an appropriate variation in component fractional occupancy coupled with independent distributions of soil and vegetation temperatures.

A two component radiative transfer model can be used to describe the angular variation in radiative surface temperature for a simple canopy architecture but quantitative data for the angular variation in fractional occupancy does not exist for such sparse vegetation.

The empirical relationship (Eq.5) is consistently valid on individual days across the annual vegetation growth cycle and describes the angular variation in radiometric surface temperature for a sparse canopy at

all expected nadir temperatures. Such a relationship can be used in conjunction with satellite retrieved radiometric surface temperatures to estimate the appropriate atmospheric correction.

REFERENCES

Brutsaert, W.B., Evaporation into the atmosphere, D. Reidel, Dordrecht, 1982

Chehbouni, A., Njoku, E.G., Lhomme, J.-P., and Kerr, Y.H., Approaches for average surface flux parameters and fluxes over heterogeneous terrain, J. Climate, 8, 1386-1393, 1995

Humes, K.S., Kustas, W.P., Moran, M.S., Nichols, W.D., and Weltz, M.A., Variability of emissivity and surface temperature over a sparsely vegetated surface, Water Resour. Res., 30(5), 1299-1310, 1994

Idso, S.B., A set of equations for full spectrum and 8-to 14-μm and 10.5-to 12.5-μm thermal radiation from cloudless skies, Water Resour. Res., 17(2), 295-304, 1981

Kimes, D.S., Idso, S.B., Pinter Jr., Reginato, R.J., and Jackson, R.D., View angle effects in the radiometric measurement of plant canopy temperatures, Rem. Sens. Env., 10, 273-284, 1980

Kustas, W.P., Choudhury, B.J., Moran, M.S., Reginato, R.J., Jackson, R.D., Gay, L.W., and Weaver, H.L., Determination of sensible heat flux over sparse canopy using thermal infrared data, Ag. Forest Met., 44, 197-216, 1989

Labed, J., and Stoll, M.P., Angular variation of land surface spectral emissivity in the thermal infrared: laboratory investigation on bare soils, Int. J. Remote Sensing, 12(11), 2299-2310, 1991

Labed, J., Li, Z.L., and Stoll, M.P., Land surface temperature retrieval from ATSR over the Niamey (Niger) area, Proc. Second ERS-1 Symposium - Space at the service or our environment, Hamburg, Germany, 11-14 October 1993, 389-392

Lagouarde, J.P., Kerr, Y.H., and Brunet, Y., An experimental study of angular effects on surface temperature for various plant canopies and bare soils, Ag. Forest Met., 77, 167-190, 1995

Nerry, F., Labed, J., and Stoll, M.P., Emissivity signatures in the thermal IR band for remote sensing: calibration procedure and method of measurement, Applied Optics, 27(4), 758-764, 1988

Stewart, J.B., Kustas, W.P., Humes, K.S., Nichols, W.D., Moran, M.S., and de Bruin, H.A.R., Sensible heat flux- radiometric surface temperature relationship for eight semiarid areas, J. App. Met., 33(9), 1110-1117, 1994

Norman, J.M., Kustas, W.P., and Humes, K.S., Source approach for estimating soil and vegetetation energy fluxes in observations of directional radiometric surface temperature, Ag. Forest Met., 77, 263-293, 1995

Van de Griend, A.A., Owe, M., Groen, M., and Stoll, M.P., Measurement and spatial variation of thermal infrared surface emissivity in a savanna environment, Wat. Resour. Res., 27(3), 371-379, 1991

Verma, S.B., Rosenberg, N.J., and Blad, B.L., Turbulent exchange coefficients for sensible heat and water vapour under advective conditions, J. Appl. Meteorol., 17, 330-338, 1978

Vining, R.C., and Blad, B.L., Estimation of sensible heat flux from remotely sensed canopy temperatures, J. Geophys. Res., 97(D17), 18951-18954, 1992

MONITORING BIOMASS BURNING USING ATSR-2 DATA

Matthew C. Perrin and Andrew C. Millington

Department of Geography, University of Leicester, University Road, Leicester, LE1 7RH, UK.
phone: +44 (0)116 2525245, fax: +44 (0)116 2523854, e-mail: mcp8@le.ac.uk, acm4@le.ac.uk.

ABSTRACT

AVHRR data have long been used for detecting biomass burning. However, the afternoon overpass time coincides with the build up of clouds in tropical regions. A second, complimentary fire sample at mid-morning may now be possible using the ATSR-2 sensor which is equipped with similar thermal wavebands. An automated, contextual fire detection algorithm, originally developed for AVHRR data, was modified and applied to ATSR-2 data acquired for lowland Bolivia during the 1995 fire season. Fixed threshold components of the algorithm were tested and the results used to make further amendments to the algorithm. Preliminary validation results are presented which suggest that ATSR-2 can be used to detect biomass burning within different tropical environments.

1. INTRODUCTION

Biomass burning has major large scale impacts on biogeochemical cycles, atmospheric chemistry, vegetation dynamics and the spatial boundaries between ecosystems (e.g. Levine 1991; Crutzen and Goldammer 1993). Currently these impacts are not well understood and there is a recognised need for regional and global fire data within the framework of global change research (e.g. IGBP, 1994). Using data from the Advanced Very High Resolution Radiometer (AVHRR) sensors, it is possible to detect active fires at suitable spatial and temporal scales and so build up maps of regional and global fire activity. The majority of fire detection studies have so far used data from the early afternoon AVHRR overpass. With the launch of the second Along Track Scanning Radiometer (ATSR-2) in April 1995, there is the potential to monitor fire activity at mid-morning. This may prove particularly advantageous in the tropics where cloud cover tends to build up during the afternoon. Discussion of nightime fire detection and other temporal sampling considerations is outside the scope of this study but are considered by Robinson (1991), Langaas (1993) and Malingreau and Eva (1995). The ATSR-2 and AVHRR sensors have comparable spatial resolutions (at nadir, 1km and 1.1km respectively) and the same thermal bandwidths making it possible to adopt AVHRR fire detection techniques for ATSR-2 that have, to some extent, already been validated (see table 1).

The objective of this investigation is to assess the potential of ATSR-2 data for monitoring active fires.

The paper describes how a contextual algorithm, originally developed for AVHRR data, has been applied to ATSR-2 data covering lowland Bolivia and then amended based on the results. Bolivia was chosen because it presents a variety of forest, savanna and agricultural landscapes with different fire types and regimes, and little is known of south American fire regimes outside of Brazil.

ATSR-2			AVHRR
Band	Range (μm)	Band	Range (μm)
V1	0.545 - 0.565		
V2	0.649 - 0.669	1	0.5 - 0.68
V3	0.855 - 0.875	2	0.725 - 1.1
1b	1.58 - 1.64		
1a	3.55 - 3.93	3	3.55 - 3.93
2	10.4 - 11.3	4	10.3 - 11.3
3	11.5 - 12.5	5	11.5 - 12.5

Table 1. ATSR-2 and AVHRR Channels

2. FIRE DETECTION METHODOLOGY

AVHRR channel 3 (3.55μm - 3.93μm) is sensitive to the radiant emittance from biomass burning because the maximum radiant emittance from typical vegetation fires occurs at wavelengths between 3-5μm (e.g. Langaas and Muirhead, 1988). Furthermore, it is possible to detect subpixel fires because the total radiant emittance from a fire is disproportionally greater than that from a cooler background. Kennedy et al. (1994) have calculated that a background environment at 300°K with a fire covering 400m^2 (0.04 per cent of an AVHRR pixel) and a temperature of 800°K would be sufficient to saturate the channel 3 sensor. Signal increases in channel 3 can also be the result of reflected solar radiation from hot, sparsely vegetated surfaces or from cloud tops (e.g. Gregoire et al. 1993). To distinguish between signal increases caused by fires and those caused by warm surfaces the difference between channel 3 and channel 4 (11.0μm) temperatures can be used. Fires will result in a much higher channel 3 temperatures than those for channel 4; whereas there will be a much smaller difference in channel temperatures over warm surfaces. To remove the effect of cloud reflectances, masking is normally

performed before applying fire detection techniques. When channel 3 and 4 temperatures of a fire pixel are known for an unsaturated fire pixel, it is possible to determine the size and temperature of subpixel fires using the method of Dozier (1981). However, the technique is concerned with fire characterisation rather than detection and is not considered here.

2.1 AVHRR fire detection algorithms

The simplest methods of fire detection use visual image interpretation or empirically derived thresholds for channel 3 temperatures and/or the temperature differences between channel 3 and channel 4. There are numerous examples of such methods which have been used for detecting a range of fire types, including: deforestation fires (e.g. Malingreau et al. 1985; Flannigan and Vonder Haar 1986; Matson and Holben 1987; Matson et al 1987; Malingreau and Tucker 1988; Kaufman et al. 1990); savanna fires (e.g. Gregoire 1993; Kennedy et al. 1994) and straw burning (Muirhead and Cracknell, 1985; Cracknell and Saradjian 1996). The main disadvantage of these algorithms is that fixed thresholds are ecosystem and season specific (Justice et al. 1993; Langaas, 1995). As a result, they are not suited to mixed landscapes like those found in Bolivia.

2.2 Contextual algorithms

Contextual approaches use variable thresholds based on the immediate environment of the pixel being tested. This overcomes most of the problems of fixed limits and means that the algorithm can be applied consistently over large areas. Two separate but similar approaches are reported in the literature. Harris and Rothery (1995) developed a contextual method to consistently identify volcanic thermal anomalies over time. They compared the channel 3 and 4 temperature difference, of each pixel in the study area, with the mean difference of its immediate background. Then the target pixel and background difference was compared to the temperature difference for all pixels in the region immediately outside of the study area. If the temperature differences were greater in all cases the pixel was flagged as hot. The second method has been developed by Flasse and Ceccato (1996) within the Local Applications of Remote Sensing Techniques group (LARST) at the Natural Resources Institute (NRI) for operational fire detection and for use in the Global Vegetation Fire Product (Stuttard et al. 1995). This algorithm has been adopted for use with ATSR-2 data. It is specially designed for the detection of vegetation fires regardless of ecosystem, season or type of fire. The algorithm consists of five main steps which are repeated here with the notation given in Flasse and Ceccato.

[1] Masking of cloud, water and desert areas to remove non-fire pixels.

[2] Selection of a pixel as a potential fire pixels if,

(a) $T_3 > 311°K$

and

(b) $T_3 - T_4 > 8°K$

where T_3 and T_4 are AVHRR channel 3 and channel 4 brightness temperatures.

[3] Masking of pixels with a very high reflectance that might contaminate the channel 3 signal. Pixels are removed if,

$$\rho_2 \geq 20\%$$

where ρ_2 is the top-of-atmosphere bi-directional reflectance for the AVHRR near-infrared channel.

[4] Computation of background statistics for potential fire pixels using a variable spatial window starting with 3 x 3 pixels. Only pixels that have not been masked and that are not potential fires can be used in the computation. The window operates until a minimum of three or at least 25 per cent of the window pixels can be used. If insufficient pixels are available the window size is increased until a maximum of 15 x 15 pixels. The neighbouring pixels are used to calculate:

T_{3b} = T_3 mean for the neighbouring pixels

σ_{T3b} = T_3 standard deviation of the neighbouring pixels

T_{34b} = $[T_3 - T_4]$ mean of the neighbouring pixels

σ_{T34b} = $[T_3 - T_4]$ standard deviation of the neighbouring pixels

[5] Testing the potential fire against its background statistics. The potential fire is confirmed if,

(a) $T_{3pf} - [T_{3b} + 2\sigma_{T3b}] > 3°K$

and

(b) $T_{34pf} > T_{34b} + 2\sigma_{T34b}$

where $_{pf}$ is a potential fire.

Although the algorithm has not been thoroughly tested, the initial results seem promising with 90% of visually identifiable fires being detected and commission errors limited to 15% (Stuttard et al. 1995; Flasse and Ceccato 1996). However, there are several weaknesses in the algorithm that have been recognised by the authors. The most important of these are the use of fixed values in the high reflectance test in step 3 and the first context test in step 5a; and the arbitrary limits set for the minimum acceptable sample size and maximum allowable window size. The validity of these values is investigated as part of this study. See Justice and Dowty (1993) for a detailed review of fire detection algorithms.

3. METHODOLOGY

The algorithm described above was firstly amended with respect only to the identification of potential fires. The ATSR-2 3.7μm band saturates at 312°K so a pixel was flagged as a potential fire if,

$$T_{1a} = \text{saturation}$$

and

$$T_2 < 304°K$$

where T_{1b} and T_2 here denote ATSR-2 3.7μm and 11.0μm channels respectively. The saturation criteria ensures that the minimum T_{1b} temperature of a potential fire is 312°K. Although this is lower than for AVHRR (saturation = 321°K), the effect of relected solar radiation in channel T_{1a} will be less marked because of the earlier overpass time.

For this study a pixel was classified as cloud if,

$$T_3 < 285°K \text{ and } V_1 + V_2 > 40\%$$

and

classified as water if,

$$NDVI < -12 \text{ and } T_{1b} < 5\%$$

where T_3 is the ATSR-2 12μm band, V_1 and V_2 are the red and green bands and T_{1b} is the short wave infrared channel. The cloud screen is a simple test to remove cold and very reflective pixels from the analysis. Use of less rigorous thresholds did not remove a sufficiently large proportion of pixels that were identifiable as cloud on the images. There was no requirement for a desert mask with the Bolivia data. The context tests were left unchanged. In order to test the response of fire detection rates to changes in the fixed thresholds, the algorithm was applied using all combinations of: high reflectance values from 15 to 25%; minimum acceptable sample sizes of 3, 6, 9, 12 and 15, and maximum allowable window sizes from 3 x 3 to 17 x 17.

3.1 ATSR-2 data processing

ATSR-2 data were obtained from the Rutherford Appleton Laboratory (RAL) as gridded brightness temperature (GBT) products. Each product consists of 512 x 512 geolocated, collocated nadir and forward-view images at a 1km resolution (Bailey 1994). For this study only nadir view data were used. The spectral bandwidths are given in table 1. Thermal data is supplied as calibrated brightness temperatures and the reflectance data was converted to top-of-atmosphere reflectance using calibration coefficients supplied by RAL. All the available images of lowland Bolivia in 1995 were examined and only those with a full compliment of nadir channel data were selected for further analysis. The images were visually inspected to remove those with approximately 80-100 per cent cloud cover. The remaining 18 images were used in the study and provide a reasonably even coverage of the 1995 fire season (May to December).

4. RESULTS AND DISCUSSION

4.1 Scattered Cloud

Visual inspection of the algorithm results showed that a significant number of fire pixels were occurring in areas of scattered cloud and at the edges of large cloud banks. In both cases it is reasonable to assume that subpixel clouds are flagged as potential fires because the cloud is sufficient to cause T_{1a} saturation and a reduction in T_4 temperatures. These pixels are not rejected by the contextual tests because the immediate background is cloud free and T_3 temperature and T_3, T_4 differences are lower. To overcome this problem a simple three pixel buffer added around cloud pixels classified which has the effect of 'infilling' areas of scattered cloud and removing false detections (see figure 1). The infilling should also improve the validity of background statistics in general.

4.2 Minimum sample size and fire counts

Figure 1 shows a plot of fire counts against the minimum sample size for three different window sizes. The high reflectance test threshold has been set at 20%. There are two important trends. First, fire counts are significantly larger for a minimum sample size of three than for other sample sizes, and second, fire counts for sample sizes between 6 and 15 are relatively stable but show a gradual decline. Interpreting these results is difficult because increasing the minimum sample size criteria has a direct effect on the mean and standard deviation estimates for the background, by increasing the number of samples used in the statistics; and an indirect effect, by forcing the statistics to be calculated on different pixels with a different proximity and relationship to the potential fire pixel. For example, a minimum sample size of 9 or over precludes the use of a 3 x 3 window. However, it is clear that sample size influences the algorithm results and that there is a trade off between getting statistics from the immediate fire background (i.e. the 3 x 3 or 5 x 5 windows) and getting a good mean and standard deviation estimate (i.e. a larger sample size). The limit was changed to a minimum sample size of 6 and appears to provide a reasonable balance between the two requirements. The minimum proportion of pixels needed for any given window size was also increased to 33% so that more representative sample of the background was used in the computation.

4.3 Maximum allowable window size

Changes in the maximum allowable window size do not have a significant effect on fire count, except that larger windows result in gradually larger fire counts because they allow more potential fires to be tested. Ideally, the choice of window size should be made with reference to the scale of the landscape. For example, the landscape of Eastern Bolivia is a mosaic of savannas and forests. Depending on which window

size is used potential savanna fires could be tested against background statistics calculated only from savanna pixels or from a mixture of savanna and forest pixels. For a contextual approach to work best, it is preferable that the a potential fire is tested against statistics calculated from a similar land cover type. One solution could be to incorporate a vegetation mask within the algorithm which would adjust the maximum allowable window size (or other parameters) automatically; or select only pixels of a similar vegetation type to the potential fire, for the background statistics.

4.4 High reflectance thresholds and fire counts.

Figure 2 shows a plot of fire counts against different thresholds for the high reflectance test with three separate curves for the periods May-August, September and October. It can be seen that fire counts generally decrease as the threshold is increased. This is explained by fewer highly reflective pixels being masked as the threshold rises. Mean T3 background temperature and T3, T4 differences are increased by the inclusion of these pixels in the statistics causing more context test failures. There is no clear point at which the threshold is more or less influential and the relationship between the threshold and fire counts is highly variable between time. This suggests that the threshold decision has a marked and arbitrary affect on algorithm performance and that this affect varies over time. In order to reduce the impacts of this test, the threshold was increased to 25% were there is a decreased rate of change in the fire count.

4.5 Context Test Adjustment

A final adjustment was made to the algorithm by changing the first context tests to:

$$T_{3pf} > T_{3b} + [3\sigma_{T34b}]$$

This removes the 3°k fixed threshold and gives more weight to the local variance in temperature difference.

4.6 Visual Interpretation

The new algorithm was re-applied to the 18 test images. Results from the re-amended algorithm have not yet been fully tested. Preliminary work indicates that the algorithm works well for the Bolivian dataset. Figure 3 shows fires identified by the algorithm for a part scene in August. The two active fires visible from their smoke plumes have both been identified by the algorithm. The fire front of the larger fire is partially described by the pattern of fire pixels. It is also worth noting that these fires are occurring in different ecosystems and that there are no obvious incorrect detections. From all fires identified by the algorithm, 30 were randomly selected and tested visually in the imagery. All were located within areas able, and likely, to be affected by biomass burning (i.e. savanna, agricultural land and at the savanna-forest boundary). Seven had associated smoke plumes or visible reflectances much lower relative to their neighbours and consistent with charred or scarred vegetation. The rest could neither be confirmed or rejected visually which is not surprising considering that the technique is detecting subpixel events. Field data listing field locations and dates of active fires during 1995 will be used to further test the algorithm.

5. CONCLUSION

Initial results suggest that it is possible to automatically detect mid-morning fire activity using ATSR-2 data with the amended contextual algorithm. Also, the contextual approach can be used to successfully discriminate vegetation fires in different environments for the duration of an entire dry season. Further work will be aimed at validating the algorithm using field data.

6. ACKNOWLEDGEMENTS

M. C. Perrin is supported by NERC CASE studentship GT4/94/356/L with Earth Observation Science Ltd. The ATSR-2 data was supplied by RAL and NERC.

7. REFERENCES

Brunette, J. M., Vices, J. B., Fountain, J., Manissadjan, K., Podaire, A. and Lavenu, F., 1991, Remote sensing of biomass burning in west Africa with NOAA-AVHRR, in Levine, J. S. (editor), 1991, *Global Biomass Burning*, MIT Press, Cambridge, MA.

Cracknell, A. P and Saradjian, M. R., 1996, Monitoring of straw burning in the U. K. using AVHRR data - summer 1995, *International Journal of Remote Sensing*, 17, 12, 2463-2466.

Crutzen, P. J. and Goldammer, J. G, 1993, *Fire in the Environment: the Ecological, Atmospheric, and Climatic Importance of Vegetation Fires*, Wiley & Sons, New York.

Dozier, J., 1981, A method for satellite identification of surface temperature fields of subpixel resolution, *Remote Sensing of Environment*, 11, 221-229.

Flannigan, M. D. and Vonder-Haar, T. H., 1986, Forest fire monitoring using NOAA satellite AVHRR, *Canadian Journal of Forest Research*, 16, 975-982.

Flasse, S. P. and Ceccato., 1996, A contextual algorithm for AVHRR fire detection, *International Journal of Remote Sensing*, 17, 2, 419-242.

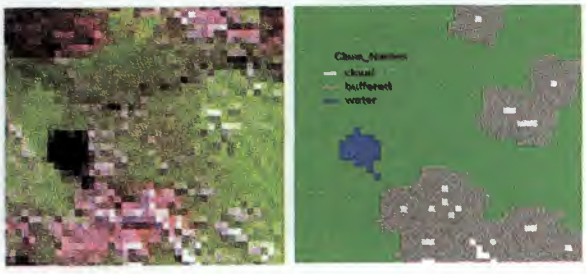

Figure 1. ATSR-2 sub-image (left) with scattered cloud over a savanna-forest landscape and masking results (right).

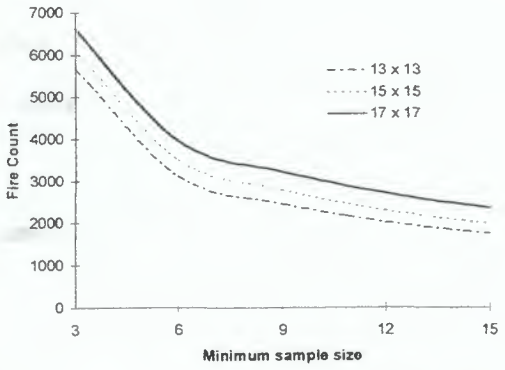

Figure 2. Effect of minimum acceptable sample size fire count. Curves are shown for three maximum window sizes. High reflectance test threshold is set at 20%.

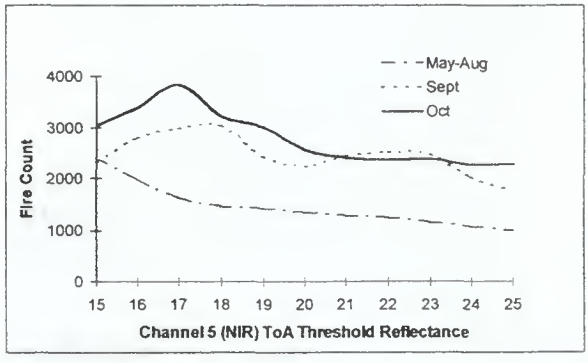

Figure 3. Effect of the high reflectance test on fire count. Minimum sample size is fixed at three and maximum window size at 15 x 15 pixels.

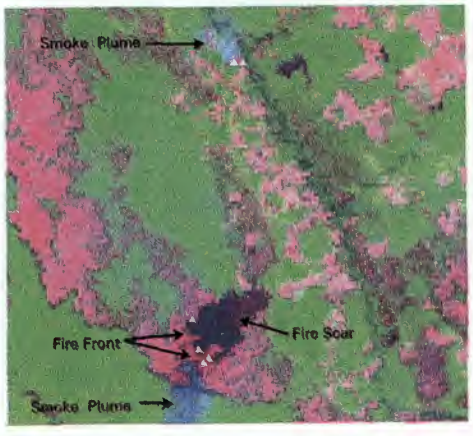

Figure 4. ATSR-2 colour composite of NE Bolivia 8th August 1995. Two active fires are visible from smoke plumes. Active fires detected by the algorithm are shown white triangles.

Gregoire, J. -M., 1993, Use of AVHRR for the study of vegetation fires in Africa: Fire Management Perspectives, *Euro courses: Advances in the use of AVHRR data for Land Applications*, Ispra, Italy.

Harris, A. and Rothery, D., 1995, Thermal monitoring of volcanoes using data from the AVHRR, In *Proceedings of the 21st Annual Conference of the Remote Sensing Society*, 11-14 September 1995, Southampton, 528-535.

IGBP, 1994, International Global Atmospheric Chemistry (IGAC) Project - the Operational Plan, *IGBP Report No.32*.

Justice, C. O. and Dowty, P (eds) 1993, IGBP-DIS satellite fire detection algorithm workshop technical report. *IGBP-DIS Working Paper No. 9*, 88pp., February 1993, NASA/GSFC, Greenbelt, Maryland, USA.

Justice, C. O., Malingreau, J. P., and Setzer, A. W., 1993, Satellite remote sensing of fires: potential and limitations. In *Fire in the Environment: the Ecological, Atmospheric, and Climatic Importance of Vegetation Fires*,
edited by Crutzen, P. J. and Goldammer, J. G, Wiley & Sons, pp77-88.

Kaufman, Y., Tucker, C. J., and Fung, I., 1990, Remote sensing of biomass burning in the tropics. *Journal of Geophysical Research*, 95, 9927-9939.

Kenndy, P. J., Belward, A. S., and Gregoire, J -M., 1994, An improved approach to fire monitoring in West Africa using AVHRR data. *International Journal of Remote Sensing*, 15, 2235-2255.

Langaas, S, 1993, Diurnal cycles in savanna fires, *Nature*, 363, p120.

Langaas, S., and Muirhead, K., 1988, 'Monitoring' bushfires in west Africa by weather satellite. In *Proceedings of 22nd International Symposium on Remote Sensing of Environment*, Abidjan, Cote d'Ivoire, 20-26 October 1988, (Ann Abor, MI: ERIM), 2, 253-268.

Langaas, S., 1995, A critical review of sub-resolution fire detection techniques and principles using thermal satellite data, submitted to *Remote Sensing Reviews*.

Levine, J. S. (editor), 1991, *Global Biomass Burning*, MIT Press, Cambridge, MA.

Malingreau, J. P. and Eva, H., 1995, Notes on the temporal sampling of remotely sensed data for active fire monitoring, *IGBP-DIS Workshop on Global Fire Monitoring* - Joint Research Centre, Ispra, Italy.

Malingreau, J. P., Stephens, G. and Fellows, L., 1985, Remote sensing of forest fires: Kalimantan and north Borneo in 1982-83, *Ambio*, 14, 6, 314-321.

Malingreau, J. P., and Tucker, C. J., 1988, Large scale deforestation in the south-eastern Amazon basin of Brazil. *Ambio*, 17, 49-55.

Matson, M. and Holben, B., 1987, Satellite detection of tropical burning in Brazil, *International Journal of Remote Sensing*, 8,3, 509-516.

Matson, M., Stephens, G., and Robinson, J., 1987, Fire detection using data from the NOAA-N satellites, *International Journal of Remote Sensing*, 8, 7, 961-970.

Muirhead, K. and Cracknell, A. P., 1985, Straw burning over Great Britain detected by AVHRR, *International Journal of Remote Sensing*, 6, 5, 827-833.

Robinson, J. M., 1991, Problems in global fire evaluation: is remote sensing the solution?, chapter 8, in Levine, J. S. (editor), 1991, *Global Biomass Burning*, MIT Press, Cambridge, MA.

Stuttard, M., Boardman, S., Ceccato, P., Downey, I., Flasse, S., Gooding, R., and Muirhead, K., 1995, *Global Vegetation Fire Product Final Report for Joint Research Centre*, Contract 10444-94-09-FIEP ISP GB, Ispra, Italy.

ERS-SAR DATA FOR LAND INFORMATION SYSTEMS
CLASSIFICATION STRATEGY BASED ON REGIONAL ASPECTS

M. GÜNZL, A. HAGEMEISTER, T. SELIGE

GSF - National Research Centre for Environment and Health
Institute for Biomathematics and Biometrics
Ingolstädter Landstraße 1, 85764 Neuherberg, Germany
phone: +49 89 3187 2255, fax: +49 89 3187 3369
Email: guenzl@gsf.de, hage@gsf.de, selige@gsf.de

ABSTRACT

The project is aimed to improve land use classification based on ERS-SAR. Classification results have to be integrated into authority linked Land Information Systems. The present study is focused on the description and determination of regional effects on ERS-SAR backscatter. Based on these results a classification strategy has been developed to consider regional differences in backscatter affected by terrain, soil distribution and climate. The classification strategy is based on agricultural knowledge rules implemented with a fuzzy logic approach. Time effects and texture changes during the growing season will be shown. The influence of local climate and soil association on sowing, plant growth and harvest time is considered to be important when classifying time series of satellite data.

1. INTRODUCTION

Land Information Systems (LIS) are increasingly used by authorities as decision tools for sustainable development and planning as well as for environmental protection. The advantages of LIS are the capacities of complex analysis and integration of different data sources on a common spatial base. The accuracy of LIS based results ultimately depend upon data quality and reliability. Next to variations of terrain, soil distribution and climate the agricultural land use is a significant factor in landscape heterogeneity and dynamics. Therefore, the detection of agricultural land dynamics is of focal interest and indispensable in the implementation of LIS. This is the domain of remote sensing. As a part of the EMAP project (ERS-SAR 1/2 Data for Monitoring Agricultural Land Use as a Long Term Project) this study is aimed to develop a satellite based system for land inventory considering regional factors affecting plant growth and crop stand morphology. The limits and the possibilities of ERS-SAR will be analysed in comparison to optical data. The advantage of radar satellite is the multitemporal availability. On the other hand the backscatter signal of radar satellites is known to be strongly influenced by regional factors such as terrain, soil differences and precipitation. Individual crops will be characterized by different backscatter signals dependant on terrain, soil, climate and local weather conditions (ULABY, 1986).

Therefore, the main task is to describe and to discriminate the influence of these factors on the backscatter signal. The following factors have been investigated due to their influence on ERS-SAR SLC backscatter signal:

- geometrical effects due to the varying local incidence angle (see Fig. 4a/b),
- direct and indirect weather influences like soil moisture and dew precipitation on the plants,
- anthropogenic effects (soil cultivation, harvest),
- several other disturbing influences (to be investigated)
- vegetational influences (species, variety, cover and biomass) representing the crop species and yield.

2. INVESTIGATION AREA

The testsite is located in southern Bavaria between Munich and the Danube river embracing an area of around 2.500 km^2 in the northwest quarter of ERS frame 2637. Different landscapes such as tertiary hilly country, cultivated low moorland, fertile plains and quaternary gravel plains are covered (Fig. 1).

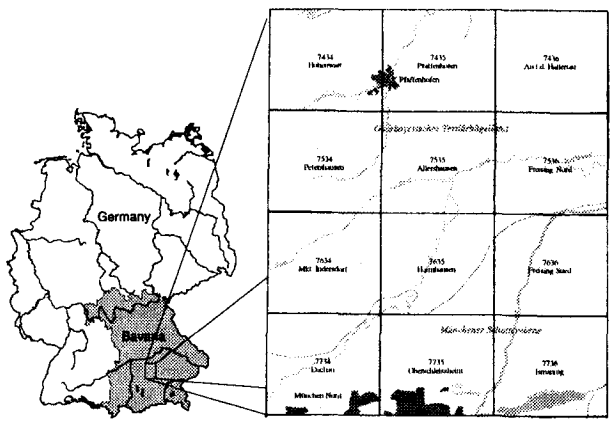

Fig. 1: Map of the investigation area

The investigation area can be divided into three different main landscape units:

- a hilly northern unit with tertiary sediments structured through alluvial plains, loess covered gentle slopes (mainly eastward exposed) and steeper slopes (mainly westward exposed) with a multitude

of tessellated soils from sandy, loamy to clayey material,

- an extensive quaternary gravel plain unit in the south with shallow soils representing dry locations adjoining to
- low moorland units in the southeast and southwest with very humus soils and humid location conditions.

Reference areas and investigated fields are spread representatively through the various landscape units. Site conditions are further characterized by different regional climate types (different zones of precipitation and solar radiation) affecting the plant growing conditions and the phenology. The average temperature is about 7.4 °C and the average amount of precipitation is about 830 mm.

3. METHODOLOGY

Ground Truth

A wide ground truth database is an indispensable requirement to consider regional aspects within the final classification process of the ERS-SAR data set. The applied ground truth program integrates three intensity levels:

- level 1: measurements of parameters, determining plant morphology and site conditions. The results are precise crisp metric data. On this level of high intensiveness only a small quantity of 30 test fields can be investigated. Those fields build core cells where the zones of level 2 and 3 are surrounded.
- level 2: estimations of parameters describing crop stand and soil surface. The results are ordinal fuzzy data.
- level 3: land use mapping at 8 reference areas, each of 4 to 5 km^2.

The spatial arrangement of the three zones is shown in Fig. 2.

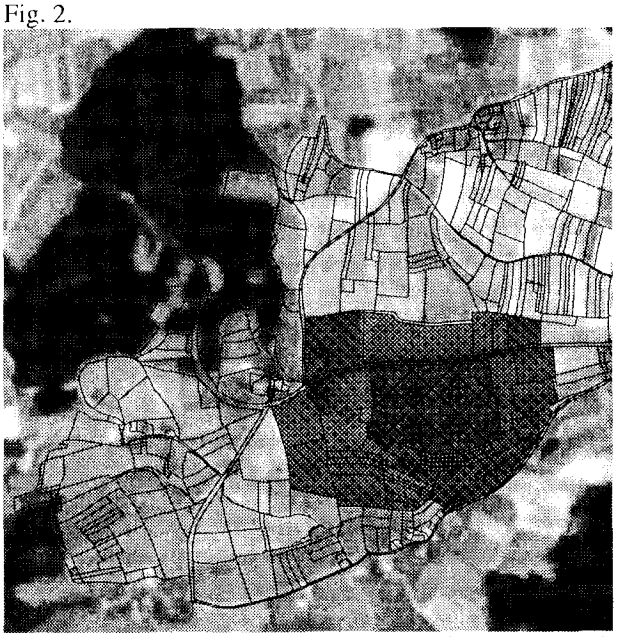

Fig. 2: Conception of the three level ground truth program and the spatial arrangement of the three zones

Some measured parameters of the 1st level are: biomass, water content of the plants, plant height, EC-stage, soil moisture, soil roughness and direction of plant rows. On the 2nd level the vegetation cover (density, height, EC-macro-stage) and the soil surface (roughness, tillage) are described by an ordinal parameter scheme. The estimations allow the investigation of about 200 to 300 test fields. This step is important to increase the spatial data base.

On the third level the land use will be mapped for an area of about 30 km^2.This data is necessary to validate the results from the segmentation and classification step. Besides ground truth data, climatological and pedological data are part of the spatial data base. Different climate and soil conditions divide the landscape into several sub-regions with specific plant growing conditions and characteristic phenological features. With this agricultural knowledge it is possible to derive a set of fuzzy rules which can be implemented within the classification algorithm. All the afore mentioned data types are stored, managed and analysed by a GIS using ARC/Info software. The ground truth program and the land use mapping are based on topographical maps 1 : 5000. The accuracy of the test field boundaries are checked by differential GPS.

Image Processing

Twelve SLC-scenes of 1996 were co-referenced by the correlation of windows around various manually chosen landmarks.

A set of dynamic combinations for the resulting multitemporal SAR scene were taken as resolution and signal-to-noise enhanced inputs for the segmentation algorithm. During the next two years this method will be used to keep track on the changes in field shapes within the whole 50x50 km observed area.

4. RESULTS

Regarding the signal-noise relationship (reciprocal value of the backscatter standard deviation) some significant differences within individual species have been found. In these cases the crop stand phenotype of test fields could be divided according to various characteristics. A representative example is given by two winter wheat plots at June 15th 1996 (Fig. 3a & 3b). The left field is situated in the northwest part of the investigation area (tertiary hilly country). The right field is located in the southeast (pleistocene gravel plain). Different climatic and soil conditions (*left*: Cambisols from loamy material, actual soil moisture 9%, *right*: dark histosols with a high content of C_{org}, actual soil moisture 24%) of the two locations when taken into consideration with anthropogenic factors like different seeding times (*left*: 30.11.95, *right*: 23.10.95) or varieties (*left*: Romos, *right*: Bussard) and different EC-macro-stages (*left*: beginning of ear emergence; *right*: end of ear emergence) lead to different signal-noise relationships.

Fig. 3a: Winter wheat (northwestern part of the testsite)

Fig. 3b: Winter wheat (southeastern part of the testsite)

Fig. 4: Influence of terrain-caused variation of the local incidence angle

Fig. 4b: DEM of the same area shown in Fig. 4a

To get enough information from single band single polarization ERS SLC data, it is important to observe time sequences and to evaluate texture features.
Speckle is not noise, since the same configuration leads to an identical speckle pattern (SCHREIER 1993). One major question that is fundamental to our task is therefore: What are the relevant parameters in agricultural land that lead to speckle patterns with separable textural features? Several different textural features are compared to vegetation and soil parameters that are expected to influence the backscatter signal.
Texture features based on window techniques have the inherent problem that small windows poorly represent the texture and large window sizes mix textural features from different fields if they are not totally embedded within the boundary of one single field.

Especially within areas of small fields, window based texture features gave poor results.
Segmentation as a pre-processing step for deriving texture features and classifications was found to give two major advantages:

- more up to date GIS data concerning field boundaries,
- possibility to calculate texture features based on segments instead of rectangular windows.

Although SAR is almost weather independent, it is indirectly influenced by changing soil moisture, dew and geometric effects due to heavy winds. The duration of these effects is mostly much shorter than the 35 days period of ERS orbit. Comparing ERS-1/2 looks from the tandem-mission with their one day interval enables the observation of changes happening within these 24 hours.

Therefore, it is possible to study the influence of short-term effects almost independent of long-term effects such as plant growth.

5. DISCUSSION

The weather independent monitoring capability of ERS-SAR has to be investigated for its ability to improve data in Land Information Systems concerning spatiality and actuality.
The studies on regional effects show that these factors have to be considered for land inventory use if based on ERS-SAR processing. It is necessary to describe the regionalisation of land by GIS in view of landscape types (soil region, climate region). The implementation of an expert system of agricultural rules described with fuzzy logic methods is expected to improve the classification results. The ground truth program is of fundamental importance to assess the reliability of the classification results. The following flowchart summarizes the various steps of data processing.

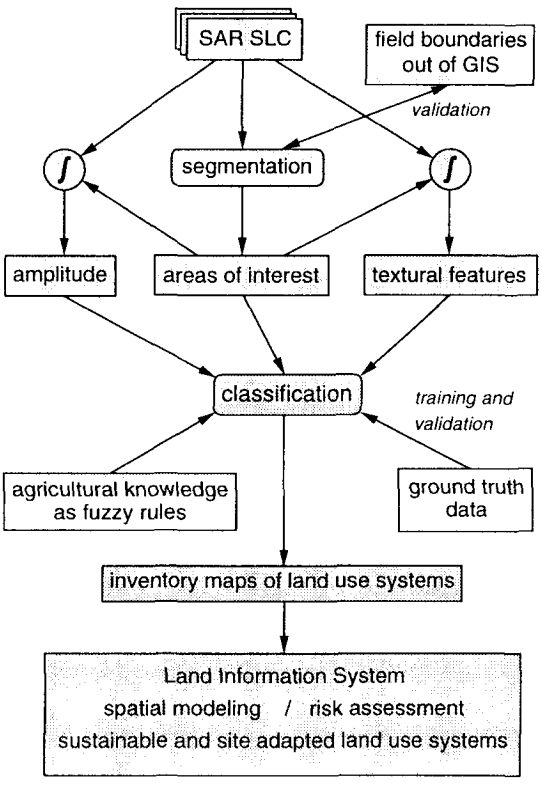

Fig. 6: Steps of data precessing

The purpose of EMAP is to analyse ERS-SAR data as a tool for agricultural crop monitoring. Continuous (35 days periods), multitemporal SAR-SLC data in conjunction with extensive ground measurements within selected test sites are used to determine correlations between the two and to separate disturbing impacts such as weather conditions and terrain slope. Therefore, in addition to amplitude and phase (interferometric analysis) the texture caused by speckle and its parameters are observed during the whole vegetation period. The characteristic time of changes due to sowing, stage of growth and harvest of different crops and their observation in conjunction with agricultural knowledge enables better crop classification. Coherence imaging of ERS-1/2 looks from the tandem mission, allows the detection even of relatively small changes such as soil cultivation. Several test sites with the same crop, but different terrain slope angles allow us to study the different effects of varying incidence angles.
A better understanding of natural effects on backscatter and further development of adapted processing strategy are still necessary. Therefore, an adapted 3 level ground truth program has been developed registering the dynamics of seasonal changes. Combining the advantage of precise measurements with more uncertain but faster and more repetitious estimation methods, will mean that backscatter will be calibrated for a broader base of ground truth information.

6. CONCLUSIONS

At the present stage of this study the influence of regional factors on the backscatter, can be summarized as follows:

- The implementation of ground truth program level 2 will give the possibility to discriminate different influences on backscatter due to the very enlarged data set produced by these estimations
- Texture information has been found to be able to improve significantly the classification result from enlarged areas. Further studies will be focused on non-window neighbourhood techniques
- The integration of remote sensing data with GIS is a central need for the future to analyse data an integrated conception.
- A fuzzy logic expert system of agricultural knowledge rules will be added to the project in collaboration with the different partners.

7. REFERENCES

SCHREIER, G. (1993): SAR geocoding: data and systems. Wichmann, Karlsruhe.
ULABY, F. T., MOORE, R.K.; FUNG, A. K. (1986): Microwave Remote Sensing: Active and Passive, Vol. 3: From Theory to Applications. Addison-Wesley, Reading.

Acknowledgement

EMAP is equally financed by the German Space Agency (DARA) and the German Federal Ministry of Agriculture (BML).

Long time scale INSAR by means of high coherence features

Stefania Usai and Ramon Hanssen
Delft Institute for Earth-Oriented Space Research (DEOS)
Delft University of Technology, Faculty of Geodetic Engineering
Thijsseweg 11, 2629JA Delft, The Netherlands
phone: +31 15 2782565, fax: +31 15 2783711
e-mail: usai@geo.tudelft.nl

Abstract

The monitoring of slow deformation processes by means of SAR Interferometry requests the observed area to mantain its correlation for more years. This usually happens only for those areas having particularly favourable characteristics, such as poor vegetation and dry and no windy climate. However, even in an area which decorrelates in a few weeks, a certain number of features has been observed, which appear to mantain high coherence values. The aim of this paper is therefore to investigate to which extent these structures, mainly man-made features, remain coherent on long time scales. For this purpose, a time series in a test area in the Northern Netherlands has been generated, with a maximum temporal extension of 3 1/2 years. Even on such a long time span, a considerable number of highly coherent features has been found. A sample of such features has then been selected and the coherence values have been traced in the whole time series. This technique has revealed to be useful in order to check the "goodness" in terms of coherence of an interferogram: in particular, in this way an interferogram could be identified having generally lower coherence, probably due to different seasonal conditions. Other tests have been performed in order to study the coherence as a function of time and of the baseline length.

1 Introduction

It is well-known that a strong limitation for time range applicability of repeat-pass differential SAR interferometry is temporal decorrelation. Therefore, we still cannot perform longterm studies of slow deformation processes like land subsidence and plate tectonics, in spite of the availability of SAR images over several years. However, we noticed that even on very long time spans, highly coherent features are still present, mainly man-made features. We thus want to investigate whether or not the coherence stability of these structures could be used for long time-scale monitoring of slow deformation processes. As a first step, we generated a time series of interferograms, which constitutes the database of the present work, spanning different time intervals between 1-day up to more than 3 years. The details and some remarks about the construction of such time series are shown in section 2. We then selected a sample of features showing high coherence on long time scale and we performed some tests on it. The first results are presented in section 3.

2 The 1992-1996 time series

The database is a time series of interferograms of the area around the city of Groningen, in the northern part of The Netherlands. The area is well known for its land subsidence, caused by the extraction of natural gas: the rate of land subsidence is up to 1 cm/yr. In order to be able to detect it by means of the INSAR technique, monitoring of the area for more years would be necessary. As a first step to assess whether this is possible, we want to study the features (mostly man-made structures) which preserve their coherence on such long periods.

master	slave	B_{par}	B_{perp}	days	no
16-3-96	17-3-96	-17	24	1	9
16-3-96	11-2-96	36	212	34	8
16-3-96	20-4-96	50	145	35	7
16-3-96	21-4-96	18	79	36	6
16-3-96	6-1-96	-109	-129	70	5
16-3-96	20-8-95	-62	-272	209	4
16-3-96	19-8-95	-26	-190	210	3
16-3-96	15-10-92	5	25	1248	2
16-3-96	10-9-92	43	52	1283	1

Figure 1: The Groningen dataset. The 5th column shows the time span in days , the 6th the serial number of the interferogram

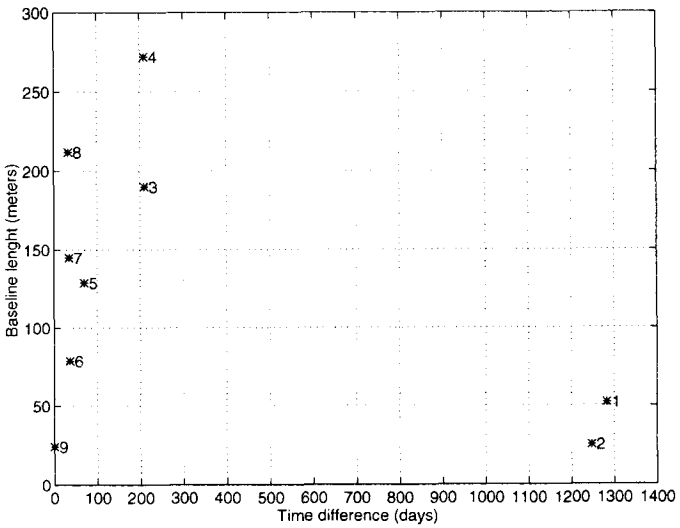

Figure 2: Perpendicular component of the baseline vs. temporal gap between the two images for each of the interferograms

The time series generated for this purpose has the following characteristics:

- The same image is used as master for all the interferometric pairs, in order to guarantee that all the slave images are interpolated on the same grid, namely the master. In this way, a given pixel represents the same area in all the interferograms.
- Azimuth filtering has been applied: our tests confirmed what was already highlighted in the literature ([1],[2]), i.e. that azimuth filtering highly improves the coherence. This is particularly important for the long time scale interferograms, where the coregistration is more difficult because of the generally low coherence. Figure 1 shows the interferograms generated, and their baseline components, column 5 contains the interferogram serial numbers, which are used as reference in the plots. In figure 2 the distribution of the time spans and of the perpendicular component of the baselines is visualized.
- The final products, i.e. the coherence and phase images, are mediated over 2 pixels $\times$ 10 lines.

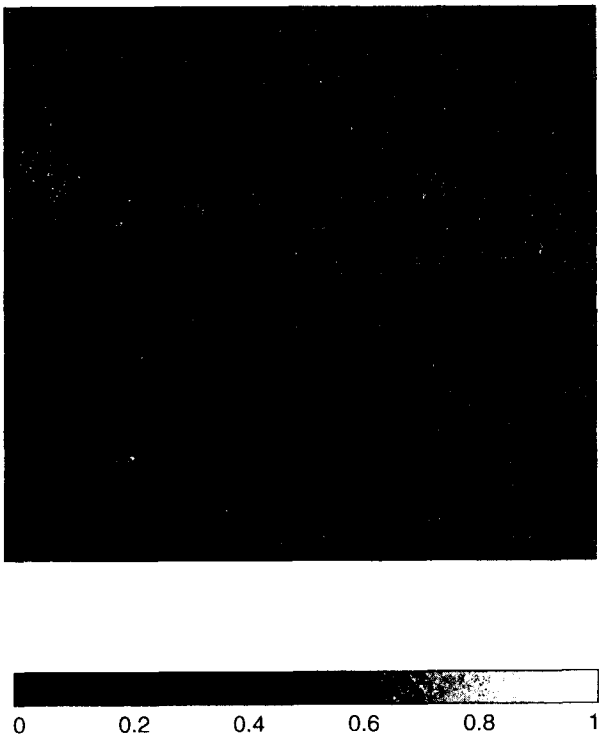

Figure 3: Coherence image of interferogram no.1 (16-3-96/10-9-92)

Figure 4: Coherence image of interferogram no.9 (16-3-96/17-3-96)

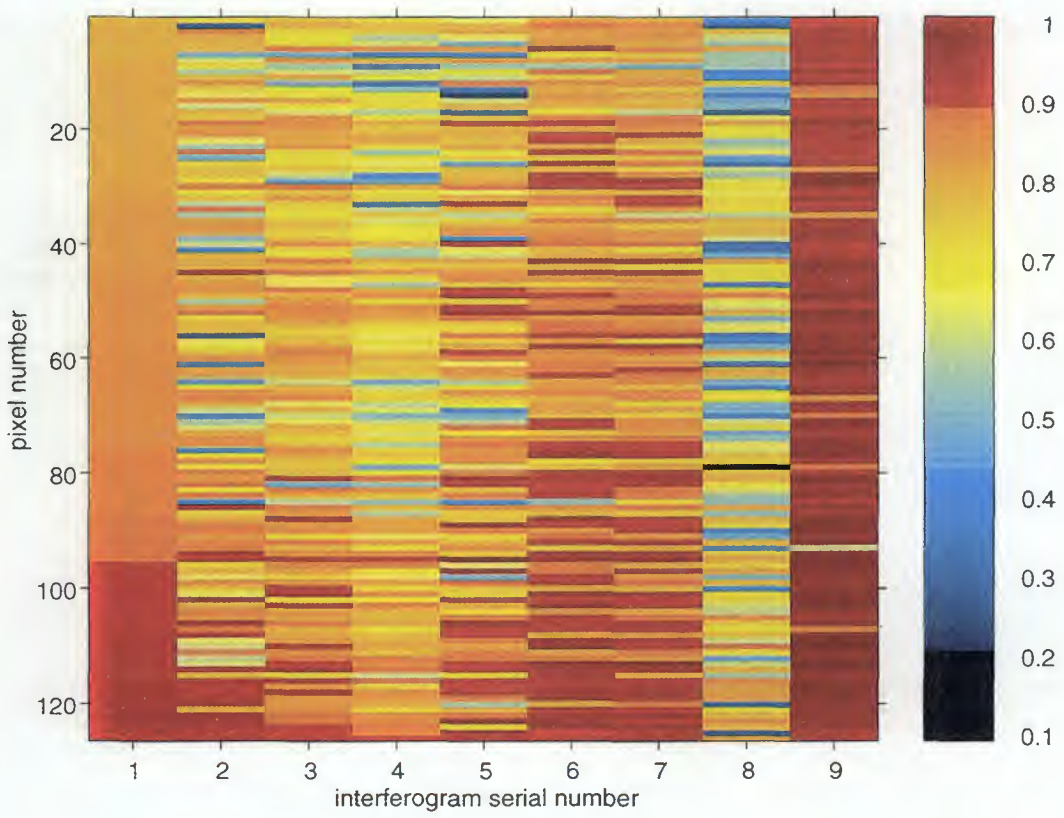

Figure 5: Coherence values for each point of the dataset and for each interferogram

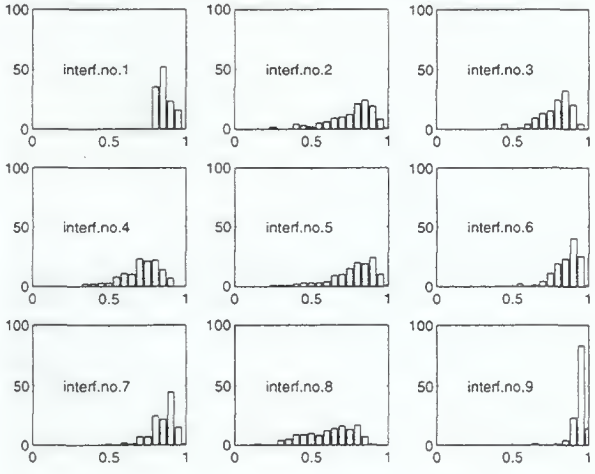

Figure 6: Histograms of the coherence values for each interferogram

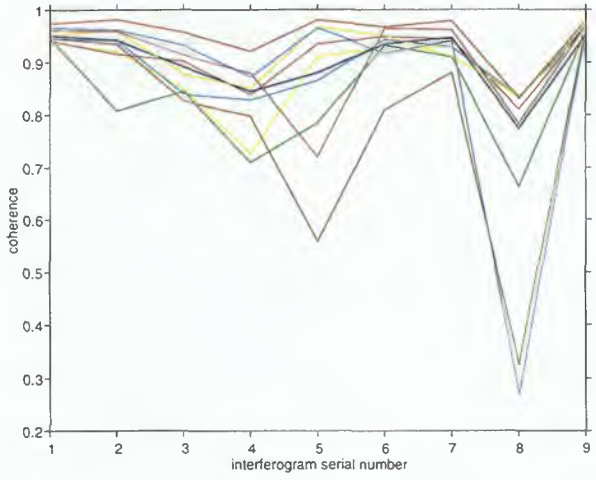

Figure 7: Coherence values in the series for the ten highest-coherence points

3 Analysis of the coherence

The coherence is estimated on a 2×10 window. Figure 4 and figure 3 are the coherence images respectively on the shortest (tandem pair, no.9) and on the longest (about 3 1/2 years, no.1) time interval considered. We selected in the coherence image no.1 those pixels having coherence higher than 0.8. We concentrated then for our tests on the area of the city of Assen (low left in figure 3), which contains a statistically significant number of such pixels. The area has an extension of 200 pixels $\times$ 300 lines. The coherence of those pixels has been traced in the whole time series. Figure 5 represents the coherence of these points as results in all the interferograms: each column represents an interferogram of the series, each horizontal line contains the values of the coherence for a given point.

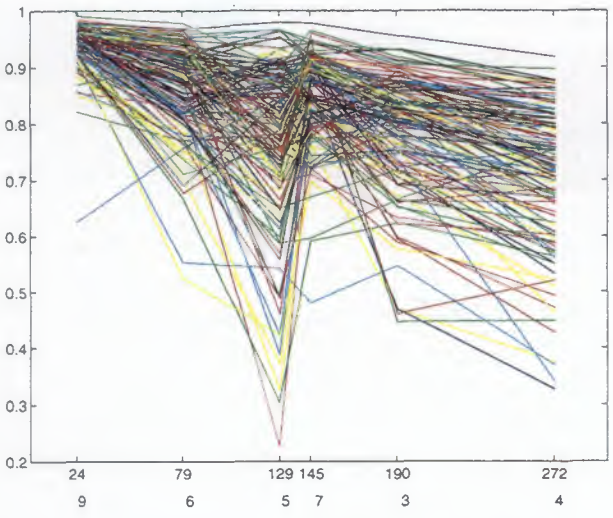

Figure 8: Coherence vs. baseline length (perpendicular component) in the series. Under the baseline values, the corresponding interferogram numbers are given.

Note that high coherence in the longest time span interferogram (no.1) doesn't seem to imply high coherence in other interferograms on shorter time intervals. As we could expect, in fact, the time gap doesn't seem to have any influence on the coherence values. This is also confirmed by the fact that any attempt to find a linear trend in the coherence as a function of time didn't give any significant result. It is also evident from figure 5 that interferogram no.8 presents a generally lower coherence. We don't know the reason for this; it can be possibly due to different weather conditions (the master image is taken in March, the second in February, during a period of snow precipitation) and to the long baseline. Figure 6 shows the coherence histograms of the time series. Figure 7 is the plot of the coherence values along the series for the ten highest-coherence points.
We also considered the possibility of a dependence of the coherence on the baseline length. For this purpose, the coherence has been plotted against the baseline length (perpendicular component) in figure 8, where under each baseline value, along the x-axis, also the corresponding interferogram serial number has been indicated. The interferogram having coherence generally lower than the others (no.8) has not been considered here. We also did not consider the two long-period interferograms (no.1 and no.2): we restricted ourselves to the temporally nearest interferograms. From the figure there seems to be some trend, but we have to perform more detailed tests in order to be able to assess it. We note also that for interferogram no.5 the coherence is worse than for the other interferograms with higher baseline. Since the slave in this pair is taken in January, this could be due to different weather conditions with respect to the time the master has been taken.

4 Conclusions

A time series of interferograms has been generated covering time spans up to 3 1/2 years. Even on such a long time span, highly coherent features could be identified. The analysis of the series in its whole permitted the identification of an interferogram showing significantly lower coherence than the others. No significant signatures of dependence of the coherence values from the time have been found. Some dependence of the coherence from the baselines could be present, but more tests are necessary in order to assess it.

5 Acknowledgements

We would like to thank P.Visser and R.Scharroo of DEOS for providing the ERS precise orbits.

References

[1] Geudtner D. *Die interferometrische verarbeitung von SAR-daten des ERS-1*. PhD thesis, Universität Stuttgart, 1994.

[2] Schwäbisch M. and Geudtner D. Improvement of Phase and Coherence Map Quality Using Azimuth Prefiltering: Examples from ERS-1 and X-SAR. In *International Geoscience and Remote Sensing Symposium, Florence, Italy, 10–14 July 1995*, pages 205–207, 1995.

PASTURES MONITORING AND LANDSURFACE CHARACTERISTICS ANALYSIS IN A SAHELIAN REGION USING MULTITEMPORAL SAR DATA: THE CHAD CASE OF STUDY

YESOU H.*, MBAIRANADJI L.**, BOLLEY A.*, TEZENAS du MONTCEL L.** et de FRAIPONT P.*

* SERTIT , Service Régional de Traitement d'Image et de Télédétection, Parc d'Innovation , bd Sébastien Brant, 67400 Illkirch, France Ph : 33 (0)3 88 65 51 95 ; Fax: 33 (0)3 88 65 51 99
e-mail: herve@sertit.u-strasbg.fr ; URL adress: http://sertit.u-strasbg.fr

**Laboratoire de Recherches Vétérinaires et Zootechniques de Farcha, LRVZ, BP 433, N'Djaména, Tchad. Tél. :(235) 52 74 75; Fax: (235) 52 83 02

ABSTRACT

In Soudano-Sahelian zone of Chad, possibilities of ERS-1 and Radarsat times series data for landscape units characteristics and pasture monitoring began to be examined. Preliminary results have been obtained using ERS data acquired by the Libreville station. Mono season data allow only to distinguish few landscape units and more themes are extractable on data acquired during the rain season. On colour composite, combining rain and dry data, identification of the major pedological units, halomorphic soils, duricrusts can be carried more easily. Plus change in land use can be pointed out such as cultivated fields. Using a long time serie Radarsat data, acquired with an high frequency, each seven days, during the 1997 rain season , an assessment on pasture monitoring will carried out.

Keywords: Multitemporal, time series, Radarsat, ERS, fusion, pastures monitoring, Sahel

1. INTRODUCTION

The purpose of this project, which received the ESA and Canadian Space Agency support within the frame of the Libreville (AO-L.F202) and Radarsat ADRO (PP 110) programmes, is the preparation of operational use of SAR data for landsurface and natural resources monitoring in Sahelian environment for their integration within Early Alert System networks. It is more precisely axed on the monitoring of the seasonal development of the herbaceous resource. It is a part of a long term though carried with the Agropastoralisme Service of the Chadian Agriculture Office on the means that have to be set up in order to insure pastures monitoring and sensitive ecosystem surveys in Chad.

A grassland observation network over the Chadian Sahelian area, the ROPONAT have been set up in 1990, and since acquires information on herbaceous phytomass, total land cover of the vegetation, etc ... Monthly synthesis of these information are compared with NOAA NDVIs. Therefore the spatial and temporal variations of herbaceous resources (natural and cultivated) need analysis at finer scales than those provide by NOAA data. Plus, the most crucial period in terms of resources gap and during which one conflicts occur between cattle farmers and settled population, corresponds with the beginning of the raining season, at this period of the year, the cloud coverage is an important disadvantage for the use of optical data (AMAN et al., 1989). With their all weather capabilities, SAR data appear as the unique source of information covering large areas as illustrated by previous studies on grassland/sensitive area monitoring over temperate area as well as over dry African countries (DALLEMAND et al., 1993; EPEMA and Van OEVELEN, 1993; GRIFFITS et al., 1993; FOLWING et al., 1994; FELLAH et al., 1994; MAJOR et al., 1994). Plus SAR data present a good to very good temporal resolution, with revisit periods ranging from 35 days for ERS-1/2 to up to two days, mainly seven days, for Radarsat and with high spatial resolutions.

The project's purpose is to set up a methodology for optimise the radar and optical synergism for grassland monitoring. SAR data will be used to localise herbaceous regrowth areas and also to point out change in landscape units. In a first step ERS1/2 data acquired by the DLR mobile station during the 1994, 1995 and 1996 Libreville campaigns are used to characterise the landscape units and their evolution through the vegetation cycle over the Ati-Mongo degree square. Radarsat data, acquired regularly all through the vegetation cycle and with a seven days frequency during the raining season, will be used for the grassland mapping and monitoring. Maps derived from SAR images will be compared with NOAA NDVI indices and also with field surveys provided by the ROPANAT network, and so as their accuracy evaluated. And assessment of the capabilities of low spatial resolution and large field coverage Radarsat data for herbaceous monitoring will also be carried out. At middle term, the results obtained during this programme will be used to propose the use of SAR data for monitoring all the

Sahelian belt and thereby to complete NOAA and future SPOT 4/ Passager Vegetation data for a better analysis and monitoring of natural resources at local scale and at least to propose the integration of SAR derived products in Early Alert Systems.

2. LOCATION OF THE STUDY AREA

The study area correspond to the Ati-Mongo square degree, 13°N-18°E, 12°N-19°E, located at 400 km at the East of N'Djaména (Chad) within the soudano-sahelian zone. Its characterises by an averaged annual rainfall less than 700mm and an annual averaged temperature of 29°C (BEAUVILAIN, 1994). It is a relatively flat area , with low topographic variations ranging from 350 to 400 m and bordered by two belts, the Abou Massif culminating at 1506 m, on the North side, and the Guéra (1613 m.) on the Southern part, delimiting a flat area cross-crossed by the Batha a temporary river, having a permanent regime during the rain season (July to October). Soils are predominantly sandy soils with halomorphic characteristics covering ferruginous duricrusts, or argillaceous soils in the topographic depressions. The vegetation, relatively sparse, consists in ligneous (dense and pseudo-bush) and herbaceous formations on the sandy halomorphic soils, plus sparse savannah and forest galleries in depressions. With this important pastures' resource, The Ati-Mongo area, all the year important travelling and farmed cattle which can locally induce an heavily over-graze. Plus, with the seasonal variations of the herbaceous vegetation, there is crucial periods of pastoral resource availability, principally at the transition between the dry and rain seasons.

3. USED DATA

A database still under development, have be built up, containing SAR data (acquired ERS and scheduled Radarsat) optical images and exogenous data.

Within the frame work of the Libreville acquisition campaigns in 1994, 1995 and 1996, ERS-1 data were acquired covering different seasonal periods (Table I). These images were coregestered with a Landsat TM mosaic (scenes 182.52 and 182.51 acquired the 10/01/87).

Acqu. date	Season	Orbit	Frame	Mode
23 / 07 / 94	rain	15789	3357	desc
09 / 08 / 94	rain	16033	3357	desc
29 / 08 / 94	rain	16320	3357	desc
19 / 11 / 95	dry	22726	3357	desc
20 / 11 / 95	dry	3053	3357	desc
09 / 12 / 95	dry	3325	3357	desc
07 / 04 / 96	dry	24730	3357	desc
26 / 04/ 96	dry	25002	3357	desc

Table I : Available ERS - 1 data

With its higher revisiting frequency due to the use of different beams and selectable incidence angles, and also with the on board tape-recording facilities, Radarsat data appeared as a powerful tool and unique information source for monitoring the pasture resource during crucial periods. Radarsat acquisition have been scheduled for the 1996 year, but have to be cancelled. A new campaign will started from April to November 1997 using the nominal 24 days cycle (standard mode, beam 1, incidence angle:20°). Based on the use of selectable incidence angles (standard mode, beam 2 and 4, incidence angles 24.2° and 33.6°), acquisitions at higher frequency, seven days, will occurred from July to October. Plus Radarsat data in ScanSAR narrow mode, will be acquired.

Exogenous data consist in topographic and pedologic maps have been rasterized and compiling within the project database.

4. LANDSCAPE UNITS RECOGNITION USING LANDSAT TM DATA

Based on Landsat TM processing, through thematic indices segmentations, Tasseled Cap and Principal components transforms, principal landscape units have been extracted: duricrusts on hill piedmonts, halomorphic soils, burned soils of savannah, forest galleries, temporary hydrographical network.

5. LANDSCAPE UNITS RECOGNITION AND PASTURES MONITORING USING SAR DATA

From a methodological point of view two approaches will be followed. The first one consists to a computer assisted image interpretation CAII, of SAR monotemporal and/or colour composite images. This method would allow the recognition and mapping of the principal landscape units. In order to improve SAR data possibilities, image enhancement techniques such as temporal average will be applied (YESOU et al., 1997 ; LAUGIER et al., 1997). Plus, a Radarsat set of four images acquired during April - May 96 will be used in order to analyse/quantify effects of the used various incidence angles, on the landscape units recognition. The second major step of processing corresponds to change detection and recognition, which would allow the pasture monitoring. Different methods will be used such as CAII, temporal image rationing (RIGNOT and Van ZYL, 1993; CIHLAR et al., 1992). Due to speckle effect, PCA would be applied only on filtered or/and enhanced summed images and also on ScanSAR data. Obtained results will be validated by comparison with fields observation from the ROPANAT network and also by comparison with NOAA derived information.

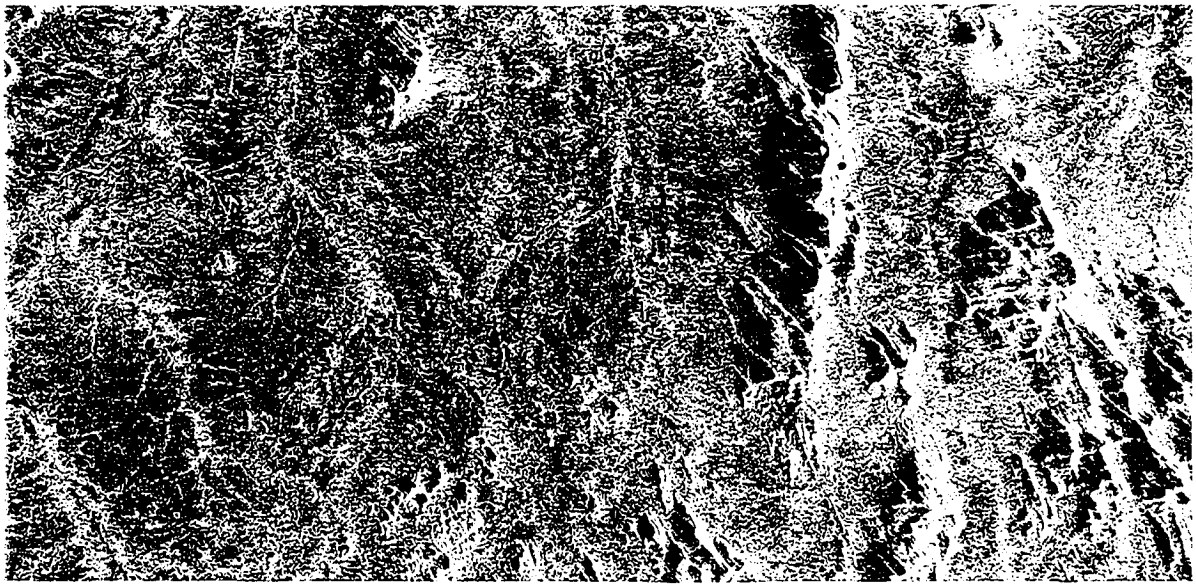

Fig. 1 : ERS- 1 derived product : Enhanced image by temporal average of ERS-1 data acquired during the 94 rainy season. Mongo sector (Chad)

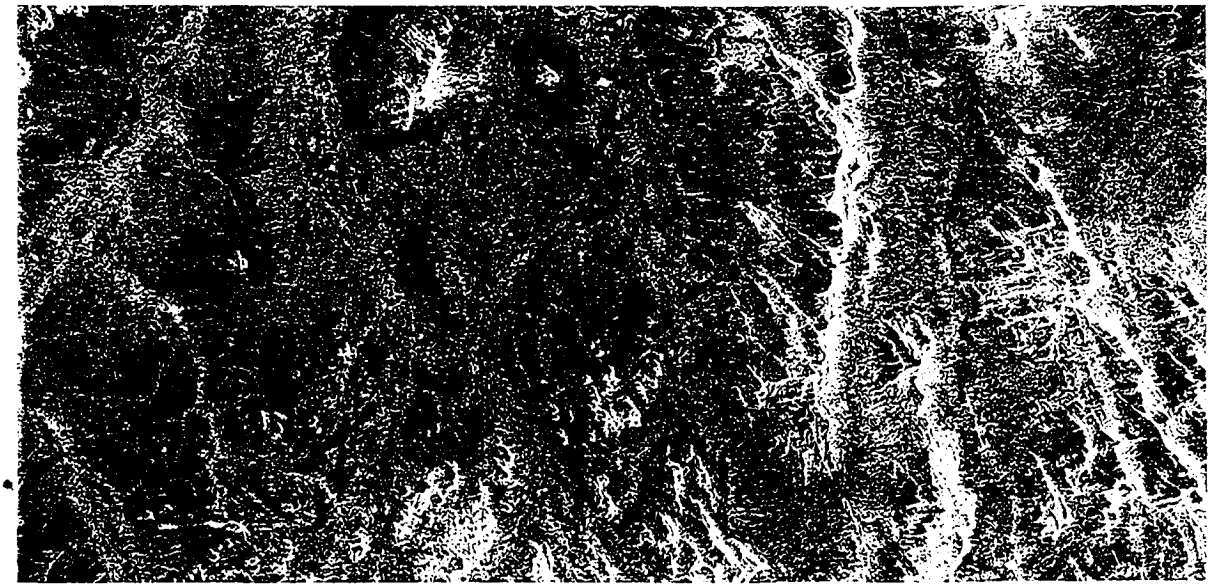

Fig. 2 : ERS- 1 derived product Enhanced image by temporal average of ERS-1 data acquired during the 95 dry season. Mongo sector (Chad)

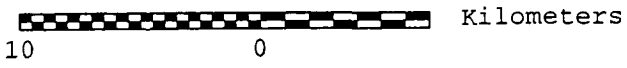

Preliminary results have been obtained using ERS data acquired by the Libreville station during rain season, July-August 1994 and dry season, November-December 95 (Fig. 1 and 2). During the dry season, SAR data allow to distinguish few landscape units such as, temporary hydrographical network, hills' piedmonts and duricrusts. Using data acquired during the rain season, only few units are recognizable. On colour composite combining dry and rain season ERS data, the recognition of pedo-morphologic units is more easy. Halomorphic soils and duricrusts are well noticeable. Plus changes in areas located around villages are pointed out, these correspond mainly to shift of cultivated fields.

6. CONCLUSION

Preliminary results have been obtained using Libreville ERS data. Their analysis is still going on. Plus using the scheduled time serie Radarsat data, acquired with an high frequency, each seven days, during the 1997 rain season , an assessment for change detection, i.e. soil large scale moisture variations analysis and pasture monitoring will carried out. At term, on the basis of obtained results, this study would propose the integration of SAR derived products in Early Alert Systems.

7. REFERENCES

AMAN A., PODAIRE A., SAINT G., PUYRAVAUD JP., MENAULT JC, MERSADIER G. SERPENTIE G., TEZENAS du MONTCEL L., 1989 - Etude de la production primaire de différentes savannes: Apports des données SPOT XS et Landsat TM. *Bull SFPT*, 114, 40-44.

BEAUVILAIN A, 1994 - Tableau de pluviométrie dans les bassins versants du Tchad et de la Bénoué. Travaux et documents scientifiques. Documents pour la Recherche III, N'Djaména.

CIHLAR J., PULTZ T.J. and GRAY A.L., 1992 - Change detection with the synthetic aperture radar. *Int. J. Remote Sensing*, 13, 3, pp. 401-414.

DALLEMAND .F., LITCHTENEGGER J., KAUFANN V., BARRY B., DIABY N. and REICHERT P., 1993 - ERS-1 SAR and optical data for land use/land cover mapping: a case of stuy in savannah zoe of Guinea. *Proceedings of "From optics to radar, SPOT and ERS applications"*, Paris, May 1993, CEPADUES Ed., Toulouse, 447-456.

EPEMA G.F. and Van OEVELEN P.J., 1993 - Monitoring landsurface characteristics in Niger using complementary SPOT and ERS-1 SAR data. *Proceedings of "From optics to radar, SPOT and ERS applications"*, Paris, May 1993, CEPADUES Ed., Toulouse, 385-396.

FELLAH K., BESNUS Y., CLANDILLON S., MEYER C and de FRAIPONT P.,1994 - Multi-temporal ERS-1 SAR data in environmental studies: researching a quantitative approach for soil moisture retrieval. *Proceedings of the First ERS-1 Worshop*, Tolédo, 1994. ESA SP 365.

FOLWING S., KENNEDY P. and McCORMICK N., 1994 - European grassland monitoring. *EARSel Newsletter*, 17, 11-12.

GRIFFITS D.G.H., WOODING M.G. and BLYTH K., 1993 - Surveillance de l'humidité du sol par ERS-1 dans les zones semi-arides. *Observation de laTerre*, ESA publ., 42, 1-5.

LAUGIER O., FELLAH K., THOLEY N., MEYER C. and de FRAIPONT P., 1997 - High temporal detection and monitoring of flood zone dynamic using ERS data around catastrophic natural events: the 1993 and 1994 Camargue flood events. *Proceedings of 3rd ERS Symposium*, Florence 17-21 March 1997.

MAJOR D.J., SMITH A.M., HILL M.J., WILLMS W.D., BRISCO B. and BROWN R.J., 1994 - Radar backscatter and visble infrared reflectance from short-grass prairie. *J. Canadien de Télédétection*, 20, 1 71-77.

RIGNOT E.J. and Van ZYL J., 1993 - Change detection tehnicques for ERS-1 SAR data. IEEE *Trans. Geosc. Remote Sensing*, 31, 4, 896-906.

YESOU H., BRAUX C., ROUZEAU O., CLANDILLON S., ROLET J. and de FRAIPONT P., 1997- Assessment of two methodologies of ERS mixing for geological investigations : ERS time-series and optical-radar fusions. *Proceedings of 3rd ERS Symposium*, Florence 17-21 March 1997.

Acknowledgement

ERS data were obtained within the framework the Libreville ESA Programme (AO-L.F202). Radarsat acquisition are scheduled within the framework ADRO (PP 110) of the Canadian Space Agency. Plus, Mr MBAIRANADJI received a grant of the Training Programme of the French Co-operation Ministry.

ERS SAR IMAGERY FOR URBAN CLIMATE STUDIES

Ludovic Basly, Francois Cauneau, Thierry Ranchin, Lucien Wald

Groupe Télédétection & Modélisation, Ecole des Mines de Paris
BP 207, 06904 Sophia Antipolis cedex, France
phone: + 33 4 93 95 74 49, fax: + 33 4 93 95 75 35
E-mail : wald@cenerg.cma.fr, Web server: http://www-cenerg.cma.fr/sophia

ABSTRACT

This study investigates the potentialities of ERS SAR imagery for the urban micro-climate and air quality, over the city of Nantes, France. The temporal variability of the SAR signal over the city has been assessed by analyzing five images in descending mode. Beside the speckle effect, the quality of the signal is highly variable from one image to the other. Meteorological effects. make contrasts between objects and their surroundings to be more or less pronounced. Urban features are mostly present in each image, but the structures are not always well perceived within a single image. It is concluded that it is necessary to have several images. Their redundancy allows a better exploitation of the urban features. Further it decreases the level of speckle. Screening of the average SAR image clearly indicates that the perception of the roads is highly dependent on the flight direction of the spacecraft. The main factors for the perception of the morphological features are the height of the buildings, its orientation relative to the spacecraft orbit, its horizontal surface, its materials. Multiresolution analysis, by means of wavelet transform or structure function, provides a good discrimination between unbuilt areas, residential areas, industrial areas, and large groups of buildings. This preliminary study has demonstrated that urban morphological features and their typologies with relation to the air flow drag were well-perceived in SAR imagery once properly processed. Further studies are required to assess definitely the benefits and the limits of such images in urban micro-climate and air quality.
Keywords: SAR imagery, urban micro-climate, air quality, roughness

1. INTRODUCTION

The city's compact mass of buildings and pavement constitutes a profound alteration of the natural landscape, resulting in a large number of micro-climates (Carnahan, Larson, 1990; Landsberg, 1981; Oke, 1987; Terjung, O'Rourke, 1980). These micro-climates may be revealed by the existence of the so-called *urban heat islands* where changes in the temperature of the atmosphere may reach several degrees compared to that of the neighbor rural area. The complex and changing mosaic of heat and cold islands influences urban ecology in a variety of ways by altering e.g., the health and physiological comfort of humans, cooling and heating requirements, vegetation, and zoological habitats. The heat islands also produce convection cells and associated air pollution diffusion patterns with increases in cloud coverage, precipitation and fog. Various scales should be taken into account in studies of urban climate, from several hundred of kilometers to the very small scales at the pedestrian level (Landsberg, 1981; Oke, 1987; Price, 1979).

The present investigation aims at the assessment of the potentialities of ERS SAR imagery for the urban micro-climate and air quality, namely urban morphological features and their typologies with relation to the air flow drag. The selected site is the city of Nantes, along the Loire River, west of France.

The investigation has three consecutive steps. The time variability of the SAR signal is analyzed in order to check whether several images may provide an useful information over a city. That demonstrates the relevance of the SAR signal for the study of urban features. Then the mean image is visually inspected with respect to a map of the city. It clearly shows the main features, that proves the significance of the SAR signal in this purpose. Finally, a mathematical method is devised for the automatic discrimination of the districts with respect to the aerodynamic roughness of the ground.

2. ACQUIRED IMAGE AND PRE-PROCESSING

Five SAR images were provided by ESA, from October 1994 to April 1995. Radial direction is almost East - West. The images were geometrically modified as follows. Six consecutive pixels belonging to the same column were averaged and replaced by their average. This reduces the number of lines and results into an approximately squared pixel of 25 m. The best image was geometrically rectified in order to fit a map with a scale of 1/100 000 in Lambert III projection by means of a bicubic interpolation, and the result constitutes the reference image. The other images were rectified with respect to this reference. The speckle was not filtered out in each image. Several tools are available which are respectful of the most pronounced structures. However we have preferred not to alter the structures any further after the geometrical rectification.

The morphological features of interest are constant

within the time span of our data set. The first step in our analysis is to assess the temporal variability of the SAR signal over the city. All images have been taken in descending mode, thus reducing the influence of the acquisition geometry. The whole set of images has been inspected visually and the mean image as well as the differences between the mean and each image have been constructed from the five superimposable images. The mean image is taken as the first component computed from a principal component analysis. This component comprises about 80 % of the total variance.

It has been found that beside the speckle effect, the quality of the signal was highly variable from one image to another. The discrepancies in the observation of the major elements of the scene were mostly explained by meteorological effects. According to the wind vector (speed and direction), contrasts between the river and its surroundings may be more or less pronounced, due to changes in wave regime. Hence the wind has a strong influence on the detection of bridges and of natural or artificial banks. It has been found that the direction has a greater effect than the speed of the wind. Rainfall has also an effect upon the quality of the image. The dielectric constant is a function of the soil humidity: therefore contrasts between natural or vegetation areas and built areas depend also upon the quantity of rain fallen in the time period before the acquisition date.

Urban features are present in each image. Each image provides a good overall description of the structures. However because of the changing quality, the structures are not always well perceived within a single image. We conclude that it is necessary to have several images. Their redundancy allows a better exploitation of the urban features. Further their averaging decreases the level of speckle without using sophisticated speckle filters which usually degrade the structures.

3. INTERPRETATION OF THE MEAN IMAGE

Figure 2 displays the mean image. The visual inspection demonstrates the importance of the relative direction of the target with respect to the radial direction of the radar wave. If the relative direction is perpendicular to the radial direction, then this object is clearly visible, even if it is flat such as a road or a railway track within a flat area. If the object is orientated in the same direction than the radar wave, then it is not visible. This is the case for the central station of Nantes and of the large railway complex in the western part of the Beaulieu island. However if the same object is surrounded by e.g., buildings reflecting the radar signal, it will be perceived because of the created contrast.

The material of the objects is also important. For example, the group Malakoff is made of several large buildings of about 20 stores each. This group does not appear in the image because the buildings are covered of ceramics which do not reflect the radar signal.

Regarding the main urban features, we conclude that

- the industrial buildings are well perceived and bright (*i.e.* highly reflective),
- the large buildings are well perceived,
- the areas comprising old buildings with more than one store are well perceived if they are mostly orientated perpendicular to the direction of propagation of the radar wave,
- the residential areas are homogeneous and low reflecting
- the unbuilt areas are low reflecting

The morphological features are likely related to the aerodynamic roughness parameters of the ground which influence the air turbulent flow. These parameters are the roughness length (noted z_0) and the zero-plane displacement. They are useful to describe and quantify the turbulent way the air flows above the ground and the structure, the reduction in wind speed and accordingly in the air turbulent mixing. They depend upon the nature of the ground and of its geometry, e.g. the buildings, their shape, their height, their spacing, their orientation with respect to the air flow, ... The main factors for the perception of these morphological features are

- the height of the buildings (mean and variance),
- their orientation relative to the spacecraft orbit,
- their surface onto the ground,
- their materials

5. CLASSIFICATION OF DISTRICTS WITH RESPECT TO AERODYNAMIC ROUGHNESS

Scherer *et al.* (1996) have conducted a study for the classification of the city of Basel (Switzerland) with respect to aerodynamic roughness parameters. They computed the principal components of a set of three ERS SAR images. Then they performed a multiple linear regression analysis between the first two components and z_0 values taken from the literature. They concluded that SAR images may be used to map the roughness length in the city of Basel. Obviously the found relationship strongly depends upon the SAR images used for this study and maybe of the site. This prevents the relationship to be used elsewhere or with other images. In order to alleviate this shortcoming, the present study investigates some mathematical operators which are a bi-dimensional function of the urban structures, which provide a good discrimination of the districts with respect to the aerodynamic roughness parameters, and which can be normalized in order to render them invariant with respect to the set of images and of the site, possibly. Then, following the work of Scherer *et al.*, a relationship may be devised by a multiple linear regression analysis, using z_0 values taken from the literature. Finally the SAR-derived image may be classified in terms of roughness length.

Figure 1.

Mean image computed from the five SAR images. The Loire river appears in grey, crossed by several bridges in bright. In dark are the major roads, and the airport in the lower left corner. The island is the island of Beaulieu, and is part of the city of Nantes. The area is mostly comprised of urban areas, but also of some agricultural lots and woods, which are not distinguished each from the other in this image.

Obviously the roughness is a function of the scale of concern. Therefore tools for multiresolution analysis have been applied onto the mean image to extract the relevant information at various scales. Two operators have been found to be the most efficient with respect to their quality in discrimination and their easiness in use and analysis: the multiresolution analysis, coupled with a wavelet transform, and the structure function, also called variogram. It is found that the multiresolution analysis is well suited to distinguish groups of buildings, with typical scale of about 100 m. This approach provides also a good discrimination between unbuilt areas, residential areas, industrial areas, and large groups of buildings. Structure functions give very similar results. Their degree of anisotropy is a function of the density and type of buildings, and of the overall orientation of the area. It depends upon the scale. Another parameter is the variance of the sample, which is given by the value for the largest scale. The closer to the pixel size the typical size of the objects and the more homogeneous the district, the smaller the variance. Privileged directions within a district and heterogeneous district increase the variance. The last parameter of importance is the value of the structure function for the scale equal to one pixel (the nugget effect). This value is comprised of the non structured noise within the image (*i.e.* the speckle), which has been reduced by the averaging of the five images, and of the sub-pixel variance, that is of the heterogeneities having a scale smaller than, but close to, the pixel size. The more heterogeneous a district at sub-pixel size, the larger the nugget effect.

For example, Figure 2 exhibits the structure function for a district made of spaced large buildings (West Beaulieu island). In this district, the storage buildings are located along the docks, with metallic parts, and components perpendicular to the radial direction. These components are clearly visible in the SAR signal while the radial components are not or less sensed. This induces a larger signal in the E-W direction than in the N-S one, which

creates an anisotropy in the structure function for sizes larger than about 70 m. The structure function exhibits a finite variance for the largest pixel sizes. This means that the size of the sample (here 7 pixels, that is about 200 m) is larger than the typical size of the structures in this district. It follows that the structure function is a suitable tool to discriminate types of buildings and their organization with respect to the aerodynamic roughness parameters.

5. CONCLUSIONS

This study has shown that the main morphological features within a city are mostly present within a SAR image. However, the quality of the signal is highly variable from one image to the other. The discrepancies in the observation of the major elements of the scene were mostly explained by meteorological effects. Because of this change in quality, the structures are not always well perceived within a single image. It is concluded that it is necessary to have several images. Their redundancy allows a better exploitation of the urban features. Further their averaging decreases the level of speckle. The screening of the average SAR image clearly indicates that the perception of the roads is highly dependent on the flight direction of the spacecraft. The morphological features are likely related to the ground roughness. The main factors for the perception of these morphological features are the height of the buildings (mean and variance), its orientation relative to the spacecraft orbit, its surface onto the ground, its materials. Relevant processing has been performed to the mean image to extract the relevant information at various scales. Multiresolution analysis, by means of wavelet transform or structure function, provides a good discrimination between unbuilt areas, residential areas, industrial areas, and large groups of buildings.

Given the importance of the orientation of the target relative to the spacecraft orbit further investigations should be made using images taken at various orientations. Image processing techniques are to be further developed and carefully assessed for an automatic detection and classification of morphological features. Campaigns of ground-measurements are necessary to establish quantitative relationships between the properties of these morphological features as observed in the SAR imagery and the roughness length.

This preliminary study has demonstrated that urban morphological features and their typologies with relation to the air flow drag were well-perceived in SAR imagery once properly processed. It is concluded that SAR images have large potentialities in the domain of urban micro-climate and air quality and that further studies are required to assess definitely the benefits and the limits of such images.

6. REFERENCES

Carnahan, W. H., Larson, R. C., 1990. An analysis of an urban heat sink. *Remote Sensing of Environment*, **33**, 65-71.

Landsberg, H. E., 1981. *The Urban Climate*. Academic Press, New York, 275 p.

Oke, T. R., 1987. *Boundary Layer Climates*, 2nd edition., Methuen & Co, London, 435 p.

Price, J. C., 1979. Assessment of the urban heat island effect through the use of satellite data. *Monthly Weather Review*, **107**, 1554-1557.

Scherer, D., Parlow E., Beha H.-D., 1996. Roughness parameters derivation from ERS-1 and Landsat-TM satellite data for the agglomeration of Basel / Switzerland. In : Proceedings of 15th Symposium of EARSeL, Progress in Environmental Research and Applications, Basel, Switzerland, September 4-6 1995, E. Parlow Ed., A. A. Balkema, Rotterdam, pp. 325-329.

Terjung, W., O' Rourke, P., 1980. Influence of physical structures on urban energy budgets. *Boundary-Layer Meteorology*, **19**, 421-439.

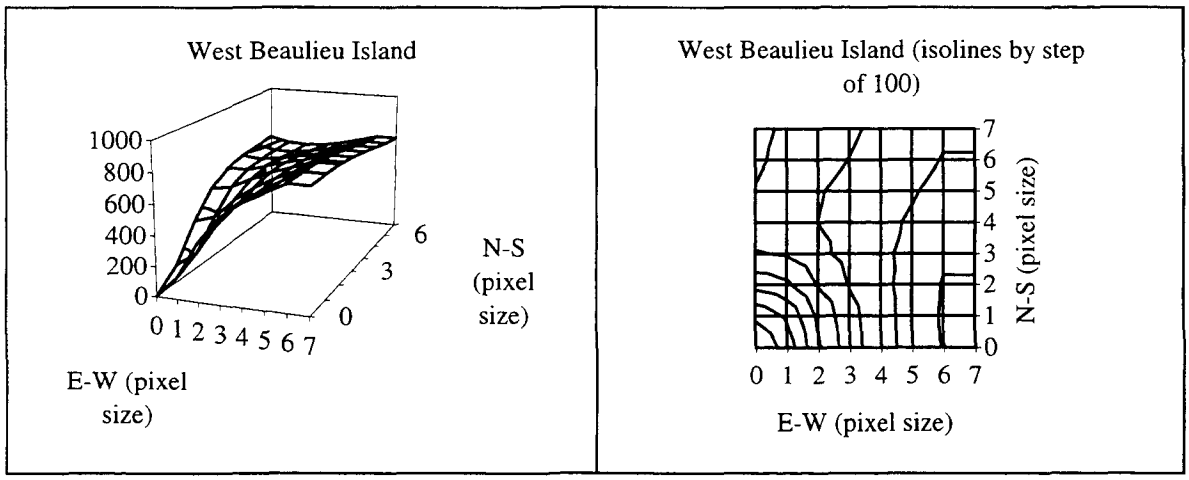

Figure 2 Structure function for a district made of spaced large buildings. The left graph (3.a) shows the structure function in 3-D, the right graph (3.b) shows its projection (in isoline) onto the x-y plane. Pixel size is 25 m.

LEAF AREA ESTIMATION FOR SUGAR BEET YIELD PREDICTION USING ERS SAR DATA

S.P.Vyas and M.D.Steven

Department of Geography, Uni. of Nottingham, Nottingham, NG7 2RD, UK
Tel : +44 115 951 5442. Fax : +44 115 9515249
E-mail : vyas@geography.nottingham.ac.uk

K.W. Jaggard

IACR Brooms Barn, Higham, Bury St Edmunds, Suffolk IP28 6NP
Tel.: +44 284 810363 Fax.: +44 284 811191

ABSTRACT

In Sugar Beet, previous studies have shown that forecasts of potential sugar yield can be provided through the growing season, based on satellite observations of crop canopy cover at various stages of development. These observations are used in conjunction with corresponding regional weather information, crop sowing dates and soil types to provide successively refined yield forecasts as harvest time approaches. 5 ERS-1 SAR and 3 ERS-2 SAR images were obtained of East Anglia. Field data were collected in two contrasting fields from June 11 to July 29, 1996, comprising radiometric and biophysical measurements of the crop canopy. A independently fitted version of the 'Cloud model' was inverted to calculate LAI from values of ERS-1 SAR backscatter and soil moisture samples. LAI estimates were in good agreement with measured values and were used to estimate canopy cover using a standard exponential relationship that has a well established coefficient for sugar beet. The study shows that Radar data can provide useful estimates of canopy cover for crop production modelling, especially in the case of loss of optical data due to cloud.

1. INTRODUCTION

In Sugar Beet, previous studies have shown that forecasts of potential sugar yield can be provided through the growing season, based on satellite observations of crop canopy cover at various stages of development.Incorporation of radar data into the crop growth model ensures the supply of data to estimate crop cover (f) when weather conditions prevent the acquisition of satellite data at optical wavelengths. Compared with optical remote sensing, radar has a more ambiguous relationship with crop canopy variables, but as shown by Xu and Steven, 1996, the relationship with leaf area in sugar beet is significant and strong enough to provide reasonable estimates of crop cover. However, the radar model used by (Xu and Steven, 1996) was calibrated and fitted to agronomic field data from a single date in 1994. This paper describes a independent study to evaluate the reliability of radar estimates of crop cover in Sugar Beet.

2. APPROACH

To test the robustness of the Xu and Steven model over time, ERS-1/2 SAR data were related to ground measurements of sugar beet for a sequence of dates through the growing season LAI was estimated from the model and used to estimate crop cover (f) for incorporation into the sugar beet growth model. The procedure used was as follows:

1. Collection of Ground truth data in selected two sugar beet fields on 10 dates with simultaneous acquisition of ERS-1/2 SAR image data.
2. Derivation of radar backscatter coefficient through ERS-1/2 SAR calibration.
3. Calculation of leaf area index from radar backscatter and soil moisture using the Cloud model
4. Crop canopy cover (f) estimation from LAI using SAR data
5. Comparison with Ground truth data

3. DATA USED

3.1 Ground truth data

The study area was chosen near Broom's barn sugar beet Research Institute, East Anglia, UK (lat/long=52.2/0.46 degrees).The field data were collected weekly from June 11 to August 16, 1996 and SAR data were acquired for 10 ERS-1/2 overpass dates. A Parkinson radiometer with 2 bands (NIR and Red respectively at 650 and 850nm) and 2 heads (radiance for 30^0 FOV and irradiance) was used for radiometric measurements of the crop canopy. In each field, 5 sample areas about 12 m apart used to collect biophysical measurements; namely row direction, plant population, canopy biomass, canopy and leaf water content, leaf area index (LAI), leaf inclination angle, soil moisture and soil roughness. The average value were used to represent each field. The detailed fieldwork and analysis procedures were as described in Xu and Steven (1996). The Ascending and Descending ERS-1/2 SAR overpasses for East Anglia were at approximately 2200 GMT and 1053 GMT, respectively. A larger set of sugar beet fields was also identified for the extension of image analysis with ERS, SPOT and ground data for a single date.

3.2 ERS-1/2 SAR DATA

The SAR precision images are multi-look, ground range, digital images generated from raw SAR image mode data using up-to-date auxiliary parameters and corrected for antenna elevation gain and range spreading loss. A full scene of ERS-1/2 SAR normally has a geographical coverage of 100 km in ground range and at least 102.5 km in azimuth (along track). Seven ERS-1 and 3 ERS-2 SAR scenes were used for this study.

4. ERS-1/2 SAR CALIBRATION

As advised by DRA (Bird, 1996), a single calibration constant was used for calibration of all ERS-1.SAR.PRI images processed by DRA based on the 131 corner reflector measurements over a period of 8 months. The calibration constant was given as 59.96 dB for ERS-1 and 55.61 dB for ERS-2 the mid-swath position. Therefore, to calculate the radar backscatter coefficient σ^0 (dB) for ERS-2, the following equation was used :

$$\sigma^0 \text{ (dB)} = 10\log_{10}(<I>) + 10\log_{10}(\sin\alpha/\sin 23^\circ) - 55.61 \text{ dB} \quad (1)$$

where <I> is the mean pixel intensity as given in Equation (2) , and α is the local incidence angle.

The two sugar beet fields where the ground data collection campaign took place were identified on the ERS-1/2 SAR images. The area for each field has been defined on the ERDAS IMAGINE image processing system together with a statistical report on the number of pixels in the selected area, the mean value of pixel amplitude and the standard deviation etc. The average radar intensity for each field could then be generated as the sum of the square of mean and the square of standard deviation, i.e.

$$I' = \frac{1}{N} \sum_{i=1}^{i=N} DN_i^2 = DN_{mean}^2 + SD^2 \quad (2)$$

where DN_{mean} is the average amplitude for the area of interest and SD is the standard deviation of the pixel values.

The local incidence angle for each field was then computed according to the centre pixel column of field and the backscatter coefficient was derived subsequently.

5. RADAR MODEL FITTING AND INVERSION

The relationship between backscatter and leaf area was as defined by Xu and Steven (1996) based on Leeuwen and Clevers' (1994) version of the Cloud model (Attema and Ulaby, 1978).

$$\sigma^0(m^2/m^2) = A\cdot\cos\theta\,(1-\exp(-2B\cdot L/\cos\theta)) + C'(1+0.0603\cdot m_s)\cdot\exp(-2\cdot B\cdot L/\cos\theta) \quad (3)$$

Where, $A=0.3259$, $B=0.167$, $C'=0.0452$ and $D' = 0.0603$

A, B and C' were coefficients fitted in previous experiment on nine fields in 1994 (Xu and Steven, 1994) and D' was predetermined from published values on soil backscatter. Sigma 0 (σ^0) is defined in power units in this equation.

$$L = -\frac{\cos\theta}{2B} - \ln\frac{\sigma^0(m^2/m^2) - A \bullet \cos\theta}{C'(1 + D' \bullet m_s) - A \bullet \cos\theta} \quad (4)$$

This model may be inverted for estimation of LAI using measured values of σ^0 and values of soil moisture content:

The canopy cover fraction or the fraction of intercepted solar radiation was estimated using following formula:

$$f = 1 - \exp(-K.L) \quad (5)$$

Where f is the fraction of incident solar photosynthetic irradiance intercepted or absorbed by leaves and L is the leaf area index. K is normally treated as a constant for a given crop type, with a typical value of K=0.71 for sugar beet.

6. RESULTS

6.1 Crop cover estimation by LAI using ERS SAR for two beet fields

Correlation coefficients of 0.92 and 0.96 were found between measured and predicted Leaf area index (LAI) for field A and B, respectively (fig 1). Figure 2 shows the comparison of crop cover (%) using ERS-1/2 SAR data for the two sugar beet fields on 10 dates from June to August. Correlation coefficients of 0.95 and 0.92 were achieved for field A and B, respectively.

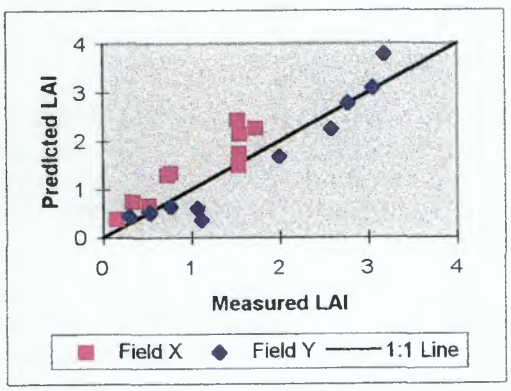

Fig.1:Comparison between Measured LAI and predicted by SAR

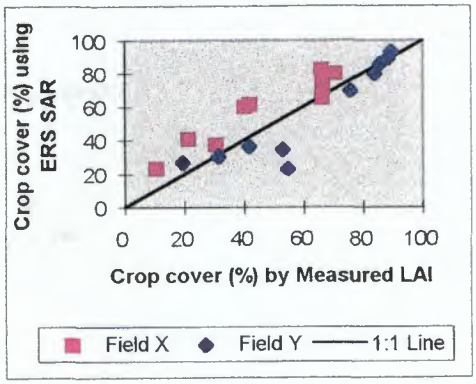

Fig.2:Comparison between Crop cover estimates by measured LAI and SAR

6.2 Extension of Radar-optical-ground data comparison

As part of a field surveys done for water stress experiment on 12 and 13 august 96, a total of 9 sugar beet fields near Brooms Barn were identified on the 13 June and 16 August, 1996 ERS-1 images. The same fields were identified on a SPOT image of 15 June, 1996. Backscatter values were calculated for each of the fields and used to estimate crop canopy cover by equation 5. The average soil moisture from field data collection in fields A and B was used in the calculations for 15 June to compare with SPOT, and the 12-13 August field data were used as the reference for the August comparison with ERS-1. Crop cover (f) was also estimated with the SPOT data using the OSAVI relationships applied to the same 9 sugar beet fields as were identified on the ERS-1 SAR images (Rondeaux et. al, 1996). In June the comparison between SPOT and ERS shows a correlation coefficients of 0.88 (Figure 3). Figure 4 shows a correlation coefficients of 0.71 between crop cover estimates from ERS SAR and from Measured LAI.

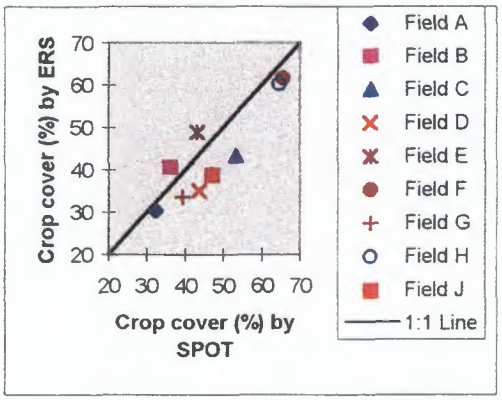

Fig.3: Comparison between crop cover(%) by SPOT and ERS SAR for 9 sugar beet fields

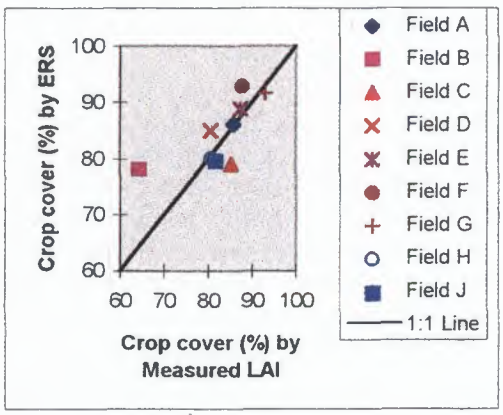

Figure 4: Crop cover (%) for 9 sugar beet fields using ERS and measured LAI

7. CONCLUSIONS

Comparison of the predicted values and measured data together with their error analysis demonstrated that ERS-1/2 SAR data can be used in the Cloud model for estimation of leaf area index and canopy cover with an acceptable accuracy and thus has the potential for operational application. The ERS SAR data have been shown to be sensitive to leaf area throughout the growing season of Sugar Beet and are a viable alternative to the use of optical remote sensing in an operational sugar beet yield forecasting system. Further validation of the model with RADARSAT C-band HH polarization, which has potentially higher temporal resolution will be made in 1997.

8. REFERENCES

Attema, E.P.W. and Ulaby, F.T., 1978, Vegetation modelled as a water cloud, *Radio Science*, 13(2), pp357-364.

Bird, P.J., 1996, Personal communication. Space and Communications Dept., Defence Research Agency, Farnborough, UK.

Leeuwen, H.J.C. van and Clevers J.G.P.W., 1994, Synergy between optical and microwave remote sensing for crop growth monitoring, Proc. *Sixth Int. Symp. Physical Measurements and Signatures in Remote Sensing*, 17-21 Jan. 1994, Val d'Isere, France, pp 1175-1182.

Rondeaux, G., Steven, M.D. and Baret, F., 1996. Optimization of Soil-Adjusted vegetation indices. *Remote Sensing Environ.*, 55, 95-107.

Vyas, S.P. and Steven, M.D., 1995, ERS-1 SAR for leaf area index (LAI) prediction. Proc. *Remote Sensing Society One Day Student Meeting*, 29 March 1995, Dept. of Geography, Uni. of Leicester, UK. pp 146-152.

Vyas, S.P. and Steven, M.D., 1996. Sugar beet yield estimation by using ERS-1 SAR data, Proceedings of the *Remote Sensing Society One Day Student Meeting*, Salford University, April 4, 96, pp 33-38.

Vyas, S.P., Steven, M.D.and Jaggard, K.W., 1996. Comparison of SPOT and SAR estimates of canopy cover in sugar beet, Proceedings of the *22nd annual conference of the Remote sensing society*, 11-14 september, 1996, Durham, UK, pp 614-622.

Vyas, S.P., Steven, M.D., Xu, H., Milnes, M. and Jaggard, K.W., 1995, ERS-1 SAR for sugar beet yield prediction. Proc. *II ERS Applications Workshop*, London, UK, 6-8 Dec. 1995, 403-405.

Xu, H. and Steven, M.D., 1996, Monitoring leaf area of Sugar Beet Using ERS-1 SAR Data. *International Journal of Remote Sensing* , 17,17,3401-3410.

APPORT DE LA FUSION MULTIDATE POUR L'INTERPRETATION DES IMAGES ERS-1 EN MILIEU TROPICAL.

William Stroobants [1], Mariline Bâ [2], Claude Pénicand [1], Jean-Paul Rudant [3], Edith Théodorakopoulos [1].

[1] Cellule d'Etudes en Géographie Numérique, 16 Bis Av. Prieur de la Côte d'Or, 94114 Arcueil Cedex, France.
Tél.: 01 42 31 88 26, Fax: 01 42 31 99 77,
E-mail: cpenican@ctme.etca.fr, wstrob@ctme.etca.fr, edith@ctme.etca.fr.
[2] Université de Dakar - Unité de traitement d'images spatiales.
Tél.: 221 27 34 13, Fax: 221 27 34 13, E-mail: diarra@chris.isra.sn.
[3] Université de Marne-La-Vallée, Laboratoire de physique et chimie des géomatériaux.
2 rue de la Butte Verte 93166 Noisy-Le-Grand, France.
Tél.: 01 44 27 38 70, Fax: 01 44 27 50 85, E-mail: jpr@lgs.jussieu.fr.

RESUME

L'exploitation d'images multidates facilite l'interprétation des images radar ERS-1 en milieu tropical. Pour illustrer les principes et l'apport d'une telle approche, cet article présente les résultats obtenus dans le cadre d'une étude cartographique menée sur le Sénégal, et plus particulièrement sur le delta du Saloum dont les caractéristiques (variété des paysages et forte dynamique temporelle) constituent un cas limite. Dans ce contexte, l'interprétation des images est gouvernée par les variations spatiales mais aussi (et surtout) par les variations temporelles de la rétrodiffusion des ondes radar. En effet, l'interprétation directe des effets liés à la rugosité des sols est peu intuitive et les transitions liées au couvert végétal sont parfois diffuses. Aussi, l'étude des paysages s'appuie sur l'analyse des différences de comportement à certaines dates d'observations (saison des pluies, saison sèche, saison post-pluie). Les images ERS sont actuellement les seules données qui soient à la fois disponibles aux dates clés et suffisamment sensibles aux variations d'états de surfaces considérés. Ainsi, une combinaison colorée d'images multidates permet d'établir rapidement les grandes unités du paysage (mangroves, forêts, savanes, etc.). Toutefois, l'exploitation individuelle de chacune des images constituant la série temporelle est ensuite nécessaire pour affiner l'interprétation de certains thèmes (milieu urbain, sols nus, sols herbacés, etc.).

I. INTRODUCTION

Le but de cette étude est de vérifier que l'imagerie radar ERS-1 rend possible l'interprétation d'une zone dans laquelle des dynamiques temporelles multiples se superposent.

Après avoir rappelé le déficit de la cartographie en milieu tropical , nous montrons comment l'imagerie radar permet de réactualiser les couvertures cartographiques existantes. Ensuite, nous analysons l'apport d'une approche multidates pour l'étude des différents changements d'états de surface qui affectent la zone d'étude.

Réalisée en partenariat, cette étude a été menée avec plusieurs organismes (CEGN, Université de Marne La Vallée et Université de Dakar) qui ont apporté leurs compétences thématiques et techniques en imagerie radar.

II. ETAT DE LA COUVERTURE CARTOGRAPHIQUE TRADITIONNELLE

Comme le montre le tableau ci dessous, l'état de la couverture cartographique des pays tropicaux est loin d'être satisfaisant [1] :

	Superficie couverture 1987 R : rythme annuel de révision (80-87)	
	1/50 000	1/100 000
Europe (sauf URSS)	96% (R = 5,7%)	79% (R = 7%)
Amérique du Nord	71% (R = 2,3%)	37% (R = 0%)
Afrique	35% (R = 2,3%)	20% (R = 3,6%)
Amérique du Sud	30% (R = 0,8%)	53% (R = 0%)
Asie, Australie, Océanie	60% (R = 5,7%)	60% (R = 7%)

Au problème de l'absence totale de cartes grandes échelles sur certaines zones, s'ajoutent les problèmes d'actualité et de qualité de l'information disponible, souvent liés aux contraintes économiques des pays concernés.

III. CARTOGRAPHIE SPATIALE DES PAYSAGES

La diversité, la complexité et l'évolution rapide des paysages tropicaux semblent être des handicaps sérieux pour tout relevé cartographique classique.

Dans les forêts tropicales d'Amérique du Sud, la difficulté de déplacement et le manque de vue d'ensemble rendent le travail sur le terrain très laborieux. En outre, l'homogénéité du paysage pousse à considérer avec attention les rares zones déforestées dont l'évolution dans le temps peut être très rapide. Dans les franges littorales plus accessibles, la dynamique côtière est également très forte. Les relevés effectués offrent donc une pérennité très faible.

Dans les régions d'Afrique concernées, l'influence anthropique (tant au niveau de l'agriculture que des infrastructures) est plus élevée, mais le couvert végétal

est généralement pauvre. Les transitions entre savanes et forêts s'effectuent de manière très diffuse. De ce fait, la partition du paysage en unités bien distinctes sollicite le jugement subjectif du cartographe. De plus, le découpage des unités de paysages sur la base des états de surface pousse à des distinctions fines au cas par cas, parfois contradictoires de l'objectif d'une cartographie homogène, et globalement peu pérennes.
Les travaux déjà menés, à l'aide des différents capteurs aéroportés ou satellitaires, ont montré que l'utilisation de l'imagerie radar, très sensible aux états de surface, apporte une perception originale de ces paysages et facilite leur étude. Utilisés sur des territoires tropicaux et équatoriaux, les capteurs radar ont permis d'obtenir des images particulièrement intéressantes dans plusieurs domaines: dynamique littorale, hydrologie, topographie, géologie et cartographie générale. En outre, la quasi-indépendance des ondes radar au couvert nuageux et la capacité de prise de vue jour/nuit des satellites radar permettent une couverture homogène des régions tropicales. Cette répétitivité permet d'acquérir un grand nombre de scènes tout au long de l'année et de s'épargner la complexité des missions aéroportées (notamment en raison de la facilité de localisation absolue des images radar ERS). Elle autorise en outre une analyse multidates des images [2][3]. On peut ainsi étudier des phénomènes soumis à des évolutions saisonnières ou annuelles (état des cultures, suivi de la déforestation en milieu tropical, etc.). Nos expérimentations menées en Guyane française ont montré que le potentiel cartographique des images radar est adapté à des paysages caractérisés par un couvert naturel relativement homogène, un faible relief et un tissu urbain peu dense [4][5]. L'utilisation d'une série d'images permettait de mettre en évidence la dynamique de phénomènes significatifs sur une région donnée. Leur analyse était d'autant plus « aisée » que les évolutions temporelles étaient peu nombreuses et que les facteurs qui les engendraient étaient connus.
Ces travaux ont débouché sur des résultats prometteurs pour la mise à jour des cartes à petite et moyenne échelles [4][5]. L'utilisation de l'imagerie radar permet la réalisation d'un produit cartographique original : la « spatiocarte » radar dont la géométrie est celle d'une carte traditionnelle, mais le fond du document est l'image elle-même. Les enjeux liés aux processus de fabrication des spatiocartes radar ont été exposés par divers auteurs [6].

Afin de valider le potentiel de la cartographie radar sur toute zone tropicale, il est toutefois nécessaire de l'évaluer sur des zones présentant des variabilités spatio-temporelles plus complexes.
A ce stade de l'analyse, il faut rappeler que ces variations temporelles interviennent sur des objets multiples. Elles concernent tout à la fois les phénomènes environnementaux et anthropiques (rythme des saisons et décalages annuels de celles-ci, importance variable des précipitations, rythme des marées, évolutions urbaines ou de la désertification, importance des brûlis, ...), les phénomènes liés au système d'observation (homogénéité temporelle des observations, dates et heures de prise de vue, périodicité de l'observation, durée des observations,...) et ceux liés à l'exploitation des observations (décalage éventuel des contrôles terrain, représentativité des données externes collectées, délai d'utilisation de l'information produite, ...).
Le delta du Saloum (Sénégal) choisi pour l'étude peut être de ce point de vue considéré comme un cas limite du fait des importantes variations liées aux conditions tidales et saisonnières.

IV. DESCRIPTION DU SITE D'ETUDE

Le centre de la zone d'étude (1000 km²) a pour coordonnées 13°80' N et 16°60' W. Le delta du Saloum est situé à l'Ouest du Sénégal à 145 km au Sud de Dakar, il forme une région plate et marécageuse recouverte par les eaux du Saloum qui serpentent dans de multiples chenaux (bôlons). Les mangroves constituent la principale végétation du delta. Localement se développent des savanes à baobab et quelques cultures vivrières (mil et arachides).

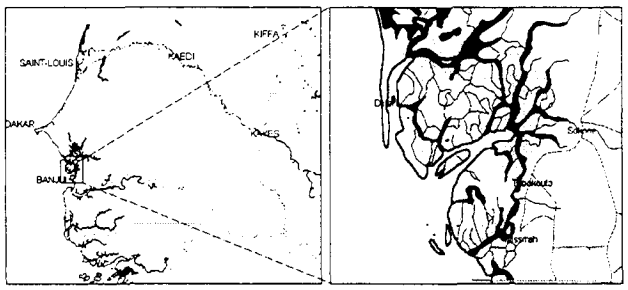

Les évolutions temporelles qui affectent la zone d'étude sont nombreuses et pas toujours cohérentes entre elles, les variations spatiales et temporelles du terrain dépendent de plusieurs facteurs dont l'influence est souvent difficile à mettre en évidence :

- rythme des saisons variable d'une année sur l'autre ;
- pluviométrie variable sur de petites distances ;
- horaires des marées différents entre les images ;
- marée haute à des heures variables dans les bôlons en raison du chemin à parcourir par la marée ; de plus, les hauteurs d'eau à l'intérieur du delta sont inconnues.

V. DONNEES UTILISEES ET TRAITEMENTS

Les données SAR du satellite ERS-1 utilisées dans le cadre de cette étude ont les caractéristiques suivantes (orbites montantes) :

Dates	Orbites	Traces	Saisons	Marées
24/05/94	14937	261	sèche	P.M. + 2 h 30 mn
16/08/93	10911	261	pluies	P.M. + 2 h 45 mn
25/10/93	11913	261	post-pluie	B.M. - 1 h

Les horaires de marée ont été calculés d'après l'annuaire, en tenant compte du décalage annoncé entre

la référence « Dakar » et la zone concernée à l'embouchure du delta (« Pointe de Sangomar »).
Une des caractéristiques des images SAR est le chatoiement (« speckle ») présent sur la totalité de l'image qui nuit à la bonne lisibilité de celle-ci. Il faut donc filtrer les images tout en préservant l'information radiométrique contenue dans les images. Nous utilisons pour cela un filtre multidates [7]. Ce filtre effectue une moyenne simple sur les zones qui ne changent pas d'une image à l'autre (i.e. zones homogènes) ; il ne moyenne pas celles dont la radiométrie est nettement différente entre les images (zones inondables) ; enfin il effectue une moyenne pondérée sur les zones dont les variations radiométriques se situent entre les deux niveaux précédents. Ce filtre préserve donc les évolutions et lisse le speckle dans les zones peu évolutives.
Une fois les images filtrées, nous les superposons pour en faire une composition colorée RVB. L'attribution des couleurs est la suivante :

- Bleu = 24/05/94
- Vert = 16/08/93
- Rouge = 25/10/93.

Nous disposons donc de deux types d'outils pour l'analyse temporelle, la juxtaposition d'une série d'images monodate et une synthèse sous forme de composition colorée.

VI. ANALYSE DES RESULTATS

Les thèmes caractéristiques du delta du Saloum (Figure 1) sont les suivants : végétation (mangroves, surfaces hétérogènes, forêts), tissu urbain, réseau routier, sols nus/herbacés, hydrographie.
L'analyse des résultats est basée sur la confrontation des interprétations sur écran et de l'indispensable validation de terrain (la première mission de validation de terrain s'est déroulée en Novembre 1996).
Pour évaluer l'intérêt respectif des images monodate et de la combinaison multidates, les matrices de confusion dont les diagonales principales sont présentées ici, ont été établies.

Classes	24/05/94	16/08/93	25/10/93	Combi. Col.
Mangroves	90%	67%	90%	100%
Savanes	75%	45%	35%	85%
Cultures	0%	100%	0%	100%
Forêts classées	80%	70%	20%	90%
Milieu urbain	100%	0%	60%	80%
Sols nus	75%	85%	80%	80%
Sols herbacés	75%	85%	80%	80%
Hydrographie	90%	97%	97%	100%

VI-1. Les mangroves

L'analyse de la combinaison colorée permet d'affiner l'identification des mangroves (amélioration de 10%) déjà bien diagnostiquées sur les images monodate. Elle ne permet néanmoins pas de lever les incertitudes restant sur un moucheté grisâtre (marque de faible évolution temporelle) qui n'est significatif, d'après nos observations de terrain effectuées 2,5 ans après la dernière prise de vue ERS, d'aucune différenciation notable de la mangrove.

VI-2. Zones agro-pastorales

Ces surfaces contiennent deux types de végétations : la savane et les cultures vivrières (arachides et mil principalement). Le contour des parcelles cultivées est plus ou moins net en fonction de l'importance de la biomasse environnante. Le cycle végétatif des cultures permet une localisation précise de celles-ci sur la composition colorée. En effet, le vert intense caractérise une forte radiométrie en saison des pluies liée au développement saisonnier des cultures. Le vert plus diffus caractérise les savanes car leur croissance est moins importante (sols non fertilisés). Enfin, la combinaison colorée améliore sensiblement la perception des zones agro-pastorales par rapport aux images monodate correspondantes.

VI-3. Forêts classées

L'exploitation du bois et les cultures y sont interdites pour éviter que la forêt ne se dégrade de façon irrémédiable. Pendant et après la saison des pluies la végétation est pratiquement la même, la rétrodiffusion est donc quasi-identique sur les images correspondantes et une teinte vert-jaune apparaît sur la composition colorée. Cette dernière permet d'améliorer l'identification des forêts (+ 10%) et de mettre en évidence la frontière entre la classe « forêts classées » et la classe « savanes + cultures », frontière d'autant plus nette quand une piste sépare la forêt de la savane.

VI-4. Milieu urbain

La localisation du milieu urbain dense ne présente aucune difficulté particulière. Cependant, il peut y avoir des problèmes quand les habitations possèdent des toits en paille, la faible rétrodiffusion de ces derniers étant quasi-identique à la savane en saisons des pluies. L'utilisation d'une combinaison colorée montre que le milieu urbain peu dense est moins net (-20%) que sur la monodate de saison sèche ; l'attention est alors portée sur les couleurs vives de la végétation environnante.

VI-5. Réseau routier.

Dans la zone d'étude il est principalement constitué de pistes en latérite avec quelques portions goudronnées. De façon générale, l'utilisation des images monodate, bien qu'améliorées par le filtrage multidates, ou de la composition colorée ne permet pas une détection systématique des pistes. Cependant, la frontière entre la forêt et la savane (cf. § VI-3) souvent marquée par des pistes permet d'en distinguer quelques unes. Quand à l'identification, elle n'est possible que parce qu'il n'y a qu'une classe à considérer. La perception du réseau routier dépend de son orientation par rapport à la direction de prise de vue et de l'angle d'incidence de l'observation. Elle est fonction en premier lieu de l'environnement et, en second lieu, de la rugosité du revêtement. Il se peut donc que les paramètres de prise

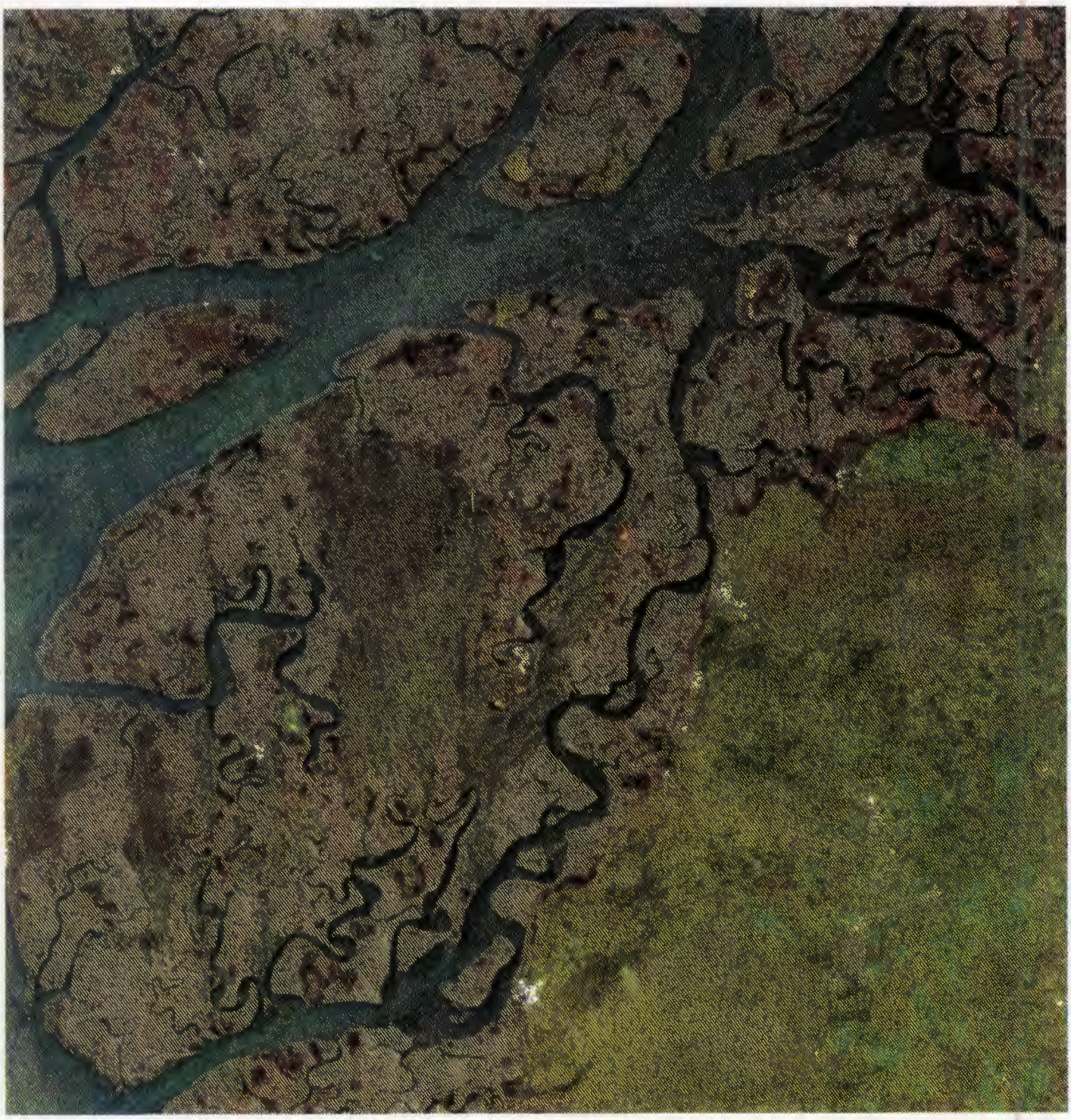

Fig1. Fusion d'images ERS-1 sur le delta du Saloum, avec:

- **Bleu : 24/05/94.**
- **Rouge : 16/08/93.**
- **Vert : 25/10/93.**

de vue du satellite ERS-1 ne soient pas adéquats pour percevoir le réseau routier du Saloum.

VI-6. Sols nus/herbacés

Les sols nus/herbacés (i.e. « slikke » / « schorre ») présentent deux types d'évolutions temporelles (saisonnières et/ou tidales) rarement quantifiables (cf. § IV). Les « slikke » (teinte violette) sont des terrains vaseux recouverts plusieurs heures à chaque marée, peu colonisés par la végétation et présentant une forte teneur en sel. Les « schorre » (teinte vert/jaune) sont des terrains colonisés par la végétation, formés de vase desséchée, granulée, et ne sont recouverts que lors des grandes marées. La composition colorée permet de localiser ces sols dans leur environnement grâce au contraste radiométrique avec les mangroves, mais ne permet aucunement une meilleure identification (-10%). En fait, les multiples transitions entre « véritables slikke » et «véritables schorre » (liées à des conditions de marées très variables dans les bôlons) induisent un éclatement des teintes dominantes pré-citées et complexifie la tâche de l'interprète.

VI-7. Hydrographie

Le réseau hydrographique ainsi que les nombreux bôlons méandriformes du delta sont clairement perçus par le satellite ERS-1. De nombreux bancs de vase affleurent à marée basse (bleu foncé), constituant ainsi un obstacle à la navigation. Leur localisation à l'intérieur du delta est importante. C'est possible pour les bôlons les plus importants où l'effet de la marée est unique à hauteur d'eau constante, mais plus difficile pour les bôlons étroits où l'on ne connaît pas précisément la hauteur d'eau à chaque marée. La perception du réseau hydrographique est quasi-identique entre la composition colorée et les images monodate correspondantes.

VI-8. Surfaces non classées

Ces surfaces présentent des caractéristiques similaires aux sols nus/herbacés.

Liserés rouge : Terrasses (i.e. vasières à marée basse) plus ou moins larges en fonction du retrait de l'eau, non cartographiables étant donné leur variabilité au sein même de l'image.

Zones oranges / blanches (centre du delta) :

Les variabilités océaniques (marées) et climatiques (saisons) ne permettent pas d'expliquer la forte radiométrie de ces zones sur les trois dates. En effet, de part la géométrie du bôlon, il semble peu probable que la marée puisse avoir un effet prépondérant sur ces zones sauf en cas de grande marée. De plus, les données pluviométriques ne sont pas assez précises sur ces zones. Les caractéristiques minérales (forte teneur en sel), l'humidité constante du sous-sol argileux et l'extrême sensibilité d'ERS-1 aux effets de rugosité fins (bande C) pourraient donner cette forte rétrodiffusion. Les zones orange seraient, quant à elles, caractéristiques d'un autre type d'argile aux propriétés similaires.

La composition colorée n'apporte ici aucune information véritablement exploitable. Au contraire, elle fait ressortir des micro-phénomènes non caractéristiques de ce qui se produit sur l'ensemble de la région.

VII- CONCLUSION

Le regroupement des informations présentes sur les trois scènes ERS-1 dans une composition colorée permet une visualisation rapide et claire des principaux thèmes caractéristiques du delta du Saloum (cultures, savanes, mangroves, hydrographie, milieu urbain dense). Il faut cependant veiller à ce que la couleur ne nuise pas à la bonne lisibilité du document cartographique final. De plus, les évolutions temporelles, souvent mal connues, l'éclatement de certaines zones en une multitude de couleurs ainsi que la sur-représentation d'objets impossible à identifier sur le terrain ne facilitent pas la tâche de l'interprète. Il semble probable que l'utilisation d'imagerie JERS (bande L), moins sensible aux effets de rugosité fins, ou RADARSAT, grâce à sa capacité de prise de vue multi-incidence et multi-résolution, permettraient une amélioration sensible de la qualité du produit cartographique final.

VIII- REFERENCES

[1] A.J. Bandenberger, S.K. Ghosh, 1992-1.
L'état de la cartographie topographique et des réseaux géodésiques du monde - les services cartographiques nationaux. Bull. S.F.P.T. N°125, pp. 3-12.

[2] M. Borgeaud, J. Noll, A. Bellini, 1994.
Multi-temporal comparisons of ERS-1 and JERS-1 SAR data for land applications. IEEE, vol2. pp. 1603-1612.

[3] D.R. Paudyal, A. Eiumnoh, J. Aschbacher, R. Schumann,.1994.
A knowledge based classification of multitemporal ERS-1 and JERS-1 SAR images over the tropics.
IEEE, vol2. pp. 1612-1614.

[4] C. Pénicand, J.P. Rudant, E. Nezry, 1995.
Utilisation opérationnelle des images de télédétection radar pour la cartographie.
Bull. S.F.P.T. N°137 (1995-1), pp. 35-41.

[5] J.P. Rudant, F. Baltzer , J.P. Deroin, M. Lointier, H. Maitre, C. Pénicand, M.T. Prost, D. Sabatier, 1994.
Possibilités cartographiques offertes par ERS1 en contexte tropicale humide, exemples en Guyane française, apports spécifiques des séquences multitemporelles. Workshop ESA, Tolède, pp. 371-376.

[6] M. Tonon, S. Sylvander, J.P. Rudant, J.P. Cantou et C. Pénicand, 1997
An operational ERS application : The mapping of French Guyana using space triangulation.
3rd ERS Symposium, Florence, 18-21 Mars 1997.

[7] W. Stroobants, C. Ledez, C. Pénicand, J.P. Rudant, P. Vallet, 1996
Une approche pragmatique de la fusion multitemporelle des images ERS-1. Fusion of Earth Data, Cannes, Février 1996, pp 131-142.

THE REQUIREMENTS FOR THE SELECTION AND PROCESSING OF SAR DATA FOR OPERATIONAL AGRICULTURAL APPLICATIONS IN EUROPE

A Sowter, *GG Lemoine and **H De Groof

National Remote Sensing Centre Limited, Delta House, Southwood Crescent, Southwood, Farnborough, Hampshire GU14 0NL, United Kingdom, Tel: +44 1252 541464, Fax: +44 1252 375014, Email: asowter@nrsc.co.uk.

*SYNOPTICS Integrated Remote Sensing and GIS Applications BV, P.O. Box 117, 6700 AC Wageningen, The Netherlands, Tel: +31 317 421221, Fax: +31 317 416146, Email: main@synoptics.nl.

**Agricultural Information Service, Space Applications Institute, T.P. 440, Joint Research Centre, I-21020 Ispra (Va), Italy.

ABSTRACT

The requirements of any operational agricultural application in Europe, using optical or SAR data, includes the timely selection and processing of image data prior to photo-interpretation. With particular reference to the MARS activities of the European Union, strict deadlines for publication of results must be adhered to if the results are to be of any use. In 1996, DG6 of the European Union awarded a contract for a pilot project to assess the potential of SAR data for the generation of rapid crop area estimates in support of MARS Activity B. This paper discusses the results of that project, particularly with reference to the timely selection of SAR scenes through the use of auxiliary data and calibrated quick looks and the subsequent ordering and pre-processing of the data for input to a photo-interpretation activity. The pre-processing included the radiometric correction, speckle filtering and terrain correction of all data used by the project.

1. INTRODUCTION

The use of SAR data for the identification of crops has had a long history but has met with only varied success. Since the launch of ERS-1 in 1991, there have been many attempts to clarify the use of SAR data in this manner. When identifying growing and developing crops on the ground, a SAR image of fixed band and polarisation appears to be less successful, on the whole, than optical data such as that gathered by the SPOT satellite. However, there have been some efforts to utilise SAR data to supplement an operational optical processsing methodology when cloud cover has been a problem (Sowter, 1995).

The sensitivity of SAR data to the properties of bare soil have been studied for some time and only recently has it been suggested that changes in soil properties may be linked to cropping and tillage practices and crop development (Lemoine et al, 1995). This implies that broad crop classes may be identified much earlier in the season using SAR than through optical-based instruments. This has implications for projects such as the EU MARS (Monitoring Agriculture by Remote Sensing) project which has amongst its programme a requirement to supply accurate yield forecasts for the EU as a whole. The supply of a more accurate early season estimate seems to be an achievable goal if SAR data is used to supplement the established optical-only methods.

Within the established MARS project, 60 sample sites across Europe of size 40km x 40km have been established that are representative of European crop trends. These sites are routinely inspected by optical sensors, primarily the SPOT satellite, and yield estimates are derived from their subsequent classification. For the pilot project, it was agreed that 20 out of the 60 sites would be chosen for analysis, primarily from Northern Europe as it was generally accepted that these sites would have a higher probability of cloud

2. DATA SELECTION

Weather conditions such as cloud cover, precipitation or light levels do not impede the ERS SAR's ability to acquire data. Unfortunately, water and temperature have an effect on the soil surface conditions and, therefore, the backscattering intensity of agricultural land. Snow cover effectively shields the SAR information that can be retrieved from the surface such that acquisitions under these circumstances are of no use whatsoever. Frozen and very dry soils have a strongly reduced backscattering coefficient which reduces the possibility of distinguishing surface roughness conditions.

A preference, based on experience, is for moist surface conditions, with normal (i.e. not extraordinarily strong) wind conditions. This is usually the case during light rain or for some time after the rain has ceased. In Autumn and Spring, we can expect that most sites will

experience such preferred conditions since, at these times, precipitation is frequent and the rate of soil drying due to evapo-transpiration is low. Thus, most soil moisture conditions will normally be at the maximum level giving a high, detailed response in an image. However, there are potentially less-than-perfect conditions for the following situations:

- During September and early October, most Southern sites will not yet have received rainfall.

- From November to March, the Northern sites are likely to encounter snow cover and the occurrence of frost. This is especially the case for ERS SAR data acquired at night (during the ascending mode).

If these problems are ignored and data is ordered at random, there may not be sufficient information in the SAR data acquired over a site to estimate crop areas to any acceptable level of accuracy. It is, therefore, advantageous to have an ability to screen the quality of the acquired ERS data before any decision to order the full product. To perform this task properly, up-to-date meteorological parameters are necessary, especially those relating to temperature and precipitation.

The most efficient method of screening ERS data for this project is through the visualisation of quick-look SAR imagery in parallel to the inspection of relevant meteorological data.

3. DATA THROUGHPUT

The first image was received by the project 9 working days after ordering. Once the first image had been received many images were received over a very short amount of time - in fact, more than 50% of the images were received within 12 working days of the receipt of that first scene, placing a great strain on the project resources which had been allocated on the basis of a steady receipt of data throughout the project.

Throughout the project, a number of important observations were made:

- Data was received sporadically, often in large batches. For example, more than half of the image tapes were received between 10-20 days after the first image had been received. This did allow some choice over which images to process, although priority was given to those sites for which we had the complete set.

- In the first ten days following the first image receipt, no complete sites were received and there was no information as to what sites would be completed soonest. Therefore, the decision over which sites to process over this time was somewhat arbitrary. When complete image sets for the sites began to be accumulated from day 10, these often did not concur with the already processed imagery, causing a slight delay. There was, consequently an early delay in despatch between days 16-22. However, the project rapidly recovered from this and from day 27 the time delay was consistently less than 5 days.

- Later in the project, the schedule suffered primarily because of the inordinate delay of only a few images needed to complete a number of sites.

In general, the initial time lags in the project between receipt and delivery were recovered to some satisfaction although the delay in the delivery of certain image data sets caused the actual completion of the pre-processing task to drag out much further than anticipated.

4. DATA PROCESSING

4.1 Introduction

Once a SAR image tape was received at NRSC, a pre-operational processing scheme was used to perform the data processing required. This scheme involved the following stages, performed sequentially:

1. Reading the SAR tape onto the system;
2. Selecting Ground Control Points (GCPs) between the SAR image and a reference SPOT image;
3. Radiometrically correcting (calibrating) the data;
4. Speckle filtering the data;
5. Geometrically correcting the data.

The main areas in the processing chain are discussed below:

4.2 GCP Collection

Tiepointing is the only manually intensive task in the SAR pre-processing chain and, until more accurate data is placed in SAR image headers, it is necessary to achieve the accuracy required by high-precision projects (Sowter et al, 1990). Tiepointing was applied with respect to SPOT data supplied by the European Commission.

Improvements in the tiepointing were applied on the basis of the following observations:

- On a site basis, there was generally a single good image out of the SAR image set that was very easy to tiepoint.

- If the three site images were either all ascending or all descending, the same GCPs could be used in each image with only a single offset applied to each.

For the task itself, tiepointing on a per-site basis has clear benefits over a per-scene basis. Unfortunately, whether this can be applied depends primarily on processing backlog which creates concerns over image delivery delays and ordering.

4.3 Calibration

The ERS calibration algorithm applied by the project follows the specifications of ESA which recommends that additional corrections be applied to standard ESA products to compensate for the effects of:

- Replica Pulse Power
- Power Loss due to the Analog-to-Digital Conversion
- Topographic Incidence Angle

The SAR data came from a number of sources (the UK-PAF and the D-PAF) and also ERS-1 and -2 data was used. Over this wide range of sources there is also a wide range of calibration constants that can be applied.so ther is certainly going to be a significant difference between pixel values due to this variation.

There are four possible ways of correcting this potentially serious variation between images:

1. Ordering ERS.SAR.RAW data only and processing using a single processor;
2. 'Normalising' a site so that only one calibration constant may be used;
3. Ensuring that no mixing of data sources occurs for any one site;
4. Identifying only a single source of data for the project.

The first of these is perhaps the best option as it is possible to order RAW data from any processing facility and still generate a consistent product; the second option is relatively easy to perform as it would only involve the multiplication of all pixel values by a factor that depended on source; the third would be difficult to manage as the same source might not be the most appropriate or timely source; and the final option is only possible when the acquisitions have been made and collected by the same processing station.

4.4 Speckle Filtering

Within the project all image interpretation/classification was performed on a per pixel basis; no field boundary information is used in order to calculate field statistics. Consequently speckle reduction is a necessity and for this purpose the GMAP filter was applied to all data.

The Refined Gamma Maximum A-Posteriori (GMAP) filter (Nezry et al. 1991) is an adaptive statistical and geometrical single point Maximum A Posteriori speckle filter. It was designed to reduce the speckle noise component from SAR imagery, while preserving texture and enhancing structural features present within the image, such as linear features and strong scatterers.

The parameter to which the filter is most sensitive is the Equivalent Number of Looks (ENL). However, this parameter is a system parameter. It characterises in practice the signal to noise ratio in the presence of speckle. The equivalent number of looks should be provided with the SAR image data. For ERS-1 PRI products this parameter should be equal to 3.

Clearly, there are methods open to the project by which the ENL can be reduced. Commonly, block-averaging the data down to, say, 25m using the 12.5m pixel values supplied will aid the performance of the speckle filter by:

- Reducing the speckle standard deviation and therefore potentially allowing a smaller window size;
- Reducing the total number of pixels to be filtered.

This clearly is very attractive indeed as there is a potential speed up in the filtering process to under 1 hour from 4 hours for a full site which, as the filtering is applied for every single SAR image, would a significant speed-up in the processing.

However, care must be taken with this approach as:

- In SAR data, although the 12.5m pixels are samples from the same distribution, they are not independent, being resampled from the independent pixels at between 25-30m using a Sinc function during imaging. Thus, block-averaging, or indeed any other form of resampling, will reduce the confidence in any mean value derived by the speckle filter.
- Resampling affects the spatial resolution of the data and therefore the window size of the filter must be adjusted accordingly to get sufficient sampling of the data.

As neither of these issues have been addressed fully in the literature, it is a point of discussion/contention as to whether for future projects the PRI data is block averaged to 25m prior to filtering.

4.5 Terrain Correction

The speckle filtered image derived from the previous step is still in the original PRI coordinate system. The purpose of the terrain correction is to undertake to rectify the image for terrain-induced distortions and place the pixel values in the required output coordinate system.

The significant amount of terrain distortion found in SAR data suggests that, in areas of even low variations in relief, terrain correction must be applied to place targets in their true relationship to each other.

The terrain correction process in SAR image data is well documented (e.g. Schreier, 1993). However, the rectification process requires a resampling of the input data to the new coordinate system, something which is not so clear as, for SAR data, point target

characteristics can be preserved but usually at the expense of the image statistics from which the reflectivity is calculated. To preserve image statistics we implemented a nearest neighbour algorithm only.

For the project, all terrain correction was applied using TSAR (an in-house SAR terrain-correction tool at NRSC), a DEM supplied by the European Commission and a GCP file derived earlier in the processing chain. The output image was provided in the required coordinate system with 20m pixel spacing in agreement with the MARS project system used for that site.

Perhaps the greatest influence in geolocation accuracy was the DEM. To demonstrate this, Table 1 below shows the absolute RMS calculated from 20 independent tiepoints of an image of the DRIF site using a fine DEM (digitised at a scale of 1 : 200 000 to 50m height spacing), the coarse DEM used for the project (with 360m height spacing for this site) and no DEM at all.

DEM Used	Absolute RMS (m)
Fine	22.47
Coarse	61.16
None	125.58

Table 1. Absolute RMS of Terrain Correction using Different Quality DEMs on the DRIF site.

From this it is clear that the fine resolution DEM provides the better accuracy, providing an absolute RMS error of less than the spatial resolution.

Although it was assumed that resampling should not affect the classification accuracy, the edges of fields were clearly broken up which could lead to a loss of definition. To alleviate this problem, it may be appropriate to use a different resampling algorithm, such as cubic convolution, which will preserve smooth 'ramps' at field boundaries. However, care must be taken to preserve the characteristic signatures of features.

5. CONCLUSIONS

During the SAR data pre-processing, 58 images were processed and despatched to the next stages in the project in an operational manner. The input and output of data was managed following strict working procedures that provided documentation for the day-to-day monitoring and identification of problems relating to the project. There were no significant problems in image despatch that cannot be related to late ordering of data or late delivery to the project from the data supplier. Therefore, in terms of the image handling and processing management aspects of the project, there are few areas of criticism.

In general, it can be clearly stated that this project has shown that high-precision processing of SAR data can be achieved in an operational European land monitoring programme. Previously, there have been no such similar projects that have generated such a large volume of high quality products within such a short timescale.

REFERENCES

Lemoine, G., De Groof, H., and van Leeuwen, HJC, 1995, 'Monitoring Agricultural Land Preparation Activities with ERS-1 to Complement and Advance Early Season Crop Acreage Estimates in the Framework of the MARS Project', Proceedings of the Second ERS Applications Workshop, London, UK, 6-8 December 1995.

Nezry, E., Lopes, A. and Touzi, R., 1991, "Detection of structural and textural features for SAR image filtering", Proceedings IGARSS 91 Symposium, pp-2169-2172.

Schreier, G. (ed.), 1993, 'SAR Geocoding : Data and Systems', Karlsruhe : Wichmann.

Sowter, A., 1995, 'The Use of Synthetic Aperture Radar Data in the 1995 Control of Area Based Arable and Forage Subsidies Contract', National Remote Sensing Centre Report AM-DC-NRL-AG-331, Issue 1.0, October 1995.

Sowter, A., Smith, D.J., Laycock, J.E., Raggam, J., Strobl, D., and Triebnig, G., 1990, 'Study on an Error Budget for ERS-1 SAR Imagery', Final Report for ESA Contract 7689/88/HGE-I.

MULTISOURCE ERS-1 AND OPTICAL DATA FOR VEGETAL COVER ASSESSMENT AND MONITORING IN A SEMI ARID REGION OF ALGERIA

Y. SMARA, A. BELHADJ-AISSA & B. SANSAL
Image Processing Laboratory, Electronic Institute, U.S.T.H.B, BP 32 El-Alia Bab-Ezzouar 16111 Algiers Algeria

J. LICHTENEGGER
European Space Agency / Earthnet, E.S.R.I.N , Via Galileo Galilei, 00044 Frascati, Italy.

A. BOUZENOUNE
Vegetal biology Laboratory, Natural Sciences Institute, U.S.T.H.B., BP 32 El-Alia Bab-Ezzouar 16111 Algiers Algeria.

ABSTRACT

This paper overviews results obtained by multisource and multidate optical data analysis and by comparing ERS-1 and Landsat TM data due to aspects of radar image enhancement techniques and the restitution of roughness of different types of vegetation in steppic regions. In effect, image data integration has become a valuable approach to integrate multisource satellite data. It has been found that image data from different spectral domains (visible, near infrared, microwave) provides data sets with complementarity information content and can be used to improve the spatial résolution of satellite images.In this communication, we present a part of the cooperation research project which deals with fusing ERS-1 SAR geocoded images with Landsat TM, investigating different combinations of integration and classification techniques. The methodology consists of several steps which are:

- Comparative performance of different filtering algorithms for the purpose of reducing Speckle noise. Several filtering algorithms (median and separable median, edge preserving smoothing filter, Lee sigma, modified Lee filter and Kuan filter) were implemented and tested with different window sizes, iterations and parameters.
- Geometric superposition and geocoding of optical images regarding GEC type SAR ERS-1 image available and resampling at unique resolution of 25 m.
- Application of different numerical conbinations of integration techniques and unsupervised classifications such as the Forgy method, the MacQueen method and other methods.

The results are compared with vegetal cover mapping from aerial photographs of the region of Foum Redad in the south of the saharian Atlas. The combinations proposed above allow us in a color composite image to distinguish different themes which exist in the image such as low and high steppic vegetation , trees, bare soil and montainous zones.

The multisource classification seem to be more efficient when the speckle is well filtered and allows us to distinguish the different themes existing in the arid and semi-arid regions in the south of the saharian Atlas and shows a good correlation between different types of land cover and land use and radar backscattering level in the SAR data which corresponds essentially to the roughness of the soil surface.

1. INTRODUCTION

Remote sensing has changed greatly over the past two decades because of advances in certain fondamental aspects. These aspects are (1) the development of sensors capable of collecting information in new portions of the electromagnetic spectrum and (2) the incorporation of computers in many aspects of data acquisition and utilization. Spaceborne remotely sensed data may be particularly useful in developing countries where frequently there is a lack of up to date, reliable spatial information (HAACK, 1994).

The launching of the ERS-1 (SAR) radar satellite in July 1991, can be mentioned as a significant achievement of the Earth resources scientific community in their efforts to improve operational monitoring of land cover changes. However, for Synthetic Aperture Radar images, speckle noise constitutes one of the main obstacles to be dealt with, since it increases variance and hampers visual interpretation as well as digital analysis of SAR data. It is therefore essential to separate noise from thematic information by filtering the speckle.

The purpose of this study is to focus on the comparative performance of different algorithms for reducing speckle noise and to assess the potentialities of the complementarity of the use of multisensor data set of optical satellite data (Landsat MSS and TM, SPOT) with spaceborne SAR data, namely here ERS-1 data for the vegetal cover assessment in a semi arid region of Algeria. In particular, the assessment of microwave data is carried out by combining these data with Landsat TM data acquired over the same site.

General characteristics of the study area are given in the first section. The second section exposes the optical data analysis and interpretation. The following section presents the ERS-1 and Landsat TM data fusion. This includes (1) analysis of the sar data, (2) image filtering and finally (3) images integration and classification. Finally, practical results obtained by this study such as spaceborne microwave data combined with optical satellite data are presented.

Proc. 3rd ERS Symp. on Space at the service of our Environment, *Florence, Italy, 17–21 March 1997* (ESA SP-414, 3 Vols., May 1997)

2. DESCRIPTION OF THE STUDY AREA

The area studied here is located on the southern piedmont of the saharian Atlas in Algeria (Djebel Amour) which is part of a unit more than 2000 kms long, related to the reliefs which extend from the Anti-Atlas in Marocco to the low mountains of the region of Gafsa in Tunisia.

The selected zone (see figure 1) is considered as a transitional zone between mountainous reliefs of the saharian Atlas and the plains of the beginning of the Sahara. This fringe, characterized by a semi-arid and arid environment, cones of dejection in river mouths, as well as the riverborne glacis , is favourable to occupation by humans who find the water necessary to support life, and land for agricultural and pastoral activities (ESTORGES , 1965 and JOLY, 1986). The remeth (Haloxylon scoparum) is the typical plant of the steppe in this piedmont. It is often altered by the presence of humans because it is grazed by cattle, and it makes efficient heating wood. These surfaces of haloxylon scoparium are mixed with the rest of the clusters of alfa on the steppe (Stipa tenacissima),armoise (artemisia herbe alba) and sparte (lygeum spartum), the most caracteristic of the saharian Atlas and of the high steppes of the northern piedmont.

This steppic vegetation is the most important object to get on the satellite images because, overgrazed in dry period, it is significant of the evolution of the whole area. This kind of environment is a fragile field submited at the mercy of hydric and aeolian agression, liable to disturb human activities seriously. Man, also, contributes to the worsening conditions of the environment by overgrazing, poor management or techniques inadapted to the environmental conditions.

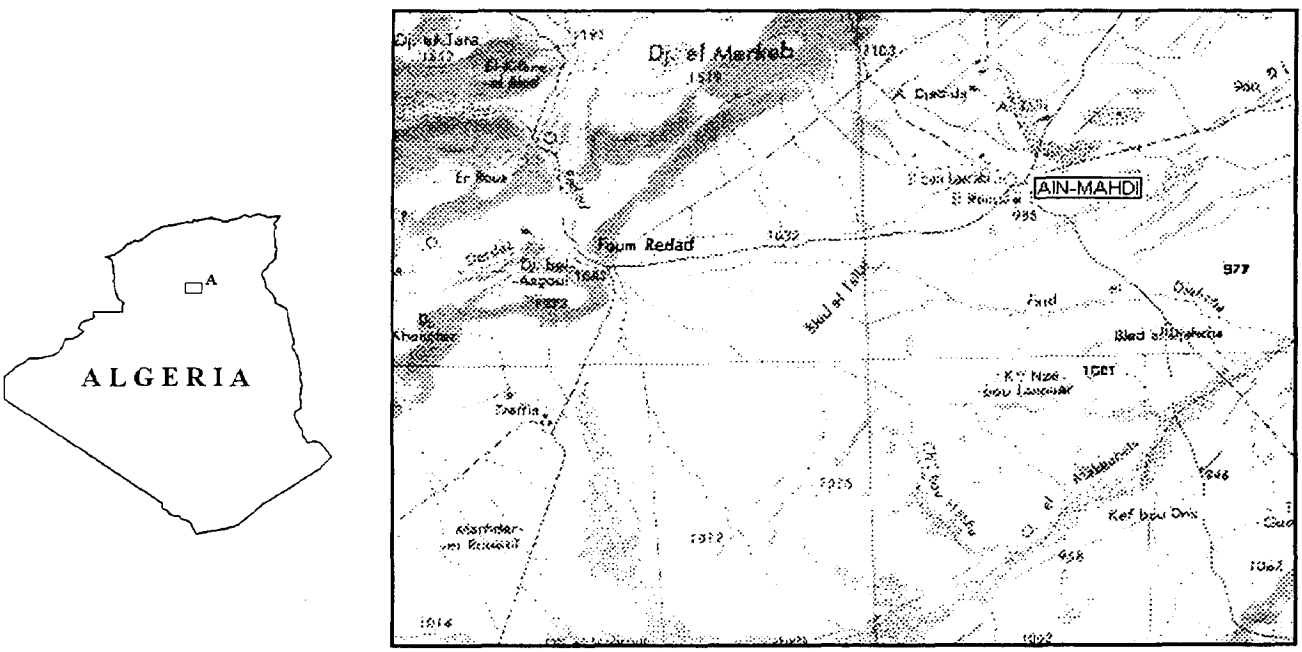

figure 1: presentation and localization of the study area A.

3. DATA USED

This study was carried out using digital satellite data (SAR ERS-1 and Landsat TM), photographic composite colors of satellite data (SPOT and LADSAT MSS), existing maps (topographic and thematic maps), aerial photographs and ancillary data.Table 1 summarizes the satellite data used.

SENSOR	DATE	SCENE
Landsat MSS	02 Dec. 1979	211 / 37
	01 Jan. 1989	196 / 37
SPOT HRV	23 Feb. 1986	50 - 282
SAR ERS-1	01Nov. 1993	12005 / 2925
SAR ERS-1	12 Oct. 1992	6494 / 2925

Table N°1: satellite data used

Ground truth data for this study (field observations and photographs) were collected during a visit to the test area in May 1992.

4. DATA ANALYSIS AND INTERPRETATION

In the charaterization or monitoring assessment of surface soils studies carried out by multisources remotely sensed data, two major categories of complemarity can be noted:

-1. When visible and microwave data are acquired at the same date; In this case, complementarity is essentially based on the use of both visible and microwave derived information. Depending on the objectives, one data source may provide information that is more accurate than the other.

-2. When visible and microwave data are acquired at different dates; in this case, information that is similar in nature is mostly used for assessing changes that could have occured between the different dates of acquisition.

the last case is particularly valuable for monitoring agricultural activities in arid and semiarid regions where we have dry and wet years and irregular rainfall. The present study shows the possibility of combining visible data , here acquired during the dry year (SPOT data) and the wet years (Landsat MSS and TM data) , and microwave data acquired in wet years for vegetation assessment.

4.1. Optical data analysis

The appearance and structure of the vegetation cover reveals the piedmont climatic conditions. We observe a thinning out towards the south and alloctones (water infiltration of the rivers). The vegetation also adapts to the edaphic conditions, so becoming then denser in the rivers depts and depressions (Dayas).
The satellite images have allowed us to grasp the vegetation in terms of cover rates. We distinguish the natural or cultivated dense vegetation of dayas and rivers from the sparse steppic vegetation of hamadas and glacis, where the cover rate is about 30%.
The dense vegetation, even if covering a limited area in this region, presents variations over time. It is limited to areas where the edaphic conditions and humidity are suitable, the zones liable to flooding, dayas, rivers and around streams.
Qualitatively, the cultivated and natural dense vegetation was highly developped in 1979 as we can see on the MSS composite color image, almost the same as in 1989 (Landsat TM image) , a wet year, when dense vegetation of rivers and dayas was relatively abundant and the cultivated area more developped than in 1986 (SPOT composite color image) , a year which followed several years of drought .
The gardens and the zone of irrigated cultures have varied little in area over this period because the lack of rainfall has been compensated by irrigation from wells and everlasting streams (gardens surrounding Ain-Mahdi village). But the "bour" culture zone without irrigation, depending on rainfall, are bare in 1986 because of the lack of water. The lower rainfall and the fall of the water table levels have equally caused a decrease in the natural vegetation of the rivers.
In spite of the importance of the soil specific reflectances in the spectral signatures of the steppic zones, linked to the sparse cover rate of this vegetation type, we manage to grasp its significant natural or man made variations over time. Notably, in the Landsat MSS images of 1979, vegetative period, but seven years after the beginning of the drought occasionally interrupted by rainy periods, we observe a certain number of areas with high albedo corresponding to bare soils.
The regeneration of the vegetation between 1986 and 1989 show that this last drought has not left any indelibile trace. The observed conditions which worsened between 1979 and 1986 have not been irreversible.

a)

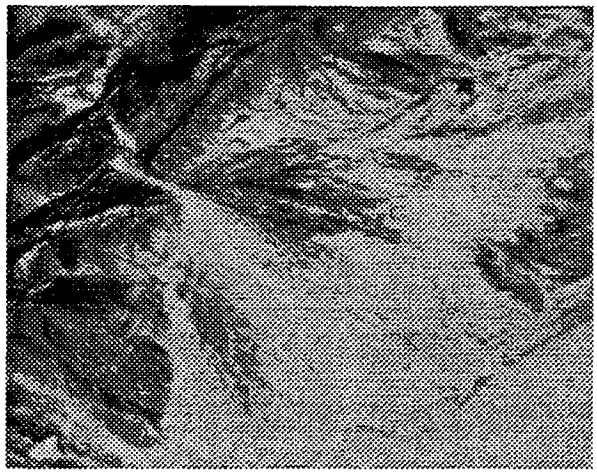

b)

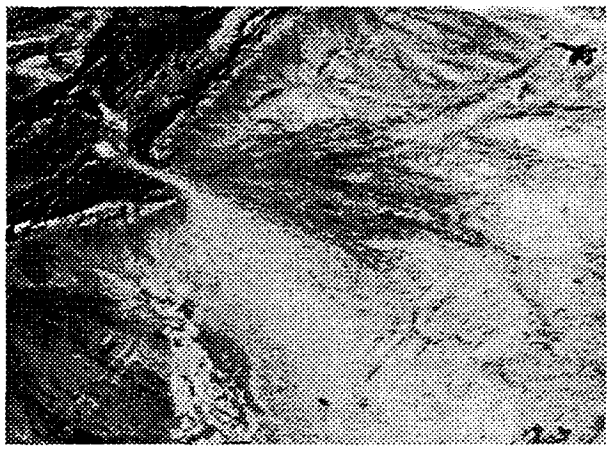

c)

Figure N°2: color composite images of a) Landsat MSS image of the 02.12.79. b) SPOT XS image of the 23.02.86 and c) Landsat TM image of the 01.01.89.

4.2. SAR ERS-1 images analysis

4.2.1. Description

The radar data were acquired by European Remote Sensing ERS-1 on 12 october 1992 and 01 november 1993. The radar was operated at C-band (5,3 Ghz, 5,66 cm wavelength) with polarization VV. The data were obtained at the incidence of 23° at the centre of image. The images are geocoded ellipsoid corrected (GEC type) and the pixel size is 12.5 m in both range (across flight) and azimuth (along flight)directions.The original 3 looks amplitude image of 12 october 1992 used in this study is shown in figure 5a.
Despite the presence of speckle, the dynamic of grey tones enables us to discriminate diffrent types of surfaces and vegetation units by visual interpretation.Very bright returns are due to the structural forms such as moutains of the saharian Atlas.Medium grey tones correspond to rubber trees mixed with steppic vegetation on mountain slopes. Black tones correspond to crops, bare soils and wetlands called dayas.

4.2.2. Interpretation of apparent grey tones

For vegetation surfaces, the backscattered energy results from different sources:(1) volume scattering by the vegetation, (2) surface scattering gy the ground and attenuated by the vegetation and (3) multiple interaction between the vegetation and the ground surface (NEZRI, 1993). Hence the radar scattering coefficient $\sigma°$ represents the incoherent sum of the three previous contributions:

$$\sigma° = \sigma° (s)\ T + \sigma° (veg) + \sigma° (int)$$

where $\sigma°$ (s) , $\sigma°$ (veg) and $\sigma°$ (int) denote the soil, vegetation and interaction contributions respectively and T is the transmission factor of the vegetation (ULABY & al, 1986).

In other respects, the two SAR images have been overlayed on a color composite image with the image of the 12 october 1992 in green and the image of the 01 november 1993 in red. the result obtained shows a large reddish part on the image which seems to correspond to a higher degree of moisture in the second image (01/11/93) than the first image (12/10/92). This conclusion is confirmed by the pluviometric information concerning this region.

5. MERGING PROCEDURES

In order to merge numerically SAR ERS-1 and TM channels where the comparison is valid because the two sets of data correspond to a wet year, we tested differents procedures derived from a general fusion data methodology. The synoptic of this methodology is shown in figure N°3. Mathematical as well as photographic procedures can be used to process the data: RGB display, linear and non-linear combinations of channels, principal components analysis (PCA) and IHS trasform are the principal image processing tools of data fusion.

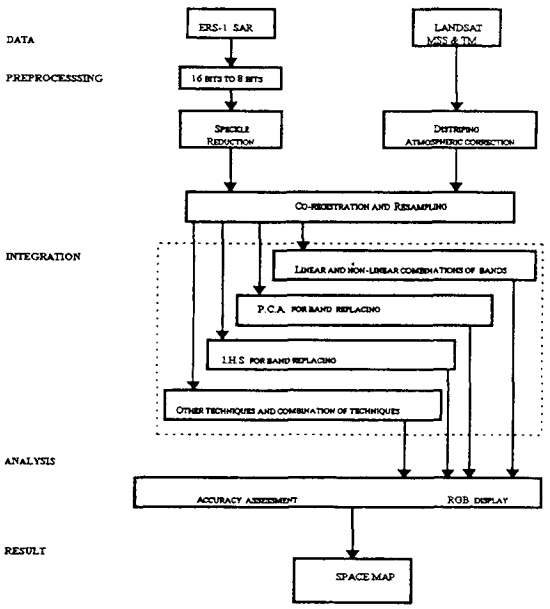

Figure N°3: synoptic of remotely sensed data integration adopted in ous methodology

5.1. Preprocessing

5.1.1. Speckle filtering

The presence of speckle in SAR images reduces the ability to perceive fine details and rules out a visual perception of systematic structures that would make it possible to describe a specific earth surface feature.

The effect of speckle in the radar image is a result of interaction of the coherent electromagnetic wave with a surface. Basically, it is the interference pattern resulting from the various returns from different scatterers on the illuminated surface. The complex amplitude of the field may be regarded as resulting from the sum of contributions from a large number of elementary scattering areas on the rough surface. Thus the phasor amplitude of the field can be represented by :

$$A(x,y,z) = \sum_{k=1}^{N} |a_k| \exp(i\phi_k)$$

Where $|a_k|$ and ϕ_k represent the amplitude and phase of the contribution from the k^{th} scattering area and N is the total number of such contributions. On the other hand, the irradiance $I(x,y,z) = A^2(x,y,z)$ obeys negative exponential statistics, and its probability density function is of the form :

$$p(I) = \begin{cases} \left(\frac{1}{\bar{I}}\right) \exp\left(-\frac{I}{\bar{I}}\right), I \geq O \\ O, otherwise \end{cases}$$

Where I is the mean of the intensity.

It is assumed that speckle has the characteristics of a random multiplicative noise (Lee, 1981) in that the noise level (or standard deviation) increases with the magnitude of radar backscattering (or the mean) (see fig.4).

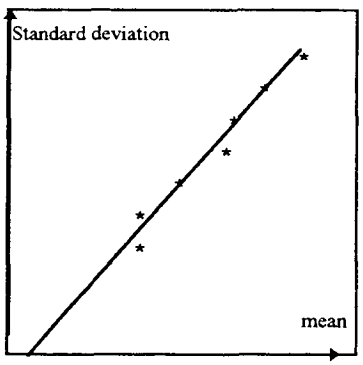

figure N°4: SAR speckle noise characteristics.

There have been many methods to reduce radar speckle described by many authors such as LEE (1981), FROST and al (1982), KUAN (1985), LOPES and al (1990), and CURLANDER and MCDONOUGH (1991). In general, these fall into one of two broad categories : pre-image (multi-look processing) and post-image (filtering) SAR processing.

On the one hand, with the advent of digital SAR correlation techniques it became easier to reduce speckle noise through multi-look processing, where several independent images (Goodman, 1976) are processed from separate portions of an aperture and recombined to reduce speckle, but unfortunately at the cost of a degraded spatial resolution. The improvement in signal to noise $(SNR)_A$ is proportional to the square root of the number of samples averaged.

$$A = \frac{1}{L}\sum_{K=1}^{L} A_K \quad \text{and} \quad (SNR)_A = \frac{(SNR)}{\sqrt{L}}$$

where :

A_K : K looks obtained by the same target.

L : Looks number.

A : Final value of pixel of multi-look image.

On a three-looks SAR image like ERS-1, the along track synthetic aperture antenna is divided into three sections or looks, and each look is processed independently. The three looks are registered and averaged. Hence, the speckle standard deviation is divided by a factor of $\sqrt{3}$ (Lee, 1981).

In the other hand, post-image speckle reduction can be achieved by spatial processing. Several studies have been carried out in order to evaluate the feasibility of different filtering techniques to reduce speckle noise (Mueller and al., 1989). Three important variables have to be defined when designing a filtering technique : i) filter algorithm, ii) window size, and iii) number of iterations.

Many filtering techniques exist and are carried out in the spatial domain as well as in the frequency domain. We have selected filters in the spatial domain because of their popularity in current literature.

There are filters which can reduce the noise effect, but only at the cost of blurred edges. Other filtering algorithms allow linear features to be preserved, but they are not effective for noise elimination purposes. In order to be considered as an ideal filter type for our investigation, three requirements should be met : i) high adaptivity : Homogeneous areas must be smoothed, edges and textures must be preserved, ii) no creation of artefacts, and iii) minimal textural information loss. For this reason, the following filtering algorithms were studied, implemented and compared.

-Median filter.

-Edge Preserving Smoothing filter (EPS).

-Local statistics method.

-Lee Sigma filter.

-Local Linear Minimum Mean Square Error Filter, LLMMSE (Kuan et al, 1985).

The filter assessment was achieved by an examination of their results according the two requirements: First a qualitative examination was carried out which comprises:

-Visual comparison between filtered images and the unfiltered image.

- Visual interpretation of the different images.

- 3D representation of different images.

Secondly, a quantitative examination was carried out by means of parameters indicating the loss of information:

- Computation of the mean and the standard deviation.

- Computation of the speckle index I_s which is given by the following expression :

$$I_s = \frac{\sqrt{\sigma_z^2}}{\bar{z}}$$

where $\sqrt{\sigma_z^2}$ is the standard deviation of the local area and $\bar{z}$ is its mean.

With the analysis of difference images (original minus filtered image) the information loss can be visualised. Median filter causes strong information loss, while the difference image for LLMMSE filter causes only minimal textural information losses.

Figures N°5 shows the original and some differently filtered images, 3D representation and image differentiation between original image and filtered images. A first visual comparison of the filters shows the superiority of the LLMMSE filter. It demonstrates good adaptivity as it smooths homogeneous areas while preserving fine details. The LSM filter shows adaptivity as well but fine details and edges are partially blurred. The median filter shows good relative results but it loses details. The EPS filter produces homogeneous regions and could be used in segmentation procedures; all details and textures are destroyed.

a)

b)

c)

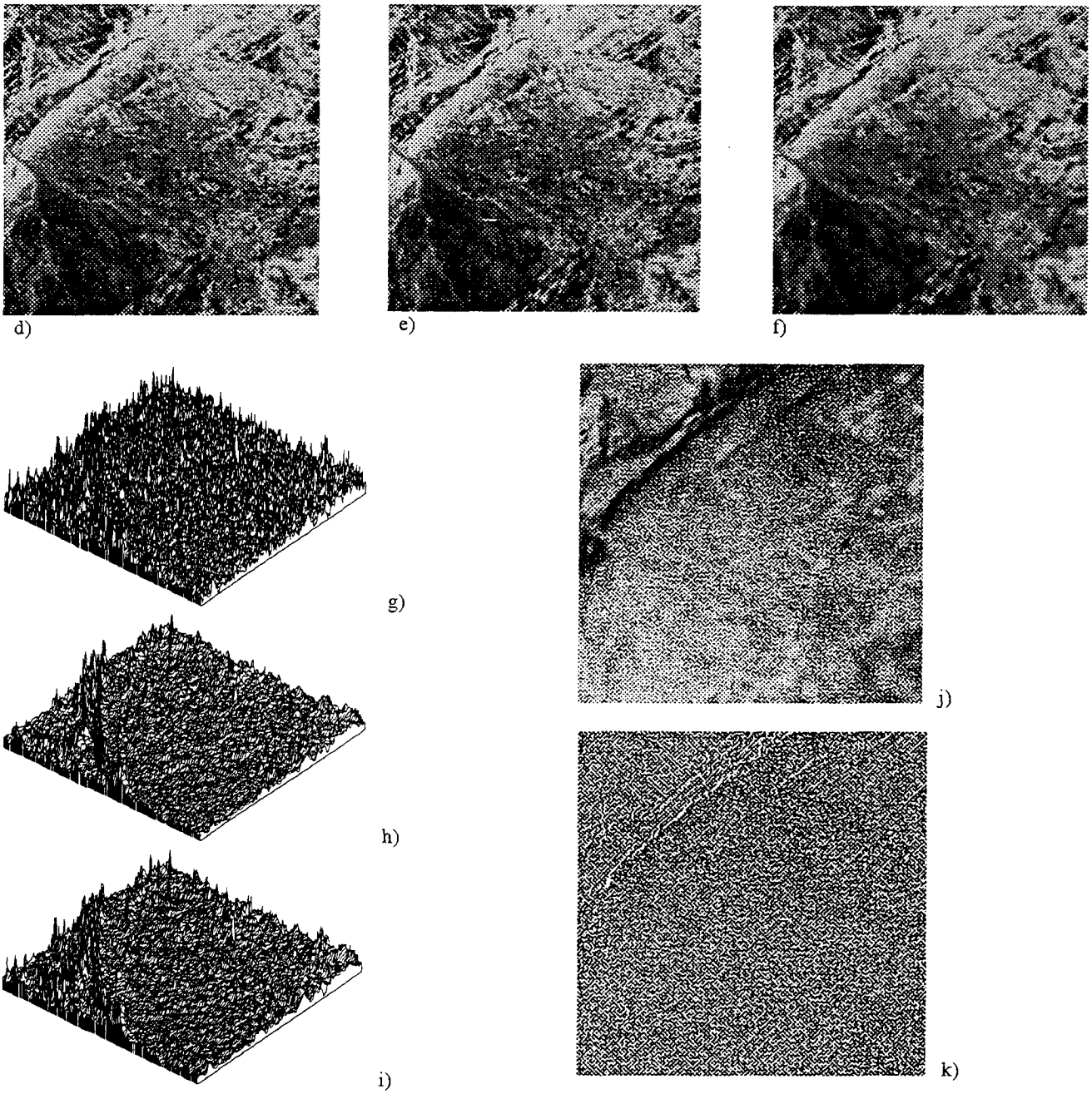

figure N°5: a) original SAR image, b) Median filtered image, c) EPS filtered image, d) Sigma filtered image, e) Modified LEE filtered image and f) KUAN filtered image. 3D representation of g) Original image, h) Median filtered image and i) Kuan filtered image. Image differentiation between original image with j) Median filtered image and k) Kuan filtered image

Filters	Variance	Mean	speckle index
original	464,54	92,04	0,23
Median 3x3	128,30	90,41	0,125
Median 5x5	94,92	88,94	0,109
Median 7x7	76,59	87,79	0,099
EPS 5x5	237,03	87,16	0,17
EPS 7x7	147,22	87,75	0,13
EPS 9x9	105,56	87,63	0,11
Sigma 3x3	223,86	90,07	0,16
Sigma 5x5	69,84	90,78	0,092
LSM 3x3	121,15	67,88	0,162
LSM 5x5	104,67	62,89	0,162
LSM 7x7	101,77	63,36	0,159
Kuan 7x7	76,39	43,94	0,198
Kuan 9x9	184,77	59,43	0,22

Table 2 : quantitative measures of the implemented filters.

It should be pointed out that a quantitative assessment (see table 2) becomes very difficult when there is no statistical easure that considers the advantages and disadvantages or describes the quality of a filter in an absolute way.

5.1.2. Geometric superposition

the TM image was coregistered to the SAR ERS-1 data and resampled to 25 m. The location of GCPs presented some dificulties, particularly in the mountainous zones .Their identification was also dificult because of, on the one hand, the limited grey level range over the land area and , on the other hand, a saturation by high backscattering on the montains. the correction was performed using 12 GCPs. The RMS error was less than 2 pixels in flat areas. A DTM is necessary to rectify the TM images with a high degree of accuracy even in the mountainous areas.

5.2. Integration techniques

Fusion of data from different sensors has been utilised in several computer vision applications. The motivation behind data fusion is to generate an interpretation of the scene not obtainable with data from single sensor. Effectively, it is interesting to combine data from optical and radar sensors, since the optical portion provided information concerning vegetation type, density and moisture content, while the microwave portion furnished information on surface roughness and texture.
The overall objective of this study is to determine if there are synergistic effects when digital spaceborne ERS-1 data are combined with Landsat TM data, and analysed using computer aided analysis techniques. The hypothesis is that the combined data set would improve the interpretation of steppic cover types compared to utilising data from either ERS-1 or Landsat TM alone. The tested different procedures are:

5.2.1. Color composite imagery

We used a color composite image with three channels whivh are: TM4 (red) corresponding to the vegetation channel, TM1 (green) corresponding to a brightness channel and SAR ERS-1 (blue) corresponding to a roughness channel. The resulting image of the figure N°6 allows us to distinguish areas with different roughness, vegetative areas and bright areas corresponding generally to bare soils.

Figure N°6: color composite image of channels TM4 (red), TM1 (green) and SAR ERS-1 (blue).

5.2.2. Principal component analysis:

Principal components analysis is a commonly used technique for remote sensing image analysis. It has been used for data enhancement (Gillespie and al, 1986) and is a statistical technique that transform a multivariate cerrelated data set into a data set consisting of new uncorrelated linear combinations of the original variables. The sum of the variance of the generated channels called principal components (PCs) is equal to the total variance of the initial variables. Each successive PC explains decreasing variance level . In this communication, we have used the PCA for merging microwaves and multispectral data using the SAR ERS-1 data and the TM channels as input data. PCA was performed over a representative 650 x 550 pixels zone (location on figure 1). The PCA was performed on centered and normalized values of the input channels. The first three principal components explain more than 99% of the variance. We note that CP1 is highly correlated with all optical channels (see figure)and negatively correlated with the radar band, and that CP2 is highly correlated with the radar band. Consequently, interesting features can be pointed out: PC1 appears to be a measure of brightness of the optical TM bands and the radar signal has a highly predominant effect on the PC2 since the hydrological network is enhanced. The following image (figure N°7) shows a color composite image of PCs channels.

Figure N°7: color composite image of Pcs channels.

5.2.3. I.H.S. transform methods

The I.H.S color transform method is a standard procedure in image analysis. It was succefully used for color enhancement of highly correlated data (GILLESPIE & al, 1986) and, more recently, to merge geophysical or geochemical data with radar images (HARRIS & al, 1990) . IHS refers to human color perception parameters. The intensity (I) corresponds to the total brightness of a color, the hue (H) to the dominant wavelenght to a color, and the saturation (S) specifies the purity of a color. For merging images, the IHS transform can be used by calculating the I,H and S parameters for a set of three original channels, which means coding the RGB display of an image in spherical or cylindrical coordinatesin the IHS color space. The merging of a fourth channel (i;e; highest resolution or microwave data) is achieved by using this one as the substitute for the

computed intensity. Then a reverse transform to RGB color space is performed. The resulting RGB composite image shows the combined information.
In such a merging procedure, the weight given to the substitute is crucial. There is a big difference between radar data on the one band and the visible or near infrared on the other. during the reverse transform, when a radar image is used as the intensity substitute, much spatial information provided by the Landsat TM data is blurred, and the hydrographic network from the SAR data is greatly enhanced. The weight accorded to SAR data is obviously too high. Best results are obtained with weighed data using the following formula proposed by YESOU & al (1993) and adaptaed to the Landsat TM data:

$$\delta . SAR + \beta . TM5 + \mu$$

TM5 is added because it provides the best information of all the themes with a good variance.
Different values of δ and β are checked (δ = 1 or 2, β = 1, 2 or 3 and μ is a scaling factor) . The use of this complex substitute replacing the computed intensity, with δ = 1, β = 1 and μ = 0, produces better results (figure N°8) than those using the radar data.

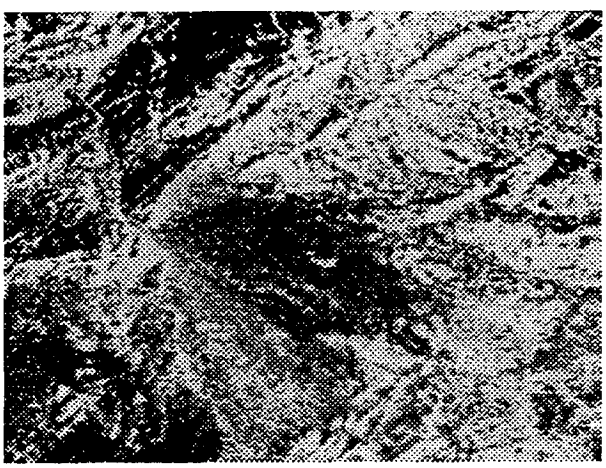

a)

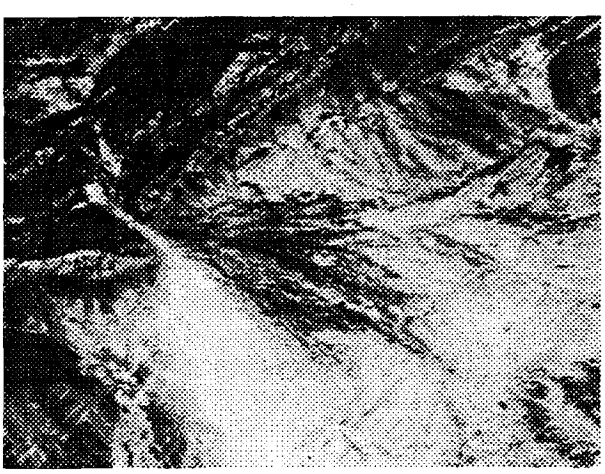

b)

Figure N°8: color composite image of obtained channels by reverse IHS trasform : a) SAR image replaces the intensity channel and b) SAR image replaces the saturation channel

5.2.4. Multisource classification:

The unsupervised classification is carried out according the following scheme described in the figure N°9:

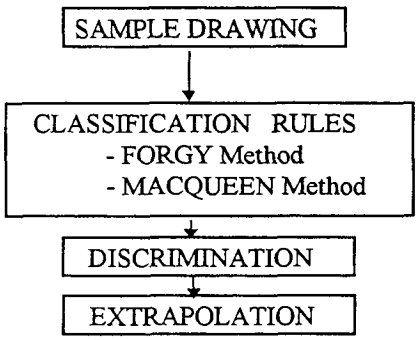

Figure N°9 : synoptic of the classification procedure

Two non supervised classification algorithms were used for this study. First, was the well-known K-means or Forgy classifier that processes the data which are sampled on a sample of 24964 pixels (about 10% of the whole image). The other algorithm used was the Mac Queen algorithm that uses only two iterations for the classification by contrast with the previous algorithm.
The classification results were evaluated with the investigation of aerial photographs (1973) which allowed us to obtain by photo-interpretation general cover types defined in the following map illustred in figure N°10:
-1- Bare soil (SN).

-2- Natural vegetation of wadi (VO).

-3- and -7- Steppe with Stipa tenacissima (SS).

-4- Presaharian species

-5- Sparse Steppe of Artrophitum Scoparium

-6-, -8- and -9- Steppe with Stipa tenacissima and hammada scoparia(SSH).

-10- Steppe with hammada scoparia (SH).

-11-Steppe with hammada scoparia and thymelaea microphylla (SHT).

-12- Cultures and fallows (CJ).

-13-, -14- and -15- Matorrals with Quercus ilex and Juniperus oxycedrus (M).

-16 and -18- Steppe with trees like Jupernicus phoenicia and stipa tenacissima (SA).

-TA-Gardens(J)

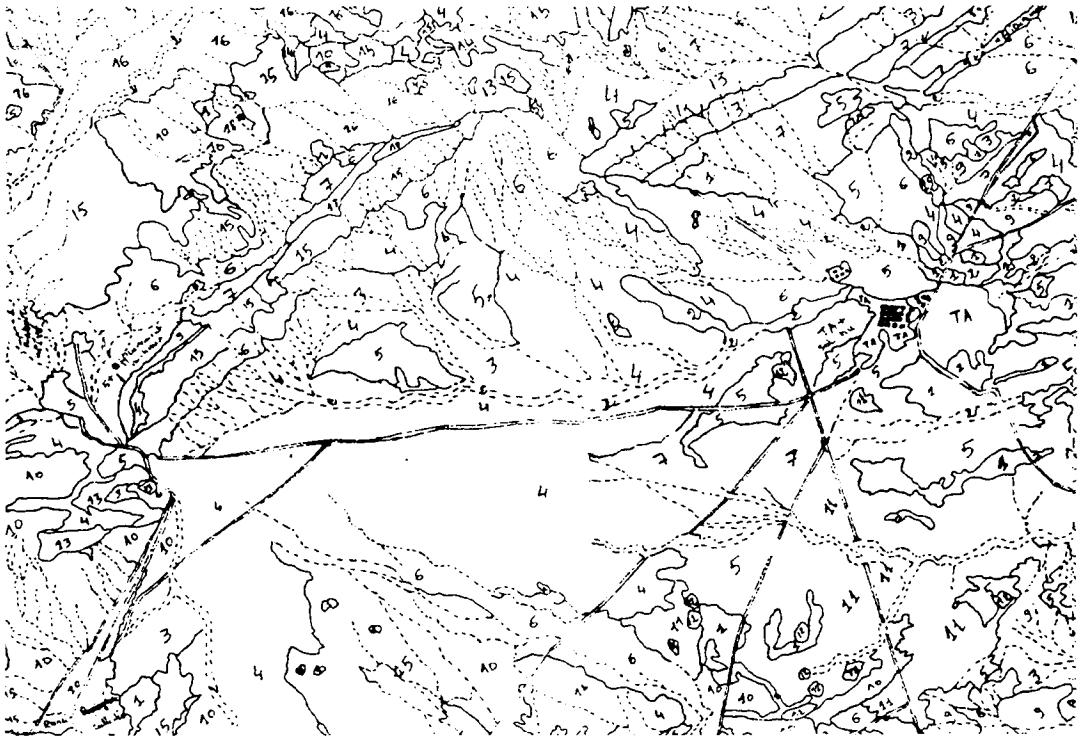

Figure N°10 : Map obtained by photo-interpretation of aerial photographs.

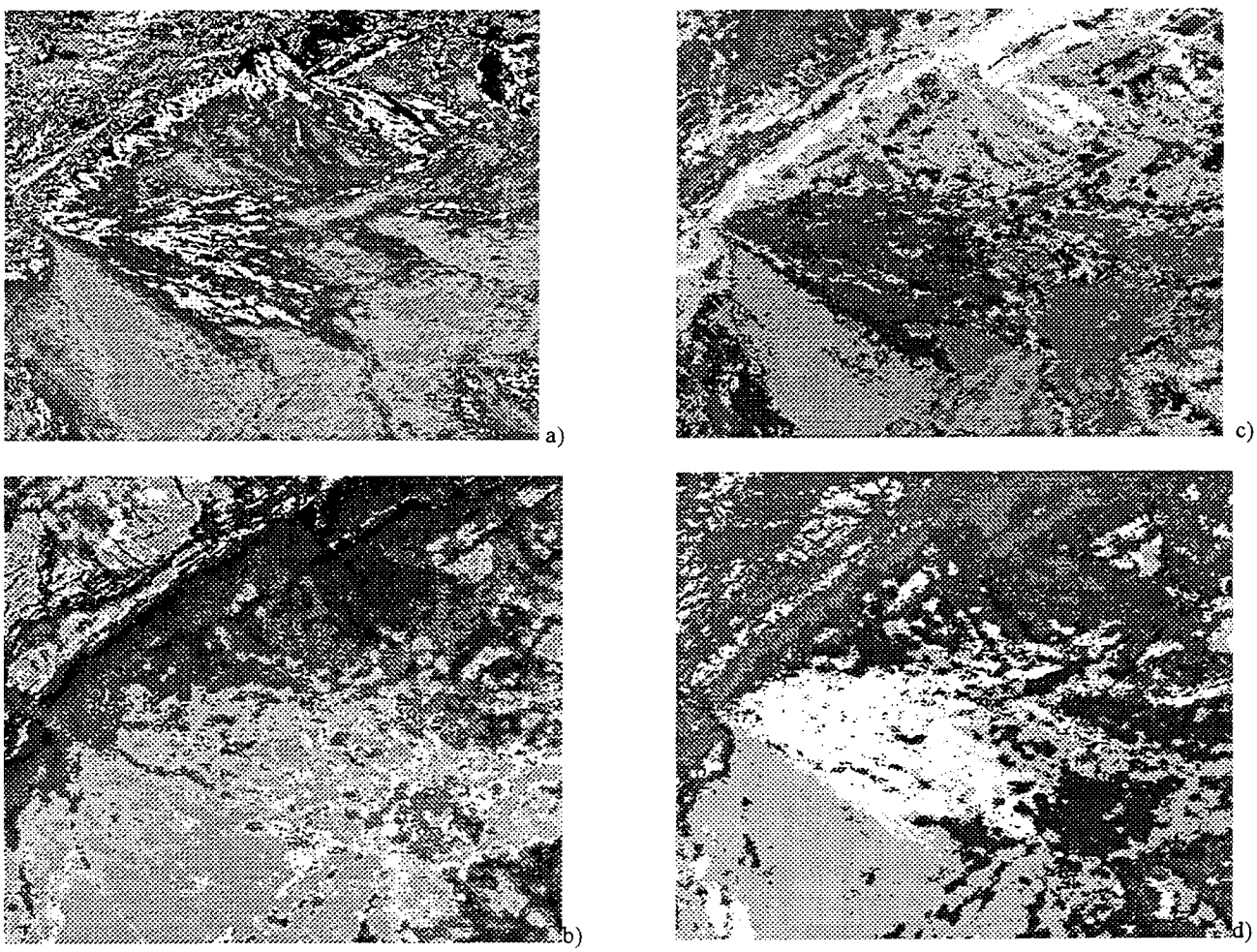

Figure N°11 : classified images of a) the Landsat TM data only by Forgy method, b) the two SAR images data by Forgy method, c) and d) the combined data (TM and SAR) by Forgy and MacQueen methods.

6. DISCUSSIONS AND CONCLUSION

This study shows the utility of remotely sensed data for vegetation cover assessment over arid and semiarid regions. The analysis of optical data obtained at different dates allowed us to determine changes concerning the natural or the cultivated areas as well as the action of the sand up in this steppic region. The satellites images have allowed us to grasp the vegetation in terms of cover rates. We distinguish the dense vegetation either natural or cultivated of dayas and rivers from the sparse steppic vegetation of hamadas and glacis (the cover rate is about 30%).

The analysis of the SAR data allowed us to distinguish the big features such as the mountains, the areas with medium roughness and the areas which appear black on the image (smoothed areas) corresponding to crops, dayas or bare soils.

When the use of merging techniques, PCA appears to be a good numerical procedure for merging SAR ERS-1 and Landsat TM data. On the PC color composite the hydrological network is greatly enhanced. In addition, wetsands (dayas) and moist soils are pointed out. The IHS transform is more difficult to use because , on the one hand, it works on only three channels and the choice of these channel is important and , on the other hand, the weight given to the substitute in the reverse IHS transform is crucial. The obtained result enhances also the hydrological network but is it more dificult to interpret than the PCA result. A judicious choice of combination of channels can improve this result.

The analysis of the multisource classification (SAR and TM data) allowed us to distinguish the big features such as the mountains, the areas with medium roughness and the smoothed areas corresponding to crops, dayas or bare soils. We can note that the spectral information (TM data) and the information concerning roughness are taken into account in these classifications.

The MacQueen classification is faster than the Forgy classification but it is less accurate (see figures 11.c and 11.d).

Considering the classification results, it seems absolutely necessary to filter speckle before any attempt at pixel-by-pixel classification. The difficulty in finding an ideal filter to reduce speckle for all types of SAR images leads the scientific community to develop specific filters according to different applications such as forested areas or vegetated areas and so on.

With the operational SARs presently in orbit (ERS-1, ERS-2, Almaz, and Radarsat) and the forthcoming spaceborne SARs (EOS-SAR, ENVISAT) such an optical and SAR data fusion is bound to become a major tool for vegetation assessment, in particular for worsening conditions of vegetation monitoring in fragile areas such arid and semiarid regions.

7. ACKNOWLEDGMENTS

The authors would like to acknowledge the European Space Agency (E.S.A) for providing the PRI and GEC type SAR ERS-1 data of the area of interest and for the image processing facilities of the European Space Research Institute (ESRIN) located at Frascati (Italy). The authors would like to acknowledge also K. CHELLAL, N. MEDJAHED and Y . BOUTABA for their contribution.

8. REFERENCES

BOUTABA, Y., BOUZENOUNE, A. & SMARA, Y., 1996. *Inventory of resources of arid region by aerial photographs and Landsat TM satellite images.* International symposium of International Space University. Preserving Earth and Improving Life.5-7 February 1996, Strasbourg, France.

CURLANDER, J.C. and McDONOUGH, R.N. 1991. *Synthetic aperture radar: systems and signal processing.* Wiley Series in Remote Sensing, Wiley & Sons, New-York, 647 p.

ESTORGES, P. 1965. *La bordure saharienne du djebel Amour.* Travaux de 'Institut de recherche saharien, vol XXIV, Alger, p. 31-46.

FROST, V.S., STILES, J.A., SHANMUGAN, K.S. and HOLTZMAN, J.C. 1982. *A model for radar images and its application to adaptative digital filtering of multiplicative noise.* IEEE transactions on pattern analysis and machine intelligence, vol. pami-4, n° 2, p. 157-165.

GOODMAN, J.W., 1976. *Some fundamental properties of speckle.* Journal of Optical Society of America, vol 66, n° 11, p. 1145-1149.

HAACK, B.N. and SLONECKER, E.T., 1994. *Merged spaceborne radar and thematic mapper digital data for locating villages in Sudan.* Photogrammetric Engineering and Remote Sensing,vol.60, n°10, p. 1253-1257.

JOLY,F., SIMONIN, A. & GUILLEMOT,J., 1986. *Interprétation géomorphologique de l'image SPOT du 23 Février 1986 concernant le djebel Amour (Algérie) et sa bordure saharienne.* Revue« Photo-interprétation », N°6,1986, pp 9-15.

KUAN, D.T., SAWCHUK, A.A., STRAND, T.C., and CHAVEL, P., 1985. *Adaptative noise smoothing filter for images with signal dependent noise.* IEEE Transactions on Pattern Analysis and Machine Intelligence, vol. pami 7, n°2, p. 165-177.

LEE, J.S. 1981. *Speckle analysis and smoothing of synthetic aperture radar images.* Computer Graphics and Image Processing, vol. 17, p. 24- 31.

LOPES, A., TOUZI, R. and NEZRI, E. 1990. *Adaptative speckle filters and scene heterogeneity.* IEEE Transactions on Geoscience and Remote Sensing, vol. 28, n°6, p. 992-1000.

METTERNICHT, G., 1993. *A comparative study on the performance of spatial filters for speckle reduction in ERS-1 SAR data.* Proceedings of the 13th EARSeL symposium, Dundee, Scotland, U.K., p. 275-282.

MUELLER,P.W. and HOFFER, R.N.,1989. *Low-pass spatial filtering of satellite radar data.* Photogrammetric Engineering and Remote Sensing, vol.55, n°6, p. 887-895.

NEZRI, E., MOUGIN, E., LOPES, A. & GASTELLU-ETCHEGORRY, J.P. 1993. *Tropical vegetation mapping with combined visible and SAR spaceborne data.* International Journal of Remote Sensing, Vol. 14, N°11, pp 2165-2184.

POHL, C. and VAN GENDEREN, J.L., 1994. *Geometric integration of multi-image information.* Proceedings of second ERS-1 symposium, 11-14 October 1994, Hamburg, Germany, p.1255-1260.

SMARA, Y., BELHADJ-AISSA, A., TAIBI, N. & MAHROUR, M. 1995. *Methodology for degradation monitoring in arid and semi arid region of southern Algeria using multidate remotely sensed data.* Proceedings of EARSeL Advances in Remote Sensing. Praha, Czech republic. p. 30-39.

SMARA, Y., LICHTENEGGER, J., BELHADJ-AISSA, A. & BOUZENOUNE, A. 1995. *Application of ERS-1 and optical data for vegetal cover assessment in a semi-arid region of Algeria.*15th Symposium of EARSeL, 4-8 September 1995, Basel, Switzerland.

SOLBERG, A.H.S., JAIN, A.K. and TAXT, T., 1994. *Multisource classification of remotely sensed data : fusion of Landsat TM and SAR images.* IEEE Transactions on Geoscience and Remote Sensing, vol. 32, n°4, p. 768-778.

YESOU, H., BESNUS, Y., ROLET, J., PION, J.C. and AING, A. 1993. *Merging Seasat and Spot Imagery for the Study of geological structures in a temperate agricultural region.* Remote Sensing of Environment, vol. 43, p. 265-279.

SENSITIVITY ANALYSIS OF ERS-1 SAR SIGNAL TO MULTISCALE-STRUCTURES OF THE TROPICAL FOREST BY MEANS OF THE WAVELET TRANSFORM

Marc Simard[1,2], Gianfranco DeGrandi[1], Keith P.B.Thomson[2], Marc Leysen[1]

[1]MTV, Space Applications Institute, Joint Research Center of CEE, Ispra, Italia.
fax: +39 332 78 9073

[2] Centre de Recherche en Géomatique, Université Laval, Ste-Foy, Québec, Canada.
phone: (418) 656-5491, fax: (418) 656-3607
E-mail: simard@crg.ulaval.ca

Abstract

The work presented here is part of the TREES Central Africa Mosaic project carried out in the Monitoring of the Tropical Vegetation Unit of the EC DG JRC Space Applications Institute. TREES (Tropical Forest Ecosystem Environment Monitoring by Satellites) in the current phase II is an EC project funded by DGXI and coordinated by MTV SAI, whose main goal is the set up of an operational tropical forest monitoring system.

This paper will focus on the sensitivity of the ERS-1 SAR backscattering to structures in the tropical forest. These structures are responsible for scene intrinsic texture in the image.

Since structures can exist at different scales, one needs a multiscale approach in order to measure the resulting multiscale texture. The analysis was done using a technique which decomposes an image into its different scales in order to identify the scales at which observable structures exist. In particular the technique is based on the Wavelet Transform.

In order to identify observable structures in the primary tropical forest at first speckle noise reduction is achieved using a technique that preserves the original space resolution.

Once a structure has been detected and observed in "low-noise" SAR image, it is possible to verify their detectability on a standard PRI format radar image. However the PRI images are heavily blurred by the presence of noise. The multiplicative characteristic of the speckle noise will modulate the image components at many scales. We must therefore also consider speckle contribution when using the wavelet decomposition for texture analysis. Such an analysis will allow us to evaluate a detection threshold for structures and intrinsic texture in the image.

Normalised scalograms or energy maps are built for different scales from the wavelet coefficients. It is seen that those maps bring complementary information related to the spatial context, and can discriminate different classes. It is also concluded that the multiscale texture are most readily detectable at larger scales.

Keywords: SAR, texture, wavelet, speckle, tropical

1. INTRODUCTION

Since space-borne radar sensors provide an all-time and all-weather surveying tool, they are ideal candidates for monitoring land cover when one needs continental-scale and on-demand coverage. One such case is the TREES Central Africa Mosaic Project [1, 2], in the framework of which the research presented in this paper is in progress. The mosaic is composed of over 450 ERS-1 images acquired over the entire bio-geographical domain of Central Africa. The images are 3-looks PRI format data with a 12.5 meter pixel size. The mosaic geographic position straddles the equator and therefore the ecosystem is imaged both in the dry and the wet seasons at the same time. Visual interpretation of the mosaic shows that a global classification is not possible on an intensity basis alone [3]. Indeed, what we observe are in some cases abrupt intensity changes in similar cover types at the space-time boundary, namely at places where due to the satellite finite imaging time (two adjacent frames in longitude are acquired roughly within 20 days), the natural target has undergone radar cross-section changes. We believe this is most probably due to meteorological factors such as rain and winds. Often, there is also a very small difference of backscatter (lower than 1dB) for different targets, such as primary and secondary forest. Therefore, a contextual parameter has to be defined. We expect a measure of texture to bring new information. But experience has shown that classical measures of texture such as first order and 2-points second order statisitics, are useless for classification purposes of ERS-1 SAR images of tropical forest. From visual inspection of the images, one can identify the large scale structures differences between targets (see Fig.2). This hints to multiscale texture analysis of the SAR images.

This paper focusses on the use of the Wavelet Transform as a contextual information extraction tool. The technique is very briefly introduced in section 2. Then the transform is applied on the SAR images and the results are discussed in section 3. We then conclude in section 4.

2. THE WAVELET TRANSFORM

The Wavelet Transform is an extension of the classical Fourier transform where a signal is decomposed onto an orthogonal basis. It is a mathematical tool which allows for mapping of a signal onto a finite support basis. The Wavelet Transform represents the original signal at different scales and positions in space. Because the basis has a finite support, contrarly to the Fourier transform, one can obtain both frequency and spatial information. The interested reader can refer to a tutorial paper by Rioul and Vetterli [4]. The transorm allows for a multiresolution analysis of the signal and is a very interesting tool for multiscale analysis of images.

The components of the signal at different scales and spatial locations is computed from the inner product of the signal I(x,y), and a wavelet $\psi(a,b)$ such that:

$$c_{a,b} =< I, \psi_{a,b} > . \quad (1)$$

where a and b are the scale and translation (position) parameters respectively. $c_{a,b}$ is the wavelet coefficient and represent the signal I at a scale a and position b.

The wavelets $\psi(a,b)$ can be thought as a band-pass filter and can be assimilated to a subband coding scheme. An efficient algorithm was developed by Mallat [5] for image analysis. It consists of a series of high-pass and low-pass filtering steps followed by subsampling. The algorithm results in the construction of low-pass versions (lower resolution) of the original image and its components on the wavelet basis. The wavelet algorithm also provides directionality information, and in this way the image structures are represented according to their orientation in the image plane.

3. APPLICATION OF WAVELETS TO THE SAR IMAGES OF THE TROPICAL TROPICAL FOREST

The Wavelet Transform is a relatively new tool for image analysis. Few authors have reported about the Wavelet Transform of SAR images in the international litterature [6][7][3], eventhough it has been extensively used for processing of other types of signal and for data compression. The implication of SAR correlated multiplicative speckle noise has been studied by Simard et al.[8], and it was concluded that to avoid multiplicative noise modulation for the analysis of texture, the wavelet coefficients should be normalised. An example of the application of this technique is illustrated next.

The original SAR image is shown on Fig.2. Two main classes are of interest in this image because they cannot be distinguished by average intensity alone: the degraded and primary tropical forest. The degraded forest is composed of patches of forest, agricultural fields and small savannas. The primary tropical forest is a homogeneous region of dense vegetation.

The image was then decomposed in the quadratic spline wavelet basis up to a scale of 200m with respect to the original 12.5m pixel size. Scalograms or energy maps can be constructed for each scale. In order to gather all available contextual information, we have added quadratically the wavelet component of the three different orientations. The resulting scalograms were then normalised by the low-pass version containing average intensity information at resolutions lower than the studied scale in order to avoid speckle modulation. Fig.3 shows the resulting energy maps which contain information due to intrinsic texture of the scene. Contribution from noise is the same for all targets independently from the average intensity. The algorithm is shown on Fig.1

The procedure was repeated for a "low-noise" and a "noise-free" image. The latter was constructed from the quadratic average of 18 images of a temporal series of the same scene, without regards to average intensity changes. It gives only a way of evaluating the structures detectable by ERS-1 configuration and does not mean the same structures can be found in a single PRI image. The "low-noise" image is constructed from the quadratic average of 3 images, where the average intensity was considered constant.

Such energy maps are presented on Fig.3. Texture distinction between degraded (top left) and primary tropical forest (center left) is very clear at a scale of 200m.

4. CONCLUSION

We conclude that texture exists at large scales in SAR images of the tropical forest enventhough it is not measurable with classical techniques. From a multiresolution analysis it is possible to retrieve that contextual information which could then be used for classification. The wavelet decomposition provides a very efficient way of analysing multiscale SAR image texture which is found at scales larger than a 100m. The energy maps provide information which is independent from the average intensity of the different classes. From the energy maps of Fig.3, it is

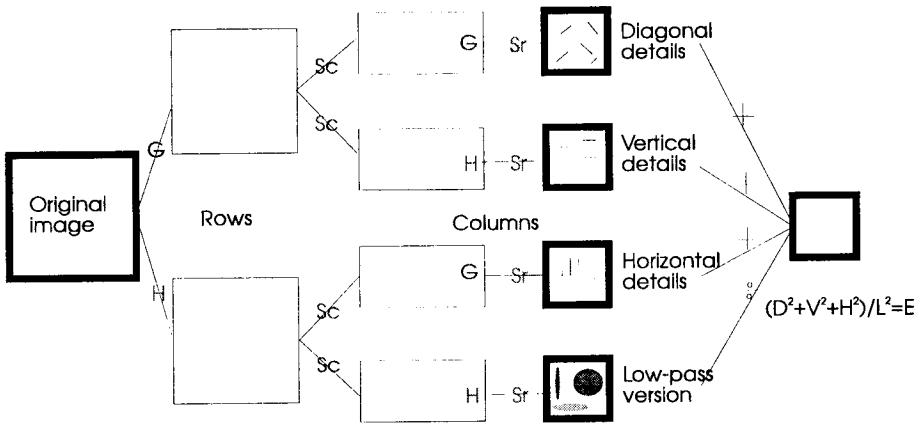

Figure 1: The algorithm for construction of energy maps. The first part corresponds to Mallat's algorithm where the rows and columns are filtered succesively with high-pass filter G, and low-pass H. Each filtering is followed by subsampling of columns (Sc) and rows (Sr). The detail images are quadratically added (+) and normalised (÷) by the low-pass image to obtain the energy map (E) at a given scale.

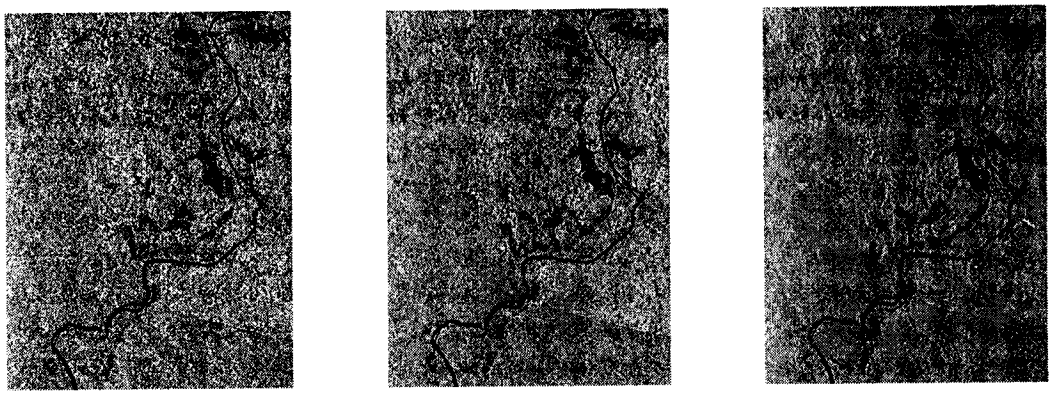

Figure 2: (left) ERS-1 PRI image with a 12.5m pixel size and 25m resolution of a tropical forest region located in Sassandra, Ivory coast. Noise is reduced by quadratic averaging of 3 (center) and 18 (right) PRI images of the scene.

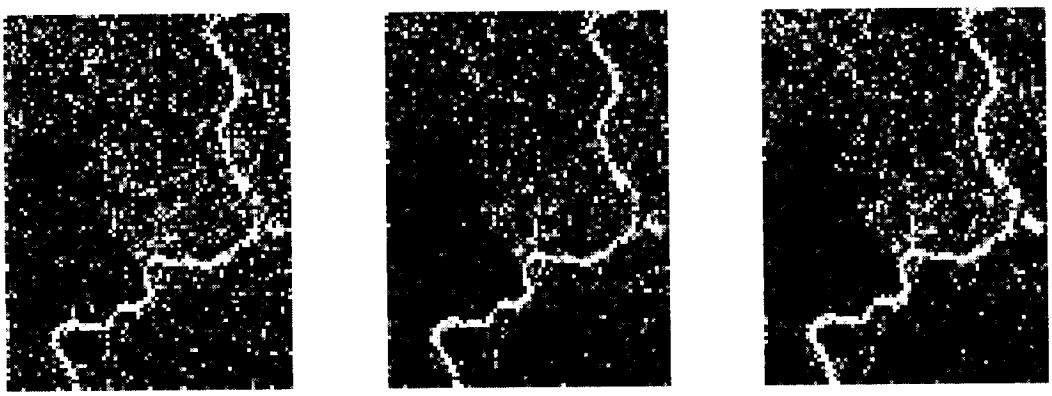

Figure 3: Energy maps at a scale of 200m constructed from a raw PRI image (left), from the quadratic average of 3 (center) and 18 (right) PRI images respectively. It is seen that the different targets such as the degraded forest (top left) and primary tropical forest (center left of river) can be discriminated from their texture content at large scales.

seen that the structures are most easily detectable for images with lowest noise, but a visual inspection of Fig.3 also demonstrates the efficiency of the algorithm in extracting multiscale intrinsic texture information from the standard ERS-1 SAR PRI images.

More work is in progress to characterise different targets (classes) and understand the information extracted from the energy maps. That new information will be at a later stage implemented in a classification scheme.

References

[1] J.-P. Malingreau, F. DeGrandi, and M. Leysen, "Trees/ers-1 study:significant results over central and west africa," *Earth observation quarterly,ESA*, vol. 48, pp. 6, 1995.

[2] J.-P. Malingreau and G. Duchossois, "The trees/ ers-1 sar'94 project," *Earth observation quarterly,ESA*, vol. 48, pp. 1, 1995.

[3] M. Simard, F. DeGrandi, K.P.B. Thomson, and G.B. Bénié, "Analyse multi-échelle de la texture de la mosaique ers-1 de la forêt tropicale africaine," *CDROM du 9^e congrès de l'association québécoise de télédétection, Québec*, 1996.

[4] O. Rioul and M. Vetterli, "Wavelets and signal processing," *IEEE SP magazine*, vol. 10, pp. 14, 1991.

[5] S.G. Mallat, "A theory for multi-resolution signal decomposition: The wavelet representation," *IEEE Transactions on pattern and machine intelligence*, vol. 11, no. 7, pp. 674, 1989.

[6] R. Fau, G.B. Bénié, J.-M. Boucher, and D.-C. He, "Segmentation markovienne pyramidale d'images," *Journal canadien de teledetection*, vol. 20, no. 2, pp. 150, 1994.

[7] L.-J. Du, J.-S. Lee, K. Hoppel, and S.A. Mango, "Segmentation of sar images using wavelet transform," *International journal of imaging systems and technology*, vol. 4, no. 0, pp. 319, 1993.

[8] M. Simard, F. DeGrandi, K.P.B. Thomson, and G.B. Bénié, "Analysis of speckle noise contribution on wavelet decomposition of sar images," *Submitted IEEE Transactions on Geoscience and Remote Sensing*, 1997.

MONITORING OF INTENSIVE AND EXTENSIVE LAND USE WITH MULTITEMPORAL ERS AND LANDSAT/TM DATASETS IN THE DISTRICT OF GOETTINGEN (LOWER SAXONY)

Bernd Schieche, Holger Schepp, Peter Hurlemann

Institute of Geography, Dept. of Cartography & Remote Sensing
Goldschmidtstr. 5, 37077 Göttingen, Germany
phone: +49 551 39 8003, fax: +49 551 39 8006
Email: bschiec@gwdg.de, hschepp@gwdg.de, phurlem@gwdg.de

ABSTRACT

The possibilities of registering the agricultural landuse of large areas rapidly and site-related are checked for the District of Göttingen, based on two LANDSAT/TM and nine ERS-1 images acquired in 1995. The data have been analyzed by the combined use of unsupervised classification (ISODATA) and supervised classification (Max. Likelihood). The analysis is based on a test site of 774 ha and related to the total crop area of the District of about 57000 ha. Four classes of arable crops and two classes of extensive landuse have been separated.

The use of LANDSAT data of the growing season was restricted to the only two available cloud-free images of the test site and to the single cloud free image of the total District. A sufficiently accurate result could not be achieved by this data.

The multitemporal analysis of the ERS data is based on time series of six and of nine images, as a consequence of an analysis of the backscatter factors and of the temporal signatures. The results of the analysis of the time series are validated by the confusion matrix of the test site and in comparison with the official statistics of the District. Related to the true acreage, the areas of the separated classes differ by less than 6 % (series of six images) and 4 % (series of nine images) as for the test site and by less than 13 % (series of six images) and 6 % (series of nine images) as for the District. The ERS system thus proves to be a useful data source for large-scale agricultural statistics.

1. INTRODUCTION

Since 1988 the European Union has been carrying out the project "*Monitoring of Remote Sensing (MARS)*" - a project on collecting and interpreting crop statistical information. Its aim is to complete, to standardize and to interpret the various national agricultural reports (TERRES et al. 1995). By combining the different data by GIS inventories can be made and changes can quickly be recognized (STADLER 1991). The European Union presently relies on area-based satellite data to control subsidized fallow land. In 1993 about 35,000 requests were under consideration in 11 member states (TERRES et al. 1995). In Germany as well, satellite remote sensing has been used as a time-saving and staff-reducing method to control fallow land. In 1995, this method was applied in about 1250 cases (OKONIEWSKI 1996). It has already been decided to extend this method.

Taking the District of Göttingen as a typical example of a Central European agricultural landscape the main aim of this investigation is to find out whether satellite data provide useful agrostatistical information (SPÖNEMANN & SCHIECHE 1997). The operational possibilities of passive (LANDSAT/ TM) and active systems (ERS) are compared. The ERS data have been received through the second ESA ERS Announcement of Opportunity (AO2). The project is supported by the Deutsche Agentur für Raumfahrtangelegenheiten (DARA).

2. DATA

As the District of Göttingen is registered by three orbits, at times daily (by the descending orbit), at times at night (by the ascending orbit) a total of twelve satellite images were acquired between April and October 1995. Nine of them were used for classi-fication.

2.1 IMAGE PROCESSING

After having geocoded and co-registrated all the ERS data as well as subsequently having corrected terrain distortions with the help of GIM it was passed through the Enhanced-Frost and the Gamma-Map-Speckle filter. In order to reduce the amount of data the grey-value spectrum of the ERS 16-Bit original data was scaled down to an 8-Bit grey-value spectrum.

2.2 GROUND CHECK

Out of the 254 - uniformly utilized - plots of the 774 ha big testsite a total of 60 fields was closely examined per overflight applying the following parameters: growth height, growth stage, coverage, row direction, surface roughness, soil moisture, dry biomass, plant moisture of the biomass.

3. BACKSCATTER FACTORS

The basic parameters of the reflecting surfaces responsible for the power of the radar echo are known. In order to make the operational analysis of radar data easier the factors which are involved in the reflection are divided into three groups, which will be treated separately (SPÖNEMANN & SCHIECHE 1997). When analyzing the data **permanent factors** will be regarded as regional constant factors. The terrain exposition has already been taken into account (SCHEPP 1996).

The **seasonal factors**, which are the result of the surface changes during the growing period, constitute the basis for the multitemporal evaluation of the satellite radar data. The regularities of the radar echo are a consequence of the regularly temporal succession of the soil cultivation, of the coverage and the biomass, of the plant structure and the surface roughness. It is only because of the resulting temporal signatures that an operational application of the radar data is possible.

Temporary factors are factors which influence the radar echo as a consequence of external effects only for a short time (see ESA SPECIALIST PANEL 1995). Actual soil moisture, interceptic water, and when images are aquired at night, dew moisture are the most important ones. Often these changes reinforce the surface's classification features, but sometimes they have the opposite effect, i.e. they must be regarded as sources of disturbance.

4. TEMPORAL SIGNATURES

As a consequence of the dominance of the seasonal reflection factors there is such a difference between the temporal signatures that 4 to 6 ERS images are sufficient to separate most crop types (see fig. 2).

Permanent grassland and fallow land show minor effects on the reflection, which - in addition - is usually relatively low throughout the year. Variations (see fig. 2) occur due to cutting and pasturing and depend on moisture contents of soil and plants. The reflection is increased as a consequence of less volume scattering or decreased because of long dry spells.

The temporal signatures of the set aside fields are normally very irregular. It depends on the state of vegetation or tillage whether seasonal or temporal factors dominate the backscatter values. Indeed the only common feature is their permanently high variation (see fig. 3).

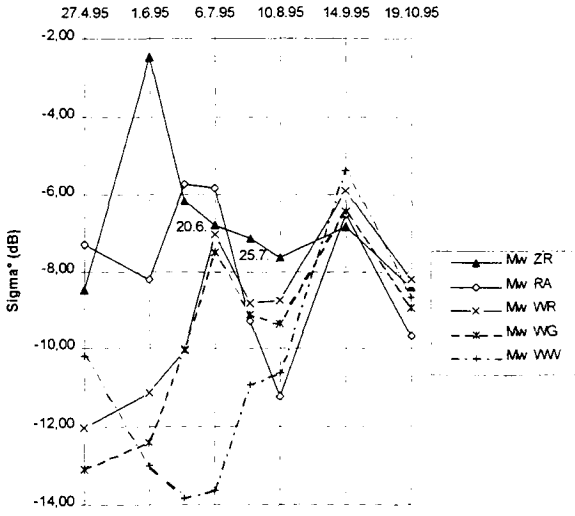

fig. 1: Mean (Mw) temporal signatures of main crops (ZR: sugarbeet (n=16); RA: rape (n=7); WR: Winterrye (n=3); WG: winter barley (n=10); WW: winter wheat (N=10))

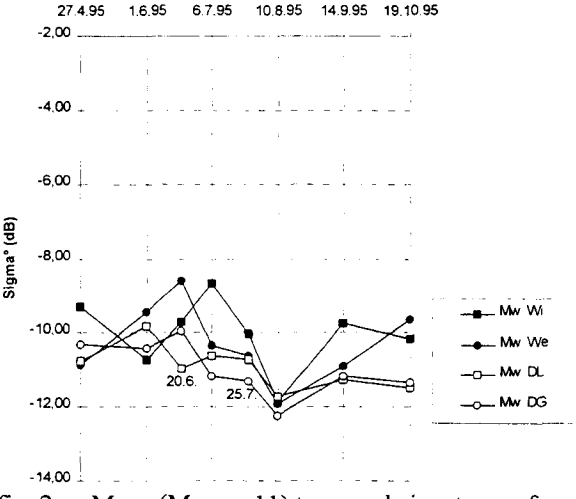

fig. 2: Mean (Mw: n=11) temporal signatures of grassland (Wi & We) and permanent fallow (DL & DG).

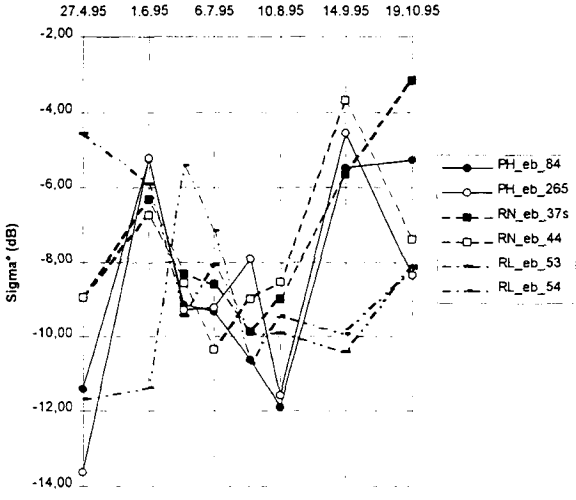

fig. 3: Temporal signatures of short term fallow (Ph: Phacelia; RN: various; RL: clover/grass)

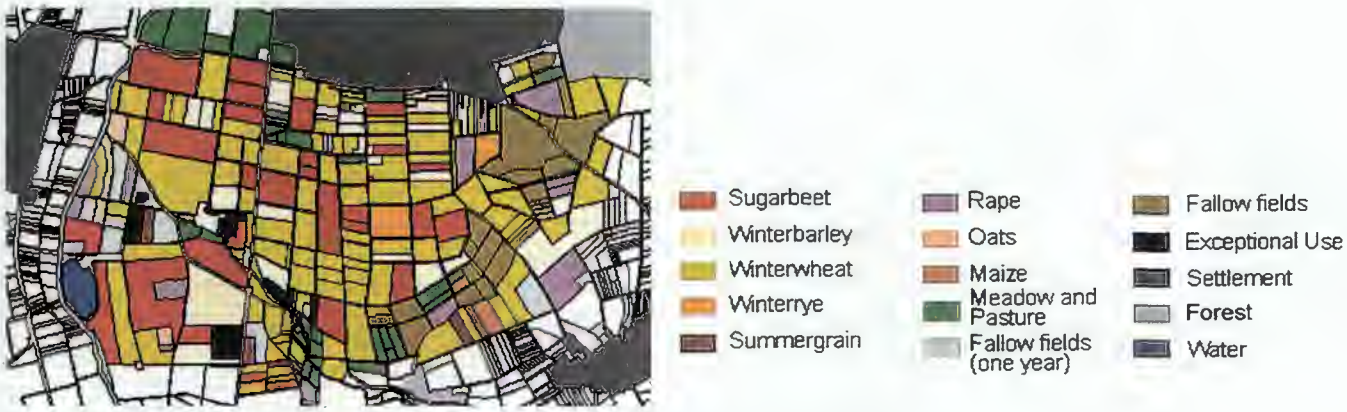

fig. 4: Reference map of landuse (from ground check) of the test site Reinshof 1995

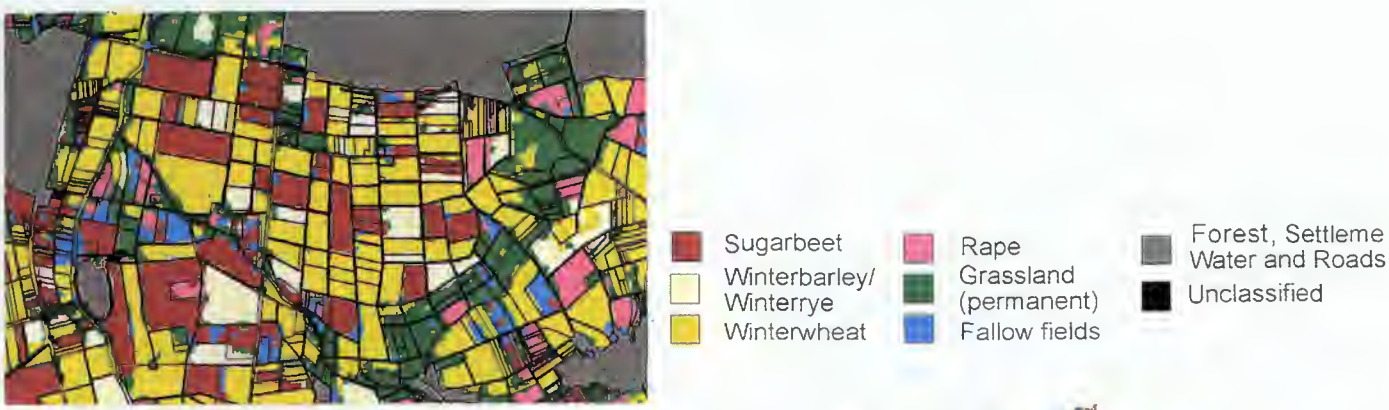

fig. 5: ERS-1 multitemporal landuse classification of the test site Reinshof (nine dates 1995)

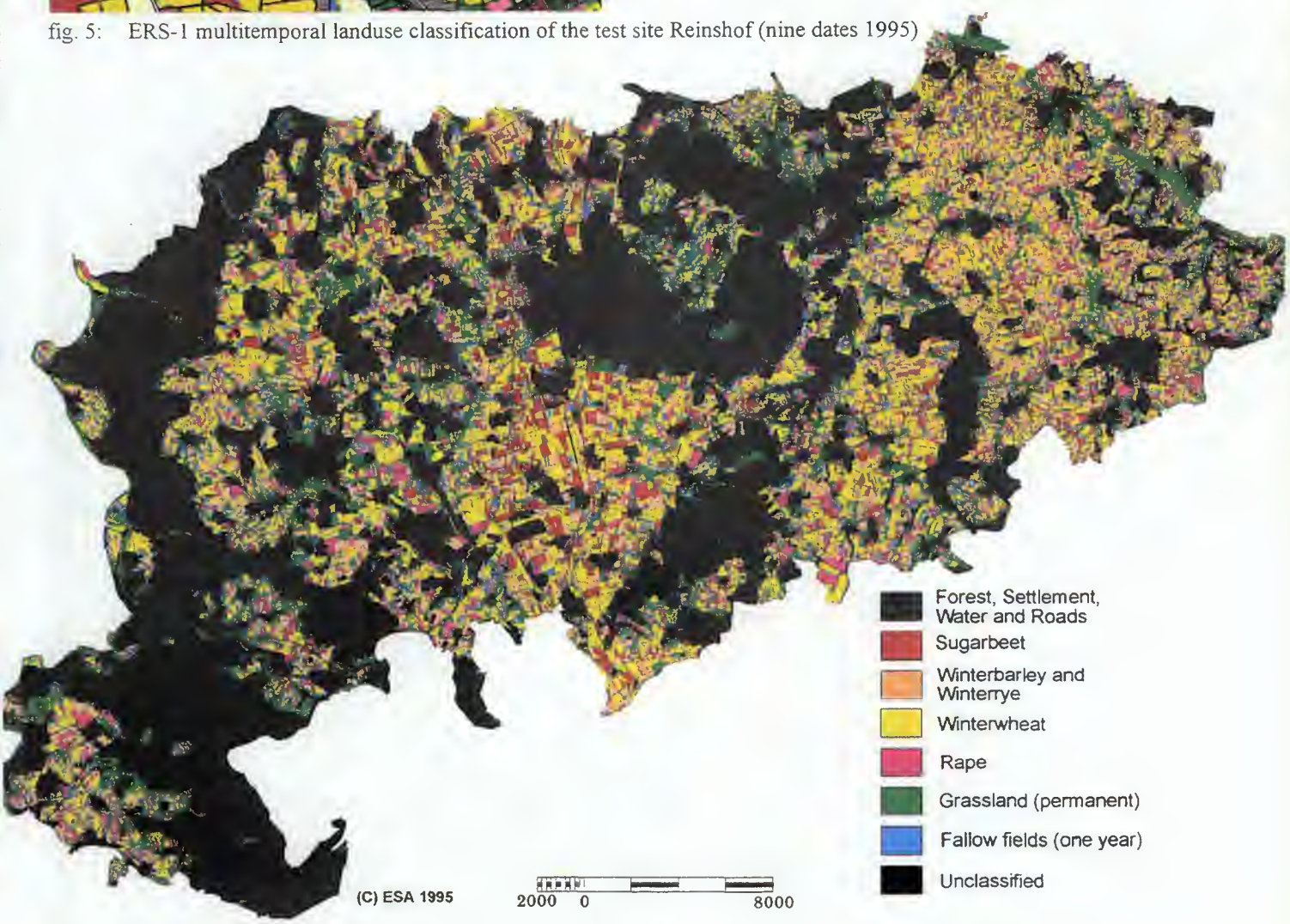

fig. 6: ERS-1 multitemporal landuse classification of the District of Göttingen (nine dates 1995) (HURLEMANN 1997)

5. CLASSIFICATION RESULTS

The cluster analysis with the help of ISODATA has proved to be the most effective procedure. But not all arable crop types were registered. Among the about 7% others (tab. 1) corn (2,6%) and oats (1,4%) represent the biggest classes, i.e. all relevant crop types were taken into account.

		(a) Tes site		(b) Di trict	
		ha	%	ha	%
Agricultural land use	Alu	773,69	100,0	5700	100,0
Winterwheat	Ww	304,11	39,3	1746	30,6
Winterbarley and -rye	Wb+Wr	98,28	12,7	1035	18,2
Sugarbeet	Sb	157,27	20,3	385	6,8
Rape	Ra	39,56	5,1	570	10,0
Grassland (permanent)	Gr	125,11	17,5	922	16,2
Fallow fields (one year)	Ff	39,36	5,1	637	11,2
Others				403	7,1

tab. 1: Reference data for classification results;
source: a) own mapping
b) Statist. Berichte Niedersachsen.

6. RESULTS

The crop types summer wheat, oats, corn and special cultivation (small experimental plots), which are only represented in a small number of fields, evidently could not clearly be separated. In contrast to the evaluation of the ERS data, winter barley and winter rye could be separated using LANDSAT/TM data. For reasons of comparison they have been grouped together in the statistics (tab. 2). The permanent grassland (pasture and meadow) had to be grouped together with the permanent fallow land as these two crop types could not be separated even in the field.

On the test site Reinshof only sugarbeet and grassland could be registered satisfactorily with the monotemporal LANDSAT/TM-classification (tab. 2). The total accuracy of 76,7% (tab. 4) is relatively small. The bitemporal classification of 83,4% can be regarded as a satisfactory result. Apart from sugarbeet and greenland winter wheat as well was distinguished relatively well. The area variations remain below 4% but the value of fallow land is not very convincing in view of the very low classification accuracy of R_{CM}= 31,1%. The ERS data with 6 dates make it possible to register the test site Reinshof with a total accuracy of 82,4%, i.e. they are as accurate as the bitemporal LANDSAT/TM-classification. The area variations as well are of that scale. With 9 dates a significantly higher accuracy of 87,7% is achieved and the area variations are adequately smaller. The most important improvement concerns the fallow land of which the low $Diff_A$- value stands for a realistic scale of registration.

The efficiency of the satellite radar is shown when a classification on the basis of 6 dates is compared with the reference map (fig. 8 & 9). Apart from the fact that by grouping some crop types together, the number of classes is reduced and the less represented crop types are neglected, the registration of the arable crops and the permanent grassland is more or less correct. The parcels of the set aside fields have also been registered to a remarkable extent.

The result of the monotemporal LANDSAT/TM evaluation with an overall accuracy of 40% is useless. The ERS data with 6 images show an total accuracy of 71%, with 9 images a total accuracy of 82% (tab. 4). With 6 classes this value represents a relatively low error rate, expressed by the very minor deviations ($Diff_A$) of the area (tab. 3).
A visual check of the classification (fig. 6) confirms a more or less correct registration. The minor deviations of the $Diff_A$-values from the official statistics can therefore be regarded as a useful result of the ERS data analysis.

	LANDSAT - TM		ERS - 1	
	monotemp.	Bitemp	6 data takes	9 data takes
Test site	76,7%	83,3%	82,4%	87,7%
District	39,8%	-	70,8%	82,4%

tab. 4: Overall accuracy of classification with different data sets.

7. CONCLUSIONS

The recent advantages of optical sensors like that of LANDSAT/TM can hardly be used operationally because of insecure weather conditions and resulting restrictions of data availability. On the contrary in Europe satellite radar offers a reliable data source for monitoring and registering of agricultural land use.
The aim of the use of remote sensing data is not to replace or to improve official statistics (BRADBURY 1994), which in Germany are regulated by law (Bundesgesetzblatt). But special requirements of agricultural statistics can be fulfilled by satellite data, i.e. the already mentioned efforts to standardize the different national agrostatistical datasets and the European Statistical Office's (Eurostat) demands to estimate the main crops acreage in spring and to make detailed inventories.
The results which have been achieved up to now by satellite radar raise expectations in even higher accuracy using new techniques like interferometry, multipolarization and multifrequency.

8. REFERENCES

BRADBURY, D. (1994): Statistische Systeme zur Messung von Fläche, Erzeugung und Ertrag. Statistisches Amt der Europäischen Union (EUROSTAT), Studie Nr. 38540006: 1-33.

ESA SPECIALIST PANEL (1995): Satellite Radar in Agriculture. Experience with ERS-1. European Space Agency ESA SP-1185. Noordwijk, 69 S.

HURLEMANN, P. (1997): Möglichkeiten der Landnutzungsklassifikation mittels ERS-1-Radar- und LANDSAT/TM-Aufnahmen im Landkreis Göttingen. Geographische Diplomarbeit Univ. Göttingen, unveröff.

OKONIEWSKI, J. (1996): Kontrolle der flächengebundenen Beihilfen durch Fernerkundung. Informationen für die Agrarberatung 9/96: 6-8.

SCHEPP, H. (1996): Die Abhängigkeit des ERS-1 Radarechos von der Exposition. Eine multitemporale Untersuchung aus dem Landkreis Göttingen. Geographische Diplomarbeit Univ. Göttingen, unveröff.

SPÖNEMANN, J. & B. SCHIECHE (1997): Satellitendaten als Mittel der Erfassung landwirtschaftlicher Bodennutzung am Beispiel des Landkreises Göttingen. Göttinger Geographische Abhandlungen, Bd. 100 (in press).

STADLER, R. (1991): Schritte zur operationalen Einbindung der Satellitenfernerkundung in die amtliche Statistik. Ber. Gesellsch. Informatik i. d. Land-, Forst- und Ernährungswirtschaft, 1: 17-25.

STATISTISCHE BERICHTE NIEDERSACHSEN (1996): Bodennutzung und Ernte 1995. Niedersächsisches Landesamt für Statistik. Hannover.

TERRES, J. M., J. DELINCE, M. VAN DE STEENE & A. HAWKINS (1995): The use of remote sensing and GIS capabilities to support the Reform of the Common Agricultural Policy of the European Community. Remote Sensing Review 12: 53-60.

	LANDSAT/TM				ERS-1			
	monotemporal [1]		bitemporal [2]		6 data takes [3]		9 data takes [4]	
	R_{CM} [%]	$Diff_A$ [%]	R_{CM} [%]	$Diff_A$ [%]	R_{CM} [%]	$Diff_A$ [%]	R_{CM} [%]	$Diff_A$ [%]
Ww	81,8	-7,1	90,5	-3,6	85,7	-5,6	90,5	-3,7
Wb+Wr	45,7	-6,1	73,1	-3,8	76,3	-3,0	83,3	-2,1
Sb	97,0	-0,6	90,7	-1,9	92,5	-1,5	92,6	-1,5
Ra	67,3	-1,7	70,7	-1,4	77,9	-1,1	80,7	-1,0
Gr	85,7	-2,5	86,5	-2,7	77,7	-3,9	86,4	-2,4
Ff	11,3	-4,5	31,3	-3,5	52,0	-2,5	68,1	-1,6
not or wrong classified		23,3		16,6		17,6		12,3

[1] 3.5.95; [2] 3.5.95 + 29.6.95; [3] 2.4., 27.4., 7.5., 1.6., 6.7., 16.7.95; [4] 2.4., 27.4., 7.5., 1.6., 6.7., 16.7., 10.8., 14.9., 19.10.95

tab. 2: Classification results of the testsite; R_{CM}: Results of the confusion matrix, $Diff_A$: Differences between reference area and classification area as proportion of the testsite area.

	LANDSAT/TM monotemporal			ERS-1 6 data takes			ERS-1 9 data takes		
	ha	%	$Diff_A$ [%]	ha	%	$Diff_A$ [%]	ha	%	$Diff_A$ [%]
Alu	59024	100,0	+3,5	59024	100,0	+3,5	59024	100,0	+3,5
Ww	15928	27,0	-3,6	17068	28,9	-1,7	17838	30,2	-0,4
Wb +Wr	4490	7,6	-10,6	6930	11,7	-6,5	8390	14,2	-4,0
Sb	8015	13,6	+6,8	5786	9,8	+3,0	5764	9,8	+3,0
Ra	3716	6,3	-3,7	5712	9,7	-0,3	5516	9,3	-0,7
Gr	23242	39,4	+23,2	16750	28,4	+12,2	12871	21,8	+5,6
Ff	1490	2,5	-8,7	5071	8,6	-2,6	6466	11,0	-0,2
not classified	2142	3,6	-3,6	1706	2,9	-2,9	2179	3,7	-3,7
			Σ |60,2|			Σ |29,2|		Σ |17,6|

tab. 3: Classification results of the District of Goettingen; $Diff_A$: Differences of proportion of area according to official statistics (see. tab. 1 and according to classification statistics)

SATELLITE-BASED CLIMATE ANALYSIS OF BASEL/SWITZERLAND

E. Parlow, D. Scherer, U. Fehrenbach, H.-D. Beha

Meteorology, Climatology and Remote Sensing Lab (MCR Lab), University of Basel
Spalenring 145, CH 4055 Basel, Switzerland
phone : +41-61-272 6480, fax : +41-61-272 6923, email : parlow@ubaclu.unibas.ch

ABSTRACT

Climate maps are a common and basic tool for planners in local and regional authorities. Especially in cities or urban agglomerations, where environmental and climatic problems are manifold, it is important to have detailed and updated maps. The paper shows an example of how satellite data of ERS-1 and LANDSAT-TM are used in combination with a digital terrain model, digital terrain analysis and a rule-based classification scheme to create climate maps in scales of 1 : 25000 to 1 : 100000. The work was carried out in close cooperation with the relevant planning agencies to guarantee full agreement and acceptance of the results. The method is now at on operational stage and can be approved for other locations.

INTRODUCTION

During recent years a series of meteorological and remote sensing projects were carried out at MCR Lab of the University of Basel. Many of these research activities are dealing with aspects of urban climatology. The two most important projects are the Regional-Climate-Project (REKLIP) (Parlow 1996) and the ERS-Pilot-Study ERSCLiP (Parlow et al. 1996). The database of meteorological and remotely sensed data for the Basel region is extremely large, and so it was decided to work out a product of a set of climate maps of different scales for the local and regional planning authorities and environmental protection agencies. The decision to use high-resolution satellite data as an important data source is connected to the fact, that (1) landuse is an important factor for the urban climate, (2) for a detailed study it must be available as a spatially distributed dataset in 20 to 30 m grid size and (3) it must be possible to update these data very easily. Together with the numerical models the whole set of spatial data and time series of point data is stored in a Geographical Information System which ensured a fast retrieval of all information and allows to simulate the climatic consequences of potential planning scenarios.

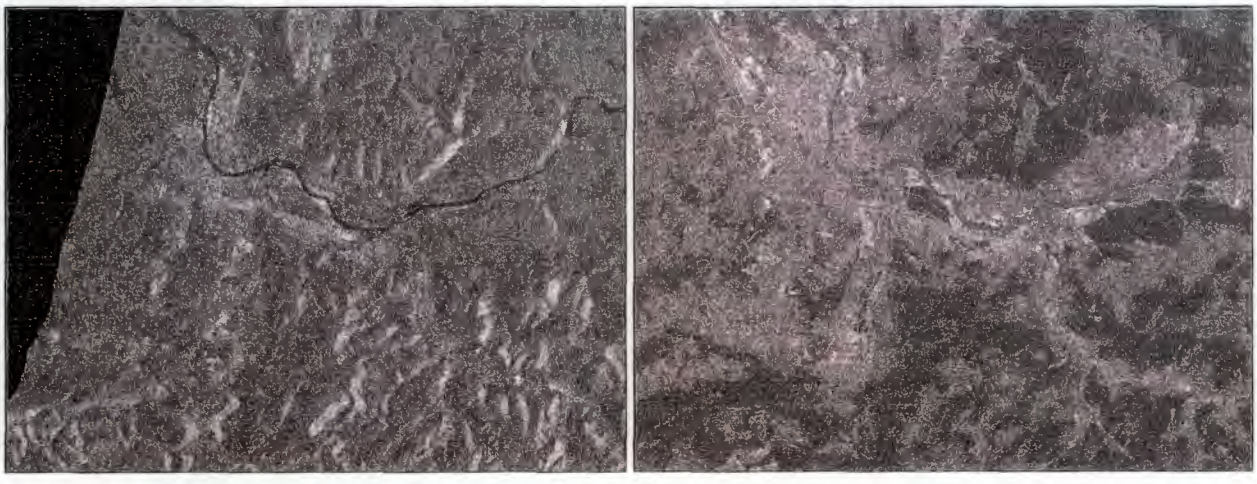

Fig. 1 : Multitemporal ERS-1 Composite (left) and LANDSAT-TM-Composite (right) of the agglomeration of Basel/ Switzerland. Data are geocoded to the Swiss National Grid.

LANDUSE AND AREAL TYPES

Landuse classifications are a widely used result of satellite data analysis. ERS-1 and LANDSAT-TM provide landuse informations in a pixel size of 30 x 30 m^2. The problems of mixed pixels (mixels) often lead to misclassifications especially where heterogeneous surfaces are predominant. Urbanized areas are characterized by complex patterns of building structures, construction works etc. To overcome these problems the concept of areal types was developed (Scherer et. al. 1996). A clear distinction between the normal

pixel-based landuse classes and aggregated areal types is made. Despite of similar class names, areal types are complex structures usually consisting of several pixel classes, which contribute to them in characteristic proportions. To make an example: low density residential areas are a mixture of houses, lawns, trees and streets. Each of the latter form an own landuse class, but in a specific combination they represent a special areal type, and water surfaces mixed with industrial areas is more likely a harbour. These areal types create individual climatological conditions which are similar in most cities. To follow the concept of landscape ecology, where areas of similar ecological conditions are called ecotopes, these climate units can be defined as climatopes. For a more detailed description it is referred to Scherer et al. (1996) and Beha et al. (1996).

Fig. 2 : Map of areal types of the agglomeration of Basel: green colours : forests, grassland and greens, brown : agricultural areas, blue : water, violet, red and yellow : build-up areas.

WIND FIELD AND VENTILATION CLASSES

The urban climate, especially in mountainous regions is very often influenced by the local wind field pattern. Nocturnal cold air production and channeling down the valleys has important climatic consequences for air quality and heat stress during summer. Therefore a climate map for the planners must include this information layer. A normal approach to the wind field of a specific area is carried out by means of numerical wind field models, which results in the information on wind speed and wind direction in a specific height above ground and for a predefined direction of the geostrophic wind. The problem of this method is that one has to compute a set of geostrophic conditions with different boundary conditions concerning wind speed. The result is a set of wind maps or a wind atlas. Normally planners are no experts in meteorology who can read these maps. They need the information in a highly aggregated form and in one single map. Therefore it was decided not to model wind speed and direction but to determine ventilation classes which are relevant to the planners. These ventilation classes can be analysed by using a digital elevation model and some surface properties of the landuse classes. Ventilation classes describe characteristic combinations of climatic factors controlling local and regional wind fields and vertical air mass exchange processes, resulting in typical and distinctive ventilation conditions. Since they are derived by means of a spatial analysis of climate factors, they do not describe atmospheric states at all. Moreover, they summarize ventilation conditions leading to characteristic probability distributions for certain atmospheric state variables in the lower planetary boundary layer. Some ventilation classes are mainly depending on terrain features, while others are delineated both by terrain parameters and landuse information. The computation was carried out by using a rule-based classification algorithm. Fig. 3 shows the digital terrain model of the agglomeration of Basel with the Swiss Jura in front reaching up to 1200 m a.s.l. in a 3D-view taken from southwest and the corresponding ventilation classes in a grid size of 100 m. By using this method all information relevant for planning can be printed in a single map (Scherer et al.).

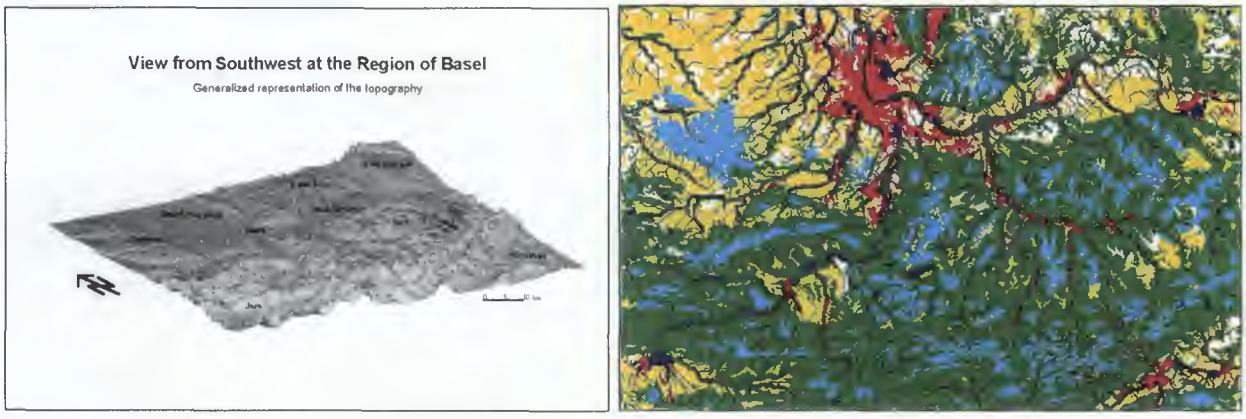

Fig. 3: 3D-Digital elevation model (left) and computed ventilation classes (right). white: indifferent ventilation, light blue: wind-exposed areas, dark green: ventilation along valley axes, light green: ventilation on slopes, yellow: undisturbed ventilation, red: reduced ventilation, dark blue: cold air accumulation areas.

CLIMATE ANALYSIS MAP

Using this technique final maps of the climate analysis of Basle were compiled which offer the planners a very detailed information on different aspects of regional climatology. Two sets of maps were constructed:

1. Climate analysis maps
   - one overview map (scale 1:100 000, see fig. 4)
   - four detail maps (scale 1 : 25 000, not presented in this paper)
2. Planning recommendations (not shown in this paper)
   - one overview map (scale 1 : 100 000)
   - four detail maps (scale 1: 25 000)

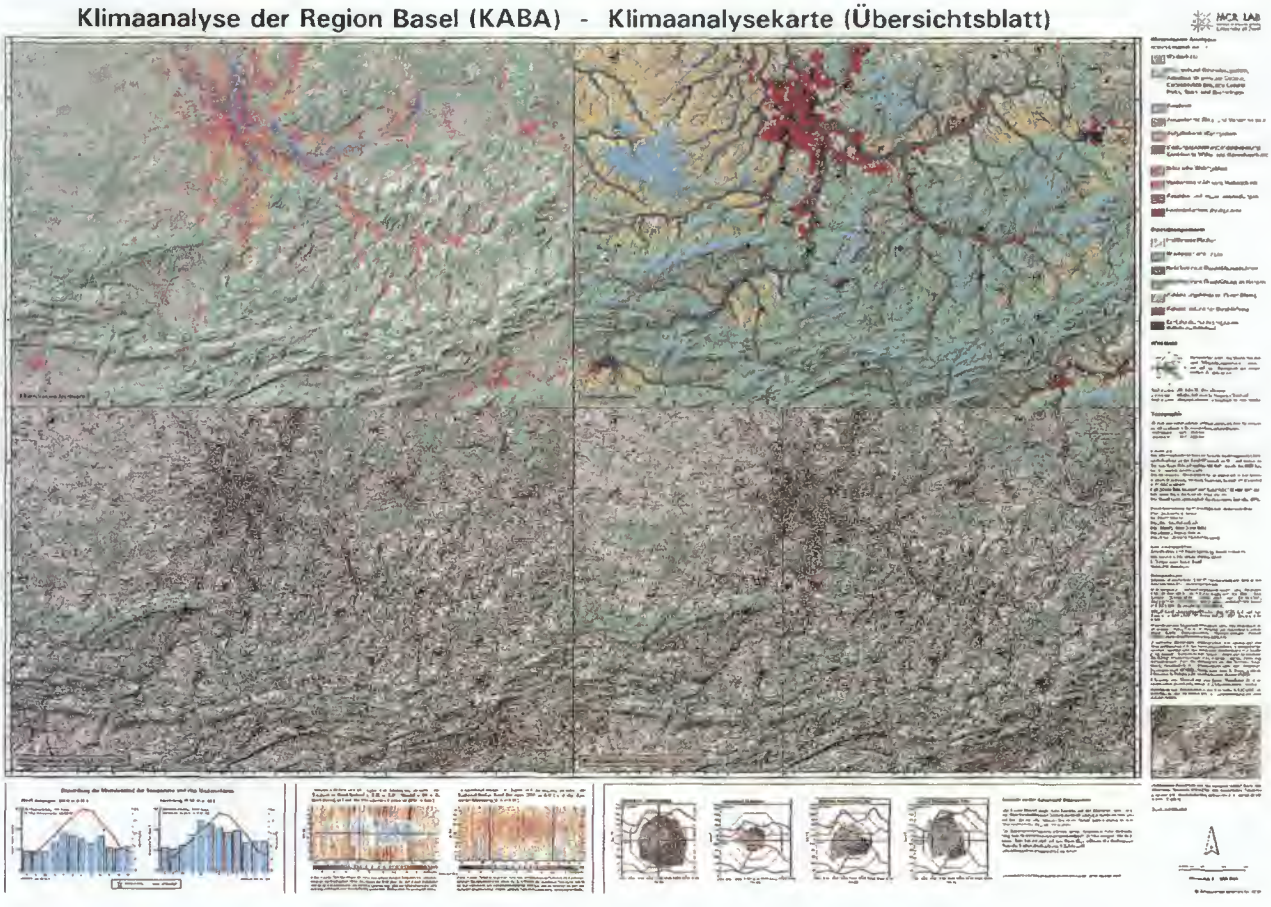

To improve the applicability of the maps additional meteorological information like wind roses and air quality data are printed as overlays into the maps or along the map borders respectively. All steps of data processing and valuation were discussed in detail with the planners to ensure that the product is accepted and used for the planning and environmental problems of the future.

CONCLUSIONS

In the Upper Rhine Valley and the region around Basel/ Switzerland several climatological projects are carried out like the Regional Climate Project REKLIP, the ERS-1-Pilot study ERSCLiP and additional single projects mostly funded by the Swiss National Foundation. Some of these projects tackle problems of basic research others are focussing application oriented results. To find a synergism of all theses research activities the presented study was started in 1995. The need of planners and decision makers to receive products and informations from research institutions which can easily be used within the political process chain and within a short time period can be achieved by the method presented. Important input data are satellite data from ERS-1 and LANDSAT-TM and a digital elevation model, which normally can be ordered from the national geodetic survey. In general meteorological data are also available from national weather surveys and so all prerequisites to work out these maps are fulfilled. It was one objective of this study to create a method to work out climate maps for application which is transferable to other regions in Europe.

REFERENCES

Beha, H.-D., E. Parlow & D. Scherer, D. (1996): Land use classification of the agglomeration of Basel/ Switzerland combining multi-sensorial satellite data from Landsat-TM and ERS-1. In : Parlow, E.: Progress in Environmental Remote Sensing Research and Applications, Balkema Rotterdam, S. 77-82.

Parlow, E., D. Scherer, H.-D. Beha, H. Gossmann & M. Braun (1996): Urban climatological parameters derived from multisensor satellite data of ERS-1 and Landsat-TM. European Space Agency, ESA-SP 383, S. 173 - 178.

Parlow, E.(1996): The regional climate project REKLIP - an overview. Theoretical and Applied Climatology, Vol. 53 (1-3), p. 3-7.

Scherer, D., U. Fehrenbach, E. Parlow & H.-D. Beha (1996): Determination of aggregated areal types from a Landsat-TM and ERS-1 based land use classification for the agglomeration of Basel/Switzerland. In : Parlow, E.: Progress in Environmental Remote Sensing Research and Applications, Balkema Rotterdam, S. 197-200.

Scherer, D., U. Fehrenbach, H.-D. Beha & E. Parlow : Improved concepts and methods in analysis and evaluation of the urban climate for optimizing urban planning processes. (submitted to Atmospheric Environment)

INTERFEROMETRIC COHERENCE MEASUREMENTS OF TROPICAL, TEMPERATE AND BOREAL FORESTS

Adrian Luckman and John Baker

Remote Sensing Applications Development Unit, British National Space Centre
Monks Wood, Abbots Ripton, Huntingdon, Cambridgeshire, UK, PE17 2LS
A.Luckman@nerc.ac.uk

ABSTRACT

The relationship between forest biomass density and interferometric coherence was investigated using SAR image pairs acquired as part of the ERS tandem mission. Temperate, boreal and tropical forest test sites were imaged although so far results are available only from Corsican Pine stands at Thetford Forest in the UK.

Interferograms were generated for a variety of repeat-pass image pairs including four 1-day pairs, one 35-day pair and one 315 day pair. Corresponding coherence maps were produced and registered to a database containing information about the distribution of stands of Corsican Pine with a variety of biomass densities estimated from their age. The relationships between the estimated biomass density and both the backscattering coefficient and the coherence were derived from this database.

The 1-day repeat coherence shows a useful dependence on biomass density up to around 100 tonnes / hectare and this dependence is stronger than that between backscattering coefficient and biomass density. The coherence in the forest areas over longer timescales is uniformly low. However, it remains high in urban areas even after 315 days.

Keywords: Forest, interferometry, ERS-Tandem, biomass density

1. INTRODUCTION

ERS SAR remote sensing has the important advantages of radiometric stability, long-term support and relative independence from atmospheric conditions. However, for forest monitoring purposes, C-band data is not ideal because in general the backscattering coefficient of forests at this wavelength is poorly related to their biophysical characteristics. SAR interferometry is expected to provide improved capability for forest applications by making use of the additional information carried in the phase differences and in the coherence (γ) between repeat-pass image pairs [Refs. 1 and 2]. The coherence is expected to decrease with forest density because there is more opportunity for small changes in scattering characteristics over time when more scatterers are present. Over time scattering characteristics might be affected by moisture, wind or growth. Also, the interferometric phase difference between clearings and adjacent forest canopies may allow tree height to be inferred.

This paper describes the preliminary findings of the ESA ERS Tandem project AOT.UK316 which aims to investigate the relationship between interferometric coherence and biomass density and to use the extra information derived from repeat-pass interferometry to assess forest characteristics at several established forest test sites. These include a temperate plantation at Thetford in the UK, a boreal forest test site at Siggefora in Sweden and tropical forest test sites at Tapajós and Manaus in Brazil.

Preliminary work suggests that 1-day interferometric coherence is very low over the tropical forest test sites but carries useful information at the temperate and boreal forests sites. As most data so far has been received and processed for the temperate forest site at Thetford, this paper describes the preliminary results from interferometric processing carried out at that site.

2. TEST SITE, FIELD AND IMAGE DATA

Thetford Forest is a predominantly coniferous plantation first developed in the 1930s on heath and low grade agricultural land in East Anglia. It consists mainly of Scots and Corsican Pine stands and includes a large range of ages of Corsican Pine from 3 years to 60 years.

Fieldwork had been carried out to measure the biomass density of Corsican Pine stands of a range of ages. This data was used to characterize the relationship between stand age and biomass density and hence to allow the biomass density to be estimated within a much larger set of forest stands. Plantation stocking maps provided by the UK Forestry Commission (now Forest Enterprise) were digitized to determine the location of forest stands of different ages of Corsican Pine within a geocoded database at a resolution of 10m.

Image data consists of four ERS Tandem image pairs from August 1995 and April, May and June 1996. This dataset allowed repeat-pass interferometry to be investigated over many time delays including 1, 35, 70, 244, 279 and 315 days.

3. IMAGE PROCESSING

Interferometric processing was carried out using the ESRIN/POLIMI ISAR software which proved to be effective though cumbersome.

All 8 images were co-registered to sub-pixel accuracy using the most recent image as a reference. Interferograms and optimized coherence maps were derived for the subset of the possible combinations of image pairs which were considered of most interest. The ones examined in this paper include all four possible 1-day repeat pairs, one of the possible 35-day repeat pairs and the maximum 315-day repeat pair.

The complex SAR images were detected and averaged to form 6-look amplitude products. These were

calibrated (taking into account only the K-factor for this preliminary analysis) and registered to a geocoded database containing the forest stand information. The coherence maps were also registered to this same database.

The relationships between the estimated biomass density and both the backscattering coefficient (σ^0) and the coherence were derived from the database using the digitized forest stand map. In each case average values were calculated over image areas of at least 150 pixels representing homogeneous forest stands of at least 1.5 ha.

4. PRELIMINARY RESULTS

Results are shown quantitatively in Figure 1 and qualitatively in Figures 2 to 11.

Although much of the Thetford area is covered by forest, strong phase fringes were developed for each of the 1-day repeat image pairs over the whole area. In the interferograms generated from image pairs spanning greater than 1-day, fringes were visible only outside the forest area.

The fringes, before and after the removal of orbital effects, for one of the 1-day repeat image pairs are shown in Figures 2 and 3. These have not been normalised but the appearance of only one fringe over the area in Figure 3 confirms the flat nature of this region. Ongoing work will determine if the phase difference between clearings and adjacent forest canopies may allow tree height to be inferred.

Figure 1 shows that there is a strong relationship between interferometric coherence and biomass density for each of the 1-day repeat pairs but that this relationship is not significant over time scales of 35 days or more. In each of the 1-day repeat cases, this relationship is stronger than that between σ^0 and biomass density. This is partly due to the soil scattering component which becomes significant at low biomass density values in some images, presumable because of higher soil moisture.

There is some variability in the relationship between biomass density and 1-day repeat coherence and future work will investigate whether this variability is related to meteorological or atmospheric conditions. This variability is also apparent in Figures 4 and 5 which show the coherence maps for two of the 1-day repeat pairs. Figure 10 shows a colour composite of three of the 1-day repeat coherence maps showing that a large amount of extra information is available using this technique. Here the area with lowest coherence indicates the mature stands of Thetford Forest.

Figures 6 and 7 show coherence maps for one of the 35-day repeat and the 315-day repeat pairs. Some coherence remains in the towns and over the Feltwell agricultural area after a month in the early growing season but little remains elsewhere. Over a time scale of nearly a year, there still remains high coherence in the urban areas and over the airfields that are characteristic of this region. Figure 11 combines coherence maps from 1, 35 and 315 days showing the limits of coherence over 1-day in red, 35 days in yellow and long term in white.

Another source of information in the ERS data lies in the difference in intensity between images from different dates. Figures 8 and 9 show composites of coherence, σ^0 and $\Delta\sigma^0$ for 1-day and 35-day repeat image pairs [Refs. 3 and 4]. This demonstrates that for 1-day repeat pairs, most information is carried in the coherence while for longer time periods more information is carried in the intensity difference than in the coherence.

5. CONCLUSIONS AND FUTURE WORK

This study has investigated the relationship between interferometric coherence and biomass density of Corsican Pine stands at Thetford Forest in the UK for repeat-pass ERS SAR image pairs over a variety of time scales.

The 1-day repeat coherence is strongly related to biomass density although this relationship is variable with the date of acquisition, probably because of environmental factors. Preliminary results show the dependence to be monotonic although noisy up to biomass densities of around 100 tonnes per hectare. Coherence over longer time scales than 1-day is uniformly low over forest areas. The relationship between biomass density and 1-day repeat coherence is stronger than that between biomass density and σ^0 suggesting that the extra information provided by SAR interferometry may be useful for forest applications.

Well developed phase fringes from 1-day repeat data may allow phase difference information to be used in the estimation of tree height.

Future work will concentrate on determining the sources of variability in the relationships and using the phase information to estimate tree height. The analysis will be repeated at the boreal forest test site at Siggefora in Sweden and further attempts will be made to perform similar analyses of the tropical forest test sites.

6. REFERENCES

[1] J. O. Hagberg, L. M. H. Ulander, and J. Askne, "Repeat-Pass SAR Interferometry Over Forested Terrain," *IEEE Transactions on Geoscience and Remote Sensing*, vol. 33, pp. 331-339, 1995.

[2] J. I. H. Askne, P. B. G. Dammert, L. M. H. Ulander, and G. Smith, "C-band Repeat-Pass Interferometric SAR Observations of the Forest," *IEEE Transactions on Geoscience and Remote Sensing*, vol. 35, pp. 25-35, 1997.

[3] U. Wegmuller and C. Werner, "SAR Interferometric Signatures of Forest," *IEEE Transactions on Geoscience and Remote Sensing*, vol. 33, pp. 1153-1161, 1995.

[4] U. Wegmuller and C. Werner, "Retrieval of Vegetation Parameters with SAR Interferometry," *IEEE Transactions on Geoscience and Remote Sensing*, vol. 35, pp. 18-24, 1997.

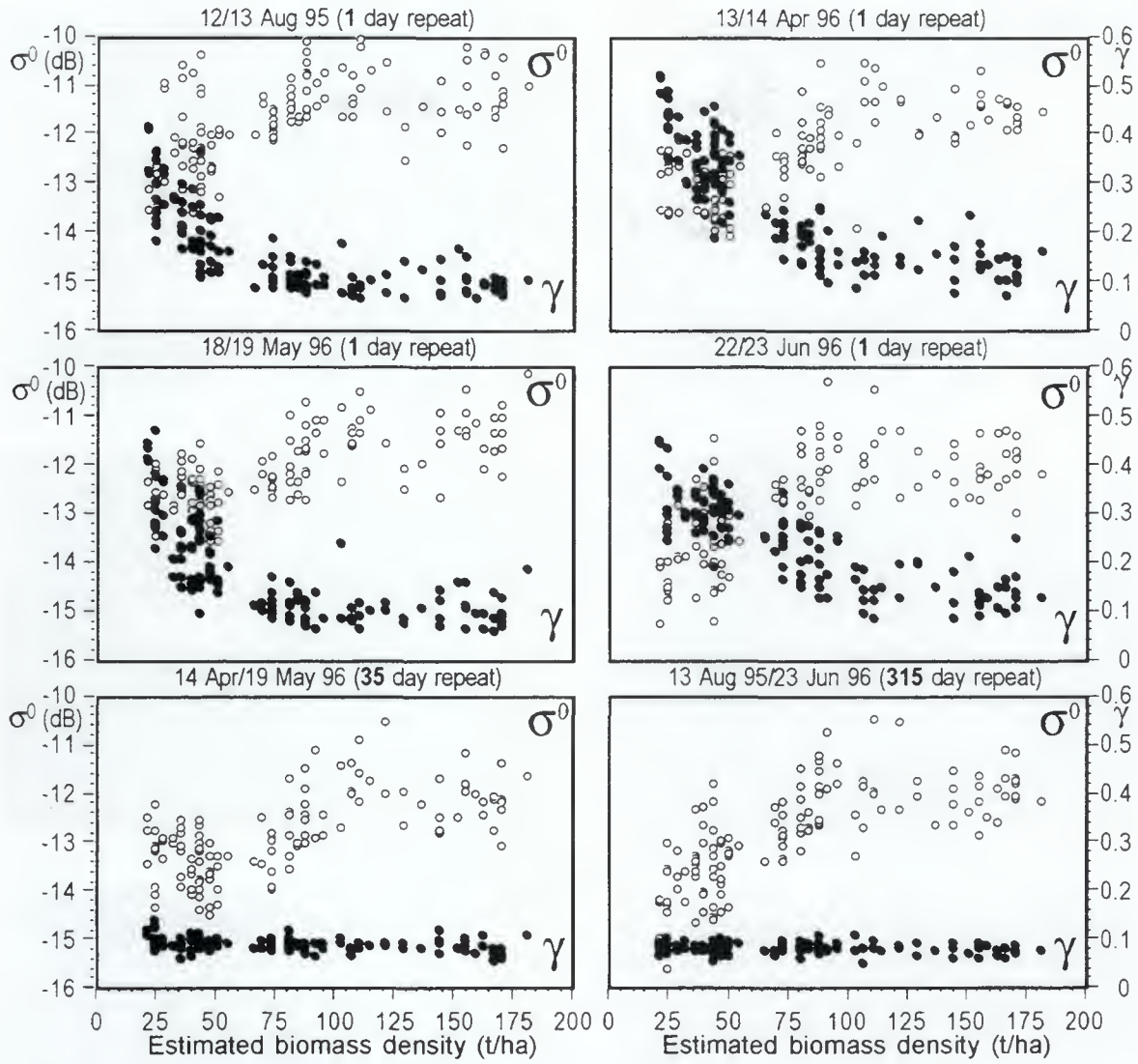

Figure 1. The dependence of σ^0 and γ on biomass density of Corsican pine stands in Thetford Forest. The relationships have been quantified for four 1-day repeat Tandem ERS pairs, one 35-day repeat ERS2 pair and one 315-day repeat ERS2 pair. The dependence of σ^0 on biomass density is variable and a strong soil scattering component is evident in some images at low biomass densities. The dependence of γ on biomass density is stronger. There is some variability for 1-day repeats and the dependence is not significant for repeat visits of longer that 1 day.

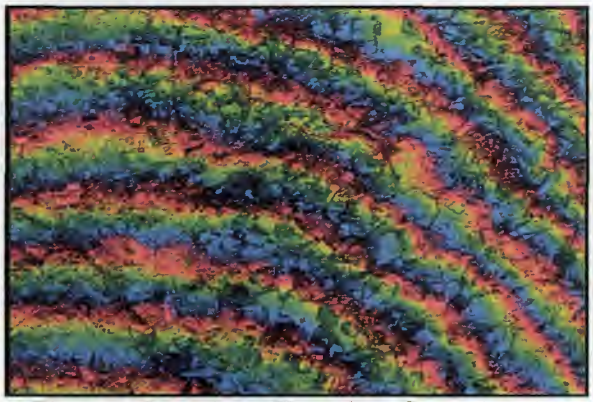

Figure 2. Intensity: γ Hue: phase Saturation: 0.5
Interferometric phase fringes modulated by the 1-day repeat coherence map (22/23 Jun 96)

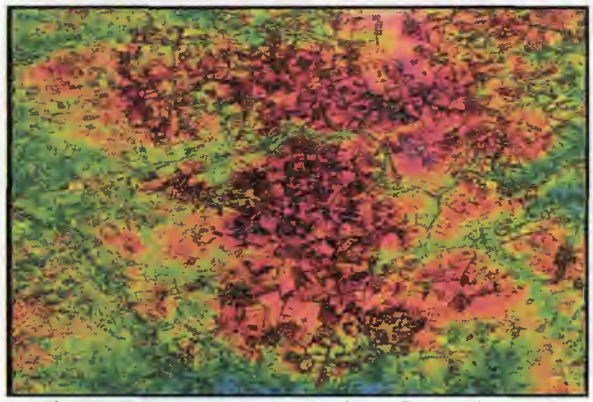

Figure 3.Intensity: γ Hue: phase Saturation: 0.5
Flattened phase map modulated by 1-day repeat coherence map (22/23 Jun 96). Note only one fringe over the region.

Figure 4. γ 18/19 May 96 (1 day)
Approx 24km by 16km

Figure 5. γ 22/23 Jun 96 (1 day)

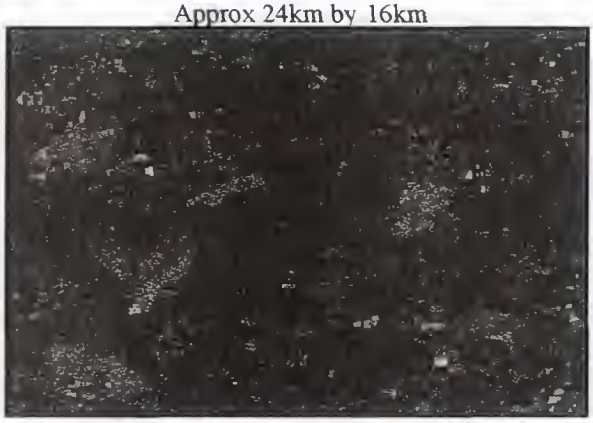

Figure 6. γ 14 Apr/19 May 96 (35 day)

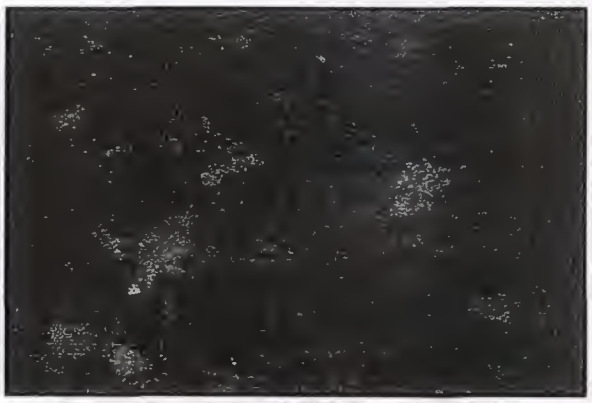

Figure 7. γ 13 Aug 95/23 Jun 96 (315 day)

Figure 8. Red: γ Green:σ^0 Blue: difference
22/23 Jun 96 (1 day)

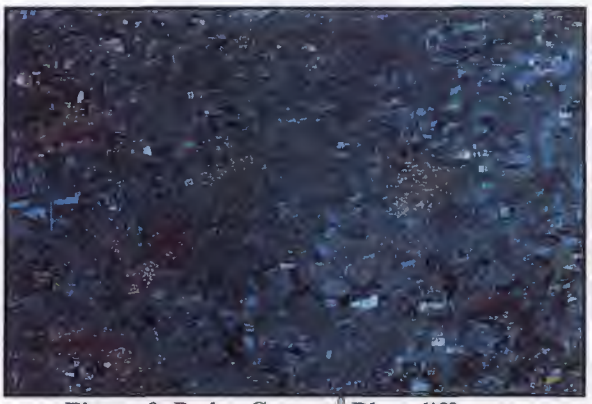

Figure 9. Red: γ Green:σ^0 Blue: difference
14 Apr/19th May 96 (35 day)

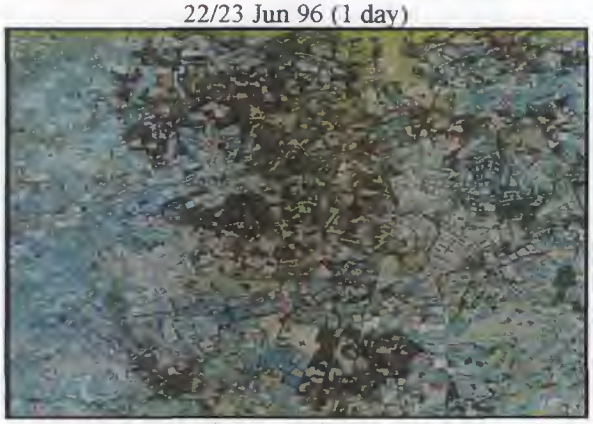

Figure 10. R: γ 22/23 Jun (1 day)
G: γ 13/14 Apr (1 day) B: γ 18/19 May (1 day)

Figure 11. R: γ 22/23 Jun (1 day)
G: γ 14Apr/19May (35 day) B: γ 13Aug/23 Jun (315 day)

REGIONAL APPLICATION OF ERS-1/2 IN THE FLEVOLAND AGRICULTURAL AREA IN THE NETHERLANDS.

Hans van Leeuwen[1] and Maurice Borgeaud[2]

[1)] SYNOPTICS, *Integrated RS & GIS Applications* BV
P.O. Box 117, 6700 AC Wageningen, the Netherlands
main@synoptics.nl
[2)] ESA-ESTEC, P.O. Box 299, 2200 AG Noordwijk, the Netherlands
maurice@xep0.estec.esa.nl

ABSTRACT

In the scope of searching applications of ERS-1/2 satellite data in agriculture this study has been formulated. This paper summarizes the state-of-the art in crop growth monitoring with use of remote sensing. The study is a follow-up of the ESA study in 1993 (ESA/ESTEC contract # 9837/92/NL/GS) where airborne RS data has been used, this study focuses on the potential of the present satellites for crop growth monitoring. Optical data has been used for calibration and validation purposes. The study has been performed by a Dutch consortium made up by SYNOPTICS AB-DLO, FEL-TNO and WAU.

Keywords: Crop monitoring, modeling, ERS-1/2

1. INTRODUCTION

In search of application of ERS-1/2 satellite data in agriculture the ESA study "Vegetation retrieval by combined microwave and optical remote sensing" (Contract nr. 11154/94/NL/NB) had been formulated. The summary of this study reflects the state of the art in crop growth monitoring with remote sensing.

For the first time a complete time-series of three successive years of the same test site in the Southern Flevoland Province in the Netherlands offered a opportunity to the Dutch research community to study the potential of radar satellite observations to crop growth monitoring. In this study three major crops in the Netherlands were subject of study: wheat, potato and sugar beet. Regional averages of the backscatter of these crops were used to calibrate and validate the semi-empirical 'Cloud-model'.

2. METHODOLOGY

The Flevoland test site in the Netherlands has been observed by ERS-1/2 for the three successive years: 1992, 1993 and 1994. In 1994 JERS-1 data has been used in order to study the potential for crop growth monitoring as well. Extensive data sets from former studies as well ground based and airborne campaigns like ROVE, Agriscatt, MAESTRO and MAC Europe, were used in order to support the theoretical microwave modeling and crop growth modeling.

Remote sensing models were selected and used in this study. The development of RS models is highly dependent on the crop type and on the physical assumptions underlying the modeling in a specific part of the spectral domain. Furthermore, in general, one can say that the modeling activities in the optical region are better understood compared to that of the microwave region. In this study three major crops in the Netherlands were subject of study: wheat, potato and sugar beet. Regional averages of the backscatter of these crops were used to calibrate and validate the semi-empirical 'Cloud-model'. The more complicated 'WSRC-model' (FEL-TNO) based on the radiative transfer theory was used in combination with well initialized crop growth models (AB-DLO) for the simulation of parameters of the 'Cloud-model' as well.

The major findings of the study and potentials for application of ERS-1/2 :

The potential of ERS-1/2 for crop growth monitoring is mainly dependent on the amount of satellite overpasses in time and on the moment of observation during the growing season. This differs for each crop. It is promising that the parameterized Cloud model for regional applications can be applied for different years. However, it is difficult to use the calibrated Cloud model for accurate yield prediction as the standard deviation of the regional backscatter is rather large. In this respect estimation of biomass by inversion of the Cloud model is troublesome and therefore not accurate enough for calibrating the crop growth model. Due to the low accuracy of estimation of biomass (plant water), calibration of the crop growth model is not possible.

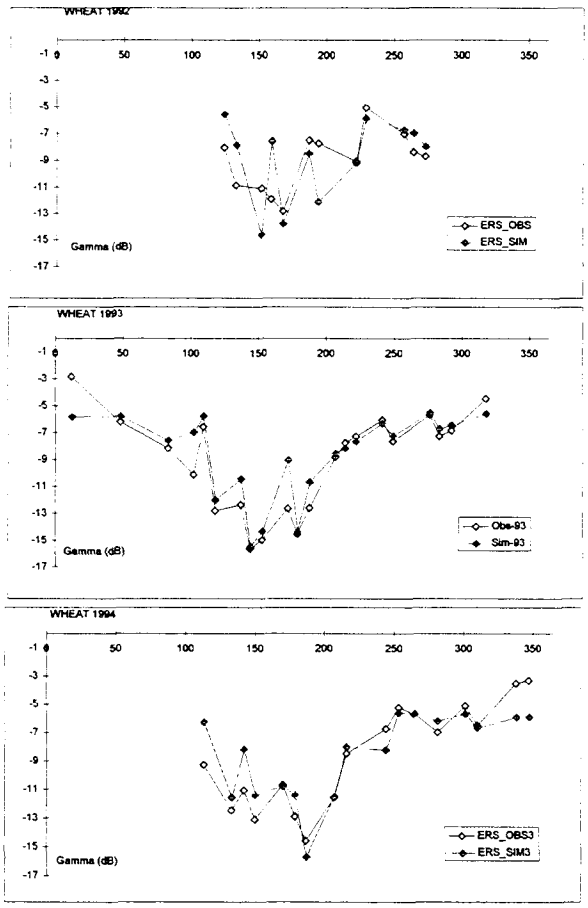

Figure 1. Comparison of ERS observations of 1992 and backscatter simulations with a CLOUD model calibrated on soil moisture derived from fruit trees backscatter (open vegetation) for winter wheat. (1-layer Cloud model Wheat, ERS 1992-1994: Soil G: 0.045 Crop C : 0.005 Soil K : 0.078 Crop D : 0.2)

Moreover, the crop growth model imposes high requirements on the accuracy of estimation of biomass from remote sensing as the crop growth model can reproduce very accurate growth information already, when the sowing date and meteorological information is present. Exhaustive studies in the past have resulted into accurate physiological descriptions of crop growth. Retrieved information from remote sensing like biomass should not exceed an accuracy of at most one unit (in kg/m^2) or a shift of few weeks in time. From simulations, it appeared that even a shift of 50 days in sowing date could not be detected by the microwave time-series. On the other hand the standard deviation in time showed interesting applications in finding the moment of regional closure of leafy crops, like potato and sugar beet.

Soil properties (especially soil moisture) appeared to have more impact on total backscatter of ERS-1/2 then was expected from the modeling. The positive result of this intensive study is that ERS-1/2 satellite time-series can provide soil moisture information under vegetated

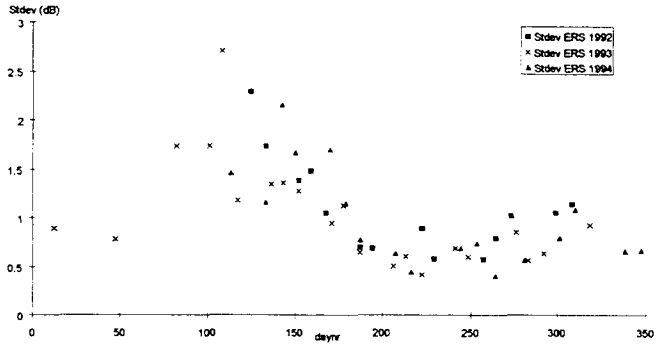

Fig 2. ERS-1 signatures of standard deviation in backscatter of sugar beet for the 1992, 1993 and 1994 growing season

conditions, which can be of particular interest for water balance studies. The latter is very important under semi-arid climatic conditions, where the soil water balance is of major importance to crop growth and possible growth limitations. The conditions in the Flevopolder are favorable and no water stress and with that growth limitation is expected to occur. Interesting is the use of crop growth models extended with a good hydrological model in those semi-arid conditions. Microwave time-series could provide these models by estimating top surface moisture conditions which are an indication of the water availability over the soil profile.

3. CONCLUSIONS

The ESA study resulted into three major conclusions relevant for applications of ERS data in the agribusiness sector:

I. ERS-1 backscatter from agricultural crops like potato and sugar beet show still clear dependency from soil moisture during the growing season. However, during the vegetative and the begin of generative growth of the winter wheat crop (day 120 till 175) almost no correlation can be noticed with soil moisture. Apparently, the canopy structure (in combination with soil) dominates the backscatter behavior.

II. The presentation of the regional standard deviation (100 fields per crop type) in backscatter gives a clear dip in backscatter during the moment of regional crop closure. While the regional intensity information of the winter wheat crop gives a clear signature in time. This information on agricultural crops are of particular interest to the agribusiness industries operating on a regional administrative level.

III. A new regional approach had been developed to model the canopy and soil contribution of the agricultural crops by using a regional crop growth model and a simplified backscatter model like the

Cloud model. The regression parameters of the Cloud model appeared to be valid also between the successive years. Modeling results on regional level show remarkable well agreement with the actual measurements.

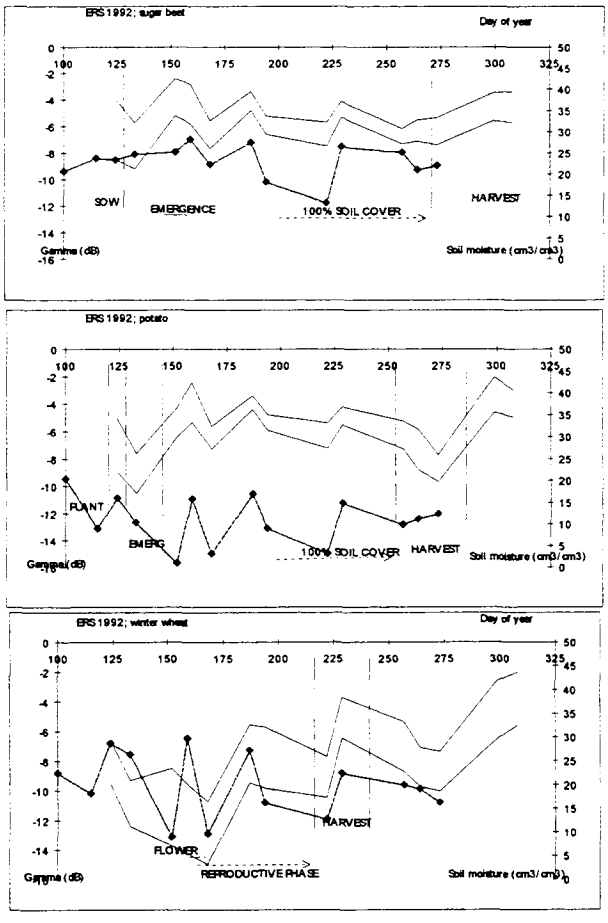

Figure 3. Average soil moisture contents for the three crops compared with the average radar backscatter signatures for the three crops in 1992.

RAPID – A JOINT PROPOSAL USING InSAR

Detlev Kosmann

German Areospace Research Est. German Remote Sensing Data Center (DLR – DFD)
82230 Oberpfaffenhofen Germany
Phone 8153 28 1376, Fax 8153 28 1445, e–mail: kosmann@dfd.dlr.de

ABSTRACT

RAPID is an approach to implement an end to end system, from the interferometric processing to application of SAR and InSAR products. It is carried out in the framework of the Announcement of Opportunites for ERS–1/2 at different Universities in Germany and Austria and the DLR. InSAR is the basic part of the project. In this CO'I project the DFD is implementing an pre–operational system to produce necessary interferometric products for some selected applications. At the current implementation level it is possible to generate coherence maps, unwrapped phase information, single Digital Elevation Models and geocoded DEM. The paper will present first results from the test area in Hungary. DEM's and coherence maps will be an essential input to the application projects in RAPID. With ERS tandem mission data coherence information are used for a monitoring project of the rainforest in Brazil. In Africa geomorphological studies uses also information from different tandem pairs to extract information like e.g. movments of sand dunes. In Germany the SAR data are input for the monitoring of two selected areas, one in the Rhine Valley and the other near the lake Steinhude. In some very hilly testareas in the Austrian alps it is planed to generate DEM with InSAR and compare them with available DEM's. In a second step a combination of ascending and descending pathes will be used to reduce geometric effects. An extraction of linear features from the SAR will show first interesting results.

Keywords: ERS–SAR, Interferometry, Processing, Applications

1. INTRODUCTION

The joint proposal RAPID (Radar Amplitude, Phase and Interferometric Detection) gathers nine research groups (from Germany, Austria, Hungary and Phlippines) with the intention to use not only the ERS SAR amplitude information but also the interferometric possibilities of the mission. Rapid is considered as innovative scientific proposal exploiting ERS data either alone or in synergy with other data for land surface processes and microwave interaction mechanisms, including also climatological purposes. The tandem mode of ERS–1 and ERS–2 will be used as well as the synergetic use of ERS data from more than one instrument on ERS–1 or ERS–2.The main reason for a joint proposal is to establish a solid interaction between researchers developing algorithms for new data types from the imaging SAR sensor (i.e. phase information, coherence maps, interferometric parameters) and those who apply these data in different regions of Europe, Africa and South America, for different research application purposes and in synergy with different remote sensing and ancillary data. The application will then give feedback in an iterative way to the group developing new software for basic SAR data.

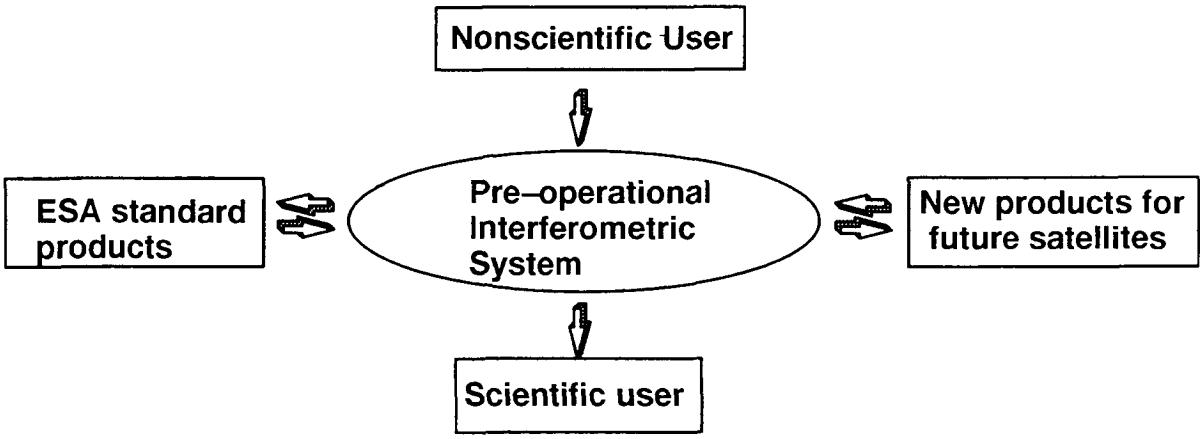

Figure 1. RAPID Project Scheme

2. DEVELOPMENT OF PRE–OPERATIONAL PROCESSING CHAIN AND GENERATION OF A LARGE AREA DEM

In the InSAR part of RAPID a pre–operational processing chain for large areas was implement and a weighted least square approach to phaseunwrapping was implemented and tested. In a test area of Hungary these approaches were tested with sufficient results. The internal accuracies of different derived DEM are in a dimension of 20 m to 40 m.

A mosaicking tool specially for terrain models was developed and implemented in a UNIX/C configuration. It was possible to generate a mosaic of 15000 square kilometers. The validation bases on national topographic maps.

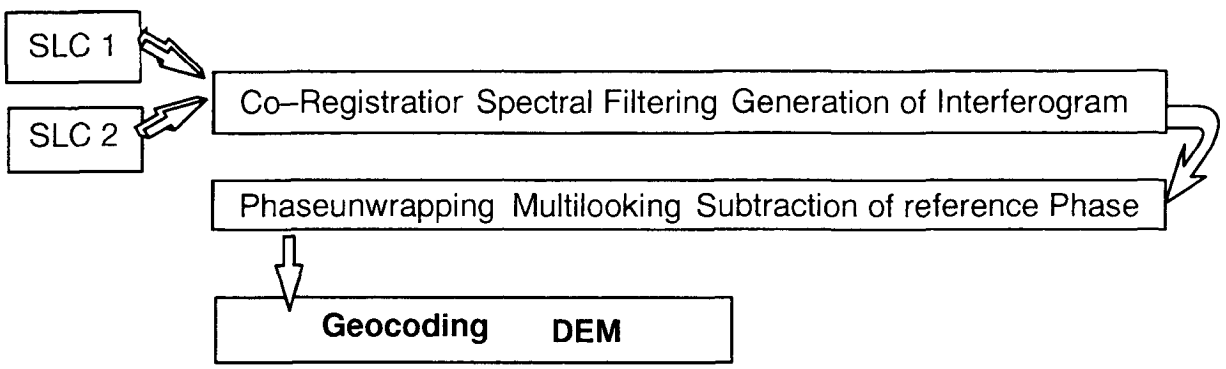

Figure 2. InSAR processing system

3. LINEAR STRUCTURE IN SAR COHERENCE DATA

The goal of the subproject from the University of Munich is to simplify mapping linear structures with Synthetic Aperture Radar (SAR) data. This is necessary as the specific conditions of SAR such as speckle and the dependence on incidence angle have resulted in either a high interactive effort or a rather insufficient output of previous approaches, especially when compared with results of mapping with optical imagery. Therefore, a specific approach is de-

veloped which accounts for SAR characteristics. It integrates several data sources such as SAR intensity images as well as coherence maps from an interferometric evaluation of two SAR scenes. Also given geographic information can be used to support the extraction.

A new approach to detect lines in noisy images using a Markov random field (MRF) model and Bayesian classification is proposed. The unobservable object classes of single pixels are assumed to fulfill the Markov condition, i.e. to depend on the object classes of neighboring pixels only. The influence of neighboring line pixels is formulated based on potentials derived from a random walk model. Locally, the image data is evaluated with a rotating template.As SAR intensity data is deteriorated by multiplicative noise, normalized intensity ratio is used as the response of the local line detector resulting in a constant false alarm rate. Besides maximum a posteriori (MAP) and iterated conditional modes (ICM) estimation of the object parameters, an implementation of local highest confidence first (LHCF) estimation is used. It is initially applied to the sites which are most probably structures in object space, and is then allowed to progress to regions less promising for line detection depending on the results of previous iterations. In this way processing times are substantially reduced.In an testarea located in Siberia it was possible to detect different linear features, probably pipelines.

4. MATCHING OF DISSIMILAR OVERLAPPING IMAGES

The primary goal is the use of interferometric methods. The component of the University of Graz is to compare results from interferometry with other 3D surface reconstruction methods, and to match dissimilar (opposite side) imagery. These investigations are assessed to evaluate the feasibility of combining data from different look angles and possible quality increasement in 3D surface reconstruction. These tasks depend on data provided by partners, which are going to be compiled. For the project data from the testsite "Hartberg" in south–east Styria/Austria were used. In particular the geocoding of ERS–data with a newly developed geocoding tool which is based on SAR simulation was done.

By matching the simulated and the actual image, the simulation is validated. If the discrepancies are below a certain threshold (usually 1 to a maximum of 3 pixels), the geocoding can be performed by resampling using the same geometric model. Remaining geometrical errors are decreased by applying a higher order polynomial adjustment between the simulated and the actual radar image. Other developments were in the field of surface reconstruction i.e. matching same–side stereo radar images with varying look–angles of ERS–1/2 with area–based template matching methods and matching dissimilar opposite side radar images of ERS–1/2 with a feature–based approach. Edge detection and grouping edge strength locations to solid edge contours together with a weighted edge–neighborhood graph makes opposite side matching feasible if a considerable amount of structural content is contained in the opposite side radar image pair. Finally, the University of Graz started on quality increasement in same–side radar image matching by detecting layover in multi–lookangle radar images of ERS–1 (roll–tilt). Matching points bordering layover areas contradict the fundamental epipolar restriction common matching software depends on. An extension capable to cope with layover arising in same–side radar image matching is currently being developed.

5. LONGTERM MONITORING

The detection and separation of ecologically important areas in the surroundings of the test area "Steinhuder Meer" is one major topic of the research part from the University of Hannover. For this investigation several

ERS−1 scenes between 1992 and 1995 have been processed and classified. All interpretation and classification methods could show that it is possible to detect for environmental studies important areas in multitemporal ERS images (GTC), but a separation into refined classes like greenland, partially covered greenland with forests and forests is very difficult. Therefore in future developments coherence maps from ERS−1 and ERS−2 tandem mission shall be considered.

The second topic was to investigate the backscatter behavior of farmland and wasteland in ERS−1 multitemporal images. The student could collect ground truth data in a test area near "Göttingen" and was able to separate the main agricultural fields. In the time range from 1992 to 1994 only a few characteristic ERS−1 scenes could be investigated. Scenes between September and December were not useful for the multitemporal interpretation methods. Nevertheless the candidate was able to detect wasteland areas without prior information. A ground truth comparison could verify his results. In the future investigations with multitemporal and multi band mission shall be carried out (X−SAR).

In the DFG−funded project "Semantic modelling of remote sensing data" also ERS−1 and ERS−2 image shall be investigated. As the main developments are in the scale 1 : 5 000 to 1 : 25 000 additional radar data sets will be considered for topographic maps in the scale of 1 : 100 000 or 1 : 200 000. For this purpose following ERS−2 coherence maps have been ordered at DLR−DFD, depending on the season there are different priorities for the data application.

6. RAINFOREST MONITORING

Embedded in a cooperation with the Brazilian Space Research Institute INPE, testsites in the state of Acre, Brazil in the Western Amazon are to be investigated for the use of complex ERS data products in rainforest monitoring.

Three tandem data products (quarter scenes SLC) have been ordered in July 96. The scenes from May 1996 cover areas in the North of Rio Branco, the capital of Acre, and an area along the Brazil Rodovia BR−364 towards Sena Madureira and Peru. The May data should be promising for using coherence data because of beginning dry season. Other tandem datasets of the Rio Branco area have been registered in October 1995. Two full scenes of ERS−1 of that orbit are already available. The scenes cover Rio Branco and surroundings with different patterns and stages of deforestation and regrowth as well as a large undisturbed primary rainforest area North of it. This data has been used for a forest / nonforest classification, also trying to separate fresh pasture areas from old pasture / regrowth areas. For classification, the EBIS texture classification approach (after Lohmann, 1994) was used. This evidence based classifier is based on texture characterization by the co−occurrence matrices in a certain window environment. Although the October scene was registered in beginning wet season, most of the known deforestation areas have been separated. In comparison to available Landsat TM reference data from July 1994, several new deforested areas have been registrated, especially Southwest of Rio Branco. On the other hand, main misclassification resulted in the peripheral areas of Rio Branco and adjacent environments. Here an overlay of backscatter signals of settlements and old pasture land exits, but also of different plantations, reaching similar levels of backscatter amplitudes as in rainforest areas. Those areas could be interesting for integrating coherence data. Based on the two ERS−1 scenes from October 1995 and

two adjacent ERS–1 scenes from August 1995 West of it (also available since July 1996), a classification has been performed. The mosaic dataset on 50 m resolution covers an area of about 200 km by 170 km and is to demonstrate large–area mapping. An accuracy assessment is under work. The data products are to be used to supplement time series data produced by the former ERS–1 rainforest pilot project. They are also to be used in preparation of a combined amplitude / phase investigation.

A combination from amplitude images and coherence results of the InSAR system shows a much higher variety in the deforestet than multitemporale ampltide images.

7. AUTOMATED LANDUSE MAPPING WITH ERS–1/ERS–2 SAR– AND INTERFEROMETRY DATA FOR FLOOD MONITORING

The Institute of Photogrammetry and Remote Sensing (IPF), University of Karlsruhe, The test area of this subproject from the Institute of Photogrammetry and Remote Sensing (IPF), University of Karlsruhe is located at the upper Rhine value with the coordinates UL N 48 ° 29'05" E 7 °45'00' LR N 48°25'00" E 7°47'50" where several water retention areas were established. These areas may be flooded to avoid disasters at the lower Rhine valley, where several flood events caused immense damage during the last few years. In addition the water retension areas are being retransferred into a natural state of fauna and flora for ecological reasons. This process is enforced by recurrent intentional flood events, called ecological flooding. In this context, several points of interest may be served by remote sensing techniques. For example the monitoring of flooded areas during ecological flooding, the distribution of water within the retention area, the water volume an area may hold and so on.

In a first step several data sets were acquired to meet the requirements of a context based SAR data analysis. From the German weather service (DWD) weather data were ordered: especially the wind conditions within our test area are of interest. On water surfaces, the wind condition is an essential mapping condition for SAR images, and can profitably be explored by an automated interpretation method for the SAR image data. Two SAR image pairs from the ERS–1/ERS–2 tandem mission have been ordered by our RAPID partner DLR for the purpose of updating the map information we gathered so far. One of the pairs was acquired during an ecological flooding within a retension area. So the IPF will study the mapping of the flooded areas by the intensity SAR image as well as the interferometric data sets to demonstrate the capabilities of this new techniques. By comparing the list of past flooding events with the available ERS–1/ERS–2 images in the archive of DLR – DFD, we found another match for a 1995 event. Since this SAR imagery has been acquired in 1995, only two pass interferometry will be possible and thus, the evaluation of interferometric products for this event is not of interest. Nevertheless a continued observation of such events by SAR intensity images would be of interest in this context. Digital terrain models are one focal point within this RAPID subproject. They are used to determine the volume of retension areas and they serve as context for an automated interpretation of actual SAR information. Therefore, the precision of different sources of DEMs is also of interest in this project.

In order to enable a higher degree of automation for the data evaluation we aim at the creation of a 'fuzzy' expert system, which holds all rules describing the relations between the actual SAR input data, the known mapping conditions such as wind force and the final event (e.g. flooded areas) the IPF want to reason about. In addition there are a lot of unknown mapping conditions influencing the final SAR signal. These condi-

tions may not be considered, but their influence on the SAR signal may be extracted by means of GIS technology directly from the SAR image. For example, the roughness of a water body may be estimated by the SAR signal within all water areas of a given minimum size, shown in a thematic base map. For that purposes a classification scheme was established and an evaluation of tools and libraries for the implementation of the classificator was realized.

8. IMPROVEMENT OF SATELLITE DATA INTERPRETATION THROUGH INTERFEROMETRIC ANALYSIS

Different datasets over the Philippines were acquired and processed since the official start in 1996. In the testareas groundstudies were made and a vegetation classification has been completed. The vegetation types were grouped into three clusters:
– vegetation types that can be identified on Spot/ Landsat images,
– vegetation type that can be identified on aerial photographs,
– vegetation type that can only be identified in the field.
The work is carried out by the University of San Carlos, Phlippines.

7. CONCLUSION

The preoperational InSAR system as basic element is capable to produce coherence maps and DEM. The availability of tandem data from the foreign station is at the moment a bottleneck, because a lot a required frames were rejected the the satellite system. For first interpretation the available ERS–products are sufficient.

The rainforst monitoring the coherence information is a very usefull dataset for interpretation and classification and will be integrated to the standard classification process. Also the detection of linear features with In SAR is an sucessfull approach.

The application institutes got and will get different dataset from their testarea und will continue with their investgation.

PRELIMINARY RESULTS OF LANDCOVER ANALYSIS OF CALANDA AREA USING ERS-1/2 SAR AND LANDSAT-TM DATA

Angel Valverde, Rogelio de la Vega

Escuela Técnica Superior de Ingenieros de Minas - Universidad Politécnica de Madrid, Madrid, Spain
Rios Rosas 21; 28003 Madrid, Spain
phone: 34.1.336.70.07, fax: 34.1.336.69.62
topytel@dexmi.upm.es

Rafael García, Constancio González

Escuela Universitaria de Ingeniería Técnica Agrícola- Universidad Politécnica de Madrid
Ciudad Universitaria s/n; 28040 Madrid, Spain
phone: 34.1.544.58.00, fax:34.1.549.30.02

Victoriano Moreno, Antonio Martínez, Iksu A. Kyun

INDRA Espacio S.A.,
Mar Egeo, 4 Pol. Ind. no.1 San Fernando de Henares, E-28850, Madrid
vmoreno@mdr.inisel-espacio.es, amar@mdr.inisel-espacio.es, ikyun@mdr.inisel-espacio.es.
phone: 34.1.396.39.35, fax: 34.1.396.39.12

ABSTRACT

Temporal evolution of land cover types was studied by means of remotely sensed data. Landsat Thematic Mapper and ERS-1 SAR data sets were available. Comparing automatic TM image classifications from different dates, we achieved detailed statistics of land cover changes. Classification schemes of ERS images were tested, and also in combination with TM data. TM classifications are more accurate than that obtained with SAR and allows temporal change monitoring of 9 classes. Although ERS-1 data had given worse results, interesting information were found.

Keywords: land cover evolution, Landsat Thematic Mapper, ERS-1 SAR, image classifications.

1. INTRODUCTION

Teruel is one of the poorer provinces of Spain. Desertization and downing economy forced to a population loss. The Calanda Desert area is one the most affected zones. Besides, an interesting geographical phenomenon can be seen: in 1981 ENDESA, an Electrical Company, started an open pit exploitation near Andorra village and in 1986 it was extended. After 11 years from the beginning of activities, 176 Has were restored for agriculture and natural vegetation. Remotely sensed data make possible a digital analysis of land cover and thus economical activities.

This paper presents the results of land cover changes using TM and the preliminary results of ERS classifications.

2. TEST AREA PRESENTATION

The study area is located at inner North East of Spain:

	UTM X	UTM Y
NW	706,451.19	4,570,386.25
SE	747,750.98	4,530,656.32

The climate is semi arid Mediterranean of cold winters, with annual rain rate of 500 mm, frequent and dominant West winds.

The soil has grown upon a geological substratum of limestone, sand and clay rocks, with fine sand texture, basic (pH = 7-8) and poor in organic materials.

These climatic and soil characteristics, in junction with roughed and gully terrain, cut by steep riverbanks of variable aspects affected by erosion phenomena determine a poor vegetation, esclerophylous high-medium shrubs, like *Juniperus comunis* and *Quercus rotundifolia*, and low shrubs, like *Rosmarinus officinalis* and *Thymus vulgaris*. There are also *Pinus pinaster*, and natural pulse herbaceous vegetation. They show that the soil is degraded and low productive.

Some olive and almond trees plantations are present within the valleys, but the main culture lands are dedicated to dry cereal farming (ENDESA, 1994).

3. METHODOLOGY

Following materials were available for this work:

- ERS-1&2 frames from 1993 to 1996
- LANDSAT-5 Thematic Mapper images, from 1984 and 1995
- CORINE digital land cover map and visually interpreted sheets
- Digital Elevation Model (DEM)

SPECKLE FILTERING AND GEOCODING OF ERS DATA.

All ERS data were read, subset and transposed in SAR data reading and handling software developed at INDRA Espacio.

Two speckle filters also developed at INDRA Espacio were tested.

a. Geometric filter: 1 iteration was enough for decreasing noise but preserving edges and linear features quite acceptable. It created homogenous zones necessary for further procedures.

b. Sigma filter: noise reduction level was poorer than the geometric filter, and there were too many isolated pixels left even using 5 by 5 window size iterations.

Thus geometric filter was chosen for this task.

Filtered data were grouped in descending or ascending stacks, and then geocoded against TM and DEM composed images. We used a shaded DEM illuminated like a SAR image combined with TM bands. TM bands were combined upon this shaded DEM, for retrieving radiometric contents.

Common point searching procedure had to be done with certain guidelines:

- Looking for zones not affected by high relief; they could be entry of gorges, top of shallow hills or the bottom of small valleys, and river junctions; railways and roads are excellent, if available.

- Once the points similarity is sure, it had to be found pixel-size level spatial and spectral pattern coincidence, i.e., the elements form and tone —even though the SAR and TM data have no correlation, it is frequent to find similarities between SAR and near-infrared channel (TM4), due to their sensitivity to surface water content. A shallow hill could have the same shape in both imagery, and its top divides quite clearly both illuminated and shaded slopes.

For ascending pass, shading required the following parameters: Sun azimuth = 255° and Sun elevation angle = 67°. Sixty five (65) control points have been initially found, with a total RMS error of 164,12 meters (6,56 pixels). After deleting points with higher errors, 20 points were left, with total RMS error of 22.95 m (0,92 pixel).

For descending pass, shading required the following parameters: Sun azimuth = 95° and Sun elevation angle = 67°. As well as ascending pass, TM bands were combined upon this shaded DEM, for retrieving optical and infrared radiometric contents. We started with 52 common points, with an initial RMS error of 181 m. After rejecting non-accurate points, 15 points were left. Total RMS error: 15.63 m. Then final ERS geocoded descending pass layer stack were generated.

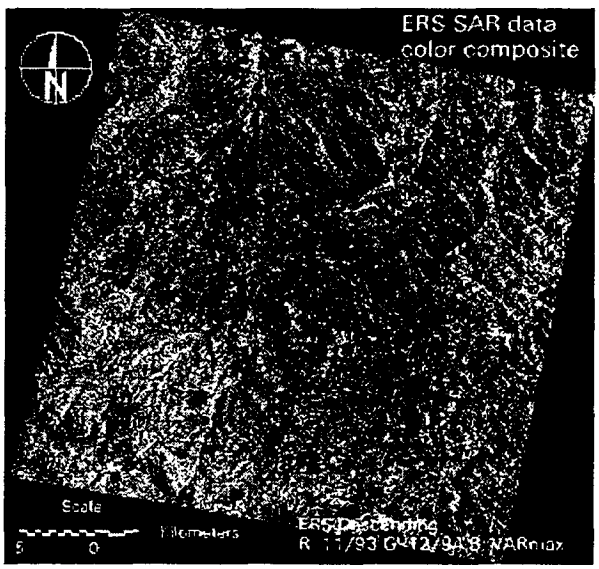

LAND COVER TEMPORAL EVOLUTION ANALYSIS.

This analysis were carried out comparing TM classifications of 1984 and 1995. Supervised method had been used. The first classification we carried on was 1995 TM. This will be used as a guide for SAR classification. CORINE legend had to be modified and generalized to better fit to our study area and classifying conditions. Therefore, this legend was established.

Training fields were delimited for retrieving spectral signatures. Maximum Likelihood algorithm was used, and mode filter was applied, for avoiding "salt and pepper" effect. An accuracy assessment was performed based on 242 stratified-random verification points, achieving a high accuracy (more than 80 %). A tabular class inventory was generated, including categories extent.

1984 TM image was also classified. In 1984 differences between croplands and natural vegetation were sharper than now. The overall accuracy level for this one was 78,64%.

NEW CATEGORIES	CORINE code #	CORINE COVER TYPE
1. Artificial surfaces	1. 10000	Artificial surfaces
2. Crop for dry farming	2. 21100	Crop for dry farming
3. Irrigated crop / riverside vegetation	3. 21210	Irrigated herbaceous crop
4. Pastures	12. 32100	Pastures
5. Shrubs	14. 32400	Shrubs with trees
6. Coniferous trees (pines)	11. 31200	Coniferous trees
7. Sparse or non-vegetated openfields / bare soil	15. 33000	Sparse or non vegetated openfields
8. Water surfaces	17. 51000	Inland water
9. Dry lagoons	No CORINE correspondence	

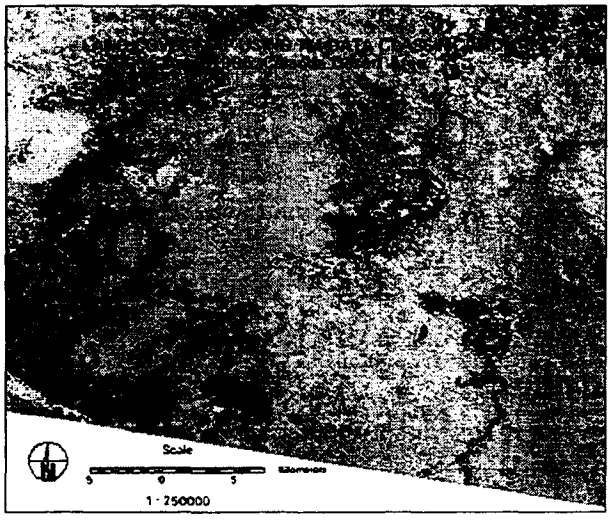

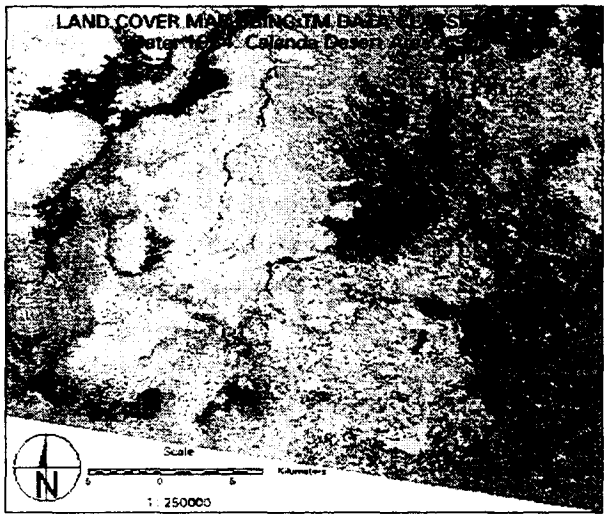

1 Artificial surfaces
2 Dry farming
3 Irrigated farming/riverside vegetation
4 Pastures
5 Shrublands
6 Coniferous
7 Bare soil
8 Water
9 Dry lagoons

1 Artificial surfaces
2 Dry farming
3 Irrigated farming/riverside vegetation
4 Pastures
5 Shrublands
6 Coniferous
7 Bare soil
8 Water
9 Dry lagoons

1995

Class names	Area (ha)	Percentage
No classified	0	0%
1 Artificial surfaces	634.23	0.48%
2 Crop for dry farming	11,299.68	8.63%
3 Irrigated crop / riverside vegetation	10,064.61	7.68%
4 Pastures	37,528.20	28.65%
5 Shrubs	62,310.51	47.57%
6 Coniferous trees (pines)	8,118.81	6.20%
7 Sparse or non-vegetated openfields and bare soil	766.89	0.59%
8 Water surfaces	217.98	0.17%
9 Dry lagoons	47.43	0.04%
Total	130,988.34	100.00%

1984		
Class names	Area (ha)	Percentage
No classified	0	0%
1 Artificial surfaces	991.80	0.76%
2 Crop for dry farming	34,253.01	26.12%
3 Irrigated crop / riverside vegetation	11,257.29	8.58%
4 Pastures	30,932.28	23.59%
5 Shrubs	47,581.11	36.28%
6 Coniferous trees (pines)	5,310.54	4.05%
7 Sparse or non-vegetated openfields and bare soil	563.22	0.43%
8 Water surfaces	172.53	0.13%
9 Dry lagoons	89.37	0.07%
Total	131,151.15	100.00%

Comparing with 95 data, we have retrieved a simple chart of changes, as can be seen in figure 3.

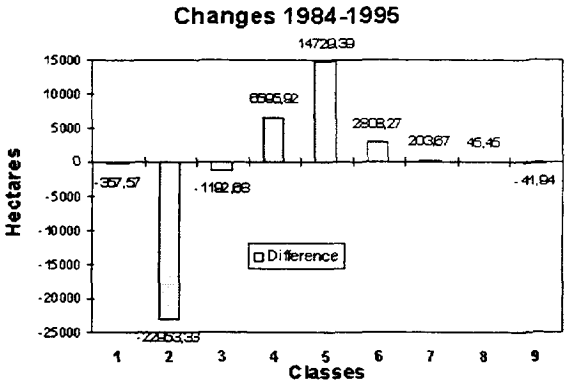

Major changing categories (more than 500 Ha) are #2 Dry Crops, #3 Irrigated Crops, #4 Pasturelands, #5 Shrublands and #6 Pines. #1 Artificial Surfaces had a significant variation, due to natural and culture lands recovering activities from open pit mining zones, in South-West of study area. Croplands, in general, have decreased, and natural vegetation of esclerophylous Mediterranean shrubs and pine plantations have increased. These phenomena show that agriculture activities are going down, meanwhile natural vegetation are recovering their original space, specially in hilly areas. The point is finding out whether the decrease of agricultural categories are caused by economic abandonment of activities.

Classification of ERS data.

At first sight, TM training sites superposed upon SAR images looked like confusing. Specially, artificial surfaces and relief slopes gave very similar response. There was no clear spectral or spatial patterns that allowed to distinguish different cover types, except water surfaces, dry lagoons, railway-looking linear features and villages. It was specially clear the V-shaped lignite processing factory and mining zone in Southwest of the area. We had to reshape training sites to match to ERS data. Finally, only descending pass data were tested.

We included two synthetic bands derived from SAR images, according to Nezry *et al.* (1995) studies: a) Multitemporal mean image and b) Maximum variation image: absolute maximum difference between dates. It would be possible to improve SAR layer separabilities by means of generating statistical bands that summarize some variables. We also introduced an artifact, adding +20 DN succession for each images, starting with the second date. Signatures means chart showed better separation between categories than former ERS attempts.

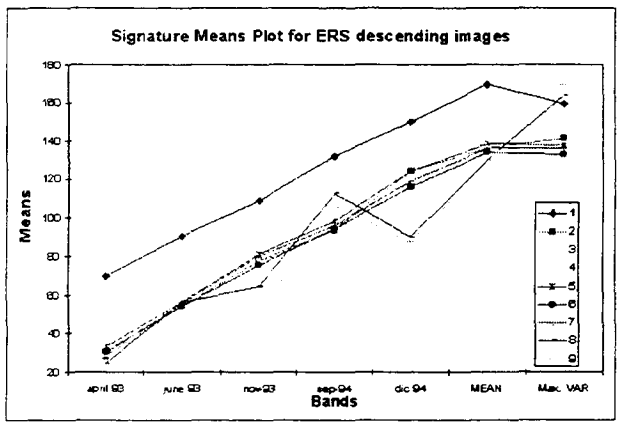

As result of separability analysis (without using a priori probability) 3 images were excluded, and following combination were used as input: 23 June 93, 10 November 93, 18 December 94 and Maximum Variation. There were some overclassified classes, like #7 and #3. Majority filters were applied two times, first

ignoring class #7 (5x5 pixels window), and second time ignoring classes #3 and #6 (3x3 pixels window).

Then classification was made and accuracy assessment was applied, with 255 stratified random points, and reached to an overall accuracy of 45.42%. This is a very low result, in spite of error filtering, but it could be considered normal, taking in account that we have used intensity images.

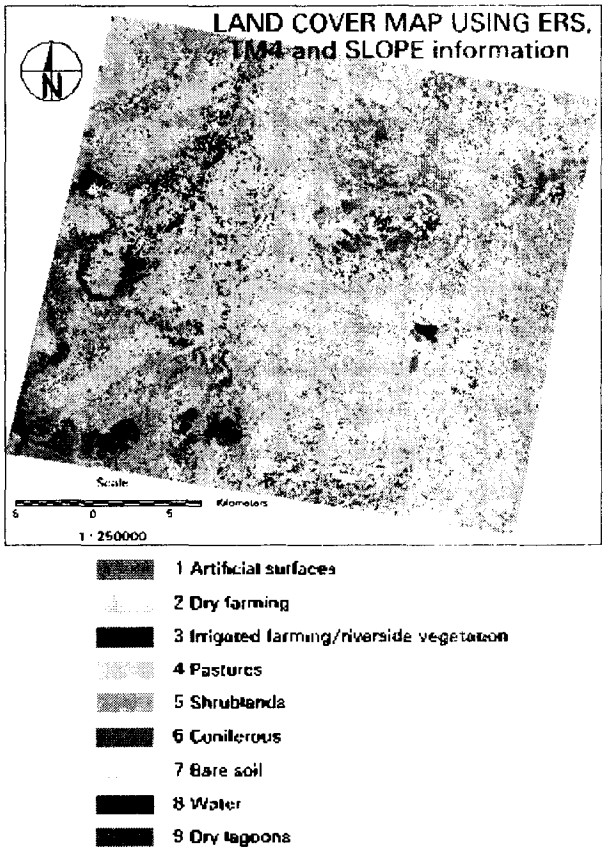

A second classification attempt was made, using as inputs: 23 June 93, 10 November 93, 18 December 94, Maximum Variation, TM band #4 (nIR) and slope information derived from DEM.

Also this time Maximum Likelihood algorithm was used, and the accuracy assessment a subtle improvement, although still low: 57.42%.

CONCLUSIONS

Plates 1 and 2 show 1995 and 1984 TM classifications respectively. Plate 3 shows both descending and ascending ERS image stacks color compositions. Plate 4 shows ERS descending pass classification.

Temporal evolution of land cover types were carried out successfully using TM classifications. More changing categories were Dry Farming, Shrublands, Pastures and Coniferous. Further studies could aim to correlate these results to possible environmental impacts of lignite mining activities, specifically that affected to dry farming. Either could be caused by actual pollution problems or another economical reasons, like Common Agricultural Policy or rural population loss.

SAR classification using descending pass and Maximum Variation images retrieved poor preliminary results. Although some unexpected classes appeared, by means of avoiding a priori probabilities in the Maximum Likelihood algorithm, such as Coniferous; and Irrigated Crops were quite well discriminated. Recognition of Coniferous could be caused not for its signature, but there exists high correlation between coniferous and steep slope areas. Water and Dry Lagoons were accurately assigned, meanwhile Dry Crops and Shrublands were significantly discriminated (over 60% of users accuracy).

Shallow relief of most part of study area allowed an accurate geocoding of SAR data. This is an important point for combining other data sources and making ground-truth analysis.

Further works will take in account other variables, like topographic data, TM bands merging, and SAR images could be enriched using sigma-naught and coherence images. Also ascending and descending pass combination variables will be tested.

REFERENCES

ENDESA, 1994, Minería a cielo abierto y medio ambiente en Andorra, Technical Notes. Zaragoza.

Nezry, E., Rémondière, S., Solaas, G. AA., Genovese, G., 1995, "Mapping of next season's crops during the winter using ERS SAR". Earth Observation Quarterly, 50 - December, pp. 1-5.

Curlander, J.C.; McDonough, R.N., 1991, "Synthetic Aperture Radar- Systems and Signal Processing". Wiley InterScience, 647 pages.

Leberl, F.W., 1989, "Radargrammetric Image Processing".Artech House, 595 pages.

POTENTIAL USE OF ERS.SAR DATA TO DISCRIMINATE NATURAL AND DEGRADED WOODY VEGETATION TYPES IN CENTRAL AFRICA

Vera De Cauwer, Robert De Wulf

Laboratory of Forest Management and Spatial Information Techniques, University of Gent
Coupure Links 653, B-9000 Gent, Belgium
phone: + 32 9 264 61 11, fax: + 32 9 264 62 40
Vera.Decauwer@rug.ac.be

ABSTRACT

The possibility to use ERS-SAR.PRI data for the discrimination of different types of tropical woody vegetation - shrub savannah, degraded forest and primary forest - was evaluated for study areas in Central Africa (Congo and Cameroon). The performance of mono- respectively multitemporal ERS.SAR data were evaluated, as well as the synergy between microwave and optical data. Texture information of the images was included. Results showed the high capacity of ERS.SAR images for a forest/non-forest distinction, but the limited potential to distinguish different types of woody vegetation. No discrimination within the superclass 'forest' was possible. Plantations could not be distinguished. Nevertheless a discrimination of shrub savannah and forest was possible for the study area in the humid tropics (Congo). On the other hand, multitemporal data sets of ERS.SAR images allowed a good distinction of dry and humid grass savannah and of different agriculture types. Hence, additional information to optical satellite images can be provided. Texture information did not enhance the classification accuracies. The pixel-based fusion of the optical and radar images gave no satisfactory results.

Keywords : ERS.SAR, Central Africa, woody vegetation, tropical forest, soil cover

1. INTRODUCTION

This study aims to contribute to a better and systematic knowledge on the capabilities of ERS.SAR for forest monitoring in Central Africa. Little is still known on the methodological aspects, constraints or particularities when dealing with tropical Africa instead of Southeast Asia or the Neotropics. More clarity is urgently needed on this subject as it is crucial in applications such as TREES or global carbon cycling projects. The distintion of woody vegetation in terms of soil cover was considered as a major topic of research.

2. STUDY AREAS

Study areas were chosen in the humid and the dry tropics in order to cover a complete range of crown cover conditions. In Northern Congo, two study areas were established at a latitude of about 0° (figure 1). A third study area is situated in Northern Cameroon at a latitude of about 10° North (figure 2).

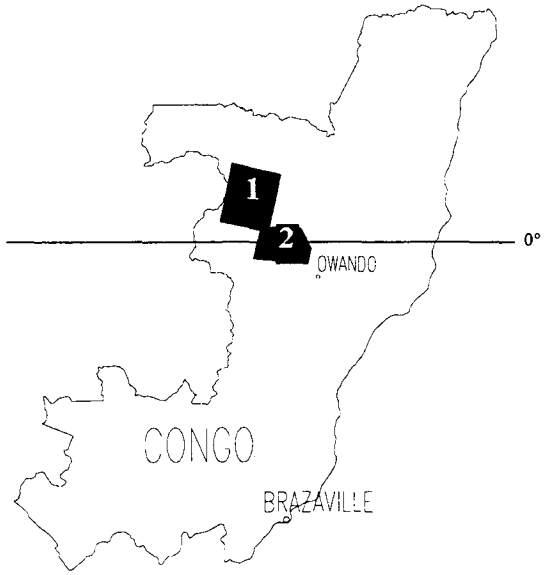

Figure 1 - Location of study areas 1 and 2 in Congo

2.1. Study area 1 : Odzala (Congo)

The study area of Odzala concerns a region covered by a mosaic of equatorial forest, marsh forest and savannah. The relief varies between 400 and 600 m a.s.l. Human influence is very limited as the region includes the National Park of Odzala, the oldest nature reserve of Congo (1935).

Available data

- 3 ERS.SAR images : one image of the dry season (20/07/94) and a tandem pair of the rainy season (22/11/95 and 23/11/95);
- 2 geocoded SPOT images (Jan. 1995);
- Digital vegetation map (Maisels *et al.*, 1996);
- Training polygons in digital format realised during a study of Maisels *et al.* (1996).

2.2. Study area 2 : Makoua (Congo)

The study area of Makoua concerns a region covered by a mosaic of equatorial forest, gallery forests, shrub savannah, grass and swamp savannahs. The relief varies between 300 and 400 m a.s.l. Human influence in the region is limited. A few industrial plantations of oil palm or cacao are present, often extensively used or even abandoned. Shifting cultivation is present near all types of human settlements. Northern Congo is among the most sparsely populated regions of Africa, with an average of 1 to 3 persons/km².

Available data

- 2 ERS.SAR images : one image of the dry season (09/08/94) and one of the rainy season (08/12/95);
- 1 geocoded LANDSAT TM image (Nov. 1990);
- Aerial photographs (1994);
- Field data collected from June till July 1994 during a study of Peirsman & Borry (1996).

2.3. Study area 3 : Dam of Maga (Cameroon)

The study area is mainly covered by formations of woody vegetation and grasses. Dense dry forest formations are rare. The relief varies between 300 and about 450 m a.s.l. Undisturbed natural vegetation has disappeared due to human activities. The population density is on of the highest in Cameroon with about 12 to 54 habitants/km². Agriculture and cattle breeding are the predominant land use. Even in the few protected zones, burning or grazing can be observed. Secondary succession of abandoned fields by native vegetation is halted at the stage of open shrub savannah. The over-exploitation ultimately leads to soil degradation, expressed by the formation of crusts in the region (Goossens & Goossens, 1994).

Available data

- 3 ERS.SAR images : one image of the rainy season (03/08/94) and a tandem pair of the dry season (14/12/95 and 15/12/95);
- 1 geocoded LANDSAT MSS image (Feb. 1991);
- Field data collected from March till April 1994 during a study of Goossens & Goossens (1994).

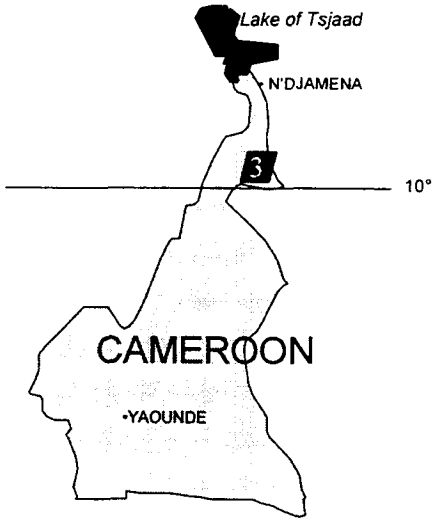

Figure 2 - Location of study area 3 in Cameroon

3. METHODOLOGY

3.1. Pre-processing

A radiometric calibration of the ERS.SAR.PRI images was performed using the formulas proposed by ESA (Laur, 1992). The calibrated 16-bit images were imported into the image processing software (MGE module of INTERGRAPH), during which they were converted to 8-bit images. A subsampling to a pixel width of 25 m - the original resolution of ERS.SAR images - was executed. The subsampling and the conversion to 8-bit reduced the data volume from 132 Mb to 17 Mb, which allowed faster processing during further analysis. A geometrical correction of the ERS images was realised with the geocoded LANDSAT and SPOT images. ERS.SAR images of the same study area were co-registrated.

3.2. Data analysis

The analysis of the images was based on a digital, pixel-based classification. Both tonal and textural information were used as input to the classifier. Following procedure was followed :

1. Filtering : It is necessary to apply a form of filtering to reduce the speckle of the radar images before a pixel-based classification can be performed. The adaptive radar filters Lee, Refined Map and Frost were tested on the data set of study area 1. The Refined Map filter gave slightly better results and was used to filter all ERS.SAR images.

2. Creation of texture images : Texture images are generated by automatic algorithms and give the spatial positions and directions of edges, lines, strong point scatters and homogeneous areas. They were created by calculating the coefficient of variation in a 7x7 window.
3.Training : Evaluation of class separability was based on training statistics i.e. the Jeffries-Matusita distance.
4. Classification : A supervised classification was executed with the Maximum likelihood and the Nearest Neighbourhood algorithms. The Maximum likelihood classifier is a parametric classifier which assumes a normal probability distribution for the data to be classified. However the information contained in the texture images are simply structure labels and no distribution can be assumed for this information. Therefore the Nearest Neighbourhood classifier, a non-parametric classifier, was used to classify the texture images (Conway *et al.*, 1993).
5. Post-classification filtering : A modus filtering with window width of 7x7 was executed to allow a further reduction of the speckle.
6. Analysis of the results : The analysis of the results was performed by a cross tabulation of a control image and the digital classification results resulting in an error matrix. Overall accuracy and Kappa-value were calculated based on the error matrix. The control images contained information not used during training.

Different data sets were used :

- Monotemporal (not for study area 3);
- Multitemporal: besides the original data, change indices were used during the multitemporal approach. Change indices can be calculated in different ways. Rignot & van Zyl (1993) concluded on the basis of a mathematical evaluation of SAR statistics that ratio images are to be preferred over difference images. Ratio images should also be relatively independent from the relief effect (Le Toan, 1995);
- Combination of optical and radar data : techniques for fully integrated analysis of optical and radar data are poorly developed. As far as visualisation of combined data is concerned, some results have been obtained using the IHS (Intensity-Hue-Saturation) technique. Few literature was found on the computer-based analysis of multi-sensor data. Schistad Solberg (1994) divided the existing sensor fusion techniques into three categories according to the stage at which the fusion is performed : the pixel-based fusion, the feature-based fusion and the decision-level fusion. Those methods assume that no changes with respect to the pattern classes have occurred between the acquisition of the different images; few studies pertained to classification in a temporally dynamic environment. For this study, a pixel-based fusion was used, without taking the temporal attribute into account.

4. RESULTS

4.1. Study area 1 : Odzala (Congo)

The classification results for study area 1 are summarised in table 1. A forest, savannah distinction was possible with the dry season image. The rainy season images seemed to have a limited potential for a forest, savannah distinction. Rainy season image 1 could not be classified, while the results for rainy season image 2 were rather poor. The differences between the images, acquired with only 1 day difference, can be explained by different soil moisture conditions.

Table 1 - Classification results for study area 1

	Overall accuracy (%)	Overall Kappa (%)
Monotemporal		
Dry season : forest, savannah	91	75
Rainy season 2: forest, sav., hab.	76	42
Multitemporal		
3 filtered images: 6 classes	85	62
3 filtered + 2 ratio images: idem	90	71
Combined		
SPOT : 7 classes	76	59
SPOT + ERS : idem	82	61

A multitemporal classification into the classes forest, savannah, swamp, marsh, water and habitations yielded an overall accuracy of 85 %. No forest types could be distinguished. The classes water and habitations were poorly classified due to confusion with shadow and layover effects of the relief. In fact, the multitemporal data set does not give much more information than the dry season image. The ratio images enhanced the classification. This may be due to the relative independence from topographic effects of ratio images (Le Toan, 1995).

Contrary to the ERS.SAR images, several forest types could be distinguished on the SPOT images : dense, open and secondary forest. Furthermore, swamp, savannah, water and habitations were separated. The addition of the ERS.SAR images ameliorated the accuracy sligthly.

The use of texture images did not enhance the classification accuracy. The modus filtering increased the overall accuracies with a maximum of 5 %.

4.2. Study area 2 : Makoua (Congo)

The classification results for study area 2 are summarised in table 2. The dry season image allowed a forest, savannah distinction. Nevertheless a confusion existed between forest and a type of grass savannah that was not present in study area 1. Probably it concerns humid grass savannah, as it shows a constant high backscatter (figure 3) and is mostly situated at lower altitudes. Corves *et al.* (1995) stated that herbaceous vegetation in floodplains of Brazil exhibited backscatter levels similar to woody vegetation. The grass type was hence called swamp savannah, although this could not be verified with the available field data.

Table 2 - Classification results for study area 2

	Overall accuracy (%)	Overall Kappa (%)
Monotemporal		
Dry season: forest, sav., burnt	82	72
Rainy season: forest,shrubs.,burnt	93	85
Multitemporal		
2 filtered images: 7 classes	69	61
2 filtered + 2 ratio images: idem	69	60
Combined		
LANDSAT TM : 7 classes	73	65
LANDSAT + ERS : idem	61	51

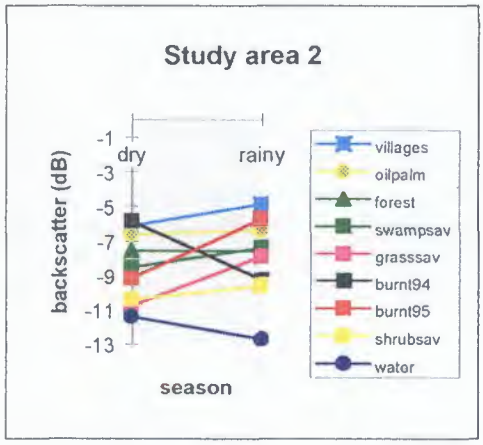

Figure 3 - Temporal evolution of training classes

A forest, savannah distinction was not possible for the rainy season image due to confusion between forest, grass and swamp savannah. Shrub savannah could be separated due to its lower backscatter than forest (figure 3). This corresponds with results of Paudyal *et al.* (1995) in Thailand. During training, slight confusion was noticed for shrub savannah with soil cover > 40 %.

Burnt savannah could be noticed on both images, especially on the dry season image. ERS.SAR images seem to have a high potential for fire monitoring.

A multitemporal classification into the classes forest, shrub savannah, swamp savannah, grass savannah, oil palm, villages and burnt yielded a overall accuracy of 69 % (figure 4). Shrub savannah with different soil cover (between 2 % and 70 %) could not be distinguished. The influence of soil moisture or soil vegetation on the backscatter of shrub savannah seemed to be more important than the soil cover. Ratio images did not enhance the accuracy. This might be explained by the relief which is less pronounced than in study area 1.

Seven classes could be distinguished on the LANDSAT image : forest, shrub savannah, grass savannah, oil palm, water, villages and short fallow. No forest types were distinguished during field work. Addition of the ERS images did not enhance the classification accuracy because many pixels were classified as zero. On the other hand, class accuracies ameliorated. Probably a decision-level fusion would give better results.

Addition of texture images did not enhance classification accuracies, neither did the modus filtering.

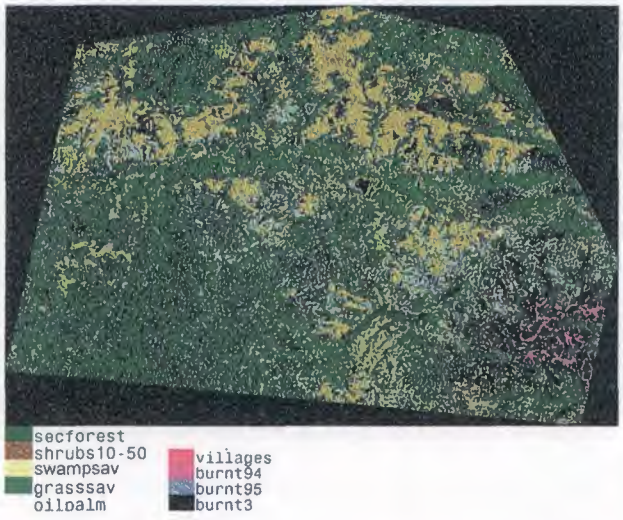

Figure 4 - Study area 2 : Multitemporal classification

4.3. Study area 3 : Dam of Maga (Cameroon)

The classification results for study area 3 are summarised in table 3. Seven classes could be distinguished during the multitemporal approach : woody vegetation, crusts, grass, water and 3 types of agriculture lands. Confusion existed between dry forest, tree savannah, shrub savannah and plantations of *Acacia albida;* they were joined in a class 'woody vegetation'. Distinctions in terms of soil cover could not be made.

Table 3 - Classification results for study area 3

	Overall accuracy (%)	Overall Kappa (%)
Multitemporal		
3 filtered images: 7 classes	66	52
3 filtered + 3 ratio images: idem	64	49
3 filtered + 3 texture images : id.	64	48
Combined		
LANDSAT MSS : 4 classes	78	63
LANDSAT + ERS : 7 classes	73	61

Only 4 classes could be distinguished on the LANDSAT MSS image : woody vegetation, crusts, grass and water. Reason is that the mean local variation on the ground surface is about the size of a pixel. Unsupervised classification is in this case more appropriate than supervised classification (Goossens & Goossens, 1994). Nevertheless, the addition of the LANDSAT MSS image to the ERS classification enhanced the overall accuracy.

5. CONCLUSIONS

Following conclusions could be made for the classification of the ERS.SAR images :

- A forest/savannah classification is feasible with a dry season image, sometimes with a rainy season image. Forest/non forest monitoring depends strongly of temporal soil moisture conditions.
- No discrimination within the superclass 'Forest' was possible. Dense and open forest, swamp forest, as well as primary and secondary forest could not be distinguished.
- In the humid tropics (Congo), shrub savannah could be separated of secondary forest. Slight confusion existed for shrub savannah with crown cover > 40%.
- In the dry tropics (Cameroon), dry forest, tree and shrub savannah could not be distinguished.
- Shrub savannah with different crown coverage percentages (between 2 % and 70 %) could not be distinguished in the dry and humid tropics.
- Distinction between forest, grass savannah, swamp savannah and shrub savannah was possible for the multitemporal approach of study area 2 (Congo).
- Plantations of oil palm and *Acacia albida* could not be distinguished.
- The pixel-based fusion of the optical and ERS images gave no good results. Probably a decision-level fusion would be more appropriate.

The results correspond with other studies that mention the poor sensitivity of ERS.SAR for biomass. This is caused by its low incidence angle (23°) and its specific wavelength (C-band). Higher wavelengths or radar interferometry could offer new possibilities.

6. ACKNOWLEDGEMENTS

Funding for the project was provided by the Belgian Federal Office for Scientific, Technical & Cultural Affairs. The ERS.SAR.PRI images were made available by ESA.

REFERENCES

CONWAY, J.A., DE GROOF, H. & SIEBER, A.J., 1993. TREES project : a suite of tools for information extraction from ERS-1 data. Proceedings First ERS-1 Symposium. Space at the Service of our Environment, Cannes, 1992.

CORVES, C., CAVES, R., QUEGAN, S., DE GRANDI, F. & NEZRY, E., 1995. Evaluating multi-temporal ERS-1 SAR data for mapping forests and detecting forest clearing in the Manaus region in Brazil. TREES ERS-1 Study '94 Final Workshop. JRC Ispra, February 1995. JRC & ESA.

GOOSSENS, E. & GOOSSENS, R., 1994. Forest resources assessment in the dry tropics : a digital alternative for the FAO Forest Resources Assessment 1990 project. University of Gent.

LAUR, H., 1992. Derivation of backscattering coefficient Sigma° in ERS-1.SAR.PRI products. ESA/ESRIN.

LE TOAN, T., 1995. Assessment of ERS-1 SAR data for forest studies in Southeast Asia. Earth Observation Quarterly, 48.

MAISELS, F.G., MBOLO, V., GULICK, S., FAY, M. & PEIRSMAN, K., 1996. Cartographie de la végétation du Parc National d'Odzala. AGRECO-CTFT en collaboration avec l'Université de Gand et WCS, 70 p.

PAUDYAL, D.R., TIANGEO, P.N., ASCHBACHER, J. & KWAN ANG, Y., 1995. Assessment of multi-temporal ERS-1 SAR data for tropical forest discrimination and mapping in southern Thailand. TREES ERS-1 Study '94 Final Workshop. JRC Ispra, February 1995. JRC & ESA.

PEIRSMAN, K. & BORRY, F., 1996. Monitoring tropical forest using spatial information techniques. TELSATIII/02/005 project, final report, University of Gent.

RIGNOT, E. & VAN ZYL, J., 1993. Change detection techniques for ERS-1 SAR data. IEEE transactions on geoscience and remote sensing, 31(4), p. 896-906.

SCHISTAD SOLBERG, A.H., 1994. Multisource classification of remotely sensed data : fusion of LANDSAT TM and SAR images. IEEE transactions on geoscience and remote sensing, 32(4), p. 768-777.

CLASSIFICATION D'UNE IMAGE RADAR : APPLICATION A LA CARTOGRAPHIE AUTOMATIQUE DE LA MANGROVE AUTOUR DE LA REGION DE DOUALA (CAMEROUN)

Annick Legeley-Padovani & Anisait Beauvais
ORSTOM, 32 rue Henri Varagnat, 93143 Bondy Cedex, France
phone : 01 48 02 55 57; fax : 01 48 47 30 88

Alain Akono & Emmanuel Tonyé
Ecole Nationale Supérieure Polytechnique (LETS), B.P. 8390 Yaoundé, Cameroun

Jean-Paul Rudant
Université PMC (LGGST), Tour 26, 4 place Jussieu, 75005 Paris, France

RESUME

Une image ERS1 est utilisée pour cartographier automatiquement les mangroves de la région de Douala (Cameroun). Cet objectif est atteint grâce à deux types de traitements : la classification non supervisée et la Morphologie Mathématique. L'image résultante a permis d'individualiser les zones de mangrove dense et celles de mangrove dégradée.

INTRODUCTION

Les mangroves constituent un écosystème de haute productivité biologique grâce au relais des éléments nutritifs d'origine continentale au profit de nombreuses espèces végétales puis animales. Elles constituent ainsi un maillon important dans la chaîne alimentaire à l'interface continent-océan [Baltzer et al., 1995]. Les cartes dont on dispose sont généralement très anciennes et les moyens requis pour en établir de plus précises sont très onéreux.

Le but de ce travail est l'élaboration d'une méthode de cartographie automatique. Cette méthode a été élaborée sur une image radar de la région de Douala (Cameroun).

ACQUISITION ET TRAITEMENT DE L'IMAGE SAR

L'image traitée est une sous scène de l'image ERS1 acquise en Août 1994 (fig. 1).

2 . METHODOLOGIE

2.1 Principe de la méthode

Les vagues provoquent une forte rétrodiffusion du signal radar et les domaines marins et terrestres présentent des parties de même radiométrie. Pour délimiter la partie terrestre nous avons eu recours à l'analyse d'image. Nous constituons ainsi un masque d'analyse qui sera utilisé pour la suite des traitements.

La cartographie automatique de la mangrove consiste à individualiser des entités connexes. Cette transformation a été effectuée uniquement par transformation d'images.

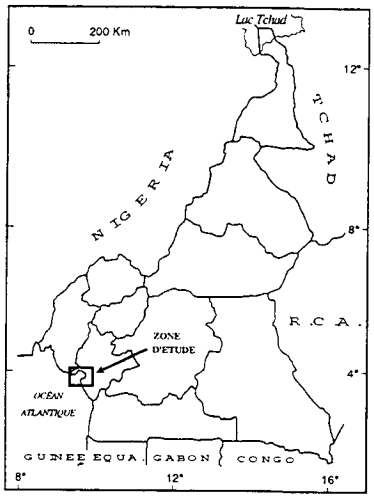

Figure 1 : Schéma de situation

2.2 outils d'analyse

Afin de rendre l'image originale plus contrastée nous avons utilisé un filtre passe bas.

Nous avons choisi de ne pas superviser les classifications; nous avons utilisé la méthode des *Nuées Dynamiques à centres mobiles* (Diday, 1971). Afin d'obtenir des surfaces plus cette dernière est lissée avec le filtre de Nagao (Nagao et Matsuyama, 1979).

L'identification d'entités connexes se fait par étiquetage automatique d'une image binaire permettant de coder différemment chaque entité connexe.

Pour délimiter des formes aux contours lisses, nous avons utilisé les transformations d'images binaires de la Morphologie Mathématique à savoir :

- la *dilatation* et l'*érosion*;
- l'*ouverture* et la *fermeture*.

Le lissage des contours a été obtenu à l'aide d'un lissage majoritaire. Seule la *reconstruction géodésique* (Coster et al., 1989) a la propriété d'éliminer les entités de faibles surface, sans modifier les contours. Elle est également utilisée pour "boucher les trous" d'une entité connexe. En effet, si on inverse l'image binaire, les trous sont assimilés à du bruit et donc éliminés par *reconstruction géodésique*. L'entité connexe "bouchée" est obtenue par une nouvelle inversion.

3. RESULTATS

3.1 Constitution du masque

L'image originale a été classifiée en 15 classes par la méthode des *Nuées Dynamiques* [Diday, 1971]. Sur le résultat de cette classification (2A) les limites de la côte se distinguent très bien. Les classes 1, 2, 3 et 4 sont extraites par binarisation.

L'image binaire a subi une *fermeture* de taille 1, elle a été nettoyée par *reconstruction géodésique* [Coster et Chermant, 1989] puis par étiquetage automatique. La dernière étape consiste à faire une *fermeture* [Serra, 1982] de grande taille puis à remplir manuellement la mer (2B). Cette dernière opération manuelle permet d'exclure du masque la terre comprise entre les bras du fleuve Wouri.

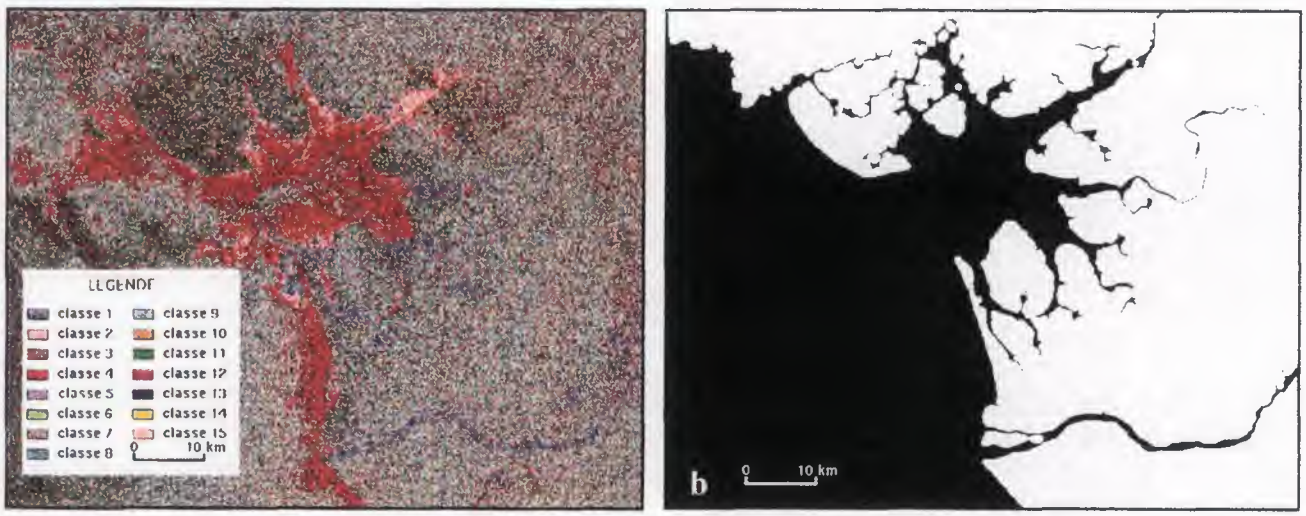

Figure 2 - Constitution du masque. (a) classification de l'image; (b) masque.

3.2 Cartographie automatique de la mangrove

L'image originale a été filtrée avec le masque inversé puis par un filtre passe bas. Nous avons fait une classification non supervisée par la méthode des *Nuées Dynamiques* qui a été lissée avec un filtre de Nagao (3A).

Les zones de mangrove sont incluses dans les classes 7, 8 et 9 qui ont été binarisées. Une *reconstruction géodésique* avec une *érosion* de taille 1 a permis d'enlever les petites entités (3B). Cette image révèle deux zones différentes qui sont traitées séparément.

Pour la zone nord-ouest, une *ouverture* de taille 1 par un carré a permis de déconnecter les entités faiblement connectées. Sur la zone Est, une *fermeture* de taille 1 par un octogone permet de connecter les entités très proches. Pour les deux zones, une *reconstruction géodésique* avec une *érosion* permet d'éliminer les entités de petite taille. La zone Est a subi un dernier nettoyage après étiquetage automatique.

Les deux zones sont ensuite réunies (4A) et une *fermeture* de taille 5 par un octogone est réalisé. Afin de boucher les trous nous avons inversé l'image. Lors des *fermetures* effectuées les entités ont pu être exagérées, pour éviter ce défaut nous avons fait une intersection avec le masque. Un *lissage majoritaire* permet une représentation plus cartographique. Une dernière *reconstruction géodésique* élimine les très petites entités (4B).

4. CONCLUSIONS

Les deux types de mangrove : une mangrove dense sur la bordure immédiate du fleuve et une mangrove naine sur la partie Est sont différenciées. La partie dense est une zone à *Rhizophora* de grande taille tandis que

l'autre partie représente des mangroves dégradées [Baltzer et al., 1995].

Nous avons obtenu une cartographie automatique satisfaisante. Il sera toutefois nécessaire de valider cette cartographie par des observations complémentaires de terrain.

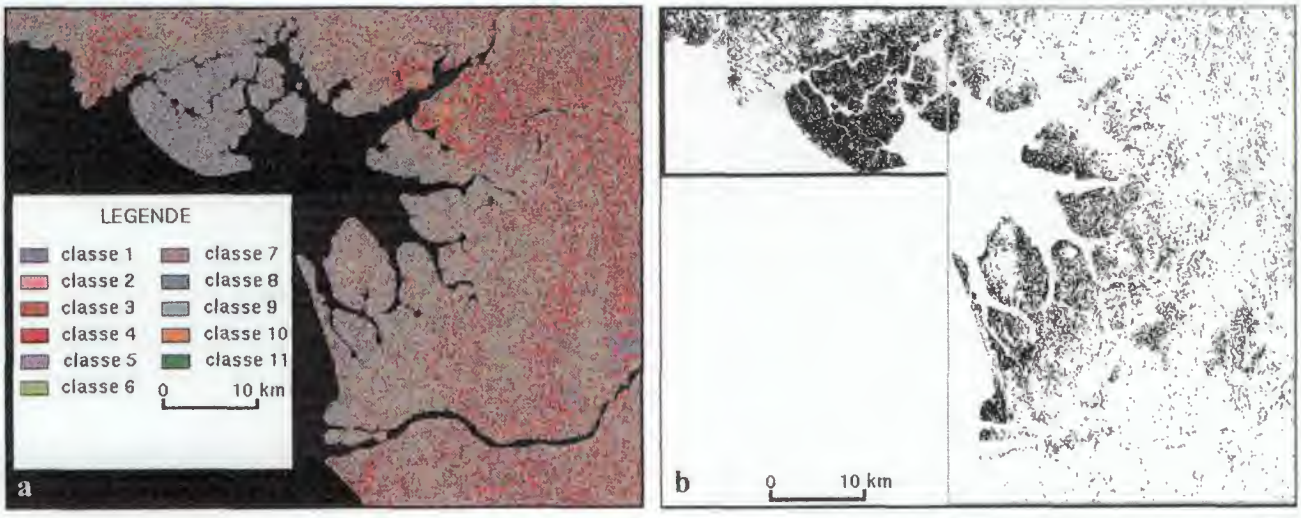

Figure 3 - Extraction de la mangrove. (a) classification de l'image masquée et filtrée, (b) zone de mangrove, les cadres noir et gris matérialisent les zones Est et Nord-Ouest.

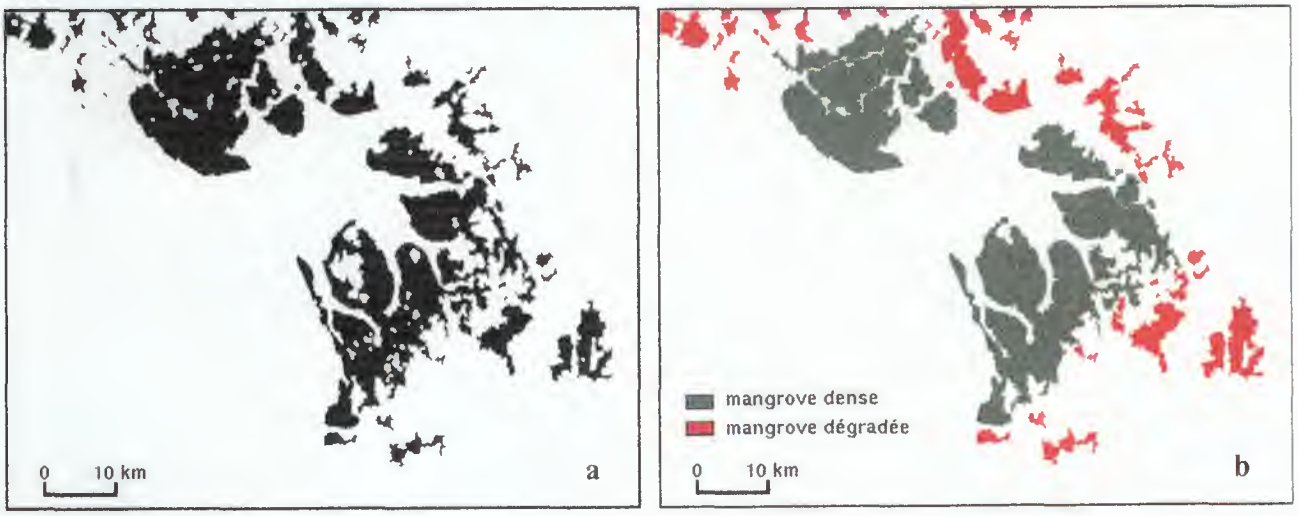

Figure 4 : Cartographie des zones de mangrove. (a) réunion des deux zones nettoyées, (b) résultat final.

REFERENCES

Baltzer F., Rudant J.P. & Tonyé E 1995, Applications de la télédétection micro onde en bande C (Aéroporté ESAR et satellitaire ERS-1 à la cartographie des mangroves de la région de Douala (Cameroun) - *Proc of the 2nd ERS Applications Worshop*, London, 6-8 Dec 1995.

Coster M. & Chermant J.C. 1989, *Précis d'analyse d'images* - (Paris : CNRS).

DIDAY E. 1971, La méthode des Nuées Dynamiques - *Revue de Statistiques Appliquées*, 19, 19-34.

Nagao M. & Matsuyama T. 1979, Edge preserving smoothing - Computer Graphic and Image Processing, Vol. 9, 391-407.

SERRA J. 1982, *Image Analysis and mathematical Morphology* - (London : Academic Press).

REMERCIEMENTS

Ce travail et ces documents ont été réalisés lors d'un stage d'accueil haut niveau à l'Institut Français de Recherche Scientifique pour le Développement en Coopération (ORSTOM), Centre de Bondy. Nous avons utilisé le logiciel PLANETES - Laboratoire d'Informatique Appliquée, Bondy et le logiciel OSIRIS V3.0 - LATICAL/ESTEL, Nouméa.

Nous remercions le l'Atelier d'Informatique et le Laboratoire des Formations Superficielles de l'ORSTOM, Bondy pour les facilités de travail offertes durant ce stage.

HEAT ISLAND STUDY IN THE AREA OF ROME BY INTEGRATED USE OF ERS-SAR AND LANDSAT TM

Giulia Abbate
ENEA-Casaccia, Environment Department, Via Anguillarese 301, 00100 Rome, Italy
Phone: +39 6 3048 4576, Fax: +39 6 3048 4925, E-mail: abbate@eca434.casaccia.enea.it

ABSTRACT

Modifications of natural land cover together with localized industrialization and enormous increase in motor traffic greatly contribute to air pollution and degradation of environmental and climatological quality in urban areas. As concentration of world population in urban areas shows an increasing trend, there is no doubt that climatological elements (i.e. temperature, ventilation, sun/shading, relative humidity) have to be integrated in urban planning and building to improve quality of life. The present study is aimed at contributing to a better understanding of climate characteristics in the "heat and roughness island" of Rome and surrounding rural areas. The satellite point of view (time synchronized dense grid of data over the whole area) allows a double-sided approach: 1) the city as a whole, with its overall interactions with neighboring areas; 2) local features within the city. As for point 1), three Landsat TM images of a large area around Rome (including sea coast, Bracciano lake, Tevere valley and Castelli Romani) for different season and meteorological conditions have been compared for all bands. Effects of interaction with the regional circulation were observed. As for point 2), multitemporal radiometric and texture properties of various land cover types (different types of building, urban fabric and vegetation) have been analysed in nine ERS-1 SAR.PRI images (acquired during 1992 under different meteorological conditions) together with Landsat TM thermal bands and NDVI. The aim is to obtain a classification of urban land-cover to be compared with temperature patterns as derived from TM thermal band. Combination of SAR data with NDVI looks very promising to this purpose.

Keywords: Land remote sensing, urban areas, multisensor analysis, environmental monitoring

1. INTRODUCTION

Urban areas all over the world are facing an increasing concentration of almost all economic, finantial and cultural activities of humanity. Together with industrialization and vehicles traffic, this concentration is leading to a progressive degradation of living environment, in terms of chemical and noise pollution, biodiversity loss and climate change. Effects of urbanization on daily mean air temperature at ground (of the order of 0.1 - 0.4 °C in the last century) have been noticed even at larger scale in data from US Historical Climatological Network, as formerly rural stations were progressively approached by urbanization (Jones et al., 1990).

Judgement of the specific urban environmental characteristics which make quality of life good, less good or unattractive, certainly involves many subjective aspects (i. e. genetical, cultural, age, etc.), neverthless a fair agreement might be reached on apparently contradictory aspects, like: no change/new opportunities, high/low population densities, privacy/accessibility, order/no planning, energy consunption/pollution, etc.

Meteorological and climatic aspects in urban areas are widely recognised to be of major importance in this context (Bitan, 1992). They can be controlled/improved by a wise urban planning and management, based on careful understanding of related physical phenomena, and knowledge of real-time situation over the whole area (Nichol, 1994, 1996). Space remote sensing techniques show a great potential of operational applications in this field (Abbate et al., 1995; Parlow, 1996; Scherer et al., 1996). A typical climatic phenomenon of urban areas is "heat island" (Oke, 1995), with related features in local and regional atmospheric circulation, cloud cover and precipitation.

Urban heat islands were observed on meteorological satellites infrared images, since the beginning of the Seventies, with relatively poor spatial resolution (7-8 Km). Several studies based on AVHRR data (spatial resolution 1.1 Km) are reported in literature (Balling and Brazel, 1988; Gallo and Tarpley, 1996). At this spatial resolution, temperature variations across metropolitan areas became evident; direct correlation was found between satellite derived surface temperature values and incidence of residential, commercial and industrial land-use, while indirect correlation was observed with values of NDVI (Normalized Vegetation Index), that is with urban-green land-use.

HCMM satellite (Heat Capacity Mapping System, Goddard Space Flight Center, 1978) acquired thermal data near the time of diurnal maximum, at a spatial resolution of 500 m, which were proven useful for placement of air monitoring stations in cities and for spatial interpolation between such sites (Price, 1979).

Ten years ago it was commonly believed that satellite images were only adequate for comparing urban-rural temperature differences and that inner structure of urban heat islands could not be studied by means of this technology, at least at that stage of development. Thoretical modelling approaches and measurements campaigns by conventional instrumentation and remote sensing from ground and aircraft were considered more useful for understanding atmospheric boundary layer

phenomena in urban areas (Plate, 1993), even if under very limiting conditions.
Just a few attempts were made afterwards of using more recently available Landsat TM data, having spatial resolution of 120 m in thermal infrared band, and 30 m in other bands (Kim, 1992). Very recently, these data have been processed in combination with other types of spatial information and accurate ground-truth measurements, by means of GIS techniques, to identify thermal characteristics of urban features down to the scale of a city block, a single row of trees, or an individual building (Nichol, 1996). ERS- SAR data (spatial resolution = 12.5 m) are being exploited to derive 3-dimensional and roughness characteristics of land (Parlow, 1996; Scherer, D., 1996), and soil moisture (Borgeaud et al., 1994), parameters which play a fundamental role in urban climate. More accurate surface temperature measurements can be obtained by ERS-ATSR, even if at spatial resolution of 1.1 Km. Digital techniques for fusion/merging of multi-sensor, multi-band, multi-temporal data allow to improve spatial resolution. Data from new sensors with improved performance characteristics will shortly be available. Thus, operational methodologies for urban planning and management, based on satellite data, are very likely to be finalized in the near future.
Many physical features can affect the climate of an urban area, including: location of the urban area within a given region, density of built-up areas, height distribution of buildings, orientation and width of streets, position and design details of green areas, design details of buildings which affect outdoor conditions (Givoni, 1992). All them can be analysed on the whole area of interest by means of techniques of Earth observation either presently available or planned to be operational in the near future. To resolve the temporal evolution of physical phenomenons - for forecasting purposes - parallel research on modelling and assimilation of satellite-derived parameters will have to be carried out.

2. ROME HEAT ISLAND EVOLUTION AS OBSERVED BY LANDSAT TM

Three Landsat TM images of a wide area around Rome (including sea coast, Bracciano lake, Tevere valley and Castelli Romani) have been compared for all bands:
Path/Row = 191/031, acquisition dates: 4 May 1994, 15 January 1995, 26 July 1995, selected for different seasons and wind conditions. In particular, regional wind was blowing from N-NW on 4 May 1994, from N-NE on 15 January 1995 (strong intensity), from SW on 26 July 1995 (pure sea breeze).
Significant variations were observed in bands 3 (red) and 4 (reflective infrared), due to vegetation species phenological cycle, and in band 6 (thermal infrared), due to changes in thermal emission. Fig. 1 (a), (b), (c), shows RGB = 6,4,3 band combination, for the study area. NDVI (Normalized Differential Vegetation Index) values were computed from bands 3 and 4:

$$(TM3 - TM4) / (TM3 + TM4).$$

Vegetated areas appear relatively bright.
Brightness temperatures were computed from band 6, according to formula (Malaret et al., 1985):

$$T(K) = 206.127 + 1.0545 * TM6 - 0.00371 * TM6^2 + (6.606 * 10^{-6}) * TM6^3.$$

Accurate thermal emissivity measurements will have to be carried out in order to derive surface temperatures.
Different heat island patterns and effects of interaction with the regional circulation can be observed. Rome heat island appears someway "pushed" downwind, at least at an intuitive level of interpretation.
In particular, on 26 July image - Fig. 1(c) - reddish colours (warmer areas) appear as "pushed" from SW towards inland reliefs and entering the Tiber valley up to a distance of about 60 Kms. This is a well known characteristic summer behaviour of sea breeze in this area (Colacino and Dell' Osso, 1978).
In visual analysis of images, different vegetation conditions have to be taken into account. To this purpose RGB = 3,2,1 band combination and NDVI maps are very useful. For instance, it can be noticed that the N-NW facing slopes of Castelli Romani, are less vegetated in May than in July. This characteristic may account for this area being relatively warmer in May. CORINE 1:100.000 land cover map (Centro Cartografico Interregionale, Roma) is also helpful in the interpretation of temperature features in rural areas as related to land-cover. The effect of wind is noticeable in the image of May, Fig. 1 (a), as the SE sector of Rome looks generally warmer than the rest of the city. In the image of 15 January, Fig. 1 (b), water and highly vegetated areas appear warmer. City area is relatively cold, as Romans experience early morning in these cold winter days (satellite passage is at 8:59 GMT). Even if the time of observation is rather early in the morning, still the presence of an heat island can be observed.
SODAR measurements carried out in the area of Rome during 1992 spring and summer gave evidence that some convective activity is still present in the urban area during night and early morning hours (plume height about 50-100 m). Convection increases due to surface heating by the sun generally between 8:00 and 9:00 local solar time (Mastrantonio et al., 1994).

3. SAR MULTITEMPORAL STUDY OF THE URBAN AREA OF ROME

Nine SAR.PRI images were selected for different meteorological conditions: Frame 2763, descending path, dates: 21 Jan., 17 Feb., 15 March, 26 May, 11 June, 16 July, 24 Sept., 29 Oct., 17 Nov. 1992.

3.1. ERS-1 SAR MULTITEMPORAL COMPOSITES

After co-registration (RMS error was generally about 0.5-0.6 pixels), various multitemporal combinations were produced and visually compared, i.e: RGB = 15 March/16 July/17 November, to look for annual variations; RGB = 11 June/16 July/24 September, summer variations; RGB = 17 February/15 March/26 May, spring-summer variations; RGB = 29 October/17 November/ 21 January, winter variations. To better locate various features, images were also registered to a 1:200.000 map. Variations in vegetated areas are seen very clearly (plant phenological cycle, irrigation / rain, ploughing, etc.). Agricultural fields appear as colour patterns, as SAR backscatter signal is very sensitive to surface water content and roughness. City appears generally bright. Structure and density features are well distinguishable at a closer look as it can be noticed in subset in Fig. 2 (a), (b), RGB = 16 July/15 March/ 17 November and 16 July/26 May/17 November, respectively. Note that the line bordering Tevere river at the left of images appears in different colour in the two combinations, this indicating highest backscattering on 15 March and, decreasingly, on 16 July, 26 May, 17 November. Interpretation requires ground-truth survey. Note also that this level of detail allows to distinguish single buildings. The impression of out-of-focus can be reduced by further co-registering subsets at this full detail.

3.2. ERS-1 SAR MULTITEMPORAL ANALYSIS

To allow quantitative comparison among data sets, radar backscattering coefficients σ° (dB) were derived, according to formula:

$$\sigma^\circ = \langle I \rangle / K(\alpha) = (\langle I \rangle / K) * (\sin \alpha_n / \text{sen } (23^\circ)).$$

Statistics were computed for twenty three training areas, covering interesting types of surfaces (different types of buildings, urban fabric, vegetation, water). Here following, they are listed and generally described in order of increasing NDVI: 1-Bracciano lake (water area), 2-Albano lake (water area), 3-Historical centre (urban, old district with narrow streets, no greenery), 4-Termini station (urban, old district, concrete, asphalt, no greenery), 5-Bologna square (not high-rising buildings, no greenery), 6-Centocelle (modern urban district, high buildings, almost no greenery), 7-Mazzini (residential, large villas), 8-Garbatella (modern urban district, wide roads), 9- Mostacciano (new villas), 10-Parioli (villas and low-rising buildings), 11-Nuovo Salario (modern new district), 12-Colosseo (ancient ruins, bare soil and some greenery), 13- Fiumicino airport (international airport), 14-EUR (modern urban district with high buildings and wide roads), 15-Ponte Galeria (crops), 16-Appia Antica (grass, some trees), 17-Isola Farnese (grass), 18-Villa Borghese (urban park), 19-Settebagni (crops), 20-Monterotondo (crops), 21-Villa Ada (urban park), 22-Mentana forest (woods), 23-Albano forest (woods).
Results are summarized in Fig.3 and Fig.4.
Plot in Fig.3 shows mean, minimum and maximum σ° values for each subset among the nine images. The lowest values are found for water areas. Some differences are observed between high density urban areas and low density urban and agricultural areas.
Plot in Fig. 4 shows for each subset, the difference between maximum and minimum values of standard deviation in the nine ERS-1 SAR images. It can be seen that this parameter better discriminates built-up areas (subsets 3-12); crops and deciduous vegetation are in fact characterized by high standard deviation due to plants phenological cycle and irrigation, while water has high standard deviation values due to waves on the surface. Grass areas (subset 17) and evergreen parks (subsets 18 and 21) have standard deviation ranges of the same order as urban areas. Consequently, while this parameter can provide useful information to discriminate and classify urban areas, it has to be used in combination with NDVI.

4. CONCLUSIONS

This study has allowed to gain insight in the heat island phenomenon of the area of Rome, and in opportunities offered by satellite data for this kind of studies. In particular, combination of ERS-SAR data with thermal and NDVI data from Landsat looks very promising.
Further work will include:
1) Further analysis of Landsat TM images to study temporal and spatial evolution of temperature patterns in the region around Roma;
2) Emissivity measurements and derivation of ground temperature maps;
3) Use of ERS ATSR data to derive temperature at ground, and comparison with the above;
4) For a subset (only urban area) co-registration with a high spatial resolution image and correlation analysis with ground cover;
5) Computation of the average σ° image from the above mentioned 9 SAR.PRI images; texture analysis and maybe classification of average image (different structure of buildings and urban fabric, direction of main roads). Maybe also use of other algorithms - to be studied - based on ascending/descending SAR images, to obtain quantitative parameters for urban structure.
6) Classification of NDVI map (different plant cover and distribution in urban districts and close surroundings);
7) Comparison of thematic layers 5) and 6) with temperature maps;
8) Integration of texture and vegetation information into ground temperature maps.
9) Integration of ground-truth data, to be acquired synchronously with satellites passages.

5. ACKNOWLEDGEMENTS

The present work was carried out under ESA Project Ref. I 102/0, "Heat Island Study in the area of Rome by integrated use of remote sensing techniques".
I wish to thank M. Fea, J. Lichtenegger, A. Bellini, M Barbieri, A. Argentieri, at ESA-ESRIN, Frascati, for support and enlightening discussions. Technical advice by K.S. Rao (Indian Institute of Technology), L. De Cecco and S. Martini at ENEA-Casaccia is also gratefully acknowledged.

6. REFERENCES

Abbate, G., Kowalewska, H., Borfecchia, F., Della Rocca, B., 1995:
Land cover characteristics of Rome urban and countryside area as observed by Landsat TM (bands 1-4) and ERS-1 SAR, *Proc. 7-th URSI Commission F Open Symposium, Wave propagation and remote sensing,* Ahmedabad, India, 20-24 Nov. 1995.

Balling, R. C., Brazel, S. W., 1988:
High-resolution Surface Temperature Patterns in a complex Urban Terrain, *Photogrammetric Engineering and Remote Sensing*, Vol. 54, No. 9, pp. 1289-1293.

Bitan, A., 1992:
The high climatic city of the future", *Atmospheric Environment* Vol. 26B, No. 3, pp. 313-329.

Borgeaud, M., Noll, J., Bellini, A., 1994:
Use of ERS-1 SAR data for land applications, *Proc. Second ERS-1 Symposium - Space at the Service of our Environment*, Hamburg, Germany, 11-14 October 1993, ESA SP-361.

Colacino, M., Dell' Osso, L., 1978:
The local atmospheric circulation in the Rome area: surface observations, *Boundary Layer Meteorology,* Vol. 14, pp. 133-151.

Gallo, K. P., Tarpley, J, D., 1996:
The comparison of vegetation index and surface temperature composites for urban heat-island analysis, *Int J. Remote Sensing*, Vol.17, No. 15, pp. 3071-3076.

Givoni, B., 1992:
Climatic aspects of urban design in tropical regions", Atmospheric Environment Vol. 26B, No. 3, pp. 397-406.

Jones, P. D., Groisman, P. Y., Coughlan, M., Plummer, N., Wang, W. C., Karl, T. R., 1990:
Assessment of urbanization effects in time series of surface air temperature over land, *Nature*, Vol. 347, pp. 169-172.

Kim, H. H., 1992:
Urban heat island, *Int. J. Remote Sensing*, Vol. 13, No. 12, 2319-2336.

Malaret, E., Bartolucci, L. A., Lozano, D. F., Anuta, P. E., and McGillen C. D., 1985:
Thematic Mapper data quality analysis, *Photogramm. Eng. Remote Sens.*, 51 (9), 1407-1416.

Mastrantonio, G.,Viola, A. P., Argentini, S. (CNR-IFA), Fiocco, G., Giannini, L., Rossini, L. (University of Rome), Abbate, G., Ocone, R. (ENEA), Casonato, M. (AMNU), 1994:
Sea breeze observation in the Roman area by a network of Doppler Sodars, Boundary Layer Meteorology, **71**: 67-80, 1994.

Nichol, J. E., 1994:
A GIS-based approach to microclimate monitoring in Singapore's high-rise housing estates, *Photogrammetric Engineering & Remote Sensing*, Vol. 60, No. 10, October 1994, pp.1225-1232

Nichol, J. E., 1996:
High resolution surface temperature patterns related to urban morphology in a tropical city: a satellite-based study, *Journal of Applied Meteorology*, Vol. 35, No.1, pp.135-146.

Oke, T. R., 1995:
The heat island of the urban boundary layer: characteristics, causes and effects", *Wind Climate in Cities,* J. E. Cermak et al. (eds.), NATO ASI Series E, Vol. 277, Kluwer Academic Publishers.

Parlow, E., 1996:
Net radiation in the REKLIP area - A spatial approach using satellite data, *Progress in Environmental Remote Sensing Research and Applications*, Parlow (ed.), Balkema, Rotterdam, ISBN 90 5410 598 4.

Plate, E. J., 1993:
Urban Climates and Urban Climate Modelling: an introduction, lecture at *NATO-ASI "Wind Climate in Cities"*, Waldbronn, Germany, July 1993.

Price, J. C., 1979:
Assessment of the urban Heat Island Effect through the use of satellite data, *Monthly Weather Review*, Vol. 107, pp. 1554-1557.

Scherer, D., Parlow, E., Beha, H. D., 1996:
Roughness parameter derivation from ERS-1 and Landsat-TM satellite data for the agglomeration of Basel, Switzerland, *Progress in Environmental Remote Sensing Research and Applications*, Parlow (ed.), Balkema, Rotterdam, ISBN 90 5410 598 4.

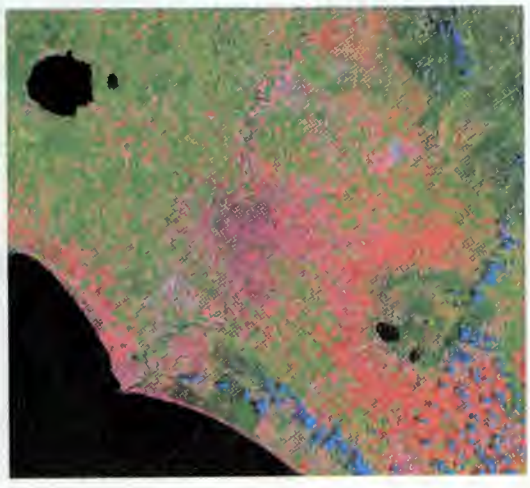

(a)

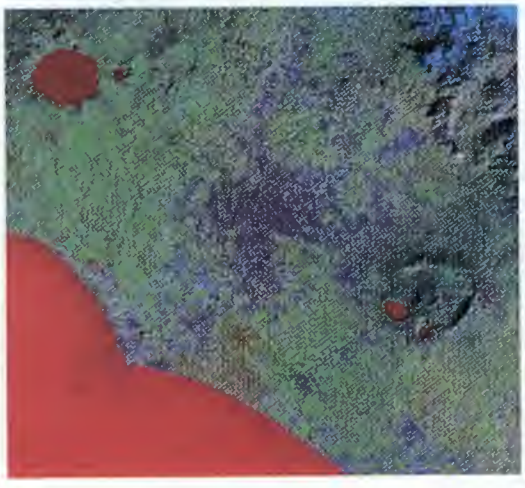

(b)

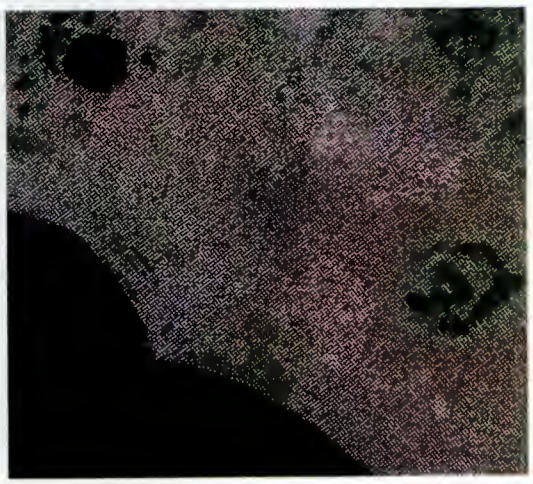

(c)

Fig. 1. Landsat TM, RGB = 6,4,3,
(a) 4 May 1994,
(b) 15 January 1995,
(c) 26 July 1995

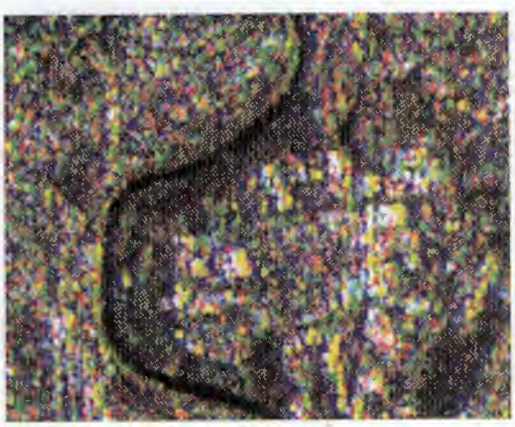

(a)

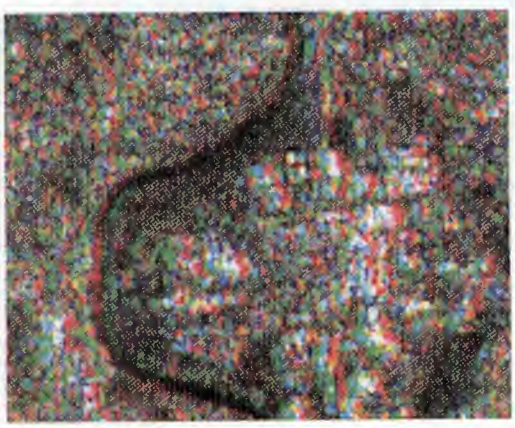

(b)

Fig. 2. ERS-1 SAR multitemporal composites:
(a) RGB = 16 July/ 15 March/ 17 November 1992
(b) RGB = 16 July/ 26 May/ 17 November 1992

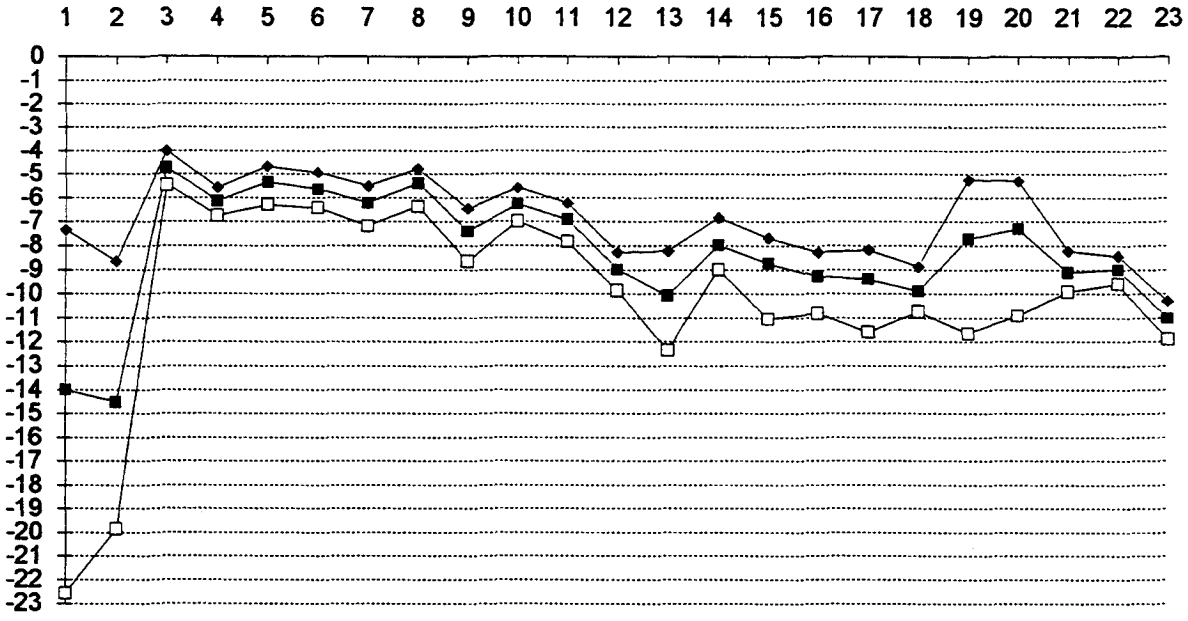

Fig. 3. σ° (dB) mean, maximim and minimim values of training areas (9 ERS-1 SAR images, 1992). Subsets are in order of increasing NDVI.

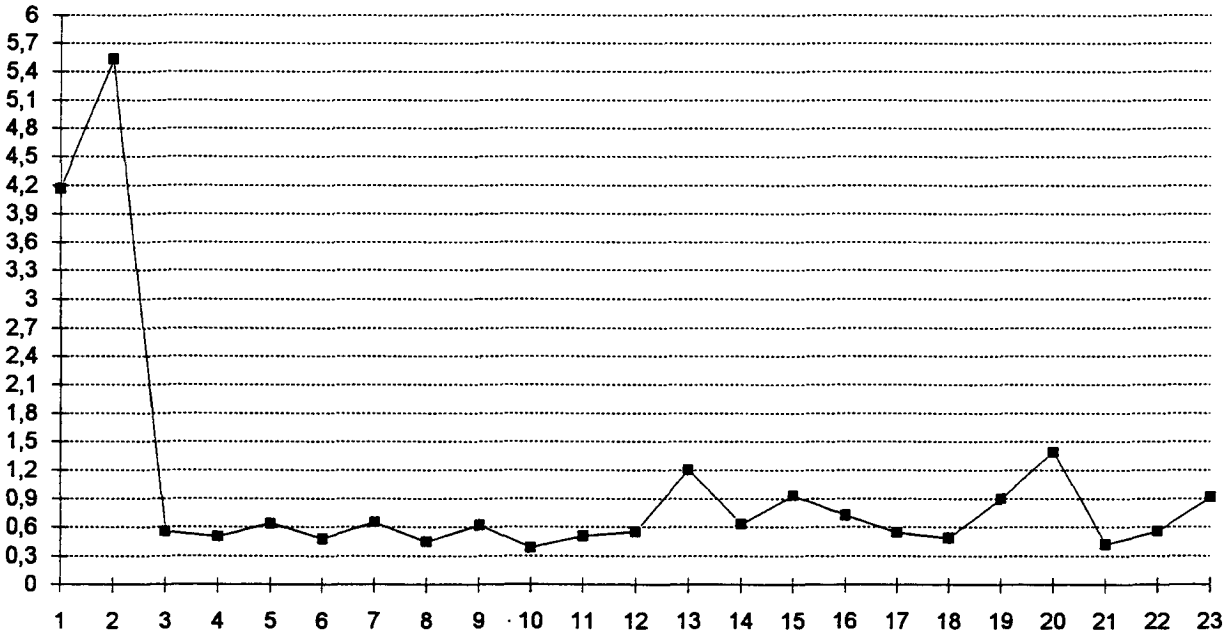

Fig. 4. σ° (dB) standard deviation range of training areas (9 ERS-1 SAR images, 1992). Subsets are in order of increasing NDVI.

WEATHER EFFECTS ON RADAR BACKSCATTER FROM CROPS

Weng Ang & Stephen E Hobbs

Systems Design Group, College of Aeronautics, Cranfield University, Cranfield, Bedford, MK43 0AL, UK

Tel: +44 (0) 1234 750111 x5137, Fax: +44 (0) 1234 750083, Email: weng.ang@cranfield.ac.uk, s.e.hobbs@cranfield.ac.uk, URL: http://www.cranfield.ac.uk/coa/

ABSTRACT

There has been recent interest in the effect of weather on radar backscatter. This paper presents work done in understanding the effect of weather, especially rain on backscatter intensity and phase coherence from crop canopies, in particular, crops typical of South-Eastern England (e.g. wheat and beans).

Current work centres on the use of a computer model to investigate the effect of rain on radar backscatter from crops over the growing season. These results will then be compared with the weather data, crop observations and SAR data for the local area. The study integrates locally collected datasets including crop observations, meteorological measurements, ERS SAR images and computational modelling in order to better understand how the change in crop radar backscatter throughout the growing season is perturbed by rainfall events.

The ultimate aim of the study will be to indicate quantitatively, the disturbance effects of rain (and possibly wind) on SAR images of crops in order to improve the monitoring and classification of crops by microwave remote sensing.

Keywords: radar backscatter, phase coherence, crops, computer modelling, ERS SAR, weather.

1 INTRODUCTION

Satellite-borne radar sensors are being used to monitor crops. In particular, the SAR data from the ERS series of satellites are being used to distinguish different crop types and identify changes in vegetation biomass. Although ERS SAR data can be obtained in all weather conditions, there is an awareness that the weather can affect the microwave backscatter from agricultural surfaces. The availability of rainfall information before or during a satellite pass is essential for the correct interpretation of data (Lichtenegger, 1996). Hence, the effects of rain and wind on radar backscatter must be corrected for in order to reduce the errors in the interpretation of crop radar signatures for agricultural monitoring.

Fluctuations in backscatter during the growing season may be explained by wind and rainfall events (Nieuwenhuis & Kramer, 1995). Rainfall of about 10 mm prior to SAR data acquisition has led to increases in backscatter of 1-4 dB from grass, bare soil and wheat-bare soil cover types (Wooding *et al.*, 1992). Moreover, there may be some evidence that a period of low observed backscatter from winter wheat corresponds to a period of low rainfall, although there may have been other causes (Wooding *et al.*, 1993).

The project described in this paper aims to quantify the weather effects on backscatter intensity and phase coherence for typical UK agricultural crops. Work is underway and the paper presents aspects of the database being compiled as well as discussing the modelling approach used.

2 METHODOLOGY

A database of crop, satellite and weather data is being created. The database includes observations of crop development and field conditions at local test sites, weather records, and a series of ERS-1 and 2 SAR images. The data collection has been designed to monitor weather-dependent radar backscatter, within the resources available, as opposed to classifying or monitoring crops. The database is being used to develop and validate a model of weather effects on radar backscatter from crops.

In addition, this database is being extended to include the 1996/1997 growing season.

2.1 Crop sampling

Measurements of the nearby winter wheat and bean crops in the Cranfield area were made (52° 04' N -0 37' E) during the growing season with a particular emphasis on crop height and moisture content during the period May-August 1996, during which time the crops developed rapidly. In addition, photographs of the crops were taken to provide a record of crop structure during the growing season.

2.2 ERS SAR data acquisition

ERS SAR images have been obtained from two sources. ERS-1 Precision Images (ERS-1.SAR.PRI) of the local area were obtained from the RAIDS service over a period spanning July 1995 to May 1996 (Graves, 1995). In addition, SAR images from the ERS-1 and ERS-2 Tandem Mission were ordered.

2.2.1 RAIDS SAR Imagery

Details of the images from the RAIDS service are shown in *Table 1a*. These are 16-bit images with a pixel size of 12.5 m x 12.5 m covering areas of approximately 25 km x 25 km. The spatial resolution of the images is about 30 m. A field that was used to grow winter wheat and a second field that was used to grow beans were identified within this set of images. Also, a field of cropped grass was used as a form of control: the small changes in the grass plants, that were deliberately kept short, over the growing season would be expected to have a relatively constant radar backscatter profile.

2.2.2 ERS Tandem Mission Imagery

Image pairs from the ERS Tandem Mission [Duchossois and Martin (1995)] are being obtained for the growing season 1995/96. Up to 25 image pairs may be required since our test sites are close to a frame edge. Each image pair covers an area approximately 50 km square. These images will be used primarily for the backscatter coherence studies although they also enhance the quality of data available for the backscatter intensity work.

2.2.3 SAR Data Analysis

Average relative backscatter intensities were obtained for the wheat and bean fields before and during the growing season. These values were converted to decibels (dB). It was not possible to calculate the absolute average backscatter intensity values for the crop fields due to the inappropriate value of the calibration constant, K supplied with the RAIDS ERS-1.SAR.PRI data. However, since the changes in backscatter due to weather effects, over the growing season, are of primary interest, analysis of relative backscatter intensity values in decibels is unaffected. The only consequence of using relative backscatter values is the large linear offset in the backscatter time series graphs.

The ISAR software developed by the Politecnico di Milano is being used to process the Tandem Mission images (Koskinen, 1995). Coherence images for each overpass are the primary output required, thus phase unwrapping is not necessary. The basic SLC images allow the calibration constant for coincident RAIDS images to be evaluated.

2.3 Meteorological data collection

An automatic weather station at Cranfield University, within 5 km of the fields under study, was used to acquire most of the weather measurements during the SAR image acquisitions and crop sampling. In addition, some data from Silsoe College (approximately 15 kilometres east of Cranfield) were also acquired. Parameters recorded include wind speed, wind direction, rainfall, solar and net radiation, air temperature, and humidity.

2.4 Radar backscatter modelling

Figure 1 describes the conceptual model underlying the radar backscatter modelling. The aim of the research is to investigate the effect of weather on backscatter intensity and phase coherence (particularly for radars similar to those of ERS-1 and 2). Previously published work allows most of the components identified to be quantified, at least approximately, and our current modelling work is concerned with refining specific components. Relative permittivity models for soil and vegetation based on those published by Dobson *et al.* (1985) and Ulaby & El-Rayes (1987) are useful since they identify the separate contribution of free and bound water. Rain / dew is assumed to modify the effective relative permittivity of the soil or vegetation by its contribution to the free water component.

A key part of the model is the component which calculates backscatter coefficient from knowledge of the scatterers' relative permittivity and their geometry. Several approaches are being evaluated, including empirical relationships, full electromagnetic scattering models (e.g. MIMICS) and simplified scattering models.

Hobbs (1996) describes the coherence simulator used. For this, all scatterers within the sample volume are

assumed to belong to one of several classes defined by their variability in response to weather (e.g. soil might be regarded as invariant, large branches to be slightly variable, and twigs and leaves to be highly variable). The simulator's inputs are the relative strengths of these different classes and their variability (phase and amplitude). A similar approach for forest applications is being developed at Chalmers University (e.g. Smith *et al.*, 1996).

3 RESULTS

Table 1 and *Figure 2* are examples of the information available from the database being compiled. *Table 1a* gives the mean relative backscatter values and standard deviations from the winter wheat, bean, and grass fields throughout the growing season. The grass fields were used as a form of control. As these were cropped, it was expected that the radar backscatter due to changes in vegetation would be relatively small and other factors would be more influential. *Table 1b* shows the mean vegetation heights of the species under study, which is a significant vegetation parameter for radar backscatter.

Figure 2 shows the mean relative temporal backscatter profile and standard deviations for the winter wheat, bean, and grass fields.

4 DISCUSSION

The results in *Figure 2* show a clear contrast between the relatively constant backscatter of the airfield's grassed areas and the annual cycle of the farmed test sites. The most significant effects appear to be related to the soil preparation in the autumn and the gradual weathering of the soil surface over the winter. Relative to this, the backscatter intensity changes during the growing season are small. These patterns are similar to those observed by other workers (e.g. Nieuwenhuis & Kramer, 1995). Similar plots for the backscatter coherence magnitude have not yet been obtained, but when available will provide an interesting comparison with the plots backscatter intensity.

5 CONCLUSIONS & FURTHER WORK

The next stages of the project are to (1) continue building the database for our test sites, (2) refine the backscatter models, and (3) derive time series for the coherence magnitude. Our aim is to develop (A) statistical relationships between backscatter intensity or phase coherence and suitable weather parameters, and (B) physically-based models to relate backscatter to weather parameters. The final stage will involve evaluating the relationships derived using our database against other similar databases, ideally for different geographic or climatic regimes (another current project at Cranfield should give access to such a database for southern Europe).

6 ACKNOWLEDGEMENTS

We would like to thank AEA Technology PLC, the Engineering and Physical Sciences Research Council, the European Space Agency, Matra Marconi Space UK Ltd., The Royal Society and Silsoe College for their support of this research.

7 REFERENCES

Dobson, M. C., Ulaby, F .T., Hallikainen, M. T. & El-Rayes, M. A., 1985:
Microwave Dielectric Behavior of Wet Soil - Part II: Dielectric Mixing Models. *IEEE Transactions on Geoscience and Remote Sensing*, Vol. GE-23, No. 1, pp. 35-46.

Duchossois, G. & Martin, P., 1995:
ERS-1 and ERS-2 Tandem Operations. *ESA Bulletin*, No. 83, August 1995, pp. 54-60.

Graves, A., 1995:
Rapid Information Dissemination System (RAIDS). IN: *Proceedings of the Second ERS Applications Workshop*, ESA SP-383, 6-8 December 1995, London, United Kingdom, pp. 383-385.

Hobbs, S. E., 1996:
Weather Effects on SAR Backscatter for Agricultural Surfaces. *Proc. ESA Workshop on SAR Interferometry*, Zurich, 30 Sept - 2 Oct 1996.

Koskinen, J., 1995:
The ISAR-Interferogram Generator Manual. Version 3.0, 7/18/95, 52pp, DEX/ED, ESA-ESRIN.

Lichtenegger, J., 1996:
ERS-1 SAR Images - Mirror of Thunderstorms. *Earth Observation Quarterly*, No. 53, pp. 7-9.

Nieuwenhuis, G. J. A. & Kramer, H., 1995:
Monitoring of Agricultural Crops with ERS-1 and JERS-1 Multi-Temporal SAR Data Crop Growth Modelling. IN: *Proceedings of the Second ERS Applications Workshop*, ESA SP-383, 6-8 December 1995, London, United Kingdom, pp. 383-385.

Smith, G., Dammert, P.B.G., and Askne, J., 1996.
Decorrelation mechanisms in C-band SAR interferometry over boreal forest. Proc. ESA Workshop on SAR interferometry, Zurich, 30 Sep - 2 Oct 1996.

Ulaby, F. T. & El-Rayes, M. A., 1987:
Microwave Dielectric Spectrum of Vegetation - Part II: Dual-Dispersion Model. *IEEE Transactions on Geoscience and Remote Sensing*, Vol. GE-25, No. 5, pp. 550-557.

Wooding, M. G., Griffiths, G. H., Evans, R., Bird, P., Kenward, D. & Keyte, G. E.,.1992:
Temporal Monitoring of Soil Moisture using ERS-1 SAR Data. IN: *Proceedings of the First ERS-1*

Symposium - Space at the Service of our Environment, ESA SP-359, 4-6 November 1992, Cannes, France, pp. 641-648.

Wooding, M. G., Zmuda, A. D. & Griffiths, G. H., 1993: **Crop Discrimination using Multi-Temporal ERS-1 SAR Data**. IN: *Proceedings of the Second ERS-1 Symposium - Space at the Service of our Environment*, ESA SP-361, 11-14 October 1993, Hamburg, Germany, pp. 51-56.

Date	Day No.	Orbit		Time	Relative Backscatter (dB)					
		Type	Frame	Track	GMT	Wheat		Beans		Grass	
						mean	st dev	mean	st dev	mean	st dev
11 Jul 95	192	Desc	2547	323	10:57	58.5	2.4	55.6	1.7	58.5	2.4
25 Aug 95	237	Asc	1035	473	22:06	57.6	1.6	59.6	2.0	58.6	2.0
19 Sep 95	262	Desc	2547	323	10:57	66.6	1.8	66.2	2.5	58.7	1.8
8 Oct 95	281	Desc	2547	094	11:00	63.4	1.4	66.3	1.9	59.9	3.2
28 Nov 95	332	Desc	2547	323	10:57	65.2	1.5	64.2	1.9	58.3	3.7
2 Jan 96	367	Desc	2547	323	10:57	64.3	3.0	64.8	2.8	57.8	1.9
6 Feb 96	402	Desc	2547	323	10:57	61.6	1.9	60.0	1.7	58.2	2.5
7 Apr 96	463	Asc	1035	201	22:03	59.9	2.4	58.9	2.2	58.4	2.8
16 Apr 96	472	Desc	2547	323	10:57	60.4	2.8	59.7	2.8	59.2	1.9
26 Apr 96	482	Asc	1035	473	22:06	59.0	2.5	59.9	2.3	57.9	3.3
5 May 96	491	Desc	2547	094	11:00	56.7	2.6	60.4	1.7	58.6	2.0
21 May 96	507	Desc	2547	323	10:57	57.8	1.5	59.1	2.4	57.8	1.5

Table 1a. The ERS-1.SAR.PRI images used to obtain relative mean vegetation backscatter profiles and standard deviations.

Date (1996)	Day Number	Crop Height (cm)	
		Wheat	Beans
16 April	471	16	-
14 May	499	30	34
21 May	506	49	39
12 June	528	70	80
24 June	540	73	92
8 July	554	76	99
19 July	565	75	100
26 July	572	74	98
1 August	578	75	93
8 August	585	73	93

Table 1b. Crop heights during growing season.

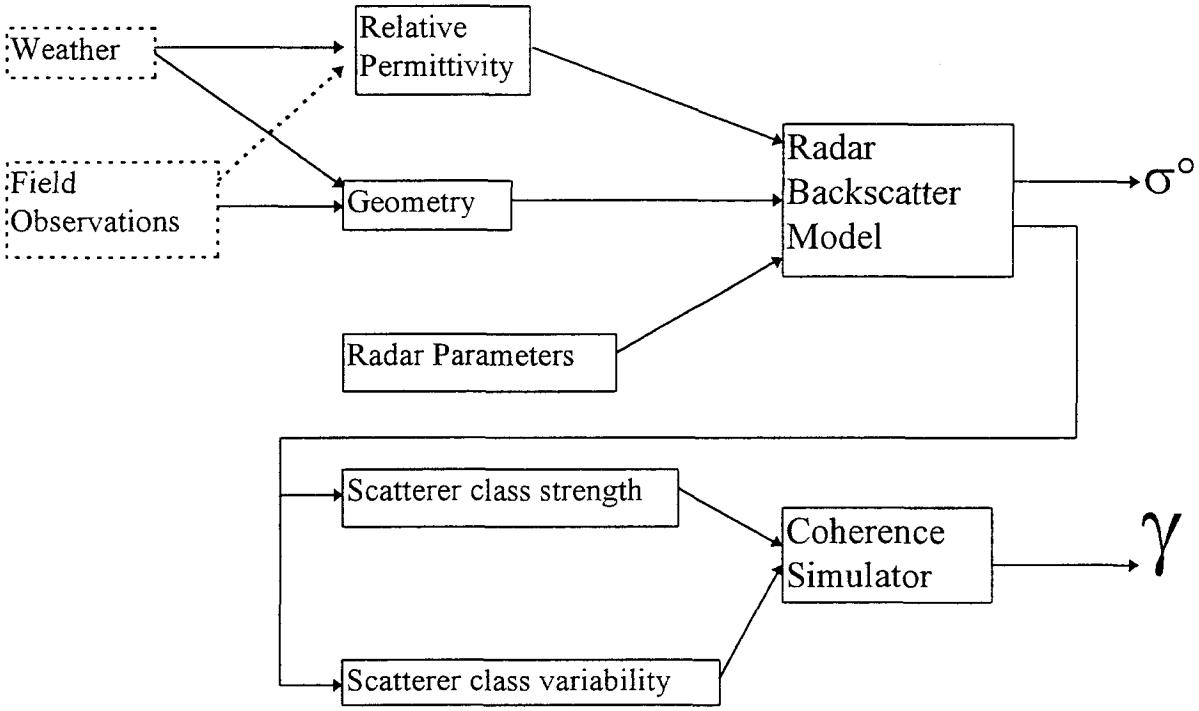

Figure 1. The conceptual basis underlying the radar backscatter modelling.

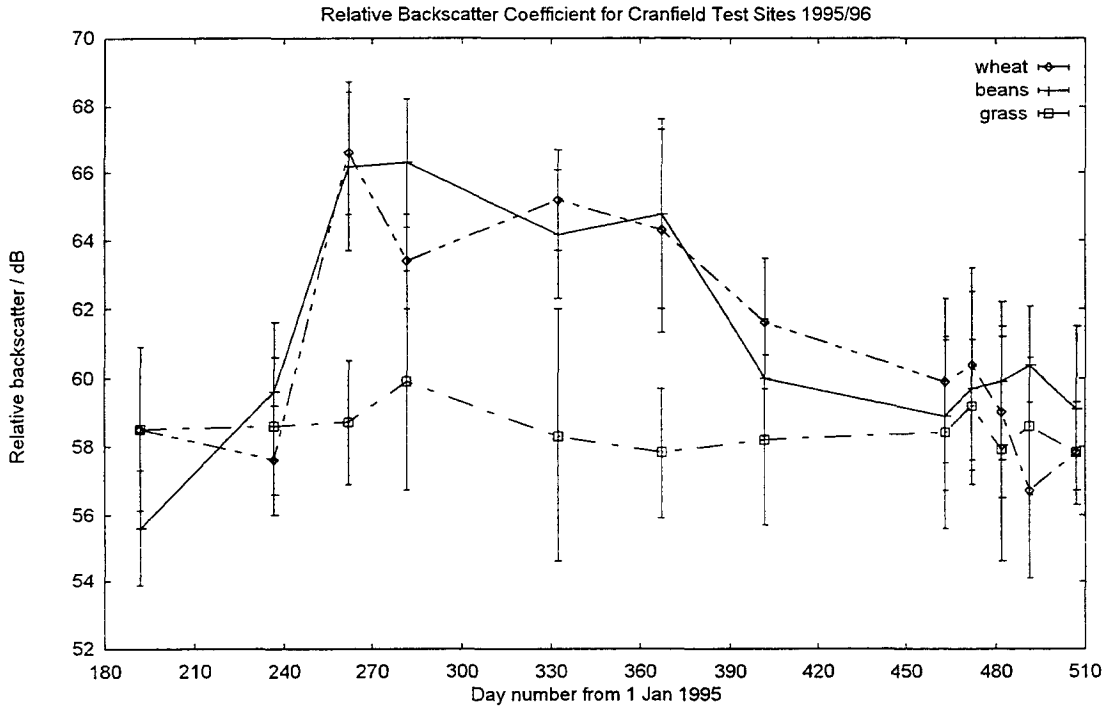

Figure 2. The mean relative temporal backscatter profile and standard deviations for the winter wheat, bean, and grass fields.

EXAMINING AGRICULTURAL AND WETLAND VEGETATION USING ERS-1 IMAGERY

Chris Keithley

Jones & Stokes Associates, 2600 V St Sacramtento, CA 95818, (916) 737-3000, chriske@jsanet.com

Miles Roberts

Geography Dept. CSU-Sacramento,CA 95819

Fiona Renton

Pacific Meridian Resources, Remote Sensing Lab, 1920 20th St, Sacramento, CA 95814

ABSTRACT

This study examined the use of multi-date ERS-1 imagery to identify crops and wetland vegetation within the Rainwater Basin in south-central Nebraska. The Rainwater basin is comprised of a dense cluster of wetlands that have been greatly modified by agricultural production. For conservation purposes techniques are needed to monitor the relationship between existing wetlands and the surrounding agricultural land use practices. The use of multi-date ERS-1 imagery was effective in dinstinguishing between agricultural and wetland vegetation. Temporal curves of radar backscatter were constructed from 150 field observations, which showed a pronounced seasonal variation in backscatter associated with crop phenology. Differences in backscatter among crop types was most pronounced in early and mid-summer images. Statistical analysis suggests that the sensitivity of radar to moisture conditions was great enough to detect a difference between crops grown on hydric versus upland soils. An unsupervised classification was performed to map the spatial distribution of crops and wetlands. Results suggest that classification performance improves when vegetation classes are grouped into structural classes.

INTRODUCTION

The Rainwater Basin is a mosaic of wetlands and agriculture stretching across 17 counties in south central Nebraska. The region provides habitat for waterfowl and is a focus of spring waterfowl migration. During the past century, conversion of wetlands to agriculture has dramatically altered this landscape and resulted in a loss estimated at 80% of the historic wetlands (Figure 1).

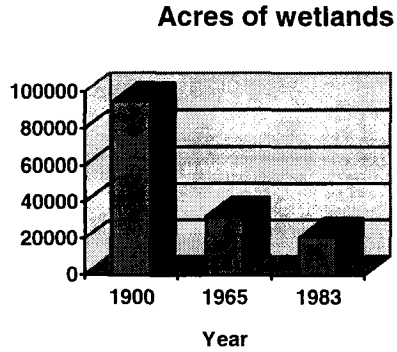

Figure 1. Estimated acres of wetlands in Rainwater Basin. Source: Nebraska Game & Parks, 1992.

Most wetlands in the Basin are shallow and small, with size dependent on recent meteorological conditions. For conservation and habitat restoration, new techniques are needed to reliably map such small yet important wetlands. This study examined the use multi-date ERS-1 Synthetic Aperture Radar (SAR) satellite imagery to identify land cover (crop type and wetlands) with radar data alone. Six SAR images were acquired covering the Rainwater Basin during the 1995 growing season (May - September). These images were used to identify typical rural land cover types such as agricultural crops (corn, soybean, milo), wetlands, and grasslands. Further analysis was conducted to test whether the sensitivity of radar to moisture conditions was great enough to detect a differnce between crops grown on hydric versus upland soils. This information would suggest a means for identifying historic wetlands that are currently under agricultural production.

The use of Synthetic Aperture Radar (SAR) to identify agricultural land cover and other vegetation characteristics has been investigated to some extent in the last two decades. Two well-documented advantages of imaging radar are cloud penetration and the capture of information about vegetation canopy structure. The strength of the SAR return is affected by target

morphological factors such as surface slope and roughness, moisture content, and molecular structure (Lillesand, et al. 1987). Thus, SAR images capture distinctly different but complementary information compared to traditional V/IR images.

For agricultural applications, the radar backscatter has been found to be dependent on plant species and age, which generally determine plant morphology. For example, sugar beets were found to give a high return due to their high water content and large leaves (Bouman, et al. 1993) In general, broad leaf crops produce a higher signal return than other crops for C band with VV polarization. VV polarized SAR reflectance is predominately caused by the physical structure of the plant canopy rather than understory characteristics (Holmes, 1990).

As with the initial applications using Landsat visible and infrared images, initial ERS-1 SAR researchers have attempted to map various crop types. Bouman and Uenk (1993), used simulated multidate ERS-1 radar to examine SAR backscatter changes over agricultural fields. They reported that a combination of early and late season SAR images provided the best discrimination between crops. Schmullis et al. (1994), reported that ERS-1 SAR returns from different fields of the same crop were more variable in the early season and converged with increasing canopy cover. Early season differences were attributed to differences in soil roughness. Thus, crop identification should be conducted using late summer data when the SAR reflectance is more affected by crop canopy than soil surface effects.

ANALYSIS OF RADAR BACKSCATTER

Six ERS-1 images were acquired between May and September 1995 covering the eastern part of the Rainwater basin in Clay County, Nebraska. These images were rectified into the UTM coordinate system using nearest neighbor resampling to 30 m resolution and assembled into a single multiband image data set where each band is a single date of imagery. Four images were from the descending ERS-1 orbit (approximately 10:30 pm EST) and two images from the ascending orbit (approximately 10:30 am EST).

One problem inherent in most SAR images is speckle, or noise, which is the result of echoes from the target surface (Leberl, 1990). This speckle is usually treated as a random effect and reduced by averaging adjacent pixels using spatial convolution filters. In this study, a 3 x 3 Sigma filter was used to reduce image speckle while retaining edge information such as field boundaries (Lee, 1981). The results of the filter were successful in reducing the heterogeneity on digital number (DN) values within agricultural fields, while preserving field boundaries.

Field observations were made in the study area to record crop type and condition for over 150 fields. The field boundaries were identified on the image data set and digitized to produce training polygons. This information provided the base for constructing temporal profiles of radar backscatter for crops and wetlands in the scene. Temporal signatures of radar backscatter were extracted for each of the 150 fields.

Histograms were used to examine the distribution of backscatter for the entire image and for individual fields. The raw data showed a high variance for the May 6, July 7 and September 23 images, although the distributions were remarkably normal. Graphs produced with the original DN values were influenced by extreme differences in standard deviation, which made comparison of profiles between agricultural fields difficult. To account for the difference in variance between dates the data was standardized to Z-scores and a scalar was added to return all Z-scores to a positive range. Inspection of covariance and correlation matrices indicated a strong positive relationship between brightness values on the July and August images.

Temporal curves were constructed to examine seasonal trends in backscatter. The mean value of backscatter was plotted using normalized Z-scores. The data revealed a strong temporal pattern of backscatter for vegetation throughout the growing season. A separation between agricultural fields, wetlands, and grasslands was apparent for some dates.

The phenological cycle of vegetation becomes important in interpreting the graphs. The first image was acquired in early May during a very wet spring, and prior to most planting. Difference in backscatter from this date are attributed mainly to differences in soil and moisture content. The second image was acquired in mid June. Due to a wet spring the planting was delayed and while agricultural vegetation was emergent, the backscatter was still influenced by the soil background. Winter wheat provided an exception to the general pattern in that the crop was mature in mid - June and close to harvest. The third image taken on July 7th consistently provided the greatest magnitude of backscatter as shown by the peak in the curve for all land cover types. This date also provided the greatest separation between crops. The temporal curves begin to converge during late July as the canopies thicken although there is still distinction between crops. The fifth image acquired in late August represented a full canopy for most crops and showed the least distinction in backscatter. The final image in September shows an increased variation in backscatter which could be attributed to the senescence of vegetation and the variation in harvesting schedules among crops.

In examining the temporal pattern of backscatter among crops a general pattern emerged as well, yet the temporal difference between crops was not as dramatic as the temporal difference between land cover classes. There was high variation between fields during the early image dates that is attributed to the soil background. Once vegetation was emergent, Corn

showed the highest backscatter followed by Milo, Soybean, and Pasture. The stubble from winter wheat provided a consistently high backscatter. As the season progressed the separation between crops was most significant in early July. The variation in backscatter among crops was less in late July, and there was little distinction between crops by the late summer.

STATISTICAL ANALYSIS of BACKSCATTER DN VALUES

To evaluate the influence of the soil background on the radar backscatter over time an analysis of variance was conducted using 50 corn fields. Using the digital field boundaries for corn fields a GIS map overlay was done with a digital soils map to identify the soil type associated with each agricultural field. The corn fields were then seperated into those that were grown on predominately hydric or non-hydric soils. The digital soils data was based on county soil surveys for Clay County, Nebraska. Across the study area there are four soils that have a hydric component (Massie, Fillmore, Butler, Scott). Of these, Fillmore soils have been altered most often for agricultural production. Table 1 shows the results of a two way ANOVA using a repeated measures design to test the hypothesis of no significant difference in the backscatter of corn on hydric versus non-hydric soils.

Table 1. Comparison of corn backscatter on hydric versus non-hydric soils using a Two-way ANOVA.

Source	DF	SS	MS	F Value	Pr > F
Group	1	1257	1257	7.11	0.01
Error	48	8480	177		

The probability of an F-value > 7.11 is 1% when Ho is true. Thus, we reject the hypothesis and conclude that a difference exists between the mean backscatter of corn fields on hydric versus non-hydric soils. By plotting the mean backscatter on hydric versus non-hydric soils the backscatter was consistently higher on hydric soils. A comparison of means using a protected Fisher's LSD test was then done to assess at which dates a differences among means could be detected.

Prior to the experiment it was thought that a difference in backscatter when comparing crops based on soil type should be most prevalent in the early season images when the soil background is dominant. By late in the summer the full canopy among corn fields should masks the influence of the soil and the backscatter should be similar regardless of soil type. This leads to expectations that the mean DN values should show significant differences in the early dates but not in the later ones. The results suggest that this pattern was generally detected with the available data set. The late season images acquired in August and September showed no difference in mean backscatter, while a differnce was detected in the images in June and early July where the soil background would still be present. The first image taken prior to planting in early May is unusual in that no difference in backscatter was detected for that date either. This image was acquired well before planting occured in this region, when the radar backscatter should be influenced by the soil background and moisture conditions. The failure to detect a difference at this date may be attributed to several factors including: the climatic conditions prior to the satellite pass and the type of statistical test choosen to evaluate means along a temporal profile.

Table 2: Results of Fisher's protected LSD test were used to evaluate the effect of time on mean backscatter. Note the astrik (*) denotes a significant difference for that date.

May 6	June 17 *	July 7 *	July 22 *	Aug. 26	Sept. 23

CLASSIFICATION OF MULTI-DATE IMAGERY

Classification was done using the multi-date data set to determine if landcover classes were easily identified. The research considered two classification schemes the first approach was a traditional unsupervised classification where the image was partitioned into agricultural and major land cover classes that included: corn, wheat, soy beans, alfalfa, milo, pasture, wetlands, and grasslands. The second approach was to emphasize the structural components of these vegetation classes and to group them based on their structural similarities. This approach involved in a reduction in the total number of classes from eight to four. The overall map acurracy for the structural approach was greater than 80%. These results suggest that the map accuracy will improve when considering structural similarities in vegetation classes.

CONCLUSIONS AND FUTURE RESEARCH

This research indicates that multi-temporal radar can be used to track temporal changes in backscatter that are related to differences in crop phenology. Results suggest that the strongest distinction between crops occurs during the early to mid growing stages. Once crops reach a full canopy the ERS-1 C-band sensor appears to provide limited penetration of the vegetation canopy. This trend has been reported in other agricultural studies as well. The extreme variation in backscatter in early season images appears to be influenced by the soil background. Other factors include the differences in planting schedules that

occurred due to wet spring weather. A clear distinction was present between major land cover types (crop, wetlands, grassland, etc.). This suggests that multi-date radar has potential for use with regional land cover mapping. Future work will explore the use of multi-date radar for classification of crops and wetlands in this region.

The significant F-value suggests that the ERS-1 data has potential for identifying hydric soils in early growing season before the crop canopy masks the soil background. Within the Rainwater basin where many of wetlands have been drained and the land has been converted to agricultural production, techniques are needed to detect and map historic losses of wetlands. Identifying and estimating the amount of crop acreage that is grown on hydric soils could prove useful as a conservation tool in assessing the impact of agricultral production on the historic extent of wetlands in this region.

ACKNOWLEDGMENTS

ERS-1 SAR images were provided by the European Space Agency (grant USA/124). Additional support was provided by the CALMIT lab at the University of Nebraska, and the Geography Dept. at CSU-Sacramento. Pat Starks, USDA provided Soils data. Additional assistance in field data collection and computer processing was provided by Brian Leavitt and Anthony Militar.

REFERENCES

Lillesand, T.M. and R.W. Kiefer, 1987. Remote Sensing and Image Interpretation, John Wiley & Sons.

Bouman, B.A.M. and D.H. Hoekman, 1993. Multi-temporal, multi-frequency radar measurements of agricultural crops during the Agriscatt-88 campaign in The Netherlands. Int. Journal of Remote Sensing. 14(8):1595-1614.

Holmes, M.G., 1990. "Applications of Radar in Agriculture," Ch. 19 in Applications of Remote Sensing in Agriculture, M.D. Stevens and J.A. Clark, Eds. Butterworth Press.

Bouman, B.A.M. and D. Uenk,1992. Crop classification possibilities with radar in ERS-1 and JERS-1 configuration, Remote Sensing of Environment. 40:1-13.

Schmullius, C, Nithack, J. and M. Kern. 1994. comparison of multitemporal ERS-1 and E-SAR image data for crop monitoring. Earth Obs. Quaterley. 43:9-12.

Leberl, F.W., 1990. Radargrammetric Image Processing, Artech House.

Lee, J.S., 1981. Speckle analysis and smoothing of synthetic aperture radar images. Computer Graphics and Image Processing. 17:24-32.

SPATIO-TEMPORAL ANALYSIS OF SAR IMAGE SERIES FROM THE BRAZILIAN PANTANAL

Geoffrey M. Henebry
Department of Biological Sciences, Rutgers University
Newark, NJ, 07102 USA
phone: +1 201 648 5053, fax: +1 201 648 5518

Hermann J.H. Kux
Instituto Nacional de Pesquisas Espaciais (INPE)
CP 515, 12227-010 São José dos Campos, SP, Brazil
phone: +55 123 41 8977, fax: +55 123 21 8743

ABSTRACT

Flood monitoring in the Pantanal Matogrossense is complicated by several environmental factors that interact to generate landscapes that appear highly heterogeneous in time and space. In light of this heterogeneity, change detection and quantification become difficult: How best to measure spatial heterogeneity through time? What constitutes an appropriate baseline? Our solution uses metrics of lacunarity to quantify land cover dynamics. We illustrate this approach using a seven-date SAR image series from 1992-93 in which a significant climatic drought follows typical seasonal inundation. Lacunarity analyses on three representative landscapes from the Nhecolândia region reveal distinct spatio-temporal trajectories that include both cyclicity and perturbation in spatial heterogeneity and anisotropy. These features correspond to the flooding cycle and the unusual drydown event.

1. INTRODUCTION

The utility of Synthetic Aperture Radar (SAR) for flood monitoring has been amply demonstrated in the past few years. This application has focused on the occasional catastrophe that affects human settlements when hydraulic loading on a regulated river system exceeds design specifications. Land cover change accompanying such a flood is obvious albeit ephemeral. In the absence of human intervention, periodic inundation of riparian lands is required to sustain the ecological dynamics that characterize river-floodplain systems. Operational flood monitoring of an unregulated river system presents a set of analytical challenges to remote sensing: How best to summarize the spatio-temporal data of an image time series? What constitutes a baseline? How to quantify spatio-temporal patterns to enable comparisons? These questions require an analytical approach that can quantify temporal development in the spatial structures that compose an imaged scene. This explicit spatio-temporal analysis contrasts with the implicit analysis found in a sequence of classified images. Indeed, dynamics of biogeophysical fields are ill-represented, both conceptually and practically, by map series.

One promising approach to identification and portrayal of patterns latent in spatio-temporal data is lacunarity analysis, a multi-scale procedure based on fractal geometry. We introduce new lacunarity metrics and a neutral model that facilitates comparisons of lacunarity decay curves. We apply these techniques to a seven-date ERS-1 SAR image series to discover spatio-temporal *landscape trajectories* found within a very dynamic tropical floodplain. This study extends our previous work on lacunarity analysis of SAR imagery (Henebry and Kux, 1996; Henebry and Kux, 1995; Kux and Henebry, 1994a; Kux and Henebry, 1994b).

2. LACUNARITY ANALYSIS

Lacunarity indices use multi-scale windowing to measure the scale dependency of spatial heterogeneity and anisotropy in binary maps in terms of departures from translational and rotational invariance (Plotnick *et al.*, 1996; Henebry and Kux, 1995; Plotnick *et al.*, 1993).

Proc. 3rd ERS Symp. on Space at the service of our Environment, *Florence, Italy, 17–21 March 1997* (ESA SP-414, 3 Vols., May 1997)

The indices are sensitive to map density and aggregation. Higher lacunarity indicates a more sparse, more clumped distribution within the map. Random maps exhibit a lack of persistent spatial structure under multi-scale windowing (i.e., correlation length approaches zero) and thus achieve low lacunarity scores. Conversely, maps containing larger aggregates maintain high lacunarity scores until the size of the sampling window exceeds the size of the aggregates.

Interval-scaled imagery must be converted into binary maps for lacunarity calculations. Slicing the image histogram into even quantiles controls map density, thereby making lacunarity sensitive only to the scale dependency of aggregation. For image time series it is useful to track lacunarity using a constant window size. Choosing the optimal window size, however, can be tricky: sampling too large or too small an extent can miss significant changes in spatial structure. It is thus prudent to conduct preliminary analyses to determine the shape of the lacunarity decay with occurs with increasing sampling extent. Comparing decays curves is rather difficult, whether it be quantiles formed from the same image or comparable quantiles across different image. We describe here a simple neutral model to facilitate comparisons.

Assume that the image histogram is sliced into quartiles and four corresponding binary maps are formed. No pixels are lost in this conversion: their values are simply collapsed to one bit. A convenient property of the basic lacunarity index is that its value at a window size equal to the image grain is the reciprocal of the map density. Therefore, the lacunarity indices sum across the quartiles to unity, when evaluated at window size of 1. This additivity forms the basis for a neutral model. We can pose an expectation that this uniform partitioning of lacunarity across the quartiles will be preserved with increasing sampling extent. At any sampling window size, we expect that the lacunarity index for any particular quartile will contribute 25 percent to the total lacunarity. In other words, we are positing a scale-invariant partitioning of lacunarity as the neutral expectation. Percent deviation from this fractal geometric expectation provides a metric that is more sensitive to change in spatial structure and easier to assess than raw decay curves. There is "conservation of spatial order", i.e., no loss of spatial elements; thus, total deviation across quartiles must sum to unity and the quartile-specific partitioning of deviation provides a means to distinguish between the textural aspects of scene object backscattering and speckle.

3. STUDY AREA

The Pantanal is the largest wetland habitat on the planet: an immense assemblage of alluvial fans formed during the Pleistocene, it covers 139,000 km^2 in Brazilian states of Mato Grosso and Mato Grosso do Sul (Klammer, 1982; Rizzini *et al.*, 1988). The Pantanal is also one of the more radiometrically dynamic landscape in the tropics due to extensive seasonal flooding by the Paraguay River and its tributaries. It has a tropical semihumid climate with mean annual temperature of 25° C and mean annual precipitation of 1100 mm concentrated into a rainy season from October to March. Altitude in the alluvial plains range from 100-200 m asl. The Pantanal is remarkable for its reduced declivity (2.5-5.0 cm/km). Local topographic features (2-4 m above the surrounding lands), resulting from either ancient Aeolian sandfields (Klammer, 1982) or termite activity (Ponce and da Cunha, 1993) are critical for determining habitat for both flora and fauna. Forested ribbons of higher ground known as *cordilheiras* are never flooded and serve as seasonal refuge for terrestrial animals. Where the water is deep, hydrophytes predominant; in areas with sufficient water flow, productive grasslands emerge. The deep sandy soils lead to a substantial seasonal drydown (June to September).

The study area lies in the Nhecolândia region of the Pantanal, located along the southern tier of the Rio Taquari alluvial fan. Nhecolândia is remarkable for the hundreds of freshwater and saline lakes that punctuate the landscape. We analyzed three typical landscapes: (1) a large quasi-perennial wetland with bordering woodlands, (2) a mosaic of lakes ringed by trees

and interspersed among grasslands, and (3) a well formed channel with riparian forest.

4. METHODS

Our ERS-1 image series spanned seven dates from 12/92 to 11/93. These acquisitions were well positioned to sample a single flooding cycle. The SAR images were georeferenced, ground-range projected, real-valued, 3-look digital data processed by INPE. The nominal ground resolution of these data was 25 m with a pixel spacing of 12.5 m in both range and azimuth. For each landscape type the same scene (1024x1024 pixels = 164 km^2) was extracted at each date and coregistered to the December 1992 scene using linear offsets. The resulting misregistration was minimal (<2 pixels) and lacunarity is robust to misregistration errors when image extent is large relative to resolution.

The quartiles (Q1, Q2, Q3, Q4) for the histograms were calculated and four binary images were thereby generated for each image subregion. In contrast to the random resampling approach of our earlier work, we calculated lacunarity using exhaustive subsampling separately for window shapes of w(2j) and w(j2), where j ranged from 4 to 1024, yielding sampling window areas from 0.125 ha to 32 ha. (For more detail on lacunarity calculation, see Plotnick *et al.*, 1993; Henebry and Kux, 1995.) Lacunarity values for Q1 and Q4 were combined into one scaled index: SLI=2-(1/Q1LI+1/Q4LI). We also calculated the combined deviation in percent for Q1 and Q4 from the neutral prediction.

5. RESULTS

We have noted previously (Henebry and Kux, 1995) that most of the spatial heterogeneity in these scenes was located in Q1 and Q4, corresponding to the lowest and highest backscattering values, while the middle 50 percent of the histogram was dominated by spatially random speckle noise. This was again the case for each scene we analyzed here; thus, we focus only on Q1 and Q4. Further, we present only results obtained from the w(j2) window shape. Although results are comparable from w(2j), the regional flooding and drainage pattern generates a stronger N-S gradient.

If we plot the Q1+Q4 scaled lacunarity index against composite Q1+Q4 percent deviation for different window sizes, we can obtain spatio-temporal patterns that captures some essential elements of the landcover dynamics (Figures 1-3). In each landscape, there is (1) quasi-periodicity evident in the spatial arrangement of backscattering, (2) more definite cyclicity with larger sampling area, and (3) clearly anomalous positions for the late 1993 acquisitions. These anomalies likely arise from an extreme drought that struck the Pantanal during the later half of 1993. How do we interpret these trajectories? Note that deviations increase as scaled lacunarity decreases with increasing sampling window area. This pattern indicates persistent aggregates in the extreme quartiles, which correspond to forested patches for Q4 and open water or wetlands for Q1. Large range in deviation values (e.g., Figs 1-2) indicates a lot of spatial rearrangement, suggesting dramatic shifts in the backscattering characteristics of large patches. Finally, are these trajectories statistically significant? This is subtle question because: (1) lacunarity index values were derived from *exhaustive and non-independent* sampling of the image; (2) the index is based on the first two moments of the sampling distribution weighted for mass; (3) the index does not have, as yet, analytically defined moments; (4) permutation tests would be prohibitively expensive. More significant is the question of whether these trajectories are representative of landscape dynamics from an inter-annual perspective; only additional image series can provide an answer to this question of baselines.

6. CONCLUSIONS

The spatio-temporal patterns revealed in this study are provocative but not yet conclusive. We have illustrated the utility in extracting spatio-temporal patterns for environmental monitoring, specifically, for definition of nominal behavior and assessment of disturbance impacts. Our long term goal is the predictive modeling of landcover

dynamics using landscape trajectories extracted from image time series derived from multiple sensors.

7. ACKNOWLEDGEMENTS

G.M.H. acknowledges support from NSF grant DEB-9696229 and a Fulbright Senior Research Fellowship at INPE during 1993-94. H.J.H.K. acknowledges ESA for support from an ERS-1 Pilot Project. Both authors acknowledge further support from ESA for an ERS-2 follow-on project. The ERS-1 SAR data were processed by and acquired through INPE.

8 . REFERENCES

Henebry, G.M., and Kux, H.J.H. 1996, Spatio-temporal land cover dynamics in the Pantanal assessed using lacunarity analysis on an ERS-1 SAR image time series, *Proc. IGARSS '96*, pp. 195-197.

Henebry, G.M., and Kux, H.J.H. 1995, Lacunarity as a texture measure for SAR imagery, *Int. J. Remote Sens,*. 16, 565-571.

Klammer, G. 1982, Die paläowuste des Pantanal von Mato Grosso und die pleistozäne Klimageschichte der brasilianischen Randtropen. Zeitschift für Geomorphologie N.F., 26, 393-416.

Kux, H.J.H., and Henebry, G.M. 1994a, Multi-scale texture in SAR imagery: landscape dynamics of the Pantanal, Brazil, *Proc. IGARSS '94*, pp. 1359-1364.

Kux, H.J.H.,and Henebry, G.M. 1994b, Evaluating anisotropy in SAR imagery using lacunarity functions. *Int. Arch. Photogram. Remote Sens.*, 30(7A), 141-145.

Plotnick, R.E., *et. al.* 1993, Lacunarity indices as measures of landscape texture, *Landscape Ecology*, 8, 201-211.

Plotnick, R.E., *et. al.* 1996, Lacunarity analysis: a general technique for the analysis of spatial patterns. *Physical Review E,* 53(5), 5461-5468.

Ponce, V.M., and da Cunha, C.N. 1993, Vegetated earthmounds in tropical savannas of Central Brazil: a synthesis with special reference to the Pantanal do Mato Grosso, *J.Biogeog*,20,219-225.

Rizzini, C.T, *et. al.*, 1988, Ecossitemas Brasileiros/Brazilian Ecosystems, Index Editora, Rio de Janeiro.

Figure 1: flooded wetland Q1+Q4

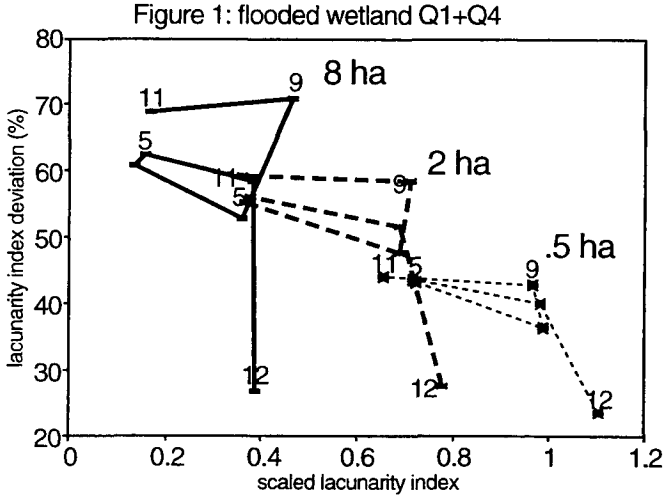

Figure 2: lake mosaic Q1+Q4

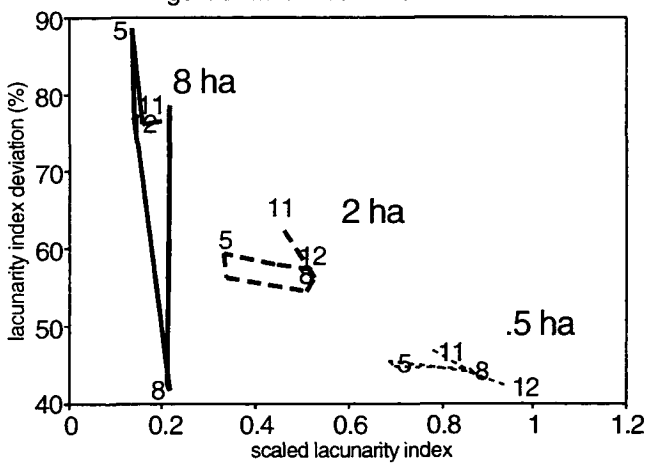

Figure 3: riparian forest Q1+Q4

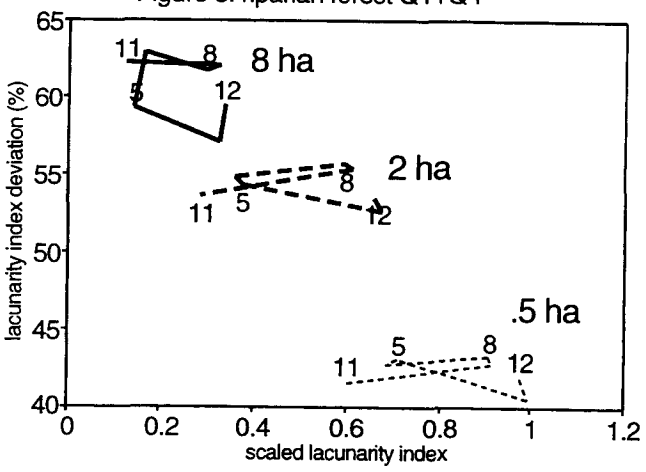

ENVIRONMENTAL MONITORING OF THE ST.PETERSBURG REGION USING ERS DATA (AO2. No 109)

Ola M. Johannessen, Lasse H. Pettersson, Stein Sandven, Kjell Kloster

Nansen Environmental and Remote Sensing Centre
Edvard Griegsvei 3a, N-5037 Solheimsvik, Bergen, Norway
phone: +47 55 29 72 88, fax: +47 55 20 00 50
E-mail: ola.johannessen@nrsc.no

Dmitry V. Ionov, Yuri M. Timofeyev

Department of Atmospheric Physics, Research Institute of Physics, St. Petersburg State University
Ulyanovskaya Str. 1, 198904, Petrodvorets, St. Petersburg, Russia
phone: +7 812 428 44 86, fax: +7 812 428 72 40,
e-mail: tim@troll.niif.spb.su

Leonid P Bobylev, Vladimir V. Melentyev, Victoria V. Donchenko

Nansen International Environmental and Remote Sensing Centre
Korpusnaya Str. 18, 197110 St. Petersburg, Russia
phone: +7 812 235 74 93, fax: +7 812 230 79 94
E-mail: nansen@sovam.com

Victor V. Ionov

Division of International Baltic and Arctic Projects, St. Petersburg State University
10th Line, 33/35 199178 St. Petersburg, Russia
phone: +7 812 218 71 46, fax: +7 812 218 13 46
e-mail: victor@baltic.lgu.spb.su

Arcadij M. Shalomiansky

A.I.Voeikov Main Geophysical Observatory
Carbysheva Str. 7, 194021, St. Petersburg, Russia
phone: +7 812 247 43 90

ABSTRACT

The work has been dedicated to some preliminary results of the Project ESA A02. No. 109 "Pilot Demonstrations of Environmental Information Retrieval from the ERS Sensors for Monitoring of the St.Petersburg Region". This is a multi-disciplinary research project with a wide scientific scope. Besides, it is a part of a long-term program - The St.Petersburg Region's Environment Monitoring System Development.

1. INTRODUCTION

The project has two main objectives:

- to demonstrate possibilities and advantages of using ERS sensors data to monitor environment conditions at a regional scale taking as an example St.Petersburg region;
- to improve algorithms of remote sensing data processing and to develop approaches to synergistic use of ERS sensors data and other types of remote sensing and in-situ measurements data.

It should be noted that St.Petersburg region is not only the city itself and St.Petersburg province but also the catchment area of the water system Onega Lake - Ladoga Lake - Eastern part of the Gulf of Finland (Fig. 1). This region is a unique testing area for improving and validation of methods of space remote ecological monitoring due to the large population density and strong anthropogenic load over environment.

Three priority directions were chosen on the initial stage of carrying out the project:

- to assess the perspectives of using ERS/SAR for monitoring pollution of such big lakes as Ladoga and Onega;
- determination of approaches to synergistic use of ERS/SAR and other satellite data for polluted areas identification for boreal forests;
- visualization and validation of GOME total ozone measurements.

Preliminary results of the investigations under the first and third directions are given in the present work. As for the second direction, it is considered in details in a special presentation made at this Symposium [Ref. 6].

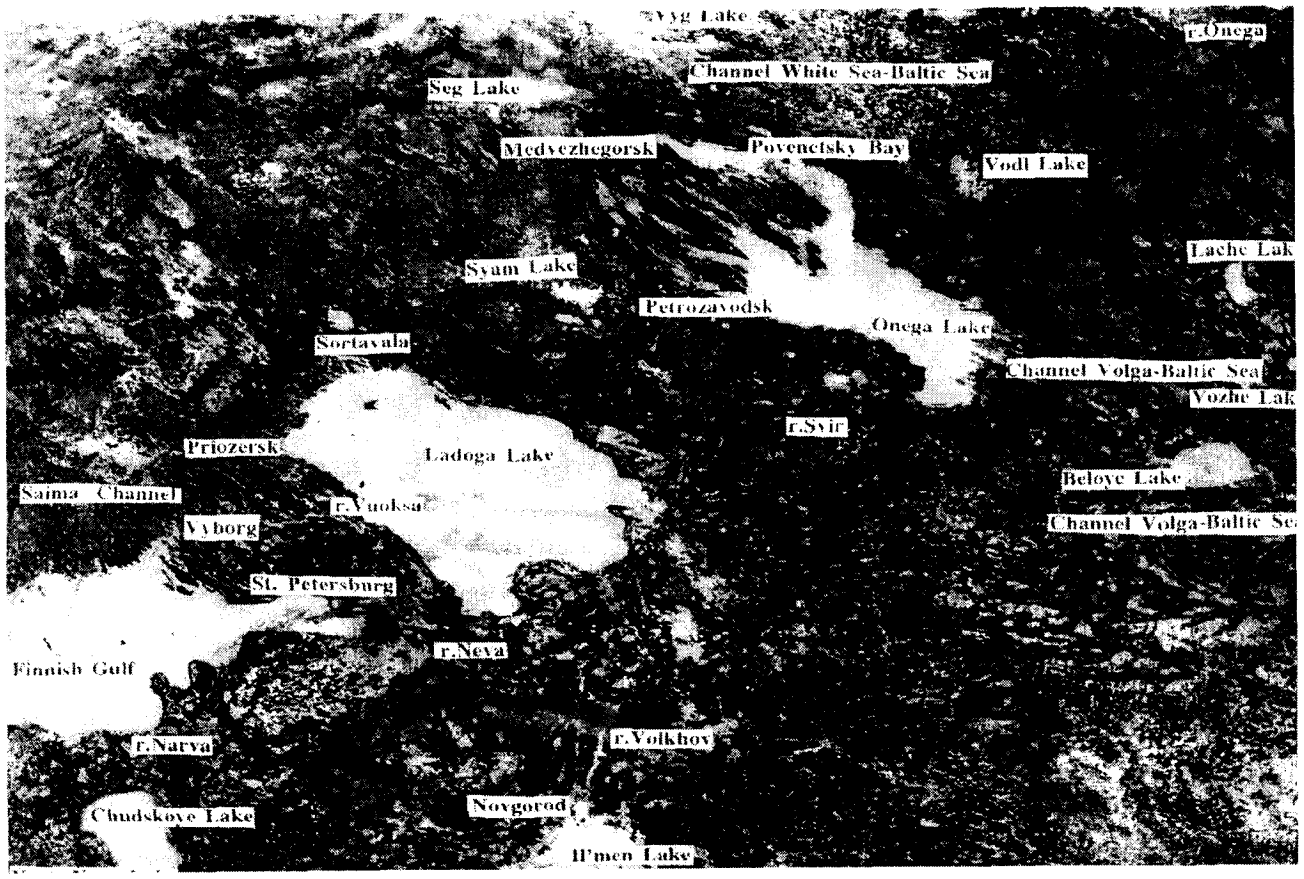

Figure 1. St.Petersburg Region (METEOR - 30 Image, 16.03.87)

2. ASSESSMENT OF NATURAL AND ANTHROPOGENIC FACTORS AFFECTING THE ENVIRONMENT OF THE REGION

This section deals with the problems of improving the techniques of remote sensing of parameters of ice cover and its regime for large water bodies of the moderate climatic zone and developing, on this basis, approaches to the remote control of natural and anthropogenic forcings on the environment from the data of space-borne SAR. Apart from the ERS-1,2/SAR images, the results of multiyear studies of the thermal structures of large lakes - Ladoga and Onega, as well as data of sub-satellite ship and aircraft experiments on these lakes were used [Ref. 1-4].

To solve the problem, consider the ice cover condition in the north-eastern part of Lake Ladoga (for 21 and 24 January, 1995 (Fig. 2a,b)). The SAR images make it possible to retrieve the history of the ice formation in this region. So, we can reliably state that initially the fast ice has settled here in conformity with the bottom relief around the shoal and the entire chain of banks, and later on the consolidated shuga ice joined the fast ice from the off-shore edge. In the first decade of January 1995 during a spell of the stormy south-westerlies the fast ice was broken here along the shore and in the mouth of the river Vidlitsa. The coastline configuration in the region considered is such that the south-westerlies can strengthen the constant cyclonic circulation of dense waters. As a result, the shoal ice preventing water masses from free motion, leads to the formation of the closed spiral of the cyclonic circulation in the near-deep layer north of the river Vidlitsy.

Thus, the satellite SAR survey gives a unique possibility to fix in winter the regulated structures forming on the surface of large lakes as a result of the atmospheric mesovortices forcing. For example, the 6 March 1996 ERS-1/SAR image (Fig. 3a,b) fixed a spiral of larger-scale cyclonic circulation appearing in the same part of Ladoga in the winter 1995-96.

Let us dwell on analysis of this phenomenon from the viewpoint of its significance for the self-clearing of the waters of large lakes and water reservoirs. The Ladoga lake is known to be the main source of fresh water for the 5-million population of St.Petersburg. The water sampling for the city is now made in the region of the Schlisselburg Bay near the source of the river Neva. The existence in this gigantic fresh-water reservoir of the cyclonic cycle of waters considerably lengthening the path of the polluted waters before they get to Neva, favours the self-clearing of the lake. At the same time, the presence in Ladoga of water masses with drastically different properties (the thermally active zonein the near-shore area and the thermally inert zone in the center of the lake) has negative consequences for water supplying: only a narrow band of the near-shore waters turns out to be involved into the cycle which, being

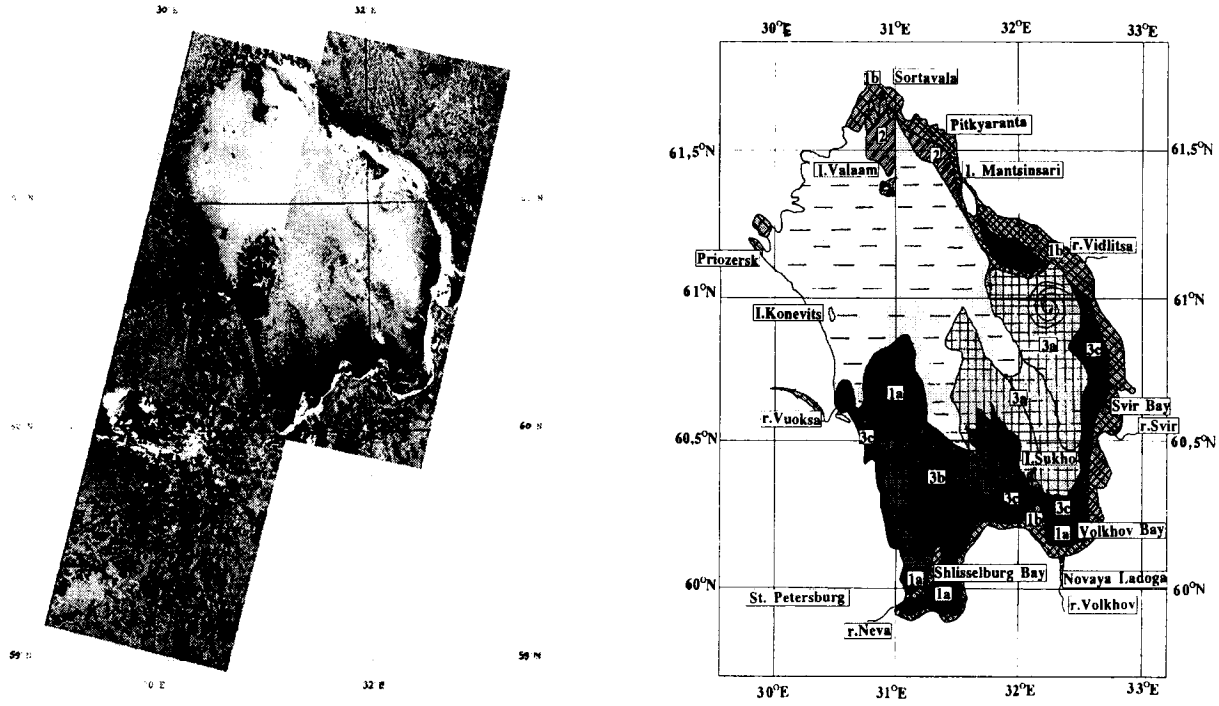

(a) (b)

Figure 2. ERS-1/SAR images of Ladoga lake, 21 and 24 January 1995 (© ESA) (a) and results of their analysis (b) 1,2,3 - freeze up phases; a,b,c - time intervals within each phase to which ice of different development corresponds

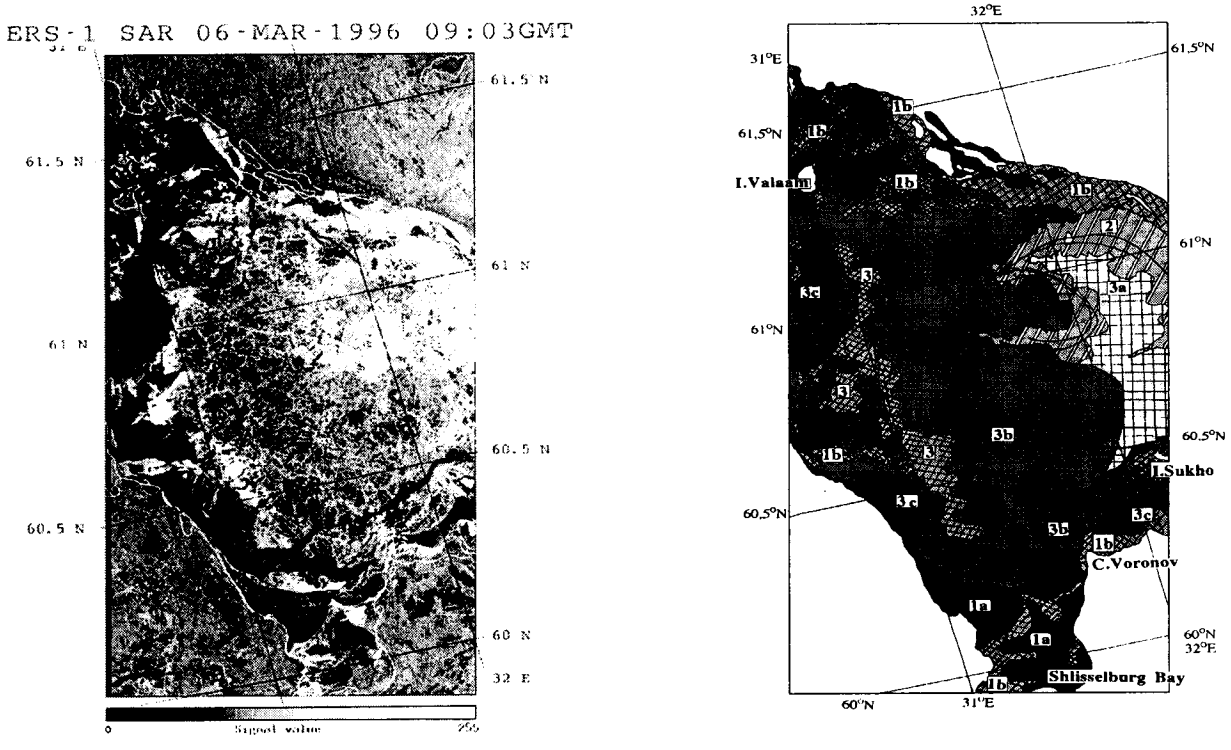

(a) (b)

Figure 3. ERS-1/SAR image of Ladoga lake, 6 March 1996, 09 : 03 GMT (© ESA) (a) and results of its analysis (b). 1,2,3 - freeze up phases; a,b,c - time intervals within each phase to which ice of different development corresponds

heavily affected by man's activity, is most polluted and needs special control and cleaning. But mesovortices of the type identified on SAR images favour the self-cleaning of the waters since under their influence the polluted waters along the coastline are thrown to the center of the lake and taken away from the cycle of

waters used by the city. Till recently these vortices have not been observed for lack of respective measuring instruments and only the ERS/SAR images have given a unique possibility to control this natural phenomenon.

Now consider the ice conditions in the northern and north-eastern part of Ladoga. An assessment of the condition and quality of the waters in this region is extremely important, since several pulp-and-paper plant, largest in the St.Petersburg region, are located here and affect substantially the ecological condition of the waters. In the skerries part of the lake, the SAR image (Fig. 2a,b) shows the fast ice, and north and north-west of the island Mantinsari over the depths 40-60 m the drifting shuga ice is seen. Note the characteristic ice formation of dark inhomogeneous exposure located in the streit between the island Valaam and the skerries region of the lake. All this vast area is covered with sufficiently even ice formed around small islands north of Valaam. Here the ice appeared during phase 2 of freezing due to circulations pushing the coastal waters to the center. This ice has formed by accretion of light nilas, by the moment of survey it preserves separate areas of open water, traces of rafting and hummocking are observed - it is these characteristics of the surface of grey ice 10-15 cm thick cause the inhomogeneities of signatures mentioned above. This area of grey ice, in our opinion, marks the boundaries of propagation of the polluted waters from the pulp-and-paper plants of Sortavala and Pitkiaranta. The strong pollution of the waters leads to a change of their surface viscosity favouring the smoothing out of capillars and the formation of a vast slick zone - this peculiarity determines the deep dark tone of signature.

The analysis made shows that the ice cover of the inland water bodies is a tracer of various natural processes and phenomena, including those climatically and ecologically important. An experience of complex decoding of ERS/SAR images of the largest lakes ice cover of Petersburg region has shown the prospects of using the SAR information to retrieve the history of the lake ice formation and its external forcings. Of considerable scientific and practical interest is an identification on SAR images of polluted water basins and the unknown-before natural phenomenon - the spiral-shaped cyclonic circulation of the ice cover.

3. VISUALISATION AND VALIDATION OF GOME TOTAL OZONE MEASUREMENTS USING GIS TECHNOLOGY

The studies of spatial-temporal variations of total ozone content (TOC) are very actual in connection with ozone layer depletion observed in the Earth atmosphere during the last decades. The basic amount of information on the ozone content comes from the ground network of ozone observing stations and as a result of interpreting the satellite data. The latter data are retrieved from the measurements of ultraviolet (UV) outgoing solar reflected and scattered radiation by the GOME device operating onboard the ERS-2 satellite. For testing the validity of the satellite data, it is necessary to provide comparing the GOME TOC data with independent measurements.

The mapping of total atmospheric ozone is the most interesting problem nowadays. Although it is the main scientific task of the GOME project [Ref. 5], in fact it is not so trivial to get a spatial distribution of total ozone from the GOME data products. This cartographic task is rather complex methodological and technical one, which can be problematic. The use of the modern computer-assisted technology of Geographical Information Systems (GIS) with its highly developed mapping and visualisation features seems to be the most effective solution.

The nominal spatial resolution of GOME is formed by 3 ground pixels across-track with 40 km along-track, 320 km across-track (see Fig. 4). As the geolocation of each pixel is described in the Level 2 Data product by the geographical coordinates of its corners, it is mostly suited for the vector model of presentation. However to take into account the overlapping pixels of different scanning modes within one orbit, pixels from different orbits within one day, and pixels from the orbits acquired on different dates - we need to come to the

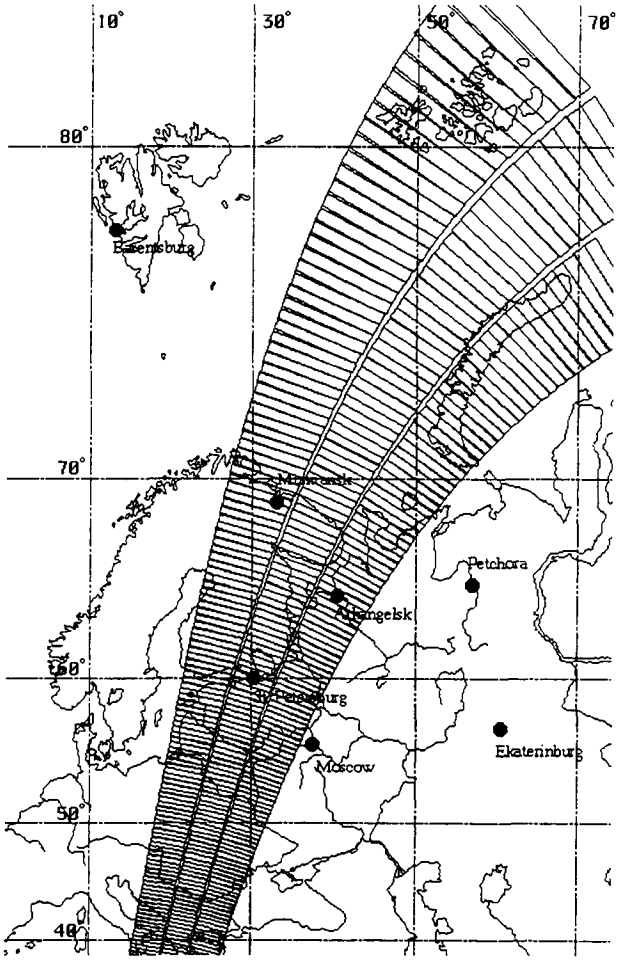

Figure 4. One of the GOME orbits with a nominal scanning mode, covering a part of Northern Europe. Symbols show the locations of Russian ground based stations for atmospheric ozone observations.

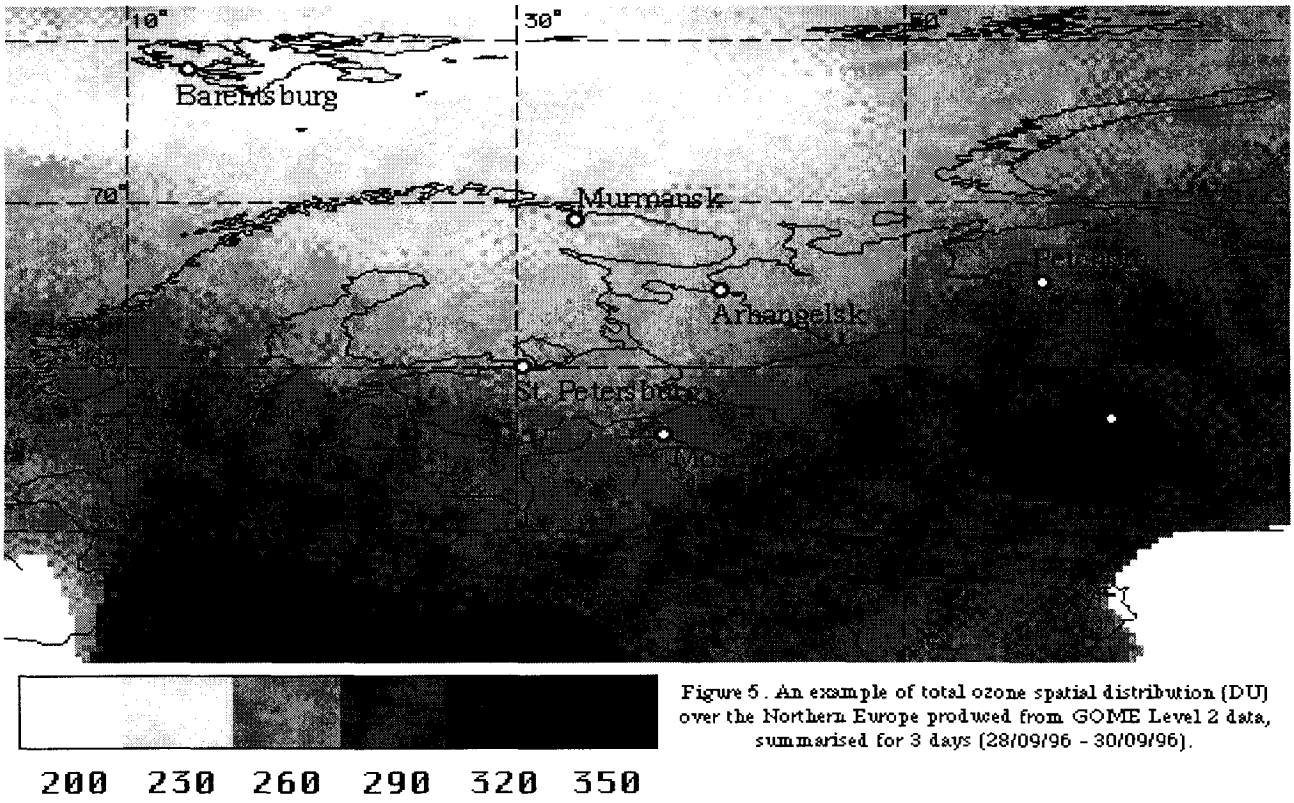

Figure 5. An example of total ozone spatial distribution (DU) over the Northern Europe produced from GOME Level 2 data, summarised for 3 days (28/09/96 - 30/09/96).

raster data presentation, getting the full power of map algebra and image processing tools.

As a pilot project, the map of the spatial distribution of total atmospheric ozone was produced from the GOME Level 2 data of 35 orbits acquired from 28/09/96 to 30/09/96. The geographical area of interest was chosen to be the Northern Europe including St.Petersburg region. The result of this work is shown in Fig.5. The TOC in the area changes approximately from 210 DU (northern-west part) to 330 DU (southern-west and southern-east part). The area of relatively low ozone is seen above the Spitsbergen. The places of relatively high ozone are above the northern part of the Mediterranean sea and near the city of Ekaterinburg. The spatial resolution of this map - about 20 geographical minutes - seems to be good enough for the purposes of the future total ozone dynamics' investigations. The spatial peculiarities of total ozone, appearing in such maps, can be understood when compared with different meteorological information, as the ability of GIS technology to integrate these data makes it possible.

Another important problem is the validation of total ozone content, derived from the GOME measurements. One of the ways to estimate the accuracy of these measurements is to compare them with simultaneous surface observations. For those purposes one needs an effective way of retrieval from the whole Level 2 data set a ground pixel located at the particular point of observation. The solution of that really complicated task (one orbit contains about 2200 pixels) is again GIS. We should consider each of the ground pixels as a spatial vector object with its unique identification number (ID). The number of these pixels will fill the spatial database of our GIS. At the same time, the whole information that corresponds to these objects will be put into the attribute database. In this case we can easily find the pixel with certain location by means of the spatial quire within GIS. We can also select pixels with different features - e.g. clouds' conditions or Sun zenith angle - when doing different attribute requests.

An example of comparison of the GOME measurements with surface observations is shown in Fig. 6. The GOME total ozone data were compared with the simultaneous measurements from 7 Russian ground

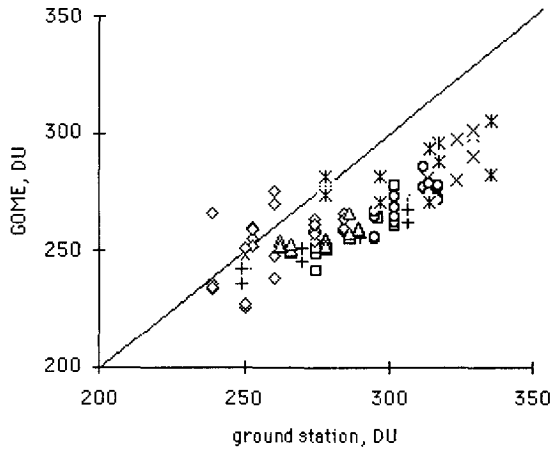

Figure 6. The comparison of the GOME total ozone measurements with surface observations at 7 Russian ground based stations (23/09/96 - 30/09/96).□ - Arhangelsk, × - Ekaterinburg, + - Murmansk, ∆ - St.Petersburg, ◊ - Barentsburg, o - Moscow, ж - Petchora

based stations. In most cases several pixels were found to cover the station at the same date - pixels from different orbits and scanning modes. All in all, about 120 GOME total ozone measurements were compared with 50 ground observations. The following statistical characteristics of the ground-based (g) and satellite (s) total ozone data - the mean values ($\bar{u}_g$ and $\bar{u}_s$), the ranges (Δu_g and Δu_s) and the RMS deviations (σ_g and σ_s) - are given in Table for each station and for overall data set (**AVG**).

Table. Some statistical characteristics of used measurement data sets

Station	$\bar{u}_g$	$\bar{u}_s$	Δu_g	Δu_s	σ_g	σ_s
Barentsburg	257	253	45	50	15	12
Murmansk	277	253	58	36	23	12
Petchora	311	285	57	36	19	11
Arhangelsk	291	256	40	36	15	10
St.Petersburg	281	255	39	17	14	4
Ekaterinburg	329	287	57	30	21	10
Moscow	313	272	31	31	9	8
AVG	293	264	129	79	27	17

Although the result of this comparison should be considered as preliminary it could be noted from Fig.6 that GOME total ozone values are considerably lower than those from surface observations. The ranges and RMS deviations of the satellite total ozone measurements are, as a rule, less than ground-based data. This conclusion is true in the most examined cases (see Table).

The comparison of the data from ground based observations with a GOME data, characterised by different measurement conditions may help to clear the reason of their discrepancies, that will be the subject of future investigations.

REFERENCES

1. Kondratyev K.Ya., Melentyev V.V., Nazarkin V.A. Remote Sensing of Water Areas and Watersheds from Space. Gidrometeoizdat, St.Petersburg, 1992. 248 pp.

2. Tikhomirov A.I. Thermal Conditions of Large Lakes. Nauka, St.petersburg, 1982. 232 pp.

3. Kondratyev K.Ya., Johannessen O.M., Melentyev V.V. High Latitude Climate and Remote Sensing. Wiley-Praxis, 1996. 200 pp.

4. Melentyev V.V., Tikhomirov A.I., Kondratyev K.Ya., Johannessen O.M., Sandven S., Pettersson L.H., Kloster K. Study of the Freeze-up Phase Changes on Large Temperate-Zone Inland Water Bodies and Possibilities of Their Microwave Diagnostics. Study of Earth from Space, No.3, 1997 pp. 13-25.

5. GOME Users manual SP-1182. ESA, ESTEC, Publications Divivsions, Noordwijk, The Netherlands, 1995

6. Donchenko V.V., Goltsova N.I., Bobylev L.P., Johannessen O.M., Kritsuk S.G., Pitulko V.M. Synergistic Use of ERS-1/SAR and Other Satellite Data for the Polluted Areas Identification for Boreal Forests of St. Petersburg Region. Ibid.

MONITORING PROCESSES OF DRYLAND DEGRADATION FROM ERS SAR DATA

G.H.Griffiths & K.H.White
The Department of Geography
The University of Reading
Whiteknights
Reading. RG6 6AB
UK

Tel. +44 118 9318733
g.h.griffiths@reading.ac.uk
k.h.white@reading.ac.uk

ABSTRACT

Land degradation is a major problem in many parts of the Sahel, adversely affecting land productivity and the livelihood of millions of people. An important component of the process of land degradation is soil erosion. This project is investigating the potential of SAR and ATSR imagery from ERS-1/2 to derive critical parameters for input into physically-based soil erosion models. Preliminary and earlier results (Griffiths et al., 1993) indicate that SAR is useful for monitoring soil moisture in the HAPEX-Sahel study area, Republic of Niger. Further work is required to retrieve other significant soil erosion parameters from the combined imagery to calibrate and validate different soil ersosion models within the same region.

1. INTRODUCTION

Soil erosion is a major factor in land degradation in semi-arid regions. Mapping the extent and severity of this process over large and frequently inaccessible areas is difficult from ground-based measurements. Earth observation data provide an ideal way to apply models spatially, thereby overcoming reliance on discrete field measurements. However, the former reliance on optical imagery (AVHRR, Landsat, SPOT) for monitoring soil erosion in the Sahel has met with limited success, largely because of restricted spectral wavebands and coarse spatial resolution. This project is using parameters derived from C- band SAR backscatter in combination with optical imagery (ATSR) to develop a methodology that combines the potential of both sensors for deriving significant soil erosion parameters.

Much recent research has concentrated upon the development of techniques for estimating soil moisture from SAR imagery (Beaudoin et al., 1990). However, the process of soil erosion is complex involving both the loss and deposition of topsoil via the agents of wind and water, resulting in a spatially variable redistribution of sediments. The type (sheet, rill, gully) and severity of erosion are dependent upon a number of key *erodibility* and *erosivity* factors:

- erodibility; soil type & moisture status, crop type & condition, slope, hydrology
- erosivity; wind speed & direction, rainfall intensity & temporal distribution.

This project is exploring the potential of combined SAR and ATSR data to derive critical soil erodibilty parameters which, in combination with field measurements of erosivity, can be input into a physically-based model to predict erosion type and severity over large areas and under different climatic, soil and vegetation conditions in the Sahel.

2. STUDY AREA

The area chosen for the project is the southern HAPEX-Sahel (Hydrological Atmospheric Pilot Experiment) study site in the Republic of Niger (Figure 1). The study area was selected for a number of reasons:

- it lies in the African Sahelian semi-arid zone and has a range of soil erodibility conditions, from highly erodible to stable;
- the area is relatively flat, eliminating the need to apply terrain corrections to the SAR data;
- there is substantial ancillary information, including data on land cover and meteorological conditions to calibrate and verify models;
- the area lies within range of a satellite receiving station, providing high bit-rate data.

3. IMAGE ACQUISITION & PROCESSING

A multi-temporal set of SAR scenes were obtained for the study area (Table 1). The images were converted to backscatter (dB) and co-registered, using standard techniques. These dates were selected to cover the transition from dry to wet soil conditions at the beginning of the wet season in May and the transition to dry conditions in October.

Orbit	Frame	Date
16070	261	11 August 1994
19012	261	04 March 1995
19964	3339	10 May 1995
20465	3339	14 June 1995
20966	3339	19 July 1995
21467	3339	23 August 1995

Table 1. SAR images acquired for the study area.

Three of the scenes (June, July & August, 1995) were registered and produced as a colour composite for interpretation. The three scenes were also examined separately and backscatter intensity sampled within a range of different cover types to produce temporal profiles of the behaviour of each cover type.

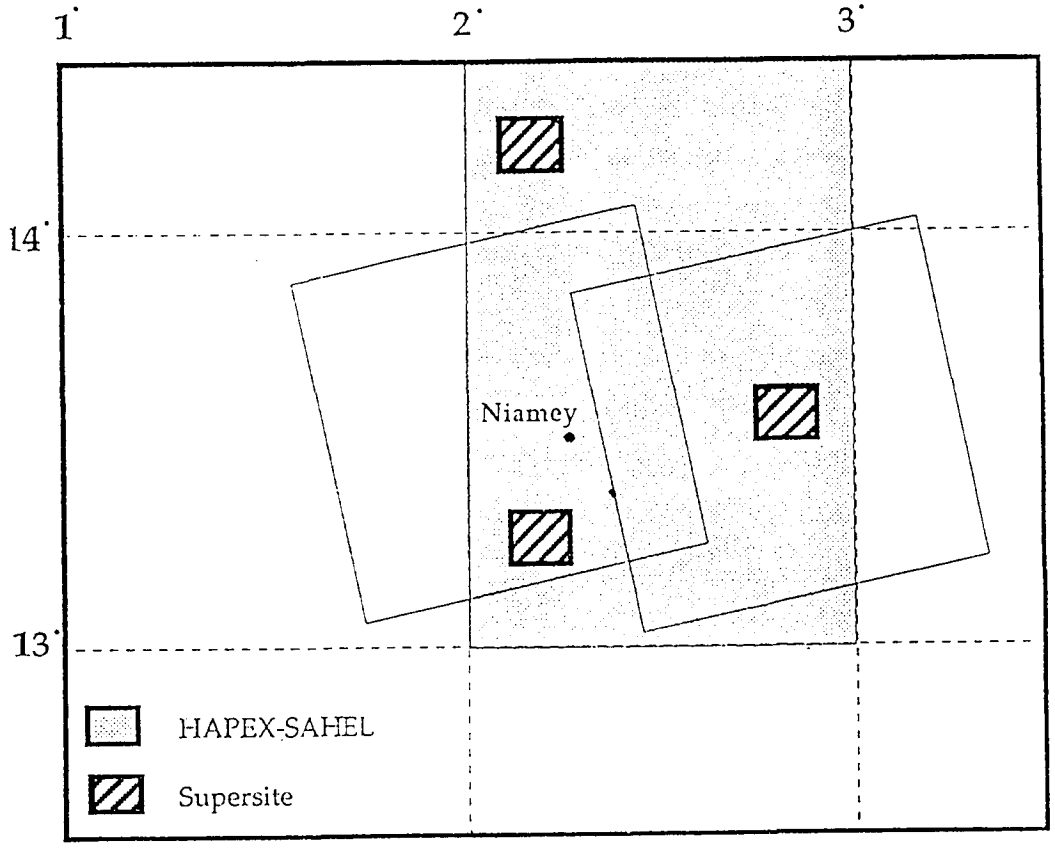

Figure 1. Location of ERS-1 scens covering the HAPEX-Sahel study are in relation to the three super sites

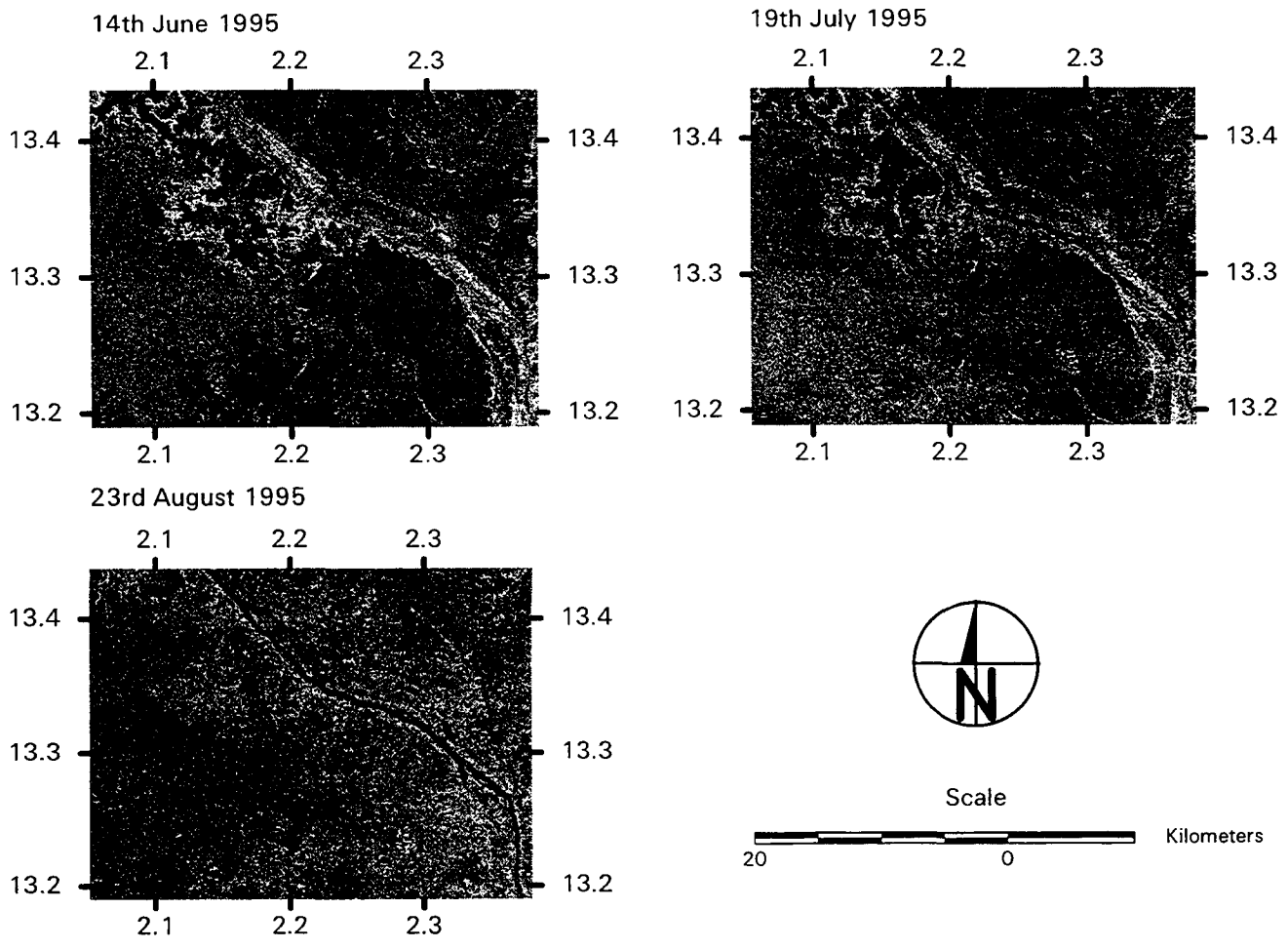

Figure 2. Three single date ERS SAR scenes of the area, showing varying contrast in backscatter between the dry season (June, 1995) and the wet season (August 1995).

4. RESULTS

Research has demonstrated (Bradley & Ulaby, 1981) that the operating frequency of the ERS-1 (C- Band) SAR combined with a low incidence angle (23°), is optimal for detecting variations in soil moisture. The set of three black and white single date images (Figure 2) display high contrast between tiger bush (*Combretum* spp.) and cultivated areas in the dry season (June 1995). Under wetter conditions (August, 1995) indicated by a low backscatter return from the flooded River Niger, this contrast has moderated suggesting that under these conditions soil moisture is the dominant control on backscatter.

The temporal profiles (Figure 3) confirm that backscatter is high for millet in August under the prevailing relatively wet conditions, suggesting a crop related moisture effect. By using a multi-temporal set of images across a single growing season, the contribution to total backscatter of surface roughness (resulting from the planting, growth and harvesting of crops) and soil moisture can be estimated.

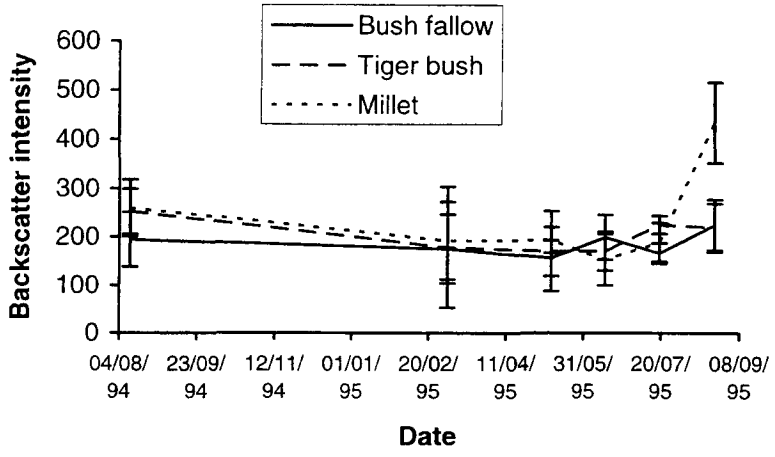

Figure 3. Temporal profile of backscatter intensity for three land cover types

5. SOIL EROSION MODELS

Several attempts have been made to model soil erosion processes. The USDA has developed models for soil conservation purposes; the Wind Erosion Prediction System (WEPS) is a process-based daily time-step model that simulates weather and field conditions to calculate soil movement. The Water Erosion Prediction Program (WEPP) is a distributed parameter, continuous simulation model which can be used for both hillslope and watershed applications.

Both models require spatial information on parameters affecting soil erodibility (e.g. texture, vegetation cover and structure, slope shape, steepness and orientation). Verification of estimates of these parameters from the SAR & ATSR imagery is possible from field and climate data collected

during and following HAPEX-Sahel. Similarly, meteorological data is available from HAPEX-Sahel and the ICRISAT Research Station for driving the climate sub-models of WEPS and WEPP. These results will be used to quantify the spatial patterns of both wind and water erosion, and geostatistics will be used to identify the processes important at different spatial scales.

Only a limited SAR image dataset has been acquired and future work will require additional imagery to coincide with planned fieldwork. The BRDF of different vegetation types within the study have been determined from field measurements. These data will enable estimates of three-dimensional vegetation canopy structure to be derived from dual look-angle ATSR data.

6. REFERENCES

Beaudoin, A., Le Toan, T. & Gwyn, Q.H.J., 1990. SAR observations and Modelling of the C-band Backscatter Variability due to Multiscale Geometry and Soil Moisture. *IEEE.*, **28**, 5, 886 - 895.

Bradley, G.A. & Ulaby, F.T, 1981. Aircraft radar response to soil moisture. *Remote Sensing Environ.*, **11**, 419 - 438.

Griffiths, G.H., Wooding, M.G. & Blyth, K., 1993. Monitoring soil moisture in semi-arid areas with ERS-1 SAR, Earth Observation Quarterly, **42**,1 - 5.

Forestry

Chairperson: **J-P. Malingreau**

INTERFEROMETRIC SAR OBSERVATIONS OF FORESTED AREAS

Jan Askne, Patrik B.G. Dammert and Gary Smith

Remote Sensing Group, Department of Radio and Space Science
Chalmers University of Technology
S-412 96 Göteborg, Sweden
phone: +46 - 31-7721843, fax: +46 - 31-164513
askne@rss.chalmers.se http://www.rss.chalmers.se

ABSTRACT

Properties of C-band repeat pass interferometric SAR (INSAR) information from forested areas in northern Sweden and from the Amazon rain forest are studied using data from the 3-day repeat cycle of ERS-1 in 1994 and from the ERS-1/ERS-2 tandem mission. Radar backscattering intensity is not sensitive to forest stem volume/biomass above a fairly low saturation level, and is limited in its use for forest/non-forest discrimination. Interferometric SAR has been shown to offer considerable improvement for mapping properties of land surfaces, particularly in forested regions. For boreal regions, coherence shows a significant advantage over intensity for classification of forest and non-forest areas. In the Amazon region, despite generally low coherence, areas of higher coherence are still visible. If the forest coherence is high enough, the interferometric height of the forest (difference between a DEM and the elevation obtained from the interferogram) can be measured. To determine the relationship between the observables and forest properties a first-order model has been developed. The observational results are compared with the model.

Keywords: Interferometric SAR, forest, model, observations

1. INTRODUCTION

Forested areas are important from a remote sensing point of view as they cover large parts of the earth, and are important environmentally and economically. In particular microwave remote sensing is important to follow fast changes, due to its independence of sun illumination and relative independence of the atmosphere and clouds.

ERS-1 SAR was intended as an experimental satellite regarding land applications, while other operations like sea ice remote sensing were considered to be semi-operational. The problem with land applications is the large variability in space as well as time, and the many parameters affecting the radar signal. The advent of repeat-pass interferometry with ERS-1/2 increased the information content in the measurements and the ability to investigate land processes. By using interferometric SAR, INSAR, and combining information using the radar backscatter, $\sigma°$, change in $\sigma°$, and coherence over time periods for which we have a reasonable interferometric coherence, the information from an area has increased considerably. By combining measurements from different acquisitions, perhaps at different seasons, information is similarly increased. However, the interpretation of the temporal changes of land cover on shorter and longer time scales is often quite complex. We will in this paper present a status report on the potential of interferometric SAR in forestry. The areas studied are mainly in Sweden, but also some scenes over the Amazon rain forest.

2. INTERFEROMETRIC SAR PROPERTIES FOR FOREST APPLICATIONS

2.1 Interferometric coherence

Interferometric coherence, γ, is an important parameter for describing the quality of different interferometric pairs. It is defined as

$$\gamma = \frac{E\{g_1 g_2^*\}}{\sqrt{E\{g_1 g_1^*\} E\{g_2 g_2^*\}}} \quad (1)$$

where $g_{1,2}$ are the complex pixel values of image 1 and 2 respectively, and E denotes expectation value. As was shown in (Ulander and Hagberg, 1995, Askne et al., 1997) the coherence can be divided into several factors

$$|\gamma| = |\gamma|_{noise} \cdot |\gamma|_{slantrange} \cdot |\gamma|_{volume} \cdot |\gamma|_{temporal} \quad (2)$$

where $|\gamma|_{noise}$ is the system noise power decorrelation, which is normally negligible, $|\gamma|_{slantrange}$ is the baseline decorrelation which can be compensated for by filtering, (Gatelli et al., 1994), $|\gamma|_{volume}$ is due to the decorrelation between scatterers within the volume illuminated by the pulse, and $|\gamma|_{temporal}$ is the temporal decorrelation of the scatterers between the two images.

Coherence estimation is only unbiased if the average is performed over a large number of pixels. The bias primarily influences low values of coherence such as over lakes and forests, (Dammert, 1996). In our case the sea outside the coast was used as reference for a zero-coherence area, for which the bias is around 0.22-0.26 using a 5x25 pixel estimation window for ERS SAR SLC images.

The coherence over a certain area is often determined by the random phase variations, σ_φ, within the averaging window. The coherence then decays like $e^{-\sigma_\varphi^2/2}$. σ_φ may be caused by random height variations σ_H, or by random displacements of the contributing scatterers, σ_R. We may also have a random thickness change, σ_l, of an intervening dielectric medium, like a snow layer, or the atmosphere, resulting in dielectric decorrelation. Assuming independent Gaussian random variables we have

$$\sigma_\varphi^2 = \left(\frac{4\pi B}{\lambda R \sin\theta}\sigma_H\right)^2 + \left(\frac{4\pi}{\lambda}\sigma_R\right)^2 + \left(\frac{4\pi}{\lambda}(\sqrt{\varepsilon}-1)\sigma_l\right)^2 \quad (3)$$

B is the interferometric baseline normal to the line of sight, R is the slant range, and θ is the incidence angle. Either σ_R=0.5 cm, σ_l = 3.8 cm (with ε=1.3), or σ_H=17 m (at B=100 m) will decrease the coherence by a factor of two.

2.2 Differential SAR interferometry

If a DEM is available of the imaged area, it is possible to generate a simulated phase image and a differential interferogram. This will display all differences between the real interferogram and the real DEM and can be used for measuring the interferometric effective tree height over forested areas. However, there are several problems with this technique. The DEM is often in a national map co-ordinate system while the SAR interferograms are in the slantrange-azimuth domain. Without having a detailed model of the sensor viewing geometry, it is not possible to accurately coregister the image and the simulated image over a large area. However, over smaller areas of approx. 20x10 km^2 a polynomial co-ordinate transformations and a set of tiepoints in the DEM and in the SAR interferogram can be used.

An interferometric pair from the winter season 1994 over an area in northern Sweden has been compared with a DEM in this fashion. Pixel mismatch (i.e. co-ordinate mismatch) is believed to be not larger than the pixel size of 20x20 m^2. Using this differential interferogram, two things can be accomplished. First, measurements of the effective forest height and, second, measurements of how accurate the interferometric DEM is. The accuracy of interferometric DEMs, in the repeat-pass case and over high-coherence areas, is limited by variations of atmospheric radar wave propagation path delays (Tarayre, 1996), and also by snow layer variations.

3. FOREST INTERFEROMETRIC SAR MODEL

In the direct remote sensing problem we describe in a model the major effects of various *in situ* parameters on the measured signal. The radar scattering aspect is described in varying detail by e.g. the water cloud model, (Attema and Ulaby, 1978), or the MIMICS program, (Ulaby et al., 1990; McDonald and Ulaby, 1993). In the interferometric SAR case the phase aspects are important as described by Eq (3), including shifts of the scatterers due to winds, but also dielectric changes due to temperature changes, rain etc.

Table 1 Describing some parameters which affect a INSAR images from a forest area.

Geometrical Properties	Temporal Properties	Dielectric Properties
shape of trees size distributions and orientation of stems, branches etc. ground roughness vegetation area-fill	wind freezing/thawing water content snow cover rain	ε_T of stems, branches etc. attenuation of vegetation

In (Askne et al., 1997) the water cloud model was used to model the scattering. The parameters of the water cloud model can be obtained by more exact models, but the model describes the essential feature; saturation at high stem volumes. As the ground and vegetation back scattering may vary over the year, some forest and open field sites with known properties should be used for reference (Pulliainen et al., 1966). In the model the extinction coefficient is assumed to be proportional to the number of scatterers, and hence to the stem volume. The extinction through the canopy layer varies with temperature, particularly for temperatures above and below the freezing point. The area fill or canopy closure at 23° incidence angle, represents the percentage of the area covered by forest canopy. This is an important parameter for sparse forests like the boreal forest in northern Sweden. Values of the area fill and the extinction were estimated in (Askne and Smith, 1996) from measurements reported by (Pulliainen et al., 1994).

The stability of the scatterers due to the wind has to be estimated, and in (Askne et al., 1997) a decrease with height was assumed. No experimental values on such stability factors are known and other height variations can also be argued for. For simplicity a constant variation has been used in this paper, resulting in minor changes compared to earlier analyses. This is a consequence of the high attenuation of the signal at C-

band, which limits the back scattering to a thin layer at the tree tops.

The interferometric effective height of the forest and the coherence are related, as the height is determined from the phase factor of the complex coherence. This is illustrated in Figure 1 where the ground term (reference height) is combined with the vegetation part from the upper part of the forestry canopy. The two terms are combined and determine the effective height.

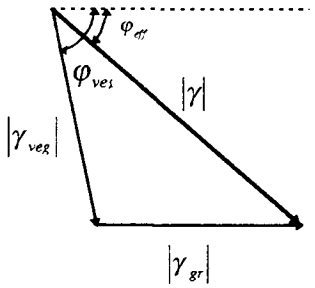

Fig. 1 Illustrating the coherence and effective height as combined by ground and vegetation components, from (Askne et al., 1997).

4. OBSERVATIONAL RESULTS

The results are concentrated to an area around Hökmark in northern Sweden using data from the 3-day repeat cycle of ERS-1 in February and March 1994. Looking at the weather statistics, melting temperatures (dielectric decorrelation) were often accompanied by strong winds (geometric decorrelation). Some results are also obtained from the Amazon rain forest not far from Manaus.

4.1 Coherence properties - Temporal decorrelation

For forests, a comparison of interferograms at different baselines, shows that decorrelation due to the baseline dependent volume scattering is unable to describe the difference between vegetated and non-vegetated areas (Smith et al., 1996). The differences seem to be related to the movement of scatterers (tree branches) on short time scales. This movement occurs so rapidly, that even decreasing the time interval between images to one day, as for the tandem mission, results in no observed increase in forest coherence (Askne et al., 1996). The authors believe that the decorrelation occurring over snow covered fields is a consequence of dielectric decorrelation resulting in phase shifts as well as amplitude shifts. This is a result of changing weather conditions, and usually occurs over a period of a few days. This is illustrated in Figure 2 for short baselines and medium baselines. The apparent differences between the decay of field coherence at different baselines is probably due to the weather conditions for the occasion of the short baselines being less stable than in the majority of medium baseline cases.

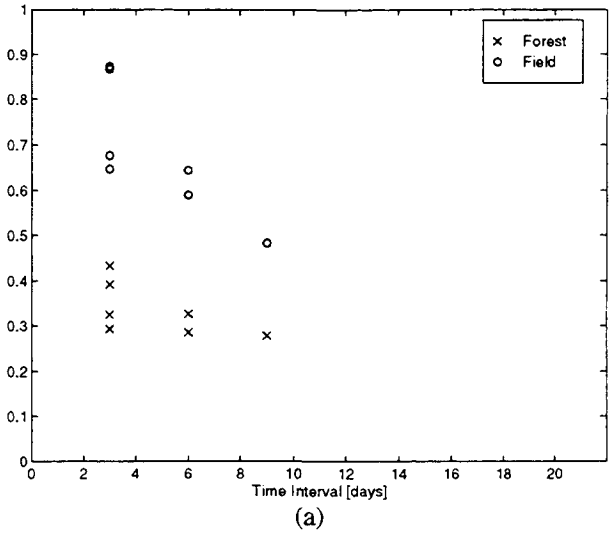

(a)

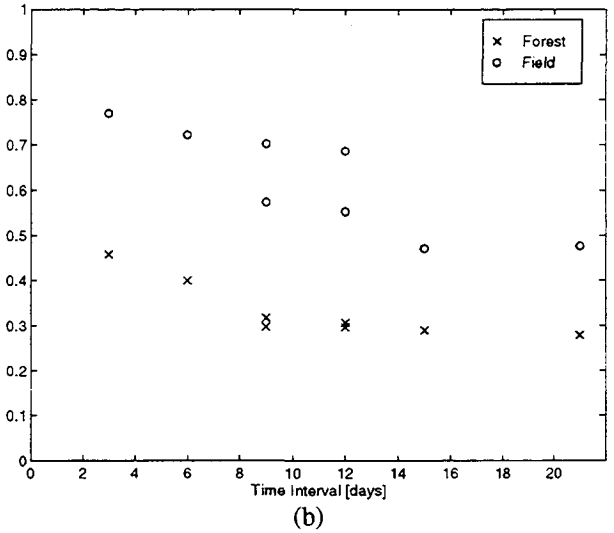

(b)

Figure 2 illustrating coherence decay with time for short baselines (21 and 30 m)in (a) and middle baselines (175 and 203 m) in (b).

4.2 Mapping of forests

A number of papers have suggested the use of SAR interferometry for improving the poor separation of forest and non-forest areas in ERS SAR backscatter measurements (Askne and Hagberg, 1993; Wegmüller and Werner, 1995b; Wegmüller and Werner, 1995a). To quantify the separability between different classes, we have used the Jeffreys-Matusita (J-M) distance (Jeffreys, 1948; Swain, 1978) to give a quantitative measure of the improvement available by including coherence information in a classification. The measure can be directly related to the probability of correct classification of Normally distributed data, for a maximum likelihood classifier (see Table 2, (Yatabe and Leckie, 1995)).

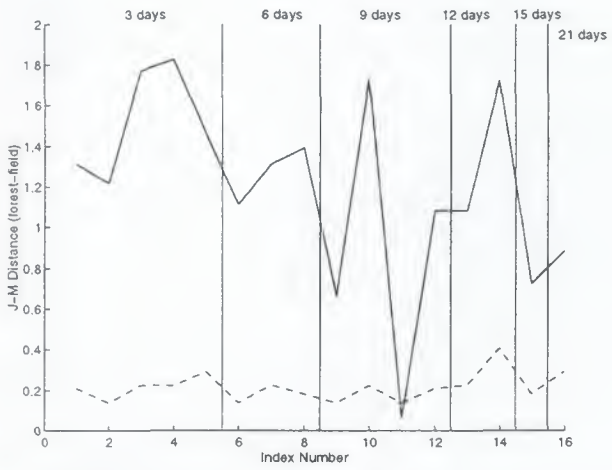

Figure 3 J-M Distance, Separability between forest and snow covered fields from Hökmark area. Solid line: using coherence; dashed line: using intensity.

Table 2

J	Probability of correct classification
0.0	0
0.4	0.60 → 0.84
1.0	0.75 → 0.94
2.0	1

The results shown in Figure 3 demonstrate how the separability of forests and snow covered fields varies for interferometric pairs where the baseline for all of the pairs is less than 600m. It can be seen that the separability is generally much better using coherence information, although in one case (index number 11), the separation is as poor with coherence as with intensity. This interferogram corresponded to images straddling a period of changing temperatures, heavy snow fall and strong winds, resulting in the fields having as low coherence as the forests.

It is also apparent from the figure that separability varies considerably between interferograms, but with a general trend towards decreased separability for increased time interval between the images of the pair. Again, this is a result of the coherence of the fields dropping as the time interval increases, and the forest (being already close to the bias level) remaining approximately constant.

In (Wegmüller and Werner, 1997) an accuracy of about 90% for the classification of forest area in an interferogram is reported for an area of mixed forest around Bern. This is consistent with the results shown here for boreal forests, although only for the better interferometric images. These images are generally characterised by high coherence for fields, which increases the separability as the forest coherence is almost always very low.

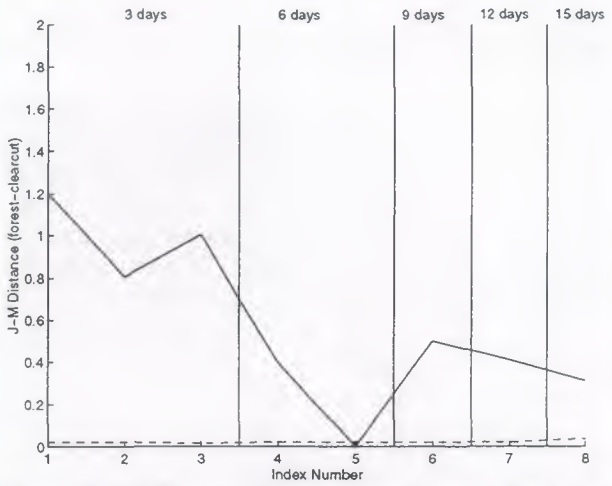

Figure 4 J-M Distance, Separability between forest and estimated fields in Amazon rain forest area. Solid line: using coherence; dashed line: using intensity.

Extension of the work on forest mapping to identifying clear-cutting in the Amazon rain forest is currently being studied. Initial results indicate that areas of higher and lower coherence (believed to be signatures of clearings and forests) have been identified, and that the areas of supposed clearings appear consistently in all interferograms of the area. However, the separability between forest and open fields is not as good, see Figure 4, as in the Hökmark area.

4.3 Image segmentation and classification

A 10 by 10 km^2 area near Hökmark has been classified using coherence, image intensity, and intensity change between the image pair from March 8 and 11, 1994, and August 1 and 2, 1995, see Figure 5.

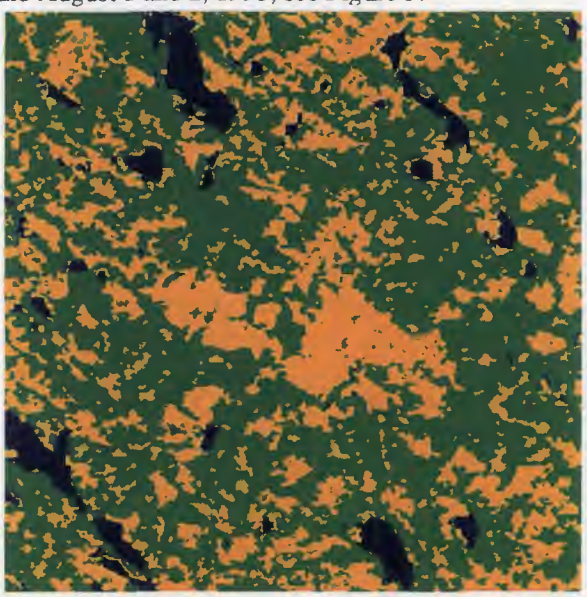

Figure 5: Classified image over Hökmark area: blue lakes green forests yellow open fields and clearcuts red buildings (Li et al., 1997).

Table 3a Measurements over Forest 1

First date	Second date	Coherence	Effective tree height (m)	σ° (dB) First date	σ° (dB Second date	Coherence adjacent open field	σ° (dB) adjacent open field
Feb 6	Feb 15	0.30	1.1	-7.4	-7.9	0.72	-10.9/-10.7
Feb 6	Feb 18	0.31	1.2	-7.0	-8.1	0.74	-10.6/-11.0
Feb 24	Feb 27	0.50	2.2	-8.1	-7.6	0.78	-10.6/-10.3
Mar 8	Mar 23	0.29	1.4	-8.7	-8.0	0.56	-10.9/-10.4
Mar 11	Mar 23	0.30	5.3	-7.9	-8.3	0.56	-10.2/-10.8
Mar 14	Mar 23	0.34	7.3	-8.1	-8.2	0.61	-10.3/-10.9
Mar 17	Mar 23	0.43	2.7	-8.0	-7.9	0.78	-10.5/-10.4

Table 3b Measurements over Forest 2

First date	Second date	Coherence	Effective tree height (m)	σ° (dB) First date	σ° (dB) Second date	Coherence adjacent open field	σ° (dB) adjacent open field
Feb 6	Feb 15	0.31	0.9	-7.0	-7.9	0.70	-12.5/-12-2
Feb 6	Feb 18	0.32	1.1	-6.6	-8.0	0.64	-11.9/-12.5
Feb 24	Feb 27	0.50	2.2	-7.8	-7.8	0.75	-12.7/-12.1
Mar 8	Mar 23	0.30	2.2	-8.5	-8.2	0.53	-12.6/-12.3
Mar 11	Mar 23	0.30	4.4	-7.7	-8.7	0.58	-11.5/-12.3
Mar 14	Mar 23	0.32	6.2	-8.0	-8.6	0.62	-12.2/-13.0
Mar 17	Mar 23	0.40	2.1	-8.2	-8.2	0.75	-12.4/-12.3

By using an image pair from the summer period and another from the winter period, problems associated with frozen lakes can be eliminated and forests, open fields, lakes, and urban areas can be discriminated (Li et al., 1997). Such a classification has been used to determine a forest mask over the 6×17 km^2 area studied below.

4.4 Interferometric effective tree height

Measurements over two small forest areas and surrounding fields in Hökmark are reported in Table 3 above. The forest coherence generally increases with the open field coherence while the effective tree height shows a more complex variation.

To create a large-scale effective tree height map, systematic phase variations over the image have to be removed. Using only the phase over fields and clear-cuts, this systematic phase variation can be estimated and, partly removed. A 2-D polynomial, up to a power of seven, fit to the field/clear-cut phase were carried out to see the large-scale phase variation. The phase variation is compared with the proposed phase fit in Table 4. (The topography in the area is below 100 m.)

The variations are believed to be partly due to mismatch between the DEM and the interferogram, and partly due to snow layer thickness variations. Another explanation is atmospheric artefacts over the image. To avoid such large scale effects an algorithm has been used to compare the forest height with close-by open fields. The observed heights are reported below.

Table 4

	Phase std.dev. (rad)	Height std.dev. (m)
Original field/clear-cut phase variation	0.201	1.66
Phase polynomial variation, field/clear-cut	0.182	1.50
Corrected phase variation, field/clear-cut	0.086	0.71

4.5 Comparison with model

From field investigations five forest areas with average stem volumes of 140, 200, 240, and 345 m^3/ha (rough estimates due to large variability within each area) have been identified together with six clear-cuts with varying regrowth. The results for σ° and the coherence (corrected for baseline decorrelation) are illustrated in Figure 5 for eight scenes and four image pairs.

For some of the results we will concentrate on observations from 24 and 27 February, due to the high forest coherence which simplifies the DEM comparison. In Figure 6 the observations are compared with the model results assuming an open field coherence of 0.9. The forest extinction is assumed to increase linearly with stem volume and equal 0.17 dB/m for a stem volume of 100 m^3/ha. The area fill is estimated to be about 70% for 100-200 m^3/ha forests.

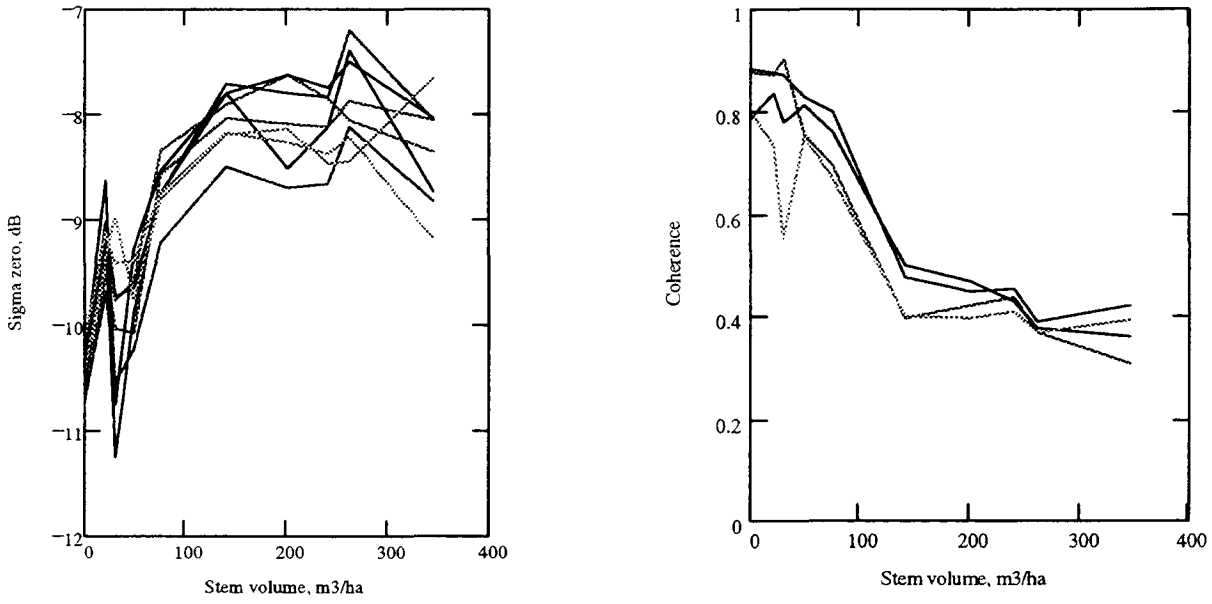

Figure 6 Illustrating σ° in figure to the left and coherence in the figure to the right for eight scenes in February and March 1994. σ° values vary quite a lot particularly over clear-cuts.

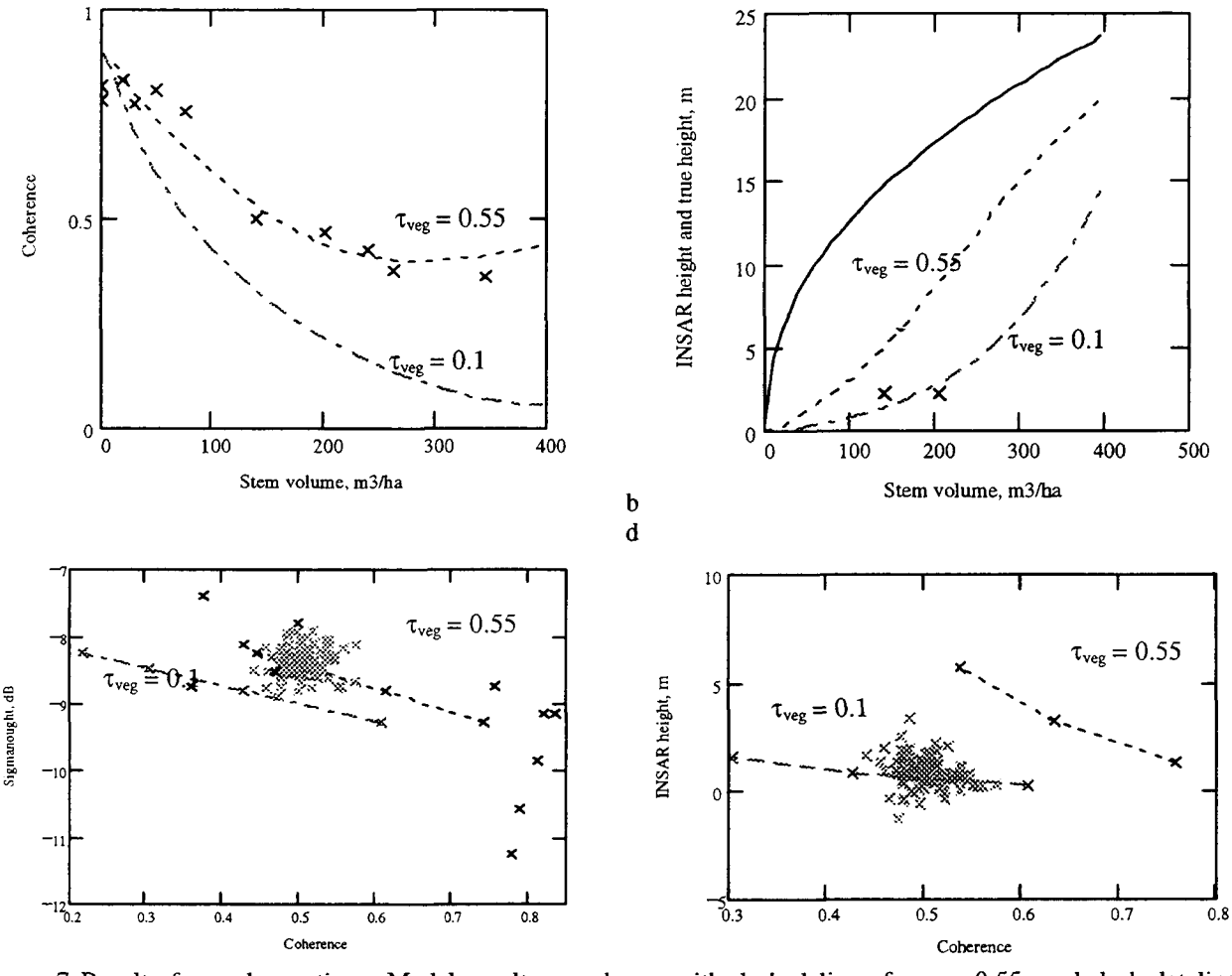

Figure 7 Results from observations. Model results are shown with dashed lines for τ_{veg}=0.55, and dash-dot lines, τ_{veg}=0.1. Solid line: estimated true height for forest as function of stem volume, x marks observations.

While coherence measurements in Figure 7c,d indicate values for τ_{veg} = 0.55 and stem volumes around 175 (stem values for 50, 100, and 150 m^3/ha marked along the model lines), the INSAR tree heights are much lower and rather in agreement with τ_{veg}=0.1 and with a stem volume of 75 - 100 m^3/ha. At present we have no field measurement of the entire area. There are many error sources in the case of interferometric heights derived using a DEM including the effects of a snow layer. The area fill factor used in the model is based on measurements in another area and believed to be too high for the area studied here. Although reasonable fits between the modelled and measured heights have been reported, (Askne et al., 1997) the results are rather sensitive to the exact location of where the measurements have been done. This indicates problems in estimating the forest effective height over large areas, and this problem will be studied further.

5. DISCUSSION AND CONCLUSION

Decorrelation mechanisms have been investigated for forest and snow covered open fields as function of time delays between pairs and baseline. Wind decorrelation is assumed to dominate for forest, and dielectric and geometric decorrelation phenomena for snow covered fields. The results show that coherence differences between fields and forest make a discrimination with high accuracy possible for image pairs acquired with less than twelve days in between them as long as no major storm or temperature variation around the freezing point occurs.

Observations and model results show decrease of coherence with stem volume, with the strongest variations for stem volumes below 200 m^3/ha. This is an interval where σ° also shows large sensitivity to stem volume. However, this is also an interval where we may experience large temporal variations, particularly of σ°. This illustrates a potential to map stem volumes in this interval as long as temporal variations can be taken into account by the use of known reference areas.

All interferometric height measurements are lower than model predictions. The measurements are performed relative to nearby snow covered open fields. The uncertainty in snow cover thickness makes these results uncertain, and interferometric effective heights should also be determined during summer time. However, this limits the study to the tandem mission, where the baselines were generally too small for reliable height estimates. Atmospheric and snow layer artefacts also influence the accuracy of the height measurements as well as the accuracy in the DEM simulated interferogram. The height estimates are dependent on the estimated area fill and extinction coefficients, for which more experimental information is necessary, in particular as function of stem volume.

The major conclusion is that the sensitivity of the ERS SAR sensors to differentiate between forest and open fields using coherence information it better than using backscatter measurements. Examples from the Amazon demonstrates that this is also possible in areas with dense forests. The time interval between the images should not exceed 3 days.

6. ACKNOWLEDGEMENTS

This project has been supported by the Swedish National Space Board, an ESA study on INSAR applications, co-ordinated by Matra Cap Systems, and by an European Union contract, EUFORA.

7. REFERENCES

Askne, J., B. G. Dammert and G. Smith, 1996: INSAR application evaluation report - Forestry. Chalmers University of Technology - Matra Cap Systems, Gothenburg.

Askne, J., et al., 1997: C-band repeat-pass interferometric SAR observations of forest, *IEEE Transactions on Gescience and Remote Sensing* 35(1): 25-35.

Askne, J. and J. O. Hagberg, 1993: Potential of interferometric SAR for classification of land surfaces. In *Proc. IGARSS'93*, edited by (IEEE, Tokyo. 985-987.

Askne, J. and G. Smith, 1996, Forest INSAR Decorrelation and Classifciation Propeties. *Fringe 96, Symposium held in Zurich, CH, on 1996,* (http://www.geo.unizh.ch/rsl/fringe96/papers/askne)

Attema, E. P. W. and F. T. Ulaby, 1978: Vegetation modelled as a water cloud, *Radio Science* 13(2): 357-364.

Dammert, P. B. G., 1996, Accuracy of INSAR Measurements in Forested Areas. *Fringe 96, Symposium held in Zurich, CH, on 1996,* (http://www.geo.unizh.ch/rsl/fringe96/papers/dammert)

Gatelli, F., et al., 1994: The wavenumber shift in SAR interferometry, *IEEE Transactions on Geoscience and Remote Sensing* 32: 855-865.

Jeffreys, H., 1948: *Theory of Probability*, (Oxford, Oxford University Press).

Li, A., et al., 1997, Fuzzy C-means clustering algorithm for classification of sea ice and land cover from SAR images. *submitted to The European Symposium on Aerospace Remote Sensing, Symposium held in London.*

McDonald, K. C. and F. T. Ulaby, 1993: Radiative transer modelling of discontinuous tree canopies at microwave frequencies, *Int. J. Remote Sensing* 14(11): 2097-2128.

Pulliainen, J. T., et al., 1994: Backscattering properties of boreal forests at the C-and X-band, *IEEE Transaction on Geoscience and Remote Sensing* 32 1041-1050.

Pulliainen, J. T., et al., 1966: Seasonal dynamics of C-band backscatter of boreal forests with applications to biomass and soil moisture estimation, *IEEE Transactions on Geoscience and Remote Sensing* 34(3): 758-770.

Smith, G., P. B. G. Dammert and J. Askne, 1996, Decorrelation Mechanisms in C-Band SAR Interferometry over Boreal Forest. *Microwave Sensing and Synthetic Aperture Radar, European Symposium on Satellite Remote Sensing III, Symposium held in Taormina, Italy, on 1996,* pp 300-310

Swain, P. H., 1978: *Fundamentals of Pattern Recognition in Remote Sensing,* (Oxford, Oxford University Press).

Tarayre, H., 1996: Extraction de modeles numeriques de terrain par interferometrie radar satellitaire: Algorithmie et artefacts atmospheriques. L'Institute National Polytechnique de Toulouse, Toulouse.

Ulander, L. M. H. and J. O. Hagberg, 1995: Radiometric and interferometric calibration of ENVISAT-1 ASAR. Res. Rep. No. 172, Dept. of Radio and Space Science, Chalmers University of Technology.

Ulaby, F. T., et al., 1990: Michigan microwave canopy scattering model, *International Journal of Remote Sensing* 11(7): 1223-1253.

Wegmüller, U. and C. L. Werner, 1995a, Farmland monitoring with SAR interferometry. *IGARSS'95, Symposium held in Firenze, Italy, on 1995a,* (IEEE), pp

Wegmüller, U. and C. L. Werner, 1995b: SAR interferometric signatures of forest, *IEEE Transactions on Geoscience and Remote Sensing* 5: 1153-1161.

Wegmüller, U. and C. L. Werner, 1997: Retrieval of vegetation parameters with SAR interferometry, *IEEE Transactions on Geoscience and Remote Sensing* 35(1): 18-24.

Yatabe, S. M. and D. C. Leckie, 1995: Clearcut and forest-type discrimination in satellite SAR imagery, *Canadian Journal of Remote Sensing* 21(4): 455-467.

FOREST INVENTORY USING INTERFEROMETRIC SAR TECHNIQUES

Marcus E. Engdahl, Juha M. Hyyppä

Laboratory of Space Technology, Helsinki University of Technology
P.O.Box 1000, FIN-02015 HUT, Finland
phone: +358-9-4512170, fax: +358-9-4512898
email: mengdahl@avasun.hut.fi

ABSTRACT

In this work the feasibility of interferometric coherence images for forest inventory was studied. Coherence images over our test site in Kalkkinen (130 km north of Helsinki) were produced from four ERS-1/2 Tandem SLC image pairs. Additionally, a normalized sum of the four coherence images was computed. All images were visually interpreted by comparing them with a base map, SPOT Pan image, and stand inventory data. Our results indicate that the coherence over boreal forest during winter is considerably higher than during other seasons. Therefore, ERS-1/2 Tandem interferograms acquired during winter seem to be ideal for DEM generation over boreal forests. Forest and non-forest may be visually discriminated from each other and discrimination between different forest types is also possible provided that the average scene coherence is not too low. Summation of normalized coherence images was found to produce images that are better suited for visual land-use and forest classification than a single coherence image.

1. INTRODUCTION

Traditional forest inventory is both expensive and time-consuming. In theory, remote sensing methods offer a good alternative and/or a supporting method for traditional forest inventory and, therefore, the utilization of remote sensing techniques has been subject of intensive investigations during the past few years. Satellite digital images, e.g. Landsat TM, have even been applied with success for operational large-scale applications, such as national forest inventory of Finland [1]. However, the Landsat TM-based estimates are rather inaccurate and there is a problem of getting cloud-free images in northern latitudes suggesting that the emphasis of development work should concentrate more on new radar-based methods. It has been shown that multi-temporal ERS-1/2 SAR PRI images do not provide accurate enough information for national forest inventory [2]. Recent advances in SAR interferometry, however, have shown an improved capability to monitor forest areas. Wegmüller et al. [3] demonstrated that the interferometric coherence, together with the backscatter intensity and the backscatter intensity change, has proved to be a useful tool for the classification of the land-surface classes. Hagberg et al. [4] suggested also that tree height and density of forests can be estimated using the interferometric phase information.

The main objective of the on-going Tandem AO project (AOT.SF301) is to evaluate the feasibility and usefulness of ERS-1/2 SAR Tandem interferometry for estimating forest resources, especially for national forest inventory. Special emphasis is in the evaluation of accuracy and cost-benefit analysis of interferometric SAR techniques compared to the present methods. This paper presents the first preliminary results from interferometric coherence images concentrating mainly on the seasonal effects on interferometric coherence.

2. SAR INTERFEROMETRY

SAR interferometry was first introduced by Graham in 1974 [5]. Previously, only the backscattered radar power was used and the information contained in the *phase* of SAR images was discarded. A SAR interferometer is formed by relating the signals from two spatially separated radar antennas. In repeat-pass satellite interferometry the SAR interferometer is formed by relating two complex SAR-images of the target area taken at separate times from a nearly exactly repeating orbit. The physical separation of the antennas at the time of the imaging is called the *interferometric baseline*. If the baseline exceeds a critical length (~1300 m for ERS-1/2) the complex images become totally uncorrelated and interferometry is no longer possible. In repeat-pass interferometry also the *temporal separation* between successive radar takes affects the amount of correlation in the interferogram. Depending on land surface type the images generally become uncorrelated when the temporal separation is long enough.

A SAR interferogram is formed by cross-correlating two complex SAR images taken with slightly differing viewing angles, and multiplying one image with the complex conjugate of the other. The two images must be

Proc. 3rd ERS Symp. on Space at the service of our Environment, *Florence, Italy, 17–21 March 1997* (ESA SP-414, 3 Vols., May 1997)

co-registered to sub-pixel accuracy. *Interferometric phase*, or the phase difference between the two images, is related to the difference in the path lengths from the two antenna positions to the ground thus permitting generation of digital elevation models (DEMs) [5].

3. COHERENCE

The correlation coefficient or *coherence* between two complex SAR images Z_1 and Z_2 is defined as the magnitude of the complex correlation [6]:

$$\gamma = \frac{E\left[Z_1 Z_2^*\right]}{\sqrt{E\left[\left|Z_1\right|^2\right] E\left[\left|Z_2\right|^2\right]}} \tag{1}$$

In equation (1), the expectation value operator E is in practice approximated with a sampled average over n samples. Sampled coherence over statistically uniform areas may be computed using:

$$|\gamma| = \frac{\left|\sum_n Z_1 Z_2^*\right|}{\sqrt{\sum_n |Z_1|^2 \sum_n |Z_2|^2}} \tag{2}$$

The interferometric phase in SAR interferograms contains information about the topography of the target area. Unless the topography is flat, this topography-induced phase must be removed. The topography-compensated coherence estimator is:

$$|\gamma| = \frac{\left|\sum_n Z_1 Z_2^* e^{-i\phi}\right|}{\sqrt{\sum_n |Z_1|^2 \sum_n |Z_2|^2}} \tag{3}$$

where ϕ is the topography-induced phase. The accuracy of the estimator (3) depends on the accuracy of the topography-compensation. Best results can be achieved by using a high-resolution DEM, if available [7].

The statistical confidence of the sampled coherence depends on the number of *independent* samples n that are used in the coherence estimation. Assuming flat or compensated topography, the standard deviation of the estimated coherence is given by [4]:

$$\sigma_\gamma = \frac{1 - |\gamma|^2}{\sqrt{2n}} \tag{4}$$

From equation (4) it can be seen that a large number of independent samples must be included in order to achieve an acceptable precision at low coherence areas. It is also known that the coherence estimators (2) and (3) are biased towards higher values especially at low coherence areas when n is small. As always, there is a tradeoff between estimation precision and achievable spatial resolution.

The correlation coefficient or coherence is a quantitative measure that is directly related to the amount of noise present in the SAR interferogram. The values of coherence range between 0 (*incoherence*) and 1 (*perfect coherence*). As long as there is some degree of coherence between the two images, interference phenomena such as fringes may be observed in the interferogram. When coherence is high, the amount of noise superimposed on the interferometric fringes is small and the observed speckle patterns in the interfering SAR images are similar [8].

Several different effects contribute to the decorrelation properties of various land surfaces [4,8]. In repeat-pass INSAR surveys with short baselines the temporal decorrelation caused by changes in the target area between the two radar passes and volume scattering in the vegetation layer are the most important causes of decorrelation. The coherence is generally low over forested areas and high over open fields which makes discrimination between forest and non-forest possible [3,4].

4. THE TEST SITE

Our three test sites are located in southern Finland, Teijo (130 km west of Helsinki), Porvoo (30 km east of Helsinki) and Kalkkinen (130 km north of Helsinki) representing a variety of different forest types and covering about 10000 hectares of forest land. Kalkkinen is the main area of activities with a large multi-source, multi-temporal remote sensing data set. From the 5000-hectare test area in Kalkkinen the following information is collected: field inventory data (ground truth), remote sensing data, and GIS information.

Field inventory data were collected by Uusimaa-Häme Forestry Center in summer 1996. About 100 parameters describing stand characteristics such as stem volume per hectare, basal area per hectare, mean tree height and tree species are measured for each stand (homogeneous forest areas of about one hectare in size). In order to evaluate the accuracy of field inventory, 40 stands were extremely carefully checked by sample plot measurements. The average value of the stem volume per hectare of the Kalkkinen test site is 141 m^3/ha. GIS information includes a digital elevation model (DEM), digital land-use map and base map 1:20000. Air/soil/vegetation temperature and precipitation monitoring statistics in selected areas have been gathered.

In this paper the first coherence images from the Kalkkinen test site are investigated.

5. THE INTERFEROMETRIC DATA SET

According to [3] the best results with SAR interferometry in forest mapping are expected using image pairs which have a short baseline and a short temporal separation between image acquisitions. Therefore, we used ERS-1/2 Tandem single look complex (SLC) image pairs which have a temporal separation of 24 hours and which also meet the baseline requirement in high latitudes. The pixel dimension in ERS-1/2 SLC images is such that one pixel in range direction corresponds to four pixels in azimuth direction. The precise orbital information used in the project was received from D-PAF. The chosen interferometric image pairs of the Kalkkinen test site are listed in Table 1.

Table 1. Interferometric pairs used in this study

Pair no.	Acquisition dates	Normal baseline	Average scene coherence
1	17-18.7.1995	0 m	0.157
2	21-22.8.1995	72 m	0.233
3	30-31.10.1995	49 m	0.201
4	8-9.1.1996	78 m	0.547

The average scene coherences were estimated using a window size of 9 x 36 pixels. The reason for the low average coherences is that the test scene in Kalkkinen is basically a mosaic of boreal forests and lakes. Pair number 4 differs from the other pairs in that it was acquired during winter time when the ground was frozen and snow-covered and the lakes were partially covered with ice.

6. INTERFEROMETRIC PROCESSING

The coherence images used in this study were produced from ERS-1/2 Tandem SLC images using the ISAR-Interferogram Generator software developed in Politecnico di Milano. The ISAR-software is distributed free of charge to the members of the ESA Fringe Group. ISAR software co-registers the two SLC images to the required sub-pixel accuracy, substracts the flat terrain phase term from the interferogram and performs common-band filtering in order to reduce baseline decorrelation. If needed, ISAR software also estimates the local directional slopes (the instantaneous frequency of the interferometric phase). In coherence estimation the ISAR software uses a Gaussian estimator window in order to reduce the deleterious effect of bright reflectors.

As mentioned earlier, there is always a trade-off between estimation precision and spatial resolution when the size of the coherence estimator window is decided. Small estimator window sizes produce high resolution estimates with large error margins. Since the forest stand size in the Kalkkinen test area is small (ca. 1 ha) and in the preliminary phase of this project only visual interpretation of coherence images was done, a rather small coherence estimator window size of 5 x 20 pixels (~50 physical looks) was chosen. The dimensions of the estimator window reflect the difference in pixel size in range and azimuth directions.

At the time of writing this report, the DEM of the Kalkkinen test site was not available to us so we approximated the terrain with a plane. The effects of this approximation on the estimated coherence should be small or negligible because the terrain height differences in the test area were small (<30m) and the baselines were short.

In post-processing, the coherence images were averaged in the azimuth direction and resampled so that the resulting pixel size was equal in both range- and azimuth directions.

7. COHERENCE IMAGES

Four coherence images were computed from the interferometric data set, one from each Tandem image pair. Additionally, a normalized sum of all coherence images (1 to 4) was computed. Here, normalization refers to the procedure of dividing the pixel values in each of the coherence images with the average scene coherence before summation. All the images were contrast stretched to two standard deviations in the data and visually compared with a SPOT Pan image. The following observations were made:

Coherence image 1 (Figure 1a):

The average scene coherence of 0.157 was very low, probably due to wind that had disturbed the scatterers in the vegetation layer. Highest coherences were observed over some fields and forest clear-cuts. Due to the low overall coherence boreal forest was not well discriminated from open water.

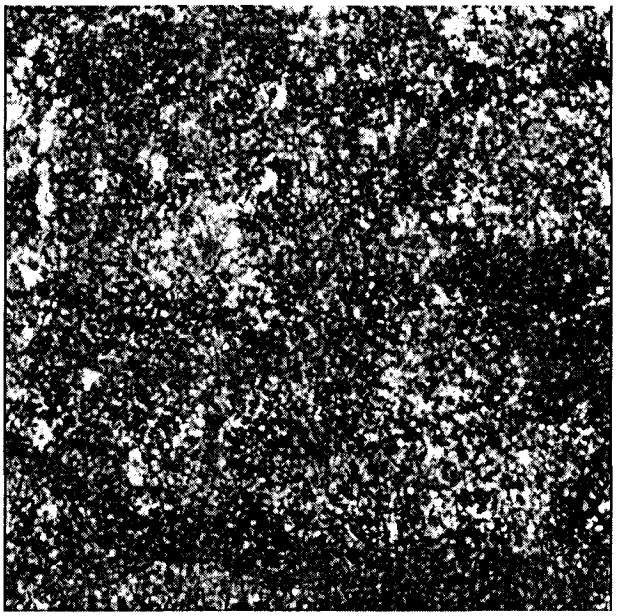

Figure 1a: Coherence of image pair 1

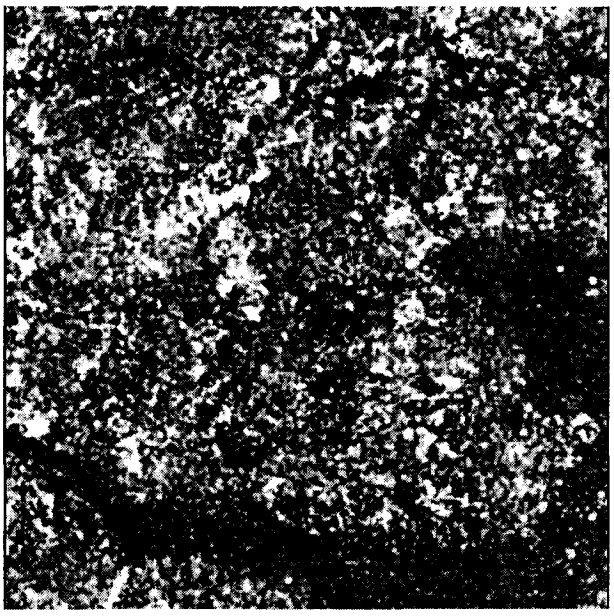

Figure 1b: Coherence of image pair 2

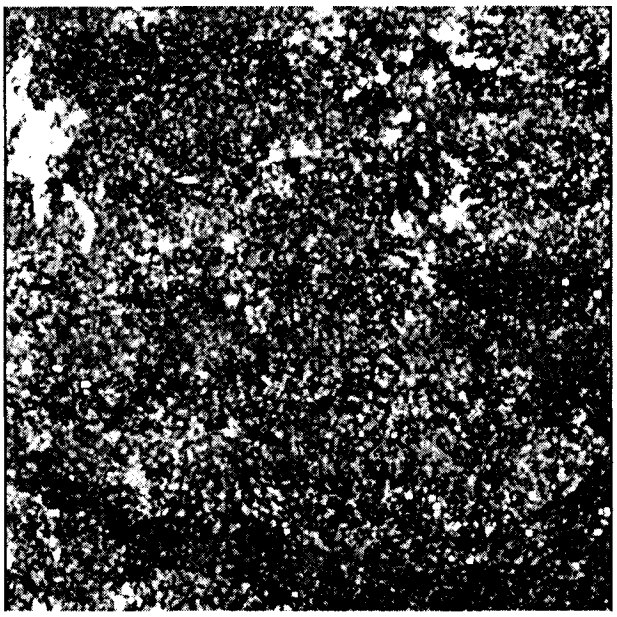

Figure 1c: Coherence of image pair 3

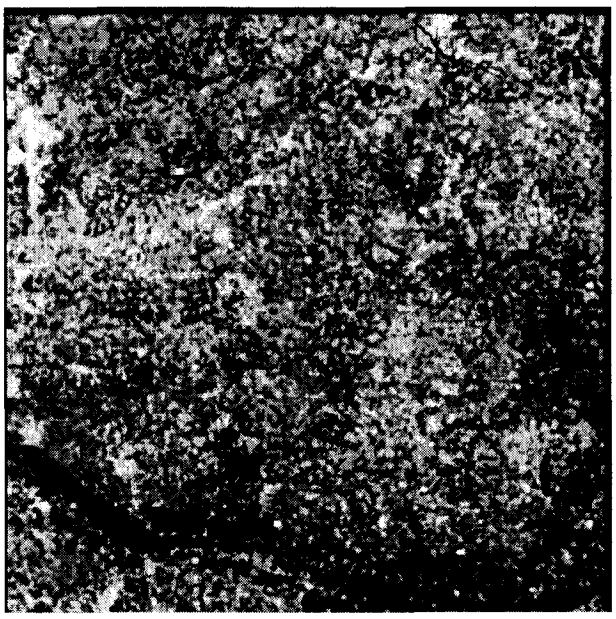

Figure 1d: Coherence of image pair 4

Coherence image 2 (Figure 1b):

Coherence image 2 is quite similar to the coherence image 1. Due to more favourable conditions the average scene coherence was higher. The highest observed coherences were in the same range as in coherence image 1. Some fields had larger coherence than in image 1, suggesting farming activity that had taken place after acquisition of image pair 1. Dense forest was visually discriminated from sparse forest.

Coherence image 3 (Figure 1c):

Due to windy conditions the coherence was low over most of the image. Coherences over some fields were significantly higher than over the rest of the image. It is reasonable to assume that in these areas the ground was almost completely vegetation-free due to recent farming activity.

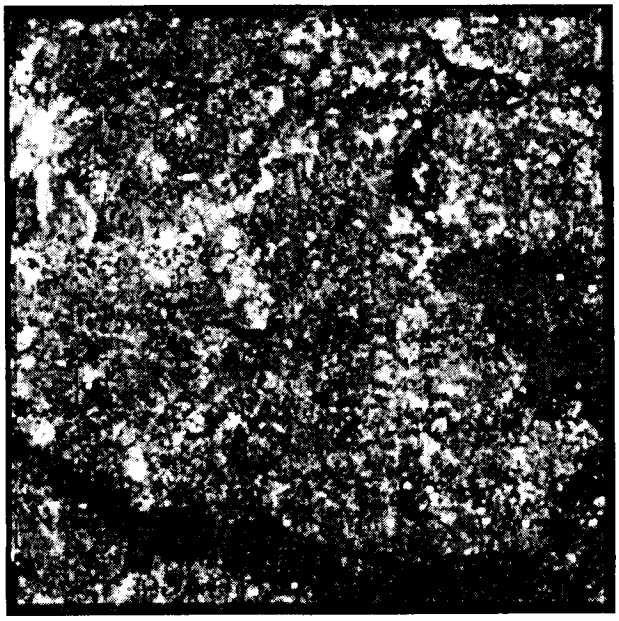

Figure 1e: Normalized coherence-sum of image pairs 1-4.

Coherence image 4 (Figure 1d):

This winter-time coherence image had by far the highest average coherence in our data set. This is because the ground was frozen and covered with snow, the lakes were partially covered with ice and the dedicuous trees had lost their leaves. Generally the coherence over forest was at least two times higher compared with the other coherence images. Coherence over fields and clear-cuts was also higher than in the other images, but to a lesser degree, thus reducing the contrast between them and the forest stands. Dense forest was visually discriminated from sparse forest. The generally high coherence reduced both the coherence estimation error and bias.

Normalized coherence-sum image (Figure 1e):

The normalized coherence-sum image was better suited for visual land-use classification than any of the coherence images alone. The image was in a good agreement with the SPOT Pan image and as expected, the coherence diminished with increasing biomass. The summing of a larger number of coherence images with high average coherences should improve the correlation between estimated coherence and biomass.

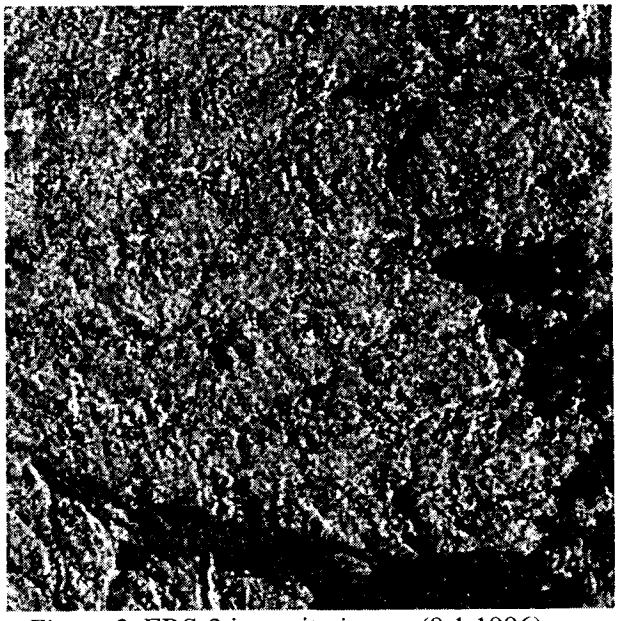

Figure 2: ERS-2 intensity image (9.1.1996).

8. CONCLUSIONS

The potential of ERS-1/2 Tandem interferometric coherence images for forest classification was studied. The following conclusions were made based on visual interpretation of coherence imagery:

- The coherence over boreal forests during winter is considerably higher than during other seasons. Therefore, ERS Tandem interferograms acquired during winter seem to be ideal for DEM generation over boreal forests.

- Forest may be discriminated from non-forest and higher average scene coherences imply better discrimination between forest types.
- Summation of several normalized coherence images produces images that are better suited for visual land-use and forest classification than a single coherence image.
- SAR interferometric coherence images provide complementary information to the SAR intensity images. This may observed by comparing the coherence images and the ERS-2 intensity image acquired 9.1.1996 (Figure 2).

9. ACKNOWLEDGEMENTS

The authors wish to thank Dr. Paolo Pasquali (Remote Sensing Laboratories, University of Zürich) for giving advice in the use of the ISAR software as well as Dr. Einar-Arne Herland (The Technical Research Centre of Finland) for handing out the code for ERS orbital propagation. The ERS-1/2 SLC images were provided by ESA as a part of the Tandem AO project AOT.SF301.

10. REFERENCES

[1] E.Tomppo, *Satellite image-based national forest inventory of Finland*, International Archives of Photogrammetry and Remote Sensing, vol.28, pp.419, 1991

[2] E.Tomppo et al., *Application of ERS-1 SAR data in large area forest inventory*, Proceedings of the Second ERS Applications Workshop, 6-8 December 1995, London UK.

[3] U.Wegmüller, *SAR Interferometric Signatures of Forest*, IEEE Transactions on Geoscience and Remote Sensing, vol.33, no.5, pp.1153, September 1995

[4] J.O.Hagberg, L.M.H.Ulander, J.Askne, *Repeat-Pass SAR Interferometry Over Forested Terrain*, IEEE Transactions on Geoscience and Remote Sensing, vol.33, no.2, pp.331, March 1995

[5] L.C.Graham, *Synthetic Interferometer Radar for Topographic Mapping*, Proceedings of the IEEE, vol.62, no.6, pp.763, June 1974

[6] M.Born, E.Wolf, *Principles of Optics*, 6th ed., New York: Pergamon, 1980

[7] P.B.G.Dammert, *Accuracy of INSAR Measurements in Forested Areas*, Proceedings of FRINGE 96 - ESA Workshop on Applications of ERS SAR Interferometry, Zürich Switzerland, 1996. Also at: http://www.geo.unizh.ch/rsl/fringe96/papers/dammert/

[8] H.A.Zebker, J.Villasenor, *Decorrelation in Interferometric Radar Echoes*, IEEE Transactions on Geoscience and Remote Sensing, vol.30, no.3, pp.560, May 1992

FOREST MAPPING IN TROPICAL REGION USING MULTITEMPORAL AND INTERFEROMETRIC ERS-1/2 DATA

Florence Ribbes, Thuy Le Toan, Jérôme Bruniquel, Nicolas Floury
CESBIO, 18 av. E. Belin, bpi 2801, Toulouse Cedex 4, FRANCE
Tel : +33 561 55 85 12 - Fax : +33 561 55 85 00 - e-mail : ribbes@cesbio.cnes.fr

Nicolas Stussi, Soo Chin Liew
CRISP, National University of Singapore, Lower Kent Ridge Road, Singapore 119260
Tel : +65 772 80 28 - Fax : +65 775 77 17 - e-mail : crsns@leonis.nus.sg

Upik Rosalina Wasrin
Forest Ecology and Mapping - SEAMO BIOTROP,
Jl Raya Tajur Km 6, PO Box 116, Bogor, Indonesia
Tel : +62-251 371 654 - Fax : +62-251 371 656 - e-mail : biotrop@indo.net.id

ABSTRACT

The paper presents a study to assess the use of ERS SAR data to map and monitor deforestation in Sumatra, a region characterized by rapid depletion of the rain forest, mainly due to logging and permanent or semi-permanent settling of transmigrated population.

Two approaches were used and compared (with reference to optical data) for forest / non forest mapping :
1- Temporal Change approach : in the frame of the TREES/ERS-1 SAR'94 project, previous studies have shown that up to a certain limit forested areas could be distinguished from non forested areas using the particularly stable temporal behavior of the backscatter values of the forest.
2- Interferometric approach : coherence images are realized from the interferometric pairs. Forest/non forest maps are realized based on the contrast between coherence of forest compared to that of the other land covers.

Both methodology have been applied over different test sites in Central Sumatra and South Sumatra. This paper presents the results obtained over one specific site : Kayuagung in Southern Sumatra which currently undergoes active deforestation.

1. INTRODUCTION

In Indonesia, the tropical rain forest is one of the major natural resources, covering about 60 % of the total area (110 MHa in 1990 [1]). Much of the existing forests have been destroyed, mainly by shifting cultivation, by logging and above all, by the increasing number of people involved in agricultural activities. Therefore the magnitude of deforestation and its consequence on natural processes need to be evaluated.

In such regions under frequent cloud cover, SAR data present optimal means for regular observations. With C band SAR data (ERS-1/2, RADARSAT) the backscatter intensity of tropical forest has stable value and the contrast between forest and other surfaces depends on the backscatter values of the non forested area, which are highly variable. Thus the use of a single SAR image is not relevant. One approach has been developed using the temporal variation of backscatter intensity to map forest covers [2]. Recently, interferometric information have been used for land cover classification [3] [4].

The aim of this paper is to assess and compare multitemporal intensity change and interferometric approaches.

2. TEST SITE AND DATA ACQUISITION

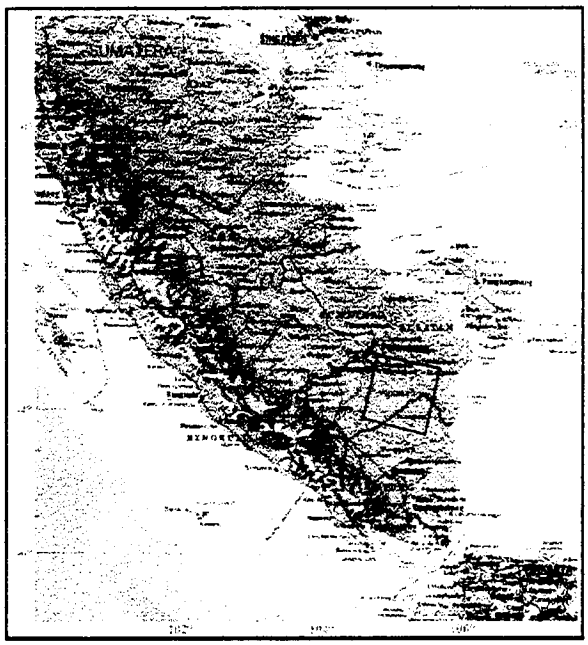

Fig. 1 : test sites

The site under study is situated in Indonesia in Sumatra island (fig. 1). It is located in South-Sumatra near the city of Kuayagung. It is a flat area with current active deforestation. Most of the primary forest of the area have been converted to secondary forest or plantation (mainly oil palm but also coconut or rubber). Moreover this site includes young tree plantations (oil palm) as well as short vegetation like shrubs mainly in swampy region.

Two ERS PRI data have been acquired in April and May 96 and one ERS-1/2 SLC pair in May 96. One SPOT HRV of May 96 was also available.

3. THE APPROACHES

The Temporal Change Approach

In this approach, the temporal change in backscatter intensity is considered.

At C-band, VV, 23°, the backscatter signal comes from the volume scattering from the foliage (leaf and stem) of the upper part of the canopy (a thickness not exceeding 4 to 5 m). The value of the backscatter depends on the distribution in size, orientation and density of the scatterers (mainly leaves). Rain forests correspond to value of -7/-8 dB, whereas temperate coniferous species have lower responses (-8/-9 dB). Oil palm and coconut can have higher responses (-5/-6 dB) due to their large leaves compared to the wavelength. Previous backscatter modeling studies on coniferous forests have shown that for a forest canopy of more than 50 tons by hectare, the backscatter reaches a stable value which also does not change significantly with time . For canopies less dense in terms of biomass (<50 t/ha), the radar signal results from both the tree backscatter and the underlying soil or undergrowth vegetation. The resulting value depends on the development of the canopy and the conditions of the underground layers which is strongly dependent on weather conditions. Thus, this category of canopy will have a temporal variation, especially between dry and wet seasons, mainly due to changes e.g. in soil moisture and underlying vegetation conditions.

For low canopies (crops), the backscatter results from the volume and surface scattering, leading to variable radar backscatter and variable temporal change.

In summary, for ERS-1 SAR, three categories of canopies can be distinguished. They are characterized by the radar backscatter values and their temporal change [2].

1) dense canopy - in terms of biomass (of an order of 50 t/ha) characterized by stable value of radar backscatter (except in mountainous areas) and small temporal change. This category includes closed primary forest, secondary forests and « older » tree plantations. Selective logging will not be distinguished, since the biomass will remain high. Different species of homogeneous tree stands (coconut, rubber, oil palms...) can be distinguished by their backscatter values resulting from the interaction of the wave with different tree structure, mainly size and shape of leaves.

2) less dense canopy (< 50 t/ha) characterized by small temporal change (± 2 dB and variable backscatter values). This category includes shrubs, thickets, logged over forests, young tree plantations.

3) low canopy characterized by highly variable radar backscatter and their temporal change (agriculture crops, clear-cut areas, young forest regrowth, new tree plantation...)

Other non temporally stable land covers include swamps, savannas and water bodies.

Urban areas appear particular with high backscatter values and no temporal variation

To distinguish forest from non forest it is necessary to have a maximum contrast between the temporal changes of forested and non forested area. This can be achieved if the delay between 2 ERS acquisitions is sufficient for significant changes in non forested areas. The optimum time interval depends on the seasonal and meteorological conditions. In most cases, the 1 day interval tandem acquisition or 3 days interval will not be sufficient. Optimal configuration would be a shortest possible interval between one acquisition during the dry season and one acquisition during the wet season.

The Interferometric Approach

In this approach, the module of the degree of coherence ρ, which is the correlation between two images acquired under slightly different geometrical configuration (fig. 3), is considered.

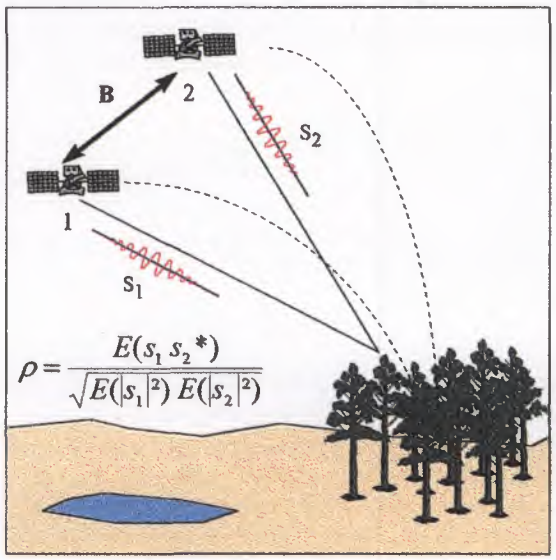

Fig. 2 : Basic principle of radar interferometry

The 2 main sources of decorrelation can be spatial or temporal decorrelation. The spatial decorrelation includes the difference in the geometry of observation between

the two acquisitions. The temporal decorrelation, which is the most important in the case of ERS-1/2 repeat pass interferometry can be due either to environmental effect (e.g. effect of wind on leaves or branches) or to vegetation growth.

In terms of degree of coherence, bare surfaces present a high degree of coherence, if they do not undergo any modification in their characteristics (geometry, dielectric, vegetation regrowth) between the two acquisitions. Volume scatterers such as leaves or branches are more sensitive to structure variations due to vegetation growth or wind effect. In the case of repeat-pass interferometry, these scatterers have a high probability to move between acquisitions. Thus the volume scattering from vegetation corresponds to a low degree of coherence. The degree of coherence, as a function of forest biomass has been analyzed in a previous study over the temperate Landes forest [5].
Fig. 3 presents the variations of the coherence versus stand biomass. High temporal coherence is obtained for clear cuts and open fields whereas it decreases with stand age.

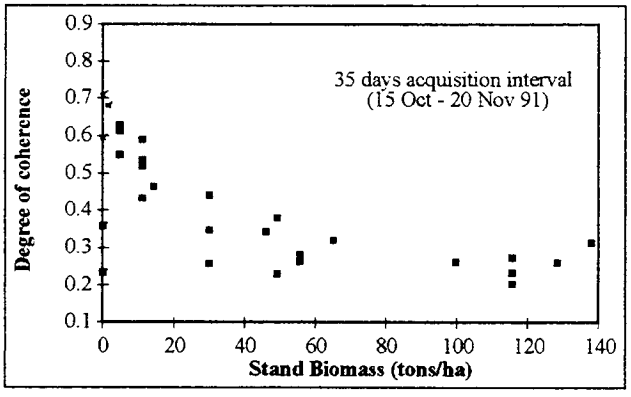

Fig. 3 : variation of the coherence *vs* stand biomass

The observations can be interpreted using the knowledge of the scattering mechanisms as follows. In the region where the soil contribution is dominant, the degree of coherence is high. On the other hand, the region where most of the backscatter comes from the volume contribution shows a low degree of coherence. In the intermediary region, the degree of coherence decreases with stands age/biomass, with a slope depending on soil/vegetation parameters. The optimum time interval is such that the contrast between the degree of coherence of forest and other surfaces could be maximized. The shortest time interval must be the best. However, depending on the study site and the seasonal, meteorological conditions, 35 days interval can provide good forest/non forest discrimination (e.g. fig. 3).

In tropical regions, the vegetation (crop, forest regrowth) growth is such that in 35 days the coherence over non forested area would be too low to be distinguished from the forested area [4]. For forest/non forest mapping the time interval should be defined so that the coherence of non forest areas remains high. Thus the shortest (1-3 days) repeat pass acquisition is more appropriate to use interferometric coherence.

3. METHODOLOGY

The Multitemporal Approach

The temporal variation of the SAR signal can be measured based on differences in the magnitude of the signal intensity between 2 dates.

Differencing and ratioing are well-known techniques for change detection. Ratioing of the multidate radar intensities is shown to be better adapted to the statistical characteristics of SAR data.

The ratio is in addition very robust to radiometric errors which are exactly reproduced in repeat-pass imagery. Those errors include the error in antenna pattern removal, and , more important, the error in the computation of the scattering element size, e.g. in sloping areas. Both errors are multiplicative factors to the total radar intensity, thus eliminated in the ratio image. Furthermore, the effect of hilly terrain which yields very important spatial variation of pixels, which is also a multiplicative effect, will also be eliminated.

However, the ratio is very sensitive to the speckle noise. To detect changes in radar intensity less than 1 dB with a confident interval better than 80 % the equivalent number of looks (ENL) must be more than 128 [6].

The forest/non forest mapping algorithm :

1. Speckle reduction filtering : in order to provide a sufficient equivalent number of looks, appropriate temporal and spatial filtering processes have been applied to the ERS-1 PRI 3 looks SAR data [7][8].

2. Temporal image ratioing : after filtering, the intensity values of two images will be divided, pixel by pixels.

3. Forest/non forest Map : as established with the experimental data, a threshold corresponding to a variation of less than 1dB will be used over the ratio image to map forested areas.

The Interferometric Approach

1. Coherence image creation : first a sub-pixel registration is realized on the phase , followed by the calculation of the phase and the coherence over a window of 2 pixels in range and 8 pixels in azimuth. Then, a projection in ground range projection and finally a resampling at 12.5m are realized

2. Forest/non forest Map : as established with the experimental data, a threshold corresponding to a coherence of less than 0.4 will be used over the coherence image to map forested areas.

4. RESULTS

Fig. 4a shows the SPOT HRV acquisition of May 1996. Dark area (e.g. area n°1) correspond to dense forest, green area (e.g. area n°2) to non forest, mainly young oil palm plantation, and light red area (e.g. area n°3) to mature oil palm plantation. Area n°4 shows an example of swampy-non forested area.

Fig. 4a : SPOT HRV image of May 1996
■ XS3 ■ XS2 ■ XS1

A ratio image have been realized with the 35 days interval SAR images, acquired in April 96 and May 96 (fig. 4b), whereas the coherence image have been calculated from the 1 day repeat pass images of 17 and 18 May 96 (fig. 4c).

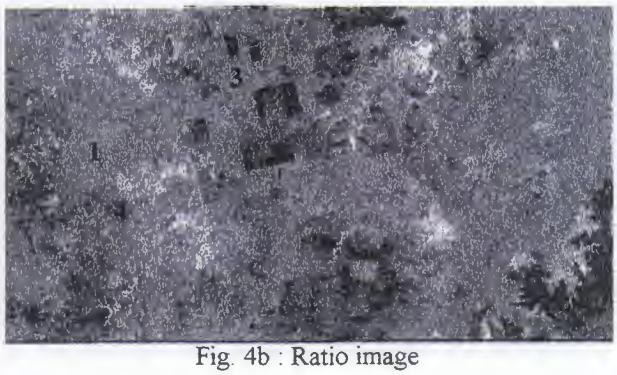

Fig. 4b : Ratio image

The resulting ratio image appears in gray tones. Areas with low temporal change have dark tones, whereas areas with a high temporal change present bright tones for a positive change ($\sigma°$ increasing between 2 acquisition) and black tones for negative temporal change ($\sigma°$ decreasing between the 2 acquisitions).

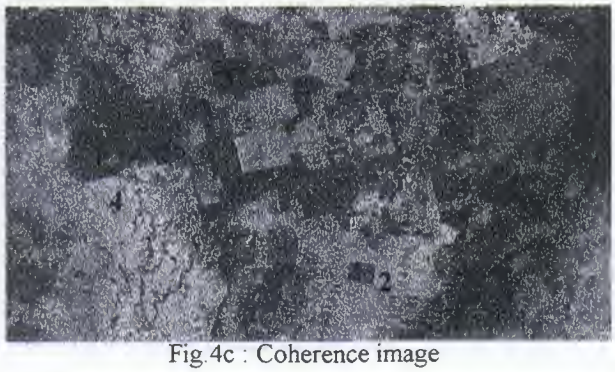

Fig.4c : Coherence image

On the resulting coherence image bright tones correspond to high coherence whereas dark tones correspond to low coherence.

Fig. 4d presents the ERS color composite image of April 96 (red), May 96 (green), and Ratio image (blue). Yellowish tones correspond to area with no temporal change whereas bluish and reddish to area with, respectively, positive and negative temporal change.

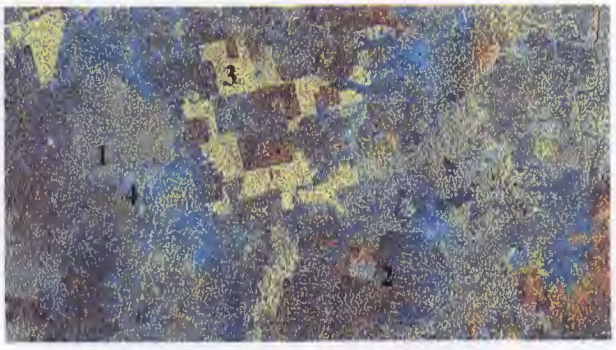

Fig.4d : Color Composite image
■ 13/04/96 ■ 18/05/96 ■ Ratio image

Fig. 4e presents the ERS color composite image of 17 May 96 (red), 18 may 96 (green) and coherence image (blue). Yellowish tones correspond to low coherence whereas bluish tones to high coherence area.

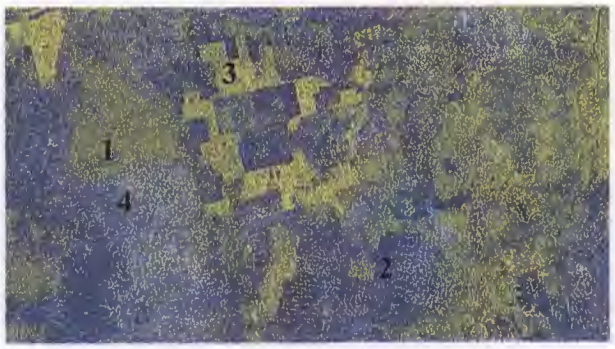

Fig.4e : Color Composite image
■ 17/05/96 ■ 18/05/96 ■ Ratio image

Area n°1 (dense forest) has a low temporal change and a low coherence. The backscattered intensity corresponds to a saturate value and the coherence, a lowest value, both not affected significantly by changes in ground conditions, since the forest backscatter results from volume contribution.

On the contrary, for area n°2 (young oil palm plantation) both temporal change and coherence are high because soil contribution is important.

For Area n°3 (mature oil palm plantation). The configuration is quite similar to the one of area n°2 (low temporal change and low coherence) because of no soil contribution. However the backscattered intensity of the mature oil palm plantation is higher than that of the forest, due, mainly, to their leaf size which are large

compared to the wavelength. This permits to distinguish them from dense forest.

Area n°4 presents a low temporal change but a clearly high coherence. This swampy area, which is non forest, would be considered as forest with the ratio approach and as non forest with interferometry, because the σ° has not changed between April and May 96 for most of the area.

This illustrates particularly well the problem of non optimum acquisition dates. April and May are situated in the same season (dry). Therefore, the moisture conditions remain the same for the 2 acquisitions as well as the sparse vegetation of this area.

A previous study has already been lead on this site with 2 images acquired in December 93 (wet season) and August 94 (dry season) [2]. Fig. 4f presents the ERS color composite image of August 94 (red), December 93 (green), and ratio image (blue). We can see that area n° 4 is no longer considered as forest because it has a high temporal change (bluish and reddish color).

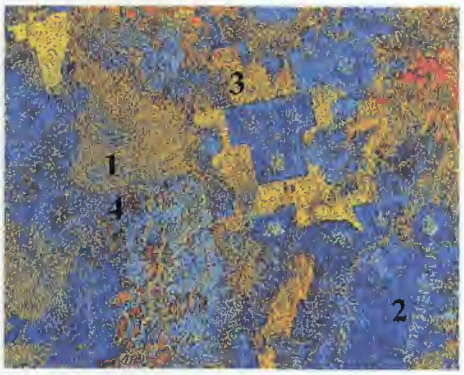

Fig. 4f : Color Composite Image
■ 05/08/94 ■ 01/12/93 ■ Ratio image

Fig. 4g and h present forest (green) / non forest (white) map using a simple thresholding of the ratio and of the coherence image.

The coherence gives more robust results for forest / non forest mapping (fig 4g and h) particularly for the swampy area.

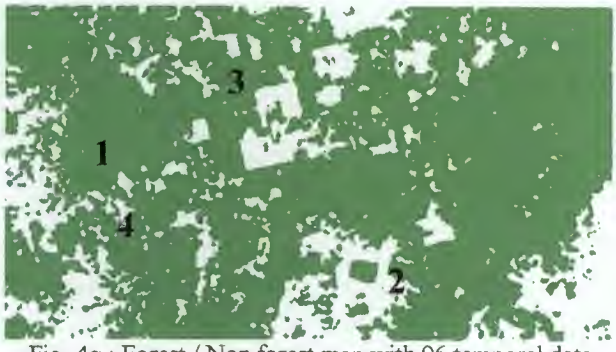

Fig. 4g : Forest / Non forest map with 96 temporal data

Fig 5 h : Forest / Non forest map with interferometric data

Fig. 4i presents the ratio image obtained from optimum acquisition dates. The mapping result is largely improved. Even areas of young oil palm plantation (area n° 2) are better delineated. This shows that the dates of acquisition are crucial for the temporal change method.

Fig 5i : Forest / Non forest map with 93/94 multitemporal data

For both methodology the use of intensity value for non mountainous area provide additional discriminations like forest / mature oil palm for example.

4. PRELIMINARY REMARKS

A comparison between Temporal Change approach and Interferometric approach have been assessed.

The criteria for forest / non forest discrimination are as follows :

For INSAR data forest classes are described by a coherence lower than 0.4. The optimum conditions are reached with a small temporal intervals as the results are more affected by changes of non forest conditions. If the delay between 2 acquisitions is too long the characteristics of non forested area will change and then their coherence will decrease, lowering the discrimination with forested area.

For ERS SAR intensity, dense forest classes area described by a temporal change lower than 1 dB. Optimum conditions are reached when using at least one dry and on wet seasons because the results are improved by the change of non forest conditions.

At C-band, the intensity of backscattered signal from bare soil surfaces depends on the soil parameters

(moisture, roughness). Consequently, bare soil surfaces can present a large range of responses. These possible variations of the soil responses may impede the forest / non-forest discrimination because of the possible confusion between some vegetated and non-vegetated areas. Therefore, optimum acquisition date are needed in the case of temporal change approach in order to improve the contrast between forested surfaces and non forested surfaces. On the contrary, the degree of coherence of a bare surface or surface with low vegetation cover is, in most cases, higher than the degree of coherence characterizing forested areas, and this independently of the soil moisture and roughness parameters.

Further investigations at various geograhical locations are needed to validate the results and to quantify the accuracy of both methodology in order to define thresholds to be used in most conditions.

REFERENCES

[1] J.P. Lanly, 1982. « Tropical forest resources ». FAO, Rome, 113 p.

[2] Le ToanT., Ribbes F., Floury N., Rosalina Wasrin U. , 1995. « Use of ERS-1 SAR Data for Forest Monitoring in South Sumatra ». Proceedings of the TREES ERS-1 94 final workshop, JRC, ISPRA, Italy, Feb. 1995.

[3] Wegmüller U., Werner C.L., Nuësch D., and Borgeaud M., 1995. « Land-surface analysis using ERS-1 SAR interferometry ». ESA Bulletin, n°.81, pp. 30-37, Feb. 1995.

[4] Stussi N., Kwoh L. K., Liew S. C., Singh K., Lim H., 1996. "ERS-1/2 Interferometry: Some Results on Tropical Forest", FRINGE 96, Zurich, Switzerland, September 1996.

[5] Floury N., Le Toan T., Souyris J.C., Singh K., Stussi N., Hsu C.C., Kong J.A., 1996. "Interferometry for Forest Studies", FRINGE 96, Zurich, Switzerland, September 1996.

[6] E.J.M. Rignot and J.J. Van Zyl, 1993. " Change detection techniques for ERS-1 SAR data ". IEEE Transactions on Geoscience and Remote sensing, Vol. 31, N° 4, pp. 896-906.

[7] J. Bruniquel and A. Lopes, 1994. « Analysis and enhancement of multi-temporal SAR data », SPIE/EUROPTO Symp., Rome, vol. 2315, pp. 342-353.

[8] A. Lopes, E. Nezry, R. Touzi, H. Laur, 1993. « Structure detection and statistical adaptative speckle filtering in SAR images ». International Journal of Remote Sensing, vol. 14, pp. 1735-1758.

FOREST MAPPING WITH ERS SAR INTERFEROMETRY

Tazio Strozzi and Urs Wegmüller

Gamma Remote Sensing, Thunstrasse 130
CH-3074 Muri b. Bern, Switzerland
Tel: +41 31 951 70 05, Fax: +41 31 951 70 08
email: gamma_rs@pingnet.ch

ABSTRACT

The geometric information contained in the interferometric phase and the potential of the interferometric correlation and of the two backscatter intensities of an interferometric pair for the classification of different surface types were combined in order to generate a forest map for a part of Switzerland. Forest was mapped based on its low interferometric correlation, low backscatter change between the two images of the interferometric pair, and backscattering intensities around -10 dB. The described approach was applied to several ERS-1/2 Tandem pairs allowing to discuss the dependence of the result on system and scene parameters, including seasonal and meteorological effects. As a result of the short one day acquisition interval (as compared to the 3 and more days with ERS-1, only) less confusion occurred between forest stands, on one side, and vegetation on agricultural fields or low correlation by farming activities, on the other side. This makes the approach with Tandem data more robust for application during spring, summer and fall. The resulting landuse maps were transformed into orthonormal coordinates using the estimated topographic heights and validated with data of the Swiss Federal Statistical Institute.

The potential of SAR interferometry for forest type discrimination was also investigated. For known forest stands the interferometric correlation was related to the forest type. A reliable separation for deciduous, mixed, and coniferous forest stands was possible only with winter Tandem pairs.

1. INTRODUCTION

Based on ERS-1 data acquired during 3-day repeat orbits a good potential of repeat-pass SAR interferometry for land applications such as landuse classification, forest mapping, and change detection was identified (Wegmüller et al., 1995a, 1995b, and 1997a). It was found that the interferometric correlation is not just a measure of the phase noise of the interferogram but a valuable source of information on scene properties. With the ERS-1/2 Tandem mission repeat-pass SAR data useful for interferometric analysis became widely available (Wegmüller and Werner, 1996). The 1-day acquisition time interval and the precise orbit control which allowed to almost permanently obtain short interferometric baselines for Tandem pairs resulted in data ideal for interferometry. In addition the 35-day repeat-orbits of the two satellites allowed to achieve nearly global coverage. With the available data interferometric techniques can now be extensively applied.

In this paper it will be shown that Tandem data are very useful for forest mapping of a part of Switzerland. The classification algorithm is based on the interferometric correlation, the two backscatter intensities of an interferometric pair, and the texture of the backscatter image. The dependence of the resulting maps on system and scene parameters, including seasonal and meteorological effects, will be discussed. The maps will be validated against available landuse inventory. Finally, the potential of SAR interferometry for forest type discrimination will be investigated.

2. INTERFEROMETRIC DATA PROCESSING

For the analysis of the interferometric signatures and for the forest mapping, the ERS SAR data were processed using Gamma's SAR and interferometric processing softwares (Wegmüller and Werner, 1997b). ERS SAR raw products were used. This has the advantage that data for full ERS frames are available. Another advantage is that by carrying out the SAR processing we have full control over this step. Data were processed to full resolution. The processing included radiometric calibration for the antenna gain and slant range distance. The resulting single look complex (SLC) images look well focused and allowed to produce interferograms of high quality.

Interferometric processing of complex SAR data combines two SLC images into an interferogram. In a first step the two images are co-registrated at sub-pixel accuracy. In the same step common band filtering of the azimuth and range spectra is applied in order to include only those parts of the spectra which are common to the two images, and thereby optimizing the interferometric correlation and minimizing the effects of the baseline geometry on the interferometric correlation. Then the two images are cross correlated, i.e. the normalized complex interferogram is computed. The azimuth and range phase trends expected for a flat Earth are then removed from the interferogram. From this "flattened" interferogram and the two registered intensity images, the multi-look interferometric correlation and backscatter intensities are estimated. In further steps the topographic height is computed. Knowing the

topographic heights allows to transform the images from SAR coordinates (slant range, azimuth) to orthonormal map coordinates. In addition, the true pixel size can be estimated and used to correct the normalization of the backscattering intensities and to avoid errors in the estimation of the interferometric correlation due to sloped terrain.

One of the main problems encountered when using SAR data for classification purposes is the strong signal noise or speckle of unfiltered SAR images. One way to solve this problem is to carry out a segmentation before estimating average signatures for the image segments. Here we did not follow this approach. The presented landuse classification scheme is based on the normalized interferogram and the two backscatter intensity images of the interferometric image pair. In a first step these data are used to estimate (1) the interferometric correlation, (2) the average backscatter intensity, (3) the backscatter intensity change, and (4) the texture of one of the backscatter images. For a wide applicability, the classification is made on a per pixel level. In order to obtain reliable values at the per pixel level appropriate estimators and filtering are required. A detailed discussion on the estimation of the parameters used for the classification is given in Wegmüller and Werner (1996). Here the main features regarding the interferometric correlation, the average backscatter intensity, the backscatter intensity change, and the texture are summarized.

The interferometric correlation is a measure of the phase noise of the interferogram. It depends on sensor parameters (wavelength, system noise, slant range resolution), parameters related to the imaging geometry (interferometric baseline, local incidence angle), and target parameters. Volume scattering and temporal change (i.e. random motion of the scatterers, change of the scatterers) decrease the interferometric correlation. The system and geometry dependent effects are pretty well understood and can be controlled by appropriate interferometric processing, as long as the system parameters are within a certain interval. The baseline dependence of the interferometric correlation, for example, may be eliminated in many cases by common spectral band filtering of the range spectrum. The estimation of the interferometric correlation requires a sufficient number of looks. As a compromise between maintaining a high spatial resolution and accurate estimation, an estimator with adaptive estimator window size was used.

In order to reduce speckle effects and obtain a backscatter intensity estimate at the pixel level which is representative for the ensemble average of the area around that pixel, the two registered SAR images of the interferometric pair are averaged. Minimum Mean Square Error filtering, as described by Frost et al. (1982), was then applied to the averaged image. Typically, the filter was applied to areas of 7x7 pixels of a 5-look image (5 azimuth looks).

The backscatter intensity change between the two images of the interferometric pair is defined as the absolute value of the ratio between the two images expressed in the logarithmic dB scale:

$$\text{change}[\text{dB}] = \left| 10 \cdot \log \frac{\langle i_2 \rangle}{\langle i_1 \rangle} \right| \quad (1)$$

Due to the speckle of the individual images it is essential to average sufficiently before the calculation of the ratio. Finally, the texture of the backscatter image is defined as the ratio between the standard deviation and the average of the backscatter intensity:

$$\text{texture} = \frac{\langle \text{stdev}(i_1) \rangle}{\langle i_1 \rangle} \quad (2)$$

Again, the estimation of the ensemble averages requires sufficiently large estimator windows. It turns out that extremely strong scatterers in an image have the unwanted effect that high texture is obtained over an area corresponding to the entire size of the estimator window. This effect can be avoided to some degree if the texture estimation is followed by filtering with a moving average filter of larger size than the texture estimator.

3. FOREST MAPPING

3.1. Classification Algorithm

Based on the interferometric signatures a simple landuse classification algorithm was developed. A hierarchical decision tree algorithm using the criteria listed in Table 1 was used to generate a landuse map. In order to account for the specific conditions under which the data was acquired the classification scheme was slightly adapted. Forest was mapped based on its low interferometric correlation, low backscatter change between the two image of the interferometric pair, and backscattering intensities around -10 dB. While forest and agricultural fields are difficult to distinguish in the backscatter image this is less difficult using the interferometric correlation. Water and forest, on the other hand, show both low interferometric correlation due to motion of the scatterers. Therefore, these categories are easier distinguished in the backscatter image.

3.2. Results

ERS-1 data acquired in November 1991 during 3-day repeat-orbits over a region around Bern (Switzerland) has previously been analyzed and used for forest mapping (Wegmüller and Werner, 1995b and 1997a). Here, these earlier results will be used for comparison purposes in order to assess the quality of the classification results achieved with ERS-1/2 Tandem data. The landuse classification of the November 1991 data is shown in Figure 1. The result was validated with a conventional forest map. An accuracy for the forest/non-forest classification of around 90% was reported by Wegmüller et al. (1997a). The November

1991 data were nearly ideal for the presented application because of the relatively short 3-day acquisition time interval, the short 58 m baseline, and the acquisition during the winter season when the forest can best be distinguished from agricultural fields because the fields are bare or only sparsely covered with vegetation.
The November 1991 data are compared with results achieved using Tandem data. The exact dates and baselines of the Tandem data are listed in Table 2. An RGB color composite of the interferometric correlation (red), the backscatter intensity (green), and the backscatter change (blue) for the November 1995 data is first shown in Figure 2. Forest appears in green because of the low interferometric correlation and backscattering change values and of the medium to high backscatter intensities. The landuse classification of the November 1995 Tandem data (Figure 3) confirm the expected usefulness of Tandem data for landuse classification. Unlike with 3-day repeat data the approach with Tandem data leads to reasonably good results during spring (e.g. Figure 4 for the April 1996 data) and summer (Figure 5 for the July 1995 data) period, too. The shorter acquisition time interval results in an increase of the interferometric correlation of fields with grass or crops, improving the potential to distinguish fields from forest. These examples allow to conclude that landuse classification based on interferometric signatures from ERS-1/2 Tandem data is feasible and has a high potential not only because of the quality of the results which may be achieved, but also because of the good spatial and temporal coverage with appropriate image pairs.

Table 1. Decision rules of landuse classification algorithm. The criteria are applied hierarchically, in the order as listed. The value ranges used are indicated for the interferometric correlation (γ), the average backscatter intensity of the two images ($<\sigma^\circ>$), the backscatter intensity change between the two images ($\Delta\sigma^\circ$), and the texture of the first backscatter image.

landuse class	γ	$<\sigma^\circ>$ [dB]	$\Delta\sigma^\circ$ [dB]	texture
urban	> 0.4	> -7.0	> 0.0	> 1.0
layover	< 0.2	> -2.0	< 2.0	
water	< 0.2	< -15.0	> 2.0	
geom. change	< 0.3		> 2.0	
dielectric change	> 0.3		> 2.0	
sparse vegetation	> 0.6		< 2.0	
med. vegetation	0.35-0.6		< 2.0	
forest	< 0.35	< -2.0	< 2.0	

Table 2: Dates, baseline and time difference Δt for interferometric data pairs used at the test site Bern (Switzerland).

Tandem pair	Sensors	Dates	Baseline [m]	Δt [days]
-	ERS-1 & ERS-1	24.11.91 & 27.11.91	58	3
1	ERS-1 & ERS-2	4.6.95 & 5.6.95	117	1
2	ERS-1 & ERS-2	9.7.95 & 10.7.95	27	1
3	ERS-1 & ERS-2	13.8.95 & 14.8.95	-46	1
4	ERS-1 & ERS-2	22.10.95 & 23.10.95	108	1
5	ERS-1 & ERS-2	26.11.95 & 27.11.95	138	1
6	ERS-1 & ERS-2	10.3.96 & 11.3.96	-9	1
7	ERS-1 & ERS-2	14.4.96 & 15.4.96	-93	1

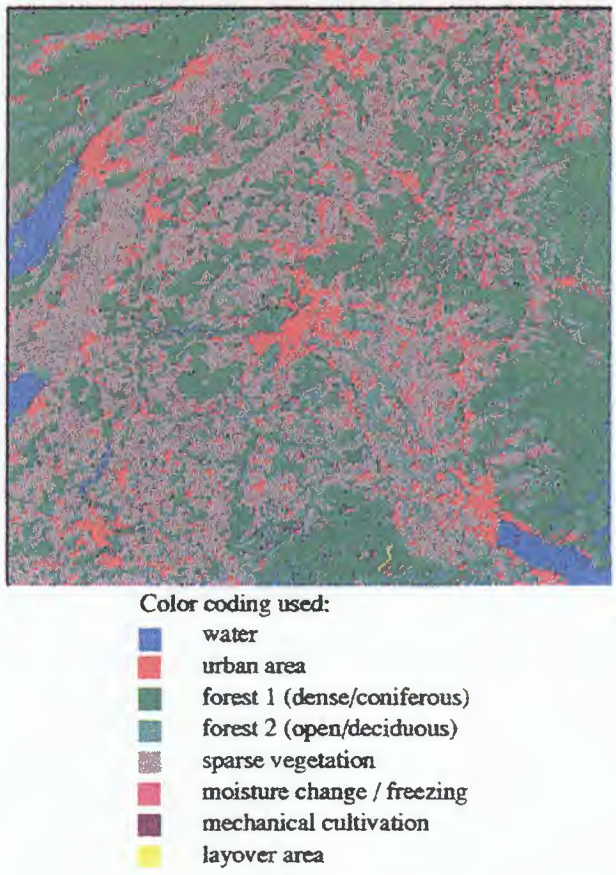

Figure 1. Landuse classification for the ERS-1 data of November 1991.

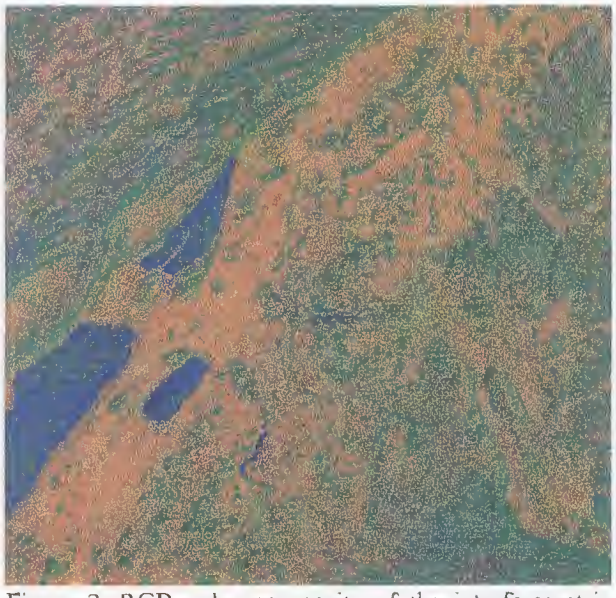

Figure 2. RGB color composite of the interferometric correlation (red), the backscatter intensity (green), and the backscatter change (blue) for the tandem pair 5 of November 1995.

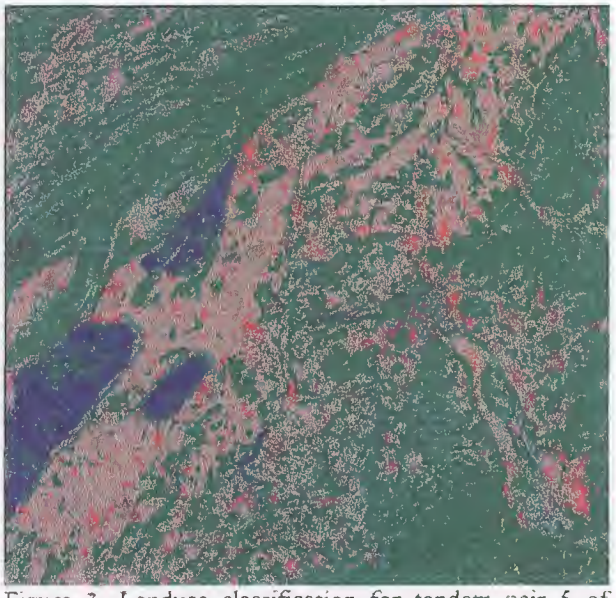

Figure 3. Landuse classification for tandem pair 5 of November 1995. For the color coding used see Figure 1.

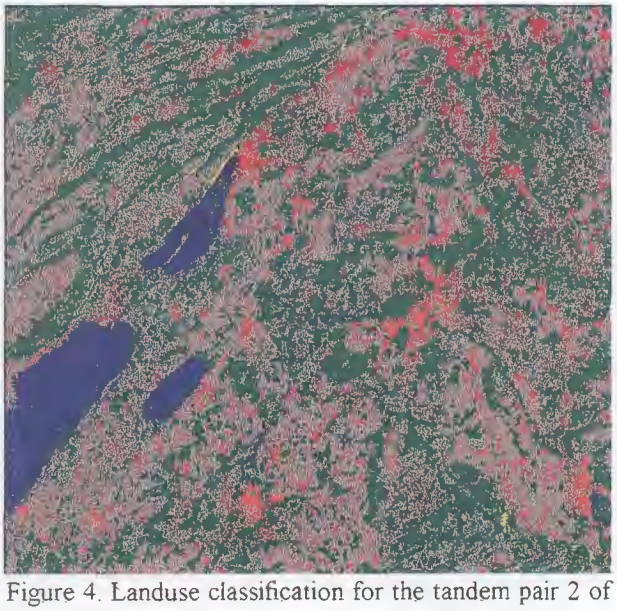

Figure 4. Landuse classification for the tandem pair 2 of July 1995. For the color coding used see Figure 1.

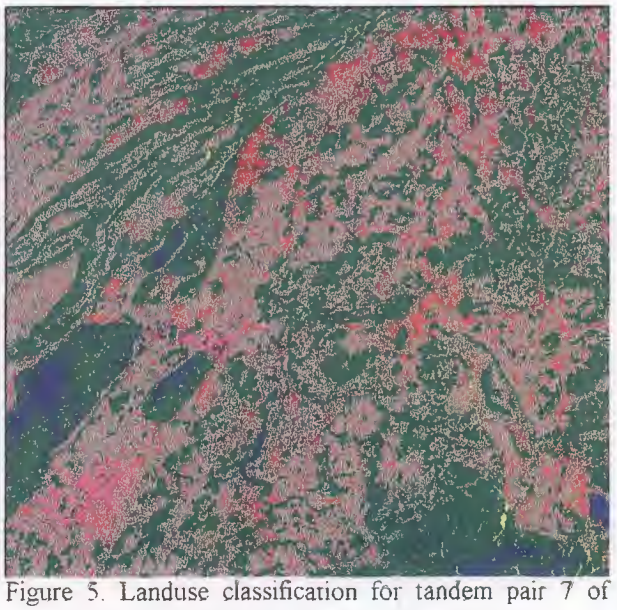

Figure 5. Landuse classification for tandem pair 7 of April 1996. For the color coding used see Figure 1.

3.3. Validation

For the November 1991 data the results were validated with a conventional forest map. An accuracy for the forest/non-forest classification of around 90% was reported by Wegmüller et al. 1997a.

Based on the landuse inventory of the Federal Statistical Institute the forest mapping accuracy achieved with the Tandem data was validated. The classification algorithm applied was adapted only very slightly to the different data sets by modifying the coherence interval between the data sets acquired during periods with leaves on the deciduous trees (coherence interval 0.05 to 0.3) and times with no leaves on the deciduous trees (coherence interval 0.05 to 0.45). This adaptation was necessary in order to account for the seasonally changing coherence observed for deciduous forest stands and agricultural fields. Apart from that, the decision intervals remained identical (texture < 1.2, backscatter ratio interval 0.5 to 2.0, backscatter intensity interval 0.02 to 0.2). The confusion matrices are listed in Table 3. The very rugged areas of the Jura, Napf and the Alps were excluded from the validation analysis. For flat to hilly terrain an overall classification accuracy between 0.79 and 0.89 was

found. These values are very satisfactory considering that the algorithm was not particularly tuned in order to achieve an optimum result. The high 0.79 classification accuracy found for the most critical data of July 1995 set is very promising. Based on a visual comparison of the RGB color composites, a classification accuracy higher than the 0.90 found previously for the November 1991 data may be expected for the more ideal data sets of the Tandem mission applying a tuned classification algorithm.

Table 3: Forest mapping accuracy obtained with the various Tandem pairs over the Bern test site.

Pair	forest class. as forest	forest class. as non-forest	non-forest class. as forest	non-forest class. as non-forest	overall class. accuracy
1	0.14	0.06	0.09	0.71	0.85
2	0.11	0.09	0.12	0.68	0.79
3	0.14	0.06	0.10	0.70	0.84
4	0.15	0.05	0.08	0.72	0.87
5	0.12	0.08	0.04	0.76	0.88
6	0.13	0.07	0.04	0.76	0.89
7	0.16	0.04	0.10	0.70	0.86

4. FOREST TYPE DISCRIMINATION

4.1. Application Description

Based on ERS-1 data acquired during 3-day repeat orbits a certain potential of repeat-pass SAR interferometry for forest type discrimination was found. Previous studies (Wegmüller and Werner, 1995b) have shown indications that higher interferometric correlation is observed over deciduous forest than over coniferous forest for data acquired in winter, when the deciduous forests are without leaves. These findings were further investigated using the multi-seasonal interferometric data of the ERS-1/2 Tandem mission. For 26 known forest stands the interferometric signatures were extracted and related to the forest type. Three classes of forest type were distinguished, i.e. deciduous, mixed, and coniferous forest stands. The results for backscatter intensity, backscatter ratio, and interferometric correlation extracted from the 7 Tandem pairs listed in Table 1 are shown in Figures 6 to 8, respectively.

Notice that the extracted signatures are mean signatures for an entire forest stand and that the investigation was restricted to segmented data, i.e. it is assumed that a segmentation is performed before the signature analysis or classification. In the Bern test-site most forest stands are in fact very small and heterogeneous and therefore not ideal for this remote sensing investigation.

Before the interpretation of the interferometric signatures some comments on the radiometric calibration have to be made The data were processed with our own SAR processor which includes radiometric calibration for the slant range distance and the antenna diagram. All filtering operations are designed in order to keep the image intensity unchanged. But in spite of that there is quite some uncertainty on the calibration of the data. First, we were informed by ESA on the data delivery that for the first two (or maybe three) ERS-2 data acquisitions something was different with the gain setting (commissioning phase). We tried to correct that but we do not know how well we succeeded. Second, the gains for ERS-1 and 2 are different. A comparison of the values of the Tandem pairs indicates that we did not use the best correction value. This also indicates that the difference may have changed. In conclusion, from the extracted backscatter intensities and ratios we conclude that a separation of the observed coniferous and deciduous forest stands does not seem to be possible.

The extracted interferometric correlation values (Figure 8), on the other hand, confirm the previous observation of higher correlation for deciduous forest stands than for coniferous forest stands during winter season or more precisely during the time when the deciduous trees are without leaves (see e.g. Tandem pairs 4, 5, 6 and 7). For the summer season (e.g. Tandem pairs 1, 2 and 3) this difference is not observed, with low interferometric correlations for all forest stands in spite of the short one day acquisition time interval. Based on these data it may be concluded that the distinction of deciduous, mixed, and coniferous forest stands based on different levels of the interferometric correlation is promising during the time when the deciduous trees are without leaves.

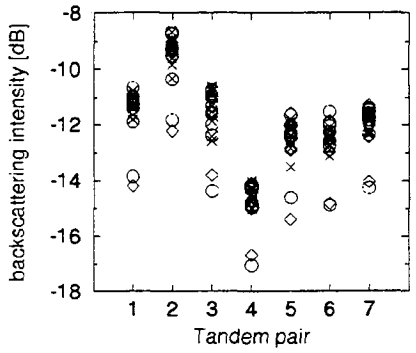

Figure 6. Backscattering of forest stands (ERS-1 images) versus Tandem pair.

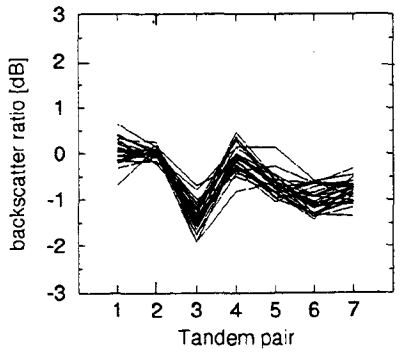

Figure 7. Ratio between ERS-1 and ERS-2 backscattering for forest stands versus Tandem pair.

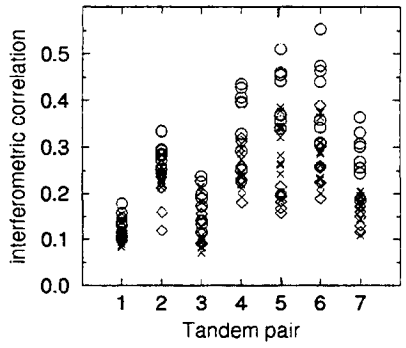

Figure 8: Coherence of forest stands for ERS-1/2 Tandem pairs. For the legend see Figure 6.

4.2. Algorithm Development and Validation

An algorithm was developed in order to classify different forest types. The forest types were distinguished based exclusively on the interferometric correlation, with the lowest interferometric correlation corresponding to coniferous forest, intermediate values to mixed forest and the highest values to deciduous forest. The exact thresholds used for the classification are listed in Table 4. The forest type discrimination results achieved with the winter Tandem pairs 4, 5, 6 and 7 for the selected 26 forest stands are listed in Table 4. A reliable separation for all three forest types was possible only with the November Tandem pair. For the other winter Tandem pairs only the two classes deciduous forest versus mixed and coniferous forest were distinguished. The achieved accuracy for the segmented data, i.e. for the test forest stands, is quite high. This is only true for the segmented data, a pixel based application of the classification with the same thresholds would lead to a much lower classification accuracy. Because of the influence of the interferometric baseline, meteorological conditions (affecting the motion of the trees), and the acquisition time interval, we did not try to develop a generally applicable forest type discrimination algorithm.

Table 4. Thresholds used for the classification of coniferous, mixed and deciduous forest, and overall classification accuracy.

Tandem Pair	Forest types classified	Coherence thresholds	Classification accuracy
4	deciduous coniferous & mixed	> 0.32 < 0.32	0.92
5	deciduous mixed coniferous	> 0.35 0.22 - 0.35 < 0.22	0.85
6	deciduous coniferous & mixed	> 0.32 < 0.32	0.81
7	deciduous coniferous & mixed	> 0.23 < 0.23	0.96

5. CONCLUSIONS

Based on the geometric information contained in the interferometric phase, on the interferometric correlation, on the two backscatter intensities of an interferometric pair, and on the texture of the backscatter image, forest maps for a part of Switzerland were generated. The maps were validated against available landuse inventory. ERS-1/2 Tandem data acquired during different seasons were analyzed. As a result of the short one day acquisition interval as compared to the 3 and more days with ERS-1 data only, the approach with Tandem data was applicable also during spring, summer and fall. During the winter season the most accurate results were obtained, because the forest can be best distinguished against agricultural fields, being the fields bare or only sparsely covered with vegetation. The distinction of deciduous, mixed, and coniferous forest stands based on different levels of the interferometric correlation for the Bern test-site was found to be promising during winter time using segmented data.

The classification algorithm used here was very general in order to allow adaptation to different test-sites, classes, seasons, and input data-sets. The key of the classification algorithm was a table with a list of lower and upper thresholds for each class and input parameter. In future work, the forest mapping and forest type discrimination algorithms should be applied to other test-sites. Boreal and tropical forest, for instance, as poorly mapped and difficult to access test-sites, represent very important ecosystems to be studied.

6. ACKNOWLEDGMENTS

This work was supported by ESA ESTEC under ESA/Contract 11740/95/NL/PB(SC) and by the Swiss Federal Office for Education and Science. ERS-1/2 raw data were provided under ESA-A02.JRC101. The Swiss Federal Statistical Institute is acknowledged for providing the digital landuse map "Arealstatisitk".

7. REFERENCES

Frost V.S., Stiles J.A., Shanmugan K.S., Holtzman J.C., 1982: A model for radar images and its application to adaptive digital filtering of multiplicative noise. *IEEE Pattern Analysis and Machine Intelligence*, 4(2), 157-165.

Wegmüller U., Werner C.L., Nüesch D., Borgeaud M., 1995a: Land-surface analysis using ERS-1 SAR interferometry. *ESA Bulletin*, 81, 30-37.

Wegmüller U., Werner C. L., 1995b: SAR interferometric signatures of forest. *IEEE Geosci. Remote Sensing*, 33(5), 1153-1161.

Wegmüller U., Werner C. L., 1996: Land applications using ERS-1/2 Tandem data. *FRINGE 96: ESA Workshop on Applications of ERS SAR Interferometry*. 30 September to 2 October, Remote Sensing Laboratories, University of Zurich, Switzerland.

Wegmüller U., Werner C.L., 1997a: Retrieval of vegetation parameters with SAR interferometry. *IEEE Geosci. Remote Sensing*, 35(1), 18-24.

Wegmüller U., Werner C. L., 1997b: Gamma SAR Processor and Interferometry Software. *3rd ERS Symposium*, Florence, 18-21 March.

MONITORING OF THE EFFECTS OF FIRE IN NORTH AMERICAN BOREAL FORESTS USING ERS SAR IMAGERY

E.S. Kasischke, N.H.F. French, and L.L. Bourgeau-Chavez

Earth Sciences Group, Environmental Research Institute of Michigan, Ann Arbor, MI USA
phone (313) 994-1200 -- *fax* (313) 994-5824 -- *email* ekas@erim.org

ABSTRACT

ERS SAR imagery collected over the boreal forest regions of North America (Alaska and Canada) have displayed a characteristic signature over regions which have recently been disturbed by fire. Studies have clearly shown that these signatures have a definite seasonal trend related to patterns of soil moisture originating from snow melt in the spring and precipitation during the growing season. At times, the fire-scar signatures are between 3 and 6 dB brighter than adjacent unburned forests. These signatures appear in all regions of the North American boreal forest, and remain visible for up to 13 years after a fire.

Keywords: fires, boreal forests, soil moisture, ERS SAR

INTRODUCTION

Fires in boreal forests disturb over 10 million ha/yr; thus they represent a major factor driving of CO_2 exchange between the atmosphere and terrestrial biome (Kasischke et al. 1995). Due to their large spatial extent and frequency, satellite remote sensor represent one of the only viable means to monitor the extent and effects of these fires (French et al. 1996a; Kasischke and French 1995).

Under the sponsorship of both NASA and ESA, investigations have been underway since 1992 to evaluate the utility of ERS SAR data to monitor boreal forests. Through these studies, we have demonstrated that: (1) ERS data can be used to monitor variations in above-ground biomass in black spruce forests (Harrell et al. 1995); (2) unique signatures associated with the effects of forest fires are present on ERS SAR imagery (Kasischke et al. 1992; 1994); (3) dominant factor responsible for these signatures is variation in soil moisture (French et al. 1996b); and (4) these signatures are persistent for at least 13 years after a fire, occur throughout the entire state of Alaska, and are present in areas covered by tundra (Bourgeau-Chavez et al. 1997). In addition to these published results, we have recently determined that these characteristic radar signatures are present in other forest types in North America and have begun to develop approaches to using the soil moisture information derived from ERS SAR data to monitor patterns of soil respiration and carbon dioxide flux from these forests.

This paper contains five sections, including this introduction. The next section of this paper illustrates fire-scar signatures which have been detected on ERS SAR imagery collected over Canada and Alaska. The following section illustrates the temporal variability exhibited throughout the growing season and presents evidence which shows these signatures are related to variations in soil moisture. The next section discusses why the ability of the ERS SAR to monitor variations in soil moisture is extremely important in monitoring carbon dynamics in the boreal forest. The final section summarizes the results.

FIRE-SCAR SIGNATURES ON ERS SAR IMAGERY

Figure 1 presents a pair of ERS SAR image mosaics collected during the summer of 1992 near the confluence of the Porcupine and Yukon Rivers in interior Alaska (Bourgeau-Chavez et al. 1997). This region experienced numerous recent forest fires which depict the bright image intensities present in the ERS SAR imagery. The boundaries of all recent fires in this region were obtained from the Alaska Fire Service and overlaid onto the ERS-1 images using GIS software. These images illustrate that: (1) there is a seasonal variation in the radar signature; (2) the boundaries of the fires match the areal extent of the radar signatures quite closely; and (3) fires up to 12 years in age are detectable. Figure 2 presents ERS SAR imagery collected over different boreal forest regions in Canada showing that the characteristic fire scar signatures observed in Alaska are not idiosyncratic to this region. These signatures were compared with fire boundary records maintained by the Canadian Forest Service, and in all cases they closely correspond to recent forest fires.

SEASONAL VARIABILITY AND THE CAUSES OF FIRE SCAR SIGNATURES

Figure 3 presents a set of ERS SAR images collected over three different fire scars in the Tanana River Valley of Alaska. These scars resulted from fires in 1987, 1990, and 1994 in forests between Delta Junction and Tok, Alaska. Studies of data from these and other sites show that the radar image intensities are brightest in the early spring immediately after the melting of the winter snow pack. The image brightness decreases during the growing

season as soil moisture decreases, but also increases immediately after significant precipitation events.

Beginning in 1992, a field campaign was carried out to monitor soil moisture in the Tok site, which burned in 1990. Figure 4 presents data from these studies clearly showing a strong correlation between radar image intensity and soil moisture (French et al. 1996b). Field studies to monitor soil moisture in the other two sites presented in Figure 3 were initiated during the summer of 1996.

The increases in vegetation cover through regrowth after fire would affect the ERS signature in two ways. First, the increases in woody plant biomass would result in an increase in radar backscatter (Harrell et al. 1995). Second, the increase in biomass would also serve to attenuate the radar backscatter signature originating from the soil surface. Since forest regrowth is extremely slow in these forests, increases in biomass do not contribute greatly to the radar signature. For example, measurements collected at the Tok site in 1995 showed that living vegetation levels ranged between 15 and 100 grams per square meter. It is more likely that increases in vegetation will mask the soil moisture signature. This may, in fact, be the reason for the less bright signature observed in the 1987 fire scar.

USING ERS SAR DATA TO IMPROVE ESTIMATE OF CO_2 FLUXES FROM BOREAL FORESTS

The organic soils of boreal forests represent one of the largest terrestrial pools of carbon (Kasischke et al. 1995). The cycling of carbon in this pool is controlled mainly by soil temperature and moisture. Both of these factors change significantly after a fire, leading to significant increases in soil respiration and an overall net loss of carbon to the atmosphere.

The patterns of soil respiration leading to biogenic emissions of carbon dioxide are largely controlled by three factors: (1) the amount of organic matter present in the soil; (2) soil temperature; and (3) soil moisture. Total soil respiration, R, (g $CO_2 \cdot m^{-2} \cdot h^{-1}$) is calculated after (Schlentner and Van Cleve, 1985) as

$$R = \frac{M}{(a_1 + M)} \frac{a_2}{(a_2 + M)} a_3 \, a_4^{(T-10)/10}$$

where M is the average forest floor moisture content (percent by dry weight), T is the soil temperature (°C) at a depth of 15 cm, a_1 is the percent soil water at half-field capacity, a_2 is percent water at half retentive capacity, a_3 is the theoretically optimal respiration rate at 10° C, and a_4 is the temperature Q_{10} value.

Efforts are currently underway to collect field and laboratory measurements of carbon dioxide emissions from the three Alaskan test sites illustrated in Figure 3. These field measurements will be used to calibrate the soil respiration equation. Estimates of CO_2 emissions will be derived using seasonal/spatial variations in soil moisture derived from ERS SAR imagery and soil temperature data derived from AVHRR and ATSR data.

SUMMARY

Our studies have clearly demonstrated that ERS SAR imagery represents a unique tool to monitor the effects of fires in boreal regions. Not only do fires in these forests result in clear, unambiguous signatures on the ERS radar imagery, but the cause of these signatures (variations in soil moisture) is an extremely important parameter in studies of a key ecological process in this biome: soil respiration. Due to this relationship, ERS SAR data are critical to monitoring the carbon cycle in boreal forests.

ACKNOWLEDGEMENTS

The research reported in this paper was supported through funding provided by NASA through grants NAGW-2645 to ERIM and NAGW-2692 to Duke, and by EPA through award number CR 823077-01-0 to ERIM. Although this research was supported by EPA, it has not been subject to agency review and therefore does not necessarily reflect the view of the agency and no official endorsement should be inferred. Finally, ERS imagery over the Canadian test sites was provided by ESA through experiment AO2. USA135. The continuing support of ESA in providing access to ERS data has been a great benefit throughout the 5 years this study has been ongoing.

REFERENCES

Bourgeau-Chavez, L.L, *et al.*, 1997
The detection and mapping of Alaskan wildfires using a spaceborne imaging radar system, *Int. J. Rem. Sens.*, **18,** pp. 355-373.

French, N.H.F., *et al.*, 1996a
Using multi-sensor satellite data to monitor carbon flux in Alaskan boreal forests, *Biomass Burning and Climate Change*, ed. by J.L. Levine, MIT Press, Cambridge, MA.

French, N.H.F., *et al.*, 1996b
Monitoring variations in soil moisture on fire disturbed sites in Alaska using ERS-1 SAR imagery. *Int. J. Remote Sens.* **17**, pp. 3037-3053.

Harrell, P., *et al.*, 1995
Sensitivity of ERS-1 and JERS-1 radar data to biomass and stand structure in Alaskan boreal forest, *Remote Sens. Environ.*, **54**, pp. 247-260.

Kasischke, E.S., and French, N.H.F., 1995
Locating and estimating the areal extent of wildfires in Alaskan boreal forests using multiple season AVHRR NDVI composite data, *Remote Sens. Environ.*, **51**, pp. 263-275.

Kasischke, E.S., *et al.*, 1992
Initial observations on the use of SAR imagery to monitor wildfires in boreal forests, *Int. J. Rem. Sens.*, **13**, pp. 3495-3501.

Kasischke, E.S., *et al.*, 1994
Observations of variations in ERS-1 SAR image intensity associated with forest fires in Alaska. *IEEE Trans. GRS*, **32**, pp. 206-210.

Kasischke, E.S., *et al.*, 1995
Fire, Global warming and the mass balance of carbon in boreal forests, *Ecol. Appl.* **5**, pp. 437-451.

Schlentner, R.E. and K. Van Cleve., 1985
Relationships between CO_2 evolution from soil, substrate temperature, and substrate moisture in four mature forest types in interior Alaska. *Can. J. For. Res.* **15**, pp. 97-106.

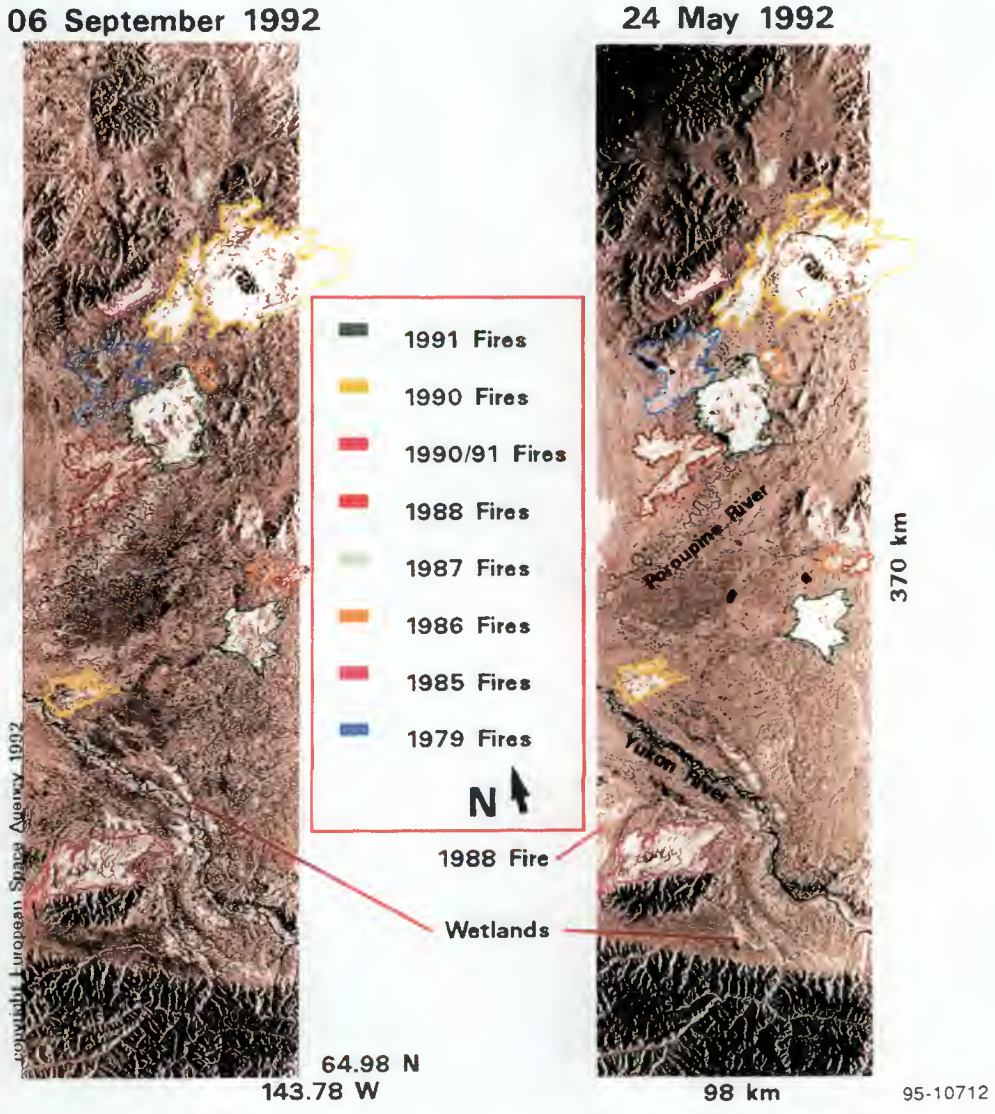

Figure 1. ERS-1 SAR Observations of Fire Scars in May and September of 1992 over the Tanana and Porcupine River Valleys, Alaska

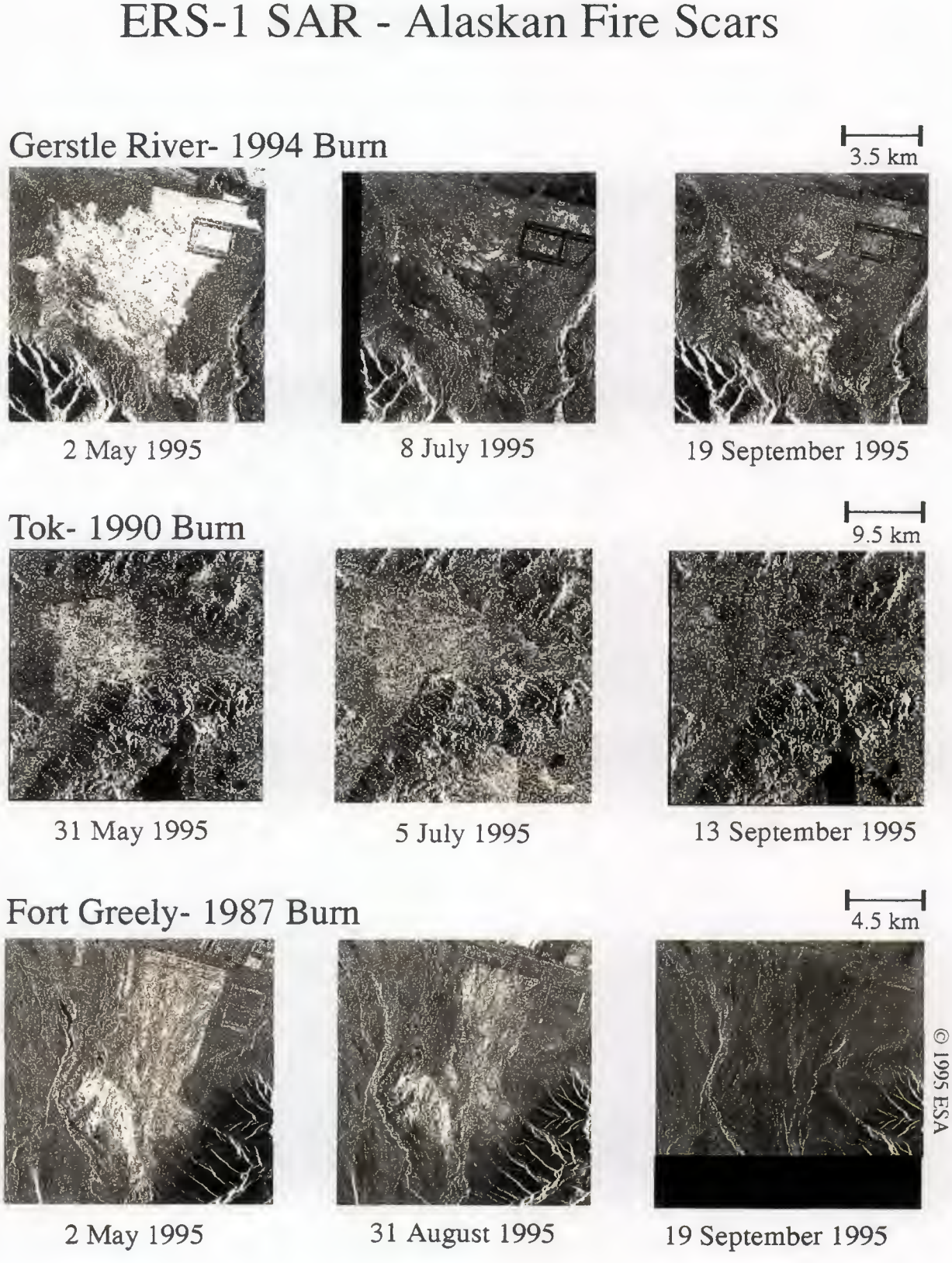

Figure 2. Seasonal Variation in Radar Image Intensities for Different Aged Fire Scars in Interior Alaska

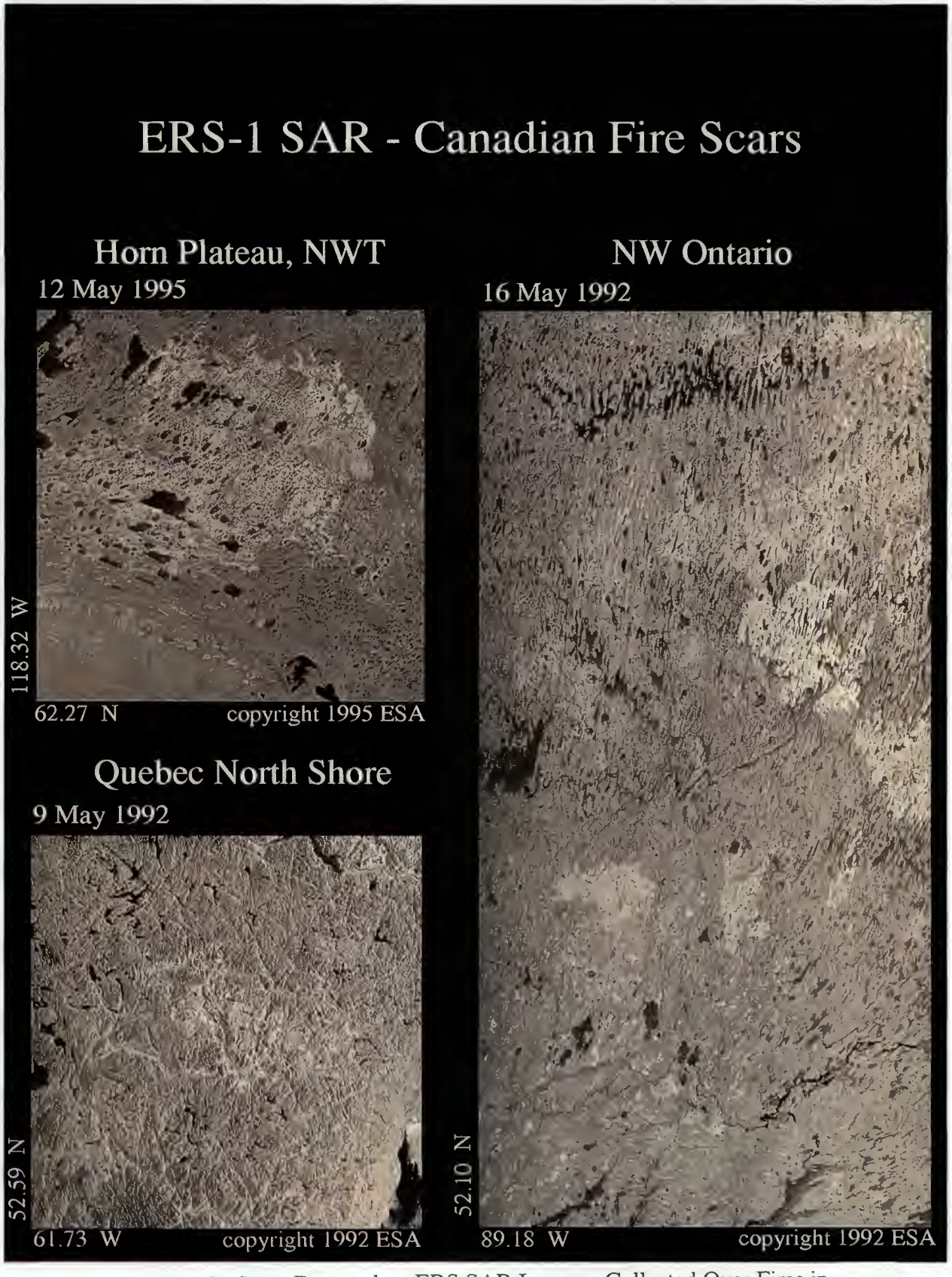

Figure 3. Scars Detected on ERS SAR Imagery Collected Over Fires in Canadian Boreal Forests

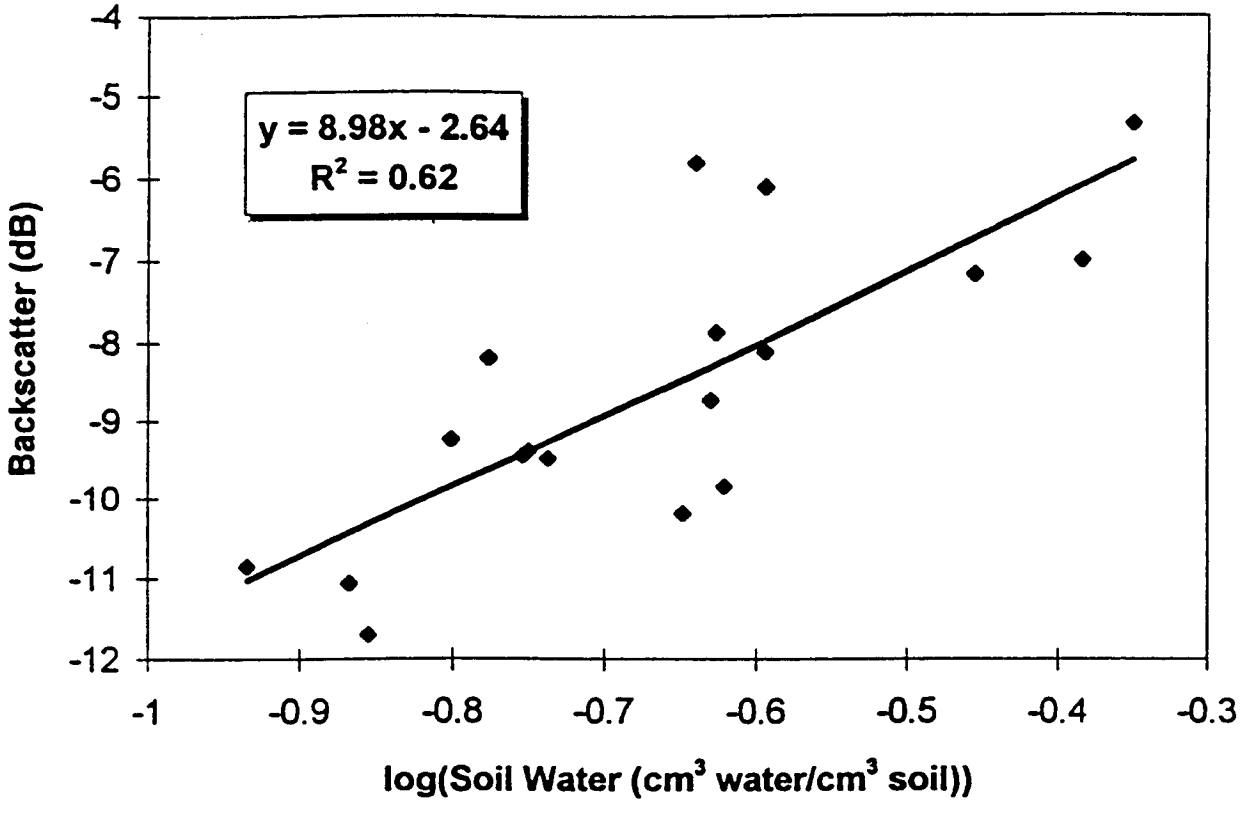

Figure 4. The Relationship Between Soil Moisture and ERS SAR Backscatter in a Fire-Disturbed Alaskan Boreal Forest

SYNERGISTIC USE OF ERS-1/SAR AND OTHER SATELLITE DATA FOR THE POLLUTED AREAS IDENTIFICATION FOR BOREAL FORESTS OF ST. PETERSBURG REGION

Donchenko V.V., Goltsova N.I., Bobylev L.P.

Nansen International Environmental and Remote Sensing Centre
Korpusnaya Str. 18, 197110 St. Petersburg, Russia
phone: +7 812 235 74 93, fax: +7 812 230 79 94
E-mail: nansen@sovam.com

Johannessen O.M.

Nansen Environmental and Remote Sensing Centre
Edvard Griegsvei 3a, N-5037 Solheimsvik, Bergen, Norway
phone: +47 55 29 72 88, fax: +47 55 20 00 50
E-mail: ola.johannessen@nrsc.no

Kritsuk S.G., Pitulko V.M.

Scientific Research Centre for Ecological Safety, Russian Academy of Sciences
Korpusnaya Str. 18, 197110 St. Petersburg, Russia
phone: +7 812 230 78 36, fax: +7 812 235 43 61

ABSTRACT

This study is dedicated to development of the interpretation basis for analysis of satellite remote sensing data in terms of indicators characterizing the ecological situation and the degree of the anthropogenic pollution of ground ecosystems. For this purpose ERS/SAR images were used together with Landsat/MSS and NOAA/AVHRR data as well as the data of ground measurements of the spectral brightness of the components of pine biocenoses and the results of studies of the moss chemistry and bioindicators. The ERS/SAR images enabled one to assess the distribution of the forested areas, to classify the forests, a combination of the ERS/SAR, Landsat/MSS and NOAA/AVHRR images obtained in different time has made it possible to trace the dynamics of changes in the forested ecosystems. The statistical structure of the samples has been studied, major factors of the variability of the complex variables such as NDVI and night temperatures have been revealed, which are most significant connected with the indicators reflecting the state of the forests. The interpretation algorithms allowed establishing correlation between the spectral features of images and the data of reference ground observances for a region with a stressed ecological situation.

1. INTRODUCTION

The most important element of the monitoring programs is the complex monitoring of forests which combines both the bioindicative and instrumental investigation techniques and has a well developed methodical basis in the form of international programs. The requirements of promptitude, field of vision, and objectivity are best met through combining the multispectral satellite survey and a network of fixed ground stations. At present an experience has been gained in interpreting the results of satellite survey to assess the distribution of pathological changes in the conifers. There are reliable reference data for the south-western areas of the Leningrad province (Slantsy - Kingisepp - Luga Bay).

The remote sensing derived Landuse information enables one to characterize the landscape basis of an ecological maps on which the proper ecological information will be imposed either in the form of initial spectral data or in the form of their transformations (e.g. NDVI), or as a complex parameter of load. The satellite imagery of a high resolution makes it possible to reliably identify the non-forested areas [Ref. 3]. In case of the forested areas one can differentiate the forest fund territory between homogeneous forest-tax formations by prevailing types, age and thickness. The reliability of decoding of the prevailing types reaches 65-80%, the error of age of trees determination - 1 class, thickness of planting - 10-15%.

Pollution of the forested territories biota of the Leningrad province has been monitored for five years by the Scientific Research Centre for Ecological Safety and Nansen Centres in St.Petersburg and Bergen (within the ICP-Forests program) over the 32×32-km grid. For the territory of the Kingisepp and Slantsy districts a grid of 16×16 km was formed and two sites of intensive monitoring were organized. Methods of sampling, defoliation assessment, lichenoindication as well as methods of chemical analysis have been intercalibrated with the countries of Europe. The coordinates of each site are in the UN EEC data base.

2. OBJECTIVES OF THE STUDY

Overall objective is the development of approaches to synergistic use of satellite remote sensing data in different spectral ranges for the assessment of

Proc. 3rd ERS Symp. on Space at the service of our Environment, *Florence, Italy, 17–21 March 1997* (ESA SP-414, 3 Vols., May 1997)

ecological situation in the study area.

Besides, one can mark out some specific objectives:
• Creation of the landscape basis of the ecological map making use of the Landuse classification of the complex of satellite data (ERS, Landsat, NOAA) with the allocation of the reliable boundaries of the proper forested territories, including the areas of the pine trees distribution.
• Study of the spectral characteristics of the pine biocenoses.
• Identification of the factors of aerotechnogenic oppression.
• Study of the dynamics of the anthropogenic change in the forest ecosystems. Assessment of the state of forests in the region.

3. TEST AREA AND DATA DESCRIPTION

3.1. Test area characteristics

This study has been accomplished for the area with the hard ecological situation (Fig 1) which is located at the Russia - Estonia boundary. Here the main sources of pollution are the energetic enterprizes of Estonia, the mining enterprizes of Narva, Slantsy, Kingisepp, and others. This zone is characterized by very high emissions of sulphur which cause serious damages to the forest ecosystems. The content of sulphur and calcium in pine-needles is much higher than

Figure 1. Territory under the study.
• - sampling points; * - sources of pollution

anywhere in toxicants is apparent not only due to huge amounts of emissions but also due to the meteo-synoptic situation.

3.2. Data used in the study

Results of field observations interpret well the area's territory by the net of test sites. Nevertheless, there is no complete spatial picture of the area on the whole, the biotic condition of its difficult-to-access sites and territories not included in the plans of previous field studies. To obtain a complete picture, an attempt has been undertaken to use satellite data.

A. In-situ (field measurements) data

Observations at the test sites are made using the ICP-Forests international techniques with the help of the intercalibration methods of data collection and analysis. The study has been focused on the indicators which can affect the spectral characteristic of pine trees - defoliation, discolouration, the longevity of pine-needles, the amount of indicative types of lichen-epiphytes, the content of heavy metals and other toxicants in soil humus and in forest mosses, a number of forest-tax parameters determining the density of forest canopy (diameters of the trunk and crown, valuation parameters, plant thickness, etc.). Changes in the pine trees' defoliation in 1995 over the investigated territory are shown in Fig. 2.

In addition to above mentioned ground measurements have been taken of the spectral brightness of the prevailing plants of the pine biocenoses.

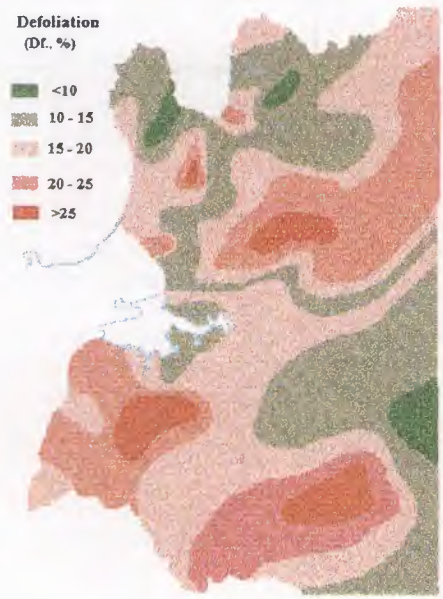

Figure 2. Changes in the pine trees' defoliation in 1995 over the territory of the Kingisepp area of the Leningrad province, from the data by N.I. Goltsova.

B. Remote sensing data

The following satellite remote sensing data have been used in the study:
- ERS-1/SAR as of 13 March, 1993; 18 March, 1994; 20 August, 1994; 13 and 29 September, 1994; 16 and 25 March, 1995; 15 and 31 August, 1995;

- NOAA/AVHRR as of 8 October, 1991; 2 and 3 June, 1992, and 15 August, 1994;
- Landsat/MSS as of 29 April, 1989 and 12 September, 1993.

4. TECHNIQUES DESCRIPTION

4.1. Initial processing of digital satellite data

To provide a comparability of the in-situ data with remote sensing data the geometric correction of the latter is carried out. To take into account the conditions of SAR scanning, the corresponding data were reduced to one level of the reflected signal by extracting the second-order trend drawn from the image lines (by the X-coordinate).

Retrieval of the surface temperature was carried out from the NOAA/AVHRR data of thermal channels 4 and 5 making use of the technique described in [Ref. 1]. The atmospheric correction was made using the standard model of the atmosphere.

The vegetation index was calculated making use of the band-difference technique described in [Ref. 2], for the NOAA/AVHRR from data of channels 1 (visible range) and 2 (near-IR range), and for Landsat/MSS from data of channels 2 and 4.

Upon correlating the coordinate system of ground observations and the geometric correction of satellite data for the area of observation points (~300 m in diameter), mean values of the following parameters were estimated:
- daytime thermodynamical surface temperature (near 03:00 p.m.) - Day T;
- nighttime thermodynamical surface temperature (near 04:00 a.m.) - Night T;
- vegetation index - NDVI;
- surface albedo - ALB;
- image brightness from the data of NOAA/AVHRR, ERS-1/SAR and Landsat/MSS.

These parameters supplemented the initial data matrix of ground survey (78 sites). Besides, over a greater area of observation points (~500 m in diameter), variations of these parameters were assessed.

After the water mask had been imposed, the factor analysis of images was made for several groups of images, which showed that the "forest-field" factor is the main factor of variability (not less than 50%). The correlation with the data of ground observations was studied for two sets:
- for the whole totality of the data available;
- for the sampled points located deep in the forests (the sampling was based both on the topographic material and on the Landsat/MSS and ERS-1/SAR data).

4.2. Elimination of non-forest areas

Despite the difficulties mentioned above, an analysis of space images makes it possible to identify the forests damaged by air pollution. However, the accuracy of pollution estimates and determination of the type of prevailing pollutants depends much on the accuracy of the contouring of the forested areas, since changes in the spectral characteristics of the surface caused by natural and anthropogenic stresses to vegetation, depend directly not only on the intensity of stresses but also on the type of the surface assessed. Therefore the targets should be thoroughly selected, especially within the areas with decreased spectral indices. It is these areas that include the sites of forests aerotechnogenically oppressed, which are, finally, an object of monitoring.

The algorithm to contour the forest areas includes the folowing two procedures:
- contouring of the urbanized territories, mining workings, agricultural fields and meadows;
- contouring of the area of marches in the remaining territories (mainly the forested ones) with differently weakened trees under the influence of natural factors.

The first procedure is accomplished most efficiently making use of the remote sensing data (Landsat, ERS-1/SAR, NOAA). The result of the forested areas allocation making use of the Landsat (Band 4) and ERS-1/SAR composite is shown in Fig. 3. One can easily identify the urbanized territories, the coniferous and broad-leaved forests.

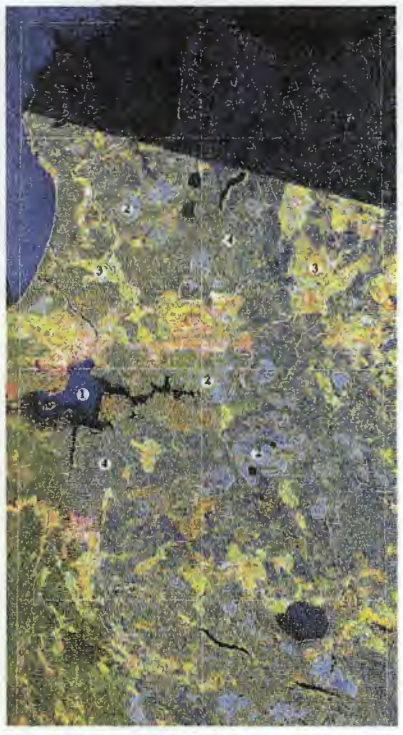

Figure 3. Allocation of the forested areas making use of the Landsat (Band 4) and ERS-1/SAR composite.
1 - water surfaces, 2 - marshes, 3 - agriculture fields, 4 - forested areas.

The second procedure is accomplished for any season from the data of SAR images as well as for spring - from the distribution of nocturnal surface temperatures, clearly reduced over the marshed areas from

NOAA/AVHRR data. The example of allocation of the marshed areas from the distribution of nocturnal surface temperatures is given in Fig. 4. In this case the territories largely covered with marshes are still cold and contrast with a warmer background of the remaining lands.

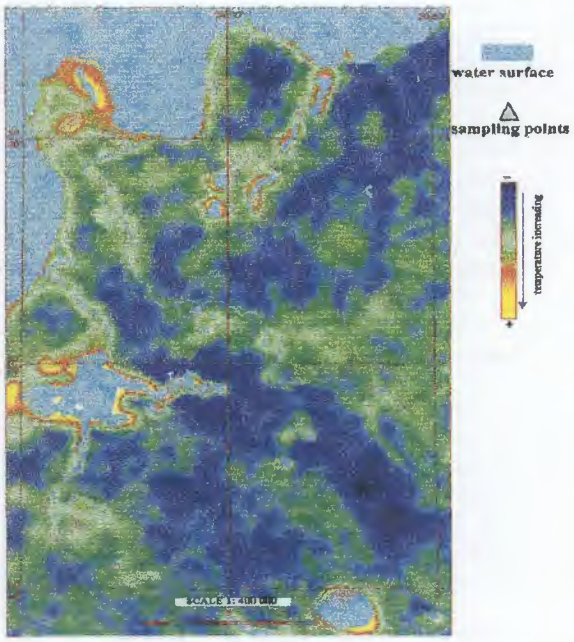

Figure 4. Allocation of the marshed areas from the distribution of nocturnal surface temperatures.

4.3. Statistical techniques

The factor analysis of the distribution of the spectral channels' intensity and the values of the spectral indices as a function of natural manifestations, which cause an oppression of the forest ecosystems, has shown that the main contribution to the variability of the studied sample is made by 3-4 parameters whose variations describe up to 95% of total dispersion. The variability of the data of all the scanners used is determined by the combination of the forested and non-forested lands (52-56%), the seasonal phases of vegetation (16-19%), and the marshed areas (8-9%). Hence, in this case the Landuse classification of the forests, agricultural and urbanized lands, and the marshes for each phase of vegetation separately is the necessary and sufficient basis of the ecological maps.

With the use of the STATGRAPHICS-3.0 software the statistic structure of the sets has been studied as well as the main factors of the variability of the complex variables (such as NDVI and Night T) have been determined which are most significantly connected with the indicators reflecting the condition of the forests (in particular, with the content of Ca in mosses, pine defoliation, etc.)

5. RESULTS

5.1. Correlation between spectral features of space images of forests and reference ground observations

Defoliation and discolouration of pine trees lead to a decrease of reflection coefficient in all spectral ranges, and with an intensive anthropogenic forcing - mainly in the near-IR range. The reflection coefficients in spectral channels 0.3-0.63 mkm (No 1), 0.63-0.8 mkm (No 2), 0.8-1.0 mkm (No 3), 1.0-1.75 mkm (No 4) for the prevailing plants of pine biocenoses at a different stage of the aerotechnogenic oppression have been used as a learning material for the interpretation of the space data (Fig. 5). For that purpose the Field Impulse Photometer (1993, Vavilov State Optical Institute, St.Petersburg, Russia) was used. The mean spectral characteristic of the pine trees has been calculated with the use of the weight coefficients of the contribution of each plant community to the reflectivity of the entire canopy of the trees.

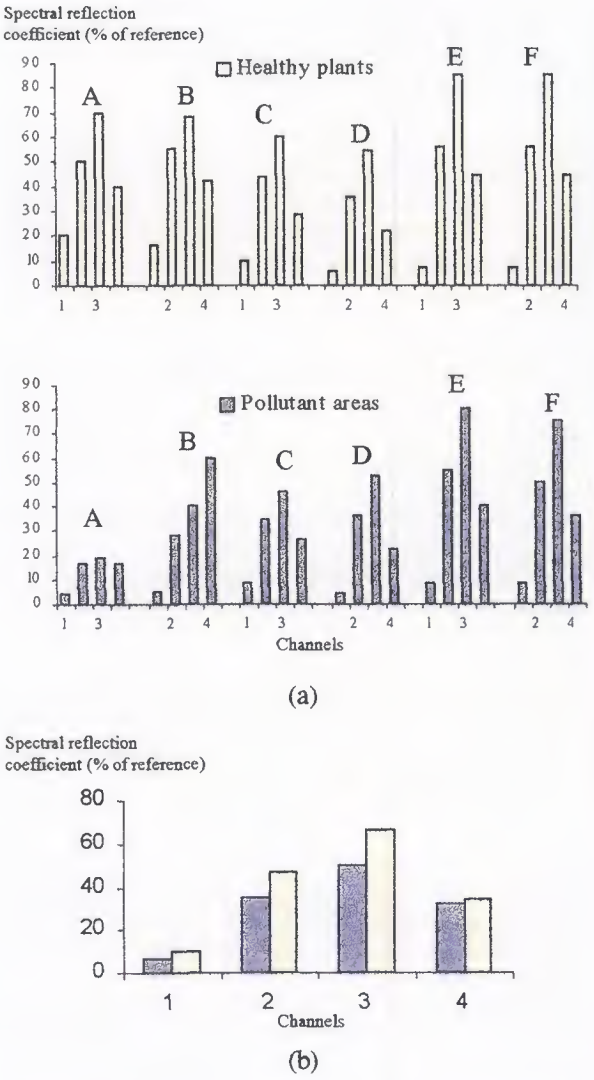

Figure 5. (a) Reflection coefficients for the prevailing plants of pine biocenoses: A - moss, B - pine (bark), C - pine (needles), D - spruce (needles), E - deciduous undergrowth, F - soil cover, (b) average reflection spectra for canopy with account of the contribution of each plant. Channels: 0.3-0.63 mkm (1), 0.63-0.8 mkm (2), 0.8-1.0 mkm (3), 1.0-1.75 mkm (4)

From average reflection spectra it is seen that differences between oppressed and healthy trees exist in every spectral range studied. There is a general decrease of spectral brightness: in channel 1 - by 30%, in channel 2 - by 25%, in channel 3 - by 26%, and in channel 4 - by 5%, which can be explained by a sharp decrease of pigmentation as a result of irreversible physiological changes with the dust-gas pollution of the vegetation cover. These dependences substantiate the information content of simple spectral indices (in particular, signal difference, simple ratios of signals from different channels, etc.).

Results of assessment of the state of forests in the investigated territory from the data of multispectral space survey (NOAA/AVHRR, 2 June 1992, NDVI change) are given in Fig. 6. In the Kingisepp district about 1050 km^2 of forests have a vegetation index below the norm, in the Slantsy district - about 600 km^2.

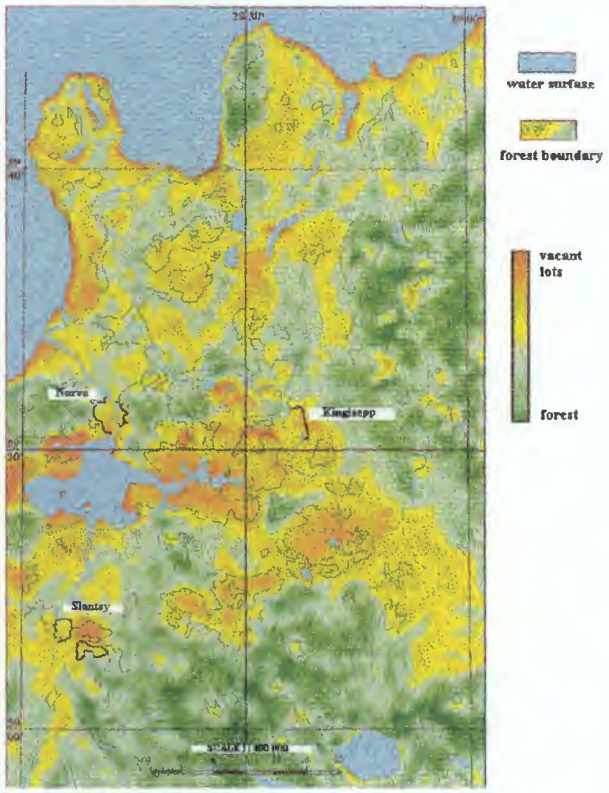

Figure 6. The vegetation index distribution.

5.2. Algorithm for identification of air pollution of the forests

For the reliably identified forests a comparison was made of healthy trees (high NDVI) and the trees weakened by air pollution. The study was completed by establishing connections and relationships between the parameters obtained by the multispectral space systems and the factors inducing the stress to the plants. The rank correlation between the distribution of some toxicants in the investigated domains and the bioindicators can be seen in Table 1.

Analysis of the covariance matrix distribution shows that the description of anomalies of heavy metals in soils, defoliation of pine trees as well as the vegetation index more closely correlate in spring, whereas changes in the values of spectral brightness for Landsat channels 2, 3 and 4 agree well with those of defoliation in the fall, there being observed an inverse dependence of spectral brightness on the pine-needles' lifetime. The impact of seasonal conditions on the statistical stability of correlations between the ground and remotely obtained data testifies to the fact that the monitoring of pine-trees of the boreal zone is more efficient in the early vegetation period.

Table 1.The rank correlation between the distribution of some toxicants and the bioindicators.

Domain toxicant,	Defoliation of the whole crown	Discolouration of the whole crown	Longevity of needles	Lichenoindication	NDVI
Mosses:					
Pb	+	+	-	+	(+)
Zn	+	-	+	-	(+)
S	+	+	+	+	+
Ca	+	-	(+)	+	++
Fe	+	-	+	(+)	-
Humus:					
Pb	+	-	-	+	(+)
Zn	+	+	+	-	-
S	+	+	++	+	(+)
Soils:					
Ca	++	++	++	++	++
S	++	+++	++	+	(+)
Fe	+	+	+	+	-
Pb	+	+	-	+	(+)
Zn	+	+	+	+	(+)
Defoliation	xxx	-	+	+	++
Discolouration	-	xxx	+	++	+
Longevity of needles	+	+	xxx	+	+
Lichenoindication	+	++	+	xxx	++
NDVI	++	+	+	++	xxx

+ consistent changes; - lack of consistent changes; ++ close consistency ; (+) unstable consistency.

The statistical structure of total set (78 stations, 16 parameters of soil, 16 parameters of mosses, 1 indicator of the density of total deposits, 4 bioindicators, 6 forest-tax characteristics, 18 remote indicators) can be informatively interpreted with the use of the correlation analysis, but without its sorting by the types of soils the meaningful correlations are established only at a 95% confidence level, and the value of partial coefficients of correlation, as a rule, exceed negligibly 0.25-0.3, which suggests nevertheless the existence of a number of basic dependences between the remotely sensed and ground data showed in Table 2.

The statistical structure of the sorted set of the points characterizing the proper forest domains differs much from total set. First of all, the correlation sharply grows between the variables (the correlation coefficients exceed 0.60 at a 99% confidence level), which makes it possible to retrieve the fields of distribution of the pollutants. For example, in Fig. 7 one can see the

dependence between some parameters determined from remote sensing data on the one hand and S and Ca concentration in soil and moss as well as the range of discolouration of pine needles on the other hand.

Table 2. Main suggested dependencies between in-situ and remote sensing data (total set)

In-situ data	Remote sensing
characrteristic of tree stand:	
crown density	SAR signal, all the channels of Landsat and NOAA/AVHRR, Day T
height and diameter of trees	Landsat channels 2, 3, 4; Day T
age of trees	Night T, all the channels of Landsat
defoliation and discoloura tion	Day T, NDVI (NOAA and Landsat)
pollution of mosses:	
total density of deposits	Day T, NDVI (Landsat)
pollution of the humus horizon:	
Al, Ca, Fe, K, Mg, V	NDVI (Landsat)
Ca, Cu, Fe, Pb, V	Day T

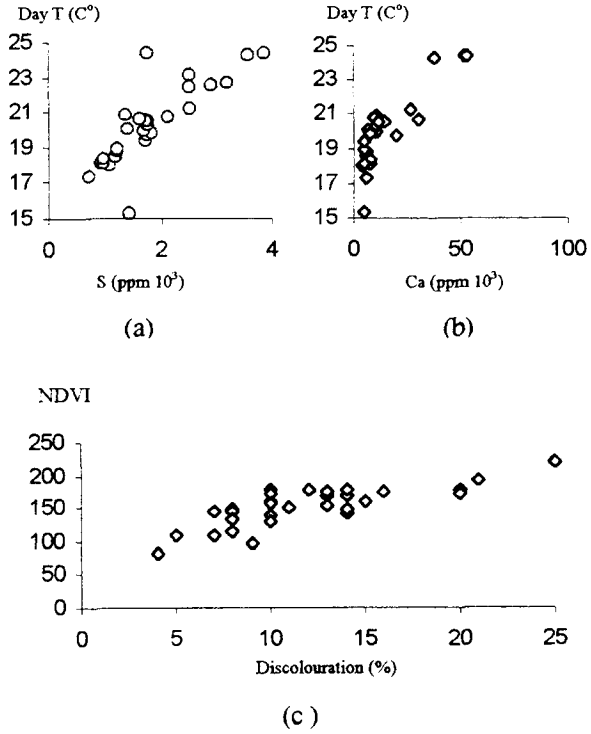

Figure 7. Dependence of (a) daytime temperatures on the content of sulphur in soils, (b) daytime temperatures on the content of calcium in mosses, (c) vegetation index on the degree of pine-needles' discolouration.

An interpretation of the statistical structure of the "forest" set can be studied more reliably, moreover, with a markedly broadened possibility of identification of the indicators of the state of pine biocenoses. The corresponding dependences between in-situ and remote sensing data are shown in Table 3.

Thus, the principal possibility has been shown to identify the density and composition of air deposits from the remotely sensed data. It should be noted that it is based on the fact that the presence of high concentrations of heavy metals and other toxicants either in soils or in deposits is manifested through the physiological and morphological changes in plants. The stress of biocenoses is expressed through cutting the biomass increase, pigmentation weakening and increase of the vegetation cover roughness.

Table 3. Main suggested dependencies between in-situ and remote sensing data (sorted "forest" set)
(r - correlation coefficient).

In-situ data	Remote sensing data
characteristic of tree stand:	
crown density	SAR signal (r = - 0.67), all the channels of Landsat and NOAA/AVHRR,Day T
height and diameter of trees	Landsat channels 2, 3 4, Day T
age of trees	NDVI Landsat, SAR (r = 0.76)
defoliation and disco louration	Day T, NDVI (NOAA and Landsat)
lichen-epiophytes	NDVI (NOAA and Landsat)
pollution of mosses:	
total density of deposits	Landsat (channels 3 and 4, r = 0.45)
Ba, Cd, Ca, Mg, S	AVHRR (channel 1, r = 0.5)
Zn	Albedo (r = 0.51)
Ba, Ca, Cu, Mg, S, Zn	NDVI (NOAA); Ba, Mg, S and Zn being meaningfully connected with NDVI at a 99% level, r = 0.5-0.6
Al, Cr, Fe, Pb	Landsat (channels 3 and 4, r = 0.45)
pollution of the humus horizon (weaker but as before statistically meaningful correlations r = 0.3)	
K, Mg	NDVI (Landsat and NOAA)
Ca, Cu, Fe, Pb	Day T, Night T, all the channels of Landsat and NOAA

5.3. Demonstration of dependence between vegetation index and Hg concentration in forest moss

As a first attempt to visualize the general distribution of healthy trees and the forests subjected to the aerotechnogenic oppression of different intensity, a comparison was made of the maps of vegetation index (NOAA/AVHRR) and Hg in forest mosses. The distribution of Hg in forest mosses over the investigated territory is shown in Fig.8. Imposing of the scheme of the distribution of Hg in mosses and distribution of weakened trees (Figs.2, 6) shows that the forests with a decreased NDVI are located within the zone of the Hg-marked emissions.

A comparison of data by the composition of indicative types of lichen on the pine trunks and by the pine-needles' longevity reveals the similar-to-space-image regularity of the distribution of the areas with the weakened forests (in these zones the pine-needles' longevity is shorter and the composition of lichen is reduced from five resistant to oxides species to their total disappearance).

Similar fields of distribution have concentrations of total Zn, Pb, Fe, S and exchange forms of Zn, Mn, Cd, S in the humus horizon of soils, as well as total amounts of Fe, Ca, Zn and S in forest mosses. The high atmospheric loading with dust and sulphur oxides, the high content of toxic heavy metals (zink, cadmium) both as exchange forms in soils and deposited on forest

moss has led during several decades to thinning of the forested ares, which is seen on the space image (see Fig.6).

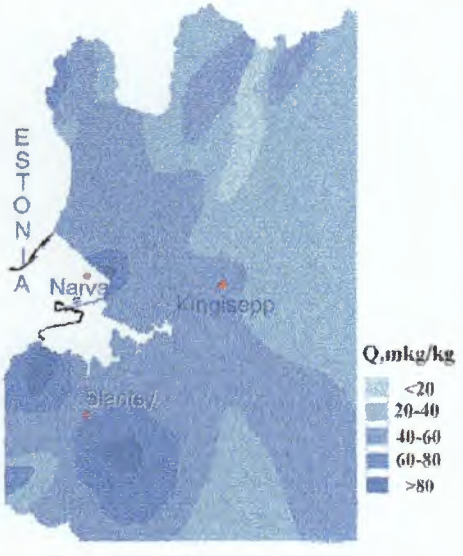

Figure 8. The distribution of Hg (Q) in HNO_3 - extracts of forest mosses over the territory of the Kingisepp area of the Leningrad province

6. CONCLUSION

"Ecological anomalies" in boreal forests which appear under the influence of aerotechnogenic pollution can be effectively revealed, identified and investigated making synergistic use of complex of remotely sensed observation data obtained from the space systems NOAA, Landsat and ERS with one bearing in mind both monitoring and forest inventory making issues.

The main conclusions of the study are the following:

1. Potential possibilities as well as the main approaches towards the synergistic use of different remote sensing data for the polluted areas of forests study are shown.

2. The suggested approach allows, taking standard areas as an example, to establish statistically important connections between parameters obtained from multi spectral space systems and factors that cause plant stresses. The study shows the principal possibility of identification of density and composition of air deposits from the complex of remotely sensed data. Statistical stability of links between ground-based and remotely sensed data subjects to seasonal conditions. Monitoring of pine trees of boreal zone is more effective in the beginning of vegetation period.

3. Stressed and healthy trees over the studied area are different in all investigated spectral diapasons owing to physiological changes of plants with dust and gas pollution of local biocenoses. The obtained dependencies ground the informativeness of simple spectral indices (in particular, difference of signals, simple ratio of signals of different channels, etc.) for the studied territory.

4. Comparison of healthy trees (high VI) with trees weakened by air pollution is reasonable to carry out over the forested areas identified for certain.

7. REFERENCES

1. Becker F., Li Z.-L. Towards a local split window method over land surfaces. Int. J. Remote Sensing, 1990, vol. 11, N3, 369-393.

2. Banninger C. Relationship between tree density, leaf area index, soil metal content and Landsat MSS canopy radiance values. IGARSS'86, p. 1401-1404. Proceedings of IGRASS'86 Symposium, Zurich 8-11 Sept., 1986, v. III.

3. E.Tomppo, M. Hallikainen, P. Mikkela, H. Henttonen et al. Application of ERS-1/SAR data in large area forest inventory. Proceeding of the first ERS-1 Pilot Project Workshop, Toledo, 1994, p. 235-240.

Wither Radar Global Mapping of the Tropical Forest: New Avenues from the TREES ERS-1 Central Africa Mosaic

F. De Grandi, J.P. Malingreau, M. Leysen, Y. Rauste, M. Simard, P. Mayaux
European Commission Joint Research Centre Space Applications Institute
21020 ISPRA (VA) Italy
phone: +39 332 789083 fax: +39 332 789073

ABSTRACT

The TREES ERS-1 Central Africa Mosaic Project CAMP has opened an entirely new perspective in radar remote sensing for the study of the earth ecosystem at large scale using radar remote sensing. The project was started in 1995 by the MTV unit (Monitoring Tropical Vegetation) of the DG JRC Space Applications Institute and consists of the assemblage of more than 450 ERS-1 images covering the whole Central African tropical region. It has so far demonstrated unequivocally the potential of this approach, in terms of thematic information content, and the capability of mapping in a short time, on demand and in all weather conditions a continental scale geographical domain. From the inception of the idea back in 1994, CAMP has evolved along several avenues; at the research and development level a rich agenda has been set up within the TREES phase 2 project to develop or refine techniques for data processing and the analysis of large scale radar maps; the thematic interpretation has progressed from an early phase based on visual inspection of the major features towards a more systematic study that takes into consideration the full spatial extent and the full gamut of vegetation types; the ERS-1 prototype mosaic has acted as a catalyst to promote new initiatives for the global mapping of the tropical forest, such the NASDA Global Rain Forest Mapping program; the CAMP information set will therefore be enriched and expanded in new dimensions with the acquisition of new global data sets using different radar sensors, such as the Japanese JERS-1, and the Canadian RADARSAT; this will also bring into the picture multitemporal aspects and the possibility of exploiting the complementary sensors' characteristics. In this paper we will give an overview of the scenario set by the several components during the evolution of the CAMP concept. Starting from a summary of the fundamental concepts underpinning the CAMP approach, we will then touch upon the following points: the derivatives and expansions of the project, such as the introduction of multi-sensors and change analysis using new global data acquisitions over Central Africa; new data processing techniques, like the wavelet multi-resolution representation; initiatives to pursue thematic studies.coordinated by the SAI MTV. Finally, projecting into the future, some guidelines are drawn for the passage of the CAMP technology into an operational phase.

1. INTRODUCTION

In the context of the TREES 94 ERS-1 Study a novel approach for large (continental) scale mapping of the tropical forest using radar remote sensing was proposed by the JRC SAI MTV (Monitoring Tropical Vegetation) unit. The new approach called for the assemblage on demand and in a short turn around time of a vast amount of high resolution radar imagery from the Synthetic Aperture Radar instrument on-board the ESA ERS-1 satellite to obtain thematic information over the whole bio-geographical domain of Central Africa at several scales and with unprecedented completeness, spatial resolution and quality. A demonstration and test bed for the new concept was put together in MTV at the end of 1995, and was henceforth referred to as the TREES ERS-1 Central Africa Mosaic Project (CAMP). A detailed description of the project can be found in [1][2]. However it is important to recall here the fundamental concepts underlying the CAMP approach, which can be summarized as follows:

- change of scale
- multiresolution
- geometric precision and consistency
- richness in information content

First of all CAMP introduces a major change in scale with respect to the conventional use of radar imagery. While typical coverage in conventional studies is in the order of $10^4 Km^2$, the CAMP radar map is extended over areas of several $10^6 Km^2$, which implies an increase of 2 orders of magnitude. However the concept of scale alone would be meaningless if it were not associated with the concept of resolution. Actually large scale coverage of the tropical ecosystem was already obtained in the past within the TREES project using the 1 km resolution AVHRR sensor. But it is indeed the scale-resolution product that gives to the CAMP approach a distinctive connotation. The availability of a large number of images at high spatial resolution over a large area - which is assured by the all-weather imaging capability and the radiometric stability of the SAR space-borne sensor - allows for the information extraction and analysis at the scale which is locally (in a spatial sense) more suitable for a certain thematic goal. In other words if suitable processing techniques are used to keep the full bandwidth-resolution product, it is possible to generate from the original high resolution data set products that best match the analysis requirements for a

Proc. 3rd ERS Symp. on Space at the service of our Environment, *Florence, Italy, 17–21 March 1997* (ESA SP-414, 3 Vols., May 1997)

certain location and a certain application. In terms of image processing techniques this links to the multi-resolution decomposition concept.

Second important characteristic is the high geometric precision and consistency of the CAMP data set over a large geographic area; this point, in conjunction with the sensor's resolution (30m) and the signal sampling rate (12.5m) makes the CAMP data set an ideal candidate for cartographic applications. The only limiting factor in this respect is the influence of topography on the geometric accuracy of the radar signal, which can become a serious drawback for certain types of cartographic applications, and in certain regions of the world.

Finally the richness in information content is one of the most striking assets of the ERS-1 CAMP mosaic. From the first analyses made per force on a visual inspection basis, a series of features related to the TREES main thematic goal (deforestation) have already emerged and indicate that these large scale radar maps can indeed pave the way to a re-assessment of our knowledge about the rain forest ecosystem. A related aspect is the mixture in the same data set of temporal and spatial variations of the ecosystem. This is due to two reasons. The entire snapshot of the Central Africa mosaic is not acquired instantaneously, but in a time frame (two months) where changes can be expected both in the ecosystem, in the meteorological conditions, and in the sensor's nominal parameters. Second the geographical area covered by the mosaic straddles the equator, and therefore there is an intrinsic seasonal reversal in the ecosystem. Time and spatial effects must therefore be taken in due account in the thematic analysis, and can of course also be exploited for monitoring the time evolution on short term (within the acquisition time of a single mosaic) or using truly multi-temporal acquisitions.

The implementation of the first ERS Central Africa mosaic allowed us to conclude at an early stage that the material provided by this large scale radar map constitutes a unique source of data on vegetation distribution at continental scale. The most celebrated "all weather" characteristic of active microwave sensing has taken its full meaning in the present case since a whole equatorial region has been covered on demand and in a minimum amount of time, and since a significant level of information on forest conditions has rapidly been extracted. The ERS-1 CAMP experience was also the precious starting point to elaborate a new application oriented research agenda and the seed that spurred a number of new activities with the goal of further improving our capability to monitor the earth's environment. It also acted, in our opinion, as a catalysts in the international remote sensing community, to promote the onset of new international projects, that start from, but capitalize and expand upon, the same concepts brought forth by CAMP. In this paper we want to trace the recent evolution of the project, along several avenues such as the expansion and diversification to new sensors and new global acquisitions within international collaborative projects; new radar science techniques to exploit at full the multi-scale concept; initiatives to bring to maturity the thematic analysis; and finally the definition of the CAMP operational aspects, to straddle the frontier of an R/D project and start approaching the operational phase of the TREES phase II project.

2. CAMP RAMIFICATIONS

The second ERS acquisition over Central Africa

The first CAMP blanket coverage over Central Africa was acquired during July and August 1994, and processed at the JRC SAI MTV during 1995. As a first natural extension to the project, a second blanket acquisition was planned in the context of the TREES phase II project (sponsored by the EC DG XI). This second acquisition was meant to explore seasonality aspects and therefore was scheduled in the dual season as far as the Central African ecosystem is concerned (January, February 1996). Under suggestion by the JRC SAI MTV a blanket acquisition over the full CAMP 1994 geographic window (6S-9N 8E-30E) was therefore performed by ESA using the DLR mobile station in Libreville, Gabon. Due to budgetary limitations in the TREES project, it was decided to partition the procurement of the correlated SAR images into batches; a first selection for 1997 was done based on the following criteria:

- thematic interest
- expectation on seasonal information strength
- local interest in the interested countries
- coincident coverage with the ERS-1 1994 mosaic

It is envisaged to set up collaborating groups for the thematic interpretation composed by a local organization, a European laboratory and the SAI MTV. Information about local interest was mainly derived through participation in the World Bank PRGIE workshop (Projet Regional de Gestion et de l'Information Environnementale) held in Libreville on October 5-11 1996. Our analysis led finally to the selection of four sites for the second ERS CAMP mosaic:

1. Transect Kindu-Uele (Zaire)
2. Bateke Plateau and Odzala (Congo Gabon)
3. Complex de Gamba (Gabon)
4. Boucle de l'Oubangui

The sites geographic position is reported in Fig. 1.

Another interesting prospect is opened up by the fact that the January-February 1996 acquisition campaign was almost entirely performed by ESA in tandem mode. An exploratory study was therefore organized in collaboration with DLR, Oberpfaffenhofen Germany, and the CNR Istituto Elaborazione Segnali e Immagini, Bari, Italy, to assess the potential of interferometric SAR image pairs

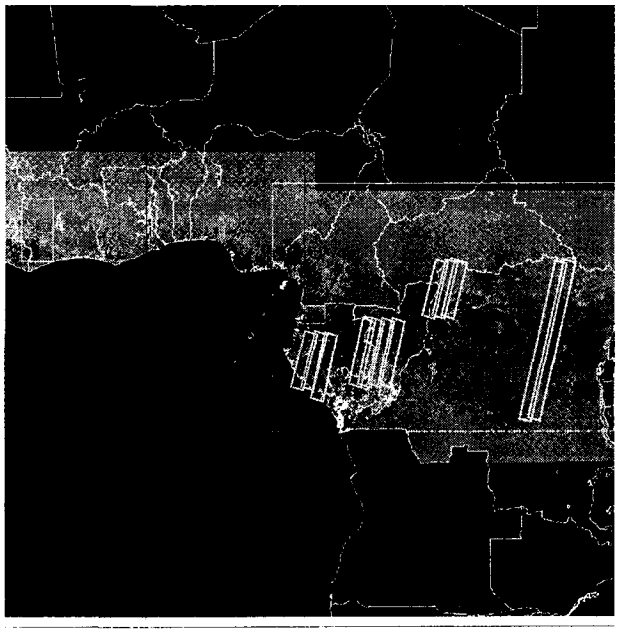

Figure 1: February 1996 ERS-2 CAMP coverage

for tropical forest mapping. The study will be conducted on a limited number of ERS-1 ERS-2 pairs over the same sites of the main CAMP acquisition, and will in particular address the use of interferometric phase information with respect to the following issues:

1. the mapping of forest non-forest classes over sloping terrain
2. the discrimination between forest types in the transition zones
3. change detection to track seasonal cycles

At the time of this writing, the processing of the second ERS coverage over Central Africa has been started at the JRC MTV, and a first mosaic over the Bateke Plateau assembled using the wavelet based processing chain (see section 4 on page 5). The next step will be clearly to put in place adequate co-registration and change detection techniques to tackle on a systematic basis the problem of multi-temporal analysis between the 1994 and the 1996 ERS data sets. Indeed the problem is even wider in scope, because as it will be pointed out in the following sections, the CAMP data set will be augmented in another dimension, namely using imagery from other radar sensors, such the Japanese JERS-1 and the Canadian RADARSAT.

As a preliminary example, and to get some feeling about what we can expect from the multi-temporal analysis, we show in Fig. 2 and Fig. 3 two overlapping frames from the August 1994 and the February 1996 acquisitions over the Bateke region. The two frames are acquired from two parallel descending orbits and their positions in the SAR ground range reference system differ only by a small translation along and across track. It is entirely justified therefore to neglect variations in the radar cross section due to incidence angle, and it is possible to co-register the two frames within one pixel accuracy using a simple Fourier domain cross correlation algorithm. By visual inspection of the frames one can clearly identify major changes in the radar backscattering in the lower left part, due probably to some abrupt event, like rain or fire. Profiles of the backscattering coefficient values taken within the two images are also reported in Fig. 4; they point out radiometric and signal dynamic differences, which are system related and should be compensated for before the change detection analysis.

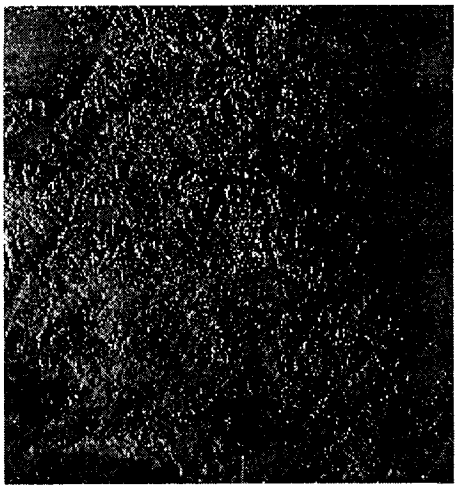

Figure 2: August 1994 ERS-1 frame
Bateke Plateau - Central Africa

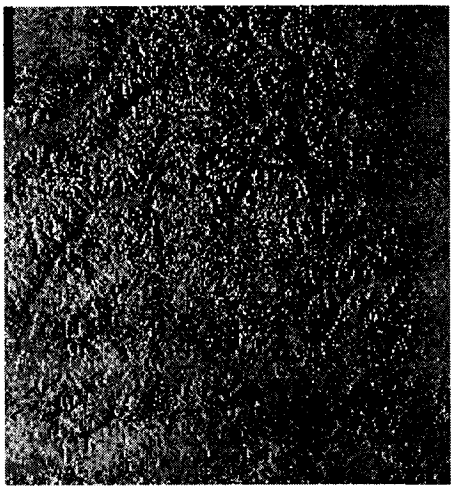

Figure 3: February 1996 ERS-2 frame
over the same area

The NASDA Global Rain Forest Mapping Program GRFM

The GRFM program is an initiative by NASDA which stems from motivations and a rationale which are very similar to the TREES CAMP project: the recognition for the need of a spatially and temporally consistent map of

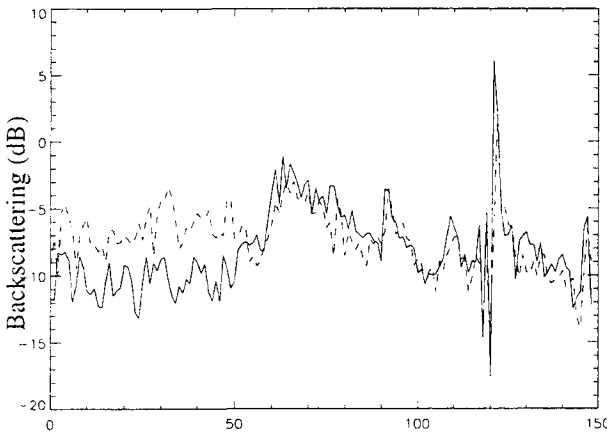

Figure 4: Backscattering coefficient profiles for the ERS-1 1994 (solid line) and the ERS-2 1996 (dotted line) over the same target.

the tropical forest at continental scale and the opportunity offered by a space-borne radar sensor, such as the Japanese Earth Resource Satellite JERS-1, to accomplish this goal. The GRFM program has set very ambitious goals in terms of coverage; planned areas comprise the entire Amazon basin, from the Atlantic to the Pacific, central and west Africa, from the Eastern coast of Kenya to Sierra Leone, and South East Asia, including Papua New Guinea. Such a breadth of scope also calls for relevant technology, knowledge and computing resources, which were pooled together through an international cooperation, which includes among others: the Earth Remote Sensing Data Analysis Centre of Japan (ERSDAC), the National Aeronautics and Space Administration (NASA), the California Institute of Technology Jet Propulsion Laboratory (JPL), the Alaska SAR Facility (ASF), the EC Joint Research Centre Space Applications Institute (JRC SAI), the National Institute for Space Research of Brazil (INPE), the National Institute for Amazonian Research of Brazil (INPA), the University of California at St. Barbara. The role of the JRC SAI MTV in the GRFM is focused on the data processing and thematic interpretation for the Central and West Africa part of the global acquisition plan. In particular the SAI MTV will act as one of three main processing centres for the project (together with NASA JPL for the Amazon basin and the NASDA Earth Observation Research Centre for the South East Asia part); the specific mandate will be to generate the baseline low resolution products and the mosaics to be distributed to all GRFM principal investigators. The thematic interpretation of the Africa data sets will be carried out in collaboration with NASA JPL, the University of California and the University of Maryland in the framework of a project approved by the NASA Office of Space Science and Applications. In this scenario a strong link will be established between the TREES CAMP project and the GRFM, in terms of cross breeding the CAMP radar technology to the GRFM machine, and in terms of synergism and complementary content of the ERS and JERS data sets. Although the GRFM data set will have some specific connotations, still we expect the fusion of all the global data sets that will become available under the different initiatives revolving around the TREES CAMP project, to maximize the information content, and therefore the potential of the large scale radar mapping approach. Preliminary results in this direction, and relative to the comparison of ERS and JERS-1 data over the Bateke plateau in Central Africa, are reported in [3].

The GRFM coverage over Africa comprises three main areas: eastern Africa (6 S - 5 N, 35 E - 40 E); central Africa and Congo basin (8 S - 8 N, 10 E - 40 E); west Africa (4 N - 10 N, 14 W - 10 E). Overall some $8^6 Km^2$ were covered from early January to early April 1996, which is tantamount to some 2000 JERS-1 radar images. Another interesting aspect which was brought into the GRFM picture is the seasonal pattern in the Congo basin, which is linked to the theme of large flooded environments' impact on global changes of the earth climate. The Congo river is the second largest tropical river basin on the Earth, and the surrounding ecosystem exhibits a peculiar temporal behaviour due to the fact that the river crosses the equator twice, and therefore there is no clear and homogeneous distinction between the dry and the rainy season. To study this seasonal pattern in the Congo basin a second acquisition was scheduled at the peak of high water in the river, namely on October - November 1986.

At the time of writing, the processing of the GRFM mosaics is under way at the MTV laboratories. As an example of one of the products which are planned for distribution to the GRFM PIs by the JRC MTV, a mosaic built from a level 3 wavelet multi-resolution decomposition of JERS-1 imagery (see section 4 on page 5) over the Sassandra forest in the Ivory Coast West Africa is shown in Fig.5.

The RADARSAT ADRO 086 Project

In response to a call for opportunities issued by the Canadian Space Agency for the utilization of RADARSAT data - the ADRO program - the JRC SAI MTV has proposed an extension of the CAMP project to explore the possibility of using wide swath low resolution radar imagery for continental scale mapping of the tropical forest. The RADARSAT sensor offers among the several imaging configurations a mode - ScanSAR - which exploits the rapid beam switching capability built into the antenna design to cover large swath (up to 500Km) by successive and almost simultaneous sub-swaths. The large coverage capability is to be traded off against a loss of image quality, which is due to the particular processing technique, whereby blocks of pulses are collected from adjacent sub-swath. A typical product in the ScanSAR 2

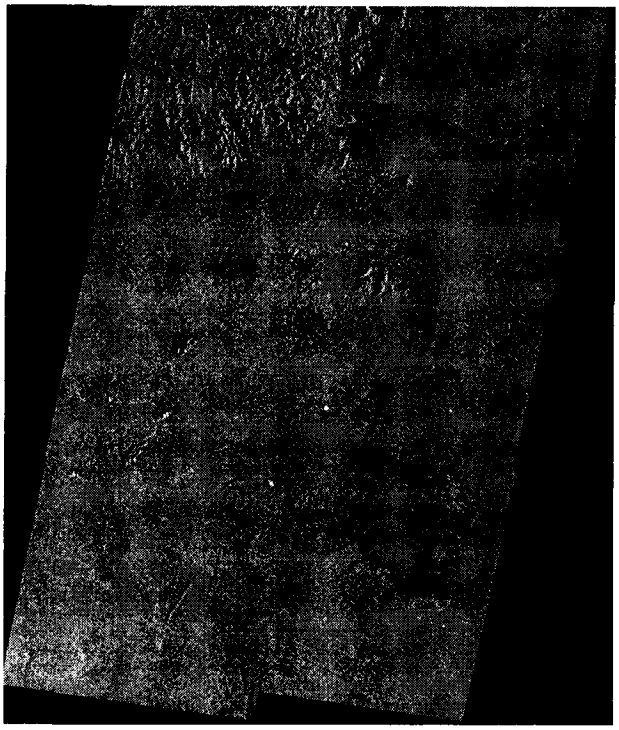

Figure 5: Prototype GRFM JERS-1 mosaic

Sassandra forest Ivory Coast West Africa

beams mode is a 14 looks detected image, with a swath width of 310 Km and a resolution of 100m. Clearly provided that the data quality (resolution, radiometry) can still be made compatible with the thematic goal, the reduced data volume would certainly be a noteworthy asset of the ScanSAR approach in view of repeated blanket coverage of the tropical regions. The science plan for this proposal calls indeed for a quantitative assessment of this trade-off.

In the original JRC proposal, two full coverages of the Central Africa site between 6 S - 9 N, 8 E - 32 E using the ScanSAR 2 beams mode were requested. Due to recent problems in the RADARSAT mission planning, only a partial coverage of the site could be obtained so far, and data were delivered only recently to the JRC. An example of the RADARSAT ScanSAR data over the Central Africa CAMP site is reported in Fig. 6. From preliminary analysis the following points have already emerged:

1. the data set shows clearly a problem with radiometric balance between sub-swaths, and in general with radiometric calibration of the data; the extent to which these problems could be fixed will strongly influence the utilization of the RADARSAT ScanSAR data in our thematic context.
2. visual inspection of the data shows very promising information content with respect to our thematic goal; in other word the degradation in resolution does not seem to affect the spatial features which are important for our analysis.
3. polarization and incidence angle are the dominant factors which influence the radar backscattering coefficient in this configuration rather than the frequency band; therefore there is much higher correlation between the RADARSAT and the JERS-1 data over the same site, rather than between RADARSAT and ERS data.

Figure 6: RADARSAT ScanSAR sample image

4. DATA PROCESSING

A new data processing chain was designed in view of the evolution and expansion of the CAMP project. The new and different data sets (JERS-1, RADARSAT) which have to be accounted for and the ever increasing data volume have dictated changes in the existing prototype CAMP software and hardware machine. Many of the changes pertain purely to the area of computer engineering, and will not be reported here. On the other hand we want to mention a new way of attacking the problem of

the low resolution mosaic products generation, because it is not only a purely computational improvement over the past approach, but introduces a completely new paradigm, which nicely stems from and reflects the concept of multi-resolution. It is therefore a computational solution which is strictly bound to one of the intrinsic characteristics of the CAMP high resolution - large scale approach. In the original implementation the high resolution (12.5m sampling) ERS-1 PRI product was directly down sampled through a classical sampling rate alteration (low pass filtering and decimation) to a 100m product. This product constituted the so called CAMP baseline product, and was used in all further transformation in the processing chain (warping, mosaicking) down to the final analysis step. The multi-resolution concept was embedded in the processing on demand paradigm; here a product at a different resolution (or the result of a different operator) was generated only in specific instances and starting always from the original high resolution PRI data sets. The new processing chain is based on a multi-resolution decomposition and on the wavelet transform. The basic theory behind this approach was developed by Stephane Mallat [4]. Details on the JRC MTV implementation can be found in [5] and in a companion paper in the same 3rd ERS Symposium proceedings [6]. We want here only to illustrate the basic concepts which underpin the new processing chain and to explain the rationale behind our choice.

The concept of multiresolution approximation is an extension of the familiar concept of vector approximation in a linear vector space. This concept permeates the realm of applied mathematics in many cases of science and engineering, such as numerical electromagnetics, to cite a field which is very important for radar science. In a conventional approximation, like the Fourier theory, a function is projected onto an ortho-normal basis of a certain vector space in such a way as to obtain a representation which is nearest to the original function, according to some criteria, such as the norm of the difference between the two vectors. In a multiresolution approximation the function is instead projected on a ladder of vector spaces, each providing the nearest approximation at a certain resolution. Moreover a space at resolution j contains all the information to compute the approximation at a smaller resolution j+1 (causality property); in other words it is possible to generate one product down to the next step in the resolution ladder (e.g. 100m spacing from 50m spacing) without tracing back to the higher resolution products. A multi-resolution representation requires that the operators that project the function into the ladder of vector spaces be numerically defined and this is accomplished defining an orthonormal basis in the spaces. It is demonstrated in [4] that this basis can be derived by translations and dilation of a unique scaling function. The wavelet representation provides the vehicle for implementing one possible multi-resolution transform; in simple conceptual terms, orthogonal wavelets can be used to construct the basis which is needed in the ladder of vector spaces, with the remarkable property that the difference in information between approximations at level j+1 and level j is used to build the multi-resolution implementation.

The mathematical properties of the multiresolution wavelet decomposition match the requirements of the CAMP data processing under several points of view. As we have seen, multi-resolution is an intrinsic concept in the CAMP approach where a high resolution sensor is used for large scale mapping; the wavelet pyramid gives the possibility of generating approximations of the original radar imagery at several dyadic scales (at each stage in the pyramid the resolution is double with respect to the previous level). The detail signals between two approximations can be interpreted as texture measures at that scale; therefore the wavelet decomposition provides at the same time the approximated image at a certain scale, and information on spatial structures that exist in the image at that scale. Moreover the wavelet representation can be used to implement a sub-band image coding scheme, which would be quite attractive for the CAMP image compression and distribution on low bandwidth media, such as the Internet. Last but not least the existence of fast discrete wavelet transform algorithms, which require only a number of operations proportional to the size of the original data, makes this approach ideal in the case of high data volume as in CAMP. These considerations led to the design of a new CAMP processing chain based on the multi-resolution wavelet representation. A block diagram of the chain is shown in Fig. 7.

In principle at each stage in the ladder, the signal (image) is passed through two conjugate quadrature filters and decimated. The signal emerging form the low pass branch constitutes the image approximation at that scale, while the part from the high pass branch represents the detail signal. In our specific implementation, the original PRI data set (12.5m pixel spacing) is passed through four stages to produce approximations at 25m, 50m, 100m, and 200m. Only the lower resolution products (100m and 200m) are used to build the mosaics; the other approximations are kept for more detailed high-resolution analyses. Moreover in the last two stages of the pyramid also images of the total energy in the wavelet coefficients are generated (scalograms) and these are retained as texture measures at that scale. In total for each original radar frame, the wavelet decomposition produces for the main CAMP database and the mosaicking phase two approximation images and two scalogram images at 100m and 200m.

5. CAMP THEMATIC INTERPRETATION

The numerous data sets that are progressively building up in the evolution of the CAMP project and its derivatives constitute a formidable database which is potentially

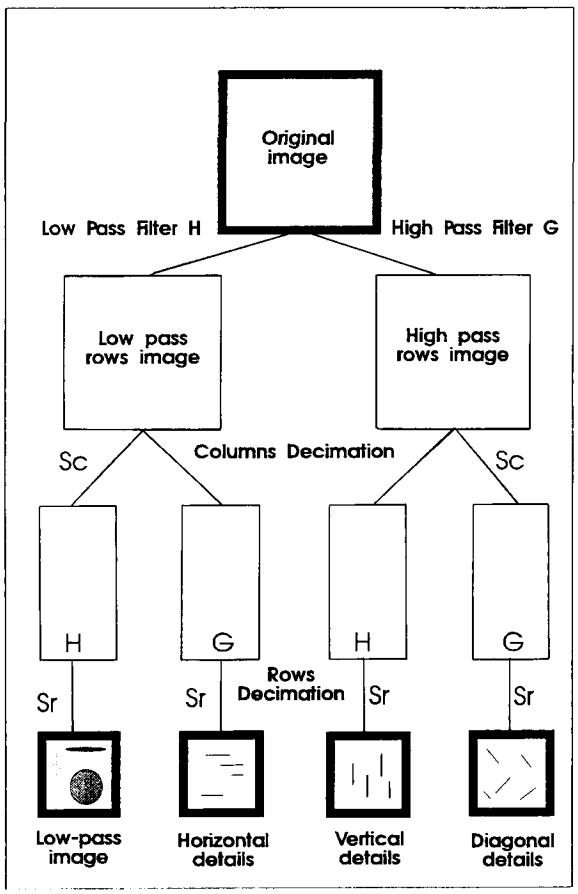

Figure 7: Block diagram of the wavelet multiresolution decomposition algorithm.

extremely rich in thematic information content. The problem of extracting this information is also a formidable one, the complexity of the task being compounded by the sheer volume of data, by the diversification of features present in the tropical ecosystem, by the combination of time and space related aspects, and by the difficulty in obtaining reference data for validation and verification. In a first phase the problem was per force driven by the need of assessing the potential of the new approach; in this context, the analysis was mainly conducted on a visual interpretation level and on sampled areas. Results from this type of analysis are for instance reported in [1] and [2]. From this baseline, two different avenues were also started under the coordination of the SAI MTV. On one side new image processing and radar science techniques were taken into consideration in order to optimize the information content retrieved by the underlying signal, given the boundary conditions of the CAMP data set (e.g. mono-temporal acquisition). Among the investigations belonging to this class we cite two examples.

Work on the retrieval of multi-scale structures in the tropical forest by means of the wavelet transform, which was conducted in the MTV unit [5][6]. The central theme here is to try to detect structures that would allow for the discrimination of secondary forest formations. Since these structures are scale dependent, a multi-scale texture measure must be used.

Work conducted by the Moscow State University Geographical Faculty and the Brunel University, UK, in the framework of the ESPRIT Project 21042. Here the main research theme was to refine image segmentation techniques to delineate thematic classes in the ERS CAMP imagery, such as undisturbed forests, secondary forest at different regrowth state, savannah and landscapes of shifting cultivation [7].

Another line of research was aimed at shifting the analysis towards a more systematic approach, in order to take into consideration the full extent of cases proposed by the large coverage of the CAMP mosaic. A first important contribution to this line is given by [8]; in this work a systematic study on the separability of a well defined set of vegetation types was established for a number of sensors (AVHRR, Landsat, ERS SAR) and for a broad sample of transition areas. This study was also the first intercomparison between the CAMP ERS-1 data set and other sensors in the TREES thematic context.

The next step will be to bring the CAMP thematic interpretation to the full breadth of the spatial extent and the thematic diversity which is by definition inherent to a global scale exercise. This ambitious goal can only be achieved pulling together the expertise and the work force of many laboratories and investigators, who can span the gamut of applications where the CAMP remote sensing data source have a relevant fall out. To this purpose, the SAI MTV is organizing a network of interested research partners who will work on several aspects of the mosaic thematic interpretation.

6. CONCLUSIONS

From the inception of the idea, back in 1994, up to now, CAMP has grown to maturity, bringing a novel approach in radar remote sensing for studying global scale problems of the earth ecosystems from the conceptual stage deep into the implementation phase. On one side new blanket acquisitions performed by the ESA ERS-1 and ERS-2 sensors, the Japanese JERS-1 and the Canadian RADARSAT are bringing new dimensions into the project and enriching our information budget on the tropical forest. On the other side new techniques in data processing and in radar science, and new experience gained in the thematic interpretation are paving the way for an ever increasing exploitation of the thematic content of these continental scale radar data sets. Last but not least the technology and knowledge base accumulated in the context of CAMP and similar projects around the world can now be exported to other remote sensing applications; among new initiatives that in a sense stem from or will benefit from the CAMP experience we cite: the EC SEARRI South East Asia Rice Radar Investigation project, a study funded by the SAI Centre for Earth

Observations and executed by the MTV unit. The investigation is aimed at the mapping of the water conditions in rice paddies at regional scale in support to crop yield modelling and methane emissions studies. And the GBRFM project launched by NASDA in collaboration with the DLR, Germany and the JRC SAI, which is an extension of the current project for the global mapping of the rain forest to the Boreal forest, and in particular to the Eurasian part of the Siberian forest.

At this point in time we can confidently say that radar remote sensing for global mapping of the earth ecosystem has passed the stage of the prove of concept, and is sailing through an advanced research and development stage. If all the new initiatives briefly described in this paper will maintain the expectations, the time will be ripe for considering the introduction of this technique into operational projects, such as the EC TREES phase 2. In this prospect, we can already now trace the major corner points that will have to be met by both the flight and the ground segment in the passage to this new phase:

- capability of global real time coverage assured by a network of receiving stations.
- fast end-to-end (acquisition, raw data processing, post-processing) turn around time.
- SAR data products consistency in time and space (signal and ancillary data).
- optimal trade-off between spatial resolution, data volume and signal to noise ratio.
- hierarchy of end products (baseline low resolution, high resolution, compressed) to meet the demands of the applications, such as automatic large scale mapping, hot spot analysis, network data distribution.
- adequate data cost policy (redefinition of the unit price from the single SAR frame vantage point, to the regional coverage mosaic).

7. ACKNOWLEDGEMENTS

The authors would like to acknowledge the efforts and contributions of all the people involved in the ever growing CAMP scenario; among these in particular: Giorgio Perna and Elisabetta Franchino, members of the CAMP software engineering team at SAI MTV. Alex Tournier and Bernard Glenat, system administrators at SAI MTV.

Alfred Hansen, visiting scientist at SAI MTV, for the precious advice on signal processing issues.

The ESA ESRIN, the DLR PAF and EURIMAGE staff members.

Dr. Ake Rosenquist, who was the major driving force at NASDA for the set up of the GRFM program; all the NASDA and ERSDAC staff members involved in the project, and particularly Dr. Tasuko Tanaka, director, and Masanobo Shimada.

Dr. Sasan Saatchi of NASA JPL who is the chief investigator for the CAMP analysis in the context of the NASA-JRC-NASDA collaboration.

The Canadian Space Agency staff members who are supporting the JRC CAMP ADRO project, and in particular Salvatore Carboni, Philippe Rolland and Adrian Bohane.

8. REFERENCES

[1] J.P. Malingreau, F. De Grandi, M. Leysen, E. Nezry, "Central Africa Mosaic Project: Using ERS-1 SAR at Continental Scale", Proc. of the Second ERS Applications Workshop, London, UK, Dec. 1995, ESA SP-383.

[2] F. De Grandi, J.P. Malingreau, M. Leysen, "The ERS-1 Central Africa Mosaic: A New Perspective in Radar Remote Sensing for the Global Monitoring of Vegetation", submitted to IEEE Trans. on Geoscience and Remote Sensing.

[3] Y. Rauste, F. De Grandi, J.P. Malingreau, "Preliminary Assessment of Complementary ERS-1 and JERS-1 SAR Observations in the TREES and GRFM Central Africa Mosaic Projects", Proc. of the 3rd ERS Symposium, Florence, 1997.

[4] S.G. Mallat, "A Theory for Multiresolution Signal Decomposition: the Wavelet Representation", IEEE Trans. on Pattern Analysis and Machine Intelligence, vol. 2 no. 7, July 1989.

[5] M. Simard, F. De Grandi, K. Thomson, B. Benie', "Analysis of Speckle Noise Contribution on the Wavelet Decomposition of SAR Images", submitted to IEEE Trans. on Geoscience and Remote Sensing.

[6] M. Simard, F. De Grandi, K. Thomson, M. Leysen, "Sensitivity Analysis of ERS-1 SAR Signal to Multiscale Structures of the Tropical Forest by Means of the Wavelet Transform", Proc. of the 3rd ERS Symposium, Florence, 1997.

[7] V.A. Sadovnichy, A.M. Berliant, A.G. Kosikov, O.R. Musin, B.A. Alexeev, A.K. Posypkin, V.N. Solntsev, "Experimental Delimitation of Vegetation Types in Central Africa on the Basis of Digital Radar Images", Preliminary Report ESPRIT Project 21042, Moscow 1996.

[8] P. Mayaux, J.P. Malingreau, "Central Africa Forest Cover Revisited: an Iterative Approach Based on Multi-Satellite Analysis", TREES Project Report July 1996.

CHARACTERIZATION OF THE LAND USE/COVER IN THE CONGO RAINFOREST WITH OPTICAL AND MICROWAVE DATA

Agnès Bégué, Serge Guillobez

CIRAD-CA, Maison de la Télédétection
500, rue JF Breton, 34 093 Montpellier, France
phone: + 33 4 67 54 87 54, fax: + 33 4 67 54 87 00, e-mail: begue@cirad.fr

Jacques Imbernon

ICRAF, United Nations avenue, Gigiri
PO Box 30677, Nairobi, Kenya
phone: + 254 252 1450 , fax: +254 252 1001 , e-mail: j.imbernon@cgnet.com

André Beaudoin

LCT, Maison de la Télédétection
500, rue JF Breton, 34 093 Montpellier, France
phone: + 33 4 67 54 87 54, fax: + 33 4 67 54 87 00, e-mail: beaudoin@lct6.teledetection.fr

Yann Kerr

CESBIO, 18 Av. Edouard Belin, 31 Toulouse, France
phone: + 33 5 61 55 85 22, fax: + 33 5 61 55 85 00, e-mail: kerr@cesbio.cnes.fr

ABSTRACT

In South Cameroon the deforestation is mainly caused by slash-and-burn agriculture. This practice is conducted on small plots within the forest, leading to a diffuse pattern of deforested areas. In such a complex farming system, with cacao plantations under tree cover and inter-cropping, the significance of high resolution satellite data can be evaluated in terms of discrimination of the main land covers : savannahs, degraded forest and dense forest. This has been done on SPOT, ERS (received at the German transportable station in Libreville) and JERS SAR images. The classification algorithm used for SAR images is based on the statistical properties of the land covers (PAPRI algorithm). The results are presented, compared to SPOT classified images and a vegetation map, and the synergy between the different sensors is discussed.

1. INTRODUCTION

The study area is in South Cameroon (Fig. 1). The humid forest of South Cameroon covers more than 40% of the country's total area. The overall climate in the forest region is subequatorial with a bimodal rainfall pattern and an annual rainfall of about 1500 mm at Yaoundé (Fig. 2).

The tropical moist forest area extends over 20.0 millions of ha of which only 4% is currently being used for agriculture production. In spite of the small proportion under cultivation, short fallows dominated by *Chromoleana odorata* characterize the land use system.

The annual deforestation rate is one of the highest in the region with 1.5% of the humid forest. This explains why a benchmark area of the ASB ('Alternatives to Slash-and-Burn') GEF project has been chosen in Cameroon close to Yaoundé. The objective of the present study is to characterize the land use of this area using multi-sensor and multi-temporal data and, particularly, to evaluate the possibilities of ERS and JERS SAR imagery at this aim.

2. DATA ACQUISITION

ERS data have been acquired by the German transportable station in Libreville (contract AOL.F207). Only the more recent acquisition campaign (winter 95/96) has been retained because the conditions of acquisition (orbit, frame ...) were consistent between the scenes. The data set we used is made of 3 ERS-1/ERS-2 tandem images (17/18 Dec. 95, 25/26 Feb. 96, and 31 March/1 April 96) acquired over two regions (Frame 3537, Fig. 1). The scenes are in GEC format.

Despite a particularly high cloud cover in the region (Fig. 2), XS SPOT images have been acquired along the same track on 3 March 1995. The scene KJ 084-342 corresponds approximately to the location of our sites as shown in Figure 1.

Proc. 3rd ERS Symp. on Space at the service of our Environment, *Florence, Italy, 17–21 March 1997* (ESA SP-414, 3 Vols., May 1997)

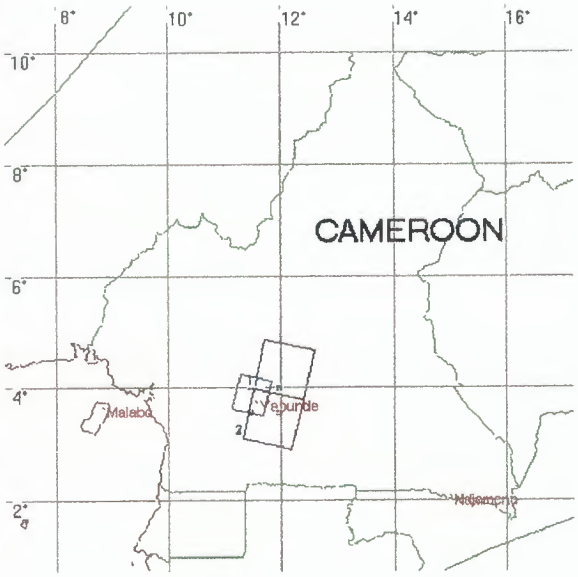

Figure 1. Location of the sites and images (ERS scene in black, SPOT scene in blue) in Cameroon.

A JERS-1 SAR GEC image of Yaoundé has been acquired too on 3 March 96.

Ground truth about land use was collected in November 1995 all over this area, for SPOT image classification. Finally, the 1/500000 Vegetation Map of Cameroon (Letouzey, 1985) is also available as a ground truth document.

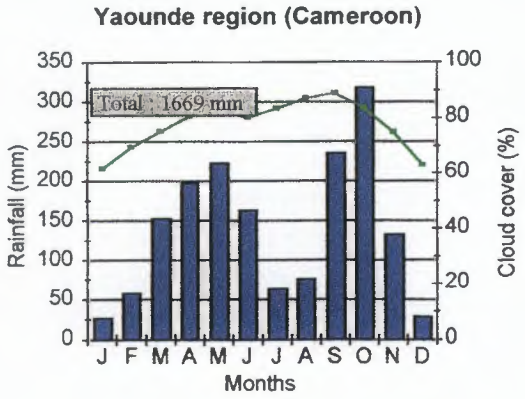

Figure 2. Monthly rainfall (blue histogram, from ORSTOM) and monthly cloud cover (green line, from Hahn et al., 1994) over Yaoundé region.

3. DATA PROCESSING

Pre-processing

First of all, the whole data set of satellite images and the vegetation map were co-registered. This operation was particularly easy for ERS images thanks to the high stability of the satellite. Between ERS, SPOT and JERS images, the operation was more time-consumming but resulted in a geometric error below 1 pixel. Then, in order to improve the processing time, the SAR images were resampled to 50m pixel spacing (simple average).

Signature analysis

We chose to work with the ERS-2 images series, as the ERS-1 tandem series were identical after calibration (coefficients from Laur et al., 1996). The images correspond to the beginning and the end of the dry season, and to the beginning of the rainy season (Fig. 2). The contrast between the dry and rainy seasons confirms the fact that these multi-temporal acquisitions can be recommended for land units discrimination in African rain-forest (Conway et al., 1994).

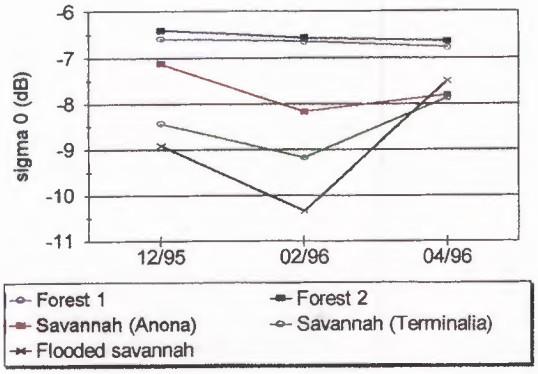

Figure 3. ERS-2 signature plots for the main training sites.

Geo-statistical analysis

The semivariogram is a relatively simple function for investigating spatial correlation among data collected in one or multi-dimensional space. This geo-statistical tool can express the textural information contained in an image. Miranda et al. (1996) developped a supervised classifier based on the information contained in the semi-variogram functions and digital number values of training sites.

We calculate the semi-variogram signatures of the above training sites, and fit them with different functions. The exponential function gave the best fit and the results are presented in Figure 4. The range value of the semi-variogram is given in meters and represents the distance at which the data are no longer correlated. The sill represents the variance of the data set. Ranges and sills are well differenciated between the vegetation units.

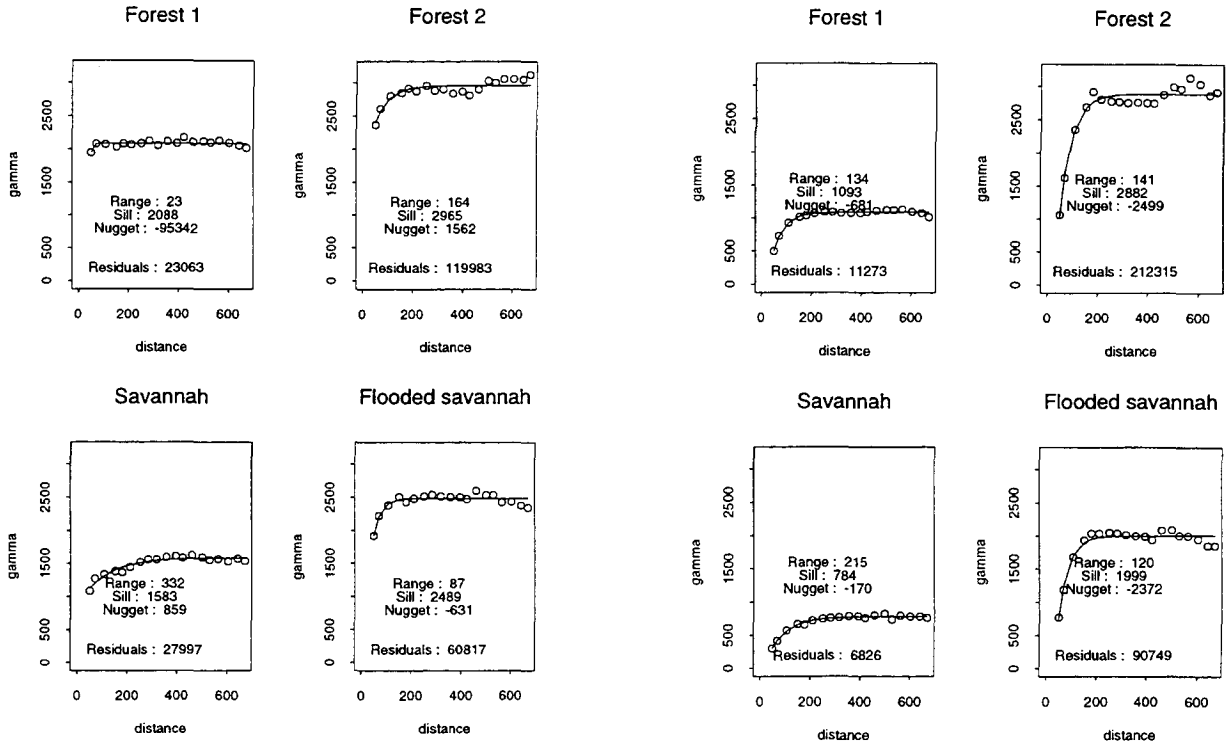

Figure 4. Semi-variograms of the main training sites calculated on ERS-2 images, and fitted with an exponential function : (a) unfiltered images and (b) temporally and spatially filtered images.

Filtering

Filtering was made in two steps : first a temporal filtering has been applied on the 7 SAR images according to Bruniquel's approach (1996). This approach permits to reduce the speckle while keeping the information of each image (no temporal smoothing). Secondly, the images were filtered using the G-map spatial filter from Lopes (1990), using a 3x3 sliding window.

4. CLASSIFICATION

In this study we chose to use a classification algorithm which is not dependent on the degree of filtering applied to the image, but which makes use of the statistical properties of the SAR image.

This algorithm is called Papri (Paysage a PRIori) and has been developed at CIRAD (Borne, 1996). Papri is a texture-based method for image segmentation, using texture in the restrictive term of ratios of colors (but not of positions of these colors). It gives an outcut of space in big units texturally homogeneous. For each pixel, the distribution of the colors is analyzed in varying-size neighbourhoods, and the results are compared to pre-chosen reference land units distributions.

Finally the pixel is classified in the neighbourhood with the closest distribution of colors. We then get an image of large land units of the original image, and two other images for quality estimation.

Papri method works on a single channel. To synthetize in an unique band the information contained in a multi-temporal and multi-sensor series of images, the simple way is to recode in a RGB image the three channels containing the maximum of information. The analysis of the temporal/spectral signatures of the main land use/ land cover units is a simple and efficient way to select the best three images.

Another way to synthetize the information in a single channel is to process to a pre-classification using the algorithms that are commonly used for optical data. The result is not satisfactory by itself, but can be used as an input image in the Papri algorithm.

To process to Papri classification, we first extract a sub-set (20 x 25 km) of the images (Fig. 5) and of the vegetation map. On this sub-image, 4 types of landscape were identified : forest, degraded forest (mixture of forest and crop-lands), savannahs and regularly flooded savannas.

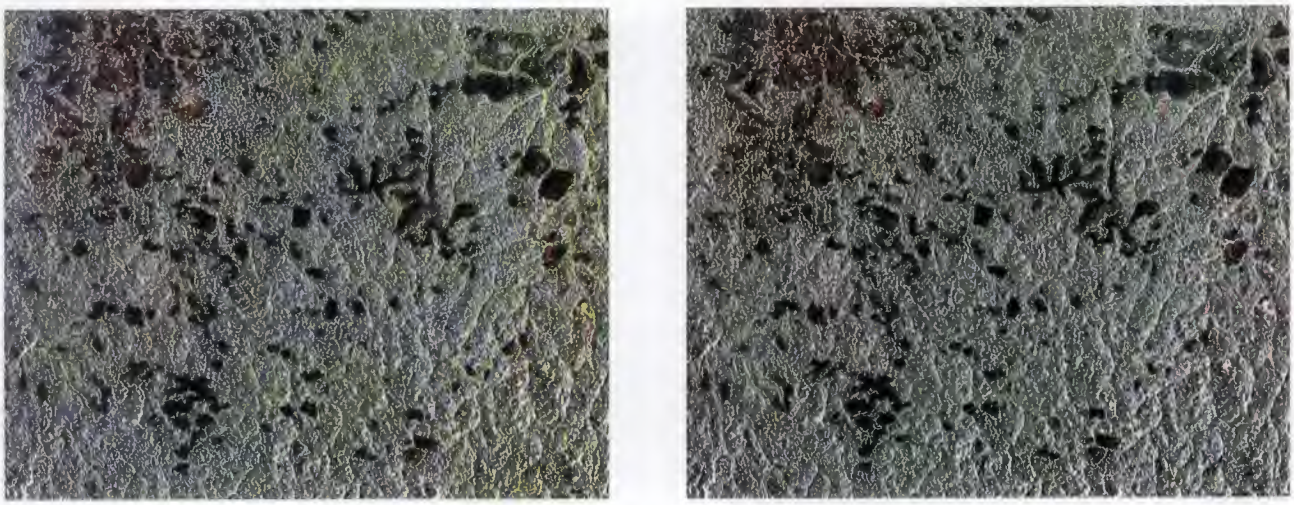

Figure 5. Colour-composite of SAR sub-images (4° 06'N;11°45'E) after temporal and spatial filtering : very few visual differences between the dry and wet ERS composition (on the left), and JERS/ERS dry and wet composition (on the right).

The maximum and minimum sizes of the windows used in Papri distributions calculations come directly from the semi-variogram analysis : windows of 1x1 to 7x7 pixels for unfiltered images, windows of 3x3 to 5x5 pixels for filtered images. Papri can be applied several times on the resulting images, conducting to larger and smoother vegetation units. The results of some Papri classifications are presented in Figures 6 and compared to Letouzey Vegetation Map and to the classified SPOT image.

Globally Papri gives satisfactory results compared to SPOT image classification. After one run of Papri (Fig. 6c and 6e, left column), the result is comparable to SPOT product (Fig. 6a). The classification is less detailed, but the classes are well retrieved and their spatial distributions are respected. Flooded savannah has a larger extend on SAR classifications which seems to be closer to the ground truth because of the high sensitivity of the microwaves to flooded vegetation (and because there is almost no chance to acquire a clear SPOT image during the rainy season when the savannahs are flooded).

On Figures 6d and 6f (right column), the representation of the vegetation units is adapted to a vision at a larger scale. Here, the results have to be compared to Letouzey map (Fig. 6b). The main units are retrieved and are located in about the same areas. But, the shape and size of the land units are rather different. This can be explained by the 10 years interval between the two map productions and by the difference in the methodology used. The differences between Figures 6d and 6f indicates that Papri method is rather sensitive to the window size. This characteristic needs to be further investigated.

5. CONCLUSIONS

Temporal and spatial filtering conducts to a high quality visual product when a sufficient number of images are available (7 images in this study). On these filtered images, one can identify visually different types of land units as noticed previously by Kuntz et al. (1996) who discriminated different types of forests, logged forest, clear-cutting ...

Combined ERS/JERS images exhibit slightly different tones in the forest domain than ERS images alone. These differences could be associated to different forest types. Unfortunatelly we do not have the information to check and label these tones variations. Globally, in this region of South Cameroon, ERS and JERS are very close and JERS does not improve in a significant way the discrimination between the land units.
Compared to SPOT, SAR images have the advantage to be acquired easily during the dry and rainy seasons. The results presented in this paper show that this temporal information is very important for land use discrimination. On SPOT images, the frequently flooded savannahs are largely under-estimated due to the season of acquisition. This is an example of the complementarity between optics and SAR.

When using algorithms of classification, the discrimination between forested and non-forested domain is almost guaranteed (Conway et al., 1994), but the discrimination between the other land units is not straighforward. In this study we used Papri which is an algorithm that can run on unfiltered SAR images and produce classifications cleared of speckle. By itself, this property is already very satisfactory. Furthermore, the result is thematically correct. Investigations are pursued on the use of Papri algorithm on unfiltered SAR images.

a) Classified SPOT image.

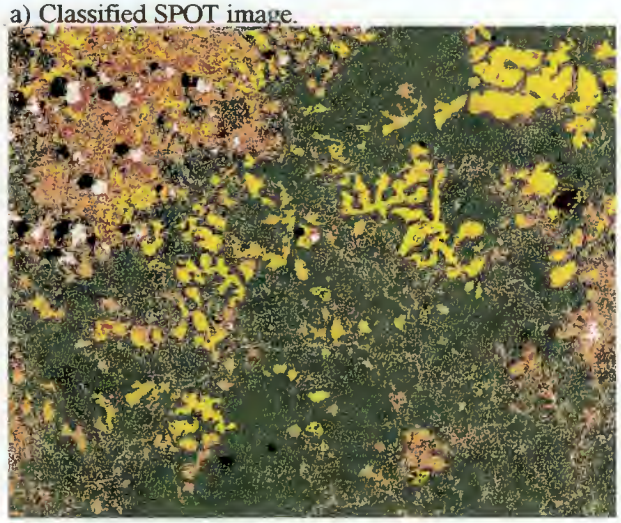

b) Extract of Letouzey 1/500000 vegetation map.

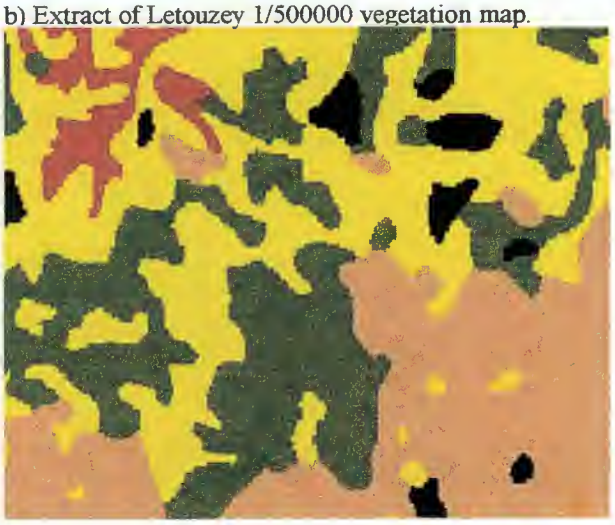

c) RGB-coded unfiltered ERS images classified with Papri : 1st run with windows from 1 to 7 pixels size.

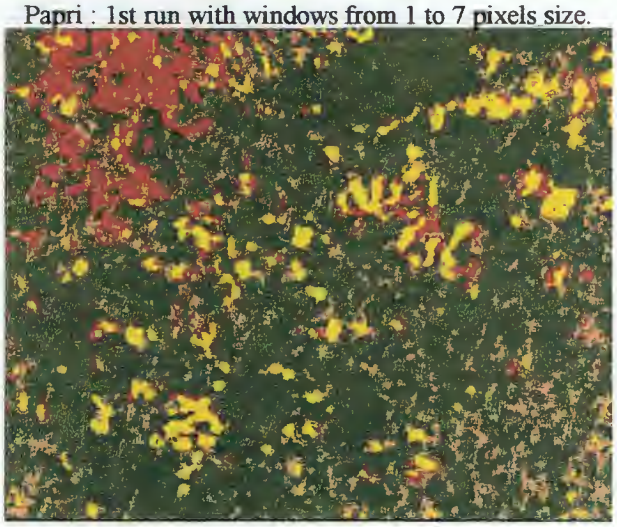

d) Fig 5c classified with Papri : 2 consecutive runs (9 to 21 window sizes, and 23 to 63 window sizes).

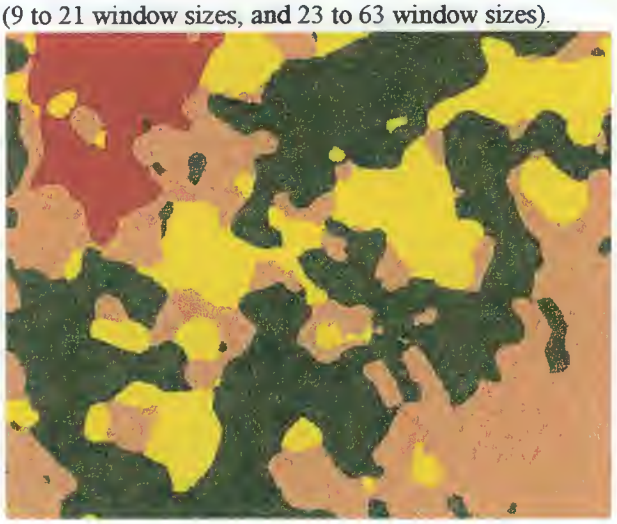

e) RGB-coded unfiltered ERS images classified with Papri : 1st run with windows from 3 to 5 pixels size.

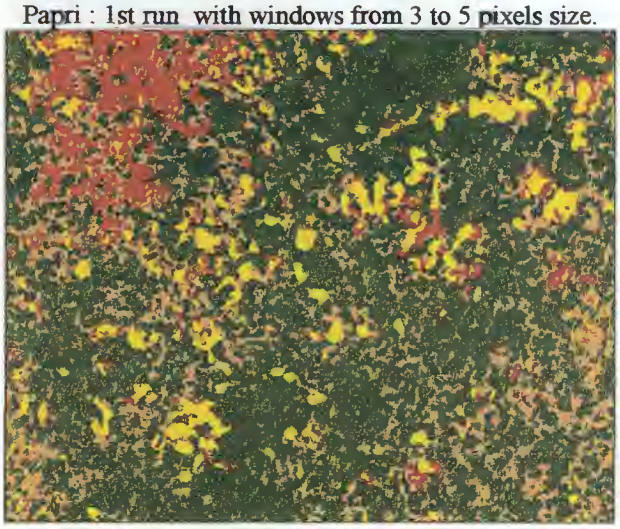

f) Fig 5e classified with Papri : 2 consecutive runs (9 to 21 window sizes, and 23 to 63 window sizes).

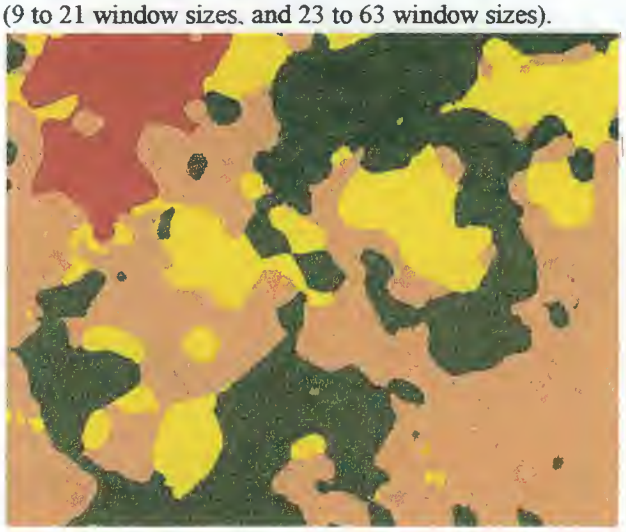

Figure 6. Comparison of different Vegetation Maps : forest (green), degraded forest (orange), low-land savannahs (yellow), frequently flooded savannahs (red).

REFERENCES

Borne F., Guillobez S., 1994, A New Approach in Remote Sensing Image Analysis for Natural Environment Cartography, in IGARSS'94 Proceedings pp. 1805-1807, Pasadena, U.S.A.

Bruniquel J., 1996. Contribution de données multi-temporelles à l'amélioration radiométrique et à l'utilisation d'images de radars à synthèse d'ouverture. Thèse de l'Université Paul Sabatier, Toulouse, 204p.

Conway J.A., Leysen M., and Sieber A.J., 1994. Evaluating multi-temporal ERS-1 SAR data for tropical forest mapping : data selection, processing and target identification. Proceedings 2nd ERS-1 Symposium "Space at the service of our environment", Hambourg, Germany, 11-14 Oct. 93, ESA SP-361.

Hahn C.J., Warren S.G., London J., 1994. Climatological data for clouds over the globe from surface observations, 1982-1991 : the total cloud edition. NDP026A, Carbon Dioxide Information Analysis Center, Oak Ridge National Loboratory, Oak Ridge, TN.

Imbernon J., 1996. Visions of landscapes and vegetation changes. CIRAD-ICRAF Joint Research Project, working paper, pp129.

Kuntz S., Streck C., Siegert F., 1996. Multitemporal evaluation of ERS-SAR data for monitoring deforestation in tropical rainforest. Proc. 2nd ERS Applic. Works., London (UK), 6-8 Dec. 95, ESA SP-383, 83-93.

Laur H., Bally P., Meadows P., Sanchez J., Schaettler B., and Lopinto E., 1996. Derivation of the backscattering coefficient sigma-0 in ESA ERS SAR PRI products, Doc. ES-TN-RS-PM-HL09, June 96, ESA/ESRIN.

Letouzey R., 1985. Carte phytogéographique du Cameroun au 500000è, IRA-ICIV, Université de Toulouse.

Lopes A., Touzi R., and Nezry E., 1990. Adaptive speckle filters and scene heterogeneity, IEEE Trans. Geosc. Remote Sens., 28:992-1000.

Miranda F.P., Fonseca L.E.N., Carr J.R., and Taranik J.V., 1996. Analysis of JERS-1 SAR data for vegetation discrimination in northwestern Brazil using the semi-variogram textural classifier (STC). Int. J. Remote Sens., 17:3523-3529.

LANDCOVER CLASSIFICATION USING ERS SAR/INSAR DATA ON COASTAL REGION OF CENTRAL SUMATRA

Nicolas Stussi, Soo Chin Liew, Leong Keong Kwoh, Hock Lim,
Centre for Remote Imaging, Sensing and Processing (CRISP)
National University of Singapore, Lower Kent Ridge Road
Singapore 119260, Republic of Singapore
e-mail: crsns@leonis.nus.edu.sg, Url: http://www.crisp.nus.sg

Janet Nichol, Kim Chuan Goh
Division of Geography, National Institute of Education
Nanyang Technological University, 469 Bukit Timah Road
Singapore 259756, Republic of Singapore
e-mail: nicholj@nievax.nie.ac.sg

ABSTRACT

In this study, we present a classification method using both optical and SAR data in order to perform landcover classification. We investigate the use of a vector of information, composed of a serie of signatures derived from both SAR and INSAR data. First, different relevant parameters are derived from ERS-SAR data using multitemporal and interferometric analysis. Optical data is then used to define a training set in to order to perform a supervised classification. Our test site is located in a tropical area, in the coastal region of Central Sumatra, Indonesia. This site has a wide variety of landcover types. The region has been undergoing rapid deforestation with the logging of commercially exploitable timber and the conversion of forest to agricultural land. Our results demonstrate that ERS-1/2 tandem data is more suitable than the 35 days repeat pass in discriminating various landcover types. The results of classification using these techniques are compared with existing landuse maps and information derived from SPOT and LANDSAT data.

I. INTRODUCTION

The use of spaceborne remote sensing for forest and landuse applications has been widely demonstrated as an important tool, particularly for forest monitoring and landcover identification. More importantly, the easy availability of data on a regular basis from operational satellites such as ERS, JERS, RADARSAT, SPOT and LANDSAT has created the potential for such an analysis to be implemented as a monitoring tool. This is immensely important in areas where extensive logging activities are prevalent. Optical data, like SPOT, remain the best source of information for forest monitoring and landuse classification, with a high resolution and a good discrimination for various lancovers. While optical sensors have been successfully exploited for such studies, their use in tropical areas is severely limited by weather conditions. Indeed, cloud cover poses the greatest restriction to the acquisition of data that may be required at different intervals.

This limitation has been somewhat alleviated by the use of Synthetic Aperture Radars (SARs) which are essentially all-weather systems. Typically such systems provide information of the ground reflectivity, in a manner which is phase preserving. The utility of the phase information was first demonstrated by Graham [1] where he used two vertically separated airborne antennas to receive simultaneously backscattered signals from the terrain. The coherent addition of the signals received by two spatially displaced antennas, which forms the basis of what is now called SAR Interferometry, provides useful information about the topography of the terrain. This technique has also been employed in spaceborne systems where the 'displacement of antennas' is achieved by a single antenna in two separate passes of the satellite [2].

It has been shown that a multiptemporal analysis of SAR data allows to monitor changes in landcover using the backscatter change intensity. Moreover, it has been demontrated in [3,4] for boreal forest and [7] tropical forest that the coherence component derived from an interferometric pair gives additional useful information for landcover classification.

In this paper, we present a supervised classification method using both optical data and radar information derived from SAR and INSAR data. First, we present the different steps to derive a serie of parameters from both amplitude and complex data. In particular, we investigate the usefulness and the limitation of tandem and 35-day repeat-pass interferometry for this application. A description of the supervised classification method is given, where optical data is used to define the training set and control the classification process.

Proc. 3rd ERS Symp. on Space at the service of our Environment, *Florence, Italy, 17–21 March 1997* (ESA SP-414, 3 Vols., May 1997)

II. TEST SITE AND DATA

The test site is located in the coastal region of central Sumatra in the Jambi province, Indonesia. This site has a wide variety of landcover types ranging from mangrove, swamp forest, primary and secondary forests and agricultural land including rice, coconut, rubber and oil palm. The region has been undergoing rapid deforestation with the logging of commercially exploitable timber and the conversion of forest to agricultural land. A landcover map of 1:100 000 scale realised in 1992 is available over this area. A set of optical data composed of two SPOT XS data (1996) and one Landsat TM data (1993) are used for the classification process. These data, in conjunction with the landcover map of 1:100 000 scale realised in 1992, are also used to validate the result of the classification.

Both SAR.SLC and SAR.PRI data are used in this study for multitemporal and interferometric analysis. A set of ERS-PRI data acquired over one year (oct 95 to december 96) are used for multitemporal studies. Interferometric pair acquired during tandem mission (April-June 1996) are used to derive the coherence component.

Sat.	Date	Orbit	Frame	Type	Baseline ($B_\perp$, $B_\parallel$)
ERS-1	95/10/07	22107	3627+20% SAT	PRI	N/A
ERS-1	96/05/04	25113	3627+20% SAT	SLC	(68, 139)
ERS-2	96/05/05	05440	3627+20% SAT	PRI, SLC	
ERS-2	96/06/09	05941	3627+20% SAT	PRI	N/A
ERS-2	96/09/22	07444	3627+20% SAT	PRI	N/A

Table 1: List of SAR Data (SAT: Shift Along the Track)

III. METHODOLOGY

First of all, we summarize the processing techniques applied on SAR data for both multitemporal and interferometric studies. Then, we will present the methodology developed to perform the classification using both optical and SAR data.

III.a Processing techniques

. Multitemporal analysis

Amplitude images SAR.PRI are analysed to derive different parameters used in the classification process:

. backscattering coefficient σ^0

. backscatter intensity change $\Delta\sigma^0$

. texture

First, an edge-preserving filter (Gamma-MAP, [8]) is performed on each amplitude image in order to significantly reduce the speckle within the image.
Then, backscatter intensity change $\Delta\sigma^0$ could be estimated correctly as follow:

$$\Delta\sigma^0_{dB} = 10 \cdot \log\left(\frac{\bar{I}_2}{\bar{I}_1}\right) \quad (1)$$

Where $\bar{I}$ is the intensity of the signal after filtering.
Texture parameters (variance and entropy) are derived from the Grey-Level Co-occurrence Matrix using a large window (15x15).

. Interferometric processing

Two main components are derived from an interferometric pair. The phase is normally used to derive terrain height. The main application is typically DEM generation, but this component could be also used to estimate the tree height. Nevertheless, the high level of noise over forested areas (especially tropical forest) can not give good estimation of height. Then, for our purpose, only the coherence component derived from the interferometric pair is used.
To generate the interferogram, the two complex images must be first co-registered to within 0.1 pixel accuracy. This step is crucial in order to obtain a good quality of interferogram. A first coarse registration is realised using a serie of ground control points. The lack of bright and clear targets over tropical areas increases the difficulty of finding a good set of GCP's. Fine registration is then perform using correlation both on amplitude and phase.

The degree of coherence γ for each pair (s_1, s_2) of co-registered complex values s_1, s_2 is given by:

$$\gamma = \frac{\langle s_1 s_2^* \rangle}{\sqrt{\langle s_1 s_1^* \rangle \cdot \langle s_2 s_2^* \rangle}} \quad (2)$$

Where the bracket <...> represents an ensemble average, which is estimated by the spatial average over a finite-size window.

$$\langle s_1 s_2^* \rangle = \frac{1}{N} \cdot \sum_{i=1}^{N} s_{1,i} \cdot s_{2,i}^* \quad (3)$$

The value N should be sufficiently large (i.e.: 3x12 or 4x16 pixels window in range and azimuth) to have a good estimation of the degree of coherence within the window.

A first study has been conducted to access the quality of the interferograms that can be generated over tropical areas. Fig.(1).a and (1).b represent the histogram of coherence obtained using tandem and 35-day repeat passes. Low coherence was expected for vegetated areas, as a high coherence value over non-vegetated areas (bare soils, grasslands and deforested areas).

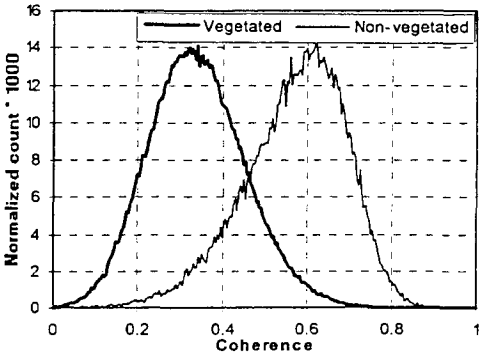

Fig. 1.a: Histogram of coherence for vegetated and non-vegetated areas. Tandem Mode

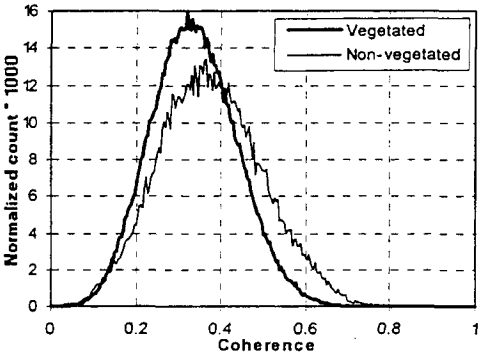

Fig. 1.b: Histogram of coherence for vegetated and non-vegetated areas. 35-days repeat-pass

For the tandem mode, there is a marked difference (of about 0.6) in the coherence level between the vegetated areas, where coherence is expected to be low due to the effect of volume scattering, and the non-vegetated areas. The latter, which comprises mainly of bare soil and deforested land, would be expected to give high coherence values. This is, however, not the case for the 35-day repeat-pass where the mean coherence level of the non-vegetated areas has a value of about 0.3, which is also the level for the vegetated areas. Plausibly, this decorrelation could be due to a change in weather conditions or land-use in the 35 days between acquisitions. Thus, while the degree of coherence in a tandem mode serves as a reliable discriminator between vegetation and non-vegetation, it is useless in the case of the 35-day repeat pass.

For forestry, tandem pairs are used to generate the interferometric components in order to reduce the effect of temporal decorrelation of the signal between the two acquisitions.
In addition, value of the baseline also plays an important role on coherence level. It has been demonstrated in [5] that γ level decreases when the baseline increases. For this reason, we have selected interferometric pairs with baseline less than 300m.

III.b Classification method

The main idea of our method is to use all available information derived from SAR and INSAR data to perform the classification process.
Using amplitude SAR images, the following parameters can be derived:
. backscattering coefficient σ^o
. backscatter intensity change $\Delta\sigma^0$ between two images
. texture
Thus, five parameters can be taken into account using two amplitude SAR images (σ^o_1, σ^o_2, $\Delta\sigma^0_{21}$, $texture_1$, $texture_2$). In addition, degree of coherence between two complex SAR images is computed using INSAR data.

On the whole, we can construct a vector of information I of n-order. The number n of discriminators depends on the number of SAR images taken into account for the analysis.
The following vector refers to a set of SAR data using two different dates:

$$I = [\sigma^o_1, \sigma^o_2, \Delta\sigma^0_{21}, texture_1, texture_2, \gamma_{21}] \quad (4)$$

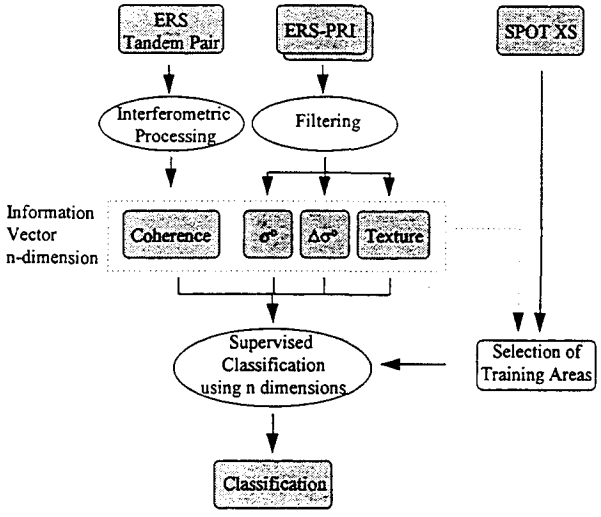

Fig. 2 : Graph of the classification method

First, a serie of training areas are selected from the SPOT XS image, given a representative set for the different types of landuse found in the image. In this case study, 5 training areas are chosen corresponding to primary forest, rubber, oil palm plantation, rice, bare soil. Then, a supervised classification is performed on the SAR components using the previous training set.

IV. RESULTS

A first analysis was conducted using 3 signatures (coherence, the backscatter intensity (σ°) and backscatter intensity change ($\Delta\sigma^\circ$)) derived from one tandem pair. The behaviour of the degree of coherence versus the backscattering coefficient is first analysed in order to demonstrate the usefulness of both components.

Fig (3) points out the good discrimination between vegetated (forest, plantation, cultivated areas) and non-vegetated areas (bare soil and deforested areas) using coherence. Nevertheless, different types of landuse could not be separated using only the coherence component. Oil palm plantation and rubber give the same degree of coherence. However, the backscattering coefficient σ° can then be used to discriminate these two types of landcovers. Unfortunately, primary forest and rubber could not be separated using both coherence and σ°.

The backscatter intensity change between two images acquired at different dates could be used to discriminate various landcover types. Different cultivated areas can then be identified by analysing the growth rate (2-3 months for rice). The change over seasons (dry and wet seasons) can alsso be a discriminator between plantation (small change over the year) and primary forest (very stable).

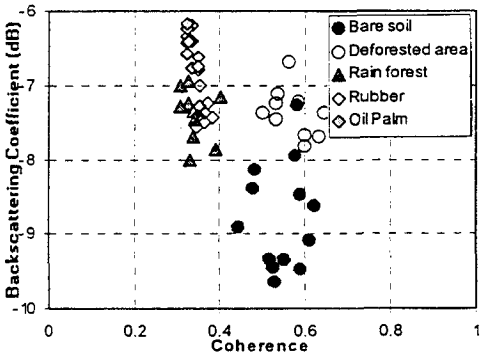

Fig. 3: Plot of σ° as a function of coherence for different classes of land-use. Tandem mode

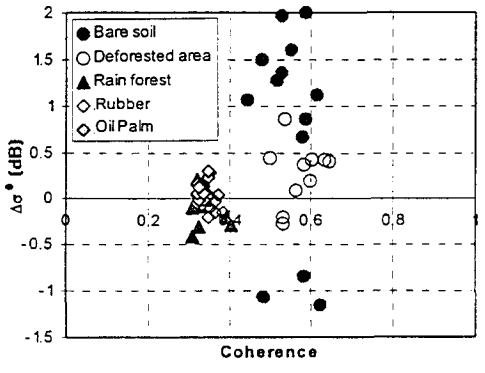

Fig. 4: Plot of $\Delta\sigma^\circ$ as a function of coherence for different classes of land-use. Tandem mode

Fig (5).a shows a color composition of three amplitude images (SAR.PRI full scene, R: 96/09, G: 96/05, B: 95/10) covering the entire test site. The bright patch at bottom right corresponds to the town of Jambi. Farming activities take place around the city and along the river Batang Hari. Bright grey areas represent primary and swamp forests. Changes in colour in the middle of the image is related to logging areas, where rapid deforestation takes place. Red patches correspond to new deforested areas, while yellow patches are related to regrowth areas. Coastal zone is composed of various cultivated areas, crops like rice (top right of the image), and different types of plantation (coconut, rubber and oil palm).

Fig (5).b is the coherence image over the same area. As expected, low coherence is found for forest. High coherence is related to bare soil, deforested areas (center of image), or small bushes. A very heterogeneous zone at the top right corresponds to paddy fields, for which various stages of growth could be found at the same time.

Fig. (5).c represents a colour composition (RGB) of coherence / σ° / $\Delta\sigma^\circ$. Areas with high coherence appear clearly in red, when areas with low coherence (primary and swamp forests) correspond to light blue areas. The discrimination between forest and non-forest appears very clearly, with very sharp edges. This image can be compared with Fig.(5).a.

Two test sites have been selected from Fig (5).a.

The first one (fig. (6.a,b,c,d)) corresponds to a forested area where intensive logging takes place, covering 25x20km.

Fig (6).a shows a colour composition of the three dates as described before. The difference between forested areas and plantation is not clear. Changes in colour can be related to change in moisture content and landuse (regrowth). For this raison, it is difficult to discriminate very clearly forest from non-forest areas.

Fig. (6).b represents the coherence. Very strong contrast between forested and non-forested areas is found. In addition, this information is recovered also in mountainous areas. In this case, fig. (6).a gives less information, when relief distortion is dominant. Notice that change index could not give a good discrimination between forest and plantation which are almost stable in time. In this case, only coherence can discriminate the two.

However, Fig (6).c represents the colour composition with coherence/σ°/$\Delta\sigma^\circ$. Clear and sharp limits between forest (yellow patches) and non-forest areas (blue) are very prominent.

The result can be visually compared with the SPOT XS image. New deforested areas can be seen in Fig (6).c at the center bottom (circle). This area is still forested on the SPOT XS image acquired 2 months before the tandem pair.

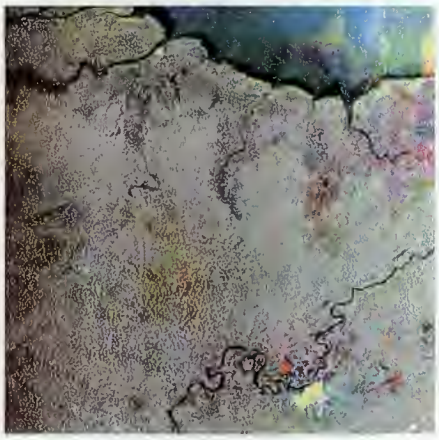

Fig. 5.a: Color Composition of 3 PRI, full scene

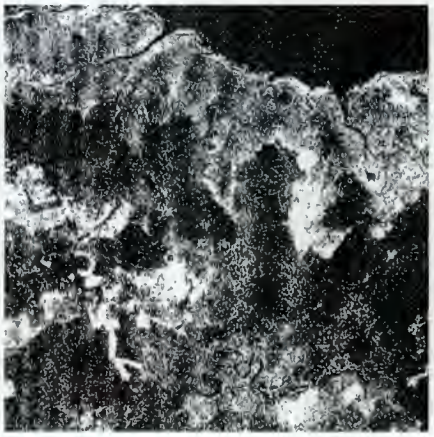

Fig. 5.b: Coherence image (tandem pass), full scene

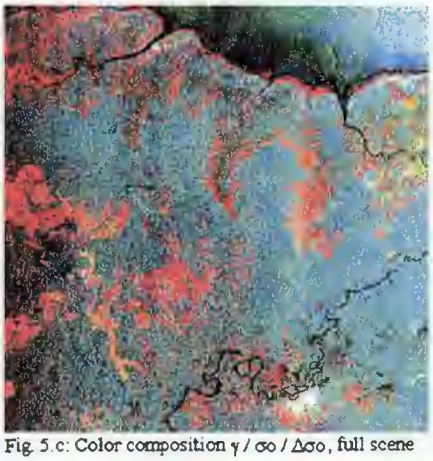

Fig. 5.c: Color composition γ / σo / $\Delta\sigma o$, full scene

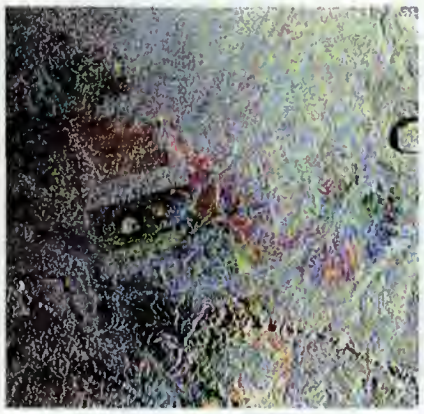

Fig. 6.a: Color composition of 3 PRI, logging area

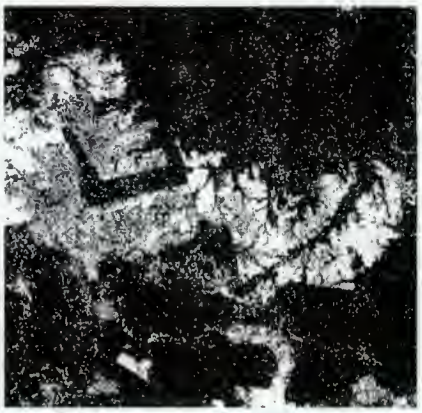

Fig. 6.b: Coherence image, logging area

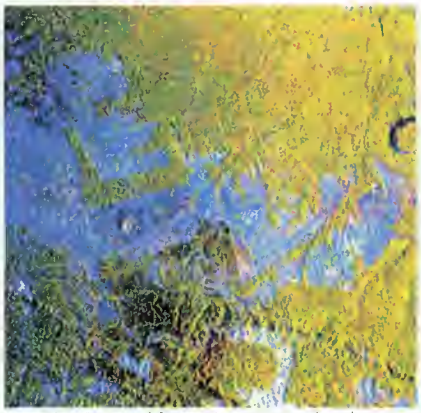

Fig. 6.c: Color Composition γ / σo / $\Delta\sigma o$, logging area

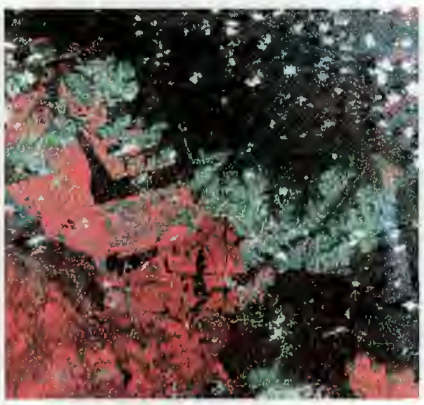

Fig. 6.d: SPOT XS Image, logging area

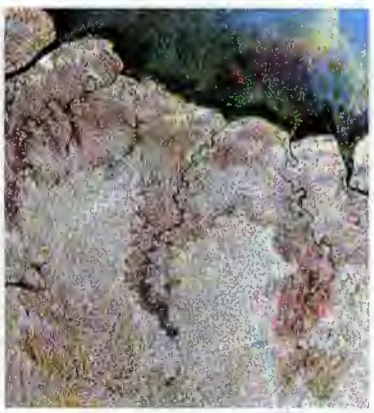

Fig. 7 a: Color Composition of 3 PRI, coastal zone

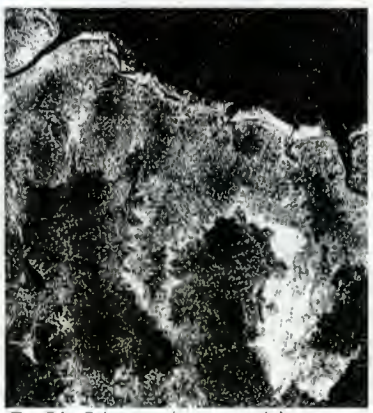

Fig. 7.b: Coherence image, coastal zone

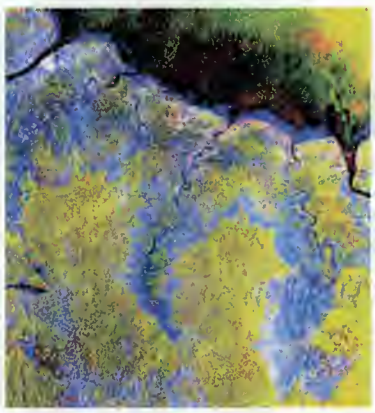

Fig. 7.c: Color composition γ / σo / $\Delta\sigma o$, coastal zone

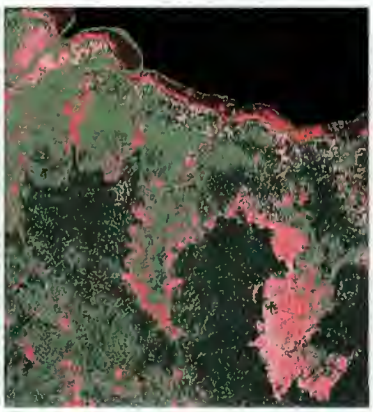

Fig. 7.e: Classification map, coastal zone

Fig. 7.d Landsat TM image, coastal zone

Color composition of 3 PRI:
. R: 96/09/22, G: 96/05/04, B: 95/10/07
. Coherence image: ERS Tandem pass 96/05/04-05
. Color composition γ / σo / $\Delta\sigma o$:
. R coherence, G: Amplitude 96/09, B Amplitude 96/05

The following example (Fig. (7.a,b,c,d,e)) shows results of the classification process over the coastal region, composed of swamp forest in the bottom of the image and cultivated areas along the coast (rice, rubber and oil palm plantation, coconut). Fig (7).a shows a colour composition of 3 PRI images. Canals, used to irrigate paddy-fields, appears in yellow at the top left of the image. Grey patches correspond to swamp forest. Linear features at the middle right correspond to intensive cultivated areas. Dark red patches along the river (top left) are related to rice.

Coherence image (Fig (7).b) shows a good contrast between plantation and forest. Logging areas located in hilly terrain (bottom left) appear clearly at the bottom left of the image. Logging routes and deforested areas then appear with a high coherence value in fig (7).b. These areas are not clearly visible in fig (7).a due to relief distortions which affect the amplitude of the radar signal.

Fig (7).c represents the colour composition with coherence/σ°/$\Delta\sigma^\circ$. This image can be compared with the Landsat TM image (Fig. (7).d) acquired in 1989. Nevertheless, some changes in lancover occured since 1989, especially along the boundary between swamp forest and cultivated areas.

Supervised classification is then performed on SAR/INSAR data set (Fig. (7).e), using training areas selected in the TM image. 4 classes was used over this site: forest, rice, coconut, rubber. Swamp forest is correctly classified (green), and a good contrast is obtained with rubber plantation (pink). Grey patches are related to coconuts. Moreover, a mixing between rubber and swamp forest is visible at the bottom left of the image. Rice appears in red (growing stage), and is located along the river. Nevertheless, some misclassifications appear, especially on heterogeneous areas (mixing between coconut and rice).

V. DISCUSSION / CONCLUSION

Multitemporal analysis is not sufficient for landcover classification over tropical areas. Some landcover types can not be discriminated, due to similar σ° and $\Delta\sigma^\circ$ (e.g.: forest and rubber).

However, it has been demonstrated that multitemporal study in combination with interferometric analysis can give useful information for landcover classification. The coherence component appears as a new discriminator. We have based our method on the use of a vector of information of n-order, composed of a serie of parameters derived from both SAR and INSAR data: coherence , σ°, $\Delta\sigma^\circ$, texture. Optical data is then used to define a training set in order to control the supervised classification. Further analysis will be conducted to improve the classification process, in order to reduce the percentage of misclassification.

Tandem pair is more appropriate for this kind of study, in order to reduce the temporal decorrelation of the signal. Moreover, small baselines are required to avoid a degradation of the level of the coherence due to baseline decorrelation.

Nevertheless, sensitivity to biomass remains low with C-band. Moreover, L-band appears to be more suitable for this type of application. To significantly improve the methodology, combination of both ERS and JERS-1 data should be used for this application. Backscattering coefficient and backscatter change intensity could then be derived from JERS-1 Data, and combined with coherence component extracted from ERS interferometric pair.

Examples presented in this paper show that the combination of coherence, σ° and $\Delta\sigma^\circ$ allows to discriminate various landcover types, and also to distinguish very fine features. For this reason, as an analogy with SPOT, this colour composite (coherence, σ°, $\Delta\sigma^\circ$) could be useful for visual interpretation in order to supplement the lack of optical data.

REFERENCES

[1] L.C. Graham, "Synthetic interferometer radar for topographic mapping", in *Proc. Inst. Electron. Eng.*, Vol 62, p. 763, 1974.

[2] A.K. Gabriel and R.M. Goldstein, "Crossed Orbit Interferometry: Theory and Experimental Results from SIR-B", *Int. J. of Remote Sensing*, 9(5), 857-872.

[3] U. Wegmuller and C. L. Werner, "SAR Interferometric Signatures of Forest", *IEEE Trans. Geosci. Remote Sensing*, Vol. 33, no. 5, 1995, pp 1153-1161.

[4] N. Floury, T. Le Toan and J.C. Souyris, "Relating forest parameters to interferometric SAR", in *Proc. IGARRS '96*, Nebraska, USA, May 27-31, 1996, pp 975-977.

[5] H.A. Zebker and J. Villasenor, "Decorrelation in Interferometric Radar Echos", *IEEE Trans. Geosci. Remote Sensing*, Vol. 30, no. 5, 1992, pp 950-959.

[6] F. Gatelli, A. M. Guarnieri, F. Parizzi, P. Pasquali, C. Prati and F. Rocca, "The Wavenumber Shift in SAR Interferometry", *IEEE Trans. Geosci. Remote Sensing*, Vol. 32, no. 4, 1994, pp 855-864.

[7] N. Stussi, L. K. Kwoh, S. C. Liew, K. Singh, H. Lim, "ERS-1/2 Interferometry: Some Results on Tropical Forest", *FRINGE 96*, Zurich, Switzerland, October 1996.

[8] J. Bruniquel, A. Lopes, "Multi-variate Optimal Speckle Reduction in SAR Imagery", *Int. J. Remote Sensing*, 1997, Vol. 18, No. 3, 603-627.

DEM

Chairperson: **F. Adragna**

POTENTIAL OF ERS-1 DERIVED ORTHOMETRIC HEIGHTS TO GENERATE GROUND CONTROL POINTS

Dowson, M.

Spatial Information Systems Unit, School of Computing Sciences,
De Montfort University, Leics LE1 9BH, UK
E-mail: mzd@dmu.ac.uk Tel: +44 116 257 7462

Berry, P.A.M.

Spatial Information Systems Unit, School of Computing Sciences,
De Montfort University, Leics LE1 9BH, UK
E-mail: pamb@dmu.ac.uk Tel: +44 116 257 7497

ABSTRACT

In order fully to utilise the high number of valid returns from the ERS-1 altimeter over the earth's land surface during the geodetic mission, the precision to which altimeter derived heights can be generated over land surfaces must be investigated

In this paper, Waveform Altimeter Product data retracked using an expert system (described elsewhere), to optimise the determination of individual heights have been used at two test sites, which include the whole of Zimbabwe, and part of the USA, to investigate the extent to which retracked altimeter data can be used to generate Ground Control Points for geodetic purposes. This paper presents results of both internal comparisons between spatially correlated returns from different orbit arcs near crossovers, and direct comparison with ground truth. The results obtained over these test areas have demonstrated that altimeter crossovers over land can be determined to an internal precision of better than one metre and show good agreement with ground truth.

1. INTRODUCTION

The orthometric height information derived by retracking ERS-1 land altimetry data from the geodetic mission has many potential applications. One possible use of such data is to generate ground control points. However, this can only be done if it can be demonstrated that under certain conditions the heights obtained are extremely accurate.

In order to investigate the behaviour of the retracked dataset, data over test areas has been analysed close to crossover points. This paper presents results of this analysis from two test areas; the whole of Zimbabwe, and part of the central USA. Comparison with ground truth is also presented.

2. DATA

2.1 Zimbabwe

A test area from Zimbabwe was chosen for the initial analysis, because of the varying nature of the terrain, which includes large areas of low to moderate slopes. Retracked altimeter data from the ERS-1 geodetic mission, previously transformed to orthometric heights referenced to the WGS84 ellipsoid, were selected over this area, at the full 20Hz resolution. Detailed discussion of the techniques used in producing this dataset can be seen elsewhere [1,2,3,4]. All crossovers where data points existed in close proximity were identified and graphed (Figure 2.11) to confirm the existence of a sufficiently dense network.

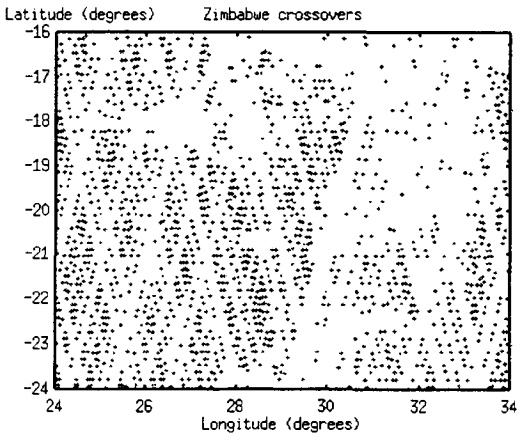

Figure 2.11 Crossovers over Zimbabwe

2.2 USA

An 8^{o} x 8^{o} test area in central USA, already being utilised for comparison with GLOBE global digital elevation model heights [2,8,9] was also used for this analysis as it contained areas of widely varying topographic roughness. Although data dropout was

found to be significant over the most varying terrain, a usable number of crossovers satisfying the same constraints as for the Zimbabwe dataset were still found to be present (Figure 2.21).

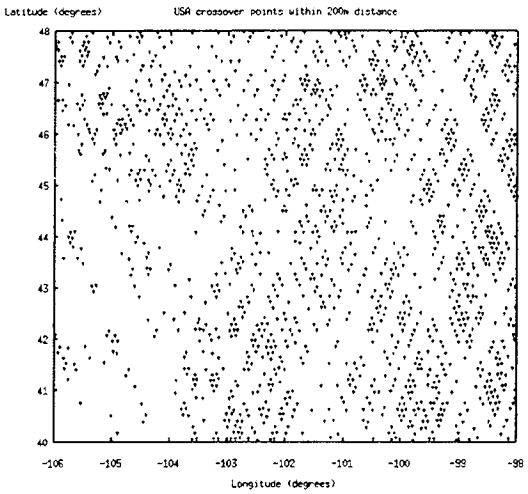

Figure 2.21 Crossovers over USA Test Area

3. ANALYSIS

Over the ocean, crossover point analysis is a well-understood and widely used technique for assessing the quality of altimeter data. However, the fundamental assumption - that the height from ascending and descending tracks should be the same when interpolated to a crossover point - is evidently invalid over land. Here, crossover points are used as a means of identifying orthometric heights from different arcs that result from echoes from the surface lying in close spatial proximity.

For the geodetic mission data, the density of crossover points means that a data driven approach rather than a global solution is more appropriate for crossover point detection. For this research, crossover points are calculated for each test area from the actual data, and all data points within a certain radius of the crossover point are identified.

In this work, the six closest pairs of points to each crossover point have been considered. The separations were calculated, and the height differences obtained. One advantage of this approach is that errors in the geoid model used to convert to orthometric heights do not appear in the height differences. This is of relevance as there are known errors in high order terms of the OSU91 geoid model.

3.1 Zimbabwe Results

For all closest data pairs whose nominal separation (calculated from the waveform latitude and longitude) did not exceed 200m, the height differences were calculated and statistics generated. Results are summarised in Figure 3.11 for all 1820 crossovers satisfying the constraints. It is evident that for 70% of the crossover pairs, agreement is reached to within 2m. This extremely good result is clearly in part a function of the comparitively gentle terrain relief over much of Zimbabwe and the surrounding area. Detailed plots of the spatial distribution of crossover pair differences over the region confirmed the clear relationship between terrain relief and crossover pair agreement. However, even in the most severe terrain, many data pairs agreed to within a few metres.

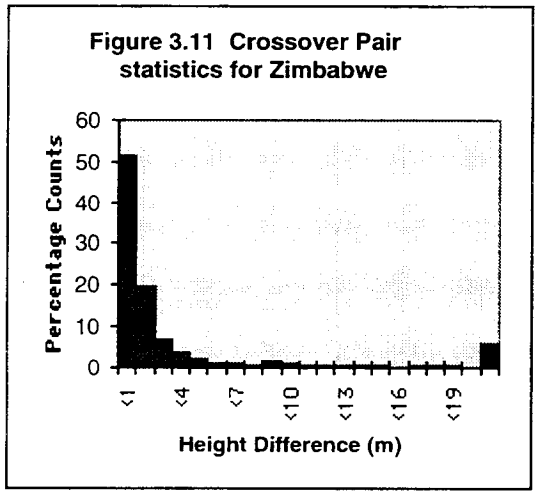

3.2 USA Results

In order to examine the behaviour of altimeter data over varying terrain, data from the USA test area were analysed, using the same constraints as for the Zimbabwe dataset. Statistics for the crossover differences are summarised in Figure 3.21.

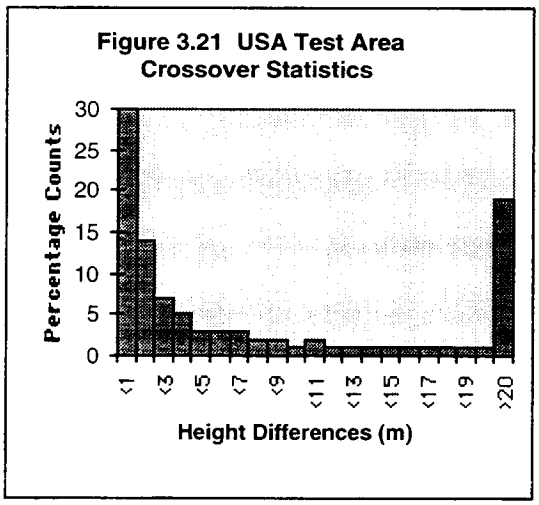

It is clear that, whilst very good agreement is found for a significant proportion of the crossover pairs, the difference distribution is less good than for the

Zimbabwe dataset. Analysis of the crossover pair distributions with height difference over the test area showed a very non-uniform distribution. Accordingly, statistics were calculated for each each 2^{o} x 2^{o} subset of the area. Sample graphs are shown in Figure 3.22

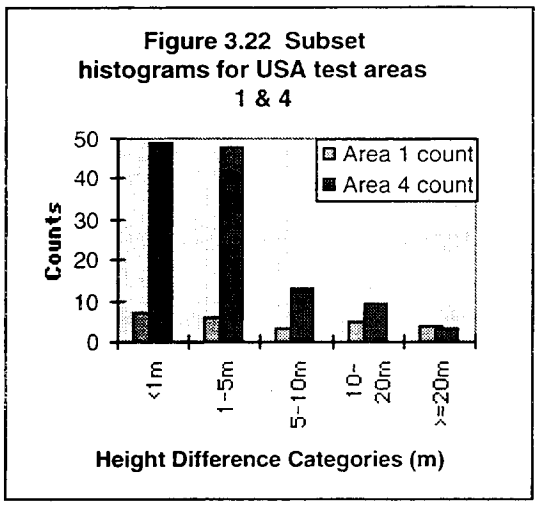

Figure 3.22 Subset histograms for USA test areas 1 & 4

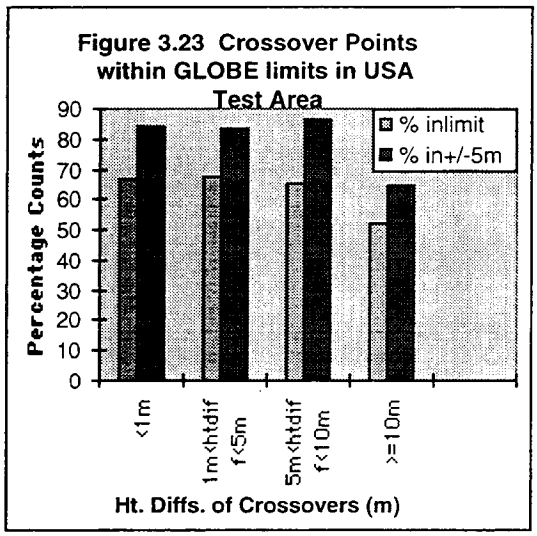

Figure 3.23 Crossover Points within GLOBE limits in USA Test Area

The availability of the GLOBE dataset enabled additional comparisons to be carried out with ground truth. It should be noted that the GLOBE dataset consists of 1km mean, maximum and minimum height pixel values with an estimated accuracy of +/- 5m at best. GLOBE heights for each crossover point (maximum, minimum and mean) were compared against the altimeter heights (higher, lower and average for each data pair) and grouped according to the crossover pair height difference. As in many cases all three GLOBE heights were found to define a very narrow height band, it was decided to relax the constraint to allow for the known inaccuracy in the GLOBE dataset and calculate all statistics for both comparison criteria. A sample output is included in Figure 3.23; this demonstrates clearly the effect of relaxing the GLOBE constraints, and also illustrates the good agreement obtained with the ground truth. More detailed comparisons with GLOBE are presented elsewhere [8,9].

4. DISCUSSION

It is clear that the agreement between values on ascending and descending tracks can be extremely good in areas of varying terrain. Discrepancy does not of itself imply error, since over rough terrain the actual height distribution illuminated may vary appreciably between returns spatially adjacent. In this context, further analysis of the altimeter performance over varying terrain is clearly required; results to date from the evaluation of the contribution of off-ranging errors are very encouraging [2,5,6,7,9]. Detailed investigation to identify those parts of the surface which have contributed significantly to the return waveform is continuing

The proportion of results where the nearest pair of points agree to within 1m is very high for both test sites. The extremely close agreement found generally (with over 70% of closest pairs agreeing in height to within 2m over Zimbabwe, together with the good results for GLOBE comparison at crossover points) also has implications for the current processing chain used for orthometric height determination. Whilst errors in atmospheric and instrument corrections, and radial orbit error have previously not been considered to add appreciably to the error budget for the majority of land altimetry data the finding that for some data consistent measurements over land can be made to high accuracy means that this approach needs to be re-addressed. It may well also prove necessary to consider regional geoid solutions rather than a global model.

5. FURTHER WORK

Currently direct comparison of results against GPS measurements over test areas are being made. Results from the research will then be incorporated in the decision process of the expert system used for altimeter retracking, to enable the generation of accurate ground control points.

6. ACKNOWLEDGEMENTS

The authors are indebted to ESA for release of the WAP dataset, and to RAL and Leicester University for the loan of equipment used in this research.

7. REFERENCES

1. Berry, P.A.M. & Blewitt, G., 1994. *Geodesy from Space.* Geoscientist, Vol. 4, No. 4, pp14 - 16.

2. Berry, P.A.M., Mathers, L., & Dong, Chang Cheng. 1995. *Comparison of Global Digital Elevation Model with Altimeter Topographic Heights.* RAL Report 2010/95-05/01.School of Computing Sciences, De Montfort University, Leicester . May 1995.

3. Berry, P.A.M., Leigh, M., Bennet, J. & Cox, D.M., 1996. *Towards Orthometric height determination from satellite altimeter data.* COSPAR, Birmingham, August 1996.

4. Berry, P.A.M. & Cox, D.M., 1996. *Orthometric Height Determination From ERS-1 Satellite Altimeter Data.* Advances in Space Research. In press.

5 Dowson,M. & Berry, P.A.M. 1996. *Potential of ERS-1 Derived Orthometric Heights to Generate Ground Control Points: First Results.* European Conference on Satellite Altimetry III, Oporto, October 96

6. Berry, P.A.M., Horton, J. & Dhillon, S., 1996. *Statistical analysis of waveform data and derived orthometric heights from ERS-1 data over Australia.* European Conference on Satellite Altimetry III, Oporto, October 96.

7. Bracke, H., Berry, P.A.M. & Dowson, M. 1996. *Geodetic Applications of ERS-1 Altimeter Data Over Land.* American Geophysical Union Fall Meeting, December 1996.

8. Berry, P.A.M., Leigh,M. & Cox, D.M., 1996. *Topographic Mapping using Satellite Altimetry.* American Geophysical Union Fall Meeting, December 1996.

9. Berry, P.A.M., & Leigh, M., 1997. *Use of ERS-1 Land Altimetry to Validate and Correct Global Digital Elevation Models.* This issue.

RETRACKING ERS-1 ALTIMETER WAVEFORMS OVER LAND FOR TOPOGRAPHIC HEIGHT DETERMINATION: AN EXPERT SYSTEMS APPROACH

Berry, P.A.M.

Spatial Information Systems Unit, School of Computing Sciences,
De Montfort University, Leics LE1 9BH, UK.
Tel: +44 1162 577497 email: pamb@dmu.ac.uk

Bracke, H.

Spatial Information Systems Unit, School of Computing Sciences,
De Montfort University, Leics LE1 9BH, UK.

Jasper, A.

Spatial Information Systems Unit, School of Computing Sciences,
De Montfort University, Leics LE1 9BH, UK.

ABSTRACT

The behaviour of altimeter echoes over land from the ERS-1 geodetic mission has been investigated. Highly complex altimeter echoes are observed over much of the terrain not sampled by previous altimeters due to loss of lock. Investigation into the effects of off-ranging has shown that for low to moderate slopes this effect is not observed as significant over validation areas; accurate height data can be determined. Attention has therefore been focussed on improving retracking performance and an expert system has been developed to retrack individual waveforms using a range of retrackers specifically configured to interpret echoes over land. Results are presented indicating the value of an expert system approach to land altimetry retracking.

1. INTRODUCTION

The ERS-1 mission resulted in the acquisition of large volumes of echoes over non-ocean surfaces. Whilst returns over ice have been the focus of considerable research, the land altimetry dataset has been much less studied.

Detailed study of data from the 35 day repeat mission demonstrated the potential for accurate height generation from ERS-1 altimeter data over land [1,2,3] with recovery of good height data found to be essentially independent of altitude, dependant primarily on the severity of the terrain relief. Subsequent retracking of the entire geodetic mission WAP dataset, and analysis of the results including series of comparisons with ground truth, confirmed this initial finding and indicated that very good agreement between ground truth and retracked altimeter data could be obtained [4, 5]. An investigation into the error budget for land altimetry was therefore carried out.

2. ERROR BUDGET

2.1 GLOBE analysis

The primary source of error for altimeter data over topographic surfaces occurs when the altimeter receives a strong return from an off-nadir sloping surface within the illuminated footprint [4].

Following initial evaluation with one cycle of 35 day data over the Rift Valley, Kenya [12] which showed less evidence of off-ranging than had been expected, a test area in the central USA was selected for a study into the effects of slope induced error on altimeter derived height estimates over land. A brief summary of the results is included here.

Figure 2.11 shows a series of sample profiles of altimeter derived 1 km mean heights plotted against the GLOBE GDEM values for the corresponding 1km pixels; overlaid on these graphs is the along track slope calculated from the GLOBE dataset. Note that these estimates refer to mean slopes over 1km pixels; these values will therefore tend to under-represent the actual slopes present in the terrain. Analysis of all profiles considered shows that for mean slopes of less than 0.8 degrees, no systematic effects of off-ranging are detected. For higher slopes, a characteristic lateral displacement of feature is occasionally observed. However, even when present, the vertical errors are lower by a factor of 2 or 3 than would be expected from a

Figure 2.11a Area 3 Profile with along track slope

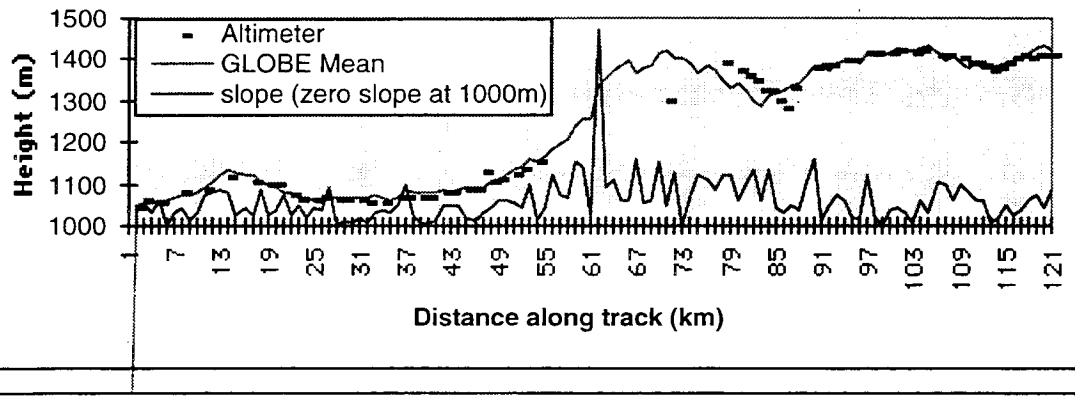

Figure 2.11b Profile Area 4 with along track slope

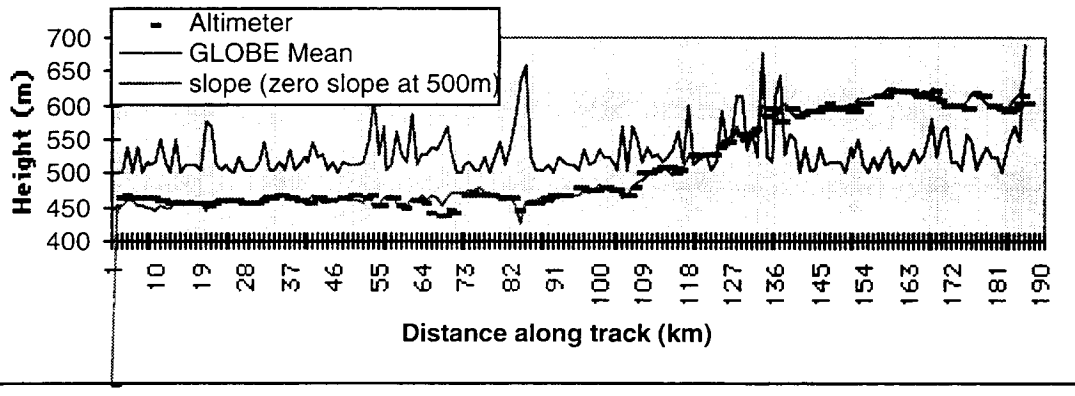

Figure 2.11c Profile Area 7 with along track slope

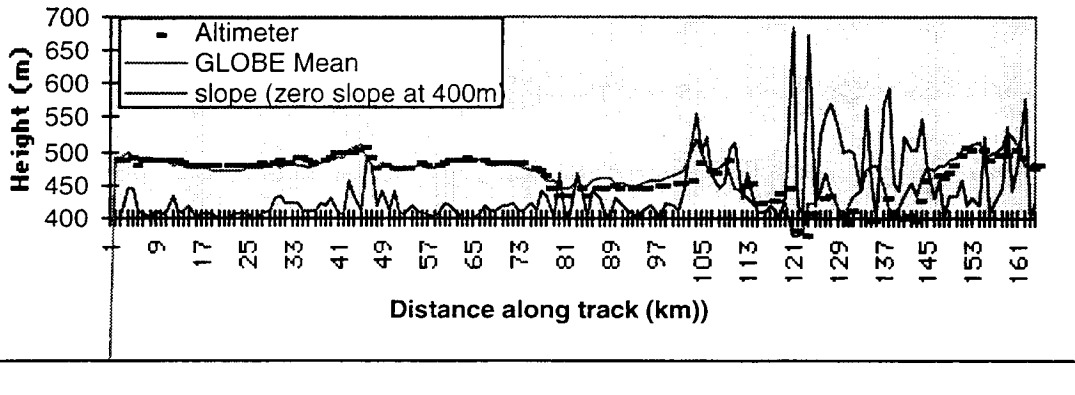

simple calculation for off-ranging from a uniform slope [4] , as are the horizontal displacements. This is a not unexpected finding, as slopes over land are not generally well characterised by a single mean value for a region, but typically comprise an aggregate of areas of differing extent and slope. A more realistic model for this effect is currently being addressed. Results from crossover analyses over Zimbabwe and the USA test areas [8,10,13] also confirm the internal consistency of the altimeter measurements.

The results over the test areas indicate that for a large proportion of data, slope induced error is not a significant error factor. This offers the possibility of obtaining orthometric height data from much of the ERS-1 geodetic mission data. However, this research also confirmed that highly complex and variable altimeter echoes are observed in this dataset, primarily over terrain not sampled by previous altimeters due to loss of lock. Initial research indicated that simple retracking techniques such as threshold retracking were not adequate to derive accurate height estimates from these complex waveforms [2,3,6,9]. To optimise the accuracy of data derived from this unique dataset, an expert system has therefore been developed to retrack individual waveforms using a range of retrackers specifically configured to interpret these echoes.

3. EXPERT SYSTEM

The expert system works within a processing chain to process data from ERS-1. From the input WAP datastream the raw altimetry data is abstracted and processed through a series of algorithms prior to input to the expert system. These algorithms include checks to exclude obviously erroneous data, or data for which vital auxiliary information is missing, but may still include 'unusable' waveforms, for example where the leading edge is missing.

Accordingly, the expert system has been developed following an interpretation system design. The method of knowledge representation within this altimetry system is the procedural knowledge representation. Input waveforms are analysed by specific rules. Following the analysis a decision is made about which retracker will be used and in which way the output will be built. Following the rule-based system the inference engine of this expert system is based on the forward chaining technique.

3.1 Rule-based expert system

A rule-based expert system is a computer program that processes problem-specific information contained in the working memory with a set of rules contained in the knowledge base, using an inference engine to infer new information.

The rule-based expert system is shown by the following model (Figure 3.11):

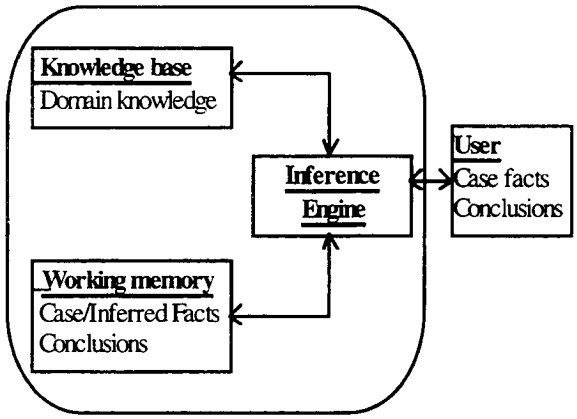

Figure 3.11 Rule-based expert system

In the rule-based system used, the rules contained in the knowledge base represent the productions contained in the long-term memory (waveform specification) and the facts contained in the working memory represent the situations in the short-term memory (altimetry data). The inference engine acts as the reasoning module of the production system model and compares the facts with the rules. Those rules that fire have their conclusions added to the working memory (using flags) and the process continues. Rule-based expert systems like this are not necessarily an exact match for human problem solving, but they provide a reasonable model for replicating this behaviour with a computer.

3.2 Design of expert system

The expert system fits within the existing processing chain (Figure 3.21), inputting and preprocessing one orbit of data at a time. The waveforms are then analysed and retracked individually. If no preference is given a decision is made according to the analysis results and the expert system rules. When the retracking of one waveform is completed, the output is generated. The process of decisions, retracking and outputting repeats for all data in the orbit file. All or a combination of the existing retrackers can also be run over all data for comparison purposes.

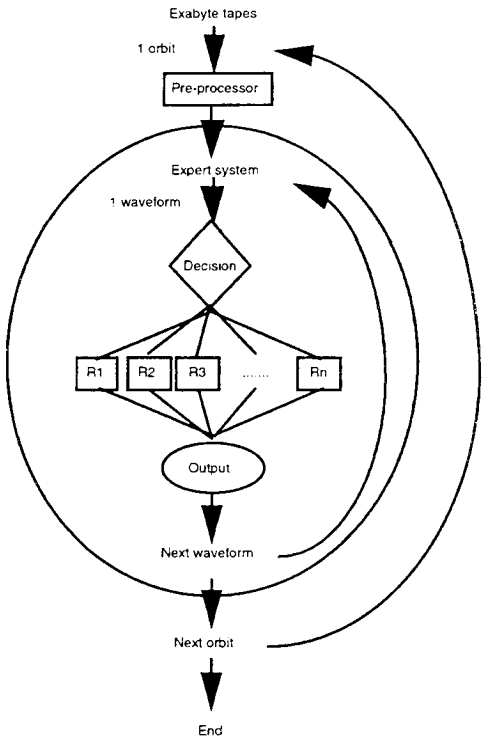

Figure 3.21 Expert System Overview

3.3 Characteristics of rule-based systems

A few notes on the advantages of rule-base systems are summarised for completeness in this section:
- Natural Expression: Because humans naturally express their problem-solving knowledge in IF...THEN type statements, it is easy to capture knowledge in a rule making the rule-based approach an easy to understand approach for the design of an expert system.
- Separation of control from knowledge: This feature is not unique to rule-based systems but is a trademark of all expert systems. This valuable feature permits a change to be made in the system's knowledge or control separately.
- Modularity of knowledge: A rule is an independent chunk of knowledge; thus its correctness can easily be reviewed and verified.
- Ease of expansion: The separation of the system's knowledge from its control permits additional rules to be included easily, allowing for a graceful expansion of the system's knowledge
- Proportional growth of intelligence: Even one rule can be a valuable piece of knowledge. As the number of rules increases, the system's level of intelligence about the problem likewise increases.
- Use of relevant knowledge: The system will use only the rules that are relevant to the problem.
- Consistency checking: The rigid structure of the rule also allows for consistency checking of the system to ensure that the same situations do not lead to different actions.
- Utilisation of heuristic knowledge: Rule-based systems are well suited for working with this heuristic knowledge. Most heuristic rules that work in a common-sense fashion draw conclusions or efficiently control the search of the knowledge base.

4. RESULTS

4.1 Initial evaluation

An analysis of typical waveform shapes over Zimbabwe [8,10,13] indicated that many waveforms were 'pre-peaked', with a significant peak appearing prior to the main peak. Under these circumstances, the performance of threshold retracking was not found to be in agreement with other retrackers used (although such differences were found to be generally fairly small, on the order of a few metres). Additionally, significant numbers of waveforms demonstrated an elongated leading edge with multiple peaks; high differences between retracker results and known GPS ground points were observed for these waveforms, often of many tens of metres. A new retracker was developed to deal with these waveforms. Following this analysis, four retrackers and a set of rules were programmed into the expert system and the data over the test area were processed.

4.2 Waveform and statistical results over test areas

For results presented here, the Delta implementation of the expert system has been used. This development version incorporates rules and retrackers based on results from the comparison of 35 day data with regional DEMs, the initial retracking analysis of the geodetic mission data and detailed analyses of these data over test areas including comparison with regional DEM and point ground truth [9,10,11,12,13].

A statistical breakdown of the retrackers called by the expert system for all valid data points over two test areas is given in Figure 4.21. A key is given in Table 4.22, together with brief notes. Note the high number of specular returns over Zimbabwe, attributed to data acquired during the rainy season.

Typical results for a 1% sample of data where the BOR retracker was used are given in Figure 4.23. Detailed analysis of expert system retracked altimeter data is presented elsewhere [12,13].

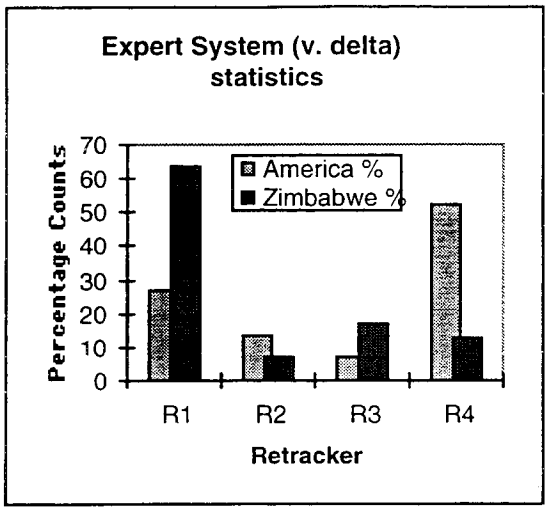

Figure 4.21 Expert System Output Statistics

ID	Retracker	Notes
R1	Threshold	The default retracker (set at 50%)
R2	Specular	Retracks specular waveforms separately
R3	Spline	Default for pre-peaked waveforms
R4	BOR	Selects complex waveform shapes

Table 4.22 Retracker Key

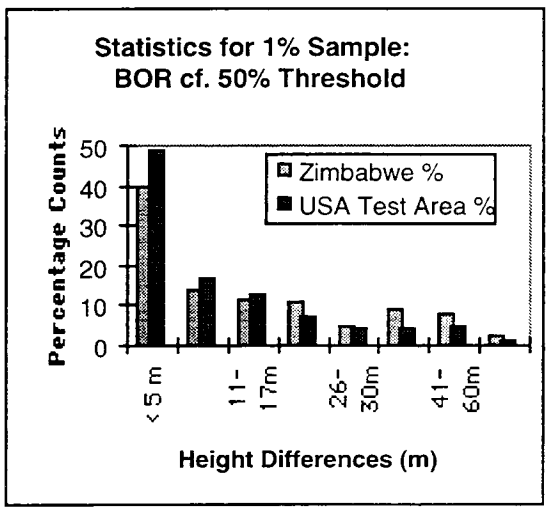

Figure 4.23 Comparison of retracker outputs for 1% sample

5. DISCUSSION

The results obtained using the expert system are currently being evaluated and the rules tuned using comparison with ground truth. However, it is already clear that each new rule increases the terrain related information returned by the expert system. Gains on well-behaved waveforms (near vertical leading edge with low retrack correction) are minimal; on more complex waveforms differences of 40m between retracker outputs are not uncommon. Examination of slope-induced error shows that the altimeter is preferentially ranging to low slope areas close to nadir; thus many returns where the mean slope is in excess of 0.5 degrees can still be retracked. However, waveforms obtained from surfaces of significant mean slope tend to have complex shapes, and threshold retracking is not found to perform well. For regions of appreciable topographic relief the advantage of an expert system approach to land altimeter retracking becomes apparent.

6. ACKNOWLEDGEMENTS

The authors are indebted to the European Space Agency for supply of the WAP dataset, and to Rutherford Appleton Laboratory and Leicester University for the loan of equipment which facilitated this research.

7. REFERENCES

1 Berry, P.A.M. & Blewitt, G., 1994. *Geodesy from Space*. Geoscientist, Vol. 4, No. 4, pp14-16.

2 Berry, P.A.M., Mathers, L., & Dong, Chang Cheng, 1995. *'Comparison of Global Digital Elevation Model with Altimeter Topographic Heights.'*. RAL Report 2010/95-05/01,School of Computing Sciences, De Montfort University, Leicester , May 1995.

3 Berry, P.A.M., 1995a. *Role of Satellite Altimetry in Determination of Land Topography*. Proceedings, IUGG XXI Assembly, Boulder, July 1995.

4 Brenner A.C., Bindschadler. R.A., Thomas, R.H. & Zwally, H.J., 1983. *Slope induced errors in radar altimetry over continental ice sheets*. J.G.R. v88, no. C3.

5 Berry, P.A.M., 1995b. *Geodetic Research using Satellite Altimetry*. Proceedings, I.M.A. Conference on Image Processing, Oxford University Press. In press.

6 Berry, P.A.M ., 1996. *Detailed Evaluation of Orthometric Height Recovery from ERS-1*. European Conference on Satellite Altimetry III, Oporto, October 96.

7 Bracke, H.W.M. & Berry, P.A.M. 1996. *An Initial Evaluation of Expert System Performance for ERS-1 Height Recovery over land.* European Conference on Satellite Altimetry III, Oporto, October 96.

8 Dowson,M. & Berry, P.A.M. 1996. *Potential of ERS-1 Derived Orthometric Heights to Generate Ground*

Control Points: First Results. European Conference on Satellite Altimetry III, Oporto, October 96.

9 Horton, J., Dhillon, S. & Berry. P.A.M., 1996. *Statistical analysis of waveform data and derived orthometric heights from ERS-1 data over Australia.* European Conference on Satellite Altimetry III, Oporto, October 96.

10 Bracke, H., Berry, P.A.M. & Dowson, M. 1996. *Geodetic Applications of ERS-1 Altimeter Data Over Land.* American Geophysical Union Fall Meeting, December 1996.

11 Berry, P.A.M., Leigh,M. & Cox, D.M. *Topographic Mapping using Satellite Altimetry.* American Geophysical Union Fall Meeting, December 1996.

12 Berry, P.A.M. & Leigh, M., 1997. *Use of ERS-1 Land Altimetry to Validate and Correct Global Digital Elevation Models.*This issue.

13 Dowson,M. & Berry, P.A.M., 1997. *Evaluation of Potential of Geodetic Applications of ERS-1 Altimeter Data over Land.* This issue.

TOPOGRAPHY OVER SOUTH AMERICA FROM ERS ALTIMETRY

Anita Brenner(1), Herb Frey(2), John DiMarzio(1), Lucia Tsaoussi(1)

(1)Hughes STX Corp.
Suite 400
7701 Greenbelt Road
Greenbelt, MD 20770
phone (301)441-4000
fax (301)441-2432
anita@ice.stx.com
john@ice.stx.com
lucia@ice.stx.com

(2)NASA/Goddard Space Flight Center
Code 921
Greenbelt, MD 20770
frey@denali.gsfc.nasa.gov
phone (301)286-5450
fax (301)286-1616

ABSTRACT

The surface topography of South America is mapped from the entire ERS-1 geodetic mission and two 35-day cycles from phase G. The Waveform Altimeter Product from the UK-PAF provides the altimeter waveforms, the range measurement, and the internal and doppler range corrections. We calculate the atmospheric corrections and solid tides, and utilize the University of Delft DGM-E04 precision orbits. Retracking range corrections are calculated using a modified version of the NASA/GSFC waveform retracking algorithm. Our editing scheme removes measurements where the altimeter is hanging onto a specular surface that is not at the subsatellite location. Additional editing is implemented to remove measurements where the tracker has bypassed the closest surface by comparison of the pre-leading edge signal to the overall waveform power. An iterative procedure is used to calculate a 1/4 degree grid from the altimetry, slope correct the altimetry elevations using this grid, and regrid the data. The gridded elevations are then referenced to the NASA/GSFC and NIMA EGM96 geoid. Comparisons of the full-rate altimetry to profiles interpolated from the 1996 ETOPO5 DEM show several instances where altimetry yields detailed topography but the ETOPO5 DEM is smooth due to lack of data. A 1/4 degree grid of the ETOPO5 DEM was created and compared with the altimetric grid. Plots of these grids delineate whole regions where the altimetry results show topographic features that are smoothed over in the ETOPO5 grid. Comparisons of Shuttle laser altimetry data to the ERS-1 altimetry grid demonstrate agreement in many locations at the sub-meter level. Future plans are to create a moredetailed topographic map combining altimetry from other missions (Geosat geodetic, Seasat, and TOPEX) to increase the resolution of the DEM.

INTRODUCTION

(Frey and Brenner, 1990) showed that the Seasat over-land measurements could be used, after post-processing of the altimeter waveforms, to measure topography. The Seasat altimeter, however, exhibited many data dropouts and the groundtracks were too sparse for detailed topographic mapping. The Geodetic mission data from Geosat had better geographic coverage, but until recently was classified and is not yet completely available. The ERS-1 altimeter was the first satellite altimeter designed to track over ocean, land, and ice surfaces. Previous altimeters, GEOS-C, Seasat, and Geosat were designed for ocean tracking only.

Two major factors make the ERS-1 altimetry the best available for overland topography. First, the ERS-1

Proc. 3rd ERS Symp. on Space at the service of our Environment, *Florence, Italy, 17–21 March 1997* (ESA SP-414, 3 Vols., May 1997)

tracker uses a coarser ice tracking mode over the continents that give it the ability to maintain track over the rougher land terrain while only degrading the resolution of the height measurement by a factor of 4 from that in ocean tracking mode. Second, the geodetic portion of the ERS-1 mission consists of two 168-day repeat cycles offset from each other to give a ground-track spacing of 8.5 km at the equator.

DATA PROCESSING, RETRACKING, AND PRECISION

To obtain precise land elevations from ERS-1 satellite altimetry, it is necessary to post-process the altimeter return waveform to correct for tracker misalignment. The UK-PAF's Waveform Analysis Product (WAP), provided through the ESA project, was used as the source of the altimeter range measurement and waveform, the internal range correction, and the doppler range correction. The atmospheric corrections were calculated using the ECMWF data and the University of Texas CSR3.0 tide model (Eanes 1994) was used to model the solid, load and pole tides. The surface elevations were calculated with respect to an ellipsoid of radius 6378137.0 m and a flattening of 1/298.257 using the DGM-E04 orbits (Scharroo et. al., 1996).

The data was retracked using the NASA/GSFC Version 4.0 retracker (Zwally et. al., 1997). The retracking process fits a single-ramp or double ramp (5 or 9-parameter) function to each waveform. The retracker is tuned to pick up distinct ramps and to ignore slight leading edge noise due to vegetation canopy. Altimeter measurements for which the waveform does not have one or two distinct ramps are edited. Analysis of the height residuals at crossing arcs on the corrected, retracked altimetry showed that 9% of the crossing arc differences were greater than 50m. Investigating the waveforms near these crossovers showed two distinct problems; 1) there was excessive signal before the first ramp which may be indicative of the altimeter missing the first return and locking onto a signal from another location, and 2) the altimeter would maintain lock on a specular surface hanging onto the surface even after the satellite moved to another location.

To correct the first problem, the retracking process was modified to edit out returns where the average pre-ramp signal was greater than 20% of the maximum count in any one gate of the whole waveform. This edited out the returns that were truly from a different location, without editing out returns that had a pre-ramp noise due to vegetation canopy. Examples of typical returns over a vegetated region of South America are shown in figure 1 where the raw waveform returns are pictured with the NASA/GSFC Version 4 functional fit and retracking locations for both the functional fit and a 20% threshold retracker. The corresponding altimeter height profile for non-retracked data, threshold retracked data and the functional retracked data is shown in figure 2. Note that the threshold retracking sometimes picks up what the functional fit considers as pre-ramp noise. The threshold retracker may be picking up canopy where the functional-retracked profile appears to follow a more realistic surface. Figure 1 also shows that there is a second distinct spike in the waveforms which increases in amplitude from measurement to measurement. South America is laced with many rivers; these returns indicate there may be a river farther away (around 12 km) that has a more specular return than the subsatellite terrain.

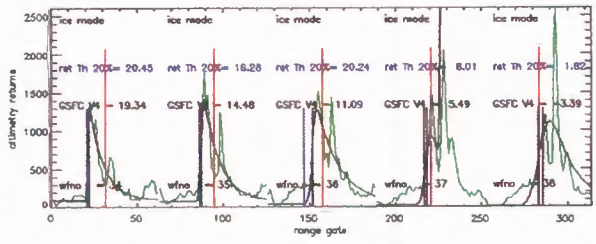

Figure 1: Typical ERS-1 Waveforms over Vegetation. Waveform numbers refer to elevation profile in Fig 2

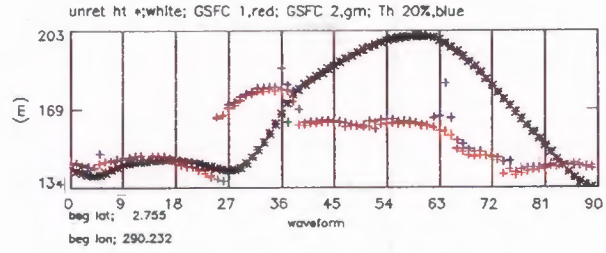

Figure 2: Typical Surface Profile

The second problem of hanging onto a specular surface is demonstrated in the altimeter height and automatic gain control, AGC, profiles shown in figures 3a and b. The AGC is a measure of the power in the return. Values of AGC greater than 45 are usually received over very flat deserts, salt flats, rivers or lakes. In figure 3 the retracked surface elevation begins at around 90m elevation with an AGC of 35. The surface elevation sharply decreases to around 75 m as the AGC slowly rises. The surface elevation remains fairly level at around 72 m until waveform 54 where it starts to systematically decrease. During that same period, the AGC has risen into the 50s and stays there until the gradual apparent decrease in surface elevation when the AGC also decreases slowly to

the mid 30s. The gradual apparent surface elevation decrease is probably due to the altimeter hanging onto the flat specular surface even after the sub-satellite terrain has changed. At waveform 62 the surface elevation abruptly rises by 25 m and the AGC is in the low 30s. At the very beginning of the elevation rise (waveform 62), there are double-ramp returns where the second ramp is following the initial decreasing profile.

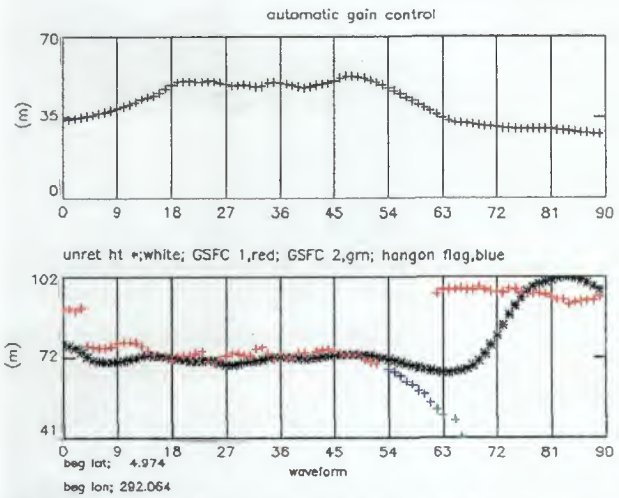

Figure 3: The Altimeter Tracker Hang-on Problem as Illustrated by: a) Automatic Gain Control, and b) Surface Profile

The following steps were used to flag measurements that appeared to be hanging onto a specular surface:

1) A running mean and standard deviation were calculated for all contiguous specular measurements. A measurement was considered specular if the AGC was greater than 45 and the product of the AGC times the maximum gate count was greater than 50,000.

2) If for one second of contiguous data, the standard deviation of (1) above was less than 2.5m then the mean elevation from the preceding specular data, mnspec, was saved.

3) If contiguous data continued to be specular and the running mean was less than four standard deviations below mnspec then that data was flagged as the beginning of a "hangon segment". All following contiguous data that met the specular criteria in (1) above, and for which the surface elevations were continuously decreasing were flagged as being in the "hangon segment".

All measurements in this "hangon segment" were edited from the final data set. Measurements for waveforms 54 through 61 of figure 3 were edited using this criteria.

The internal precision of the final data set can be measured by calculating the mean and standard deviation of the surface elevation differences for crossing arcs. The mean and standard deviation of these crossovers for all the ERS-1 data used in the calculation of the grid was 15cm and 1.55m respectively.

GRIDDING AND SLOPE CORRECTION

The altimetric-derived surface elevations were gridded onto an evenly spaced 1/4 degree grid in latitude and longitude. The elevation at each grid node was calculated by taking a weighted average of all data within a given circular region surrounding the node referred to as the cap size. The data was weighted by the inverse of the distance to the grid node. Four different cap size radii were used; 27.75 km, 41.63 km, 55.5km, and 83.25km. The spacing of the altimetry groundtracks over northwest South America with the grid size and different cap sizes is shown in figure 4 for a 5 by 5 degree region.

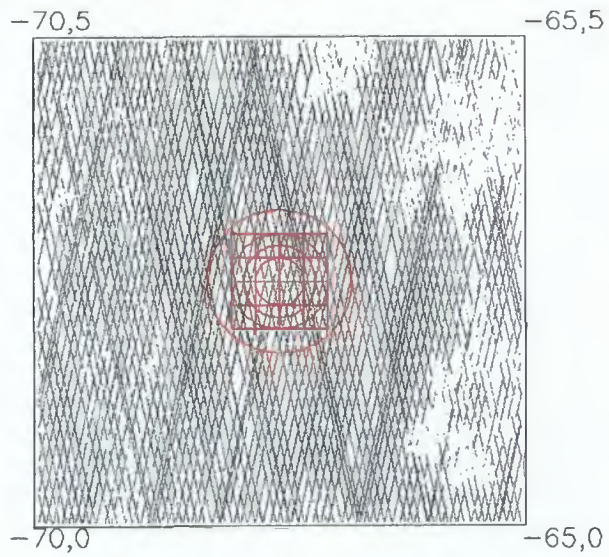

Figure 4: ERS-1 Geodetic Phase Groundtracks with Grid and Cap Sizes

The gridding procedure begins with the smallest cap size and calculates the weighted average. If there are less than 15 elevations or data are not present in at least 3 quadrants of the cap size region, the cap size is increased until these criteria are met. The standard deviation of the data to the weighted average is calculated and data which

differ from the gridded elevation by more than 3.5 times this standard deviation are edited. If data are edited, the gridded elevation is recomputed using the remaining data.

This initial grid was used to calculate the slope-induced error for each of the altimeter measurements using the methodology explained in (Brenner et. al., 1983). This error is caused by the altimeter always measuring to the closest surface within the footprint, which over a sloping surface is not the sub-satellite location. For planar-sloping surfaces this error is approximated as

$$Htcor_{slope} = H*\alpha^2/2$$

where
H = altimeter range measurement
α = the local surface slope

This planar approximation was used to slope correct all the altimeter surface elevations and the data were regridded. The EGM96 geoid (Lemoine et. al., 1996) was subtracted to reference the grid to sea level.

Results

The ERS-1 gridded elevations are shown in figure 5a. The standard deviations of these elevations from the gridding procedure range from under 1 m in the flatter regions to over 200 m in the mountain ranges. The National Imaging and Mapping Association, NIMA, released a new 5 minute DEM in 1996 hereafter referred to as ETOPO5. For most of the continents this included very detailed data. For South America, however, only the data on the northern coast appear updated from the previous ETOPO5 model. We gridded the ETOPO5 data using the same procedure as for the altimetry data for comparison. The ETOPO5 gridded elevations are shown in figure 5b. The same major features are present in both gridded data sets, except the altimetry shows more detail where the ETOPO5 appears to generally smooth out the topography. Differencing the two grids shows a mean difference of -106m with large differences in the mountain ranges where the altimetry is more than 150m lower than the ETOPO5 grid. The altimeter will always measure to the highest elevation in the footprint and the slope correction is an attempt to correct for this. The values of the slope corrections in the mountainous regions range from 5 to 75 m so they cannot account for the large differences we are seeing between the ETOPO5 and altimetry grids.

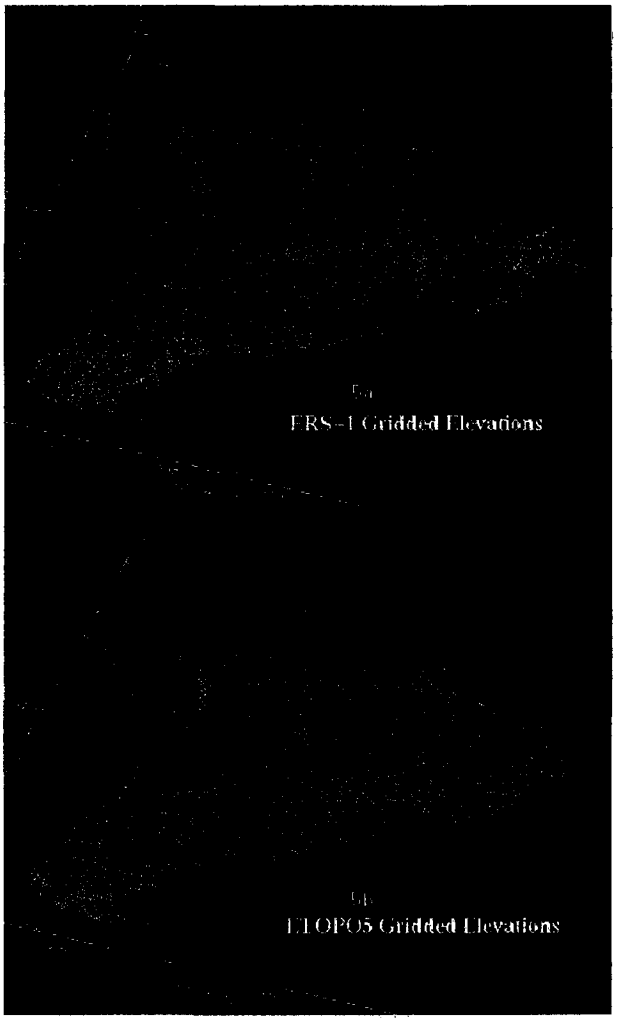

Figure 5: Gridded Elevations from: a) ERS-1 Altimetry, and b) ETOPO5 DEM

To try to determine how the altimetry differed from the ETOPO5 DEM on a smaller scale, we compared along-track altimetry profiles against a profile interpolated from the full resolution ETOPO5 DEM. A typical example is shown in figure 6 for rev 17793 that runs down the eastern bulge of South America. The altimetry is out of phase with the ETOPO5 DEM data and shows more apparent detail, though it is also noisier. The general trends are similar but the height differences in many locations are more than 100m.

To obtain a quantitative assessment of 1) the accuracy of the ERS-1 grid, 2) the affect of applying the slope correction to the altimetry, and 3) the accuracy of the ETOPO5 grid, we compared all three grids to Shuttle Laser Altimeter, SLA, observations. The SLA has a 100m footprint. The processed elevations over land are believed to be at the 1-2m accuracy level (Garvin et. al., 1997).

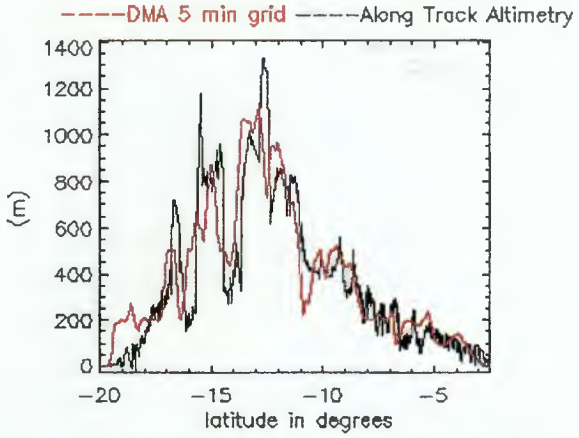

Figure 6: Along-track Altimetry Compared with ETOPO5 5 min DEM

We compared the SLA measurements to each of the 3 grids; the slope corrected ERS-1 grid, the non-slope corrected ERS-1 grid, and the ETOPO5 grid by performing a bi-linear interpolation of the grid elevations at the SLA location. Histograms of the differences of the SLA measured elevations minus the grids are shown in figure 7 for all SLA data that agreed to within 100m of each grid respectively. The laser characteristics, the small footprint, and the effect of cloud coverage or canopy height cause many unusable SLA measurements.

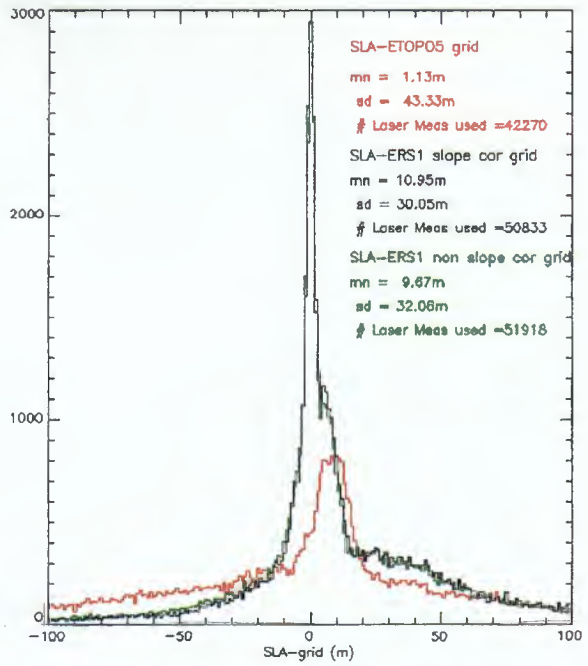

Figure 7: Histograms of Shuttle Laser Altimetry differences with Altimetric and ETOPO5 DEMs

The 100m cutoff removes any cloud measurements, but the canopy top measurements still remain.

The histograms show that in many locations the SLA data agrees well with the altimetry grids. Over 2500 SLA measurements agree within +/-0.5m and the peak of the histogram is centered at zero. The large amount of differences between 5 and 50 meters are probably due to the laser measuring the vegetation canopy. In contrast, the SLA measurements have much poorer agreement with the ETOPO5 grid where only 500 agree to within 0.5m and the histogram peak is centered at around 10m indicating a general bias in the ETOPO5 grid compared to the SLA.

Figure 8 shows the locations of the SLA data where it agreed to within 1 m of the slope-corrected ERS-1 grid. Note that some of these locations are in regions of rougher terrain though the majority are in the flatter

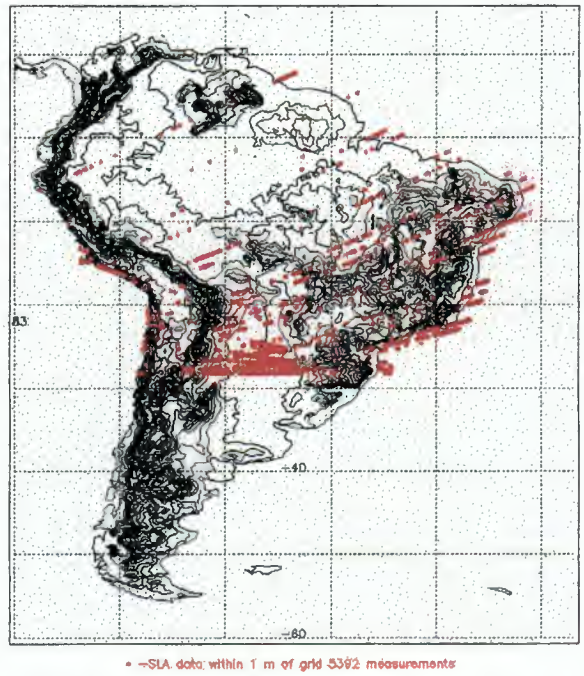

Figure 8: ERS-1 Gridded Heights with repect to the EGM96 Geoid with Locations of SLA data that agree to within 1m

regions.

The histograms also show that more of the SLA data agrees to within +/- .5 m of the non-slope-corrected ERS-1 grid than with the slope-corrected grid ERS-1. However the standard deviations of the differences are less with the slope-corrected ERS-1 grid at 30.05m compared to 32.06m for the non-slope-corrected ERS-1 grid. This indicates that the slope correction may be

adding error in the regions with low slopes, but in general it is improving the precision of the overall grid.

CONCLUSIONS

Satellite radar altimetry data, especially the geodetic phase measurements from ERS-1 can be used to improve on the topographic knowledge of the continents at least for those regions where poor elevation data currently exists such as in South America. The accuracy of the radar altimeter is limited by the large size of the footprint over rougher, mountainous terrain where the errors probably range between 100 and 200 m in contrast to the sub-meter accuracy in the plateau regions. However these results show that this data provides a valuable resource for those areas in which the current models lack in detail due to the sparsity of available measurements.

Future plans are to combine altimetry data from Seasat and the geodetic mission of Geosat to increase the resolution of the DEM.

ACKNOWLEDGEMENTS

This research was supported by NASA's Solid Earth Science Program. We wish to thank Dr. H. Jay Zwally of NASA/Goddard Space Flight Center for the use of his computational resources and Bryan Dixon of Hughes STX Corp. for processing the data.

REFERENCES

Brenner, A.C., R. A. Bindschadler, R. H. Thomas, and H. J. Zwally, 1983, **Slope-Induced Errors in Radar Altimetry Over Continental Ice Sheets**. *J. of Geophys. Res.*, Vol. 88, No. C3, pp 1617-1623

Eanes, R.J., 1994, **Diurnal and Semidiurnal Tides from TOPEX/Poseidon Altimetry**. Presented at Spring 1994 AGU Meeting Baltimore MD.

Frey, H. and A.C. Brenner, 1990, **Australian Topography From Seasat Overland Altimetry.**. *Geophysical Research Letters*, Vol. 17, No. 10, pp 1533-1536.

Garvin, J.B., J.L. Bufton, J.B. Blair, D.J. Harding, S.B. Luthcke, J.A. Marshall, J.J. Frawley, 1997, **Observations of the Earth's Topography from the Shuttle Laser Altimeter (SLA): Laser-Pulse Echo-Recovery Measurements of Terrestrial Surfaces and Clouds**. Submitted to *Science*.

Lemoine, F.G., et al., 1996, **The Development of the NASA GSFC and NIMA Joint Geopotential Model**, Presented at the International Symposium on Gravity, Geoid, and Marine Geodesy , Tokyo, Japan.

Scharoo R.,P. Visser, and G. Mets, 1997, **TOPEX-class Orbits for the ERS Satellites**. Submitted to *J. of Geophys. Res.*, ERS Special Section.

Zwally, H.J., A.C. Brenner, J.P. DiMarzio, M. Giovinetto, 1997, **Ice Sheet Topography, Slopes, and Flow Directions from ERS Altimetry**. Presented at the 3rd ERS Symposium , Florence, Italy.

Merging of Elevations from SAR Interferometry, Satellite Altimetry, GPS and Laser Altimetry in Greenland

Cecilia Svenné Nielsen, René Forsberg and Simon Ekholm

National Survey and Cadastre, Dept. of Production and Research
Rentemestervej 8, DK-2400 Copenhagen NV, Denmark
Phone: +45 35 87 52 43, fax: 45 35 87 50 52, e-mail: csn@kms.min.dk

Johan Jacob Mohr

Danish Center for Remote Sensing, Dept. of Electromagnetic Systems
Technical University of Denmark, B-348, DK-2800 Lyngby, Denmark
Phone: +45 45 25 38 00, fax: +45 45 93 16 34

ABSTRACT

The merging of elevation data from different sources in order to produce a consistent elevation model is a major challenge, especially in rugged areas like the coastal regions of Greenland. In this paper early results from the combination of SAR data from the ERS-1/2 tandem mission with photogrammetric, GPS and airborne laser ranging data are presented for local areas in East Greenland. It is anticipated that SAR interferometry in the future will provide a significant improvement of the ice surface and rock digital elevation model of Greenland, currently produced from a mixture of satellite and airborne altimetry over the ice and surveying / photogrammetry in the ice-free regions.

INTRODUCTION

Greenland is a perfect target region for operational mapping projects based on SAR interferometry. Current maps of the ice-free coastal parts are to a large degree inaccurate, with large planimetric distortions, and for a few regions no official maps exist at all, even at the basic mapping scale of 1:250.000. Apart from the mapping needs, there is also a basic need for digital elevation models, especially to support airborne gravity field mapping and exploration.

A large-scale airborne survey was carried out in 1991-92 [Greenland Aerogeophysics Project - GAP; cf. Brozena, 1992], covering all of Greenland with gravity measurements and precise radar altimetry. Airborne gravity measurements are very sensitive to topographic variations, and a good DEM of surface (and ideally also sub-ice) topography is essential for optimal use of airborne gravity data, especially when combined with other surface data.

Whereas ERS-1 and GEOSAT satellite altimetry provide good and accurate elevation mapping at the center of the ice sheet, the marginal ice zones and the ice-free coastal areas can not be mapped this way. For these regions airborne profiling radar data from the GAP project, and equivalent laser ranging data from the NASA AIM (Arctic Ice Mapping) project [Krabill et al., 1995] were used.

In the ice-free areas elevation data were derived from a variety of traditional sources: scanned photogrammetry, digitized contours from new stereophotogrammetric mapping, manually read profiles of existing maps, and - in a few areas - DMA Digital Terrain Elevation Data (DTED) average data.

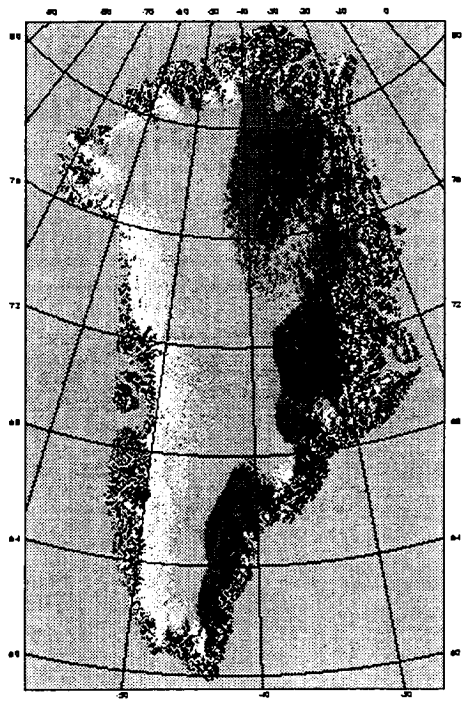

Figure 1: Shaded relief plot of Greenland surface topography with an average resolution of 2 km [Ekholm, 1996]

In this way a composite "best" DEM of Greenland was compiled [Ekholm, 1996]. This DEM is shown in Figure 1. The quality of the Greenland DEM is highly varying, and for roughly half the coastal region inaccurate, with basic resolution of no more than 5 km, with possible systematic errors of 100's of meters. Here ERS-1/2 SAR interferometry obviously offers the potential for significant improvements.

In the present paper we will look at SAR interferograms and derived DEM's in the context of improving the Greenland basic DEM. Independent checks of the accuracy of a SAR derived DEM using geodetic control points from GPS and conventional triangulation, and airborne laser altimetry collected as part of the Danish national project: Elevation Changes Of the Greenland Ice Sheet (ECOGIS) will also be made.

INSAR DEM FORMATION

The selected region of study is the central East Greenland region around Scoresbysund fjord. This region is very rugged, especially south of Scoresbysund, a tertiary basalt area with steep topography rising 2000 m above the fjord, divided by numerous glacial streams and topped by local ice caps.

This region is the most poorly mapped area of Greenland, and the local Geikie ice cap was selected as study area for marginal ice cap elevation changes in the ECOGIS project, covered with laser altimetry flights

Figure 2: Flight tracks from July 15 and 16/96. Payload includes GPS receiver and laser altimeter

(Figure 2) and GPS-positioned corner reflectors for airborne SAR interferometry mapping experiments.

Two SAR interferograms covering the Geikie area were created from four descending ERS-1/2 scenes acquired in January, February 1996 respectively during descending passes. Of the two frame pairs selected, the first has a short (8 m) and the second a fairly long (115 m) perpendicular baseline.

The SAR interferograms were formed using the DCRS processing system, starting from ESA raw data [Mohr

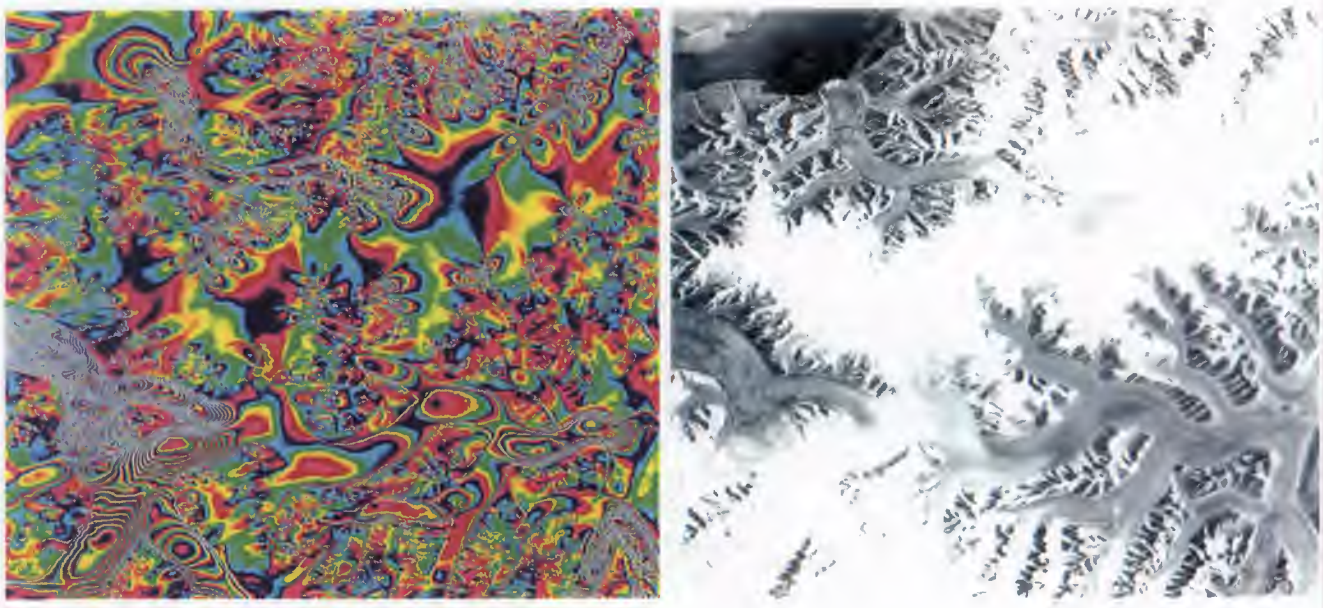

Figure 3: Interferogram and amplitude image created from an ERS-1 scene (January 07/96, orbit 23430, frame 2187) and an ERS-2 scene (January 08/96, orbit 3757, frame 2187). One color cycle represents a phase change of 2π [Nielsen, 1996]

al., 1996]. A reasonably good correlation was obtained over much of the Geikie plateau and surrounding mountains, but with many breaks and shadows due to the very steep topography. Figure 3 shows an example of a the SAR interferogram with the shorter baseline. With the large share of glaciers and ice caps with virtually unknown topography and dynamics in the interferograms it was not realistic to try to obtain a phase-unwrapped SAR DEM for this region.

An unwrapped SAR interferogram was therefore formed for the more benign Jameson Land area just north of the Scoresbysund Fjord. This region is characterized by a rather smooth sloping topography, broken by deeply incised rivers, with a maximal elevation of 909 m attained close to the steep cliffs of Hurry Inlet. To the east of this fjord an alpine style topography is found in Liverpool Land.

For Jameson Land a SAR interferogram was formed from a tandem SAR pair from February 1996, again starting from the raw ESA product, utilizing precise orbits from ESA as well. Coherence was good across the scene, but the steep cliffs of Hurry Inlet and some river valleys in southern Jameson Land produced breaks. The multi-looked interferogram (100 by 100 m) was subsequently phase-unwrapped.

The interferometric phase was then inverted to absolute 3-D position utilizing 8 geodetic control points across the region in effect calibrating the corresponding baseline and removing the absolute phase. Note that due to the utilization of precision orbit data the tie points need not be identified in the interferogram neither for baseline calibration nor for geocoding. The final DEM quasigrid expressed in radar coordinates was finally converted to a set of WGS84 geographic coordinates, with corresponding heights converted to orthometric heights by the geoid model [Mohr et al., ibid.].

DATA GRIDDING AND MERGING

The incorporation of SAR-derived elevations is straightforward, provided data are checked and calibrated for systematic errors. When this is the case, SAR data may enter together with other data in a collocation / Kriging prediction, where an a priori standard deviation is assigned to all data, and predicted values (s) are obtained from a vector of observations (x) by

$$s = C_{sx}^{T}\left[C_{xx} + D\right]^{-1} x$$

where C is the covariance matrix of the topographic heights, and D the associated noise matrix which is assumed to be diagonal. Here it should be noticed that, in principle, it is possible to estimate the uncertainty of each SAR pixel by means of correlation images and an error model.

In the implemented scheme [based on GRAVSOFT program GEOGRID, cf. Tscherning et al., 1992] an efficient quadrant search algorithm is utilized, and only a set of closest neighborhood points used in the actual prediction, giving the capability to handle very large data sets by this method. As covariance model a second-order Markov model

$$C(d) = C_0(1+\alpha d)e^{-\alpha d}$$

is used, where d is the spherical distance between two points. Correlation lengths, typically around 10 km, and variances are empirically scaled from the data. If the SAR data have systematic errors, such data can also be handled by the collocation methods by either estimating such parameters along with the gridding process, "least squares collocation with parameters", or - more operational - pre-estimating trends between different data sets in a least-squares collocation "draping" technique.

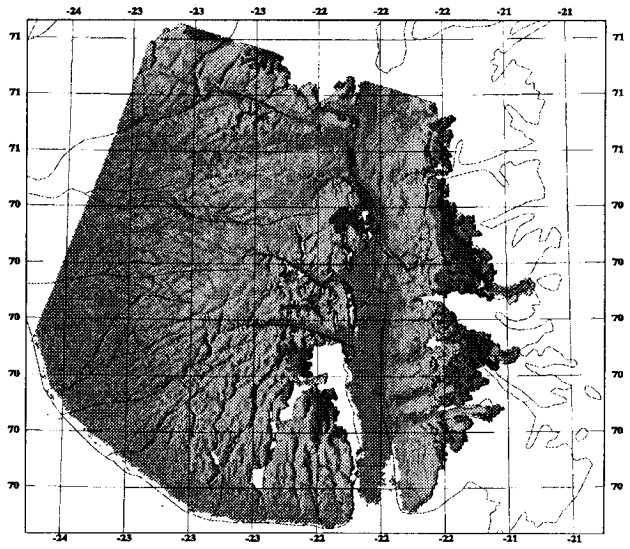

Figure 4: Shaded relief plot of SAR Digital Elevation Model. The colors are separated with 200 m equidistance. The darkest gray corresponds to elevations larger than 600 m

Figure 4 shows the results of this gridding process using SAR only data, and Figure 5 the corresponding complete model incorporating other data such as manually scanned maps and some DTED data for the areas outside the SAR DEM data coverage.

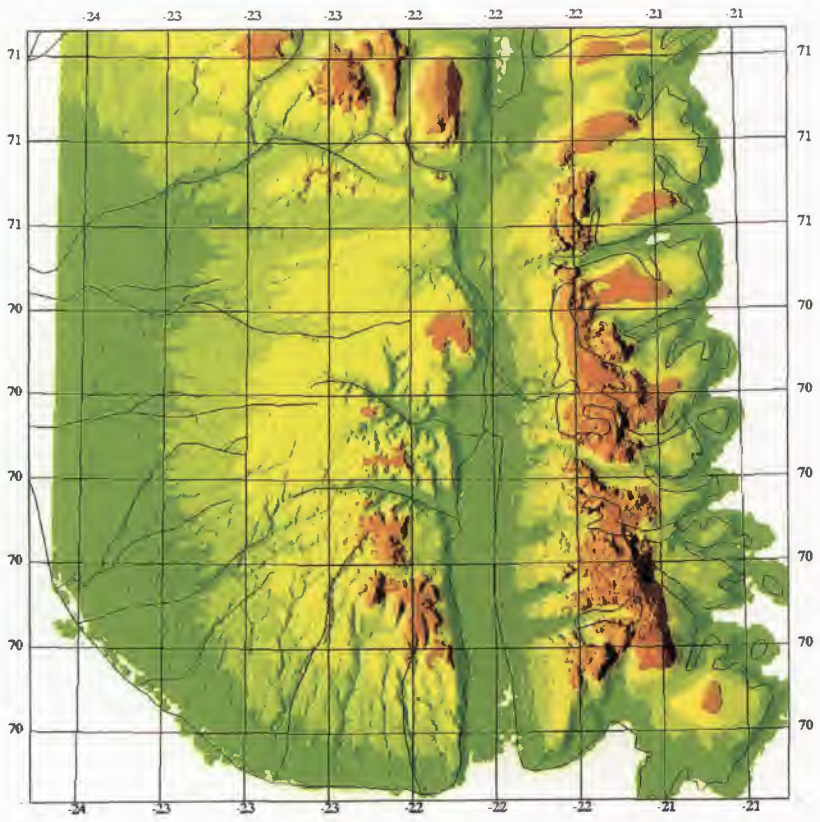

Figure 5: Shaded relief plot of complete Digital Elevation Model. The colors are separated with 200 m equidistance. Brown corresponds to elevations larger than 600 m

COMPARISON OF THE SAR DEM AND CONTROL DATA

A set of approximately 200 geodetic control points exists in southern Jameson Land (Figure 6), along with a couple of laser altimetry airborne profiles. The majority of the geodetic control points were derived by traditional triangulation in the late 60's, and as such the points are typically located at local high points in the topography.

The comparison of the elevations derived from the SAR DEM and the geodetic values, transformed to WGS84 by newer GPS measurements, is given in Table 1. To evaluate possible systematic errors in the SAR DEM two experiments were performed: First a sequence of trend surfaces of linear, quadratic and cubic polynomials

$$z^{(1)} = a_0 + a_1 x + a_2 y \quad ;$$

$$z^{(2)} = z^{(1)} + a_3 x^2 + a_4 y^2 + a_5 xy \quad ;$$

...

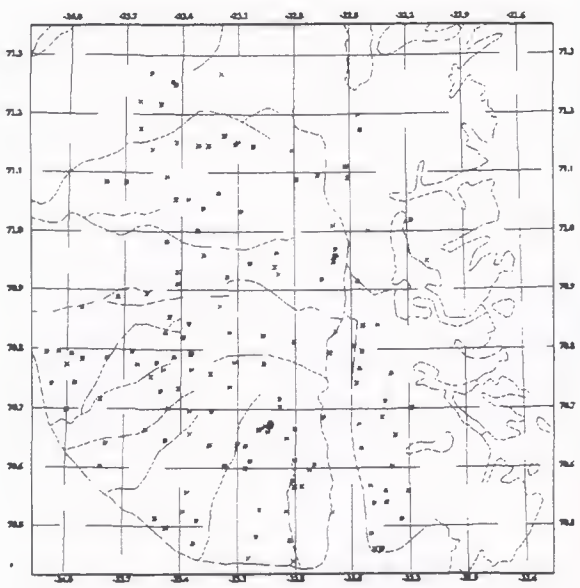

Figure 6: Distribution of Geodetic points

		Mean	Std. dev.
Direct difference H_{SAR} - $H_{geodesy}$		1.81	20.74
Direct difference H_{SAR} - H_{Laser}		14.50	22.20
Direct difference $H_{Existing\ DEM}$ - $H_{geodesy}$		97.50	158.20
H_{SAR} - $H_{Geodesy}$ difference with surface detrending	Linear	0	20.22
	Quadratic	0	20.17
	Cubic	0	19.82

H_{SAR} - $H_{Geodesy}$ difference with DEM shifted

Easting	-300		-100		0		100		300	
Northing	Mean	St.dev.	Mean	St.dev.	Mean	St.dev.	Mean	St.dev.	Mean	St.dev.
-300	17.44	33.90			16.02	31.95			18.36	34.79
-100			4.42	21.83	4.41	22.15	4.72	22.55		
0	3.53	28.48	1.16	19.90	1.81	20.74	2.02	21.50	3.03	23.73
100			-0.52	20.55	-0.23	21.03	0.31	22.29		
300	5.50	29.90			4.85	29.62			5.63	33.11

Table 1: Comparison of control point elevations and SAR DEM elevations in Jameson Land. Unit: meter

were estimated and removed prior to comparison, and secondly the SAR DEM was subjected to shifts in north and east directions prior to comparison, to check for possible mislocation errors. The results of these comparisons are additionally given in Table 1.

From Table 1 it is seen that the SAR DEM apparently is free of systematic errors of the above mentioned kinds, and the overall fit of the model is around 21 m r.m.s. Because this number represent the comparison of *point* elevations to DEM 100 m *average* elevations, this number is in part due to unavoidable aliasing, and the true DEM error must thus be smaller. Looking at the actual discrepancies there seems to be no systematic pattern in the outliers and there is no correlation with surface slope.

To get an additional evaluation, airborne laser profiling data were used. These data originate from two flights to the Geikie plateau from Constable Pynt airport, carried out July 1996 as part of the ECOGIS project. The laser data were sampled at 10 Hz from a low-flying Twin-Otter aircraft, positioned with kinematic GPS to an accuracy of a few dm.

The maximal range of the used Optech laser unit was approximately 500 m, giving loss of return signal over some deeper valleys and cliffs. The orientation of the laser has been done by a dual-axis accelerometer, mounted next to the laser, which together with GPS-derived accelerations may be converted into approximate roll and pitch. The laser profiling was demonstrated to yield dm-level results in marine tests [Forsberg et al., 1996], but due to the lack of an accurate orientation reference (no INS) only a m-level level laser accuracy are expected on the Jameson Land profiles.

Since the laser footprint is very small, typically < 1m, the laser data may be considered point values just like the geodetic control points, but since the laser randomly samples the topography, including the river valleys, larger discrepancies are expected. This is illustrated in Table 1, and Figure 7. Again the a majority of the discrepancy can probably be described to aliasing relative to the 100 m resolution of the SAR DEM, but it is also apparent that there are systematic, unexplained errors in the laser comparisons.

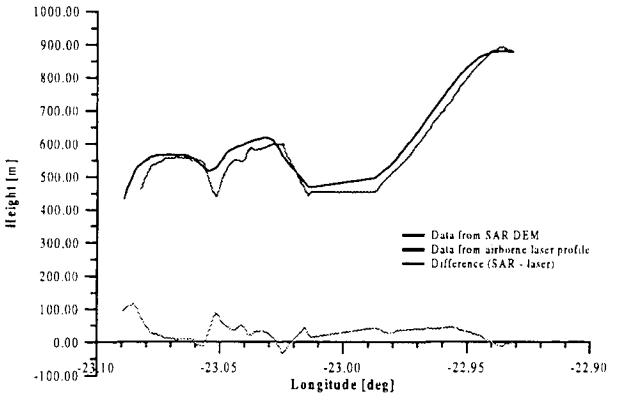

Figure 7: Example of elevation comparison between laser altimetry track and the SAR Digital Elevation Model. The depicted data are from the central parts of Jameson Land.

CONCLUSIONS

In the present paper a SAR derived DEM with a multi-look (averaging) resolution of 100 m has been evaluated by comparisons to point data, yielding an accuracy around 21 m r.m.s., partially expressing the resolution problem of point versus mean elevations. Given the rough topography, this kind of accuracy will be very useful for aiding small-scale mapping, and especially for generating DEM's for geophysical applications.

However, it is clear that for a more general use in Greenland, with glaciers bounded by steep topography, additional InSAR method development is required, e.g. utilizing combinations of ascending and descending orbit data, preferably with a range of different baselines, in order to enhance phase unwrapping, allow ice velocity estimation, and reduce the number of shadows and layovers. In the most severe nunatak topography, auxiliary photogrammetric or geodetic information is required.

REFERENCES

Brozena, J. M., 1992: The Greenland Aerogeophysics Project: Airborne Gravity, Topographic and Magnetic Mapping of an Entire Continent, *In: O. Colombo (Ed.): From Mars to Greenland, Proc. IAG Symposia 110*, Vienna 1991, Springer Verlag, pp. 203-214.

Ekholm, S., 1996: A Full Coverage, High-resolution, Topographic Model of Greenland Computed from a Variety of Digital Elevation Data, *J. of Geophysical Research*, Vol. 101, No. B10, 21961-21972.

Forsberg, R., 1993: Impact of Airborne Gravimetry on Geoid Determination - the Greenland Example, *Bull. International Geoid Service*, no. 2, Milano, pp. 32-43.

Forsberg, R., K. Hehl, L. Bastos, A. Gidskehaug, U. Meyer, 1996: Development of an Airborne Geoid Mapping System for Coastal Oceanography (AGMASCO), *Proc. Int. Symp. on Gravity, Geoid and Marine Geodesy (GRAGEOMAR)*, Tokyo, in print.

Krabill, W.B., R.H. Thomas, C.F. Martin, R.N. Swift and E.B. Frederick, 1995: Accuracy of Airborne Laser Altimetry over the Greenland Ice Sheet, *J. Remote Sens.*, 16, 1211-1222.

Mohr, J.J. and S.N. Madsen, 1996: Multi-pass Interferometry for Studies of Glacier Dynamics, *Fringe 96*, Zurich, http://www.geo.unizh.ch/rsl/fringe96/papers/mohr-madsen

Mohr, J.J., S.N. Madsen and N. Reeh, 1997: ERS Tandem Study of Glacier Dynamics in NE-Greenland, *3rd ERS Symposium*, Florence, Italy

Nielsen, C.S., 1996: ERS-1/2 SAR Interferometri Anvendt til Estimering af Geikie Plateau Gletscherens Topografi, *M.Sc. thesis in geodesy (in Danish)*, Geophysical Dept., University of Copenhagen.

Tscherning, C.C., R. Forsberg and P. Knudsen, 1992: The GRAVSOFT Package for Geoid Determination, *Proc. 1st continental workshop on the geoid in Europe*, Prague, pp. 327-334.

INSAR TERRAIN HEIGHT ESTIMATION USING LOW-QUALITY SPARSE DEMS

Mike Seymour and Ian Cumming

University of British Columbia
Dept. of Electrical and Computer Engineering
2356 Main Mall, Vancouver, B.C.,Canada V6T 1Z4
seymour@ee.ubc.ca, ianc@ee.ubc.ca
http://www.ee.ubc.ca/sar/

ABSTRACT

SAR interferometry (InSAR) is a technique for estimating topography using the phase difference between coincident SAR images. Many regions of the Earth have existing topographic data that can be used to assist interferometric SAR processing. In the following, we show how coarse low-quality DEMs can be used in the InSAR processing chain. In particular, coarse low-quality DEMs facilitate phase unwrapping by removing as much of the low resolution topographic phase as possible. The problem of unwrapping the residual phase is easier than unwrapping the flat earth corrected interferogram phase because the local phase bandwidth is reduced in addition to the demodulation of the flat earth correction. Lower local fringe frequency reduces the probability of residues and hence the probability of phase unwrapping difficulties. In addition, the coarse DEM can also be used to calibrate the interferogram phase by providing a height template for a fitting process.

Keywords: SAR interferometry, DEMs, terrain height estimation, baseline estimation.

1. INTRODUCTION

SAR interferometry exploits the travel time phase information in the complex-valued SAR images to derive terrain heights or terrain height changes [1]. In a single ERS SAR image, the travel time phase information is lost because of the disparity between the size of resolution element and the wavelength of the SAR. However, if two well-correlated SAR images of the same ground scene are available, one can extract a noisy estimate of the travel time phase *difference* from the phase difference between the images. Through careful processing, trigonometry, and some external parameters, the off-nadir angle of a pixel in an ERS scene can be estimated to accurately place the pixel in the ground range plane ($<$ 10 m error). In effect, SAR interferometry can be used to derive a digital elevation model (DEM) of a SAR scene.

Estimation of topography using SAR interferometry is usually seen as a four step process: firstly, produce the interferogram; secondly, unwrap interferogram phase; thirdly, calibrate the interferometer fourthly, convert unwrapped phase to terrain height. For InSAR processing, specific signal processing steps are required to produce an interferogram phase estimate which has the highest SNR possible (*e. g.* registration of the SAR images and filtering of the interferogram phase). Phase unwrapping is the difficult non-linear problem of estimating how many 2π phase ambiguities are required to reconstruct a (possibly discontinuous) interferogram phase surface. The difficulty of this task is evidenced by the plethora of published algorithms for phase unwrapping. Calibration of the interferometer geometry refers to estimating the baseline magnitude (B) and the baseline orientation (θ_B) or equivalently, the normal ($B^{\perp}$) and parallel ($B^{\parallel}$) baselines.

Clearly, there are two ways that a low-quality low resolution DEMs could possibly simplify InSAR processing: by facilitating more sophisticated flattening to aid in the phase unwrapping process, and by providing a template of terrain heights to aid in the calibration of the interferometer. Both stages seem interdependent: one needs unwrapped phase and the geometry of the interferometer to perform height estimation and one needs height estimates which require unwrapped phase to perform the calibration of the interferometer. However, one can decouple these two operations by using the image registration relation [2]. In the following, we develop an algorithm for estimating topography which makes use of low-quality sparse DEM data.

2. DEMS AND INSAR

While the main purpose of InSAR processing is to estimate an accurate DEM, if a coarse or inaccurate DEM is available, it can be used to aid in several steps in the InSAR processing chain. There are a number of low-quality low resolution DEMs publicly available. In particular, the United States Geological Survey (USGS) has made a 30 arc-second DEM of most of the world available While these data are

certainly low resolution (approximately 1 km posting) and low accuracy (90 % confidence interval of ± 650), we can show that these DEMs can aid in InSAR processing.

2.1. Using Low Quality DEMs for Calibration

The accuracy requirements for the baseline components (normal and perpendicular baseline) are approximately 5 cm to provide RMS height errors on the order of 10 m for ERS data (assuming no other error sources). Although precision orbit modeling could give this accuracy, the orbit data for ERS SAR products does not quite meet these exacting requirements [3, 4] and alternative methods of calibration must be used. One method is terrain height tiepointing [5]. In this case, registration between the known locations of height values and the SAR image must be made. The method pre-supposes locally accurate measures of topography which are easily registered to the reference SAR image.

Consider estimating the interferometer geometry by minimizing sum of squared error (SSE) between the InSAR and the DEM height estimates:

$$\min \sum_k (h_{insar,k} - h_{dem,k})^2. \quad (1)$$

Assuming no other errors, one can write that the InSAR estimated terrain height is a combination of the true terrain height (h_k) and the perturbation of the terrain height ($\Delta h_{insar,k}(\Delta B, \Delta\theta_B)$) due to errors in the baseline magnitude (ΔB) and the baseline orientation ($\Delta\theta_B$) respectively: $h_{insar,k} = h_k + \Delta h_{insar,k}(\Delta B, \Delta\theta_B)$. Similarly, the DEM terrain height estimate can be written as the true topography plus an error term ($\Delta h_{dem,k}$):$h_{dem,k} = h_k + \Delta h_{dem,k}$. The restated calibration problem is then to minimize

$$E_R = \sum_k (\Delta h_{insar,k}(\Delta B, \Delta\theta_B) - \Delta h_{dem,k})^2. \quad (2)$$

Using differentials, the error due to a calibration error at a particular data point p, can be approximated by

$$\Delta h_{insar,p} \approx 1.1 x_p \left[-\frac{B^{\parallel}}{B^{\perp}} \frac{\Delta B}{B} + \Delta\theta_B \right]. \quad (3)$$

InSAR height errors due to mis-calibration of the interferometer are proportional to the ground range (x_p) of the true data. In the case of no shadow and no layover, the ground range of radar data is a monotonically increasing function which can be approximated by a line of constant slope with an offset. Combining the error due to baseline orientation and baseline magnitude into one variable $\alpha = -\frac{B^{\parallel}}{B^{\perp}} \frac{\Delta B}{B} + \Delta\theta_B$ yields

$$\min \sum_k (1.1\, \alpha\, x_k - \Delta h_{dem,k})^2. \quad (4)$$

For α to be zero, e.g. no error in the estimated geometry of the interferometer, it must be true that

$$\mathsf{E}\,[x_k\, \Delta h_{dem,k}] = 0. \quad (5)$$

If there are no trends in the DEM errors that are correlated with the ground range variable, one can theoretically get accurate estimates of the InSAR geometry. Note that this relation also means that the mean error in the input coarse DEM is translated directly to the output error in the InSAR DEM. The solution is to process data sets which are as large as possible to minimize the possibility of biases in the coarse low-quality DEMs.

2.2. Using Low-Quality DEMs for Phase Unwrapping

One common step in InSAR processing is referred to as phase flattening where the interferogram phase component that is due to a flat earth is removed. Flattening facilitates interpretation of the topography in the interferogram phase and reduces phase wrapping complexity. The residual phase after flattening is directly proportional to terrain height so the residual interferogram looks much like a contour map of terrain height. The complexity of phase unwrapping varies directly with the number of residues and the number of phase residues is a function of local frequency [6]. Therefore, reducing the local frequency of the interferogram simplifies the phase unwrapping problem. If a low-quality DEM is available, flattening which is more sophisticated then flat earth flattening could be used to remove frequency content from the interferogram.

The real difficulty here is to find some way of deriving an appropriate geometry to jump-start the flattening process. It is a circular problem: one needs the interferometer geometry to derive the topography but one needs some measure of topography to derive the geometry. However, the registration relation between the SAR images gives us a crude estimate of the unwrapped phase. This relationship can be used to derive a rough estimate of the interferometer baseline to allow initial flattening using the coarse DEM data.

In practice, the slope error of a reconstructed DEM depends on the method of reconstruction, the fidelity of the data, and the variability of the terrain under consideration. In addition, for radar applications, terrain height errors translate into errors in slant range position. Therefore it is difficult to predict

in advance whether or not a DEM will actually help in the InSAR processing algorithm. However, one can examine the influence of terrain height errors on the phase slope by considering the relationship between slant range and ground range and the error in terrain heights. For the 30" DEM from USGS, the accuracy statistic cited for the terrain height data is ±650 meters at 90 % confidence interval. Since we reconstruct the gridded DEM in the slant range coordinates using triangulation, the averaging reduces the 90% confidence interval to $650/\sqrt{3} \approx 375$ meters. For height differences, the 80% confidence interval is therefore about 750 meters. Each of the points in the is separated on the ground by approximately 900 meters so the average slope error at 80% confidence interval is about 0.84 meters of height per horizontal meter on ground. Nominally, for flat earth and a range sampling interval of 4 meters in range, the 80 % confidence interval in slope error is about 8 meters which is not enough to cause unwrapping errors for normal baselines on the order of 300 meters.

The algorithm is summarized in Table 1. It consists of three general parts which are iterated to increase the SNR of the output: preliminary flattening, residual phase unwrapping, and calibration. Currently, we unwrap the residual phase using a weighted least squares algorithm [7]. We take the current estimate of the topography and use it again in the preliminary flattening stage. The iteration is terminated when the number of unwrapped pixels stabilizes. The iterations allow the algorithm to cope with isolated residues due to noise.

3. SIMULATIONS

To test the efficacy of the algorithm, a simulation of a noisy interferogram ($\mu = 0.5$) was generated with the following parameters $B = 360m, \theta_B = 3\pi/8, B^{\perp} \approx 260$ (see Figure 1). The "true" height model Figure 2 was generated by gridding scattered data samples of a Terrain Resource Information Map [8]. These are publicly available digital mapping products generated by the Surveys and Resource Mapping Branch of the government of British Columbia. The 90% confidence interval of the DEM is 5 m for unobscured ground areas. The nominal sampling interval is 100 meters for flat areas and 75 meters for areas of steep terrain. 30" DCW data was gridded for the overlapping area of the TRIM elevation data (see Figure 2) and the algorithm was applied. After 3 iterations, the algorithm successfully unwrapped 96 % of valid data. The success of pre-flattening using the coarse DEM is shown in Figure 1 where the filtered residual interferogram phase was generated by simply low-pass filtering the flattened noisy interferogram. The mean error of the InSAR DEM is the same as the mean error of the DCW DEM: ≈ -35 meters. This is as expected because minimizing the sum of squared height errors will conserve the mean of the input data model. We are using the equivalent of only about 100 DCW data points to reconstruct the input topography model. Since the 90% confidence interval of the data is 650 meters, we would expect that the standard deviation of the mean height estimate to be about 40 meters which agrees well with our result.

The global error performance of the algorithm is summarized by the percentile plot of the residual error after the mean error was removed is shown in Figure 3. The value of InSAR deviation at the 90^{th} percentile is approximately 10 meters while the original DCW data had a value of 122 m at the 90^{th} percentile. This represents an improvement of approximately 20 dB. Note also the large tail in the percentile distribution of height errors from the InSAR DEM due to phase unwrapping errors.

4. SARDINIA - PRELIMINARY RESULTS

The ERS FRINGE group distributed ERS-1 scenes from frame 801, orbit 241, August 2, 1991 and orbit 327, August 8, 1991 of Sardinia as test data. These data are well known for their high coherence and their mountainous character which causes phase unwrapping difficulties. We extracted the overlapping 30" DCW DEM data for the scene and processed a subsection of the data. The interferogram and reconstructed DCW DEM were coarsely registered by hand.

The sub-scene processed is 400 azimuth pixels by 1000 range pixels large and is approximately 4 km in slant range by 3.2 km in azimuth. According to the FRINGE baseline listings [9], $B \approx 142$ meters while $B^{\perp} \approx 126$ meters. The phase and coherence magnitude of the interferogram are shown in Figure 4. The raw interferogram phase was smoothed by a factor of four in azimuth and half-band filtered [10] but not downsampled in range. The coherence magnitude estimate was made over 11 by 11 pixel blocks using a simple linear phase compensation in range.

The modeled interferogram phase and residual phase after unwrapping are shown in Figure 5. The estimated terrain height model is shown in Figure 6. The range of InSAR estimated terrain is between 0 and 1000 meters which is approximately the range of topography in the region. Detailed comparison of the estimated terrain heights with the true topography is difficult because of lack of a detailed DEM. However, we do have access to some topographical maps. A line of topographical data was extracted from the map sheets and converted to slant range representation. The line of data corresponds to azimuth line

130 in the processed InSAR data.

A comparison of two output height estimates, the input 30" DCW topography and the map topography is shown in Figure 6. The "InSAR w/DEM" topography was generated using the DCW DEM for calibration. The "FRINGE Data" topography was generated using the FRINGE baseline listings as calibrating the interferometer using the orbit data and the flat earth assumption yielded results which had very large errors. It is clear that the "FRINGE Data" has a very large slope bias in comparison with the "InSAR w/DEM" approach. Using the DCW DEM to calibrate the interferometer is a substantial improvement over the calibration using the "FRINGE Data".

However, it is clear that the DCW topography is not well registered to the interferogram/map data. The offset is approximately 500 m in slant range or about 1.25 kilometers in ground range. Considering that the original spacing of the DCW sample points is on the order of 900 meters and that no special processing was done for the registration, the results are reasonable. Despite the misregistration, the valid portion of InSAR data from 5500 meters to 7000 meters in slant range agrees well with the map data. However the first part of the scene does not fair as well with an obvious ambiguity error starting at approximately 4000 meters which gets worse as one reaches approximately 5000 meters slant range. Although the range of terrain height is reasonable, there are still ambiguity errors present in the data which could possibly be eliminated by iterating the estimated terrain height with the DCW model to get better registration between the DCW data and the interferogram.

5. CONCLUSION

We have presented an algorithm for processing InSAR data using coarse low-quality DEMs. The algorithm takes advantage of the prior knowledge in the low-quality DEM to ease the difficulty of phase unwrapping. In addition, the input coarse low-quality DEM is used to calibrate the interferogram. We showed that the primary cause of error in the output terrain height estimates is the correlation between the true ground range of the data and the DEM height errors. In practice, this means one should process as large an amount of DEM data as possible to minimize bias in the InSAR estimated topography. We showed some simulations which yielded an improvement of approximately 20 dB in the 90^{th} percentile value of error. Finally, some preliminary results for the ERS-FRINGE Sardinia data set were shown where the improvement in output terrain height accuracy using the coarse DEM as input was clearly demonstrated. The topography estimated using the FRINGE listing had a substantial range slope in comparison to the true topography of the region.

REFERENCES

[1] L. C. Graham, "Satellite interferometer radar for topographic mapping," *Proceedings of the IEEE*, vol. 62, no. 6, pp. 763–768, 1974.

[2] M. Seymour and I. Cumming, "An iterative method for estimating baseline geometry," in *PIERS'96*, (Innsbruck), July 1996.

[3] D. Small and D. Neusch, "Validation of height models from ERS interferometry," in *FRINGE'96*, (Zurich, Switzerland), ESA, 1997. *http://www.geo.unizh.ch/rsl/fringe96/papers/*.

[4] C. Reigber et al, "Impact of precise orbits on SAR interferometry," in *FRINGE'96*, (Zurich, Switzerland), ESA, 1997. *http://www.geo.unizh.ch/rsl/fringe96/papers/*.

[5] D. Small, C. Werner, and D. Nüesch, "Baseline modelling for ERS-1 SAR interferometry," in *IGARSS '93*, (Tokyo), pp. 1204–1206, Aug 1993.

[6] U. Spagnolini, "2-D phase unwrapping and instantaneous frequency estimation," *IEEE Trans. Geo. Remote Sensing*, vol. 33, pp. 579–589, May 1995.

[7] D. Ghighlia and L. Romero, "Robust two-dimensional weighted and unweighted phase wrapping that uses fast transforms and iterative methods," *J. Opt. Soc. Am. A*, vol. 11, pp. 107–117, January 1994.

[8] Surveys and Resources Mapping Branch, *British Columbia Specifications and Guidelines for Geomatics*. Ministry of Environment, Lands and Parks, Province of British Columbia, release 2.0 ed., January 1992.

[9] G. A. Solaas, "ERS-1 interferometric baseline algorithm verification," Tech. Rep. ES-TN-DPE-OM-GS02 version 1.0, ESA, 1994. *http://gds.esrin.esa.it:80/CEFB565F/CORBITS*.

[10] F. Gatelli, A. Monti Guarnieri, F. Parizzi, P. Pasquali, C. Prati, and F. Rocca, "The wavenumber shift in SAR interferometry," *IEEE Trans. Geoscience and Remote Sensing*, vol. 32, pp. 855–865, July 1994.

1: Grid the DEM in the SAR reference image slant range geometry.
2: Register the DEM to the reference SAR image.
3: **while** Number of unwrapped pixels changes significantly **do**
4: Make a preliminary estimate of the interferometer geometry using interferogram registration relation.
5: Calculate residual interferogram by demodulating with current interferogram phase estimate.
6: Filter residual interferogram.
7: Unwrap residual filtered phase.
8: Estimate topography by minimizing the MSE between InSAR topography and the original DEM. (θ_B).
9: **end while**

Table 1: Preliminary algorithm for estimation of topography using coarse low-quality DEMs.

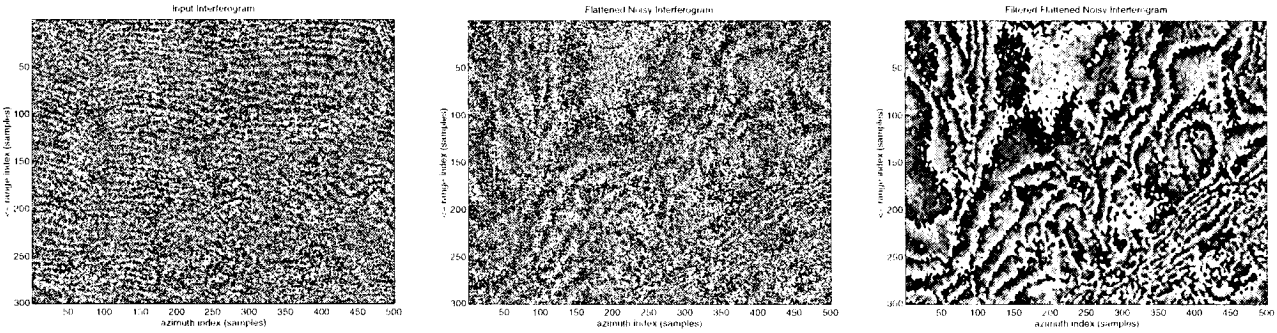

(a) Input interferogram, $\mu = 0.5$. (b) Flattened noisy interferogram (c) Filtered interferogram.

Figure 1: Simulation results: example of pre-flattening using coarse DEM data.

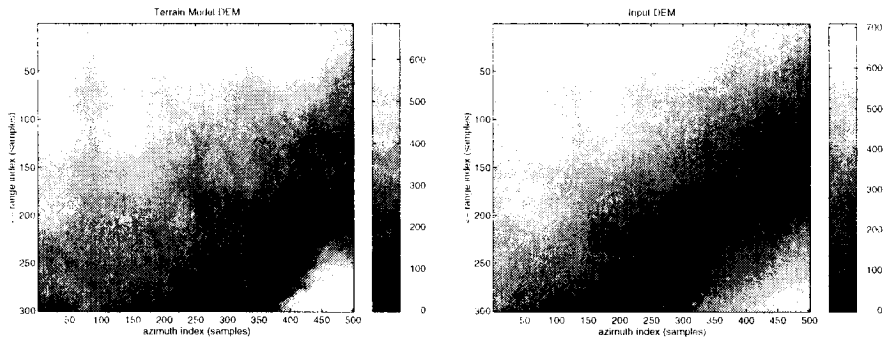

(a) Simulated terrain model. (b) Input DCW low-quality DEM.

Figure 2: TRIM data based simulated topography and DCW DEM used for simulation.

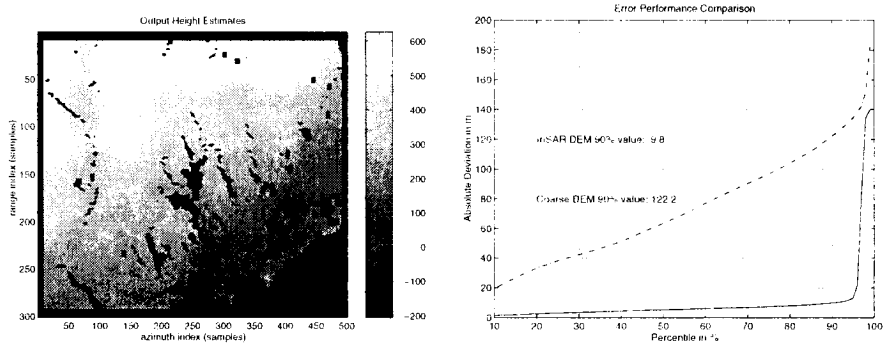

(a) Output InSAR DEM. (b) Percentile distribution of InSAR DEM errors.

Figure 3: Simulation results.

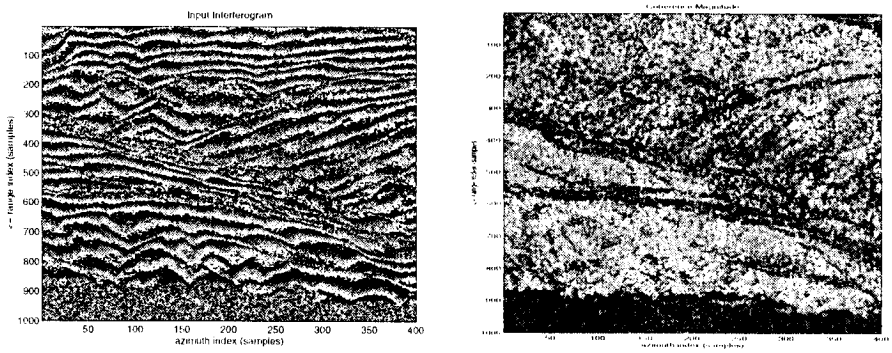

(a) Input interferogram. (b) Coherence magnitude estimate.

Figure 4: Interferometric SAR data for Sardinia dataset.

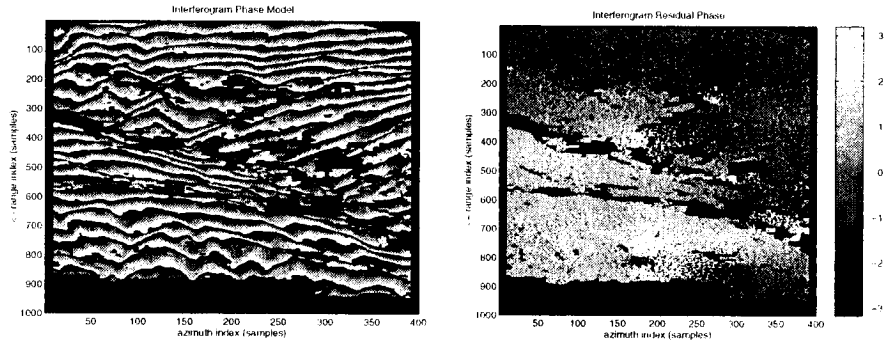

(a) Modeled interferogram phase. (b) Residual phase.

Figure 5: Interferogram phase for Sardinia dataset.

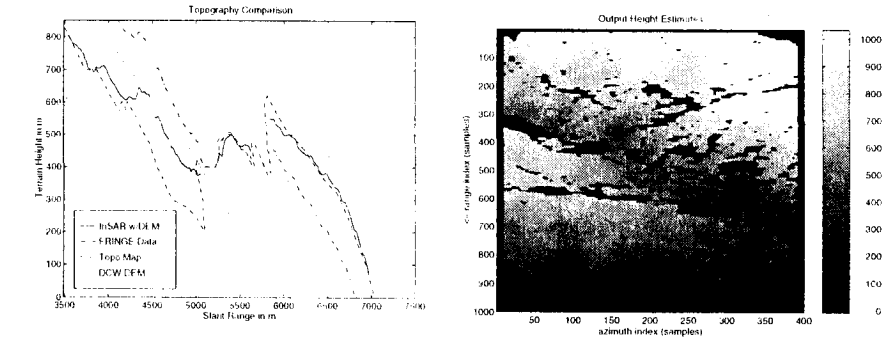

(a) DEM comparison. (b) Output height estimates.

Figure 6: InSAR topography estimate for Sardinia dataset.

Geology

Chairperson: **J. Bodechtel**

THE FIELD EXPERIMENTS SYNCHRONOUS WITH ERS-1 AND 2 TANDEM MISSION FOR THE SIMULATION OF NEOTECHTONIC MOVEMENT

K.S. Rao and Y.S. Rao
CSRE, IIT, Powai, Mumbai-76, India
E-mail: **ksrao@disha.csre.iitb.ernet.in**

ABSTRACT

Using differential SAR Interferometry technique, it is possible to detect subtle changes in the Earth's land and ice surfaces over a period of time to an accuracy of millimetres. The technique involves interferometric phase comparison of successive SAR images. The results so far available related to the above technique are limited and there is a need to conduct further experiments to strengthen the earlier results. Taking advantage of ERS-1 and 2 tandem operation, experiments were conducted to simulate Earth crust movement by installing corner reflectors (CRs). The CRs were exclusively designed, fabricated and installed for the simulation. From April to June 1996, the corner reflectors were lifted systematically with tandem passes and accurately measured on the ground. The movements will be estimated using differential SAR interferometric technique.

Keywords: Differential SAR Interferometry, corner reflectors, SAR, Earth crust movement.

1. INTRODUCTION

In SAR interferometry, phases of the two images of the same area of the earth's surface, but gathered from different view points of the satellite are combined to give information on terrain elevation. The accuracy with which the terrain height can be estimated depends on the base line, however the reported accuracy so far is about 5 meters. Extensive work was carried out by several investigators on terrain elevation mapping using SAR Interferometry technique (Zebker & Goldstein (1986), Rodriguez & Martin (1992), Zebker et al. (1994) and Prati et al (1994)).

In differential SAR interferometry, three or more SAR images are processed for the detection of small changes over a period of time. The relation between the change in the height (δh) and the corresponding phase difference (Φ in radiance) is given by

$$\delta h = (\lambda \Phi) / (2. \pi . \text{Cos} (\varphi))$$

For ERS SAR system $\varphi = 23$ degrees and $\lambda = 5.66$ cm. Substituting these values, we get

$$\delta h = (0.9786119) \Phi$$

Using the Differential SAR Interferometry technique, Coulson et al (1993) reported that two corner reflectors moved one cm during experiments were identified and the lifting heights were estimated as 9mm and 7mm respectively. Using continuous ERS-1 SAR data over 18 months period, Massonnet et al (1995) measured surface deformation of an active volcano at Mount Etna. Wegmuller et al (1995) extended the differential SAR technique for Land-surface analysis and classified various features. Massonnel et al. (1993, 1994) and Zebker et al (1994) generated coseismic interferogram using ERS-1 SAR data for the Landers earthquake and measured the surface deformation

We have taken up a project, Sponsored by ISRO-IIT(B) Space Technology Cell, to study the Lathur Earthquake, India using Differential SAR Interferometry technique. As a part of the above project, we conducted experiments synchronous with ERS-1 and 2 tandem operation to get experience in processing and analysis of SAR data over Indian test site and also to confirm the reported results. The aim of this paper is to present our experience and the results of our experiments. In the subsequent sections, the test site, design - fabrication and mounting of corner reflectors, ERS-1 and 2 tandem passes, sequence of lifting of CRs and processing of data were discussed.

2. TEST SITE

The test site for carrying out the experiments was selected near Bhavnagar city, north-western part of India, Gujarat state with latitude 22^0 and longitude 72^0. The area was extensively surveyed as a part of SIR-C ground truth data collection program. Another reason for selecting this area was that it was covered by two adjacent passes of the satellites according to the ESA acquisition program. It means that we selected overlapping portion (side-lap area) of two passes of ERS-1 and 2 satellites so that the CRs will be imaged once in every 17 days. The area is flat and not covered by electric poles, buildings etc. The test site location along with ERS-1 and 2 passes is given in Fig. 1

Most of the area in the SAR scene comes under coastal wasteland and is affected by tidal waters through numerous streams. In summer, the area

is dry and some places plowing practices were growing on for the cultivation of Bajra and Jowar in rainy season. Sea and rainy water inundates the area particularly in the rainy season. From rainy season to the end of the winter, the area is covered by the grass and is used as a gangland. In a few locations, salt is cultivated using either underground salt water or sea water that comes through streams. The only vegetation present throughout the year is prosopis Juliflora and can be seen along the roads and many places in the agriculture fields. The soil colour varies from grey to black and texture varies from sandy to clay. The roughness of the locations where the CRs mounted varies from smooth to medium. A small part of scene covers hilly terrain with varying elevations up to 500 metres from the sea level.

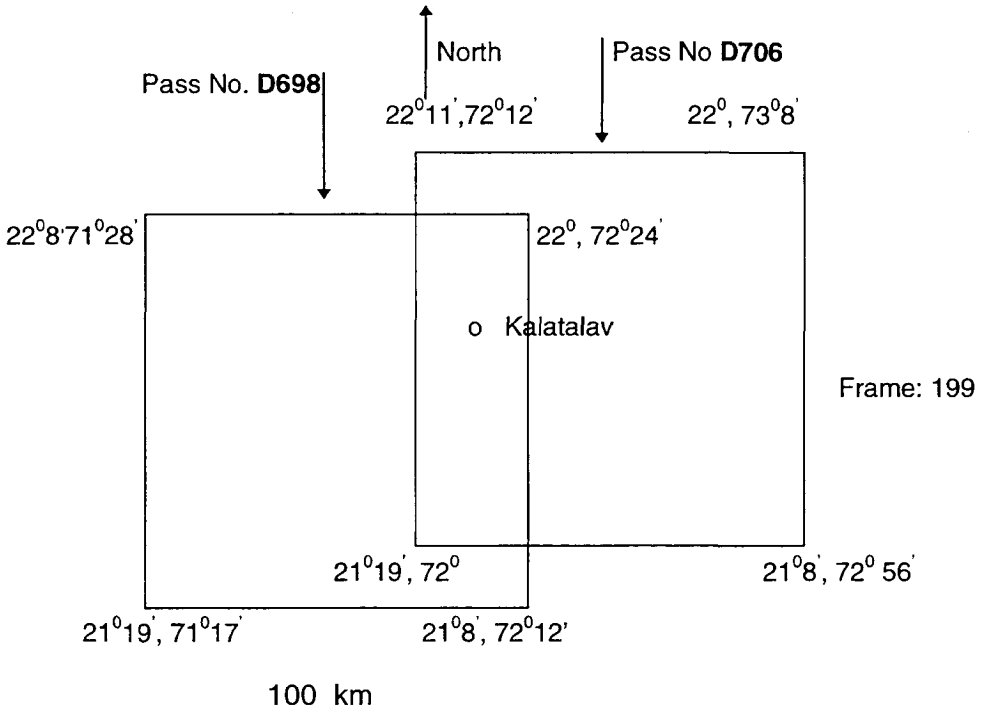

Fig. 1 ERS frames with test site location at Kalatalav

3. FIELD WORK PREPARATIONS

3.1 DESIGN AND FABRICATION OF STAND FOR CORNER REFLECTORS

Generally, corner reflectors are used for the absolute calibration of SAR signals. In this experiment, our purpose of using corner reflectors is to simulate Earth crust movement by moving or lifting the position of corner reflectors from one pass to another pass of the satellite. In order to measure the movement of corner reflectors, there should be a proper mechanism for moving the corner reflector and then taking an accurate measurement. In order to incorporate these facilities, a stand was prepared and attached to each corner reflector. The stand can be dismantled from the corner reflectors for easy transportation.

For strongly holding the corner reflector, an iron pole with height of 58 cm and diameter of 2.8 cm were chosen. One side of the pole is slightly cut at a fixed position for the movement of a screw over the cuts. The screw is attached to other iron pipe with slightly bigger diameter (3 cm) than the iron rod. The pipe can be slided over the rod using the screw and can be locked at any required position. This screw can be used for vertical movement of corner reflector. The maximum range that can be lifted over the rod is upto 18 cm. For measuring the vertical movement of corner reflector, a scale and a pointer are attached. The accuracy of the scale is 1 mm.

Two couplings were attached to the pipe one at the bottom and other at the top. To these couplings, two small rods are fixed and they joined in such a way that the corner reflectors will sit on the top rod. There is a screw arrangement for the bottom rod. By moving this screw at the bottom rod, corner reflector can be oriented to boresight angle to get the highest gain of radar signal. By moving the screw, the rod length changes and thereby the orientation angle of corner reflectors. For 61.2 cm of the rod length, the corner reflector will orient properly to the radar look direction. For the top rod, another two rods were welded perpendicularly. To these parallel rods, holes were made for fixing the corner reflectors. Corner reflectors can be

mounted on the cross rods. The dimensions of the stand are designed in such a way that for any possible orientations of the CRs, the stand will be completely masked by the CR from the view of the satellite. This care is taken to see that no signal will be reflected from the stand.

3.2 DESIGN AND FABRICATION OF CORNER REFLECTORS

Four corner reflectors with size of 81.5 cm were fabricated. The material used for CRs is a single aluminium sheet with thickness of 1 mm. A single sheet for each CR was moulded in such a way that it forms a corner reflector. These CRs could not be dismantled for transportation. A few small holes were made on the three sides of corner reflectors for smooth flowing of air and there by avoiding damage due to strong winds. More information on fabrication and installation of CRs can be found from Polcal user manual (vanZyl et al. 1990). The gain of the corner reflectors for ERS-1 and 2 SAR parameters is 27.6 dB.

3.3 CONSTRUCTION OF BASE FOR THE CR STANDS

To avoid any shrinkage or swelling of soils during the three months period of the experiments and also for exact re-fixing of the CRs, a base is constructed by digging the soil. The ground was dug to a depth of 15 cm of 30 x 30 cm area. First 5 cm depth was filled with sand and then 5 cm depth was filled with gravels and the remaining portion was filled with concrete. A mark was fixed on the centre of the base which will serve as a reference point for GPS measurements. Four metal projections were fused on four corners of the base to fix a wooden plank of thickness 5 cm to cover the concrete base from the view of the satellite.

3.4 INSTALLATION OF CRS IN THE FIELD

After the fabrication of stands, CRs and the base, the CRs were installed in the field by mounting them to the stands and then to the wooden plank of the base. The front two bottom corners of CRs were tightly tied to the wooden base with wires to avoid oscillations of CRs due to strong winds.

The locations at which the four corner reflectors are mounted are shown in Fig.2 as No. CR1, CR2, CR3 and CR5. They were well separated by 500 metres to avoid the influence of one on another adjacent corner reflectors. They were also away from electric poles and buildings. For orienting the corner reflector's boresight towards the radar beam, we tilted the CRs by 31.7^0 from the horizontal. It is the difference between boresight angle (54.7^0) and SAR incidence angle. While orienting CR towards the radar beam direction, another important parameter, one has to consider, is satellite orbit inclination angle. This angle for ERS-1 and 2 satellite is 98.5^0 and with respect to north it is 18.5^0. Using magnetic compass, magnetic north and south were identified and offset between geographic north and magnetic north were considered for orienting corner reflector perpendicular to the satellite orbit pass. The corner reflector was turned by 12^0 from magnetic north so that the boresight of CR will coincide with the radar look direction.

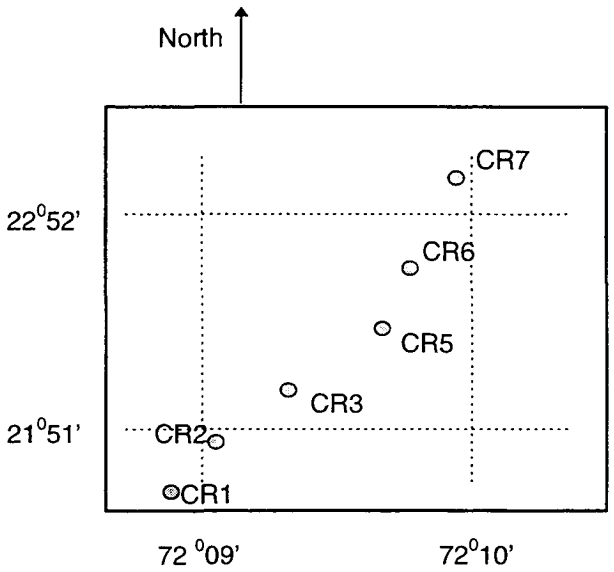

Fig. 2 Locations of 6 CRs (not to scale) based on Differential GPS measurements: CR1 (Lat 21°50'39" Long. 72°8'54"), CR2 (Lat 21°50'56" Long. 72°9'7"), CR3 (Lat 21°51'13" Long. 72°9'18"), CR5 (Lat. 21°51'32" Long. 72°9'42") and CR6 (Lat. 21°51'44" Long 72°9'45")

Two more corner reflectors (No. CR6 and CR7) without stand were mounted on the base at two places. They were fixed all through the experiment without any movement. The sizes of these corner reflectors are 90 cm and 60 cm. These can be used for the calibration of the SAR signal and also as a fixed reference points required for the computation of differential SAR Interferometry.

4. LIFTING OF CRS

As shown in Fig. 1 the test site is covered by two adjacent passes. ERS-1 satellite imaged the area with path No. 706 on April 4, 1996 around 11.30 a.m.. Next day i.e. April 5, 1996 ERS-2 satellite collected data over the same area. The test site was also covered through adjacent path number 698 on April 23 and 24 1996 by ERS-1 and 2 satellites respectively. After 35 days from April 4,

1996, the same area was again covered through path No. 706 and collected data over the test site on May 9 and 10, 1996 by ERS-1 and 2 satellites respectively. Acquisition of data by both ERS-1 and 2 satellites over two adjacent passes are given in Tables 1 and 2.

To lift the corner reflectors, systematically synchronous with satellite passes, knowledge on differential SAR interferometric technique is essential. For obtaining a change or movement of earth objects, minimum three SAR scenes over the same area are required. Within the period of three acquisitions, the object on the Earth should not be moved more than once. If so, movement of the objected could not be measured. Keeping the above principle in mind, we moved the three corner reflectors (No 1, 2 and 3) to different heights at different dates for different passes. The corner reflector 5 was 0.0 cm. throughout the period of the experiment. The lifting heights for Path 706 and 698 are given in Table 1 and 2 respectively.

Table 1. Lifting height (cm.) information of corner reflectors synchronous with ERS-1 and ERS-2 passes (1996) in path number 706 of NRSA, India

S.No.	Satellite	Date of pass	CR1	CR2	CR3	CR5
1	ERS-1	April 4,	0.0	0.0	0.0	0.0 cm.
2	ERS-2	April 5,	0.0	0.0	0.0	0.0 cm.
3	ERS-1	May 9,	2.0	4.1	5.9	0.0 cm.
4	ERS-2	May 10,	3.1	6.1	8.9	0.0 cm.
5	ERS-2	June 14,	1.0	4.9	7.1	0.0 cm.

Table 2. Lifting height information of CRs synchronous with ERS-1 and 2 passes in Path number 698 of NRSA, India

S.No.	Satellite	Date of pass	CR1	CR2	CR3	CR5
1	ERS-1	April 23,	0.0.	0.0	0.0.	0.0 cm.
2	ERS-2	April 24,	0.0.	0.0	0.0	0.0 cm.
3	ERS-1	May 28,	3.1	3.1	8.5	0.0 cm.
4	ERS-2	May 29,	1.0	4.9	8.9	0.0 cm.

5. GPS MEASUREMENTS FOR THE POSITION OF CRS

The main aim of taking Global Positioning System (GPS) measurements in this experiment is to identify geographical Latitude and Longitude of each corner reflectors and their absolute heights. Using these position measurements, mis-identification of corner reflector in the image can be avoided. Differential GPS measurements were taken at the centre of each corner reflector base and the values are given in Fig. 2. A few measurements were also taken at hilly region for topography.

6. PROCESSING OF A TANDEM PAIR

SAR Interferometry software developed by ESA (ISAR) was successfully installed at CSRE, IIT - Bombay and being used for the above research work. The ERS-1 and 2 tandem data acquired on April 4 and 5, 1996 through pass D706 with baseline of 117 m were processed using ESA, INSAR. To get experience in using ISAR software, A small window of 256 by 256 pixels were extracted from big scene of 50 km x 50 km at two locations, one for smooth surface and the other for hilly terrain. The fringes generated, with orbital parameters, for smooth surface and hilly terrain appear to be alike with small differences. We are trying to analyse the causes for getting such fringes.

7. CONCLUSIONS

Experiments were conducted synchronous with ERS-1 and 2 tandem operations for simulating the earth crust movement by installing several corner reflectors in the field. For this purpose, CRs were specifically fabricated along with stands and bases for lifting their heights with greater accuracy and reproducibility. Tandem data were processed using ESRIN, INSAR software for generating fringes. The work for estimating the heights of CRs is in progress.

ACKNOWLEDGEMENTS

The authors are thankful to Prof. V. S. Chandrasekaran, Head, CSRE, IIT-B for his constant encouragement. We are also thankful to other colleagues of CSRE who have extended their fullest co-operation for the successful conduction of the experiments. Finally we thank ISRO-IITB Space Technology Cell for sponsoring the project.

REFERENCES

Coulson, S.N, Rocca, F. Prati, C., and Monti Guarnieri, S., 1993: SAR interferometry with ERS-1, Earth Observation Quarterly, No.4, pp.20-23.

Mossonnet D., Rossi M., Carmona C., Adragna F, Peltzer G., Feigl K.,and Rabaut T., 1993: The displacement field of the Landers earthquake mapped by the radar interferometry, Nature, 364, pp.138-142.

Mossonnet D., Feigl K., Rossi M., and Adragna F., 1994: Radar interferometric mapping of deformation in the year after the Landers earthquake, Nature, 369, pp.227-230.

Massonnet D., Briole P., and Arnaud A., 1995: Deflation of mount Etna monitored by space borne Radar Interferometry, Nature, Vol: 375, pp. 567-570.

Prati, C., Rocca, F., Monti Guarnieri, A., and Pasquali, P., 1994: Report on ERS-1 SAR interferometric techniques and applications, Dept. of Electrical Engineering, Politicinico di Milano, PizzaL. da Vinci, 32-20133 Mileno, Italy, June 1994.

Rodriquez, E., and Martin, J., 1992: Theory and design of interferometric SAR's, Proc. IEEE, 149, 147-159.

Wegmuller U., Werner C.L., Nuesch D., and Borgeand M., 1993: Land surface analysis using ERS-1 SAR interferometry, ESA Bulletin, No. 8, pp.30-37.

VanZyl, J.J., Burnette C.F., Zebker, H.A., Freeman A., and Holt, J., (1990), Polcal user's manual, JPL, NASA. CA 91109.

Zebker, H.A., and Goldstein, R, 1986: Topographic mapping from interferometric synthetic aperture radar observations, J. Geophys. Res., 91, pp.4993-5001.

Zebker H.A., Rosen, P., Goldstein R., Gabrid, A., and Werner C., 1994: On the derivation of coseismic displacement fields using differential radar interferometry: the Landers earthquake, J. Geophys. Res. 99, pp.19617-19634.

Zebker, H.A., Werner C., Rosen P.A., and Hensley S., 1994: Accuracy of topographic maps derived from ERS-1 interferometric radar, IEEE Trans. Geosci. Rem. Sens. 32, pp.823-836.

ASSESSMENT OF TWO METHODOLOGIES OF ERS MIXING FOR GEOLOGICAL INVESTIGATIONS : ERS TIME-SERIES AND OPTICAL-RADAR FUSIONS

YESOU H.*, BRAUX C.**, ROUZEAU O.**, CLANDILLON S. *, ROLET J.*** and de FRAIPONT P.*

* SERTIT , Service Régional de Traitement d'Image et de Télédétection, Parc d'Innovation , bd Sébastien Brant, 67400 Illkirch, France Ph : 33 (0)3 88 65 51 95 ; Fax: 33 (0)3 88 65 51 99
e-mail: herve@sertit.u-strasbg.fr ; URL adress: http://sertit.u-strasbg.fr

**BRGM, Direction de la Recherche, Département Géophysique et Imagerie Géologique, BP 6009 - 45060 ORLEANS Cedex 2 - France - Ph: (33) (0)2 38.64.34.34
e-mail: ROUZEAU@sgn.brgm.fr, URL adress: http://www.bgrm.fr

*** Dpt. Sciences de la Terre et Groupement Ouest Image, Avenue le Gorgeu 29287 Brest Cedex, France, Ph: (33) (0)2 98 01 62 72. e-mail.: Joel.Rolet@catamaran-gw.univ-brest.fr

ABSTRACT

An appraisal of the performance for geological feature mapping potential for ore exploration survey of ERS-1 and fused optical data/ ERS was carried out. Firstly, multilook multitemporal images were produced and analysed. In a second step, the merging the best multitemporal multilook image (a 27 ENL image) and a multispectral data was achieved using both photographic and numerical techniques. The assessments of the derived data were done through multisources analysis using the SynARC software. It have be pointed out that ERS added value products, such as multitemporal average image, are very interesting for the studies and analysis of geological structural features and that the synergism between optical and SAR data have to be promoted.

Keywords: Multitemporal fusion, SAR, multisensors, mapping, exploration, mineral, structure

1 - INTRODUCTION

Within the frame of the Project Pilot PP2-F10, an appraisal of the performance for geological feature mapping potential for ore exploration survey of ERS-1 and fused optical data/ ERS was carried out over the South Armorican Shear Zone (Brittany, Western France). This study area was selected on the basis of the availability of data base of remotely sensed imagery, including times series ERS, SPOT, Landsat, Seasat data, and because this area presented a metallogenical interest. The SASZ and the related granites are known to control mineralisation such as Au, Sb, Pb (CHAURIS et al., 1977; FOUQUET, 1980; BONNEMAISON and MARCOUX, 1987; BRAUX et al., 1990). Plus, a regional survey of identification of gold bearing areas have been recently carried out by the BRGM, the French geological Survey Office, pinpointed out few sectors in this area having a great potential for gold mineralization (BRAUX et al., 1991).

2 - LOCATION OF THE STUDY AREA

The study area corresponds to an erosional palaeo-surface with low topographic amplitude. The bedrock is hidden by alterites (weathered crystalline and sedimentary rocks) and Quaternary formations. The ancient agricultural system has made Brittany a region intensively criss-crossed by hedges delimiting small ordered fields, woodlands, hamlets, and villages. In such countryside, changes in the parcel arrangements reflect relationships between land use and geological pattern (ROLET and YESOU, 1990; BRAUX et al., 1991).

The major geological object is the South Armorican Shear Zone, SASZ (JEGOUZO, 1980). In the landscape, the SASZ appears as a succession of narrow valleys and elongated depressions where some wetlands and lakes take place. The SASZ, trending N90-100°E, was active for over 360 My. At a first stage, it corresponded to a senestral shear zone (BRUN and BURG, 1982), then functioned as a dextral transcurrent faulting system, characterised by the development of early ductile mylonite and then latter brittle breccias. A 40 km dextral offset has been proposed for this accident (JEGOUZO and ROSSELO, 1988). During the Carboniferous active regional shear, along the SASZ, the Central and South domains were intruded by aluminous leucogranites, 345 to 290 My. Replays of the SASZ occurred during upper Carboniferous (Stephanian), Tertiary and Quaternary. Seismical data show that it is still an active zone (NICOLAS et al., 1990; BESNUS et al., 1993).

3 - USED DATA

Fourteen images acquired from October 92 to August 1993 were used (Table I). From this set, on the basis of their radiometric qualities, mostly tonal variations and nine images were selected for further investigation. These corresponding to data acquired in descending mode are indicated in bold in the table I. During the

pre-processing step the SPOT panchromatic images was georeferenced in Lambert system. Then, the multispectral optical images and the SAR data were co-registred to the georeferenced SPOT image.

Orbit	Frame	date	mode
6566	2637	92 10 17	des
7067	2637	92 11 21	**des**
7568	2637	92 12 26	**des**
8069	2637	93 01 30	**des**
8305	9639	93 02 15	ass
8534	963	93 03 03	ass
8570	2637	93 03 06	**des**
9035	963	93 04 07	ass
9071	2637	93 04 10	**des**
9536	963	93 05 12	ass
9572	2637	93 15 05	**des**
10073	2637	93 06 19	**des**
10574	2637	93 07 24	**des**
11075	2637	93 08 28	**des**

Tableau I : Characteristics of the used ERS SAR data. Data merge in the temporal ERS averaged image are indicated in bold.

Sensor	SPOT	SPOT	Landsat 5
Scene	26-253	27-253	203/26- 27
Date	23-02-90	22-04-87	24-02-85
Mode	PAN	XS	TM
Resol.	10 m	20 m	30 m
Incidence	7°5 R	23,4°L	0

Tableau II : SPOT and Landsat characteristics

4 - ASSESSMENT OF ERS DATA ALONE

In a first step an assessment of raw ERS and multitemporal colour composites was done. On the used ERS-1 data, textural variation and contrast are so weak that geomorphologic and tectonic features are not accentuated. It was not possible to extract an useful lineament map, interpretation of these data would been hazardous. Thus, the use of these monotemporal data and colour composites did not appeared as valuable remote sensing technique for structural mapping and mineral exploration in this context of temperate agricultural region. Thus enhancement techniques, such as multitemporal average and fusion of optical plus radar data, were tested

5 - ERS ENHANCEMENT VIA MULTITEMPORAL AVERAGE TECHNIQUES

Radar image enhancement by multitemporal average is a relative new technique allowing to improve the radiometric resolution, preserving the nominal spatial resolution of the SAR sensor (PENICAND et al., 1993; FELLAH, 1995; LAUGIER et al., 1997). In the case of invariant /stationary objects, the final ENL corresponds to the product of the initial ENL (3 for GEC data) and the number of summed images. Temporal averaged images have been produced by summing ERS data acquired under the same acquisitions parameters (mode, incidence angle) and during the same vegetative cycle: November 1992 to January 1993; March 1993 to May 1993; June 193 to August 1993. These images were noted, *winter*, *spring* and *summer image*. Plus, an image with a ENL of 27, noted *total imag,e* was produced by the fusion of 9 descending images. From these enhanced images, high resolution negative films were produced, as well as prints enlarged at scales of 1/100 000 and 1/ 80 000.

The *summer image* presents weak contrast. The parcelling is not well noticeable. Major structures are not well marked excepted those facing the radar beam. The *winter and spring images* are similar, the winter image being a little bit more contrasted. On these data, the agricultural parcelling is well noticeable and so as it is possible to access to the major part of the structural features enhanced by this parcelling. Whereas, structures associated with the hydrological network are sometime a little bit difficult to extract. In the *total image*, the good restitution of geometric information, such as the agricultural parcelling, with an effective spatial resolution in the same range than high resolution optical data. From this total image fine interpretative results with the mapping of the regional foliation, shear zones and of the late fracturing networks, can be expected. This will be present later.

6 - INFORMATION ENHANCEMENT BY ERS AND OPTICAL FUSION

The merging the multitemporal multilook image and a multispectral data, derived from the mixed data, call *optical enhanced image* and resulting from the fusion a Landsat TM and a SPOT panchromatic image[1], was achieved using robust procedures, photographic techniques and Principal Component Analysis (PCA) (YESOU et al., 1993a; POHL, 1996).

[1] The merger of the Landsat and SPOT was realized as following. Firstly, a PCA was achieved in order to extract spectral contrast from Landsat TM.. Then, to increase the spatial resolution, a SPOT panchromatic was combined by selective linear combination with the extracted spectral image. SPOT merging was done selectively in order to avoid the distorsion of the spectral content of Landsat TM. Only the PC corresponding to the visible part of the spectrum domain, the thrird PC in this case, was combined with the SPOT (YESOU et al., 1993b). The final optical product, having three channels, $PC1_{TM}$, $PC2_{TM}$ $PC3_{TM}$*PAN, is call the *optical enhanced image*.

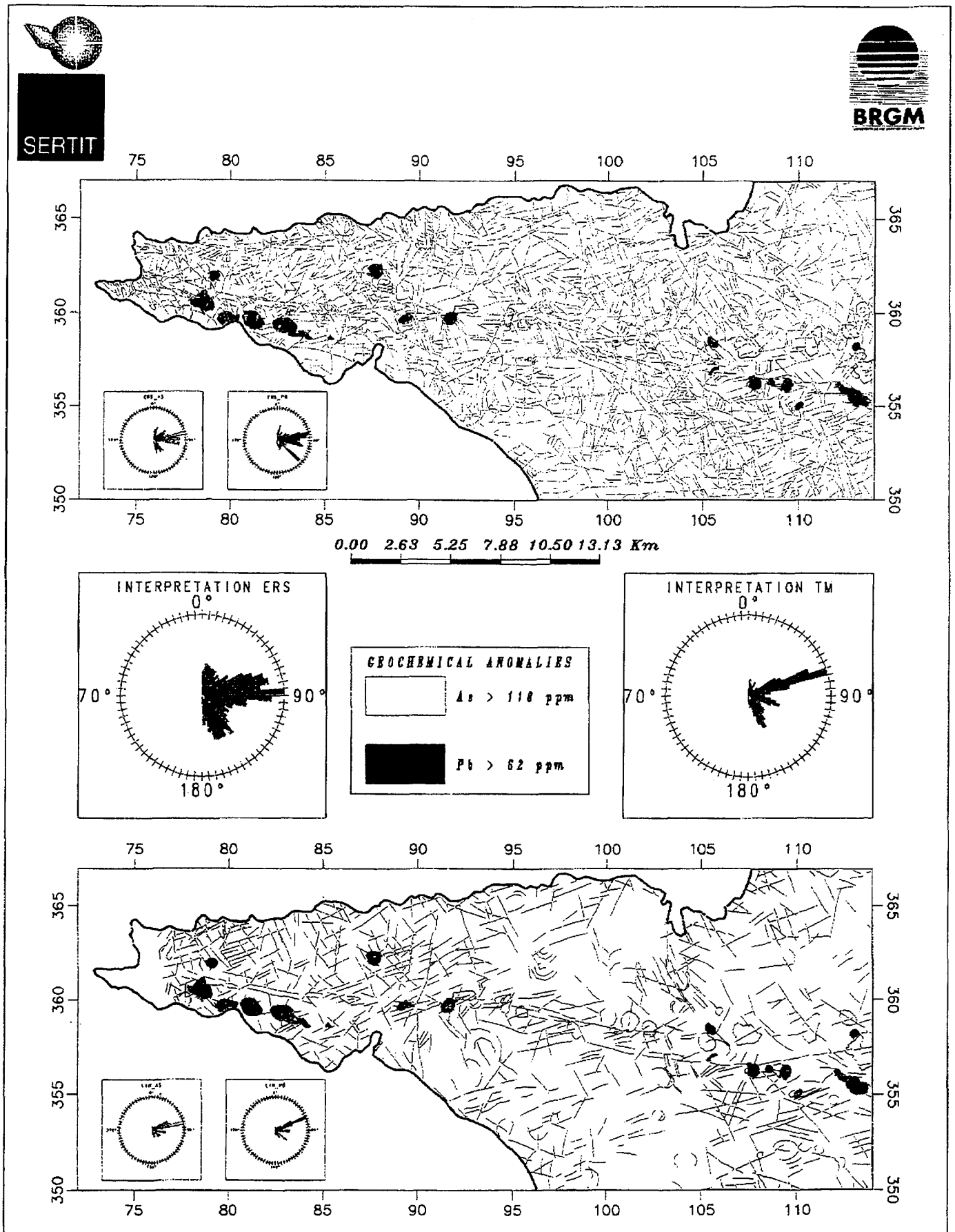

Figure 1 : Lineament maps derived from ERS enhanced image and Landsat TM data and direction frequency diagrammes obtained both by sensors type (great diagramme) and by family of mineralization anamalies (little diagrammes).

Photographic techniques, simplest and efficient ones, were used to merge the *optical enhanced image* and the *total image* derived from ERS data. It corresponds to the attribution during the colour printing of one of the three colour planes (cyan, magenta, yellow) to the radar image and the two last to two optical channels. Eighteen combinations are possible, the best results were obtained with the $PC3_{TM}$*PAN, *total image*, $PC1_{TM}$, on Cyan, Magenta and Yellow.

A PCA was also achieved in order to merge the optical and radar data corresponding to the following set $PC1_{TM}$, $PC2_{TM}$, $PC3_{TM}$*PAN, and the ERS *total image*. The three first obtained PCs present the merging of the information derived from radar and optical data

7 - ERS DERIVED MAPS ANALYSIS

From the enhanced radar image and from the fused optical-radar images which combine information derived both from radar and optical data, lineament maps were produced (Fig. 1). Four families of linear elements could be discerned:

- The first one, oriented N50-70°E, corresponds to a regional foliation defined in the crystalline rocks (western area), and to a regional cleavage in the sedimentary Palaeozoic and Proterozoic series (eastern area).
- A N90-105°E family corresponds to mylonite shear zones. The most important one is located in the axial part of the studied area and corresponds to the SASZ. Replies of this accident are developed on its southern border.
- Two later fracturing systems could be also distinguished, a NS and a N150°E, respectively late-Variscan and post-Lias in age.

Few curvilinear and circular elements were also extracted. These might indicate plutonic domes (ROLET et al., 1993).

8 - ERS DERIVED MAPS APPRAISAL

The maps derived from enhanced ERS and fused optical-ERS data were compared with those obtained during previous studies from Seasat, merged Spot -Seasat data and Landsat TM images (YESOU et al., 1993; ROLET et al., 1993; BRAUX et al., 1991). Mapped features derived either from the ERS multilook multitemporal image or from optical-ERS merged image are, but with a finest level of detail, the same than those observed derived from the Landsat and the merged Seasat-SPOT data.

The assessment of ERS derived products for ore exploration was carried at the BRGM. This was done though a GIS multisources using the SynARC software. The lineament map derived from the multitemporal multilook ERS image was compared with a previous lineament map derived from Landsat TM image (BRAUX et al, 1991). Lineaments density and characteristics were analysed both at regional scale and by geological entities. Then derived maps were compared with geophysical and geochemical data (Fig. 1).

Comparing directions of structures derived from ERS and Landsat, a global concordance can be mentionned with some differences concerning relatives proportions. All known families of structures have been extracted on either the ERS derived documents or Landsat TM one. Plus, numerous of elements of four major families, have been detected as common: N°65-80 foliation, N°95-100° shear zones and N150-170° late fracturing. Structures N150-170°E are dominant on the ERS derived interpration and the N65-80°E on the Landsat TM one. This fact could be related with the orientation of the sensors, the N150-170°E structures are in fact facing the radar beam, so are well enhanced on the ERS derived image rather than EW structures are when the Landsat TM data where acquired outlined by the sun shadow.

From a general point of view, considering number and length of the detected structures, there is a report of three considering either the number of elements extracted or the total length and a report between one point five and two for the cumulated length, mean and standard deviation of length (Table III). These results indicated that if more structures have been detected their extension is smaller. this means that more details are available on the geometry of the geological structures. The fact that ERS interpretation provides more diversified information than Landsat TM data could be linked with two point ; the improvement of the apparent spatial resolution of the multitemporal average ERS image and the followed approach. The Landsat data were analysed during a operational survey, when the investigation of the ERS data was more deeper due to the exploratory aspect of the Project Pilot programme.

	TM	ERS1
Lineament number	1514	4745
Cumulated length	927 km	1605 km
Mean length	582 m	338 m
Maximal length	2787 m	2279 m
Length standard deviation	414 m	259 m

Table III : Statistical comparison of lineaments derived from the enhanced ERS image and the Landsat TM data

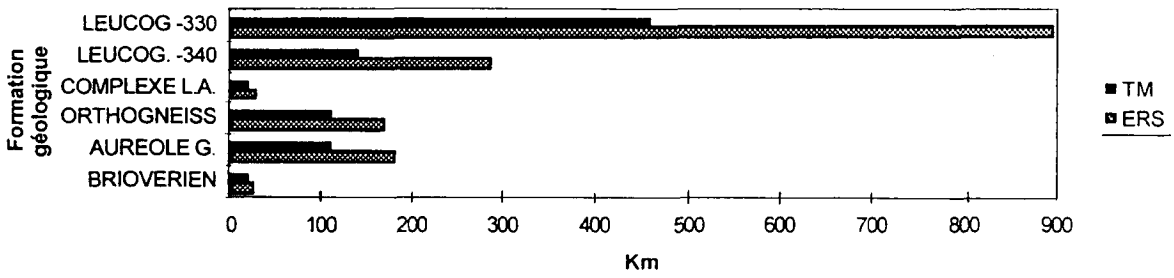

Figure 2 - Lineament cumulated length by geological entity

The analysis conducted by geological entities (granite, sedimentary etc ..) confirm that extracted lineaments from ERS enhanced image are more numerous and systematically smaller than those derived from the Landsat TM (Figure 2).

The Landsat TM data provide a clear information concerning the early structures such as the South Armorican Shear zone, that is pointed out also by the good correlation between As anomalies and lineaments derived from Landsat TM data. The ERS lineaments map provides a dense information over all the studied area, and a precise mapping of the late fracturing networks the SASZ. This fact is confirmed by the statistics analysis and by the correlation between the Pb anomalies and lineaments derived from ERS data.

The derived ERS and Landsat TM map where integrate with multisources sources (geophysical, geochemical, such as As, Ag, Sb and Pb distributions) to analyse the relationship of the extracted lineaments and the ores location. The relationship between Ag and As anomalies and EW fracturing network is obvious on the integrated Landsat TM plus ore map. Whereas the confrontation between the ERS derived lineament map and the ore locations the relationship between the late fracturing networks and the PB and Sb ores is well pointed out. Plus, on the integrated map ERS lineament and ore location, the structural control of located ores is better documented

9 - CONCLUSION

Firstly, from this assessment programme, it appears that ERS multitemporal average images, are very promising tools for geological applications. With the summing of at least three images, good results can be obtained. providing improved ERS data useful at relative fine scale. Costs of this ERS added value product, including acquisition and processing, are of the same order than optical current data ones.

Secondly, when possible, i.e. when both type of images are available, the synergism between optical and SAR data have to be promoted. There is a good complementarity between the ERS and Landsat data. The Landsat TM derived map provides a clear information concerning the early structures such as South Armorican Shear zone. Good correlation between As anomalies and lineaments derived from Landsat TM data is observed. The ERS lineament map provides a dense information over all the SASZ study area and mainly on late fracturing networks. This fact is confirmed by the statistics analysis and by the correlation between the Pb anomalies and lineaments derived from ERS data.

10 - REFERENCES

BESNUS Y, CAILLEUX Y., ESNAULT D., FLYNN R., ROLET J. et YESOU H., 1993 : Réalisation d'une base de données sismotectonique avec utilisation d'images satellitaires, sur le Massif armoricain (France). *Actes du Symposium Canadien de Télédétection*, Sherbrooke, Québec, Canada, 7-13 juin 1993, pp. 903-908.

BONNEMAISON M. et MARCOUX E., 1987 : Les zones de cisaillements aurifères du socle hercynien français. *Chron. rech. min.*, **488**, pp. 29-42

BRAUX C., DELPONT G., BONNEFOY D., CASSARD D. et BONNEMAISON M., 1990 : Interpretation of remote sensing data over the South Armorican shear zone (Brittany-France) : a contribution to exploration for gold mineralization. *Proceedings of Remote sensing an operational technology for mining and petroleum industries*, London, 29-31 october 1990.

BRAUX C., CASSARD D., DELPONT G., BONNEFOY D., CORPEL J. et LAGNY Ph., 1991 : Identification de secteurs à vocation aurifère dans un couloir tectonique régional par interprétation de données satellitaires, géologiques, géophysiques intégrées dans un système d'information géographique. L'exemple du

cisaillement sud-armoricain. *Chron. Rech. Min.*, **505**, pp. 19-34.

CHAURIS L., FOUQUET Y et MOELO Y, 1977 : Les occurences autimonifères de l'île de Sein et du Cap Sizun (Finistère). Leur place dans la métallogénie armoricaine. *Bull. Soc. fr. Min. Cristallogr.*, **100**, pp. 208-213.

FELLAH K., 1995 : The impact of the observation scale in hydrological applications of SAR data, *ESA-ESTEC/VRL*, Earth Sciences Division, Land/Surface Unit, Stagiaire report, April 1995. 35 p.

FOUQUET Y., 1980 - Les districts antimonifères de Quimper et du Cap Sizun (Finistère). Leur place dans la métallogénie de l'antimoine dans le massif Armoricain. Thèse 3eme cycle, Clermont-Ferrand.

LAUGIER O., FELLAH K., THOLEY N., MEYER C. and de FRAIPONT P., 1997 : High temporal detection and monitoring of flood zone dynamic using ERS data around catastrophic natural events: the 1993 and 1994 Camargue flood events. *Proceedings of 3rd ERS Symposium*, Florence 17-21 March 1997, this issue.

NICOLAS M, SANTOIRE J.P et DELPECH P.Y., 1990 : Intraplate seismicity : new seismotectonic data in Western Europe. *Tectonophysics*, **179**, pp. 27-53.

PENICAND C., CHAMPSEIX N., LEDEZ C., LENTZ C. and RUDANT JP., 1994 : Utilisation de l'imagerie satellitaire radar pour la cartographie de base en milieu tropical. *Proceedings of the 5th EUR Conf EGIS*, Paris, 29, 3-1.4.

POHL C., 1996 : Geometric aspects of multisensor image fusion for topographic map updating in humid tropics. *ITC Publ.*, **39**, 159 p.

ROLET J. et YESOU H., 1990 : Apport de l'imagerie SPOT à la reconnaissance en pays couvert de plans de cisaillement C et de schistosité S. Le cas du Cisaillement Sud Armoricain. *C. R. Acad. Sc.*, **301, Série II**, pp. 1075-1080

ROLET J., YESOU H. et BESNUS Y., 1993 : Structures circulaires et réseaux de fractures. Analyse des données Seasat, SPOT et Landsat TM sur le Massif armoricain (France). *Bull. Soc. géol. Fr.*, **164**, **2**, pp.199-214.

ROUZEAU O., BRAUX C., KING C. et MAURIZOT P., 1996 : Recherche et gestion des ressources renouvelables et non renouvelables à partir de données radar ERS-1. Etude de la fracturation géologique et implications en prospections. *Rap. BRGM R 39154*, 47p., 1996

YESOU H., BESNUS Y., ROLET J., PION J.C. and AING A., 1993a : Merging SEASAT and SPOT imagery for the study of geological structure in a temperate agricultural region. *Remote Sensing of Environment* , **43**, pp. 265-279

YESOU H., BESNUS Y. et ROLET J., 1993b : Extraction of spectral information from Landsat TM data and merger with SPOT panchromatic imagery. A contribution to the study of geological structures. *ISPRS, J. Photogrammetry Remote Sensing*, **48**, pp. 23-36.

YESOU H., BESNUS Y. et ROLET J., 1994 : Perception of a geological body using multisources remotely sensed data - The relative influence of the spectral content and of the spatial resolution. *Int. Jour. Remote Sensing*, **15**, **12**, pp. 2495-2510.

YESOU H., MEYER C. and FRAIPONT (de) P., 1996 : Evaluation of ERS-1 SAR data for set aside lands monitoring. *Proceedings of ERS Applications Workshop*, Londres,6-8 December 1995. *ESA SP-383*, pp. 473-478

Acknowledgement

ERS data were obtained within the framework of the Pilot Project PP2-F10 of the ESA. This work has been also supported by the Aval-SAR programme of the CNES (Décision d'aide à la Recherche 94/CNES/0378). The authors thank A. AING (ORSTOM - Bondy) for providing the high quality enlarged prints and C. KING (BRGM, Direction Recherche) for her project management at the BRGM and also her help and comments on this work.

INVESTIGATION OF ERS SAR DATA OF THE TANDEM MISSION FOR PLANNING AND MONITORING OF SIBERIAN PIPELINE TRACKS

Claudia Streck & Urs Wegmüller

Kayser-Threde GmbH, Dept. of Environmental Monitoring, Wolfratshauser Str. 48, 81379 Munich - Germany, Phone: +49 (0)89-7 24 95-217, Fax: +49(0)89-7 24 95-291, http://www.kayser-threde.de, Email: sc@kayser-threde.de

Gamma Remote Sensing AG, Thunstr.130, CH-3074 Muri, Bern, Switzerland, Phone: +41 (0)31-9 51 70 05, Fax: +41(0)31-9 51 70 08 http://www.primenet.com/~gamma/gamma.html, Email:gamma_rs@pingnet.ch

ABSTRACT

Siberian pipelines, embedded in a mosaic of boreal forest, bogs, rivers, lakes and tundra, are undergoing stress due to varying heave displacements by thawing and freezing of the active permafrost layer. Problems such as the upward movement of the lighter gas pipelines arise due to the melting of frozen surface water in spring, or the downward movement in winter caused by the melting of the frozen soil around the pipeline. These varying movements of the pipeline, depending on the underground, the surface cover and the pipeline itself, may lead to cracks and severe damage. These problems require a permanent monitoring of existing and a careful planning of new pipeline tracks. Currently the pipelines are regularly monitored by visual inspection via helicopter. Planning information such as a DEM and a classification of the surface cover is derived mainly from optical remote sensing and field work. The potential of radar data as a possibly more reliable and cost effective source of information for the monitoring and planning of gas pipelines in the remote and hardly accessible regions of Nadym, Siberia, was investigated. Methods used included the interpretation of multitemporal SAR backscattering as well as SAR interferometric products using ERS-1/ERS-2 Tandem data. ERS SAR data proved to be a valuable alternative for the mapping of the pipelines. The study is being carried out as an ESA Pilot Project (A02.D129) and funded by the German Space Agency (DARA).

1. INTRODUCTION

The all-weather capacity and illumination independence of spaceborne Radar remote sensing offers new opportunities for the planning and monitoring of pipeline tracks in the remote and inaccessible areas of the West Siberian Lowlands. In this taiga biome, land surfaces and their artificial structures undergo up and downward displacements caused by the thawing and freezing of the active permafrost layer. A careful monitoring of existing pipeline tracks and a precise planning of new pipeline tracks is required. The localization of these impacts improves the assessment of the potential hazards. The Active Microwave instruments on board ERS 1- and ERS-2 satellites, launched by ESA, deliver SAR data for this task. A promising technique, where the ERS-SAR data of two passes are combined, is Interferometry. This technique allows the derivation of height and height displacement maps. Further, SAR Interferometry has shown great potential for the mapping of land surfaces (Wegmüller et .al, 1995).

2. TEST SITE AND DATA DESCRIPTION

A test site in the environs of Nadym (latitude 65°30´N, longitude 73°15´E), located in the northern part of the West Siberian Lowlands, has been selected for investigation. Most of the region underlies Permafrost the gas pipelines and other man made structures are exposed to heave displacement. Fig. 1 shows the area of investigation as seen by Landsat TM. Two gas pipeline tracks, surrounded by a mosaic of vegetation, meandering river channels and little thawing ponds cross the test site. In the TM image the pipeline tracks and dust roads appear in bright blue colors. They are embedded in open boreal forest (coniferous forest) which appear in light greenish brown colors. The sparse woods with moss show up as violet and the closed forest of the floodplain (mixed forest) as brown. The greenish areas with little lakes indicate peatland and swampy areas. The red regions are moist depressions with grasses and light green tones occur on burnt areas where fresh vegetation now grows.

In general, pipelines are constructed subsurface, as shown in Fig. 2B. The pipelines themselves are not visible but can be detected indirectly by changes in the vegetation cover caused by their construction. The large pipeline track running from NE to SE consists of 9 subsurface pipelines and has a width of about 1 km. In some areas the pipelines are not covered with sand, but are exposed on the surface (see Fig. 2A). This is mainly in areas where surface water occurs and where the active permafrost layer is very thin and ice is close to the surface (peatland and swamp). Ground truth campaigns were carried out during August 1995 and 1996 and for additional verification the Landsat TM scene of 26/07/95 (see Fig. 1) has been studied. All the subsets which will be discussed later are displayed as rectangles

Proc. 3rd ERS Symp. on Space at the service of our Environment, *Florence, Italy, 17–21 March 1997* (ESA SP-414, 3 Vols., May 1997)

in Fig. 1. Radarsat Fine mode data, acquired on 05.09.1996 (pixel spacing of 6.25 m), was included for analysis.

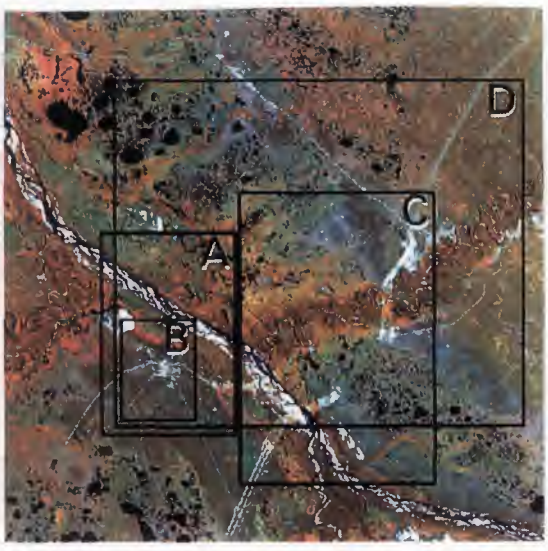

Figure 1: Test Site Nadym, Siberia, as seen by TM RGB(4,5,3) Composite

Figure 2: Pictures of a surface (A) and subsurface (B) pipeline

The following data sets from the tandem phase of ERS-1 and ERS-2 (descending orbits, frame 2277) have been analyzed. The scenes are listed together with meteorological data acquired next the airport of Nadym in Tab.1. The empty cells indicate unavailable information.

Orbit	Date	Temp.C	Precipitation
E1-22839	27.11.95	-29.0	Snowh. 15cm
E2-03166	28.11.95	-24.8	
E1-24843	15.04.96	-2.5	Snowh. 60 cm
E2-05170	16.04.96	-3.5	
E1-25334	20.05.96		
E1-25845	24.06.96	17.7	
E2-06172	25.06.96	12.4	

Table 1: ERS-SLC Tandem data sets and meteorological information

3. DATA PROCESSING

The ERS-SLC scenes have been processed by Gamma Remotes Sensing AG using their Interferometric SAR Processor (ISP). Common spectral-band filtering in azimuth and range was applied. The scenes have been co-registered to a subpixel accuracy. The 5-look intensity images have been calibrated and Frost filtered using a 5x5 pixel window. The coherence was computed adaptively with varying window sizes from 3 x 15 looks for areas of high coherence up to 9 x 45 looks for areas of very low coherence. RGB composites composed of the adaptive filtered coherency images in red, the amplitude of the first date in green and the ratio of the two dates in blue, have been produced. Prior to the ratio calculation (intensity ERS1/ERS2) the amplitudes have been Frost filtered using large 15 x 15 pixel windows, in order to account for the strong signal noise of SAR images.

A useful combination of ERS SLC pairs has been selected for evaluation. The next table lists the orbits for each pair, the time difference in days, the perpendicular baseline and adaptive coherence mean.

InSAR Pair	Time diff. days	Baseline B perp in m	Coh. Mean
22839_3166	1	77	0.73
24843_25344	35	42	0.09
24843_5170	1	57	0.67
25344_25845	35	100	0.09
25344_6172	36	17	0.08
25845_6172	1	82	0.51
5170_25344	34	99	0.10

Table 2: Orbit, Time difference, Baseline and Coherence for investigated ERS Tandem Data

All the tandem pairs show a high coherence mean, whereas the 34,35,36 day repeat cycles with an average coherence around 0.1 do not meet the requirements for Interferometric exploitation. Consequently, the image pair 22839_3166 has been selected for DEM generation. The absolute height information has been derived using 15 Ground control points of known topographic height from the map. The only topographic map available has a scale of 1:500,000. For the 15 GCPs, the average deviation between the interferometric height estimates and the reference height error standard deviation of the control points is about 5m. The elevation is given in the geometry of the map which is used to select the control

points (probably related to Geoid surface as the used Geoid of the reference map is unknown).
All the data sets (ERS, Radarsat, TM) have been geo-referenced to the ortho-rectified coordinate system which is represented in UTM, WGS 84.

4. DATA INTERPRETATION

The figures 3 A and B (see Annex) show the intensity and coherence data for the subset A as indicated in Fig. 1. Following features are indicated: compressor station (reference point (rp) 1), pipeline track (rp 2) and a power line corridor (rp 3). One can clearly depict the linear structures in the coherency image (see Fig. 3B) which can hardly be detected in the intensity image (see Fig. 3A). In the coherency image the non forested areas do have a high coherence compared to the low coherence of the forested areas. The major reasons are orientation of the sensor to the object (see rp 2 and 3) and the ground resolution (rp 3). This clearly demonstrates that the coherency image successfully allows the detection of pipeline tracks and other man-made objects whereas the intensity image does not.
The Fig. 4A (see Annex) shows the uncalibrated amplitude of the frost filtered Radarsat Fine Mode (descending orbit) for the subset B (see Fig. 1). A delineation, derived from Radarsat Fine Mode data Fig. 4B (see Annex) gives an overview of the prominent features. In the Radarsat image the pipeline tracks are black. This is most likely due to the low incidence angle (causing a broader radar shadow). A zoom-in along the power lines shows the typical effect of a bright signal for the pylons caused by the HH polarization. The higher resolution (pixel spacing of 6.25 x 6.25 m) allows a clear detection of all features.
Multitemporal intensity images for the subset C (seeFig. 1) are displayed in Fig. 5 A, B and 6 A, B (see Annex).
Fig. 5A shows the pipeline tracks Yamburg (rp 2) and Urengoi (rp 5) during dry winter conditions on the 27.11.95. The temperature is -29.0 °C and the area is snow-covered (15 cm). The 1 km wide pipeline track Yamburg (which includes 9 subsurface sand- or short vegetation covered pipelines) is clearly visible in the environs of the open boreal forest (see region around rp 2). The backscatter of the pipeline varies due to changing surface cover which depends on the locality and construction work (grasses, bushes (region around rp1); no trees and only sand (region around rp 3); or mosses in the peatland areas or no cover at all (rp 6).) In the floodplain forest the pipeline track (south of rp 3) is almost invisible due to the similar backscatter. In the environment of peatland and permafrost (rp 6) the pipelines are detected very well. This may be due to the snow-covered frozen tundra which has low intensities contrasting increased intensities of the single pipeline itself.
Fig. 5 B shows the same situation on 15.04.96, at an air temperature of -2.5 °C and a snowheight of 60 cm. From personal communication we know that the area is extremely frozen. At the pipeline track Urengoi (rp 5) construction work has been undertaken. In order to replace the sand-buried pipelines, they first need to be dug out. Furthermore, an ice road has been built to cross the river and to access the pipeline track. The change of geometry (slope of the sand hills exposed to the sensor look direction) increased the backscatter. The moist depression (linear dark features) next to rp 1 is extremely frozen. The dirt road (rp 10) is now very bright and gives a high reflection caused by the change of geometry due to traffic and snow removal. All the construction work along the pipeline has to be undertaken in winter because there is no access.in the summer
Fig. 6 A shows the area of investigation on the 20.06.96, when thawing starts and the snow is melting. A clear distinction between the moist loamy peatland areas with short vegetation (rp 6) and the well drained sandy soils where the open forest and sparse forest is located (rp 5), is obvious. An increase in backscatter of about 3 dB due to moisture changes can be observed for the peatland environs. Sparse forest stands with moss can also be distinguished from open forest stands. The border is located near rp 5.
Fig. 6 B shows the date of 24.05.96 at a temperature of 17.7 °C. The area is snow-free, a lot of surface water occurs and the thawing ponds are ice-free (environs of rp 6). The pipeline track Urengoi is now better depicted at location rp 6. Burnt areas appear very bright (west of rp 3).
The interpretation of the multitemporal images gave the following results: detection of construction work during winter, occurring moisture changes in the pipeline vicinity (extreme changes on badly drained loamy soils (peatland, bog, swamp)), and small changes on the well drained sandy soils where forest stands; this allows the determination of freezing and thawing, whereas the pipeline itself is stable and shows hardly any changes in the backscatter.
The figures 7 A,B and C (see Annex) show the multi-temporal coherence for subset C (see Fig. 1). The value of the coherence depends on the following factors: geometry (baseline) and parameters related to the land surfaces. The latter can be further separated into volume scattering and temporal changes such as movement of the scattering object (wind effect) or variation in dielectric constant (freezing and thawing).
The overall coherency for the 27./28.11.95 tandem pair, displayed in Fig. 7 A, is very high (0.7). The small baseline and the stable meteorological conditions (frozen, snow-covered environment) favors this. Clearly visible by its low coherence are moist depression, thawing ponds and river channels. This is due to the temporal de-correlation induced by movement of the scatter and change in the dielectric constant (freezing) see Fig. 9 in the Annex.
Fig. 7 B presents the coherence information for the ERS tandem pair of 15./16.04.96. Clear differentiations between forested and non-forested areas are visible. The low correlation due to volume scattering in the mixed forest of the floodplain (rp 2) is obvious. The areas

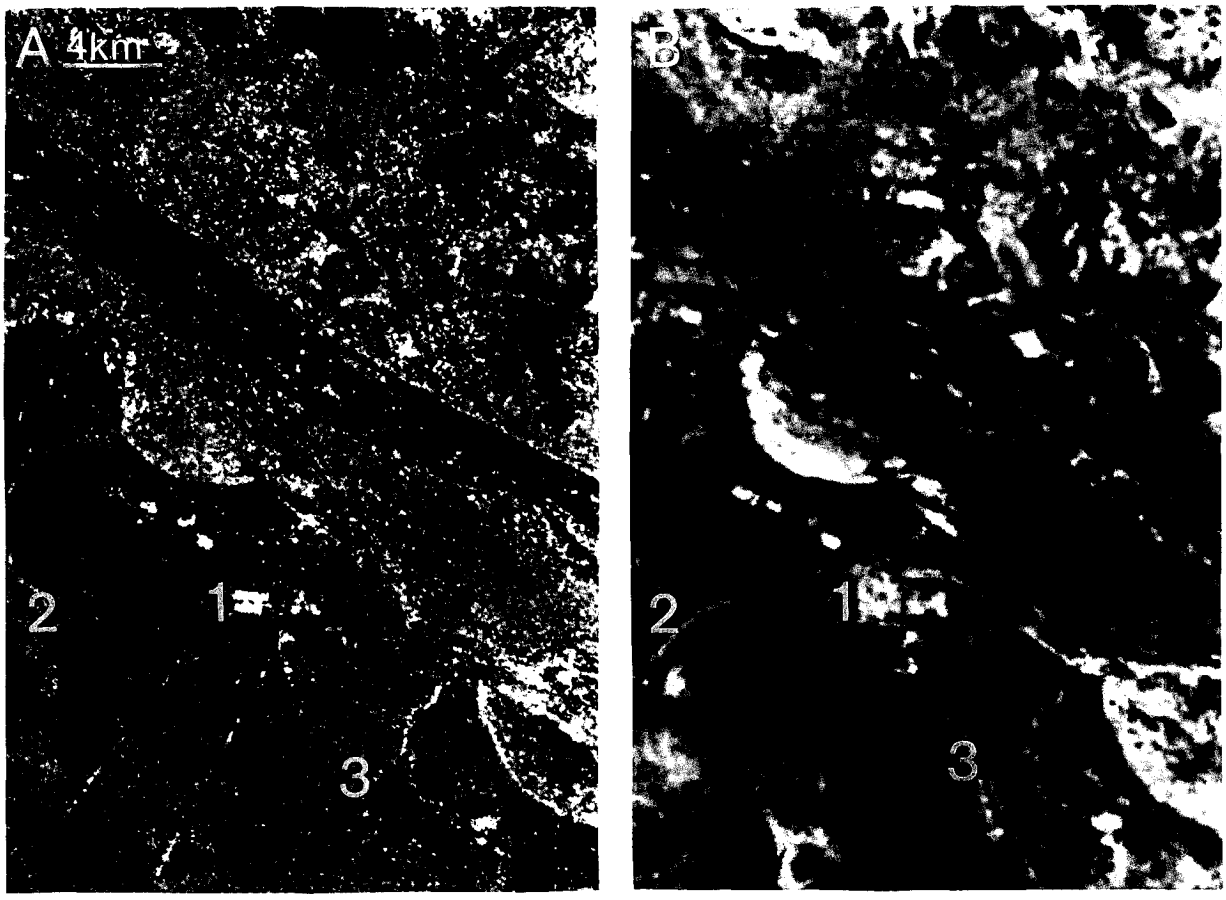

*Figure 3: **A** ERS Intensity Image 25.06.95 **B** ERS Coherence Image 24/25.06.97*

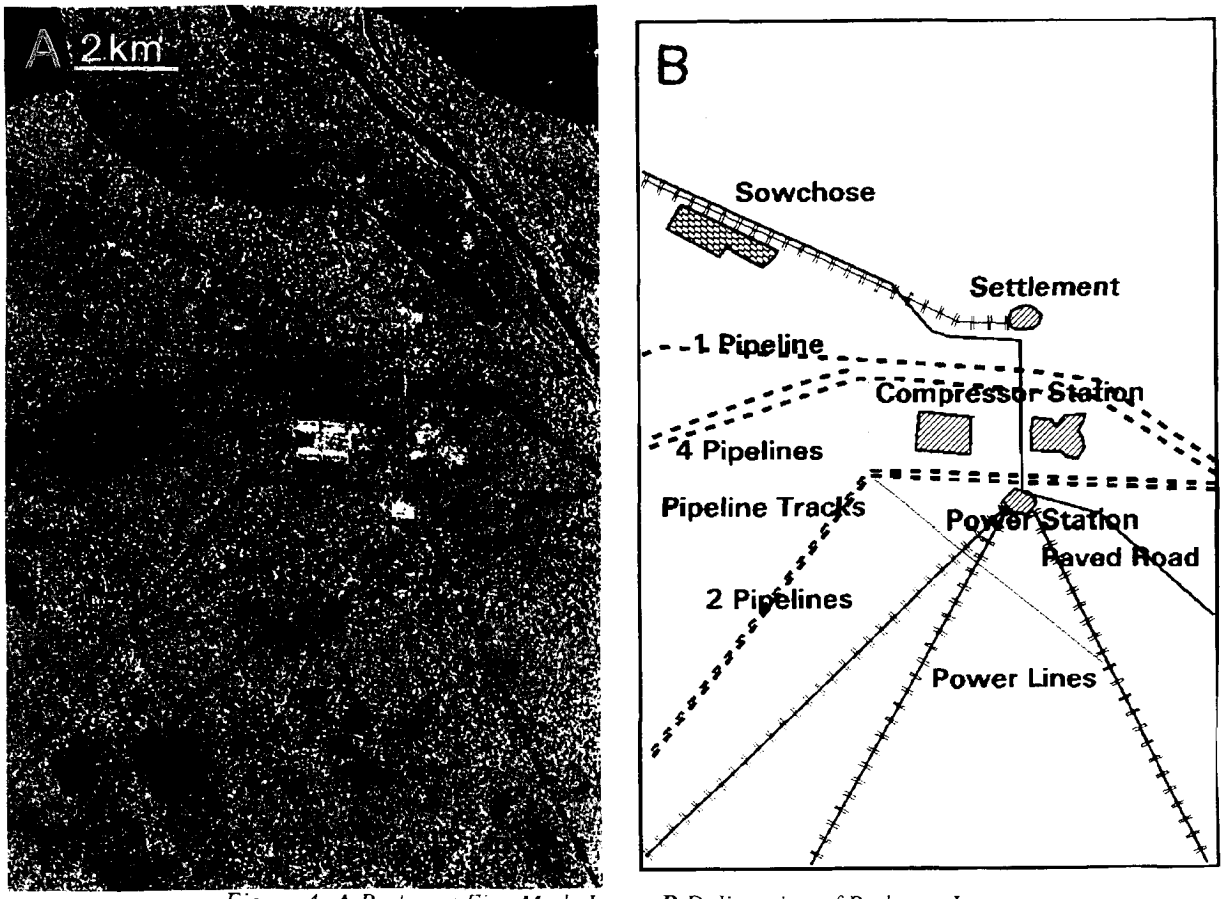

*Figure 4: **A** Radarsat Fine Mode Image **B** Delineation of Radarsat Image*

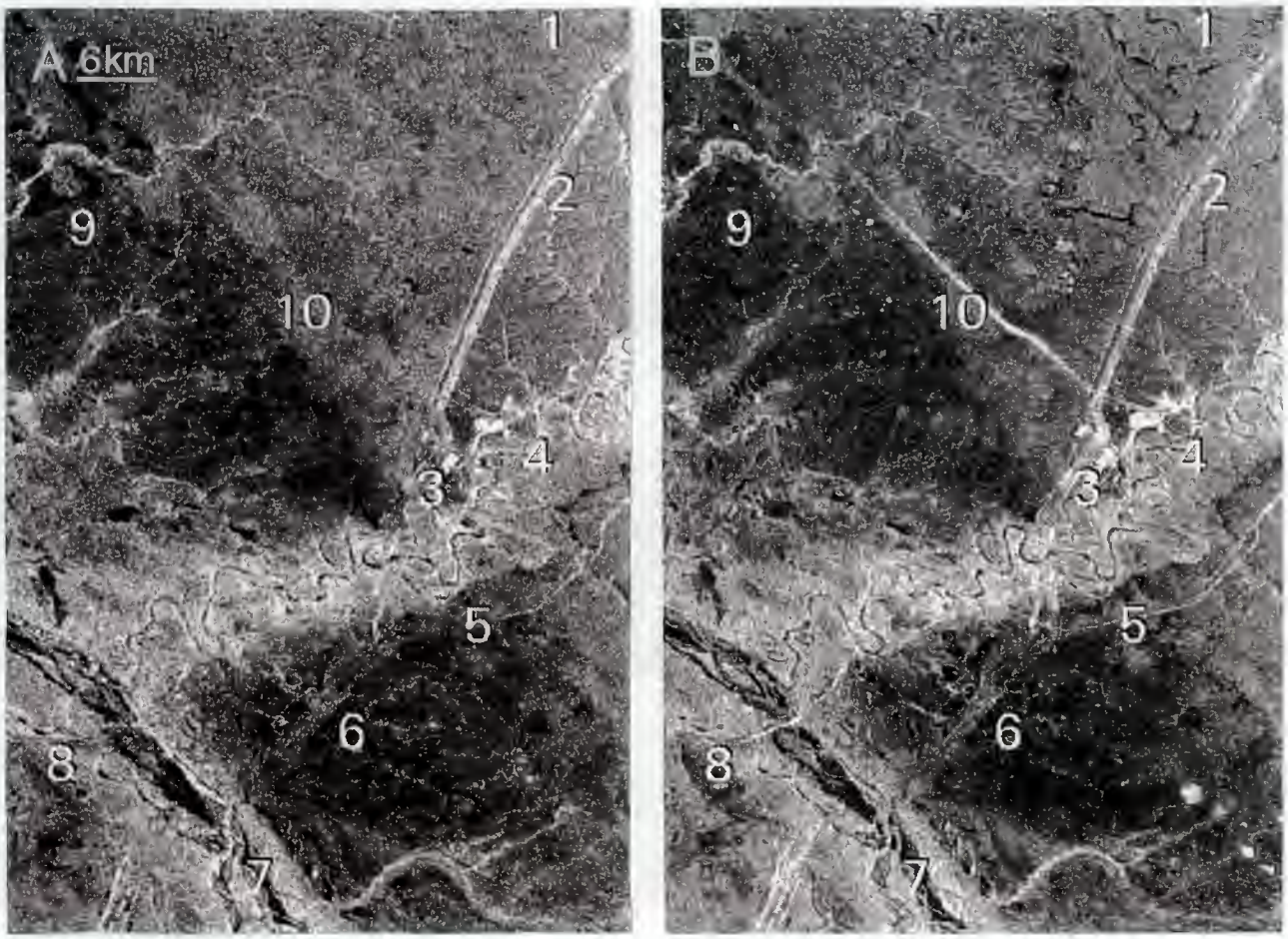

*Figure 5: **A** ERS Intensity 27.11.95 **B** 15.04.96*

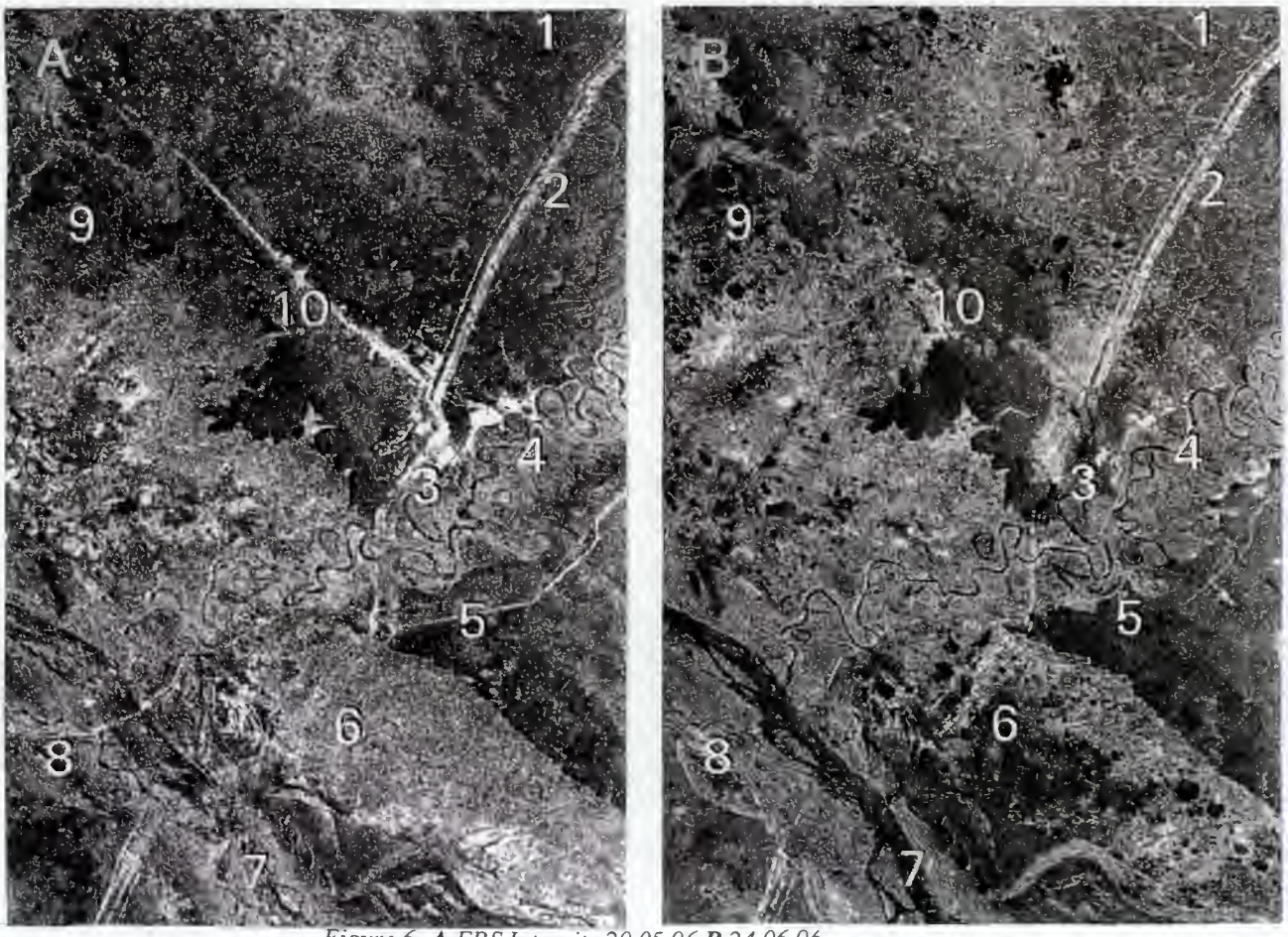

*Figure 6: **A** ERS Intensity 20.05.96 **B** 24.06.96*

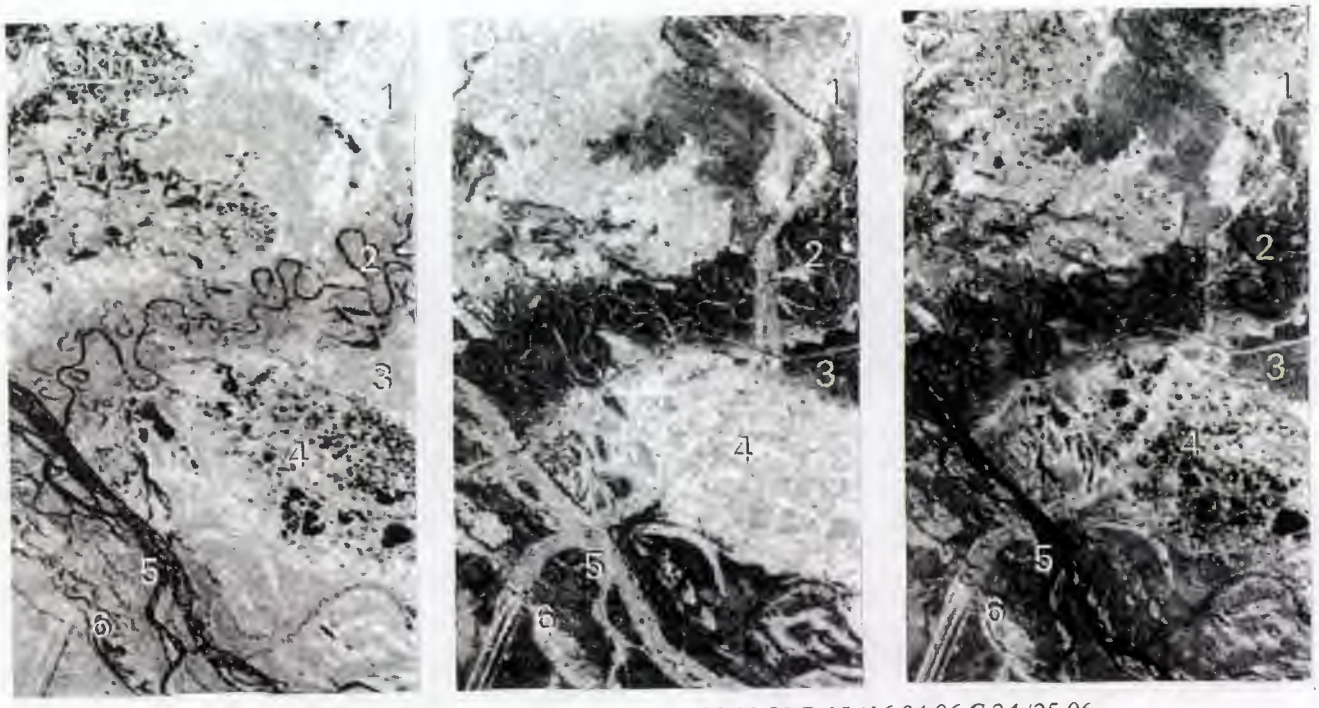

Figure 7: A Coherence Image 27./ 28.11.95 B 15./16.04.96 C 24./25.06

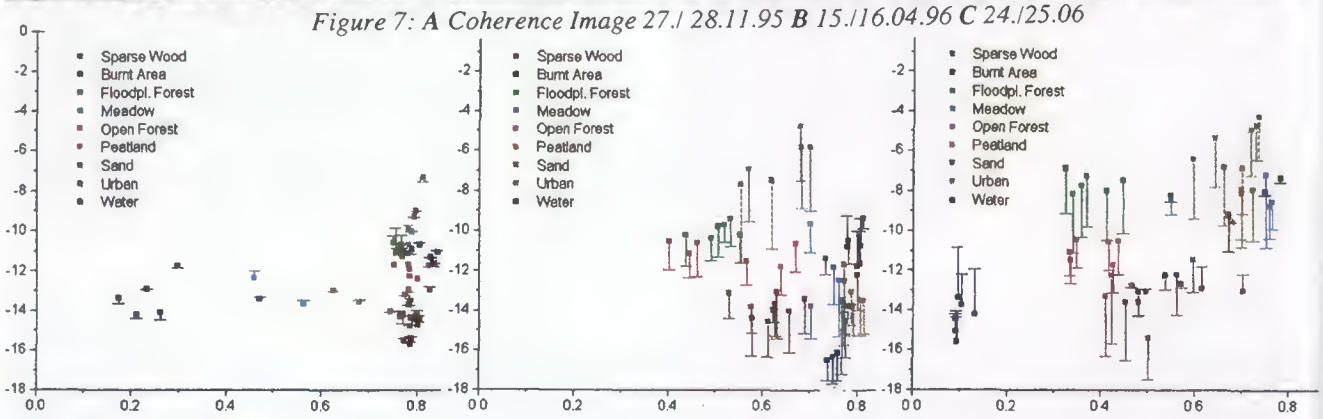

Figure 9: Backscatter Changes/Interferometric Correlation for ERS Pair of Nov 95, April 96, June 96

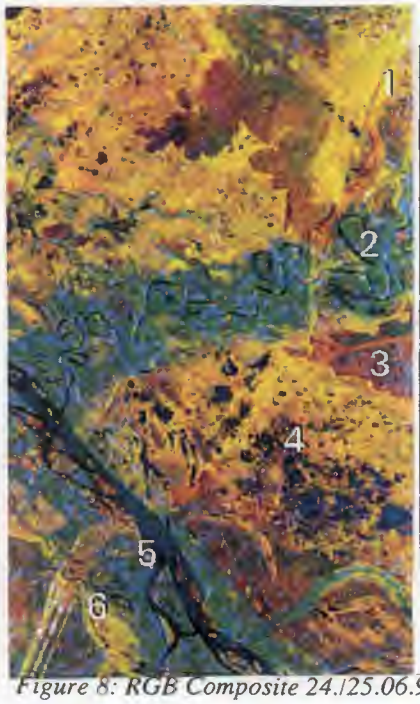

Figure 8: RGB Composite 24./25.06.96

Color	Coherence of ERS 24./25.06.96 (R)	Intensity of ERS SLC 24.05.96 (G)	Ratio of the Intensity 24./25.05.96 (B)	Feature
Blue	Low	Low	High (Change)	River, surface water (rp 4)
Green	Low	Medium	Medium (No Change)	Flood plain forest (rp 2)
Yellow	High	High	Medium (No Change)	Young short vegetation (rp 1), pipeline track in peatland environment (rp 4) and covered with short vegetation
Red	High	Low	Medium (No Change)	Sand covered pipeline tracks

Table 3: Legend for Fig. 8

covered with short vegetation show high coherence due to frozen environment. The decrease in the correlation of the floodplain forest (see Fig. 9) might be related to the particular snow conditions. Currently we are not certain about the exact reason. The road below rp 1 shows low coherence due to truck traffic (in the Intensity Images the roads appear bright). The frozen river (north of rp 5) shows a high coherence.
Fig. 7 C provides an overview of the subset for the ERS Tandem Pair 24./25.06.96. The varying coherence gives a better differentiation. Now all the thawing ponds (see rp 4) and the river (rp 5) have a low coherence due to movement of water by wind. Even the string bogs crossing the pipeline track next to rp 6 can be detected.
Fig. 8 (see Annex) shows the same subset C (see Fig. 1) for the area investigated in an RGB composite combining coherence of the ERS pair 24./25.06.96 as red, the intensity of 24.06.96 as green and the backscatter changes as blue. The table 3 (see Annex) indicates the colors and the associated features.
The investigation of the multitemporal coherence images together with the backscatter changes enables a classification of the landscape itself and a classification of the surface of the pipeline tracks. It also allows the determination of the freezing and thawing conditions of the area investigated.

5. CONCLUSIONS

It has been demonstrated that, in general, the following products can be derived from InSAR processing of ERS- SAR Tandem data for Planning and Monitoring of pipeline tracks in boreal environments:

A. Digital Elevation Model (relative accuracy 5-20 m rms in height, horizontal resolution is about 20 - 30 m) which is important for planning of new pipeline tracks. Products such as shaded relief, slope maps and contour lines can be derived.

B. Landcover Classification showing the

1. hydrological situation (lakes, rivers and moist areas) for planning of placing concrete weights to prevent up-stroke of lighter gas pipelines in spring when ice thaws.

2. geo-location of pipeline tracks, power lines, roads, compressor stations and settlements.

3. vegetation cover and its classification in potentially hazardous areas (through freezing and thawing of moist areas).

The next table (Tab. 4) indicates the tasks used as input for planning and monitoring of pipeline tracks in boreal environments, and the products used.

TASK	PRODUCTS USED
DEM for planning of new pipeline tracks	Tandem pair most preferably in stable climatic condition during winter (Nov. .Dec.)
Landcover classification for planning and monitoring	Multitemporal coherence images (For the Nadym test site the coherence of Nov. pair shows very well the hydrological situation; the April pair is best for forest and non-forest classification.)
Geo-location of pipelines and related infrastructure	Coherence images and Radarsat images (for the Nadym test site April and Nov. pair)
Determination of potentially hazardous areas	Multitemporal ERS intensity. Most preferable are data sets from winter and spring when thawing starts
Monitoring of construction work	Multitemporal ERS intensities

Table 4: Requirements and products used for Pipeline Monitoring and Planning

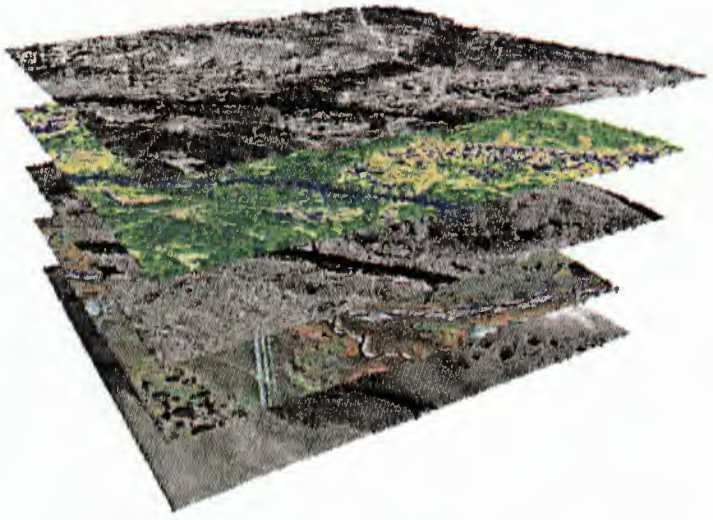

Figure 10: Multi-Layer 3 D Animation for the Pipeline Tracks

6. ACKNOWLEDGMENTS

We would like to thank ESA for the provision of data in the framework of a pilot project (A02.D129) and the German Space Agency for funding of the project. We further appreciate the provision of Radarsat data by the Canadian Space Agency.

7. REFERENCES

Rignot, E., Way, J. B. 1994, Monitoring Freeze and Thaw Cycles along North-South Alaskan Transects Using ERS-1 SAR. RSoE. 49, pp.131-137.
Rosen, A., et. al. 1994 , Interferometric Detection of Freeze-Thaw Displacements of Alaskan Permafrost Using ERS-1SAR. Proc. PIERS ´1994, pp.842-845.
Streck, C., O. Hellwich , 1996, Retrieval of Man-Made Structures in Siberia with INSAR-Techniques using ERS SAR Data. Proc. IGARSS 96, p.p. 1836-1838.
Wegmüller, et al., 1995, Land surface analysis using ERS1/2 SAR Interferometry. ESA Bulletin, No. 81, pp.30-37.

ETUDE DE FAISABILITE : DETECTION DE SITES ARCHEOLOGIQUES ET CARTOGRAPHIE GEOMORPHOLOGIQUE EN SYRIE PAR L'EXPLOITATION D'IMAGES DES SATELLITES ERS1 ET SPOT2 INTEGREES DANS UN SYSTEME D'INFORMATION GEOGRAPHIQUE.

Damien Closson, André Ozer, Önhan Tunca, Assia Kourgli, Yves Cornet

Université de Liège. Laboratoires de Géomorphologie et de Télédétection
Allée du 6 Août, 2, Bâtiment B11, 4000 Liège (Sart-Tilman)
tél.: + 32 4 366 53 35 fax : + 32 4 366 57 22

ABSTRACT

Cette étude de faisabilité s'attache à rechercher les parties du spectre électromagnétiques utilisées en télédétection qui peuvent éventuellement fournir une aide pour la prospection archéologique. Une image ERS1 (capteur AMI-SAR) et une image Spot2 (capteur HRV) sont interprétées et analysées au sein d'une base de données géographiques. La comparaison est effectuée au niveau des traitements numériques, de superpositions et juxtapositions de données au sein du S.I.G. La qualité des documents est également évaluée au cours de travaux de terrain.

L'étude démontre que l'image de Spot2 fournit des informations plus pertinentes que l'image de ERS1, notamment à propos du parcellaire agricole. Celui-ci met clairement en évidence les limites de terrasses alluviales et les paléoméandres. La plupart des données de Spot sont également visibles sur ERS mais avec moins de précision. Cependant, compte tenu de l'expérience SIR-A effectuées au début des années '80, l'étude ne permet pas de conclure de façon définitive que les informations prélevées dans les longueurs d'onde centimétriques sont toujours moins efficaces que celles issues des longueurs d'onde micrométriques.

1. Introduction

L'usage de la télédétection en prospection archéologique n'est mentionné que très rarement dans la littérature scientifique. Pourtant, dans les régions où la couverture cartographique est relativement ancienne, peu précise ou inexacte et où les photographies aériennes sont peu disponibles, les images satellites devraient constituer des documents d'analyse de premier choix en favorisant la généralisation des observations de terrain.

Cette étude répond à deux questions : 1 - La télédétection peut-elle contribuer à augmenter les connaissances relatives au système paléogéographique et de quelle façon? 2 - Quelles sont les images les plus intéressantes en prospection archéologique?

La région étudiée correspond à un tronçon de la plaine alluviale de l'Euphrate syrien localisé une cinquantaine de kilomètres au sud de Deir ez Zor, en aval de la confluence entre le Khabour et l'Euphrate. Deux sites archéologiques de première importance y sont localisés: Doura Europos et Terqa. La vallée y est encaissée de 30 à 40 m dans un vaste plateau caillouteux subdésertique. Elle constitue un territoire bien délimité qui, quoique soumis à des conditions climatiques très dures (moins de 150mm de pluie par an), est aisément mis en valeur. De grandes surfaces couvertes de dépôts limoneux d'origine alluviale constituent des sols fertiles facilement irrigables par gravité.

2. Inventaire et traitements numériques des données du S.I.G.

2.1. Inventaire des données du S.I.G.

- Image AMI SAR de ERS1 - 10/10/1995.
- Image panchromatique HRV de SPOT2 - 01/06/1991.
- Image panchromatique MSS « Landsat 1 » du 18 novembre 1973.
- Mosaïque de cartes topographiques syriennes au 1/25.000 établies entre 1960-1965.
- Extrait d'une carte géologique russe de 1966 au 1/200.000.
- Extrait d'une carte topographique britanique de 1942 au 1/200.000.
- Levés géomorphologiques de A. Ozer (Belgique-1989) et B. Geyer (France-1988).
- Mission française de reconnaissance de l'Euphrate en 1922.

2.2. Les traitements numériques.

Les données de ERS1 sont noyées dans un bruit qui empêche une délimitation précise des rares éléments identifiables. L'utilisation d'un tel document pour la cartographie géomorphologique n'est pas à conseiller.

3. Analyse des images au moyen de la base des données du S.I.G.

L'intérêt de la télédétection s'exprime par un enrichissement de la base de données du S.I.G. :

● les images améliorent les données cartographiques en augmentant la précision de certains tracés (limites géologiques, ancien canal, etc.) et permettent une actualisation;
● l'interprétation des documents permet de réaliser des prévisions (p.ex. le sens de déplacement d'un méandre);
● les images contiennent un ensemble d'informations thématiques (p.ex. le parcellaire agricole) introuvable sur les documents cartographiques courants;
● la résolution des données provenant du satellite SPOT2 est légèrement inférieure à celle des photos prises à basse altitude mais permet une analyse presque aussi détaillée.

4. Télédétection et travaux de terrain.

Les excursions ont montré de manière explicite les niveaux de perception extrêmes que représentent les données satellitaires et les données terrain. Les images satellites interviennent significativement au niveau de la conception d'un modèle théorique de localisation de sites antiques ou préhistoriques par la mise en évidence d'éléments géomorphologiques qui, interprétés dans un contexte de prospection et moyennant l'apport d'autres informations, peuvent conduire à des découvertes archéologiques.

5. Conclusions.

● La télédétection augmente les connaissances du système paléogéographique en accroissant le nombre et la qualité des données de la surface terrestre. L'observation de l'affectation du sol dans différentes longueurs d'ondes participe à la mise en évidence d'éléments géomorphologiques remarquables ainsi qu'à la découverte des relations entre tous les éléments du paysage. Par exemple, l'image panchromatique de SPOT2 met clairement en évidence l'étroite corrélation entre les limites des champs irrigués et le tracé des anciennes berges. Le professeur A. Ozer, au cours de ses travaux de terrain, a, entre autres, montré que la compréhension de l'histoire des sites de Terqa et du tell Jebel Masaïkh passait obligatoirement par la reconnaissance des anciens lits de l'Euphrate. Dans ce cas, l'apport de l'image satellitaire est primordial pour la reconnaissance des paléoméandres du fleuve.
● Le croisement des images avec des données thématiques (courbe de niveau, limites géologiques, etc.) permet d'ajuster et/ou de compléter des informations (le prolongement d'un canal très ancien) et d'effectuer des prévisions (migration de méandres).
● Les images satellites sont rarement d'une utilité directe dans les travaux de terrain du fait de l'échelle. Elles fournissent cependant des spatiocartes qui donnent un autre point de vue que les cartes topographiques généralement utilisées. En fournissant des données originales, elles contribuent à améliorer la réflexion sur le problème de la localisation de sites à prospecter.
● Des deux capteurs analysés (AMI SAR et HRV), celui du satellite SPOT2 fournit les images qui conviennent le mieux pour cet usage. L'étude est cependant beaucoup trop limitée pour diminuer la valeur des images « radar ». En effet, seule la partie du spectre électromagnétique utilisée par l'AMI SAR (bande C) de ERS1 a été utilisée. Dans l'étude de certaines régions désertiques, les capteurs utilisant la bande L (p. ex. expérience SIR A) ont fourni de meilleurs résultats que les capteurs micrométriques (« visibles »). La variation de l'angle d'incidence des ondes pourrait également modifier les résultats que nous avons obtenus.

6. Bibliographie.

European Space Agency (E.S.A.) satellite ERS-1. 10 octobre 1995 19:35:25:000. Image radar. Orbit 22160, frame 693. Instrument AMI SAR.

Besançon J., Sanlaville P. 1981, Aperçu géomorphologique sur la vallée de l'Euphrate syrien. *Paléorient*, vol. 7/2, 5 - 18.

Cartes topographiques de Syrie, 1:25.000. 1960 - 1965. Feuilles 1-37-XVII-4-C-c, 1-37-XVII-4-C-a, 1-37-XVII-4-C-b, 1-37-XVII-3-D-d.

Geyer. B 1988, Le site de Doura Europos et son environnement géographique. *SYRIA*, tome LXV, fascicules 3-4. 285-295.

Lillesand T.M., Kiefer R.W.1987, *Remote sensing and image interpretation* - second edition. 721 pages.

Ozer A. 1996, Prospection géomorphologique dans la région de Terqa. *M.A.R.I.*, 8, 115 -124.

Ponikarov V.P. 1966, The geological map of Syria, 1:200.000. Department of Geological and Mineral Research, Syrian Arab Republic.

Spot Image, satellite SPOT2. 01/06/1991 08:09:36. Image panchromatique. K-J 128-280. Instrument HRV1.

Survey de la X^{ème} Armée Britannique. Mai 1942. Carte topographique 1:200.000.

Velud C., Geyer B., Pascuel J-P. 1995, Une mission de reconnaissance de l'Euphrate en 1922. Les enjeux économiques, politiques et militaires d'une conquête, deuxième partie. Rapport du Lieutenant Charles Hérault. Institut français de Damas.

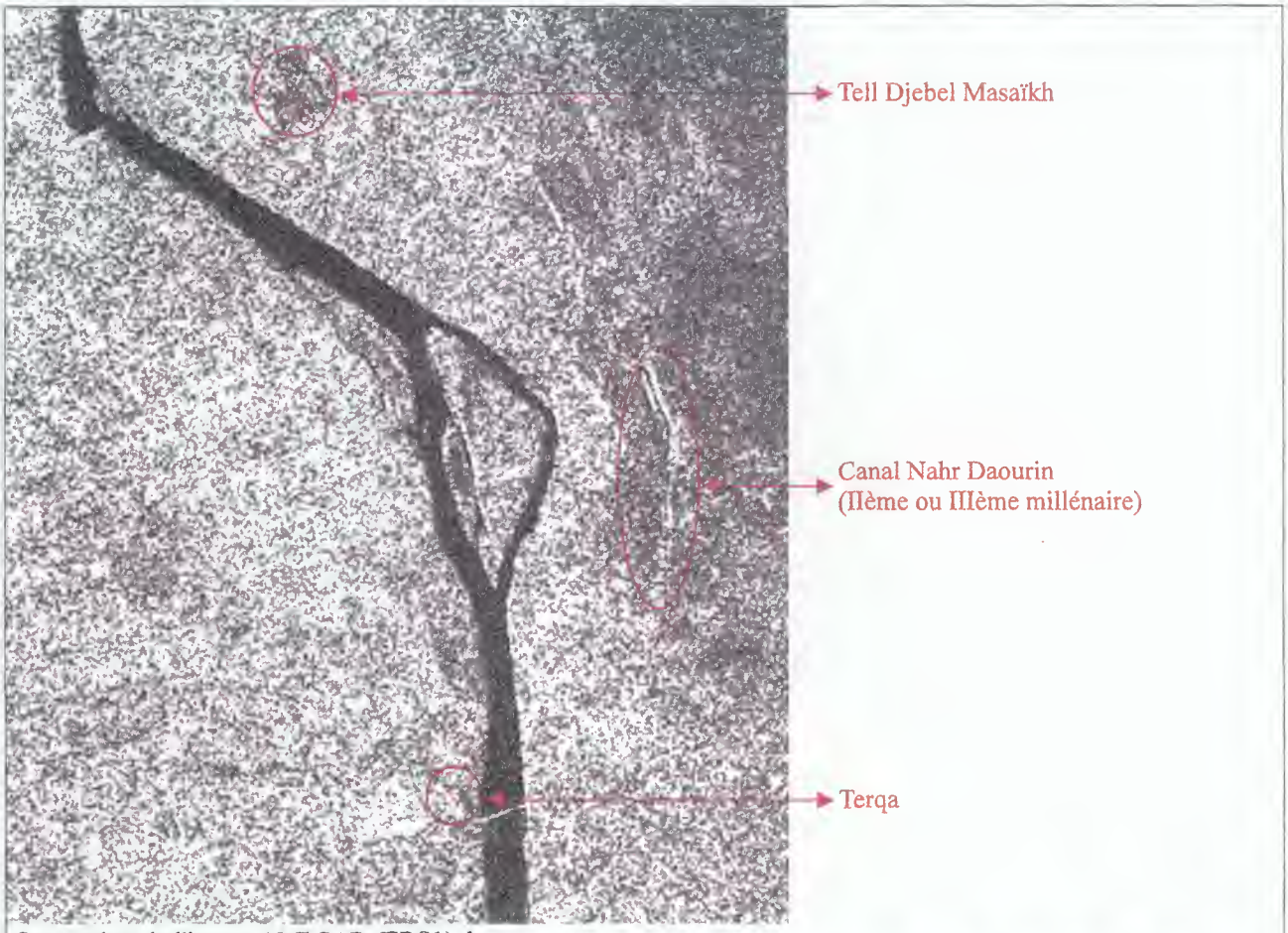

Sous-scène de l'image AMI SAR (ERS1) du 10 octobre 1995. Orbit 22160, frame 693.

Sous-scène de l'image HRV1 (Spot2) du 1 juillet 1991. K-J 128-280.

Figure 1. Comparaison des données brutes de ERS1 et de Spot2. Localisation des principaux sites archéologiques.

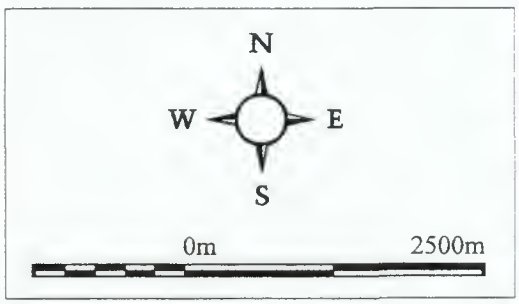

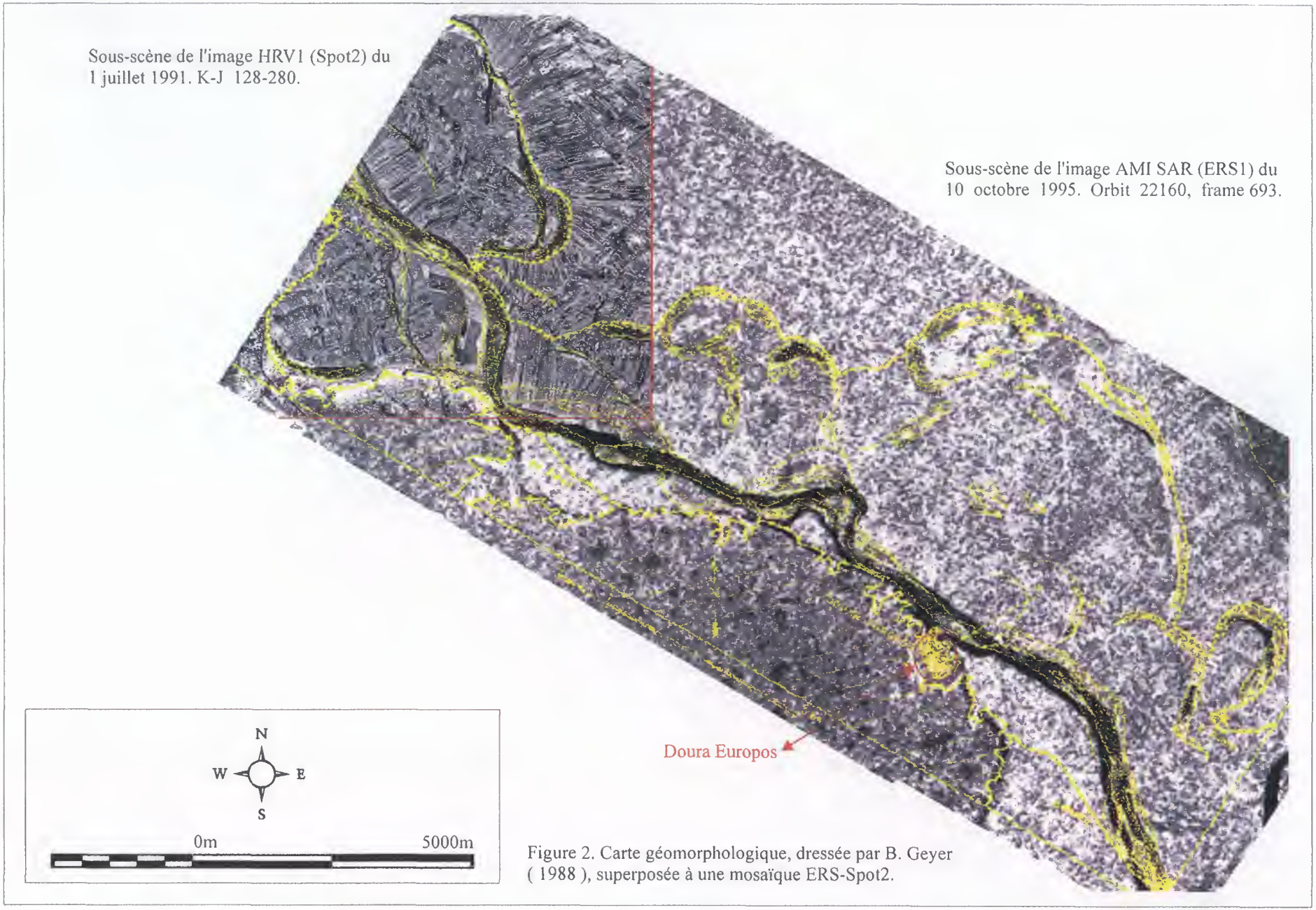

Figure 2. Carte géomorphologique, dressée par B. Geyer (1988), superposée à une mosaïque ERS-Spot2.

MAPPING OF SAND WAVES AND CHANNELS IN THE TAIWAN TAN AREA WITH ERS SAR

Ming-Kuang Hsu Department of Oceanography, National Taiwan Ocean University, 202, Keelung, Taiwan, R.O.C., Phone: (886) 2.462.2192ext.6313, Fax: (886) 2.463.1764, hsumk@ind.ntou.edu.tw

Leonid M. Mitnik, Pacific Ocanaological Institute, FEB RAS, Vladivostok 6900041, Russia, Phone: (4232).312-854, Fax: (4232).312.573, toi@iasnet.ru

Shyuer-Ming Shih Institute of Oceanography, National Taiwan Ocean University, 107, Taipei, Taiwan, R.O.C., Phone: (886).2.366.1238, Fax: (886)2.362.6092, mingshih@ccms.ntu.edu.tw

Abstract

Regular ERS-1/2 SAR survey of the Taiwan area was carried out in 1993-1996. The Taiwan Tan Shoals located in the southern Taiwan Strait were selected for study the surface manifestations of shallow water topography. The Taiwan Tan shoals have an area about 10,1000 km^2 and the depth of the shallowest water is about 8m - 10m. Typical water depth is around 30m. The sand waves in Taiwan Tan Shoals are clearly show on the ERS-1 SAR images during favorable weather condition and when the tidal current is strong. The height of these sand waves range from 3m - 25m; wavelength range from 300m - 1100m.

Keywords: ERS SAR, bottom topography, sand waves, Taiwan Tan

Introduction

ERS-1 SAR survey of the Taiwan Strait was carried out as a part of the project " Study of Kuroshio Current and its branches" selected by ESA. The surface manifestations of underwater relief were reliably separated from other oceanic features against the background of the brightness variations caused by the wind speed variability. It was due to their static locations and radar signatures. Visibility of the bottom irregularities depended on a number of environmental factors such as sea surface wind speed and direction, current velocity and direction, shape of the underwater features etc.

Generally, it is accepted that the imaging mechanism consists of three steps (Van Kooij et al, 1995):

(1). Interaction between tidal current and sand waves causes spatial modulations in the surface current velocity;

(2). Modulations in the surface current velocity give rise to variations in the spectrum of wind-generated waves (wave-current interaction); and

(3). Variations in the wave spectrum show up as intensity modulations in radar imagery.

It had been found that depth, steepness of the slope, and the height of sand waves are the shape parameters which determine the radar backscatter modulation. The extreme (max. or min.) radar backscatter is located at downstream end of the steep slope. Actually, under suitable condition, we can 'see' the sand waves and other types of sea bottom topography form SAR images.

Subsurface Signatures observed on SAR Images in Taiwan Tan area

A comparison of SAR brightness distribution and bathymetry were carried out for the Taiwan Tan Shoals, where extensive sand waves field were developed. Taiwan Tan Shoals are located in the middle part of the southern Taiwan Strait between 22.5-23.3°N and 117.8-119.2°E. It is the most extensive one in the world, having an area of about 10,1000 km^2. The shoals deflect the northward Taiwan Current to the east.

The Taiwan Tan sand wave field is characterized by ridged and shoals separated by deeper channels. Typical water depth is around 30m. The depth of the shallowest place is about 8m. The corresponding areas are shown by dark in Figure 1. The areas over the range 10m to 20m are shown by hatching in Figure 1. The depth increases slowly and then fast in the south of the shoals.

The dominant topography feature of Taiwan Tan Shoals appears to be sand-wave field. The sand-wave field is well developed in the area with water depth less than 40m, although similar topography features were also found in waters deeper than 300m (Boggs, 1974). The wave height of the sand waves is in the range of 3 to 25m, their wavelength varied from about 300m to 1100m and is about 900m in average. The orientation of the sand waves varies between NNW-SSE to NWW-SEE and is perpendicular to the prevailing ebb and flood tidal currents. The depth variations through the Taiwan Strait are shown in Figure 2 (Lan et al., 1991). Where the B and B' sections cross the Taiwan Tan. Sand waves with large amplitude and deep canyons are seen in profiles.

Most of the top sediments on the Taiwan Tan Shoals were

composed of medium sands except for the eastern side where it is composed of medium coarse sand. From the grain-size distribution it follows that the Taiwan Tan Shoals were composed of riverine and near shore deposits and the sediment have been reworked under high energy environment. The average content of heavy minerals of sediment is 1.22% compared to 0.90% for the adjacent area. The heavy minerals are mainly in sand and mud carried into the sea from the rivers of the Mainland China or from Penghu islands.

Base on the sediment characteristics and the bottom topography features, it is believed that the Taiwan Tan Shoals were likely formed during the post glacial period. The sediments were formed in the near shore zone, fluvial deltas, beaches. The sand wave field was built by strong tidal currents after transgression. Detailed bathymetric survey has been not conducted to date. Thus, satellite SAR is a powerful instrument providing the detailed pattern of bottom topography.

The ERS-1 SAR images of the southern part of the Taiwan Strait was taken on 27 July 1994 (Figure 3), 3 June 1995 (Figure 4) and 22 June 1995 (Figure 5). Rectangles on the bathymetry map (Figure 1) shows their location. All three images were obtained at favorable weather conditions. From the surface analysis maps of the Japan Meteorological Agency it follows that the large area between Mainland China and Taiwan was characterized by light wind (2-5 m/s). The brightness variations of the SAR images reflect the main bathymetric features depicted on the chart as well as reveal new ones. The alternating curved dark and gray bands result from an interaction of tidal current with the underwater sand waves. The sand waves are seen with amazing clarity as the straight or curved bands with alternating brightness. The deeper longitudinal channels with varying width and length cut the sand waves. Near the channels the crests of the waves bend. A ratio of a width of the lighter signatures to a width of the neighboring darker ones varies over a wide range due to the variations of depth, shape of the sand waves and tidal current velocity.

In general, the bottom features are visible under strong currents (greater than 0.5 m/s). At the time of the SAR pass, local tide was near its high level. At point 23°20'N, 119°20'E rate of northward flood tidal current is 3.5 kn. and rate of southward ebb tide current is 2.5 kn. However, the detailed information about tidal currents for the Taiwan Tan area was unknown for us. Thus, we used the results of numerical simulations to estimate current velocity during ERS-1 pass. Calculations were carried out at the Central Weather Bureau, Taipei, Taiwan. The model covers the region 21.375 - 26.75°N, 116.375 - 122.75°E. There are 52 x 44 grid points and a resolution is 1/8 degree. The time interval of integration is 45 s. Figure 6 depicts the tidal currents in the Taiwan Tan area reaches 60cm/s - 65cm/s. It may be assumed that the velocity is large than 60cm/s - 65cm/s, if take into consideration of the complicated underwater relief. This enables the bottom relief to be visible.

Conclusions

It is found that under favorable weather condition and when current is strong enough, the subsurface topography can be reliably separated from other anomalies of radar backscatter associated with oceanic and atmospheric phenomena. The height of the sand waves formed by tidal currents is in the range of 3m -25 m. The distance between the bands changes from about 300 m to about 1300 m. They are directed almost along latitude, at right angle to prevailing currents. In addition to the currents, their orientation is determined also by configuration and depth of the channels and the steepness of their slopes. The channels are aligned almost along longitude and direction of the sand waves changes near them. Three ERS-1 SAR images of the shoals took at favorable weather conditions on 1994 and 1995 summer. The SAR signatures reveal a lot of new details which were not shown on the navigation maps. The sand waves are seen as the straight or curved bands with alternating brightness. The bathymetric features were detected at different weather conditions and current directions. The dedicated in-situ measurements are vital to get more insight into the details of the surface roughness modulation and decrease the discrepancy between the theories and measured data.

Acknowledgment

We thank the European Space Agency for providing ERS-1/2 SAR images. We also thank the staff at ESRIN and the Center for Space and Remote Sensing Research, National Central University, Taiwan for their enthusiastic help in data acquisition and processing. We are grateful to Miai Mitnik, S.S. Yu for assistance in processing of SAR images. This research was sponsored by the National Science Council through research grants NSC-83-0209-M019-010, NSC-84-2611-M019-009 and NSC-85-2611-M019-011 k2.

References

Boggs, S. Jr., 1974
Sand-wave fields in Taiwan Strait: *Geology*, **2**, pp. 251-253.

Lan, D., W. Zhand, C. Chen and Z. Xie, 1991
Preliminary study on age and origin of medium-coarse sands in Taiwan Shoal in Taiwan Strait., *J. Oceanography*, **10**, pp. 151-161.

Van Kooij, M.V.A., J. Vogelzang and C.J. Calkoen, 1995
A simple analytical model for brightness modulation caused by submarine sand waves in radar imagery, *J. Grophys. Res.*, **100**, (C4), pp. 7069-7082.

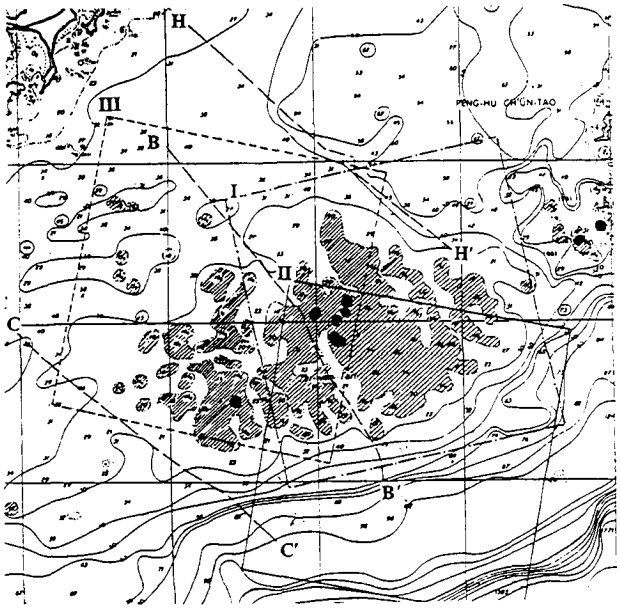

Figure 1: The bathymetry Map, SAR covered regions and the survey lines for the topography profile of Taiwan Tan area (from Chinese Navy Chart No.0312). The depth of the shallowest water is about 8-10m, the corresponding area are shown by dark. The areas over the range 10 to 20 m are shown by hatching. Block I, II and III are the corresponding to the SAR images shown on Figure 3, 4 and 5. Line H-H', B-B' and C-C' are measured depth variations shown on Figure 2.

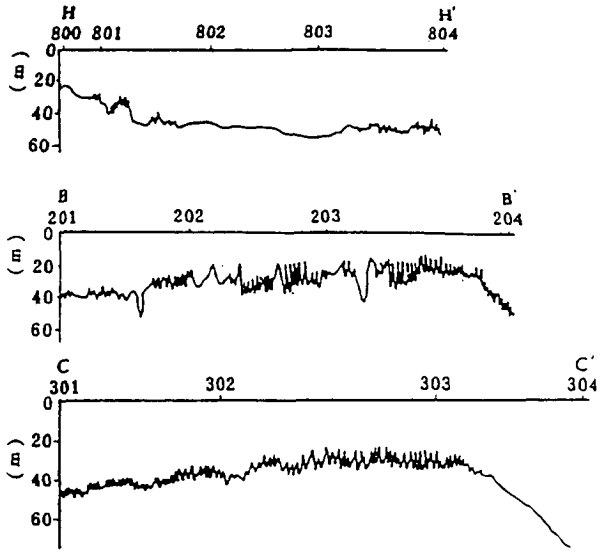

Figure 2: Depth variations along sections H-H', B-B' and C-C' through the Taiwan Tan. (from Lan, et. Al 1991)

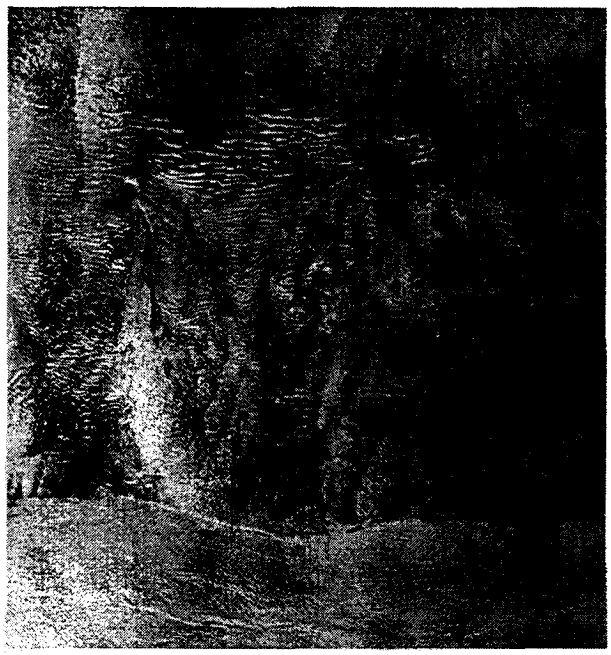

Figure 3: ERS-1 SAR image (copyright ESA) taken at 14:31 UTC 27 July, 1994 showing the surface manifestations of bottom topography in area I.

Figure 4: ERS-1 SAR image (copyright ESA) taken at 02:38 UTC 3 June, 1995 showing the surface manifestations of bottom topography in area II.

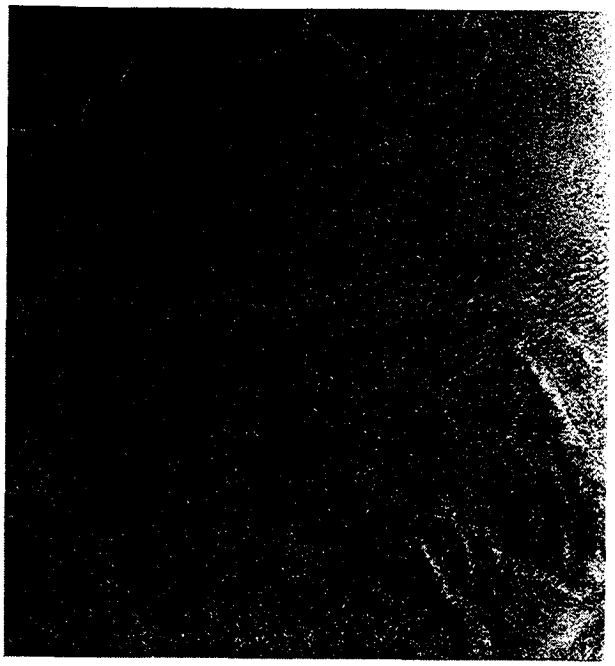

Figure 5: ERS-1 SAR image (copyright ESA) showing the surface manifestations of bottom topography in the area III.

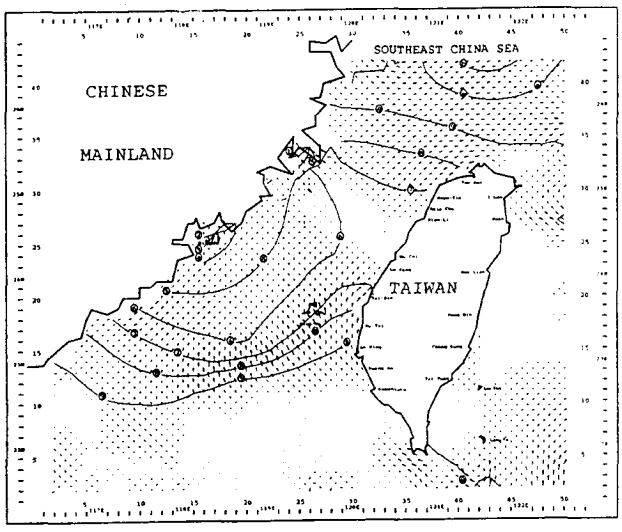

Figure 6: Tidal currents in the Taiwan Strait at 02:37:30 3 June 1995. Numerical calculations of the Central Weather Bureau. Isolines shows the sea level 1- -120cm; 2 - -100cm; 3 - -80cm; 4 - -60cm; 5 - -40cm; 6 - -20cm; 7 - 0cm; 8 - +20cm; 9 - +40cm; a - +60cm.

TEXTURE ANALYSIS OF SAR-ERS1 IMAGES FROM SOUTH CAMEROON

Annick Legeley-Padovani, Anicet Beauvais, Frédérique Seyler & Boris Volkoff

ORSTOM, Centre d'Ile de France, 32 rue Henri Varagnat, 93143 Bondy Cedex, France
phone : 01 48 02 55 00, fax : 01 48 47 30 88

Pascal Sailhac

Institut de Physique du Globe de Paris, J.E. CNRS n°335, Case 89, 75252 Paris Cedex, France

Alain Akono

Ecole Nationale Supérieure Polytectnique (LETS), B.P. 8390 Yaoundé, Cameroon

Jean-Paul Rudant

Université PMC (LGGST), Tour 26, 4 place Jussieu, 75252 Paris Cedex, France

ABSTRACT

Texture characterisation of SAR images from a forested smooth landscape of South Cameroon was performed using mathematical morphology and multifractal analysis processing. The first method involves to apply gradient-oriented filters according to directions perpendicularly to the radar emission - after removing the speckle and smoothing the original image by using a centre connected and a Nagao filter successively. Reconstruction and erosion was then operated to delineate the drainage network structures - reflecting geological and environmental patterns. The second method consists to analyse the inner multifractal structure of an image with a set of regional multifractal spectra - each was computed for a given area. Regional multifractal spectra were obtained using a naïve estimator based upon the statistics of the singularity maps in subscenes - according to different textures. Our preliminary results indicate that the coupling of classical processing with multifractal analysis could be promising to SAR image segmentation.

1. INTRODUCTION

Detailed field studies carried out in the South Cameroon rain forest have allowed to determine relationships between (i) soil formation and processes and (ii) slope morphology and drainage pattern [Bitom et al., 1997]. The texture of SAR-ERS1 images emphasises the typical slope and drainage network patterns on which depends the landscape roughness. Two processing methods have been performed to analyse the texture of SAR images in the dense homogeneous rainforest of the South Cameroon (Fig. 1).

Mathematical morphology consists to extract dark continuous lines corresponding to stream networks performing binary morphologic processing and geodesic transformations - these latter ones keeping structure outlines. We have also used grey-scale morphological transformations - an extension of the morphologic transformation of binary images.

Multifractal method was used to provide a number of descriptor parameters well suited to radar images analysis. These parameters were integrated in an image segmentation algorithm that fully describes the variations of natural textures. This method consists to examine the inner multifractal structure of the image with a set of regional multifractal spectra, each of them being computed for a given area of the original image.

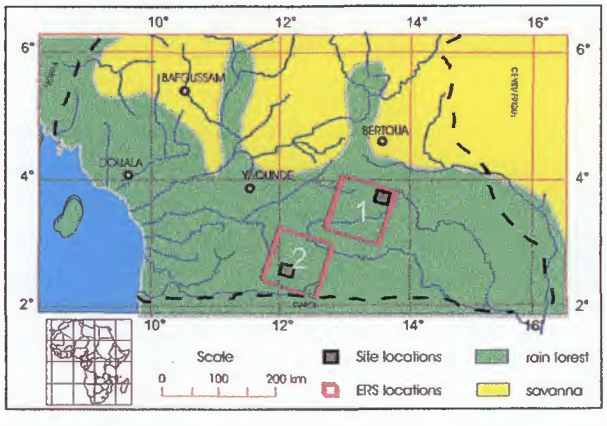

Figure 1. Location of the SAR images and study area.

SAR IMAGE ACQUISITION AND PROCESSING

The two methods have been tested on two subscenes of C band radar images (SAR-ERS1, frequency 5.3 GHz, wavelength 5. cm), with a nominal resolution of 25 m in range and 22 m in azimuth. The two radar images were acquired on August, 1994, (image 1) orbit 15947, frame 3519, (image 2) orbit 16191, frame 3555 with the scene centre located at 04° 19' N - 13° 37' E and 02° 32' N - 12° 29' E respectively (Fig. 1).

Mathematical morphology was applied to delineate the drainage network of a 1600 * 1400 pixels subscene of image 1, while multifractal analysis was used to describe the texture of a 800 * 700 pixels subscene of image 2.

2. METHODOLOGY

2.1 Mathematical morphology

First of all, the speckle of radar images was removed by applying a connected central filter [Mering & Parrot, 1995] (Fig. 2a). Then the resulting image has been smoothed out by a Nagao filter that fractionates each neighbour 5*5 into 9 sectors [Nagao & Matsuyama, 1979], (Fig. 2b)- the mean and variance of which was calculated to select the neighbour exhibiting the lowest values. The following processings were then applied to both the ""unspeckled"" and the Nagao filtered images.

The channel network structure was delineated using an oriented gradient filtering procedure along three directions NW, W and SW which are suitable to depict the valleys, while the east direction outlines the ridges. The south and north directions only yield a low signal as they are parallel to the radar satellite transmission. Directions NW, W and SW were equally processed after smoothing by a Nagao filter. Then, a low threshold was applied, and it was cleaned up by a geodesic reconstruction [Coster & Chermant, 1989] using a high threshold as a marker.

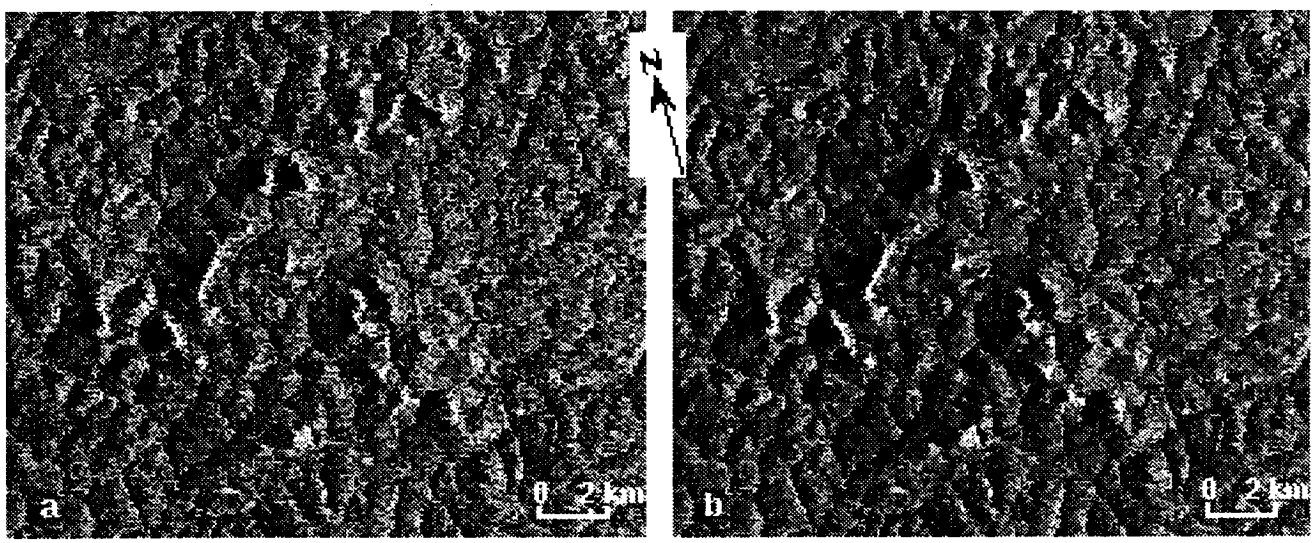

Figure 2. Processing of a subscene of the original image 1 (a) "unspeckled" image , (b) "unspeckled" image smoothed by a Nagao filter.

The three cleaned up directions are then merged. Although the network is pretty well delineated, small entities still remain. To remove these entities a closing of size 1 was applied [Serra, 1982] using an octagonal shape, and then cleaned up again by a geodesic reconstruction with an erosion of size 1. The real width of the channels is then restored by the intersection of the resulting image with the merged image.

2.2 Multifractal analysis

A multifractal formalism was used to calculate the singularity map and the spectra from the original intensity map (Fig. 3). The singularity map is a map of the local Pointwise Hölder exponent obtained by regression analysis based on surfaces of 2190m x 2190 m. The global image singularity spectrum have been computed by the Moment Method (or Legendre Method). As the Legendre Method application is limited by the size of the images, due to the speckle, another $f(\alpha)$-estimator have been used to obtain local singularity spectrum on 100 x 100 pixels sub-images (see [Sailhac & Seyler, 1997] for further details on the calculation method).

3. RESULTS

3.1 Mathematical morphology

The result obtained from Nagao smoothed images is fairly better than that of the simply "unspeckled" image. The resulting image was further processed by testing the opening residuals to enhance the directions, in particular the very thin elements. The residuals or "top hat" forms are processed either by a morphologic opening or by reconstruction if we apply a connected opening [Grimaud, 1991]. In both case the residuals have been cleaned up by a a geodesic reconstruction using a low threshold as a marker. The resulting directions have

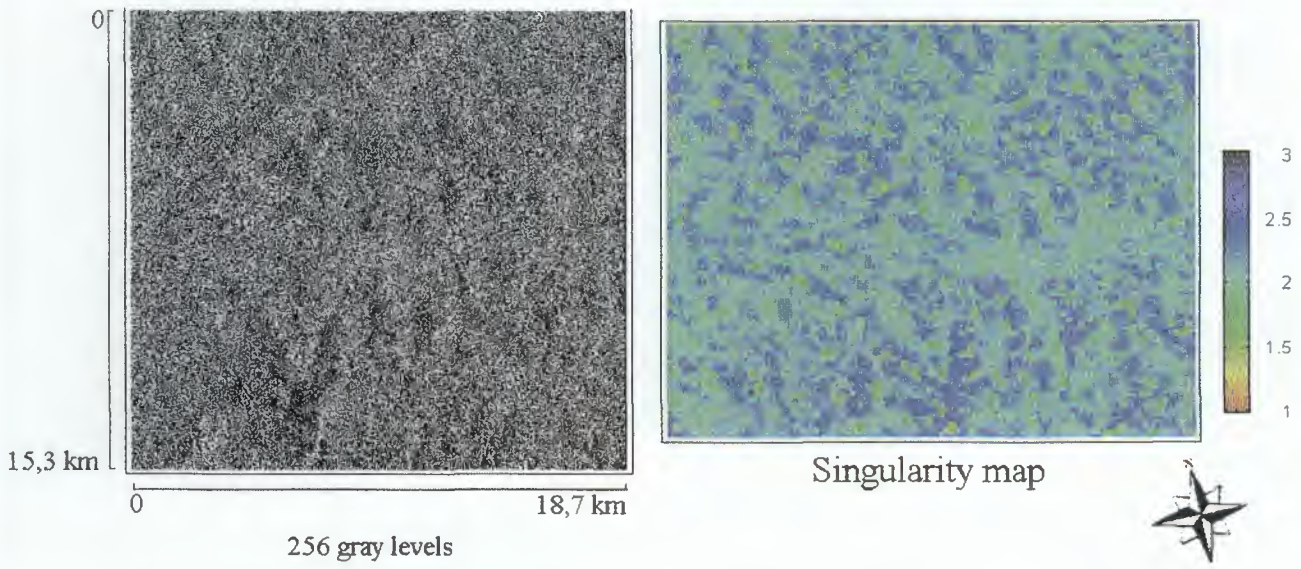

Figure 3. Maps of (a) intensity and (b) singularity of image 2 subscene.

been then merged and processed as above.
The difference between the four processes was quantified by a transformation allowing to compare two binary images - here, the results obtained on two extracts of the studied subscene are compared (Fig. 4). Comparison of two equally looking binary sets A and B implies to makes the symmetric difference between A and B as: $A \Delta B = A \cup B - A \cap B$ [Callot et al., 1994]. The resulting set C is a binary image composed of all pixels discriminating A and B. Then the intersection of this image with A and B permits to quantify the respective contribution of A and B (Fig. 4). Figure 5 shows the structure of drainage network delineated by the above processing.

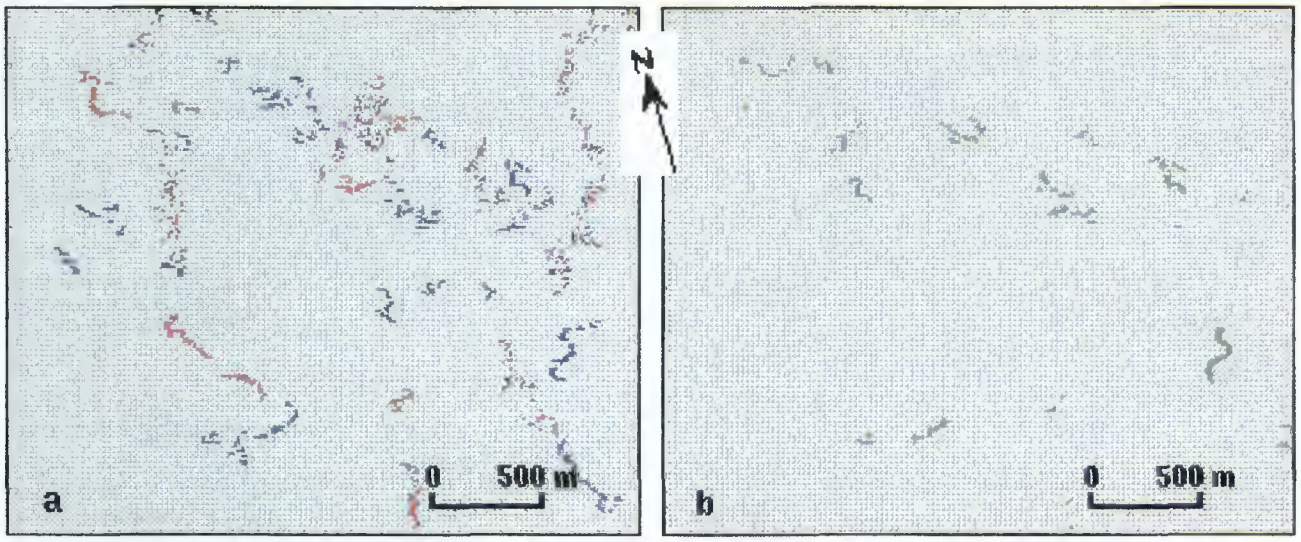

Figure 4. Comparison of results got from two extracts of image 1 subscene between (a) "unspeckled" image (blue) and smoothed image (red), (b) smoothed image (red) and the morphologic 'top-hat' on smoothed image directions (green).

3.2 Multifractal analysis

The singularity map is another representation of the texture perceived on the intensity image (Fig. 3). Unlike other image textures we have analysed, that does not show any orientated structures. A Fourier transform performed on this image also featured this lack of any linear structure, likely due to the half circular shape of the hills that prevail here. The values of the map are increasing with the heterogeneity of the topography, low values about 2 for the large flat area occupied by swamps, and high values ranging from 2.5 to 2.8 for the

forested hills whose the slope forms induce systematic changes of orientation with regard to the radar emission angle.

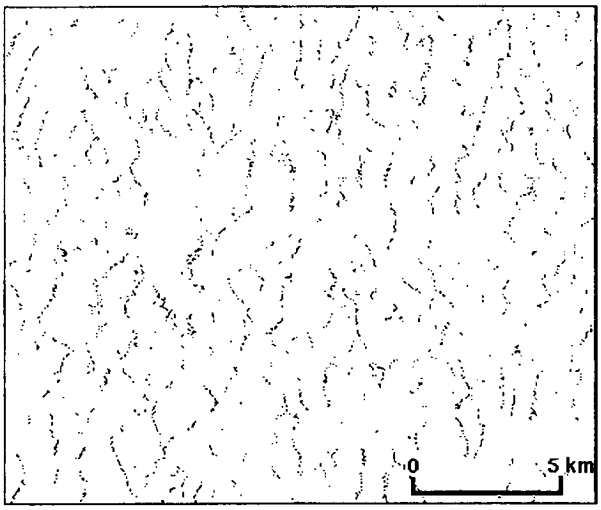

Figure 5. Channel network delineation of image 1 subscene applying mathematical morphology

The comparison of various multifractal spectrum indicates that the spreading of the spectrum to the left is related to the anisotropy of the image (Fig. 6). This part of the spectra thus characterises at best the different textural features prevailing in the studied area.

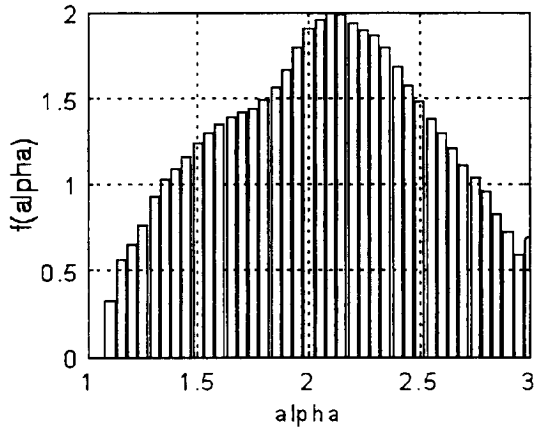

Figure 6. Global singularity spectrum of image 2 subscene.

4. CONCLUSIONS

Mathematical morphology was relatively efficient to delineate drainage network structures, in particular, those oriented perpendicularly to the radar satellite emission - characterised by better incised valleys. This processing will be applied to the whole SAR images - that will allow, we believe, to draw a mosaic of different network structures which will be compared to the other environmental patterns of the forested landscape of South Cameroon. Multifractal analysis was able to discriminate between representative natural textures- the method used to textural characterisation seems promising to ERS1 images segmentation based on the landscape patterns recognition. It may also be of great importance for the measure and the modelling of the landscape evolution and its involved processes. This method will be also tested out to analyse the scaling properties of network structures.

5. REFERENCES

Bitom D, Volkoff B, Beauvais A, & Seyler F 1997, Influence d'une remontée du niveau hydrostatique sur l'évolution des couvertures pédologiques et des modelés en zone intertropicale humide. (submitted to C. R. Acad. Sci., Paris)

Calot Y., Mering C. & Simonin A., 1994, Image analysis and cartography Sand hill massifs on resolution images : application to the Great Western ERG, *International Journal of Remote Sensing*, **15** (18), 3799-3822.

Coster M. & Chermant J.C., 1989, *Précis d'analyse d'images*, (Paris : CNRS).

Grimaud M., 1991, La géodésie numérique en Morphologie Mathématique. Thèse Docteur-Ingénieur, Ecole des Mines de Paris, Fontainebleau.

Mering C. & Parrot J.F.., 1995, Filtering of radar images for geological structural mapping, *SPIE*, 2315, 743-754.

Nagao M & Matsuyama T 1979, Edge preserving smoothing, Computer Graphic and Image Processing, Vol. 9, 391-407.

Sailhac P & Seyler F 1997, Texture characterisation of ERS1 images by regional multifractal analysis: A tool applied to the study of South Cameroon Rain Forest landscape and bio-geo-hydrological processes, to be published in: Fractals in Engineering, June 25-27, 1997, Arcachon, France.

Serra J., 1982, *Image Analysis and mathematical Morphology*, (London : Academic Press).

Hazards

Chairperson: **J. Bodechtel**

SAR ERS IMAGERY FOR THE STUDY OF RELATIONSHIPS BETWEEN TECTONICS AND VOLCANISM: EXAMPLES IN ICELAND AND ANATOLIA

Jean Chorowicz, Pierre Chotin, Damien Dhont
LGGST, Case 129, Paris 6 University, 4 place Jussieu, 75252 Paris cedex 05, France
phone: (33) 01 44 27 50 89, fax: (33) 01 44 27 50 85, Email: choro@lgs.jussieu.fr

Tekin Yürür
Department of Geology, Hacettepe University, Beytepe Ankara, Turkey

Jean-Luc Froger
CRV, Université Blaise Pascal, 5 rue Kessler, 63038 Clermont Ferrand, France

Jacques-Marie Bardintzeff, Georges Rasamimanana
Laboratoire de Pétrographie-Volcanologie, Université Paris-Sud, Bâtiment 504, 91405 Orsay Cedex, France

ABSTRACT

Our approach is based on the mapping of tectonic and volcanic structures using high resolution imagery, mainly SAR ERS. We show that most of the volcanic edifices are located on tension fractures responsible for fissure eruptions, volcanic linear clusters and elongate volcanoes. This relationships is studied first in Iceland, using SAR ERS-1 imagery. It is then applied to Central Anatolia, using also a Digital Elevation Model and field structural analysis. We have evidenced different types of volcanic emplacement such as tension fracture, tail-crack or horse-tail features, and releasing bend basin along the strike-slip faults. Caldera complexes of Cappadocia seem to be associated to horse-tail type fault termination. Deformation was determined from the tension fractures and from field structural analysis. In Central Anatolia, the tectonic regime is extension and not compression.

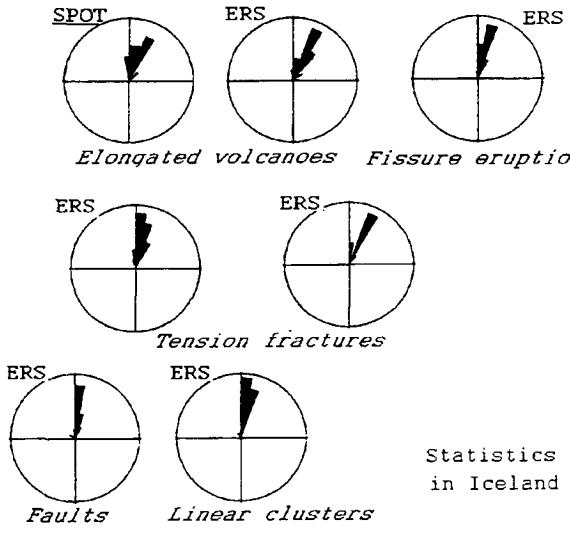

Fig. 1. Statistics in Iceland. Rose diagrams are percentages of cumulative lengths.

1. INTRODUCTION

Observation of geometric relationships between volcanism and tectonics is a fruitful approach in geology. On one hand, analysis of the distribution and types of volcanic vents provides information on the geodynamics. On the other hand, tectonic analysis explains the location of volcanic vents. In this paper, we analyse tectonics and emplacement of volcanic vents in Iceland and in the Central Anatolia region, using satellite and Digital Elevation Models (DEM), complemented with field structural analysis.

3. METHODOLOGY

For the Iceland study, we have used the scenes of orbit 5894, frame 2277, acquired on 92-08-31, and orbit 5436, frame 2277, acquired on 92-07-30, both on descending orbits. These two scenes largely overlap and the common area can be observed in stereoscopy (Fig. 2). We also have used the scene of orbit 6115, frame 1323, acquired on 92-09-15, in ascending node.

Before measuring fault strike and elongation of volcanoes, it is necessary to assess the distortion effects for different geometric configurations. We considered the outlines of lowermost floors of volcanic edifices, which are generally horizontal. To estimate elongation, we determined the ratio of the largest against smallest diameters (L/l). We checked the distortion to study a test area where both SAR ERS-1 and SPOT data (SPOT Panchromatic KJ 717-214) are available. Figure 1 shows that the differences between the two sets are not significantly distinct from uncertainty of the diagrams (10°).

SAR ERS images were produced at 1/200,000 scale, in positive or in negative (Fig. 6). This last type of presentation of the image has the advantage to display in dark the bright slopes facing the radar and affected by shortening and layover effects, giving the impression

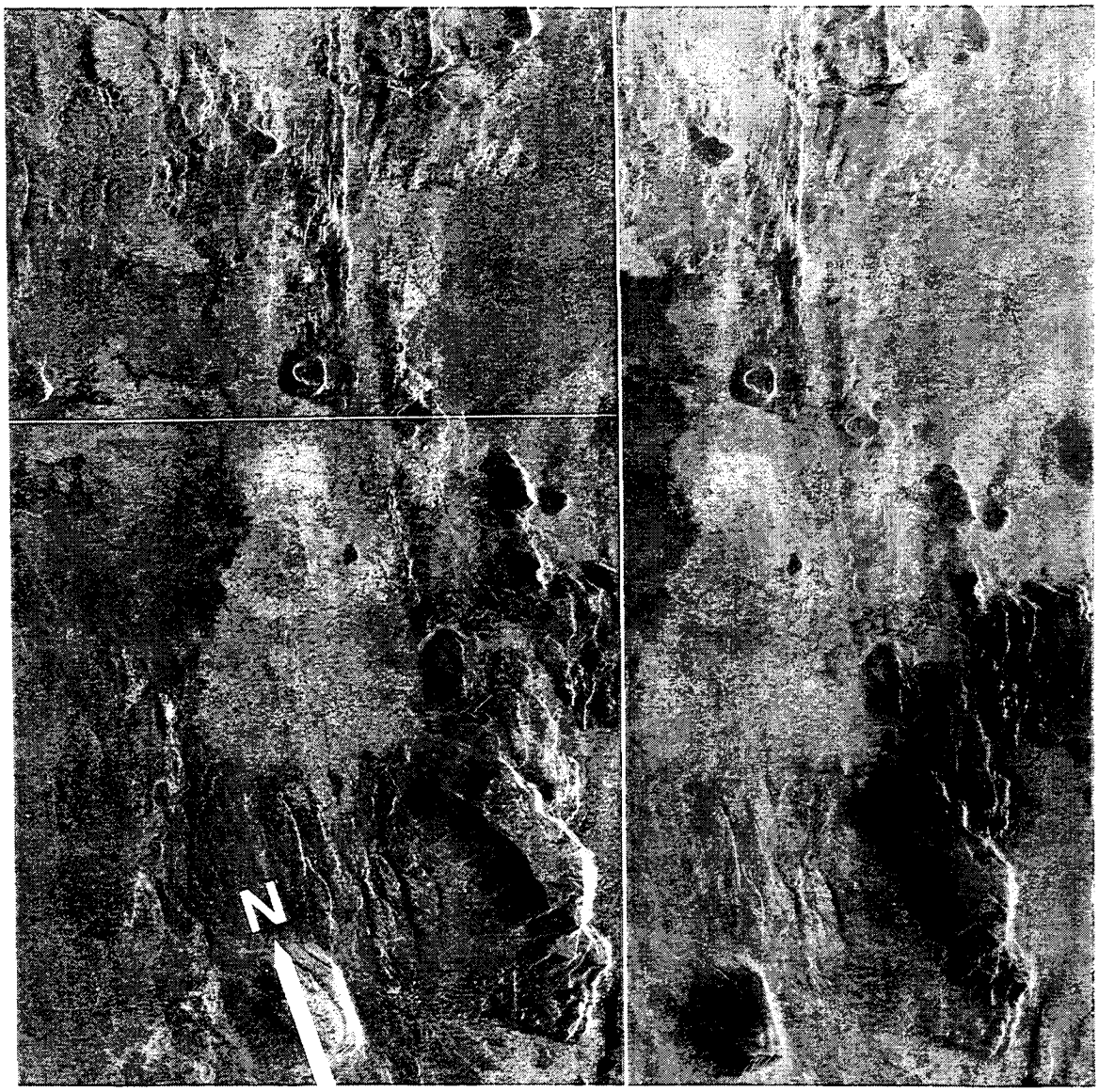

Fig. 2. Sample of the stereopair of SAR ERS-1 images (descending nodes) acquired over the test area in Iceland. See location on Fig. 3.

of shadow. Slopes backing the radar are then clear and give the impression to be illuminated.

2. OBSERVATIONS IN ICELAND

In the Holocene Krafla fissure swarm, straight scarps mark recent faults (Fig. 2). In some places, volcanic material fills open fissures which gradually thin out along strike and have the shape of tension fractures (Fig. 3). Main trends of these fissure eruptions range from N350°E to N40°E, with maximum from N10°E to N20°E (Fig. 1). Some variations in trend of the fissure eruptions may be locally linked with the occurrence of calderas.

Nearly all volcanoes are located on faults or in the prolongation of faults. some volcanic edifices are aligned and close to each other, forming linear clusters composed of several volcanoes. Directions of linear clusters range from N350°E to N30°E with maximum from N00°E to N20°E (Fig. 1).

Several faults face each other at a distance of 200 to 800 m, delineating narrow grabens (e.g., T in Fig. 3) which progressively close at one or both ends. These are interpreted as tension fractures by Opheim and Gudmundsson (1989). They strike N0-40°E, with maximum between N20°E and N30°E (Fig. 1). The rose diagram of graben strikes has the same shape as of tension fractures. Normal faults in Iceland are considered to have formed from tension fractures or joints (Forslund and Gudmundsson, 1992). The rose diagram of fault strike is very similar to that of tension fractures: faults have a preferred strike between N350 and N30°E, with maximum between N00 and N10°E, except for faults striking about N125°E, parallel to the west-north-west striking Husavik fault (Fig. 3), considered to belong to the Tjörnes transform fault.

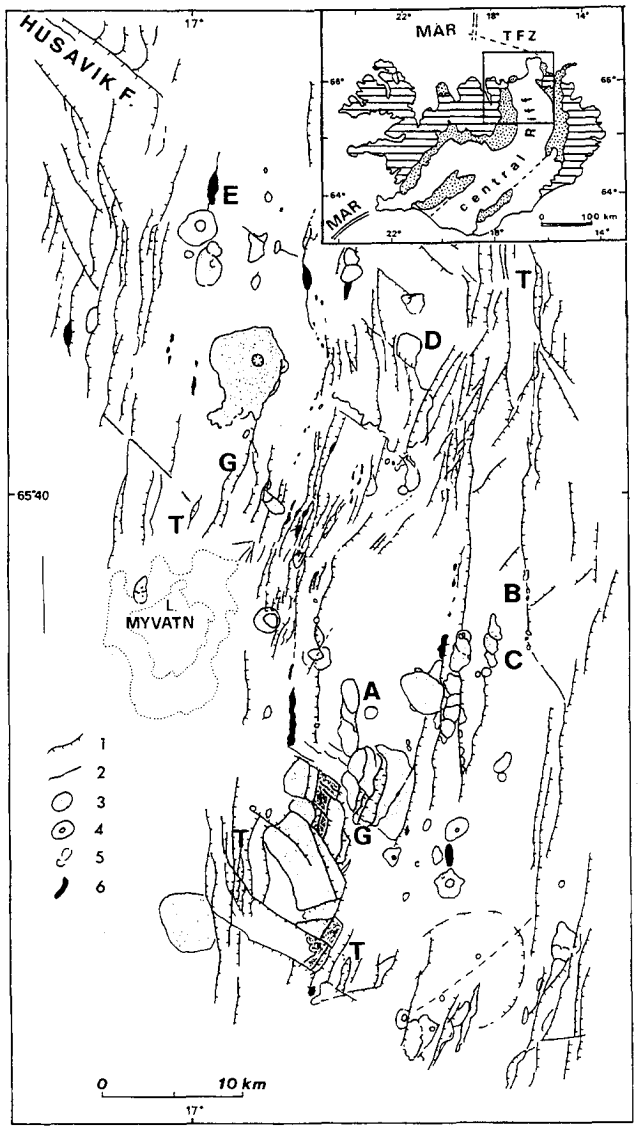

Fig. 3. Interpretative map of the test area in Iceland, from the SAR ERS stereopair.

The study of Iceland, with the use of SAR ERS-1 imagery, shows that (1) volcanic vents are located on tension fractures, (2) direction of elongation of volcanoes coincides with the strike of tension fractures, (3) a cluster of aligned volcanoes commonly represents a tension fracture or several tension fractures aligned on a fault, (4) the trend of tension fracture tips indicate the perpendicular local tension.

4. OBSERVATIONS IN CENTRAL ANATOLIA (TURKEY)

The Central Anatolia region in Turkey (Fig. 4) has been submitted to Mio-Plio-Quaternary deformation and volcanism (Le Pennec et al., 1994). This region is part of the Anatolia block moving westward by lateral extrusion as a consequence of north-south convergence between Africa-Arabia and Eurasia.

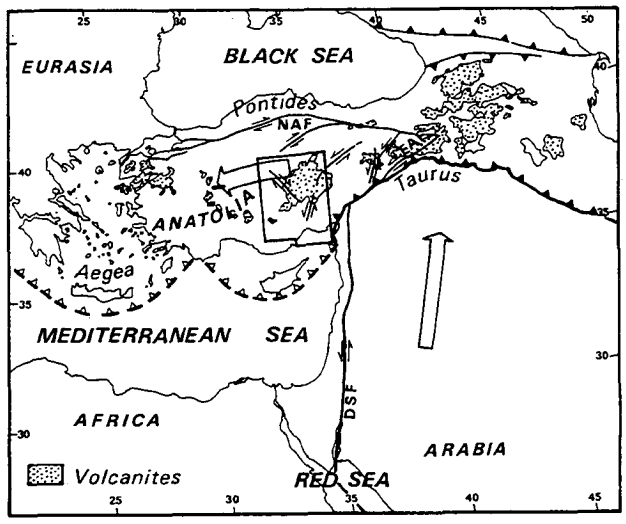

Figure 4. A. Geodynamic context of the Central Anatolia region since the late Miocene. Large arrows show Africa-Arabia and Anatolia plate motions relative to Eurasia. Thick lines: plate boundaries. Rectangle: location of Central Anatolia. DSF: Dead Sea Fault; EAF: East Anatolian Fault; NAF: North Anatolian Fault.

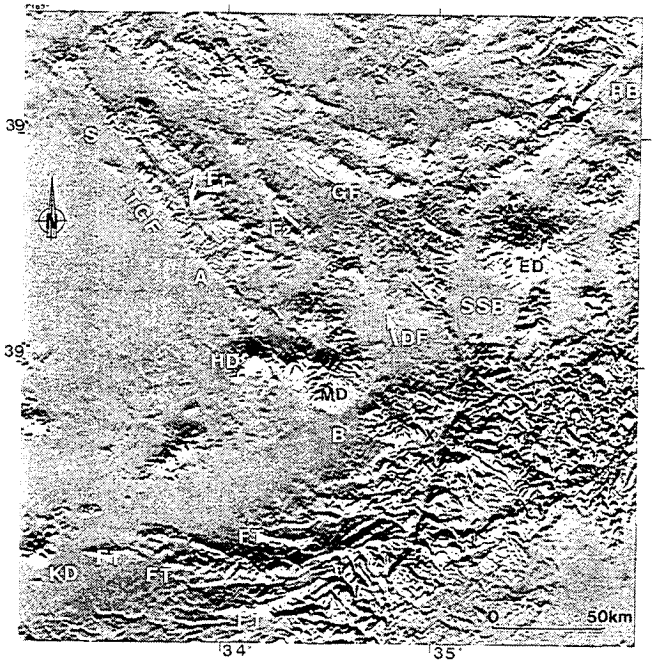

Fig. 5. Image of the Digital Elevation Model of the studied area, at 500 m ground resolution, illuminated from south. A: Aksaray; B: Bor; DF: Derinkuyu fault; ED: Erciyes Dag; FT: normal faults of the Central Taurus range; GF: Gumuskent fault; HD: Hasan Dag; KD: Kara Dag; MD: Melendiz Dag; S: Sereflikoçhisar; SSB: Sultan Saz basin; TGF: Tuz Gölü fault.

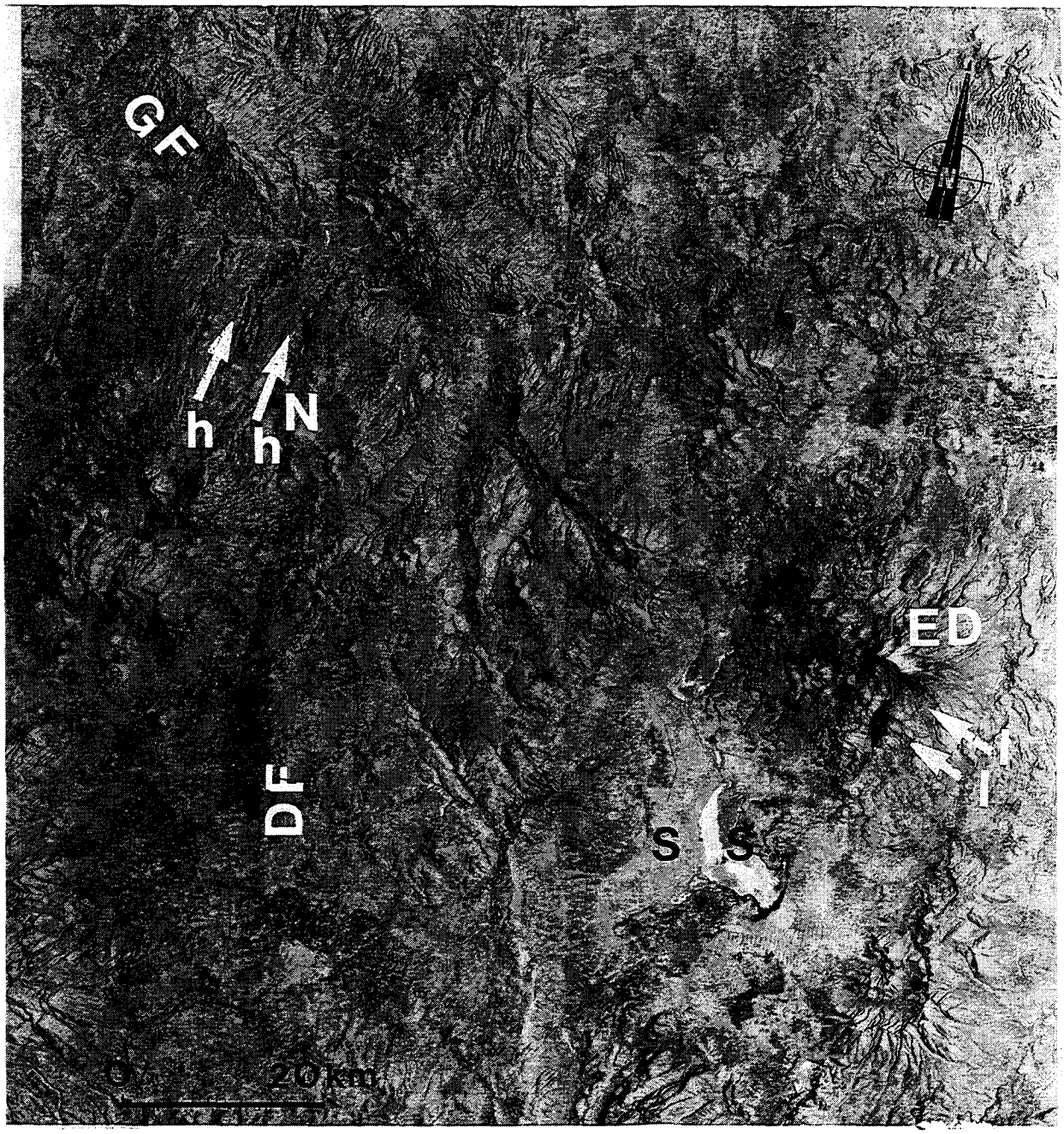

Fig. 6. SAR ERS-1 image (negative view) of the Sultan Saz basin (SS) and part of the Cappadoce region, including the Gumuskent and Derinkuyu faults (respectively GF and DF). h: NNE-striking faults south of Nevsehir (N) forming a horse-tail pattern. l: NW-SE structural lines affecting the Erciyes Dag (ED). Location on Fig. 7.

Volcanic edifices form elongated strato-volcanoes, linear clusters or volcanic ridges. They evidence volcanic emplacement on tension fractures and tail-crack or horse-tail features (Fig. 6). Caldera complexes of Cappadocia are associated to horse-tail type fault termination. The Erciyes Dag is situated in the Sultan Saz releasing bend opening along the strike-slip Ecemis fault. The common characteristics of these structures is to open at local scale and give way up to the magma.

Deformation was analysed from tension fractures - which are at right angle to the direction of extension - and field structural analysis. At regional scale, the tectonic regime responsible for distribution of volcanic vents in this area of convergence and lateral extrusion, is extension, not compression. Volcanism is related to crustal scale faults and tension fractures, arguing that extension in the Central Anatolia plateau is not of lithospheric scale but rather related to crustal blocks moving above sub-horizontal detachment surfaces located in the lower crust.

6. CONCLUSIONS

SAR ERS data have synoptic views permitting to describe structures which cover large surfaces. The data provided concern objects of large dimensions and can be considered as complementary to detailed microtectonic field analysis.

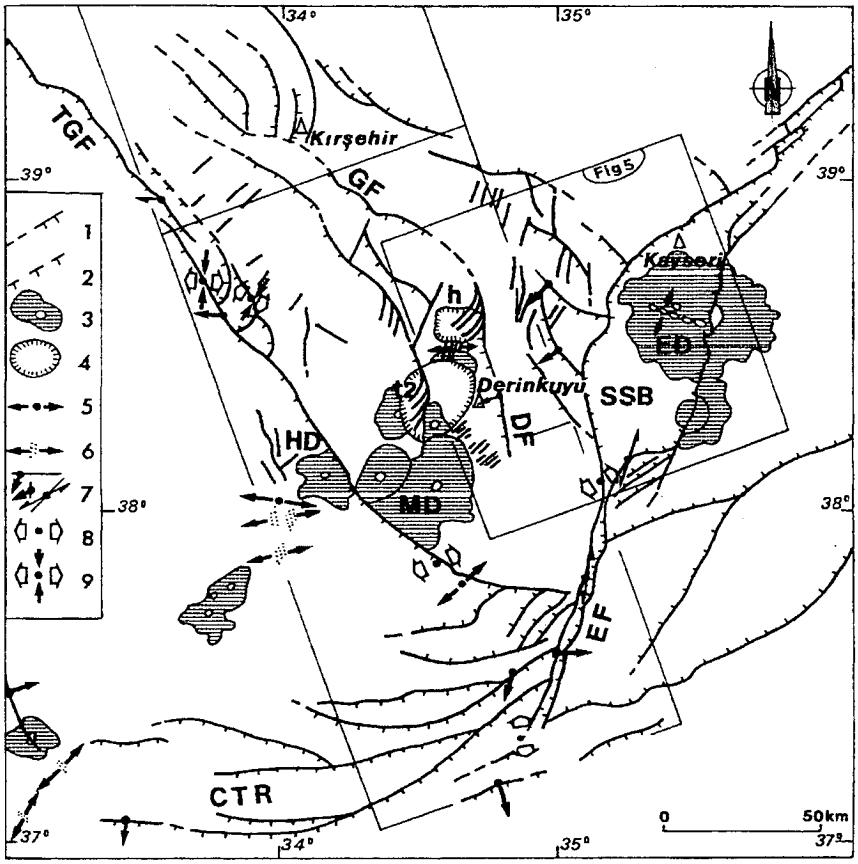

Figure 7. Synthetic map of tectonic and volcanic features observed from above data. CTR: Central Taurus Range; DD: Develi Dag; DF: Derinkuyu fault; ED: Erciyes Dag; EF: Ecemis fault; GF: Gumuskent fault; h: horse-tail pattern; HD: Hasan Dag; MD: Melendiz Dag; SSB: Sultan Saz Basin; t2: horse-tail structure at southern end of fault F2; TGF: Tuz Gölü fault. 1 and 2: normal faults (2: inferred), barbs indicate downthrown side; 3: volcanic vents and strato-volcanoes; 4: caldera complexes; 5: observed in the field; 6: direction of extension from tension fractures determined by linear clusters or volcanic ridges; 7: main slip vector along major faults; 8 and 9: direction of $\sigma 3$ from inversion of fault-slip data (9: strike-slip regime).

Radar imagery is particularly convenient because it accentuates topographic features, specially scarps which mainly express neotectonic structures (Chorowicz et al., 1995).

This approach to analyse tectonic-volcanism geometric relationships is new. It uses the mapping of structures from high ground resolution remote sensing systems, including SAR, an all-weather sensor. Attention is paid to elongate volcanic edifices or craters, and clusters of aligned vents, considered to be rooted on tension fractures.

Acknowledgements

SAR ERS-1 data have been provided by the European Space Agency in the frame of project AO2.F112 (J. Chorowicz, Principal Investigator).

7. REFERENCES

Chorowicz, J., B. Koffi, C. Chalah, P. Chotin, B. Collet, J.-T. Poli, J.-P. Rudant, O. Sykioti, and G. Vargas 1995, Possibilités et limites de l'interprétation géologique des images (SAR) ERS-1, *Bulletin de la Société Française de Photogrammétrie et Télédétection*, 138(2), 82-95.

Forslund, T. and Gudmundsson, A. 1992, Structure of Tertiary and Pleistocene normal faults in Iceland. *Tectonics*, 11(1), 57-68.

Le Pennec, J.-L., J.-L. Bourdier, J.-L. Froger, A. Temel, G. Camus, and A. Gourgaud 1994. Neogene ignimbrites of the Nevsehir Plateau (Central Turkey): stratigraphy, distribution and source constraints, *Jl. of Volcan. and Geotherm. Res.*, 63, 59-87,.

Opheim, J.A. and Gudmundsson, A. 1989, Formation and geometry of fractures, and related volcanism of the Krafla fissure swarm, northeast Iceland. *Geol. Soc. Am. Bull.*, 101: 1608-1622.

VOLCANO MONITORING USING INTERFEROMETRIC SAR

Wadge, G.[1], Achache, J.[2], Ferretti, A.[5], Francis, P.W.[3], Morley, J.[4], Muller, J-P.[4], Murray, J.B.[3], Prati, C.[5], Rocca, F.[5], Stevens, N.F.[1], Upton, M.[4] and Williams, C.A.[1]

1. Environmental Systems Science Centre, University of Reading, Reading, UK
phone: +44 (0)1189 318741, fax: +44 (0)1189 755865 email: gw@mail.nerc-essc.ac.uk
2. BRGM, Orleans, France
3. Dept.of Earth Sciences, Open University, Milton Keynes, UK
4. Dept. of Photogrammetry and Surveying, University College London, UK
5. Politecnico di Milano, Milano, Italy

ABSTRACT

At a volcano like Etna, which is under continual scientific observation, differential interferometry using ERS SAR has the potential to become a useful operational tool to monitor surface displacements caused by internal changes in magma pressure and movement. Our approach to achieve this is firstly to create geocoded differential interferograms corrected by a DEM from which surface displacement maps can be derived. Then in conjunction with contemporary ground survey measurements, we can analyse the surface displacements in terms of pressure changes in a 3D finite element model of the volcano and the crust. Preliminary results using ERS-1 and -2 SAR data from September 1995 to June and September 1996 suggest that the volcano expanded over this period. Often it is only the historical lava flows on the flanks of the volcano that supply areas with sufficiently high phase coherence to produce good results. To work well this approach needs a time series of suitable SAR data so that transient atmospheric and surface effects are minimised. We also show that ignoring the topography of the volcano when analysing internally-induced deformation will distort the pattern of apparent surface displacements.

1. INTRODUCTION

The surfaces of volcanoes move in response to the movement of magma within them. Generally speaking, increasing internal magma pressure will make the surface bulge upwards and outwards. Following an eruption of magma at the surface, this deformation will tend to be reversed. The scale of this deformation is centimetric to decimetric over tens of square kilometres, over periods of weeks to years. Hence differential interferometry from spaceborne SAR should be a good means of monitoring such deformation. No other technique will produce such a dense spatial sampling of the displacement field.

There are two obvious monitoring strategies: early warning and forecasting. In the former, relatively infrequently sampled pairs of images (e.g. 0.5 - 1 year separation) at non-erupting volcanoes could be checked to detect any signs of deformation. At volcanoes with established observatories a more intense observation programme (e.g. every 35 days) could be integrated with other observations to analyse the internal behaviour of the volcano.

This study is concerned with the latter strategy applied to the Etna volcano in Sicily. Etna has been the focus of most work on this technique to date because it is the most active European volcano with an observatory. A substantial volcano-wide deflationary signal was detected from ERS-1 data and reported by Massonnet et al. (1995) for the 1992-93 period during and after a major lava flow eruption. Briole et al. (1997) also showed from the same data that a much more localised deformation anomaly was correlated spatially with earlier lava flows from 1986-89, suggesting that post-emplacement stress relaxation was responsible. There are 2 main elements to our approach, though the results presented here are preliminary. First, we create differential interferograms using repeat-pass pairs of ERS-1 and ERS-2 SAR images and map them onto ground range coordinates. Then we validate and compare these interferometric observations with contemporaneous field survey observations and 3-D finite element models of surface deformation due to magmatic/tectonic stress variations at depth.

2. SAR DATA AND PROCESSING

ERS-1 and-2 SAR data for Etna were chosen from the ERS-1 phase G (1992-93), the tandem experiment (May 1995- May 1996) and the ERS-2 period (May 1996-present). The relevant data from ERS-1 phase G were discussed by Massonnet et al. (1995). Here we concentrate on data from the 1995-96 period. Scenes from two frames (frame 747 from ascending passes and frame 2853 from descending passes) were selected. For differential interferometry, short perpendicular baselines (Bp) are required. Choosing a minimum Bp threshold of 200 m reduces the number of potential interferometric pairs to 137. We find that during the winter months (November - April) the summit of the volcano, which is covered in snow, has its phase coherence reduced to levels that are too low in interferograms with at least one winter image. In practice, therefore, we use the following criteria to select and prioritise the image pairs for processing:

Proc. 3rd ERS Symp. on Space at the service of our Environment, *Florence, Italy, 17–21 March 1997* (ESA SP-414, 3 Vols., May 1997)

1. Bp < 200 m
2. Selection only from summer month acquisitions
3. Prefer pairs with at least one image contemporaneous with a field survey

This reduces the number of pairs to about 20, essentially between summer 1995 and summer 1996.

Our processing uses the method that requires 2-pass data together with a DEM. The data shown here were produced using the UCL 3D Image Maker System for differential SAR interferometry (UCL-3DIM/dIfSAR) that is described by Upton et al. (1996). This employs a modified version of the IfSAR interferogram creation software from POLIMI (Feretti et al., 1996) together with a further set of programmes developed at UCL for converting the results to ground coordinates (WGS84 elipsoid is used throughout to allow easy comparison of GPS with IfSAR results).

3. DEMS

The quality of the DEM used to remove topography affects the quality of the interferogram. We have experimented with a number of different DEMs of Etna to assess this effect and early results are reported in Muller et al. (1996). Two of the DEMs we have used are :

CNR-DEM
This is derived from vector contour data supplied by CNR- Gruppo Nazionale per la Vulcanologia which was compiled from aerial photogrammetric data captured mainly in September 1985. It is a 1arc-second DEM in WGS84 ellipsoid co-ordinates gridded using a minimum curvature interpolator. Its use in this context suffers from errors introduced via the digitisation process and the patching together of sub-areas and from the fact that the topography over the areas that were subject to lava flows of 1986-7, 1989 and 1991-3 are now incorrect.

ERS-IfSAR DEM
Tandem data (ascending pass) from 5/6 September 1995 were used to generate a 1 arc-second DEM using the UCL 3D Image Maker (IfSAR) system (Muller et al., 1996b) and PRC vectors from D-PAF to model the SAR geometry. The model is very noisy in places, especially over the forested lower slopes where there is low phase coherence between the two images. Much higher quality DEM results are possible using a multi-baseline approach (Ferretti et al., 1997). The estimates of height for each pixel can be compared to eliminate those pixels affected by local transients (e.g. atmospheric effects). This serves the dual purpose of providing a very high quality DEM for differential work and mapping areas affected by path-effect noise.

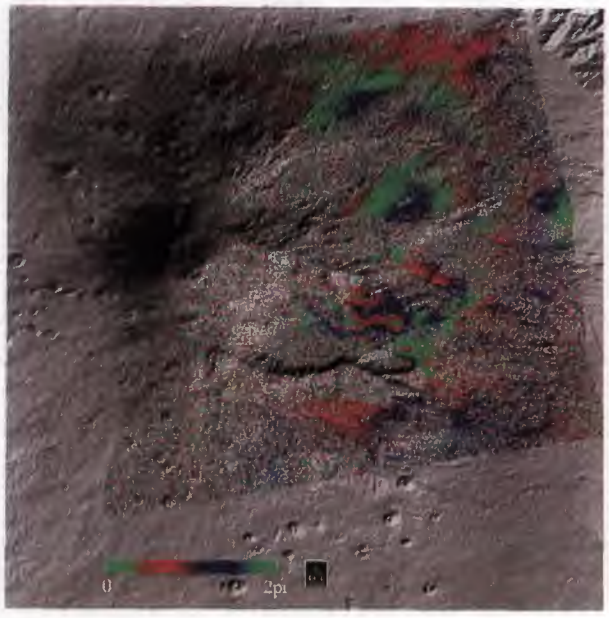

Figure 1. Geocoded differential interferogram for ERS-1/ERS-2 ascending pass data (Bp = 5 m) from September 1996 to June 1996 superimposed on a shaded relief image (25 km E-W) of the CNR-DEM of the summit area of Etna. A threshold of > 0.13 for coherence has been used to display the phase data. The large valley feature in the centre of the scene is the Valle del Bove. © UCL 1997

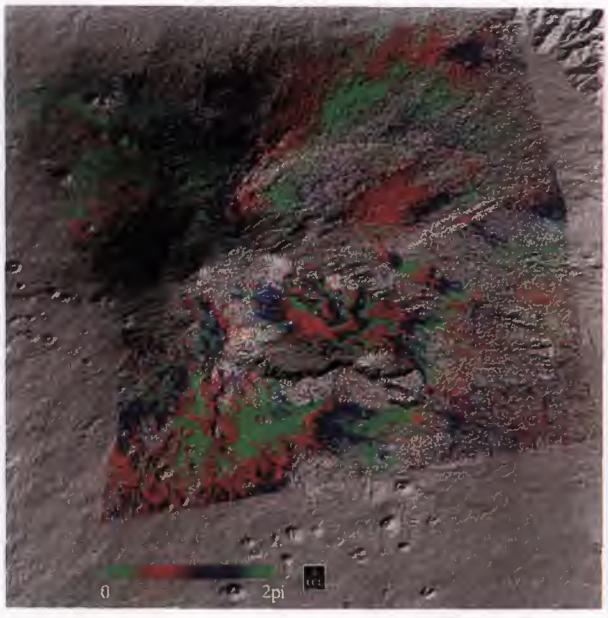

Figure 2. Geocoded differential interferogram for ERS-2/ERS-2 ascending pass data (Bp = 112 m) for the same period as (a). A threshold of > 0.2 for coherence has been used to display the phase data. © UCL 1997

The existence of DEMs before and after the emplacement of lava flows on a volcano can be put to use in calculating the volume and morphology of the flows. We have used the difference between the 1985 CNR-DEM and the 1995 ERS-IfSAR DEM to measure the 1991-93 lava flow-field in this way (we know from ground survey that this flow is up to 95 m thick in places, Stevens et al. (1997)). The principle difficulty with this approach in this case is the correct registration of the DEMs due to the unknown datum shifts between the CNR maps and WGS84 ellipsoid.

4. SAR-DERIVED SURFACE DISPLACEMENTS

Our analysis is in its preliminary stage. Here we discuss two pairs of differential interferograms created from ascending pass images from September 1995 and June 1996. The first pair is an ERS-1 /ERS-2 pair (orbits 21660 and 5995), the second an ERS-2 / ERS-2 pair (orbits 1987 and 5995). These geocoded interferograms are shown in figures 1 and 2. They should represent either (i) displacements of the surface of the volcano in the intervening 9 months, or (ii) effects due to changes in properties of the atmosphere. In the absence of some independent means of distinguishing these two effects, for any given pair, we can only rely on generalisations such as ionospheric anomalies should be of small (< 10 km) size and lower tropospheric effects will be related to weather or systematic change in moisture content with height. We can potentially avoid atmospheric problems using multi-image data as described previously, though this is not done here.

Assuming that the fringes seen in a differential interferogram are due to surface displacements, there are two main possible causes of such displacements on Etna: internal deformation and movements associated with lava flows. Internal deformation displacements should have the characteristic of being wide-scale (e.g. volcano-wide) except perhaps before and close to eruptive fissuring. The surfaces of lava flows can move due to thermal contraction, downslope creep or relaxation of the substrate. The spatial pattern of such displacements should be related to the shape of the flow. Recently emplaced flows (few years) may show such displacements, but older flows should be more stable. It is the historical lava flows on the flanks of the volcano that are the most coherent surfaces over periods of months to years. We see this effect clearly in figure 1 when a threshold minimum level of coherence is used. On the eastern flanks of Etna, north of the Valle del Bove the flows of 1865 and 1971 are distinct in figure 1 whilst south of the Valle del Bove the flow of 1766 is obvious. There are two problems associated with qualitative interpretation of these type of results. Firstly, it is difficult to see regional displacement patterns from isolated patches of information. Secondly, these individual patches (the lava flows) may have their own local displacement signal, superimposed on the regional one.

The clearest pattern evident from these, albeit limited extent, differential interferograms is in the northern Valle del Bove (Fig. 2). Here 2-3 fringes (5-8 cm) of displacement towards the satellite indicate uplift towards the west or summit of the volcano. Superimposed on these are the lava flow-related displacements of the 1989 and 1986-87 lava flows described by Briole et al. (1997) which are in the opposite sense (displaced away from the satellite). Interestingly, most of the 1991-93 flow in the southern part of the Valle remains incoherent over this 9 month period though the north central edges (in Fig. 2) are now coherent. There is some indication that the volcano-uplift pattern seen in the northern Valle del Bove also exists in the northeastern parts of figures 1 and 2 and southwestern part of figure 2 though only 1-2 fringes appear to be involved. The ERS-directed vector of motion detected by differential interferometry is largely a measure of the vertical component of displacement.

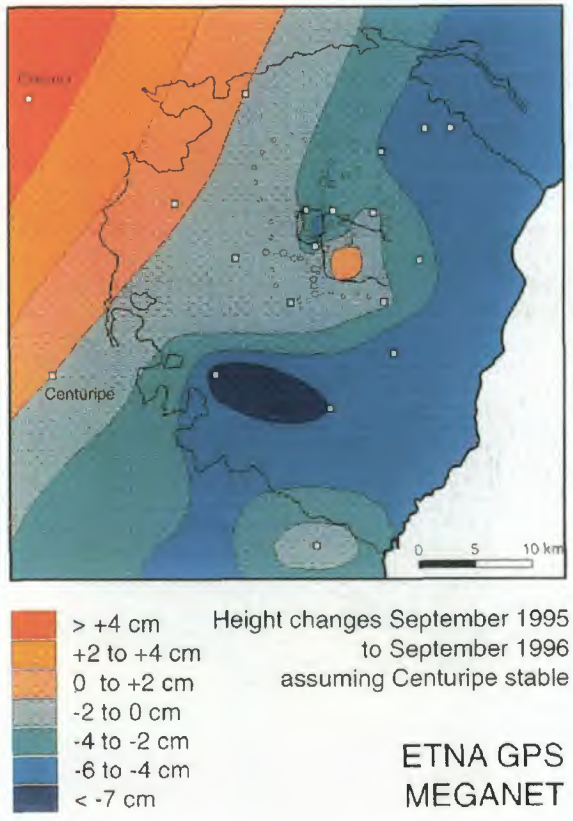

Figure 3. Contour map of the vertical component of relative displacements measured by the MEGANET GPS network between September 1995 and September 1996. White squares are station positions.

5. GROUND SURVEY DISPLACEMENTS

There are a large number of ground surveying measurements made on Etna. We report on the preliminary findings of two such sets of GPS measurements made with Wild GPS system 200 receivers in September 1995 and September 1996 (Murray and Sargent, 1997), a period that includes the SAR data acquisition. This Etna MEGANET GPS network consisted of 52 stations and error ellipsoid dimensions for changes between the two occupations average 10 mm horizontally and 16 mm vertically. Horizontal displacements show a radial pattern of movement away from the volcano by up to 10 cm. Vertical movements show a pattern of depression of the flanks of the volcano relative to the summit by 4-6 cm superimposed on an apparent NW-SE gradient (Fig. 3). The pattern of relative outward and downward movement of the flanks of the volcano is qualitatively compatible with the weakly-defined SAR-derived displacements from the September 1995 - June 1996 period.

6. 3D MODELLING

Apparent agreement of the SAR- and ground survey-derived displacements suggests that the volcano's magma storage system may be re-pressurising after the 1991-93 eruption, which was very voluminous. To properly test this type of hypothesis the observations must be compared to a realistic model of internal behaviour. We are developing such a model using 3D finite elements (Williams et al., 1997). The model incorporates the major structural surfaces and appropriate material property constants of the volcano and the crust

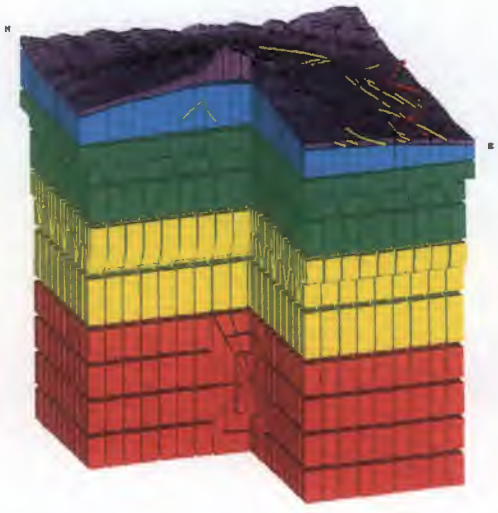

Figure 4. Cut-away view of a simplified 3D finite element model of the structure of Etna. Some of the surface faults (yellow) and the coastline (red) are shown and the putative location of a magma chamber at 16 km. The model dimensions are 40 km horizontally and 20 km vertically with twofold vertical exaggeration.

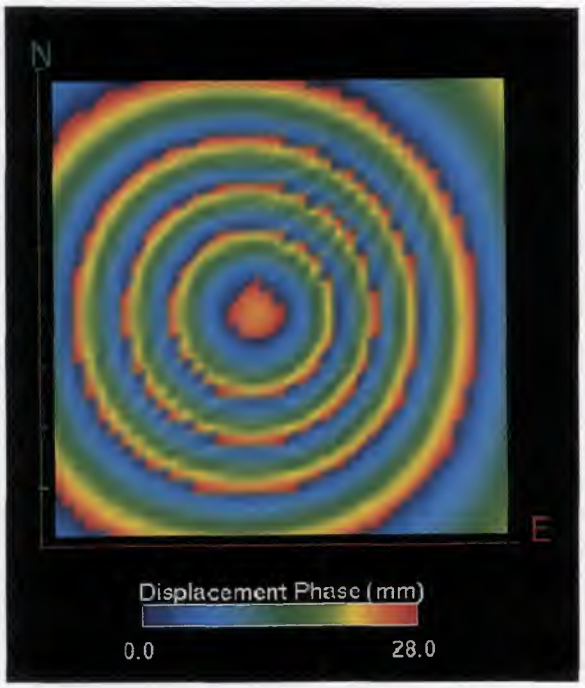

a

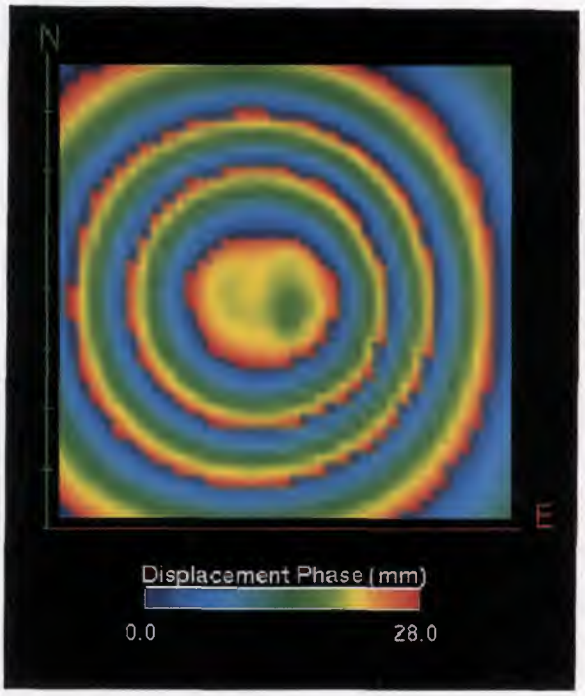

b

Figure 5 (a) Synthetic differential SAR interferometric fringes (from an ascending pass pair) due to pressurisation at a 16 km deep magma chamber as seen on a flat surface (c.f. same numerical result as the analytical one shown by Massonnet et al., 1995). (b) Equivalent result taking into account the surface topography of the volcano. Both results created using the finite element model approach of figure 4. Models are 40 x 40 km.

beneath. These surfaces include: surface topography, sedimentary basement, shallow decollement surface, acoustic basement, plutonic body beneath the Valle del Bove, deep decollement surface, crustal magmatic reservoir and the Moho (Fig. 4).

The benefits of this approach compared to that which seeks a best-fit solution to an analytical model for an elastic half-space (e.g. Massonnet et al., 1996) can be seen in figure 5. This shows the difference that ignoring the substantial (> 3 km) surface relief of Etna makes in the pattern of surface displacements, expressed as a synthetic interferogram, due to a buried pressure source at 16 km. Because the summit of the volcano is further from the pressure source than the flanks nearly a whole fringe of displacement is, correctly, removed from the flat surface model version near the summit region of Etna.

7. ACKNOWLEDGEMENTS

We thank ESA for the ERS SAR data supplied under ERS AO2.UK117 and for the CNR - Gruppo Nazionale di Vulcanologia for DEM data. We are also grateful to our colleagues in the EC-funded MADVIEWS project whose work overlaps with that reported here. GW, JPM and PF thank the UK NERC for funding under grant GR3/09745 and GW thanks the UK NERC for general support to ESSC under grant F60/G6/12.

8. REFERENCES

Briole, P., Massonnet, D. & Delacourt, C. 1997. Post-eruptive deformation associated with the 1986-97 and 1989 lava flows of Etna detected by radar interferometry. *Geophysical Research Letters*, 24, 37-40.

Ferretti, A., Monti Guarnieri, A., Prati, C. & Rocca, F. 1996. Multi baseline interferometric techniques and applications. *Proc. ESA Fringe 96*. http://www.geo.unizh.ch/rsl/fringe96.

Ferretti, A., Monti Guarnieri, A., Prati, C. & Rocca, F. 1997. Multibaseline SAR interferometry for automatic DEM reconstruction. *Proc. ESA 3rd ERS Conf.*, Florence, 17-21 March.

Massonnet, D., Briole, P. & Arnaud, A. 1995. Deflation of Mount Etna monitored by spaceborne radar interferometry. *Nature*, 375, 567-570.

Muller, J.-P., Mandanayake, A., Morley, J.G. & Upton, M. 1996a. Accuracy assessment of DEMs derived from ERS tandem interferometry and comparison with SPOT-stereo. *Proc. ESA Fringe 96*. http://www.geo.unizh.ch/rsl/fringe96.

Muller, J.-P., Mandanayake, A., Murrary, K., Holland, D. 1996b. Assessment of interferometric SAR DEM for UK National Mapping. *Proc. ESA Fringe 96*. http://www.geo.unizh.ch/rsl/fringe96.

Murray, J.B. & Sargent, P. 1997. Deformation mega-network at Mt. Etna volcano. *J. of Conference Abstracts*, 2(1), 53, Cambridge Publications.

Stevens, N.F., Murray, J.B. & Wadge, G. 1997. The volume and shape of the 1991-93 lava flow field at Mount Etna, Sicily. *Bull. Volcanol.*, 59, (in press).

Upton, M., Muller, J.-P., & Smith, A. 1996. The UCL 3D Image Maker system for automated differential SAR interferometry. *Proc. ESA Fringe 96*. http://www.geo.unizh.ch/rsl/fringe96.

Williams, C.A., Wadge, G., Morley, J.G., Muller, J-P., Upton, M. & Murray, J.B. 1997. Three-dimensional numerical modelling of the deformation field at Mt. Etna volcano, Sicily, constrained with SAR interferometry, *European Geophysical Society General Assembly abstract*, Vienna, 21-25 April, 1977.

ERS-TANDEM-INTERFEROMETRIC OBSERVATION OF VOLCANIC ACTIVITIES IN ICELAND

Karl-Heinz Thiel, Xiaoqing Wu, Philipp Hartl

Institute of Navigation, University Stuttgart
Keplerstr. 11, 70174 Stuttgart, Germany
phone: +49 711 121 3413, fax: +49 711 121 2755

ABSTRACT

Applying SAR-Interferometry in remote areas has shown the high potentials for monitoring of surface changes. ERS-tandem-interferometric observations of the natural phenomena of an volcanic activity in Iceland demonstrated once again the powerful ability of SAR-interferometry to detect small surface changes of large areas. With the available data sets from the ERS tandem phase, the topography and the surface changes due to the recent eruption of the Vatnajökull volcano in Iceland are estimated.

Key words: SAR interferometry, ERS-1/ERS-2 tandem phase, volcano, small change detection

1. INTRODUCTION

SAR-interferometry is a powerful technique for the generation of digital elevation models (DEMs) and the monitoring of small surface changes. With the ERS-1 data sets, an INSAR derived DEM with an accuracy of 4.3 m was demonstrated for an area near Bonn, Germany with a ground resolution of 50×50 m^2 [1]. The ability of SAR-interferometry to detect the small changes was demonstrated for several sites and cases: the monitoring of the Landers earthquake of 28 June 1992 [2] and the ice movement in the Antarctic [3,4]. In this paper, the ERS tandem interferometric observation of the ice surface changes caused by the recent volcanic eruption on Sep. 30, 1996 in the Vatnajökull-Glacier in south Iceland will be presented.

SAR interferometry is based on the generation of an interferogram by using two SAR images of the same area. The two images are acquired at two different times. In the case of ERS tandem mission, the time interval is 24 hours. The phase of the interferogram contains the topographical information if the two look angles are different, and the information about the surface changes. The following equation describe the relation between the phase Ψ of the interferogram, the topographical elevation Δz and the surface change δr in slant range direction:

$$\Psi(P) - \Psi(P_0) \approx \frac{4\pi}{\lambda}\left\{\frac{B}{R \cdot \sin\theta}\Delta z + \delta r\right\}, \qquad (1)$$

after the phase of the "flat earth" is removed. In eq. (1), P is a point and P_0 is a reference point, B is the baseline between the two orbits of the two acquisitions, R is the slant range to the point P and θ is the incidental angle.

If there is no surface change between the two acquisitions of the two images, the topographical elevation can be derived from the phase of the interferogram. And if the topographical elevation is known, the surface change in slant range can be also obtained from the phase. In the following sections, we will use two ERS tandem pairs acquired on Dec. 30/31, 1995 and Oct. 21/22, 1996 to estimate the DEM of the Vatnajökull area and its surface changes happened between Oct. 21 Oct. 22., 1996 due to the Vatnajökull volcanic eruption on Sep. 30, 1996 and the following seismic activities.

2. 1996 VOLCANIC ERUPTION IN VATNAJÖKULL

The recent volcanic eruption beneath the biggest glacier in Europe, the Vatnajökull glacier in Central Iceland happened on Sep. 30, 1996, after an earthquake with a magnitude of 5.4 on Sep. 29, 1996. This event continued for more than one month. As a result, a 4 km long fissure beneath the glacier, which is 400-600 m thick in this location, was formed. Around the eruption fissure, an evident ice sinking was observed. A large amount of melt water drained into the Grimsvotn Lake, which is located just in the south of the eruption fissure and about 350 m lower than the eruption site. The ice cover of the Grimsvotn Lake has been raised.

Fig. 1 shows the topography around the eruption location.

3. DEM OF VATNAJÖKULL OBTAINED FROM ERS-INSAR

Because of the continuous surface changes caused by the volcanic activities, no repeat path INSAR with an acquisition time interval of 35 days except the ERS tandem INSAR with one day acquisition time interval can provide enough coherence to obtain a good quality

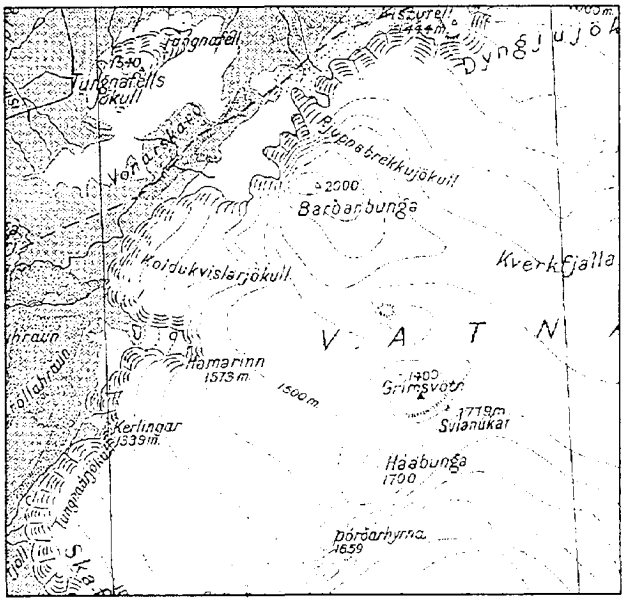

Fig. 1 Topographical map of Vatnajökull of Iceland.

interferogram. In the eruption duration, only the descending pair on Oct. 21/22, 1996 and the ascending pair on Oct. 23/24, 1996 are available. Due to the raining on Oct. 23 [5], the coherence of the ascending pair is too poor to allow to get a useful interferogram. Therefore only the descending pair will be used to detect the surface changes resulting from the volcano activities.

Before the phase of an interferogram can be used to detect the surface changes, the DEM of the area must be known according to eq. (1). One possibility is to use a known DEM. Another alternative is to use an interferogram with no surface changes. In this case the ERS tandem data of Dec. 30/31, 1995 (frame: 2295, orbits: 23315/03642) are used to generate the DEM of the Vatnajökull.

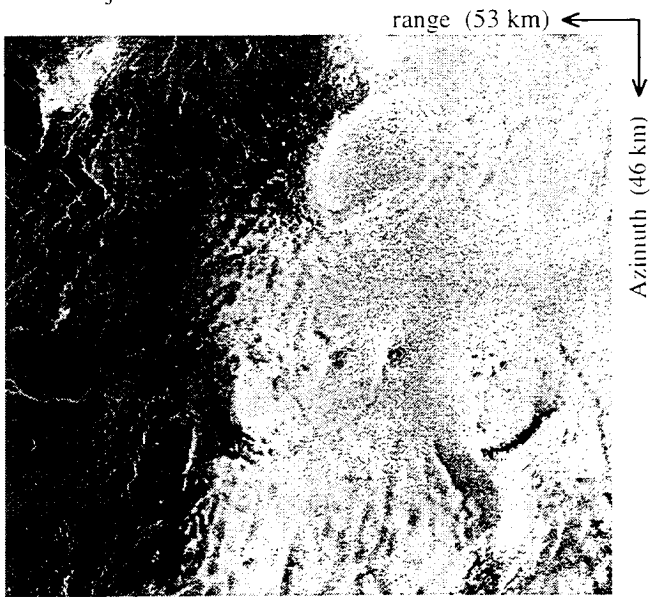

Fig. 2 ERS-1 SAR amplitude image of Vatnajökull from Dec. 30, 1995

Fig. 2 shows the amplitude image of ERS-1 SAR obtained from Dec. 30, 1995 and Fig. 3 shows the phase of the interferogram obtained from the ERS tandem pair of Dec. 30/31, 1995, where the 2π elevation is about 68m. The corresponding coherence image is given in Fig. 4. By comparing the interferogram of Fig. 3 with the topographic map in Fig. 1, we find that they have a good agreement at the three control points: the top of the Tongnafellsjökull (1540 m), the top of the Barðarbungar (2000 m) and the bottom of Grimsvotn (1400 m). The number of fringes between Barðarbungar and Grimsvotn is 8, which corresponds to 550 m elevation difference. In the map, this elevation difference is 600 m. On the other hand, the number of fringes between Barðarbungar and Tongnafellsjökull is 7.5, which corresponds to about 500 m relative elevation. This has also a rough agreement with the elevation difference in the map. Therefore the DEM represented by the interferogram in Fig. 3 can be accepted, except for some areas with great surface changes.

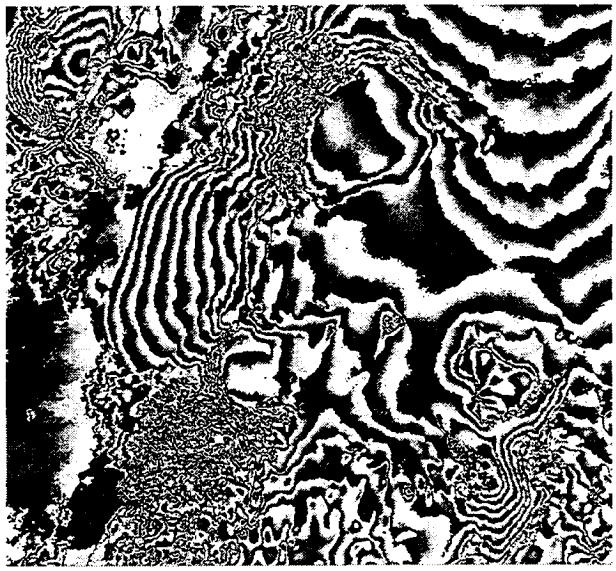

Fig. 3 ERS-1/ERS-2 tandem INSAR phase image of Vatnajökull from Dec. 30/31, 1995 with 2π elevation of 68 m.

These areas include area 1 (refer to Fig. 4) in the west of Hamarinn, where the coherence is low and the fringes are dense and area 2 (Fig. 4) between Barðarbungar and Grimsvotn, which is enlarged in Fig. 5, where the center should be lower than the surroundings for more than 700 m (more than 10 fringes). From the map in Fig. 1, we know this is not correct. Most of the fringes can only be the result of surface changes (about 30 cm surface increase). This suggests that some kind of small seismic activities must have happened between the two SAR data acquisitions on Oct. 21 and 22, 1996. Unfortunately, we have no information about the seismic activities, if any, near Grimsvotn at end of Dec. 1995 to confirm the suggestion.

Fig. 6 gives the 3D perspective view of the eruption area, produced with the INSAR-DEM of Dec. 30/31, 1995.

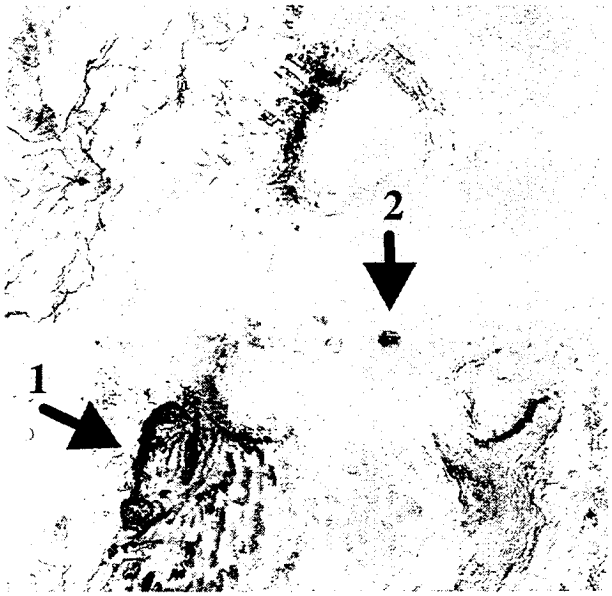

Fig. 4 ERS-1/ERS-2 tandem INSAR coherence image of Vatnajökull obtained from Dec. 30/31, 1995

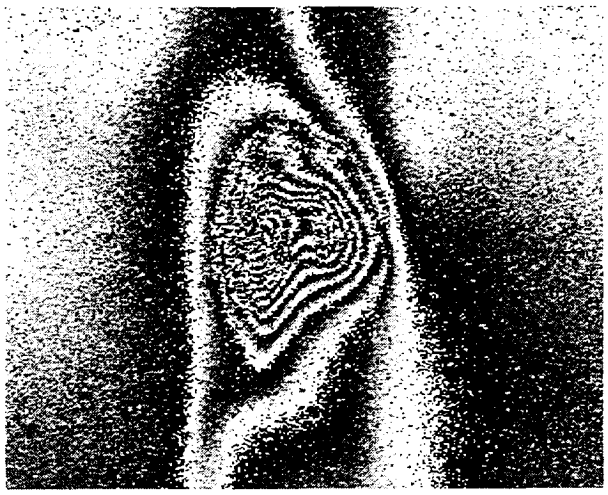

Fig. 5 Surface changes of subregion 2 between Dec. 30 and 31, 1995. One fringe corresponds to 3 cm elevation change.

Fig. 6 3D elevation model obtained from the interferogram phase of Dec. 30 and 31, 1995.

4. SURFACE CHANGES OBSERVED BY INSAR

The amplitude image of ERS-1 SAR acquired on Oct. 21, 1996, three weeks after the volcanic eruption, is shown in Fig. 7. The most significant difference between the ERS SAR images before (Fig. 2) and after (Fig. 7) the eruption is the new 6 ~ 8 km long eruption fissure between Barðarbungar and Grimsvotn. The other changes can not be clearly and quantitatively determined from these two amplitude images.

Fig. 7 ERS-1 SAR amplitude image of Vatnajökull from Oct. 21, 1996

But with the help of the coherence image (Fig. 8), obtained from the ERS tandem data of Oct. 21/22, 1996, we can get more information about the effects resulting from the volcanic activities. A pear-formed area around the fissure shows very poor coherence. Just below the area around the Grimsvotn Lake, there is a narrow handle-shaped area with low coherence. The other three low coherence areas around the fissure are a small circle area at the west of the fissure, a small area at the margin of Barðarbungar and north of the fissure and a large area in the east of Barðarbungar. These low coherence areas must have suffered surface changes. The amount of the surface changes can be determined from the interferogram in Fig. 9 and the DEM in Fig. 6.

In order to measure the surface changes between Oct. 21 and 22, 1996 due to the volcanic activities according to the interferogramm in Fig. 9, the DEM of this area has to be removed. Fig. 10 shows the corrected interferogram phase, which is also geocoded in UTM. In Fig. 10 each fringe represents 2.8 cm surface change in slant range. Because the horizontal movement of the ice surface is very small, the surface changes result mainly from the elevation changes. In this case, one fringe represents about 3 cm elevation change.

Fig. 8 ERS-1/ERS-2 tandem INSAR coherence image of Vatnajökull from Oct. 21/22, 1996.

Fig. 9 ERS-1/ERS-2 tandem INSAR phase image of Vatnajökull from Oct. 21/22, 1996 with 2π elevation of 70 m

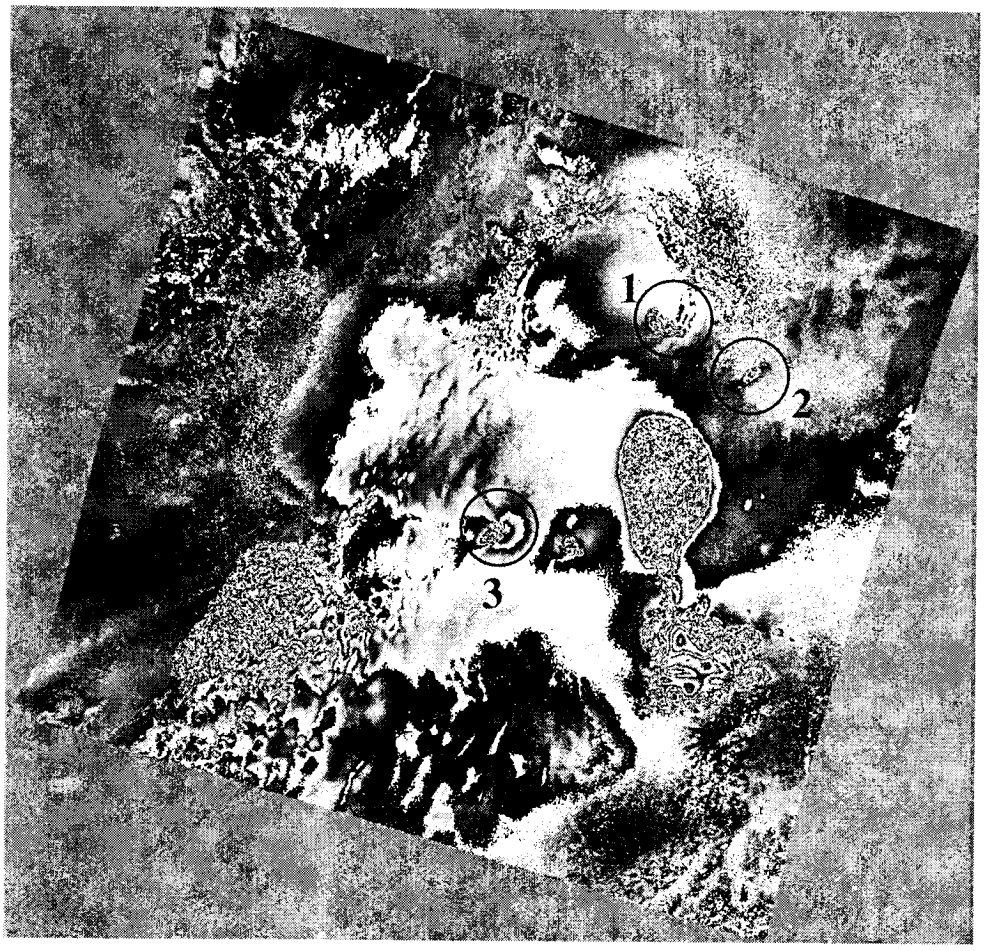

Fig. 10 Geocoded surface changes between Oct. 21 and 22, 1996. One fringe corresponds to 3 cm elevation change.

The largest surface changes happened around the eruption fissure and has a pear form. The changes within one day are so large that the coherence is lost and the fringes in the center of the area is not countable. Fig. 11 gives an enlarged version of the north part of the pear-formed region. About 20 fringes are clear to count. Therefore the center of the pear-formed region is at least 25 fringes lower than the surroundings, which corresponds to about 80 cm sinking within the 24 hours.

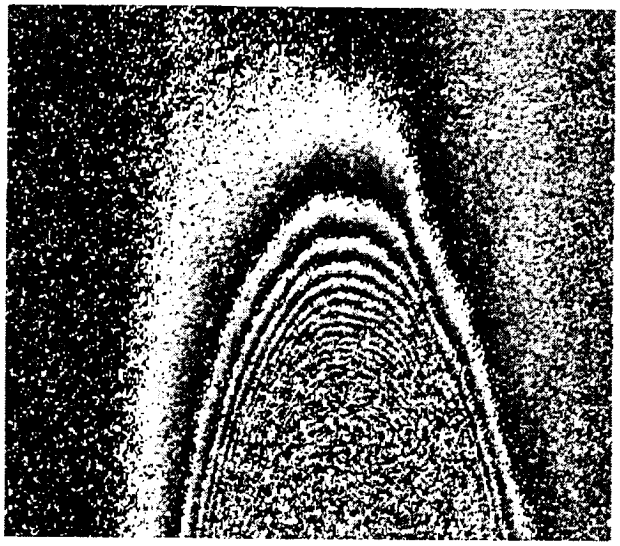

Fig. 11 Enlarged version of the surface sinking of the north part of the eruption region

The melt water flows into the Grimsvotn below, so that the ice cover of Grimsvotn is raised. The rising of the ice surface can be clearly seen in the Fig. 12a and Fig. 12b, which is the enlarged version of the north part of Fig. 12a. According to Fig. 12b, the up-right peak in Fig. 12a is 18 fringes higher than the surroundings, which corresponds to 54 cm surface increase. The highest point in Fig. 12 is the middle peak, which is 23 fringes higher than the surroundings, i.e., about 70 cm surface increase. The point with the least increase (27 cm increase or 9 fringes) is located near the bottom of Fig. 12a. Whereas the center of the Grimsvotn has about 40 cm surface increase (13 fringes higher). A measurement with a GPS from Oct. 21 to 25, 1996 shows about 2 meter surface increase, or an average surface increase of 50 cm per day [5], which is in good agreement with the results derived from the INSAR measurement. The unhomogeneous surface increase of the ice cover in Grimsvotn Lake reveals probably the unhomogeneity of the ice thickness, which however must be further confirmed.

The other three areas around the eruption fissure with great surface changes are enlarged and shown in Fig. 13, Fig. 14 and Fig. 15, respectively. The two small regions near Barðarbungar suffered a surface sinking of about 30 cm (10 fringes, Fig. 13), and 6 cm (2 fringes, Fig. 14), respectively, whereas the small region at the west of Grimsvotn Lake has a surface increase of at least 21 cm (7 fringes) at the center.

Fig. 12a Enlarged version of the surface increase of the ice cover on the Grimsvotn Lake.

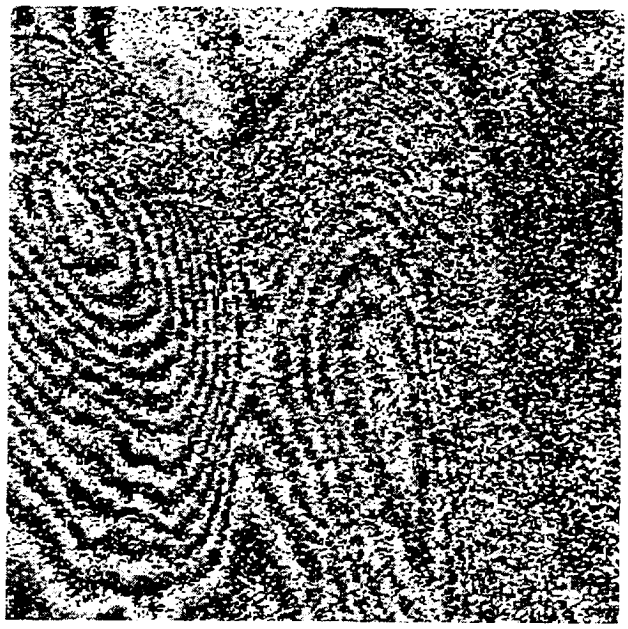

Fig. 12b Enlarged version of the north part of Fig. 12a.

Another large area with only small surface changes is located at the northeast corner of Fig. 10. The location of the area can be also clearly identified in Fig. 8. The surface increase of the large area is, however, small, only about 1 cm (1/3 fringe). The reason, why the surface of this area is increased, must be studied further.

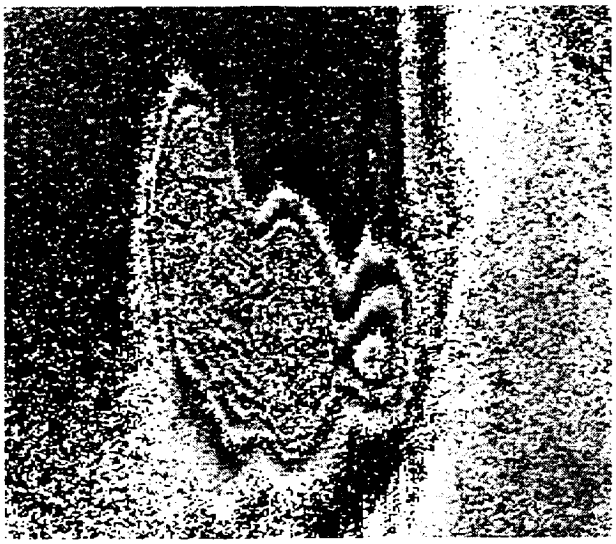

Fig. 13 Enlarged version of the surface sinking of the subregion 1 in Fig. 10.

Fig. 14 Enlarged version of the surface sinking of the subregion 2 in Fig. 10.

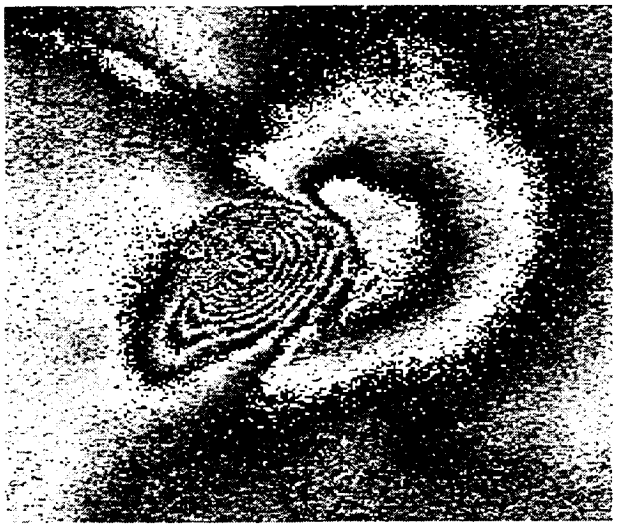

Fig. 15 Enlarged version of the surface increase of the subregion 3 in Fig. 10.

5. CONCLUSIONS

ERS-1/ERS-2 tandem data with only one day time span allow to observe and measure accurately the ice surface changes of large areas resulting from volcanic activities. The INSAR technique enables us to observe all the possible surface changes in volcanic or other endangered areas in larger time scale, if continuous data acquisitions are available. With the December 1995 acquisitions, a surface change could be detected, which might have been a first indicator of the volcanic activities 9 months later.

The INSAR measurement will be valuable information sources to monitor, assess and even predict the effects of volcanic activities. It can not be replaced by other techniques such as optical imaging and GPS measurement. It will become one of the most useful remote sensing tools for monitoring the natural phenomena.

6. ACKNOWLEDGMENTS

This work was supported by German Ministry of Science and Research (BMBF) and DARA project „DYPAG" (FKZ:03PL016A4) and also by European Space Agency, which provided all the ERS SAR data used.

7. REFERENCES

[1] Wu, X., Thiel, K.H., Wehr, A.: The effect of different land covers on the accuracy of interferometric DEM, Workshop on ERS SAR Interferometry, Zürich, Switzerland, Sept. , 1996.

[2] Massonnet, D., et al.: The displacement field of the Landers earthquake mapped by radar interferometry, Nature, vol. 364, pp. 138-142, July 1993.

[3] Hartl, Ph., Thiel, K.H., Wu, X., "Information extraction from ERS-1 SAR data by means of INSAR and D-INSAR techniques in Antarctic research", second ERS-1 symposium, Hamburg, Germany, pp. 697-702, Oct. 1993.

[4] Goldstein,R.M., Engelhardt, H., Kamb, B., Frolich, R.M., "Satellite Radar Interferometry for Monitoring Ice Sheet Motion: Application to an Antarctic Ice Stream", Science, Vol. 262, pp. 1525-1530, Dec. 1993.

[5] Villi Knudsen, "The Volcano Show: glacier eruption filming diary", http://www.centrum.is/cgi-bin/vol-news.cgi, Nov. 1996.

VOLCANO MONITORING USING DATA FROM THE ERS ALONG TRACK SCANNING RADIOMETER

Martin J. Wooster and David A. Rothery

Department of Earth Sciences, The Open University, Milton Keynes, MK7 6AA, U.K.
phone: + 44 1908 653012, fax: +44 1908 655151 email: m.j.wooster@open.ac.uk, d.a.rothery@open.ac.uk

ABSTRACT

We demonstrate the use of time-series shortwave (1.6 μm) and longwave (11 μm) infrared spectral radiance data from the ERS Along Track Scanning Radiometer (ATSR) in identifying active lava domes and lava flows and for monitoring changes in the thermal output of these volcanic features. At Lascar Volcano (Chile) and Unzen Volcano (Japan), variations in lava dome radiative output are shown to be indicative of physical changes that have importance for the prediction of explosive eruptions and/or pyroclastic flow generation. At Fernandina Volcano (Galápagos Islands), gross characteristics and physical properties of the largely unmonitored 1995 lava flow are determined from ATSR spectral radiance data, allowing the lava flow volume to be determined from the estimated total energy losses. Results agree with post-eruption field survey data and analysis of high-spatial resolution SPOT imagery. Though it is of a relatively low spatial resolution, data from ATSR is shown to be of use for the monitoring of a variety of effusive volcanic phenomena. It is likely that data from ATSR, AATSR and EOS MODIS could be used to supplement existing geophysical techniques at many of the worlds poorly monitored volcanoes.

1. INTRODUCTION

The Earth is a volcanologically very active planet, with around 60 eruptions occurring every year from a total of over 1500 potentially active volcanoes [Ref. 1]. A multitude of geophysical techniques has been developed to assist volcanological science and to provide means of monitoring activity with a view to eventual eruption prediction [Ref. 2]. However lack of funding and political will mean that these techniques are often inadequately applied, even to volcanoes that pose a significant threat to local population and infrastructure [Ref. 3]. In addition, remote volcanoes that pose no direct threat to human life remain largely unmonitored using traditional techniques, though their activity may be of scientific interest and they may pose a risk to aircraft traffic if explosive eruptions are of sufficient magnitude.

Satellite remote sensing is capable of providing repetitive data on all potentially active terrestrial volcanoes, with ERS interferometric SAR data already being used to map volcano surface deformation that is the result of large-scale magma movement [Ref. 4]. This paper concentrates on the thermal monitoring of effusive volcanic activity using infrared radiance data from the ERS Along Track Scanning Radiometer (ATSR). High spatial resolution commercial datasets, such as those from the Landsat Thematic Mapper (TM), have already been shown to be of use in this regard [e.g. Ref. 5] but the infrequent repeat cycle and high data cost hinders their routine use. If ATSR's low spatial resolution (~ 1 km²) radiance measurements can be shown to be of similar value, the frequent, low-cost data could potentially provide a useful supplement to established geophysical monitoring techniques.

2. BACKGROUND

2.1 The thermal structure of active lava bodies

Lava flows and domes are both products of magma being exuded out of an active volcanic vent. The viscosity of the magma generally controls whether the lava flows in a fluid-like manner or whether it piles up around the vent, forming a lava dome. Highly viscous, dome-forming magma generally contains a high proportion of dissolved volatiles, which leads to an increased likelihood of explosive activity. Such explosive eruptions are often associated with the formation of vertical eruption columns and extremely hazardous, fast-moving pyroclastic flows of pumice, ash and hot volcanic

Proc. 3rd ERS Symp. on Space at the service of our Environment, *Florence, Italy, 17–21 March 1997* (ESA SP-414, 3 Vols., May 1997)

gas, the most dangerous form of eruptive activity. In contrast, a lava flow moves relatively slowly and often poses no direct threat to human life, though it may do enormous infrastructure damage.

Whilst the chemical composition of lava flows and domes may differ, their thermal structures are relatively similar. The internal core temperature of both are close to magmatic (~ 1000 °C), whilst the upper surface of lava crust is generally much cooler (~ 70 - 400 °C), having lost heat by radiative cooling [Ref. 6]. The crustal layer is an efficient insulator and effectively retards heat loss from the inner core, allowing near-magmatic temperatures to be maintained for a long duration. However, the continual movement of a lava flow generally causes cracks and fissures to appear in the crustal surface, which exposes the interior and allows radiative cooling from the high temperature core to continue. Lava domes are more static than lava flows, with the formation of cracks related to the cooling and contraction of the dome structure. These cracks act as fumarolic vents for the degassing of the magma held below the dome, with neighbouring dome surfaces heated by the escaping gas, often to temperatures approaching those of the dome interior [Ref. 7].

With respect to surface temperature structure, both lava flows and domes can thus be considered as relatively low temperature, broad-area surfaces, interspersed with smaller high temperature regions.

2.1 Radiance observations at 1.6 and 11 μm

ATSR makes measurements of thermal infrared radiance at 3.7 μm, 11 μm and 12 μm, primarily for conversion into accurate estimates of sea surface temperature. Daytime cloud detection is enhanced by the use of pseudo-reflectance data from the 1.6 μm shortwave infrared (SWIR) waveband, which is allied to an onboard calibration system on ATSR-2 and has had a post-launch calibration applied on ATSR-1 [Ref. 8].

Night-time SWIR data is also useful for thermal investigations of high-temperature surfaces (> 400 °C) since, as Fig. 1 indicates, these emit significant amounts of infrared radiance at 1.6 μm. Furthermore, the highly non-linear relationship between surface temperature and 1.6 μm spectral radiance indicates that SWIR radiance measurements made at volcanologically active locations are likely to be dominated by radiance from surfaces at or near magmatic temperatures, even if these cover a very small fraction of the sensor field-of-view (FOV). The 3.7 μm waveband is similarly sensitive to high temperature surfaces but the instrument gain settings make it susceptable to detector saturation, making this channel unsuitable for quantitative radiance measurements over hot features.

In contrast to the shorter wavelengths, the near-linear relationship between surface temperature and 11 μm spectral radiance indicates that signals in this waveband are dominated by surfaces covering large areas of the sensor FOV. Additionally 11 μm data of active lava bodies will be largely insensitive to changes in the highest temperature surfaces since they will generally cover only a very small fraction of the FOV.

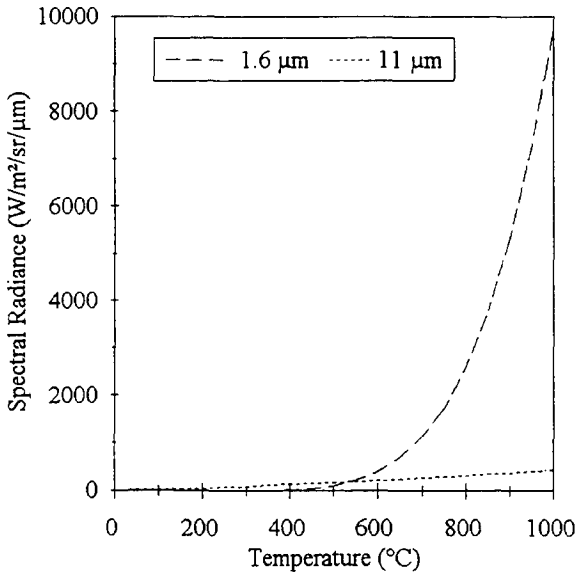

Figure 1. The 1.6 μm and 11 μm spectral radiance vs. temperature relationships for the potential range of geothermal surface temperatures.

3. LAVA DOMES

3.1 Lascar Volcano, Chile (22.37 °S, 67.73 °W)

Lascar is a highly active but largely unmonitored volcano in the central Andes. Lascar is known to possess an active lava dome (diameter ~ 150 - 400 m) whose subsidence is believed to impede degassing and so lead to pressure build-up and

thus explosive activity [Ref. 9]. Most eruptions are reasonably small but large events do occur, the most notable being that of 18-20 April 1993 which produced a 7.5 km long pyroclastic flaw and an eruption column 24 km in altitude that rained ash 1500 km downwind. Using high spatial resolution data from the Landsat Thematic Mapper (TM), Ref. 9 indicates that certain Lascar eruptions are preceded by a significant decrease in thermally emitted 1.6 μm spectral radiance, modelled as a cooling of the domes fumarolically heated surfaces as gas flux decreases. To determine whether low-spatial resolution data could provide a similar monitoring capability, 125 ATSR-1 and ATSR-2 ascending node (night-time) scenes covering Lascar between 1992 and 1995 were selected and subjected to cloud screening tests designed to eliminate data affected by gross and sub-pixel clouds [Ref. 10]. The nadir-view 1.6 μm signal at Lascar's location was then extracted, there being no 3.7 μm data for the majority of the time-series due to the failure of the ATSR-1 3.7 μm channel in May 1992.

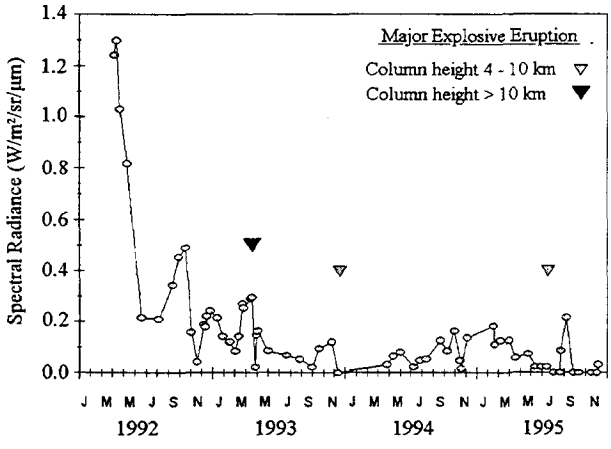

Figure 2. The time-series of ATSR 1.6 μm spectral radiance measurements made at Lascar Volcano. Though ash clouds may have been present during certain of the measurements the closely spaced nature of the time series allows overall trends in emitted radiance to be determined.

The cloud-cleared 1.6 μm dataset is plotted as Fig. 2, and shows a rapid April-June 1992 decrease in SWIR spectral radiance, this change exactly paralleling that found using TM SWIR data and agreeing with *in situ* observations of May and November 1992 which noted a growing and subsequently collapsed lava dome [Refs. 7, 9]. We suggest that the magnitude of the April 1993 eruption, the largest in Lascar's recorded history, may have been related to the long (10 month) duration between the apparent collapse of the dome and the subsequent vulcanian explosive eruption, which may have allowed pressure inside the volcano to reach uncharacteristically high levels. The dome collapse is evident from the ATSR data six months before it was noticed during the November 1992 summit visit. After the April 1993 eruption, the shortwave infrared radiance is seen to fall to zero, indicating that the dome was destroyed in the eruption. A subsequent aircraft overflight indicted the rapid re-growth of a new lava dome, which is also evidenced by the return of a 1.6 μm signal in late April 1993.

After April 1993 there are two further significant periods of signal rise and fall, October-November 1993 and April 1994-May 1995. We attribute both these periods to dome growth/collapse events or to other phenomena that caused variations in magmatic degassing. As predicted by the Lascar model [Ref. 10], both cycles were followed by large explosive eruptions, with columns extending between 4 and 10 km height. A final signal rise in August 1995 is interpreted at the arrival of a new lava body, or an increase in magmatic gas flux increasing the temperature of crater surfaces.

3.2 Unzen Volcano, Japan (32.77 °N, 130.28 °E)

Unzen Volcano is situated in a densely populated region of Kyushu, the southern-most of the four principal islands of Japan. A new lava dome began to grow at the volcano summit in May 1991 and rock-fall collapses from this growing dome generated more than 10,000 pyroclastic flows over the following four years, these being most frequent when lava effusion rates were high [Ref. 11]. Periods of most intense flow necessitated the evacuation of 12,000 local inhabitants. Because of the strong relationship between lava dome growth rate and the frequency of pyroclastic flow, the lava effusion rate was monitored throughout the eruption using trigonometric and photogrammetric data of the summit [Ref. 11]. These data provide a quantitative comparison for the 1.6 μm time-series of Unzen, produced from 159 cloud-screened ATSR scenes of the volcano and shown alongside the effusion rate dataset in Fig. 3.

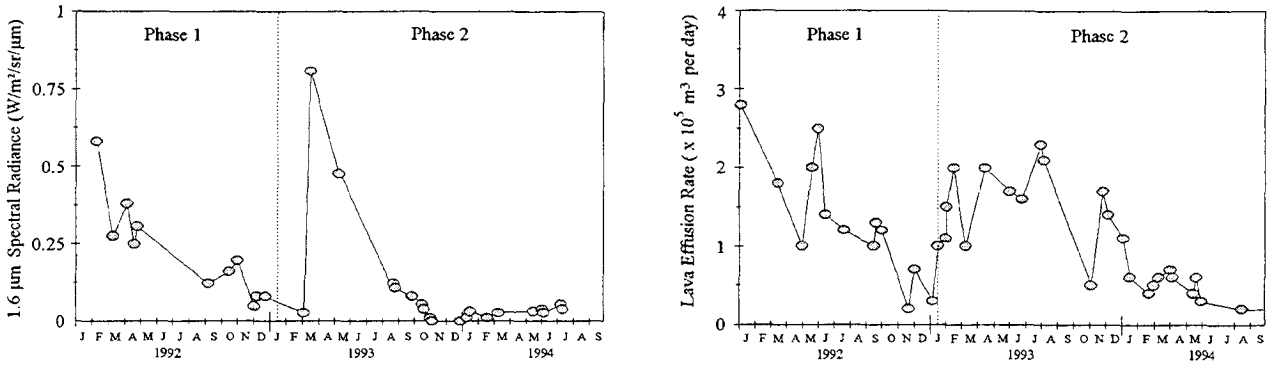

(a) (b)

Figure 3. (a) The 1.6 μm spectral radiance data of Unzen Volcano , (b) the lava effusion rate, with estimated error ± (0.3 x 10^5 to 1.0 x 10^5) m^3/day.

During the Unzen activity, two phases of magma supply were identified from the lava effusion rate data. The monotonic fall in effusion rate during phase 1 is paralleled by a near-linear decrease in 1.6 μm spectral radiance over the same period, with an r^2 value of 0.8 between these two datasets. The onset of phase 2 of magma supply is also correctly identified by a sharp rise in the SWIR spectral radiance, though the peak is considerably narrower than that evidenced in the effusion rate data. Studies of TM data and airborne thermal imagery have identified the dominant source of shortwave infrared spectral radiance as areas of the Unzen dome that were heated by the release of fumarolic gas (temperature ~ 800 °C) [Ref. 12]. During phase 1 the rate of gas release was observed to be in direct proportion to the effusion rate of lava, thus explaining the positive and significant relationship between effusion rate and SWIR spectral radiance of phase 1. However, the degassing rate was noted to be significantly more variable during phase 2 [Ref. 12] and we believe this variability caused weakening of the phase 2 effusion rate - SWIR radiance relationship.

3. LAVA FLOWS

3.1 Isla Fernandina, Galápagos (0.37 °S, 9.53 °W)

The island of Fernandina is a single shield volcano in the Galápagos archipelago. Fernandina's frequent eruptions are of great volcanological interest but the remote and uninhabited nature of the island has prevented detailed studies of previous eruptions in-progress. The most recent Fernandina eruption occurred in January - April 1995 and was first spotted from a fishing vessel. Fig. 4 shows the first cloud-free ATSR 11 μm data of the 1995 activity at Fernandina, which was later reported to have lasted for around three months duration.

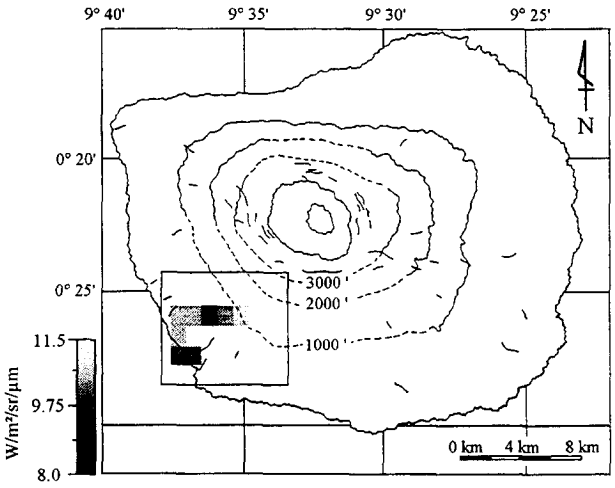

Figure 4. The 11 μm data recorded on 8 February 1995. The data are masked to show thermally anomalous (lava flow-field) pixels only and have a map of previous eruptive fissures superimposed.

Using techniques described in Ref. 13, values of 1.6 μm and 11 μm thermally anomalous spectral radiance [Fig. 5] were extracted from eight cloud-free ATSR scenes of the eruption and were respectively converted into areal estimates of exposed core and cooling crust.

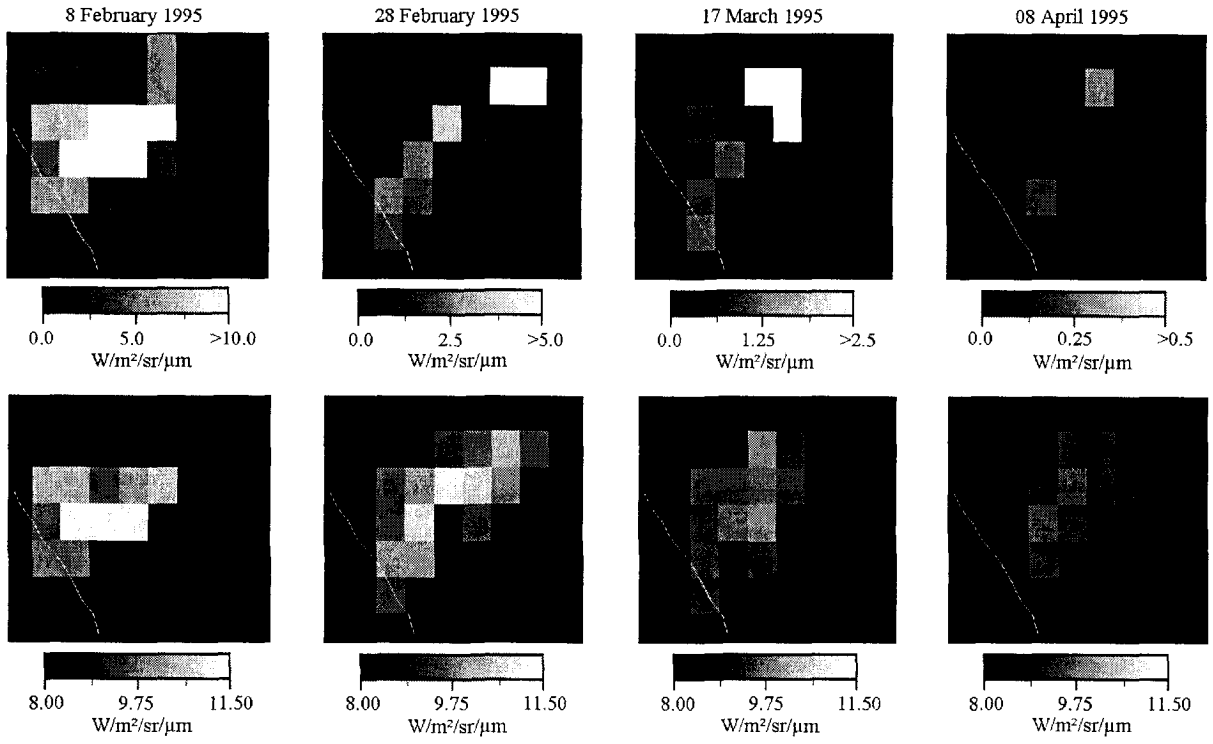

Figure 5. 1.6 µm (upper row) and 11 µm (lower row) data from four of the eight available scenes of the 1995 Fernandina eruption. The data are masked to show lava flow-field pixels only and the geographical area covered is that box outlined in Fig. 4. Large changes in the 1.6 µm signal reflect the rapid formation of sub-surface lava tubes whilst the more slowly varying 11 µm signal reflects cooling of the surface crust.

The indeterminacy of the solutions was addressed by performing the calculations for a realistic range of surface temperatures, allowing maximum and minimum areal estimates to be determined. An adaptation of the Stefan-Boltzmann equation was then used to calculate the radiative power losses, with estimates of the convective loss provided by numerical models. Addtion of these heat losses allowed the total power losses from the upper flow surface to be determined [Fig. 6].

Integration of the upper surface power loss over the period of the eruption, coupled with model-based estimates of conductive energy losses, confirmed the total energy lost from the lava as 5 x 10^{16} - 9 x 10^{16} J. Equating this to the total energy supplied by complete cooling and solidifying of the lava allowed the volume of erupted magma to be estimated as 10 - 20 million m^3. This agrees with estimates produced from high spatial resolution SPOT imagery combined with DEM data [Ref. 14] and is within the range observed for previous Fernandina lava flows.

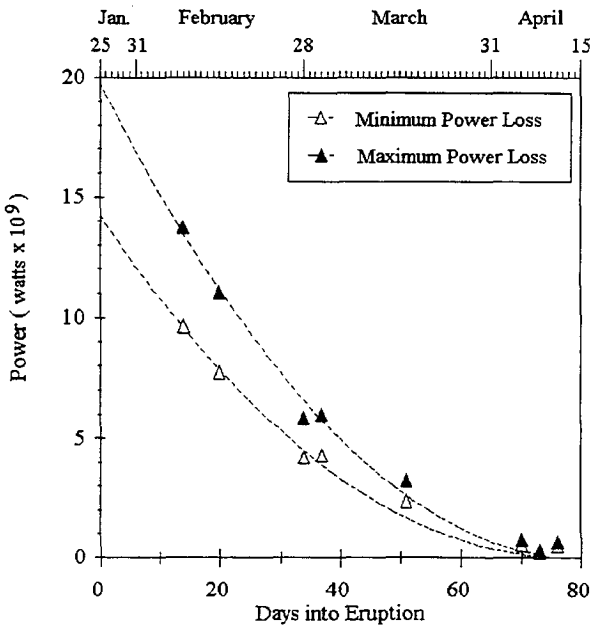

Figure 6. The minimum and maximum estimates of total power loss from the upper flow surface, with best-fit polynomials fitted to the data.

4. CONCLUSIONS

These studies lead us to the conclusion that low-spatial resolution infrared spectral radiance data can be used to observe the thermal emittance from sub-pixel sized active lava bodies such as lava domes and lava flows. As such, ATSR and similar satellite-based instruments offer a means of monitoring effusive volcanic activity on a regular, danger-free, low cost basis and can be used to provide evidence of changes in activity which, at certain types of volcanoes, may then be related to the possibility of forthcoming eruptions and pyroclastic flow. At certain other volcanoes analyses of such data can also provide a means to estimate the characteristics of remote lava flows, which may remain uninvestigated using traditional techniques. Infrared spectral radiance data will in future be readily available, both from ENVISAT's Advanced ATSR and from the MODIS instrument onboard NASA's EOS satellites. It is likely that use of such data can positively contribute to the scientific and monitoring studies carried out at a wide range of volcanological locations.

5. ACKNOWLEDGEMENTS

This work is supported by research studentship GT12/94/ATSR2/37 from NERC and the Natural Resources Institute, University of Greenwich (UK). Rothery and Wooster are investigators on ESA ERS project UK-101 and are indebted to staff of the RAL ATSR project for their invaluable support. ATSR data are courtesy of ESA/RAL/BNSC/NERC.

6. REFERENCES

Simkin, T. and Siebert, L. 1994, *Volcanoes of the World*, Geoscience Press (Tuscon)

McGuire, W., Kilburn, C. and Murray, J. 1995, *Monitoring Active Volcanoes: Strategies, Procedures and Techniques*, UCL Press (London)

Tilling, R. I. 1989, Volcanic hazards and their mitigation: progress and problems, *Rev. Geophys*, 27, 237-269

Massonnet, D., Briole, P. and Arnaud, A. 1995, Deflation of Mount Etna monitored by spaceborne radar interferometry, *Nature*, 375, 567-570.

Rothery, D. A. and Pieri, D. C. 1993, Remote sensing of active lava (Chap. 8), in *Active Lavas* (C. R. J. Kilburn and G. Luongo, Ed.), UCL Press (London)

Fink, J. H., 1990, *Lava Flows and Domes, Emplacement Mechanisms and Hazard Implications*, Springer-Verlag (Berlin)

Oppenheimer, C., Francis, P. W. Rothery D. A. and Carlton, R. W. T. 1993, Infrared image analysis of volcanic thermal features: Lascar Volcano, Chile 1984-1992, *J. Geophys. Res.*, 98, 4269-4286

Wooster, M. J. 1996, In Orbit Calibration of the ATSR-1 1.6 μm Channel Using High Resolution Data from the JERS-1 (Fuyo-1) Optical Sensor, *Int. J. of Remote Sens.*, 17, 1069-1074

Matthews, S. J., Gardeweg, M. C. and Sparks, R. S. J. 1997, Crater collapse and explosive eruptions as a result of magma degassing; the 1984 to 1996 cyclic activity of Lascar Volcano, Northern Chile. *Bull. Volcanol.*, in press

Wooster, M. J. and Rothery, D. A. 1997, Thermal monitoring of Lascar Volcano, Chile using infrared data from the Along Track Scanning Radiometer: a 1992-1995 time-series, *Bull. Volcanol.*, in press

Sato, H., Fujii, T. and Nakada, S. 1992, Crumbling of dacite dome lava and generation of pyroclastic flows at Unzen Volcano, *Nature,* 360, 664-666

Wooster, M. J. and Kaneko, T. 1997, Time-series analysis of lava dome development at Unzen Volcano, Japan using low spatial resolution infrared radiance data from the ERS-1 ATSR, *J. Geophys. Res.*, submitted

Wooster, M. J. and Rothery, D. A. 1997, Time-series analysis of effusive volcanic activity using the Along Track Scanning Radiometer : the 1995 eruption of Fernandina Volcano, Galápagos Islands, *Remote Sens. Environ.*, in press

Rowland, S. K. 1996, Slopes, lava flow volumes and vent distributions on Volcán Fernandina, Galapagos Islands, *J. Geophys. Res.*, 101, 27657-27672

INTERFEROMETRIC PHASE ANALYSIS FOR MONITORING SLOW DEFORMATION PROCESSES

Ramon Hanssen and Stefania Usai

Delft Institute for Earth Oriented Space Research (DEOS)
Delft University of Technology, P.O. Box 5030, 2600 GA, Delft, the Netherlands.
phone: +31 15 2782565, fax: +31 15 2783711

E-mail: hanssen@geo.tudelft.nl

Abstract— **SAR interferometry has proven to be a feasible tool for detecting ground deformations caused by earthquakes or volcano activity. However, the application of the technique for deformation processes which take place on a longer time scale remains difficult for a number of reasons. Limiting factors for monitoring slow deformation processes are mainly temporal decorrelation and atmospheric delay differences within a SAR scene. Especially areas with agricultural activity lose coherence typically within an interval of days, which is too short to unravel the slow deformation rates. The systematical analysis of series of interferograms seems to be the only possibility for extracting feasible subsidence rates from SAR interferometry. In this paper we will give an overview of the possible error sources and propose a method for the analysis of severely decorrelated phase interferograms.**

I. Introduction

The feasibility of differential SAR interferometry for detecting and quantifying deformation is limited by the characteristics of the deformation and the terrain, the time interval between the two or more SAR acquisitions, and a number of additional phase effects, whether or not coherence preserving.

The characteristics of the deformation can be expressed as the size of the displacement in slant range versus the width of the phenomenon. The size of the displacement is limited by the phase noise and the slope/pixel size ratio which should not exceed aliasing criteria. The detectability of a phenomenon with these parameters is dependent on wavelength, pixel posting, image size, and time. However, this relationship is complicated due to the influence of the time interval between the two consecutive SAR acquisitions. For large areas in the world coherence decreases significantly if the epoch between the acquisitions exceeds more than a couple of days. What remains in the interferogram are isolated patches of coherent information which do contain information but can be ambiguous to interpret. The decrease in coherence is referred to as temporal decorrelation. Moreover, the phase interpretation of such an interferogram suffers from additional coherence preserving phase effects, like the influence of the atmosphere and signal penetration differences in the imagery. These cause a coherent bias in the phase measurement. Naturally, additional coherent phase effects can be caused by the interferometric processing, where e.g. orbit inaccuracies and inconsistencies in the applied Digital Elevation Model (DEM) can cause phase variations in the image. In the present work, we will try to give an overview on the different phase effects and study the effects of propagation heterogeneities, penetration change and temporal decorrelation for slow subsidence studies using SAR interferometry. Approaches are being proposed to use preferably all SAR imagery of a study area to subsequently detect coherent phase errors, identify them, and correct for them.

II. The interferometric phase

The phase observation in a SAR image contains the superposition of a number of effects. If we concentrate on the effects which are independent of the SAR and INSAR processing, the first and most important influence is the geometric distance between the antenna and a resolution element at the earths surface. The signal propagation is a second effect that influences the phase: a delay or acceleration of the velocity of the signal yields a bias in the phase observation. A third effect is the reflection depth and the interaction with the surface. The radar signal, dependent on the wavelength and intensity, does not reflect at the geometrical boundary between the soil and the atmosphere, it penetrates the soil to some extent and is influenced by the dielectric characteristics of it. Apart from phase biases due to geometry, propagation and penetration, a fourth influence on the phase of a SAR resolution cell is the arbitrary superposition of single scatterers within the resolution cell. In equation (1) this summation is given for resolution element p and acquisition i (with $i = \{1, 2\}$).

$$\phi_{p,i} = \phi_{geom,i} + \phi_{prop,i} + \phi_{penetr,i} + \phi_{scat,i} \quad (1)$$

$$\Delta\phi_p = \phi_{p,2} - \phi_{p,1} \quad (2)$$

In the interferometric phase image, the interferogram, the phase observations of acquisition 1 and 2, for a specific resolution element are subtracted from each other, as in equation (2). The geometrical difference between both signals conveys information on (relative) height, deformation, orbit aberrations and the choice of the reference surface. For a single resolution element this information is hard to interpret, and especially the relation between adjacent pixels reflects the above mentioned information. Due to this relative character, the absolute propagation delay caused by the atmosphere is not relevant for SAR interferometry. However, propagation delay heterogeneities within the interferogram scene can easily produce phase differences which are hard to discern from e.g. geometrical phase differences due to topography or deformations. For penetration effects the same line of reasoning holds. As long as the

Proc. 3rd ERS Symp. on Space at the service of our Environment, *Florence, Italy, 17–21 March 1997* (ESA SP-414, 3 Vols., May 1997)

penetration differences in the first SAR image are equal to those in the second one, the effect is cancelled out. Local penetration change in time yields an interferometric phase effect. Finally, the effect of a temporal change of the scatterers in a resolution cell causes decorrelation, resulting in an increase in phase variance, which decreases the reliability of that particular interferometric phase.

III. Propagation heterogeneities

The effect of propagation differences in the interferometric phase is caused by the spatial and temporal variability in the refractive index in the atmosphere. The phase variations caused by this variability are independent from the interferometric configuration. However, if this interferometric phase is processed to a height estimate, the errors in height increase with the height ambiguity. Therefore large baselines can be used to suppress the influence of atmospheric heterogeneities on DEM generation. For deformation maps, the errors are independent of the baseline. Analysing the effects of the atmosphere on SAR interferometry, we can distinguish between the influence of ionosphere and troposphere. In the following we will discuss both propagation effects.

A. Ionospheric propagation

The SAR phase signal is accelerated if the number of free electrons in the ionosphere increases. To estimate the number of free electrons, the ionosphere is modelled as a single layer at a certain effective height. The electron density is now translated to the Total Electron Content (TEC) at this effective height. To achieve reasonable units, one TECU (TEC Unit) is equal to 10^{16} electrons/m^2. The total range of electron activity varies between 0 and approximately 30 TECU, dependent on solar activity, time of day, latitude, and geomagnetic activity.

The ionospheric range error for a two-way SAR signal can be determined in first approximation using the following equation

$$\Delta R = \frac{2K}{f_{SAR}^2}\mathrm{TEC}\cdot\left(1-\left(\frac{r_e\sin\theta}{r_e+h_{sp}}\right)^2\right)^{-\frac{1}{2}} \qquad (3)$$

In this equation, $K = 40.28$ is an empirically determined constant, f_{SAR} is the specific SAR frequency, and the right multiplication factor is the mapping function, which maps the zenith delay to the SAR incidence angle θ, using the earth radius r_e and the height of the single layer h_{sp}. For TECU values between 0 and 30, the range error for a C-band SAR is between 0 and 0.97 meter. As a rule of thumb for repeat pass interferometry, we can therefore say that 1 TECU difference within a SAR image yields approximately one fringe in the interferogram. Note that if the difference in TEC units is equal in both SAR images, both effects are cancelled out in the interferogram.

In figure 1 it is shown how the TEC units vary for a specific time of day. These values are determined using the network of the International GPS Service for Geodynamics (IGS), and are mainly tidal effects (Jungstand 1997)(Williams 1996).

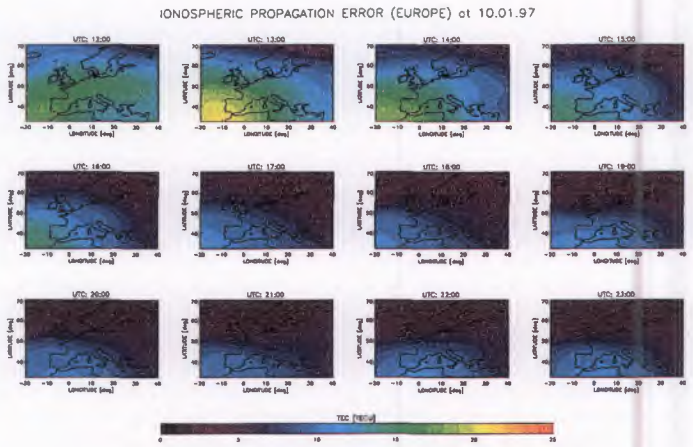

Fig. 1. Example of a hourly map of the Total Electron Content over Europe (Jungstand 1997)

Since the long wavelength features are only causing a small ramp in the interferogram, this ionospheric effect will be hard to recognise and can easily be misinterpreted as an orbit error. Especially if the SAR acquisitions are acquired at the same time of day, it is expected that the effects cancel each other in the interferogram. Travelling Ionospheric Disturbances (TID's), however, are recognised at different spatial wavelengths: large, medium and small, respectively thousands, hundreds and tens of kilometers (Spoelstra 1996),(Williams 1996) and are mainly caused by auroral disturbances which propagate equatorward. Finally small scale ionospheric phenomena, also referred to as acoustic waves (Williams 1996), are characterised as irregularities in the ionosphere's E-region and F-region. Here, nighttime density fluctuations of 10–20% are observed for wavelengths of 30–300m, corresponding with a phase shift of 35–70 degrees. Therefore, ionospheric heterogeneities can be a disturbing influence for SAR interferograms.

B. Tropospheric propagation

The propagation velocity in the troposphere is determined by the refractive index, which is dependent of temperature, pressure and relative humidity. The incremental path length compared to the propagation in vacuum can be determined integrating these parameters over the total path length in the troposphere. The Smith-Weintraub approximation, which is accurate to about 0.5% yields (Smith, Jr. and Weintraub 1953):

$$\Delta\rho = 7.76\cdot10^{-5}\int_0^{top}\frac{P}{T}dx + 3.73\cdot10^{-1}\int_0^{top}\frac{e}{T^2}dx \qquad (4)$$

where P is the total pressure, T is the absolute temperature, and e is the partial pressure of water vapour, which is related to the relative humidity rh with

$$e = \frac{rh}{100}\exp\left(-37.2465 + 0.213166T - 0.000256908T^2\right). \qquad (5)$$

The first term in equation 4 is referred to as the hydrostatic term, which can be relatively well determined using

surface measurements. The evaluation of the second term, however, imposes severe problems due to the high spatial and temporal variability of the relative humidity, especially in the atmospheric boundary layer (the first 1.5 kilometers) and in cloud layers. Although in terms of absolute delay the hydrostatic term accounts for about 90% of the delay, the relative character of the SAR phase observations is mainly sensitive for the variations of the second, 'wet', term (Hanssen and Feijt 1996).

Since cloud cover can be an indication for variations in relative humidity, the interferometric effect of different types of cloud layers is shown in the figures 2, 3, and 4. Figure 2 represents a tandem interferogram of a relatively stable atmosphere with homogeneously distributed cloud cover for both acquisition dates. At the right side of the image, some diagonal internal or gravity waves are visible. In a current study, the atmospheric conditions within this epoch are additionally examined using a local GPS network. In figure 3, the effect of a frontal zone is visible as a diagonal feature in the interferogram. In Hanssen and Feijt (1996), these data were compared with additional surface and satellite meteorological data, which confirmed the hypothesis of a tropospheric change in humidity connected with a frontal zone. Finally, figure 4 shows the effect of convective cells on the interferometric phase. Up to two fringes phase difference are visible, which indicates the presence of convective phenomena with an associated change in humidity characteristics.

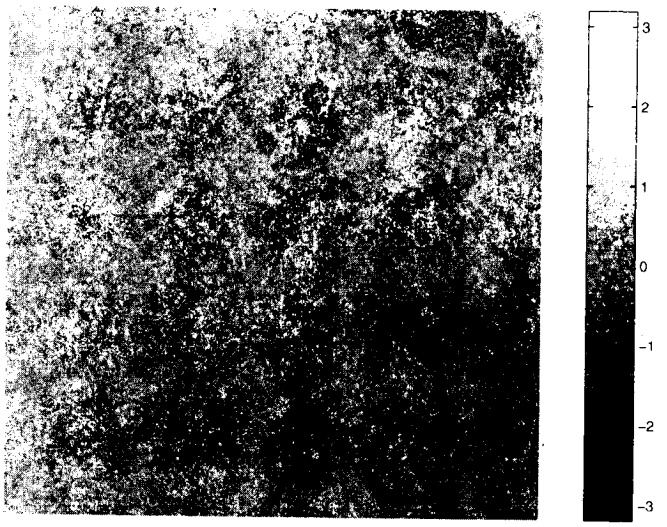

Fig. 2. The effect of internal gravity waves in a homogeneously cloudy troposphere on the interferometric phase

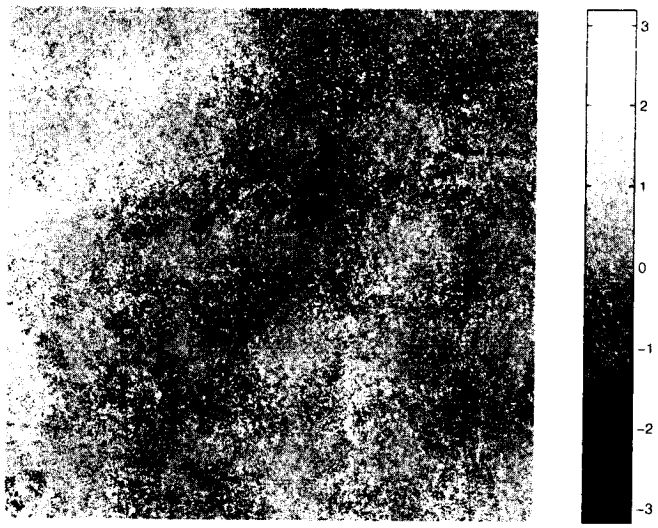

Fig. 3. The effect of a meteorological frontal zone on the interferometric phase

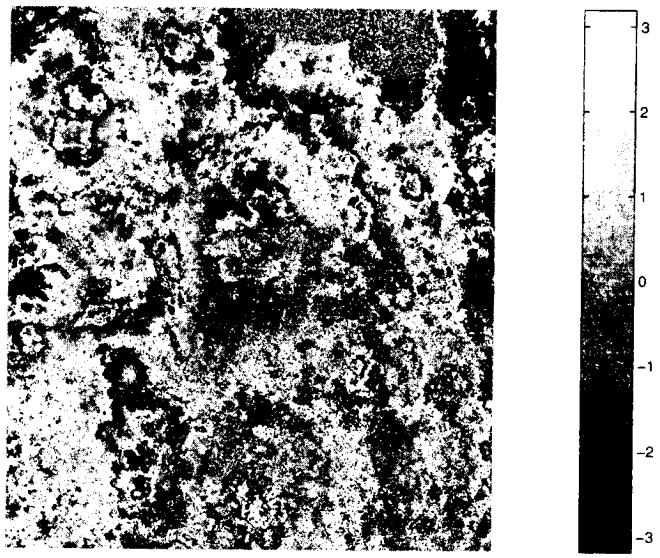

Fig. 4. The effect of convective cells on the interferometric phase

IV. Penetration differences

A coherent change in penetration difference between different types of soil can yield localised phase biases in the interferogram. In figure 5 it is shown how a coherent phase bias of approximately 0.15 phase cycles (corresponding with 5 mm path length change), acts on specific areas in the interferogram which are clearly correlated with areas of different land use. The interferogram is based on a tandem SAR image pair. A change in the dielectric properties of the soil influences the Fresnel reflection coefficient which might yield a coherent phase effect. Another possibility would be a height change due to the expansion of the entire field as a reaction on a localised change in the fields water content (Gabriel, Goldstein, and Zebker 1989). However, since temperature, pressure, relative humidity, wind speed and cloud cover had identical characteristics at both SAR acquisitions and no watering took place in this period, it is considered unlikely that expansion effects dominate for this phase change. Changes in penetration or in the dielectric constant seem to be more likely, although unambiguous interpretation of the effects is difficult without a priori information. If a penetration error propagates in a height estimate, with this effective baseline of 25 meter, an error of 48 meters can be reached when comparing two

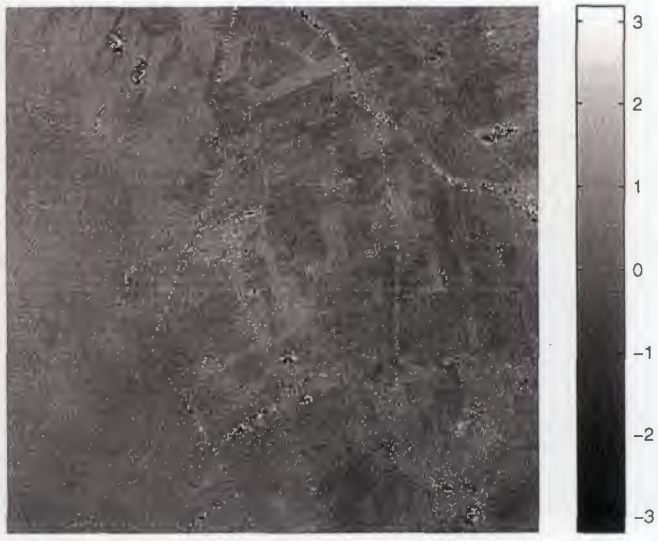

Fig. 5. A 5 × 5 km zoom of an interferogram showing penetration differences

isolated positions.

V. Temporal decorrelation

In figure 6 it is shown how the coherence over a specific area has decreased over a time interval of 3.5 years. From this coherence image it may seem that no significant information can be retrieved in this interval, since the overall tone of the image has a constant and low value. On the other hand one might conclude that this average coherence value of approximately 0.3 is still interpretable in terms of a reasonable stable interferometric phase. After closer analysis of the data, isolated points with a relatively high coherence estimation can be detected.

As described by Touzi, Lopes, and Vachon (1996), the discrimination between areas of different coherence is mainly influenced by the number of independent samples in the coherence estimation window. If this number is chosen too small, low coherence areas become biased towards a higher coherence estimation. Figure 6, for which an estimation window of 2 × 11 samples was used, displays this effect—although almost all coherence in this (mostly agricultural) area has disappeared, a bias of approximately 0.3 is apparent in the data. Therefore discrimination between different coherence levels becomes difficult.

As shown in figure 7, an increase of the coherence estimation window to 20 × 110 samples yields an increased discrimination between areas of different coherence, which is due to the corresponding drop in coherence bias. In the figure, this can be observed in the red tone of the decorrelated areas[1]. On the other hand, areas with a relatively higher coherence can be detected as the yellow and green spots. Naturally, the larger estimation window implies a decrease in the absolute coherence levels with respect to

[1]Note that although a continuous colour wheel proved to be the best visualisation for these data, coherence levels above 0.95 which are also coloured red can be neglected with this estimation window.

Fig. 6. Coherence image after a 3.5 year time interval, using 2 × 11 independent samples for the coherence estimation

those of small window sizes. Therefore, the range of coherence values in the image reduces, whereas the reliability of the estimates increases.

Due to the better possibilities to discriminate between coherence levels, thresholding at a chosen low level becomes possible. Figure 8 shows how the interferometric phase values corresponding with pixels with a coherence higher than 0.1 still reveal interpretable phase information. In this masked interferogram, a multilook window equal to the coherence estimation window (20 × 110) was applied. Although disturbing influences of the satellite orbits or atmospheric heterogeneities still form a major restriction for an unambiguous interpretation, this method of phase analysis reveals promising prospects for the study of long time interval and severely decorrelated interferograms. The coherence preserving areas are in this case mainly of anthropogenic origin.

VI. Conclusions

Phase bias effects due to atmospheric heterogeneities and local temporal penetration differences hamper an unambiguous interpretation of the interferometric phase in terms of geometric path length differences. For slow deformation processes, the need to use interferometric pairs over long time intervals introduces decorrelation effects, which results in an increased phase noise for major parts of the interferogram. Using large coherence estimation windows, the coherence bias is suppressed. This enables the discrimination of different low coherence levels, and the extraction of useful phase information. Finally, strong multilooking reduces the phase variance for the selected parts of the in-

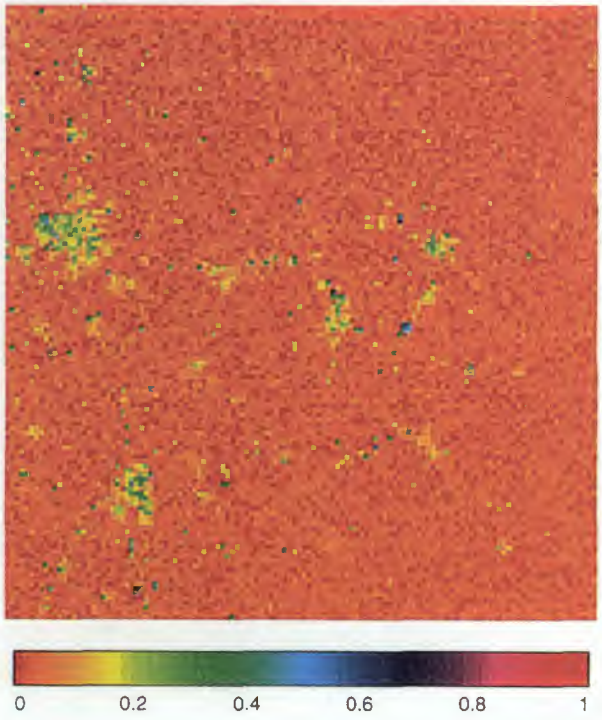

Fig. 7. Coherence image using 20 × 110 independent samples per pixel

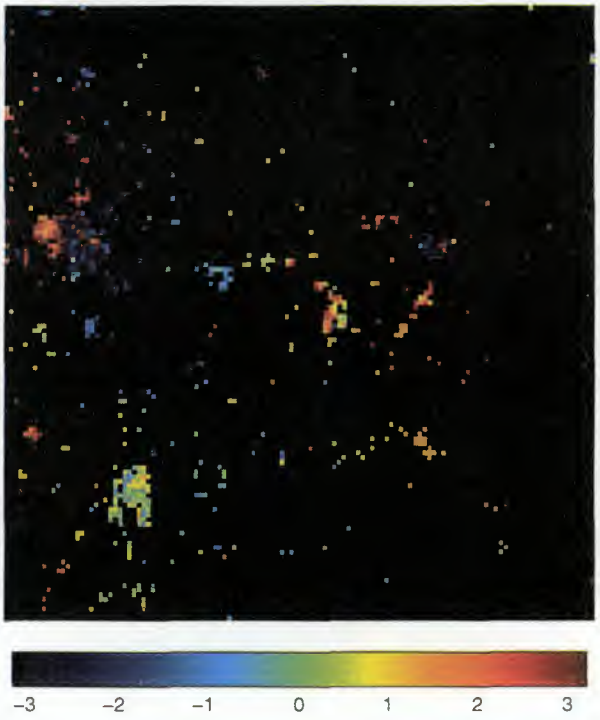

Fig. 8. Interferogram, masked under a coherence level of 0.1 with a multilook window of 20 × 110 pixels

terferogram.

VII. Acknowledgements

The authors would like to thank the European Space Agency for the provision of the SAR data, and dr. A. Jungstand from DLR Neustrelitz for the kind provision of the ionospheric maps over Europe. Also the support of the group of dr. R.Bamler from DLR Oberpfaffenhofen is kindly appreciated.

References

Gabriel, A. K., R. M. Goldstein, and H. A. Zebker (1989). Mapping small elevation changes over large areas, differential radar interferometry. *Journal of Geophysical Research 94*(B7), 9183–9191.

Hanssen, R. and A. Feijt (1996). A first quantitative evaluation of atmospheric effects on SAR interferometry. In *Fringe workshop Zurich*, http://www.geo.unizh.ch/rsl/fringe96/papers/hanssen/. ESA.

Jungstand, A. (1997). Ionospheric maps and GPS satellite and receiver biases. http://www.nz.dlr.de/gps/gps-ion.html. DLR Remote Sensing Ground Station Neustrelitz.

Kohl, H., R. Rüster, and K. Schlegel (Eds.) (1996). *Modern Ionospheric Science*. Katlenburg-Lindau, FRG: European Geophysical Society.

Smith, Jr., E. K. and S. Weintraub (1953). The constants in the equation for atmospheric refractive index at radio frequencies. *Proceedings of the I.R.E* (41), 1035–1037.

Spoelstra, T. A. T. (1996). A climatology of quiet/disturbed ionospheric conditions derived from 22 years of Westerbork interferometer observations. *Journal of Atmospheric and Terrestrial Physics 58*(11), 1229–1258.

Touzi, R., A. Lopes, and P. W. Vachon (1996). Estimation of the coherence function for interferometric SAR applications. In *EUSAR'96, Königswinter, Germany*, pp. 241–244.

Williams, P. J. S. (1996). *Tides, Atmospheric Gravity Waves and Travelling Disturbances in the Ionosphere*, pp. 136–180. In Kohl et al. Kohl, Rüster, and Schlegel (1996).

USE OF ERS TANDEM DATA TO PRODUCE DIGITAL ELEVATION MODELS BY INTERFEROMETRY AND STUDY LAND MOVEMENTS BY DIFFERENTIAL INTERFEROMETRY IN CALABRIA AND JORDAN

Y. Cornet, J.-Y. Doulliez, J. Moxhet, D. Closson, A. Kourgli, P. Ozer, A. Ozer

Laboratoire de Géomorphologie et de Télédétection
Université de Liège
2, allée du 6 août, 4000 Liège, Belgium
Yves.Cornet@physun.geo.ulg.ac.be

D. Derauw

Centre Spatial de Liège
Avenue du Pré Aily, 4031 Angleur, Belgium
dderauw@ulg.ac.be

ABSTRACT

This paper summarises 2 case-studies of neotectonic in Calabria and Dead Sea area. Their scope is the evaluation of ERS 1-2 interferometry and differential interferometry products. We show the successive steps of the realization, correction and georeferencing of these interferometric products. After this technical approach we present some examples of geomorphometric exploitation of the DEM to detect structural, lithological and active or passive neotectonic influences. The results of these applications are compared with those reached using traditional DEMs to evaluate qualitatively the validity of the interferometric products.

INTRODUCTION

This summary presents the work of our laboratory concerning the uses of radar interferometry in the aim of morphological analysis and natural hazards evaluation. The technique of radar interferometry is promising since it theoretically allows the realization of digital elevation models (DEM) and even the measure of displacements of the ground with a good precision [Ref. 1, 2, 3 and 4]. In this study, the technique was tested essentially in Calabria and Jordan. Some image correction and geomorphological analysis techniques have also been developed. This step of geomorphological applications of SAR DEMs is obviously essential. In fact, the quality of a DEM must be evaluated quantitatively by the estimation of an absolute precision (RMS error), but has also to be validated qualitatively in function of the use that we can do of this DEM [Ref. 5] : geomorphometry, hydrologic network analysis, or analogical interpretation of morphostructural features, for instance.

1. STUDIED SITES

For this study, two test sites were selected, one in southern Italy (Calabria) and one in the Dead Sea area (Jordan). Those sites were selected because of several reasons :

– Jordan : the Dead Sea graben in Jordan was selected first because of its very active tectonics connected with the pull-apart rift along the Jordan River strike slip fault system. The system is characterized by focal mechanisms mainly normal and transverse [Ref. 6-13]. But another quality is the desert nature of this area which is particularly appropriate for radar interferometry. Our objective was also to detect structural features potentially correlated with brittle behavior of the upper crustal regions and sudden seismic movements as well as slow pre, inter and post seismic deformations with differential interferometry. The dynamic aspect is also influenced by diapiric deformations [Ref. 13] of ground in the Dead Sea graben.

– Calabria : we have a good coverage of this zone with topographical maps, geological maps and aerial pictures, what is an advantage to compare with the digital elevation model obtained by interferometry; this area of Southern Calabria and particularly the Strait of Messina is one of the most seismically active in the Mediterranean basin, and the geomorphic record of tectonic activity is particularly perceptible [Ref. 14-20]; lastly, this zone is ideal to apply some 3D analysis methods because of the high slopes gradients.

2. INTRODUCTION TO RADAR INTERFEROMETRY

A radar image is primarily composed of two components : an amplitude value, which is correlated

with the physical properties of the ground, and a phase value, which represents the path length of the signal. The purpose of the interferometry is to use this phase value to calculate DEMs and even ground displacements (differential interferometry).

The basic principle is to use two frames of the same zone and coregistrate them in order to produce an interferogram, which is an image of the phase differences between the two frames. This interferogram, in the general case (two frames sensed at two different times from two different places) represents as well the parallax as the displacement of the ground between these two frames. So it is directly related to the elevation at the cost of an ambiguity of $2k\pi$. Thus, after the coregistration which eliminates the influence of the distance between the frames, an intermediate operation, the *phase unwrapping*, is necessary to eliminate this ambiguity. This is generally a step by step algorithm where the altitude of a pixel is arbitrarily fixed and the altitude of its neighbors is derived from it, postulating the continuity of the surface. As radar images are exposed to layover and shadowing phenomena, this hypothesis is not always verified, so one obtains generally a set of polygons where the altitude is coherent inside but not between them.

The same technique can be used for monitoring the displacements of the earth crust. It is necessary, in that case, to use three or more images. The technique we used with this project was to use two pairs of ERS tandem images. The images within a pair were taken by ERS-1 and ERS-2 within a short interval, but the two pairs were separated by a long interval. This permits to minimize the influence of other factors such as humidity or land cover variations.

3. REALIZATION OF DIGITAL ELEVATION MODELS

The digital elevation models of Calabria and Jordan were processed by the « Centre Spatial de Liège » with the technique described above [Ref. 21]. The drawback of the process is that the digital elevation model is in slant range projection (fig. 1a). So it was necessary to geometrically correct the model to be able to compare it with other cartographic sources.

We performed this correction by using a local spherical approximation of the WGS84 ellipsoid, considering a sphere with a radius equivalent to the earth radius (measured on the ellipsoid) at the center of the scene. Each pixel is projected on this sphere in function of its azimuthal projection which determines the position of the antenna and in function of its height. The corrected positions (in planimetry) are then coherent in a polygon but not between two or more polygons, and the relative position of independent polygon is not the same as on a map. After this process, it is required to perform an interpolation in order to obtain a continuous surface (fig.1b). This operation was achieved with the module MODEL MAKER from the ERDAS IMAGINE software. We had to take into consideration the fact that the spatial resolution is not the same in range and azimuth but is defined by the CSL to get unspeckled interferograms, and also for the range direction by the operations of geometrical correction and interpolation.

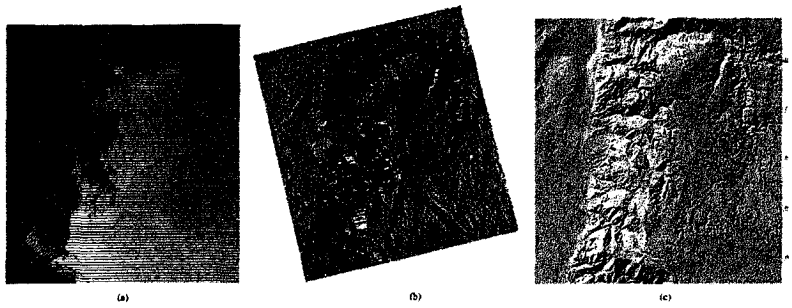

Figure 1 : from left to right : (a) DEM in slant range projection (independent zones in different colors); (b) geometrically corrected DEM in shaded relief; (c) DEM from the Geological Survey of Israel in shaded relief.

This technique was applied only on the digital elevation model of Jordan, because the DEM of Calabria was too uneven to apply this technique.

4. RESULTS AND VALIDATION

Thanks to this correction procedure, we obtain satisfactory results when the topography is not too uneven, because in that case the coherence zones (where the phase has been unwrapped uniformly) are broad enough. But in the zones with major topographic variations, where the third dimension of geomorphologic features is useful, this procedure is globally unsatisfactory.

The digital elevation model in *slant range projection* of Calabria has been compared with a DEM produced by digitization of topographic maps. This permitted us to validate the results by comparing the respective altitudes of some control points. Those control points are very difficult to determine and the spatial representativity of the topographical surface is not satisfying. We obtain a standard error of estimation of 40.23 and 51.30 m for the two DEMs produced by interferometry (2 and 4 SAR images DEMs) (see fig. 2). We also noticed some artefacts in the shape of the section of some valleys by the formation of double and parallel valleys (fig. 3). This phenomenon , which can influence negatively the analogical interpretation of the DEM (digitization of

lineaments) is due to the *lay-over* of some sides oriented to the sensor.

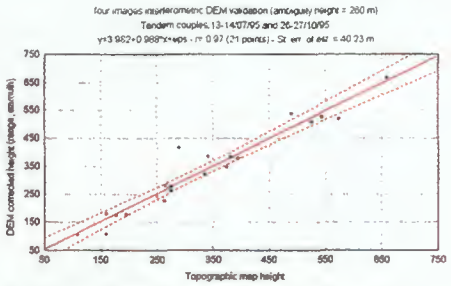

Figure 2. Validation of one DEM of Calabria

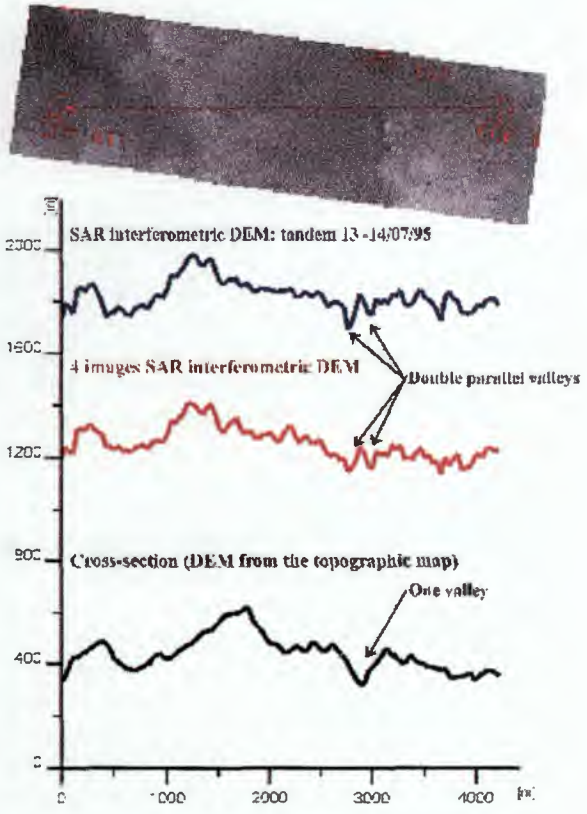

Figure 3 : Double parallel valleys on the SAR interferometric DEM (4 SAR images interferometric DEM - ambiguity height = 260 m -, tandem 13-14/07/95 - ambiguity height = 400 m - and the corresponding topographic cross-section)

In the Dead Sea area, we didn't dispose of reliable topographic maps so we were not able to produce a cartographic DEM. The DEM produced by interferometry was composed of many independent polygons where the altitude is coherent but related each with a different altitude. That's why we studied essentially the larger coherent zone which covers most of the Jordan plateau in the vicinity of Kerak. We can see visually (fig. 1b) that the technique of radar interferometry puts well in evidence the topography of the plateau and particularly the graben of Wadi El Batra.

The comparison of the corrected DEM with a poster of a DEM provided by the Geological Survey of Israel (fig. 1c) shows also a good conformity in a planimetric point of view, even of the deep valley that incises the plateau in the north-east part.

5. GEOMORPHOLOGICAL ANALYSIS OF THE DEMS

5.1. COPLANARITY ANALYSIS

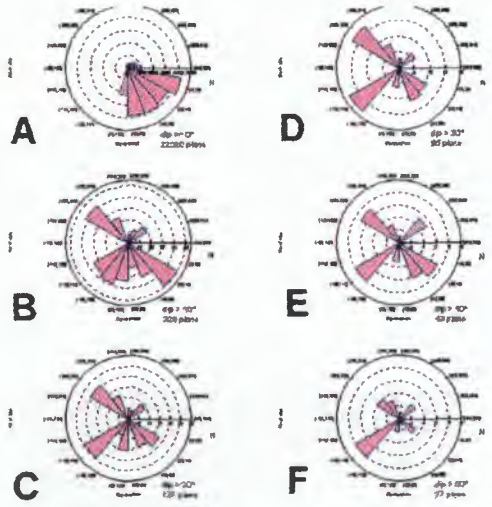

Figure 4. Planes frequency in function of their dip direction and magnitude. A : dip > 0°; B : dip > 10°; C : dip > 20°; D : dip > 30°; dip > 40°; dip > 50°

This geomorphometric application of SAR interferometric DEM is inspired by [Ref. 22]. We have described the technical aspects of this procedure [Ref. 23]. Nevertheless, some corrections and refinements have been adopted : distance tolerance to test the multiple coplanarity of lineaments and planimetric representation of the determined planes by computation of the intersections between selected planes and the DEM used to detect and digitize the lineaments. The orientation of the planes depends on the number of coplanar lineaments per plane and the dip of these planes (fig. 4). We then have to select the planes before the analysis of their planimetric representation (fig. 5). We have to maximize the number of coplanar lineaments per plane and to extract only the planes with high dip value because of the predominant strike slip and normal faulting system of the area. The results obtained in Jordan from SAR interferometric DEM (fig. 6) are unfortunately less accurate and less rich in geomorphologic information than those obtained in Calabria from a DEM computed on the basis of the digitized hypsometry. Nevertheless, the main structural orientations are enhanced by this kind of analysis applied on interferometric DEM but the low rate of height variation that allow the continuity of the

interferometric DEM avoids the computation of planes defined by high dip value.

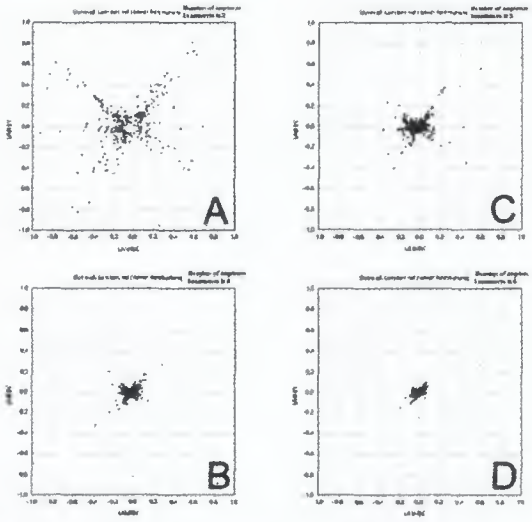

Figure 5. Schmidt-Lambert representation of the planes in function of the number of coplanar lineaments. Poles of planes resulting of 2 (A), 3 (C), 4 (B), 6 (D) coplanar lineaments.

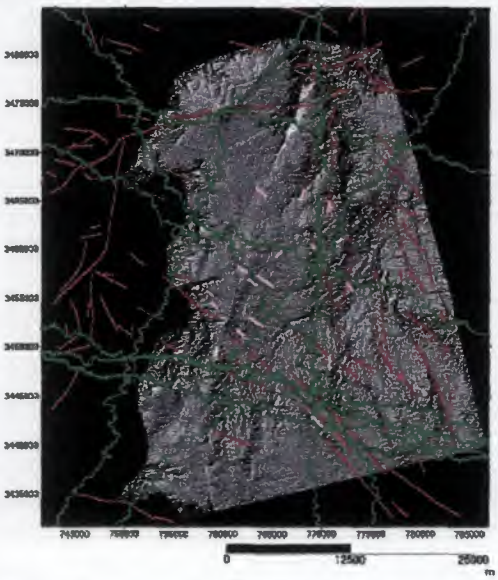

Figure 6 : Results of the coplanarity test (angle tolerance : 2°, distance tolerance : 61 m, minimum dip : 30°, minimum number of coplanar lineaments : 3) : green : intersections between planes and SAR interferometric DEM; fuchsia : coplanar lineaments; red : structural features (see references)

5.2. HYDROLOGIC ANALYSIS

In order to analyze qualitatively the digital elevation model, we also achieved a simple hydrographic network analysis. This allowed us to characterize the continuity of the surface. We can see on the figure above that many streams are discontinuous because of small dips in the DEM (in blue on the picture)

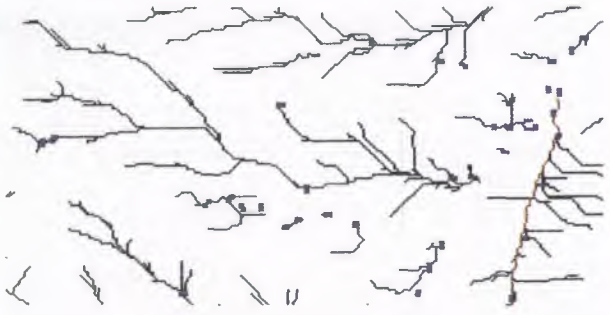

Figure 7. Hydrographic network.

6. DIFFERENTIAL INTERFEROMETRY

As we mentioned above, the interferometry technique can also be used in order to detect movements of the earth crust. This technique was tested here on the images of Jordan with two ERS-1 & ERS-2 tandem pairs (November 10-11, 1995 and December 15-16, 1995). In the end we obtained what is called a *differential interferogram*, composed of closed polygons where the phase has been unwrapped independently. So, the differential movements are consistent only within each polygon and not between the polygons. Because of the residual noise of the radar images, we first had to eliminate the smallest ones in order to preserve only the interpretable information.

However, this study could not put in evidence significant movements. The few observed fringes could only be related to optical path variations due to variations in humidity and variation of the distance between the satellite and the earth [Ref. 24]. The reduced time interval between the scenes (one month) is probably the main explanation for this.

We couldn't apply this technique for the region of Calabria because we didn't have a couple of usable interferograms. In fact, only one couple of images did produce a usable interferogram (with well developed fringes); on the other couples, the phase was preserved only on the villages and some dry streams.

7. FIELDWORK

In order to facilitate the interpretation of the differential interferogram and the features observed or completed from the DEM, a field study was conducted in Jordan from September 17 to October 2, 1996. We particularly centered our investigations about : (i) the global and local fracturation, after an interpretation on the satellite images; and (ii) the landslides and natural wells which could eventually generate fringes on the interferograms.

Despite the fact that this zone is seismically very active, and that several earthquakes have affected the Dead Sea valley during the period of interest, this study was not able to show movements at a detectable scale occurring during this too short period.

The graben of Wadi El Batra (visible in the South-west of the image) has been studied by a student of the University of Jordan in Amman. It seems to be inactive since a long time.

CONCLUSIONS

The geometrical quality of interferometric products expressed in function of the geomorphologic and geomorphometric mapping possibility must be estimated in function of the application. In our case two cases of potential applications of SAR interferometric DEMs and differential interferograms have been described. The first case is a geomorphometric analysis of which the result is the static determination of morphostructural features. The comparison of this kind of analysis performed on an interferometric DEM and computed from digitized hypsometry shows the actual limits of the first one however after correction and georeferencing : height incoherence, variable planimetric accuracy due to layover and shadowing (discontinuities), isolated noisy pixels... Moreover, some artifacts on SAR interferometric DEM (double valleys) can lead to misinterpretation of geomorphologic features.

The second case is the automatic extraction of hydrographic network from SAR interferometric DEM. The discontinuity of the network is regrettable and the use of this kind of product must be considered with care in an operational 2 and 3D analysis of the hydrographic network to detect abnormalities that could be investigated on the tectonical point of view.

The two instances presented above are static, the dynamic or cinematic point of view of tectonics has been investigated using differential interferometric products computed in Jordan. Till now we got no exploitable information on pre-, co-, post- and inter-seismic motions (brittle and epeirogenic deformations) of the superficial crust. In Calabria no satisfying differential interferogram has been computed. These results leads us to the following operational establishment : in such seismic areas the monitoring must go on but the actual question is how is it possible to get enough SAR frames that allow the interferometric processing in function of orbit geometry and terrain condition and how is it possible to insure the results before ordering SAR data to avoid trial and error procedure.

REFERENCES

[Ref. 1] Massonnet D., Feigl K., Rossi M. & Adragna F., 1994, Radar interferometric mapping of deformation in the year after the Landers earthquake, *Nature,* **369**, 227-230.

[Ref. 2] Massonnet D., Rossi M., Carmona C., Adragna F., Pelzer G., Feigl K. & Rabaute T., 1993, The displacement of the Landers earthquake mapped by radar interferometry, *Nature,* 364, 139-142.

[Ref. 3] Zebker H.A., Rosen P., Goldstein R.M., Gabriel A. & Werner C.L., 1994, On the dérivation of coseismic displacement fields using différentiai radar interferometry: the Landers earthquake, *J. Geophysical Research,* **99**, 19617-19634.

[Ref. 4] Zebker H.A., Werner C.L., Rossi P.A. & Hemley S., 1994, Accuracy of topographie maps derived from ERS-1 interferometric radar, *IEEE Trans. Geosci. Remote Sensing,* **32**, 823-836.

[Ref. 5] Weibel R. & Brändli M., 1996, Adaptative methods for the refinement of digital terrain models for geomorphometric applications, *Zeitschrift für Geomorphologie N.F.*, **101**, 13-30.

[Ref. 6] Abou Karaki N.; 1987, Synthèse et carte sismotectonique des pays de la bordure orientale de la Méditerranée: Sismicité du système de failles du Jourdain-Mer Morte, *Thèse de doctorat,* IPGS, Université Louis Pasteur (Strasbourg I), France, 430 pages.

[Ref. 7] Ben-Avraham Z., Ten Brink U. & Chuarrach J.; 1990, Transverse faults at the northern end of the southern basin of the Dead Sea graben, *Tectonophysics,* **180**, 37-47.

[Ref. 8] Gardosh M., Rf-Ches Z. & Garfunkel Z.; 1990, Holocene tectonic deformation along the western margins of the Dead Sea, *Tectonophysics,* **180**, 123-137.

[Ref. 9] Hatzor Y & Reches Z, 1990, Structure and paleostresses in the Gilboa' region, western margins of the central Dead Sea rift, *Tectonophysics,* **180**, 87-100.

[Ref. 10] Kovach R.L., Andreasen G.E., Gettings M.E. & El Kaysi K., 1990, Geophysical investigations in Jordan, *Tectonophysics,* **180**, 6169.

[Ref. 11] Reches Z., 1987, Mechanical aspects of pullapart basins and push-up swells with applications to the Dead Sea transform, *Tectonophysics,* **141**, 7588.

[Ref. 12] van Eck T. & Hofstetter A., 1990, Fault geometry and spatial clustering of microearthquakes along the Dead Sea-jordan rift fault zone, *Tectonophysics,* **180**, 15-27.

[Ref. 13] Abou Karaki N.; 1995, The gravity survey. *In: Center for Consultation, Technical Services and Studies; 1995. Assessment of the hazard of subsidence and sinkholes in Ghor Al-Aditha area - Final report,* University of Jordan, non publié, 117-124.

[Ref. 14] Bottari A. & Lo Giudice E.; 1987, Structural studies on the strait of Messina. The seismotectonic data,. *Doc. et Trav. IGAL,* **11**, 115-125.

[Ref. 15] Dumas B. & Raffy J., 1993, Validité et précision de la mesure des mouvements verticaux par référence aux paleoniveaux marins: exemples en

Calabre méridionale, *Bull. Inst. Géol. Bassin d'Aquitaine*, Bordeaux, **53**, 141-150.

[Ref. 16] Ghisetti F., 1981, L'evoluzione strutturale del bacino Plio-Pieistocenico di Reggio Calabria nel quadro geodynamico dell'arco Calabro, *Boll. Soc. Geol. It.*, **100**, 433-466.

[Ref. 17] Miyauchi T., Dai Prà G. & Sylos labini S., 1994, Geochronology of Pleistocene marine terraces and regional tectonics in the Tyrrhenian coast of South Calabria, Italy, *Il Quaternario*, 7(1), 17-34.

[Ref. 18] Neri G., Caccamo D., Cocina O. & Montalto A., 1996, Geodynamic implications of earthquake data in the southern Tyrrhenian sea, *Tectonophysics*, **258**, 233-249.

[Ref. 19] Ott d'Estevou P., Barrier P., Bousquet J.C., Chabellard J.G., Coppier G., Jarrige J.J., Lanzafame G. & Laniece C.; 1987, Evolution structurale pliocène et quaternaire du Détroit de Messine, *Doc. et Trav. IGAL*, **11**, 105-114.

[Ref. 20] Vachard D., Barrier P., Montenat C. & Ott d'Estevou P., 1987, Dykes neptuniens, brèches internes et éboulis cimentés des escarpements de faille du détroit de Messine au Plio-Quaternaire, *Doc. et trav. IGAL*, Paris, **11**, 127-141.

[Ref. 21] Derauw D. & Moxhet J., 1996, Preliminary results of Tandem SAR interferometry and differential interferometry over the Dead Sea area. *FRINGE 96, ESA Workshop on Applications of ERS SAR Interferometry*, 30 September to 2 October 1996, Remote Sensing Laboratories, University of Zurich, Switzerland, http://www.geo.unizh.ch/rsl/fringe96/papers/derauw.

[Ref. 22] Eliason J.R., 1992, Mapping fractures remotely for earthquake hazard assessment by the use of topographie and seismic hypocenter data, *Episodes*, **15**, 1, 75-82.

[Ref. 23] Cornet Y. & Ozer P., 1996, The contribution of ERS1 SAR data in neotectonics, *Deuxième Symposium International "ERS Applications Workshop"*, Londres, Grande-Bretagne, décembre 1995, 265-272.

[Ref. 24] Zebker H. A. & Rosen P.A., 1996, Atmospheric artefacts in interferometric SAR surface deformation and topographic maps, submitted to *Journal of geophysical Research - Solid Earth.*

ERS TANDEM DATA FOR EARTHQUAKE PREDICTION: PRELIMINARY RESULTS

Salvatore Ponte

Department of Aerospace Engineering, Second University of Naples
Via Roma, 29 - I-81301 Aversa (CE), Italy
Phone: +39-81-5010223; Fax: +39-81-7682160
E-mail: ponte@unina.it

ABSTRACT

First results related to the research activity carried out in the framework of the ESA Project AOT.I302 are presented. The project is aimed at integrating spaceborne techniques to measure ground deformation with traditional means of seismic activity monitoring. The Sannio-Matese area, one of the most earthquake-damaged zones in southern Italy, has been chosen as test-site and equipped with 20 corner reflectors and 16 GPS benchmarks, in order to have high-coherence ground control points suitable for DEM validation and phase analysis. Fringe maps and coherence analysis for three available tandem datasets, acquired in May and June, 1996, are presented, together with preliminary results on land use classification and parameters extraction based on the coherent information gathered by the Synthetic Aperture Radar (SAR) sensors. The capability of measuring small crustal deformation by means of differential SAR interferometry (DINSAR) is also investigated by analyzing non-tandem datasets.

Keywords: SAR Interferometry, Coherence, Classification, Differential SAR interferometry.

1. INTRODUCTION

This paper presents some preliminary results related to the activity which is being carried out in the framework of the ESA project "Use of ERS-1/ERS-2 Tandem Data for Earthquake Prediction In Tectonic Active Areas" (AOT.I302, in response to an ESA's Announcement of Opportunity AO-Tandem issued January 16, 1996), aimed at monitoring and forecasting small crustal deformations and tectonic movements in the area of the Matese Chain (Campano-Molisano Apennines, Southern Italy), which extends from Isernia to Benevento, along the direction NW-SE, and is known as one of the most seismically active segments of the Apennine chain (Siro and Slejko 1989, Barbano *et al.*, 1989), being subject to destructive earthquakes of intensity up to XI MCS (in 1688) and, in the last three centuries, to many other strong events (X MCS in 1702, 1732 and 1805, IX MCS in 1962, X MCS in 1980). The project, planned on three-year work packages and started in January, 1997, focuses its objectives on processing methods, validation and science in the areas Interferometry/Land topography, Land classification and Land motion detection with differential phase analysis. Co-ordinated by the Department of Aersopace Engineering of the Second University of Naples, Italy, the project involves national (Consortium for Research and Development of Advanced Remote Sensing (CO.Ri.S.T.A., Naples), Dept. of Space Science and Engineering, University of Naples, Italy) and European (Wageningen Radar Surveys, Wageningen, The Netherlands) partners. The main activities to be performed can be grouped into the following categories:

- Generation of digital elevation models (DEM) from interferometric SAR data;
- Attitude and orbit determination, and baseline components estimation from raw data analysis;
- Differential SAR interferometry;
- Characterization/classification of land use by using interferometric radar information (coherence maps) and multi-temporal SAR products;
- Characterization of a tectonically sensitive area located in Southern Italy by means of seismotectonic models derived from historical seismicity, tectonics and geodynamical modeling.
- Integration of SAR observations and Global Positioning System (GPS) measurements and classical techniques of ground deformation measurements (high-precision leveling and tilt monitoring) and earthquake prediction.

Results are foreseen both in a short-term analysis, through the study of historical and actual seismicity and of ground deformations which precede and accompany earthquakes, and in a long-term study involving the analysis and characterization of geodynamical processes which affect the Matese Chain.
The project has its predecessor in an international joint research, funded in 1994-1996 by the Commission of the European Communities (CEC), which involved partners from Italy (Dept. of Space Science and Engineering, University of Naples, Consortium CO.Ri.S.T.A., Vesuvius Observatory), Germany (Institut für Navigation, University of Stüttgart) and France (Bureau de Recherche Gèologiques et Mineraries, Marseille) (Luongo *et al.*, 1996). During this program, the principal seismogenetic areas around the Matese Chain have been identified, and the Sannio-Matese test-site has been equipped with instrumentation

for ground deformation measurement with differential GPS and SAR techniques, as described later, collecting seismic data from May, 1994 to August 31, 1996.
In this paper, after a description of the Sannio-Matese area from a seismotectonic viewpoint, the monitoring network is presented. Successively, the activities performed on the ERS tandem pairs are summarized. Results on the coherence analysis and a simple unsupervised classification scheme based on the coherence maps are presented. Moreover, a feasibility study on the potentialities of DINSAR technique on the test area. Concluding remarks describe the future steps of the research activity.

2. DESCRIPTION OF THE TEST-SITE AND GROUND EQUIPMENT

2.1. Historical seismicity and current seismic events of the Sannio-Matese area

The first phase of the research activity has been an overall assessment of the seismic characteristics of the area. Fig. 1 shows the main tectonic features of the Matese complex, which is a transitional area from the structure of the Calabro and the Umbro-Marchigiano-Toscano Archs, affected by complex regional stress fields and by significant variations of the deformation fields, due to stress fields acting in the southern and mid-northern parts of the Apennines (Hippolyte *et al.*, 1994, Lavecchia, 1988).

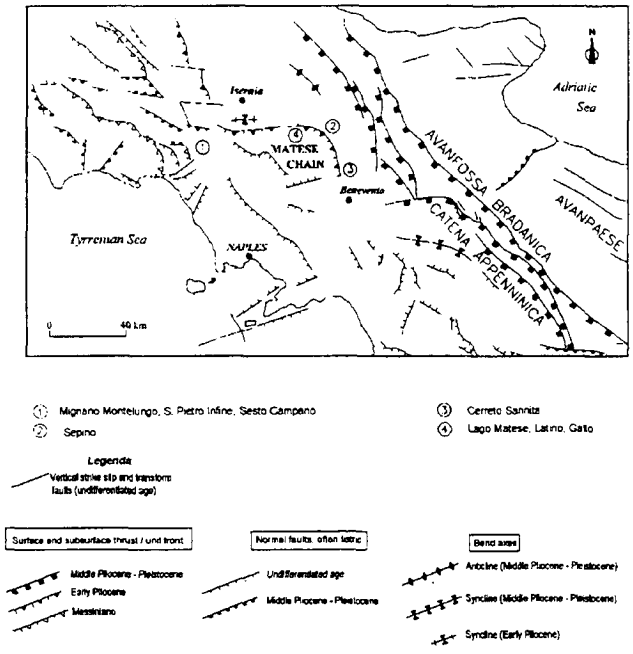

Figure 1. The Sannio-Matese area and its main tectonic features.

Focal mechanisms are mainly dip-slip for earthquakes of major energy, and strike-slip for the others (Westaway, 1987). The dip-slip mechanisms show the tensile axis perpendicular to the chain due to the rifting process migrating from the Tyrrhenian coast to the chain, whereas strike-slip mechanisms can be related to strike slip movements perpendicular to the chain axis. In short, the analysis of historical seismicity of the area under investigation shows that:

- The isoseismals are extended in the direction of the chain and follow the principal tectonic features, and the magnitudo of historical events ranges from 6.2 and 7.5 (Tab. 1), with a maximum length of seismogenetic faults, L,.of 100 km.

Date	*Magnitudo*	*L(km)*
1456, Dec. 5	7.5	100
1688, Jun. 5	6.8	45
1694, Sep. 8	7.0	53
1732, Nov. 29	6.8	45
1805, Jul. 26	6.8	45
1857, Dec. 16	7.0	53
1930, Jul. 23	6.8	45
1980, Nov. 23	6.8	45

Table 1. Major seismic events in the Sannio-Matese area.

- In major earthquakes, complex rupture mechanisms are prevailing, as inferred from the earthquake of 1456 (Luongo *et al.*, 1991). The numerous fractures in the medium account for the complexity of the rupture mechanism; the structures longitudinal to the chain can be divided into fault segments that are generated by rotation and migration of the peninsula towards East.
- The structures transverse to the chain can be triggered by earthquakes along the axis of the chain itself, or they may have the function of channels of seismic energy.
- Seismic activity is mostly found on the eastern side of Matese and the mechanisms are prevailingly extensive, with the main planes in the NW-SE direction.

As far as the current seismicity is concerned, low-energy earthquakes have characterized the period 1980-1991, with the majority of seismic events located in a narrow strip of the peninsula, with focal depths reaching up to 20 km. Seismicity sources are various, not necessarily linked to the Apennine fault, as a confirmation of the complexity of the stress field acting on the area (Alessio *et al.*, 1995). Four main seismogenetic areas have been identified:

- Southern Abruzzo, with mid/low-level energy of seismic activity in historical and recent times;
- Molise, with past high-energy earthquakes and recent seismic activity in swarms vith low energy;
- Area of Benevento, with strong earthquakes in the past (>X grade) and current low-level but frequent seismic events;

• Campania and Basilicata, with high-intensity events in historical times and recently (for example, the 6.8-magnitudo earthquake occured in Irpinia in 1980).

2.2. Monitoring and ground equipment

Currently, the deformations in the Matese area are being measured through analysis of seismicity data and ground slow motion. Seismicity is monitored through a number of stations of the national seismic network, managed by the National Institute of Geophysics (ING, Istituto di Geofisica Nazionale), together with a regional network monitored by the Vesuvian Observatory (OV, Osservatorio Vesuviano) and a set of temporary stations installed by the Department of Geophysics and Volcalonogy (DGV) of the University of Naples (Fig. 2).

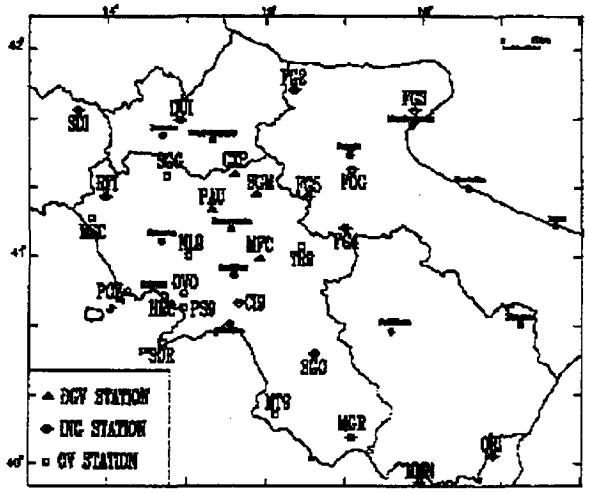

Fig. 2. Seismic network of the Sannio-Matese area.

Ground motion is monitored by high-precision leveling and inclination measurements with a leveling route (129.300 km) equipped with 164 benchmarks, of which 61 have horizontal displacement monitoring capability, and 103 are able to measure vertical components of ground displacements. Last August, 1996, a preliminary leveling campaign has been performed (Luongo *et al.*, 1996): currently, a correlation between the experimental data gathered and seismotectonic models of the area is being performed.

Moreover, twenty triangular trihedral corner reflectors (CR) and sixteen GPS benchmarks have been installed (Fig. 3): the CRs, deployed by a team headed by Prof. P. Murino (Dept. of Space Science and Engineering, University of Naples, Italy), are suitable ground control points for image registration, can give reliable and stable radar cross-section values, thus giving radiometric standards for absolute image calibration, and can be exploited as phase references when monitoring height variation and horizontal slips by means of differential interferometric data, whereas the GPS benchmarks, fixed to the ground by excavation and concrete cages, enable to determine with good accuracy the horizontal component of the displacement field, by means of ionosphere-corrected differential GPS measurements. Recent campaigns conducted in the area (November 1994 and June/July 1995, Luongo *et al.*, 1996) gave a first statement of stability of the site, with differential displacements not greater than 10 mm.

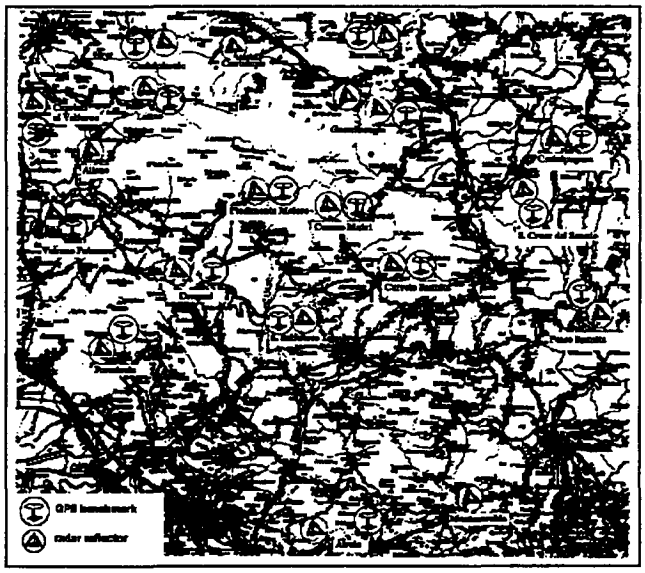

Fig. 3. Deployment configuration of corner reflectors and GPS benchmarks.

3. INTERFEROMETRIC SAR PRODUCTS GENERATION

The availability of several tandem acquisitions over the Sannio-Matese area during the last three years has greatly improved the possibility of obtaining highly correlated SAR datasets, due to the one-day ground-site revisiting period. The criterion adopted for tandem pair selection was aimed at finding sets of at least three passes at the shortest time intervals, and with suitable baseline components. The consequent constraints on the baseline component perpendicular to the line of sight, B_{perp}, lock the suitable values of $|B_{perp}|$ to be in the range from 70 to 130 m, for efficient phase unwrapping and avoiding baseline decorrelation (Li and Goldstein, 1990, Prati and Rocca, 1990): the tandem pairs with such values of B_{perp}, selected from the listings provided by the ESA Guide and Directory Service (GDS), are reported in Tab. 2.

Acquisition date	*Orbit numbers*	B_{perp} *(m)*
May 7-8, 1996	25167(ERS-1) / 5494 (ERS-2)	122
May 23-24, 1996	25396 (ERS-1) / 5723 (ERS-2)	81
June 27-28, 1996	25897 (ERS-1) / 6224 (ERS-2)	78

Table 3. Tandem pairs analyzed and correspondent baseline estimates. The theoretical value of B_{perp} suitable for interferometry applications is of the order of 100 m.

The tracks of interest are ascending passes, labeled 129 (second quarter) and 358 (first quarter). Fig. 4 depicts the imaged area.

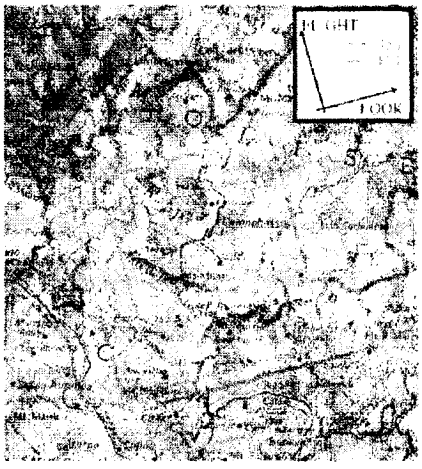

Fig. 4. Sketch map of the ground swaths of ERS Tracks 129 (Quarter 2) and 358 (Quarter 1), Frame 819. The approximate co-ordinates of the test area are 41°33' N, 14°04' E(upper left corner), 41°33' N, 14°52' E (upper right), 41°01' N, 14°04' E(lower left), 41°01' N, 14°51' E(lower right). The extension is about 1800 km².

Single-look complex (SLC) images, processed by ESA/ESRIN, have been requested for the investigation. The average dimensions of each frame is of the order of 15000 lines of 2200 range samples. Fig. 5 shows, as an example, one of these images, multilooked by a factor 5 in the azimuth direction in order to get a square pixel (about 20x20 m²), and mirrored about its horizontal axis, to obtain a north-south image. The Matese Chain and the Matese Lake are well visible on the central portion of the frame, and a division of the massif into three blocks with respect to the NW-SE-oriented Matese Lake-Letino structure is suggested by the radar image.

The capability of producing DEMs on different 10x10-km² subareas of the test-site has already been accomplished by using November 1995 and February 1996 ERS tandem pairs and implementing an efficient end-to-end procedure, from geometric registration to baseline components estimation from the propagated state vectors available in each CEOS formatted SLC header (Rufino *et al.*, 1996).

The logic flow of the operations performed for fringe maps generation has been as follows:

- Coarse registration by rigid translation. A number of visually-inspected bright points common to both images has been used to cut non-overlapping areas, obtaining a residual misregistration of the order of three pixels.
- Fine registration by localization in each 512x256 pixel subset of the brightest point target as a Ground Control Point (GCP). The evaluation of the pixel shifts to be applied for registration has been performed by 10-time oversampling each subset (cubic B-splines have been used for interpolation) and cross-correlating the GCP amplitudes. The average number of suitable GCP, after elimination of poorly correlated subsets and inconsistent shifts derived from the procedure, has found to be from 150 to 200, depending on the size of the images: such an high number, as compared to past experience with 3-day ERS-1 pairs (Moccia *et al.*, 1994), can take account for possible nonlinearities due to the pointing geometry and/or attitude differences.

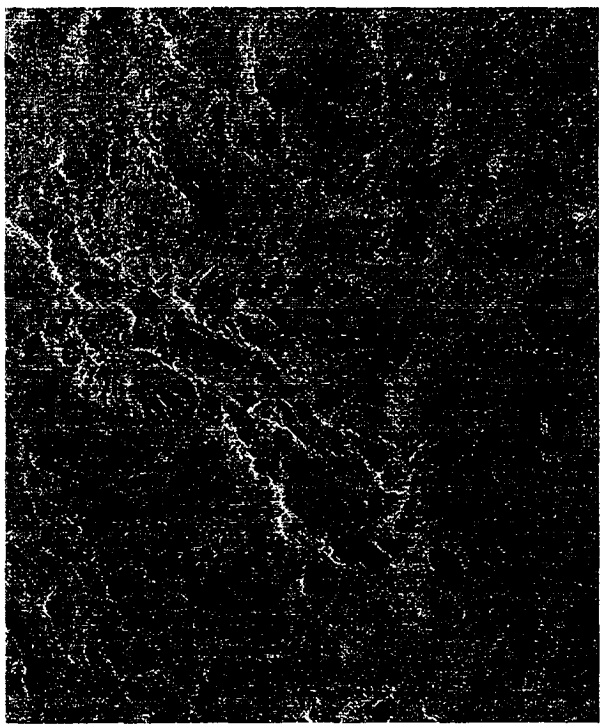

Fig. 5.SAR SLC image of the Sannio-Matese area, gathered on May 7, 1996 by the ERS-1 AMIinstrument (orbit number 25167, frame 819, track 129), processed by ESA-ESRIN (© ESA 1996).

- Co-registration by means of bicubic polynomials, whose coefficients have been computed with least-square approximations, by using as input the sub-pixel shifts. As a remark, we noted that the range and azimuth residual shifts are quite constant for the three pairs analyzed, with a slight increase of azimuth sub-pixel displacement from near to far range, probably due to small differences in attitude (i.e. pointing geometry) between the two passes, or to non perfectly parallel orbits.
- Complex product between the co-registered SLC images (the second one being complex conjugated). No common spectral band filtering before computation of the fringe map has been performed, thus leaving a residual baseline decorrelation.
- Coherent multilook for coherence enhancement and maximum likelihood estimation of the interferometric phase (Werner *et al.*, 1992). Fig. 6 shows one of the resulting interferograms: the shorter ERS-1/ERS-2 temporal baseline gives good quality fringes, and comparatively small decorrelated areas.

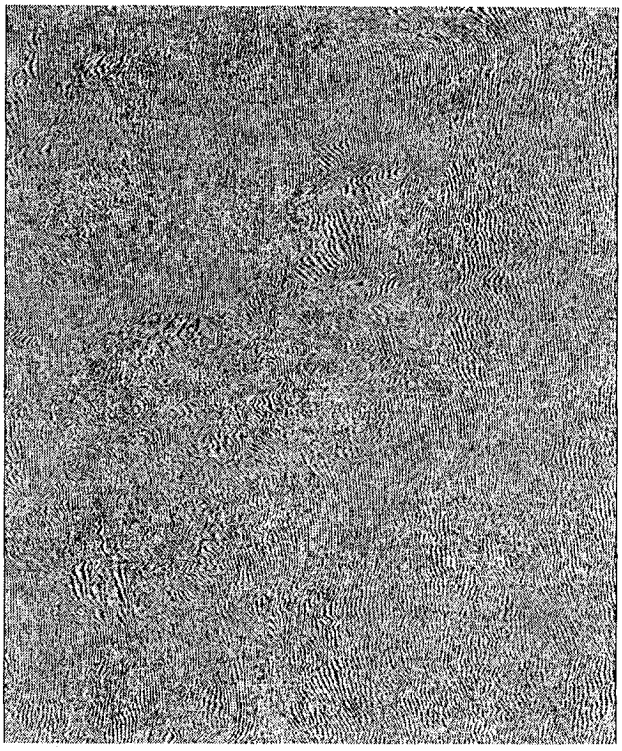

Fig. 6. 5-look interferogram obtained from the ERS tandem pair of May 7-8, 1996 (see Tab.3). The image dimensions are 2400x2400 pixels (ERS-R).

4. COHERENCE ANALYSIS AND CLASSIFICATION

Fringe quality has been evaluated by means of the correlation coefficient γ:

$$\gamma = \frac{p_{i1} p_{j2}^{*}}{\sqrt{\langle p_1^2 \rangle \langle p_2^2 \rangle}}$$

where * denotes complex conjugation, p_{i1} and p_{j2} are homologous pixels in the two co-registered images, and <>denotes the average operator. Fig. 7 shows coherence histograms of the multilooked interferograms, and Table 4 gives a statistical characterization of γ.

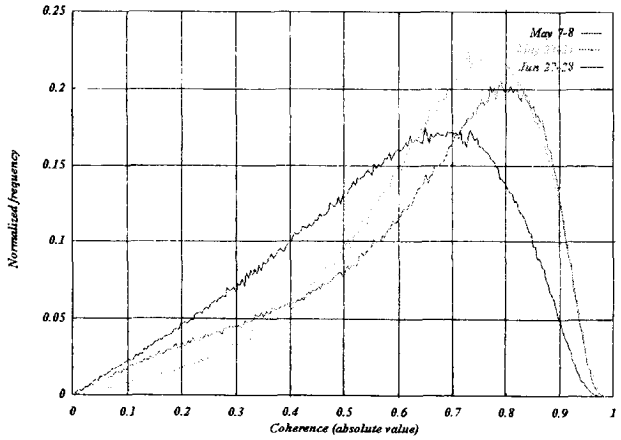

Fig. 7. Coherence histograms of the three tandem pairs selected.

The good values found are a consequence of the reduced temporal gap between the two observation, and it is expected that stripping off mountainous areas and zones in which layover due to high slopes occur could even increase the average coherence. As a remark, layover areas reduce the possibility of efficient phase unwrapping for DEM generation, as shown by analyses conducted on different pairs of the illuminated area by Rufino *et al.*, 1996.

Tandem couple	*Average*	*St. dev.*
May 7-8, 1996	0.55	0.21
May 23-24, 1996	0.59	0.05
June 27-28, 1996	0.63	0.04

Table 4. Coherence statistics.

Fig. 8(a) shows the coherence image relative to the June 27-28, 1996 pair, and Fig. 8(b) is a color-composite image obtained by superimposing (red and blue channels) the interferogram to the coherence map, in order to visually inspect areas of low coherence. The Matese Chain, a densely vegetated mountainous area, shows, as expected, low coherence, whereas flat areas and bare soil exhibit larger correlation. With respect to the corresponding SAR images (Fig. 5), some ground features are more identifiable: for example, rivers Volturno and Calore are clearly visible in the lower left part.

Temporal decorrelation shows changes in land use, vegetation cover and moisture, as well as roughness and hydro-meteorological changes (Wegmüller *et al.*, 1995). This suggests strategies of classification based on feature extraction from the coherence maps. At this stage, a straightforward attempt has been performed, based on a common iterative, self-organized unsupervised clustering algorithm (ISODATA, ERDAS™, 1991). The initial number of clusters has been chosen to be 4, on the basis of available thematic maps of the area, and the corresponding broad classes have been labeled as woods and water courses, pasture, bare soils, sown areas. Fig. 9 shows the resulting classified area, with color-coding of the different classes. The comparison with thematic data is encouraging, even if refinements need to be done, for the identification of narrower classes, possibly by means of multi-source imagery (for example, woods and water basins are grouped in the same class in the coherency image, whereas are distinguishable in the backscatter image) and for accuracy evaluation.

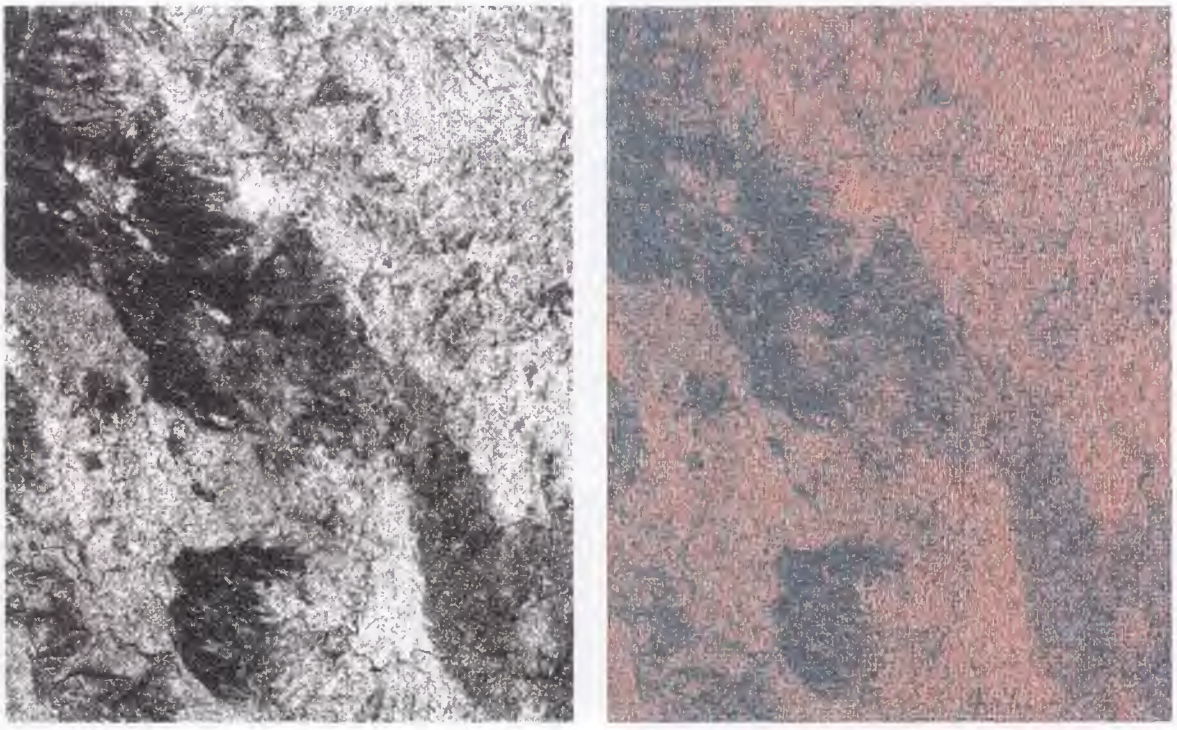

Fig. 8. Coherence map (a) of the June 1996 ERS tandem pair. Brighter areas correspond to high coherence values. (b)Composite image of coherence+interferogram (ERS-R).

5. FEASIBILITY OF DIFFERENTIAL SAR INTERFEROMETRY

The potentiality of differential SAR interferometry (DINSAR) for measuring small displacements (of the order of centimeters) occurred between the acquisition of three radar images has been widely demonstrated (Gabriel et. al., 1989, Prati *et al.*, 1993). DINSAR data, though, rely heavily on quantitative changes of the scattering mechanisms of the imaged area, i.e. on the well-known temporal and baseline decorrelation effects (Zebker and Villasenor, 1992), and therefore are strictly related to the terrain morphology and land use. Since the test-site is a densely vegetated area, with little urbanization and sparse bare-soil regions, the loss of coherence is significantly high even after few days, a constraint which gives non-tandem data of the area (e.g. ERS-1/ERS-1, ERS-2/ERS-2 pairs, or ERS-1/ERS-2 passages with more than 1-day separation) a relatively low information content. This section will justify quantitatively this observation, also showing the possibility of obtain DINSAR maps on some non-vegetated areas present in the illuminated scene. The investigation has been conducted on two tandem pairs, namely, the May 23-24 and the June 27-28 couples (see Tab. 3), chosen because of their suitable B_{perp} values (81 and 78 m for the tandem pairs, about 80 m between non-tandem observations). Fig. 10 shows the coherence histograms obtained from the processing of two non-tandem combinations of the available SLC products. The low γ-values are due to the wide temporal baseline (34 and 35 days respectively) and to possible cultivation in vegetated areas (harvesting).

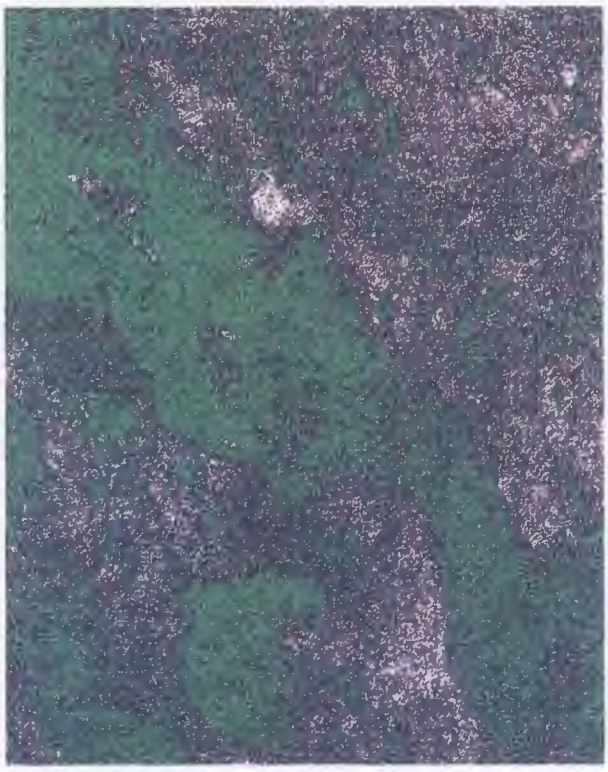

Fig. 9. Colour-coded classified map of a portion of the Sannio-Matese area. Classes are woods/water (green), pasture (blue), bare soils (indigo/white), sown areas (blue/red) (ERS-R).

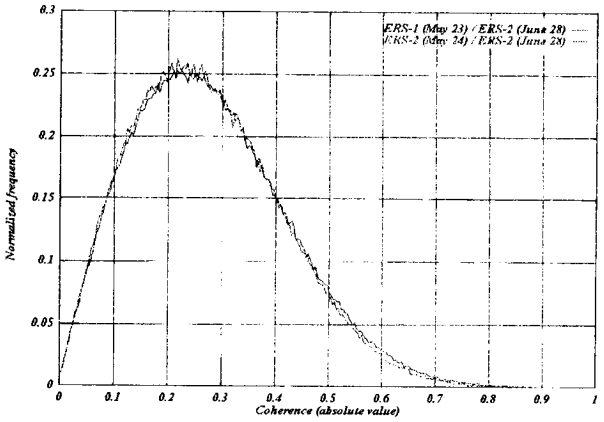

Fig. 10. Coherence histograms of the analyzed non-tandem pairs. Average values found are 0.28 and 0.27 for the ERS-1/ERS-2 and the ERS-2/ERS-2 pairs, respectively, with standard deviation of 0.02.

As a result, only in little portions of the image fringes are visible. Fig. 11 shows such an area, corresponding to Mount La Gallinola (in the Matese Mount Maggiore unit, direction NE with respect to the Matese Lake, see Fig. 5), a non-vegetated site formed by milestones, clay and marl.

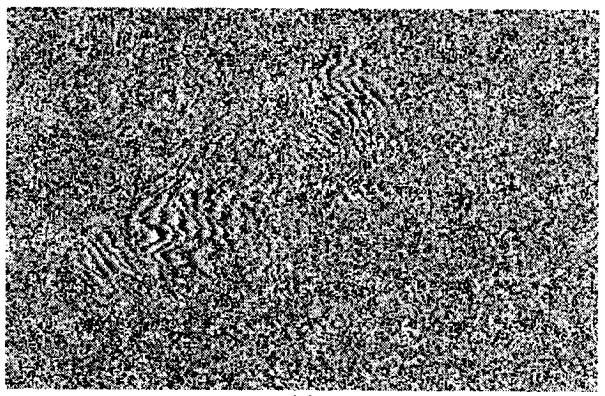

(a)

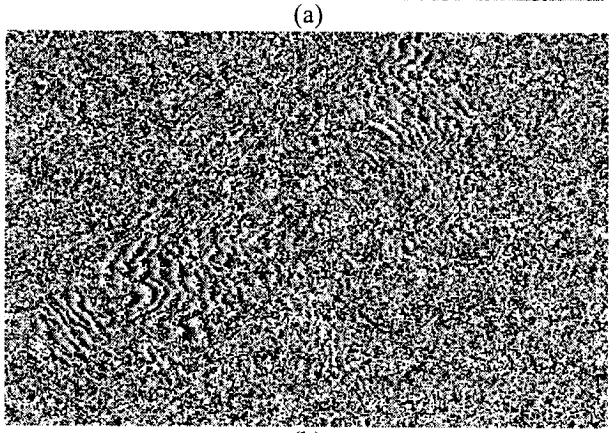

(b)

Fig. 11. Portion of the interferograms obtained from ERS-1 (May 23)/ERS-2 (June 28) images (a) and ERS-2(May 24)/ERS-2 (June 28) pairs(b). Poor-quality fringes are visible on a bare-soil area, which exhibits an average coherence of 0.4. The dimension of this subset are 128x128 pixels (a 5-look coherent summing has been applied in the azimuth direction).(ERS-R)

We are exploring the possibility of obtaining DINSAR information in this small region: at the moment, no double-difference interferogram has been produced.
The lack of large and representative high-coherence areas seems to reduce the impact of change detection by means of DINSAR data. Nonetheless, the presence of a number of CR deployed on the test-site could allow us to obtain a correct phase sampling on a small subset of high-coherence points (the point target images), whereas GPS measurements on the absolute CR locations should permit the reconstruction of the absolute phase of each reflector, and, as a consequence, the possibility of detecting surface changes in the vicinity of the CRs.
In a first attempt of this procedure, the identification of the CR responses in the images and the extraction of geometric and radiometric image quality parameters (range and azimuth resolutions, integrated and peak sidelobe ratio (ISLR, PSLR)) by means of appropriate algorithms (Moccia *et al.*, 1994, Rufino *et al.*, 1996), has allowed us to obtain a set of control points with good phase quality. The problem of retrieving the relative phase of the CRs is still open, because unfortunately the CRs are immersed in low-coherence areas. Simulation approaches are under study.

6. CONCLUSIONS AND FURTHER WORK

First results relative to the analysis of ERS tandem pairs of the Sannio-Matese area have been presented in this paper. The study has been focused on three available SAR SLC couples, from May to June, 1996: good quality interferograms have been obtained, and the coherence analysis has shown reasonably good coherence values. A first approach in classifying land use from the coherence information has been presented, and critical analysis on the feasibility of differential interferometry on the area has shown potential application of the technique only in small subsets of the scene. In the future, the research activity related to the project will be concentrated on the following points:

- Development of differential interferometry by means of phase information derived from the installed CRs. We are investigating the approach proposed by Massonnet *et al.*, 1996, who suggests to use a course DEM for generating synthetic fringes due to relief. To this end, computer simulation of the SAR system will allow us to create artificial fringe maps, generate the reference function necessary to compress the raw data and enhance the interferogram coherence. The simulation technique has been successfully applied on SIR-C/X-SAR data (Ponte and Moccia, 1995), which shown better resolutions when compressed with the simulated 2D impulse response function.

• Correlation between GPS measurements and differential interferometry. Synergistic use of multi-source imagery for geological analysis.
• Refinement of baseline estimation methods and orbital modeling. Work is underway for producing computer code for the extraction of the platform attitude during data acquisition, starting from the ERS raw data and restituted state vectors. A comparison with SIR-C/X-SAR attitude information, derived from the postflight attitude trajectory history (PATH) data, shows little interpolation errors in recostructing the attitude (Rufino and Ponte, 1997).
• Implementation of classification strategies based on coherence maps and SAR backscatter images. A promising multi-source approach, which does not require normal distribution of data and seems to improve classification accuracy, is the evidential reasoning (Peddle, 1995). Study on the application of this theory to signatures provided by INSAR products is being performed.
• Development of three-dimensional seismo-tectonical models of the Sannio-Matese area.

ACKNOWLEDGMENT

ERS-1/ERS-2 SLC images have been provided by ESA-ESRIN, Frascati, Italy. The activity has been performed in the framework of the ESA project AOT.I302.

REFERENCES

Alessio, G., Gorini, A., Vilardo, G., Iannaccone, G., 1995: Low energy sequences in areas with high seismic potential: Benevento (Southern Apennines), April 1990. *Natural Hazard*, **3**, pp. 300-307.

Barbano, M. S., Egozcue, J. J., Fernandez, G., Kijko, A., Lapajne, J., Mayer-Rosa, D., Schenk, V., Schenkova, Z., Slejko, D., Zonno, G, 1989: Assessment of seismic hazard for the Sannio-Matese area of Southern Italy - A summary. *Natural Hazard*, **2**, pp. 217-228.

ERDAS™ Field Guide, 2nd Edition, Version 7.5, July 1991, Atlanta, GA, USA, Chap. 6.

Gabriel, A. K., Goldstein, R. M., and Zebker, H. A., 1989: Mapping small elevation changes over large areas: differential radar interferometry. *J. Geoph. Res.*, **94**, B7,pp. 9183-9191.

Hippolyte, J. C., Angelier, J., Roure, F., 1994: A major geodynamic change revealed by Quaternary stress patterns in the Southern Apennines (Italy). *Tectonophysics*, **230**, pp. 199-210.

Lavecchia, G., 1988: The Thyrrenian-Apennines system: structural setting and seismotectogenesis. *Tectonophysics*, **147**, pp. 263-296.

Li, F. K., Goldstein, R. M., 1990: Studies of multibaseline spaceborne interferometric synthetic aperture radars. *IEEE Trans. Geosc. Rem. Sens.*, **1**, pp. 88-97.

Luongo, G., Cubellis, E., Obrizzo, F., and Petrazzuoli, S. M., 1991: A physical model for the origin of volcanism of the Thyrrenian margin:the case of Neapolitan area. *J. Volcan. Geoth. Res.*, **48**, pp. 173-185.

Luongo, G., Ereditato, D., Mucciacciaro, G., Obrizzo, F., Cubellis, E., Hartl, P., Thiel, K.-H., Becker, D., Reich, M., Bles, J. L., Sauret, B., Murino, P., Ferri, M., Russo, L., Fanelli, A., Castellano, L., Parente, R., Rufino, G., Esposito, S., 1996: *Earthquake Prediction in Tectonic Active Areas Using Space Techniques - Final Report.* Contract No. EV5V-CT94-0461.

Massonnet, D., Vadon, H. and Rossi, M., 1996: Reduction of the need for phase unwrapping in radar interferometry. *IEEE Trans. Geosc. Rem. Sens.*, **34**, pp. 489-497.

Moccia, A., Esposito, S., and D'Errico, M., 1994a: Height measurement accuracy of ERS-1 SAR interferometry, *EARSeL Adv. Rem. Sens.*, **1**, pp. 94-108.

Moccia, A., Vetrella , S., and Ponte, S., 1994b: Passive and active calibrators characterization by using a spaceborne SARsystem simulator. *IEEE Trans. Geosc. Rem. Sens.*, **32**, pp. 715-721.

Peddle, D. R., 1995: Knowledge formulation for supervised evidential classification. *Photogr. Eng. & Rem. Sens.*, **61**, pp. 409-417.

Ponte, S., Moccia, A., 1995: Validating a spaceborne SAR simulator by using SIR-C/X-SAR data. *46th IAF Congress*, Oslo, Norway. Paper IAF-95-B.6.03.

Prati, C., Rocca, F., 1990: Limits to the resolution of elevation maps from stereo SAR images. *Int. J. Rem. Sens.*, **11**, pp. 2215-2235.

Prati, C., Rocca, F., and Monti Guarnieri, A., 1993: SAR interferometry experiments with ERS-1. *Proc. 1st ERS-1 Symposium*, Cannes, France, pp. 211-218.

Rufino, G., Moccia, A., Esposito, S., 1996: DEM generation by means of ERS tandem data. Pres. at the *ESA Workshop on Applications of ERS SAR interferometry (FRINGE 96)*, Zurich, Switzerland, Sep. 30-Oct. 2, 1996.

Rufino, G., Ponte, S., 1997: Extracting attitude information from spaceborne SARraw data: results from SIR-C/X-SAR acquisitions. Submitted to *IEEE Trans. Geosc. Rem. Sens.*

Siro, L., and Slejko, D., 1989: Different approaches to the seismic hazard of Sannio-Matese (Southern Italy). *Natural Hazard*, **2**, pp. 329-348.

Wegmüller, U., Werner, C. L., Nüesch, D., Borgeaud, 1995: Land-surface analysis using ERS-1 SAR interferometry. *ESA Bulletin*, **81**, pp.30-37.

Werner, C. L., Goldstein, R. M., Rosen, P., and Zebker, H. A., 1992: Techniques and applications of SAR interferometry for ERS-1 topographic mapping, slope measurement and change detection. *Proc. 1st Workshop ERS-1 FRINGE Working Group*, ESA/ESRIN, pp. 11.

Westaway, R., 1987: The Campania, Southern Italy, earthquake of August 21, 1962. *Geophys. J. R. Astr. Soc.*, **88**, pp. 1-24.

Zebker, H. A., and Villasenor, J., 1992: Decorrelation in interferometric radar echoes. *IEEE Trans. Geosc. Rem. Sens.*, **30**, pp. 950-959.

THE ANTOFAGASTA 1995 EARTHQUAKE: CRUSTAL DEFORMATION PATTERN AS OBSERVED BY GPS AND D-INSAR

Ch. Reigber, Y. Xia, G.W. Michel, J. Klotz and D. Angermann

GeoForschungsZentrum Potsdam
Division 1: Kinematics and Dynamics of the Earth
Telegrafenberg A17, D-14473 Potsdam, Germany
phone: +49 331 288-1101, fax: +49 331 288-1111, e-mail: reigber@gfz-potsdam.de

ABSTRACT

Combinations of different ground and space techniques provide promising tools for the assessment and understanding of Geo-Hazards. We studied the spatially distributed surface deformation related to the 30 July 95, Antofagasta, Chile, subduction earthquake. In order to do this, we applied two space techniques: the Differential Interferometric SAR technique using three sets of ERS-1 SLC data and repeated GPS-measurements in a regional 70-sites' network. Results indicate that: a) coseismic surface deformation reached values of 90 cm in the vicinity of the epicenter along the coast and values of 10 cm in a distance of 200 km to the epicenter in the direction normal to the trench; b) both the GPS-method and the D-INSAR technique provided highly comparable deformation; c) the co-seismic surface deformation field is fairly homogeneous and shows little perturbations; d) we are not yet able to distinguish between the long-term secular deformation and the earthquake event triggered deformation. Combining both methods, however, results suggest that where long-term accumulation rates of deformation are apparently high, i.e., in the western part of the investigated area, they must be homogeneously distributed.

1. INTRODUCTION

„Geo-Hazards" such as earthquakes, volcanic eruptions, and those created by land instabilities are among the strongest sudden impacts on modern life and property. Due to the increasing vulnerability of western and developing countries, future hazards appear to be increasingly disastrous with future events causing further superlatives in death and property loss. Social development in a variety of third world countries is in addition strongly hindered by recent natural hazards and the United Nations claimed the 90s as the International Decade for Natural Disaster Reduction. The assessment and mitigation of „Geo-Hazards" hence appears as an - and probably is *the* - obligatory task of the geoscience community. Hazard assessment studies are multifold and combine investigations of recurrence intervals or probability of occurrence of events together with their probable impact on life and property, and the investigation of deformation and rates within different time scales, including geological studies, paleoseismology, and the monitoring of seismicity and currently accumulating deformation. In addition to the assessment of hazards, the above mentioned studies aim at providing a better understanding of the processes acting. Studies of the regional co-seismic and post-seismic earthquake deformation embrace information about crustal and upper mantel behavior and rheologies. Within the last few years, the Global Positioning System (GPS) technology became one of the most powerful tools to derive the distribution of deformation in zones of high tectonic activity. However, measurements are conducted at discrete points and hence could miss important information between sites. A combination of the GPS-technique with the fast developing Differential Synthetic Aperture Radar Interferometry (D-INSAR) technology promises to become a major tool for the monitoring of the spatial distribution of deformation related to volcanic dome growth, mass movements or the seismic cycle (Masonnet et al., 1993, Zebker et al., 1994). This contribution presents results of the Ms:7.3 Antofagasta, Chile, of 30 July 1995 earthquake deformation study as obtained from GPS-measurements and D-INSAR.

Aims of the study are to:

- investigate the 2-years' GPS-derived motions that include (pre-, co-, and post-) seismic and secular deformation and information about the amount of coupling between the Nazca and the S-American Plates;
- correlate results from the GPS measurements to the D-INSAR observations;
- study the co-seismic spatial distribution of surface deformation, structure-related perturbations etc.;
- relate the surface deformation patterns to the along-fault quake deformation; and
- (in future) investigate the post-seismic behavior of the crust and upper mantle.

Proc. 3rd ERS Symp. on Space at the service of our Environment, *Florence, Italy, 17–21 March 1997* (ESA SP-414, 3 Vols., May 1997)

2. THE STUDY AREA

The study area shown in Fig. 1 is located in N-Central Chile along the western rim of Southern America. Here, partial coupling of the subducting oceanic Nazca Plate with the upper S-American Plate causes current straining within the latter. Frequent major earthquakes occur that accommodate a large part of the ongoing deformation. Recurrence intervals of major quakes are in the order of 10s to 100s of years (Comte & Pardo, 1991; Papadimitriou, 1993). For the study area a major earthquake had been forecasted (Nishenko, 1985). Partitioning of the oblique Nazca-S-American Plate convergence has been assumed and several teleseismically derived subduction related focal plane solutions indicate almost pure thrusting. The July, 30, 1995 Ms:7.3 Antofagasta earthquake apparently ruptured 220 km of the subduction zone that starts beneath N of the Mejillones Peninsula (22.5°S) and continues to the area of Taltal to the S (25°S). The hypocentral depth was estimated between 48 km (USGS, NEIC) and 28 km (Harvard, CMT) and the corresponding fault plane indicates E-dipping thrusting apparently on the subduction interface. Second-order quake-related surface movements were not detected except for some open ruptures along the Atacama Fault, a major N-S trending system of faults that display a long history of transcurrent and normal faulting. Overall damage was relatively low.

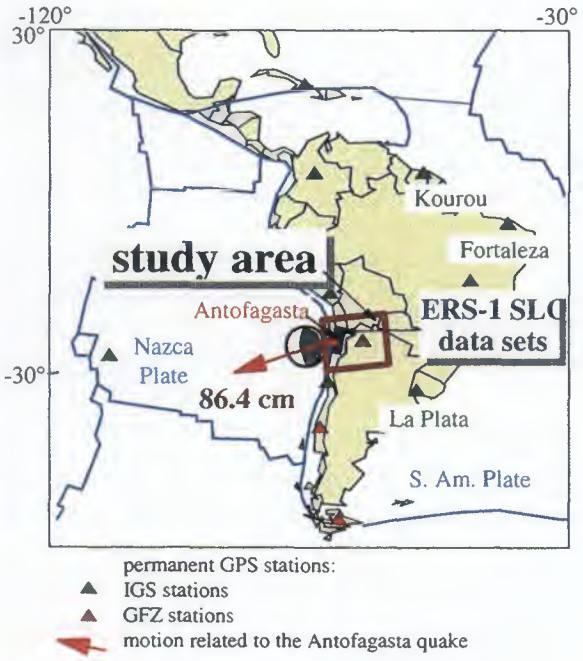

Fig. 1: Study area

3. GPS CAMPAIGN RESULTS

Within the SAGA project (South American Geodynamic Activities) the GeoForschungsZentrum Potsdam (GFZ) established in cooperation with many partner institutions of the hosting countries in 1993/94 a network of 200 GPS stations covering the whole territory of Chile and the western part of Argentina (Klotz et al., 1996). This periodically re-observed network is embedded in a network of permanently operating stations in South America and world-wide which is primarily managed by the International GPS Geodynamics Service (IGS) (Beutler et al., 1995). The main purpose of the SAGA network is to observe station velocities over at least one decade. In combination with geologic, seismic, neotectonic, gravity and magnetic data, these velocities are used to study the ongoing deformation processes in the Andes. In the northern part of the network a dense traverse of 72 points extending from Antofagasta to the Argentine Chaco was observed 21 months before the July 1995 earthquake and 3 months after the event. Using more than 20 Trimble 4000 SSE receivers, about 3 days of continuous data were acquired on each site in each campaign. The station distribution in the subnetwork around Antofagasta is shown in Fig. 2.

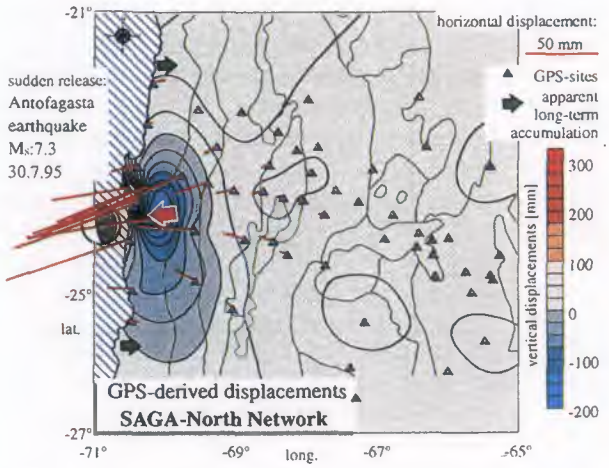

Fig. 2: SAGA-North GPS network and displacements.

The GPS data were processed with the GFZ software EPOS (Earth Parameter and Orbit Processing System). The precise GPS software package is based on undifferenced phase and pseudo-range observations. The network computation is done in form of daily solutions with the ionosphere-free linear combinations of phases and pseudoranges. In order to tie the network to the International Terrestrial Reference Frame (ITRF), the campaign data were processed simultaneously with globally distributed IGS station data and the data of permanent GFZ stations in South America. The parameters solved for are station coordinates, clock parameters, ambiguities and tropospheric parameters. Optional is the processing of orbit and Earth Orientation Parameters (EOP) in a dynamic solution. Using EPOS, different processing strategies are possible (Angermann et al., 1996). The most efficient strategy is to fix the orbits and the Earth orientation parameters to the IGS mean solution calculated by seven different centers, including GFZ Potsdam. Doing this and solving for the coordinates of all network stations and a set of global IGS sites, daily average network solutions are obtained

which are referred to a system defined by the IGS orbit and EOP's. This fiducial-free network solutions were transformed to the ITRF93 using those IGS stations that were included in the global computations.

The network accuracy is assessed using the repeatability of the daily network solutions. The SAGA horizontal position accuracy depicts 1-3 mm, the vertical accuracy 5-6 mm. In the global IGS frame this network is positioned with an accuracy better than 1 cm horizontally and 1-2 cm vertically. The displacement vectors, derived from the geocentric coordinates of the two campaign solutions (see Fig. 2), are related to three sites on the stable eastern part of the South American plate: Kourou, Fortaleza and La Plata. The geometry of this station configuration is stable within 1 cm between the two measurement epochs. The displacements in the Antofagasta region are about 100 times larger than the motion in the eastern part of the network. The entire city of Antofagasta moved by about 90 cm westwards, but was only marginally moved in vertical direction. This abrupt co-seismic position change was recorded by our permanent GPS station in Antofagasta. Stations north of the epicenter were uplifted by about 30 cm, whereas the region about 100 km east of the epicenter is subsided by up to 20 cm. Figure 2 shows that an area of almost 300 x 300 km is deformed in a relatively regular form by this magnitude 7 earthquake.

4. DIFFERENTIAL SAR-INTERFEROMETRY RESULTS

The study region is hyperarid with almost no vegetation. The area is hence perfectly suited for applying the differential SAR Interferometry technique (D-INSAR) for surface motion detection. The D-INSAR principle can shortly be described using the geometry of the Interferometric radar as shown in Figure 3.

Assume the surface point 0 with an orthometric height h was acquired at three different times from three different orbital positions S, S_1 and S_2 by the radar sensor. From the Interferometric pair S-S_1 with baseline B1 and the second pair S-S_2 with baseline B_2 one can obtain two interferograms with the phases Φ_1 and Φ_2, respectively, which read after removal of the Interferometric phase term of the reference surface

$$\Phi_1 = \frac{4\pi h}{\lambda r \sin\theta} B_1 \quad and \quad \Phi_2 = \frac{4\pi h}{\lambda r \sin\theta} B_2 \qquad (1)$$

From these Interferometric phases the height of the surface point 0 can be determined with high resolution if the orbits are of high (5-10 cm) quality (Reigber et al., 1996). If prior to the third acquisition, point 0 was shifted by a natural or manmade event to position 0', the slant range r_2 would be changed to (r_2 - ρ). This change ρ registered by the radar sensor corresponds to the projection of the displacement vector $\overline{00'}$ onto the slant range and is independent of the baseline itself. The second phase can, therefore, be written as

$$\Phi_2' = \frac{4\pi h}{\lambda r \sin\theta} B_2 + \frac{4\pi\rho}{\lambda}. \qquad (2)$$

From equations (1) and (2) the change in slant range ρ can be derived as

$$\rho = \frac{\lambda}{4\pi}\left(\Phi_2' - \frac{B_2}{B_1}\Phi_1\right) \qquad (3)$$

Before multiplying with the baseline ratio B_1/B_2, phase Φ_1 must be unwrapped. Under normal conditions one would also unwrap phase Φ_2'. But sometimes, as it was the case in our study, the baseline B_2 is too long, leading to a difficult unwrapping process of phase Φ_2'. In this case, the alternative procedure is to use the wrapped phase Φ_2' and unwrap the phase term of ρ.

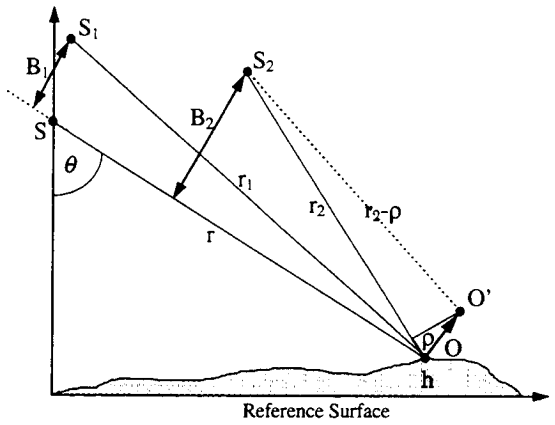

Fig. 3: Geometry of the D-INSAR.

In order to generate the D-INSAR deformation pattern from the rather complex SAR image pairs used, we followed the algorithms and procedures described in Xia (1997). A major basis for the recovery of the baselines and the reconstruction of the scene geometry is to determine the precise PRC orbits of ERS-1 using a combination of satellite laser ranging and altimeter crossover data (Massmann et al., 1994).

Unfortunately, we could find up to now only three useful ERS-1 SLC image data sets for our study area from the orbital segments

- 19623 - April 14, 1995; acquired before the earthquake,
- 21126 - July 30, 1995; acquired just a few hours after the earthquake, and
- 22128 - October 8, 1995; two months after the earthquake.

The location of these images is shown in Figure 1.

The repetition frequency (PRF) was different for the three data takes. Therefore, data sets 21126 and 22128 were first resampled and then registered with PRF 1679.90 Hz of data set 19623. The calculated baselines and fringe frequencies are given in Figure 4. The total image size is 140 km in along-track direction and 40 km cross track.

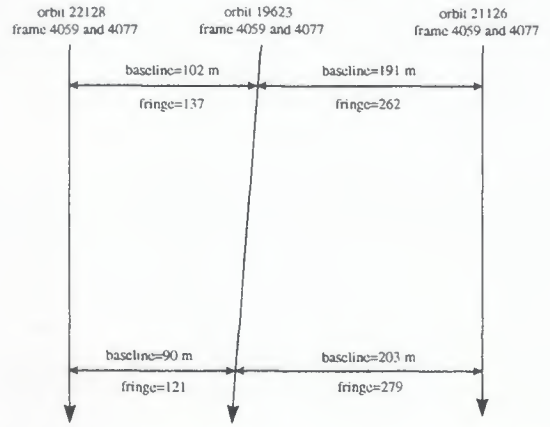

Fig. 4: Distribution of the baselines and fringes.

Because the baseline of image pair 19623/22128 is better suited for phase unwrapping, this pair was chosen for generating the reference topography. The images 19623/21126 were taken as second pair. Due to the timely distribution of the images, it is evident that in our case both data pairs are affected by earthquake-induced dislocation and that equation (1) therefore has to be modified in the same way as equation (2). This leads to the modified equation (3).

$$\left(1-\frac{B_2}{B_1}\right)\rho=\frac{\lambda}{4\pi}\left(\frac{B_2}{B_1}\Phi_1-\Phi_2\right) \qquad (4)$$

The $(1 - B_2/B_1)$ scaling factor of the change ρ is in our case approximately 3 (B_1 = -96 m, B_2 = 197 m). Thus the phase difference of 2π in the differential interferogram will correspond to a displacement of 0.9 cm in slant range direction.

Fig. 6 displays the radar intensity and the Interferometric fringe images. Fig. 7 shows the coherence image, the differential interferogram with the topography removed and representing the deformation in slant range direction, and the topography derived from data pair 19623/21126 from which the displacement term was removed. A few facts become immediately evident from these pictures. The dark stripes in the coherence image indicate unstable operation of the SAR sensor (orbit 22128, frame 4059). The orientation of the Interferometric fringes is considerably perturbed by the crustal deformation. The differential interferogram clearly shows that the deformation increases from the top to the bottom of the image.

5. COMPARISON OF D-INSAR AND GPS-DERIVED DEFORMATION

From its spatial resolution D-INSAR is a one-dimensional observation technique whereas GPS provides three-dimensional position information. To compare results from both techniques we projected the GPS-derived 3D-displacement vectors into slant range direction using the precise orbital positions of ERS-1 as computed by the D-PAF. Figure 5 shows two „deformation in slant range" surfaces, one from D-INSAR and one derived using the interpolated GPS data. They coincide largely. Five GPS points 0, 3, 4, 34 and 2014 are located in the processed D-INSAR deformation image (Fig. 7). Direct comparison of results from both techniques is hence possible for these sites. In order to further test the D-INSAR results we extrapolated the resolving deformation patterns beyond the lower bound of the image, i.e., to the south where the GPS stations 1 and 6 are located. Table 1 includes a comparison of results for these seven points.

Station Nº	GPS absolute	GPS relative	D-INSAR relative	Difference
0	-25.09	0	0	0
3	-5.32	197.7	189	8.7
4	-27.25	-21.6	-18	-3.6
2014	-19.56	55.3	54	1.3
1	6.43	315.2	about 300	15.2
6	-25.27	-1.8	about -1	-0.8
34	3.86	289.5	282	7.5

Table 1: Comparison of displacement results from GPS and D-INSAR (all in slant range direction in mm).

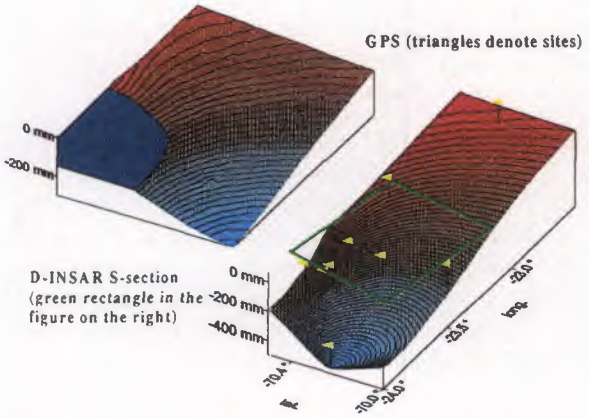

Fig. 5: Comparison of D-INSAR and GPS derived deformation in slant-range direction.

The average difference for the directly comparable points 0, 3, 4, 2014 and 34 is 5 mm and for the extrapolated points less than 20 mm.

The deformation patterns derived using both techniques coincide, suggesting that a major part of the resulting deformation happened between April 14 and July 30 and

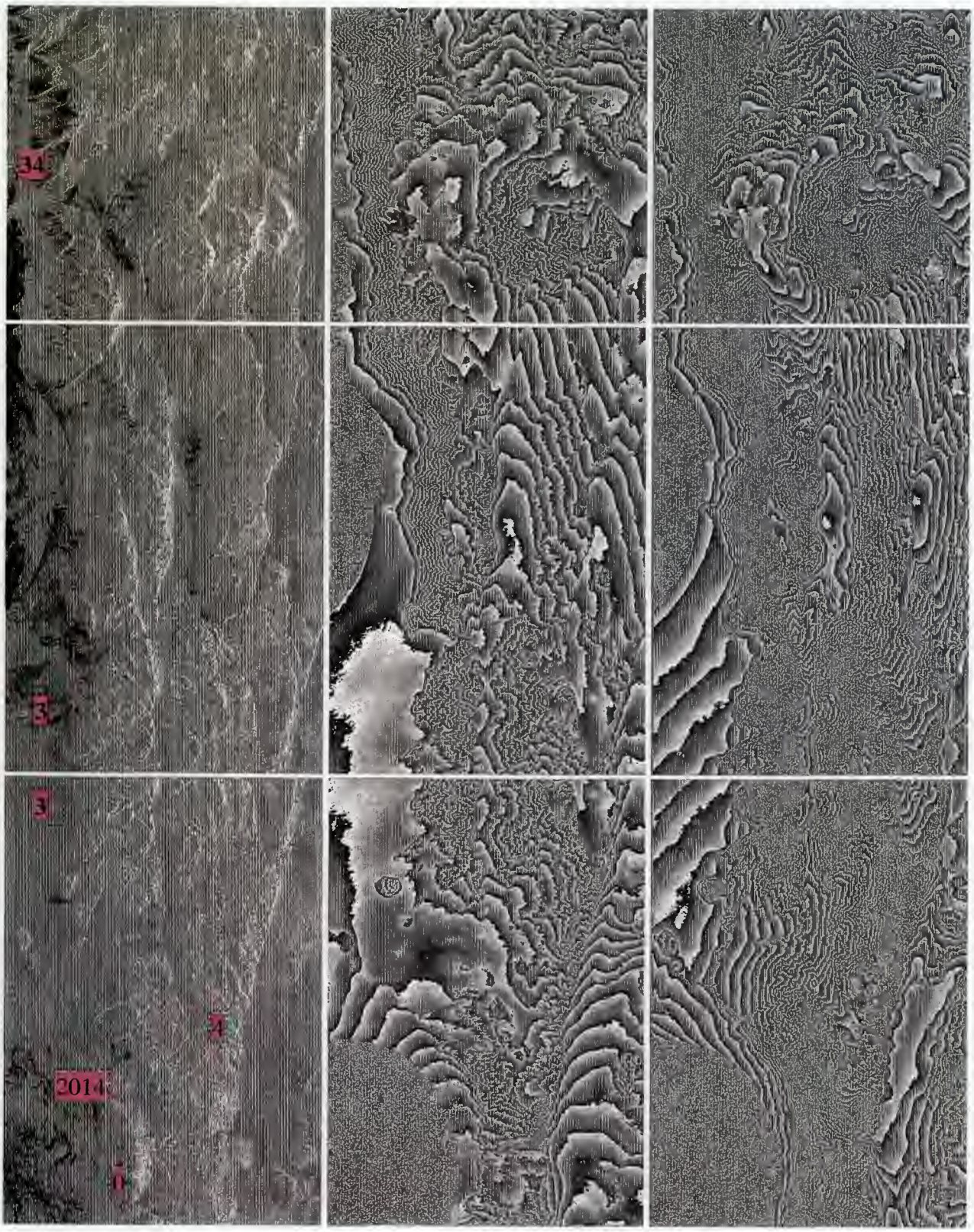

Fig. 6: Intensity and fringe images.

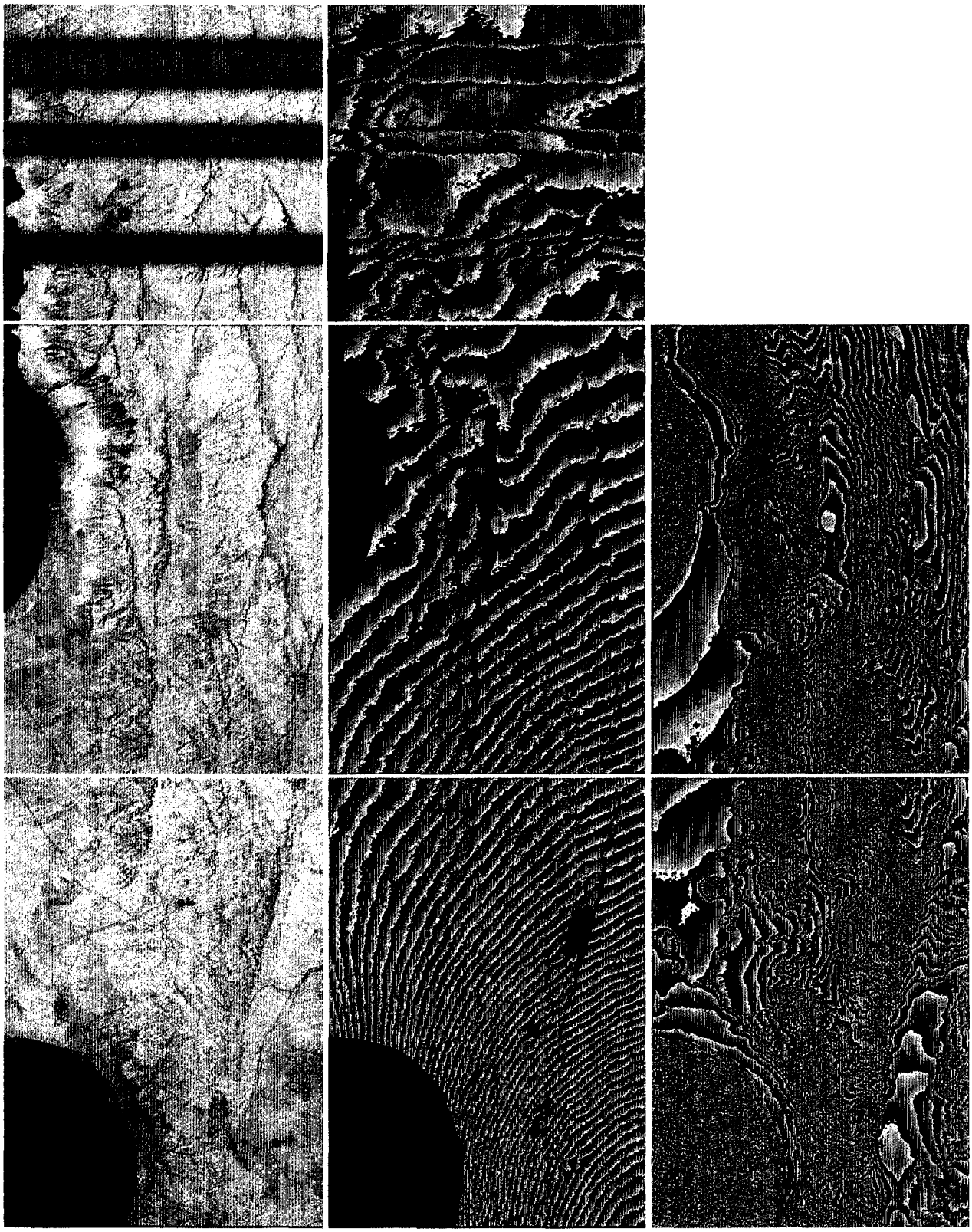

coherence (19623/22128)

deformation (0.9 cm per fringe)
derived from 19623/22128
and 19623/21126

topography (50 m contour)
derived from 19623/21126
and differential interferogram

Fig. 7: coherence, deformation and topography images.

hence is co-seismic. However, we cannot exclude that a minor part of the deformation is not related to the event but indicates pre-seismic or inter-seismic straining or a-seismic deformation. We suggest that the eastward directed movements detected at the northernmost and southernmost GPS stations (Fig. 2) indicate apparent inter-seismic accumulation of deformation prior to the earthquake event. Further studies are necessary to distinguish long-term straining from short-term event-induced deformation.

Only minor perturbations were found in the D-INSAR fringes. In addition, deformation patterns interpolated using the GPS-derived motions suggest that the major part of the deformation was fairly homogeneous. Second-order movements along crustal faults triggered by the major quake are therefore not depicted by the data. Minor perturbations, which are evident in the fringe patterns, correlate with marked changes in topography and changes in lithologies. This is especially true a) adjacent to the coast where soft coastal sediments border crystalline Jurassic volcanic rocks and b) locally within neotectonic fault zones where fine cataclastic material facilitate quake-induced sediment redeposition.

6. CONCLUSIONS

A combination of D-INSAR and GPS techniques was used to depict co-seismic deformation triggered by the Ms: 7.3 1995 Antofagasta, Chile, subduction earthquake. The 72-sites' GPS network covers an area of over 300 km normal to the Chilean trench. Results indicate significant co-seismic deformation over at least 200 km off the epicenter and normal to the trench. The D-INSAR data cover only a limited area - near the coast and adjacent to Antofagasta - where 7 GPS sites are located. Deformation patterns derived using both techniques coincide and show only minor differences. This suggests that a) the major part of the 2-years GPS-monitored deformation was co-seismic and b) co-seismic deformation was distribute almost homogeneously. The latter is backed up by the fact that movements along second-order crustal faults, which might have been triggered by the major quake, were not detected. We are not yet able to distinguish between long-term accumulation of deformation and event-triggered release. Applying both techniques, their high accuracy and low relative differences in motion encourage us, however, to use these techniques further-on to quasi-monitor the expected elastic inter-seismic accumulation of deformation as well as the post-seismic visco-elastic deformation expected. The latter embraces information on the rheology of the crust and upper mantle and about the long-term emergence of the Coastal Cordillera. Monitoring future deformation will be especially interesting in the north of the study area where an earthquake has long been expected. In spite of the high earthquake magnitude, damage was low in the area of Antofagasta. This can be explained partly by the behavior of the underground. We think that the high-resolution D-INSAR deformation data entangle further information on the quake-induced behavior of the underground and soil and may thus - together with GPS -in future directly assist hazard assessment studies.

Altogether, the results obtained so far are encouraging for various modeling groups within GFZ and motivated us to start operation of the 4 m mobile ground station recently purchased by DLR and GFZ. First measurements were conducted in Cordoba/Argentina in January 1997. ERS-1 SAR data have already been processed and will be integrated into our studies of the post-earthquake surface deformation processes. In addition, we will soon install a few corner reflectors in the study area to increase the recovery accuracy of the image geometry and the GPS station identification in the images (<1 pixel).

7. REFERENCES

Angermann, D., G. Baustert, J. Klotz, J. Reinking, S.Y. Zhu: Hochgenaue Koordinatenbestimmung in großräumigen GPS-Netzen. Allgemeine Vermessungs-Nachrichten, Heft 5, Wichmann-Verlag, 1996.

Beutler, G., I.I. Mueller & R. Neilan: The International GPS Service for Geodynamis (IGS): The Story, Proc. IAG Symposium No 115, Springer Verlag, 1996, ISBN 3-540-60872-6.

Compte, D. & M. Pardo: Reappraisal of great historical earthquakes in the Northern Chile and Southern Peru seismic gaps. Natural Hazards, 4, 23-44, 1991.

Klotz, J., J. Reinking & D. Angermann: Die Vermessung der Deformation der Erdoberfläche, Geowissenschaften, 14, 389-394, 1996.

Masonnet, D., M. Rossi, C. Carmona, F. Adregna, G. Peltzer, K. Feigl & T. Rabaute: The displacement field of the Landers earthquake mapped by radar interferometry, Nature, 364, 138-142, 1993.

Massmann, F.-H., Ch. Reigber, R. König, J.C. Ralmondo & C. Rajasenan: ERS-1 orbit information provided by D-PAF. Proc. 2nd ERS-1 Symp. - Space at the Service of our Environment, Hamburg, Oct. 1993, ESA SP-361, 765-770, 1993.

Nishenko, S.P.: Seismic potential for large and great intraplate earthquakes along the Chilean and southern Peruvian margins of South America: A quantitative reappraisal, J. Geophys. Res., 90, 3589-3615, 1985.

Papadimitriou, E.E.: Long-term earthquake prediction along the western coast of South and Central America based on a time predictable model, PAGEOPH, 10, 301-316, 1993.

Reigber, Ch., Y. Xia, H. Kaufmann, F.-H. Massmann, L. Timmen, J. Bodechtel & M. Frei: Impact of the Precise Orbit on the SAR-Interferometry, Proc. ESA Workshop on the Applications of the ERS SAR Interferometry, Zürich, 1996.

Xia, Y.: Processing of SAR data from the mobile DLR/GFZ antenna, GFZ Scientific Technical Report, 1997 (in prep.).

Zebker, H., P.A. Rosen, R.M. Goldstein, A. Gabriel & Ch. Werner: On the derivation of coseismic displacement fields using differential radar interferometry: The Landers earthquake, J. Geophys. Res., 99, 19617-19634, 1994.

EARTHQUAKE HAZARD ZONATION IN THE LAKE CONSTANCE AREA — CONTRIBUTION OF SATELLITE RADAR (ERS-1, SIR-C) - DATA

Barbara Theilen-Willige

Birkenweg 2, D-78333 Stockach, Germany
phone and fax: +49 7771 1868

ABSTRACT

The integrated analysis of geologic and seismologic data, field observations, lineament data derived from satellite radar images (ERS-1, SIR-C) data from Southwest-Germany, especially the Lake Constance Area, allows a better understanding of the tectonic setting and a more detailed identification of fault zones. Especially the **lineament anlysis** of satellite radar data contributes to the tectonic inventory. Comparisons of lineament maps with **seismotectonic data** suggest that some of the most prominant visible lineament zones are deap-seated structures. Determining the location of faults and main fracture zones and estimating their influence on seismic waves is an important component of seismic risk analysis. The lineament analysis of satellite radar contributes to a better knowledge of the **influence of local structural conditions on seismic wave radiational propagation** and **on ground motions**. As potentially hazardous secondary effect earthquake triggered landslides might occur as reported from the 16 Nov 1911- event. The detailed interpretation of satellite radar data allows the detection of lineaments that are coincident with fault and fracture systems influencing **slope instabilities.** Comparison of slope gradient maps of the northwestern Lake Constance Area with radar imageries derived lineament maps help to delineate areas objected to landslides.

1. INTRODUCTION

Although awareness of earthquake risk has been increasing on the part of scientists and engineers, the scope and magnitude of the problem is not yet fully understood by local and regional public officials responsible for implementary land use policy. Estimating the likelihood of seismic hazard and the degree of damage is essential for damage mitigation planning as certain lifeline facilities such as oil, gas and water pipelines and electrical and telephone transmission lines can be equipped with means for limiting damage.

Investigations of groundstructure interactions form the necessary basis for the analysis and evaluation of the earthquake damage risk (Ahorner & Rosenhauer, 1993). Damage resulting from an earthquake varies spatially. Within the same zone of shock intensity, the damage may vary locally, being a function of both the type of structure and ground conditions, as for example of faults and fractures, lithology or ground water table. Seismic waves traveling in the subsurface will be refracted at sharply outlined discontinuities as for example faults, and, thus, arrive at a summation effect that might influence the damage intensity. Earthquake damage can be amplified by guided seismic waves along fault zones. Precise delineation of those faults can be a veritable input to seismic risk analysis.

The present study is an attempt to integrate various data sets (satellite radar data, seismotectonic data, geologic and geomorphologic field data) to obtain a general better understanding of the tectonic setting and to improve earthquake vulnerability maps. Aim of this study is to investigate the contribution of satellite lineament analysis for the detection of fault zones being of importance during an earthquake.

One purpose of this study is to research the possible relationships presented in Fig.1a and b:

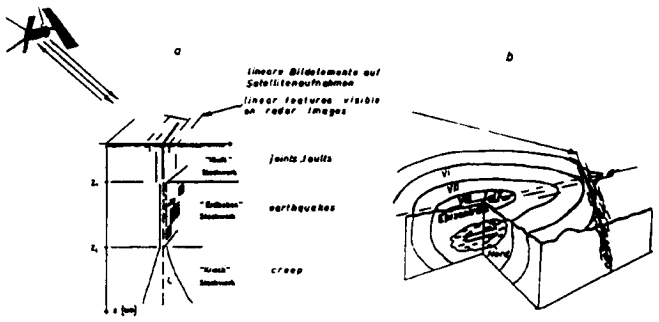

Figure 1a. Possible relations of linear features visible on radar-images to fault planes in the subsurface (according to Schneider, 1996, modified)
Figure 1b. Detectability of linear features on radar imagery tracing tectonic discontinuities as faults, fractures, etc. that might influence seismic wave propagation

Proc. 3rd ERS Symp. on Space at the service of our Environment, *Florence, Italy, 17-21 March 1997* (ESA SP-414, 3 Vols., May 1997)

Fig.1a illustrates a situation which would be optimal for radar image interpretation and evaluation of radar derived lineament analysis: The rupture pattern might be the result of a spatio–temporal evolution due to repeated earthquakes. It is reasonable to hypothesize that the fracture pattern occurs in response to stress from one or more seismotectonic significant events: The fault planes causing earthquakes are traced by fractures and faults and, thus, are visible as linear features on the radar images. This situation can be find especially in areas where earthquake related faults are visible at the surface as for example in California. In many areas the situation is not as clear as shown schematically in Fig.1a. It cannot be excluded, however, that repeated earthquake shock influences successively the fracture pattern of surficial rocks (Schneider, 1996).

Fig.1b shows schematically a situation where lineament analysis might contribute to the detection of faults influencing the contour and degree of seismic shock.

Reducing damage in areas subject to one or more **earthquake–induced processes** (landslides, displacements, etc) involves **hazard zonation** or mapping. These hazard maps form a necessary base for seismic safety planning. The use of radar lineament mapping is investigated to detect zones of weakness (faults, fractures) controlling movements of slopes, especially signs of possible further instabilities.

2. GEOTECTONIC SETTING

Southern Germay as a tectonic and seismo–tectonic unit has a shape of a triangle, bordered by the following structures: the Upper Rhinegraben in the west, the Prealpine Molasse basin in the south and the Bohemian Massif in the northeast. Beginning with the Swabian Jura earthquake in 1911 the seismic activity in the Central Europe is concentrated to this area. As far as it can be seen from historic records from the time before 1800 a shock of the quality as those in 1911, 1943 and 1978 has not been observed in this area before (Schneider, 1979, 1980, 1996). As can be deduced from fault–plane solutions, the prominent type of seismotectonic motions consists of horizontal strike slip motiones along NNE or NW directions (Fig.2). From the distribution of epicenters and the orientations of fault planes it is possible to conclude that the axis of main principal stress is oriented about NNW (Schneider, 1980, Gruental & Stromeyer, 1995).

3. RADAR LINEAMENT ANALYSIS

ERS–1 data as well as SIR–C – L–, C– and X–Band data from the Überlingen test site were used for lin-

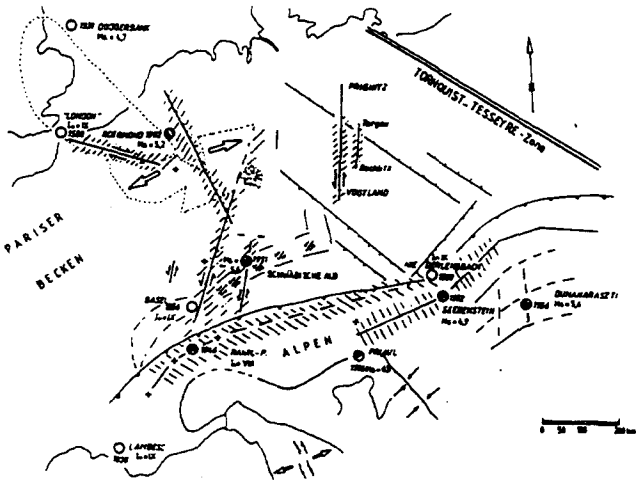

M_s= surface wave magnitude, M_l= local magnitude,
I_o= epicentral intensity, R= radius of perceptibility

Figure 2. Directions of largest principal stresses in central Europe and earthquakes according to Schneider, 1996

eament analysis. (The term lineament is a neutral term for all linear, rectilinear or slightly bended image elements.) Lineaments often represents the surface expression of faults, fractures, lithologic discontinuities, etc. .

3.1 Evaluation of ERS–1 DATA

The ERS–1 radar satellite has taken several complete SAR coverages from entire Germany. The processing of the data was done in the German Processing and Archiving Facility (D–PAF) at the German Remote Sensing Data Center (DFD) of the DLR/ Oberpfaffenhofen. The geocoded terrain corrected SAR images are the basic input data set for the generation of mosaics, the Radarmap Germany (Kosmann *et al.*, 1994). The precise gecoding procedure guarantees a geometic accurancy of 30 m.

The nature of the linear traces visible on ERS–1–image mosaics from SW–Germany varies along strike and is represented by some combinations of linear steep valleys, especially in the Black Forest Area, and depressions, linear hydrographic features and drainage segments, linear hills, ridges and abrupt ending straight scarp lines. Available geologic and geophysic data indicate correlations of the distinct expressed lineaments with fault zones in the subsurface. Comparisons of lineament maps with seismotectonic and aeromagnetic data suggest that some of most prominent lineament zones represent deep–seated structures as for example the Hegau–fault zone (Theilen–Willige, 1996). The pattern of linear features corresponds to the tensional stress field

known in this area. Radar imageries from SW–Germany, thus, provide essential clues to the tectonic setting. The radar images allow an interpretation of lineaments and of structural trends that would have been impossible from field mapping alone. This is demonstrated by an ERS–1– image from Southwest–Germany (Fig.3) and ERS–1–derived lineament map (Fig.4). The lineament map is combined with the representation of known epicenters. Epicenters are concentrated predominantly in areas of crossing lineaments (Theilen–Willige, 1995). According to Schneider (1993) agglomerations of seismic activity are related to intersecting fault zones. There are agglomerations of sesmic foci near the intersectings between fault–zones striking with an angle of maximum shear stress considering the recent orientation of the tectonic stress field.

Until recently few attempts have been made to correlate seismic events to known surface faults and to study possible relationship between large seismic events and structural framework in this area. Comparisons of focal mechanisms with local neotectonic structures in the Lake Constance area and in northern Switzerland have shown in many cases a good correlation between the orientation of nodal planes of the fault plane solutions and the orientation of fault systems observed at the surface (Pavoni, 1987, Smit, 1989).

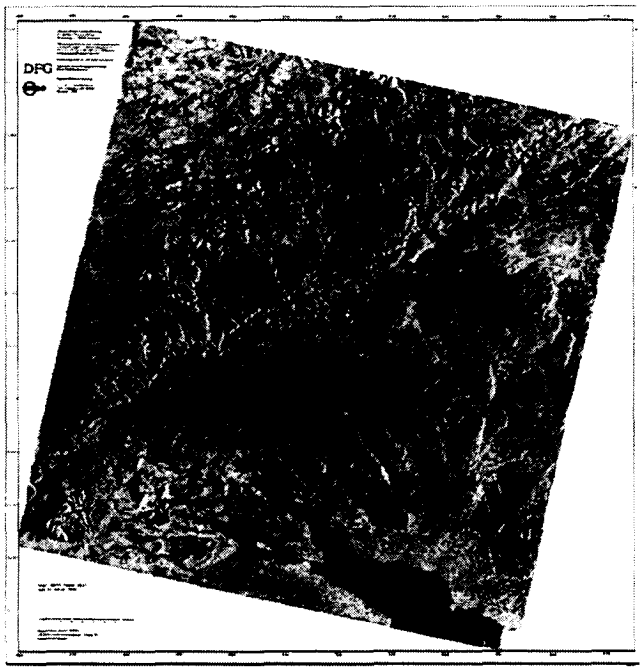

Figure 3. ERS–1 satellite radar image (22 Jan 1995) of southwest Germany

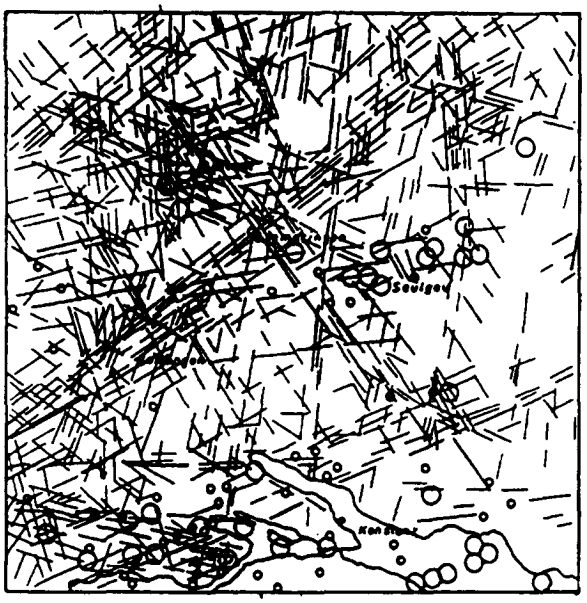

Figure 4. Comparison of earthquake epicenter distribution with ERS–1 image derived lineaments (Map of epicenters: Bundesanstalt für Geowissenschaften und Rohstoffe, Hannover, 1991, Deichmann, N., ETH Zürich, 1996, person. commun.)

3.2 Evaluation of SIR–C–L and C–Band and X–SAR–Data

Shuttle Imaging Radar (SIR–C) data, L– and C–Band, have been provided by NASA's Jet Propulsion Laboratory (JPL), SIR–C Radar Data Center, Pasadena (USA) and SIR–C – X–Band data by DLR, DFD, Oberpfaffenhofen. Based on the SIR–C–data (L– and C–Band, HV, and X–Band, VV, Überlingen test site) from the northwestern Lake Constance area, Überlinger See, a lineament analysis has been carried out. Different amplifications of the radar imageries were interpreted to see the influence of scale on the manifestation of lineaments as 1 : 200.000, 1 : 100.000 and 1 : 50.000. Fig.5 shows the SIR–C–Band image, Fig.6 the derived lineament map. To identify the mapped lineaments, the lineament maps were compared with topographic and geologic maps.

Although the area is covered by vegetation radar return is more influenced be the local topography and SAR viewing geometry. Most of the linear features visible in the SIR–C–radar imageries, especially C– and X–Band, correspond to linear morphologic units as linear valleys, linear scarps or hills.

For the structural inventory radar illumination is a limiting factor, as for example in this case N–S striking geologic features are suppressed and therefore the lineament inventory based on SIR–C data alone must

be incomplete. To get a complete inventory of the structural setting an additional analysis of other data sets is neccessary as for example geologic maps and of structural field data. Comparing the SIR–C – C–Band lineament map with geologic maps it is clearly detectable, that some faults identified in the field are expressed as lineaments on the radar image. This is confirmed by field check of features seen on the radar imageries. Correlations of tectonic inventories in the field with mapped lineaments show a clear coincidence between the strike and position of prominent lineaments on the radar imageries and the strike of faults or principal strike directions of the fracture system. This seems to justify the assumption that many of these linear features correspond to geologic features as fractures and faults.

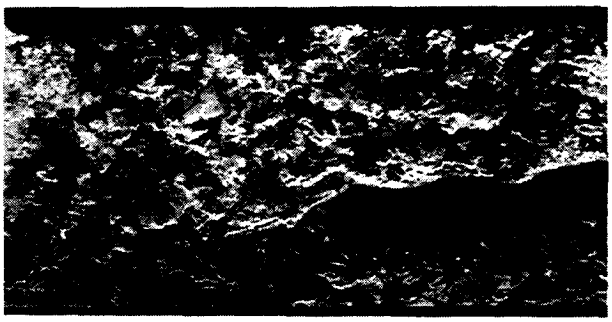

Figure 5. SIR–C – C–band (HV) imagery from the Überlingen test site (NASA/JPL, Radar Outreach Program, USA, April 1994, digital image enhancement by Ch. König, BVBK, Dießen, 1996)

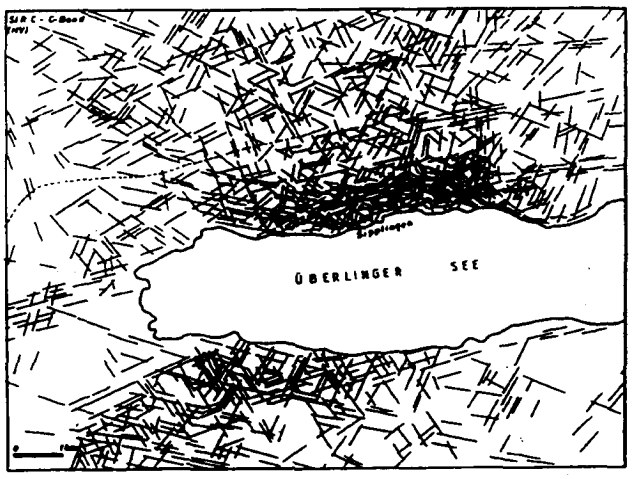

Figure 6. Lineament maps based on SIR–C data of the Überlingen test site — SIR–C – C–band (HV) derived lineament analysis

4. COMPARISON OF ISOSEISMAL MAPS WITH LINEAMENT MAPS

Lineament maps derived from interpretation of ERS–1–data and SIR–C–data were compared with available macroseismic observations of stronger earthquakes (intensities of 7 to 8 on the MEDVEDEV–SPONHEUER–KARNIK–Scale). As an example is shown the isoseismal map of the 3. September 1978 event (Fig.7). The correlation and combination of the 3. September 1978–isoseismal map with the ERS–1 derived lineament map clearly indicates that **areas of high damage intensities are related to surface traces of larger faults and to areas with a dense lineament pattern** . The more affected areas are concentrated where larger lineaments are crossing.

Lineament evaluations based on the different SIR–C–data of the Überlingen test site at the northwestern border of the Lake Constance were compared as well with isoseismal maps of earthquakes occuring during the last decades of the Lake Constance area. These maps have been provided by the Geophysical Survey of Baden–Württemberg / Freiburg. It is obvious that stronger affected areas correspond to areas on the lineament maps with distinct expressed lineaments crossing each other (Fig.8). The contours of areas with higher damage intensities on the isoseismal maps seem to be influenced by structural patterns in the subsurface.

5. LANDSLIDES

In the northwestern part of the Lake Constance area landslides cover a wide variety of landforms as rockfall, rockslide (translational and rotational slide), debris slide and even earth flow. Landslides occur after nearly every wet season of the year, often activated when the water table is high. However, casualty and damage statistics pertaining to landslides are very fragmentary.

it is documented that landslides have been triggered by seismic shock in this area: **Slope–instabilities developed in the superficial quaternary deposits and tertiary Molasse sediments during the 16 Nov 1911– event demonstated the existence of potentially hazardous secondary effects of earthquakes in this area** as rockfalls and rockslides (Sieberg & Lais, 1925).

The movements of slopes in this area are structurally controlled by surfaces or planes of weaknes, such as faults, joints and bedding planes. The steep slopes bordering the northwestern Lake Constance / Lake Überlingen consist of tertiary Molasse sandstones containing many prominent open fractures

Figure 7. Combination of the Swabian Jura – earthquake (3 Sep 1978) macroseismic map for main shock in southwest Germany (MSK–scale, Schneider, 1992) and the ERS–1 mosaic (radarmap) derived lineament map

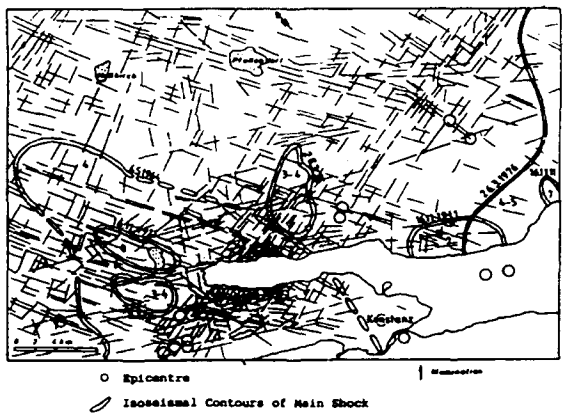

Figure 8. Comparison of isoseismal maps of the Lake Constance area with SIR–C / X–SAR imagery derived lineament maps; areas of main shock during seismic events clearly correspond to areas with distinct expressed lineaments.

and faults. A careful search to locate areas with close spacing of faults and joints, especially where they cross, helps to look for evidence of possible continued movement. The most significant sign of possible futher instability is the presence of cracks on the crown of slopes. SIR–C– imageries have been investigated to detect lineaments or curvilinear features in the areas of the headwall scarps in order to find traces of possible failure surface–traces. The lineament map based on the SIR–C – C–Band (HV)–imagery is represented in Fig.6.

Fig.10 shows a combination of a SIR–C – C– and L–Band lineament analysis and a slope gradient map. This combined representation provides important clues for delineating landslides. Movements can be detected in the field exactly in those areas where prominent lineaments cross steep slope areas.

Environmental pollution as a consequence of broken pipes after a strong earthquake is one of greatest problems in a densely populated and industrialized area. Surveying of piplines that might be affected by earthquakes or earthquake induced effects as for example landslides, liquefaction or displacements is important for the maintainance of supply. Water of the Lake Constance is needed for the supply of more than 3,5 million people.

Updating and digitalization of all available piping documentations, integrating the data into existing digital topographic map and at least comparing them with ERS–1/2– and SIR–C satellite–radar derived lineament maps is an important step toward seismic hazard prevention measurements.

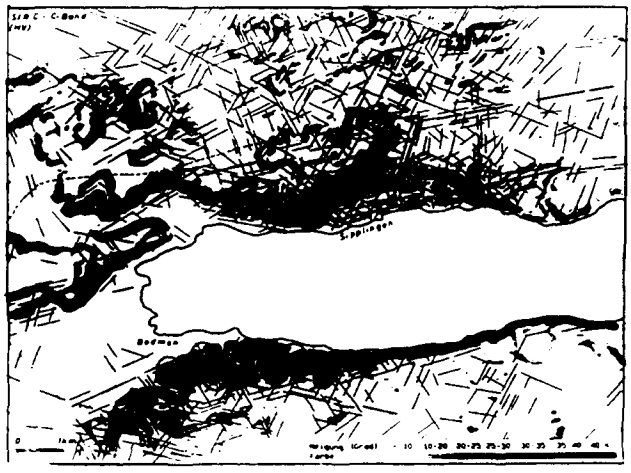

Figure 9. Slope gradient map of the northwestern Lake Constance area combined with the SIR–C – C–band lineament map to delineate areas objected to slope failures

—— linear features visible on the radar image

⬭ areas objected to land slides

CONCLUSIONS

Lineament analysis based on satellite radar data contributes essentially to the tectonic inventory.

In comparison with the available ERS–1–data from the Lake Constance area SIR–C–data provide a more

accurate representation of lineaments mainly because its higher resolution and viewing geometry, whereas ERS–1–data provide a valuable overview about the tectonic setting. Lineament analysis based on SAR imageries can help to delineate local fracture systems and, thus, provide informations about types of seismic wave motion associated with earthquakes. When lineament maps based on ERS–1– and SIR–C–data are merged with isoseimal maps, the correlation of sub–surface structural information with the damage intensity occuring after earthquake shock contributes to a better delineation of hazard prone areas.

The combined interpretation of satellite radar data and isoseismal maps improves the understanding of the influence of local soil and structural conditions on seismic wave radiational propagation and on ground motions .

Lineament analysis provides important clues for delineating slope failures as probable secondary effects of stronger earth– quakes.

ACKNOWLEDGEMENTS

The author is indebted to the German Research Association (DFG)/Bonn for financial support and a grant. Prof. Dr. G. Schneider, Institute of Geophysics, University of Stuttgart is kindly acknowledged for supplying literature and base maps and for helpfull discussions. Dr. W, Bruestle, Geophysical Survey, Freiburg and Dr. N. Deichmann, ETH Zürich are acknowledged for delivering geophysical data as isoseismal maps and epicentre maps. The author thanks H. Runge and D. Kosmann, DLR, Oberpfaffenhofen, E.O. Leary, JPL, California for providing ERS–1– and SIR–C–/ X–SAR–data and SIR–C– L– and C–band – data. Dr. Ch. König, Bildverarbeitungs–Büro König, Dießen, is acknowledged for the digital image enhancement.

REFERENCES

Ahorner, L., Rosenhauer, W. 1993, Seismische Risikoanalyse. *Deutsche Forschungsgemeinschaft (Hrsg.): Naturkatastrophen– und Katastrophenvorbeugung — Bericht zur IDNDR* VCH–Verlag, Weinheim, pp. 177–190.

Gruental, G., Stromeyer, D. 1995, Rezente Spannungsfelder und Seismizität des baltischen Raumes und angrenzende Gebiete — ein Ausdruck aktueller geodynamischer Prozesse. *Brandenburgische Geowiss. Beitr.*, **2**, No. 2, Berlin, pp. 69–76.

Kosmann, D., Winter, R., Sties, M., Wiggenhagen, M. 1994, Mosaicing and Classification for the Radarmap Germany. *Proceed. Second ERS–1 Symposium — Space at the Service of our Environment, Hamburg,* 11–14.10.1993, ESA SP–361, Noordwijk, pp. 629–633.

Pavoni, N. 1987, Zur Seismotektonik der Nordschweiz. *Eclogae geol. Helv.*, **80**, No. 2, Basel, pp.461–472.

Schneider, G. 1979, The Earthquake in the Swabian Jura of 16 Nov 1911 and Recent Concepts of Seismotectonics. *Tectonophysics*, **53**, Amsterdam, pp. 279–288.

Schneider, G. 1980, Seismic Stresses in Southern Germany. *Rock Mechanics Suppl.***9**, pp 69–73.

Schneider, G. 1992, Erdbebengefährdung. *Wissenschaftliche Buchgesellschaft* , Darmstadt, 167 pages.

Schneider, G., 1993, Beziehungen zwischen Erdbeben und Strukturen der Süddeutschen Groß–Scholle. *N.Jb. Geol. Palaeont. Abh.*, **189**, Nos. 1–3, Stuttgart, pp. 275–288.

Schneider, G. 1996, Erdbebengefährdung in Mitteleuropa — Hinweise aus Geodäsie und Gravimetrie auf Scherzonen mit seismischem Bewegungscharakter. *Deutscher Verein für Vermessungswesen*, **43**, No. 1, March 1996, Stuttart, pp. 47–56.

Sieberg, A., Lais, R. 1925, Das mitteleuropäische Erdbeben vom 16.11.1911, Bearbeitung der makroseismischen Beobachtungen. *Veröffentl. Reichsanstalt für Erdbebenforschung Jena*, H.4, Jena.

Smit, P. 1989, Seismotektonische und aeromagnetische Untersuchungen in der Region Ramsen (Kanton Schaffhausen). *Diplomarbeit an der Abt. für Naturwiss.*, ETH Institut für Geophysik, Zürich.

Theilen–Willige, B. 1995, Erdbebengefährdung im Bodenseegebiet. *Geowissenschaften*, **13**, No. 2, Berlin, pp. 40–46.

Theilen–Willige, B. 1996a, Satellitenaufnahmen Südwestdeutschlands und der Bodenseeregion als Hilfsmittel bei der Erfassung erdbebengefährdeter Bereiche. *Publ. der Deutschen Gesellschaft für Photogrammetrie und Fernerkundung (DGPF)*, **4**, Vorträge 15. Wissenschaftl. Techn. Jahrestagung, 4–6.10.1995, Universität Hannover, Hannover, pp. 63–74.

Theilen–Willige, B. 1996b, Seismic Risc Analysis in Southwest Germany Based on Satellite Radar Data. *Intern. Archives of Photogr. and Remote Sensing*, **XXXI**, Part B7, Vienna 1996, pp. 705–708.

DETECTION OF ASEISMIC CREEP ALONG THE SAN ANDREAS FAULT NEAR PARKFIELD, CALIFORNIA WITH ERS-1 RADAR INTERFEROMETRY

Charles L. Werner, Paul Rosen, Scott Hensley, Eric Fielding, and Sean Buckley
Jet Propulsion Laboratory,4800 Oak Grove Drive, Pasadena, California *

ABSTRACT

Parkfield, California lies an area along the San Andreas fault in Southern California that has experienced strong earthquakes at apparently regular intervals in historic times. Differential interferometric analysis of ERS data of this region reveals the wide-area distribution of creep along the moving fault segment over a 15 month interval. Removal of the interferometric phase related to the surface topography was done by simulation of an interferogram in the absence of motion given a topographic map of the region. A sharp phase discontinuity in the differential interferogram is equivalent to approximately 1.5 cm change in the line of sight. This displacement is consistent with current models of motion along the fault. We compare the observed phase signature with a predictions of the differential phase based upon the Okada model for elastic deformation. The ERS differential interferometric data are compared with a 6 month differential interferogram collected by the NASA SIR-C L-Band instrument in 1994.

1. INTRODUCTION

Parkfield, California lies an area along the San Andreas Fault (SAF) in Southern California that has experienced moderate earthquakes at apparently regular intervals in historic times [Bakun and Lindh 1985]. It is a site of intense study in anticipation of a significant earthquake ($M_w > 6$) that according to predictions appears long overdue [Roeloffs 1994]. Such an event is expected because the section of the San Andreas Fault northwest of the town of Parkfield, measured by conventional geodetic methods, is creeping aseismically at a rates consistent with the right lateral secular plate motion, whereas these data also strongly suggest a region beneath Parkfield that is locked and has accumulated a slip deficit greater than the displacement that occurred in the 1966 earthquake [Harris and Segall 1987].

ERS-1 has clearly demonstrated the capability to map earthquakes, [Massonnet et al. 1993] and [Peltzer and Rosen 1995], post seismic rebound, [Peltzer et al. 1995], as well as volcanic deformation, such as at Kilauea in Hawaii [Rosen et al. 1996]. Based on the earlier work on coseismic detection of motion, we proposed to attempt detection of aseismic creep along the San Andreas Fault.

The San Andreas fault is divided into several major sections. The Parkfield segment of the fault is a section of the North American-Pacific plate boundary. Below depths of 10 to 20 km the Pacific and North American plates have a secular motion of 3.5 cm/year. North of Parkfield, aseismic slip and small shocks account for the plate motion, while south of the town, infrequent large earthquakes ($M_w > 7$) release stress buildup. The last time there was motion on this segment of the fault was the 1857 Fort Tejon earthquake. Parkfield lies in the transition zone and because of constraints on the length of fault rupture in this region, is the site of moderate earthquakes that occur at shorter intervals. Earthquakes of approximately M_w 6 have occurred on 2 February 1881, 3 March 1901, 10 March 1922, 8 June 1934 and 28 June 1966. Based upon statistical analysis of these past events, Parkfield has been the site of a concerted monitoring effort in anticipation of an earthquake that was to have occurred before 1993. Careful measurements of the fault motion have been made using creep meters, two-color geodimeters, and GPS receivers. These in-situ data are an ideal data set for comparison with the creep and deformation measurements derived from ERS-1 repeat track interferometry. The high spatial sampling density of SAR interferometry may give additional insight into the distribution of strain for transition zone.

ERS interferometric analysis must often contend with significant temporal decorrelation. In order to detect fault creep long time intervals between data acquisitions are required such that measureable displacements can occur. While the short ERS wavelength of 5.66 cm has good sensitivity to displacements, small scale surface changes arising from vege-

*This work was carried out by the Jet Propulsion Laboratory, California Institute of Technology, under a contract with the National Aeronautics and Space Administration

tation and precipitation can completely decorrelate a scene [Zebker and Villasenor 1992]. The region around Parkfield is semi-arid and the hope is that correlation over long time intervals should be present.

2. ERS-1 AND SIR-C DATA PROCESSING

Criteria for selection of the ERS data scenes for Parkfield was a combination of interval between acquisitions and the baseline length. The catalog of interferometric baselines supplied by ESA were searched to find combinations acquisitions with time durations exceeding 6 months and with baselines less than 200 meters. Data were ordered from frames 2871 and 2889 and orbits including 4180, 5182, 10192, and 11194. The most promising interferometric pair was 4180 and 10192 covering a time interval of 420 days and a perpendicular baseline B_{perp} of only 3 meters. Starting with the raw ERS data, SLC images were produced to maximize the interferometric correlation by choosing a common doppler centroid. An interferogram was produced using standard processing algorithms [Zebker et al. 1994].

The interferometric phase is a combination of topographic and displacement related components. If the phase trend associated with the curved earth is removed, then the interferometric phase is given by:

$$\phi_{flat} = -\frac{4\pi}{\lambda} B_{perp} \frac{z}{r_0 \sin\theta_0} + \frac{4\pi}{\lambda}\delta_r \qquad (1)$$

where λ is the wavelength, r_0 and θ_0 the slant range and look angle at the center of the scene respectively, and δ_r the motion of the surface along the line of sight between data acquisitions [Rosen et al. 1996]. For this interferometric pair the sensitivity to displacement is 1.0×10^5 the sensitivity to topography. None the less, the topographic contribution to the phase must be subtracted to detect any fault creep.

The interferometric simulator described in [Rosen et al. 1996] was used to generate a synthetic interferogram of the ERS frame using USGS 30 and 90 meter DEMs as input. The simulated interferogram has continuous phase, and does not require phase unwrapping. After precise corregistration and resampling the simulated interferogram relative to the ERS interferogram it can be can be subtracted leaving the residual phase containing the deformation or creep signature. Tropospheric water vapor contributes significant noise on the order of 2π radians to the 2-pass differential interferogram [Goldstein 1995]. The only effective means, at present, for removal of the tropospheric water vapor phase distortion is by averaging of multiple interferograms. The differential interferogram from our single pair is shown in Fig. 1.

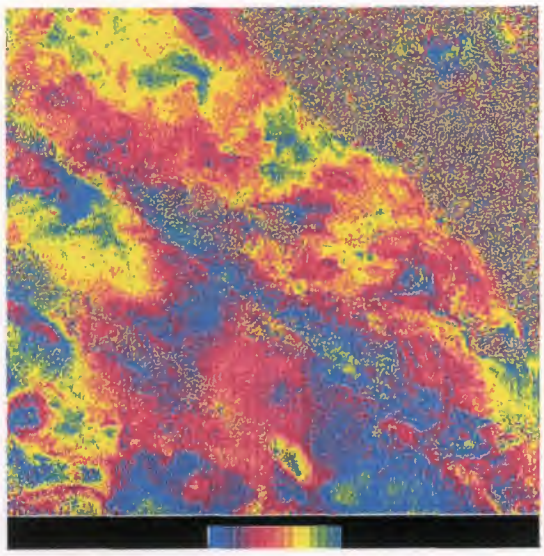

Figure 1: ERS-1 differential interferogram of San Andreas Fault slip near Parkfield California. One color cycle corresponds to a fault motion of 2.84 cm. along the line of sight. Image covers ERS-frame 2871 from orbits 4180 and 10192.

Temporal decorrelation of th data places this data set at the limits of what can be processed. The interferometric correlation coefficient was extremely low (< 0.2) over much of the scene such that only by a extensive averaging could the creep signature be made visible. A new variable resolution filtering algorithm [Goldstein and Werner 1997] was applied that makes use of the fact that the fringe spectrum is generally narrow band relative to the uncorrelated noise spectrum. In this algorithm, the normalized interferogram is divided into 32x32 patches. Each of the patches $S(x,y)$ is Fourier transformed to give $S(u,v)$ and then weighted by the scaled magnitude of the spectrum:

$$\tilde{S}(u,v) = |S(u,v)|^{\alpha} S(u,v)\ . \qquad (2)$$

The filtered signal is obtained by inverse Fourier transform of the filtered patch $\tilde{S}(u,v)$. The output image is formed by summing overlapping filtered patches using triangular window weighting in both range and azimuth. The interferogram filtered using the new algorithm had significantly better resolution and fringe visibility compared with the interferogram filtered using a fixed resolution smoothing kernel.

Similar processing was performed for tracks of the SIR-C radar that crossed the Parkfield fault zone with a 6 month interval (April and October) be-

tween passes in 1994 [Rosen et al. 1996]. Data were acquired at both C- and L-Band, but only the L-Band data had sufficient coherence to be of any value. These data were processed similarly as the ERS data and mosaiked into the ERS scene. One of the advantages of the 2-pass simulation approach to differential interferometry is that geocoding of the data once the simulation has been performed is a simple because the correspondence between the image and topographic map can be stored as a mapping file. Once the data are geocoded, different passes and tracks can be merged. In this case the ERS and SIR-C were mosaiked and then compared.

3. SAN ANDREAS FAULT SLIP MODEL

The Parkfield deformation modeling was performed using a finite-source dislocation buried in an elastic half-space [Feigl and Dupre 1996] based upon the original work by Okada [Okada 1985]. Specifically, the model was used to determine the component of the displacement field in the direction of the radar line-of-sight direction. One cycle of the color wheel corresponds to 28.4 mm of surface deformation in the radar line-of-sight direction.

The creep meters used in the modeling were located at Slack Canyon (xsc1), Middle Mountain (xmm1), Parkfield (xpk1), Work Ranch (wkr1), Carr Ranch (crr1) and Gold Hill (xgh1). The creep meters were assumed to be co-located with the SAF such that their positions could be used to defined fault segments. Specifically, the fault segments were defined by the creep meter locations as follows:

segment i Easting = creep meter i Easting (x)

segment i Northing = creep meter i Northing (y)

segment i length = $sqrt(x^2 + y^2)$

segment i strike = atan2$(x, y) + 2\pi$

segment i dip = 90 degrees

For the northern most fault segment (which corresponded to one creep meter location), the length was set to a sufficiently large number and the strike was set to the adjacent fault segment strike.

The slip along each fault segment was modeled as two separate slip mechanisms: shallow slip and at-depth slip. The shallow slip was modeled with faults segments as defined above with depths of 14 km, widths of 25 km [Harris and Segall 1987] and right lateral fault slip rates as determined from USGS creep meter data spanning the decade 1987.22 to 1997.14

Figure 2: Simulation of ERS differential interferogram based based upon deformations predicted by the Okada model as implemented by Feigl and Dupre. Image covers ERS-frame 2871 from orbits 4180 and 10192. One fringe cycle is equivalent to a displacement along the LOS of 28.4 mm

with the secular trend removed [Langbein 1997]:

Slack Canyon (xsc1)	21.15 mm/yr
Middle Mountain (xmm1)	16.68 mm/yr
Parkfield (xpk1)	10.02 mm/yr
Work Ranch (wkr1)	8.49 mm/yr
Carr Ranch (crr1)	3.66 mm/yr
Gold Hill (xgh1)	3.45 mm/yr

The at-depth slip was modeled with a locking depth of 14 km and a right lateral fault slip rate of 25 mm/yr [Harris and Segall 1987] for all fault segments. The expected signature for the differential interferometric pair is shown in Fig. 2

4. CONCLUSIONS

The fault is clearly visible in the differential interferogram. The magnitude of the tropospheric water vapor phase distortions is greater than the signal an hinders quantitative analysis beyond order of magnitude calculations. A linear phase discontinuity, coincident with the 100 km long fault trace, is equivalent to approximately 1.5 cm change in the line of sight distance. This displacement is consistent with the model of fault motion that we have derived from the creep meter data as input to the Okada elastic deformation model.

The SIR-C data suffer also from tropospheric phase noise, and a shorter time interval. None the less, the

higher correlation over the time interval suggests that L-Band decorrelates less rapidly than C-Band. The observed phase signature is consistent with the ERS-1 results.

Quantitative analysis of aseismic creep requires multiple data acquisitions to suppress atmospheric noise. Further study of this region will require systematic processing of all candidate interferometric pairs.

References

[Bakun and Lindh 1985] Bakun, W. H. and A. G. Lindh, The Parkfield, California earthquake prediction experiment, *Science, 229,* 1985.

[Feigl and Dupre 1996] Feigl, K. L. and E. Dupre, RNGCHN: A Program to calculate displacement components from dislocations in an elastic half-space with applications for modeling geodetic measurements of crustal deformation, *Computers and Geosciences,* July 10, 1996.

[Goldstein 1995] Goldstein, R. M., Atmospheric limitations to repeat-track radar interferometry, *Geophysical Research Letters 22,* 2517-2520, 1995.

[Goldstein et al. 1988] Goldstein, R. M., H. A. Zebker, and C. L. Werner, Satellite radar interferometry: two-dimensional phase unwrapping, *Radio Science, 23,*, 713-720, 1988.

[Goldstein and Werner 1997] Goldstein, R. M., and C. L. Werner, Radar ice motion interferometry, to appear in *Proceedings of the* 3^{rd} *ERS Symposium,* Florence, Italy, 18-22 March, 1997.

[Harris and Segall 1987] Harris, Ruth A, and P. Segall, Detection of a locked zone at depth on the Parkfield, California, segment of the San Andreas Fault, *Journal of Geophysical Research, 92,* 7945-7962, 1987.

[Langbein 1997] Langbein, J., Parkfield creep meter data: detrended measurements from the past 10 years,
http: //quake.wr.usgs.gov /QUAKES/geodetic /twocolor/ creep_pkf_10yr_det.gif.

[Massonnet et al. 1993] Massonnet, D., M. Rossi, C. Carmona, F. Adragna, G.Peltzer, K. Fiegl, and T. Rabaute, The displacement field of the Landers earthquake mapped by radar interferometry, *Nature, 364,* 138-142, 1993.

[Okada 1985] Okada, Yoshimitsu, Surface deformation due to shear and tensile faults in a half-space, *Bulletin of the Seismological Society of America, 75,* 1135-1154, 1985.

[Peltzer et al. 1995] Peltzer, G., P. A. Rosen, Francois Rogez, and Ken Hudnut, Postseismic rebound in fault step-overs caused by pore fluid flow,, *Science, 273,* 1202-1204, 1996.

[Peltzer and Rosen 1995] Peltzer, G. and P. A. Rosen, Surface displacement of the 17 May 1993 Eureka Valley, California, earthquake observed by SAR interferometry, *Science, 268,* 133-1336, 1995.

[Roeloffs 1994] Roeloffs, E., The earthquake prediction experiment at Parkfield, California. *Reviews of Geophysics, 32,* 315-335, 1994.

[Rosen et al. 1996] Rosen, P. A., S. Hensley, H. A. Zebker, F. H. Webb, and E. J. Fielding, Surface deformation and coherence measurements of Kilauea Volcano, Hawaii, from SIR-C radar interferometry, *Journal of Geophysical Research 101,* 23109-23125, 1996.

[Zebker et al. 1994] Zebker, H.A., C. L. Werner, P. A. Rosen, and S. Hensley, Accuracy of topographic maps derived from ERS-1 interferometric radar, *IEEE Trans. Geosci. Remote Sens., 32,* 823-836, 1994.

[Zebker and Villasenor 1992] Zebker, H. A., and J. Villasenor, Decorrelation in interferometric radar echoes, *IEEE Trans Geoscience and Remote Sensing, 30,* 950-959, 1992.

MINING SUBSIDENCE LAND SURVEY BY SAR INTERFEROMETRY

Richard J Stow
Environmental Science Dept., Doncaster College, Waterdale, Doncaster, DN1 3EX, UK
phone:+44 1302 553 892, fax: +44 1302 553 559, email: dick.stow@don.ac.uk

Patricia Wright
Space Division, GEC-Marconi Research Centre, Chelmsford, Essex CM2 8HN, UK
phone: +44 1245 242 668, fax: +44 1245 475 244, email: patricia.wright@gecm.com

ABSTRACT

The overall philosophy of this collaborative project, between Doncaster College, RJB Mining (UK), GEC Marconi Research Centre and Matra Marconi Space (UK), is to improve the accuracy of subsidence prediction models implemented in the mining industry. These models help mine management, in terms of productivity, conformity with regulatory consent, and minimised environmental and economical impacts. However, the models currently produce actual to predicted subsidence results in the range 43%-773%, which then have to be adjusted using local knowledge. The project aims to provide accurate data on elevation change due to mining activity, via the application of radar interferometry with ERS synthetic aperture radar (SAR) data. These elevation change data can then be fed into subsidence models to improve predictions about subsidence. Initial interferometry results are presented showing evidence of subsidence. Validation is underway and preliminary interpretations are offered and discussed.

Keywords: SAR, Radar, Interferometry, Differential Interfeometry, Mining Subsidence.

1. INTRODUCTION

The Bonn Experiment [Ref. 1] demonstrated the capability of SAR interferometry to measure surface movement to centimetre resolution under experimental conditions. It is desirable to extend this to more realistic operational situations where ground motion occurs. Due to the relative predictability and continuity of mining subsidence compared to natural tectonic movement, and the availability of precision ground survey data, there is an unequalled opportunity to use mining subsidence to validate interferometric techniques for measuring surface movement and advance them a step further towards operational application.

In the UK, mining subsidence is typically limited to 1 metre by planning consent. The dynamics of subsidence involve vertical movement, spreading beyond the worked panel at around 37° and to a depth of about 70% of its thickness. Variation in subsidence rate occurs due to inconsistency of geological formations, rock mechanical properties and the overall uniqueness of the situation. The dynamics of mining subsidence are difficult to model; the industry standard [Ref. 2] is applied largely by use of generalised graphs, which are usually empirically derived from observation, with the results adjusted by local experience. Computer models are generally based on input parameters of seam thickness, depth of mining, and amount and direction of seam gradient. The reliability of this modelling is extremely variable, with reported actual to predicted subsidence results in the range 48-773% [Ref. 3]; these results have to be adjusted by local knowledge. Part of this can be accounted for by the empirical nature of the models which makes them highly sensitive to the accuracy and extent of survey data available.

Currently, mineral surveyors conduct line surveys of subsidence along roads and canal banks, which represent a very small proportion of the area of influence of the mine working, and this small sample size contributes to the wide variation in modelling results. Remote sensing data has the potential to improve modelling subsidence accuracy by significantly increasing the quantity of feedback data compared to that available by traditional survey methods.

ERS SAR data, used in conjunction with SAR interferometry techniques (in particular differential interferometry) may be able to provide such information to the mining industry with a potential elevation change resolution of the order of 1cm and horizontal resolution of about 20m. However, the technique is not yet proven, and the project aims to investigate whether SAR data can provide elevation change information at the level of confidence required by the mining industry. Once this has been established, it is intended that subsidence maps be produced that can be linked into appropriate subsidence models, the results of which can be

compared with subsidence predictions based solely on line survey data.

2. DIFFERENTIAL INTERFEROMETRY

The use of differential interferometry is aimed at the detection and measurement of small scale surface movements. The technique commonly involves the generation of two interferograms from three images [Ref. 4], one interferogram spanning some surface change, the other a 'reference'. The former is expected to contain fringes due to the terrain and the surface movement, whereas the latter contains terrain fringes only. By differencing the two interferograms, the terrain effects can be removed from the "surface" change measurement, leaving only the effects of the surface movement. It is also possible to use a single interferogram, encompassing the surface change, and a reference digital elevation model (DEM) from some other source to remove the terrain effects from the data [Ref. 5]. In addition, it is likely that where topography and baseline are favourable, terrain correction will not be necessary, and therefore a single interferogram will suffice for "differential" interferometry.

3. TEST SITE AND GROUND DATA

The project intends to study two sites, the Selby Coalfield in the UK, where subsidence is limited to 1m, and the Silesian coalfield in the Czech Republic, where up to 40m subsidence has been experienced from cumulative working of coal seams. Work is currently concentrated on the Selby site in order to demonstrate the capability of ERS data to detect and measure mining subsidence. The site occupies a predominantly flat river plain, with the majority of terrain under 10m, and is covered in arable farm land. The Selby site is preferred to establish a capability, as detailed ground data exist, which have been made available by RJB Mining. These data consist of maps of mined areas, dates of mining activity, subsidence measurements acquired along survey lines, and subsidence predictions. In an area of concern, lines surveys are typically acquired every 6 months and measurements are made to millimetric accuracy. Once a subsidence monitoring capability has been established, it will be applied to the Silesian site.

4. IMAGE DATA

Both 35 day repeat and tandem ERS single-look complex (SLC) data are available to the project for interferogram generation. In selecting the initial data for interferogram generation, the following criteria were applied to optimise interferogram coherence.

1. Interferometric baseline under 200m.
2. Temporal separation 35 days or less.
3. Acquisitions between September and March.
4. No rainfall during or immediately before acquisition.

The SLC data is processed using the interferometric processor developed at MRC [Ref. 6]. This processor facilitates the rapid production of large area interferograms and performs complex image registration, interferogram generation and formation of associated interferogram products, such as DEMs, differential DEMs and coherence maps. Developed under the Application Visualisation System (AVS) environment, the processor is highly flexible, in that it can be rapidly reconfigured to include enhanced processing steps such as the addition of new phase unwrapping algorithms, but it is also easy to use, with a range of "standard" networks for interferometric processing.

5. INTERFEROMETRY RESULTS

To date, two tandem pairs and one 35 day repeat pair of ERS SLC data have been processed at MRC. Initially, effort has been concentrated solely on interferogram generation and analysis for these three data sets, in order to determine if subsidence can be detected and measured. Due to the baselines selected and the low relief of the terrain at the Selby site, it has not been necessary, so far, to remove terrain effects from the "surface change" interferogram using a reference data source.

The 35 day repeat interferogram was generated using data from February and March, 1993, with a baseline of -161m. A small section of the interferogram is shown in Figure 1. The data has been filtered to improve the phase statistics and is represented in approximately ground range with 50m horizontal resolution. Although the data has been acquired outside the growing season, coherence is relatively low due to the length of separation between the two images, but provides coherent coverage of more than 50% of the site.

Interest here is focused on the circular, concentric fringe features. By comparison with ground data, it has been established that these do not correspond to terrain features. A colour cycle in this image corresponds to an elevation change of about 50m, implying that we would have to be seeing a terrain feature several hundred metres in height, when the highest elevation in the image is only about 20m.

The features themselves are quite localised (about 500m in horizontal scale) and regular in shape and would therefore appear not to be due to atmospheric effects or any residual geoid effects that might be visible. The circular features have been visually compared with areas of known mining activity and the locations compare well, suggesting that they are probably due to ground subsidence.

Each fringe in a subsidence feature represents a surface movement of 28mm in the radar look direction. Some of the features have evidence of three or more fringes, suggesting a surface change of about 8cm in 35 days. Features with at least one fringe are clearly visible in the image, provided that they occur in relatively coherent regions, indicating that the vertical measurement accuracy is at least of the order of a few centimetres, given favourable coherence conditions, or better given ideal conditions.

Two pairs of tandem data have also been processed and analysed; although the interferogram coherence is far superior to the 35 day repeat data, no obvious subsidence features can be seen. It is probable that the amount of subsidence occurring in a 24 hour period at the Selby site is too small to be detected by this technique (we might expect 2.3mm of subsidence in 24 hours, based on 8cm in 35 days).

6. VALIDATION RESULTS

The interferometric phase image (Figure 1) shows a number of distinctive concentric fringe features, which after geocoding to mine working drawings and Ordnance Survey 1:25000 maps have been shown to align precisely with areas of mining activity up to and including the acquisition dates. These phase data can be converted to elevation changes by phase unwrapping.

The close up phase image of the largest subsidence feature (Figure 2), geocoded to a 1:10560 Ordnance Survey map and overlaid with a mine workings plan (without surface detail), shows two sets of fringes centred on mining activity between two satellite passes. Active seams (H430 and H626) during the period of image coverage are illustrated in Figure 3, with dates and locations of the working face also marked. In particular, the records of progress in coal extraction of panels H430 and H626 show a close correlation to the fringe position. That is to say that the fringe centres occur at the location of the working face of the panel. For instance, in seam H430 the working face was almost at the end of the panel (these panels were worked north-west to south-east), reflected in the location of the fringe centre, whereas in seam H626 the working face had not passed the half way stage, which is again reflected in the fringe centre

The east-west asymmetry of the outer fringes is explained by residual subsidence from panels visible to the east, especially panel H623, which was completed at its southern end in July 1992, 7-8 months prior to the satellite passes. Residual subsidence typically continues for a year (sometimes longer) after mining has ceased.

A north westward vector in the fringes is caused by residual subsidence behind the working face on the productive panels. The displacement of the fringe centres from the panel centre line is generally concurrent with expected subsidence displacement of around 50m in the direction (75°) of the strata dip in this area. However, there is unexplained variance in the degree of subsidence above the two active panels; subsidence is greater at the centre of panel H626 compared to panel H430 (approximately 2.25 fringe cycles and 2 cycles, corresponding to 63mm and 56mm, respectively). This difference may be explained by variance in productivity, relative position along the panels of the two active areas or by the proximity of previously worked seams.

Unfortunately, for this image pair there is no surface survey data available close to the acquisition dates and so quantitative validation of the amount of subsidence is not possible.

7. CONCLUSIONS AND FUTURE DIRECTIONS

Initial results suggest that mining subsidence can be detected using 35 day repeat SAR data and SAR interferometry techniques, and that this subsidence can be measured at the very least to an accuracy of a few centimetres. However, there would appear to be a central dilemma in applying this technique. A balance needs to be found between a useable temporal separation between images (in terms of interferogram coherence) and allowing a suitable length of time to lapse for a measurable amount of subsidence to occur.

From the results so far, it is also clear that it is unlikely that the tandem data can be used to *directly* measure surface change in the UK. However, it may be the case that at the Silesia site, tandem data will reveal subsidence effects due to the greater amount of subsidence occurring. In addition, tandem data has an important role to play in providing reference terrain information when terrain effects have to be removed from the surface change data.

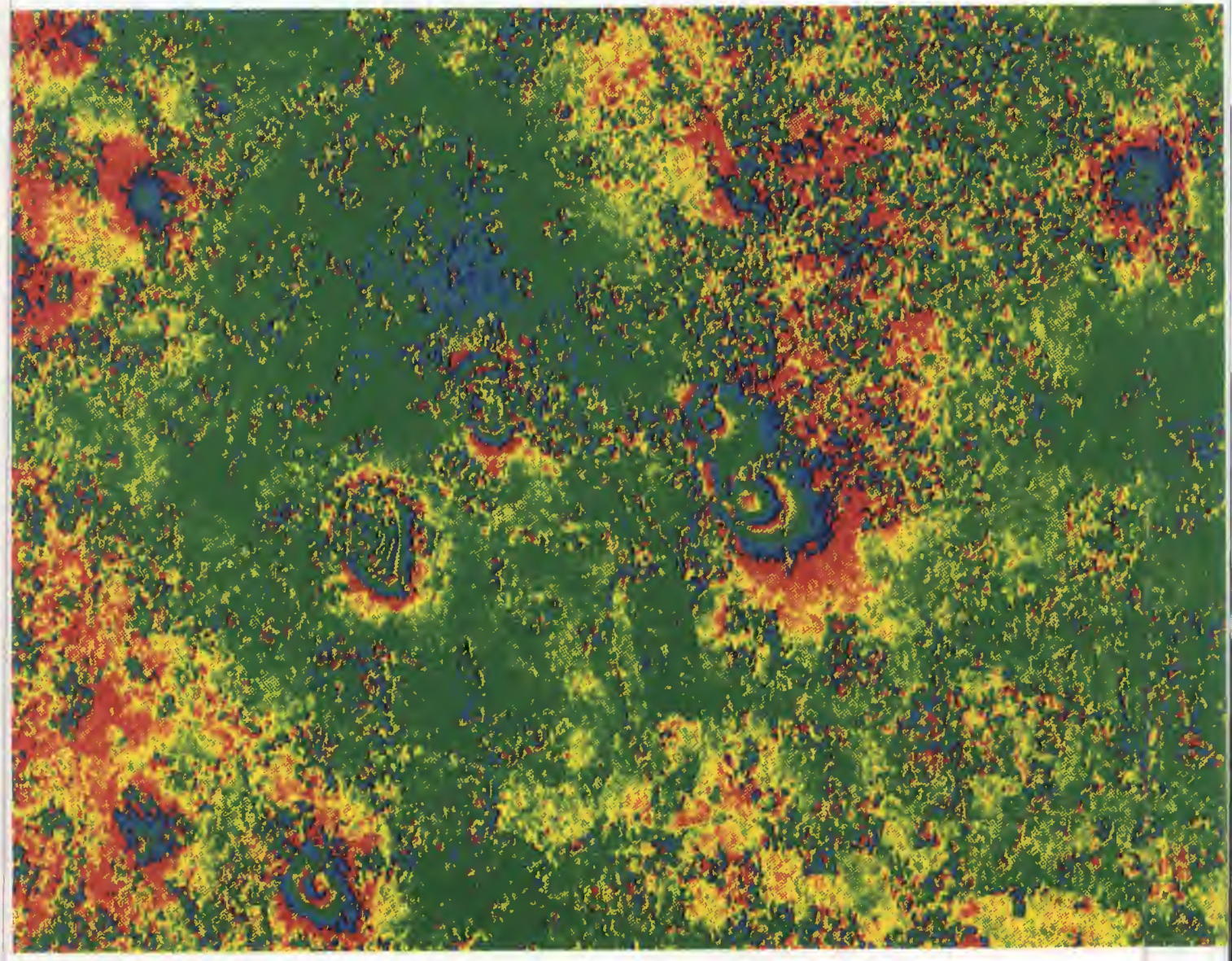

Figure 1 Portion from a phase image of the Selby test site (generated using ERS SLC data from 12/2/93 and 19/3/93) showing interferometric fringes corresponding to mining subsidence.

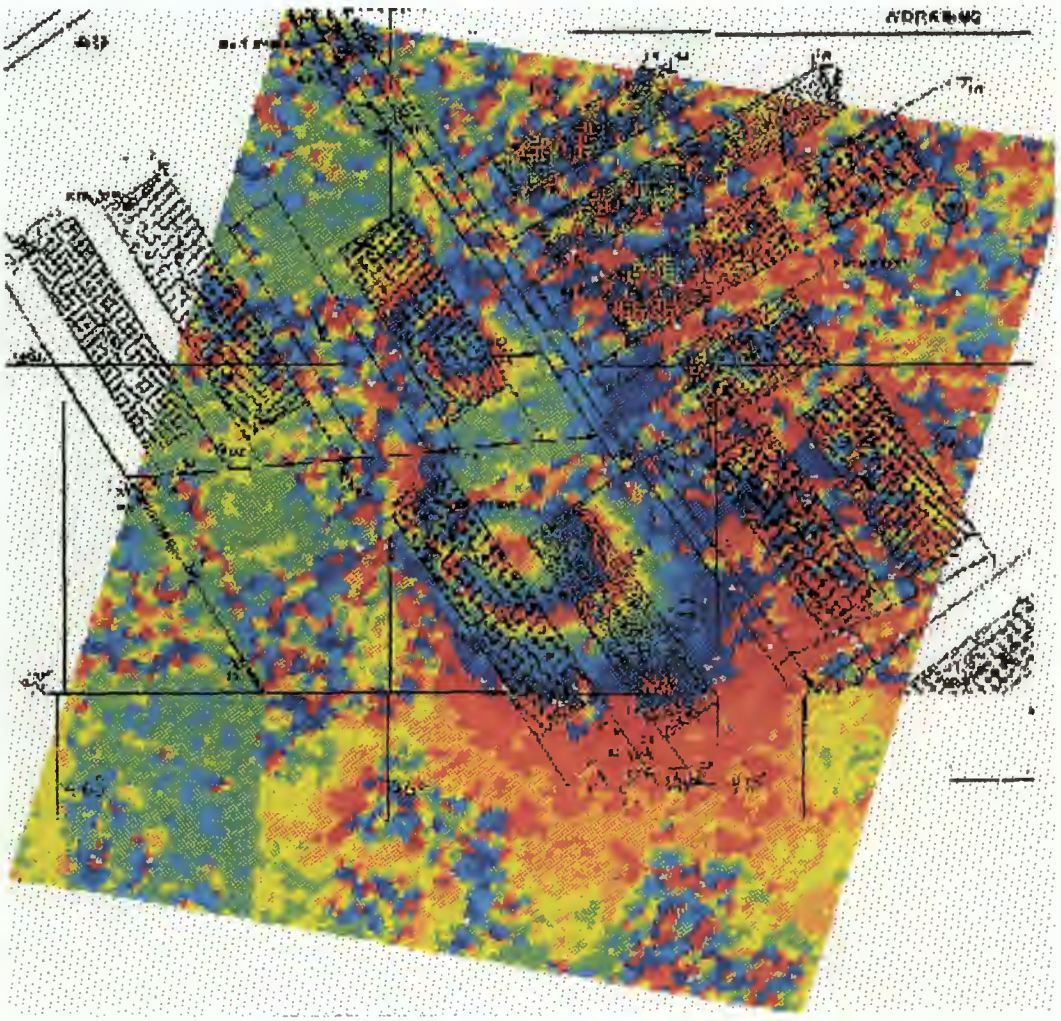

Figure 2 Geocoded interferometric fringe features from a small portion of Figure 1, overlaid with mine working plans showing mine panels and a roadway.

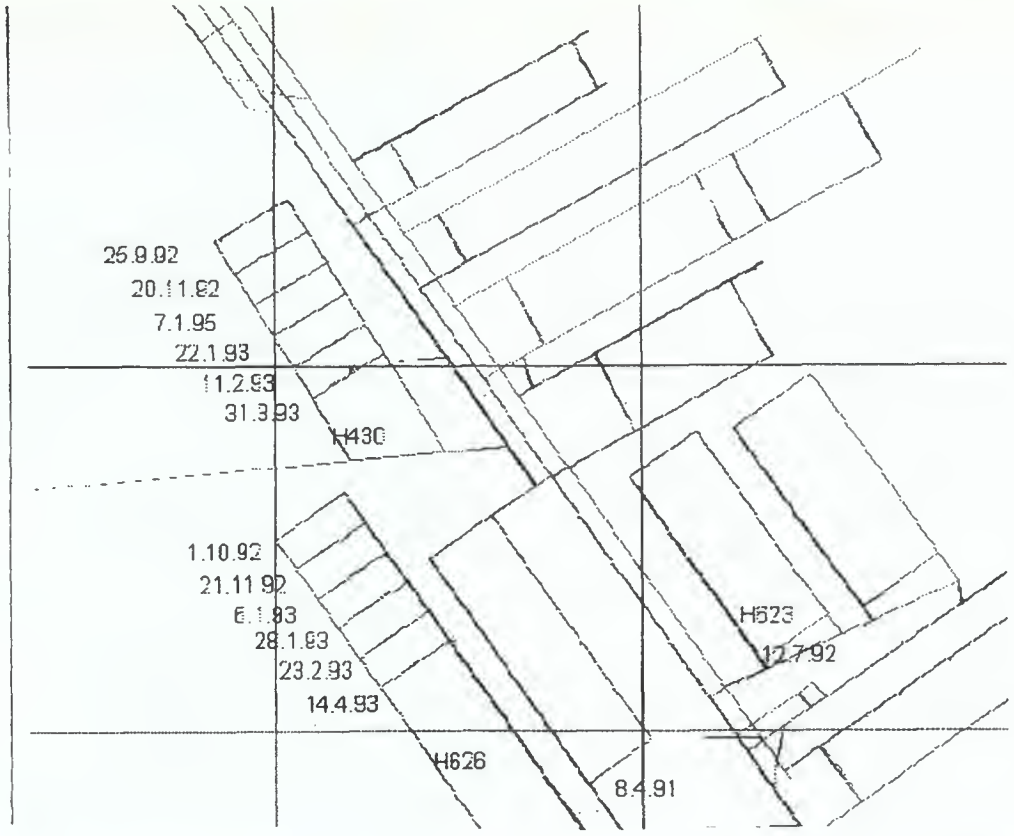

Figure 3 Plan of mine workings with date and position of the working face indicated for active seams.

We are pleasantly surprised at such positive results in the 35 day repeat data, given the reduced levels of coherence (for this site) which result from such a long repeat interval. This gives encouragement that a mission with an appropriate repeat interval might be an effective tool for detailed routine monitoring of ground subsidence.

Work will continue on producing and validating surface change measurements for the Selby site. The issues of all year coverage, extended temporal measurements (i.e. covering a 6 month period) and optimal image temporal separation for accurate and reliable subsidence measurements will be addressed. Once a capability has been firmly established, it will be applied to the Silesian coalfield site.

In order to carry out a quantitative evaluation of subsidence measurements using this technique, ground surveys, at Selby, of currently productive mine areas have recently been carried out by RJB Mining, timed to coincide with ERS data acquisition.

8. ACKNOWLEDGEMENTS

This work has been supported by the British National Space Centre (BNSC) under the BNSC Earth Observation Link Programme (project R2/002), Matra-Marconi Space and by RJB Mining. ERS SAR data have been provided by the European Space Agency under projects AO2.UK137 and AOT.UK303.

9. REFERENCES

[1] Coulson, S.N.,1992, ERS-1 FRINGE Activity Review, *Proc. of 1st ERS FRINGE Workshop*, ESA.

[2] Subsidence Engineers Handbook, 1975, *National Coal Board, Mining Department.*

[3] Ferrari, C.R., 1995, The Case For Continuing Coal Mining Subsidence Research, *Proc. of the UK Minerals Industry Conference.*

[4] Gabriel, A.K., Goldstein, R.M., & Zebker, H.A., 199, Mapping Small Elevation Changes Over Large Areas: Differential Radar Interferometry, *Journal of Geophysical Research*, 94, 9183-9191.

[5] Massonet, D., Rossi, M., Carmona, C., Ardagna, F., Peltzer, G., Feigel, K., & Rabaute, T., 1993, The Displacement Field of the Landers Earthquake Mapped by Radar Interferometry, *Nature*, 364.

[6] Partington, K.C., Rye, A.J., Wright, P.A., & Smith, P.J., 1995, High Level Software Design for the Production of Synthetic Aperture Radar Derived Digital Elevation Models, *GEC-Marconi Research Centre* MTR 95/52A.

FLOOD MAPPING USING ERS TANDEM COHERENCE IMAGE : A CASE STUDY IN SOUTHERN FRANCE

L. MARINELLI
GEOIMAGE
Les Espaces de Sophia, 80 route des Lucioles, 06560 Valbonne, France
tel: 33 4 93 00 40 00, fax: 33 4 93 00 40 01, email: dev@geoimage.fr

R. MICHEL
Commissariat à l'Energie Atomique,-DASE/LDG
91680 Bruyères-le-Chatel, France
tel: 33 1 69 26 62 76, fax: 33 1 69 26 70 23, email: michel@ldg.bruyeres.cea.fr

A. BEAUDOIN
LCT Cemagref-ENGREF
34093 Montpellier; France
tel: 33 4 67 54 87 52, fax: 33 4 67 54 87 00, email: beaudoin@teledetection.fr

J. ASTIER
BRL-Ingénierie
33001 Nîmes, France
tel: 33 4 66 87 50, fax : 33 4 66 87 51 09

ABSTRACT

Flood mapping proved to be feasible using multitemporal ERS SAR amplitude images. However, it allows to map the flood extent only at given acquisition dates, rarely corresponding to the maximal flood extent. In this paper, we report first results of a study on the use of coherence images, in order to improve the flood detection which can be difficult in some flood conditions. We focused our study on a major flood that occured in 1996 in southern France. In this area was available a large data set including water height measurements, DEM's, different thematic vector layers in a GIS and Tandem INSAR ERS images. Then, we compared the results of flood detection, obtained using respectively amplitude and coherence images, to flood simulations derived from a simple hydraulic model. We showed that coherence images should detect areas where flood-induced surface changes occured, possibly corresponding to the maximal flood extent within the repeat-pass acquisition window.

1.INTRODUCTION

Flood detection using ERS amplitude images have largely demonstrated its faisability (ESA, 1995 ; MacIntosh and Profeti, 1995 ; Oberstadler *et al.*, 1995 ; Smith, 1997). A common method relies on a multitemporal approach based on ERS false-color composites made of two or three amplitude images (Noyelle *et al.*, 1995). However, the use of backscatter amplitude is somewhat limited in some flood conditions. First, flood detection in urban and vegetated areas is poorer because of enhanced double-bounce scattering adding to the direct backscatter from the water surface (Hess *et al.*, 1990); even in open flooded areas, the usually low backscatter increases with higher surface roughness due to wind and/or strong currents. A second constraint is that the torrential type of flood, often encountered for example in Mediterranean countries, usually have a rapid dynamic. Therefore, the ERS given acquisition dates do not necessarily catch up the maximal flood extent, which is of greater interest for applications such as flood prevention through *a posteriori* validation of flood models.

In this paper, we evaluate the possible contribution of ERS INSAR correlation (degree of coherence) in order to improve the flood detection and to possibly obtain an integrated view of the flood within the INSAR acquisition window. Thus, if the flood peak occurs within this acquisition window, we could possibly detect the flood maximal extent.

2. STUDY AREA AND FLOOD EVENT

We focused our study on a major flood that occured in southern France in January 1996, in the surroudings of the town of Béziers, located in the Hérault *Département* (County). This flood was caused by heavy rainfalls during the night of January 28. In some places, 200 mm of rain felt within few hours, with rainfall rate up to 70

mm/hour. Two basins were mainly hit within the available ERS coverage : the Orb river and its affluents, and the Aude river. Several flood types occurred in these basins : 1) a violent torrential flood in the Lirou river (one of the Orb's affluent) that killed 3 persons and heavily damaged a riverside village, 2) the Orb river that was subject to a huge flood in its floodplain mainly between Béziers and the sea, and 3) the lowlands of the Aude river that were filled up to an exceptional level due to direct rain catchment. Globally, 80 villages across the whole region were declared disaster areas, with damages running into many millions of dollars.

Available data set concerning this area and the flood event includes:

- a 1 :25000 topographic numerical map (SCAN 250 © IGN) ;
- a GIS database (BD CARTO © IGN) including a DEM (50m grid) and different vector layers for roads & railways network, rivers, administrative boundaries... ;
- a fine DEM with centimetric precision over the lowlands of the Aude basin, obtained within an interdepartmental management project against floods;
- daily measurements of the water levels during the flood, starting on January 29.

Available SAR data consists of two interferometric Tandem ERS pairs. One of the pair corresponds to the flood event, where the two images were acquired respectively on January 28 & 29 1996, i.e. during and after the heavy rainfall including the flood peak. The other pair was acquired on April 7 & 8 1996 and corresponds to a low water level of rivers.

3. METHODOLOGY

From the two interferometric Tandem pairs we computed two coherence images. This was done through interferometric processing by using a Maximum Likelihood Estimator to retrieve the complex correlation coefficient :

$$\rho . e^{j\Delta\varphi} = \frac{< s_1 . s_2^{*} >}{\sqrt{< |s_1|^2 >< |s_2|^2 >}} \qquad (1)$$

where s_1, s_2 are the two complex matched images, ρ is the degree of coherence, $\Delta\varphi$ the interferometric phase and $< >$ denotes a spatial averaging. In order to improve this estimation, the degree of coherence was estimated using a sliding Hanning window with compensation of the interferogram local slope (Michel *et al.*, 1997).

Moreover, we also used the backscatter images for comparison, which were processed using a post-processing chain developed at LCT (Beaudoin *et al.* 1994). This processing was necessary as hills are found in the area, causing radiometric confusion between flooded areas and terrain slopes opposed to the radar. Images were previously filtered using a combination of temporal and spatial filtering (Bruniquel *et al.*, 1997), in order to reduce the speckle noise while preserving the best resolution. Then, slope and backscatter angular corrections were performed in order to retrieve a normalized $\sigma°$ closely equivalent to the one over a flat terrain.

Both $\sigma°$ and ρ images were then orthorectified using the 50m DEM, to put them into the Lambert II cartographic projection of the BD CARTO database, allowing to overlay SAR images to other data (drainage network for instance) for analysis purposes.

Then, $\sigma°$ and ρ images, or flooded areas extracted from image tresholding, were combined to the topography and the drainage network, allowing to create different types of flood maps. Finally, these images and space maps were compared to a simulated flood map obtained from water level measurements used in a simple hydraulic model over the 3 hydraulic compartments of the Aude basin lowlands (BRL).

4. RESULTS & INTERPRETATION

First, we present the results of flood mapping from the hydraulic model on the Aude river. Fig. 1 shows the topography of the Aude river Lowlands (shaded DEM), including a transect (white line) with related height profile of the 3 main ponds A, B and C, and measured water levels on January 29. Simulated flooded areas appear as 3 polygons in fig. 1.

In the following, we visually analyse $\sigma°$ images for January 28 & 29, included respectively in fig. 2a and 2b, and the coherence image of fig. 3, for inter-comparison and comparison with the simulated flooded area. For all three images, we included the drainage network to ease the visual analysis.

In fig. 2a, the acquisition time corresponds to the beginning of the flood. Along the Orb river, upstream from the town of Béziers, we can observe several small black patches correponding to known flooded areas. However, most of this part of the river and its affluents were known to be flooded, which can not be seen in this image. Along the Aude river we recognize the tree main temporary ponds which are already filled up to a high level. However, in the bottom left corner, we can see a very large disturbing bright patch, probably

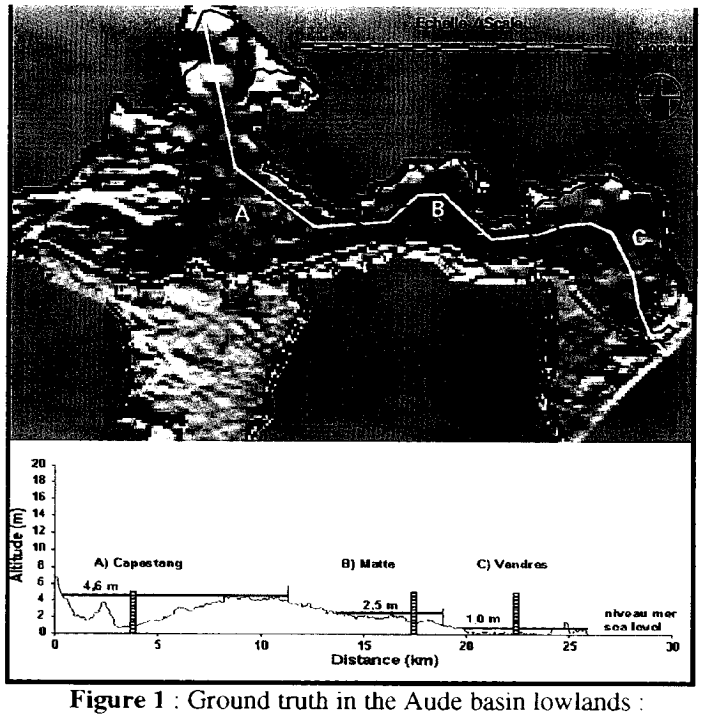

Figure 1 : Ground truth in the Aude basin lowlands :

- B&W background : shaded DEM ;
- white line : transect through the lowlands with related height profile & water levels in the bottom part ;
- 3 polygons A,B,C : simulated flooded areas from hydraulic modelling and water level measurements.

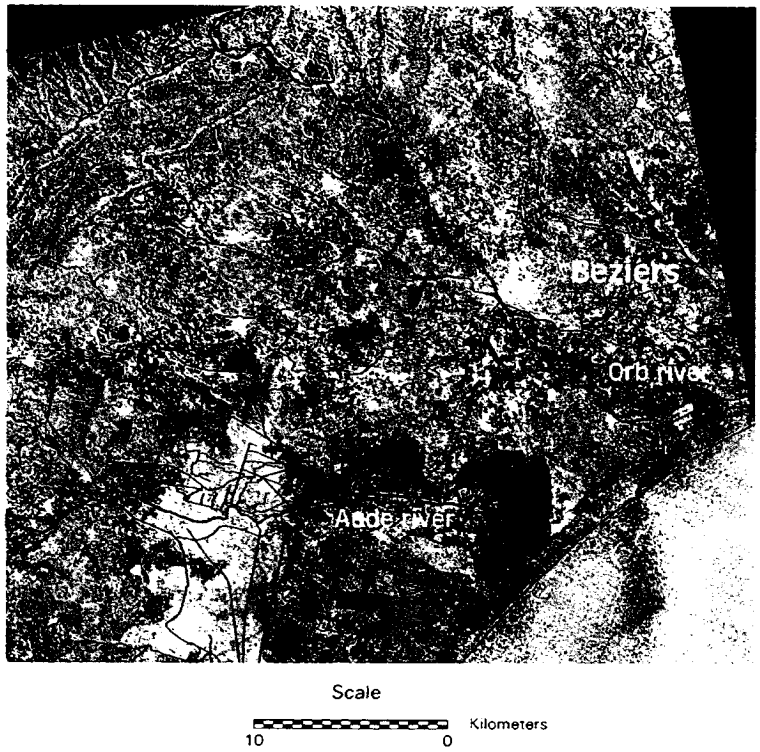

Figure 2a): ERS backscatter amplitude image (PRI) acquired over the flooded area in the Hérault *département*, southern France : January 28 at 23 pm (ERS-1) during the heavy rainfall. Black lines represent the main drainage network.

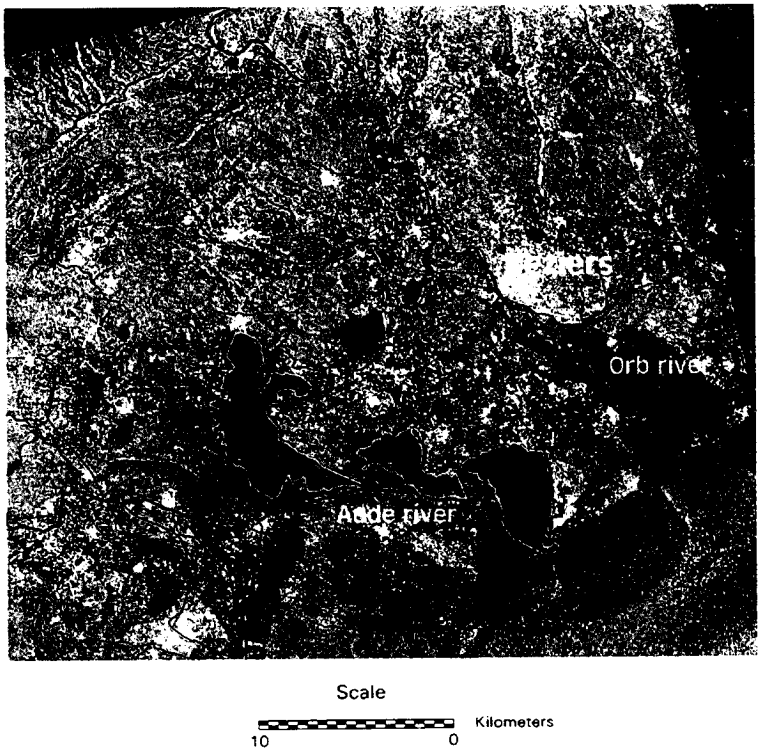

Figure 2b): ERS backscatter amplitude images (PRI) acquired over the flooded area in the Hérault *département*, southern France : January 29 at 23 pm (ERS-2) after the heavy rainfall and close to the flood peak. Black lines represent the main drainage network.

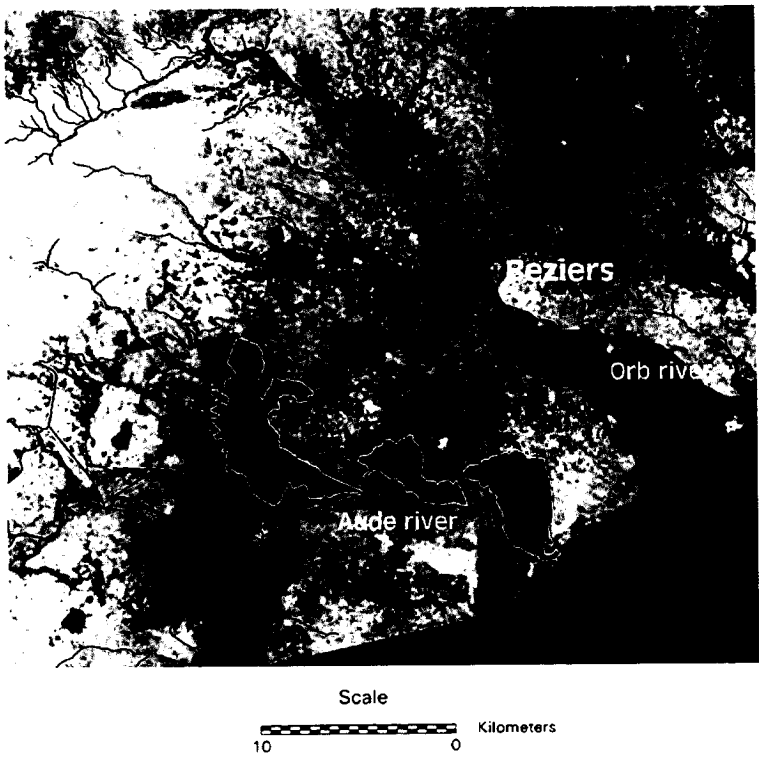

Figure 3 : Degree of coherence from INSAR ERS-1/2 Tandem acquisition on January 28_& 29 1996, including the the flood peak. Black lines represent the main drainage network.

corresponding to volume scattering from dense and big rain drops during the heavy rainfall. This hypothesis will be checked using measurements from a meteorological ground-based radar (Météo-France) that tracked this precipitation.

24 hours later in figure 2b, we can see that for the Orb river, the flood spread heavily in the floodplain down to the sea. For the Aude river, the ponds were filled up to an exceptional level from direct rain catchment. For this image, we overlaid the flood boundaries (in white) obtained from hydraulic modelling (fig. 1), to show the good agreement with flooded areas as seen by ERS.

However, several known flooded areas, as observed by rescue and hydrological services, were not detected in this backscatter image. As an example, the backscatter stay high in the western part of Béziers and in riverside villages south of it, despite heavy flooding. The same high backscatter is observed along the Lirou river where a torrential flood occured (western affluent of the Orb). Hence the interest of studying coherence images, in order to improve the flood detection.

Looking at the coherence image of fig. 3, it exhibits many areas of very low coherence for all the major rivers of the area. Compared to figure 2a and b, low coherence areas include all the dark patches found in amplitude data, indicating that the coherence also detected flooded areas. But more striking are the continuous stripes of low coherence along most rivers that were flooded, but were not detected as such, in amplitude data. This is especially visible for two rivers north-eastern of the Orb river, the Orb's north-western affuents and the small rivers upstream from the Aude Lowlands.

As a first interpretation, lost of coherence comes mainly from the temporal geometric unstabilility of the surface (Wegmuller and Werner, 1997), which is evident for 1) areas that were flooded at either one or the other date (more or less vegetated soils <--> water), or 2) areas that were flooded at both dates (moving water). Therefore, it seems that the lowest coherence in this image corresponds to flooded areas within the maximal extent for a 24 hours period. In addition, as the flood peak was luckily within this period, probably we could map the maximal extent of this particular flood.

However, some unflooded areas also show low coherence. It can be observed in the image upper left corner, where decorrelation occurs in wooded areas, due to wind-induced random movements of the scatterers (leaves and branches). Also, large areas of low coherence (but slightly brighter than those where flood occured) are observed between the rivers. We expect this to be caused by more or less soaked and dampened soils, with surface changes of the dielectric constant and roughness (moisture content, water pools, smoothing due to heavy rainfalls). Also, possible atmospheric perturbations should be considered.

Despite this, contextual visual analysis allows to distinguish flooded areas from the rest, except in areas where the edges are not clear (upper right corner).

5. PRELIMINARY CONCLUSIONS

Flood mapping using the usual backscatter coefficients gave good results in large and flat areas, as expressed by the good agreement between flooded areas derived from SAR data and those obtained from hydraulic modelling. However, the coherence image seems to do a better job for the following flood conditions encountered on our site : tall vegetation and built-up areas, windy conditions, torrential flood with strong currents or flood occuring in some relatively narrow valleys.

In addition to improved detection, Tandem INSAR coherence gave an integrated view of the flooded areas within the 24 hours window, and as the flood peak occured during this period, we can possibly map the maximal flood extent by applying simple appropriate classification methods.

Obviously, in the perspective of operational flood mapping using ERS INSAR data, the potential of 35-day repeat pass acquisitions must be addressed. In this case, it is expected that the flood detection will be poorer, as many more surface types would temporally decorrelate (farming activities in crop areas, decorrelation in tall vegetation due to wind and growth, etc). However, such a larger acquisition window would increase the chance of catching the flood peak. This will be investigated on our site.

Nevertheless, as for other recent studies in other application fields, degree of coherence from INSAR couples acquired within a short time interval appear to be an efficient and complementary SAR information source for flood mapping.

ACKNOWLEDGMENTS

Single Look Complex ERS SAR images were supplied by ESA as part of a Tandem AO (AOT.F309) and within the Earth Watching program of EURIMAGE (Roberto Biasutti). We thank the Association SIG-LR based in Montpellier, France, who provided us with information from the BD CARTO database (© IGN).

REFERENCES

ESA, 1995. Proceedings of first ERS Thematic Working Group Meeting on Flood Monitoring, ESA-ESRIN, Frascati, Italy, 26-27 June 1995.

Bruniquel, J. and A. Lopes, 1997. Multi-variate optimal speckle reduction in SAR imagery, *Int. Journal of Remote Sensing*, Vol. 18 No 3, pp. 603-628.

Beaudoin, A., M., Deshayes, L. Piet, N. Stussi and T. Le Toan, 1994. Retrieval and analysis of temperate forest backscatter signatures from multitemporal ERS-1 data acquired over hilly terrain, *1st Symposium on ERS-1 Pilot Project*, Toledo, Spain, 23-25 June 1994, pp. 283-289.

Hess, L.L., J.M. Melack and D.S. Simonett, 1990. Radar detection of flooding beneath the forest canopy : a review, *Int. Journal of Remote Sensing*, Vol. 11 No 7 , pp. 1313-1325.

MacIntosh and Profeti, 1995. The use of ERS SAR data to manage flood emergencies at the smaller scale, *Second ERS applications workshop*, London, UK, December 6-8 1995, pp. 243-246.

Michel, R., J.P. Avouac and J. Taboury, 1997. Processing low noise interferograms from ERS-1 SLC radar images, *Proc. of the 3rd ERS symposium, florence*, Italy, March 17-21 1997.

Noyelle, J., S. Delmeire and L. Marinelli, 1995. Identification of flooded areas in the Rhône and Var river, France, using ERS-1 amplitude data, *Proceedings on first ERS Thematic Working Grip Meeting on Flood Monitoring*, ESA-ESRIN, Frascati, Italy.

Oberstadler, R., H. Hönsh and D. Huth, 1995. Assessment of the mapping capabilities of ERS-1 SAR data for flood mapping : a case study in Germany, *Second ERS applications workshop*, London, UK, December 6-8 1995, pp. 247-255.

Smith, L.C., 1997. Satellite remote sensing of river inundation area, stage and discharge : a review, *Hydrological processes*, Vol 11.

Wegmuller, U. and C Werner, 1997. Retrieval of vegetation parameters with SAR interferometry, *IEEE Trans. On Geoscience and Remote Sensing*, Vol. 35, No 1, pp. 19-24.

FLOOD MAPPING FROM PHASE DECORRELATION OF TANDEM ERS DATA: OB' RIVER, SIBERIA

Laurence C. Smith

Department of Geography, University of California, Los Angeles
P.O. Box 951524, Los Angeles, CA 90095-1524 U.S.A.
phone: +310 825 3154, fax: +310 206 5976
email: lsmith@geog.ucla.edu

Douglas E. Alsdorf

Department of Geological Sciences, Cornell University
Snee Hall, Ithaca, NY 14853-1504 U.S.A.
phone: +607 255 6329, fax: +607 254 4780
email: alsdorf@geology.cornell.edu

ABSTRACT

A major difficulty with using ERS PRI products to map the extent of river flooding, lakes, and other water bodies is found where wind-induced waves increase backscattering from the water surface. However, strong temporal decorrelation of interferometric phase is found over open water surfaces because they are in constant motion. When phase coherence from surrounding land surfaces is sufficiently high to provide a contrast with low coherence from water surfaces, inundated areas may be clearly delineated even under conditions of strong wind or turbulence.

INTRODUCTION

The Ob' River, Siberia delivers $4X10^{11}$ m^3 of fresh water each year to the Arctic Ocean, ranking it thirteenth in flow volume among the worlds largest rivers (Meade, 1996). Like the Pechora, Yenisei, Lena, and Indigirka Rivers, peak discharge occurs in June, and at least half of the total annual flow occurs during the spring flood period (Gordeev et al., 1996). During this time, the floodplain experiences a dramatic increase in inundated area. Floodplain lakes that are normally isolated from the river channel become connected to each other and to major channels, permitting exchanges of water, sediment, and nutrients to occur. A better understanding of the timing and magnitude of this process will allow identification of sediment sinks and nutrient source areas that contribute to total loads of organic material delivered by the Ob' River to the Kara Sea.

Temporal ERS SAR images of the Ob' River near Salekhard (approximately 66N; 66E) permit observation of floodplain inundation patterns throughout the seasonal cycle. In support of this objective, the European Space Agency scheduled, acquired, and processed 88 PRI scenes over this test site from 1991 - 1995. However, the presence of wind was found to be a serious impediment to using ERS PRI data to delineate inundation patterns on Ob' River. Incident microwaves scatter strongly from wind-induced waves at the water surface, yielding backscatter values similar to those of surrounding non-inundated areas. Only 8 of 88 processed PRI scenes were acquired under sufficiently calm wind conditions to permit the inundated areas to be clearly distinguished over most of the floodplain. In an effort to mitigate this problem, interferometric phase coherence images were derived from four tandem ERS-1 and ERS-2 pairs (Table 1), to explore the value of phase coherence for mapping inundation.

Sensor	Orbit	Track	Date
ERS-1	21050	2259	25 July 95
ERS-2	1377	2259	26 July 95
ERS-1	21093	2259	28 July 95
ERS-2	1420	2259	29 July 95
ERS-1	21551	2259	29 Aug 95
ERS-2	1878	2259	30 Aug 95
ERS-1	21594	2259	01 Sept 95
ERS-2	1921	2259	02 Sept 95

Table 1. Tandem interferometric pairs acquired over the Ob' River near Salekhard.

July 25 amplitude (ERS–1)

July 26 amplitude (ERS–2)

July 25/26 phase coherence (ERS–1/2)

Figure 1. Marshy floodplain of the Ob' River near Salekhard, Siberia. Each image is approximately 20 km X 20 km. Two multi–looked amplitude images acquired 25–26 July 1995 are shown along with the corresponding phase coherence image. Increased backscattering from wind is present in both amplitude images; this problem is eliminated in the phase coherence image.

INTERFEROMETRIC PHASE COHERENCE

The use of interferometric phase coherence is growing in popularity for surface change detection. The information it provides is particularly useful in forest and land-use applications. For example, while cleared fields are often difficult to discriminate from surrounding forests using ERS amplitude (backscatter) data, interferometric phase coherence is typically high from fields but low from forest canopies. The interferometric correlation coefficient is a measure of the accuracy of the interferometric phase; its value decreases with temporal surface change and/or increasing volume scattering (Wegmuller and Werner, 1995). Open water surfaces provide an extreme example of temporal phase *de*correlation. Because the water surface is constantly in motion, the aggregate phase return on a first acquisition date will be radically different from the phase return from a second acquisition, resulting in very low phase coherence from open water surfaces. If the surrounding land surface yields sufficiently high coherence to provide a contrast with the low coherence of the water surface, this contrast may be used to provide unambiguous classification of water, regardless of wind or turbulence.

Phase coherence images for the tandem scenes listed in Table 1 were produced from raw ERS data provided by ESA. Interferometric processing was carried out with the Gamma SAR Processor and Interferometry software. Processing steps included baseline estimation from orbit data, precision registration of interferometric image pairs to a registration accuracy of 0.2 or better, interferogram generation, and estimation of interferometric correlation (Wegmuller and Werner, 1997). Correlation was computed within a 3X3 moving window. Only one-day interferometric pairs were used in order to minimize the effect of temporally changing water level on the derived phase coherence images. One-day pairs also yield much higher levels of phase coherence from non-inundated surfaces.

RESULTS

A strong contrast in phase coherence between inundated and non-inundated areas was found in all four tandem pairs, permitting clear delineation of river channels and floodplain lakes. Figure 1 illustrates this result for the Ob' River, with a tandem pair acquired July 25/26, 1995. Wind effects seen in in the PRI data are eliminated in the phase coherence image. Note the many small lakes obliterated in one or both of the amplitude images that may be clearly seen in the coherence image. Our observations also suggest that wetlands, which often display high backscatter returns due to a double-bounce mechanism between the water surface and emergent aquatic vegetation, may be seen in interferometric phase coherence images.

Flood inundation maps derived from July and September interferometric phase coherence images confirm the existence of a strong seasonal variation in inundation area on this dynamic Arctic river. Wind-free portions of other PRI images acquired throughout the summer cycle show that different floodplain lakes are alternately connected or isolated from the primary river channels. This seasonal inundation pattern appears to be the major control on free water exchange between the main channel and adjacent aquatic ecosystems. This phenomenon is believed to exert a strong control on the storage and exchange of sediments, nutrients, and contaminants between the Ob River and its floodplain.

ACKNOWLEDGEMENTS

ERS-1 and ERS-2 PRI and RAW products were provided by ESA, through a Second Announcement of Opportunity (AO2) data grant to Cornell University. The Gamma Modular SAR Processor (MSP) and Interferometric SAR Processor (ISP) were used to process the raw data and derive the phase coherence images.

REFERENCES

Meade, R H 1996, River-sediment inputs to major deltas, in Milliman and Haq (eds.), *Sea-Level Rise and Coastal Subsidence*, Kluwer Academic Publishers, 63-85.

Gordeev V V, Martin J M, Sidorov I S, and M V Sidorova 1996, A reassessment of the Eurasian river input of water, sediment, major elements, and nutrients to the Arctic Ocean, *Amer. J. Sci.*, 296, 664-691.

Wegmuller U, and C L Werner, SAR interferometric signatures of forest, *IEEE Trans. Geosci. and Remote Sens.*, 33(5), 1153-1161.

Wegmuller U, and C L Werner, Gamma SAR processor and interferometry software, Proc. Third ERS Sci. Symp., 17-21 March 1997, *ESA SP-394*.

ERS1 - SAR INTERFEROMETRY; POTENTIAL AND LIMITS FOR MINING SUBSIDENCE DETECTION

Daniel Raymond and Jean-Paul Rudant

Université Pierre et Marie Curie
Département de Géotectonique
(U.R.A. C.N.R.S. 1759)
case 129, T26 E1
4, Place Jussieu, 75252 Paris Cedex, France
phone: 33 1 44 27 58 83, fax: 33 1 44 27 50 85
e-mail: dra@osiris.lgs.jussieu.fr

ABSTRACT

In the Mulhouse potassic mining district (E France), the mining working involves ground subsidence phenomenons . This subsidence is increasing during 12 to 15 months after the caving processes, with a maximum vertical speed of 10 mm/day. Subsidence areas (0.5 km^2 maximum) are dissymetrical, with an active slope moving in the same direction as the mining. Movements in the active areas are followed by the mining Society. Three interferograms SAR ERS1 images of Mulhouse area have been provided by the French Centre National d'Etudes Spatiales (C.N.E.S). The topographic effects have not been geometrically corrected, because the smoothed relief of the studied area. On the third interferogram, subsidence effects have been identified. Nevertheless the active slopes (100m wide, or two pixels) are not visible, and the subsidence rate is too rapid with respect to the resolution of the interferogram (interval; 35 days). Interferograms with an interval of one or three days would be necessary for a real survey of the subsidence.

1. INTRODUCTION

ERS1 - SAR interferometry has been used for ground deformation analysis at various times, e.g. deformation linked to an earthquake (Landers, California) (Massonnet & al, 1993 and 1994, Zebker & al, 1994, Peltzer & al.1994); post-eruption deflation of a volcanoe (Mt Etna) (Massonnet et al, 1995); landslide (S France) (Fruneau & Achache, 1996). Below, we test potential and limits of this method for mining subsidence studying.

In France various areas are affected by mining subsidence; coal fields (Carnec, 1996), evaporitic accumulations, iron ore deposits. For this work we have selected the Mulhouse Potassic Basin (E France) where active mining subsidence is well documented.

2. POTASSIC BASIN OF MULHOUSE GEOLOGICAL FRAMEWORK AND SUBSIDENCE PROCESSES

The Rhinegraben is filled by a thick saliferous succession from Oligocene age. The potassic basin of Mulhouse (200 km^2) is located to the S of the graben. Two sylvinite levels are worked at a depth increasing from 400m (N) to 1100m (S). The levels thickness is included between 1m and 5m. The operating Company (Mines de Potasse d'Alsace) extracts 10MT to 13MT/year of ore. The mining method is a complete holing followed by caving. The latter involves the collapse of the immediatly overlying strata, followed by a slow creep of the whole evaporitic succession. Upwards the ground is subsiding, and hollows (0.5 km^2 maximum) expand.

(1) The gap equals closely the volume of extracted ore.
(2) The hollows are dissymmetrical with a 20mm/m slope in front of the working face.
(3) The slope is moving forward progressively at the rate of the underground working advancing.
(4) The subsidences increases with a 10mm/day maximum vertical speed during the active phase (12 to 15 months) and becomes stable after 36 months.

One may notice various disorders concerning buildings, roads, railway tracks etc.... Therefore, the mining Company takes safety provisions before the beginning of new works, and, during the mining working, the subsidence is followed by successive levellings along control lines.

Proc. 3rd ERS Symp. on Space at the service of our Environment, *Florence, Italy, 17–21 March 1997* (ESA SP-414, 3 Vols., May 1997)

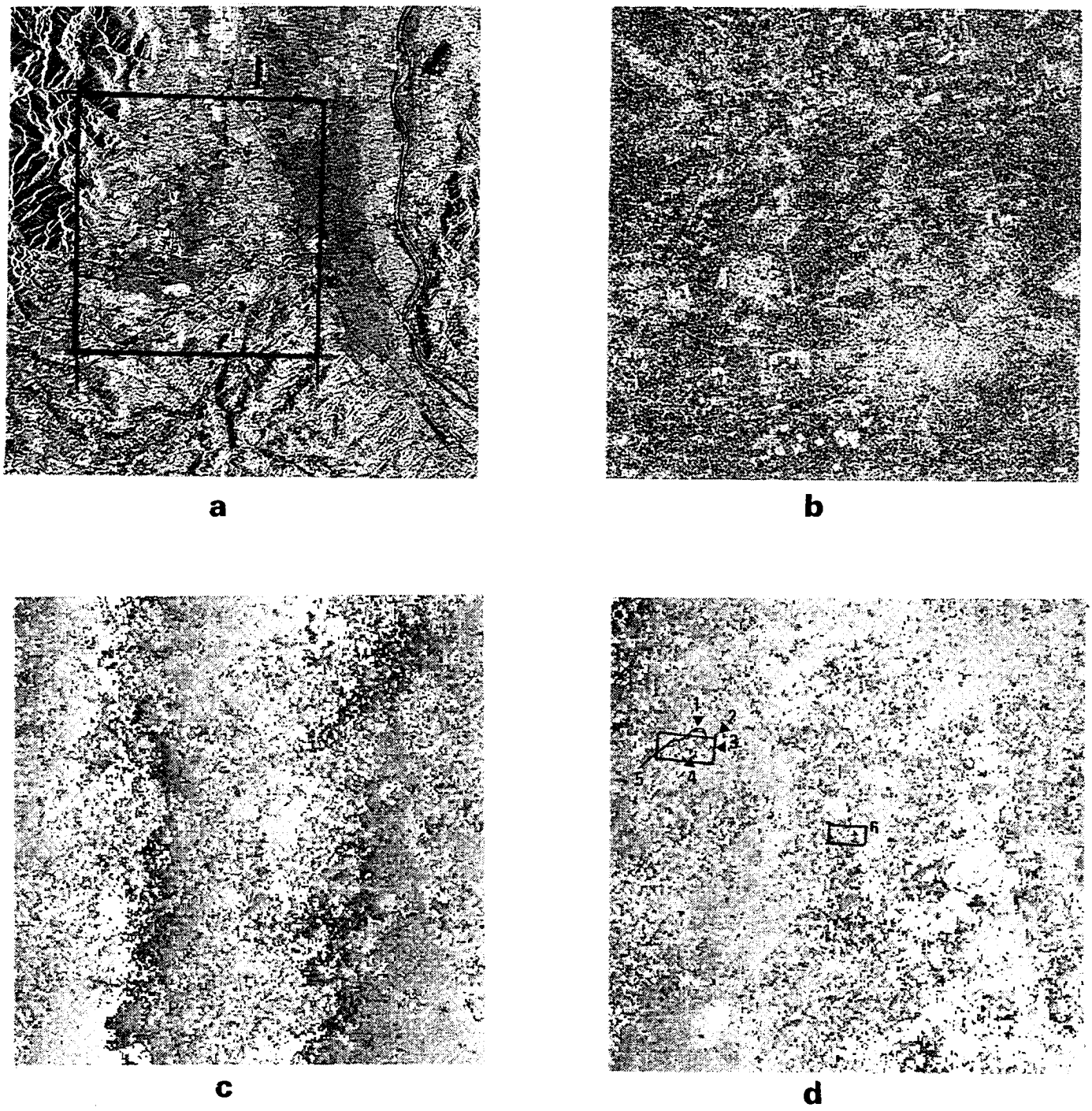

Fig. 1. SAR ERS1 Images of the Mulhouse area
(master-orbit n°11461, date 24.09.93, slave-orbit n°11962, date 29.10.93; interval 35 days)
a. Amplitude Image (with localisation of b). b. Coherence Image (see also fig. 2). c. Phase difference Image.
d. "local unrolling " Image (1 to 3. N Bollwiller; 3 bands of alternatively dark and light pixels according to "mini-fringes". 4. S Bollwiller. Dark band of pixels, according to the active slope bordering the S of the subsidence area. 5. Bollwiller subsidence area border. 6. Pulversheim. "phase hill ")

3. SAR IMAGES ACQUISITION AND PROCESSING

The C.N.E.S has provided us three interferometric pairs. The images have been acquired between September 1992 and October 1993, during the phase C of ERS1 descending orbits. For each pair we have collected an amplitude image (fig. 1, a), a coherence image (Zebker &Villasenor, 1992)(fig. 1, b), and an image of phase differences(fig. 1, c). For the latter, the distance effects have been eliminated, but not the topographic effects according to the smoothed topography of the studied area, located within an alluvial plain. The phases difference is algebraic (8 bits coding) and the interval (0/255) corresponds to a complete phase rotation (360°).

$$\Delta\Phi 1\_2 = DP\ 1\_2 = ((2 / \lambda) * (O2 - O1)* 256) + 128 + (\Delta\Phi 2 - \Delta\Phi 1)_{reflexion} * 256/360 + GC$$

the whole modulo 256

[DP: phase difference. O; optical way (antenna/target single path). Index 1 →Master-orbit. Index 2→Slave-orbit. GC. geometrical corrections].

Therefore a ground subsidence involves an increasing optical way ($\Delta\Phi>0$), and a "phase hill" signature on the images.

The first pair (interval:168 days, altitude of ambiguity: 230m) and the second pair (interval: 35 days, altitude of ambiguity: 64m) display a very important decorrelation. On the other hand, the average coherence is better on the third pair (master-orbit n°11461, date 24.09.93, slave-orbit n°11962, date 29.10.93; interval 35 days; altitude of ambiguity: 39m). Otherwise the acquisition period of the third pair is in accordance with an active phase of subsidence for various areas within the basin.

For the above-mentionned reasons, we have principally analysed the third pair. First one may notice ellipsoidal parasitic fringes centred over the Rhine River (fig. 1, c). The origin of this artefact is unknown. In order to obtain interpretable phase images of the subsidence areas, we have carried out a local "phase unrolling" over the working area (fig. 1,d).

4. RESULTS

With the help of a geographic information system (data provided by the mining company M.D.P.A), we have located with precision the subsidence areas on the various images. During the interferometric acquisition, the subsidence is important in two selected areas; Bollwiller (maximum 205mm/35 days) and Pulversheim (maximum 80mm/35 days).

4.1. Bollwiller area

On the coherence image, one may notice a "dark spot"" within Bollwiller area (signature of a coherence loss due to the subsidence?) (fig. 2).

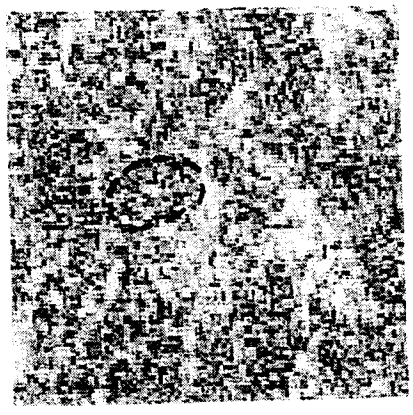

Fig. 2. "Dark spot" (circled) within Bollwiller area (extracted of fig. 2b)

A dark spot also occurs on the "phase unrolling" image (fig. 1, d).

- this spot coincides with the subsidence area position during the interferometric acquisition.
- on the other hand, to the N of the spot, one notices an area where the pixels are unvarying; according to the M.D.P.A. data, this area is under stabilisation (subsidence less than 5 mm/35 days).

A detailed analysis of the dark spot displays

- Northwards 3 alternately dark and light pixel alignments; maybe corresponding to "mini-fringes" generated by a vertical motion of 9mm. This latter is in accordance to M.D.P.A. data for this area.
- Southwards a dark alignment corresponding to the active slope, with a complete phase fading.

4.2. Pulversheim area

In this area, one may notice a "phase hill" (light pixels zone surrounded by dark pixels). The latter ($\Delta\Phi>0$) is the signature of a ground subsidence, but the information is only qualitative.

5. CONCLUSIONS

5.1 Size of phenomenons

Within the potassic basin, the subsidence areas are lying on 0.5 km^2 maximum (300 pixels) and the active slopes are 2 pixels wide. Consequently,

- One may detect subsidence areas by the interferometric method
- But they are too narrow for a reliable subsidence measurement.

In the studied case, for the time, the SAR interferometry is not competitive in comparison with classical levellings; nevertheless, this method provides a global vision of the subsidence areas.

5.2.Speed of phenomens

In the studied case, the subsidence speed is important (Bollwiller, 5mm/day, Pulversheim, 2.3 mm/day). 3 days or 1day/intervals (ERS1-ERS2 "tandem" phase°) would be necessary for a better understanding of ground motion. From 35 days-interferograms, the analysis must be limited to high coherence urbanized areas.

5.3. Prospects

Our work opens new prospects in use of SAR-interferometry for the detection and the analysis of the subsidence. Nevertheless it is necessary to fit the interferometric interval according to the subsidence rate previously measured on the field. For 35 days acquisitions; the interferometry is only valid for desertic or urbanized areas, where the coherence remains high during a long time.

Acknowledgements. We thank J Breniaux and Y. Lourdel (MDPA) for their informations about subsidence data and C.N.E.S. for his financial supporting.

6. REFERENCES

Bonte G. Godefroy Y. et Lourdel Y. (1983). Havage intégral en grande hauteur au quartier 75 de la mine Amélie (MDPA). Annales des Mines, 4, p. 71 - 74.

Carnec C. (1996). Interférométrie SAR différentielle. Application à la détection et au suivi des mouvements de terrain. Thèse doct. Univ. Paris VII,. Méthodes physiques en Télédétection, 195 p.

Fruneau B. et Achache J. (1995). Détection du glissement de terrain de La Clapière de Saint-Etienne-de-Tinée par interférométrie SAR et modélisation. C. R. Acad. Sci. Paris, t. 320, série IIa, p.809-816.

Massonnet D., Rossi M., Carmona C., Adragna F., Peltzer G., Feigl K., et Rabaute T. (1993). the displacement field of the Landers earthquake mapped by radar interferometry. Nature, 364, p. 138-142.

Massonnet D., Feigl K., Rossi M., et Adragna F. (1994). Radar interferometric mapping of deformation in the year after the Landers earthquake. Nature, 369, p. 229-230.

Massonnet D., Briole P. et Arnaud A. (1995). Deflation of Mont Etna monitored by spaceborne radar interferometry. Nature, 375, p.567-570.

Peltzer G., Hudnut K.W., et Feigl K.L. (1994). Analysis of coseismic surface displacement gradients using radar interferometry: new insights into the Landers earthquake. Jl Geophys. Res., 99, n° B11, p. 21971-21981.

Zebker H.A et Villasenor J. (1992). Decorrelation in interferometric radar echoes . IEEE Trans. Geosci. Remote Sensing, 30, p.19, 617-634.

Zebker H.A., Rosen P. , Goldstein R.M. Gabriel A. et Werner C.L. (1994). On the derivation of coseismic displacement fields using differential radar interferometry: the Landers earthquake. J. Geophys. Res., 99, p. 19617-19634.

CRUSTAL DEFORMATION IN SOUTHERN CALIFORNIA USING SAR INTERFEROMETRY

G. Peltzer, P. Rosen, F Rogez

Jet Propulsion Laboratory, California Institute of Technology, Pasadena, CA 91109

K. Hudnut

US Geological Survey, Pasadena, CA

ABSTRACT

By combining pairs of ERS-1/2 SAR images of Southern California spanning long time intervals (1-4 years), we were able to measure the rate of slow deformation processes along faults activated during the Landers 1992 earthquake. Interferograms revealed several centimeters of post-seismic rebound in step-overs of the 1992 break, with a characteristic decay rate of ~280 days. We interpreted this process as due to pore fluid flow as pore pressure gradients caused by coseismic stress changes dissipate. The data also revealed evidence of after-slip on different sections of the fault. The southern branches of the 1992 break experienced surface creep producing sharp phase cuts in the interferometric maps. The same approach was used in the Los Angeles basin, which is currently undergoing NS shortening at a rate of ~8 mm/yr. The tectonic signal in interferograms of the Los Angeles basin is intermingled with signals due to other sources such as ground subsidence caused by oil and water withdrawal.

1. INTRODUCTION

Repeat pass radar interferometry allows scientists to produce surface change maps combining millimeter precision in range displacement and high spatial resolution (Gabriel et al., 1989). The first application of the technique to seismology has been the mapping of the surface displacement related to earthquakes (e.g., Massonnet et al., 1993; Zebker et al., 1994; Peltzer and Rosen, 1995). Although spectacular, these results essentially corroborate the information brought by seismic and geodetic data, which, when combined with dislocation models, provide relatively precise descriptions of the static displacement produced by an earthquake. A more challenging application of InSAR is the detection of slow deformation processes such as post-seismic or interseismic strain occurring in the absence of earthquake. Such processes do not radiate seismic waves and are therefore not as well documented as earthquakes. We have used ERS-1 SAR images spanning time intervals of 1 to 4 years to study slow deformation processes in Southern California (Figure 1). We first focused on the Landers area, which has been the locus of an earthquake of magnitude 7.3 on June 28, 1992 and is undergoing post-seismic deformation since then. We also looked at the Los Angeles basin area, which is currently undergoing north-south shortening at a rate of 8 mm/yr and has been the site of a magnitude 6.7 event in 1994. In addition to tectonic movements, the activity related to water and oil extraction in the Los Angeles region results in significant ground subsidence and uplift, which dominate the tectonic signal is many areas.

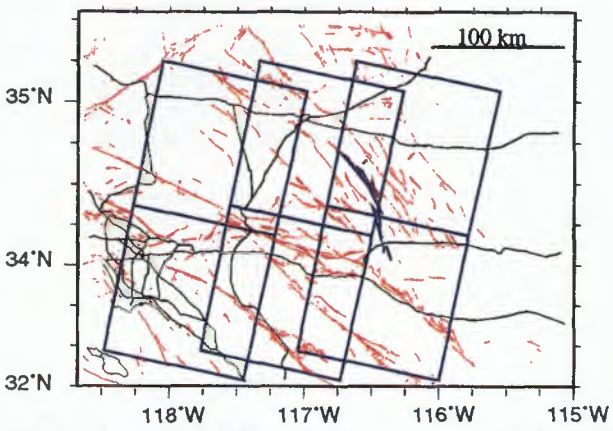

Figure 1: Map of active faults in study area, southern California with ERS-1 image frames. Thick line shows surface rupture of the Landers, 1992 earthquake.

2. POST-SEISMIC ACTIVITY AFTER THE LANDERS EARTHQUAKE

2.1 PORO-ELASTIC REBOUND IN FAULT STEP-OVERS:

The Landers, California, 1992 earthquake produced a surface rupture of more than 70-km in length and a maximum left-lateral offset of 6.2 m (Sieh et al., 1993). The surface break was formed of three right-stepping echelons forming two pull-apart structures (2 and 3 in Fig. 2a). A bent in the central section of the northernmost branch made a compressive jog (1 in Fig. 2a). We analyzed the post-seismic surface deformation in the vicinity of the 1992 rupture using 3 interferograms spanning 3 different time intervals

Proc. 3rd ERS Symp. on Space at the service of our Environment, *Florence, Italy, 17–21 March 1997* (ESA SP-414, 3 Vols., May 1997)

after the earthquake (Fig. 2b). All three interferograms depict intense deformation in the three structures described above, corresponding to range increase (subsidence) in the compressive jog and range decrease (uplift) in the pull-apart structures (Fig. 2b) in opposition to co-seismic movements.

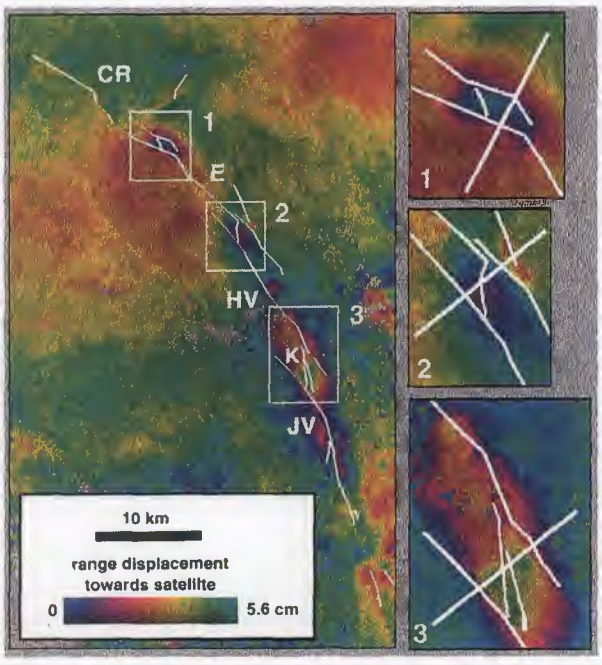

Fig. 2a. Three-pass interferogram of the Landers area generated with SAR image acquired on August 7, 1992 - September 24, 1995 - 11 June 1995. White line depicts 1992 surface rupture. Straight lines in zoomed areas are profiles shown in Fig. 2b. Fault labels are CR: Camp Rock fault, E: Emerson fault, K: Kickapoo fault, JV: Johnson Valley fault, and HV: Homestead Valley fault. After Peltzer et al., 1996.

The volumes of rock in the step-overs of the 1992 fault experienced dilation or compression during the earthquake and subsequently post-seismic relaxation. Analysis of the profiles shown in Fig. 2b indicates that the relaxation process occurred at a rate decaying exponentially with time, with a characteristic time of 270±45 days, similar to processes involving pore fluid flow in the upper crust (Anderson and Whitcomb, 1975; Muir-Wood and King, 1993). We interpret the observed deformation as the result of the slow dissipation of pore fluid pressure gradients produced by the earthquake in the step-overs of the fault. Because the Poisson's ratio of undrained porous media is larger than their Poisson's ratio under drained conditions, the transition from undrained (co-seismic) to drained (post-seismic) conditions implies a post-seismic rebound, as we observe in the interferograms (Peltzer et al., 1996).

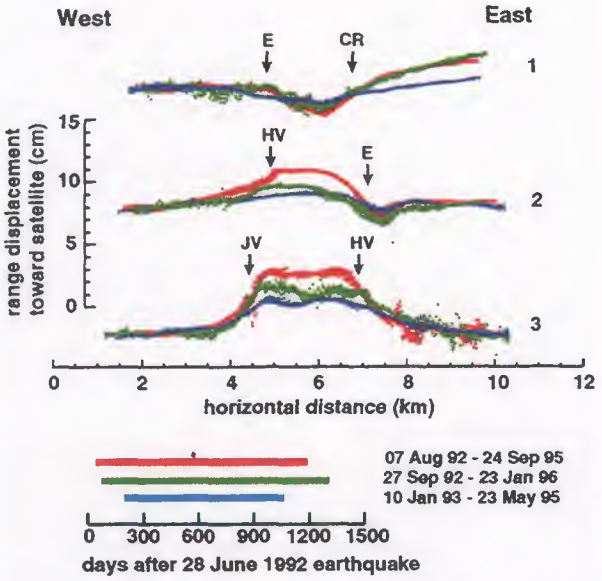

Fig. 2b. Line of sight surface displacement along profiles 1, 2 and 3 shown in Fig. 2a for three triplets of SAR images. Dots are displacement of individual image pixels within ~400 m from profile line and solid curves indicate averaged values in ~160 m-long bins along profiles strike. Fault labels are same as in Fig. 2a. After Peltzer et al., 1996.

2.2 CREEP ALONG SOUTHERN FAULT BRANCHES:

Sharp phase cuts are clearly visible in the interferograms along the two branches forming the southernmost section of the 1992 rupture (Fig. 2a, 3a, and 3b).

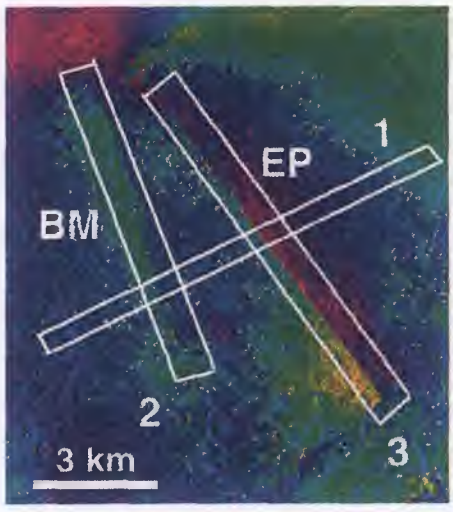

Fig. 3a. Detail of interferogram spanning time interval between September 27, 1992 and January 23, 1996 along the southern end of the 1992 surface break. EP is Eureka Peak fault and BM is Burnt Mountain fault. Boxes show location of profiles in Fig. 3b.

These cuts correspond to fault creep occurring after the earthquake. The profiles of Fig. 3b provide

information about the depth of the creeping section of the fault (approximately equal to the distance from the fault over which surface displacement vanishes, i.e. ~3km), as well as about the distribution of slip along the fault strike. Creep along a 10-km long section of the Eureka Peak fault occurred at an average rate of ~3.3 cm/yr resulting in ~14 cm of right lateral surface slip in 3 years. Using these parameters, we were able to determine that the geodetic moment released by creep on the Eureka Peak fault between January 10, 1993 and May 23, 1995 equals 5.4 10^{16} Nm. The fact that a seismic moment of only 1.6 10^{14} Nm was released by aftershocks during the same period in the vicinity of the this fault suggests that the observed post-seismic creep is essentially aseismic. Similarly, creep on the Burnt Mountain fault appears to have produced up to 17 cm of right-lateral surface slip in the three months following the earthquake.

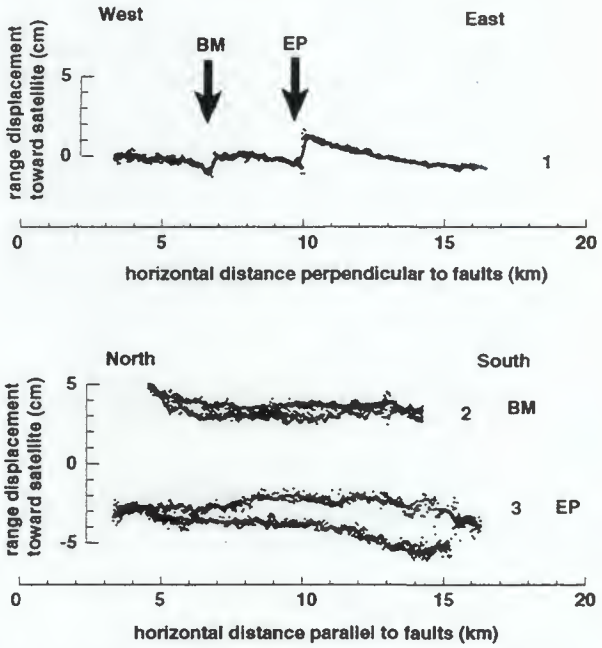

Fig. 3b. Top: transverse profile of range displacement across the Eureka Peak (EP) and Burnt Mountain (BM) faults. Bottom: Distribution of image pixels displacement in boxes parallel to faults in Fig. 3a. The distance between the two groups of dots in each profile indicate the line of sight offset on faults.

3. SURFACE DEFORMATION IN THE LOS ANGELES BASIN

Surface displacement in the Los Angeles region is primarily due to the tectonic activity. In addition to large surface displacement induced by earthquakes, geodetic data gathered at permanent GPS sites indicate that the basin is currently undergoing north-south shortening at a rate of ~ 8 mm/yr. In an attempt to detect surface displacements related to the inter-seismic accumulation of strain within the basin, we have analyzed interferograms spanning 1-4 years between 1992 and 1996 (e.g., Fig.4). Several reasons make it difficult to extract subtle tectonic signal from the interferograms. First, there is a 1.5 year gap in the ERS-1 data acquisition of 35-day repeat passes over the Los Angeles area between 1993 and 1995, limiting the temporal resolution of the data set. Second, during this period of no acquisition, the M 6.7, Northridge earthquake occurred, resulting in up to 50 cm of vertical uplift over the Santa Susana Mountains (Hudnut et al., 1996), a signal dominating by far that of elastic strain accumulation which may have occurred in the area during the same period. Third, ground subsidence related to water and oil withdrawal produces patterns of strong signal in the interferogram which also dominate the tectonic signal in many areas.

Fig. 4 depicts surface changes in the Los Angeles basin between October 1993 and December 1995. the concentric rings visible along the western edge of the SAR swath result from the surface uplift produced by the M6.7 Northridge earthquake of January 17, 1994.

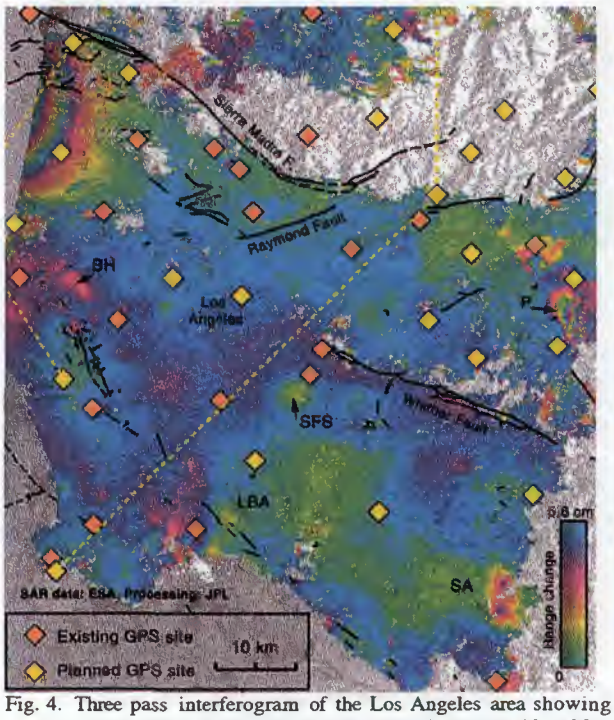

Fig. 4. Three pass interferogram of the Los Angeles area showing surface change between October 20, 1993 and December 22, 1995. Diamonds depict the location of existing and future GPS stations of the Southern California Integrated GPS Network (SCIGN). Black lines are mapped active faults. Gray areas are zones where the radar correlation is lost due to seasonal change of the vegetation. Location labels are P: Pomona, BH: Beverly Hills oil fields, LBA: Long Beach Airport, SFS: Santa Fe Springs oil fields, SA: Santa Ana.

Other clear features on the image are probably related to human activity such as water and oil withdrawal. For example, the area of Pomona, east of Los Angeles is the locus of ground subsidence probably related to the pumping of water (Fig. 5). The extent of the Pomona ground subsidence has not been recognized so far and may become a hazard for structures and people. In all the interferograms we analyzed, the area showed a volume deficit (subsidence), suggesting that, over the years, seasonal water recharges do not cope with the effect of the intensive use of water. Fig. 5 emphasizes the fact that ground subsidence can produce damages to structures such as freeway bridges or pipelines, which are numerous in the area.

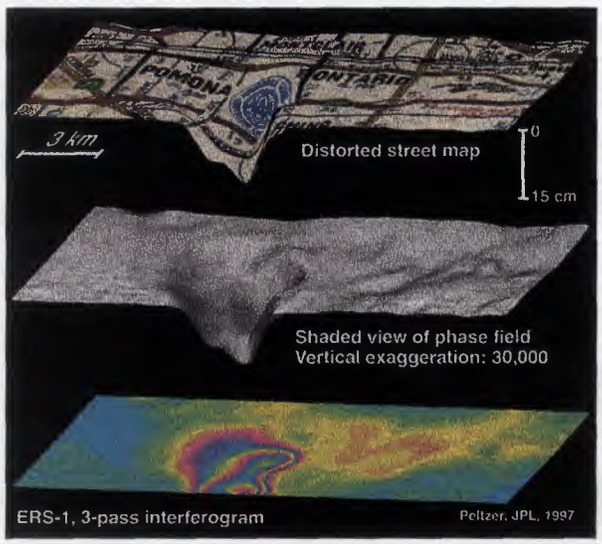

Fig. 5. Ground subsidence in the Pomona area. Bottom: Detail of interferogram of Fig. 4 over the Pomona area shown in perspective. One color cycle represents 5.6 cm of range displacement. Center: Shaded view of phase field displayed with 30,000 vertical exaggeration. Top: Distorted AAA street map wrapped on phase field. AAA map (c) 1988 Automobile Club of Southern California, reproduced by permission.

Other regions of ground subsidence include the Beverly Hills oil field (oil) and localized spots in the San Pedro and Long Beach area (probably oil industry activity) (Fig. 5). Noticeable surface uplift is observed in Santa Fe Springs (oil field) and east of Santa Ana. Surface uplift in these areas may result from the recharge of aquifers or oil fields with water, or from the poro-elastic response of the ground subsequent to water or oil withdrawal.

A large effort is currently being made by a consortium of universities and government agencies such as the USGS and NASA to set up a dense array of continuously operating GPS instruments in the Los Angeles area (SCIGN). The distribution of existing and planned stations over the radar maps of Fig. 4 emphasizes the complementary character of the two techniques. The combined analysis of SCIGN data and radar inteferometric maps provides scientists with unprecedented temporally and spatially dense information about movements of the surface, bringing new insights into long term motion on faults and their seismic cycle, and into effects of human activity.

Acknowledgment: The ERS radar data were provided by the European Space Agency. The research described in this paper was carried out at the Jet Propulsion Laboratory under contract with NASA.

4. REFERENCES

Anderson D.L. and J.H. Whitcomb, Time-dependant seismology, J. Geophys. Res., 80, 1497 (1975).

Gabriel, A.G., R.M. Goldstein, and H.A. Zebker, Mapping small elevation changes over large areas: Differential radar interferometry, J. Geophys. Res., 94, 9183-9191, 1989.

Hudnut, K.W., Z. Shen, M. Murray, S. Mcclusky, R. King, et al., Coseismic displacement of the 1994 Northridge, California earthquake, B. Seism. S. Am., 86, S19-S36, 1996.

Massonnet, D., M. Rossi, C. Carmona, F. Adragna, G. Peltzer, K. Feigl, and T. Rabaute, The displacement field of the Landers earthquake mapped by radar interferometry, Nature, 364, 6433, 138-142, 1993.

Muir-Wood, R. and G. C. P. King, Hydrological signatures of earthquake strain, J. Geophys. Res., 98, 22,035, 1993.

Peltzer, G. and P. Rosen, Surface displacement of the 17 May 1993 Eureka Valley, California, earthquake observed by SAR interferometry, Science, 268, 1333-1336, 1995.

Peltzer, G., P. Rosen, F. Rogez, and K. Hudnut, Postseismic rebound in fault step-overs caused by pore fluid flow, Science, 273, 1202-1204, 1996.

Sieh, K., L. Jones, E. Haukson, K. Hudnut, D. Eberhart-Phillips, T. Heaton, S. Hough, K. Hutton, H. Kanamori, A. Lilje, S. Lindvall, S. McGill, J. Mori, C. Rubin, J. Spotila, J. Stock, Hong Kie Thio, J. Treiman, B. Wernicke, and J. Zachariasen, Near-field investigations of the Landers earthquake sequence, April to July 1992, Science, 260, pp171-176, 1993

Zebker, H. A., P. Rosen, R.M. Goldstein, A. Gabriel, and C.L. Werner, On the derivation of coseismic displacement fields using differential radar interferometry: the Landers earthquake, J. Geophys. Res., 19,617-19,634, 1994.

RECENT INTERDISCIPLINARY RESEARCH IN THE NEOVOLCANIC ZONE OF ICELAND USING SAR DATA

Ulrich Münzer[1], Sigurjón Jónsson[2], Páll Einarsson[3]

[1] Institute of General and Applied Geology,
Ludwig-Maximilians University, Luisenstrasse 37, 80333 München, Germany,
phone: +49-89-5203-417, fax: +49-89-5203-286

[2] Iceland Geodetic Survey, Laugavegur 178, 105 Reykjavík, Iceland

[3] Science Institute, University of Iceland, Dunhagi 3, 107 Reykjavík, Iceland

ABSTRACT

The ESA project "Monitoring of Natural Land Surface Change in Iceland using ERS-1/ERS-2 and Other Remote Sensing Systems" was initiated to investigate the possibilities of radar remote sensing to observe glaciers and volcanic areas in Iceland. In this context, the ERS-1/2 Tandem Missions (August 17, 1995 - May 16, 1996, and October 21-24, 1996) offered a unique opportunity to employ interferometric methods. In 1995/96 an international team of scientists carried out a preparatory work, marking test sites in Iceland with corner reflectors, obtaining GPS and soil moisture measurements, and determining surface roughness. Radar data processing, interferometric software development and processing were undertaken. The importance to explore the limitations of the technique as well as the advantages was demonstrated in autumn of 1996 when a volcanic eruption took place within the Vatnajökull glacier in Iceland. The usefulness of the Tandem data is presented by one example where a cm-scale uplift is observed in two surface depressions within the Vatnajökull glacier. The depressions are due to subglacial geothermal activity and the uplift is a result of an iceflow into the depressions.

Keywords: ERS, SAR, Iceland, volcanism, glaciers, disaster monitoring, interferometry.

1. INTRODUCTION

Iceland is located on the Mid-Atlantic ridge where the plates of North America and Eurasia spread apart. Volcanic and seismic zones form the plate boundary in Iceland (Figure 1). Glaciers presently cover about 11.200 km^2 of Iceland, or about 10.8% of the country (Björnsson, 1988). They are mainly in the southern part of the island where precipitation is considerably higher than in the northern part. Some of the volcanoes and geothermal areas in south Iceland are covered by glaciers that makes Iceland interesting for studies of glacier-heat and glacier-volcanic interactions.

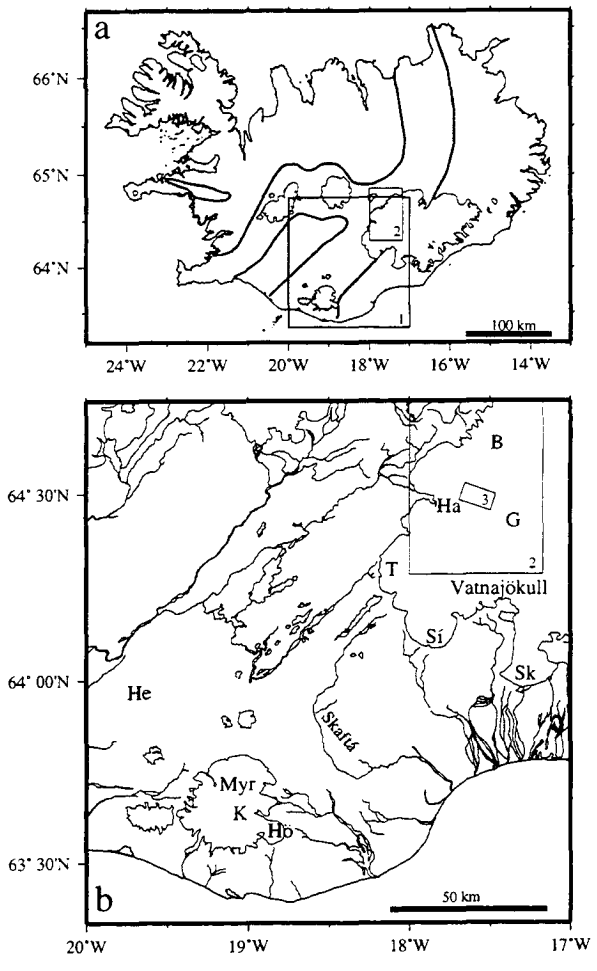

Figure 1. a) Map of Iceland showing the location of volcanic zones as well as the specified test area of the ESA project (frame 1). b) A map of the test area in central south Iceland where the volcanic zone is partly covered by the glaciers of Mýrdalsjökull (Myr) and Vatnajökull. Frames 2 and 3 mark the areas covered in figures 2 and 3, respectively.
Central volcanoes: Katla (K), Hekla (He), Bárðarbunga (B), Hamarinn (Ha), Grímsvötn (G).
Glacier tongues: Tungnaárjökull (T), Síðujökull (Sí), Skeiðarárjökull (Sk), Höfðabrekkujökull (Hö).

Several of the sub-glacial geothermal areas cause a sudden burst of water from the glacier on a regular basis, a phenomenon that is called jökulhlaup (an Icelandic term to express the phenomenon). Ice melts continuously within the geothermal areas and a reservoir of the meltwater is formed underneath the glacier. When the waterlevel within the reservoir has reached a certain level, high enough to overwin the overburden ice pressure around the reservoir, the water rushes out and a jökulhlaup starts. Jökulhlaups can also occur from a drainage of meltwater from subglacial eruptions and from marginal ice-damed lakes (Björnsson, 1992).

Jökulhlaups can be large and very destructive and can have a major effect on the landscape. They have destroyed large vegetated areas, formed canyons, and they transport huge amounts of sediments. They have caused loss of lives, ruined farms and farmlands in Iceland. Jökulhlaups also threaten electrical power plants, roads, bridges, electrical transmission lines, and other constructions (Björnsson, 1992).

It is therefore of considerable interest that the ESA project no. AO.2 D116 "Monitoring of Natural Land Surface Change in Iceland using ERS-1/ERS-2 and Other Remote Sensing Systems" (Principal Investigator U. Münzer) was initiated to investigate the possibilities of radar remote sensing to observe the ongoing dynamical processes, to detect changes on glaciers due to subglacial geothermal areas and due to volcanic activity, and to observe geomorphological effects of the jökulhlaups as well as changes at the fore-fields of retreating, advancing, and surging outlet glaciers. The project will help to understand further the ongoing processes and will be a demonstration of how the SAR technique can be used in other areas where similar processes are at work.

The test area covers the Eastern Volcanic Zone which is partly covered by the glaciers of Mýrdalsjökull and Vatnajökull (Figure 1). The central volcano of Katla, underneath the Mýrdalsjökull glacier, has erupted approximately every 50 years during last centuries. The eruptions have been accompanied by destructive jökulhlaups reaching peak discharge of 100 000 - 300 000 m^3/s (Thórarinsson 1957). The western part of the Vatnajökull glacier covers the central volcanoes of Bárðarbunga, Hamarinn and Grímsvötn (Björnsson and Einarsson, 1990). During the last decades jökulhlaups have occurred regularly from the caldera of Grímsvötn (Guðmundsson et al., 1995) and from two subglacial geothermal areas between Hamarinn and Grímsvötn (Björnsson, 1977).

A volcanic eruption started within the Vatnajökull glacier on September 30, 1996, several kilometers north of the Grímsvötn caldera (Figure 2) (Einarsson et al., 1997). The eruption lasted nearly two weeks. Huge amounts of meltwater drained into the caldera were it accumulated in a subglacial lake. On November 5-6, 1996, the water rushed out to the south coast, forming the century's most destructive jökulhlaup from the Grímsvötn caldera. The consequences were serious. Several bridges and more than 10 km of the ring road were destroyed, electrical transmission lines and communication cables broke.

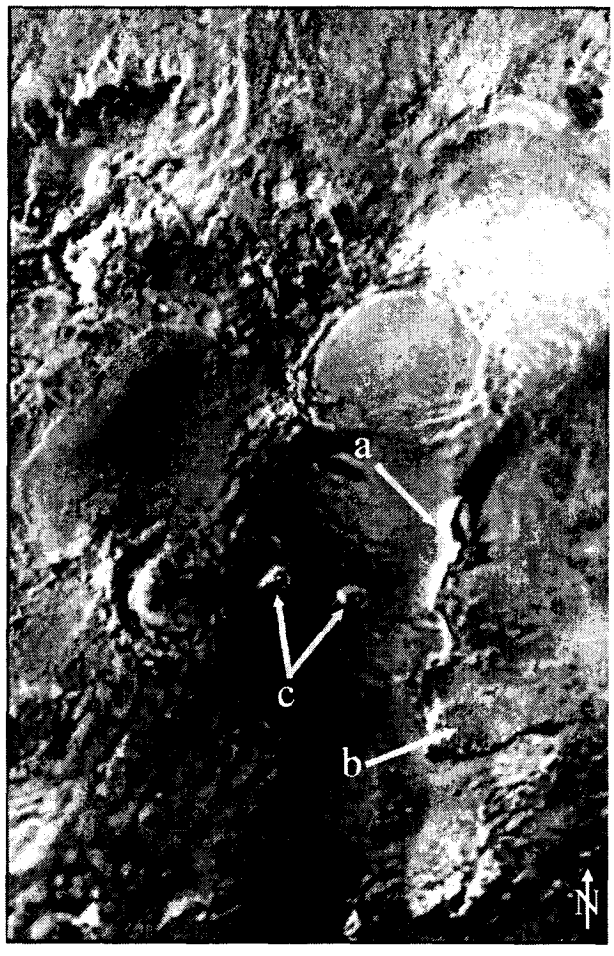

Figure 2. ERS-2 subscene of the western part of the Vatnajökull glacier from October 6, 1996, about one week after the volcanic eruption started. The eruption fissure within the glacier is clearly visible (a). The subglacial tunnel where the melt-water drained south from the eruption site to the caldera of Grímsvötn (b) can also be detected. The two round features (c) are surface depressions in the ice cap due to subglacial geothermal activity. ©ESA 1996

2. DISASTER MONITORING - A RESEARCH PROJECT IN PROGRESS

The ESA project referred to above was initiated in 1995. Participants are from institutions in Germany, Iceland, Austria and Poland. Difficulties in funding have had a restraining effect on the project, so the joint effort had to be carried out on a smaller scale than previously planned.

Much of the preparatory work was carried out in 1995. 20 corner reflectors were established in the field,

specifically designed to withstand Iceland's climate. The corner reflectors are mainly situated around the Mýrdalsjökull glacier and the Hekla volcano. They have played an important role in geocoding radar images of the area. During the scheduled acquisition times of the Tandem Mission in August and September 1995, soil moisture measurements were made at the reflector sites at depths of 0-2 cm, 2.5 cm and 5-10 cm. In addition, surface roughness was determined in the vicinity of the reflectors. The corner reflectors were located with accuracy better than 2 cm using Global Positioning System (GPS) receivers, a work carried out by co-investigators of the Nordic Volcanological Institute, Reykjavík, the Iceland Geodetic Survey (IGS), and the Institute of Applied Geodesy, Germany (IfAG). The corner reflectors will be in use during the whole time of the project. Co-investigators from the Institute of Geography of the Nicholas Copernicus University in Torun, Poland, made geomorphological field investigations at the fore-fields of the outlet glaciers of Síðujökull, Tungnaárjökull, and Skeiðarárjökull (Figure 1).

The following year, 1996, was dedicated to in-situ research in Iceland as well as to data processing and interpretation of the first results. The geomorphological mapping was continued at the western margin of the Vatnajökull glacier and east of the Mýrdalsjökull glacier. A detailed map of the Skeiðarárjökull glacier fore-field was completed before the catastrophic flood occurred in November 1996 (Wisniewski et al., an unpublished map), and will serve as an invaluable reference for future studies of the changes that occurred during the jökulhlaup. Aerial photography, with a Wild RC 10 metric camera, of the eruption site and the flooded areas was carried out by the IGS in November.

Most of the radar data processing and interferometric software development has been in the hands of co-investigator German Aerospace Research Establishment (DLR), Oberpfaffenhofen, Germany. A Digital Elevation Model (DEM) of the test area was generated for geocoding of radar images and for differential interferometry, using topographic maps (1:50 000) from the IGS. The co-investigator from the Institute of Meteorology and Geophysics at University of Innsbruck, Austria, has investigated backscatter patterns of the glaciers, soil moisture, and surface roughness, as well as analysed the coherence of interferograms.

3. SAR INTERFEROMETRY OF THE VATNAJÖKULL GLACIER

The ERS-1/2 Tandem Missions (August 17, 1995 - May 16, 1996, and October 21-24, 1996) gave a unique opportunity to use SAR interferometry on areas where deformation rate is relatively high and where the coherence disappears quickly, like on glaciers. The Tandem Mission in October 1996, was especially valuable in observing the changes caused by the eruption site within the Vatnajökull glacier.

Among other interesting features on the Vatnajökull glacier that can be observed using SAR interferometry is uplift of two depressions in the ice-cap west of the Grímsvötn caldera (Figure 1-3). These two depressions are due to sub-glacial geothermal activity. Every few years the meltwater underneath the depressions reaches a level high enough to overcome the surrounding overburden pressure. When this happens, a jökulhlaup starts in river Skaftá (Figure 1). Therefore, these depressions have been called the western and the eastern Skaftá cauldrons (Skaftárkatlar). The ice surface in the depressions drops down by tens of meters following a jökulhlaup, but it is uplifted again in the following months and years, by the inflow of ice into the depression.

Several interferograms of this area, made out of Tandem data, were investigated. They show uplift of these depressions. The uplift rate depends on the surface slope into the depressions, or the time since the last jökulhlaup occurred (Jónsson et al., 1997). Figure 3 is a differential interferogram of the cauldrons showing the uplift during one day of October 21-22, 1996 (descending orbit). The topographical effect was removed using a DEM of the area, information about the satellite orbits, and the differential interferometry software of the DLR. One fringe in the interferogram represents a 2.8 cm change of distance in line of sight to the satellites. The western cauldron is uplifting more than 15 cm per day, but the rate of the deformation is too high in the center to quantify the uplift. The uplift rate of the eastern cauldron is estimated to be about 9 ± 3 cm/day. The reason for higher uplift rate of the western cauldron is that a jökulhlaup occurred there in August 1996, only about two months before this observation. Therefore, the western cauldron is relatively deep with steep slopes, causing relatively fast inflow of ice and rapid uplift. The last jökulhlaup from the eastern cauldron occurred in July 1995. Hence, the eastern cauldron is closer to being full again than the western cauldron.

The estimated uplift rates are assumed to be accurate to about 3 cm. The altitude of ambiguity (Massonnet and Rabaute, 1993) of this interferogram is about 70 m. The accuracy of the DEM is not assumed to be better than several tens of meters in this area. Consequently, the errors in the DEM may account for up to one fringe in the differential interferogram. More detailed analysis of the ice-flow dynamics of these two depressions can be found in Jónsson et al. (in preparation 1997).

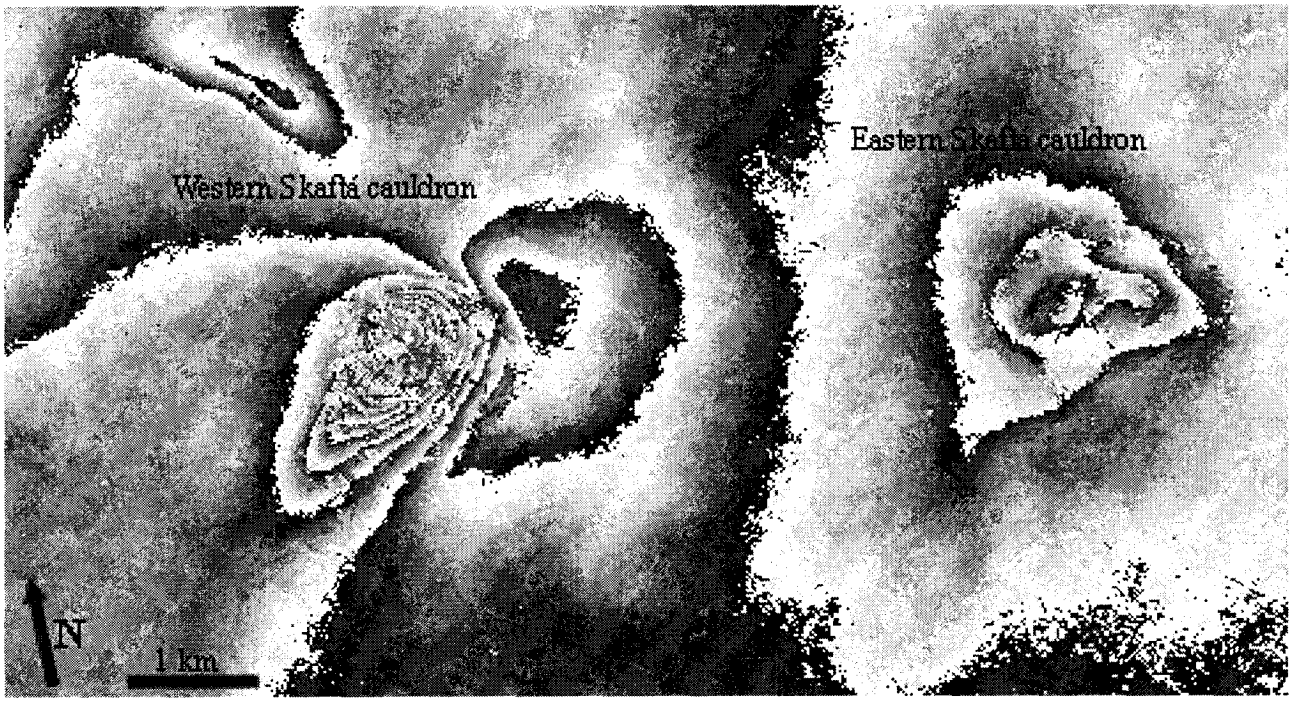

Figure 3. A differential interferogram of the Skaftá cauldrons in Vatnajökull from ERS-1/2 Tandem data of October 21-22, 1996. The rate of deformation in the western cauldron is to high to quantify the uplift, but it is more than 15 cm/day. The uplift of the eastern cauldron is estimated to be about 9 ± 3 cm/day. ©ESA 1996

4. OUTLOOK

The status and the first results of the project, as well as future plans, were discussed at a Workshop in Reykjavík in August 1996, attended by all co-investigators. The importance of investigating the possibilities of the SAR technique to monitor glacier-volcanic interactions were clearly demonstrated by the volcanic eruption within the Vatnajökull glacier that started on September 30, 1996.

During the summer of 1997, several new corner reflectors near the western margin of the Vatnajökull glacier will be installed. Soil moisture measurements will be done near the new corner reflectors and repeated near the old reflectors. Field investigation and geomorphological mapping will be repeated in the fore-field of the Skeiðarárjökull glacier to detect the changes caused by the jökulhlaup in November 1996, based on multitemporal SAR data (Münzer et al., 1995). A continued geomorphological investigations will also be carried out of the Höfðabrekkujökull glacier, as well as in-situ investigations in the unstable, threatened Mýrdalsjökull area.

The data obtained from different radar imaging systems (ERS-1/2, JERS-1, and RADARSAT) will be compared and evaluated as to their suitability for disaster monitoring and hazard detection and prediction.

5. ACKNOWLEDGEMENTS

The research is now funded by DARA - German Space Agency, Bonn, No. 50EE9706. The Iceland Science Fund supported the work. Thanks are due to ESA, Frascati, for assistance in providing the required data, especially for repeating the ERS-1/2 Tandem Mission in October 1996 and in March 1997. We thank all participants of the project for their contribution.

6. REFERENCES

Björnsson, H., 1977: The cause of jökulhlaups in the Skaftá river, Vatnajökull, *Jökull, 27*, 71-77.

Björnsson, H., 1988: *Hydrology of Ice Caps in Volcanic Regions*, Soc. Sci. Islandica, Reykjavík, Iceland, 139 pp.

Björnsson, H., 1992: Jökulhlaups in Iceland: prediction, characteristics and simulation, *Annals of Glaciology, 16*, 95-106.

Björnsson, H., and P. Einarsson, 1990: Volcanoes beneath Vatnajökull, Iceland: Evidence from radio echo-sounding, earthquakes and jökulhlaups, *Jökull, 40*, 147-167.

Einarsson, P., B. Brandsdóttir, M. T. Guðmundsson, H. Björnsson, K. Grönvold, and F. Sigmundsson, 1997: Unrest near the center of the Iceland Hotspot: The October 1996 subglacial eruption in Vatnajökull, *Eos* (in press).

Guðmundsson, M. T., H. Björnsson and F. Pálsson, 1995: Changes in jökulhlaup sizes in Grímsvötn, Vatnajökull, Iceland, 1934-1991, deduced from in-situ measurements of subglacial lake volume, *J. Glaciology, Vol. 41*, 263-272.

Jónsson, S. et al., 1997: Surface depressions caused by subglacial geothermal activity within the Vatnajökull glacier, Iceland: Ice-flow dynamics observed using Synthetic Aperture Radar Interferometry (in preparation).

Massonnet, D., and T. Rabaute, 1993: Radar interferometry: limits and potential, *IEEE Trans. Geoscience & Rem. Sensing, 31*, 455-464.

Münzer, U., Á. Guðmundsson, H. Weichelt, R. Winter, T. Bahr, C. Böhm, B. Müschen, 1995: Geologic Mapping of Selected Areas in Iceland and Verification of Results. NASDA Reg. No. J-0410, Final Report of JERS-1 System Verification Program, Vol. 1, pp. 587-601, Ministry of International Trade and Industry, National Space Development Agency of Japan, Tokyo.

Thorarinsson, S., 1957: The jökulhlaup from the Katla area in 1955 compared with other jökulhlaups in Iceland, *Jökull, 7*, 21-25.

FLOOD MONITORING STUDY IN THE JAMUNA & GANGES FLOODPLAIN IN BANGLADESH USING ERS-1

Hans van Leeuwen
Synoptics, *Integrated Remote Sensing & GIS Applications* BV
PO Box 117, 6700 AC Wageningen, the Netherlands
main@synoptics.nl

Timothy Martin, Iffat Haque and Ahmadul Hassan
Bangladesh FAP 19 GIS / EGIS
House 49, Road 27, Banani, Dhaka, Bangladesh
Tel. 880-2-881570 / Fax. 880-2-883128
egis@egis.pradeshta.net

Dirk Werle and Brian Tittley
AERDE Environmental Research, Canada

ABSTRACT

In this study we investigate the use of ERS-1 SAR data, digital image processing and GIS integration methods to combine and analyse SAR imagery, ground reference data. We outline a simple methodology for monitoring flood conditions in Bangladesh with satellite SAR data. Then we demonstrate and illustrate the usefulness of ERS-1 SAR multi-temporal image analysis during the 1993 flood season for selected test areas in Jamuna and Ganges River flood plains. The results strongly indicate the potential of the ERS-1 SAR to provide water surface delineation during monsoon flood conditions. When used in conjunction with flood model results and topographic data, satellite SAR can provide valuable information about localised flooding conditions.

Keywords: Flood monitoring, ERS-1/2, Bangladesh

1. INTRODUCTION

This project represents the first effort to evaluate the usefulness of multi-temporal satellite SAR imagery in Bangladesh. The ability to acquire local and regional SAR data of flooded terrain during adverse weather conditions and the usefulness of SAR image analysis have been demonstrated in numerous studies. The capability to incorporate SAR data into flood monitoring activities, land use analysis, and coastal zone management is currently limited in Bangladesh. Substantial technical and logistical support, training, and technology transfer is required in the form of consultance given presently by SYNOPTICS and AERDE research.

In 1993 within the framework of the Flood Action Plan (FAP) program, the Government of Bangladesh and the World Bank have assigned the USAID sponsored FAP 19 GIS (Geographic Information Systems) program component a supporting role to provide leadership in the development, application and institutionalization of GIS technology in Bangladesh. In order to organise, process and interpret spatial information for resource management and environmental monitoring, GIS relies on up-to-date remote sensing data as a source.

2. OBJECTIVE

The objective of the work is mapping the extent of monsoon flooding in 1993 using radar remote sensing. The main approach consisted of several steps, including: (1) SAR data acquisition by the ERS-1 satellite over a selected study area in July and August, 1993, and collection of ground reference data; (2) digital SAR image processing and analysis; (3) integration of SAR image analysis results with ground reference data as well as optical satellite imagery and GIS data sets; and (4) assessment of results.

3. STUDY AREA, TEST SITES AND DATA SETS

The flood plains of the Jamuna and Ganges Rivers in Central Bangladesh were selected as a study area. The area exhibits floodplain conditions representative during the onset and height of the monsoon season. Much of the land is affected by flooding which begins with pre-monsoon rainfall in May and June; it reaches a peak in July and August. Inundation is caused by rainwater and river water. The areal extent of flooding is more or less defined by topographic features within

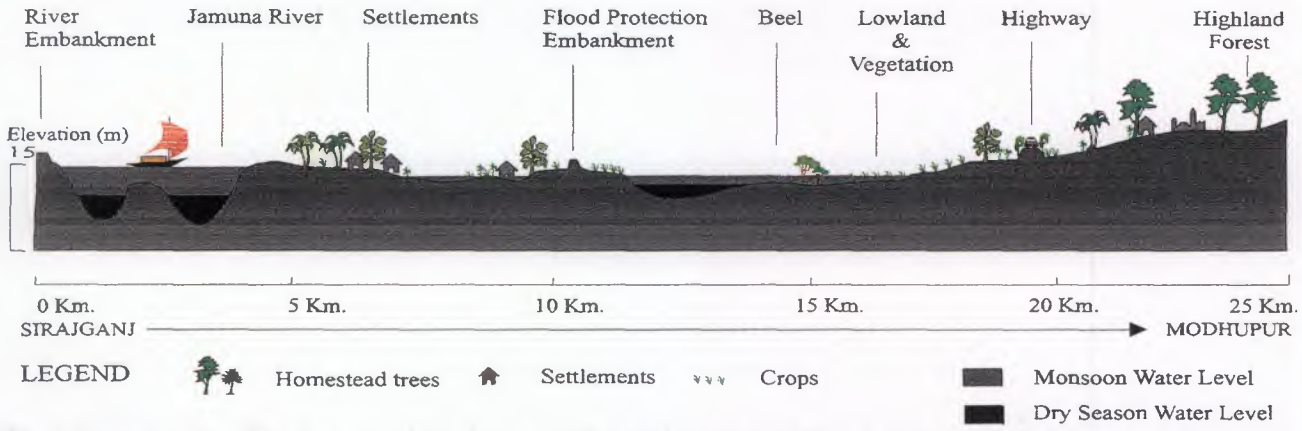

Fig. 1 Schematic profile of a typical landscape in Bangladesh. *Included is the Jamuna River, the recent floodplain and Pleistocene upland terraces. Land and floodscape elements are idealised; heights and distances are relative and can vary considerably. In the case of flood levels and terrain, local variations are in the order of a few meters and subtle changes can greatly influence cultivation and land use practices.*

the floodplain. Agricultural land use is dominated by rice crops; other crops include jute, wheat, mustard, sugarcane and pulses. Fishery is another important source of nutrition and income. The Tangail district was selected as a test site for detailed image analyses and GIS data integration exercises. The area is located at the east bank of the Jamuna River. Approximately 70% of the land is cultivable land and 30% is homesteads and homestead forest, roads, and permanent water bodies like rivers and beels. The area has some flood protection from a low embankment, and some degree of controlled flooding from inlet sluices; however, the drainage that exists is uncontrolled. There is a provisional division into flood compartments which are formed by roads, rivers, embankments or major landscape feature (see figure 1). The ERS-1 SAR image processing and analysis effort concentrated primarily on two scenes which were acquired over part of the Jamuma and Ganges River floodplains in central Bangladesh on July 24, 1993 (orbit 10570/frame 3123) and August 28, 1993 (orbit 11071/frame 3123).

4. ANCILLARY DATA

In order to assist the ERS-1 SAR data analysis, a GIS database was created using existing GIS data for the Tangail District. The following features were included in the GIS: major roads; embankments; permanent water bodies; settlements; and bio-physical data such as crops, soils, and topography. A digital elevation model (DEM) of the greater Tangail area was generated from the Bangladesh Water Development Board (BWDB) 1960s ground survey at 4- and 8-inch to the mile maps. Digital elevation values were interpolated to a 25-meter grid pixel size. By rasterising and integrating flood model data with the DEM for the Tangail area, flood depth and flood extent maps can be generated in a 25-meter grid cell format. Flooding is assumed to be caused by the modelled drainage network.

Ground observations of the area covered by the ERS-1 satellite were made at more than 40 sites on July 24 and August 28, 1993. The field data were systematically compiled into a hierarchical classification and coding scheme. The information gathered included amount of flooding, crop or vegetation canopy (if crops were present), geographic position, and general observations. Map polygons of varying extent representing the areas of data collection were digitised and tagged with a reference identification. The SAR signatures associated with the prevailing land use in those polygon areas were then subjected to further analysis. Meteorological data provided by the Bangladesh Meteorological Department suggest that on July 24, 1993, the cloud cover was 100%; occasional light precipitation and no winds were recorded. On August 28, 1993, the cloud cover was 100%; there was no precipitation, and light winds at 5 knots from the south-east were recorded.

5. METHODOLOGY

Pre-processing

The full ERS-1 precision processed images were geo-referenced using SPOT panchromatic images of previous years and co-registered in order to integrate ancillary data. Various SAR filter options were introduced and tested. A 3 x 3 Maximum a-posteriori (MAP) filter produced the best overall results for the flood mapping application. In order to reduced data volume, both July and August SAR images were scaled from the original 16-bit to an 8-bit format using 1.5 standard deviations from the mean distribution value in the 16-bit image. A contrast stretch was applied in order to improve the visual appearance of the imagery.

Classification

A procedure for discriminating flooded and non-flooded areas was developed using July and August SAR images of the Tangail test area. A method was chosen that used a simple density slice to segregate the image into two discrete classes and one mixed class. Then, a series of knowledge-based algorithms were applied to the mixed class pixels, resulting in their assignment to one of the two known classes. When results for the test area were considered satisfactory, the classification process was then applied to the entire SAR images. The classification was based on the principle that the amount of SAR return from standing water is significantly lower than that of soil, vegetation, and other features occurring on dry land. It was recognised, however that backscattering on wind-agitated water surfaces and volume scattering and multiple reflections from vegetation in standing water can create bright SAR return, thus confusing these areas with features on dry land.

6. RESULTS

After the classification and post-processing procedure was accepted for the Tangail test area, it was applied to the entire July and August ERS-1 SAR scenes of central Bangladesh. In table 1 the results of the classification for the July and August image are given.

Flood Maps

The flooded and non-flooded classes in the flood maps show large continuous areas of flooding throughout the ERS-1 SAR scenes. In the floodplain east of the Jamuna River, the flooding pattern is more irregular with interspersed areas of non-flooded crops and settlements. The overall area classified as flooded increased slightly from July to August: 48% and 53%, respectively (see figure 2). The acquisition frequency (July and August are both Monsoon months) for flood need to be optimised even more.

Assessment of SAR Classification Accuracy

The SAR image classification results were examined by FAP 19 analysts and by persons from several other projects familiar with flood conditions within the study area. In addition, the classification results were compared with other maps and flood model results and determined to be reasonable and useful. A more quantitative assessment of the SAR image classification then was carried out by comparison with information obtained from the ground surveys. The detailed ground reference data, from some 45 observations on a variety of land uses, were simplified into the following four categories: (1) urban, settlement, homestead; (2) non-flooded crops; (3) flooded crops; and, (4) river, floodwater, and beels (remnants of former river meanders, or isolated river bodies). These categories were compared with the two-class SAR image

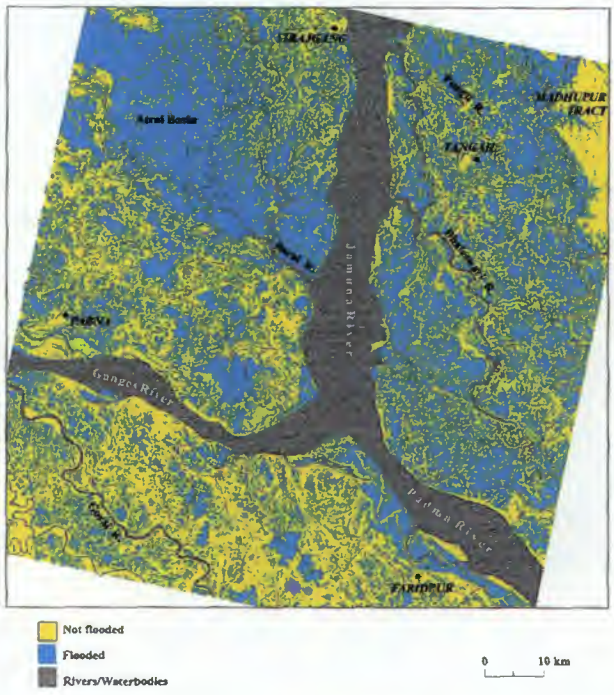

Fig. 2 ERS-1 SAR classification for central Bangladesh, August 28, 1993. *The results for the main rivers have been excluded from the classification.*

classification results, flooded and non-flooded, and presented in Table 1. The statistics show a reasonably high overall accuracy: 84% for July and 81% for August. Agreement of near 90% and better was achieved for the settlement and water classes in both images. The lower agreement of the non-flooded crops (82% and 60%) is most logically attributed to the broad range of SAR signatures for the crops included in the class. The flooded crop category, with 77% and 80% accuracy for the respective July and August images, also includes a variety of flood water characteristics and a range of crop type, canopy, and condition.

Table 1. Classification results of the July and August 1993 ERS-1 SAR Image

Class	July	August
Overall	84%	81%
Settlement	90%	90%
Open water	90%	90%
Non-flooded crops	82%	60%
Flooded crops	77%	80%

Visual Interpretation

The July and August 1993 SAR data were merged into a composite image for an area north-west of the confluence of the Ganges and Jamuna rivers. This composite was produced by displaying the July and August SAR images and an August/July ratio image in

the respective red, green and blue colour planes of the image processing system (see figure 3)

The resulting colour image provided an effective display of change between July and August flood conditions. For example, open water and areas of transplanted *aman* (paddy) that are flooded in both July and August were associated with distinct colour signatures. Changes were also clearly detected in areas where crops became flooded in August.

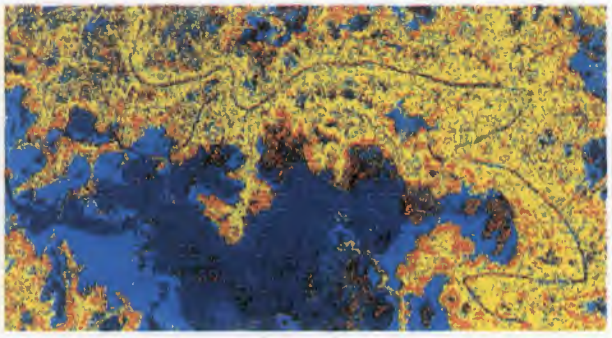

Fig. 3 Multi-temporal ERS-1 SAR image. *Composite image of July 1993 (red plane) and August 1993 (green plane) of the image processing system. A ratio image (July/August) is displayed in the blue plane.*

7. CONCLUSIONS

- The SAR delineation of flooded and non-flooded areas compared favourably with ground information collected simultaneously to the radar data
- The overall agreement was over 80% agreement was greatest for open water surfaces, non-flooded settlements, and for certain crops.
- Difficulties were encountered in the classification of crop canopies that were partially flooded. Ground reference data collection is essential.
- Multi-temporal data were useful for showing changes in flood extent and for assessing the dynamics of hydrology and cropping patterns.
- It appears that classified SAR imagery can be especially useful for verifying FMM results. The radar classification also compared favourably with the most detailed land type (flood depth) maps of Bangladesh.
- ERS-1 - Landsat TM composite imagery provides an understanding of complex land use practices, which vary greatly between the dry season and the monsoon flood period.

HIGH TEMPORAL DETECTION AND MONITORING OF FLOOD ZONE DYNAMIC USING ERS DATA AROUND CATASTROPHIC NATURAL EVENTS: THE 1993 AND 1994 CAMARGUE FLOOD EVENTS.

LAUGIER O., FELLAH K., THOLEY N., MEYER C. and DE FRAIPONT P.

SERTIT, Boulevard Sébastien Brandt, F-67400 Illkirch, Tel : +33 (0)3 88.65.52.00, Email: sertit@sertit.u-strasbg.fr

ABSTRACT

Within the framework of a Pilot Project, SERTIT has investigated the usefulness of high temporal ERS-1 SAR data acquisitions for flood detection and monitoring. The 1993 and 1994 floods in the Camargue region (France) are taken as the subject matter of the case study. An extensive data base has been developed which is composed of satellite data and exogenous data. The satellite data include twenty ERS-1 SAR scenes acquired essentially with a 3 day cycle before, during and after the floods. The detection and cartography of flooded zones is produced by the photo-interpretation of multi-temporal ERS-1 images together with auxiliary information and change detection techniques (colour composition, ratioing and differencing). The analysis of the detected flood evolution maps enables the understanding of flood dynamics. In addition, by taking the opportunity of the large number of georeferenced multi-temporal ERS-1 SAR scenes, a high radiometric resolution ERS SAR image was produced by the temporal merging of eighteen ERS-1 SAR images showing the usefulness of multi-temporal SAR data in cartography. These results lead to the interesting prospective of applications of high temporal acquisition SAR data in the forecasting, monitoring, impact and understanding of catastrophic natural events.

Keywords: ERS-1 SAR, 3 day mode, flood monitoring, temporal merging

1. INTRODUCTION

Within the framework of Pilot Project AO-F112 supported by the CNES and ESA, SERTIT has investigated the usefulness of high temporal acquisition ERS-1 SAR data for hydrological applications in exceptional hydrological conditions (Fellah *et al.*, 1997). The 1993 and 1994 floods in the Camargue region (France) were taken as the subject matter of the case study. One of the tasks was to study the backscattering coefficient behaviour in relation to different soil hydric conditions (flooded, saturated, moist). As a first step, in order to delimitate the hydric conditions, the detection and monitoring of flooded zones was carried out. This is the subject matter of this paper.

This study's originality lies in the number of processed ERS-1 SAR scenes and their temporal coverage of the floods. The study focuses on the 1994 flood as ERS-1 was in the Second Ice Phase (phase D) and therefore covered the Camargue flood every 3 days.

2. THE DATA BASE

SERTIT had already investigated the Camargue 1993 floods using ERS-1 SAR data (de Fraipont *et al.*, 1994 ; Tholey *et al.*, 1995), a data base concerning this event had been already built. This data base was completed in order to obtain an historic background to the 1994 flood and to acquire further information concerning the natural environment of the Camargue region. The data base is composed of georeferenced satellite and exogenous data.

2.1. Satellite Data

The satellite data include a SPOT XS scene plus twenty ERS-1 SAR scenes acquired before, during and after the floods. Most of these scenes were acquired during a three day ERS-1 acquisition mode. The SPOT XS scene was acquired on March the 26th 1993 and contains information concerning the Camargue's land cover. The ERS scenes were acquired between the 26th of September 1993 and the 16th of March 1994 (Table 1). The products of the SAR scenes are either ERS.SAR.PRI or ERS.SAR.GEC standard products (ESA, 1992). All the scenes have been georeferenced and then integrated into a GIS.

Table 1: The ERS-1 SAR scenes

Date	Product	Orbit (Track 2727)
27/09/93	GEC	11504
16/10/93	GEC	11776
01/11/93	GEC	12005
20/11/93	PRI	12277
25/12/93	PRI	12778
31/12/93	PRI	12864
03/01/94	PRI	12907
06/01/94	PRI	12950
12/01/94	PRI	13036
15/01/94	PRI	13079
18/01/94	PRI	13122
21/01/94	PRI	13165
24/01/94	PRI	13208
27/01/94	PRI	13251
02/02/94	PRI	13337
08/02/94	PRI	13423
14/02/94	PRI	13509
26/02/94	PRI	13681
04/03/94	PRI	13767
16/03/94	PRI	13939

2.2. *Exogenous data*

The exogenous data include topographic maps, aerial photography, meteorological data, a flood report and flood evolution maps. The IGN topographic maps cover the entire Camargue region at a scale of 1/25000. Aerial photography were taken during the 1993 flood for the Mairie d'Arles. The meteorological data include daily precipitation for the period lasting from September 1993 to March 1994 and wind information (speed and direction) during ERS SAR image acquisitions. These data were recorded by METEO FRANCE at the Tour du Valat station located in the Camargue region. The flood report (Vianet, 1994) and flood evolution maps (Scale: 1/50 000) were established by the Parc Naturel Régional de Camargue (PNRC), the Camargue nature reserve authority, which plotted the 1993 and 1994 flood areas daily with conventional techniques during the flood-level rise.

3. THE CAMARGUE FLOOD EVENTS

For the first time since the building of the Rhone river embankments in the XIX century, the Camargue region was flooded in October 1993 and January 1994.

3.1. *The Camargue Region*

It is located in the delta of the Rhône river in the South of France near the town of Arles (Fig. 1). The landcover of this region includes rice fields and other croplands, grassland and protected natural marshlands. A complex hydraulic network insures an artificial balance between the agricultural zones, which use a lot of fresh water, and the natural salt marsh zones. The Camargue is a very flat plain normally protected from Rhône floods by embankments. The study area is comprised of the October 1993 and January 1994 Camargue flood zones.

3.2. *The 1993 and 1994 Floods*

The PNRC's flood report analysis allowed a better understanding of the flood evolution. The October 1993 and January 1994 floods were caused by the formation of breaches in Petit Rhône river dikes. During the flood-level rise, Rhône water spread from breaches successively to the four Camargue flood basins. These flood basins are the Saliers, Tête de Camargue, Bernacles and Grand Mar basins (Fig. 1). The hydraulic network played a great role in the flood propagation. In particular, the Rousty canal had enabled the flood water to go from the Bernacles to the Grand Mar flood basin.

The evacuation of the flood water to the Mediterranean sea was a natural process with the water flowing from the Grand Mar basin to the étang du Vaccarès and its tributaries via the Rousty Canal and then to the sea helped by a northerly wind. Pumping stations were also used to transfer flood water from flood basins to the Rhône river and from the étang du Vaccarès tributaries to the sea. This process took much time and was only partial since large quantities of flood water were trapped in the Camargue soils.

4. METHOD AND RESULTS

Firstly the principle of the flood detection method used to map the Camargue floods is presented. Then the flood evolution maps employing ERS SAR data are analysed. Taking the opportunity that the multi-temporal ERS-1 SAR scenes available where georeferenced, SERTIT developed a radiometric enhancement method of SAR data which is described.

4.1. *Flood Mapping Method*

ERS-1, the earth observation satellite of the European Space Agency (ESA) carries a C band (wavelength = 5.6 cm), VV polarisation and 23° average incidence angle SAR which acquires images of the earth's surface in all meteorological conditions.

Theoretically, the interaction between the signal pulsed by ERS-1 SAR and open water which can be considered as flat surfaces is specular generally making the detection of open water possible on a SAR image. Practically, the specular effect can be decreased or even cancelled out by bad weather conditions (in particular wind and precipitation) and/or the presence of vegetation making the detection of open water using a single ERS SAR scene difficult or even impossible.

The distinction between flooded zones and the hydrological network is done with the use of auxiliary information (topographic maps, ...) and/or with a change detection approach between multi-temporal ERS SAR scenes. Change detection techniques of multi-temporal ERS SAR images which are generally used are photo-interpretation (Matthews *et al.*, 1994), colour composition (Blyth *et al.*, 1993), ratioing (Rignot *et al.*, 1993) and differencing (Badji *et al.*, 1994).

Due to the number of scenes which had to be processed and in order to have quick but accurate flood delimitations, the detection and cartography of flooded zones were produced by the photo-interpretation of the multi-temporal ERS-1 images. In addition, auxiliary information were employed in order to try to analyse various surface parameters (soil moisture, surface roughness,...) which affect the backscattered signal. Colour composition, ratioing and differencing techniques were also used to facilitate the detection of flooded zones (Fig. 2).

Once all the scenes where processed, flood-level evolution maps showing the rise (Fig. 3) and the fall (Fig. 4) of flood-level were established. On these images the digitised flood extents are coloured from light blue to light purple and are superimposed on a high radiometric resolution ERS SAR image (see 4.3).

4.2. *Flood Evolution Analysis*

The analysis of flood evolution maps enable the understanding of floods dynamics since this analysis provides information which are comparable to those

Figure 1: The Camargue region its different flood basins (A: Tête de Camargue, B: Bernacles, C: Saliers, D: Grand Mar) and the Rousty Canal in red

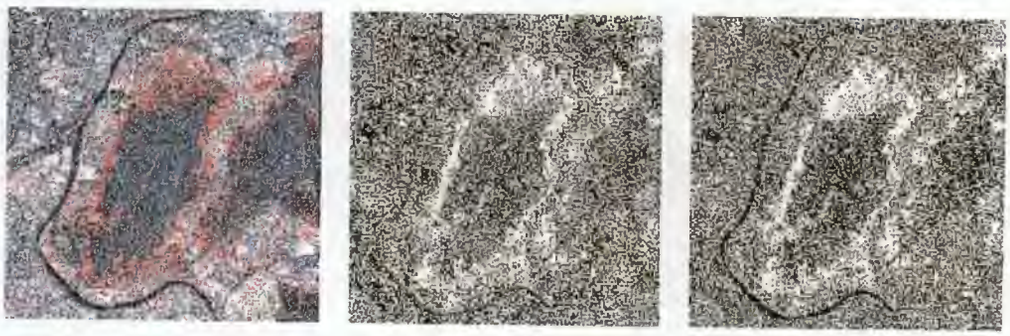

Figure 2: Change detection techniques: Colour composition (left), ratio (centre) and difference (right) images showing the drop of the flood-level in the Saliers basin between 21/02/94 and 27/02/94

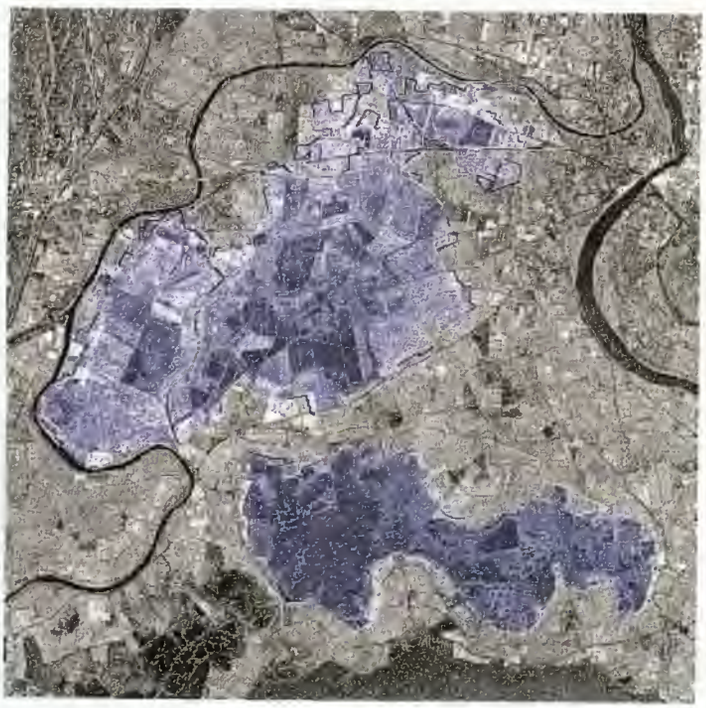

Figure 3: The rise of the flood-level between 12/01/94 and 18/01/94

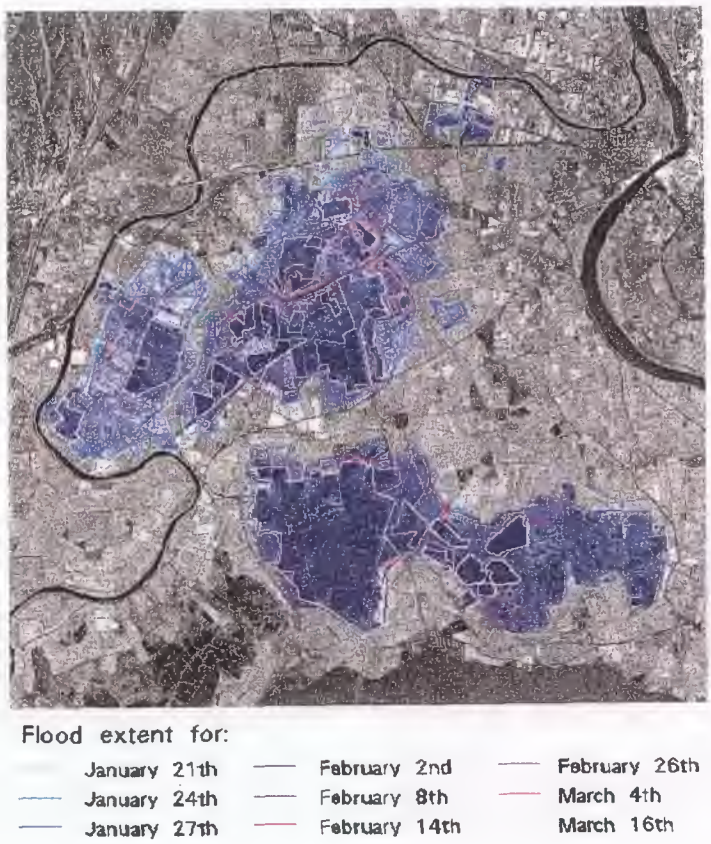

Figure 4: The drop of the flood-level between 21/01/94 and 16/03/94

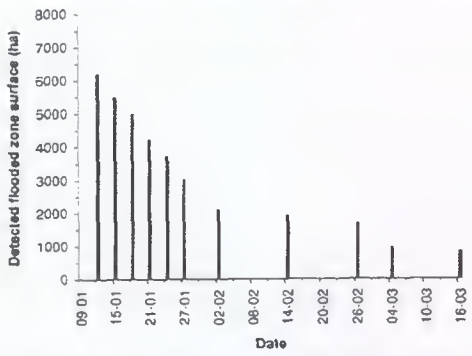

Figure 5: Evolution of detected flooded zone surfaces relating to ERS-1 SAR scene acquisition dates

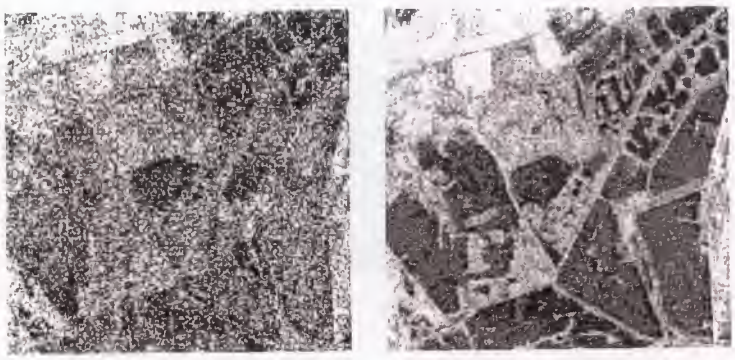

Figure 6: ERS-1 SAR.PRI scene acquired the 06/01/94 (left) and the high radiometric resolution ERS SAR image (right)

extracted from the flood report and flood evolution maps established by PNRC:

- The Tête de Camargue, Saliers, Bernacles and Grand Mar basins are clearly detected on Fig. 3 and Fig. 4;
- The flood evolution maps show the spreading of the flood water in the different flood basins. On Fig. 3, the detected flooded zone surfaces decrease in the Tête de Camargue and Saliers basins between February 12th and 15th whereas the detected flooded zone surfaces increase in the Bernacles and Grand Mar basins. Fig. 4 clearly shows that the speed of the fall in the flood-level in the different flood basins are not the same;
- The flood water evacuation process took a long time. A figure showing detected flooded zone surfaces relating to ERS SAR image acquisition dates is presented (Fig. 5). It shows that in agreement with the flood report, the flood water evacuation process took much time. Indeed, there is a fast diminution of detected flooded zone surfaces until the beginning of February and a stagnation during the February 2nd-26th and March 4th-16th periods.

The study of flooded zone limits with respect to roads and field's limits also shows that multi-temporal ERS-1 images enable the cartography of flood evolution with a satisfactory accuracy for a field process analysis.

4.3. Radiometric resolution enhancement method of ERS SAR images

Taking the opportunity that all the ERS images were georeferenced and integrated into a GIS and following theoretical studies (Fellah, 1994 ; Bruniquel *et al.*, 1997), SERTIT developed a SAR data temporal merging method which showed the usefulness of SAR data in cartography.

In fact, one of the greatest problems with SAR imagery is the speckle which affect the radiometric resolution. This problem is usually resolved by spatial averaging methods of SAR acquisitions which increase its radiometric resolution but alter its geometric resolution. A technique which is not yet often used is the temporal merging of SAR acquisitions which greatly enhances its radiometric resolution and preserves its spatial resolution as it is shown in Fig. 6. The high radiometric resolution ERS image results from the temporal merging of eighteen ERS-1 SAR scenes. One notices that in Figs. 3 and 4 road and hydrological networks, field limits and bridges can be detected. These images show that SAR data can be useful in precise cartography.

The number of processed ERS scenes (18) seems to show that the temporal merging of SAR data is not an economic method. However, the minimum number of SAR scenes which should be used in order to produce an accurate and cost effective cartography of a region may be much smaller than eighteen and it depends on the study's objective. For example, for geological applications a number of about three images seems to be a good compromise (Yesou *et al.*, 1997).

5. CONCLUSION

The analysis of 3 day mode ERS-1 SAR images allowed a flood evolution cartography with a satisfactory accuracy for a field process analysis and enabled an accurate description of flood dynamics. The comparison between this method and conventional mapping techniques shows the usefulness of SAR data in producing a quick and effective cartography of flood evolution.

Moreover, the high radiometric resolution ERS SAR image shows that multi-temporal SAR data can also be used for precise cartography, in particular for regions where adverse meteorological conditions make the use of optical space or air borne instruments difficult.

Since the ERS-1 3 day mode was only temporary, all these results show the great potential of high temporal SAR data acquisitions. In that context, the SAR data acquisition cycle seems to be a key factor in the environmental monitoring. The low resolution and high temporal acquisition mode of RADARSAT SAR and with a perspective towards the future ENVISAT ASAR will therefore certainly open up numerous applications in the anticipation, prevention, impact and monitoring of major environmental hazards.

ACKNOWLEDGEMENTS

The ERS-1 SAR data were available under ESA Pilot Project A02-F112. This study was supported by CNES within the AVAL SAR programme. The authors would wish to thank the Mairie d'Arles and the Parc Naturel Régional de Camargue which kindly furnished information and data concerning the floods.

REFERENCES

Badji M., Dautrebande S., Mokadem A.I., Dewez A, 1994, ERS-1 SAR Imagery Applied to Rural Bassins Hydrological Studies I: The Flood Inundation Mapping and Monitoring, Proceedings of the First Workshop on ERS-1 Pilot Projects, Toledo, Spain, 22-24 June 1994, ESA SP-365, pp 117-124.

Blyth K., Diggin D.S., 1993, Surveillance des Inondations par le SAR d'ERS-1, Earth Observation Quaterly, ESA, N° 42, pp 6-8.

Bruniquel J. and Lopes A., 1997, Multi-variate speckle reduction in SAR imagery, Int. J. Remote Sensing, Vol 18, No. 3, pp. 603-627.

de Fraipont P., Guerre L.F., Tholey N., 1994, Complémentarité SPOT-ERS pour le suivi d'événements hydrologiques exceptionels. La crue d'octobre 1993 en Camargue. Rapport SERTIT-SPOT Image, 13p. plus poster.

ESA, 1992, ESA ERS-1 Product Specification, ESA SP-1149.

Fellah K., 1995, The impact of the observation scale in hydrological applications of SAR data, Internship report, November 94 - March 95, ESA-ESTEC/VRL, Noordwijk, the Netherlands.

Fellah K., Meyer C., Laugier O., Besnus Y. and de Fraipont P., 1997, Potential and limitations of multi-temporal SAR data in a quantitative SAR approach for multi-scalar hydrological applications. Synthesis of ERS Alsace/Camargue Pilot Project. Proceedings of the 3rd ERS Symposium, Florence, Italy, 18-21 March 1997.

Rignot J.M. E. and Van Zyl J.J., 1993, Change Detection Techniques for ERS-1 SAR Data, IEEE Transactions on Geoscience and Remote Sensing, Vol 31, No. 4, pp 896-906.

Matthews J. and Gaffney S., 1994, A study of Flooding on Lough Corrib, Ireland During Early 1994 Using ERS-1 SAR Data, Proceedings of the First Workshop on ERS-1 Pilot Project, Toledo, Spain, 22-24 June 1994, ESA SP-365, pp 125-128.

Tholey N., de Fraipont P., Clandillon S., Fellah K., Yesou H., 1995, Monitoring Flood Events with Remote Sensing Data : An Exemple of ERS-1's contribution to Floods Events in Northern and Southern France Regions, Proceedings of the First ERS Thematic Working Group Meeting on Flood Monitoring, ESRIN, Frascati, Italy, 26-27 June 1995, ESA.

Vianet R., 1994, Rapport sur les inondations, Parc Natural Régional de Camargue (unpublished).

Yesou H., Braux C., Rouzeau O., Clandillon S., Rolet J. and de Fraipont P., 1997, Assessment of two methodologies of ERS mixing for geological investigations: ERS time-series and optical-radar fusions, Proceedings of the 3rd ERS Symposium, Florence, Italy, 18-21 March 1997.

EVOLUTION OF OIL SLICK PATTERNS AS OBSERVED BY SAR OFF THE COAST OF WALES

Pablo Clemente-Colón, William Pichel

National Environmental Satellite, Data, and Information Service
National Oceanic and Atmospheric Administration
Washington, DC 20233, USA
phone: + 1 301 763 8231, fax: + 1 301 763 8020

Xiao-Hai Yan

Graduate College of Marine Studies
University of Delaware
Newark, DE 19716, USA
phone: + 1 302 831 3694, fax: + 1 302 831 1199

ABSTRACT

Imagery from three different Synthetic Aperture Radar (SAR) spaceborne sensors were obtained over the coast of Wales, UK. These observations indicated the persistence of slick features associated with the grounding on February 15, 1996 of the Sea Empress tanker at the entrance of the Milford Haven estuary and the resulting massive oil spill that followed. RADARSAT, ERS-1, and ERS-2 SAR images revealed the evolution of these features from February 22 to February 26, 1996. The feature tracking Maximum Similarity Shape Matching method (MSSM) developed at the University of Delaware College of Marine Studies (CMS) was applied to the pair of ERS SAR images. MSSM calculated drift speeds of about 10 cm/s. Observations of the slick pattern evolution in the SAR imagery were compared to available reports of ground conditions. Deformation of the slick features was also evident in the SAR data throughout the five-day period.

1. INTRODUCTION

Ocean features such as current fronts and eddies can be detected by visible, thermal, and Synthetic Aperture Radar (SAR) satellite sensors and can potentially be tracked by any of these systems if adequate temporal coverage relative to the movement and deformation of the feature exists. In particular, the detection by these sensors of ocean features associated with the presence of surface oil slicks has also been documented. Surface oil slicks produce changes in sun-glitter patterns that can be detected and mapped using the visible bands of remote sensing sensors such as the Landsat, SPOT and NOAA AVHRR radiometers (Wald et al., 1984). Due to differences in the emissivity of oil and sea water, surface temperature differences can be developed to a level that will also make slick patterns detectable by satellite thermal sensors (Park et al., 1989; Stringer et al., 1992). Changes in the surface tension due to the presence of oil will tend to dampen the capillaries and short gravity waves that are responsible for most of the backscattered signal received by a SAR instrument. These relatively smoother areas will appear as darker or low backscatter regions in radar images (Goodman, 1990). The advantages of the SAR over AVHRR IR data are higher spatial resolution and the capacity to make observations both day and night and under cloud covered conditions.

The ability of SAR to detect oil slick features depends greatly on the wind conditions at the time of the observation. Low winds will not produce enough roughness over the unaffected sea surface to create sufficient contrast with the oil covered areas. On the other hand, very high winds will tend to destroy frontal features due to mixing and may create enough backscatter clutter to make it impossible to detect any oil covered areas. Wave action and tidal mixing can also greatly affect the development and detection of oil slicks. In spite of this, many cases of oil spill detection by spacecraft SAR have been documented since the launch of ERS-1 satellite.

The use of satellite data for ocean feature-tracking is becoming more and more commonly accepted as a valuable tool for applied and basic research (Vastano, 1995; Emery, 1985; Kelly and Strub, 1992; Yan et al., 1994; Breaker et al., 1992). The technology has been evolving from the early use of hardcopy satellite images to computer assisted analysis and more recently to automated feature recognition techniques such as the Maximum Shape-matching Method (MSSM) developed at the University of Delaware Center for Remote Sensing (Kuo and Yan, 1994).

The detection, mapping, and tracking of oil spills, in particular, is of critical importance in a wide range of emergency response activities after a major oil spill. This information, along with additional information on local environmental conditions and model output, can be used to devise protection responses and cleanup strategies. Knowing the extent and trajectory of an oil spill can increase the efficiency of the emergency response effort. The Exxon Valdez oil tanker spill on March 24, 1989 in Alaskan waters was the first major spill widely studied with the use of spacecraft visible and thermal remote sensing (Park et al., 1989; Stringer et al., 1992).

The Sea Empress oil tanker spill on February 15, 1996 off the coast of Wales was much larger than that of the Exxon Valdez spill in Alaska and has given us the first opportunity to study the evolution of a major spill using spaceborne SAR. Although, at least 12 scenes from three different SAR satellites were acquired between February 22 and March 17 (Bjerkelund, 1996), only three images were available for this study. The objectives of this paper are to apply the MSSM method to two of the spaceborne SAR images of the Wales oil spill and to study the potential use of spaceborne SAR for oil detection and tracking.

2. SAR DATA

The ERS-1 and ERS-2 satellites are multi-sensor satellites operated by the European Space Agency (ESA). ERS-1 was launched on July 17, 1991 and almost four years later, ERS-2 was launched on April 21, 1995. The Active Microwave Instrument (AMI) aboard has a single SAR mode with a resolution of 25 m, a fixed incidence angle of 23 degrees at the center of the scene and 100 km swath. The Tromsø Satellite Satation (TSS, 1996) acquired and processed the SAR data over the southwest Wales region. Two full resolution images, for February 25 and 26, 1996, were available from ESA for this study. A third RADARSAT STANDARD MODE 1 SAR image of the region was produced from data acquired on February 22 by the Canada Centre for Remote Sensing (CCRS) and processed by RADARSAT International (RSI). This RADARSAT mode is analogus to the ERS-1/2 SAR with a resolution of 25 m. The image was available through the world wide web from the Canadian Space Agency (CSA, 1996) but at a much lower spatial resolution of about 300 m.

3. SEA EMPRESS OIL SPILL

The Sea Empress oil tanker ran aground off Saint Ann's Head, just outside the Milford Haven estuary in Wales, under gale-force winds of up to 40 knots and 10 ft waves conditions on February 15, 1996. At the time, it was transporting a cargo of 37.6 million gallons of medium to light crude oil to the Texaco refinery in Milford Haven, a major oil refinery and loading port in the UK. Unfortunately, the Milford Haven Estuary is also an important natural conservation area and forms part of the Pembrokeshire Coast National Park, Britain's only marine wildlife sanctuary. In addition, Milford Haven is an important fishing port for lobster, crab, and mackerel fisheries.

After the initial grounding, around 1.7 million gallons were estimated to have spilled out of the tanker. On February 18, the tanker ran aground again with spill estimates jumping to about 9 million gallons. Thousands of gallons of dispersant were sprayed by aircraft to dissipate the increasing spill. By February 21, the estimated spill had jumped to 12 million gallons with gale winds and raging seas also reported. A NOAA Advanced Very High Resolution Radiometer (AVHRR) satellite image taken at 08:08Z on February 21 at the Natural Environment Research Council (NERC) Satellite Receiving Station in Dundee (Dyrynda and Symberlist, 1997) , showed a long streak of oil spreading eastwards along the coast towards the Caldey Island. Southwesterly winds were credited with initially spreading much of the oil offshore but shifting winds throughout this period pushed large amounts of the crude toward the coastlines and into beaches from the Saint Brides Bay, north of Saint Ann's Head, to the Carmarthen Bay to the east. By February 26 oil sheen had been reported as far as the Lundy Island in the middle of the Bristol Channel, about 65 km SSE of Saint Ann's Head. Three weeks after the initial oil spill, persistent beach contamination from new oil coming ashore was being reported over beaches on the western Carmarthen Bay. The final official spill estimate for this disastrous event stands at 16 million gallons (72 thousands tonnes) of oil.

4. MSSM ANALYSIS

The MSSM technique was used to derive velocity vectors from observed oil slick patterns on the ERS-1/2 SAR images. This method uses the concept of maximum similarity between features for which a centroid is calculated through a radius weighted mean. In theory, the features may have any shape and can not only translate but also rotate and suffer some deformation from one image another. Features are matched between the two images based on selectable confidence levels. Once this is done, the corresponding velocity vectors can be calculated and plotted for different parts of the feature. A more detail description of the method is presented in Kuo and Yan, 1994.

The February 25 and February 26 images (figures 1 and 2, respectively) show several recognizable slick features from one image to the other. The effort concentrated over the Carmarthen Bay were a large slick pattern was observed in both images. A sub-image was cropped out for this region. Co- registration of the sub-images was done with an IDL/ENVI geometric transformation routine using selected coastline control "tie" points between the two sub-images. An adaptive Lee filter was used to reduce speckling and a median filter was then applied to further enhance some of the slick features. The sub-images were then sampled down by one third for final MSSM analysis. Edge detection and contrast enhancement were finally applied to binarize the image and better define slick boundaries

5. RESULTS

The SAR images used in this project represent the first time that the evolution of a slick feature from a major oil spill has been observed throughout several days and by multiple spacecraft SAR instruments. The RADARSAT image (CSA, 1996) indicates very low backscatter over the western Carmarthen Bay, relative low backscatter also to the south and to the west along the coast, and a bright region over the eastern Bay. The bright region indicates that eastern Bay areas were not yet impacted by the spill as of February 22. The low backscatter regions indicate general oil contamination with the most intense slicks hogging the western Carmarthen Bay coastline and

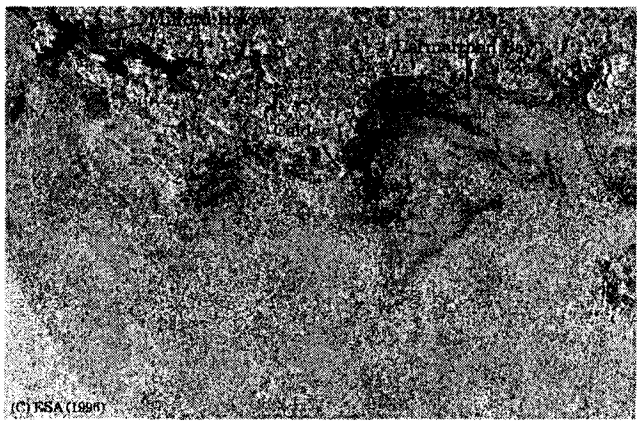

Figure 1. ERS-1 SAR image acquired on February 25,1996 at 22:24 UTC. Darker areas represent lower backscatter returns caused by the presence of a large oil slick on the Carmarthen Bay .

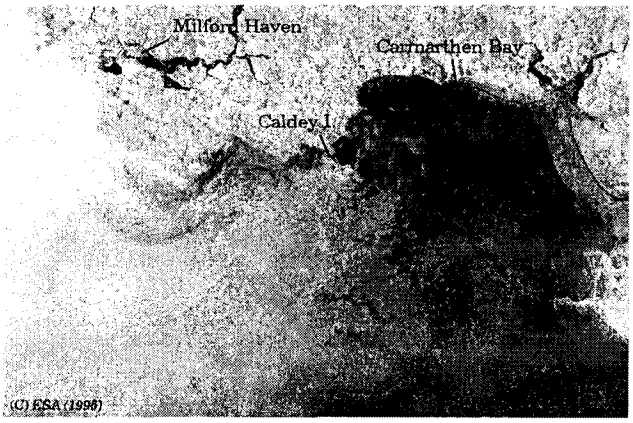

Figure 2. ERS-1 SAR image acquired on February 26,1996 at 22:24 UTC. Darker areas represent lower backscatter returns caused by the presence of a large oil slick on the Carmarthen Bay .

rapidly advancing further into the Bay as suggested by the AVHRR observations of the previous day. Available meteorological information can help explain the observed distribution of the oil slick. Hourly data for February 21 and 22 from the weather buoy 62303 located just southwest of the Carmarthen Bay at 51.5°N, 49.0°W, show persistent strong winds between 8 and 20 knots in a west northwest direction throughout those days. Further advance of the oil slick into the Carmarthen Bay is evident in the ERS-1 image for February 25 with some of the low backscatter filaments extending more than half way into the eastern Bay. The observed drift appears to be related to a relaxation in wind speed and a change in the wind direction toward the southeast earlier that day. The filaments extend even further on February 26 reaching the eastern Bay. The drift and dispersion of the slick pattern in the Carmarthen Bay during the 24 hours between the February 25 and 26 images was more rapid than during the 3 days between the February 22 and 25 observations. This fast spreading of the slick over most of the bay is probably due to a combination of the reported airborne spraying of thousands of gallons of dispersant over the Carmarthen Bay on February 25 (SOUTHERNAIR, 1996) and very rapidly shifting winds throughout the day.

Figures 3 shows the output obtained from MSSM analysis with the calculated vectors plotted over the February 25 ERS-1 Carmarthen Bay sub-image. The elongated feature extending into the eastern Bay is the most identifiable feature after a large amount of slick dispersion occurred between the two days. The velocity vectors were computed and plotted by the MSSM program and represent speeds of 12.6 (label 1), 10.8 (label 2), 8.9 (label 3), and 8.1 $\pm$ 0.45 cm/s (label 4). These velocity vectors show a southeastward drift of the pattern which is consistent with the visual inspection of the images. It is obvious that different parts of the slick drifted at different rates and that large deformation of the overall shape of the slick occurred in one day. Velocity vectors from other features on the south and western side of the slick pattern indicated a generally slower southward drift with an averaged magnitude of 3.79 cm/s (not shown). The much faster southeastward drift of the northeastern part of the slick pattern again reflects significant deformation of the slick as it evolved. In general, the estimates from MSSM appear to be reasonable. ERS-1/2 SAR coverage of the region extending from the southern Carmarthen Bay to the Bristol Channel during February 25 and 26 is shown in figure 4. These data show that some of the slick actually drifted even faster reaching as far south as the Lundy Island in the Bristol Channel.

Figure 3. MSSM velocity vectors output for the elongated oil slick pattern on Carmarthen Bay superimposed on ERS-1 SAR sub-image for February 25, 1996. The vectors represent the displacement of the pattern between 22:24 UTC, February 25 and 22:24 UTC, February 26, 1996.

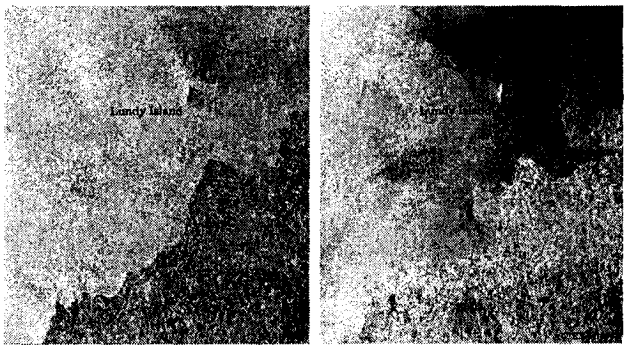

Figure 4. ERS-1(left) and ERS-2 (right) SAR images of the region extending from the southern CarmarthenBay to the Bristol Channel on February 25 and 26, 1996, respectively. Darker filaments observed on February 26 represent lower backscatter returns associated with oil slicks reaching the Bristol Channel.

6. CONCLUSIONS

The evolution of an oil slick pattern resulting from one of Britain's largest oil spills was observed using spacecraft SAR imagery. Much of the low backscatter patterns observed in three images acquired by RADARSAT, ERS-1, and ERS-2 satellites were consistent with reported ground conditions. In particular, a persistent oil slick pattern was observed between February 22 and February 26. This pattern was observed to drift from the western Bay, where many heavily polluted beaches were found, into the eastern Bay during the observing period. Evidence of slicks as far as 65 km south of the initial spill location was also shown.

The MSSM feature tracking technique developed at the Center for Remote Sensing, University of Delaware was used. The exercise demonstrated the possibility of using feature tracking techniques on spaceborne SAR images of oil slick features. In general, frequent observations of the oil slick patterns are desirable and would allow for better tracking under rapidly changing conditions. The high resolution SAR data can provide for good delineation of features and should allow for accurate estimates of oil slick drifts.

7.0 ACKNOWLEDGMENTS

This study was partially supported by NSF under grant OCE-9453499, and by NOAA Sea Grant under grant NA56RG0147. ERS-1 and ERS-2 SAR data was provided by the European Space Agency under the National Ice Center ERS-1/2 Proposal.

8.0 REFERENCES

Bjerkelund, C., 1996, Canadian Center for Remote Sensing, personal communication.

Breaker, L. C., V. M. Krasnopolsky, D. B. Rao, and X.-H. Yan, 1994, The feasibility of estimating ocean surface currents on an operational basis using satellite feature tracking methods, *Bulletin of the American Meteorological Society*, 75(11):2085-2095.

CSA, 1996, Canadian Space Agency, "http://radasat.space.gc.ca/ENG/Activities/Early_Images/" (HTML).

Dyrynda, P. and R. Symberlis, 1997, Sea Empress Oil Spill, "http://www.swan.ac.uk/biosci/empress/", (HTML).

Emery, W. J., A. C. Thomas, M. J. Collins, W. R. Crawford, and D. L. Mackus, 1986, An objective method for computing advective surface velocities from sequential infrared satellite images, *J. Geophys. Res.* 91(12):865-878.

Goodman, R., 1994, Overview and future trends in oil spill remote sensing, *Spill Sci. Technol. Bull.* 2(1):11-21.

Kelly, K. and P. T. Strub, 1992, Comparison of velocities estimates from advanced very high resolution radiometer in the coastal transition zone, *J. Geophys. Res.* 97(6):9653-9668.

Kuo, N.-J. and X.-H. Yan, 1994, Using the shape-matching method to compute sea-surface velocity from AVHRR satellite images, *IEEE Trans. Geosci. Rem. Sens.* 32(3):724-36.

Park, P. K., J. A. Elrod and D. R. Kester, 1989, Satellites as tools to study marine pollution, Eighth International Ocean Disposal Symposium, 9-13 Oct. 1989, Inter-University Center of Postgraduate Studies, Dubrovnik, Yugoslavia, 1989, pp. 16-17.

SOUTHERNAIR, 1996, Southern Air Transport works to disperse Wales oil spill, "http://www.southernair.com/news/walesoil.htm", (HTML)

Stringer, W. J., K. G. Dean, R. M. Guritz, J. M. Garbeil, J. E. Groves, and K. Ahlnaes, 1992, Detection of petroleum spilled from the MV Exxon Valdez, *Int. J. Remote Sens.* 13(5):799-824.

TSS, 1996, Troms Satellite Station (agency) "http:i//www.tss.no/oilserv/exa.html" March.

Vastano, A. L., S. E. Borders, and R. E. Wittenberg, 1985, Sea surface flow estimation with infrared and visible imagery, *J. Atmos. & Oceanic Technol.* 2:401-403.

Wald, L., J. M. Monget, M. Albuisson, H. M. Byrne, and J.-M. Massin (ed.), 1984, A large scale monitoring of the hydrocarbons pollution from the LANDSAT satellite, Remote Sensing for the Control of Marine Pollution, NATO Challenges, *Mod. Soc.* Vol. 6, pp. 347-358.

Yan, X.-H., N.-J. Kuo and V. Klemas, 1994, Automated techniques for obtaining ocean surface current velocities from satellite images, Proc. of the Second Thematic Conf. on Remote Sensing for Marine and Coastal Environment, New Orleans, LA, 31 Jan.-2 Feb., 1994, Vol. 1, pp. 85-95.

COMPLEMENTARY ANALYSIS OF SAR ERS AND SPOT-P DATA FOR THE MAPPING OF PINATUBO LAHAR AND PYROCLASTIC FLOW DEPOSITS

Fredy Z Garcia, Jean Chorowicz

Paris VI University, LGGST. Case 129. 4, Place Jussieu, 75252 Paris cedex 05, France.

Phone +33 01 44 27 52 60 Fax +33 01 44 27 50 85

Email address: garcia@lgs.jussieu.fr - choro@lgs.jussieu.fr

Perla Delos Reyes

Philippine Institute of Volcanology and Seismology, Q.C., Philippines.

Email address: peejay@x5.phivolcs.dost.gov.ph

ABSTRACT

SAR ERS and SPOT-P satellite data acquired in 1995 and 1993 over the western side of Pinatubo Volcano were analyzed and compared with field data. Multi-temporal SAR ERS-1 data acquired on 9 July and 13 August 1993, with 35 days interval, show that there was significant lahar development. Active lahars manifested as rough surfaces with high degree of brightness in the August data. Active channels can also be identified and delineated, reflected as white and light to dark gray tones, respectively, depending on moisture and textural features. The high capability of ERS-1 to detect moisture content and surfaces covered by water permitted easy recognition of lakes and flooded areas, appearing black when there is quiet standing water or light gray surface when water is wavy due to windy conditions. The analysis of stereoscopic SPOT-P data for the mapping of ancient (pre-1991) and recent lahar and pyroclastic flow deposits is based on differences in morphology, texture and brightness. Both multi-temporal SPOT and SAR ERS-1 images show temporal and spatial development of the lahars since the eruption of Pinatubo in June 1991.

1. INTRODUCTION

The Pinatubo stratovolcano (Fig. 1) dome complex is located 15°08' N and 120°21'E, to the northern end of the Bataan volcanic arc (Wolfe & Self 1982; Newhall & al 1993, 1996). It is built-up of Eocene and Mio-Pliocene rocks (Hawkins & Evans 1983; Delfin & al 1996). The last plinian eruption occurred in June 1991. The volume of pyroclastic materials ejected during this eruption was estimated 5 to 7 cubic kilometers with the bulk of the deposits emplaced on the western flank of the volcano. These deposits are the main source materials for lahars which occur each year by the erosion and remobilization during the rainy season. Observations and mapping of lahars are done yearly (Punongbayan & al 1993). Active lahar deposits have been identified on multitemporal black and white SAR ERS images and keys to their identification have been established (Chorowicz & al 1997).

Our present objective is to assess the usefulness of satellite imagery for (1) the mapping of pre-1991 eruption (ancient) and post-1991 eruption (recent) lahar and pyroclastic flow deposits, and (2) identification of geomorphic changes in the watershed areas and the river channels draining from Pinatubo Volcano.

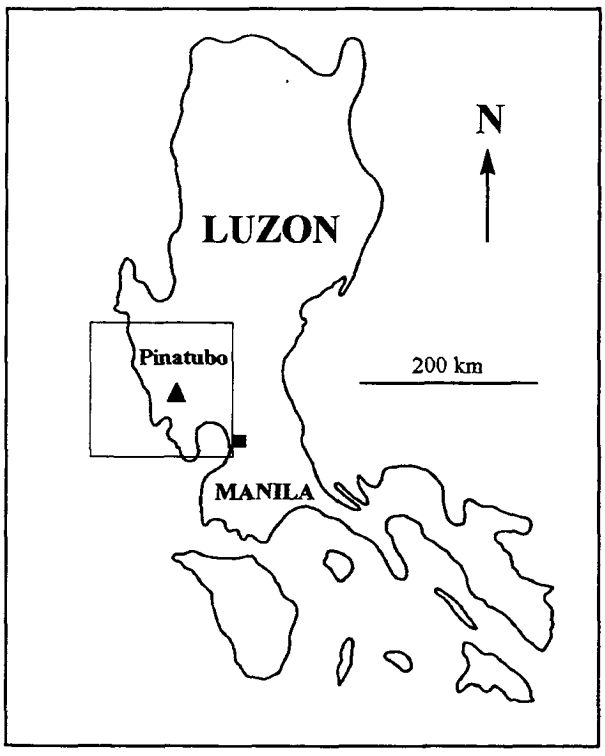

Figure 1. Location map of the study area.

2. METHODOLOGY

SAR ERS-1 and optical SPOT-P images acquired over the western side of Pinatubo Volcano in 1993 and 1995 were analyzed and compared with field data. Analysis was made on high resolution SAR ERS-1 images dated 9 July and 13 August 1993 with pixel 12.5 m size. We also analyzed a stereopair of SPOT panchromatic images (KJ-302,319) with pixel size 10 m, dated 12 February 1995 and 14 March 1995.

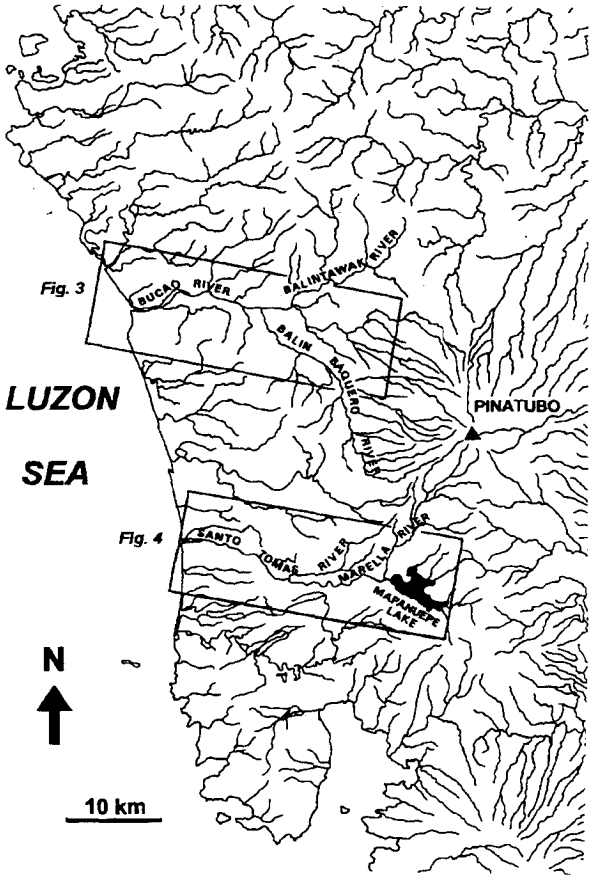

Figure 2. Drainage pattern of the Pinatubo Volcano and location of selected test areas on SAR ERS and SPOT-P data.

3. ANALYSIS ON 1993 SAR ERS IMAGES

a) Bucao Basin

Along the upper streams of the Balintawak River (Fig. 2), the SAR ERS-1 data acquired on 9 July and 13 August 1993 show that there was significant lahar development during the 35 days interval. Both ERS-1 images show pre-existing lahar terraces which are relatively differentiated by white color and high brightness that represent the slopes of the terraces. The active flow channel in the July image is represented by black sufaces or narrow curved and black lines, located generally at the base of the terraces. These active channels probably are permanent stream flows. They were replaced in the August scene by the wide, white, curved surface displaying rough textural feature (Fig. 3), along this stretch of the Balintawak River. The temporal changes in brightness are due to the increase in load of coarse sediments during an active lahar flow. These observations are supported by field data which reported that a debris flow event occurred from 0508H to 2242H local time (Punongbayan et al, 1994). The 13 August 1993 SAR ERS-1 data was acquired at 1028H, local time.

Along the middle reach of Balintawak river, both SAR ERS-1 images show changes in color and texture. In the July SAR ERS-1 data, the surface shows fine texture and black color with well defined drainage pattern indicating that the surface is relatively flat, with a cover of fine sediments and high moisture content. In the August SAR ERS-1 data, the surface has rough texture and light color with the main channel braiding into divergent streams, creating a radial pattern of fan-shaped lahar deposits. The divergent radial lines have high brightness which represents the active channels developing the fan lahar deposits during this time. The damping of lahar deposits dammed a non-Pinatubo tributary north of this section resulting in the increase of the lake surface, reflected as a black surface.

Figure 3. Bucao Basin. August 13, 1993 SAR ERS-1 data. The lahar deposits developed during the 13th August event formed a fan radial pattern in the upper stream of the basin. In the middle, the Bucao valley has a rough texture and white tone with definite drainage

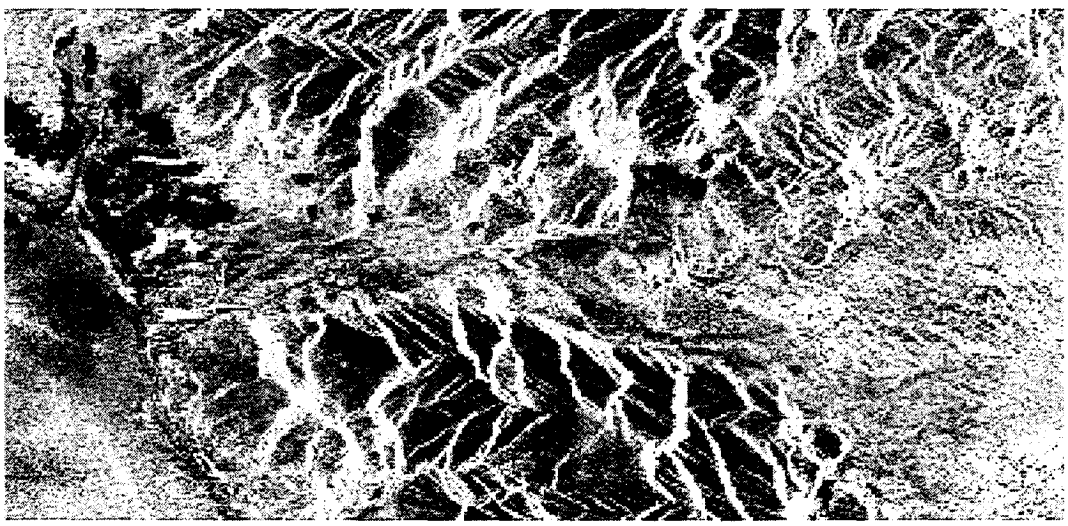

lines indicating that the surface is filled by coarse grained sediments with high moisture content.

Figure 3A. February 12, 1995 SPOT-P image. The white color represents terraces formed of lahar deposits and grey tones are the humid zones.

b) Pinatubo pyroclastic flow field

Both in the SPOT and ERS-1 data, the surface of the 1991 pyroclastic flow is shown to be extensively incised by dense, pinnate rill network during the early stages of erosion, then becoming wider and deeper creating dendritic channel patterns. Most of these recent pyroclastic flow deposits drain towards existing pre-eruption tributaries of the major river systems around Pinatubo. On the western side, the northwestern drainages of Balintawak, Balin-Baquero, Bucao rivers and the southwestern drainages of Marella-Sto. Tomas rivers deliver a major bulk of the 1991 eruption pyroclastic flow materials towards distal low-lying areas (Fig. 2). On the SAR ERS-1 data, the pyroclastic flow appears to be not distinctive in texture from the ancient and recent pyroclastic flow units. By comparing the delineated boundaries in the SPOT image, one can recognize an increase in relief of the ancient deposits. Likewise, on SPOT-P data the boundary between the 1991 pyroclastic flow and post-1991 lahar deposits can be discerned from the difference in textural features, smooth for lahar deposits and rugged/rough for pyroclastic flow. On SAR ERS-1 images the boundary of the ancient and recent pyroclastic flow deposits is not discernible except for distinctive white surface boundary between the two types. Boundary between the 1991 pyroclastic flow and lahars is likewise not distinctive.

c) Santo Tomas - Marella Basin

Along the upper reach of the Marella river (Fig. 2), the SAR ERS-1 images both reflect presence of recent lahar terraces indicating that it was emplaced even before July 1993. However, in August 1993, the shifting of the active lahar flow towards the western side indicates overtopping and deposition of additional sediments.

Along the middle reach of the Marella river, lahar terraces are also evident on the August and July 1993 images, indicating that probable emplacement is from 1991 to 1993. However, the active channel was on the eastern side of this terrace. The July flow had anastomotic channel appearing as black surface bounded by narrow white surface, reflecting minor lahar terraces in border of the main thalweg. The August flow has a linear shape and wider channel appearing as white surface with rough texture, indicating that there was an ongoing lahar flow. Major aggradation during and after 13 August 1993 lahars could have resulted in the shifting of flows towards the west side (Rodolfo & al 1996; Punongbayan & al 1993).

Figure 4. Santo Tomas Basin. August 13, 1993 SAR ERS-1 image. The black tone is due to free water on the Mapanuepe Lake and the flooding plains during the typhoon of 13th August. The bright tones on the whole of the valley correspond to runnig lahars with high brightness.

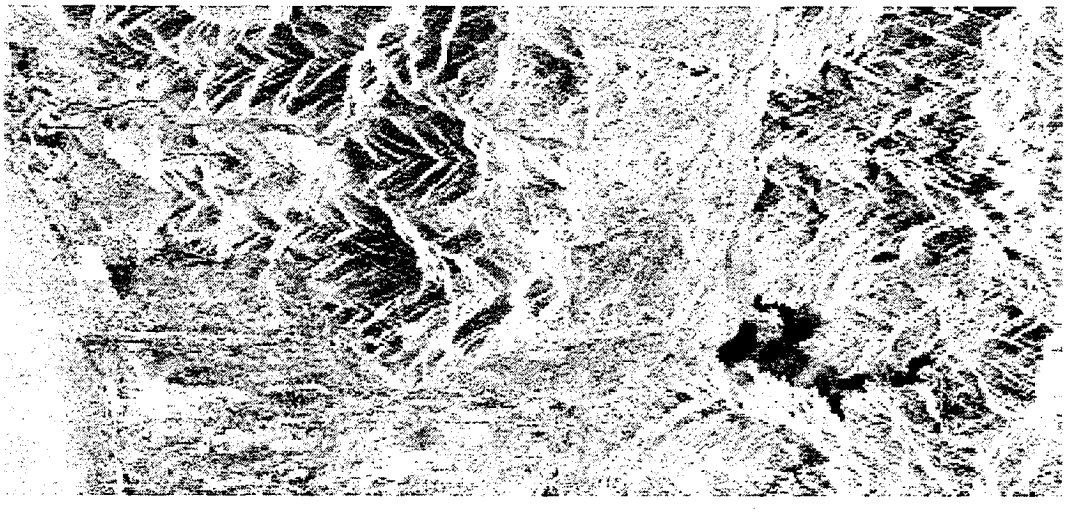

Figure 4A. Santo Tomas Basin. February 12, 1995 SPOT-P image. The high level of the stream flow, manifested by darker tone along the main active channel, has emphasized the distinct boundary of the existing high lahar terraces, in white color.

4. STEREOSCOPIC SPOT-P DATA ANALYSIS

a) Comparison of 1995 SPOT images

Analysis was made on a stereopair of SPOT panchromatic images (KJ-302,319) with pixel size 10m, dated February 12, 1995 and March 14, 1995, with 31 days interval. Analysis of SPOT stereopair, shows particular textural and morphological features which can be used to differentiate various types of volcanic deposits, specially applicable to ancient deposits, and even assign relative dating. There seems to be no distinction between lahar deposits from 1991 to 1995 because they have similar spectral response. However, the high level of the normal stream flow in the February image, manifested by darker color along the main active channel, emphasized the distinct boundary of the existing high lahar terraces. Furthermore, comparison of the two SPOT images cannot provide significant lahar development since both images were taken during the relatively dry season.

b) Comparison of SPOT and SAR ERS-1 data

The side looking high resolution SAR ERS-1 data taken during rainy season has permitted the recognition of relative changes along the main thalwegs, and the development of active lahar flows. Furthermore, the analysis on stereoscopic SPOT data acquired during the onset of the 1995 dry season has allowed differentiation of ancient and recent lahar deposits.

CONCLUSIONS

The use of SAR ERS and SPOT-P remote sensing data, has proven to be effective in mapping lahar and pyroclastic flow deposits in the western side of Pinatubo Volcano, especially in sections not accessible in the field. On SAR ERS-1 images one can recognize the morphological and surface features even through cloud cover. Cartography with optical SPOT data is limited by frequent cloud cover in tropical and volcanic areas such as the Philippines. Comparison of ERS-1 and SPOT images is useful in verifying relief features, identifying active lahars, and delineating areas affected by flooding and formation of lahar-dammed lakes. These mapping tools still need to be verified with field data.

REFERENCES

Chorowicz J & al 1997, Keys to analyse active lahar from Pinatubo on SAR ERS imagery. Remote Sensing Environment (in press)

Delfin F G & al 1996, Geothermal exploration of the pre-1991 Mount Pinatubo hydrothermal system. Fire and mud: eruptions and lahars of Mount Pinatubo, Philippines. PHIVOLCS - University of Washington Press, Seattle, p. 197-212.

Hawkins J W & Evans C A 1983, Geology of the Zambales Range, Luzon, Philippine Islands: Ophiolite derived from an island arc-backarc basin pair, in D.E. Hayes, ed., The Tectonics Evolution of the southeast Asian seas and islands, v. 2: Amer. Geophys. Union, Geophys. Monograph 27: 124-138

Newhall C G & al 1996, Eruptive history of Mount Pinatubo. Fire and mud: eruptions and lahars of Mount Pinatubo, Philippines. PHIVOLCS - University of Washington Press, Seattle, p. 165-195.

Newhall, C.G..1993. Eruptive history of Mount Pinatubo [abstr.]: Eos, Transactions of the American Geophysical Union, 74(43): p. 666-667.

Punongbayan R S & al 1993, Impacts of the 1993 Lahars and longterm lahar hazards and risks around Pinatubo volcano. Philippine Institute of Volcanology and Seismology, UNESCO report. p. 1-40.

Rodolfo K S & al 1996, Two years of lahars on the western flank of Mount Pinatubo: initiation, flow processes, deposits, and attendant geomorphic and hydraulic changes. Fire and mud: eruptions and lahars of Mount Pinatubo, Philippines. PHIVOLCS - University of Washington Press, Seattle, p. 989-1013.

Wolfe J A & Self S 1982, Structural lineaments and Neogene volcanism in southwestern Luzon, in The tectonics and Geological Evolution of Southeast Asian Seas and Islands. Part 2. Hayes. D. Editor. Amer. Geophys. Union, monograph 27: p. 157-172.

This work is supported by UNESCO IUGS-GARS programme on the Asia Natural Hazard Mapping Project.

MAJOR URBAN SUBSIDENCE MAPPED BY DIFFERENTIAL SAR INTERFEROMETRY

Mark Haynes, Ren Capes

Nigel Press Associates, Crockham Park, Edenbridge, Kent TN8 6SR, UK
Phone: + 44 1732 865023, Fax: + 44 1732 866521, E-mail: info@npagroup.co.uk

Geoff Lawrence

TREIC°L, 46 Pondcroft Road, Knebworth, Hertfordshire SG3 6DB, UK
Phone: + 44 1438 813681, Fax: + 44 1438 816513, E-mail: geoff@treicol.demon.co.uk

Andy Smith

Phoenix Systems, 60 St. Albans Road, Kingston-upon-Thames, Surrey KT2 5HH, UK
Phone: + 44 181 5498878, Fax: + 44 181 5498878

David Shilston, Geoff Nicholls

WS Atkins Consultants Ltd, Woodcote Grove, Ashley Road, Epsom, Surrey KT18 5BW, UK
Phone: + 44 1372 726140, Fax: + 44 1372 740055

ABSTRACT

At NPA we have investigated a variety of ground displacement phenomena using our *CivInSAR* differential interferometric system, as part of our BNSC ADP2 programme. We report here a spectacular case of major urban subsidence, over a 100km^2 area, amounting to 78mm over almost 3 years. This has been validated by a GPS ground survey for which both the calculated displacements rates and overall trend are in close agreement with our interferometric results.

1. INTRODUCTION

The capability of differential SAR interferometry to map catastrophic ground movements such as earthquakes is now well established, having been demonstrated several times recently. Examples have included the events at Landers (California) in 1992, Kobe (Japan), as well as the 1995 Grevena (Greece) earthquake which the authors investigated [1]. Very often for these single, sudden events the temporal bracketing with a suitable interferometric pair of SAR images (given acceptable orbital criteria) can be optimised to a minimum since the time and date of occurrence are unique. However more subtle, long-term ground displacement events, such as subsidence and volcanic deformation present more of a challenge to this technique since the timeframes (on the scale of years for subsidence) often result in low coherence conditions which in turn degrade any interferometric results.

As part of our *Application Demonstrations Programme 2* with the British National Space Centre, we have investigated a variety of ground displacement phenomena world-wide, using our proprietary *CivInSAR* differential interferometric processing system at NPA. Most recently, and in spite of the above-mentioned obstacle, we succeeded in detecting and clearly mapping a major and ongoing urban subsidence event, stretching over a period of several years. However, due to the sensitive nature of these results at the time of writing, we have been bound to keep location details confidential, which means that some of the specifics in our data description and geology discussion have been withheld. Nevertheless this paper provides an otherwise detailed account of our investigation and results of this major ground displacement phenomenon.

2. SAR AND ANCILLARY DATA

Raw SAR scenes from the ERS-1 and ERS-2 platforms (descending orbits) were used in our interferometric processing, together with a 50m DEM of the area. The time span of the pairs ranges from almost 3 years down to a 25-hour, tandem pair. The pairs were selected with low perpendicular baseline (B_{perp}) values. Parameters are summarised in Table 1 overleaf.

After preliminary full-scene (100km × 100km) SAR processing, the region of interest was limited to approximately 16km × 12km. This area is mostly urban and completely encompasses a major city.

α	20.7	2 years 11 months
β	6.7	2 years 4 months
γ	41.8	7 months
δ	27.9	25 hours

Table 1. Temporal and perpendicular baseline parameters of 4 interferometric pairs.

3. INTERFEROMETRIC PROCESSING

The raw SAR format scenes were first processed to ground-range single-look-complex using a commercial SAR processing package (*PulSAR*), with pixel dimensions of 12.5m in range and 3.125m in azimuth (4:1 ratio). In doing so, the nominal orbit state vectors of each scene header were enhanced (and the orbits propagated) using the ESA/DLR precise state vector (PRC) data.

Due to the variation in coherence with time, degrees of pixel averaging were necessary during the interferogram generation process. The amount of averaging was raised for pairs with increasing temporal separations, and using a 1:4 averaging ratio, square cell interferograms were generated, ranging from 12.5m for the tandem pair (δ) to approximately 60m for the 2 year 11 months pair (α).

The differential interferometric approach we employed here is the 2-pass-plus-DEM technique, as opposed to the 3-pass approach. Our system imports the elevation and synthesises the phase due to topography to generate the differential phase image from the initial interferogram. Orthorectification and mapping into a suitable projection are in addition applied to this differential result.

The *CivInSAR* processing system also provides residual phase detrending tools which were employed for some pairs - resulting from orbital errors (despite the use of precise state vector data which has a 1m nominal radial accuracy). In addition, and as part of our subsequent analyses and visualisations, coherence maps are also generated with our system, however space does not permit reporting of these additional results and analyses.

Phase unwrapping and deformation map generation complete the process. These and other results and data can then be incorporated into our GIS/value-adding system which was described in our work on the Grevena earthquake [1].

4. RESULTS

The sequence of 4 differential interferograms is displayed in Figure 1. The rate of ground displacement is well illustrated by this sequence of increasing time separations. This ranges from zero movement in the (δ) tandem pair, to part of one fringe cycle in the (γ) 7-month pair, and strikingly to 3 distinct fringe cycles in the β and α pairs (2 years 4 months and 2 years 11 months respectively). For the β pair we estimated this downward movement at a maximum of 78mm over 2.33 years.

5. GROUND VALIDATION

The *CivInSAR* team is grateful to WS Atkins Consultants Ltd, a major civil engineering company who agreed to undertake a GPS ground survey through the region corresponding to our detected area of subsidence on the interferograms. Heights from benchmarks were surveyed at 7 GPS points along a physical path length of just over 8km in total. The survey points and path overlaid onto the fringe outlines are also illustrated in Figure 1. Recorded height differences were translated to a yearly rate using the number of years back to the previous known benchmark year. These yearly rates (with scaled tolerances) were then projected to the 2.33 years time frame of interferogram pair β for comparison. Table 2 lists these results, and the height profiles of the ground survey results are contrasted with the interferometrically-derived deformation map for pair β at the corresponding GPS stations in Figure 2.

6. GEOLOGICAL INTERPRETATION

Displacements of this magnitude mapped as distinctly as this have been recorded only for earthquake events, for example as we demonstrated over the Grevena earthquake in northern Greece. Slight seismic shocks are not unknown in this area (most associated with collapse of coal workings!) but these are rare slight shallow local events that dislodge chimney pots. Nothing has been recorded that would have produced this amount of displacement.

We do not have to look very far for a reason for this ground displacement. Subsidence over underground coal workings has long caused problems in the conurbation, although there is no complete survey of the hundreds of workings.

There is an unusually thick sequence of Coal Measures in the region, with 52 individual seams from 1cm to 3.5m thick occurring over 1100m of rock succession dipping gently beneath the conurbation in a deep trough.

By superimposing the fringe contours over the geology map of the area, we noted that 30 of the 52 coal seams occupy the fringe core. These seams trend north-northwest, exactly parallel to the strike of the core of fringe pattern. This "grain" is shared by the strike of the geological strata, the topography (there is a height range of 80m to 100m across the core of the fringes) and the trend of minor landslips, along steeper slopes where harder sandstone outcrop. These landslips, the largest about 1km long and 150m wide, are nowhere large enough or consistent enough to result in displacement adequate to yield a fringe.

The stacked coal seams reach the surface to the east of, and within, the core of the fringes. They dip westward, mostly consistently, at 10° to 20°, beneath the core of the fringes. The generalised sub-surface distribution of these seams in the geological section shows a coincidence of stacked seams and the fringes that is so strong that this is unambiguous, if circumstantial, evidence for subsidence of the coal workings.

There are an estimated 8000 disused shafts in this conurbation and at least 200 abandoned adits within the area defined by the fringe patterns. There are almost no active coal workings in the area and none whatsoever within the fringe core. There is a very close coincidence of the fringe contours and the outline of the areas of all underground coal workings and, displaced updip (that is to the east), the area of mine workings within 30m of the surface. Many of these workings are ancient and predate systematic survey and recording. As there are only piecemeal survey of these workings, sudden unexpected collapse over mining voids or over areas where the pillars of the old seams, or the mouths of shafts collapse, are a feature of the whole conurbation.

What we have here is subsidence at relatively shallow depths, probably no more than 100m and maybe no more than 30m depth. Extensive underground shafts, "bell-pits", adits and workings, many by pillar and stall (in which pillars of coal are left standing, usually on a rectangular grid to support the workings) underlie the whole conurbation. Mining has been almost totally abandoned, and collapse of roof supports and pillars in particular, and seasonal water logging is causing subsidence.

7. CONCLUSION

Using our *CivInSAR* interferometric processing system, we have demonstrated our capability to detect, monitor and quantify subtle ground displacement events over a period of years and across a wide physical area. The demonstration reported here was a recent case of major urban subsidence. We were able to both replicate interferometrically this phenomenon and have had our results validated by an independent GPS ground survey team.

8. ACKNOWLEDGMENTS

We gratefully acknowledge the technical support of the UK Defence Evaluation and Research Agency (DERA), who are a partner in the *CivInSAR* programme.

9. REFERENCES

[1] Capes, R., Haynes, M., Lawrence, G., Smith, A., Muller, J-P., Parsons, B., England, P., Clarke, P. 1996 *CivInSAR Quake Assessment: An integration of differential SAR interferometry into a GIS to assist in earthquake risk management*, FRINGE 96, ESA Workshop on Applications of ERS SAR Interferometry, Sept/Oct 1996, Zurich

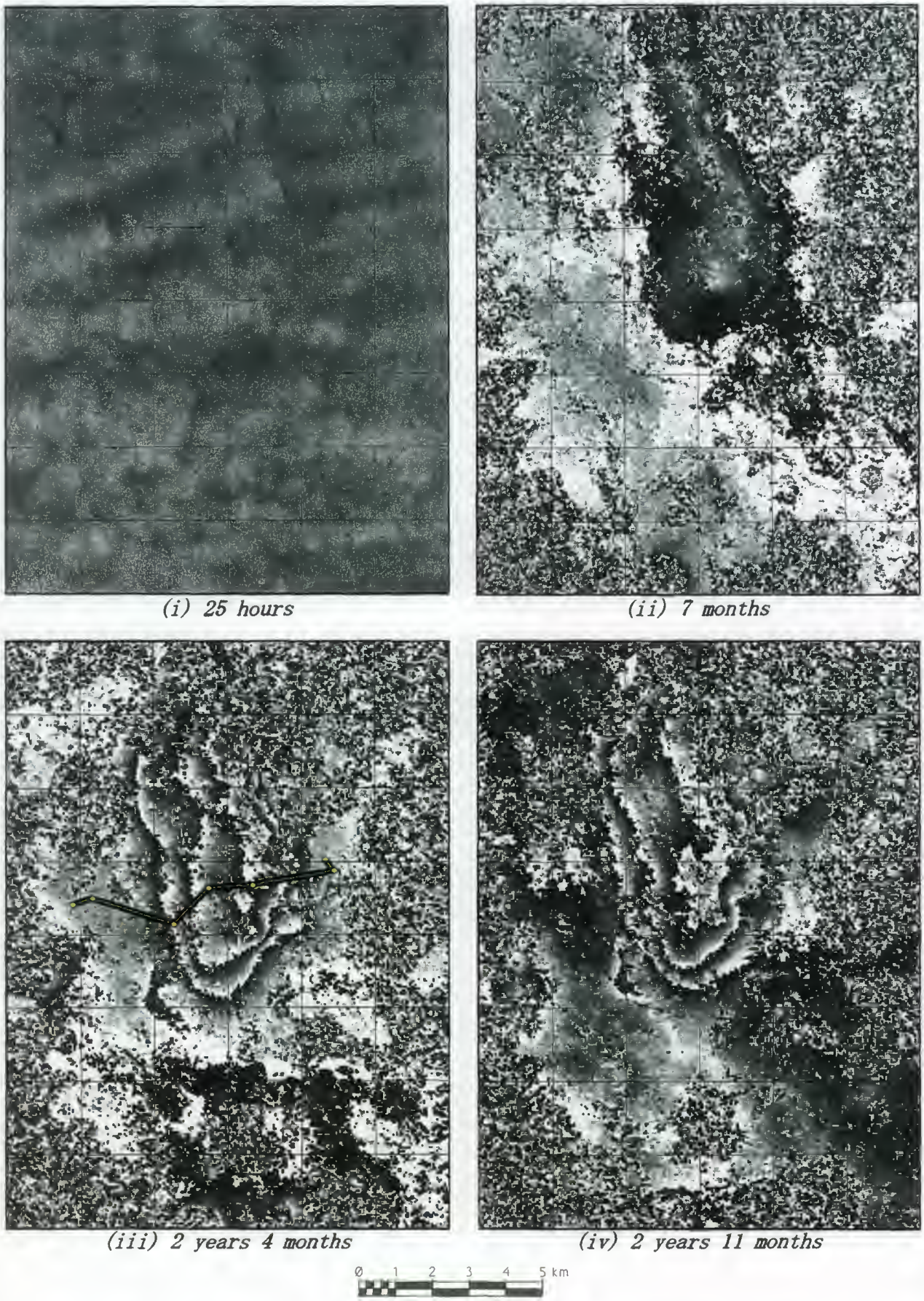

Figure 1. Sequence of differential interferograms with increasing temporal baselines over subsidence region. Interferogram (iii) includes GPS ground survey path described in Section 5.

GPS Station Reference Number	GPS Movement since previous recorded benchmark year (mm)	GPS Movement/year (mm)	GPS Movement over 2.33 year interferogram span	Movement at corresponding location in 2.33 year interferogram deformation map (mm)
10	0.0 ± 30	0.0 ± 2.4	0.0 ± 5.6	-4.9
11	+61.0 ± 30	+2.0 ± 1.0	+4.7 ± 2.3	-3.8
12	-62.0 ± 30	-2.0 ± 1.0	-4.7 ± 2.3	-32.6
13	-451.0 ± 30	-15.0 ± 1.0	-35.0 ± 2.3	-72.0
14	-983.0 ± 30	-32.0 ± 1.0	-75.7 ± 2.3	-78.1
15	-100.0 ± 30	-8.0 ± 2.4	-18.7 ± 5.6	-26.3
16	-115.0 ± 30	-9.0 ± 2.4	-21.0 ± 5.6	-26.0

Table 2. Comparison of GPS heights survey (with tolerances) scaled to interferogram time span and interferometrically derived displacements at corresponding locations ('-'sign indicates downward displacement).

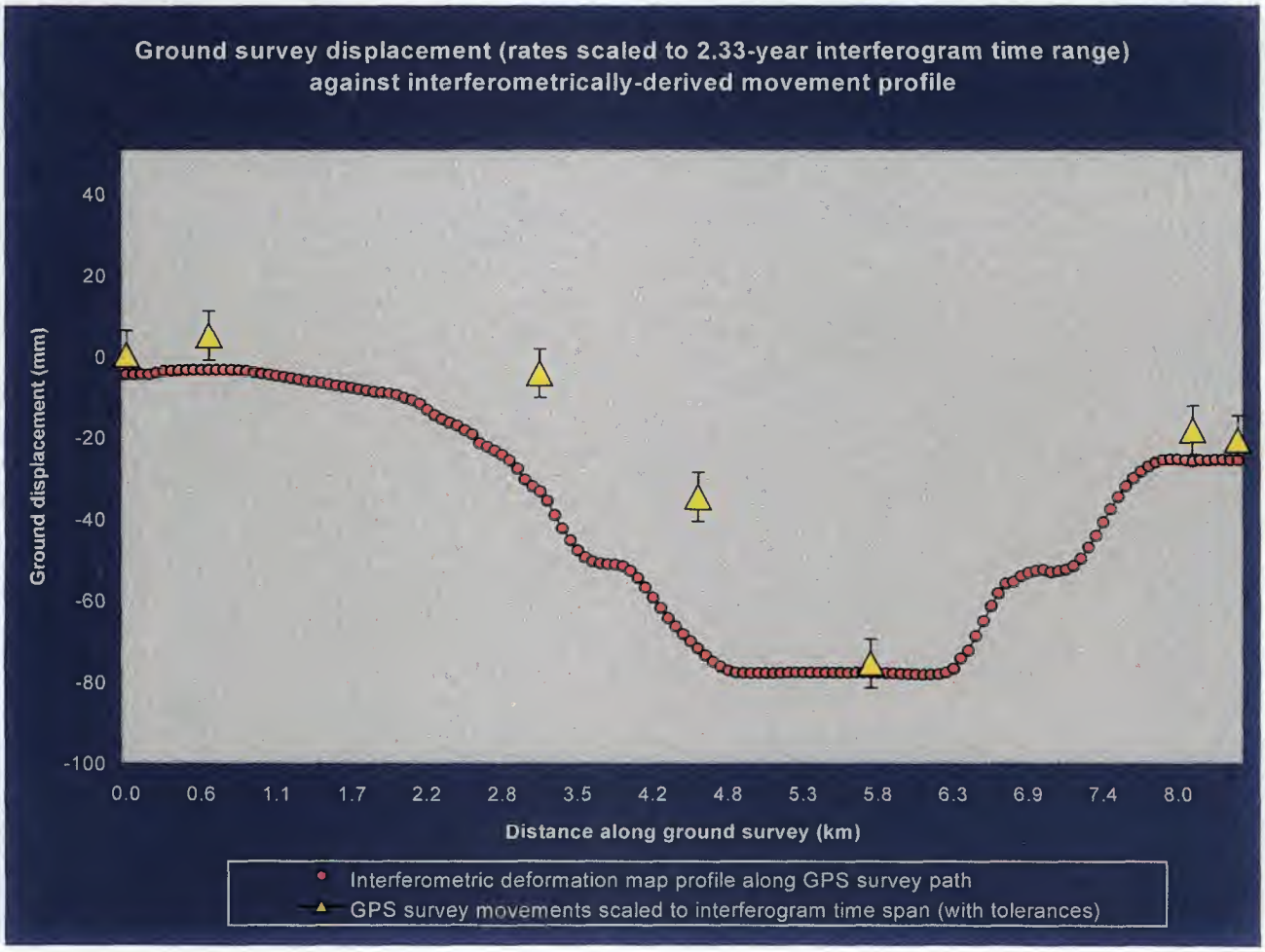

Figure 2. Comparison of subsidence values from GPS survey and interferometric deformation map

RECENT TECTONIC EVIDENCED BY SAR INTERFEROMETRY IN THE EAST AFRICAN RIFT. ESA PROJECT AOL.B201

François Kervyn

Royal Museum for Central Africa
13, Leuvensesteenweg, 3080 Tervuren, Belgium.
Phone: 32-2-769 54 20, fax: 32-2-769 54 32
E-mail: geoldept@africamuseum.be

ABSTRACT

SAR interferometry and related tools open new possibilities for geological applications in regions where field access is limited. Production of interferometric DEM with good vertical resolution offers facilities for geomorphologic interpretations. We are using such DEMs for the study of the Rukwa rift situated between the Tanganyika and Malawi tectonic troughs which is showing both highly pronounced and subtle tectonic features that the interferometry technique can evidence.
The Rukwa rift is a deep NW-SE trending sedimentary basin where both normal and strike-slip movements are recorded in the recent times. Field experience has demonstrated the support of such DEMs for slight topographic features identification which are not visible on existing topographic maps.
This work is taking place within a more global and pluridisciplinary study of that part of the East African rift.

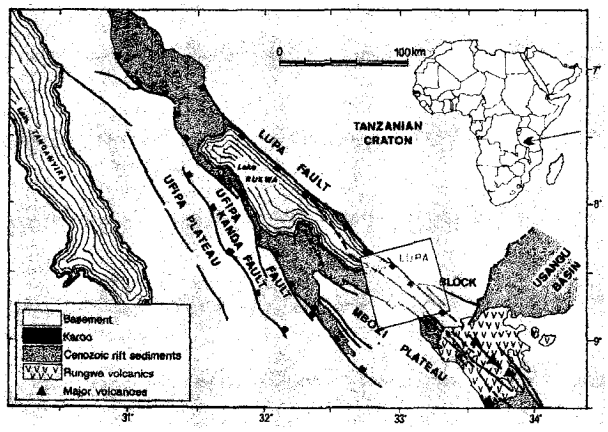

Figure 1: Tectonic sketch map of the Rukwa Trough. Investigated zone is highlighted. (Adapted from Delvaux et al. [1])

1. INTRODUCTION

In the frame of the ESA project AOL.B201, ERS1 & ERS2 scenes have been acquired over three zones of the investigated area (fig. 1.). The first selected zone was the South-Eastern part of the Rukwa basin because of its easiest access for field check, its important coverage of external informations (seismic profiles, coring, ...), and of course because of its higher geological interest.

The scenes were first processed in order to compute the interferogram (fig. 2) which was unwrapped and gives a DEM in the slant range projection. In the mean time, the corresponding topographic map at the 1/50.000 scale were digitized and a map DEM (DEM_m) was created (fig. 3a).
DEM_m allowed the geocoding operation via the tie points collection between a simulated SAR and the real one. Once geocoded, the DEM_i is calibrated in meters by reffering to the DEM_m. After this « preparation» phase, the DEMs can be processed and compared.
Two different approaches are applied here for the tectonic analyse of the DEMs: drainage computation and hill shading. Both methods are showing that DEM_i has a higher vertical resolution than DEM_m and allows to increase the amount of valuable information specially in the flat areas.

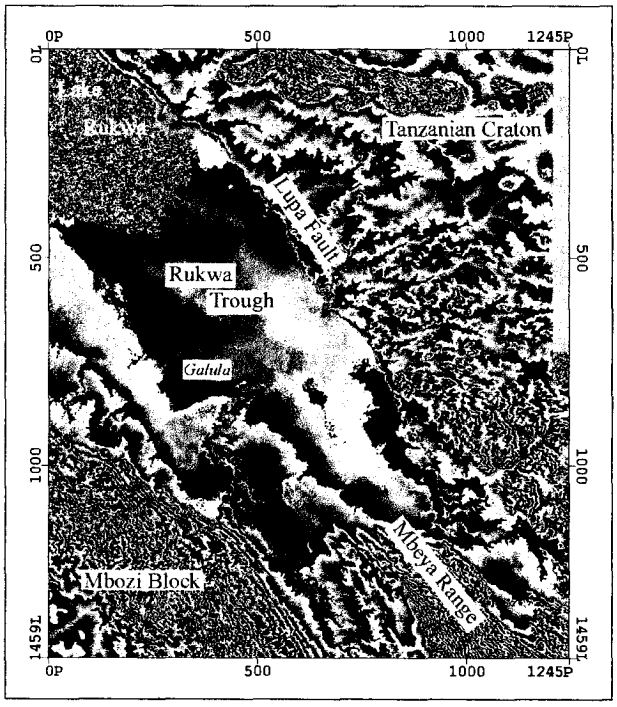

Figure 2: Interferogram in slant range projection computed with the ERS1 & ERS2 scenes acquired on 4th and 5th December 1995.

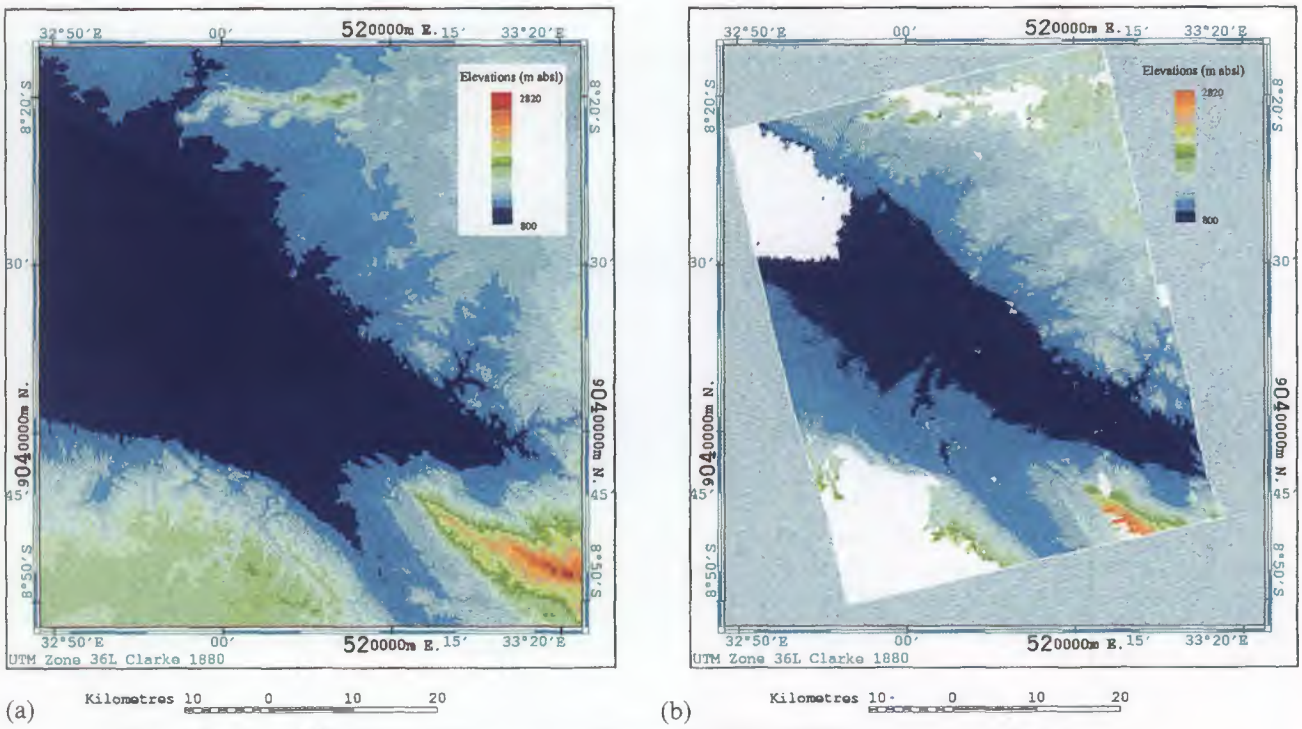

Figure 3: Digital Elevation Models: a) Interferometric DEM (DEM_i) computed after phase unwrapping of the corresponding interferogram and geocoded via control points collection on a simulated SAR image created with DEM_m; after zoning, the unvaluable zones are left in blank. b) computed from the 1/50.000 scale topographic maps (DEM_m) with a 20m contour interval.

SOURCES

ERS data involved in this paper (orbits: ERS1 22947, ERS2 3274, frame 7011) were acquired on December 4th and 5th 1995, at the end of the dry season. The available topographic maps are at the scale of 1/50.000 and all the 20m contour lines have been digitized. These numeric data were then interpolated using a minimum curvature method for the DEM_m computation.

2. DATA PROCESSING

The interferometric process of both SAR images was performed with the software developped at the CSL (Centre Spatial de Liège - Belgium).
Baseline and altitude of ambiguity are respectively 177m and 64m resulting in a good quality interferogram especially in the flat area i.e. in the recent sedimentary deposits of the lake. Around the basin however, due to the higher relief, shadowing is affecting the coherence and complicates the phase unwrapping. Consequently the resulting DEM_i contains several zones with independent phase unwrapping.

3. METHODOLOGY

3.1 Geocoding of the interferometric DEM

One of the major problems of SAR is the conversion from slant range to ground range projection. Depending on the imaged area, deformation is stronger where relief is important. In this case geocoding was performed by collecting control points between a simulated SAR image and the real SAR image. A simulated SAR scene is computed from the orbital parameters and the DEM_m elevation data. Fourty points almost uniformly distributed have been identified and allowed the geocoding of both SAR scenes and of course all related interferometric products (coherence map, DEM_i, ...).
At this stage DEM_i and DEM_m are superimposable and therefore allow any further comparisons.

3.2. Zoning and calibration of the interferometric DEM.

Depending on the DEM_i quality, certain values need to be rejected; it is the case for example for the low coherence zones involving a loss of reliable elevation data. A zoning operation is then performed by isolating the unvaluable or incompatible areas. By selection of corresponding valuable zone on DEM_m, one can define
the relevant elevation values and therefore re-scale the DEM_i between the proper bounds (fig.3b).
Since we are interested in the recent and present day tectonic, the zone chosen for this study is of course the one containing the flat area with the young lacustrine sediments.

3.3. Drainage computation

The technique used in this work for drainage computation is the one described by S.Jenson and J.Domingue (1988).

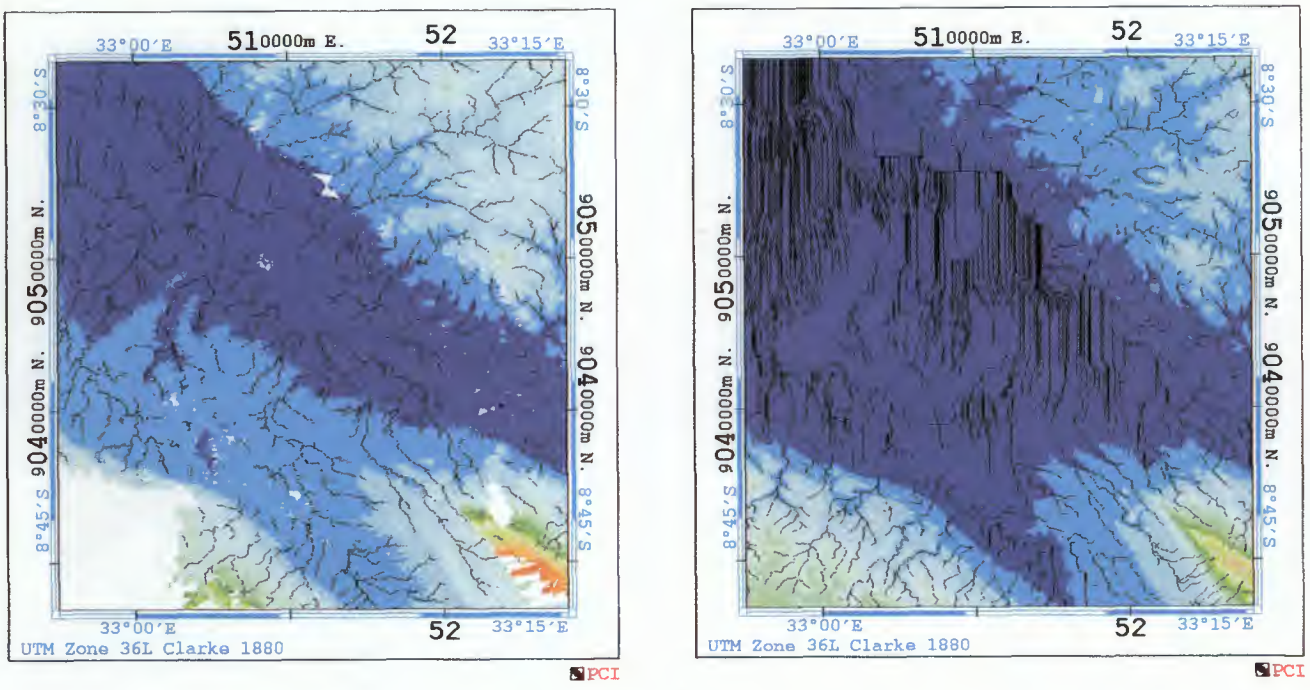

(a) (b)

Figure 4: Drainage computed from the two DEMs. In the high relief regions, one can observe a high level of similitude between DEM_i (a) and DEM_m (b). In the region where the relief is less pronounced, drainage is highly corrupted by the lack of topographic information while the DEM_m was interpolated.

They propose an iterative spatial technique leading to the extraction of the morphological features from DEMs and specifically topographic depressions and flow directions.These are conducting to further process such as delineation of watershed or overland flow paths.

The calculations involve a « conditionning phase » providing three data sets that are to be used in the next process steps.

Firstly, a DEM where depressions have been filled; then a data set indicating the flow direction for each cell; and finally, a flow accumulation data set where each cell receives a value equal to the total amount that drain to it.

From the drainage network computation, it appears that an important amount of information is brought trough the interferometric method by comparison with the map based DEM_m (fig.4a).

Drainage computed in the region of high relief shows a high level of similitude but an inhomogeneous offset is observed and is attributed to the geocoding inaccuracy.

Where the relief is less pronounced, the difference increases and the drainage of the DEM_m is highly corrupted by the lack of topographic information while the DEM_m was interpolated (fig.4b).

Drainage computed from the DEM_i may be incomplete or inaccurate in some places, but is mostly in agreement with our field knowledge and the tectonic setting of the region.

3.4. Shaded relief

Subtle topographic features in the recent sediments of lake Rukwa appear thanks to the shaded relief operation. One can observe a curved lineament parallel to the major Lupa border normal fault extending towards the SE and the tanzanian craton. Another and even more visible lineament is continuing north-westwards the Mbeya Range strike-slip fault. These structures are likely to belong to the same family than the faults recorded by micro seismic prospection on the lake. The two lineaments are meeting near the Galula village and seems to be affected by a SW-NE oriented structure extending in the craton (fig.5).

4. DISCUSSION

Occurrence of important tectonic structures in the today sediments as this analyse and related field work suggest, could provide high value information for further interpretation of the basin evolution.

The geological interpretation of the lineaments evidenced in the lacustrine sediments via SAR interferometry suggests that they are likely to correspond to the strike-slip movement of the Mbeya Range. This hypothesis is also supported by the seismic profiling managed on the lake (De Batist *et al.* 1996), and by field observations.

The curvilinear lineament might be explained with a perpendicular movement according to a SW-NE

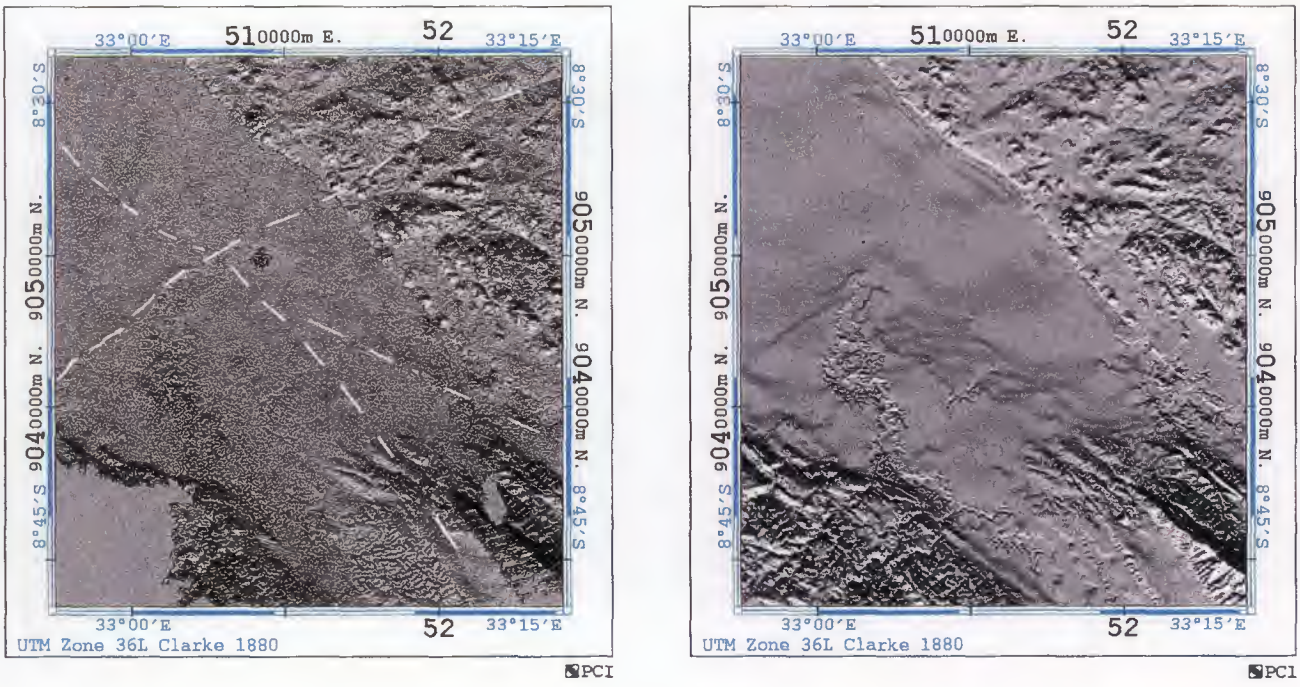

(a) (b)

Figure 5: Shaded relief operation lead on DEM_i (a) evidences subtle linear and curvilinear structures in the Rukwa Trough. SE-NW oriented structures may be affected by perpendicular one. Shaded DEM_m shows only the major features (b).

direction along a linear structure crossing the curved lineament in the neighbourhood of the Galula village. Actually, this structure extending within the craton and clearly visible on the imagery seems also to be responsible for the deviation of the Songwe river flow path.

5. CONCLUSION

In conclusion, the elevation model provided by SAR interferometry (DEM_i) has a higher vertical resolution than the elevation model computed from the topographic maps (DEM_m). DEM_i allowed to identify subtle topographic features in the Rukwa sedimentary plain that are invisible in DEM_m. Two different tools have been applied to both DEMs to demonstrate the existence of these topographic steps: drainage computation and hill shading. Field observations where access allows it has confirmed the occurrence of such features; but even if they are in agreement with the general geological setting, their relation with tectonic is still to be established.

The study will now be extended to the other set of SAR data available for this region in order to guide next field campaigns.

6. REFERENCES

De Batist, M.; Versteeg, W.; Vanhauwaert, P.; Van Cauwenberghe, T.; Broone, C.; Kilembe, E.; Kajara, R.. High resolution reflection seismic investigation of Lake Rukwa, *in Rukwa Project. Investigation of the sediments of Lake Rukwa (Tanzania): A clue for reconstructing the South equatorial climate during the last 130,000 years. EEC, DG XII: Programme Environnement; Area I: Global Change. I.1 Natural Climatic Change. 1994-1996.*

Delvaux,D.; Kervyn,F.; Vittori, E.; Kajara, R.S.A.; Kilembe, E. Late Quaternary tectonic activity and lake, level change in the Rukwa Rift Basin.. Submitted to *Journal of African Earth Sciences, march 1997.* [1]

Delvaux, D.; Levi,K.; Kajara, R.S.A.; Sarota, J. 1992, Cenozoic paleostress and kinematic evolution of the Rukwa - North Malawi rift valley (East-African rift system). *Elf Aquitaine production, BCREDP 16.* [2]

Jenson, S.K., Domingue,J.O. 1988, Extracting topographic structure from digital elevation data for geographic information system analysis. *Photogrammetric Engineering and Remote Sensing, vol. LIV, 11.*

Vittori, E.; Delvaux, D.; Kervyn, F. Kanda Fault: a major seismogenic element west of the Rukwa rift (East Africa, Tanzania). *Journal of Geodynamic, in press.*

European Space Agency
Agence spatiale européenne

Contact: ESA Publications Division
c/o ESTEC, PO Box 299, 2200 AG Noordwijk, The Netherlands
Tel (31) 71 565 3400 - Fax (31) 71 565 5433